LIGHTWEIGHTING MATERIALS

VEHICLE TECHNOLOGIES PROGRAM

Less dependence on foreign oil today, and transition to a petroleum-free, emissions-free vehicle tomorrow.

2007

annual progress report

U.S. Department of Energy
Energy Efficiency and Renewable Energy
Bringing you a prosperous future where energy is clean, abundant, reliable, and affordable

U.S. Department of Energy
Office of Vehicle Technologies
1000 Independence Avenue S.W.
Washington, D.C. 20585-0121

FY 2007

Progress Report for Lightweighting Materials

Energy Efficiency and Renewable Energy
Office of Vehicle Technologies

Patrick Davis
Acting Program Manager, Office of Vehicle Technologies

Rogelio Sullivan
Advanced Materials Technologies Team Leader

Joseph Carpenter
Technology Area Development Manager

December 2008

CONTENTS

1. INTRODUCTION 1

2. AUTOMOTIVE METALS – WROUGHT 7

A. Thermo-Mechanical Processing Design for Lightweight Materials 7
B. Development of High-Volume Warm Forming of Low-Cost Magnesium Sheet 29
C. Die Face Engineering Project for Advanced Sheet Metal Forming 36
D. Electromagnetic Forming of Aluminum Sheet 42
E. Ultra-fine Grained Foils and Sheets by Large Strain Machinging Processes 47
F. Aluminum Automotive Closure Panel Corrosion Test Program 49

3. AUTOMOTIVE METALS – CAST 59

A. Improved Automotive Suspension Components Cast with B206 Alloy 59
B. Magnesium Powertrain Cast Components 68
C. Ultra-Large Castings of Aluminum and Magnesium 76
D. High Integrity Magnesium Automotive Castings (HI-MAC) 85
E. Casting/Solidification of Magnesium Alloys 89

4. AUTOMOTIVE METALS – TITANIUM 101

A. Low-Cost Titanium Powder for Feedstock 101
B. Production of Heavy Vehicle Components from Low-Cost Titanium Powder 110
C. Powder-Metal Performance Modeling of Automotive Components 116
D. Examining Fundamental Mechanisms of Tooling Wear for Powder Processing 127

5. AUTOMOTIVE METALS – STEEL 133

A. NSF Funding for the Development of 3rd Generation Advanced High-Strength Steels 133
B. High-Strength Steel Joining Technologies 136
C. Hydroform Materials and Lubricants 144
D. Sheet-Steel Fatigue Characteristics 151
E. Tribology 159
F. High-Strength Steel Stamping 161
G. Strain-Rate Characterization 168
H. High Strain-Rate Deformation of Steel Structures 174
I. Future Generation Passenger Compartment - Validation 179
J. Lightweight Rear Chassis Structure 184
K. Characterization of Thermo-Mechanical Behaviors of Advanced High-Strength Steels (AHSS): Formability, Weldability and Performance Evaluations of AHSS Parts for Automotive Structures 190
L. Characterization of Thermo-Mechanical Behaviors of Advanced High Strength Steels (AHSS): Weldability and Performance Evaluations of AHSS Parts for Automotive Structures 197

M. Materials Design for Steel Alloys 209

6. AUTOMOTIVE METALS – CROSS-CUTTING 221

A. Magnesium Research and Technology Development 221
B. Magnesium Front-End Design and Development 224
C. Magnesium Front-End Research and Development 231
D. Self-healing Coating Systems for Corrosion Control of Magnesium Alloys 239
E. Ferrate Conversion Coating for Corrosion Protection of High-Temperature Die-Cast Magnesium Alloys 245
F. Integrated Computational Materials Engineering 251
G. Simulation-Based Design Optimization 257
H. Fatigue of Lightweight Automotive Materials 272
I. Materials Design for Magnesium Alloys 282
J. Multiscale Microstructure-Property Plasticity Considering Uncertainty 301
K. Cyberinfrastructure 323

7. LOW-COST CARBON FIBER 339

A. Low-Cost Carbon Fiber from Renewable Resources 339
B. Improved Lignin Purification/Recovery Process for Carbon-Fiber Applications 352
C. Advanced Stabilization of PAN Fiber Precursor 357
D. Advanced Oxidation of PAN Fiber Precursor 365
E. Carbon-Fiber Systems Integration 370

8. POLYMER COMPOSITES R&D 377

A. Automotive Composites Consortium Focal Project 4 377
B. Development of Manufacturing Methods for Fiber Preforms 391
C. Development of Next-Generation Programmable Preforming Process 398
D. Low-Cost Carbon Fiber Composites for Lightweight Vehicle Parts 408
E. High-Volume Processing of Composites 417
F. Natural-Fiber Composite Retting, Preform, Manufacture, and Molding 422
G. Natural-Fiber Composites for Structural Component Design 431
H. Interphase Analysis and Control in Fiber-Reinforced Thermoplastic Composites 463
I. Composite Crash Energy Management 482
J. Engineering Property Prediction Tools for Tailored Polymer Composite Structures 493
K. Predictive Modeling of the Structure and Properties of Polymer-Matrix Composites: NSF/DOE Grant Projects 505
L. Structural Nanocomposite Design 516

9. JOINING 525

A. Forming Limits of Weld Metal in Aluminum Alloys and Advanced High-Strength Steels 525
B. Impact Modeling and Characterization of Spot Welds 531
C. Friction-Stir Spot Welding of Advanced High-Strength Steels 539
D. Thermal-Drilling Application Development 545
E. Weld Element and Joining-Process Technology Development 550

10. NONDESTRUCTIVE EVALUATION 561

A. Nondestructive Evaluation (NDE) Inspection of Resistance Spot Welds in Automotive Structures Using an Ultrasonic Phased Array 561
B. Nondestructive Inspection of Adhesive Metal/Metal Bonds 572
C. Laser-Utrasonic Inspection of Adhesive Bonds Used In Automotive Body Assembly 580
D. In-Line Resistance Spot Welding (RSW) Evaluation System for Lightweight Materials 585

11. RECYCLING 593

A. Recycling Assessments and Planning 593
B. Baseline Assessment of Recycling Systems and Technology 600
C. Development of Technology for Removal of PCBs and Other Substances of Concern (SOCs) from Shredder Residue 608
D. Compatibilization/Compounding Evaluation of Recovered Polymers 615
E. Post-Shred Materials-Recovery Technology Development 624
F. Development of High-Speed Multispectral Imaging for Sorting Automotive Plastics 634
G. Microwave Assisted Gasification for Recycling Polymer Matrix Composites 638

12. MATERIALS CROSS-CUTTING R&D 647

A. Technical Cost Modeling 647
B. Intermediate-Rate Crush Response of Crash Energy Management Structures 651
C. High-Rate Damage and Fracture, Experimentation, Simulation and Visualization 657
D. Multi-Materials Vehicle (MMV) Research and Development (R&D) Initiative 666
E. Mission Eggcellence – K-12 Outreach Program 671

APPENDIX A: ACRONYMS AND ABBREVIATIONS 679

1. INTRODUCTION

Automotive Lightweighting Materials R&D

As a major component of the U.S. Department of Energy's (DOE's) FreedomCAR and Vehicle Technolgies (FCVT) Program, Lightweighting Materials (LM) focuses on the development and validation of advanced materials and manufacturing technologies to significantly reduce automotive passenger-vehicle body and chassis weight without compromising other attributes such as safety, performance, recyclability, and cost.

Increased fuel economy is the most obvious effect of lighweighting. This term is used instead of "lightweight" so as not to imply just the use of lower-density materials. Steel, for instance, is not a low-density material, but by increasing its strength, less can be used for net weight reduction. It has been estimated that with every 10% drop in weight, the fuel economy increases 6–8% (with mass compounding and everything else the same). Mass compounding means that, in addition to the fuel economy increase due to the direct loss of weight by the given component or structure, other mass may be shed elsewhere in other vehicle components or structures such as the powertrain, the suspension and the braking.

In addition, lightweighting offsets the increased weight of features (e.g., audio, video and navigation systems), vehicle upsizing and performance (e.g., acceleration, safety, exhaust-gas pollution abatement) demanded by the customer or mandated by regulations. This has been the primary use of lightweighting in the recent past. In the future, lighweighting will be needed to offset the added weight and cost per unit of power of hybrid and fuel-cell powertrains.

The specific goals of LM are to develop material and manufacturing technologies by 2010 that, if implemented in high volume, could cost-effectively reduce the weight of passenger-vehicle body and chassis systems by 50% with safety, performance, and recyclability comparable to 2002 vehicles.

LM is pursuing five areas of research: cost reduction, manufacturability, design data and test methodologies, joining, and recycling and repair. The current long-range plan for activities in these areas is found at www.eere.energy.gov. Because the single greatest barrier to the use of lightweight materials is cost, priority is given to activities aimed at reducing costs through development of new materials, forming technologies, and manufacturing processes. Priority lightweighting materials include advanced high-strength steels (AHSSs), aluminum (Al), magnesium (Mg), titanium (Ti), and composites including metal-matrix materials and glass-, natural-, and carbon-fiber-reinforced thermosets and thermoplastics. The inclusion of AHSSs is an example, explaining the term "lightweighting," as opposed to "lightweight," in order not to imply focus on only lower density materials.

Collaboration and Cooperation

LM coordinates, cooperates and even collaborates extensively to identify, select and conduct its research and development (R&D) activities with others. The primary interfaces have been and still are with entities of Chrysler, Ford, and General Motors, namely, the FreedomCAR Materials

Technical Team (MTT), the Automotive Composites Consortium (ACC), the United States Automotive Materials Partnership (USAMP) and the Vehicle Recycling Partnership (VRP). These are the main means for determining critical needs, identifying technical barriers, prioritizing, assessing and selecting projects. Other important U.S. partners include the Auto/Steel Partnership (A/SP) of the American Iron and Steel Institute (AISI), the Plastics Division (formerly the American Plastics Council - APC) of the American Chemistry Council (ACC-PD), the American Foundry Society (AFS) and the North American Die Casting Association (NADCA). LM closely coordinates some of its R&D activities with those of Natural Resources Canada's (NRCan's) CANMET Materials Technology Laboratory due to common interests in automotive lightweighting in North America. Contacts with similar efforts in other countries are maintained. A major thrust in magnesium was initiated in fiscal year (FY) 2007 with CANMET and the China Magnesium Center of the Chinese Ministry of Science and Technology (MOST); see 6.A-C. Six projects at six universities are jointly funded with the U.S. National Science Foundation (NSF); see 8.L. Eight new projects, also jointly funded with the NSF and the A/SP, in the AHSS area were started in FY 2007; see 5.A. Another project at a university (see 8.I) is jointly funded with DOE's Office of Science. Sixteen projects (see 2.A, 3.E, 4.B and E, 5.M, 6.G-K, 8.H and M, 9.E, and 12.C and E) at the Mississippi State University (MSST), funded under a Congressional mandate, are coordinated with the mainstream LM activities. Five projects (6.D and E, 8.D, 10.C and 11.F and G) are funded under the DOE Small Business Innovation Research and Small Business Technology Transfer (SBIR/STTR) program.

Research areas and responsible organizations

Coordinated area	Organization
Fabrication of Mg	NRCan
Recycling and reuse of automotive parts and materials	Vehicle Recycling Partnership, Plastics Division of the American Chemistry Council (ACC-PD)
Fabrication of steel	American Iron and Steel Institute, the Auto/Steel Partnership
Fundamental materials and manufacturing research	National Science Foundation (NSF)
Production and fabrication of composites	ACC-PD

Projects Development and Selection

In cooperation with the USAMP and the MTT, a procedure has been established to help facilitate the development of projects. The LM has only rarely done open solicitations of projects. Most projects are usually developed by informal contacts with original equipment manufacturers (OEM) and/or national lab researchers and are brought forth for consideration, assessed and selected on the bases of recommendations of either the USAMP or the MTT. The LM, however, retains final say as to what is funded. This flexibility allows the LM to select the most appropriate partners to perform critical tasks that have optimal chances of migrating to OEMs or suppliers as application-engineering projects and eventually being implemented in production vehicles.

Once selected, R&D projects are pursued through a variety of funding mechanisms, including cooperative research and development agreements (CRADAs), cooperative agreements (CAs), university grants, R&D subcontracts, and directed research. Those developed through the USAMP CA are usually cost-shared equally (dollar-for-dollar) with the LM funds by the USAMP or other non-Federal sources, either in cash or in-kind. No LM funds are paid to the USAMP. Those projects developed through the MTT are usually performed at national laboratories and universities and not cost-shared.

Laboratories currently involved include Argonne National Laboratory (ANL), Oak Ridge National Laboratory (ORNL), Pacific Northwest National Laboratory (PNNL), and Sandia National Laboratories (SNL). ANL oversees the LM's recycling efforts (see 11A-E) and ORNL provides overall technical support and coordination, including for the CA with USAMP. The National Energy Technology Laboratory (NETL) provides external projects management including the CA with the USAMP and the NSF jointly-funded projects. ORNL and NETL monitor the MSST projects.

R&D projects are assigned to one of three phases as depicted in the figure and defined below: concept feasibility, technical feasibility, and demonstrated feasibility. Projects are guided to meet the requirements of each phase before they move on to the next phase. Not all projects must go through these phases under LM funding; some may enter the technical or demonstrated feasibility stages from efforts funded elsewhere.

Typical phases/stages of projects

Concept Feasibility: Concept-feasibility projects focus on a specific idea to address a need or to create something new. Projects are usually exploratory and small in monetary requirements and time, typically less than $200,000 total over 1–2 years, to provide a yes/no answer to the value of the idea. All projects are required to have a detailed research plan, budget, and timing. They can be ended before proceeding to technical feasibility if there is a lack of technical progress or if the preliminary business case turns out to be unfavorable. The SBIR-STTR Phase I projects are of this nature as well.

Technical Feasibility: Technical-feasibility projects typically continue R&D for ideas with proven concept-feasibility merit or potential. These projects should identify the key barriers to implementing the technology and focus on overcoming them. Technical-feasibility projects should have well-defined, industrial OEM and/or supplier participation and pull. They are usually larger and longer term than the concept feasibility projects with typical investment in the $1M to $2M (or more) range and length of 2–3 years (or more). Technical-feasibility projects can be ended before proceeding to demonstrated feasibility if there is a failure to overcome the key barriers to

implementation or if the cost or business case does not develop as favorably as initially assessed. SBIR-STTR Phase II projects fit this paradigm.

Demonstrated Feasibility: Technology projects that need larger-scale validation may become demonstrated-feasibility projects. Not all technical-feasibility projects will need a demonstration or validation phase. These projects are few in number, much larger in scale, and may involve component or system fabrication and tests. Support and leverage from the industrial OEMs and/or suppliers is a key requirement.

FY 2007 Accomplishments

The High-Integrity Magnesium Automotive Castings (HI-MAC) project (see 3.D) is developing the metal-casting-process technologies necessary to cost-effectively manufacture high-integrity, cast Mg automotive-chassis components exhibiting high ductility and strength, low porosity, and which are free of objectionable oxides and inclusions. This project is developing the capability to cast Mg structural components based on existing Al low-pressure permanent-mold and squeeze casting processes. During this fiscal year, Mg control arms were produced from two of the Mg casting processes and will be provided for static and vehicle testing. The low-pressure die-casting machine and the Mg control arm produced therein are shown in Figures 1 and 2, respectively.

In addition, two new and emerging casting processes, ablation and T Mag, are also being investigated for potential use in casting structural Mg components. The use of controlled, molten-metal transfer and filling by an electromagnetic pump is being implemented to eliminate many of the production and environmental issues associated with the standard cover gas over Mg melts and yield higher-quality castings. Success in this project will result in increased production of Mg components requiring geometries and properties not possible with conventional high-pressure die-casting process limitations.

Figure 1. CMI Equipment and Engineering low-pressure casting cell.

Figure 2. Low-pressure, permanent-mold cast Mg control arm.

In the High-Volume Processing of Composites project (ACC 115, see 8.F), a measurement system was developed to objectively quantify the severity of bondline read-through (BLRT) in a way that correlates to visual assessment. BLRT is a visual defect that can occur where adhesive is used to bond a reinforcement to a Class "A" exterior panel and has been a deterrent to using composites because the "solution" is often to increase gage thus thwarting achievement of the theoretical weight savings available from carbon-fiber sheet-molding compound (SMC).

The Recycling End-of-Life Vehicles (ELVs) thrust (see 8.A-E) made significant progress during FY2007. The importance is that recovery and reuse of polymers and materials from ELVs will increase materials supply options and decrease costs for automakers and decrease the carbon footprint of lightweighting materials over the product life-cycle. The thrust developed and demonstrated effective recovery of high-quality polyolefins (at greater than 90% yield) from shredder residue, developed process conditions for selective recovery of acrylonitrile-butadiene-styrene (ABS), polystyrene (PS) and polycarbonate (PC) from shredder residue, and confirmed the technical feasibility of converting ELV shredder residue to fuels and chemicals. Commercialization of some of these processes is expected in the near future.

This thrust is conducted by a team consisting of personnel from ANL, the VRP, and the ACC-PD under a CRADA. The team received the Society of Plastics Engineers (SPE), Environmental Division Global Plastics Environmental Conference (GPEC) award in 2007 for "Enabling Technologies and Processes" in recognition of the team's contribution to development of ELV recycling technology.

The Low-Cost Carbon Fiber from Renewable Resources project (see 7.A) demonstrated that solvent-extracted, purified hardwood lignin can be continuously melt-spun into fiber form. This is a significant milestone in the search for low-cost carbon fiber.

The USAMP nondestructive Evaluation (NDE) Steering Committee issued a report entitled "Strategic Plan for Nondestructive Evaluation Development in the North American Automotive Industry" calling for increased development and application of NDE tools in the automotive industry to reduce waste, save money and energy, and help accelerate the introduction of new materials, processes, and vehicle technologies. The report looks at the expanding role of NDE in automotive production; identifies emerging challenges and prescribes a path to greater NDE development. The document represents a consensus between researchers at the U.S. Department of Energy (DOE) and the domestic automotive industry in suggesting that greater NDE use would also advance energy and environmental goals while improving production efficiency and reducing waste.

The Magnesium Front End (MFE) thrust (see 6.A-C and 6.F), the projects at MSST and the eight under NSF Funding for the Development of 3rd Generation Advanced High Strength Steels (see 5.A) began in FY 2007. MFE is a joint Canadian, Chinese, and U.S. effort aimed at development of automotive Mg technologies and, as such, may be the first of its kind. Other new starts included Ultra-fine Grained Foils and Sheets by Large Strain Machining Processes (see 2.E), Self-healing Coating Systems for Corrosion Control of Magnesium Alloys (see 6.D), Ferrate Conversion Coating for Corrosion Protection of High-Temperature Diecast Magnesium Alloys (see 6.E), and Development of High-Speed Multispectral Imaging for Sorting Automotive Plastics (see 11.F); the latter three short-term, SBIR-STTR projects were one-year projects and were thus also completed in FY 2007.

Besides the three short-term, SBIR-STTR projects, other projects that were completed included the Die-face Engineering Project for Advanced Sheet Metal Forming (2.D), Electromagnetic Forming of Aluminum Sheet (2.D), Improved Automotive Suspension Components Cast with B206 Alloys (3.A), and Thermal-Drilling Application Development (11.D). Science-base sub-projects of the Magnesium Powertrain Cast Components (3.B) also were concluded.

Future Directions

The current emphases on carbon-fiber-reinforced polymer-matrix composites and Mg will continue, as they have the greatest weight-reduction potential and costs. However, there will be some efforts on AHSSs, Al, and Ti because these materials will contribute in niche roles to the overall FreedomCAR weight-reduction and cost-neutrality goals. Material-crosscutting work in general manufacturing, will continue in joining, nondestructive evaluation (NDE), and recycling. Though technical-feasibility (see above) projects will dominate as before, concept-feasibility and demonstrated-feasibility projects will also be pursued as will some university base-technology projects.

2. AUTOMOTIVE METALS - WROUGHT

A. Thermo-Mechanical Processing Design for Lightweight Materials

Esteban B. Marin: Co-Principal Investigator (PI)
Senior Structural Analyst
Center for Advanced Vehicular Systems (CAVS)
Mississippi State University (MSST)
200 Research Blvd.
Mississippi State, MS 39762
(662) 325-6696; fax: (662) 325-5433; e-mail: ebmarin@cavs.msstate.edu

Paul T. Wang: Co-PI
Manager, Computational Manufacturing and Design
CAVS, MSST
P.O. Box 5405
Mississippi State, MS 39762-5405
(662) 325-2890; fax: (662) 325-5433; e-mail: pwang@cavs.msstate.edu

Christy Burton: Research Associate II
CAVS, MSST
200 Research Blvd., Rm 2147
Mississippi State, MS 39762
(662) 325-3822; fax: (662) 325-5433; e-mail: cburton@cavs.msstate.edu

Sebastien Groh
CAVS, MSST
200 Research Blvd
Mississippi State, MS 39762
(662) 325-5576; fax: (662) 325-5433; email: groh@cavs.msstate.edu

Wei Chen: Co-PI
Associate Professor of Mechanical Engineering
Robert R. McCormick School of Engineering and Applied Science
Northwestern University (NWU)
Department of Mechanical Engineering
2145 Sheridan Road
Evanston, Illinois 60208-3111
(847) 491-7019; fax: (847) 491-3915; e-mail: weichen@northwestern.edu

Jian Cao: Co-PI
Associate Professor of Mechanical Engineering
Robert R. McCormick School of Engineering and Applied Science
NWU
Department of Mechanical Engineering
2145 Sheridan Road
Evanston, Illinois 60208-3111
(847) 467-1032; fax: (847) 491-3915; e-mail: jcao@northwestern.edu

Balasubramaniam Radhakrishnan
Oak Ridge National Laboratory (ORNL)

1 Bethel Valley Road
Oak Ridge, TN 37831-6164
(865) 241-3861; fax: (865) 241-0381; e-mail: radhakrishnb@ornl.gov

Gorti Sarma
ORNL
1 Bethel Valley Road
Oak Ridge, TN 37831-6164
(865) 574-5147; fax: (865) 241-0381; e-mail: sarmag@ornl.gov

Joe Horton
ORNL
1 Bethel Valley Road
Oak Ridge, TN 37831-6115
(865) 574-5575; fax: (865) 574-7659; e-mail: hortonja@ornl.gov

Sean Agnew
University of Virginia (UVa)
116 Engineer's Way, P.O. Box 400745
Charlottesville, VA 22904-4745
(434) 924-0605; fax: (804) 982-5660; e-mail: sra4p@virginia.edu

---

Contractor: MSST
Contract No.: 4000054701

Objective

The main goal of this task is to develop physics-based, experimentally-validated, thermo-mechanical processing models and design methodologies for improving the manufacturability and forming technology of lightweight materials such as wrought heat-treatable aluminum (Al) and magnesium (Mg) alloys.

Approach

The technical approach of this task is to (i) build an experimental material database that captures the important features of the microstructure evolution during hot and cold rolling and stamping processes of Al and Mg alloys, (ii) develop a multi-scale material model using an internal state variable (ISV) formalism that is able to predict the microstructure evolution (hardening, recovery, recrystallization, grain growth, texture-induced anisotropy and precipitate hardening) of metals during thermo-mechanical processing, (iii) construct numerical models of metal forming (rolling and stamping) for process design, and (iv) introduce optimization techniques under uncertainty to develop a simulation-based design tool for integrated material-process design.

Main activities (subtasks) planned to perform the proposed research are:

- Develop plane-strain compression (rolling) and bi-axial stretching (stamping) techniques for Al/Mg alloys at room and elevated temperature.
- Build an experimental database capturing microstructure evolution of Al alloys.
- Perform pilot-scale rolling experiments and material characterization of Mg alloys.
- Extend experimental database with microstructure information for Mg alloys.
- Develop multi-scale ISV model to predict microstructure evolution of Al and Mg alloys during thermo-mechanical processing.
- Construct thermo-mechanical process models and develop manufacturability metrics for process design (rolling and stamping).

- Develop methodologies for uncertainty quantification and reliability-based design optimization of metal-forming processes.

Team members participating in this task are:

MSST: Paul Wang (PI), Esteban Marin (macroscale ISV model development), Christy Burton (mechanical/microstructure characterization of Al 6022), Sebastien Groh (support ISV model development with micro-scale/discrete dislocation simulations), Reza Yassar (scanning electron microscopy (SEM)/transmission electron microscope/microscopy (TEM) characterization and microstructure evolution modeling, moved to Michigan Tech in Aug. 2007).

ORNL: Balasubramaniam Radhakrishnan and Gorti Sarma (support ISV model development with meso-scale/crystal plasticity simulations), Joe Horton (pilot-scale rolling experiments and characterization of Mg alloys).

NWU: Jian Cao (biaxial stretching experiments and stamping simulations), Wei Chen (design optimization under uncertainty).

UVa: Sean Agnew (anisotropy and twinning of Mg alloy).

Accomplishments

- Developed a fixture for channel die compression (CDC) experiments and performed preliminary plane-strain compression tests on Al 6022 rolled sheets (reduction from 1/8" to 1/32"). Modifications of the fixture and the test procedure are being carried out to improve the outcome of the tests (uniform deformation of specimen).
- Rolled, tested and analyzed 13 out of 97 experimental Mg alloy slabs that were cast by Magnesium Elektron North America Inc (MEL Inc). A recipe adapted to the mill size at ORNL was developed to allow hot rolling of these slabs to a thickness of 1.5 mm. Several of the analyzed alloys have strengths and ductilities close to those of AZ31.
- Extended an ISV constitutive framework to account for important features of the microstructure evolution typically observed during the high-temperature deformation of metals, in particular lightweight materials. These extensions are physically-based and account for recrystallization and grain-growth phenomena, aspects that add up to the dislocation hardening and recovery mechanisms already considered in the original model. A parametric study of the enhanced model is underway.
- Established a preliminary, hierarchical multi-scale modeling approach to predict the inelastic deformation of face-centered cubic (fcc) metals. This approach builds a clear bridging methodology connecting nano-, micro- and meso-scales: dislocation mobility data numerically generated using molecular dynamics (MD) simulations (nano-scale) are used by a discrete dislocations approach (micro-scale) to determine the material parameters for a particular slip-system hardening law typically employed in crystal-plasticity models (meso-scale). This bridging methodology has been validated by using the multiscale crystal-plasticity model to predict the mechanical response of an Al single crystal deformed under uniaxial compression. The computed strain-stress response agrees well with experimental data from the literature.
- Applied meso-scale models (crystal-plasticity and Monte Carlo (MC) techniques) to predict the texture evolution during thermo-mechanical processing of Al 6022 sheet. Good agreement was obtained between model predictions and experimental textures obtained for direct annealing of the hot band and after cold rolling and annealing of the hot band. Benchmark simulations of microstructural deformation of hexagonal close-packed (hcp) polycrystals were carried out using a finite-element code developed at ORNL and the results were compared with those obtained using material point simulations as well as the models developed at MSST. Excellent agreement was obtained.
- Developed framework for stamping-process optimization with considerations of both robustness and reliability requirements. This framework identified the sources of uncertainty and process characteristics that are to be studied as the responses of interest. Forming limits of rolled Al 6022 sheets were examined using limit-dome tests at room temperature.

Future Direction

- Finalize the CDC tests on Al 6022 at room temperature. Perform subsequent annealing tests (temperature of 380°C and different times) to generate data for recrystallization and grain-growth modeling. Design fixture for high-temperature CDC tests.
- Finish survey of experimental Mg alloys and do a detailed annealing, recrystallization-kinetics study to better understand the minimum times and temperatures needed for roll processing of Mg alloys as an aid to cost reduction. Apply what has been learned to the continuous-casting processes such as twin-roll casting.
- Calibrate and validate the current ISV model framework using the experimental database being generated in the project as well as the output of the meso-scale simulations at ORNL. Implement model framework in finite-element codes. Continue extension of the material model to account for texture-induced anisotropy and precipitate hardening.
- Apply the numerical and hierarchical multi-scale framework to study the deformation of a fcc bicrystal. Evaluate the extension of the methodology to model the deformation of polycrystalline fcc metals.
- Refine the meso-scale models to obtain closer agreement with experimental deformation and recrystallization textures for Al and Mg alloys, extend the models to include the effect of particles on textures, support the development of analytical models for recrystallization kinetics at MSST based on the output of the meso-scale models, and investigate the effect of surface- and through-thickness shear on texture evolution during thermo-mechanical processing of Al and Mg alloys.
- Quantify the sources of uncertainty for stamping processes through data collection, develop numerical simulations to predict the process characteristics of interest, and develop efficient uncertainty-propagation and statistical-sensitivity analysis techniques.
- Explore extrusion modeling and structure evolution as compared with rolling results in Mg alloys.

Introduction

Thermo-mechanical processing (TMP) is typically used to improve the mechanical properties of a material by inducing changes in its microstructure (grain structure, texture, precipitates). Properties such as plasticity, strength, ductility and formability can be tailored by a proper design of different steps in TMP (e.g., hot/cold rolling, heat treatment, stamping). In this context, building robust design methodologies for TMP can contribute to improve current manufacturing processes and/or fix many technical problems (e.g., formability) that at present hinder the production of selected lightweight materials such as Mg alloys.

The present task is focused on developing a simulation-based design approach of TMP that integrates recent advances in materials science, mechanics and optimization and that could be applied to improve the manufacturability and forming technology of lightweight materials. This approach relies on building an extensive material database with microstructure/property information, developing a multi-scale material model with ISVs tied to the physics of lower length scales and able to capture history effects during processing, constructing process models that describe the geometry and boundary conditions of the processing system, and applying optimization and uncertainty techniques to optimize the TMP design accounting for inherent variabilities in the material, geometry and processing conditions.

Material Database for Al and Mg alloys

The material database will need to capture the microstructure-property-processing relationship of lightweight materials (Al and Mg alloys). It will provide the needed information about microstructure evolution and stress response as a function of processing parameters, information that can be used to develop / calibrate / verify a class of continuum ISV models.

In a general context, the class of constitutive models for TMP has the functional form:

$$\sigma = f(\varepsilon, \dot{\varepsilon}, \theta, s_i)$$

where the variables $\varepsilon, \dot{\varepsilon}, \theta$ (strain, strain rate and temperature) reflect the processing conditions and the parameters s_i are ISVs, representing the state

of microstructure of interest (e.g., hardness, statistically-stored dislocations)

In this project, to build the material database supporting the development of our particular ISV model, we will perform accurate microstructural analyses of deformed material and populate the database with quantitative parameters that are representative of microstructural heterogeneity and that can be included in our physically-based constitutive model. Typical measures of microstructure evolution to be determined are: grain morphology (size, shape), texture, dislocation structures (cell size, dislocation wall thickness, dislocation density), lattice curvature (geometrically-necessary dislocations (GNDs), grain-orientation spread, grain average misorientation), precipitate morphology (inter-particle spacing, volume fraction of precipitates, radius of precipitates), and recrystallized fraction of material.

As examples of extracting specific microstructural information from deformed material, researchers at CAVS have performed preliminary studies on annealed Al 6022 specimens deformed under uniaxial tension at room temperature. Figure 1 shows electron backscatter diffraction (EBSD) micrographs depicting the effect of precipitates on the formation of dislocation substructures. Figure 2, on the other hand, presents a technique to extract, indirectly, dislocation structure information by measuring grain / sub-grain misorientations. In the context of this task, similar studies will be reproduced for Al and Mg specimens deformed under conditions resembling a rolling process (plane-strain compression) and a stamping process (biaxial stretching) as well as heat treatment (annealing).

In the following, a brief description of the activities that have been done to build the materials database is presented. Specific activities are: plane-strain compression on Al 6022 and pilot-scale rolling experiments of a number of Mg alloys. The description of the biaxial stretching tests (formability studies) of Al 6022 sheets is presented in "Framework for Integrated Robust and Reliability Optimization of Sheet Metal Stamping Process" below.

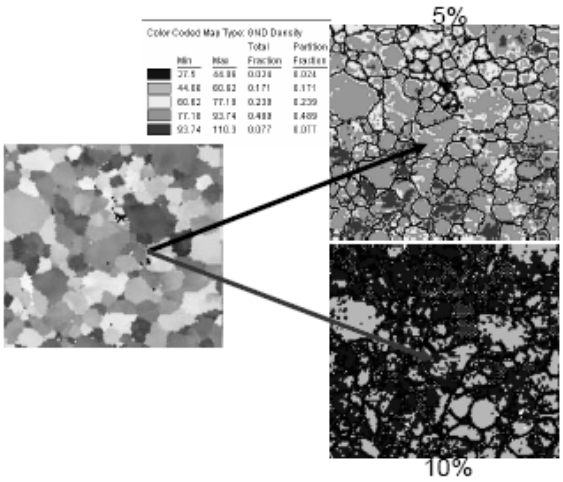

Figure 1. GND density maps, specimen aged for 8 hrs at 170°C. Note that in the presence of peak-aged precipitates, by increasing deformation from 5% to 10 %, dislocation substructures start to interfere with each other. This leads to the annihilation of GNDs, and, consequently, to a decrease in lattice orientation spread.

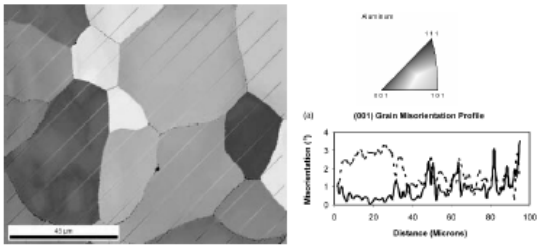

Figure 2. A procedure to extract dislocation structure information using misorientation plots.

Channel Die Compression of Al 6022 (MSST)

Plane-strain compression tests and annealing studies are being performed on Al 6022 to obtain microstructural data for modeling recrystallization and grain growth. Room-temperature CDC tests are being carried out on specimens extracted from a 1/8" Al rolled sheet; see Figure 3.

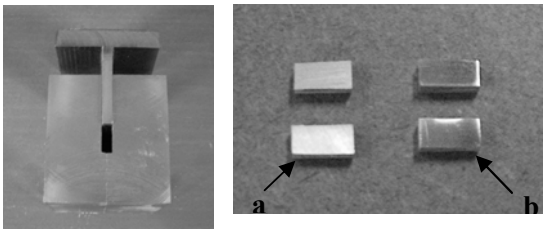

Figure 3. CDC fixture and (a) un-polished and (b) polished test specimens from 1/8" Al sheet. Specimens are 5 mm x 10 mm.

For the tests, the polished specimens are lubricated with polytetrafluoroethylene (PTFE) powder to reduce friction at the interface. The specimens are then loaded into the test fixture and compressed at a fixed displacement rate to a final gage thickness of 1/32". The deformed specimens are shown in Figure 4. Currently, reasons for the non-uniform deformation of the specimens are being investigated. Testing parameters, lubrication application methods, and fixture design are being varied.

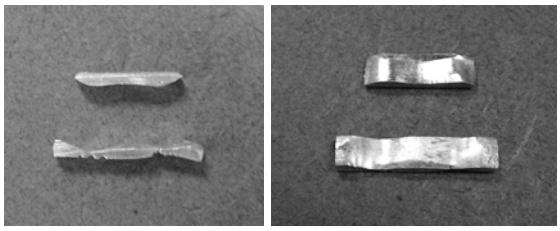

Figure 4. Preliminary deformed CDC specimens. Adjustments to the testing procedure are being done to improve the outcome of the tests.

After the plane-strain compression tests are successfully completed, the heavily-deformed specimens will be annealed isothermally for various times in a molten salt bath maintained at a temperature of 400°C. The specimens will then be quenched within 2 sec after removal from the annealing furnace to keep the partially recrystallized structure. The microstructural examination of these annealed specimens using SEM will provide experimental data for studying the recrystallization kinetics in these alloys as well as set the stage for grain-growth experiments.

Rolling Experiments of Mg Alloys (ORNL)

Pilot-scale rolling experiments on a number of Mg alloys produced by MEL Inc were performed at ORNL. Besides generating information for the material database, this study will help to develop a wrought Mg alloy and/or processes for the cost-effective production of Mg sheets which are both economical and formable enough for practical applications in vehicle structures. Activities are being concentrated in three areas: evaluating the feasibility of using innovative roll processing together with lower-cost alloyed ingots to reduce the total cost of sheet materials; developing a basic understanding of the mechanisms of deformation and recrystallization in order to develop inexpensive alloys for applications in the transportation industry; and optimization of Mg alloys for warm or superplastic forming.

It is worth noting that previous work centered on demonstrating the feasibility of utilizing infrared processing to enable continuous processing of wrought Mg alloys as one part of cost reduction. This work, on the other hand, is centered on alloy development to produce a lower-cost wrought alloy with properties close to that of AZ31. At approximately $4/lb for finished sheet, cost is one impediment to wider use of Mg in transportation applications. Possible ways to reduce cost mostly center on reducing the number of processing steps to the point of continuous processing, and some potential cost savings in the composition elements and methods associated with the initial alloying of ingots. Previous studies of infrared or plasma-arc-lamp reheats have shown potential to facilitate continuous-strip rolling operation. Also, a more thorough understanding of recovery and recrystallization will allow optimization of any chosen process. These innovations coupled with continuous casting should result in significant cost savings.

Suggestions of a rolling schedule for a lab-sized, 6-inch mill and experimental conditions were made by MEL Inc and were used as a starting point. MEL cast practice slabs with representative compositions of the alloys to be studied. The process developed and then used for subsequent tests consists of: 1) Overnight anneal at 400°C.

The minimum times and temperatures necessary for this step have not been investigated; 2) Slabs were then covered with 1.1-mm-thick sheets of stainless steel. The sheets were oxidized and sprayed with dry film graphite lubricant. The rolls are cold so the stainless steel sheets help to retain heat; 3) Hot rolling at 400°C with 10% reductions per pass and 10-min reheat between passes down to approximately 1.5 mm; 4) One half of the sheet was saved and the second half was cold rolled 10%. Figure 5 shows a successful hot-rolled sheet of alloy 129.

Figure 5. MEL Mg alloy #129 as hot rolled at 400°C clad to a thickness of 1.5 mm.

Tensile stress and elongation at failures are tabulated in Table 1. Results from comparison AZ31 specimens from some of our previously published papers are also tabulated.

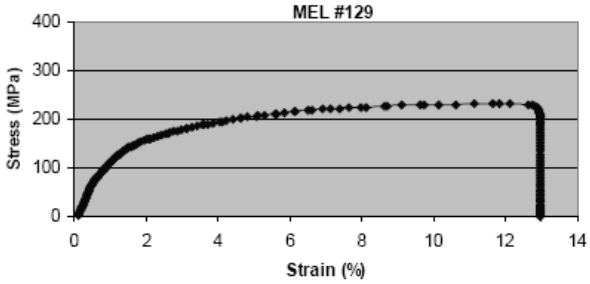

Figure 6. Tensile test data for MEL Mg alloy #129. Specimen axis is along the rolling direction.

These comparison results used the same flat dog-bone specimen size with a 25-mm gage length and the same strain rate of 10^{-3}/sec. Figure 6 presents a sample of the experimental stress-strain curve obtained during the tensile tests.

Optical metallography was done on all specimens; however, grain-size determinations were difficult on many of the hot-rolled and cold-rolled specimens due to the very fine microstructures present (see Figure 7 for a sample). The incomplete data were not tabulated. A second try will be made with a slightly different procedure. One alloy for which the metallography was adequate was alloy 113 with American Society for Testing and Materials (ASTM) grain sizes between 8 and 9, approximate grain diameters of 20 μm. It is vital to have accurate grain-size measurements to determine trends in mechanical properties.

Examination of Table 1 shows many of the alloys have tensile stress and elongations comparable to AZ31. All but one alloy hot rolled successfully. While the aim was 10% cold work, it is apparent from the tensile stresses and elongations that substantial cold work was present in the hot-rolled alloys. This also needs to be quantified. These results do suggest that the alloying approach may work and an alloy based on the compositions MEL suggested could be produced with low cost. In summary, a series of new compositions that were cast in lab-sized ingots by MEL Inc. were successfully hot rolled and tested at ORNL. Some of the compositions showed comparable results to AZ31. This alloying approach may achieve the goal of designing a less-expensive sheet alloy with desirable properties similar to AZ31.

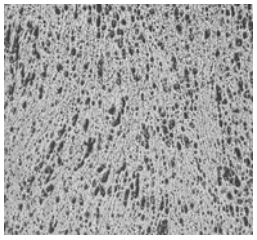

Figure 7. Optical micrograph for MEL Mg alloy #129 (20X magnification).

Table 1. Mechanical properties of experimental wrought Mg alloys.

Tensile Stress and Ductility of Experimental Alloys, 10^{-3} strain rate, 25°C, 25-mm gage length					
alloy #	**as hot rolled or with CW**	**Tensile Stress, MPa**	**Elongation, %**	**Rolled thickness, mils**	
100	**HR**	**225**	**10**	**59**	
	cw	**265**	**6**	**52**	**aim was 10%**
103	**hr**	**253**	**9**	**60**	
	cw	**254**	**8**	**54**	
104	**hr**	**270**	**8**	**60**	
	cw	**287**	**4**	**58**	
113	**hr**	**213**	**6**	**54**	
	cw	**212**	**5**	**52**	
115	**hr**	**206**	**8**	**55**	
	cw	**222**	**1**	**50**	
117	**hr**	**293**	**10**	**58**	
	cw	**305**	**8**	**55**	
123	**hr**	**221**	**3**	**59**	
	cw	**223**	**4**	**52**	
127	**hr**	**254**	**3**		**fr practice rolling batch**
128	**cw**	**249**	**6**		**fr practice rolling batch**
129	**hr**	**224**	**11**	**60**	
	cw	**248**	**2**	**53**	
159	**hr**	**217**	**7**		**fr practice rolling batch**
171	**hr**	**269**	**15**	**60**	
	cw	**312**	**3**	**54**	
191	**hr**	**192**	**3**	**did not roll**	
Comparisons					
az31	**as received**	**270**	**24**	**arc lamp rolling paper[1]**	**tested at ORNL, same geometry as above**
az31	**as infrared rolled**	**312**	**5**	**infrared rolling paper[2]**	**tested at ORNL, same geometry as above**
az31	**as extruded**	**270**	**20**	**extrusion paper[3]**	
az31	**as received**	**294**	**12**	**roll bonding paper[4]**	**tested at ORNL, same geometry as above**
az31	**half hard**	**270**	**5**	**MEL web site**	

[1]J. A. Horton, C. A. Blue, and S. R. Agnew, "Plasma Arc Lamp Processing of Magnesium Alloy Sheet," Magnesium Technology 2003, ed by H.I. Kaplan, TMS (2003) 243-246.

[2]J. A. Horton, C.A. Blue, T. Muth, A. L. Bowles, S.R. Agnew, "Infrared Processing of Magnesium Wrought Alloys", Magnesium Technology 2005, ed. By N. R, Neelameggham, H.I. Kaplan, and B.R. Powell, TMS (2005) 155-158.

[3]S.R. Agnew, J.A. Horton, T.M. Lillo and D.W. Brown, "Enhanced Ductility in Strongly Textured Magnesium Produced by Equal Channel Angular (ECA) Processing", Scripta Mater, 50, #3 (2004) 377-381

[4]A. Bowles and J.A. Horton, "Accumulative Roll Bonding of Magnesium Alloy AZ31", Magnesium Technology in the Global Age, ed. by M.O. Pekguleryuz and L.W.F. Mackenzie, The Canadian Institute of Mining, Metallurgy and Petroleum (2006) 183-192.

Constitutive Model Development

Modeling thermo-mechanical processes of metals requires an ISV material model that can accurately predict the microstructure evolution during cold/hot deformation and heat treatment. To develop such a model, a multi-scale material modeling methodology is being pursued. In this section, we present a summary of the work performed in this context. The first part explains our current ISV constitutive framework and its extension to capture, for now, recrystallization and grain growth; the second part presents a preliminary multi-scale modeling methodology that clearly links nano-, micro- and meso-scales; and the last part describes the meso-scale modeling approach that is being used to predict recrystallization and grain growth. Although not related yet, these three developments will be tied later on to come out with a predictive multi-scale ISV constitutive framework.

ISV Model (MSST)

The approach to model the deformation of Al and Mg alloys during thermo-mechanical processing is to enhance a current ISV constitutive framework to account for additional aspects of the microstructure evolution observed during the high-temperature, large plastic deformation of metals. These extensions will be physically-based and experimentally-validated, with the corresponding mathematical expressions (functional forms of evolutionary equations) justified using multi-scale modeling strategies for dislocation plasticity (nano-scale, micro-scale and meso-scale approaches).

The constitutive equations of the current "evolving microstructural model of inelasticity" are formulated in a consistent thermodynamic framework using large-deformation kinematics [Marin, 2006A]. The plasticity aspects of the model are described based on two ISVs: a scalar strength κ (isotropic hardening) and a tonsorial back stress $\boldsymbol{\alpha}$ (kinematic hardening). The evolution equations for these variables, in particular the equation for the strength, account for dislocation hardening and dynamic / static recovery mechanisms. The final equations of the model are written in non-dimensional form, a feature that simplifies the form of the equations, facilitates the fitting-parameter procedure and increases the robustness of the numerical implementation. The specific equations of the three-dimensional model, which are valid for small elastic strains, isotropic plasticity and isotropic thermal expansion, are given by

$$\mathrm{dev}\breve{\mathbf{d}}^{\mathrm{e}} = \mathrm{dev}\breve{\mathbf{d}} - \breve{\mathbf{d}}^{\mathrm{p}},\ \mathrm{tr}\breve{\mathbf{d}}^{\mathrm{e}} = \mathrm{tr}\breve{\mathbf{d}} - 3\mathrm{f}_{\breve{\theta}}\overset{*}{\breve{\theta}},\ \breve{\boldsymbol{\omega}} = \breve{\boldsymbol{\omega}}^{\mathrm{e}}$$

$$\breve{\mathcal{L}}_{\mathrm{v}}^{\mathrm{e}}\mathrm{dev}\breve{\boldsymbol{\tau}} = \mathrm{dev}\breve{\mathbf{d}}^{\mathrm{e}}$$

$$\overset{*}{\breve{\mathrm{p}}} = \mathrm{tr}\breve{\mathbf{d}}^{\mathrm{e}}$$

$$\breve{\mathbf{d}}^{\mathrm{p}} = \sqrt{\frac{3}{2}}\overset{*}{\breve{\varepsilon}}^{\mathrm{p}}\breve{\mathbf{n}},\quad \overset{*}{\breve{\varepsilon}}^{\mathrm{p}} = \breve{\mathrm{f}}(\breve{\theta})\sinh^{\breve{\mathrm{n}}(\breve{\theta})}\left[\left\langle\frac{\breve{\sigma}_{\mathrm{eq}}}{\breve{\kappa}+\breve{\mathrm{Y}}(\breve{\theta})}-1\right\rangle\right]$$

$$\breve{\mathcal{L}}_{\mathrm{v}}^{\mathrm{e}}\breve{\boldsymbol{\alpha}} = \breve{\mathrm{h}}(\breve{\theta})\breve{\mathbf{d}}^{\mathrm{p}} - \breve{\mathrm{r}}_{\mathrm{d}}(\breve{\theta})\overset{*}{\breve{\varepsilon}}^{\mathrm{p}}\sqrt{\frac{2}{3}}\|\breve{\boldsymbol{\alpha}}\|\breve{\boldsymbol{\alpha}}$$

$$\overset{*}{\breve{\kappa}} = \left[\breve{\mathrm{H}}(\breve{\theta}) - \breve{\mathrm{R}}_{\mathrm{D}}(\breve{\theta})\breve{\kappa}\right]\overset{*}{\breve{\varepsilon}}^{\mathrm{p}} - \breve{\mathrm{R}}_{\mathrm{S}}(\breve{\theta})\breve{\kappa}\sinh\left(\breve{\mathrm{Q}}_{\mathrm{S}}(\breve{\theta})\breve{\kappa}\right)$$

In these equations, a bold letter denotes a second order tensor and the symbols $(\breve{\mathrm{a}},\overset{*}{\breve{\mathrm{a}}})$ represent a dimensionless quantity and a dimensionless time derivative, respectively. Also, $(\breve{\boldsymbol{\tau}},\breve{\mathrm{p}})$ are the Kirchhoff and hydrostatic stresses, $(\breve{\mathbf{d}},\breve{\mathbf{d}}^{\mathrm{e}},\breve{\mathbf{d}}^{\mathrm{p}})$ are the total, elastic and plastic deformation rates, $(\breve{\boldsymbol{\omega}},\breve{\boldsymbol{\omega}}^{\mathrm{e}})$ are the continuum and elastic spins, $\breve{\mathbf{n}}$ is the plastic flow direction, $(\breve{\sigma}_{\mathrm{eq}},\overset{*}{\breve{\varepsilon}}^{\mathrm{p}})$ are the equivalent stress and equivalent plastic strain, $\breve{\theta}$ is the temperature, and $\mathrm{f}_{\breve{\theta}}$ is a function describing the thermal-expansion characteristics of the material. The symbol $\breve{\mathcal{L}}_{\mathrm{v}}^{\mathrm{e}}$ denotes a co-rotational time derivative, (dev(•), try(•)) indicate the deviatoric and trace operators, and $\|(\bullet)\|$ represents the norm of a tensor. This version of the model has nine normalized temperature-dependent plasticity functions represented by the parameters: $\breve{\mathrm{f}},\breve{\mathrm{n}},\breve{\mathrm{Y}},\breve{\mathrm{r}}_{\mathrm{d}},\breve{\mathrm{h}},\breve{\mathrm{R}}_{\mathrm{D}},\breve{\mathrm{H}},\breve{\mathrm{R}}_{\mathrm{S}},\breve{\mathrm{Q}}_{\mathrm{S}}$.

Typically, these parameters are used to fit the predicted plastic response of the model to experimental stress-strain curves for a particular

material obtained at different temperatures and strain rates.

As mentioned before, the above constitutive framework is being extended to capture important features of the microstructure evolution during thermo-mechanical processing. In this context, as a first step, the model has been modified to account for recrystallization, grain growth and the resultant softening behavior in the stress response [Brown, 2006]. For this purpose, the specific changes being introduced in the above constitutive equations are:

1. Add the effect of grain size to both the initial mechanical strength $\breve{Y}$ and the evolution of the isotropic hardening variable $\breve{\kappa}$ ($\breve{\kappa}$ physically represents the evolution of statistically-stored dislocations, defects that are mainly responsible for most of the hardening in polycrystals),
2. Add a recovery (softening) term to the evolution of $\breve{\kappa}$ whose effect is triggered when the energy stored (driving force for recrystallization) in the material during deformation reaches a critical value,
3. Develop physically-based evolution equations for the fraction of recrystallized grains and the grain size,
4. Incorporate a model for GNDs through a stress-like variable (misorientation variable) which effectively accounts for the stored energy due to misorientations of the deformation-induced dislocation boundaries, and
5. Incorporate deformation texture effects to account for its influence on the initiation of recrystallization.

The preliminary version of the extended model accounts for aspects 1–4 above and substitutes the previous set of ISVs $(\breve{\kappa},\breve{\alpha})$ for the set $(\breve{\kappa},\breve{\varsigma},\breve{X},\breve{D})$, where $\breve{\varsigma}$ is the stress-like misorientation variable, $\breve{X}$ is the fraction of recrystallized grains and $\breve{D}$ is the average grain size. For the case of uniaxial extension (one-dimensional case), the non-dimensional constitutive equations for the deviatoric (isochoric) response of this extended model are:

$$\overset{*}{\breve{s}} = \frac{2}{3}(1+\nu)(\breve{d} - \breve{d}^{p} - f_{\breve{\theta}}\overset{*}{\breve{\theta}})$$

$$\breve{d}^{p} = \breve{f}\sinh^{\breve{n}}\left[\left\langle \frac{3}{2}\frac{|\breve{s}|}{\breve{\kappa}+\breve{Y}(\theta,\breve{D})} - 1\right\rangle\right]\mathrm{sign}(\breve{s})$$

$$\overset{*}{\breve{\kappa}} = \left(\breve{H} + \frac{\breve{H}_2}{\breve{\kappa}\breve{D}} + \frac{\breve{H}_3\breve{\varsigma}}{\breve{\kappa}}\right)\left|\breve{d}^{p}\right| - \left(\breve{R}_D\left|\breve{d}^{p}\right| + \breve{R}_S\sinh(\breve{Q}_S\breve{\kappa})\right)\breve{\kappa} - \breve{R}_x(\breve{C}_{\breve{\kappa}}\breve{\kappa}^2 + \breve{C}_{\breve{\varsigma}}\breve{\varsigma}^2)\breve{\kappa}\breve{X}$$

$$\overset{*}{\breve{\varsigma}} = \frac{\breve{H}_4}{\breve{D}}\breve{\varsigma}^{1-1/\breve{r}}\left|\breve{d}^{p}\right| - \breve{R}_x\left(\breve{C}_{\breve{\kappa}}\breve{\kappa}^2 + \breve{C}_{\breve{\varsigma}}\breve{\varsigma}^2\right)\breve{\varsigma}\breve{X}$$

$$\overset{*}{\breve{X}} = \breve{R}_x\left(\breve{C}_{\kappa}\breve{\kappa}^2 + \breve{C}_{\varsigma}\breve{\varsigma}^2\right)\breve{X}(1-\breve{X})$$

$$\overset{*}{\breve{D}} = \frac{\breve{B}_D}{\breve{D}^{\breve{m}}}$$

Here, $\breve{R}_x$ and $\breve{B}_D$ are temperature-dependent material functions defined by

$$\breve{R}_x = \frac{\breve{M}_x\breve{\bar{\mu}}(\breve{\theta})}{\breve{\theta}}\exp(-\frac{\breve{Q}_x}{\breve{\theta}}),\quad \breve{B}_D = \breve{C}_D\exp(-\frac{\breve{Q}_D}{\breve{\theta}}).$$

In the above equations, $\breve{s}$ is the deviatoric stress, ν is the Poisson ratio, and $\breve{\bar{\mu}}(\breve{\theta})$ is a function defining the temperature dependence of the shear modulus. As noted, in this extended model there are ten additional material parameters $(\breve{H}_2,\breve{H}_3,\breve{H}_4,\breve{C}_{\breve{\kappa}},\breve{C}_{\varsigma},r,\breve{M}_x,\breve{Q}_x,\breve{C}_D,\breve{Q}_D)$ which are to be determined from mechanical tests and microstructural characterization studies that describe the evolution of $\breve{X}$ and $\breve{D}$. Currently, this extended model is being implemented in MatLab to perform a parametric study and to set up the fitting procedure for the material parameters. In addition, the integration scheme of the three-dimensional equations is also being developed for implementation in material-user routines of commercial finite-element codes, e.g., ABAQUS and LS-DYNA.

A Hierarchical Multi-Scale Materials Modeling Approach (MSST)

A multi-scale materials modeling approach bridging MD and discrete dislocation (DD) to crystal plasticity (CP) in fcc single crystals has been established in this task. In this approach, the material parameters of a dislocation-based hardening law typically used in crystal-plasticity models are numerically computed from DD simulations results. These simulations use dislocation-mobility information obtained from MD computations. A schematic of the bridges connecting these different length scales as well as the simulation tools used at each length scale are summarized in Figure 8. A brief description of the approach follows.

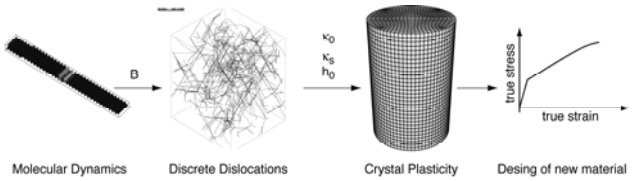

Figure 8. The link between nano-scale, micro-scale and meso-scale in the hierarchical multi-scale modeling approach.

At the crystal plasticity level, the plastic strain in fcc single crystals results from dislocation glide on well-defined lattice planes. A glide system (α) is defined by the dislocation Burgers vector $\mathbf{b}^{(\alpha)}$ and the normal vector of the gliding plane $\mathbf{n}^{(\alpha)}$. Two expressions are needed to relate the evolution of the plastic shear strain rate (i) to the applied stress on the glide system τ_α and (ii) to the evolution of the slip-system strength κ_α.The flow law relates the shear strain rate to the applied shear stress using a power-law relationship

$$\dot{\gamma}_\alpha = \dot{\gamma}_{0,\alpha}\left(\frac{\tau_\alpha}{\kappa_\alpha}\right)^{1/\mathrm{m}}$$

Here, m is the strain-rate sensitivity exponent, taken in the order of 0.05, and $\dot{\gamma}_{0,\alpha}$ is a reference shear strain rate, chosen in the order of $10^{-3}\,s^{-1}$. Assuming that all glide systems harden at the same rate, i.e. $\kappa_\alpha \to \kappa$, one can write the evolutionary law for the strength κ as

$$\dot{\kappa} = h_0\left(\frac{\kappa_s - \kappa}{\kappa_s - \kappa_0}\right)\sum_\alpha \dot{\gamma}_\alpha$$

Here, κ_s, κ_0 and h_0 are the saturation strength, the initial strength and the initial hardening rate, respectively. In general, these parameters are determined by correlating the model response to experimental strain-stress curves. However, in this work, they are numerically computed using DD simulations.

At the discrete dislocations level, as the Peierls stress is low in fcc crystals, the velocity ν of a single dislocation in these materials can be correlated to a linear form given by

$$v = \frac{\kappa b}{B}$$

Here, b is the magnitude of the Burgers vector and B is the drag coefficient. This coefficient is determined using MD simulations and the computed value for Al is presented in Figure 9. It is noted that B increases from $2.5\text{x}10^{-5}$ Pa-s to $5.5\text{x}10^{-5}$ Pa-s when the temperature varies from 100K to 500K. Such a range of values for the drag coefficient is in agreement with experimental data.

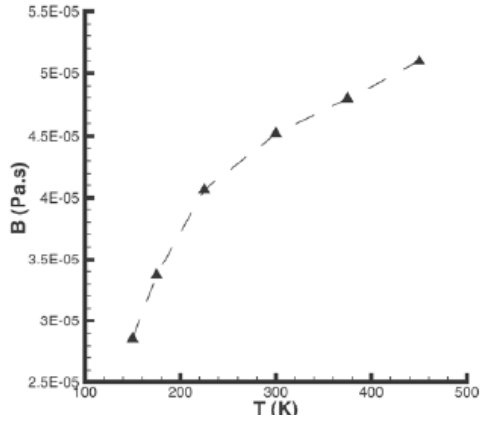

Figure 9. Dislocation drag coefficient as a function of temperature computed from MD.

The above mobility law is used to simulate the tensile test of a dislocation box using DD. A deformation rate of 20 s^{-1} is applied along the [421] axis. The analysis starts with an initial dislocation density of $10^{12}\,m^{-2}$, uniformly

distributed over all the slip systems. During the deformation of the simulation box, the plastic strain rate generated by the gliding dislocations equilibrates the applied strain rate. Hence, with $\sum \dot{\gamma}_\alpha$ being a constant, the evolution equation of the slip system strength can then be integrated to recover the Palm-Voce equation

$$\kappa = \kappa_s - (\kappa_s - \kappa_0)\exp\left(-\frac{h_0}{\kappa_s - \kappa_0}\sum_\alpha \dot{\gamma}_\alpha t\right)$$

The hardening (strength) computed from DD is plotted in Figure 10. The same figure also shows the fitted response using the above equation for four sets of parameters. The value of these parameters depends on the time range used to correlate the above equation and the predicted hardening from DD. The initial strength ranges between 3.29 MPa and 3.39 MPa, the initial hardening rate ranges between 25.83 MPa and 34.98 MPa, and the saturation strength varies between 47.75 MPa and 49.10 MPa.

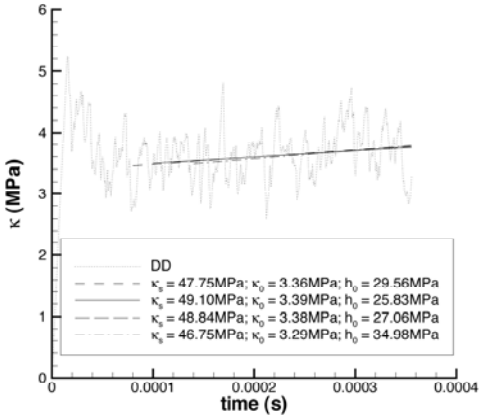

Figure 10. Evolution of hardening as predicted by DD and fit to the integrated evolution equation for the strength κ.

The set of parameters shown in Figure 10 has been used in a crystal-plasticity framework [Marin, 2006B] to calculate the stress-strain responses of an Aluminum single crystal under compression loading along the [421] direction. The predicted curves are compared to the experimental one [Hughes, 2000] in Figure 11. A good agreement between numerical predictions and experimental data is observed for the range of hardening parameters determined from DD. In addition, the deformed mesh at a strain of 0.6 presented in Figure 12 clearly shows that the crystal cross-section ovals during deformation. Note that the experimental cross-section of the deformed crystal agrees well with the predicted deformed shape.

Currently, the multi-scale material modeling procedure described above is being extended to predict the mechanical response of an Al bi-crystal. The application of the approach to model the behavior of polycrystalline fcc metals will also be explored.

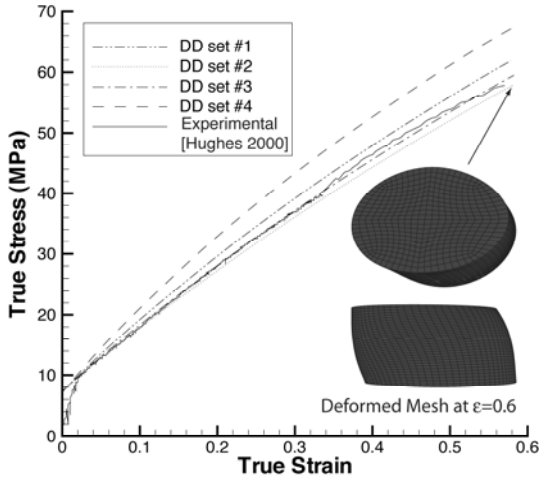

Figure 11. Stain-stress response using the crystal-plasticity parameters calculated by DD.

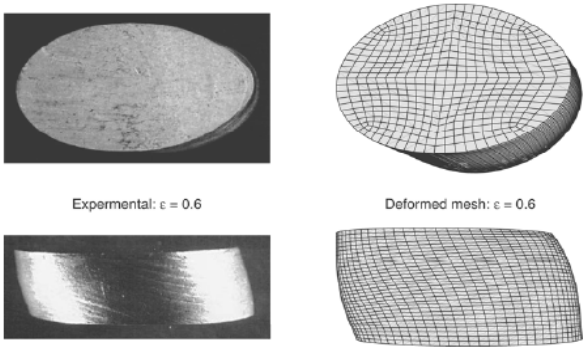

Figure 12. Experimental versus predicted deformed shape of Al single crystal.

Recrystallization and Grain Growth Studies using a Meso-scale Approach (ORNL)

The objective of these studies is to develop and validate meso-scale simulations of microstructure and texture evolution during thermo-mechanical processing of Al- and Mg-alloy sheets and provide a comprehensive microstructure module that can be integrated with the ISV material model being developed by MSST for capturing the main features of microstructure evolution and corresponding history effects occurring during cold / hot working and heat treatment of Al and Mg alloys.

This work involves large-scale, crystal-plasticity modeling of microstructural deformation, extracting the deformation substructure, and evolving the substructure during annealing using a meso-scale technique that includes a nucleation model for recrystallization based on orientation-dependent recovery of subgrains. The input for meso-scale models was obtained by a realistic mapping of the initial experimental microstructure to the simulation domain.

Coupled Deformation-Recrystallization Simulations

Thermo-mechanical processing to produce optimum grain structure and texture is essential for the successful utilization of commercial Al and Mg alloys as sheet products. Several modeling techniques have been developed in the past with a reasonably good predictive capability for bulk deformation textures [Kocks, 1998]. Significant progress has also been made in the last decade in the development of advanced measurement techniques for characterizing micro textures with high spatial resolution both in two- and three-dimensions. However, prediction of micro-texture evolution during deformation and its subsequent evolution during recrystallization remains very challenging because of uncertainties involved in predicting the mechanisms that lead to the formation of recrystallization nuclei with specific crystallographic orientations, and the uncertainties involved in predicting the grain/sub-grain boundary properties that determine the growth kinetics of the nuclei. With the availability of large computers and advances in software, it is now possible to perform simulations of polycrystalline deformation with a high enough resolution to capture the formation of in-grain misorientations [Sarma, 1998]. Meso-scale simulations of annealing have been combined with the output of deformation simulations to predict the evolution of recrystallization textures [Radhakrishnan, 1998, 2000, 2004A, 2004B]. In these simulations, nucleation is modeled by heterogeneous sub-grain growth incorporating misorientation and structure-dependent boundary properties. A recent development in the modeling of nucleation is based on an assumption of orientation-dependent recovery of sub-grains [Crumbach, 2004, Radhakrishnan].

Such an orientation-dependent recovery has been demonstrated in Al [Theyssier, 1999], copper [Ridha, 1982] and steels [Humphreys, 1995; Barnett, 1999; Yoshinaga, 1998]. It has also been shown that the cell morphology in the deformed structure is a function of the grain orientation. In the case of polycrystalline Al, it was shown that orientations in the vicinity of the Cube had equated cell structure while the other deformation orientations had a cell structure that had a linear morphology [Liu, 1998]. The orientation-dependent cell morphology was explained on the basis of the number of different non-coplanar active slip systems [Liu, 1998]. For example, a high number of non-coplanar active slip systems was correlated with a more equiaxed cell morphology than when only a few co-planar slip systems are active during deformation. It has also been experimentally observed in Al polycrystals that orientations such as the Cube that have equiaxed cell structures also recover extremely fast compared to other deformation components.

Computational Approach

Generation of Input Microstructures: In order to obtain realistic comparisons between model and experiment, the input microstructures used for modeling should accurately capture the microstructural features present in the experimental system. The important microstructural features include the grain

structure, the bulk texture and the micro-texture that includes the grain misorientation distribution. The experimental data were in the form of EBSD scans performed on specific two-dimensional sections. A computational approach was developed for mapping the texture information obtained in the two-demensional sections to a three-dimensional grain structure. The approach is based on reducing the large number of experimental texture points to a finite number of orientations and assigning the orientations to the grains in the three-dimensional structure. The assignments were done on the basis of a weighting function that describes the probability of existence of a given orientation. Because a three-dimensional grain structure has a range in the grain size, the texture obtained after the initial assignment does not usually have a good match with the experimental texture. Also, there is usually a poor match between the model and experimental grain-misorientation distribution functions. A computational approach that minimizes the error both in the texture and the misorientation distribution was developed.

Microstructural Deformation: Meso-scale deformation simulations were performed using a polycrystal plasticity model incorporating neighboring grain interactions in which grain deformation is distributed in a non-uniform fashion among the polycrystals [Sarma, 1996]. Interactions with surrounding crystals are incorporated in the calculation of the deformation rate of each crystal through an appropriately-defined local neighborhood. A compliance tensor is computed for each crystal based on a viscoplastic constitutive relation for deformation by crystallographic slip. The compliance of the crystal relative to that of its neighborhood provides a means for partitioning the macroscopic deformation rate among the crystals. Deformation modeling was also carried out using a finite-element implementation of the crystal plasticity model with grain-level discretization. The details of finite-element implementation are described elsewhere [Sarma, 1998].The deformation of fcc polycrystals was simulated using 12 slip systems consisting of the 12 {111}<110> octahedral slip systems.

Recrystallization simulations were performed using a three-dimensional MC approach in a cubic grid. For local-energy calculations, the energy of the site and a neighborhood consisting of the first, second and third nearest neighbors was used. The input microstructure for the MC simulations was obtained from the output of the crystal-plasticity simulations. The details of the MC procedure are described elsewhere [Radhakrishnan, 1998].

New Nucleation Model: The nucleation step during recrystallization was modeled as follows. For each site in the simulation domain, the total shear rate on each {111}<110> slip system was calculated for the entire deformation. For each site, the total shear rate on the non-coplanar systems was calculated by adding the shear rates belonging to a given (111) plane. The shear rates were then normalized by the maximum shear rate for each site and added. The resulting quantity was further normalized by the maximum value in the system to give nucleation probability for each site as a fraction with an upper bound of 1.0. The above definition is different from the definition of the active number of slip systems proposed by Crumbach et al. [Crumbach, 2004; Crumbach, 2006]. While Crumbach et al. defined the orientation-dependent recovery based on the total number of active slip systems, we specifically identify the non-coplanar slip systems (slip systems with different slip plane) and base our nucleation probability on the relative shear rates in the non-coplanar slip systems.

Results

Coupled Deformation-Recrystallization Simulations

The application of the grain-mapping code using the EBSD data generated for an Al 6022 hot band by MSST is shown in Figure 13. The agreement in texture between the mapped grain structure and the experimental texture is excellent.

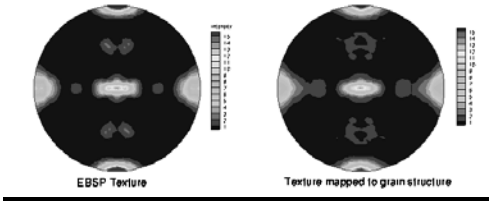

Figure 13. <100> pole figures showing textures from EBSD and the grain structure obtained by mapping.

The three-dimensional grain structure to which the texture was mapped is shown in Figure 14. The grain structure was generated by a MC grain-growth code with isotropic grain-boundary energy and mobility. The assumption is that the grain structure in the hot band is equiaxed. Further refinement of the mapping with simulated non-equiaxed grain structures is an extension of the current capability that will be pursued in the future.

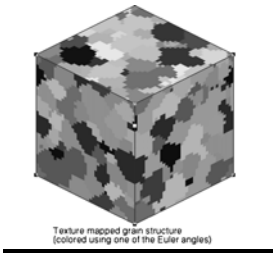

Figure 14. Three-dimensional grain structure to which the EBSD texture is mapped.

The above grain structure was deformed in plane-strain compression to a total cold deformation of 75% reduction in height using the neighborhood compliance model described previously. The final texture that results from the deformation simulation was compared with experimental EBSD texture data for the 1/32" sheet obtained by cold rolling the 1/8" hot band. Figure 15 shows <111> pole figures for the initial texture and the computed texture after cold deformation. The Cube component is generally unstable during cold deformation, and other deformation components form at the expense of the Cube component. However, there is still some residual Cube orientation present after cold deformation.

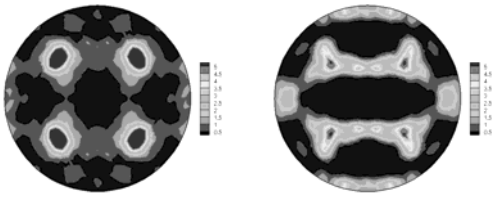

(a) (b)

Figure 15. <111> pole figures showing the texture in (a) 1/8" hot band and (b) computed texture in 1/32" sheet after plane-strain compression.

The experimental texture obtained by EBSD scan is shown in Figure 16 in the form of a <111> pole figure. The agreement with the simulated texture shown in Figure 15(b) is quite reasonable. The agreement can be improved using the more rigorous finite-element technique with a high degree of mesh refinement, and these simulations are underway.

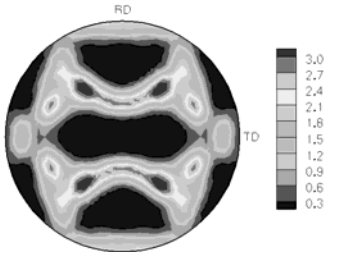

Figure 16. EBSD texture after cold rolling to 1/32".

Figure 17 shows the recrystallization texture obtained using the meso-scale recrystallization model that used the simulated deformation texture in Figure 15(b) as the input. The recrystallization texture shows a strong Cube component, although orientations rotated from Cube are also present. This is in general agreement with the results seen in the literature, although a direct comparison of the model with experiments will await measurements on the 1/32" sheet. The recrystallization simulations used the nucleation model based on orientation-dependent recovery described previously.

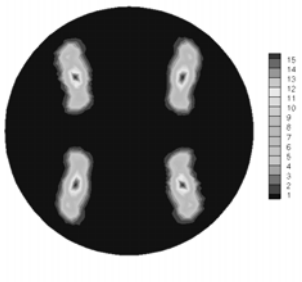

Figure 17. Simulated recrystallization texture in the annealed 1/32" sheet.

The nucleation probability as a function of the site number in the microstructure is shown in Figure 18. The orientations that recovered quickly to form the recrystallization nuclei correspond to those sites that had a high value for the nucleation probability.

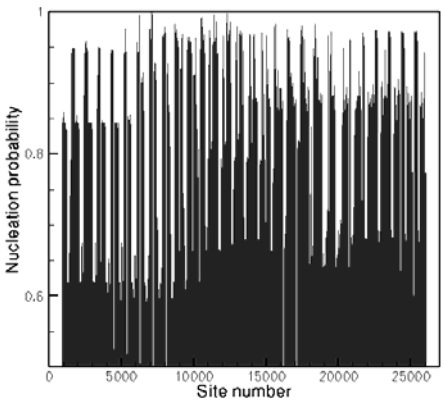

Figure 18. Nucleation probability as a function of site number.

The meso-scale model, in addition to capturing the texture, also captures the recrystallization kinetics, as shown in Figure 19. The simulations currently do not have the capability to model the recrystallization as a function of real time and temperature. However, it is possible to convert the Monte Carlo time step (MCS) shown as the time axis in Figure 19 to real time using a technique that was developed for modeling grain growth in a temperature gradient.

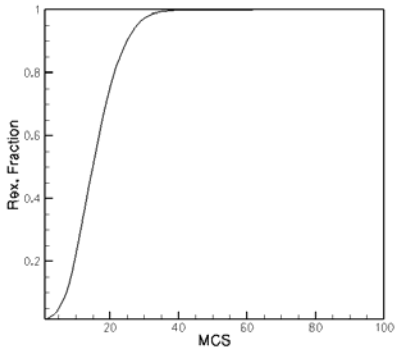

Figure 19. Recrystallization kinetics obtained using the meso-scale annealing simulations. MCS represents the Monte Carlo time step.

Simulations are also being carried out using the crystal-plasticity finite-element approach to deform the polycrystalline microstructure that was obtained by reconstruction based on experimental EBSD data (Figure 14). A finite-element mesh of $40 \times 40 \times 40$ elements is being used for these simulations, and the microstructure will be deformed in plane-strain compression to a compressive strain of 1.4, which corresponds to a 75% reduction in height in terms of rolling. The high strains involved can lead to problems with severe element distortion and, therefore, the mesh needs to be adjusted periodically with regular parallelepiped elements of the appropriate aspect ratio based on the overall strain. Recrystallization simulations that make use of the finite-element modeling results as input will be performed in the future.

Benchmark deformation simulations for fcc and hcp polycrystals

Simulations using the crystal-plasticity finite-element model were carried out using a single finite element containing an aggregate of 256 orientations within the element for computing the material response. These simulations were compared with the results from a material point simulation (MPS) program, where the mechanical response and texture evolution of an aggregate of grain orientations is computed for a given velocity gradient, and the velocity gradient for each orientation is assumed to be the same as the applied velocity gradient (under the Taylor

hypothesis). These simulations were intended to serve as a verification of the implicit integration scheme used to evolve the material state.

The response of both fcc and hcp crystals under plane-strain compression was simulated. The fcc crystals were assumed to deform on the twelve {111}<110> slip systems, while the hcp crystals were assumed to deform on the three (0001)<2 −1 −1 0> basal, the three {1 0 −1 0}<1 −2 1 0> prismatic and the twelve {1 0 −1 1}<1 1 −2 3} pyramidal slip systems. The material parameters for the fcc and hcp crystals were taken from [Marin, 2006]. The slip system strength for the fcc crystals was assumed to be the same for all the slip systems, and the evolution in strength was assumed to be isotropic. For the hcp crystals, the pyramidal slip systems typically have higher strength and, in these simulations, the strength of these systems was initially assumed to be five times the strength of the basal and prismatic systems and this initial strength difference was maintained through the deformation. A value of 1.633 was assumed for the axial (*c/a*) ratio for the hcp crystals.

The results from these simulations are shown in Figure 20 in the form of the stress-strain response, and in Figures 21 and 22 in the form of pole figures to show the texture evolution for the fcc and hcp crystals. The stress values have been normalized by the initial slip-system strength. These results show that the response of the aggregate with initially random orientation distribution is very similar from both the MPS program and the finite-element model (FEM). There are small deviations in the stress-strain response with increasing strain, and this is thought to be a consequence of the velocity gradient in the finite element model deviating slightly from the exact plane-strain compression that can be enforced in the MPS program. These results serve to verify the implementation of the integration scheme for the elasto-viscoplastic crystal plasticity model in the finite-element model.

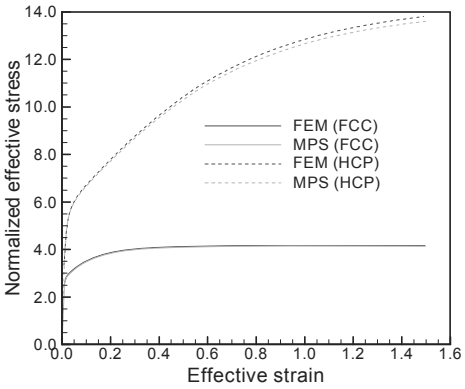

Figure 20. Stress-strain response for an aggregate of 256 fcc and hcp crystals deformed in plane-strain compression computed using material point simulation and one-element finite-element model.

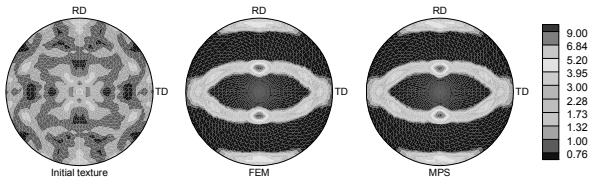

Figure 21. <111> pole figures showing texture evolution for plane-strain compression of an aggregate of 256 fcc crystals computed using MPS and one-element finite-element model.

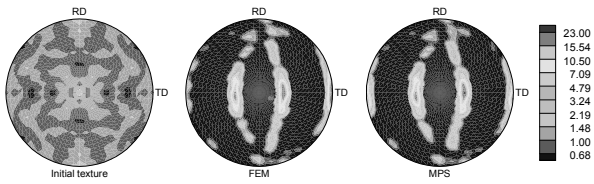

Figure 22. <0001> pole figures showing texture evolution for plane-strain compression of an aggregate of 256 hcp crystals computed using MPS and one-element finite-element model.

The finite-element model was used to simulate fcc and hcp polycrystals with each element representing a single crystal of a different orientation. A unit cube was discretized using a 7×7×7 element mesh, and each element was initially assigned an orientation from a random distribution. The polycrystals were subjected to three different deformation modes: plane-strain compression, uniaxial compression and simple shear. The material parameters for all simulations and the slip systems for both fcc and hcp

polycrystals are the same as described above for the one element simulations.

The deformed mesh for the fcc polycrystal subjected to plane strain compression is shown in Figure 23. The differences in orientations between the elements lead to the highly heterogeneous deformation that is evident from the distorted mesh. The textures after deformation are shown in Figure 24 in the form of <111> pole figures, and are consistent with the textures expected for the different modes of deformation for fcc polycrystals.

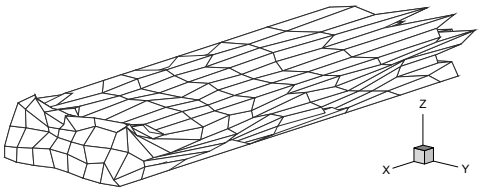

Figure 23. Deformed mesh for 7×7×7 element mesh fcc polycrystal deformed under plane-strain compression ($\varepsilon = 1.3$).

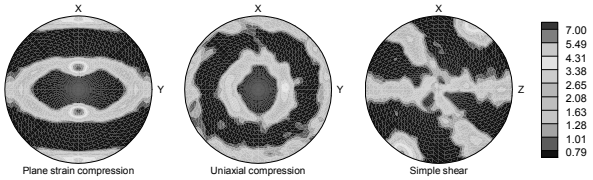

Figure 24. <111> pole figures showing texture evolution for 7×7×7 element fcc polycrystals subjected to various modes of deformation.

Similar results for textures after deformation of the hcp polycrystal are shown in Figure 25 in the form of <0001> pole figures. As in the case of the fcc polycrystals, the textures for the different modes of deformation are consistent with those typically observed for hcp materials. The results from these simulations also compare well with similar results presented in [Marin, 2006], and have been used to verify the performance of the finite-element implementation for materials with hcp crystal structure.

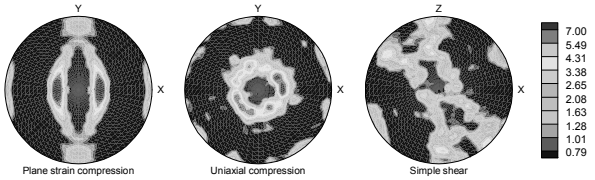

Figure 25. <0001> pole figures showing texture evolution for 7×7×7 element hcp polycrystals subjected to various modes of deformation.

As a summary, the coupled deformation-recrystallization simulations are able to capture the texture evolution in Al 6022 during deformation and static recrystallization reasonably well. However, further improvement can be obtained by more rigorous deformation models using grain-level discretization and more efficient incorporation of the nucleation model to evolve the deformation substructure. These simulations are currently being carried out. Extension of the current capability for modeling the deformation using the crystal-plasticity-based finite-element method to hcp polycrystals has been verified using benchmark problems. This capability will be used in the future to model the deformation and recrystallization of Mg alloys.

Framework for Integrated Robust and Reliability Optimization of Sheet-Metal Stamping Process

Sheet-metal forming processes have been widely used to fabricate a desired sheet-metal product in many industries such as automotive, appliance, aerospace, and others. Productivity and high strength but lightweight products are among the key attributes that sheet-metal forming processes could offer. However, uncertainties due to uncontrollable conditions (e.g., metal suppliers, forming conditions, and numerical errors) play an important role and need to be taken into account in the design process.

The process characteristics considered in this work are related to the margin of safety/failure of the sheet metals. Failures in sheet-metal fabrications generally come from three main phenomena: springback, tearing and wrinkling. In this stamping study, our focus is on tearing and wrinkling. Tearing is a failure due to an excessive

localized load leading to a local instability causing the sheet metal to split [Swift, 1952; Keeler, 1964; Marciniak, 1967; Cao, 2002]. Wrinkling is an unstable phenomenon mainly due to excessive in-plane compressive loads [Wang, 2000].
The first step in characterizing uncertainties in sheet metals is to examine the forming limits of Al sheet AA6022 provided by MSST.

Characterization of Forming Limits

Forming-limit diagram has been a popular tool in industry to characterize the material resistance to thinning since Keeler and Backofen introduced the concept in 1964. Figure 26 shows the limit-dome test apparatus at the Advanced Materials Processing Laboratory at NWU.

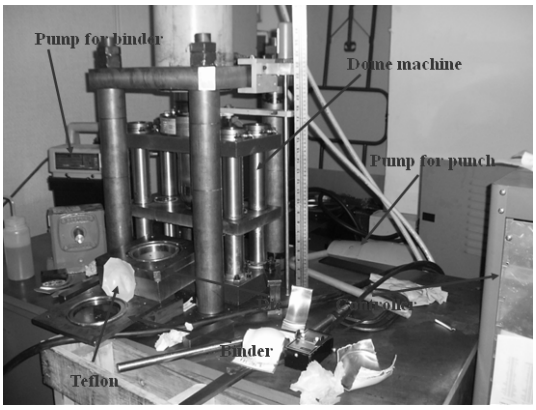

Figure 26. Limit-dome test at NWU.

Sheets were first marked by grids and then clamped between binder rings and deformed by the punch. To reduce friction between the sheet metal and the punch, a Teflon sheet is used between the metal and the punch. Before and after the deformation, grid sizes were measured using microscopes as shown in Figure 27. Various widths of samples (Figure 28) were used to obtain various strain paths. Finally, the forming-limit diagram can be obtained as shown in Figure 29. It can be seen that there exists a 0.025 strain variation in the forming- limit curve (FLC).

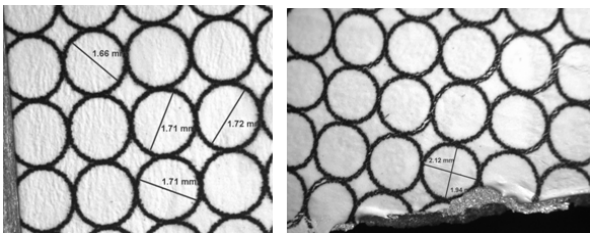

Figure 27. Grids on sheet metal: (a) before deformation, (b) after deformation (near a crack).

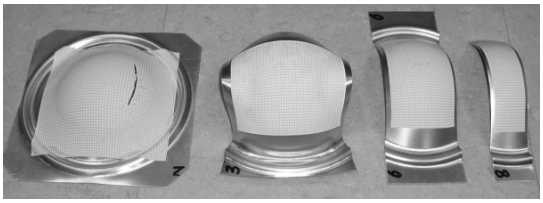

Figure 28. Samples used in the limit dome tests.

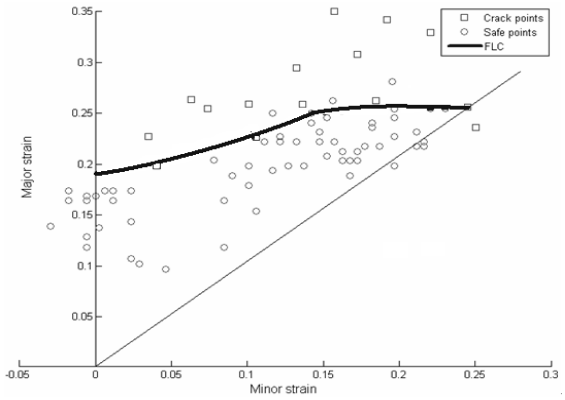

Figure 29. Forming limit diagram of AL6022.

Flowchart of Probabilistic Design of Stamping Process

The design process for a stamping process is summarized in the following flowchart. The main focus of this work is to create an integrated framework for robust and reliability design of a stamping process that achieves a design specification in terms of failure-free and takes into account uncertainty.

The design process considering uncertainties for sheet-metal forming processes requires integration of finite-element analysis (FEA), statistical analysis, and decision making. Design and optimization under uncertainty provides a means

such that unacceptable failures are unlikely to occur with an acceptable confidence.

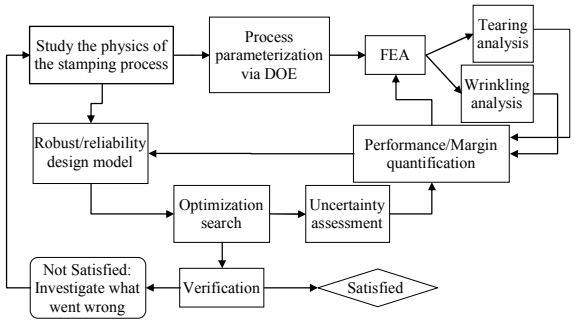

In most engineering applications, mean and variance are the parameters of interest to define a probabilistic system. Uncertainty-propagation techniques for statistical moments have evolved from analytical probabilistic models and a sampling-based approximation technique called Monte Carlo simulation. Analytical probabilistic models mostly are very difficult to develop. Monte Carlo simulation, on the other hand, is a powerful approximation technique that relies on pseudo- random numbers but it requires a large (and often impractical) computational effort. In this work, we will employ the state-of-the-art uncertainty propagation techniques to improve the efficiency of this process.

A Probabilistic Design Model For Optimizing Stamping Process

A sheet-stamping process is subjected to tearing and wrinkling failures due to process set-ups and material properties. In addition, variations associated with process set-ups and material properties play a role in the quality of the product. Here, we formulate a probabilistic design model by incorporating uncertainty and both tearing and wrinkling criteria. In sheet-metal forming design, we consider failure margins as design requirements that a forming process needs to satisfy. A design solution needs also to satisfy all reliability requirements in failure analysis (wrinkling and tearing), when uncertainties are taken into account. The constraint statements are defined as follows:

- Probability of **tearing** occurrence must be less than *X* (the probability of not having tearing must be larger than *R*). The statement is mathematically written as follows

$$P(f > 0) = P(|\varepsilon_{appl}| < |\varepsilon_{cr}|) \geq R = 1 - X,$$

where *f* is the margin, which is defined by a strain-based criterion. The simplest case is to monitor if strain $|\varepsilon_{appl}|$ at one point exceeds the limit value $|\varepsilon_{cr}|$. By using the stress-based forming-limit diagram as the failure criterion, we have another equivalent statement as follows

$$P(f > 0) = P(\text{sign}(\sigma - \sigma_{critical}).\min\|\sigma - \sigma_{critical}\| > 0) \geq R = 1 - X$$

- Probability of **wrinkling** occurrence must be less than *X* (the probability of not having wrinkling must be larger than *R*). The statement is mathematically written as follows

$$P(f > 0) = P(|\sigma_{appl.comp.}| < |\sigma_{critcal}|) \geq R = 1 - X,$$

where *f* is the margin, which is defined by a stress criterion.

To simplify the probabilistic design model, we utilize the moment matching technique [Du, 2000] to create an equivalent model in a format of robust/reliability design. While the objective is used to achieve the robust design goal, the constraints are used to ensure reliability. The moment-matching method is an approximation technique that does not need to estimate the entire probability density function (PDF) not by assuming the response follows normal distributions (only need the mean and variance of the system response). As a result, the need of the resources on the uncertainty propagation is reduced. The probabilistic design model is written as follows:

Minimize

$$y = W_1 \frac{-\sum_i w_i \cdot \mu_{f_i}}{M_f^*} + W_2 \frac{\sum_j w_j \cdot \sigma_{f_j}^2}{\Sigma_f^{2*}},$$

Subjected to $g_i = -(\mu_{f_i} - k_i \sigma_{f_i}) \leq 0,$

$x \in \Omega.$

where y is the objective function; g_i is the i^{th} constraint function; W_1 and W_2 are weighting factors for normalized means and normalized variances, respectively; w_i is a weighting factor for the i^{th} component; μ_{f_i} is the mean value of f_i; $\sigma^2_{f_i}$ is the variance value of f_i; M^*_f and Σ^{2*}_f are used to normalize the two aspects of the robust design objective; k_i is the i^{th} moment factor (corresponding to a minimum reliability) to capture the feasibility of a robust design constraint under uncertainty. The uncertainty-propagation techniques previously presented before are utilized for these statistical moment calculations. In particular, we will use the weighted three-point-based method for the mean and variance estimation.

The objective of the model is to minimize the negative value of the expected value of the total margin and its total variance while to maintain the minimum reliability requirements.

Conclusions

Good progress has been made since the beginning of the project in February 2007. Experiments are underway to build the material database needed for constitutive modeling development. Materials modeling work using molecular dynamics, discrete dislocations, crystal plasticity and ISVs (macroscale) is being performed to relate the physics at different length scales and come out with a physics-based and robust material model. Meso-scale simulations (Monte Carlo, crystal plasticity) of recrystallization and grain growth are being performed on Al alloys and are also being extended to Mg alloys. Process models are being constructed and used to simulate rolling and stamping of lightweight materials. Finally, a probabilistic framework has been developed to include uncertainties due to different sources when modeling thermomechanical processes, in particular, stamping processes. As noted previously, all this work will contribute to the development of thermo-mechanical processing models and design methodologies for improving the manufacturability and forming technology of lightweight materials.

Presentations/Publications/Patents

1. S. Groh, E.B. Marin and M.F. Horstemeyer, "Multiscale Modeling of the Plasticity in Al Single Crystal", Plasticity'08, Hawaii.
2. S. Groh, E.B. Marin and M.F. Horstemeyer, "Multiscale Modeling of the Plasticity in Al Single Crystal", in preparation.

References

1. [Marin, 2006A] E.B. Marin, D.J. Bammann, R.A. Regueiro, G.C. Johnson, Sandia National Laboratories, CA, SAND2006-0200 (2006).
2. [Brown, 2006] A.A. Brown, D.J. Bamman, M.L. Chiesa, W.S. Winters, A.R. Ortega, B.A. Antoun, N.Y.C. Yang, "Modeling static and dynamic recrystallization in FCC metals", Plasticity'06, Halifax, Canada.
3. [Marin, 2006B] E.B. Marin, Sandia National Laboratories, CA, SAND2006-4170 (2006).
4. [Hughes, 2000] D. Hughes, D.J. Bammann, A. Codfrey, V. Prantil, E. Holm, M. Miodownik, D. Chrzan, and M. Lusk, Sandia National Laboratories, SAND2000-8232 (2000).
5. [Kocks, 1998] U.F. Kocks, C.N. Tomé, H.-R. Wenk, Texture and Anisotropy, Cambridge University Press, Cambridge, 1998.
6. [Sarma, 1998] G.B. Sarma, B. Radhakrishnan, T. Zacharia, Comput. Mater. Sci. 12 (1998) 105-123.
7. [Radhakrishnan, 1998] B. Radhakrishnan, G. Sarma, T. Zacharia, Acta Mater. 46 (1998) 4415-4433.
8. [Radhakrishnan, 2000] B. Radhakrishnan, G. Sarma, H. Weiland, P. Baggethun, Model. Simul. Mater. Sci. Eng. 8 (2000) 737-750.
9. [Radhakrishnan, 2004A] B. Radhakrishnan, G. Sarma, Phil. Mag. A22 (2004) 2341-2366.
10. [Radhakrishnan, 2004B] B. Radhakrishnan, G. Sarma, JOM 56 (2004) 55-62.
11. [Crumbach, 2004] M. Crumbach, M. Goerdeler, G. Gottstein, L. Neumann, H. Aretz, R. Kopp, Model. Simul. Mater. Sci. Eng. 12 (2004) S1-S18.
12. [Crumbach, 2006] M. Crumbach, M. Goerdeler, G. Gottstein, Acta Mater. 54 (2006) 3275-3289.

13. [Radhakrishnan] B. Radhakrishnan and G. Sarma, Materials Science and Engineering A, in press.
14. [Theyssier, 1999] M.C. Theyssier, J. H. Driver, Mater. Sci. Eng. A272 (1999) 73-82.
15. [Ridha, 1982] A.A. Ridha, W.B. Hutchinson, Acta Metall. Mater. 30 (1982) 1929-1939.
16. [Humphreys, 1995] F.J. Humphreys, M. Hatherly, Recrystallization and Related Annealing Phenomena, first ed., Elsevier, New York, 1995, pp. 335-337.
17. [Barnett, 1999] M.R. Barnett, L. Kastens, ISIJ International 39 (1999) 923-929.
18. [Yoshinaga, 1998] N. Yoshinaga, D. Vanderschueren, L. Kestens, K. Ushioda, J. Dilewijns, ISIJ International 38 (1998) 610-616.
19. [Liu, 1998] Q. Liu, D. Juul Jensen, N. Hansen, Acta Mater. 46 (1998) 5819-5838.
20. [Sarma, 1996] G. Sarma, P.R. Dawson, Int. J. Plast. 12 (1996) 1023-1054.
21. [Swift, 1952] Swift, H.W., J. Mech. Phys. Sol., 1 (1952) 1-18.
22. [Keeler, 1964] Keeler, S.P., Backofen, W.A., ASM Transactions Quarterly, 56 (1964) 25-48.
23. [Marciniak, 1967] Marciniak, Z., Kuczynski, K. Int. J. Mech. Sci., 9/9 (1967) 609-620.
24. [Cao, 2002] Cao, J., Yao, H., Int. J. Plast., 18/8 (2002), 1013-1038.
25. [Wang, 2000] Wang, X. and Cao, J., Int. J. of Mech. Sci., Vol. 42/12 (2000) 2369-2394.
26. [Du, 2000] Du, X. and Chen, W., ASME J. of Mech. Design, 122/4 (2000) 385-394.

B. Development of High-Volume Warm Forming of Low-Cost Magnesium Sheet (AMD 602[i])

Principal Investigator: Peter Friedman
Ford Motor Company
Ford Research and Innovation Center
2101 Village Road, MD 3135
Dearborn, MI 48121-2053
(313) 248-3362; fax: (313) 390-0514; e-mail: pfriedma@ford.com

Principal Investigator: Paul Krajewski
General Motors (GM) Corporation
GM, R&D and Planning
Mail Code 480-106-212
30500 Mound Road
Warren, MI 48090-9055
(586) 986-8696; fax: (586) 986-9204; e-mail: paul.e.krajewski@gm.com

Principal Investigator: Jugraj Singh
Chrysler Corporation LLC
Body Materials Engineering
Mail Code 482-00-11
800 Chrysler Drive
Auburn Hills, MI 48326-2757
(248) 512-0029; fax: (248) 576-7490; e-mail: js329@chrysler.com

Technology Area Development Manager: Joseph A. Carpenter
(202) 586-1022; fax: (202) 586-1600; e-mail: joseph.carpenter@ee.doe.gov

Field Project Officer: Aaron D. Yocum
(304) 285-4852; fax: (304) 285-4403; email aaron.yocum@netl.doe.gov

Expert Technical Monitor: Philip S. Sklad
(865) 574-5069; fax: (865) 576-4963; e-mail: skladps@ornl.gov

---

Contractor: United Sates Automotive Materials Partnership (USAMP)
Contract No.: FC26-020R22910 through the DOE National Energy Technology Laboratory.

Objective

Develop the technology and material-supply base for cost-effective, lightweight body panels fabricated from sheet magnesium (Mg). A warm-forming system will be designed and built to develop a suitable process for forming Mg sheet as well as a test bed to evaluate potential low-cost Mg sheet from various global producers. Specific deliverables from this project will include the following:

- Design and build a warm-forming die and demonstrate a deep-draw capability on conventional direct-chill (DC) material.
  - Demonstrate pan forming of at least 100 mm.
- Evaluate materials and compare the formability of continuous-cast (CC) and DC materials.
  - Evaluate high-temperature elongation equal or greater in CC material compared to DC material.
- Demonstrate high-volume cycle times with CC material on an integrated forming cell.
  - Part-to-part cycle time with CC material of 5-10 jobs per minute (jpm).

Approach

- CC is a key technology for enabling the development of low-cost Mg sheet. This project will drive material development in the supply base by giving them a mechanism for evaluating materials. The project will receive material from major global Mg suppliers including Magnesium Elektron, CSIRO, ThyssenKrupp, LY Copper, and POSCO. These materials will be characterized via tensile testing at the University of Virginia (UVA), biaxial forming at CANMET-Materials Technology Laboratory (CANMET-MTL), and through stamping trials at Troy Tooling Technologies.

- Novel die systems will be designed and constructed that enable the use of warm forming in a conventional single-action press. The die will be used to determine critical forming parameters for Mg sheet including lubricant thickness, preheat temperature, die temperature, forming speed, etc. The forming windows for the different materials will be determined to see the effect of processing via different methods, e.g., CC vs. ingot (DC) casting.

- Full automation, including loading of pre-heated sheet and part extraction, will be developed to achieve acceptable cycle times (5-10 jpm) demonstrating the high-volume feasibility of warm forming.

Accomplishments

- Mg-sheet materials have been received from four of the five suppliers (100 blanks each, 1 mm x 600 mm x 600 mm). These materials have been provided to UVA (Prof. Sean Agnew) and CANMET-MTL (Dr. Kevin Boyle) for characterization. Material from the fifth supplier (LY Copper) will be arriving in the fourth quarter of 2007 (4Q07).

- Material-characterization work has been completed on the first of the five test alloys at UVA and CANMET-MTL. Work has concentrated on high-temperature tensile testing and biaxial forming as well as microstructural characterization.

- Significant modifications have been made to the warm-forming pan die originally designed and built in the previous Warm Forming of Aluminum II (AMD 307) project complete in 2006. This includes improvements in the thermal stability of the die as well as significant instrumentation so that temperature, press tonnage and forming speed can all be captured with a new data acquisition system.

- The forming of DC-cast Mg sheet utilizing the warm-forming pan die to full die depth of 125 mm has been demonstrated, thus achieving the first project gate.

- A press has been purchased by team member, Troy Tooling Technologies, to be used for all forming-trial work as well as the development of the fully-automated, warm-forming line.

Future Direction

- The dedicated press at Troy Tooling Technologies will be modified to achieve the speeds required to achieve 5 to 10 parts per minute.

- Material-characterization work through microscopy, elevated-temperature tensile testing and formability experiments will continue with work performed on all five candidate alloys.

- Next, forming trials will concentrate on: 1) establishing a forming window for the conventional DC-cast material; 2) comparing the formability of the CC alloys with the conventional alloys; and 3) a demonstration of a fully-automated, warm-forming line.

Introduction

The major barrier to the application of Mg-sheet components in vehicle structures is a combination of two factors: the limited formability of Mg sheet and the cost of producing the sheet itself. Warm-forming processes, similar to what was demonstrated in aluminum (Al) by the predecessor AMD 307, can be used to significantly improve the formability of Mg sheet. This project is leveraging the accomplishments of the AMD 307 project to develop equipment, lubricant, simulation, and forming equipment for the cost-effective forming of Mg sheet. A warm-forming cell based on the lessons-learned of AMD 307 will be designed and built to demonstrate the efficient forming of Mg sheet. The target application for this process is deep-draw panels with specific interest in door inners.

The cost of Mg sheet is driven by the high conversion costs of rolling an ingot into sheet form. This is a direct result of the hexagonal close-packed (hcp) structure of Mg that requires the sheet to be rolled in small increments, often with annealing steps between rolling passes. CC is a technology with the potential to reduce this cost dramatically. By casting directly into sheet form, CC offers a higher production rate, a smaller capital investment, and significantly less energy and labor as compared with the conventional DC ingot-casting process. The opportunities for decreasing the cost of Mg sheet via CC have been described by Hunt et. al in their 2005 report to the DOE (see 2005 annual). Suppliers globally are working on developing CC technology. In this project, all of the major global Mg suppliers will be included to determine if their materials are suitable for the warm-forming process. The new warm-forming system will be used as a standard test bed for the evaluation of these materials as well as new Mg sheet materials produced in the future.

Low-Cost Mg Sheet

The project includes Mg sheet from five major global Mg suppliers. This includes two DC-casters (Magnesium Elektron and ThyssenKrupp) and two continuous casters (CSIRO, LY Copper, and POSCO). Four of the five suppliers have provided 100 blanks of 1 mm x 600 mm x 600 mm of AZ31B-O material (LY Copper is targeting 4Q07 for delivery). All of the materials will be used at three locations: UVA, CANMET-MTL, and Troy Tooling Technologies.

Materials in this work have been coded so that the technical results can be shared with all the material suppliers without providing company information.

Deliverable:

- Determine the best AZ31 alloy for warm forming, and provide guidance to the materials community on how continuous-cast materials compare with DC cast materials.

Design and Build Warm-Forming Tool

The previous AMD 307 project provided a great deal of information about the design and fabrication of a die for warm forming. This current project is leveraging these lessons learned and the existing equipment to create an optimized die system for warm forming.

Figure 1. Modified warm-forming die.

Key elements of this optimization are using advanced simulation techniques for both thermal control (General Motors (GM)) and formability (Ford). A photograph of the warm-forming die is shown in Figure 1.

Evidence of the improvement attained in the thermal control of this die system is shown in Figure 2 where the temperature across the die face is held within a 10^{o}C range. This is a significant improvement from the door die that was previously used in AMD 307. This excellent temperature uniformity is the result of the computer-aided engineering (CAE)-led design of the heating system. The hot zone is isolated from

the rest of the die system with strategic use of insulation and water-chilled plates. As noted in Figure 3, this new design also shows very good thermal stability over time.

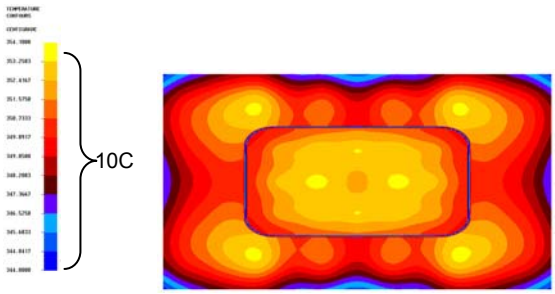

Figure 2. Thermal distribution across the die face.

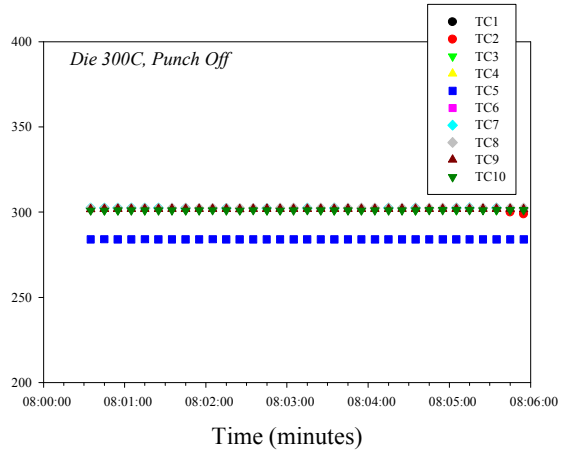

Figure 3. Temperature of the die and punch plotted as a function of time.

Successful pans from DC-cast material were produced during the first forming trial to a full depth of 125 mm as shown in Figure 4. More recently, the die has been modified to allow for the capture of both thermal and forming data through a new data-acquisition system. Data such as temperature across the tool, pressing force, and forming rate will now be recorded for each formation. The first forming trial using this new instrumentation is planned for the 4Q07.

Deliverables:

- Warm-forming die with improved thermal control and instrumented to record critical forming data such as temperature, press tonnage and deformation rate.
- Established feasibility to form conventional DC-cast material to a minimum of 100 mm depth. [Gate 1 Achieved]

Figure 4. Rectangular pan formed to full depth from DC-cast AZ31.

Material Characterization

Samples of the materials from the various Mg suppliers have been provided to Professor Sean Agnew at UVA and Dr. Kevin Boyle at CANMET-MTL. Preliminary results of the research efforts are summarized below.

The University of Virginia

The specific deliverables include:
1) microstructure analysis, 2) mechanical property data, 3) constitutive relations, and 4) digital and paper copies of reports describing and discussing items (1-3).

A suitable system for elevated-temperature tensile tests has been designed and built at UVA. The system, shown in Figure 5, is based on a modified American Society for Testing and Materials (ASTM) standard for superplastic tensile tests and has shown to provide excellent data. Experimental work with this equipment has begun under a variety of temperatures and strain rates.

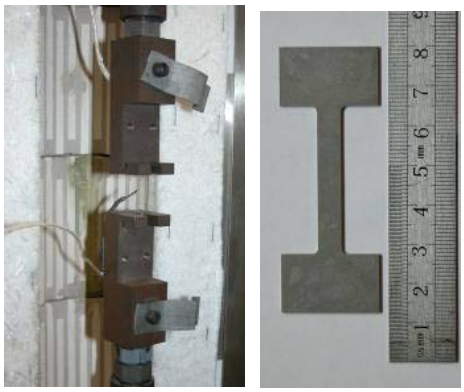

(a) (b)

Figure 5. Photograph of the (a) grip and (b) tensile specimen used for elevated-temperature tensile testing at UVA.

Results of the first set of experiments are shown in Figure 6. Not surprisingly, the flow stress decreases with increasing temperature while the elongation to failure increases. However, there does appear to be an interesting result in that there is almost no difference in elongation-to-failure for temperatures between 200°C and 275 °C . This is further explored in Figure 7 which shows that the flow stress continues to decrease with increasing temperature but the elongation-to-failure plateaus from 200 °C to 275 °C . More work will be required to understand this phenomenon.

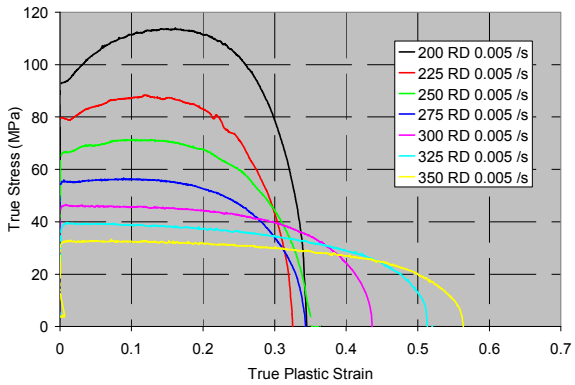

Figure 6. True stress versus true strain for DC-cast material at various temperatures (RD=rolling direction).

The microstructures of the conventional DC-cast Mg alloy have been characterized in a variety of conditions including: a) as-received, b) heat-treated (required to compare various tempers), c) pre-heated, and d) post-deformation. Grain size, grain shape, and the level of mechanical twinning present in the sheets in their various conditions have been measured, as well as the size and distribution of second-phase particles.

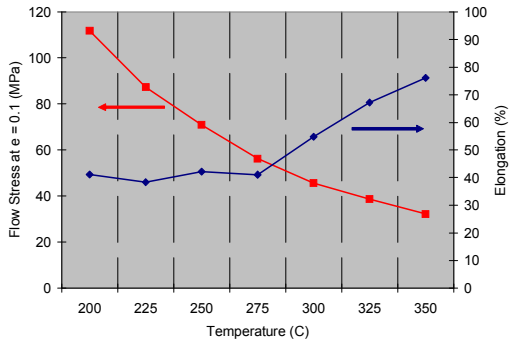

Figure 7. Flow stress and elongation to failure plotted as a function of temperature for the DC-cast material.

Although crystallographic texture is not a first-order microstructure feature by which all engineering materials are examined, the texture of the various sheets will be measured using x-ray diffraction. Electron backscattered diffraction (EBSD) may be used to further examine texture (e.g., gradients in texture) or for identifying the crystallography of twins in the microstructure.

Initial work has been performed with scanning electron microscopy (SEM) and will be applied on a limited basis to answer questions regarding fracture-surface morphology and/or energy-dispersive x-ray spectroscopy (EDS) to determine the chemical composition of specific particles in the microstructure. EDS could also reveal a lack of homogenization in the chemical composition of continuous-cast sheets, which is of great interest due to the potential of CC processes to lower the cost of sheet materials.

Deliverables:

- Complete tensile characterization for Mg-sheet alloys as a function of temperature and strain rate.
- Comparison of CC and DC AZ31 materials.
- Constitutive equations for inclusion in formability simulation.

CANMET-MTL

CANMET-MTL has developed a custom-designed apparatus for generating warm forming-limit diagrams (FLDs) based on the Marciniak in-plane stretching test (Figure 8). It is proposed that full FLDs will be generated for a select number of alloys and temperatures. Ideally, full FLDs for all temperatures and strain rates of interest would be measured; however, generating a full FLD is costly. An estimate of the FLD can be obtained by measuring forming limits in tension, plane-strain tension and pure biaxial stretching.

Preliminary forming data for two of the test materials are shown in Figure 9 for plane-strain samples. For both materials, the maximum strain that can be attained increases with temperature. This is not surprising and consistent with data from the literature. However, for material “O”

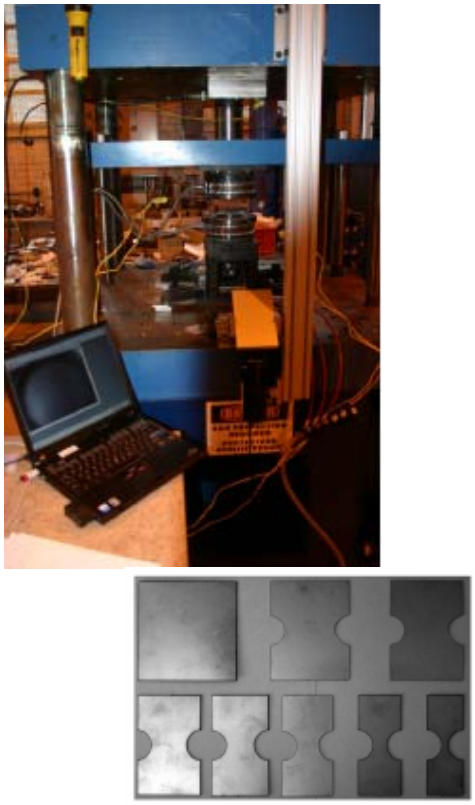

Figure 8. Custom-build test apparatus and specimens for determining FLDs at elevated temperature at CANMET-MTL.

there appears to be a strong dependence on orientation with the material transverse to the rolling direction showing increased strain to failure. More work is needed to fully understand this effect.

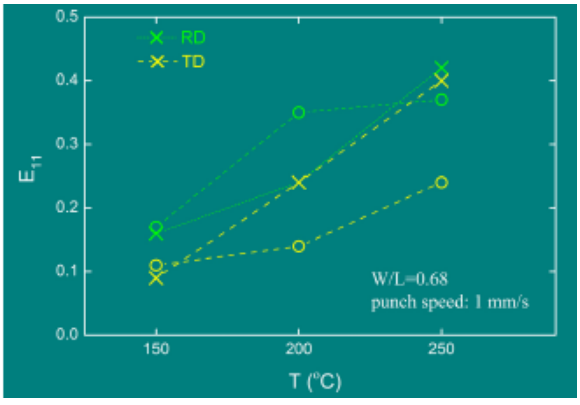

Figure 9. Major strain plotted as a function of test temperature for two materials in two orientations (TD = transverse to rolling direction; W/L = ratio of specimen width to length).

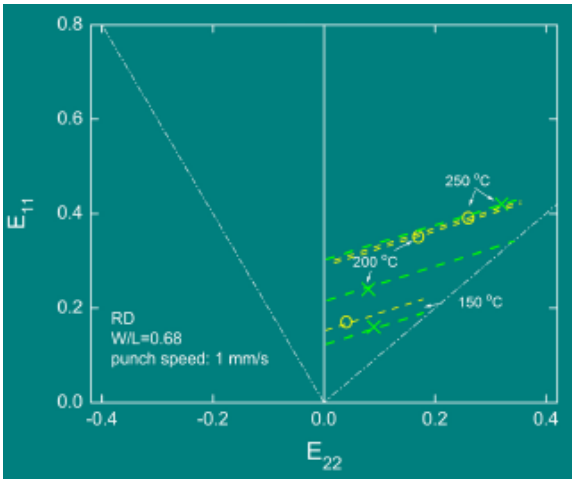

Figure 10. Preliminary forming data plotted on an FLD for two materials.

The preliminary forming data are plotted on an FLD in Figure 10. It appears that the strain path is a function of temperature with the higher-temperature samples moving away from plane-strain toward biaxial stretching. This is a very important finding which will need to be better understood and characterized to design optimized-forming processes.

Deliverables:

- Determine FLDs for Mg-sheet alloys provided in the current study. These results will be used to evaluate which materials have the best formability and, combined with the constitutive equations developed at UVA, provide accurate warm-forming predictions for Mg sheet.

Lubrication

The preliminary work in AMD 307 demonstrated that the warm-forming lubricant developed for Al also works for Mg sheet. This lubricant, provided by Fuchs, will be used in the present project. Application of the lubricant will be done by Jay and Kay Manufacturing, as in AMD 307.

Die Tryout and First-Phase Trials

As noted above, the first forming trial has been competed and established the ability to form conventional DC-cast Mg sheet to the full die depth of 125 mm. The following forming trials are planned to complete the deliverables for this project.

(1) Establish the optimum forming window (temperature, preheat, lubricant, binder pressure, press speed, etc.) for Mg sheet using existing DC sheet as the baseline. This trial will be executed in the 4Q07 and will use a convection oven for preheating and manual part handling.

(2) The second trial will evaluate the performance of the five (5) different Mg-sheet alloys and compare those results with the forming window developed in (1). [Achieve Gate 2]

(3) The third trial will demonstrate the fully-automated, warm-forming line with the forming windows shown in (2).

(4) Additional trials may be necessary depending on press availability and the results from trials (2) and (3).

Automated Cell and Demonstration

The final phase of the project will involve constructing a fully-automated warm-forming cell using the optimized pan die. A conduction preheater has been loaned to the project by GM. Troy Tooling Technologies will integrate the preheater and die using automated material handling to create a warm-forming cell that can produce a formed pan every 10 seconds. The process will be demonstrated to the OEMs and DOE.

Deliverable:

- Demonstration of a fully-integrated, warm-forming system. [Achieve Gate 3].

Cost Model

AMD 307 developed a cost model for warm forming in cooperation with Camanoe Associates. This model will be modified to understand the costs of warm forming of Mg sheet and to establish the benefits of using lower-cost CC materials.

Deliverable:

- Cost comparison of forming Mg sheet from DC and CC materials.

Figure 11. Photograph of new dedicated press and pre-heater for the development of the fully automated warm forming cell.

Conclusions

The goal of this project is to develop the technology and material supply base for cost-effective, lightweight body panels fabricated from sheet Mg. Deliverables include the development of forming parameters, equipment design and simulation tools for forming sheet magnesium and a standard evaluation of sheet magnesium from all potential low cost suppliers.

Next steps of the project include forming trials with lower cost, continuously-cast alloys as well as development of an automated, warm forming system.

[i] Denotes project 602 of the Automotive Materials Division (AMD) of the United States Automotive Materials Partnership (USAMP), one of the formal consortia of the United States Council for Automotive Research (USCAR, see www.uscar.org), set up by Chrysler, Ford and General Motors to conduct joint, pre-competitive research and development.

C. Die-Face Engineering Project for Advanced Sheet-Metal Forming (AMD 408[i])

Project Investigator: Thomas B. Stoughton, Ph.D.
General Motors Corporation
GM Research & Development Center, MC 480-106-359
30500 Mound Road
Warren, MI 48090-9055
(586) 986-06303; fax: (586) 986-0574; e-mail: thomas.b.stoughton@gm.com

Project Investigator: Laurent Chappuis
Ford Motor Company
VOGO – Advanced Stamping Engineering
17000 Oakwood Boulevard
Allen Park, MI 48101
(313) 805-5230; fax: (313) 322-4359; e-mail: tchappui@ford.com

Project Investigator: Chang-Quing Du, Ph.D.
Chrysler Corporation
ASME Stamping Technology Center, CIMS 482-60-05
800 Chrysler Drive
Auburn Hills, MI 48326
(248) 576-5197; fax: (248) 576-2230; e-mail: cd4@chrysler.com

Project Administrator: Manish Mehta, Ph.D.
TRC-National Center for Manufacturing Sciences
3025 Boardwalk
Ann Arbor, MI 48108-3266
(734) 995-4938; fax: (734) 995-1150; e-mail: manishm@ncms.org

Technology Area Development Manager: Joseph A. Carpenter
(202) 586-1022; fax: (202) 586-1600; e-mail: joseph.carpenter@ee.doe.gov

Field Project Officer: Aaron D. Yocum
(304) 285-4852; fax: (304) 285-4403; e-mail: aaron.yocum@netl.doe.gov

Expert Technical Monitor: Philip S. Sklad
(865) 574-5069; fax: (865) 576-4963; e-mail: skladps@ornl.gov

---

Contractor: United States Automotive Materials Partnership (USAMP)[i]
Contract No.: DE-FC05-02OR22910 through the National Energy Technology Laboratory

---

Objective

- The main goal of the recently-concluded AMD 408 Die-Face Engineering Project (DFEP) was to develop and implement robust, new simulation technology by improving the certainty, computational accuracy, and turn-around speed of critical formability and springback analyses performed for die design and die-fabrication/stamping tryout that can greatly help reduce manufacturing costs for all sheet-metal parts using newer lightweight sheet metal such as advanced high-strength steel (AHSS) and aluminum (Al).

- The project has demonstrated significant progress towards this goal by generating optimized sheet stamping dies using computer-aided design (CAD) surfaces (generated from finite-element modeling [FEM] mesh) that compensate for springback while maintaining formability. The project has also shown that major savings can accrue from the elimination of the soft tool prototyping phase, with corresponding major reductions in costs and lead time for structural automotive components utilizing AHSS and Al.

Approach

- The original collaborating partners included Alcoa, TK-Budd, Chrysler Corporation, Ford Motor Company/Volvo Cars Division, General Motors Corporation, US Steel, Livermore Software Technology Corporation (LSTC), and over a dozen test laboratories and stamping-technology vendors, all of which were facilitated and coordinated by Technologies Research Corporation of the National Center for Manufacturing Sciences (TRC-NCMS), which served as Technical Project Administrator.
- The LS-DYNA engineering package was the team's reference modeling package for demonstrating and evaluating new technology advances. The USAMP DFEP approach has involved the USAMP original equipment manufacturer (OEM) partners working collaboratively with key technology vendors and test laboratories to significantly improve the accuracy of material models for new high-strength, lightweight sheet materials. The OEMs and suppliers jointly assessed and evaluated the impact of new material properties on springback-prediction technology using proprietary prototype numerical-code modules. They also contracted with other die-construction and CAD vendors to perform lab and field validation activities, before industrializing and applying it across a broader range of closure and structural parts. This last task is in progress.
- The project deliverables include:
  - Integrated product-process finite-element analysis (FEA) capability that will more accurately predict springback for both closures (>90%) and structural parts (~80%)
  - Test results from simulations, panel trials and springback measurements that were used to guide and validate the software development (done at private expense by vendors)
  - Capability to automatically and consistently generate a numerical-control (NC) quality, machinable CAD surface of acceptable quality from FEM mesh.
- The DFEP project research tasks, performed and overseen by nominated expert team leaders, are hereby reported under four main technology areas described below. An OEM-led industrialization team is performing the industrial-scale implementation feasibility and justification analyses based on the deliverables from each technology thrust area:
  - Numerical technology
  - Material testing/modeling
  - Surface technology
  - Field validation

Accomplishments

- Completed Springback Classification Study of closure and structural parts with information and results pooled from the DFEP team, as well as an Industrialization Progress Survey to determine which die-face engineering software advances offer the largest benefit to each OEM.
- Developed, validated and implemented new algorithms (e.g., smooth contact, adaptive mesh refinement around radii) for better contact treatment and demonstrated improved stress calculation on benchmark parts that improves the computational accuracy and efficiency without compromising the quality of springback predictions.
- Developed and implemented material models with higher predictive accuracy for portraying isotropic hardening and kinematic hardening to better represent materials work-hardening phenomena, i.e., the Bauschinger effect using extensive uniaxial, biaxial, shear test data, and fracture-surface data

measurements. Developed a minimum set of specified material tests required to represent the formability behavior of a sheet.

- Completed Common Rail Die CAD surface morphing, re-cut and tryout-panel stamping experiments, and collected all needed die and panel scan data to enable the comparison of the engineered die-face to baseline forming and springback simulations. A new die surface was automatically generated for tryout and a second set of structural panels formed and measured to validate these prediction and morphing technologies.

Future Direction

- The "Holy Grail" of virtual stamping lies in achieving an expanded, integrated, product design-analysis-compensation-formability assessment of virtual product-process-tool design capability. Such a capability remains to be demonstrated for multi-stage forming processes that seamlessly combine the draw-restrike-flange-hemming steps, enabling the computer-aided engineering (CAE) analyst to simultaneously perform formability and springback simulations while utilizing proven CAD-based, die-face modification algorithms in a FEM environment.
- Accompanying such technology development, a cost-benefit analysis should also be performed; comparing cost, quality, and user-effort attributes of the improved simulation and tool-development capability with the conventional (baseline) die build and tryout process.

Introduction

The USAMP AMD 408 DFEP has concluded, culminating with validation of the diverse modules and packages of developed stamping simulation technology on a large structural Common Rail Die automotive component.

In Year 1, the DFEP team identified and classified part categories for which springback was a challenge to predict (e.g., underbody parts), and then conducted new simulations utilizing significant LS-DYNA improvements (developed at vendor expense) and its linked modules. The OEM end-users tested these progressive numerical improvements and identified the attributes of new material models needed to predict optimized tool geometry along with relevant sheet-material formability process parameters. An extensive material-testing and electronic-archival activity was initiated to develop and validate material-property data and specify constitutive models applicable to a wider variety of AHSS sheet grades and Al alloys. A Common Structural Rail Die geometry with challenging features was selected in order to demonstrate technology advances.

In Project Year 2, several test laboratories were contracted to conduct measurements of critical formability and springback properties of AHSS and Al sheet materials being pursued for new vehicle lightweighting initiatives. Material properties determining isotropic and kinematic hardening, such as tension-compression, shear, and bending-unbending, were measured and verified by the team. The resulting datasets were used to develop or refine several new material models for implementation in predictive CAE code. Several CAD vendors were approached with a list of critical requirements for mesh-to-CAD surface morphing that could facilitate NC machining of a die surface.

In Project Year 3, the DFEP team integrated various developed software modules and material models, testing them on parts of increasing complexity such as NUMISHEET benchmark geometries, and later extended the analyses to production automotive parts. Springback-prediction experiments were run to compare baseline simulations with experimental stamped panels of the Common Rail Die. Towards the end of the reporting period, the DFEP team collaborated with one down-selected CAD vendor to evaluate the feasibility of morphing directly from FEA meshes to smooth CAD surfaces, while meeting all NC surface-quality requirements. The Common Rail Die was re-cut to the recommended morphed (compensated) surface and used to stamp new trial panels. Scan data gathered from AHSS and Al panels and compared with the nominal CAD product surface confirmed that significant advances were made in predicting springback and compensation technology. These advances are

currently being evaluated for industrialization in an automotive design environment.

Significant project accomplishments are reported below under each sub-task heading.

Material Testing/Modeling

An extensive design-of-experiment test matrix was assembled by the DFEP team, listing factors thought to influence springback prediction such as: bend/unbend cycles, constitutive equations describing high-bending conditions, change of the elastic modulus as a function of strain state, anisotropy models, etc. The resulting material-modeling and testing phases with AHSS and Al focused on two areas: yield criterion and hardening-law parameter determinations.

Material test laboratories in the United States, Poland, Germany, France and Japan, reputed for possessing domain expertise and proprietary test methodology or equipment, were contracted for characterization, material testing and model fitting. The overarching goal was to develop a combined isotropic kinematic hardening model that, when implemented into NC, could significantly improve springback predictions. A commercial material test capability for meeting these advanced parameter requirements does not presently exist in North America.

For yield criterion areas, uniaxial tension, plane-strain tension, biaxial tension and shear tests were carried out and yield stresses were determined from those tests based on an equivalent-plastic-work concept. The data on yield-surface expansion at large plastic work or plastic strain were also available from those tests. Those yield-surface and associated expansion data can be used to validate any available yield criteria.

For the hardening law, single-cycle tension and compression tests at various strain levels, multiple-cycle tension and compression tests, full-cycle tension and compression test, strain-memory tension and compression tests, prestrained-tension and compression tests were carried out using the best testing technology available. Material-model parameters for Chaboche and Yoshida combined isotropic and kinematic hardening laws were determined and validated using those test data. A new, modified Yoshida model was also developed based on the unique hardening behavior of AHSSs, and the material model parameters were also determined. The model was implemented in the LSTC DYNA code, and was used in validating the Common Rail Die springback simulations.

Numerical Code Development

The following new numerical solution approaches and features were proposed and evaluated by the DFEP team:

- Conducted extensive benchmark testing of new, smooth-contact algorithms for improving geometric description of the products and springback predictive accuracy in FEM. The effect of the number of elements on the tooling radius was studied using benchmark parts. Other studies have involved using different contact scale factors combined with initial coarse mesh, initial coarse mesh with smooth contact, and initial fine mesh with smooth contact.
- New shell-element formulations were evaluated which had indicated high potential in improving forming simulation and springback prediction, especially in regions with small radius. This work may also be valuable in extending the analysis techniques to secondary forming steps such as hemming and flanging.
- The team conducted modeling tests on a new element with improved through-thickness stress variations that could help improve springback prediction.
- Three new material models were formulated and implemented in the code with preliminary testing completed on benchmark parts.

The general conclusions of the NC validation effort were:

- Material hardening rule: For Al, the standard Yoshida kinematic hardening model is recommended, while for AHSS, the modified Yoshida model is recommended.

- Smooth contact reduced the computational "noise" introduced by regular contact treatment in part-process-formability simulations.
- Fully-integrated shell element with thickness stretching reduced the twisting, but it also simultaneously suppressed the side-wall curl in the springback prediction of Common Die. This element formulation has the potential to improve the overall accuracy, and further research is suggested in the future.
- Selective mass scaling can speed up the springback computation without affecting the result and is recommended.

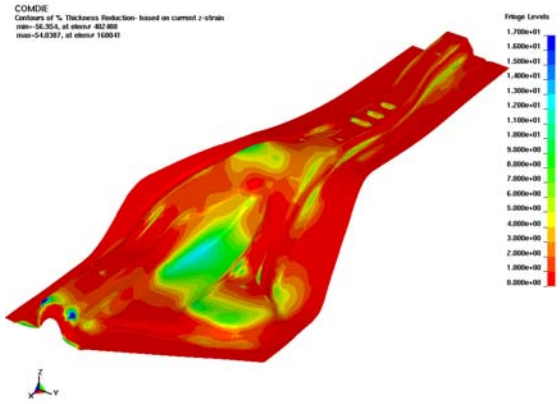

Figure 1. Thinning map of DP600 full rail model predicted with new numerical technologies.

Surface Development

The goal of the DFEP Surface Technology development tasks was to assist the CAE/Stamping Development engineer to rapidly and robustly translate CAE die design (or modification information) directly into CAD data that can be used in machining dies. Recent highlights are discussed below:

- Based on the team's assessment of the most promising, production-friendly, morphing capability, during the second phase of CAD Surface R&D, the team worked with one down-selected vendor to continue more detailed evaluations of algorithmic, surface-quality and computational-efficiency improvements to commercial mesh-to-CAD software. Seven automotive parts were tested in this phase.

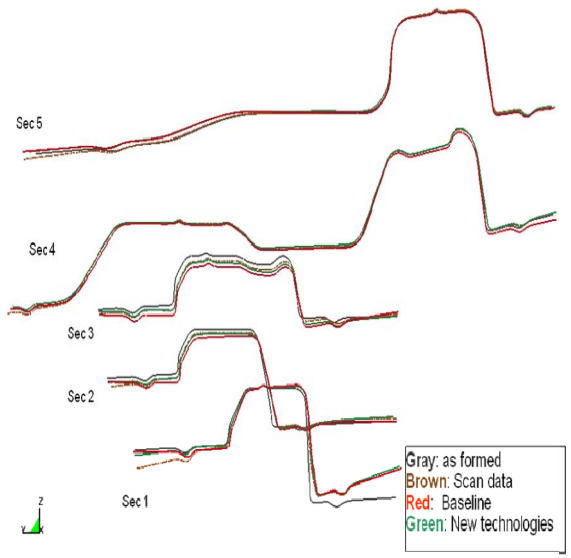

Figure 2. Section comparison of springback of formed part between new technologies and baseline.

Finally, the prototype-morphing technology was applied to the compensated FEM model of the Common Rail Die geometry, and resulting CAD surface used to NC re-cut the die-face prior to stamping trials.

Field Validation

A verification run of the compensated die was conducted using new simulation technology features and compared with stamping trials as shown in Figure 1 (thinning map). Figure 1 shows the thinning map of dual-phase (DP) 600 full panel formed with a compensated die.

Scan comparison of five scanned trim panels (for compensated mesh to design-intent surface of die) indicated that, while there are minor deviations between trim panel scans and design-intent, the comparisons are quite good. Figure 2 shows these deviations across several cross-sections of the Common Rail.

Figure 3 shows the predicted deviation between the trimmed sprung Common Rail part and the design-intent (nominal) part. The maximum deviation is 7.5 mm.

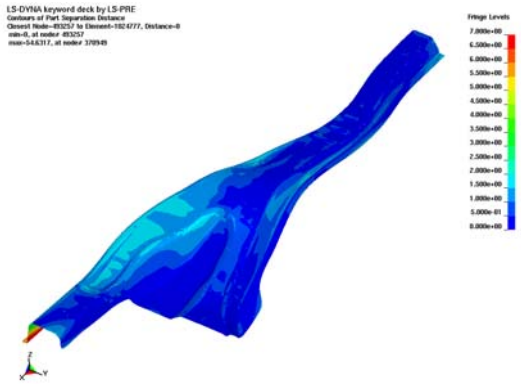

Figure 3. Predicted deviation between the trimmed sprung common-rail part and the design-intent (nominal) part.

Conclusion

Over the three-year DFEP project, the USAMP Team performed a series of comprehensive material testing with new AHSS and Al sheets, as well as mesh-to-surface morphing and numerical modeling studies which were further validated by the OEM/supplier team on a focus structural component. New numerical solution approaches were formulated and evaluated (such as smooth contact), while some existing material modeling theories were modified (such as the modified Yoshida non-linear kinematic hardening model). All new technology improvements were implemented in commercial simulation code LS-DYNA®. The validation and industrialization studies performed by the OEM partners indicate the springback prediction accuracy has been significantly improved, the results are more robust, and the dependence of prediction results on the user experience has been greatly minimized.

[i] Denotes project 408 of the Automotive Materials Division (AMD) of the United States Automotive Materials Partnership (USAMP), one of the formal consortia of the United States Council for Automotive Research (USCAR, see www.uscar.org) set up by Chrysler, Ford and General Motors to conduct joint, pre-competitive research and development.

D. Electromagnetic Forming of Aluminum Sheet

Principal Investigator: Richard W. Davies
Pacific Northwest National Laboratory (PNNL)
P.O. Box 999, Richland, WA 99352
(509) 375-6474, fax: (509) 375-5994, e-mail: rich.davies@pnl.gov

Technical Coordinator: Sergey Golovashchenko
Ford Motor Company
Ford Research Laboratory, Dearborn, MI 48121-2053
(313) 337-3738, fax: (313) 390-0514, email: sgolovas@ford.com

Technology Area Development Manager: Joseph A. Carpenter
(202) 586-1022; fax: (202) 586-1600; e-mail: joseph.carpenter@ee.doe.gov

Expert Technical Monitor: Philip S. Sklad
(865) 574-5069; fax: (865) 576-4963; e-mail: skladps@ornl.gov

Participants:
Nick Bessonov, EMF Simulations, University of Michigan-Dearborn
Jeffrey Johnson, EMF System and Control, PNNL
Jeffrey Bailey, EMF Capacitor Bank Control, PNNL
Vladimir Dmitriev, EMF R&D, Ford Motor Company

Contractor: PNNL
Contract No.: DE-AC06-76RL01830

Objective

- The purpose of this project is to develop electromagnetic-forming (EMF) technology that will enable the economic manufacture of automotive parts made from aluminum (Al) sheet. EMF is a desirable process because the dynamic nature of the deformation results in benefits including increased forming limits and reduced springback. These benefits would result in increased use of Al and, therefore, more fuel-efficient vehicles due to mass reduction.

Approach

The project will address three main technical areas:
- Analysis methods for forming-system design
- Development of durable actuators (coils)
- Industrial embodiment of the EMF process

Accomplishments

- Completed installation and operational qualification of new EMF power supply for the PNNL coil-durability test equipment that will provide faster capacitor-charge time and allow increased coil-cycle rates.
- Completed fabrication of EMF tooling for component-forming demonstrations, and demonstrated initial forming capabilities with a Ford-developed component. Initiated coil modifications to enhance durability.
- Completed modeling and experimental validation of the EMF process using three-turn coil and simulated Al forming blank. Modeling simulations of coil current as a function of time correlate well with experimental measurements.

- Completed documentation of major EMF modeling-code elements and initiated evaluation of code parallelization approaches for reduced model run times.
- Initiated conversion of the code to run on a Unix-based platform and established a follow-on subcontract effort for this code development with Oakland University.

Future Direction

- Continue to develop a modified EMF model code to run on Unix-based parallel-cluster workstation, and evaluate parallelization of code elements for reduced run time.
- Document EMF modeling code and develop enhanced user interface.
- Continue to investigate the industrial embodiment of EMF systems for automotive manufacturing.

Introduction

In the electromagnetic-forming (EMF) process, a transient electrical pulse of high magnitude is sent through a specially-designed forming coil by a low-inductance electric circuit. During the current pulse, the coil is surrounded by a strong, transient magnetic field. The transient nature of the magnetic field induces current in a nearby conductive workpiece that flows opposite to the current in the coil. The coil and the workpiece act as parallel currents through two conductors to repel one another. The force of repulsion can be very high, equivalent to surface pressures approximately tens of thousands of pounds per square inch. Thin sheets of material can be accelerated to high velocity in a fraction of a millisecond.

A recent interest in understanding the electromagnetic forming of metals has been stimulated by the desire to use more Al in automobiles. The high workpiece velocities achievable using this forming method enhances the formability of materials such as Al. In addition, the dynamics of contact with the forming die can help reduce or mitigate springback, an undesired effect that cannot be avoided in other forming techniques such as stamping. The commercial application of this process has existed since the 1960s. The large majority of applications have involved either the expansion or compression of cylinders (tubes). The forming of sheet materials is considerably more complex and receives relatively little attention.

Approach

The project addresses three main technical areas. The first technical area involves establishing analysis methods for designing forming systems. These methods will be based on developed knowledge of forming limits and relations between electrical-system characteristics and deformation response for specific Al alloys of interest. The second area of technical challenge is in coil durability. Existing knowledge of electromagnetic forming and relevant knowledge from pulsed-power physics studies will be combined with thermo-mechanical analyses to develop durable coil designs that will be tested experimentally. Finally, the third technical area involves the industrial embodiment of the EMF process. In this project, EMF is expected to be hybridized with conventional sheet-metal stamping. Different approaches to hybridization will be analyzed for issues affecting the economic implementation in a modern stamping plant. Different system concepts will be developed and studied. Existing knowledge of the EMF process and technical achievements in this project will be combined to establish a methodology for designing hybrid-forming systems that can be readily integrated into modern manufacturing facilities for the economic production of automotive sheet-Al components. Some of the project focus areas and results are discussed in the following sections.

PNNL EMF System

The EMF system at PNNL has been operational since 2001. The system is typically operating at 6,500 V and current levels in excess of 225 kA have been demonstrated. Figure 1 shows a typical response of the EMF system during a 15 kJ discharge of the capacitor bank. The figure shows that the half-current (measuring half the total system current) of the system is approximately 86 kA, so that a total current of 172 kA passed through the load coil within 26 μs.

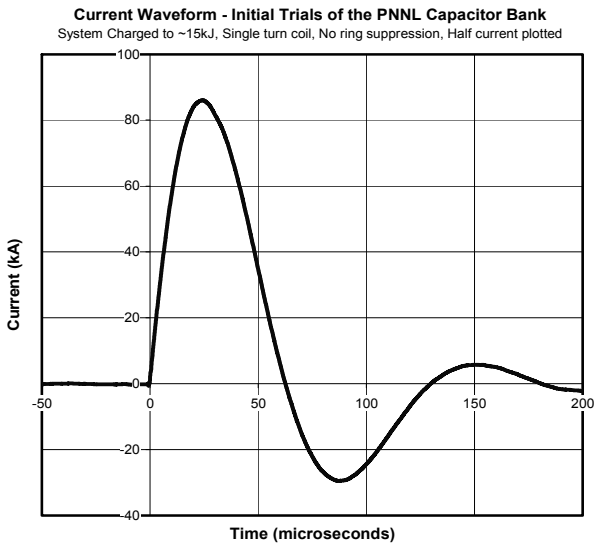

Figure 1. Typical EMF system waveform.

The system has also been cycled several thousands times at high current levels while supporting our coil-durability experimental work. The custom-designed control system was successfully demonstrated in automated, cyclic-loading operating modes. In the second half of fiscal year (FY) 2007, a new power supply was installed and operationally validated. The power supply has significantly faster charge-rate capacity, which will allow faster recharging of the capacitor banks and will allow coils to be fired at higher cycle rates. This will reduce the experimental run times required to test coil designs for coil durability.

Coil Design Concepts and Durability

During EMF, the high-intensity electromagnetic forces are applied to the turns of the coil. The coil, insulators and support structure must resist these forces, as well as related thermal cycles, without significant permanent deformation or material failure. In contrast to typical cylindrical coils, sheet forming will require coils with general three-dimensional shapes that are inherently less resistant to forces induced during forming. The key issues involve materials selection and design. Materials must be selected for both electrical conductivity and mechanical properties, and they must lend themselves to manufacturing. Materials may also need to be compatible with the presence of coolants and the forces generated during hybrid forming that combines conventional stamping and EMF. The design must integrate these elements while delivering the primary function of a spatial and temporal load distribution that achieves the desired deformations. Coil systems will have to be low-cost, modular, and have high durability (nominally 100,000 cycles) if they are to be relevant to automotive manufacturing.

The PNNL coil-durability experiments in the second half of FY2007 focused on increasing the frequency of capacitor discharge to simulate high-repetition rate of automotive manufacturing. PNNL has increased the charge rate of the capacitor bank and refined the control system to achieve cyclic-discharge rates to fewer than 10s. This has allowed the project team to evaluate the structural performance of the coil and to understand the effect of coil operating temperature.

The second half of FY 2007 was primarily spent on further development of an EMF-process simulation tool. This predictive EMF-process simulation tool will allow us to design the process by predicting the EMF field, stresses and strains in the blank, and the temperature distribution in the coil. Another focus area was the continued development of the flat-coil design. Improvements were made to both simplify and lower the cost of the manufacturing of flat coils. Furthermore, the packaging of the flat-coil assembly has been improved for robustness and ease of handling. Efforts have been initiated to modify the code to run on Unix-based workstation clusters and to investigate advantages in parallelizing the code for faster run times.

Results of Numerical Simulation of EMF Process

The EMF process is challenging to simulate due to the need to simultaneously model electromagnetic, thermal, and elastic-plastic deformation of materials. Many of the commercial research codes have serious limitations and an inability to predict the results of EMF processes accurately. This project originally focused on integrating portions of existing commercial research codes to predict the important characteristics of a three-dimensional EMF process accurately. However, work that is more recent has focused on more accurate, custom, process simulations. The current modeling work involves collaboration with Dr. Nick Bessonov, in cooperation with Oakland University and Dr. Sergey Golovashchenko at Ford.

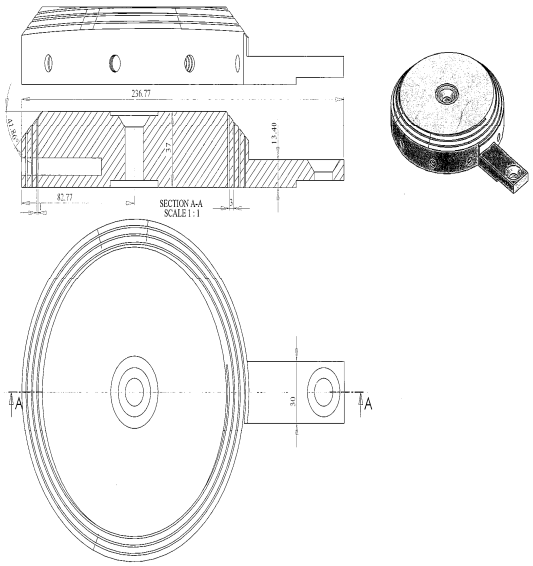

Figure 2. Design of the three-turn coil.

To validate the capability and accuracy of the code, simulations were run of a three-turn coil forming Al sheet. The design of the coil is shown in Figure 2, and the geometry for the coil and Al-sheet blank is shown in Figure 3. The numerical mesh for modeling the coil and the blank are shown in Figures 4 and 5. Based on actual EMF experimental parameters, forming of the Al blank using the 3-turn coil was simulated and experimentally validated. Key measure of the simulation accuracy is to evaluate coil current as a function of time with and without simulation of the Al-sheet blank. In Figure 6, the comparison of experimental curves and numerical results is shown for voltages of U_0=5kV, 7kV and 9kV with and without the blank positioned on top of the coil at the distance of 1 mm.

Correlation of the results is similar to the case when the discharge was produced without the blank. Comparing the duration of the discharge with and without the blank (Figure 6), it was observed from both experimental and numerical curves that with the blank the period of discharge was shorter, while the amplitude of current was larger. These results served as an indication that the numerical model predicts the inductance of the coil-blank system reasonably accurately. Therefore, analysis of the blank deformation should also produce appropriate results.

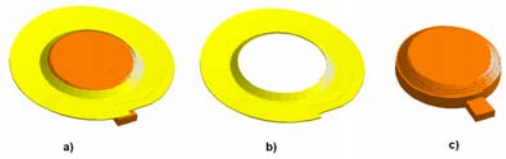

Figure 3. The geometry for the coil and the blank.

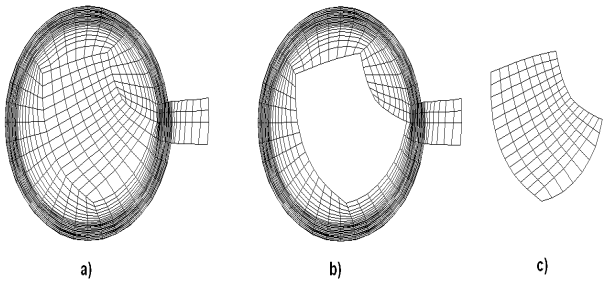

Figure 4. The mesh for the coil is a combination of two meshes b) and c).

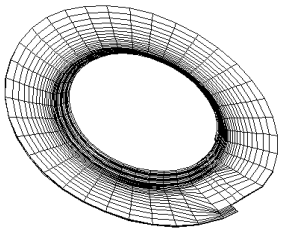

Figure 5. The mesh for the Al-sheet blank.

Additionally, EMF-modeling work has focused on improving the modeling code computational efficiency, documenting and enhancing the user operations and interface. To improve computational

efficiency, work has been directed at conversion of the operating system to a Unix-based system, which will allow future parallelization of the code. Additional efforts at Oakland University are focused on documenting the user inputs, automating several of the iterative steps and inputs for the code to improve the user interface. Documentation of the code's operating principles, input requirements, and operational assumptions has been, and will continue to be, documented over the remainder of the project effort.

Conclusions

This work has developed numerical models that describe three critical elements of the EMF process: 1) propagation of the electromagnetic field through the coil-blank system and generation of pulsed electromagnetic pressure in specified areas, 2) high-rate deformation of the blank and, 3) heat accumulation and transfer through the coil with an air-cooling system. The process models provide capability to analyze EMF restrike processes from the perspective of coil design, blank deformation, and cooling systems for the coil.

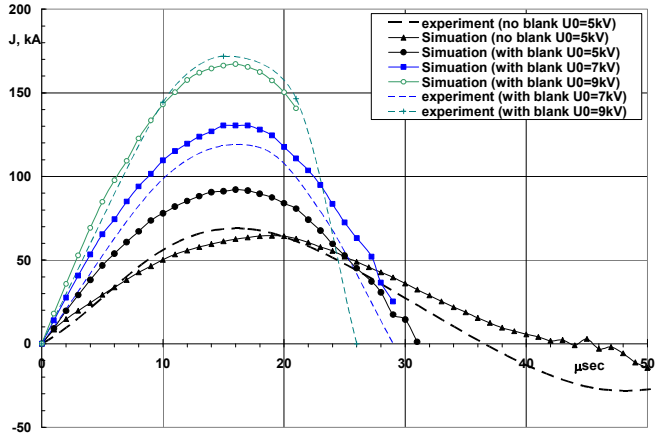

Figure 6. Results of 3-turn coil simulation and experimental validation. Current in the coil vs. time with and without blank.

E. Ultra-fine Grained Foils and Sheets by Large-Strain Machining Processes

Principal Investigator: S. Chandrasekar
Purdue University
West Lafayette, Indiana
(765) 494 3623; e-mail: chandy@ecn.purdue.edu

Principal Investigator: Mark T. Smith
Pacific Northwest National Laboratory (PNNL)
P.O. Box 999, Richland, WA 99352
(509) 375-4478; fax (509) 375-4448; e-mail: mark.smith@pnl.gov

Technology Area Development Manager: Joseph A. Carpenter
(202) 586-1022; fax (202) 586-1600; e-mail: joseph.carpenter@ee.doe.gov

Expert Technical Monitor: Philip S. Sklad
(865) 574-5069; fax: (865) 576-4963; e-mail: skladps@ornl.gov

---

Contractor: PNNL
Contract No.: DE-AC06-76RL01830

Objective:

- The goal of this project is to demonstrate the feasibility of producing magnesium (Mg) sheet and shaped products having superior formability and strength properties through the application of severe plastic deformation developed by large-strain extrusion machining and peeling techniques. The resulting microstructure and properties of the ultra-fine grain (UFG) and nano-grained Mg alloys will be characterized for mechanical properties and formability, and the commercial economics of the process will be evaluated. The benefit of the project will be the demonstration of processing techniques that can be used economically to produce Mg sheet materials and shapes with significantly enhanced strength and formability.

Approach:

- Establish the process and tooling capabilities for Large-Strain Extrusion Machining (LSEM) and Peeling in the context of creating bulk foil/sheet from Mg alloys. Specific attention will be paid to design of process conditions (e.g., pre-heating of sample, avoiding shear localization) to realize continuous-chip formation.
- Carry out preliminary optimization of process conditions for foil/sheet production.
- Characterize the hardness and microstructure of the foil/sheet as a function of strain using Vickers indentation, nano-indentation, optical microscopy and transmission electron microscopy (TEM). Microstructure characterization will involve examination of grain size and dislocation substructures. Note: Uniaxial strength measurements and Electron Backscatter Diffraction (EBSD) characterization (for grain-size distribution) will be done at PNNL.
- Identify the best processing conditions based on the property and microstructure characterization.
- In conjunction with PNNL, assess process scale-up, conduct cost-analysis and suggest guidelines for process development for specific automotive applications.

Accomplishments

- This new project began at the end of fiscal year 2007. It will continue into FY 2008. PNNL has initiated a subcontract with Purdue University to conduct the large-strain extrusion machining (LSEM) and Peeling experimental processing of two Mg alloys. In addition, PNNL is procuring Mg feedstock materials to support the Purdue experimental efforts.

Future Direction

- Purdue University will process samples of two Mg alloys using the LSEM and Peeling processes, and will characterize microstructural features. Samples of the large-strain-processed materials will be supplied to PNNL for grain-size and mechanical-property evaluations. PNNL and Purdue will develop a cost model for scale-up of the process at the conclusion of the project.

Introduction

Shear strains in the range of 1-10 can be imposed in a variety of materials, including those of moderate to high initial strength, in a single pass of a machining operation. Two variants of the chip-formation process—Large-Strain Extrusion Machining (LSEM) and Peeling - appear to be particularly attractive for the direct production of foil and sheet with UFG microstructures. *Peeling* is removal of material in the form of a strip (chip) with superimposed tension applied to the chip. The strain and, hence, the microstructure of the resulting strip are controlled by the tool rake angle and applied tension. LSEM combines microstructure refinement by large-strain machining with simultaneous shape and dimensional control of the chip by ‘extrusion’.

Publications/Presentations/Patents

None in FY 2007.

F. Aluminum Automotive Closure Panel Corrosion Test Program (AMD 309[i])

Project Co-Chair: Tracie Piscopink-Jafolla
General Motors Corporation
3300 General Motors Road
MC: 483-370-101
Milford, MI 48380-3726
(248) 676-7014; Fax (248) 685-5279, e-mail: tracie.l.jafolla@gm.com

Project Co-Chair: Francine Bovard
Alcoa Technical Center
100 Technical Drive
Alcoa Center, PA 15069
(724) 337-3249; fax (724) 337-2044, e-mail: tracie.l.jafolla@gm.com

Technology Area Development Manager: Joseph A. Carpenter
(202) 586-1022; fax: (202) 586-1600; e-mail: joseph.carpenter@ee.doe.gov

Field Project Officer: Aaron D. Yocum
(304) 285-4852; fax: (304) 285-4403; e-mail: aaron.yocum@netl.doe.gov

Expert Technical Monitor: Philip S. Sklad
(865) 574-5069; Fax (865) 576-4963; e-mail: skladps@ornl.gov

Contractor: United States Automotive Materials Partnership (USAMP)[i]
Contract No.: DE-FC26-020R22910 through the DOE National Energy Technology Laboratory

Objective

- Develop a standardized cosmetic corrosion test for finished aluminum (Al) automotive body panels that provides a good correlation with in-service testing and field performance.

Approach

- Conduct laboratory testing, outdoor exposures, test-track exposures and in-service testing.
- Evaluate test data to determine which accelerated tests correlate with in-service testing.
- Conduct iterative laboratory testing to improve correlation between lab tests and on-vehicle exposures.

Accomplishments

- Multiple iterations of laboratory tests, test-track exposures and outdoor exposures have been completed.
- On-vehicle tests have been exposed for nearly four years.
- Corrosion-product analyses have been conducted for some laboratory tests and for two-year, on-vehicle exposures.
- Three key parameters have been identified for replication of on-vehicle corrosion:
  1. Relative ranking of substrates based on extent of corrosion observed.
  2. Corrosion morphology of localized blisters along scribe line with some filiform at leading edges.
  3. Sulfur in the corrosion products.

Future Direction

- Modifications of the more promising accelerated laboratory tests are being evaluated in an effort to find a lab test with improved correlation to on-vehicle exposure results in terms of the extent and morphology of the corrosion as well as the composition of the corrosion products. On-vehicle exposures will continue until the panels have been exposed on vehicles for four years.

Introduction

Although Al closure panels have been used on numerous vehicles for several years, the degree of confidence in predicting service performance has not been high due to the lack of an accelerated corrosion test that mimics field performance. Automotive manufacturers and their suppliers often rely on accelerated corrosion tests that were developed for evaluating steel, but these tests are not always consistent with in-service Al closure-panel performance.

In order to address the need for an accelerated Al corrosion test, a group comprised of representatives from the US automotive manufacturers, Al suppliers, coating suppliers, and other associated suppliers was formed in 2000. The goal of this group has been to identify and implement a standardized accelerated corrosion test for cosmetic corrosion of Al that exhibits the same appearance, severity, and corrosion products that are exhibited on in-service Al components. This report provides an update on the efforts of this group.

Experimental

Materials

In 2001, the first step in the development of a new cosmetic corrosion test occurred with the establishment of a reservoir of painted panels. These panels would then be used in the subsequent evaluation of all test methods. As listed in Table 1, the substrate- materials, metal-finish and paint-processing variables were selected to give a range of cosmetic corrosion performance. Several Al alloys used in the Unites States and in Europe, both current and historical, were included. Electro-zinc-coated steel and uncoated cold-rolled steel were included as reference materials. Two Al alloys were processed to simulate metal finishing in an automotive assembly plant body shop. Two sizes of panels, 2" x 4" and 4" x 6", of each of the materials were painted with a typical automotive paint system. This paint system included zinc phosphate pretreatment, medium-build cathodic electrophoretic priming (E-coating), and spray painting with a primer surfacer and white basecoat/clear topcoat system for a total paint film thickness of approximately 100 μm. One set of alloy 6111 panels (Panel Code B) was processed through the phosphate pre-treatment with lower fluoride concentration (comparable to the fluoride level used for steel only vehicles which results in lower phosphate coating weight). Also, since qualification testing is often done on panels that are processed only through the electrophoretic primer (E-coat) step, another set of alloy 6111 panels (Panel Code C) was processed only through the E-coat step (i.e., standard fluoride for Al but no basecoat or clear-coat applied). Panel code C was evaluated in accelerated tests only (no on-vehicle or proving- ground exposures).

Table 1. Materials.

Panel Code	Alloy Substrate	Metal Finish	Paint System
A or 1	AA6111-T4PD	Mill	Standard
B or 2	AA6111-T4PD	Mill	Low F
C or 3	AA6111-T4PD	Mill	Ecoat Only
D or 4	AA6111-T4PD	Sanded	Standard
E or 5	AA6016-T4	Mill	Standard
F or 6	AA6022-T43	Mill	Standard
G or 7	AA2036-T4	Sanded	Standard
H or 8	EG 60 Steel	Mill	Standard
I or 9	Cold-Rolled Steel	Mill	Standard

Panels were prepared as needed for testing with two parallel scribes penetrating through the coatings to the substrate. The panels were provided to the testing laboratories as fully-prepared painted and scribed panels. Triplicate sets of the painted and scribed samples have been exposed in a variety of environments, including laboratory, static outdoor exposure, proving-ground, and on-vehicle tests.

Evaluation Method

For this study, an optical imaging system developed by Atlas Material Testing Technology LLC was employed to quantitatively interpret the degree of cosmetic corrosion. The imaging system employs controlled illumination conditions, high-resolution digital image capture and advanced algorithm-based image- and data-analysis methodologies. [1].

Four geometrical attributes of the cosmetic corrosion were measured: area of corrosion, maximum length, minimum length and average length. The area of corrosion was found to be the most representative and comprehensive measurement. Because the size of the panels and therefore the scribe lengths for the lab tests were

different from the other tests, the corrosion area was normalized to the length of the scribe (i.e., area per length). The normalized corrosion areas for triplicate panels (2 scribes per panel) were then averaged and the results are reported as "normalized average area."

On-Vehicle (In-Service) Exposures

It is critical when developing a laboratory-based test that test-to-field correlation be performed. In an effort to capture real-world data in developing this test, it is necessary to expose these panels to severely corrosive environments that represent "worst case" real-world service environments. Suitable environments exist in the northeastern United States, southeastern coastal areas of the United States, and southeastern Canada. The five sites selected for this study were: 1.) Detroit, Michigan; 2.) Florida; 3.) St. Johns, Newfoundland; 4.) Montreal, Quebec; and 5) an Ohio-to-New York Truck Route.

Two sets of 2" x 4" test panels are exposed on each vehicle (two vehicles per site). Each set of 24 (three each of eight material variables) are attached to a mounting panel (16" x 12") using double-backed tape prior to mounting on the vehicle. At the Detroit, St. Johns, and Montreal sites, one set is mounted on the hood of each vehicle (horizontal orientation) and one set on the right front door of each vehicle (vertical orientation). At the Florida and Ohio-New York sites, the panels are mounted beneath the trailer frame behind the front wheels (vertical orientation only). Each panel contains 2 diagonal scribe lines which are 2" long and 1" apart. The panels will be exposed for a total of 5 years of in-service exposure. Intermediate evaluations will be conducted when possible.

Laboratory Tests

Several rounds of laboratory testing have been conducted to date. A list of the accelerated laboratory tests that were evaluated and reported previously is given in Table 2.

Table 2. Laboratory Tests Evaluated and Reported Previously.

Test Procedure	Exposure (s)
SAE J2334	40, 60 & 80 cycles
GM 9540P	40, 80 cycles
Ford APGE	35 & 70 cycles
ASTM D2803 (50,80 & 100% RH)	6 weeks
ASTM G85 Annex 2	3 weeks
VDA 621-415	10 cycles / 70 days
ASTM B117	500 & 1000 hours
CCT IV	70 cycles
HCl Dip	8 weeks
KWT	6 weeks
Ford APGE (Manual & Automated Humidity Cycle)	70 cycles
ASTM G85 Annex 2	1 & 2 weeks
HCl Dip	3 & 6 weeks
ASTM G87	20 cycles
ASTM G85 Annex 4	500 hours
ASTM G85 Annex 5	500 hours
GM9511P	4 weeks
GM9682P	4 weeks

In 2007, the following laboratory tests were conducted:

- Repeat of American Society for Testing and materials (ASTM) G85-A4 [2] - Constant salt-spray test acidified by periodic introduction of SO_2.
- GM9511P [3] - GM Scab Test 60C/85%RH exposure with daily cycles of neutral NaCl immersion and weekly cycles of thermal shock to -25^{o}C
- GM9682P [4] - GM wheel filiform test w/ 6hr CASS + 4 weeks @60^{o}C and 85% relative humidity (RH) (CASS = 5%NaCl + 0.25g $CuCl_2 \cdot H_2O$ acidified with acetic acid)
- Modified ASTM G85-A2 [5] - Cyclic spray/RH test with acidified (acetic acid) NaCl with following modifications:
  - substitute H_2SO_4 for acetic acid
  - pH of 3.5 or 5.0
  - add 0.1% $CaCl_2$
- Modified ASTM G85-A4 [3] - Constant salt-spray test acidified by periodic introduction of SO_2 with the following modifications
  - substitute H_2SO_4 for SO_2
  - pH of 3.5 or 5.0 (two tests)
  - add $CaCl_2$

Corrosion-Product Analysis

Corrosion-product analysis was performed on selected panels to determine the extent of cosmetic corrosion and its morphology, and the composition of the corrosion products. For the top-down analysis of the corrosion products, the paint layer was stripped in 1-methyl-2-pyrrolidone solvent. Water was not used during the stripping procedure so as to preserve any chloride/sodium species present within the corrosion product.

The panels were examined using a Leo 440 scanning electron microscope (SEM) equipped with a Quartz XOne energy-dispersive X-ray (EDX) analysis system. SEM/EDX technique was chosen for this examination because the amount of corrosion product on Al closure panels is very small, making more traditional analytical procedures impractical. In addition, the use of SEM/EDX allows not only for a measurement of the chemical species present, but also for an analysis of the distribution of these species in and around the corroded area on the panel.

Results and Discussion

On-Vehicle Results

A consistent result from the on-vehicle exposures conducted to date is that panels D, G, and I exhibit more corrosion than the other substrates, as illustrated by the images in Figure 1.

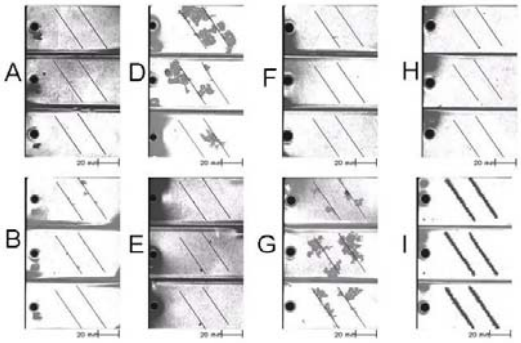

Figure 1. Images of the 3 replicate panels of each substrate from a Detroit On-Vehicle Test with ~2 Years Exposure.

The Al panels with metal finishing (D & G) generally have more corrosion than the other Al substrates and cold-rolled steel (I) has more corrosion than the electro-galvanized (EG) steel (H). The normalized average area from on-vehicle service relevant exposures in Detroit, Montreal and the Ohio-New York Truck route are plotted in Figure 2. Based on these two-year, on-vehicle results, accelerated tests that show a significant difference between the substrates with metal finishing (i.e., sanding) and those without metal finishing are candidates for further investigation. After the first round of testing, the APGE (one lab only), ASTM G85-A2 test and HCl dip tests appeared to show the expected differences on panels with metal finishing.

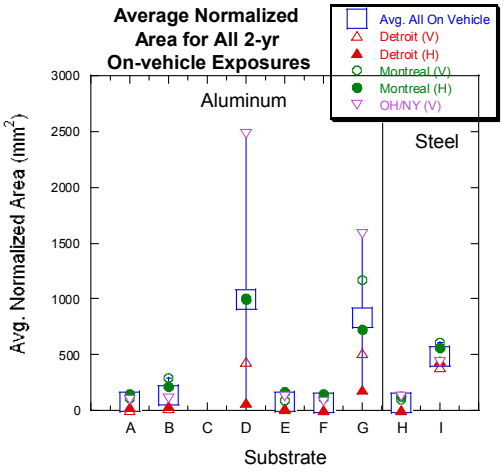

Figure 2. Normalized average area for on-vehicle exposures after two years.

In addition to comparing the extent of corrosion from the accelerated tests to on-vehicles results, the corrosion morphology was also examined. Figure 3 shows the corrosion morphology found on substrates A, D, and I that were exposed in Montreal. The corrosion on Al is not continuous along the scribe as it is for steel.

Substrate A AA 6111 | Substrate D Sanded AA 6111 | Substrate I CRS

Figure 3. Images of corrosion on panels exposed in Montreal.

Figure 4 shows the morphology of corrosion on substrate D from the three previously evaluated accelerated tests – ASTM G85-A2, HCl Dip, and APGE. The morphology of the corrosion produced in ASTM G85-A2 and the HCl Dip tests occur more uniformly along the scribe line than is typically observed in on-vehicle exposures.

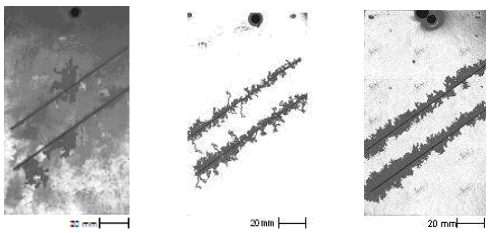

APGE 70 cycles | HCl Dip 8 weeks | ASTM G85-A2

Figure 4. Images of corrosion on substrate D after accelerated corrosion testing.

The morphology of the corrosion produced from APGE is closer to that found on the on-vehicle panels, but only one out of four laboratories running the test were able to produce those results.

Corrosion products were examined on Al and steel panels from three different on-vehicle exposures (St. Johns, Detroit and Montreal). SEM/EDX and x-ray photoelectron spectroscopy (XPS) analyses were performed at several areas on each panel. The results of this examination were reported previously.

The corrosion-product analyses for two-year on-vehicle exposures can be summarized as follows;

- St John's – Sulfur detected in the corrosion products on all three Al panels examined (A, D, G). Chloride detected on panels D & G.
- Montreal – Chloride detected in the corrosion products of all panels examined. Little or no sulfur present in the corrosion products.
- Detroit – Chloride and sulfur found in the corrosion products of the Al panels (A, B, D). Chloride only found in the corrosion products on steel.

Therefore, based on the two-year, on-vehicle results, the following criteria have been used to evaluate the correlation with accelerated lab test results:

- Relative Ranking of Extent of Corrosion
  - D,G > I >> B > A,E,F,H.
- Composition of Corrosion Products
  - In addition to usual species, sulfur should be present.
- Morphology of Corrosion
  - Blisters with filiform on leading edge
  - Sporadic sites along scribe line unlike the relatively uniform creepback typically observed on CRS.

Laboratory Test Results

After observing the sulfur in the corrosion products from the on-vehicle exposures, the task group investigated three existing accelerated corrosion tests that included sulfur in the exposure: ASTM G85-A4, ASTM G85-A5 and ASTM G87. The differences in the exposures are summarized below.

ASTM G85-A4 – Continuous NaCl spray with intermittent SO_2 gas

ASTM G87 – SO_2 and humidity (no NaCl)

ASTM G85-A5 – NaCl, $(NH_4)_2SO_4$ fog

In ASTM G85-A4, significant corrosion occurred on most of the panels while very little corrosion occurred from exposure to ASTM G87 or ASTM G85-A5 as illustrated in Figure 5. Although relative to the two-year, on-vehicle exposures, ASTM G85-A4 over-predicted the corrosion for most substrates (A, B, E, F and H). The test results indicate that an addition of SO_2 gas to a neutral NaCl salt-spray exposure accelerates the corrosion of Al significantly. Exposure to SO_2 and humidity in the absence of NaCl in the ASTM G87 test, however, did not accelerate the corrosion on the Al panels D and G and, therefore, does not appear to correlate with the on-vehicle results. Likewise, the presence of dilute ammonium sulfate in the ASTM G85-A5 test did not accelerate the corrosion on the Al panels D and G and, therefore, does not appear to correlate with the on-vehicle results.

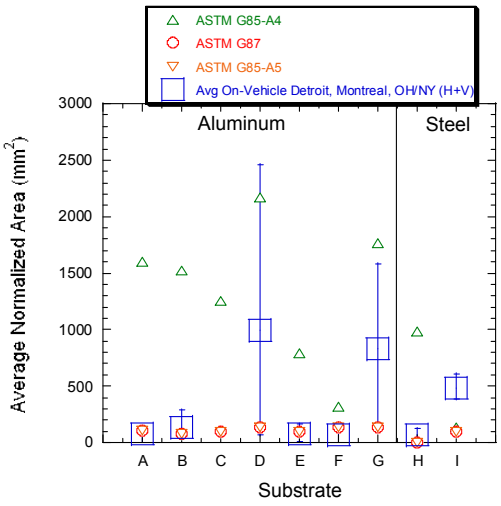

Figure 5. Average normalized area of corrosion for sulfur-bearing ASTM lab tests ASTM G85-A4, ASTM G85-A5, and ASTM G87 and for on-vehicle exposures.

Sections from panels A, D, G and I exposed to ASTM G85-A4 test were examined using the SEM/EDX technique to determine the corrosion product morphology and its composition. Figure 6 presents the backscattered electron micrographs of the representative corroded regions from these panels. The letters on each micrograph identifies the panel and the numbers present the locations where the corrosion product chemistry data has been reported in Table 3. In addition to these spot analyses, detailed elemental distribution maps (not presented in this report) from various locations of interest were also collected.

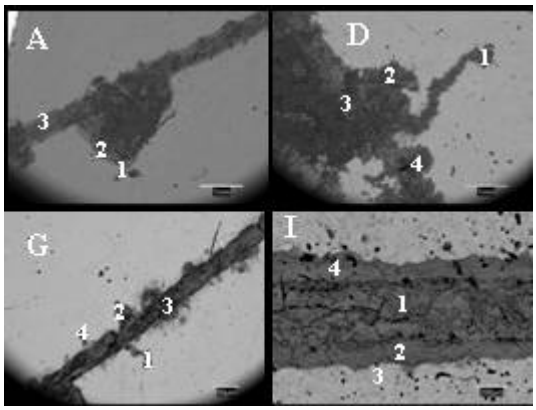

Figure 6. Backscattered electron micrographs of the representative corroded regions from four panels exposed to ASTM G85-A4 test. The numbers on these figures indicate the locations where corrosion product chemistry data has been reported in Table 3.

Table 3. Corrosion Product Composition (wt.%) for Panels Exposed to ASTM G85-A4 Test.

Panel ID	Area Analyzed	Elements Detected (Wt. %)				
		O	Na	Al	P	S
A	Spot 1	55.9		32.5	2.5	0.9
	Spot 2	73.8		92.6		
	Spot 3	25.4		71.4		2.9
D	Spot 1	33.5		40.7	5.1	
	Spot 2	48.4		26.3	6.8	0.2
	Spot 3	45.4		37.6	0.6	5.7
	Spot 4	39.3	1.4	19.9	13.7	2.3
G	Spot 1	33.5		40.7	5.1	
	Spot 2	48.4		26.3	6.8	0.2
	Spot 3	45.4		37.6	0.6	5.7
	Spot 4	39.3	1.4	19.9	13.7	2.3
I	Spot 1	31.2				4.9
	Spot 2	24.8			2.5	1.8
	Spot 3	13.0			4.6	
	Spot 4	24.7		0.3	1.3	1.9

Table 3. (continued) Corrosion Product Composition (wt.%) for Panels Exposed to ASTM G85-A4 Test.

Panel ID	Area Analyzed	Elements Detected (Wt. %)				
		Cl	Mn	Fe	Cu	Zn
A	Spot 1	1.3	0.5			6.5
	Spot 2					
	Spot 3					
D	Spot 1	15.0			1.2	4.5
	Spot 2	2.0	3.0	0.1		13.2
	Spot 3	4.1			6.3	
	Spot 4	14.0	2.4	0.3	0.6	6.2
G	Spot 1	15.0			1.2	4.5
	Spot 2	2.0	3.0	0.1		13.2
	Spot 3	4.1			6.3	
	Spot 4	14.0	2.4	0.3	0.6	6.2
I	Spot 1	1.5		62.4		
	Spot 2	0.8	0.6	65.8		3.7
	Spot 3		1.2	71.3		9.8
	Spot 4	1.1	0.5	68.3		2.0

The micrographs presented in Figure 6 indicate that filiform corrosion was observed on the Al panels (A, D and G), whereas undercutting of the paint film was observed on the steel (panel I). Moreover, the tip of the filiform filaments (spot #1 on panels A, D and G) were enriched in chloride species. Small amounts of sulphur were also detected at these locations. By contrast, the scribe marks and thicker deposits (such as spot #3 on A, D and G) were enriched more in sulphur. Such distinct differences in the distribution of sulphur and chloride species have also been previously observed for panels removed from field exposures.

Finally, the steel panels tend to exhibit greater sulphur enrichment than chloride enrichment.

From the results of these initial sulfur-bearing tests, it appears that SO_2 gas may be more effective at accelerating corrosion on painted Al than sulfate. However, the use of sulfate species would be preferred over SO_2 gas from a safety and handling perspective. Therefore, a plan was developed to further evaluate sulfate additions by modifying two tests, ASTM G85-A2 and ASTM G85-A4, to include both chloride and sulfur in the form of sulfate ions (SO_4^{2-}) rather than SO_2 gas. For these modified tests, the salt solution used in the cabinet exposures consisted of a 5% NaCl, 1% $CaCl_2$ solution with sulfate added in the form of sulfuric acid to modify the pH to either 3.5 or 5. For the Modified ASTM G85-A2, no acetic acid was used. For the Modified ASTM G85-A4, no SO_2 gas was used.

Results from these modified tests are shown in Figure 7. The modified ASTM G85-A2 test with pH adjusted to 3.5 (Lab 1 only) showed some moderate acceleration of corrosion on substrates B, D, and G but significantly less than the average on-vehicle results.

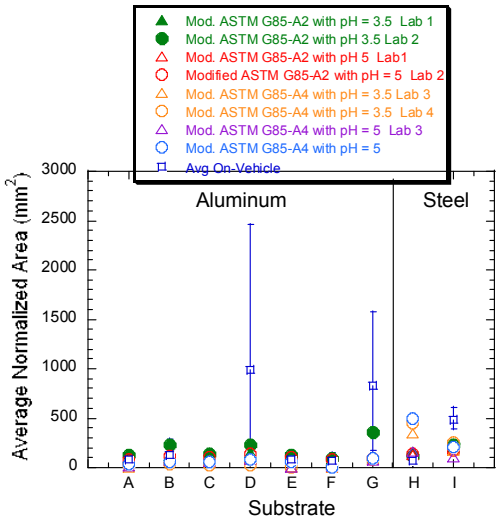

Figure 7. Average normalized area of corrosion for modified ASTM G85-A4, modified ASTM G85-A2 and for on-vehicle exposures.

Figure 8 presents the backscattered electron micrographs of the representative corroded regions from the four panels of interest. The letters identify the panels and the numbers indicate the locations for the corrosion-product analysis data reported in Table 4.

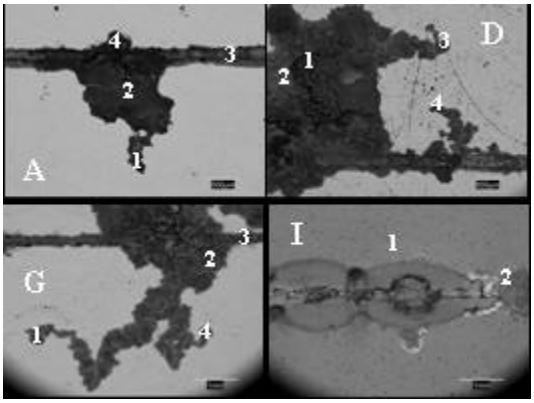

Figure 8. Backscattered electron micrographs of the representative corroded regions from four panels exposed to the modified ASTM G85-A2 test. The numbers on these figures indicate the locations where corrosion-product chemistry data have been reported in Table 4.

Table 4. Corrosion Product Composition (wt.%) for Panels Exposed to modified ASTM G85-A2 Test.

Panel ID	Area Analyzed	Elements Detected (Wt. %)				
		O	Al	P	S	Cl
A	Spot 1	51.3	28.6	5.1		4.4
	Spot 2	60.7	32.7			4.8
	Spot 3	48.1	22.4	6.6		1.6
	Spot 4	60.2	32.9	1.5	0.4	3.1
D	Spot 1	56.3	33.6			10.1
	Spot 2	60.3	18.5	0.9		2.1
	Spot 3	56.8	30.2	2.8		6.1
	Spot 4	55.5	28.4	5.1		5.6
G	Spot 1	51.2	32.1	4.3		6.6
	Spot 2	61.2	32.4			6.4
	Spot 3	58.3	22.4	3.0		2.0
	Spot 4	46.3	23.6	7.3		5.1
I	Spot 1	27.5		6.4		6.8
	Spot 2	30.3				3.3

Table 4 (continued). Product Composition (wt.%) for Panels Exposed to modified ASTM G85-A2 Test.

Panel ID	Area Analyzed	Elements Detected (Wt. %)				
		Ca	Ti	Mn	Fe	Zn
A	Spot 1			1.6		9.1
	Spot 2	1.8				
	Spot 3	9.3		1.8		10.3
	Spot 4	1.9				
D	Spot 1					
	Spot 2	18.1				0.1
	Spot 3			0.1		4.1
	Spot 4					5.5
G	Spot 1			1.2		5.4
	Spot 2					
	Spot 3	11.0	1.1	2.2		0.1
	Spot 4			3.2		14.4
I	Spot 1			1.7	40.6	17.0
	Spot 2	4.1			62.4	

A major difference in the corrosion-product chemistry between this test and the ASTM G85-A4 test is the absence of sulphur species in the corroded regions. The data presented in Table 4 indicate that very low levels of sulphur were detected at one location on Panel A. This observation was also confirmed by the detailed elemental distribution maps collected from several locations of interest. Another difference is the extensive presence of chloride species throughout the corrosion-product region; greater concentrations of chloride species were detected at all locations within the corroded regions. This is in contrast to ASTM G85-A4 test where chloride species were detected only at the tip of the filiform filament. Finally, greater amounts of calcium, especially within the scribe marks, were also detected. These results suggest that the corrosion-product chemistry from this test is significantly different from that observed in ASTM G85-A4 test and also from the trends observed in the field-exposure samples.

Finally, none of the other modified tests utilizing sulfates showed any acceleration of corrosion on substrates D and G relative to the other substrates and, therefore, do not appear to correlate with the on-vehicle results.

In addition to the sulfur-bearing tests, two additional accelerated tests were recently evaluated, GM9682P and GM9511P (Figures 9 and 10, respectively). The GM9682P test showed significant acceleration of corrosion on substrates D and G at Lab 4, but far less at Lab 1, the second lab conducting that test. GM9682P test results form Lab 4 also significantly over-predict the corrosion on substrate B. GM9511P did not show any acceleration of corrosion on substrates D and G relative to the other substrates and, therefore, does not appear to correlate with the on-vehicle results.

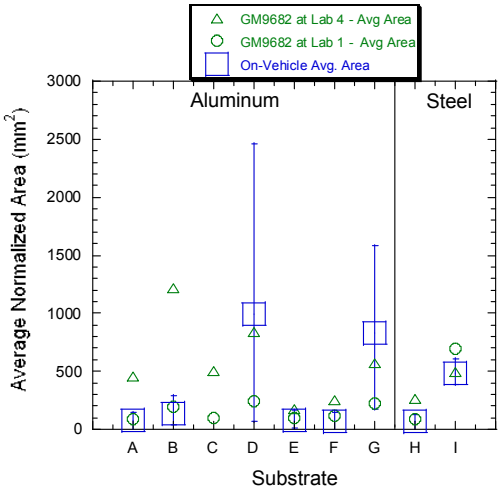

Figure 9. Average normalized area of corrosion for GM9682P and for on-vehicle exposures.

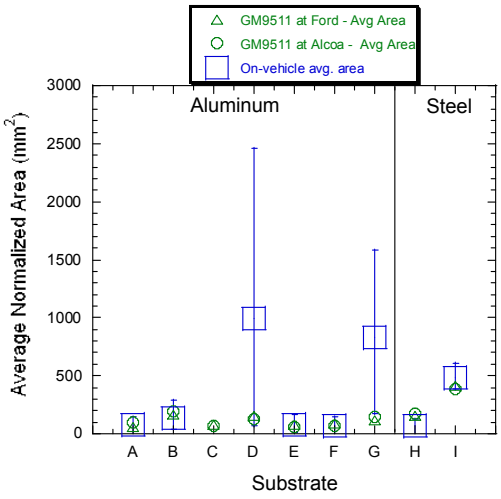

Figure 10. Average normalized area of corrosion for GM9511P and for on-vehicle exposures.

The morphology of the corrosion observed in these tests is illustrated in Figures 11 and 12. It has more of a filiform appearance than is typically seen for on-vehicle exposure (see Figure 1). As there is no source of sulfur in these tests, the corrosion products are not expected to contain sulfur.

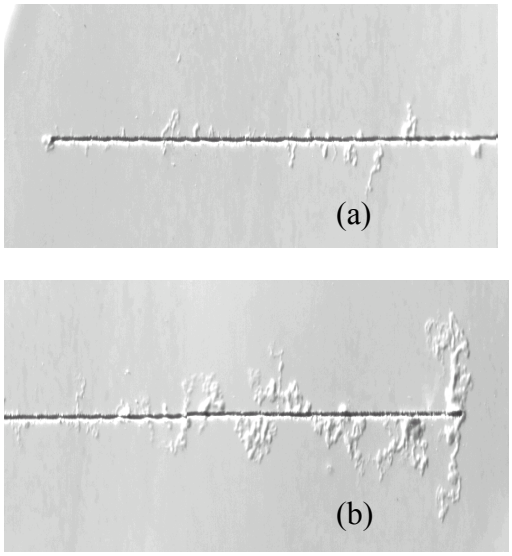

Figure 11. Appearance of cosmetic corrosion on substrates A (a) and D (b) after GM9682P test.

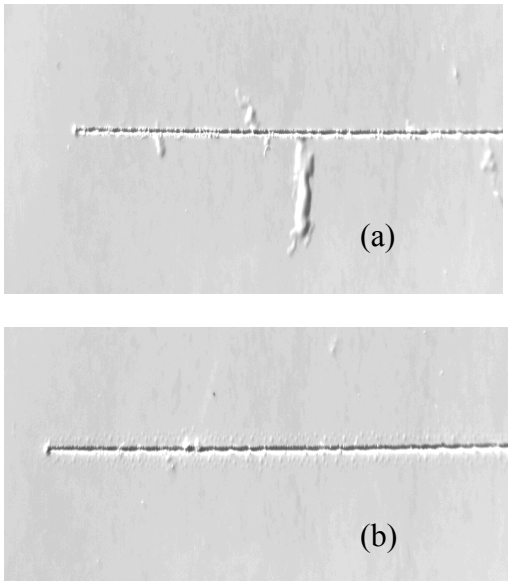

Figure 12. Appearance of cosmetic corrosion on substrates A (a) and D (b) after GM9511P test.

Conclusions

Based on the two-year, on-vehicle results, the following criteria have been identified as requisites for accelerated lab tests that replicate on-vehicle performance:

- Relative Ranking of Extent of Corrosion D,G > I >> B > A,E,F,H.
- Composition of Corrosion Products - In addition to usual species, sulfur should be present.
- Morphology of Corrosion - Blisters with filiform on leading edge at sporadic sites along scribe line.

In addition to these criteria, the repeatability and reproducibility of the test method are also important considerations. Table 5 is a summary of the tests conducted in 2007 relative to these criteria. Of the tests evaluated to date, only the standard ASTM G85-A4 test appears to result in the appropriate relative ranking, the correct morphology and has sulfur in the corrosion products. However, the repeatability of the test was not very good and it requires the ability to have SO_2 gas in the exposure. The use of sulfate species would be preferred over SO_2 gas from a safety and handling perspective, but from the results of these initial sulfur-bearing tests, it appears that sulfur dioxide gas may be more effective at accelerating corrosion on painted Al than sulfate.

Table 5. Summary of Tests Performed in 2007.

Procedure	Relative Ranking Similar to On-Vehicle?	Sulfur Corrosion Products	Morphology Similar to On-Vehicle?	Lab-to-Lab reproducible and/or repeatable?
ASDTM G85-A4	Yes	Yes	Yes	Ranking different in 2 runs at same lab
Modified ASTM G85-A4	No	No	No	Good lab-to-lab reproducibility
Modified ASTM G85-A2	Yes (1/2)	No	Yes	Poor lab-to-lab reproducibility
GM9511P	No	No source in test	No	Good lab-to-lab reproducibility
GM9682P	Yes (1/2)	No source in test	No	Poor lab-to-lab reproducibility

References

1. Lee, F., Pourdeyhimi B, and Adamsons, K, "Analysis of Coatings Appearance and Surface Defects Using Digital Image Capture/ Processing/Analysis, The International Symposium on a Systems Approach to Service Life Prediction of Organic Coatings, Breckenridge, Co, Sep 14-19, 1997.

2. ASTM G85-98 Annex 4, "Salt/SO2 Spray Fog Testing", Annual Book of ASTM Standards, Vol. 3.02, 2005.
3. GM9511P, "Scab Corrosion Creepback of Paint Systems on Metal Substrates", General Motors, 1998.
4. GM9682P, "Filiform Corrosion Test Procedure for Painted Aluminum Wheels and Painted Aluminum Wheel Trim", General Motors, 1997.
5. ASTM G85-98 Annex 2, "Cyclic Acidified Salt Fog Testing", Annual Book of ASTM Standards, Vol. 3.02, 2005.

Presentations/Publications/Patents

SAE 2002B-203
SAE 2003-01-1235
SAE 2005-01-0542
SAE 2006 Oral Only
SAE 2007-01-0417

[i] Denotes project 309 of the Automotive Materials Division (AMD) of the United States Automotive Materials Partnership (USAMP), one of the formal consortia of the United States Council for Automotive Research (USCAR, see www.uscar.org) set up by Chrysler, Ford and General Motors (GM) to conduct joint, pre-competitive research and development.

3. AUTOMOTIVE METALS – CAST

A. Improved Automotive Suspension Components Cast with B206 Alloy (AMD 405[i])

Principal Investigator: Dr. Murat Tiryakioğlu
MT Technical Services
157 Hunters Run Drive, Moon Township, PA 15108
(412) 264-4632; fax: (412) 264-4632; e-mail: murat.tiryakioglu@gmail.com

Technology Area Development Manager: Joseph A. Carpenter
(202) 586-1022; fax: (202) 586-1600; e-mail: joseph.carpenter@ee.doe.gov

Field Project Officer: Aaron D. Yocum
(304) 285-4852; fax: (304) 285-4403; e-mail: aaron.yocum@netl.doe.gov

Expert Technical Monitor: Philip S. Sklad
(865) 574-5069; fax: (865) 576-4963; e-mail: skladps@ornl.gov

---

Contractor: United States Automotive Materials Partnership (USAMP)[i]
Contract No.: DE-FC26-020R22910 through the DOE National Energy Technology Laboratory

---

Objective

- The objective of this project is to establish the commercial viability of B206 alloy for suspension components, by providing needed fundamental information on this alloy system and by overcoming technical issues that limit the lightweighting applications of this alloy. The B206 alloy has the potential to provide near net-shaped castings with mechanical properties equivalent to forged aluminum (Al) suspension components and ferritic ductile iron.

Approach

Four major technical focus points have been identified for this project. Accordingly, the work will be conducted in four separate phases:

1. Determine the effect of alloy composition on mechanical properties in the T4 and T7 heat-treated conditions and establish the feasibility of using less expensive versions of the alloy.
2. Study heat treatment of B206 alloy and establish combinations of aging time and temperatures which produce desirable stress-corrosion immunity. This portion of work will also determine the feasibility of using improved T7 heat-treatment cycles to increase elongation in this temper.
3. Create cost models for automotive suspension components produced by different processes and different materials.
4. Produce control-arm castings using two different casting processes. Test components produced in the T4 and T7 tempers to provide required engineering information and establish the feasibility of using cast B206-alloy components to replaced forged Al parts.

Accomplishments

- The project was officially kicked off in October 2005.
- Dr. Geoffrey Sigworth, the initial Project Technical Consultant (PTC), resigned from the program. Dr. Murat Tiryakioğlu took over the PTC responsibilities in March 2006.
- Phases 1, 2 and 3 have been completed.

- Phase 4 is ongoing. As of December 2007, 30 B206-T4 and T7 suspension control-arm castings were produced at Nemak and delivered to Chrysler. The project was extended until April 2008 to produce castings and complete Phase 4. Ballard Brass & Al, Inc. was selected to produce semi-permanent-mold castings, an economically favorable process that is typically used for the B206 alloy. Eck Industries/Alotech was selected to produce castings using the ablation process; a direct-chill process that is well suited to the B206 which responds better to fast cooling rates. Both suppliers are scheduled to start production of the castings in early January 2008, with mechanical testing planned for February 2008.

PHASE 1:
Phase 1 is complete and consisted of two separate studies. The first study was to identify the optimum chemistries for the T4 and T7 tempers and the second study was to evaluate the effect of cooling rate on the properties of B206 in the T4 and T7 tempers.

Phase 1, Part 1:
A study of tensile properties versus alloy composition was conducted by researchers at Alcan International. These results show that best results for the T4 and T7 tempers are obtained with two separate alloy compositions. The two alloy compositions and expected properties are provided below (in wt.%):

1. T4 Temper
The alloy contains 4.7 to 4.9% copper (Cu), 0.35 % magnesium (Mg) and 0.2 % manganese (Mn). The expected tensile properties are yield strength (YS) 250-260 MPa, ultimate tensile strength (UTS) 430-450 MPa, and elongation 18-22%.

2. T7 Temper
For a ductile T7 version, the alloy contains 4.2 to 4.4% Cu, 0.15% Mg, 0.2% Mn, 0.10% iron (Fe), 0.10% silicon (Si). The expected average tensile properties would be YS: 370-390 MPa, UTS: 445-455 MPa, and ~9% elongation.

In addition to the above results, a set of casting guidelines has been prepared for foundrymen who want to pour B206 alloy.

Phase 1, Part 2
A second stage of Phase 1 casting trials was completed in September 2005 by Nemak researchers at their Central Development and Technology Center near Monterrey, Mexico. Several different alloy compositions were prepared and 'wedge' castings were made. The 'wedge' castings were poured to establish the tensile properties of the alloy as the solidification rate varied from 30 seconds to 30 minutes. In addition, hot-crack-test castings were poured to determine the effect of alloy composition on castability.

PHASE 2:
Phase 2 was conducted at the University of Windsor under the direction of Prof. Jerry Sokolowski. Alcan International also assisted this phase of the project by providing additional testing. A survey study of the aging of B206 alloy was completed. Samples were aged at temperatures between 125^{o}C and 225^{o}C for times ranging from two to forty-eight hours. The hardness and electrical conductivity were measured and the samples were subjected to a corrosive medium to establish their vulnerability to intergranular attack. A report of these experiments was issued in October 2005. Additional studies were conducted to establish the kinetics of the solution heat-treatment process. Attempts to develop an alternative T7 aging process to increase elongation in that temper were mostly unsuccessful.

PHASE 3:
Phase 3 has been completed. A cost model was developed by Edmund A. Herman, P.E., of Creative Concepts Company, Inc. in March 2006. A Microsoft Excel spreadsheet was developed which can be used to compare costs of producing castings using A356-T6, B206-T4 and B206-T7 alloys.

PHASE 4:
Phase 4 is in progress. The intent of Phase 4 was to produce and test B206 castings using green sand at Hayes Lemmerz and precision sand at Nemak. Mercury Castings was added in September 2005 to produce castings using their Slurry-on-Demand process.

Hayes Lemmerz
The design work for the castings was completed in April 2006. Dr. Tiryakioğlu and Prof. John Campbell provided the optimum gating and filling system to minimize the entrainment of surface oxide films and therefore maximize mechanical properties. However, Hayes Lemmerz closed their Ferndale, Michigan facility and discontinued their involvement in the program before castings could be made.

Mercury Castings
Mercury Marine attempted to make castings but was unable to produce acceptable quality castings. No further work with Mercury Marine is planned.

Nemak
The gating system design concepts proposed by Tiryakioğlu and Campbell were adopted by Nemak and final gating system design, as shown in Figure 1, was developed with the assistance of Prof. Campbell. Mold-filling simulations using Magma software showed significant improvement over previous designs.

Figure 1. The gating and feeding system design used by Nemak.

Initial trial castings poured at Nemak with complete sand cope and drag showed extensive porosity and metal-mold reaction problems. Consequently, the mechanical properties, especially elongation, and surface finish of castings did not meet expectations (YS=270 MPa, UTS=310 MPa, elongation=10%). Based on Phase 1 results, the Project Team concluded that the solidification rate in the full sand mold was the primary reason why the castings did not achieve the desired properties.

To increase the cooling rate, Nemak machined an Al drag, poured thirty castings and heat-treated the castings in the T4 and T7 tempers. The results were encouraging but neither temper fully achieved the targeted mechanical properties. The T4 temper missed the target yield stress by 5%. The T7 temper greatly exceeded the UTS and YS targets but failed to achieve the targeted 10% elongation. Unfortunately, due to business conditions, Nemak had to withdraw from the program. Nemak delivered the metal drag and sand cope to Chrysler in the event that another supplier may be able to cast the parts.
Ballard Brass & Al, Inc.

Ballard will produce 50 castings using the semi-permanent-mold process. First four castings are scheduled to be produced in December 2007 and subsequently heat-treated to T7 condition. The team will decide whether any changes on the tooling are necessary, based on the tensile properties of the first four castings. Once the process has been optimized to produce castings with pre-targeted properties, 25 castings will be produced using the T7 chemistry and heat-treated to the T7 condition followed by 25 castings with the T4 chemistry heat-treated to the T4 temper.

Eck Industries/Alotech
Eck Industries and Alotech will produce 50 castings, 25 of the T4 temper and 25 of the T7 temper, with the ablation process, which generates high cooling rates and low levels of porosity. Castings are scheduled to be poured in early January 2008 using the same T4 and T7 chemistries and heat-treat schedules as the semi-permanent-mold castings.

Component Testing
General Motors and Westmoreland Mechanical Testing and Research are currently awaiting castings to be tested in component fatigue, tensile, fracture toughness, compressive testing and corrosion. This testing has been postponed since suppliers have been unable to produce castings to the desired quality and mechanical properties.

In addition to component testing, deformation characteristics will be evaluated to determine whether any outliers in tensile tests are due to structural defects that can be avoided with better melt quality and modifications to mold-filling system design. A full project report will be available in May 2008.

Future Direction

- The Project Team believes that it is possible to achieve the targeted properties and is currently investigating a lean chemistry to boost the T4 yield and direct cooling (ablation) or heat-treat optimization to improve the T7 elongation. The two casting processes selected for the production of the control-arm castings, namely, ablation and semi-permanent-mold, are expected to meet the target mechanical properties. The project will be finalized in May 2008.

Introduction

B206 alloy is significantly stronger than 356 alloy, and has mechanical properties approaching some grades of ductile iron. It also has excellent high-temperature tensile and low-cycle-fatigue strength. Consequently, this material could be used in a number of applications to reduce vehicle weight. Cost savings may also result, because less material would be required to provide the strength needed for the application. In spite of its excellent properties, 206 alloy is seldom used because of its propensity for hot cracking. GKS Engineering has discovered a better method to grain refine this alloy, which reduces the tendency for hot cracking. This material has a number of potential applications, but its high strength and excellent ductility make it an ideal candidate for suspension components. Consequently, in the first stage of work (Project AMD 305 -- completed in May 2002) control arms were produced via a tilt-pour/permanent-mold casting process to establish the viability of this material for these safety-critical components.

The work completed under AMD 305 showed that extremely high mechanical properties can be obtained. The tensile properties of permanent-mold B206-alloy control arms were nearly the same as (or slightly better than) those found with many forged Al components, and the low-cycle-fatigue life of B206 alloy is ten times that of A356 alloy castings for an equivalent stress level. AMD 305 also showed that the permanent-mold-casting process, although suitable, may not be the best manufacturing process for 206 alloy. Traditional sand-casting and composite-casting methods (such as Nemak´s semi-permanent-mold, precision-sand-casting process) are more forgiving of hot cracking. The additional work in this present project examines the technical feasibility of producing B206 alloy suspension components in three other casting processes. Other important technical and commercial issues related to B206 will also are addressed. The object is to provide the technical and economic data needed to justify

commercial use of this material in suspension components.

Justification

Automakers are under increased pressure to reduce carbon dioxide (CO_2) emissions and improve fuel economy through increased Corporate Average Fuel Economy (CAFÉ) standards. Because of its higher strength, B206 alloy structures have the potential to reduce vehicle mass, which is directly linked to improved CAFE and vehicle performance. There is also a potential for cost savings, because less material would be required when compared to conventional Al castings.

Program and Deliverables

This project was initially planned to be completed in 30 months and preceded in four stages. Below is a description of the deliverables for each of the four phases of the project.

Phase 1
The main alloying elements in 206 alloy (Cu, Mg, Mn) will be varied in a series of statistically-designed experiments. Test bars will be cast at each composition and heat-treated to the T4 and T7 tempers. Hot-crack-test castings will be made to study the effect of alloy composition on castability, and 'wedge' castings will also be poured to determine the effect of solidification rate on tensile properties. These tests will determine the effect of alloy composition on mechanical properties and castability, and will allow design and casting engineers to better tailor mechanical properties for any specific application. The minor impurity elements (Fe and Si) will also be varied to determine the effect of these elements on mechanical properties. It appears that the maximum limits for Fe and Si, presently listed in the Aluminum Association (AA) specifications for the 206 alloys, are lower than necessary for most automotive applications. Increasing these limits by a modest amount would reduce the cost of the alloy. These tests will be conducted at the Research and Development Center of Alcan International and at Nemak.

Phase 2
Parts made in 206 alloy are immune to stress corrosion in the T4 and T7 tempers. Parts that have been aged to peak strength (T6), however, are susceptible. Published information on other Al-Cu-Mg alloys suggests that relatively short aging times may induce stress corrosion, and that the susceptibility to stress-corrosion may occur before any change in hardness is found. For example, the temperatures and times used in powder coating may cause a problem. This part of the study will map out the dangerous areas which must be avoided. It will also examine alternative T7 treatments, to see if there is a way to improve material properties (especially elongation) in this temper. The use of alternative methods to test for stress corrosion resistance will also be evaluated. The standard test is cumbersome and takes 30 days to complete. A simpler, more rapid test is desirable. This phase of work will be carried out at the University of Windsor in Windsor, Ontario, and at Westmoreland Mechanical Testing Laboratories. Additional support will be provided by the laboratories of Alcan International.

Phase 3
A cost model will be constructed for suspension components manufactured using different processes and materials. A General Motors front-left control arm (FLCA) forged in 6xxx alloy will serve as a mule for this economic study. The following component cases will be considered:

- -forged 6xxx alloy
- -sand-cast B206 alloy
- -semi-permanent-mold-cast B206 alloy
- -permanent-mold-cast A356 alloy

Creative Concepts will assist the project group in formulation of the cost models in this portion of the study. Sync Optima will also do finite-element modeling (FEM) studies of the different cases, to determine changes required in the design (and weight) of the control arm as the material is changed from the base condition (forged 6xxx alloy).

Phase 4
In this final stage of work, a control arm 'mule' casting will be manufactured by the composite precision-sand-casting process at Nemak. Semi-solid cast parts will also be made at Mercury Castings.

In AMD 305, parts were made and heat-treated to the T4 temper. In this new work, additional castings will be made and tested in both the T4 and T7

tempers. In this way, a complete set of mechanical-property data will be obtained for the castings.

For this portion of the project, the compositions used to produce castings will be the optimum alloy compositions mapped out in Phase 1 of the project.

Westmoreland Mechanical Testing and Research will do testing of castings made in this phase of work.

Measurable Success Indicators

The successful results desired from each of the four phases of work are outlined below:

Phase 1
Mechanical properties as a function of cast material composition will be provided, allowing automotive design engineers to optimize component properties at lowest possible cost. Information will be provided that may allow us to increase upper limits for dissolved Si and Fe and reduce costs in 206 alloy.

Phase 2
Optimum heat-treatment schedules, which avoid stress-corrosion problems, will be established and recommended. Simple and rapid tests for stress-corrosion susceptibility will also be evaluated.

Phase 3
Cost models will be provided for the production of suspension components using several manufacturing processes and different materials. This model will assist automotive design engineers to optimize component performance and, at the same time, to help realize production cost savings.

Phase 4
Control-arm castings will be produced using two different casting processes and a complete battery of material property tests of the components will provide the technical database needed to design, manufacture and use suspension components cast in B206 alloy.

Technical Results

The results of the Phase-1 casting trials have been used to map out the range of mechanical properties that can be obtained from B206 alloy castings. For permanent-mold test bars, which have a relatively rapid solidification rate (20-30 seconds), the tensile properties found in the T4 temper are shown in Figure 2. The irregular polygon in these figures indicates the variation of tensile properties (UTS or YS and elongation) that one may expect as the composition is varied between the upper and lower limits for this alloy in the AA specifications. The amounts of Cu, Mg, Mn, Fe and Si in the alloy were all allowed to vary. The corresponding range of mechanical properties available in the T7 temper is indicated below in Figure 3.

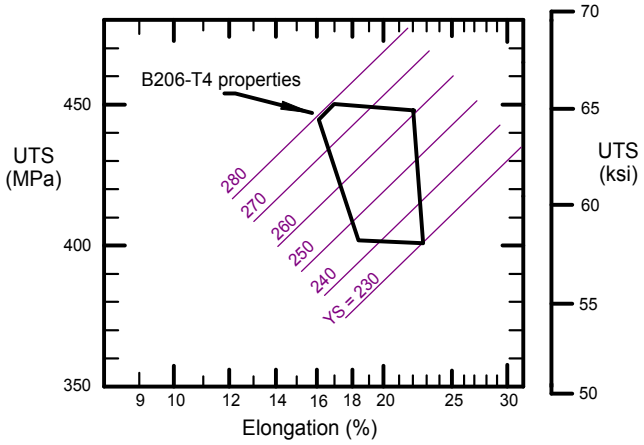

Figure 2. B206-T4 tensile properties.

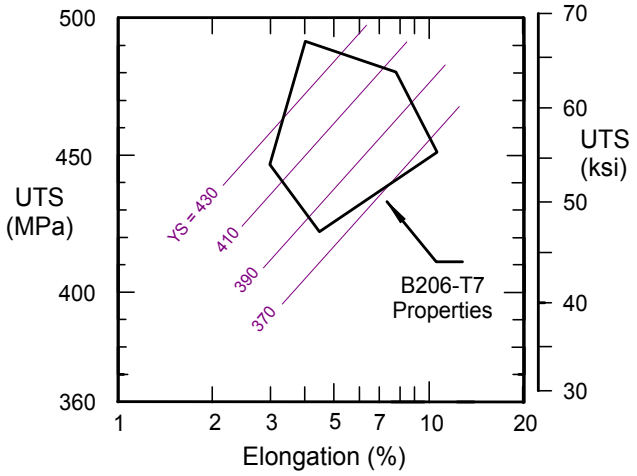

Figure 3. B206-T7 tensile properties.

In addition to the above results, two of the Alcan alloy compositions were poured into an end-chill mold. Tensile samples were cut at three distances from the chill (ranging from 12.5 to 50 mm (½ to 2 inches)). The tensile properties obtained from these castings are shown Figure 4, together with data published for the more commonly used Al casting alloys.

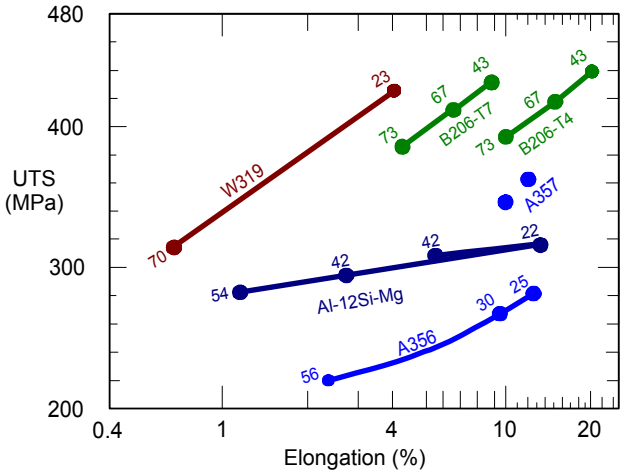

Figure 4. Range of mechanical properties in five Al casting alloys.

The solidification time is indicated in this figure by numerical values for the secondary dendrite-arm spacing (SDAS), or the cell size in the case of B206 alloy. (The data for A357 alloys is for heavily-chilled sections of aerospace castings only.) It can be seen that B206 alloy exhibits mechanical properties superior to the conventional Al-Si-Mg and Al-Si-Cu casting alloys.

A number of B206 alloy samples were aged and tested for intergranular attack by corrosion. A test procedure outlined in Mil Spec MIL-H-6088 and American Society for Testing and Materials (ASTM) specification G110 was used. This procedure correlated well with the results of a standard alternate immersion test in 201 alloy, [1] and so it was adapted for use in Phase 2 of this study. The average depth of the intergranular attack by corrosion (in microns) is plotted in Figure 5, as a function of aging time and aging temperature. In Figure 5, the safe aging conditions are indicated by the hatched areas. (These areas indicate aged samples where the average intergranular-corrosion depth was less than 20 μm deep.) The areas of worst corrosion attack are between the safe areas, at aging temperatures between 100°C and 180°C.

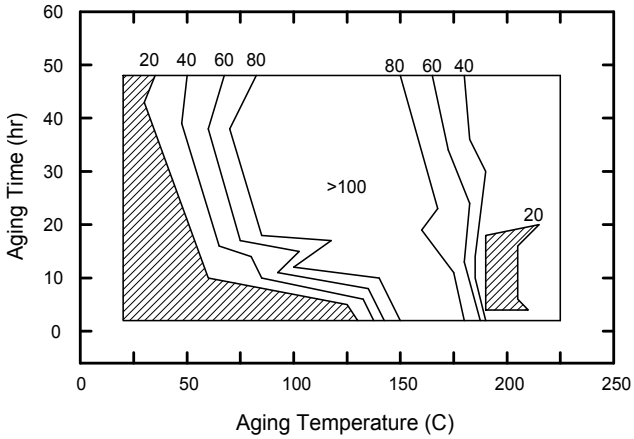

Figure 5. Average depth of corrosion.

In Phase 2 of our program, immersion stress-corrosion tests were conducted in accordance with the ASTM G47-98 standard. Specimens were all naturally aged for 3 days and artificially aged for different durations at temperatures between 100°C and 225°C. The stress-corrosion cracking (SCC) life contour plot is provided in Figure 6 as a function of artificial aging temperature (T) and time. The worst stress-corrosion life occurred between 100°C and 175°C, which is consistent with intergranular-corrosion results outlined in Figure 6. More analysis will be conducted for possible correlation between the results from the two test methods.

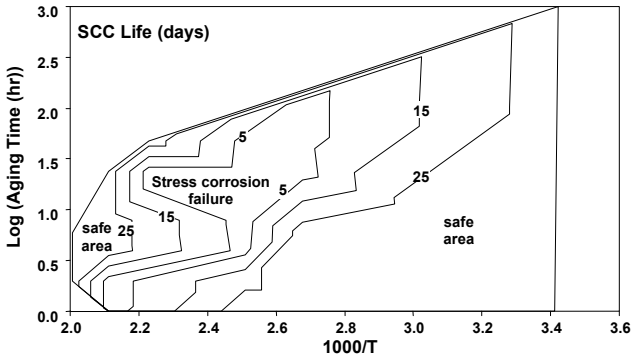

Figure 6. Stress-corrosion cracking life contours as a function of artificial aging time and temperature.

Contour plots of tensile properties after artificial aging at temperatures between 100°C and 225°C for various durations are presented in Figure 7. Highest UTS and elongation are obtained at an artificial

[1] M.S. Misra and K.J. Oswalt: "Corrosion Behavior of Al-Cu-Ag (201) Alloy," Metals Engineering Quarterly, Vol. 16, pp. 39-44 (1976).

aging for 12-24 hours at 125°C. A small set of experiments is planned at Alcan Laboratories to obtain more detailed results.

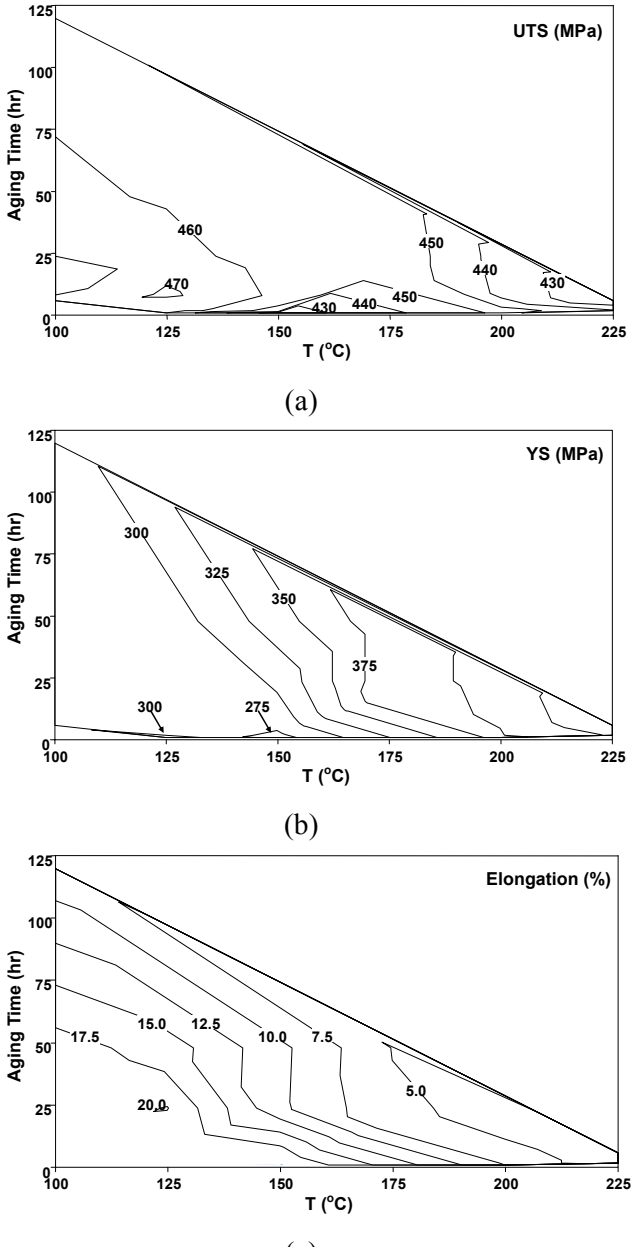

Figure 7. Contour plots for (a) ultimate tensile strength, (b) yield strength and (c) elongation as a function of artificial aging time and temperature.

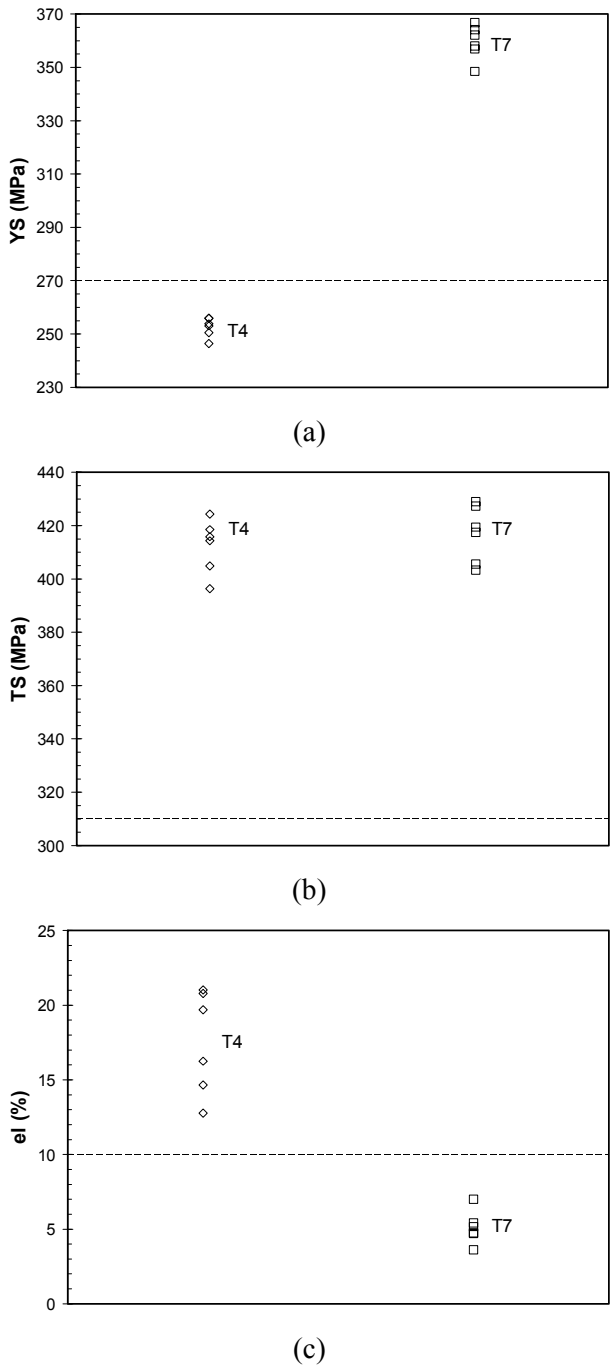

Figure 8. The tensile properties of semi-permanent-mold castings in T4 and T7 tempers produced by Nemak.

Two castings produced by the semi-permanent-mold process (with an Al drag) at Nemak were tested by excising tensile coupons from three locations in each casting. The tensile properties are summarized in Figure 8. The desired level of each property is indicated by a dashed line.

Note that the yield strength for T4 and the elongation for T7 tempers are barely below the desired levels. It is the believed by the entire project group that these properties can exceed the desired levels by the optimization of the heat-treatment process.

Presentations and Publications

The results from this project so far have generated two presentations and papers:

- G.K. Sigworth, J.F. Major: "Factors Influencing the Mechanical Properties of B206 Alloy Castings", Light Metals 2006, pp. 795-799, 2006 (presented at 2006 TMS Annual Meeting)
- J.F. Major and G.K. Sigworth, "Chemistry / Property Relationships in AA 206 Alloys," paper 06-029, AFS Transactions (presented at 2006 AFS Congress).

[i] Denotes project 405 of the Automotive Materials Division (AMD) of the United States Automotive Materials Partnership (USAMP), one of the formal consortia of the United States Council for Automotive Research (USCAR, see www.uscar.org) set up by Chrysler, Ford and General Motors (GM) to conduct joint, pre-competitive research and development.

B. Magnesium Powertrain Cast Components (AMD 304[i])

Principal Investigator: Bob R. Powell
General Motors Research & Development Center
30500 Mound Road, Mail Code 480-106-212
Warren, MI 48090-9055
(586) 986-1293; fax: (586) 986-9204; e-mail: bob.r.powell@gm.com

Technology Area Development Manager: Joseph A. Carpenter
(202) 586-1022; fax: (202) 586-1600; e-mail: joseph.carpenter@ee.doe.gov

Field Project Officer: Aaron D. Yocum
(304) 285-4852; fax: (304) 285-4403; e-mail: aaron.yocum@netl.doe.gov

Expert Technical Monitor: Philip S. Sklad
(865) 574-5069; fax: (865) 576-4963; e-mail: skladps@ornl.gov

---

Contractor: United States Automotive Materials Partnership (USAMP)[i]
Contract No.: DE-FC26-02OR22910 through the DOE National Energy Technology Laboratory

---

Objective

- Demonstrate and enhance the feasibility and benefits of using magnesium (Mg) alloys in place of aluminum (Al) in structural powertrain components and achieve at least 15% mass reduction of the cast components.

  Note: the final engine achieved a cast-component mass reduction of nearly twice the original target.

Approach

- Identify, benchmark, and develop a design/material property database of the potentially cost-effective, high-temperature Mg alloys and, using this cast-specimen database, select the alloys that are most suitable for the Mg components as determined by the design requirements of the components. (Task 1)
- Design, using finite-element analysis (FEA), an ultra-low-mass engine containing potentially four Mg components (cylinder block, bedplate, structural oil pan, and front-engine cover) using the most suitable, low-cost, recyclable, creep- and corrosion-resistant Mg alloys. (Task 2)
- Create a cost model to evaluate alloy, manufacturing, and technology costs to predict the cost-effective performance of the engine. (Task 2)
- During the execution of Tasks 1 and 2, identify and prioritize the critical gaps in the fundamental science of Mg alloys and their processing that are barriers either to the progress of the project or to the use of Mg in future powertrain applications. Seed-fund the most critical research and promote additional identified needs to support further development of the Mg scientific infrastructure in North America, thereby enabling more advanced powertrain applications of Mg. This will be one of the technology-transfer deliverables of the Mg Powertrain Cast Components (MPCC) Project. (Task 3)
- Note that before addressing Tasks 4–6 and funding Task 3 research, an in-depth review of the engine design, including performance and durability predictions, alloy requirements and measured alloy properties, cost model, and predicted mass reduction was conducted. Passing this gate review was necessary for entry into the second half of the project, which has the goal of demonstrating/validating the engine design with respect to castability, manufacturability, performance, durability, and cost.

- Refine the engine component designs as necessary (updating to match the properties of the alloy selected for each component), design and build tools and patterns, and cast the engine components. (Task 4)
- Excise specimens from the cast components and develop a full mechanical- and corrosion-design database for the alloys. Create an original equipment manufacturer (OEM)-common material specification for Mg powertrain alloys. (Task 5)
- Conduct Mg component testing, assemble and dynamometer-test the complete engines (with the Mg components), and conduct end-of-test teardowns. Refine the cost model to support determining the cost-effective performance of the engine. (Task 6)
- Document the completed MPCC Project: work, results, lessons learned, and recommendations. (Final Report)

Accomplishments

- In the years 2001-2004, Tasks 1 and 2 were completed. A successful gate review for entering Phase II was accomplished, involving (1) the selection of alloys for each Mg engine component and revision of the component designs based on the properties of the selected alloys, (2) the issuance of contracts to project teams for tooling and casting each component, and (3) the selection of five basic research projects in support of the objectives of Task 3.
- In 2005 and 2006, substantial progress was made toward accomplishing the objectives of Task 4, with the completion of component tooling design and build and the initiation of casting trials to produce the cylinder block, the structural oil pan, the front-engine cover, and the rear-seal carrier.
- The FY2007 accomplishments are as follow:
- Casting of the prototype Mg cylinder blocks was completed. The blocks that passed X-ray inspection and leak testing were machined and then delivered to Gehring Corporation for application of wear-resistant coatings in the cylinder bores. Coating of the bores and finishing and honing of the blocks were completed. Ten blocks were thus successfully completed. This number is sufficient to support component and engine testing, including back-up engines for unforeseen test events.
- The machining behavior of the sand-cast cylinder block Mg alloy was observed and documented, as was that of the machining behavior of the die-casting Mg alloys used in the other components. From a machining process and materials perspective, the creep-resistant alloys comprising the MPCC engine components were indistinguishable from the well-known AM and AZ Mg alloys.
- The other Mg components (structural oil pan, front engine cover, and rear-seal carrier) were also completed and delivered to Roush Industries for use in engine testing. Friction-stir welding (FSW) was used to attach the cover to the structural oil-pan reservoir.
- The Honeywell coolant was also delivered to Roush in support of engine testing. Coolant and oil aliquots will be analyzed during dynamometer testing.
- Engine testing was begun. The first assembled engine test was successful. The test, hot scuff, is a key test of the integrity of the coating in the bores of the Mg cylinder block. In addition, the first thermal-cycle test of the assembled components was successfully completed.
- The patent application for the structural details of the Mg cylinder block was accepted by the United States Patent Office (USPTO) examiner. US Patent No. 7,284,528 was issued on October 23, 2007. It is assigned to USAMP.
- The five basic-research projects which were launched in previous years in support of the Task 3 objectives were completed. A review article about the Task 3 research was published in the August 2007 issue of the TMS Journal of Materials. The Task 3 projects are: 1) Computational Thermodynamics and Phase Equilibria (Penn State University); 2) Hot Tearing Susceptibility (CANMET – Materials Technology Laboratory (MTL)); 3) Creep Mechanisms of Mg Alloys (The University of Michigan at Ann Arbor); 4) Mg Corrosion and Corrosion Mechanisms (the Universities of Michigan at Dearborn and Ann Arbor); and 5) Recycling of Creep-Resistant Mg Alloys (Case Western Reserve University).

Future Direction

- Excise specimens from cast Mg engine components and test to create an excised-specimen property database of the three selected Mg alloys, which database will complement the cast-specimen database completed during Phase I.
- Complete sub-assembly testing of the Mg engine components.
- Complete engine dynamometer testing, teardown, and analysis of the Mg-intensive engines.
- Input data from all stages of the manufacture of the die-cast oil pan and front-engine cover and the sand-cast cylinder block into the cost model to determine the cost-effective performance of the Mg-intensive engine.
- Complete the project by March 31, 2008.

Introduction

The MPCC Project will be completed in 2008. This project was launched in 2001 to realize the vision of a Mg-intensive engine that would meet OEM manufacturability and durability requirements, be cost effective, and be 15 percent lighter than the total mass of the cast Al engine components which would be converted to Mg. In the intervening nearly seven years of work, this vision remains intact. Figure 1 shows the range and depth of work accomplished by the project team.

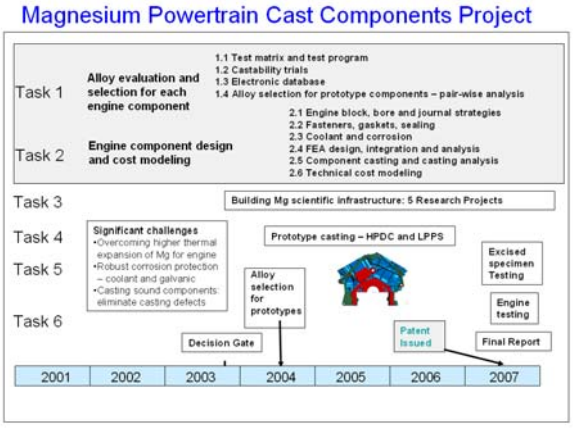

Figure 1. Timeline for the MPCC Project showing organization by task, milestones, and significant challenges encountered.

Beginning with an Al production engine, the Ford 3.0L V6 Duratec, the MPCC project team: 1) designed the Mg version of the engine; 2) extracted from the design, the material requirements of the "Mg-intensive engine;" 3) cast and property-tested a broad range of promising, creep-resistant Mg alloys, including sand-casting alloys for the cylinder block and high-pressure die casting alloys for the structural oil pan, front engine cover, and rear-seal carrier; 4) created technical cost models (sand casting and high-pressure die casting) for manufacturing the engine; 5) designed and built tooling to cast the engine components; 6) cast and machined the four Mg components for the engines; 7) tested two generations of ethylene glycol-based coolants which had Mg corrosion inhibitors and selected one for the engine test program; and, 8) began component (subsystem) and fully-assembled, engine-dynamometer testing of the Mg-intensive engines. Completion of component and engine testing is scheduled for the first calendar quarter of 2008.

Tasks 1 and 2, which yielded the engine design, and alloy property electronic database, have been reviewed in previous reports. Together, the successful completion of these tasks determined that it would be possible to design a Mg-intensive V6 engine and that the material properties required by the design could be satisfied with existing creep-resistant Mg alloys. These results were the basis of the successful gate review of the MPCC Project in October 2003. Phase 2 of the project commenced at that time. Task 1 created an extensive electronic database of creep-resistant Mg alloys. This database has since been combined with a complementary database of materials properties of primarily non-creep-resistant Mg alloys, generated by the Structural Cast Mg Development (SCMD) project (AMD 111) completed in 2006. The common architecture to house them was developed over the course of both projects and has been renamed the Automotive Lightweighting Materials (ALM) database. The ALM database is the core for materials properties data that will be generated in future AMD

projects. The design and maintenance of this database is an area of active effort at USCAR.

Completing Task 2 required overcoming a major design challenge--that of the higher coefficient of thermal expansion (COE) of Mg relative to the other engine structural materials, Al and iron. To maintain acceptable clearance between the crank shaft and crank bore, it was necessary to use iron inserts in the cylinder block bulkheads and to replace the bedplate (lower crankcase) with bearing caps. The design resulted in the issuance of a US patent. The patent, which is assigned to USAMP, was issued on October 23, 2007. Figure 2 show a schematic of the cylinder block with the crank bore inserts and bearing caps.

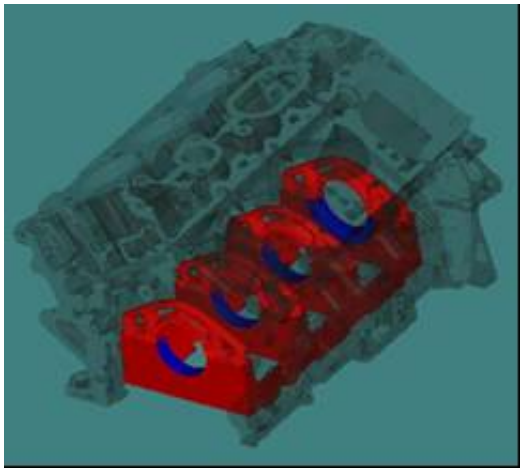

Figure 2. The MPCC Mg-intensive engine showing the crank-bore inserts and bearing cap assembly.

Task 3: Basic Research in Support of Mg Powertrain Advances

During Phase 1 of the MPCC Project, the project team identified critical scientific needs which, if not overcome, would be barriers to the production implementation of Mg-intensive powertrains. For example, an effective, Mg-corrosion-inhibited coolant was identified which will be used for MPCC engine dynamometer testing. While the coolant enables the Project test program, it is too early to predict how the coolant will perform in commercial application. Understanding corrosion performance across various test methods and how those results depended on the corrosion mechanisms and products inherent in the test would be a significant advance toward the development of robust coolants for a Mg-intensive engine. Basic research addressing the above questions was one of five MPCC/DOE-supported projects.

The research projects supported were:
1) Computational Thermodynamics and Alloy Development of Mg Alloys, under the leadership of Prof. Z.K. Liu at Penn State University; 2) Hot Tearing Behavior of Mg Alloys, under the leadership of Dr. D. Emadi at CANMET-MTL;
3) Creep, Bolt Load Retention, and Microstructural Analysis of High Temperature Mg Alloys, under the leadership of Prof. J.W. Jones at the University of Michigan at Ann Arbor;
4) Evaluation of Mg Corrosion by Various Methodologies and Surface Composition of Mg Alloys by Rutherford Backscattering, under the leadership of Prof. P.K. Mallick at the University of Michigan at Dearborn; and 5) Fluxless Recycling Methods and Process Control for Creep-Resistant Mg Alloys, under the leadership of Prof. D. Schwam at Case Western Reserve University and Dr. E. Es-Sadiqi at CANMET-MTL.

A thorough review of these completed "Task 3" projects, including citing of their publications, appeared in the August 2007 issue of JOM, a publication of The Minerals, Metals & Materials Society; see Figure 3.

Task 4: Casting the Components for the Mg-Intensive Engine

Assembling the "bill of materials" for engine testing was completed in 2007. The bill-of-materials included the Mg cylinder blocks, oil pans, front-engine covers, rear-seal carriers, and other components that were specifically designed or selected for the engine, e.g., the head gasket, Al bolts for the pan and front cover, bearing-cap ladders assembly, Mg-protected coolant, etc. All other parts were carry-overs from the Al production Duratec. Ten such production engines were obtained to provide parts for building the Mg-intensive engines.

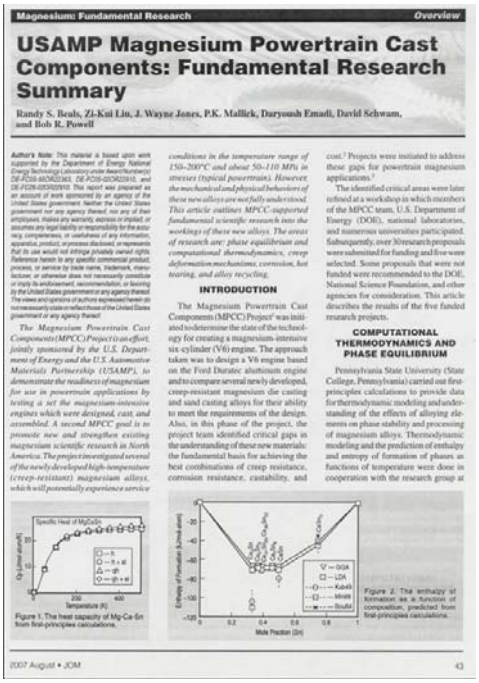
Magnesium: Fundamental Research Overview

USAMP Magnesium Powertrain Cast Components: Fundamental Research Summary

Randy S. Beals, Zi-Kui Liu, J. Wayne Jones, P.K. Mallick, Daryoosh Emadi, David Schwam, and Bob R. Powell

INTRODUCTION

COMPUTATIONAL THERMODYNAMICS AND PHASE EQUILIBRIUM

2007 August • JOM 43

Figure 3. Cover page of the review article about the MPCC basic-research projects published in the August 2007 issue of JOM.

Cylinder Block: Six dozen "prototype-production" blocks were sand cast by Fonderie Messier using Australia Mg Technologies alloy SC-1. Of these, half were cast during the development phase to achieve sound castings. At this point, the casting process was fixed and the remaining blocks cast. These were X-ray inspected, machined, and leak tested. Some required impregnation. The resulting set of "testable blocks" had their cylinder bores coated with a wear-resistant thermal spray. After honing the blocks, metrics were obtained for the blocks and then they were delivered to Roush Industries to await engine assembly and dynamometer testing. A partially-machined cylinder-block casting is shown in Figure 4.

Structural Oil Pan: Two-hundred oil pans were cast by Spartan Light Metal Products. This was a difficult component to cast, as has been described previously. Of these, about fifty were machined, leak tested, impregnated or weld repaired as necessary and delivered to Hitachi America so that the cover could be friction-stir welded on to the reservoir. A finished pan is shown in Figure 5. The welded reservoir cover, heat-staked baffle, and the cast-in groove for the gasket are evident in the figure.

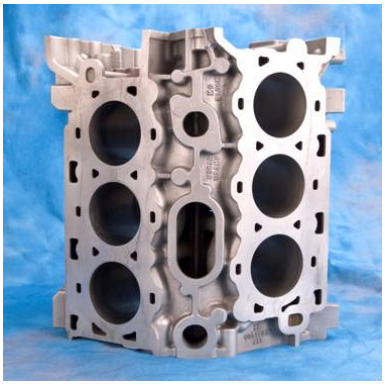

Figure 4. Partially-machined MPCC Mg block.

Figure 5. Finished, cast Mg structural oil pan.

Front-Engine Cover: The front-engine cover is also a difficult part to cast. Two-hundred castings were made at Intermet. These were sorted, and the sound castings machined, leak tested, and impregnated as necessary. Finished parts were delivered for engine testing during the reporting period. A finished casting is shown in Figure 6.

Figure 6. The MPCC Mg front-engine cover.

Rear-Seal Carrier: These Mg parts were thixomolded by Thixomat and delivered for engine testing in the prior reporting period. A finished casting is shown in Figure 7.

Figure 7. The MPCC Mg rear-seal carrier.

Head Gasket: Dana Corporation designed the head gasket for the MPCC Mg-intensive engine. It is a 3-layer, stainless-steel design, which contains a wave stopper sandwiched between the two active layers. Pulsator testing of the gasket validated the design and the head gaskets were manufactured and delivered.

Mg-Protected Coolant: Three-hundred gallons of proprietary Honeywell coolant, which was selected after a set of MPCC corrosion tests, were delivered during the reporting period.

Fasteners: The Mg-intensive engine used both steel and Al fasteners. The head bolts and mains were steel and the bolts for the oil pan and front-engine cover were Al. Torque testing, completed at Ford, determined that the specification for the head bolts in the Al production block could carry over to the Mg block.

Task 5: Excised Specimen Testing for the Mechanical Property Database

Phase 1 of the MPCC Project comprised building a database of mechanical, thermo-physical, and corrosion properties of the considered sand-casting and die-casting Mg alloys. These were cast specimens. The cast-specimen database was completed and has been released in combination with that of the SCMD project data. The databases from each project reside in common architecture. This database will be housed at USCAR and will continue to be populated with properties of structural automotive materials. It will henceforth be called the Automotive Lightweighting Materials (ALM) Database.

Specimens excised from each of the four Mg components cast in the MPCC project will be tested at the results included in the ALM database. The Mg components were delivered to Westmoreland Mechanical Testing & Research. Specimen blanks were excised and then X-ray inspected at Chrysler; from these, a set of specimens will be tensile tested at room temperature and 150°C.

Task 6: Mg-Intensive Engine Testing

Engine testing is the ultimate measure of the technical readiness of Mg for powertrain applications. The MPCC test program was developed to validate the engine design and its predictions about the durability and the noise, vibration, and harshness (NVH) performance of the engine.

The MPCC test program is based on that used for the Al production Duratec. Six tests are included in the program, as is teardown analysis. The engine tests are:

- Hot Scuff
- Cold Scuff
- 150-hour Deep Thermal Cycle
- 300-hour High Speed Durability
- 480-hour Key Life Thermal Cycle
- 675-hour Engine System Test

In addition to completing the assembly of the bill-of-materials for testing, the other major effort in 2007 was acquiring and testing the necessary software, engine-control modules and other communications between the engines and the dynamometer-control systems. This major challenge was completed, a production Al engine was run to validate the dynamometer communications, and the first of the engine tests was completed.

Hot scuff is primarily a test of the bore coating and sizing of the bore, piston, and ring assembly. It was critical that we successfully complete hot scuff and cold scuff before beginning the durability tests. The hot-scuff test consisted of running the engine at 4000 revolutions per minute (rpm) for 30 minutes and then inspecting the bore walls and pistons for scratches (“scuff”). The test results were excellent. The cold-scuff engine has

been assembled and is ready for testing. Engine testing is expected to be completed in the first calendar quarter of 2008. Figure 8 shows the assembled Mg-intensive engine that was used for the hot-scuff test.

Figure 8. Hot-scuff MPCC Mg-intensive engine.

Conclusions

The MPCC Project has made excellent progress since its inception in 2001. In retrospect, the significant challenges for the Mg-intensive engine have been revealed to be designing for the thermal expansion coefficient of Mg, which is greater than that of Al, and casting the various components. That both challenges were overcome will be determined on the basis of the ongoing engine testing, as will the performance of the coolant-corrosion package. Progress in coolant-corrosion protection was significant, but before the Mg-intensive engine enters the commercial market, further development of robust corrosion protection is recommended.

Project objectives under the sponsorship of USCAR and DOE enabled sharing the costs and risks of this project and avoided duplication of effort by the OEM participants. The Project renewed interest in using Mg in automotive powertrains within the Mg-supplier and manufacturing community as well as the automotive industry. The project is promoting greater competition and rapid development of Mg sources, manufacturing capability, and engineering expertise, and has already encouraged the development of scientific- research projects into the properties, processing, and behavior of Mg at various universities and national laboratories in North America. The successful completion of the Project in 2008 will add to this momentum.

Presentations/Publications/Patents

1. R.S. Beals, Z.-K. Liu, J.W. Jones, P.K. Mallick, D. Emadi, D. Schwam, and B.R. Powell, "USAMP Mg Powertrain Cast Components: Fundamental Research Summary," published in JOM, 59, [8] 43-8 (2007).
2. P.P. Ried, B.R. Powell, W.L. Miller, L.J. Ouimet, J.F. Quinn, J.E. Allison, J.A. Hines, R.C. McCune, R.S. Beals, and L. Kopka, "Development of a Mg-Intensive Engine," presented at NADCA Chapter 39, Stevensville, MI, May 10, 2007 (R&D-10,688).
3. J.A. Hines, R.C. McCune, J.E. Allison, B.R. Powell, W.L. Miller, L. Ouimet, R.S. Beals, L. Kopka, and P.P. Ried, "Casting and Testing the USAMP Mg-Intensive Powertrain," presented at SAE World Congress, Detroit, MI, April 17, 2007 (R&D-10,688).
4. B.R. Powell, W.L. Miller, L.J. Ouimet, J.A. Hines, R.C. McCune, J.E. Allison, R.S. Beals, L. Kopka, and P.P. Ried, "Project Update: The USAMP Mg Powertrain Cast Components Project," presented at 18th IMA Mg in Automotive Seminar, Livonia, MI, March 28, 2007.
5. R.C. McCune, P.K. Mallick, D. Sivaraj, and Z. Shi, "Film Formation on Mg Alloys in Aqueous Solutions and Detection by Rutherford Backscattering Spectroscopy," presented and published at TMS Mg Technology Symposium 2007, Orlando, FL, March 1, 2007.
6. H. Zhang, A. Saengdeejing, J. Saal, and Z.-K. Liu, "Enthalpies of Formation of Mg Compounds from First-Principles Calculations," presented and published at TMS Mg Technology Symposium 2007, Orlando, FL, February 28, 2007.

7. J. TerBush, A. Suzuki, N. Saddock, J.W. Jones, and T. Pollock, Microstructure and Creep of Die-Cast Mg Alloys," presented at TMS Mg Technology Symposium 2007, Orlando, FL, February 26, 2007.
8. F. Hunt, H. Badarinarayan, K. Okamoto, and D. Platt, "Friction Stir Welding of Dissimilar Mg Alloys for Automotive Applications," presented and published at TMS Mg Technology Symposium 2007, Orlando, FL, February 26, 2007.
9. J.A. Hines, R.C. McCune, J.E. Allison, Bob R. Powell, W.L. Miller, L. Ouimet, R.S. Beals, L. Kopka, and P.P. Ried, "Casting and Testing the USAMP Mg-Intensive Powertrain," TMS Mg Technology Symposium 2007, Orlando, FL, February 26, 2007.
10. H. Zhang, Y. Wang, L.-Q. Chen, and Z.-K. Liu, "Thermodynamic Modeling of the Mg-Ca-Ce System by Combining the First-Principles and CALPHAD Methods," presented at Materials Science and Technology 2006, Cincinnati, OH, October 15-18, 2006.
11. D. Emadi, "Understanding Hot Tearing Behavior of Al and Mg Casting Alloys," presented at Innovation in Light Metals Casting Research Symposium, McMaster University, Hamilton, Canada, October 5, 2006.
12. Bob R. Powell, "Enabling the Mg-Intensive Engine: From the Microstructural Basis of Creep to Engine Testing," Michigan State University, Lansing, Michigan, October 5, 2006.
13. R.J. Natkin, B. Oltmans, T.J. Heater, J.E. Allison, J.A. Hines, G.K. Tappen, and D. Peiskammer, "Crank Shaft Support Assembly," Utility Patent Application 11/373,544, filed March 10, 2006; 1st examiner response March 2007.

Acknowledgements

The author would like to acknowledge the members of the AMD 304 project leadership team for their hard work in successfully completing the work to date: Randy Beals and Lawrence Kopka (retired) of Chrysler Corporation; Joy Hines, John Allison, Robert McCune (retired) of Ford Motor Company; William Miller, Larry Ouimet, and Jim Quinn of General Motors Corporation; and Peter Ried of Ried and Associates. Extensive involvement of the other members of the project team was essential and enabled this project. The member organizations are listed in Table 1.

The continuing support of our respective companies and the U.S. DOE is gratefully acknowledged.

Table 1. The MPCC Project Team

Core Team:	J. Allison, R. Beals, J. Hines, L. Kopka, R. McCune, W. Miller, L. Ouimet, B. Powell, J. Quinn, P. Ried
Product Design:	Ford, GM, DCX, Magna Powertrain
Alloy Suppliers:	AMC, Dead Sea Mg, GM, Noranda, Norsk-Hydro, Solikamsk, VSMPO -Avisma
Casters	Eck, Gibbs, Intermet, Lunt, Meridian, Nemak, Spartan,
Bore Treatment:	Gehring, Flame Spray
Tooling:	Becker, Delaware, EXCO, HE Vannatter
Coolants:	Ashland/Valvoline, ChevronTexaco, Honeywell/Prestone, CCI
Fasteners:	RIBE
	Hitachi
Gaskets:	Dana/Victor Reinz
Testing Labs:	Amalgatech, CANMET, Stork, Westmoreland, Quasar
Casting Modeling:	EKK, Flow Science, MAGMAsoft, Technalysis
Prof. Organizations:	IMA, NADCA
Project Administration :	Ried and Associates

[i] Denotes project 304 of the Automotive Materials Division (AMD) of the United States Automotive Materials Partnership (USAMP), one of the formal consortia of the United States Council for Automotive Research (USCAR) set up by Chrysler, Ford and General Motors (GM) to conduct joint, pre-competitive research and development.

C. Ultra-Large Castings of Aluminum and Magnesium (AMD 406[i])

Principal Investigator: Michael H. Maj
Ford Motor Company
Research and Advanced Engineering
2101 Village Road
Dearborn, MI 48121
(313) 337-6700; fax: (313) 390-0514; e-mail: mmaj@ford.com

Project Administrator: Thomas N. Meyer, Ph.D.
TNM Contract Engineering and Consulting Services
3987 Murry Highlands Circle
Murrysville, PA 15668
(412) 860-7946; e-mail: tnmeng@aol.com

Technology Area Development Manager: Joseph A. Carpenter
(202) 586-1022; fax: (202) 586-1600; e-mail: joseph.carpenter@ee.doe.gov

Field Project Officer: Aaron D. Yocum
(304) 285-4852; fax: (304) 285-4403; e-mail: aaron.yocum@netl.doe.gov

Expert Technical Monitor: Philip S. Sklad
(865) 574-5069; fax: (865) 576-4963; e-mail: skladps@ornl.gov

---

Contractor: United States Automotive Materials Partnership (USAMP)[i]
Contract No.: DE-FC26-020R22910 through the DOE National Energy Technology Laboratory

---

Objective

- Assess the manufacturing feasibility, economics and mass reduction potential of thin-wall structural castings of aluminum and magnesium applied to automotive weight reduction.

Approach

The Ultra-Large Casting (ULC) project builds on the findings of a U.S. Department of Energy funded contract to the American Foundry Society (AFS, Project ORNL-12401) which benchmarked various casting processes to assess their suitability to manufacture large, light-metal castings. This annual report will address three technical areas focusing on the ULC objective. These include demonstration and evaluation of two semi-solid processes the Sub-Liquidus Casting (SLC Process) for magnesium (Mg) and aluminum (Al) and a multiple hot-runner direct-injection Thixomolding process for Mg. In addition, the project has been expanded to include a study of a new Large Thin Casting (LTC) concept which examines reducing total casting cycle times by a factor of four. The SLC and Thixomolding efforts address improvements to mechanical properties while the LTC effort addresses cycle time and, hence, cost. A "real world" application of a ULC made from one of the casting processes is intended to demonstrate the weight-savings potential and other benefits of ULCs. Based on this background work and continuing research, the ULC project approach is listed below.

- Further describe and substantiate the rationale for using light-metal castings in place of conventional stamped- and welded-steel automotive body structures to reduce vehicle weight.
- The project is executed in two concurrent phases. *Phase I* is focused on process selection and capability analysis. Pha*se II* is focused on designing, analyzing and testing a "real-world" vehicle application meeting the ULC Team's criteria of a ULC.

  - The main objective for *Phase I* is to utilize the selected processes to improve the quality of cast components vs. conventional casting processes by achieving homogeneous distribution of properties and demonstrate consistent and predictable mechanical properties with improved strength and ductility.
  - The major tasks for *Phase I* will consist of Flow and Solidification Modeling, Tool Design/Analysis/Fabrication, Correlation with Casting Trials, Material Characterization, Process Capability Studies and an Economic Analysis.
  - The main objective for *Phase II* is a "Real-World" application of a ULC will demonstrate a mass reduction of 40% to 60% at a competitive cost compared to conventional steel construction. Additionally, it is desired to demonstrate parts consolidation, reduced investment cost in tooling and dies and improved energy absorption.
  - The major tasks supporting *Phase II* are finite-element analyses (FEAs) for Static, Durability, Noise, Vibration and Harshness (NVH) and Crash Analyses; System-Level and Full-Vehicle Prototype Fabrication; Durability Testing; Dynamic Crash Testing; and an Economic Analysis.
- In addition, the ULC project initiated the exploration, analytical development and engineering evaluation of a process concept to establish the process parameters and machine configurations required to produce LTCs with thicknesses as low as 1 mm at production rates of 240 pieces per hour.

Accomplishments

LTC

- On a theoretical basis, the process technical feasibility of making large (e.g., automotive door inner panels) Mg and Al castings 1.00-mm thick was established.
- Determined processing requirements.
- Concepts for the engineering methods, equipment, tooling and controls necessary were developed.
- A preliminary assessment of the potential cost competitiveness of LTC castings was completed.

"SLC" Process

- In 2007, casting-system modifications were completed that facilitated changeover between Mg and Al. Installation included sulfur hexafluoride (SF_6) cover-gas distribution system and a METAMAG centrifugal pumping system to transfer Mg from the holding furnace to the bottom-pour ladle.
- The shot tip diameter was reduced from 20" to 12" diameter, improving the cycle time, casting yield, and die-temperature control.
- Initial die designs included bidirectional flow from each gate location. Preliminary casting trials revealed this gate configuration yielded inconsistent (non-repeatable) test results. The gate configuration was revised to direct metal flow through one gate in one direction only and repeatable test results were achieved.
- Integral to the test plan during the "fluidity" portion of the test sequence, the depth of the die cavity was increased from 2 mm to 3 mm by 0.5 mm increments, subsequent to evaluation of each material (A356, AM60 & AM50).
- Subsequent to completion of the "fluidity" trials, the die was reconfigured to accommodate the die inserts to manufacture the three structural shapes (waffle, structural rib & cylindrical node). The flow path from the gate to the inserts was reset to 2.5-mm depth and the profile modified from a flat plate to a C-channel, to better simulate a typical casting geometry.
- All casting trials defined in the statement of work (SOW) were completed in 2007 for both Al A356, and Mg AM60B and AM50 alloys. The designs-of-experiment (DoEs) were designed to determine the relative significance of the following process variables:
  - Metal Temperature (% solids)
  - Die Temperature
  - Vacuum (die-cavity pressure)
  - Gate Velocity
  - Casting Thickness (fluidity test only, other tests at 2.5-mm depth)
- Four die configurations were evaluated for each of the three materials:
  - Fluidity (flat plate (2 mm -> 3 mm)
  - Structural Rib (2.5-mm depth runner, C-runner)

- Waffle (2.5-mm depth C-shaped runner)
- Cylindrical node (2.5-mm depth, C-runner)

Thixomolding Process to Produce "Shotgun"

- Operation of the 4-Drop hot runner continued to improve.
- Overcame serious part-ejection problems by increased ejector pins and pin diameter, support pillars, and increased radii.
- Completed hot-runner validation effort with improved runner sequence and thermal control with improved material flow.
- Executed a DoE assessing the effects of :
  - Injection speed
  - Barrel temperature
  - Mold temperature
  - Hold time
- Alloys of AM60 and AZ91D were used to produce hundreds of samples in an effort to obtain maximum elongation preferred for structural parts. Initial trials were conducted with AZ91D with the majority of the castings produced with AM60.
- X-rays were obtained for approximately 75 shotgun and representative tensile, yield, and elongation (TYE) testes were obtained along with porosity, solids fraction, dimensional variation for numerous parts and operating conditions. Dimensional performance was found to be excellent.
- Elongation is a critical property for such structural castings and values noted at this time do not meet the 10% target. A trial is set for 1st quarter of 2008 to demonstrate improved elongation.

Application Demonstration

- Performed lateral and vertical bending tests on Mg shotguns.
- Constructed three full body-in-white (BIW) Ford F-150 cabs with all-Mg front-end structures consisting of two shotgun castings from the thixomolding process and a carry-over high-pressure die-cast (HPDC), Mg radiator support. (See Figure 8).
- Full front-end structure system-durability testing indicates the Mg shotgun equals the performance of the current steel version and weighs approximately 50% less than the steel components.

Future Direction

LTC

- Prepare and present competitive analysis.
- Identify and describe future projects key to proving out feasibility of LTC concept.
- Document all findings in a "Project Close-Out Report."

SLC Process

- As noted, the casting trials are complete with the remainder of the work focused on:
  - Characterize the mechanical properties of the castings.
  - Completing a statistical analysis of DoE results to determine process capability.
  - Develop conclusions and recommendations for further process improvements.
- Document findings in a "Project Close-Out Report."

Thixomolded Shotgun

- As a result of the casting trials conducted this year, the design of the shotgun is being modified with the associated tool changes in preparation for a final trial planned for 1st quarter of 2008. This is expected to yield elongation values in excess of the targeted 10%.
- Parts produced during the trial in 1st Quarter 2008 will be fully evaluated by x-ray, TYE, and durability.
- Document all findings in a "Project Close-Out Report."

Application Demonstration

- Dynamic Crash Testing of Mg shotgun
- Cost Comparison Study of ULC Structure vs. Conventional Steel Structure

The Rationale for ULCs

The majority of mass-market automobile and light-truck body structures are constructed of sheet metal stampings fastened together with resistance spot welding. This method of construction tends to increase the weight of the body because it introduces structural redundancies. For example, an outer panel requires an inner panel for stiffness, which in turn might require local reinforcements. The casting process enables all of these structural elements and features to be integrated into a single piece and, thus, has the potential to significantly reduce weight. This logic is illustrated with the example in Figure 1, which shows how a multi-piece, stamped-steel liftgate inner structure could be integrated into a single casting. There are numerous examples in the industry literature to be cited; however, the basic justification for ULCs is the ability to *reduce cost* by integrating components and *reduce weight* by taking advantage of the casting process to eliminate structural redundancies and, additionally, using lower- density material such as Mg or Al.

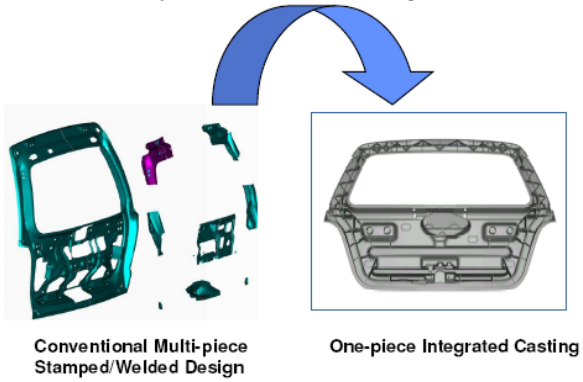

Figure 1. Example of parts integration.

Preliminary studies indicate large castings can be cost competitive with conventional stamped steel; however, a comprehensive, definitive case study comparing a true structural casting to conventional multi-piece stamped and welded construction has yet to be completed. Such a case study is essential for substantiating the rationale for ULCs and is undertaken by the ULC Team.

Existing Applications of Large Light-Metal Castings

There are many examples in the industry of what are considered ULCs such as die-cast Mg instrument panel structures, seat structures, closure inner structures, etc. However, it is more appropriate to describe these applications as quasi-structural because they are not totally integrated into the body structure. These quasi-structural components demonstrate the lightweighting potential of large castings replacing conventional stamped steel structures.

A notable example of an ultra-large structural casting is the current Ford F-150 radiator support structure. It is a one-piece, thin-walled Mg casting (see Figure 2) that replaces seven major stamped steel parts for a 25 lbs. weight savings. It is integrated into the body structure where it contributes to torsional stiffness and plays a role in crash. If applications of ultra-large structural castings like the F-150 radiator support and other large quasi-structural parts already exist, why is there a need for an ULC project?

Figure 2. Cast Mg radiator support.

These particular components are manufactured using the conventional HPDC process, which has some inherent limitations in achieving consistent mechanical properties.

Current Manufacturing Processes for Producing Large Light Metal Castings

The F-150 radiator support and most large quasi-structural automotive light-metal castings are manufactured with the HPDC process. While they

perform adequately in many applications, HPDCs may not be suitable for other primary structures like pillars, rails or bodysides that have to manage large amounts of crash energy. HPDCs lack the level of ductility and other desirable mechanical properties for these structural applications. Therefore, further uses of HPDCs beyond today's applications are limited by the process capabilities and by the mechanical properties achievable with conventional die-casting.

Utilizing a relatively simple process such as HPDC to make structural parts is highly desirable by the industry. Unfortunately, the presence of porosity in HPDCs has a detrimental effect on mechanical properties. A plethora of countermeasures have been developed to combat porosity (and other shortcomings) of the HPDC process by introducing into the process vacuum, non-turbulent filling of the shot sleeve, and "squeezing" during solidification. There are also expensive, specialty, heat-treatable alloys that are used along with one or more of the countermeasures to lower porosity levels and improve quality, but not without significant increase in cost. In spite of these enhancements and spin-off HPDC-based processes, HPDCs continue to be challenged by tradeoff between quality and cost. This inhibits the wide use of HPDCs as primary structural parts.

Besides porosity and non-uniform mechanical properties, adapting HPDC to ULCs presents other challenges such as low yield. In some cases, over 50% of the shot weight consists of biscuits, runners and overflows. This has an effect on economics, especially for Mg die-castings since Mg is not able to be recycled in-process. As casting size increases, runner systems become larger and more complex, increasing tooling cost and necessitating the use of larger tonnage die-casting machines. This significantly increases the cost of capital equipment.

LTCs

There have been significant developments in die-casting machines and processes over the past 30 years (1975 – 2005). Nearly all of that development has focused on making castings that are more structurally sound. Squeeze casting and several semi-solid processes such as "thixocasting", Thixomolding™ and "rheocasting" are examples.

There have been a few examples of moderately - large thin castings but large, thin (1 mm) Al castings have not become common in the marketplace. Thin Mg castings (such as cellular telephone housings) are common, but they are small. The design freedom intrinsic with castings leads one to believe that there must be a market for large, thin Al and Mg castings if they can be made with a consistently high quality and at a low-enough cost.

This is not a study of the costing and pricing dynamics of the industry. If the castings can be made one-millimeter thick and cast at 240 castings per hour from a single cavity die, requirements for mass reduction and cost parity should be satisfied.

A casting process concept has been proposed and this engineering evaluation is to determine its technical and economic feasibility. For demonstration, a large, thin panel (e.g., pickup truck door inner) was chosen for a full analysis.

The procedure follows the North American Die Casting Association (NADCA) 23-step ***"Process Engineering and Design for Die Casting"*** flow chart. Questionable, missing data and physical relationships are identified. Concept designs for a casting-machine die and work cell to meet the processing requirements are created and will be described in the NADCA paper[1]. Following this engineering analysis, the economics of operation are developed.

Finally, detailed descriptions of possible follow-on projects were developed and are described in a separate section of this report. At this point, the following conclusions can be stated:

- It is feasible to pressure-cast components having a projected area of one square meter and a substantial area having a thickness of one millimeter. A door inner for a full-size pickup truck is an example.
- Such panels can be cast at a rate of 240 per hour.
- High investment cost and unproven technology are significant barriers.

- Cost model shows that such castings may be cost competitive with stamped-steel, door-inner panels.
- Direct material remains the largest single cost factor accounting for over half of the part cost without considering the amortized cost of tooling.

SLC Process Development/Demonstration

Although the SLC process has been described in previous annual reports, some review is provided here. It is a unique process that offers the potential to produce thin-wall Al castings having greater properties (i.e., no heat treatment) than typically achieved by conventional sand, permanent-mold or die-casting processes. The THT hardware system offers the possibility to operate as many as four injectors; thus, the metal flow length can be kept low while producing large parts. The machine operates as a vertical casting machine at elevated pressures with the injectors providing metal with a vertical stroke. The time that molten metal is held in the injector determines the solid fraction of metal injected.

SLC Approach

To conduct this evaluation, a test part was designed that met the following criteria:

- Producable on an existing 1000-ton machine
- Part reflects the flow length for a ULC
- Part casting features/challenges are representative of a structural ULC
- Enables the assessment of knit-line quality
- Same tool set can be readily used for fluidity (Figure 3) test, part geometric features of rib section (Figure 4) and step (waffle) section (Figure 5) and knit-line node (Figure 6) evaluation
- Fluidity picture frame (Figure 3) measures 395 mm by 395 mm
- Flow length from gate thru the rib section (Figure 4) is 580 mm and the same holds for the step section. For example, the metal flows from the gate thru the grid section and exits the grid section after flowing approximately 580 mm.
- Flow length from the gate to the far side of the knit-line node is approximately 530 mm. The node is a cylinder 50-mm high with a 63.5-mm inner diameter (ID) and 6.5-mm wall. NOTE: the runners for the grid, step and node are primarily a U-section with the width 53.6 mm, height 40 mm, and nominal wall thickness of 3 mm.

Figure 3. Fluidity test part.

Figure 4. Rib geometry.

SLC Experimental Results

The flow length was conducted first. The total flow length for the fully-filled part is in excess of 1.5 m. The sides of this fluidity picture frame measures 395 mm square (Figure 3).

With respect to fluidity (Figure 4), a DoE was conducted with the following results:

- Primary variables were determined to be gate velocity (flow turbulence & fill time), die temperature, and section thickness.
- Secondary variables were determined to be metal temperature and vacuum level.

With respect to part geometries (see Figures 5 and 6) quality (x-ray), a DoE was conducted with the results summarized:

- Primary variables are gate velocity (lower velocity is better) and vacuum level
- Secondary variables are metal temperature, section thickness and die temperature.

Figure 5. Waffle geometry.

Figure 6. Knit-line node geometry.

For the above tests, the die lubricant was found to significantly impact the test results. Casting quality noted by x-ray appears to degrade as the distance from the ingate increases and the ingate velocity increases and this is particularly true following a change in flow direction. The simulation results were confirmed with the actual testing trials.

SLC Conclusions

- Low flow velocity and short flow distances, thus, hot-runner technology (Mg) and multiple in-gates for Al are desirable for quality parts
- Stable die temperatures yield consistent casting quality and reduced process scrap.
- Elevated die temperatures enable manufacture of components having reduced cross-section.

The remaining effort will include:

- Property determinations
- Process assessment for Al and Mg parts with economics
- Project Close-Out Report

Thixomolded Shotgun

G-Mag is modifying tooling in preparation for one more casting trial utilizing the Thixomolding process to produce a Mg shotgun. The Thixomolding process has the potential to produce Mg ULCs with properties compatible with structural applications at costs competitive with steel components. The effort exploits the semi-solid process licensed by Thixomat, Inc. of Ann Arbor, Michigan. It can be best described by its similarity to plastic injection molding. Mg is prepared in chip form and supplied to the casting machine where the chips are partially melted and injected into the mold cavity.

To evaluate and develop the process, a shotgun for a Ford F-Series vehicle was chosen. The shotgun (see Figure 7) joins the A-pillar to the radiator support structure. The radiator support structure is a Mg casting produced by the HPDC process. For such a part, a full evaluation of the component can be conducted.
Before 2007, the part design and the tooling was evaluated by FEA and casting simulations and reported in the annual report for 2006. The major part of the activity for 2007 involved actual casting trials.

Figure 7. F-Series "Shotgun."

Figure 8. Full-cab with Mg shotguns.

Casting Trials

A DoE was performed to determine optimized process settings. Various factors including injection speed, melt temperature, shot size and mold temperature were reviewed extensively. The best parameter values were chosen based upon part appearance. For example, 100% part appearance is completely filled, no visual cold flows, no holes in the ribs, no underfill, no sink marks, no cracks, no distortion and no warpage. The other extreme (0%) is a part with voids, cold flows, underfill areas, cracks, distortion, broken ribs, warpage, and non-uniform fill due to blocked gates.

Thixomold DoE

A Taguchi DoE design was conducted with L8 table having 6 factors and 2 values.

The nominal parameters are:

- AM60 material
- Injection Machine-Husky Hydroelectric 1000t
- Hot runner, 4-drop shotgun tool

DOE Parameters

- Metal Temperature (1120°F, 1145 °F)
- Mold Temperature (400°F, 500°F)
- Injection Speed (3 m/s, 6 m/s)
- Hold Pressure (500 psi, 1000 psi)
- Hold time (0.5 s, 1.0 s)
- Cool time (20 s, 30 s)

Based upon the part appearance criterion, the following was concluded:

- Injection speed, melt temperature and mold temperature have the greatest impact
- Holding pressure and cooling time have minimal impact on part appearance.

Dimensional Variation

Fifteen lefts and fifteen right shotguns were randomly selected and examined dimensionally with the following information:

- The overall length varied from 843.67 mm to 845.510 mm (i.e., less than +/- 1 mm)
- An important hole-to-hole spacing varied from 353.756 mm to 354.518 (i.e., less than +/- 0.5 mm)

In addition, parts were checked for distortion or flatness. Again, parts were selected randomly and found to be flat within an average of 0.044 mm with a max of 0.091 mm and a minimum of 0.007 mm.

Tensile, Yield and Elongation

TYEs were measured for a large group of parts with elongation as high as 17% with an average of approximately 5% in the areas evaluated. Representative yield and tensile strengths are 18 ksi and 27 ksi, respectively. It was the goal to achieve a 10% elongation over much of the part area, but this has not been achieved.

Porosity

In area of the buckling zone, the solid % was determined to be an average value of 6% solids (4.22% to 7.99%) with an average porosity of 0.77% (0.51 to 1.04 %) established by Archimedes method.

Full Component Durability Test

Ford conducted a durability test on a shotgun selected at random with its life exceeding that of the steel shotgun being used today. The Mg shotgun weighed approximately half that of the steel part.

Conclusions

As a result of the effort expended this year the following conclusions are provided:

- Dimensional control was very acceptable.
- The critical property of elongation fell short of expectations (i.e., seeking 10%). Changes in the part design are being made that are expected to result in a 10% elongation.
- Solids content varies significantly over a relatively small area of the part and around the same drop.

Future Direction

As a result of the evaluations reported, the part design was modified with casting simulations currently underway. The tooling will be subsequently modified and another series of castings will be produced for evaluation. Again, these changes are expected to result in the desired 10% elongation.

Presentations/Publications/Patents

1. Edmund Herman, *USCAR/USAMP Large-Thin Casting Project*. NADCA/AFS 112th Metalcasting Congress at CastExpo '08, May 17, 2008, Atlanta, GA.
2. Ultra Large Casting (USCAR) "Shotgun" awarded 1st Place in the Process Category, IMA 2007 Awards Competition, May 15, 2007 Vancouver, BC.
3. Michael Maj, *Ultra-Large Castings for Lightweight Vehicle Structures*, IMA Automotive Seminar, March 28, 2007, Laurel Park Manor, Livonia, MI.
4. Michael Maj, *Ultra-Large Castings for Lightweight Vehicle Structures*, TMS 2007 Annual Meeting, 2/21 thru 3/1, Orlando, FL.

References

1. Edmund Herman, *USCAR/USAMP Large-Thin Casting Project*. NADCA/AFS 112th Metalcasting Congress at CastExpo '08, May 17, 2008, Atlanta, GA.

[i] Denotes project 406 of the Automotive Materials Division (AMD) of the United States Automotive Materials Partnership (USAMP), one of the formal consortia of the United States Council for Automotive Research (USCAR) set up by Chrysler, Ford and General Motors (GM) to conduct joint, pre-competitive research and development.

D. High-Integrity Magnesium Automotive Castings (HI-MAC) (AMD 601[i])

Principal Investigator: Bruce Cox, Senior Specialist Casting
Chrysler Corporation
CIMS 481-01-41
800 Chrysler Drive
Auburn Hills, MI 48326-2757
(248) 576-0235; fax: 248-576-7288; e-mail: bmc8@chrysler.com

Technology Area Development Manager: Joseph A. Carpenter
(202) 586-1022; fax: (202) 586-1600; e-mail: joseph.carpenter@ee.doe.gov

Field Project Officer: Aaron D. Yocum
(304) 285-4852; fax: (304) 285-4403; e-mail: aaron.yocum@netl.doe.gov

Expert Technical Monitor: Philip S. Sklad
(865) 574-5069; fax: (865) 576-4963; e-mail: skladps@ornl.gov

---

Contractor: United States Automotive Materials Partnership (USAMP)[i]
Contract No.: DE-FC26-020R22910 through the DOE National Energy Technology Laboratory.

Objective

- Develop and validate casting-process technologies needed to manufacture squeeze- and low-pressure-cast magnesium (Mg) automotive suspension components.
- Address critical technology barriers inhibiting Mg application and component affordability.
- Deliver components for static and/or vehicle testing.
- Evaluate potential of emerging Mg-castings technologies.

Approach

- The approach of the HI-MAC project is to develop the metal-casting-process technologies necessary to cost-effectively manufacture high-integrity (high ductility and strength, low porosity, free of objectionable oxides and inclusions), cast Mg automotive-chassis components.
- This project will develop existing aluminum (Al), low-pressure permanent-mold and squeeze-casting processes for the production of Mg structural castings.
- The project aims to facilitate production of Mg components requiring geometries and properties not possible with existing high-pressure die-casting (HPDC) process limitations.
- Two new emerging casting processes (ablation and T Mag) will be investigated.
- The project will also develop enabling technologies critical to increased cast-Mg automotive applications—microstructure control, porosity and hot-tearing computer models, thermal treatments, and controlled mold filling.

Accomplishments

- Cost expenditures match original budget numbers and in-kind support meets or exceeds forecasted numbers.

- The HI-MAC Project team has 46 active participants from Chrysler, Ford, General Motors (GM), other industrial firms and academia.
- All project participants support the project functions including visits to project member's facilities and universities; participation in conference calls and quarterly review meetings (QRMs).
- Four, new, Mg-casting processes have been and are being developed. Rear lower control arms have already been produced from two of the processes.
- Seven different universities are actively involved in the HI-MAC project, including students from undergraduate to PhD levels.
- Microstructure properties and modeling techniques are being identified for the different types of Mg alloys that have already been cast.
- The *Magnesium Vision 2020 Document* (developed by the previous Structural Cast Magnesium Development [SCMD] project) is used as reference by the HI-MAC Project Team as the new Mg-casting processes are developed.

Future Direction

- Accomplishment of the four, new, Mg-casting processes will provide industry with higher-integrity, Mg, automotive castings that can be manufactured at a more economical initial set-up cost than is currently used by industry.
- The HI-MAC Project Team will provide Mg castings from two of the four new casting processes by year-end (YE) 2007 for testing and evaluations (Figure 2).
- Complete all statement-of-work (SOW) tasks in accordance with the original project timeline and budget figures.

Introduction

The overall introduction for this project has not changed since the original SOW was established. However, as each report is submitted to the Department of Energy (DOE), various aspects within the Introduction will be mentioned as progress is made in the completion of tasks. Perhaps the quickest, near-term path to increased Mg content in automobiles is through increased use of metal castings, and the HI-MAC Project is well on its way to support this goal.

HI-MAC addresses the near- and mid-term metal-casting development needs identified in the published document, *Magnesium Vision 2020.* Understanding and eliminating the technical barriers that currently inhibit Mg-casting production will move the automotive industry into a better position to realize emerging automotive Mg-component needs, build needed Mg-industry infrastructure and develop tools that will be needed to reduce the cost of Mg components and enable sustainable production requirements. The HI-MAC Project has already started to address these three key issues:

Development of Casting Tools: Develop technologies and tools that will be required for sustainable, long-term procurement of cast-Mg automotive-components (Tasks 3, 4, 5 and 6). These tasks will address the science and technological barriers that currently inhibit production and affect the affordability of cast-Mg components.

Casting Process Development: Develop casting processes to facilitate production of cast-Mg automotive chassis components that cannot be manufactured using current process limits (Tasks 1, 2 and 7). A new squeeze-casting cell (Figure 1) has already been built and is in operation by Contech, one of the HI-MAC Project participants.

Figure 1. Contech squeeze-casting cell.

A similar, low-pressure casting cell was also built (Figure 2) and Mg control-arm castings have already been produced (Figure 3).

Figure 2. CMI Equipment and Engineering low-pressure casting cell.

Figure 3. Mg control arm.

Infrastructure Development: Development of casting processes (Figures 1 and 2) and tools will include industry participation by automotive suppliers currently producing Al components (Tasks 1, 2, 7), the development of equipment uniquely suitable for the production of Mg components (Task 2, 6) and development of a broader research and science base (Tasks 3, 4, 5, 8).
New casting processes and tool development will be demonstrated by production of a Mg control arm by low-pressure cast, squeeze-cast, and newly-emerging casting processes. Control arms will be delivered for static and/or vehicle testing. To support the achievement of these processes, the project is divided into eight tasks to address key technology barriers that limit cast-Mg, automobile suspension and chassis applications and affect the manufacturing costs of these components as they are defined today:

Task 1: Squeeze-casting process development

Task 2: Low-pressure casting process development

Task 3: Thermal treatment of castings including research into stepped heat-treatment and fluidized beds

Task 4: Microstructure control during casting including grain refining and property improvement

Task 5: Computer modeling and properties to enable prediction of casting quality and microstructure

Task 6: Controlled molten-metal transfer and filling

Task 7: Emerging casting technologies

Task 8: Technology transfer Steering Committees have been formed to independently assist the Core Project Team in the achievement of these tasks.

Conclusions

The HI-MAC project addresses the critical barriers to Mg casting implementation, as stated in the *Magnesium Vision 2020* document. The four new casting processes will provide industry with higher-integrity, Mg, automotive castings for applications such as control arms, knuckles, and wheels that may ultimately enable weight savings of 35 to 60%. The new enabling technologies will reduce Mg-component processing and facility costs and enable the production of high-integrity Mg castings. The use of controlled, molten-metal transfer and filling (electromagnetic pump) will eliminate many of the production and environmental issues associated with the standard cover gas over Mg melts and yield higher-quality

castings. In addition to all of the above, the HI-MAC project will provide technical support to the Magnesium Front End Research and Development Project (AMD 604. See 6.B/).

Presentations/Publications/Patents

1. Beckerman,C., Prediction of Porosity and Hot Tears in Magnesium Castings at Materials Science and Technology (MS&T)2007 Conference, Detroit, MI September 2007.
2. Xue,Y., Horstemeyer, M., McDowell, DL., El Kadriri, H., Fan, J., Microstructure-based multistage fatigue modeling of cast AE44 magnesium alloys, Int J of Fatigue 2007; 29:666-76.
3. El Kadiri, Xue, Y., Horstemeyer, MF, Jordan, B., and Wang, P., Fatigue Crack Growth Mechanisms in a Die Cast AM50 Alloy, Acta Materialia 2006; 54:5061-76.
4. Low-Pressure Casting of Magnesium Alloys for Automotive Components; Greg Woycik, CMI Equipment & Engineering; American Foundry Society-111th Metalcasting Congress, May 15-18, 2007.
5. Magnesium Casting Technology Update; David Weiss, Eck Industries, Inc.; American Foundry Society-111th Metalcasting Congress, May 15-18, 2007.
6. HIMAC; Magnesium Squeeze Casting Update; Brian Szymanowski, Contech; American Foundry Society-111th Metalcasting Congress, May 15-18, 2007.
7. High-Integrity Magnesium Automotive Components (HI-MAC); Bruce Cox, Chrysler NA, American Foundry Society-111th Metalcasting Congress, May 15-18, 2007.

Acknowledgements

Within 14 months after project approval, the HI-MAC Project team had cast three Mg castings from three new casting processes. This success would not have been possible without the support and help from: the DOE; the USAMP Steering Committee; the USAMP AMD Board; Chrysler, Ford and General Motors; the other-industrial and academia support teams; the Canadian and US National Labs. In addition, the USCAR Office and American Foundry Society staff members were available to assist our Project Team during monthly and quarterly review meetings that were held at their respective facilities. The Project Chairmen appreciates the support from all of the teams mentioned above.

[i] Denotes project 601 of the Automotive Materials Division (AMD) of the United States Automotive Materials Partnership (USAMP), is one of the formal consortia of the United States Council for Automotive Research (USCAR), set up by Chrysler, Ford and General Motors (GM) to conduct joint, pre-competitive research and development. See www.uscar.org.

E. Casting/Solidification of Magnesium Alloys

Sergio D. Felicelli: Co-Principal Investigator
Associate Professor
Mechanical Engineering
Carpenter Engineering Bldg, Rm 210
Mississippi State University (MSST), MS 39762
(662) 325-1201; e-mail: felicelli@me.msstate.edu

John T. Berry: Co-Principal Investigator
FEF Key Professor and Coleman Professor of Mechanical Engineering
MSST
210 Carpenter Bldg.
Mississippi State, MS 39762
(662) 325-7309; e-mail: berry@me.msstate.edu

Douglas J. Bammann: Co-Principal Investigator
Professor, Mechanical Engineering
MSST
210 Carpenter Bldg.
Mississippi State, MS 39762
Office: (662) 325-3260; Home: (662) 294-2585; e-mail: djb215@me.msstate.edu

Liang Wang: Postdoctoral Associate
Center for Advanced Vehicular Systems, CAVS 2182-B
MSST, P.O. Box 5405
Mississippi State, MS 39762-5405
(662) 325-9235; Home: (662) 325-5421; e-mail: liangw@cavs.msstate.edu

A. Sabau
Oak Ridge National Laboratory (ORNL)
1 Bethel Valley Road, Oak Ridge, TN 37831-6083
(865) 241-5145; fax: (865) 574-4357; e-mail: sabaua@ornl.gov

Qingyou Han
Purdue University
Mechanical Engineering Technology Department
401 North Grant Street
Knoy Hall - Room 107
West Lafayette, IN 47907-2021
(765) 494-7528; fax: (765) 494-6219; e-mail: hanq@purdue.edu

Technology Area Development Manager: Joseph A. Carpenter
(202) 586-1022; fax (202) 586-6109; email: joseph.carpenter@ee.doe.gov

Field Project Officer: Aaron D. Yocum
(304) 285-4852; fax: (304) 285-4403; email aaron.yocum@netl.doe.gov

Expert Technical Monitor: Philip S. Sklad
(865) 574-5069; fax: (865) 574-6098; email: skladps@ornl.gov

Contractor: MSST
Contract No.: 4000054701

Objective

- Identify the root causes for porosity, segregation, and other defects in magnesium (Mg) cast parts and propose practical solutions for the improvement of casting processes.

Approach

- Mg-alloy cast parts are gaining increasing attention from the automotive sector, aiming at weight saving. However, the casting of Mg alloys is still plagued with problems that are difficult to solve: porosity, macro-segregation, oxide entrainment, irregularity of microstructure, corrosion, machining safety, etc. This research project addresses the fundamental behavior of solidification phenomena that lead to undesired defects (e.g., porosity, macro-segregation, mushy zone) in Mg cast parts, with the objective of developing new or improved casting methods for these alloys.

Accomplishments

- Task 1 – Add pore nucleation and growth models to MULTIA solidification simulator. Completed. Model validated with A356; validation with AZ91 coming next. Results presented at 2007 American Foundry Society (AFS) and The Minerals, Metals and Materials Society (TMS) conferences.
- Task 2 – Upgrade MULTIA with an ORNL algorithm for coupled micro-porosity and interdendritic flow. 70% completed. A MSST Master of Science (MS) student is working in the project.
- Task 3 – Perform measurement of density and permeability in mushy zone of Mg alloys. 50% completed. Density measurement to be performed at High-Temperature Materials Laboratory (HTML). Samples of AZ91, AM60, and AE44 are being prepared. Permeability will be determined with indirect method from measurement of cooling rate and dendrite-arm spacing in cast samples made at ORNL. Cast ingots of various sizes were made of AM60B and AZ91D, with measurement of cooling curves. Additional die-cast samples of AE42, AE44, and AM50 were also sent to MSST. Characterization is in progress.
- Task 4 – Perform thermodynamic calculations of physical properties of Mg alloys. 20% completed. Curves of temperature (T) vs. fraction liquid calculated at ORNL for AM60B, AZ91D, AE42, AE44 and AM50. MSST just purchased ThermoCalc Mg database. Calculations of other physical properties are in progress.
- Task 5 – Apply MULTIA to simulate porosity and segregation in Mg-alloy castings. To be started once a full data set can be obtained. First alloy to be simulated will be AZ91, then AM60 and AE44.
- Task 6 – Perform validation experiments for Mg-casting simulations. Scheduled for year two, but we are gathering literature experimental data on AZ91 to validate several aspects of the model.

Future Direction

- Task 1 – Validate model with permanent-mold (PM) castings of AZ91, AM60 and AE44.
- Task 2 – Task to be completed by end of 2007.
- Task 3 – Supply round bar samples of AZ91, AM60 and AE44 to HTML for measurement of density in mushy zone, specific heat and thermal diffusivity (collaboration of A. Sabau and W. Porter, ORNL). MSST to characterize Mg-alloy samples made at ORNL for determination of permeability (collaboration of Q. Han, Purdue Univ.).
- Task 4 – Finish thermodynamic calculations of properties of AZ91, AM60 and AE44. Assemble a complete MULTIA data set for these alloys, obtaining remaining properties from experiments or literature.
- Task 5 – Perform simulations of segregation and porosity formation for the above alloys in PM casting.

Project Staffing Overview

After visiting us for an invited seminar in the last week of March, Prof. William Griffiths (University of Birmingham, UK) has just returned to MSST for a sabbatical leave. He will spend four months working with us. Professor Griffiths has an extensive experience in Mg alloys and oxide films defects, and he will be a valuable support to the project. A section summarizing his recent research on oxide bifilms in Mg castings is included in this report.

Graduate students Sandeep Poola and Hebi Yin have been recruited for the project. Sandeep (MS student) spent two weeks at ORNL working with Dr. Qingyou Han on casting of Mg-alloy samples for determination of permeability. Hebi (Ph.D. student) is developing a cellular automaton model for calculation of solidification microstructure in Mg alloys. Ph.D. student Claudio Pita is developing a meshless method for simulating the dynamics of oxide bifilms, under our National Science Foundation (NSF) project "Modeling of oxide bifilms in aluminum castings." A new Ph.D. student, Udaya Sajja, has recently joined this project.

Sergio Felicelli attended a High-Integrity Magnesium Automotive Casting (HI-MAC. See 3.D) quarterly report meeting in March 2007 at the AFS headquarters to stay informed on the progress in that project directly related to ours. We continue monitoring their progress through access to the HI-MAC viewroom.

Dr. Felicelli contacted Prof. Jeff Wood at University of Western Ontario to become informed of their work for the AUTO21 initiative. Though their research has been in the area of high-pressure die casting (HPDC), a potential collaboration link was established.

We purchased a license of thermodynamic software ThermoCalc, plus additional licenses for the steel, aluminum (Al) and Mg databases. Training on the software was held on site for several researchers of the ORNL/MSST project.

Graduate student Enrique Escobar de Obaldia, who worked in the porosity model development, graduated in May 2007 with a MS degree and is now a project engineer at MAGMA Foundry Technologies, IL.

Modeling the Onset and Evolution of Hydrogen Pores During Solidification

Team Members: Sergio Felicelli, Claudio Pita, Enrique Escobar de Obaldia

Abstract

A quantitative prediction of the amount of gas microporosity in alloy castings is performed with a continuum model of dendritic solidification. The distribution of the number and size of pores is calculated from a set of conservation equations that solves the transport phenomena during solidification at the macro-scale and the hydrogen diffusion into the pores at the micro-scale. A technique based on a pseudo-alloy solute which is transported by the melt is used to determine the potential sites of pore growth, subject to considerations of mechanical and thermodynamic equilibrium. Two critical model parameters are the initial concentration of the pseudo-solute and the initial size at which pores start to grow. The dependence of the model prediction on these parameters is analyzed for Al A356 plate castings and the results are compared with published experimental data.

Introduction

Although porosity occurring during alloy solidification is very harmful to the mechanical properties of alloys, the control or elimination of this defect is still a formidable task in modern foundries. The formation of microporosity in particular is known to be one of the primary detrimental factors controlling fatigue lifetime and total elongation in cast Al components [Major, 1997]. Microporosity refers to pores which range in size from micrometers to hundreds of micrometers and are constrained to occupy the interdendritic spaces near the end of solidification. The micropores can form due to microshrinkage produced by the pressure drop of interdendritic flow or because of the presence of dissolved gaseous elements in the liquid alloy. In this work, we focus on the calculation of gas microporosity and, unless noted otherwise, we use the term porosity to mean gas-induced microporosity. In the case of Al alloys, hydrogen is the most active gaseous element leading to gas porosity [Felicelli, 2000]. Many efforts have been devoted to the

modeling of porosity formation in the last 20 years, particularly in Al alloys [Felicelli, 2000, Han, 2002, Lee, 2001, M'Hamdi, 2003, Poirier, 2001, Zhu, 2005] and, in a lesser degree, to nickel superalloys [Felicelli, 2000, Guo, 2003] and steels [Carlson, 2003, Sung, 2002]. More recently, rather sophisticated models have been developed to include the effect of pores on fluid flow (three-phase transport) [Sabau, 2002], multiscale frameworks that consider the impingement of pores on the microstructure [Lee, 2004], and new mechanisms of pore formation based on entrainment of oxide bifilms [Yang, 2004]. A recent review on the subject of computer simulation of porosity and shrinkage related defects has been published by Stefanescu [Stefanescu, 2005].

Mathematical Model

The model presented here is based on a robust and well-tested, multicomponent solidification program that calculates macrosegregation during solidification of a dendritic alloy with many solutes [Felicelli, 1998]. The model (named MULTIA) solves the conservation equations of mass, momentum, energy, and each alloy component within a continuum framework in which the mushy zone is treated as a porous medium of variable permeability. In order to predict whether microporosity forms, the solidification shrinkage due to different phase densities, the concentration of gas-forming elements and their redistribution by transport during solidification, were later added to the model [Felicelli, 2000]. In this form, the model was able to predict regions of possible formation of porosity by comparing the Sievert's pressure with the local pressure, but it lacked the capability of calculating the amount of porosity. This model has already been presented in detail in [Felicelli, 2000] and [Felicelli, 1998], and references therein; only the main assumptions and governing equations are presented here. In particular, we discuss a method that adds to MULTIA the capability of calculating the volume-fraction of porosity and the pore-size distribution during solidification. In this method, the growth of pores is simulated with a micro-scale growth model that is coupled to the macro-scale governing equations in MULTIA. The criterion for the formation of pores is based on equilibrium conditions between the pores and the alloy and on the transport of a pseudo-solute that represents inclusions or impurities dissolved in the alloy. The pore volume fraction as well as the pore-size distribution can be determined from the evolution of the population and size of pores during solidification.

Governing Equations

The following assumptions are invoked: the liquid is Newtonian and the flow is laminar; the Boussinesq approximation is made in the buoyancy term of the momentum equation; the solid phase is stationary; the gas phase does not affect the transport equations (two-phase model); and the densities of solid (ρ_s) and liquid (ρ_l) are different but constant. Additional assumptions are made at appropriate places in the article. With these assumptions, the conservation equations can be written as [Felicelli, 2000]:

Mass and momentum:

$$\nabla \cdot \mathbf{u} = \beta \frac{\partial g_l}{\partial t} \tag{1}$$

$$g_l \frac{\partial}{\partial t}\left(\frac{\mathbf{u}}{g_l}\right) + \mathbf{u}\cdot\nabla\left(\frac{\mathbf{u}}{g_l}\right) = -\frac{g_l}{\rho_l}\nabla p + \frac{\mu}{\rho_l}\nabla^2\mathbf{u} - \frac{\mu}{\rho_l}\frac{g_l}{\mathbf{K}}\mathbf{u} + \frac{\mu\beta}{3\rho_l}\nabla\left(\frac{\partial g_l}{\partial t}\right) + \frac{\rho g_l}{\rho_l}\mathbf{g} \tag{2}$$

Energy:

$$\overline{\rho c}\frac{\partial T}{\partial t} + \rho_l c_l \mathbf{u}\cdot\nabla T = \nabla\cdot\overline{\kappa}\nabla T - \rho_s\left[L + (c_l - c_s)(T - T^H)\right]\frac{\partial g_l}{\partial t} \tag{3}$$

Solutes:

$$\frac{\partial\overline{\rho C}}{\partial t} + \rho_l \mathbf{u}\cdot\nabla C_l = \nabla\cdot\overline{\rho D\nabla C} - \beta\rho_l\frac{\partial g_l}{\partial t}C_l \tag{4}$$

In the above equations, **u** is the superficial velocity, g_l is the volume fraction of liquid, *t* is time, ρ is density, β is the shrinkage coefficient $\beta = (\rho_s - \rho_l)/\rho_l$, *p* is pressure, μ is viscosity, **g** is gravity, **K** is the permeability, *T* is temperature, *c* is specific heat, κ is the thermal conductivity, *L* is latent heat, T^H is a reference temperature, *C* is the solute concentration in weight per cent, and *D* is solute diffusivity. The subscripts *"s"* and "*l*" refer to solid and liquid, respectively, while a bar over a

variable means a volume average of the variable over the solid-plus-liquid mixture; for example, $\overline{\rho} = g_l\rho_l + g_s\rho_s$, where g_s is the volume fraction of solid. Several equations (4) are solved in the model, one per each solute. A particular solute is hydrogen, which can precipitate in gas form when its dissolved concentration in the liquid exceeds the solubility at the local temperature and pressure. The energy and solute equations are rearranged in modified form depending whether the solute is assumed to have negligible or complete diffusion in the local solid (like hydrogen). [Felicelli, 2000] and [Felicelli, 1998] provide more specific details on the model regarding additional rearrangement of equations and numerical solution procedures.

Calculation of Porosity

A pore-growth model is implemented at the microscopic scale together with a criterion for nucleation of pores. The term nucleation is here used in the general sense to refer to the origination of pores, without necessarily implying any particular mechanism of classical nucleation. We assume that, dispersed in the liquid, there is an initially-known distribution of microscopic inclusions. These can be oxide bifilms that were entrained during melt pouring, old oxide bifilms that existed in the melt before pouring, or other impurities that serve as possible nucleation sites for hydrogen pores. We call $n(\mathbf{x},t)$ the number of these inclusions per unit volume of alloy, where $n(\mathbf{x},0)$ is known. The inclusions are transported with the velocity field **u** of the liquid, and they can partition to the solid like the other solutes of the alloy. For implementation purposes, the inclusions are treated as another alloy solute with negligible diffusion.

We assume that hydrogen pores can nucleate and grow only at places where the following two conditions are met:

$$n > 0 \tag{5a}$$

$$p + \frac{2\sigma}{r} < p_S \tag{5b}$$

in which p_S is the Sievert pressure [Flemings, 1974], r is the pore radius and σ is the surface tension of the pore-liquid interface. Most of the mechanisms that have been proposed for the nucleation of pores are based on the size of interdendritic cavities and the theory of heterogeneous nucleation on non-wetted surfaces. These ideas have been challenged by John Campbell [Yang, 2004, Campbell, 2003, Campbell, 2006] and others, who propose a nucleation-free mechanism for pore formation based on the concept of double oxide films or bifilms. In this scenario, during pouring in a casting process, the liquid surface of the alloy can fold upon itself. Because the liquid surface is covered by an oxide film, the folding action leads to bifilms, which are entrained into the bulk melt as a pocket of air enclosed by the bifilm. In effect, the bifilm with its air pocket is the beginning of a pore. After entrainment, the turbulence causes the bifilm to convolute and contract. Posterior pore growth can occur by the simple action of unfurling of the bifilms which in turn can be caused by mechanical action of the surrounding melt and by the aid of hydrogen diffusion into the pore.

It is interesting to note that if the bifilm theory is correct, then it follows that Eq. (5b) is irrelevant because there is no direct contact between gas and liquid and, hence, no surface tension is involved. However, the unfurling of bifilms is probably affected by the diffusion of hydrogen into the bifilm through the oxide layer. Consequently, a threshold amount of hydrogen in the liquid may be necessary to produce sufficient unfurling.

In this work, we keep (5b) as a criterion for pore origination and test the modeling results thus obtained against experimental data. When conditions (5) are met, we assume that a concentration, *n,* of spherical pores form with a known average initial radius, r_0. If the pores are in a supersaturated environment, they will grow by hydrogen diffusion. Assuming that the pores maintain the spherical shape during growth in the liquid, the rate of hydrogen mass, m^H, entering the pore by diffusion from the liquid is given by:

$$\frac{dm^H}{dt} = 4\pi r_P^2 \rho_l D_H \left.\frac{\partial C_l^H}{\partial r}\right|_{r=r_P} \tag{6}$$

where r_P is the pore radius, r is the radial coordinate measured from the center of the pore,

and D_H is the diffusivity of hydrogen in the liquid. We assume that the hydrogen gas inside the pore behaves as an ideal gas and that the partial pressure of other gases in the pore is negligible compared to that of hydrogen (this is reasonable in Al alloys given the high diffusivity of H compared to other gases). In this case, the rate of increase of the volume of the pore, v_p, can be calculated as:

$$\frac{dV_P}{dt} = \frac{R_H T}{p_S}\frac{dm^H}{dt} \tag{7}$$

where R_H is the hydrogen gas constant. The radius of the pore, r_p, is then obtained as:

$$r_P = \left(\frac{3}{4\pi}V_P\right)^{1/3} \tag{8}$$

To estimate the radial derivative in Equation (6), we follow Yin and Koster [Yin, 2000] and consider the thickness of the diffusion boundary layer around the pore:

$$\left.\frac{\partial C_l^H}{\partial r}\right|_{r=r_P} \cong \frac{C_l^H - C_P}{\delta} \quad ; \quad \delta = 4\sqrt{D_H t} \tag{9}$$

where C_P is the solubility of hydrogen at the local pressure and temperature, given by Sievert's law [Flemings, 1974], and t is the time measured since pore nucleation. We must keep in mind that the pore growth model exists at the microscopic scale; there are no actual pores that are part of the geometry of the macroscopic model (the radial direction has no meaning in the macroscopic model). The pore radius calculated in Equation (8) should be interpreted as the average radius of pores in a location ***x*** where there are ***n(x, t)*** pores per unit volume.

Equation (6) is valid for pores that grow in the liquid. For pores growing in the mushy zone, the diffusion flux is taken as an average for liquid and solid [Poirier, 2001] and the pore area is multiplied by a shape parameter, α, in order to account for the distortion of the pores as they impinge into dendrites, with:

$$\alpha = \frac{r_P S_V}{3} \tag{10}$$

where α is the pore shape parameter and S_V is the specific area of the pore (ratio of pore area to pore volume). For spherical pores, $\alpha = 1$, while $\alpha > 1$ for pores distorted by dendrites.

The pores grow while there is liquid remaining around them and lock in size after complete solidification. The total fraction of porosity in the casting as a function of time can be calculated as:

$$f_P(t) = \frac{1}{V}\int_V n(\mathbf{x},t)V_P(\mathbf{x},t)d\mathbf{x} \tag{11}$$

where V is the volume of the casting.

To close the model, we need to provide some mechanism by which the concentration of dissolved hydrogen in the bulk liquid around the pore decreases to compensate the hydrogen provided to the pore (otherwise the pore will continue to grow indefinitely). That is, the transport equation for hydrogen needs to be modified to include a sink term. In the liquid, this equation is:

$$\frac{\partial C_l^H}{\partial t} = D_H \nabla^2 C_l^H - \mathbf{u}\cdot\nabla C_l^H - nC_l^H\frac{dV_P}{dt} \tag{12}$$

where the last term in the right-hand side represents the amount of hydrogen entering the pores from the liquid by diffusion. Because MULTIA is a two-phase code (liquid and solid), the gas phase is not included in the transport equations. Therefore, the validity of the proposed model needs to be restricted to small volume fraction of porosity, which is reasonable for the usual level of hydrogen microporosity measured in Al castings (< 1%). In this case, we can assume that the presence of the pores does not considerably affect the transport of other quantities like energy and momentum.

Model Application and Discussion

The solidification model is discretized in space and integrated in time using a finite-element algorithm that is described by Felicelli *et al.* [Fang, 1989, Felicelli, 1998]. Al A356 alloy is solidified by simulation in a bottom-cooled, two-dimensional mold. The two-dimensional simulated casting has dimensions of 26 mm in width and 300 mm in height. Gravity acts downwards. In addition to the alloy solutes in A356 (Si and Mg),

the gas-forming element, H, is considered. The computational domain is the casting; the top boundary is left open in order to allow for liquid flow to feed shrinkage. A no-slip condition is used for velocity at the bottom and two vertical boundaries, a stress-free condition is used on the top open boundary, and solute diffusion flux is set to zero on all closed boundaries. The thermal boundary conditions utilized in Poirier *et al* [Poirier, 2001] are used here, which are extracted from a measured thermal history in the plates cast by Fang and Granger [Fang, 1989]. The simulations start with an all-liquid alloy of the nominal composition initially at a uniform temperature of 958 K, which is 70 K of superheat. The thermodynamic and transport properties of the alloy, including the alloy elements and hydrogen, are the same as the ones in [Poirier, 2001], with the exception of the partition coefficient of hydrogen, for which we used the developments of Poirier and Sung [Poirier, 2002] to include the effect of the high eutectic fraction in A356.

We performed simulations for the following values of initial hydrogen content: 0.11, 0.25, and 0.31 cc/100g (Note: 1 wt% = 1.12 x 10^4 cc/100g), for which measured volume fraction of porosity and pore diameters were reported in the experiments by Fang and Granger [Fang, 1989]. In their work, these represented three different castings with the same geometry.

For all the calculations presented in this work, we used an initial pore diameter of 3 μm and a density of inclusions of $2x10^{11}$ m^{-3}. Taking the density of alumina as 4000 kg/m^3 and spherical inclusions of size equal to the initial pore size, this inclusion density corresponds to a concentration of approximately 5 ppm. This selection was guided by the work of Simensen and Berg [Simensen, 1980], who found that the smallest alumina particles in Al and Al-alloys ranged from 0.2 to 10 μm, while the concentration of oxides varied between 6 and 16 ppm.

Figure 1 shows the variation of pore volume fraction and pore diameter vs. cooling rate in the solidified casting for all three values of initial hydrogen content. In this figure, the light-grey dots are calculated values that span all the casting; each dot represents the pore volume fraction or pore diameter calculated at a mesh node in the casting.

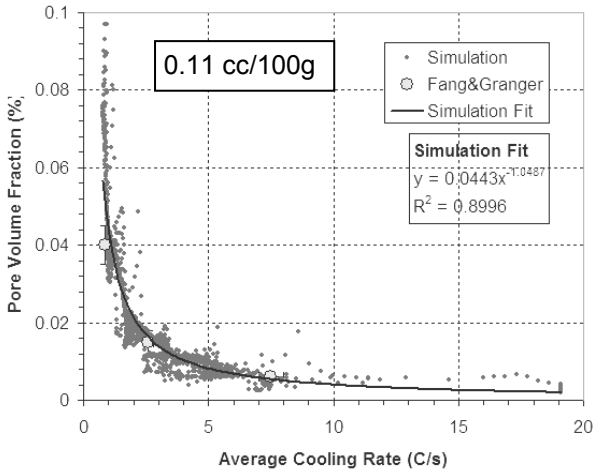

(a)

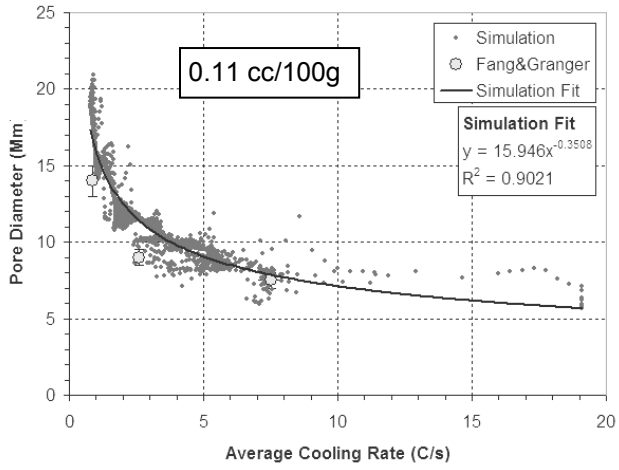

(b)

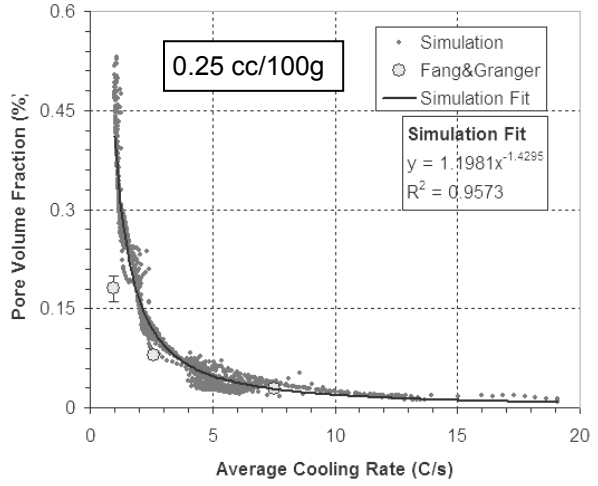

(c)

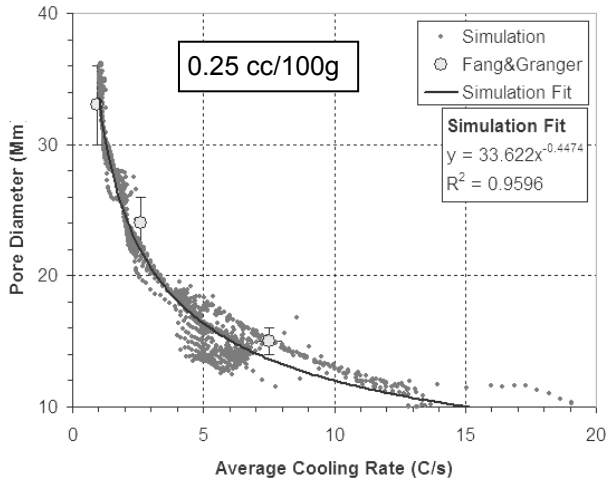

(d)

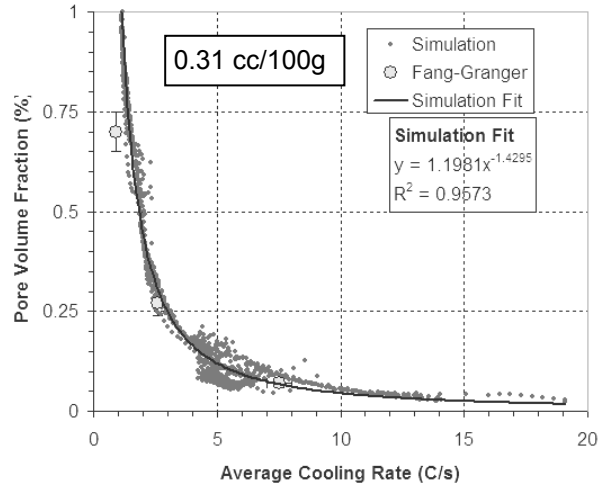

(e)

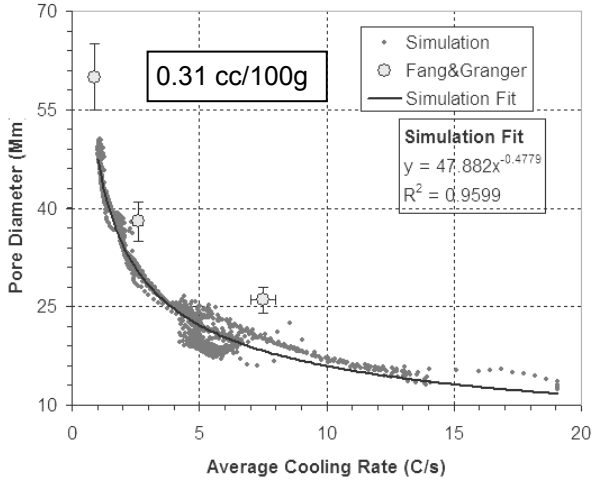

(f)

Figure 1. Pore volume fraction and pore diameter vs. cooling rate for different H contents.

A least-square fit of the calculated values is also shown as a solid black line. The experimental data of Fang and Granger [Fang, 1989] are indicated as larger light-grey dots; these were taken by manual reading from their paper, so bars estimating possible reading error are added. The experimental, larger, light-grey dots represent average values measured at a certain section of the casting, while the simulation shows the space variation within the entire casting. Certainly, the pore volume fraction and diameter are affected by other solidification variables in addition to cooling rate, but an average trend can be identified which is that they both decrease for higher cooling rates.

The quantitative agreement of simulated results with the experimental data is reasonable, considering that we are using a relatively simple, two-dimensional continuum model. As previously mentioned, all the results in Figure 1 were obtained using the same values of the initial pore diameter (d_0 = 3 μm) and concentration of inclusions ($n = 2\text{x}10^{11}$ m^{-3}). Although the selected values fall in the experimentally measured range reported in [Simensen, 1980], it is possible that pores originate with a range of sizes and that the concentration of inclusions may differ from one casting to another in the experiments of Fang and Granger [Fang, 1989]. A closer agreement with the experimental data can be obtained if the parameters d_0 and n are individually adjusted for each level of hydrogen content, but this approach was not pursued. In this sense, it is interesting to note that a same set of parameters works rather well for all three castings.

In addition to d_0 and n, a pore-shape parameter $\alpha = 1$ was used to obtain the results for the castings with 0.25 and 0.31 cc/100g of hydrogen content, indicating that the growth of pores in these castings was apparently not significantly affected by impingement of the pores on dendrites. However, we needed to use $\alpha = 4$ to reproduce the results of the 0.11 cc/100g casting, probably indicating that, in this casting, the pores were significantly distorted during growth. This observation is supported by the calculated fraction of liquid at which pores activate in each casting: 0.45, 0.75 and 0.85, for the 0.11, 0.25 and 0.31 cc/100g castings, respectively. We observed in the

simulations that, once activated, pores grew very fast, indicating that in the 0.25 and 0.31 cc/100g castings, the pores developed most of their size at high fraction of liquid and were not significantly affected by dendrite impingement. In contrast, in the 0.11 cc/100g casting, pores started to grow at an already high fraction of solid and were most probably largely distorted by dendrites during growth.

Conclusions

A continuum solidification model was extended to calculate the volume fraction of porosity and the pore-size distribution during solidification of Al alloys. The formation and growth of individual pores are calculated with a new hydrogen-diffusion technique in which the inclusions are treated as an additional alloy solute and subject to transport equations in the liquid and mushy zone. The method requires two parameters, the initial pore size and the concentration of inclusions, which are of physical nature and can be linked to measured data. The simulations show that the same set of these parameters is able to reproduce with reasonable agreement experimental data of different castings with varying levels of hydrogen content. A limitation of the method occurs when pores grow at high fraction of solid, which happens for the lowest level of hydrogen content. In this case, the growth of pores is highly affected by impingement on dendrites. Although the experimental data can still be reproduced through the use of a pore shape factor, a micro-model that links the pore shape parameter to physical quantities in the mushy zone would be desirable.

Acknowledgements

This work was partly funded by the National Science Foundation through Grant Number CTS-0553570. The authors gratefully appreciate the financial support provided by the Center for Advanced Vehicular Systems (CAVS) at MSST.

Appendix - Oxide Bifilms in Mg Castings (by Prof. W. Griffiths)

Double oxide film defects in castings occur when the oxidized surface of the liquid metal is folded over onto itself and recombined into the bulk liquid. The characteristic of a double oxide defect in Al and Mg alloys is, therefore, that of a thin layer of gas separating unbonded oxide surfaces—an ideal site for initiation of failure of the microstructure under load [Campbell, 1991]. There is much evidence for their occurrence in Al castings, and recent investigations into the casting of pure Mg have demonstrated the presence of double oxide films in this alloy also, where their unbonded nature has been demonstrated by SEM examination [Griffiths, 2007]. Al-alloys casting manufacture has been governed by process design principles involving a minimum ingate velocity of $<0.5\ ms^{-1}$. This has been shown experimentally to be valid in the case of Mg alloys also [Lai, 2004]. Double oxide film defects in Al have been shown to be nucleation sites for hydrogen (H) porosity [Raeiszadeh, 2006], and it is to be expected that gas porosity can be nucleated more easily in this way in Mg alloys, because a MgO film is porous and should allow diffusion of H gas, whereas alumina forms a protective film. Double oxide film defects in Mg have also been shown to be ideal sites for the nucleation of shrinkage porosity [Griffiths, 2007, Lai, 2004].

While the role of oxide film defects in Al alloys has been the subject of much research, their role in Mg alloys is still to be investigated. However, it is to be expected that they have similar, deleterious effects on properties due to the similar nature of the two alloy classes.

Presentations/Publications/Patents

1. S.D. Felicelli, E. Escobar de Obaldia and C.M. Pita, "Simulation of hydrogen porosity during solidification," *American Foundry Society Transactions*, vol. 115, paper 07-078, pp. 1-13 (2007) – BEST PAPER AWARD.
2. S.D. Felicelli, C. Pita and E. Escobar de Obaldia, "Modeling the onset and evolution of hydrogen pores during solidification," *Shape Casting: The 2nd International Symposium*, edited by P. Crepeau, M. Tiryakioglu and J. Campbell, TMS (The Minerals, Metals & Materials Society), ISBN: 978-0-87339-660-8, 2007, pp. 201-208.

References

1. [Campbell, 1991] "Castings", J. Campbell, Butter-worth-Heinemann, London, 1991.
2. [Campbell, 2003] Campbell J: Castings 2nd Edition – The New Metallurgy of Cast Metals. Butterworth-Heinemann, Oxford, UK, 2003.
3. [Campbell, 2006] Campbell J: Entrainment Defects, Materials Science and Technology Vol. 22, n 2, (2006), pp 127-145.
4. [Carlson, 2003] Carlson K D, Zhiping L, Hardin R A and Beckermann C: Modeling of porosity formation and feeding flow in steel casting *Modeling of Casting, Welding and Advanced Solidification Processes X*, D.M. Stefanescu, J. Warren, M. Jolly, and M. Krane (Eds.), The Minerals, Metals, & Materials Society, 2003, 295-302.
5. [Fang, 1989] Fang Q T and Granger D A: Porosity formation in modified and unmodified A356 alloy castings, *AFS Trans.* Vol. 97 (1989), 989-1000.
6. [Felicelli, 1998] Felicelli S D, Heinrich J C and Poirier D R: Finite element analysis of directional solidification of multicomponent alloys, Int. *J. Numer. Meth. Fluids* Vol. 27 (1998), 207-227.
7. [Felicelli, 2000] Felicelli S D, Poirier D R and Sung P K: A model for prediction of pressure and redistribution of gas-forming elements in multicomponent casting alloys, *Metall. Mater. Trans. B* Vol. 31B (2000), 1283-1292.
8. [Flemings, 1974] Flemings M C: *Solidification Processing* (New York: McGraw-Hill), pp 203-210.
9. [Griffiths, 2007] W. D. Griffiths and N.-W. Lai, *Met. and Mat. Trans. A*, Jan. 2007, vol. 38A, 190-196.
10. [Guo, 2003] Guo J and Samonds M T: Microporosity simulations in multicomponent alloy castings, *Modeling of Casting, Welding and Advanced Solidification Processes X*, D.M. Stefanescu, J. Warren, M. Jolly, and M. Krane (Eds.), The Minerals, Metals, & Materials Society, 2003, 303-311.
11. [Han, 2002] Han Q and Viswanathan S: Hydrogen evolution during directional solidifications and its effect on porosity formation in aluminum alloys, *Metall. Mater. Trans. A* Vol. 33A (2002), 2067-2072.
12. [Lai, 2004] N.-W. Lai, PhD Thesis, University of Birmingham, UK, 2004.
13. [Lee, 2001]Lee P D and Hunt J D: Hydrogen porosity in directional solidified aluminum-copper alloys: a mathematical model, *Acta Mater.* Vol. 49 (2001), 1383-1398.
14. [Lee, 2004] Lee P D, Chirazi A, Atwood R C and Wang W: Multiscale modeling of solidification microstructures, including microsegregation and microporosity, in an Al-Si-Cu alloy, *Mater. Sci. Eng. A* Vol. A365 (2004), 57-65.
15. [M'Hamdi, 2003] M'Hamdi M, Magnusson T, Pequet Ch, Amberg L and Rappaz M: Modeling of micropososity formation during directional solidification of an Al-7%Si alloy, *Modeling of Casting, Welding and Advanced Solidification Processes X*, D.M. Stefanescu, J. Warren, M. Jolly, and M. Krane (Eds.), The Minerals, Metals, & Materials Society, 2003, 311-318.
16. [Major, 1997] Major J F: Porosity control and fatigue behavior in A356T61 aluminum alloy, *AFS Trans.* Vol. 105 (1997), 901-906.
17. [Poirier, 2001] Poirier D R, Sung P K and Felicelli S D: A continuum model of microporosity in an aluminum casting alloy, *AFS Trans.* Vol. 109 (2001), 379-395.
18. [Poirier, 2002] Poirier D R and Sung P K: Thermodynamics of hydrogen in Al-Si alloys, *Met. Mater. Trans. A* Vol. 33A (2002), 3874-3876.
19. [Raeiszadeh, 2006] R. Raeiszadeh and W. D. Griffiths, *Met. Mat. Trans. B*, Dec. 2006, vol. 37, 865-871).
20. [Sabau, 2002] Sabau A S and Viswanathan S: Microporosity prediction in aluminum alloy castings, *Metall. Mat. Trans. B* Vol. 33B (2002), 243-255.
21. [Simensen, 1980] Simensen C J and Berg G, A survey of inclusions in aluminum, *Aluminium*, Vol. 56, No. 5, pp. 335-340.
22. [Stefanescu, 2005] Stefanescu D M: Computer simulation of shrinkage related defects in metal castings – a review. *Int. J. Cast Met. Res.* Vol. 18 (2005), 129-143.
23. [Sung, 2002] Sung, P K, Poirier D R and Felicelli S D: Continuum model for predicting microporosity in steel castings, *Modelling Simul. Mater. Sci. Eng.* Vol. 10 (2002), 551-568.

24. [Yang, 2004] Yang X, Huang X, Dai X, Campbell J and Tatler J: Numerical modeling of entrainment of oxide film defects in filling of aluminium alloy castings, Int. *J. Cast Met. Res* Vol. 17 (2004), 321-331.
25. [Yin, 2000] Yin H. and Koster J., "In-situ observed pore formation during solidification of aluminium", *ISIJ International*, vol. 40(4), pp. 364-372.
26. [Zhu, 2005] Zhu J D, Cockcroft S L, Maijer D M and Ding R: Simulation of microporosity in A356 aluminium alloy castings, *Int. J. Cast Met. Res.* Vol. 18 (2005), 229-235.

4. AUTOMOTIVE METALS – TITANIUM

A. Low-Cost Titanium Powder for Feedstock

Principal Investigator(s): Curt A. Lavender and K. Scott Weil
Pacific Northwest National Laboratory (PNNL)
Richland, WA 99352
(509) 372-6770; fax: (509) 375-4448; e-mail: curt.lavender@pnl.gov
(509) 375-6796; fax: (509)375-4448; e-mail: scott.weil@pnl.gov

Technology Area Development Manager: Joseph A. Carpenter
(202) 586-1022; fax: (202) 586-1600; e-mail: joseph.carpenter@ee.doe.gov

Expert Technical Monitor: Philip S. Sklad
(865) 574-5069; fax: (865) 576-4963; e-mail: skladps@ornl.gov

Participants:
Lance Jacobsen, International Ti Powder, Inc., 20634 W. Gasken Drive, Lockport, IL 60441
Michael Hyzny, DuPont, (302) 999-5252 e-mail:michael.t.hyzny@USA.dupont.com
Tim Soran, ATI Allvac, (509) 372-1711; e-mail:Tim.Soran@Allvac.com

---

Contractor: PNNL
Contract No.: DE-AC06-76RLO1830

Objective

- Investigate alternate powder and melt-processing methods for low-cost titanium (Ti) materials.
- Evaluate processing methods to produce powder metallurgy (P/M) Ti products with International Ti Powder, Inc. (ITP) powders.
- Evaluate the suitability of emerging Ti technologies for the production of low-cost Ti products for automotive applications.

Approach

- Perform characterization and analysis of the sintering behavior of commercial-purity (CP)-Ti and Ti-alloy ITP powder. Provide feedback of results to ITP for use in process design.
- Develop low-cost feedstock for P/M use in automotive applications from low-cost Ti tetrachloride ($TiCl_4$).
- Survey the emerging technologies for the low-cost production of Ti powders and evaluate for use in automotive applications.

Accomplishments

- Observed decreased swelling in a series of lower-purity, $TiCl_4$-produced powders relative to those synthesized from standard $TiCl_4$. The improvement is attributed to the increase in the onset of sintering temperature, which mitigates the entrapment of volatile impurities that would otherwise lead to pore formation and growth. The net effect is that the use of a lower-purity $TiCl_4$ may be beneficial in two ways: (1) it is a potentially lower-cost precursor to Ti powder production and (2) the trace impurities allow higher-density components to be fabricated via a typical, low-cost, press-and-sinter approach. Preliminary mechanical test results indicate that the impurities have no effect on tensile strength.

- An instrumented powder-pressing die was fabricated and used in die-pressing experiments, to measure the effectiveness of in-die and admixed powder lubrication in increasing green body density and reducing pressing pressure.
- The ITP powder particle-size distribution was modified by various milling techniques, including Spex, attrition and ball milling. Parameters have been developed, which minimize the production of fines (less than 400 mesh) that tend to cause die sticking and lead to an increase in the general oxygen content of the powder.

Future Direction

- On an ongoing basis, perform the necessary process characterizations, such as dilatometry and chemical, thermo-gravimetric, microstructural, and x-ray diffraction (XRD) analyses required to develop sintering cycles for Ti-alloy powder compositions of potential interest to the automotive industry that yield high-density components.
- Complete static mechanical properties testing of pressed-and-sintered test compacts produced from the milled and lubricated powders discussed above.
- Identify one or more suitable "automotive" components on which to focus a demonstration fabrication study. Press and sinter the demonstration components in an industrial P/Mfacility to validate findings from the milling, die lubrication, and sintering investigations.
- Contract with ITP to produce a low-cost, metastable, beta-type alloy powder for potential automotive applications.
- Evaluate alternate low-cost Ti feedstocks for P/M or wrought (melt-processing) products.

Introduction

The use of low-cost ilmenite to produce the $TiCl_4$ employed in the ITP process was demonstrated in the previous reporting period. It was determined that the low-cost $TiCl_4$ did not adversely affect ITP's powder-synthesis process. However, during a series of high-rate die-pressing trials using commercial P/M equipment, it was determined that the low-purity powder would require further modification to mitigate the high friction forces measured in the pressing studies, eliminate die sticking through better control of powder size distribution, and establish robust sintering conditions that simultaneously accommodate current commercial practice. Thus, during this reporting period, three key studies were performed: 1) the sintering behaviors of the low- and high-purity powders, 2) an instrumented powder-pressing die was constructed and trials were performed to measure the forces that lead to high friction, and 3) a series of milling trials to determine how the powder size distribution could be properly modified.

Results and Discussion

Sintering Investigation

As part of this activity, a study was initiated last year to examine the use of low-cost, ilmenite-derived $TiCl_4$ as the precursor in Ti powder synthesis. The $TiCl_4$ was synthesized by DuPont at their TiO_2 pigment-production facility. However, unlike the high-purity chloride precursor used in pigment synthesis, the low-cost $TiCl_4$ underwent only one stage of distillation to remove iron chloride impurities. Both this source of $TiCl_4$, and a second, high-purity source (refined via the typical multistage distillation process) were employed in synthesizing CP-Ti using the Hunter process at DuPont and the Armstrong process at ITP.

As shown in Table 1, there is little difference in the concentrations of interstitial and key reduction-reaction by-product (i.e., NaCl) impurities between the high- and low-purity-Armstrong-produced powders. Similar results were observed in the Hunter materials. However, results from induction-coupled plasma/mass spectroscopy (ICP/MS) analysis did indicate that trace impurity elements transfer from the proprietary, single-stage, $TiCl_4$ distillation product to both forms of low-purity powder. Low- and high-magnification micrographs of the various powders, shown in Figure 1, indicate that little difference in particle morphology was observed between the high- and low-purity forms of each powder type. From Figure 1, it is apparent that both the Hunter and Armstrong powders are actually agglomerates composed of fine-scale

crystallites. In general, the size of the constituent crystallites is smaller in the Hunter material than in the Armstrong-produced powders. The corresponding size distributions for the four different powder types are presented in Figure 2. Again, little difference was observed between the high- and low-purity versions of each powder type and the Hunter powder agglomerates tend to be several times smaller on average than the Armstrong powders.

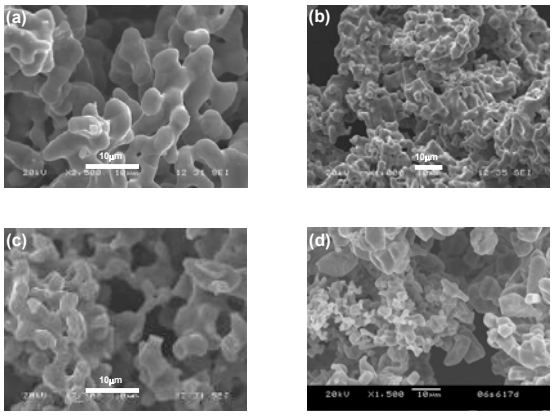

Figure 1. High-magnification images of: (a) high-purity Armstrong powder, (b) high-purity Hunter powder, (c) low-purity Armstrong powder, and (d) low-purity Hunter powder.

Element	High-purity Armstrong powder (ppm)	Low-purity Armstrong powder (ppm)
C	93	55
N	77	47
O	2400	1780
Na	330	110
Cl	19	21
BET (m^2/g)	0.31	0.31

Table 1. Concentration of interstitial and key reduction-reaction by-product (i.e., NaCl) impurities between the high- and low-purity, Armstrong-produced powders. BET = Specific surface area measurement.

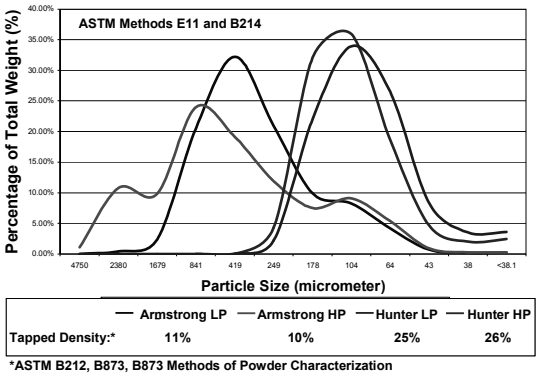

Figure 2. Particle-size distributions of high- and low-purity powders produced by the Armstrong and Hunter processes.

As discussed in the fiscal year (FY) 2006 annual report, prior dilatometry measurements indicated a significant difference in the sinterability of the high- and low-purity, Armstrong-produced materials. Specifically, in the high-purity powder, the onset of sintering takes place at ~400ºC whereas in the low-purity powder it is delayed to nearly 900ºC. Interestingly, however, tensile bars prepared from the high-purity powder exhibit substantially lower densities when sintered at 1250ºC than do comparable, low-purity specimens, as seen in the plot of as-sintered density vs. sintering time shown in Figure 3. A comparison of the internal microstructures of both specimen types in Figure 4 shows this difference more dramatically. As shown in Figure 5, swelling occurs in the high-purity specimens sintered for extended periods.

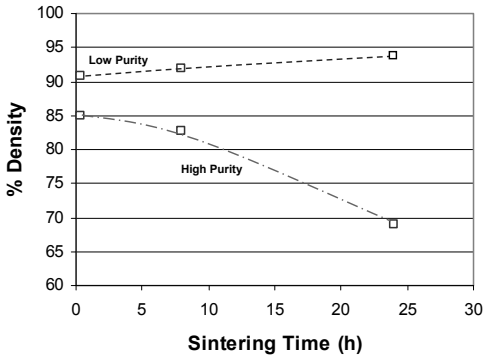

Figure 3. A plot of final density versus sintering time at 1250°C for two series of tensile specimens fabricated from high- and low-purity Armstrong powders.

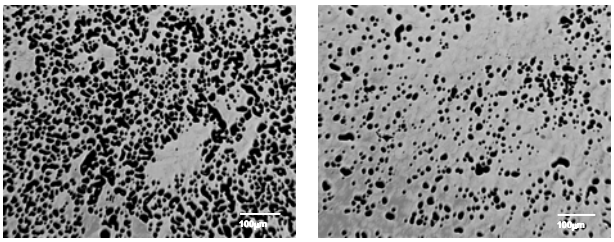

Figure 4. Cross-sectional scanning electron microscope (SEM) images of the internal microstructures of sintered bodies fabricated from: (a) high-purity and (b) low-purity Armstrong powders.

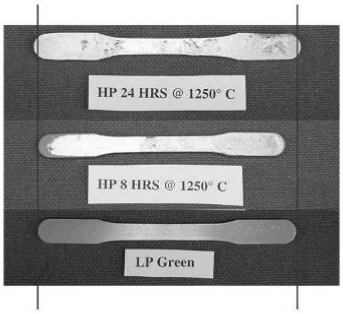

Figure 5. A comparison of the lengths of three tensile bars. Top two were prepared from high-purity Armstrong powder; bottom is representative of a tensile bar in the as-pressed condition.

At 1250ºC, the flow stress of CP-Ti is quite low (< 100 psi) i.e., the material will readily creep when placed under an external load or subjected to an internal pressure. It is suspected that a species susceptible to volatilization at high temperature (still undetermined) is present in the Armstrong-produced CP-Ti powder. If trapped within the Ti body during sintering, this species could lead to excessive pore formation and growth with the increase in time at elevated temperature. Recalling that the high-purity powder is far more sinterable than the low-purity material, it is, therefore, more prone to this type of entrapment/swelling mechanism, as shown schematically in Figure 6. Note that swelling has not been observed in Armstrong-produced Ti alloy powders (e.g., Ti-6Al4V) synthesized from high-purity $TiCl_4$, presumably because the alloying agents cause a delay in sintering that allows volatile species to escape the compact and avoid entrapment. The net effect is that the use of the lower-purity $TiCl_4$ source may be beneficial in two ways: (1) it is potentially a lower-cost precursor for use in Ti powder production and (2) the trace impurities allow higher-density components to be fabricated via a low-cost, press-and-sinter approach. Preliminary mechanical test results indicate that the impurities have no effect on tensile strength.

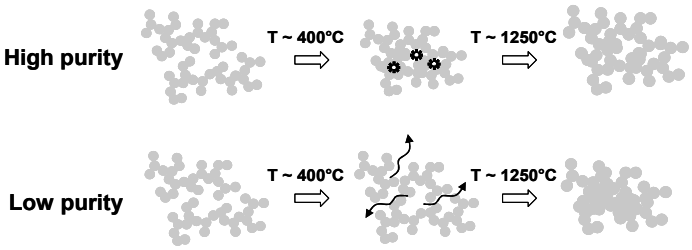

Figure 6. Schematic representations of the mechanisms speculated to occur during sintering of the high-purity and low-purity Armstrong processed CP-Ti powders.

Die Lubrication

In addition to the historically high material costs associated with Ti part manufacture, there are those inherent to conventional primary and secondary material processing, such as rolling, forging, and machining. One means of reducing production cost is to employ near-net-shape processing such as P/M techniques, where possible. A common P/M practice used in manufacturing small steel automotive parts (gears, pump bodies, etc.) is uniaxial die compaction. However, this has found limited application in fabricating high-quality Ti components because of the high powder and die-wall friction forces (i.e., particle/particle and particle/die-wall interactions) typically encountered during die compaction of Ti powder. High friction forces lead to inhomogeneous green densities, subsequent internal porosity, and part distortion during sintering. Porosity is particularly problematic in components designed for high fatigue life (i.e., springs and gears). In addition, excessive die-wall friction increases the force required to eject the part from the die cavity, which leads to increased die-wall galling, higher die wear, and shorter die life.

Both powder and die-wall friction can be reduced by incorporating an appropriate lubricant. The key is to identify a transient material that promotes the formation of high-density green bodies, yet is readily removed from the component prior to or during sintering, leaving behind no residual interstitial impurities (i.e., C, O, or N) that can embrittle the final part. Recognizing the potential

economic value of effective P/M processing for Ti automotive components, an instrumented die was designed at PNNL to measure die-stress profiles *in-situ* during compaction and to evaluate the efficacy of various lubricants in increasing compact green density and reducing die wear. Shown schematically in Figure 7(a), is a cross-sectional view of the die. Thirteen, radially-aligned, strain-gage pinholes have been machined into the die along at 30° angular increments and 2.54-mm height intervals to form a helical radial-stress measurement array. As shown in Figure 7(b), the instrumented die employs a matching pair of punches and four linear springs to simulate the double-action compaction process commonly employed in industry. Continuous monitoring of top-punch position, compaction load, and radial die stress affords real-time analysis of both die-wall stress and die-wall and powder friction. As shown in Figure 7(c), radial stress is measured via strain-gage pins that are axially constrained between the die wall and a hollow setscrew at each of the thirteen hole locations.

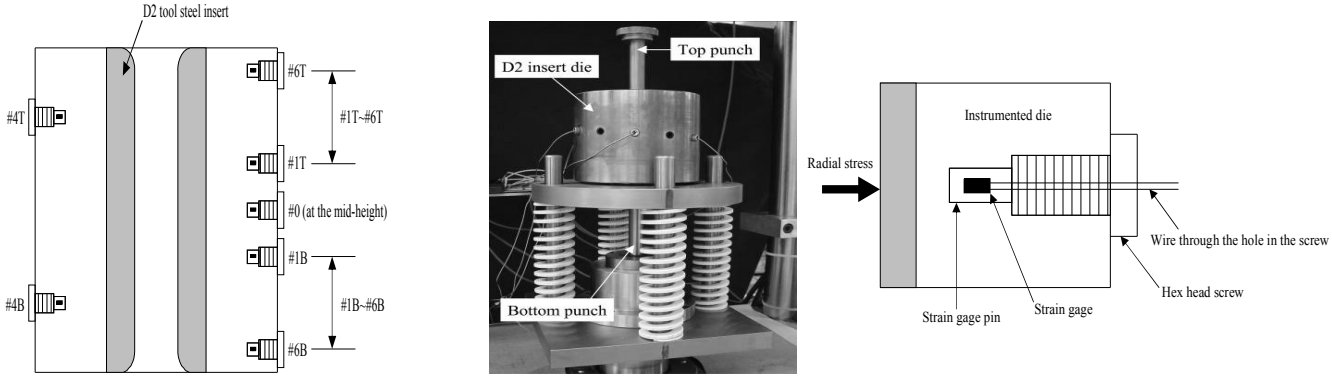

7(a) 7(b) 7(c)

Figure 7: (a) A schematic of the enhanced instrumented die: a cross-sectional side view. The strain-gage pin holes in the die are located helically with 30° angular and 2.54-mm height intervals. (b) The experimental set-up to simulate a double-action pressing. Two strain-gage pin holes were left open to clearly show the location of the holes. (c) A schematic of the assembly of a strain-gage pin and the enhanced instrumented die.

Using a pre-set maximum axial stress of 80 ksi, unmodified (i.e., no lubricant/binders added) Ti powder obtained from DuPont, Inc. CP-Ti powder produced as Hunter fines (apparent density = 0.87 g/cc, d_{50} ~ 131μm) was compacted to ~85% of theoretical density. For comparative analysis, a similar series of compactions was conducted using a commercial iron (Fe) powder obtained through Western Sintering, Inc. (blended with 0.75 wt% ethylene bistearamide wax, apparent density = 2.94 g/cc; d_{50} ~ 116μm), which compacted under the same axial stress to green densities averaging ~88% of theoretical. Shown in Figures 8(a) and (b) are the histories of the applied axial stress and the associated radial stress (measured at the vertical center of the die) as a function of time for the Ti and Fe powders, respectively. For both powders, the mid-height radial stress increases in nearly linear fashion with a linear increase in axial compaction stress. After a brief hold period, the axial stress drops to zero as the top punch is withdrawn for compact ejection. Note that a residual radial stress remains in each case due to friction between the powder particles within the compacts. In turn, this residual stress induces a die-wall frictional resistance force that must be overcome to eject the compacted part from the die. The radial stress generally decreases as the part is ejected. However, note that, for the Ti compact, there is a sharp increase in axial stress required for final ejection due to a higher static coefficient of friction for the Ti powder vis-à-vis Fe.

There is a correlation between the high ejection stress and the uniformity of radial stress in the green body both during the compaction and hold periods of the pressing process. Shown in Figure 9(a) are the radial stress profiles at maximum axial stress for the Ti and Fe powder compacts.

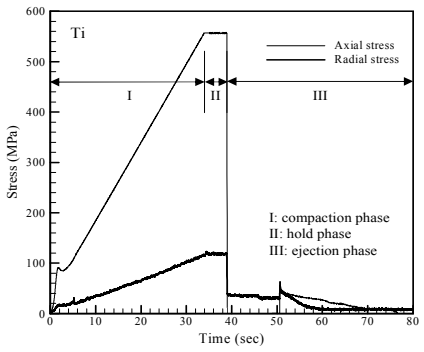

(a)

Figure 8. The histories of the applied axial stress and the radial stress, which was measured at the mid-height of the die, as functions of time for (a) the Ti powder and (b) the Fe powder.

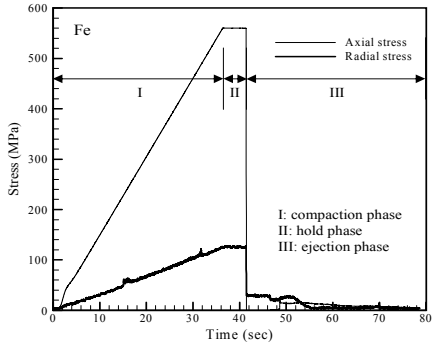

(b)

Note that for the Fe powder, the radial stress distribution is relatively uniform, which is not the case for the Ti material. The latter material displays a peak stress in the center of the compact, which is expected to be accompanied by a distinct gradient in density across the compact, i.e., also peaking at the center and tailing off near the top and bottom. Similarly, the graphs shown in Figure 9(b) display the residual radial-stress profiles for each compact recorded at the start of the hold period. Again, the profile measured from top to bottom for the Fe compact is uniform, while that for the Ti compact exhibits a maximum in the center of the body.

The Fe powder employed in these experiments is generally considered "ideal" for P/M processing via uniaxial die compaction. With that in mind, one of our objectives in lubricant selection for the

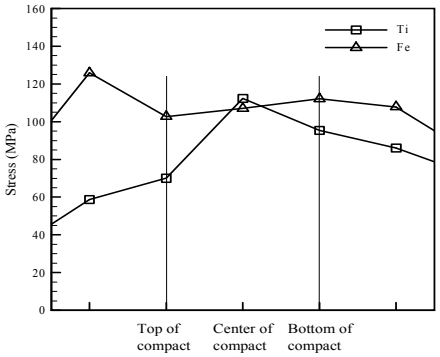

(a)

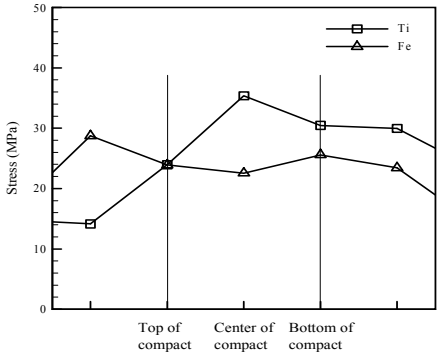

(b)

Figure 9. (a) Typical profiles of the radial stress at the limit axial stress for the CP-Ti and commercial Fe powders. (b) Typical profiles of the residual radial stress for the CP-Ti and commercial Fe powders. Note that each tick on the abscissas represents the stress measurement location of the die.

Ti powder is to duplicate the same type of pressing behavior in Ti as was observed with Fe, i.e., achieve moderately-low, residual, radial stresses and uniform radial stresses profiles during the compaction process and eliminate the spike in ejection stress. A series of polycyclic aromatic hydrocarbon (PAH) compounds was examined as potential powder lubricants, including: naphthalene, pyrene, anthracene, anthragallol, and camphor. In several cases, stearic acid (a well-known lubricant for Fe and copper (Cu) powders) was added as a secondary lubricant and a die-wall lubricant was employed. The PAHs were chosen because they are relatively easy to remove after powder compaction via sublimation under vacuum. To date, a series of 18 experiments has been conducted to explore the effects of powder lubricant composition and powder-to-lubricant ratio on radial stress distribution, die-wall friction distribution, and green density in CP-Ti compacts. While these experiments are still in the final stages of data acquisition, preliminary analysis indicates

that both powder and die-wall lubrication can substantially improve the compaction behavior of Ti. For example, shown in Figures 10 and 11 are the compaction test results (at an applied axial pressure of 80 kpsi) for unmodified CP-Ti and CP-Ti mixed in a 10:1 ratio with camphor, both in comparison with the previously described commercial Fe powder. Note the greater uniformity in radial stress across the lubricated powder compact and the corresponding reduction in die-wall friction. This leads to an increase in green density of 3 – 5%, which, in turn, can increase the sintered density from ~90% of theoretical to 96 – 98% while extending the life of the die. Without optimization, the compaction behavior of the lubricated CP-Ti powder is similar to that of the commercial Fe powder. Future work will focus on measuring what effects these lubricants may have on material chemistry in the as-sintered state. It is anticipated that the use of PAH-based lubricants will not cause a measurable increase in the concentration of interstitial elements, in particular carbon.

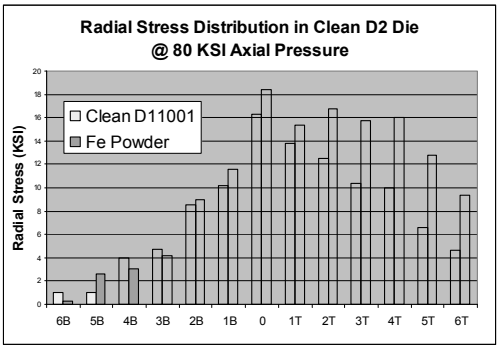

(a)

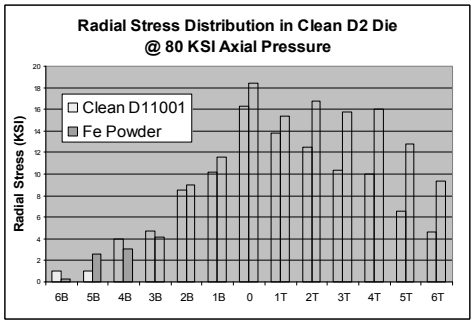

(b)

Figure 10. (a) Typical profiles of the radial stress at the limit axial stress for unmodified CP-Ti and commercial Fe powders. (b) Typical profiles of the die-wall friction for unmodified CP-Ti and commercial Fe powders.

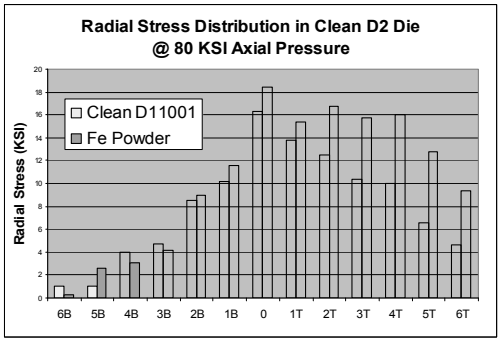

(a)

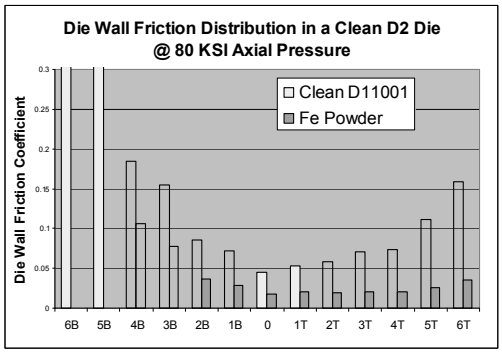

(b)

Figure 11. (a) Typical profiles of the radial stress at the limit axial stress for CP-Ti + camphor (10:1 volumetric ratio) and commercial Fe powders. (b) Typical profiles of the die-wall friction for CP-Ti + camphor (10:1 volumetric ratio) and commercial Fe powders.

Milling Studies

Although the ITP process has been demonstrated to produce high-quality Ti powder, the current size distribution will limit the potential automotive uses. The enhanced flow characteristics (as measured by the Hall meter in previous studies) and uniform die-fill required for very highly-detailed, net-shape automotive parts, will require additional milling of the powder. The challenge of milling the ITP Ti powder is to produce a size distribution that is fine enough to pour through the Hall meter without generating a large fraction of fine powders that increase interstitial element content and become trapped between the die and punch, causing die sticking (typically considered to be less than 400 mesh). Therefore, a study to

modify, in a controlled manner, the particle size distribution was initiated. Milled powders were evaluated based on powder morphology, particle-size distribution and oxygen content. Three separate milling techniques were evaluated using variations of the applicable parameters of each methodology. High-energy Spex milling, low-energy ball milling, and high-production-throughput attrition milling were selected for the study. Each system was modified for milling operations to take place in an argon-rich environment.

Many parameters, including milling aids, time, media, and intensity, were evaluated and each milling process selected produced a powder size and morphology that poured easily through the Hall meter. The typical appearance of the powder produced by each method is shown optically in Figure 12. The most important finding was that ball-milling and attrition-milling compacted the agglomerates rather than fracturing the agglomerates, as was observed in the SPEX-milled powders. As expected, the attrition- and ball-milled powders produce fewer particles less than 230 mesh and had correspondingly lower oxygen content. Several iterations on the process parameters for the three milling methods have been made and, as reported previously, the high-intensity SPEX-milling process produced large fractions of fine powders and a nearly 2000 ppm increase in oxygen content and, as such, has been eliminated from the test matrix. A small sampling of the effectiveness of ball and attrition milling has been included in Figure 13, where samples of the powder, with equivalent particle distribution, are compared for oxygen content for powder sizes above and below 230 mesh. As shown by Figure 13, for powders of an equivalent powder size distribution, large differences in oxygen content were observed depending on parameters used. For example, attrition milling could produce powders that ranged in oxygen content from a minimum of 2500 to greater than 4200 ppm, for conditions labeled #3 and #1, respectively.

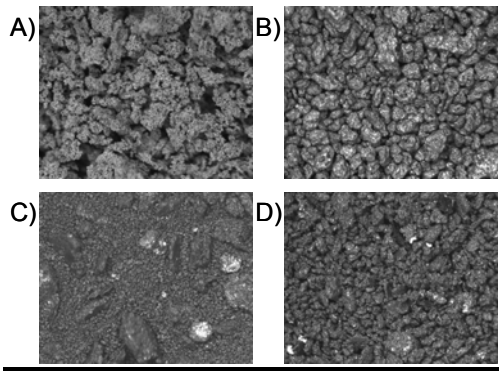

Figure 12. CP-Ti powder. A) As-received from ITP. B) Ball-milled powder. C) SPEX-milled powder. D) Attrition-milled powder.

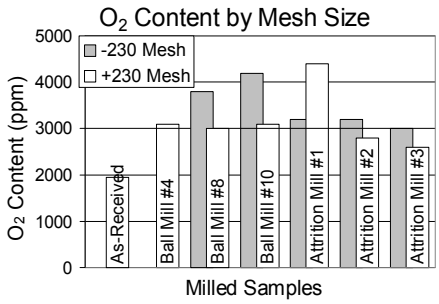

Figure 13. Chart comparing oxygen contents of Ti powders exposed to several milling conditions. The powders reported here were selected based on morphological similarity.

Conclusions

The low-purity powders produced by ITP are suitable for many bulk part applications and have been used in powder rolling and cold-hearth melting with a high degree of success. However, the highly-detailed parts used in automotive applications, such as valves, gears, springs, and fasteners that are candidates for Ti, require a finer, uniform powder distribution in order to meet the lowest part-cost, net-shape, P/M processing methods. During this reporting period, the following conclusions regarding the low-cost ITP powder for automotive P/M applications were reached:

- Sintering conditions that lead to increased part density can be established based on the proper control of the onset temperature for sintering.
- Die lubrication can be used to mitigate galling and, thereby, reduce part ejection forces,

potentially improve part quality, and reduce part cost by increasing die life.

- Similarly, admixed powder lubricants increase green body density and reduce part-ejection forces.
- Controlled powder-milling processes can yield particle-size distributions and oxygen contents that are suitable for high-volume P/M applications.

Publications/Patents

1. Lavender CA, and KS Weil. 2006. *Low-Cost Ti Powder for Feedstock.* Pacific Northwest National Laboratory, Richland, WA.
2. Lavender CA, 2007. *Cost-Effective Production of Powder Metallurgy Ti Components for High-Volume Commercial Applications.* Pacific Northwest National Laboratory, Richland, WA.
3. Lavender CA, 2007. *Low-Cost Ti Powder for Feedstock.* 2006 Annual Report: Automotive Lightweighting Materials. Pacific Northwest National Laboratory, Richland, WA.

Presentations

1. Hovanski Y, CA Lavender, KS Weil, and LA Jacobsen. 2007. *Net Shape Powder Metallurgy Processing Using ITP Ti Powder.* Presented by Yuri Hovanski at TMS 2007 Annual Meeting & Exhibition, Orlando, FL on February 27, 2007.
2. Weil K, Hovanski Y, and CA Lavender, 2007. *Investigation of Potentially Low-Cost Ti Powders for Use in Automotive Applications*. Presented by Scott Weil at TMS 2007 Annual Meeting & Exhibition, Orlando, FL on February 27, 2007.
3. *The Development of Low-Cost Ti Powder Processing,* Presented by CA Lavender at MS&T 2007 Detroit, September 10, 2007.
4. *Modification and Analysis of Ti Powders Synthesized by the Armstrong Process,* Presented by CA Lavender at MS&T 2007 Detroit, September 10, 2007.

B. Production of Heavy Vehicle Components from Low-Cost Titanium Powder

Co-Principal Investigator: Randall German
Director and Professor
Center for Advanced Vehicular Systems (CAVS)
Mississippi State University (MSST), P.O. Box 5405
Mississippi State, MS 39762-5405
(662) 325-5431; fax: (662) 325-5433; e-mail: german@cavs.msstate.edu

Co-Principal Investigator: Seong Jin Park
Associate Research Professor
CAVS, 2215
MSST, P.O. Box 5405
Mississippi State, MS 39762-5405
(662) 325-8565; fax: (662) 325-5433; e-mail: sjpark@cavs.msstate.edu

Co-Principal Investigator: Haitham El Kadiri
Assistant Research Professor
CAVS
MSST, P.O. Box 5405
Mississippi State, MS 39762-5405
(662) 325-5568; fax: (662) 325-5433; e-mail: elkadiri@cavs.msstate.edu

Co-Principal Investigator: Youssef Hammi
CAVS
MSST, P.O. Box 5405
Mississippi State, MS 39762-5405
(662) 325-5452; fax: (662) 325-5433; e-mail: yhammi@cavs.msstate.edu

Co-Principal Investigator: Paul T. Wang
Manager, Computational Manufacturing and Design
CAVS
MSST, P.O. Box 5405
Mississippi State, MS 39762-5405
(662) 325-2890; fax: (662) 325-5433; e-mail: pwang@cavs.msstate.edu

Co-Principal Investigator: Pavan Suri
Assistant Research Professor, CAVS
MSST
Mississippi State, MS 39762-5405
(662) 325-8278; fax: (662) 325-5433; e-mail: pks44@msstate.edu

Co-Principal Investigator: Craig A. Blue
Oak Ridge National Laboratory (ORNL)
Oak Ridge, TN 37831-8063
(865) 574-4351; fax: (865) 574-4357; e-mail: blueca@ornl.gov

Co-Principal Investigator: William H. Peter
ORNL
Oak Ridge, TN 37831-8063
(865) 241-8113; fax: (865) 574-4357; e-mail: peterwh@ornl.gov

Technology Area Development Manager: Joseph A. Carpenter
(202) 586-1022; fax: (202) 586-1600; e-mail: joseph.carpenter@ee.doe.gov

Expert Technical Monitor: Philip S. Sklad
(865) 574-5069; fax: (865) 574-6098; e-mail: skladps@ornl.gov

Contractor: MSST
Contract No.: 4000054701

Objective

Design and produce titanium (Ti) structural components by using math-based, experimentally-validated, powder-compaction and sinter models.

Approach

We examine lower-cost, blended-elemental (BE) and prealloyed (PA) Ti powders that are responsive to the powder metallurgy (P/M) process and synthesize new combinations and innovations in powder composition. Recent developments, such as using hydride powders, have enabled the fabrication of BE parts to over 99% of full density, resulting in significantly improved properties. Additives such as carbon or boron can then generate carbide or boride reinforcing phases – dispersed phase composites. Further studies and developments show that this approach may be well suited to reduce the cost of producing automotive parts, making Ti more cost-competitive with other materials commonly used. The work includes powder modifications, novel organo-metallic lubricants (the composition is proprietary), finite-element analysis of the compaction to minimize wall friction and wear, and evaluation of novel tooling materials and coatings. New computer tools for modeling porosity and size change during both compaction and sintering are tailored to Ti systems, with the ability of performing computer-aided design for the tooling and processes to attain dense and net-shaped final products.

Accomplishments

- Completed the literature survey for low-cost Ti powder, Ti alloys for automotive application with cost analysis, and their processing techniques.
- Designed new Ti alloys and proposed three Ti-alloy candidates.
- Continued development of simulation tools for powder injection molding (PIM), die compaction, sintering, hot isostatic pressing (HIPing), and incorporated optimization.

Future Direction

- Design and perform the experiments for PIM.
- Evaluate the proposed alloys in terms of processing windows and mechanical properties.
- Establish modeling and simulation with ORNL experiment data for die compaction, sintering, and HIPing.
- Select a cost-effective and better-preformed Ti alloy and fabricate a prototype component for demonstration.

Introduction

Lower-cost Ti could be the catalyst for Ti losing its perception as an expensive material and allow it to break into the automotive industry. The goal is to produce a market-competitive Ti component by low-cost manufacturing methods. The proposed research on Ti and Ti-matrix composites is the first step toward the application of P/M net-shape technology of lightweight materials into the domestic automotive industry. P/M techniques offer designers the flexibility of producing complex, near-net shape parts with the potential of significant cost savings due to very little waste in materials.

Table 1 shows the overall task structure, including the involvement of the ORNL team based on previous discussions between MSST and ORNL. Note that IAP Research will also provide hydride-dehydride (HDH) Ti powders with nanoscale additives for PIM.

Table 1. Overall structure of Task 1

	experiment	simulation
die compaction	ORNL	MSST
PIM	MSST	MSST
sintering	ORNL	MSST
HIPing	ORNL	MSST

Current Progress Based on Schedule Planned

Table 1 shows the current progress based on the schedule planned. Subtasks related to experiments are behind schedule now. We need experiment data from die compaction, sintering, and HIPing for modeling purposes. As for PIM, we need to find a sponge- powder supplier or obtain timely assistance from ORNL.

Table 2. The proposed schedule of Task 1 with marks of progresses

Subtasks	Year 1				Year 2			
	Q1	Q2	Q3	Q4	Q1	Q2	Q3	Q4
1.01 literature review, first simulation	100							
1.02 powder evaluation	100							
1.03 microstructure and interfacial study	80							
1.04 processing evaluation	80							
1.05 modeling and simulation		60						
1.06 optimization		30						
1.07 experimental verification		30						
1.08 mechanical properties and fatigue								
1.09 defect evaluation by non-destructive method								
1.10 corrosion and oxidation								
1.11 cost modeling								
1.12 process verification								

Summary of the Progress

The task consists of three research categories: literature survey, Ti-alloy design and evaluation, and modeling and simulation for Ti-powder processings.

Literature Survey

The literature survey was completed for Ti powder production methods of gas atomized, HDH, and sponge Ti powders, Ti alloys, P/M processes, and previous Ti alloys in use for automotive applications. The cost of Ti alloys is at least 10 times higher than the cost of aluminum (Al) alloys and 30 times higher than the cost of steels. Table 3 summarizes the consumption of Ti alloys in the automotive market between 1998 and 2002. It is seen that Ti alloys were never used in massive production mode. They were only limited to components requiring extra-high stiffness. For example, Ti is superior in maximum strength and fatigue strength scaled to density when compared to Al, magnesium (Mg), and steels. However, manufacturers show tendencies to use slightly-expensive Ti alloys rather than Al in the powertrain if rotating and oscillating masses in design are required to be substantially reduced.

Table 3. Ti alloys' uses in automotive applications

year	component	material	manufacturer
1998	brake guide pins	Grade 2	Mercedes
1998	sealing washers	Grade 1s	Volkswagen
1998	gear shift knob	Grade1	Honda
1999	connecting rods	Ti-6Al-4V	Porsche
1999	valves	Ti-6Al-4V	Toyota
1999	turbocharger rotor	Ti-6Al-4V	Mercedes
2000	suspension spring	LCB	Volkswagen
2000	valve cups	b-Ti alloy	Mitsubishi
2000	turbocharger rotor	g-TiAl	Mitsubishi
2001	exhaust system	Grade 2	GM
2002	valves	Ti-6Al-4V	Nissan

We also analyzed the cost for several Ti alloy candidates, as shown in Figure 1. This analysis indicates that the type of Ti powders (i.e., gas-atomized, HDH, and sponge Ti powders) is the most important factor in cost control.

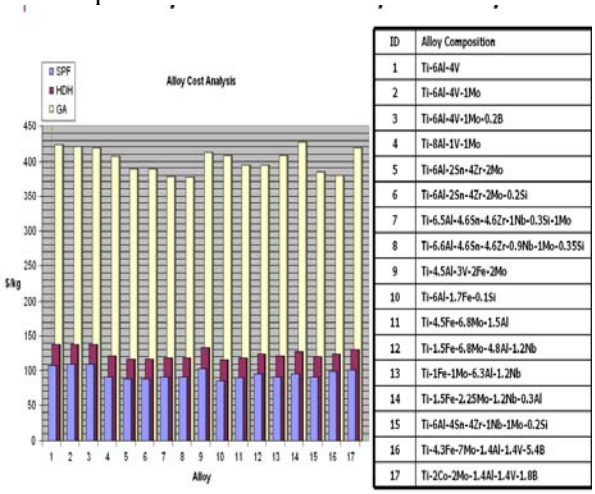

Figure 1. Cost analysis plot for candidate Ti alloys.

Ti Alloys Design and Evaluation

Ti alloys can be a predominant monophase structure; α (hexagonal close-packed, hcp) or β (body-centered cubic, bcc), or a dual-phase structure α+β, depending on the composition strength ratio between the α stabilizing elements and β stabilizing elements. Figure 2 schematically illustrates the main properties of potential Ti alloys falling in different crystallographic classes. α alloys only enclose traces of β phase. Near-α alloys contained predominantly α and the microstructure may appear to be similar to an α alloy. A dual-phase, α-β alloy consists of α and retained or partially-transformed β. Metastable β alloys predominantly contain retained β, which is susceptible to a fine transformation upon post-heat treatments. All of these alloys are used for temperatures less than 600°C, although the melting temperature is higher than that of typical steel. The thermal expansion coefficient is less than half of Al.

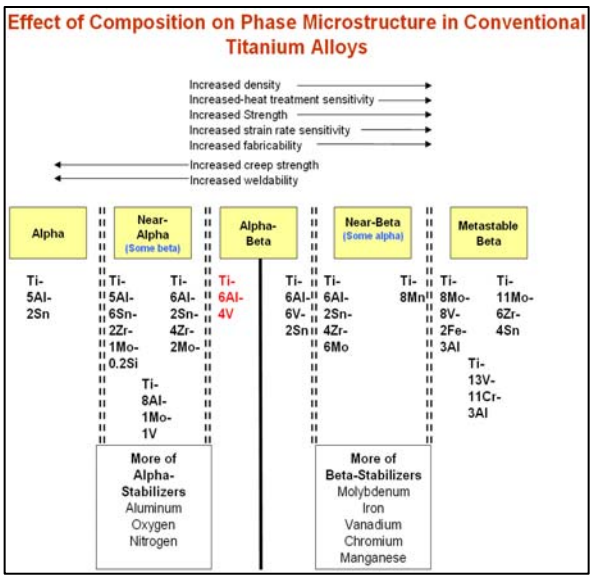

Figure 2. General classification of Ti alloys with respect to properties and microstructure.

Based on our research activity, we recommend starting with the following three compositions using a master-alloy powder for generating the eutectic systems:

I) Ti-(2 to 3%)Fe- (3% to 6%)Zr- (2% to 4%)Sn- (1% to 3%)Mo- (0% to 1%)Cr)

II) Ti-(2 to 3%)Fe- (3% to 6%)Zr- (2% to 4%)Sn- (2% to 3%)Mn- (1 to 2%)Mo- (0% to 1%)Cr)

III) Ti-(2 to 3%)Fe- (3% to 6%)Zr- (2% to 4%)Sn- (2% to 3%)Mn- (1 to 2%)Mo- (2% to 5%)Cr_3C_2.

Currently, we have purchased all required powders for evaluating the proposed Ti-alloy compositions. The evaluation will be performed through powder mixing, die compaction, sintering, and mechanical property measurement. Figure 3 shows the optimization algorithm for liquid-phase sintering of Ti-alloy powder.

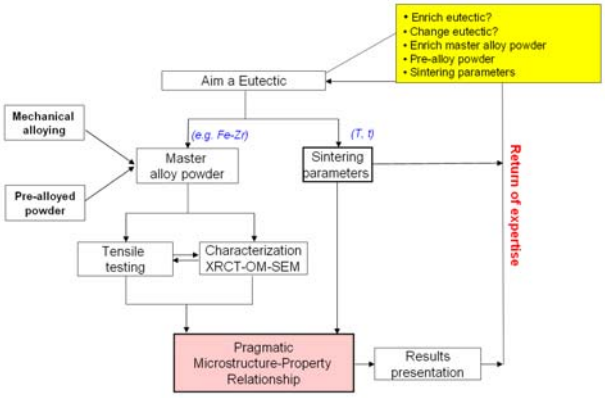

Figure 3. Composition optimization algorithm for liquid- phase sintering of Ti-alloy powder.

As for the PIM, we prepared PIM feedstock based on the standard, wax-polymer binder system with 50 % solid-loading percentage. We are now measuring the viscosity using a homemade capillary rheometer to obtain material properties for simulation.

Modeling and Simulation

PIM: We compared the flow behavior of three different Ti powders (gas atomized, HDH, and spherodized HDH Ti), as shown in Figure 4a. From the literature, material properties of HDH Ti powder for PIM were made available. We used PIMsolver® code donated by CetaTech, Inc. to simulate the PIM process. A tensile-specimen geometry was selected for simulation as shown in Figure 4b. The simulation results inferred possible processing windows (Figure 4c), and optimized the filling time for minimum injection pressure (Figure 4d).

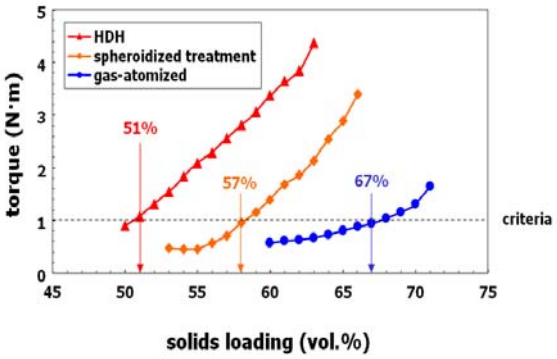

Figure 4a. Torque vs. solid loading.

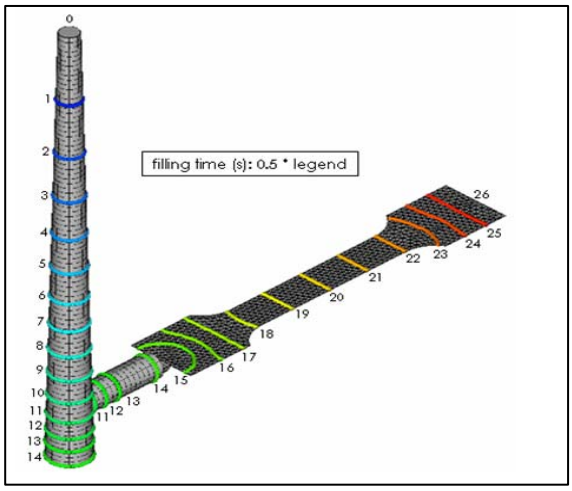

Figure 4b. Filling pattern.

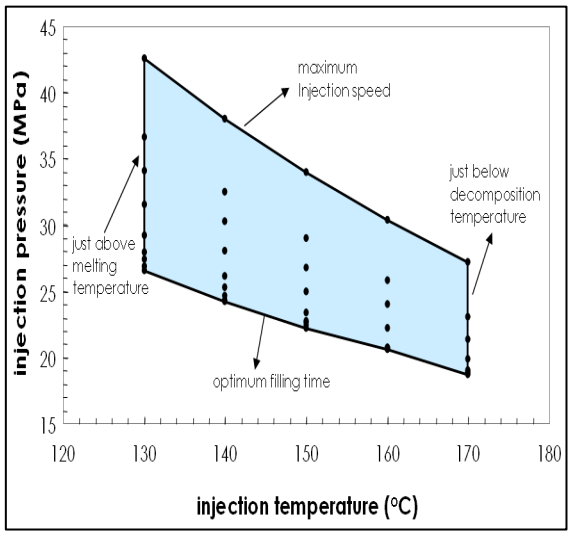

Figure 4c. Processing window

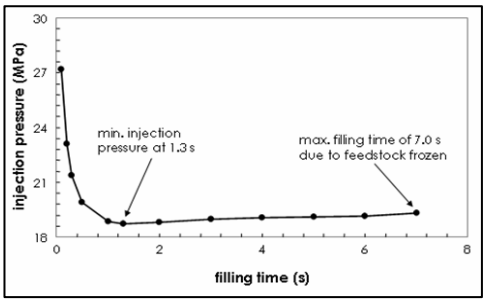

Figure 4d. Optimum filling time.

Figure 4. The first trial of PIM simulation and optimization with HDH Ti powder.

Die Compaction: We obtained all material properties of CP-Ti powder including the compressibility curve (Figure 5a) from literature for die-compaction simulation using ABAQUS. A gear geometry was considered as the first demonstration and simulations were performed, as shown in Figure 5b. In addition, we employed optimization algorithms to determine the loading schedule for reaching uniform green compact density.

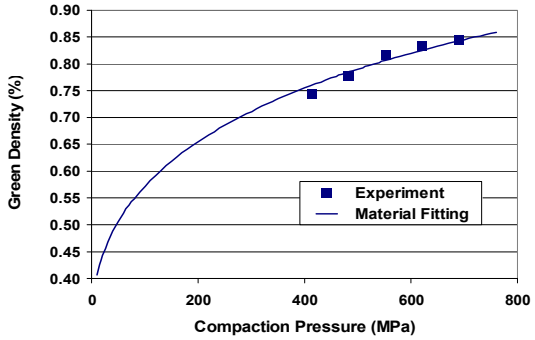

5a. Compressibility curve

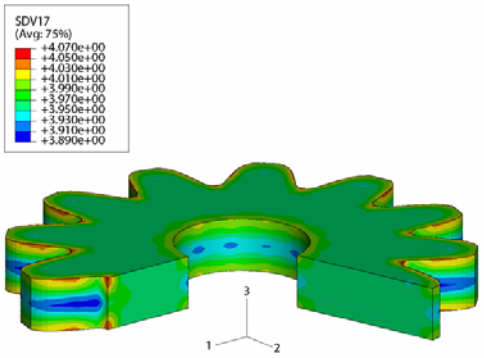

5b. Density distribution after compaction

Figure 5. The first trial of die-compaction simulation with CP-Ti powder.

Sintering and HIPing: We also have the capability to simulate sintering and HIPing processes. As for the HIPing, we obtained all material properties from a creep test with pressure and temperature dependency of Ti-6Al-4V powder and performed simulations of powder HIPing. In addition, we developed the algorithm to optimize can geometry to obtain accurate final HIPed component dimensions. Currently, we could not find through literature survey any Ti powder or Ti-alloy powder material properties for simulation of the sintering.

Conclusions

In the last six months, we accomplished the following (technically):

- Completed the literature survey for low-cost Ti powder, Ti alloys for automotive application with cost analysis, and their processing techniques.
- Designed new Ti alloys.
- Developed a simulation tool for powder injection molding, die compaction, sintering, and HIPing with some optimization.

Presentations/Publications/Patents

Conference Presentation:

1. Haitham El Kadiri, William Peter, Robert Whitehorn, Seong Jin Park, Youssef Hammi, Randall German, Craig Blue, Jim Kiggans, "Microstructure and Mechanical Properties of Sponge Ti and Its Alloy Powders with Various Powder Metallurgical Processes," *TMS 2008*, March 9-13, 2008: New Orleans, LA.

Patents (in preparation)

Three Ti alloy compositions.

C. Powder-Metal Performance Modeling of Automotive Components (AMD 410[i])

Project Manager: Howard Sanderow
Management & Engineering Technologies (MET)
161 Copperfield Drive
Dayton, OH 45415
(937) 832-1583, fax: (937) 832-0858; e-mail: metgroup@earthlink.net

Principal Investigator: Mark F. Horstemeyer (Paul T. Wang, Youssef Hammi)
Center for Advanced Vehicle Systems (CAVS) Chair in Solid Mechanics & Professor, Mechanical Engineering
Mississippi State University (MSST)
206 Carpenter Bldg., P.O. Box ME
Mississippi State, MS 39762
(662) 325-7308; fax: (662) 325-7223; e-mail: mfhorst@me.msstate.edu

Russell Chernenkoff, (retired from Ford Motor Company)
Metaldyne Sintered Component, Inc.
Metaldyne Powertrain Global Operations and Technical Center
47603 Halyard Drive
Plymouth, MI 48170
(734) 582-6227, fax: (734) 582-6250; email: russellchernenkoff@metaldyne.com

Jean Lynn, Senior Specialist
Chrysler, LLC
800 Chrysler Drive, CIMS 482-00-15
Auburn Hills, MI 48326
(248) 512-4851; fax: (248) 576-7490; e-mail: jcl6@chrysler.com

Shekhar G. Wakade, Technical Specialist Materials Engineering
General Motors (GM)/ Powertrain
823 Joslyn Ave.
Pontiac, MI 48340
(313) 322-0175, fax: (248) 857-4425; e-mail: shekhar.g.wakade@gm.com

Glen Weber, Technical Specialist Engine Metals
Ford Motor Company
Building #1, Cube 12A037
Dearborn, MI
(248)) 568-1143; e-mail: gweber@ford.com

Technology Area Development Manager: Joseph A. Carpenter
(202) 586-1022; fax: (202) 586-1600; e-mail: joseph.carpenter@ee.doe.gov

Field Project Officer: Aaron D. Yocum
(304) 285-4852; fax: (304) 285-4403; e-mail: aaron.yocum@netl.doe.gov

Expert Technical Monitor: Philip S. Sklad
(865) 574-5069; fax: (865) 576-4963; e-mail: skladps@ornl.gov

Contractor: U.S. Automotive Materials Partnership (USAMP)[i]
Contract No.: DE-FC26-02OR22910 through the National Energy Technology Laboratory

Objective

- The objective is to develop and experimentally validate math-based models for powder-metallurgy (P/M) component design and performance prediction. The effort will extend an existing USAMP microstructure-property model from casting to PM for practical application in low strain-rate (design and durability) and high strain-rate (toughness-driven impact strength) environments. This model will be used to evaluate and optimize an automotive-component design (main-bearing cap) as affected by materials (ferrous and non-ferrous) and manufacturing processes (compaction and sintering). This model will be implemented into various software platforms (such as ABAQUS). It will be robust enough to facilitate the insertion of various lightweight materials such as aluminum (Al) and titanium (Ti) for future component applications.

Approach

- Determine current PM standards publications, component-design guidelines, manufacturing, and evaluation methodologies. Provide a selection of metal powders that can satisfy design-performance requirements, component-design guidelines, and manufacturing and testing specifications across industry participants (Task 1).
- Evaluate and develop numerical-modeling techniques to predict mechanical properties throughout P/M-component sections. The transition of current materials/design requirements to advanced, structural P/M components has created a need to predict the properties of components in all sections of design. In addition, design processes should consider the least-cost, lowest-mass product designs and reduced development lead-time. An existing, math-based framework will be extended with the abilities to predict P/M-component structures and properties accurately throughout the compaction and sintering processes (section size, density variation, dimensional tolerances, potential for cracking) and with the input of alloys and process parameters (machine functions, tool and powder temperatures, friction and pressure). It will capture the history of a P/M part through its pressing, sintering, and life-cycle performance using the developed multiscale methodology (Task 2).
- Develop component- and vehicle-level testing to validate durability, quality control and performance of P/M parts. Quality-control process factors (powder properties, press settings, tooling design, and furnace conditions) will be determined for P/M parts production in terms of their impacts on process variations and quality improvement. Optimization and statistical techniques will be used to help determine the main factors affecting the final component. Validation experiments considering actual boundary conditions from real processes to fracture the components will be performed (Task 3).
- Manage and report program activities: There will be bi-weekly teleconferences and two technical review sessions per year. Intermittent meetings will be held throughout the year to report progress and discuss issues. Proper execution of this task will greatly enhance the visibility and the value of this project. Reports generated from this program will follow the guidelines suggested by Department of Energy (DOE) and United States Council for Automotive Research (USCAR) (Task 4).
- Perform technology/commercial-transfer throughout the product value-chain. To date, there exists limited accountability for major research and development (R&D)/technical institutions to foster the infrastructure to support large-scale applications of P/M components. If the auto industry wishes to take advantage of P/M's potential weight and cost-reduction opportunities, they must nurture P/M development through programs sponsored and directed by USCAR. The project team will request the professional support of societies to publish notices of meetings and project information, as released by the project team (Task 5).

Accomplishments

- Continued to characterize powder and green-compact, comprising FC-0205 Ancorsteel powder provided by Hoeganaes and 205Q powders provided by Metaldyne. Obtained structure/property data during sintering on FC-0205 and 205Q powders (Task 2).
- Measured the density distributions of the green and sintered main-bearing caps provided by Metaldyne using immersion density and image analysis. Measured the density distribution of the sintered main-bearing cap using the two-dimensional (2D) x-ray computed tomography (CT) (Task 3).
- Compaction Modeling Status: Validated modeling and simulation efforts for cylindrical samples under compaction with Al 6061, tungsten carbide and FC-0205 experimental data. Validation on Cincinnati part and on main-bearing cap are ongoing (Task 2).
- Sintering Modeling Status: Developed and implemented in ABAQUS/Standard code (Task 2).
- Received from Metaldyne 205Q and 223 powders, transverse rupture strength (TRS) test bars and bearing caps in green and sintered conditions. Also received tensile bars and material samples to be machined into tension, compression, torsion and fatigue specimens (Task 3).
- Performed tension, compression, torsion, notched and smooth fatigue tests on samples provided by Metaldyne to calibrate the internal state variable (ISV) performance model and a fatigue model (Task 3).
- Hosted meetings at CAVS with USCAR P/M team members in March, August and December 2007 (Tasks 4-5).
- Submitted two conference papers at PowderMet2007 (Task 4).
- Completed semi-annual and annual reports for release to USCAR and DOE (Task 4).

Work Plan for 2008

- Enhance the compaction model with additional features, i.e., springback responses during ejection (March 2008).
- Correlate the FC-0205 and 205Q sintering data with the models (February 2008).
- Validate the experimental results on the main-bearing cap with the sintering simulation results (February 2008).
- Validate the plasticity/fatigue model with the information provided by Metaldyne – main-bearing cap. (April 2008).
- Use the model to optimize the compaction and sintering processes for a main-bearing cap (April 2008)
- Apply the modeling to lightweight material such Al powder using literature data and predict the performance and fatigue property in a bearing cap (May 2008).
- Tech Transfer and Training (April 2008).

Introduction

The objective of this project is to develop and experimentally validate math-based models for P/M component design and performance prediction.

During this past year, different powder material tests have been conducted on the FC-0205 and 205Q powders to characterize and calibrate the compaction, sintering and performance parameters. The characterizations of the FC-0205 and 205Q powders during compaction and sintering are nearly completed. Using the 205Q powder material samples from Metaldyne (powder, TRS bars, tensile bars, material blanks and bearing caps), CAVS has performed tensile, compression, torsion and fatigue tests at different densities. Three different methods of density

measurements have been used to determine the density distribution of the green and sintered bearing caps.

Regarding the modeling, the compaction model has been validated on cylindrical, Cincinnati and main-bearing cap (MBC) parts. Data from the literature and other material were used to validate the model as well. The compaction model for the ejection stage is currently being implemented. The sintering model has been developed, implemented and tested for algorithm efficiency.

Powder Characterization

A number of experimental tests and density measurements have been performed to gather the data necessary for characterization and validation of the constitutive equations of compaction and sintering. A brief description of these experimental tests follows.

Brazilian and Compression Tests

To determine material cohesion and interparticle-friction parameters, d and β, compression and Brazilian disc tests were performed on cylindrical green samples of different densities ranging from 5.2 to 7.3 g/cc [Coube and Riedel, 2000]. Two different FC-0205 powders were tested: powder 1 and powder 2 with 0.6% and 1.0% Acrawax, respectively. The Brazilian tests were performed according to American Society for Testing and Materials (ASTM) D3967-95a (2005): Standard Test Method for Splitting Tensile Strength of Intact Rock Core Specimens. The compression tests were performed according to ASTM E9-89a: Standard Test Methods of Compression Testing of Metallic Materials at Room Temperature. The fracture stresses, σ_c and σ_t, were measured in these two tests with different degrees of stress multiaxiality (Figure 1).

Closed-die Compaction Tests

The goal of this experiment is to determine the cap eccentricity parameter in the Cap Model. Six strain gages were attached to the external surface of a 2-inch-diameter steel die to measure the hoop strain. Gages 3 and 4 were located at the same distance from the bottom of the die. Compaction tests were performed on several FC-0205 powder cylinders of 0.5-inch diameter with different heights. The cap-eccentricity parameter in the Cap Model was determined with an inverse method by comparing the numerical hoop to measure the hoop strain. Gages 3 and 4 were located at the same distance from the bottom of the die. Compaction tests were performed on several FC-0205 powder cylinders of 0.5-inch diameter with different heights. The cap- eccentricity parameter in the Cap Model was determined with an inverse method by comparing the numerical hoop strains to the measured hoop strains at different locations on the die as illustrated in Figure 2.

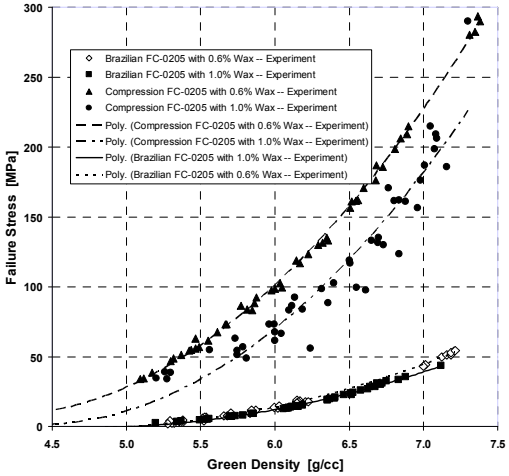

Figure 1. Failure stress vs. green density for FC-0205 cylindrical samples.

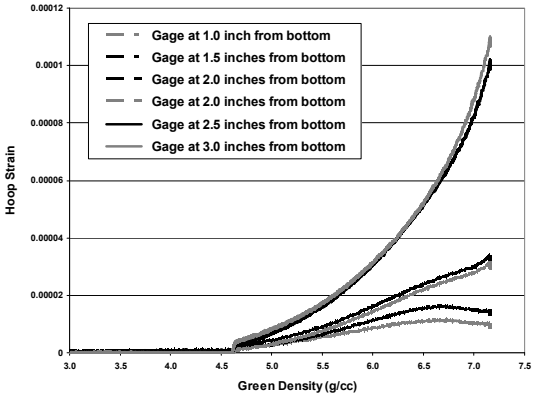

Figure 2. Experimentally-measured hoop strains for FC-0205 cylindrical samples.

The equivalent stresses, q_c and q_t, and the hydrostatic stresses, p_c and p_t, are calculated from the interpolation of the fracture stresses to

determine the ordinate (d) and slope (tan β) of the straight-line failure envelope in the Drucker–Prager Cap Model at different densities (Figures 3 and 4).

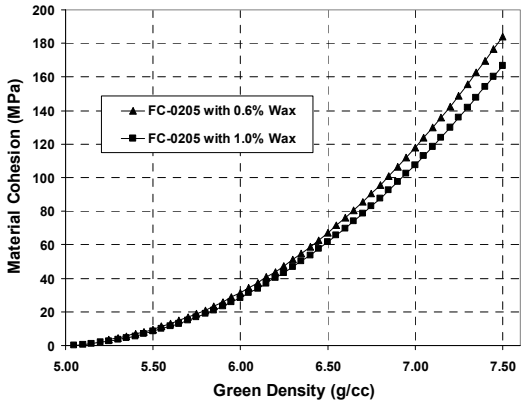

Figure 3. Material cohesion (d) vs. green density for FC-0205 cylindrical samples.

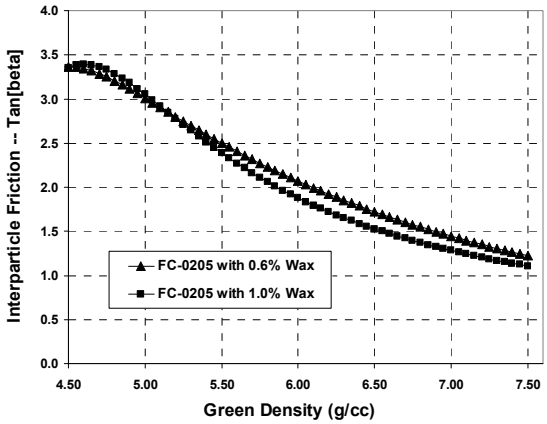

Figure 4. Interparticle friction (tan β) vs. green density for FC-0205 cylindrical samples.

Resonant Frequency Tests

Using the resonant frequency method [Yu et al., 1992, McIntire, 1991], the Ultra RS laboratory in France determined the Young's modulus, E, and Poisson ratio, ν, of FC-0205 rectangular bars sized 1.25 in x 0.5 in x 0.25 in. with green densities ranging from 5.6 to 7.2 g/cc [Figure 5]. The bulk modulus, K, and shear modulus, G, were then derived from the E and ν functions of density.

Density Measurements

Green-density measurements were made on the first press trial of the Cincinnati, Inc. samples. The first three sample parts of this press trial were cut into quarters. Each quarter was then further divided into twelve pieces (Figure 6), resulting in forty-eight total pieces for each sample part.

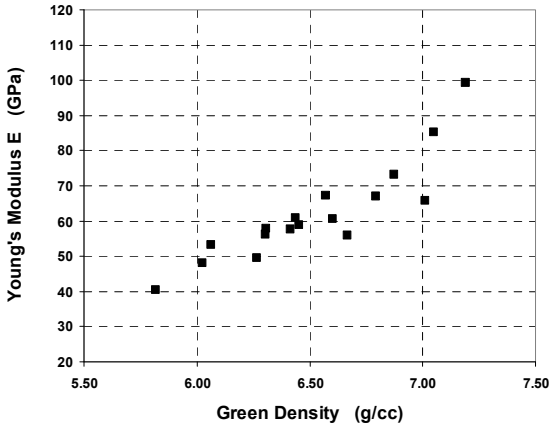

Figure 5. Young's modulus, E, as function of the density for the FC-0205 powder.

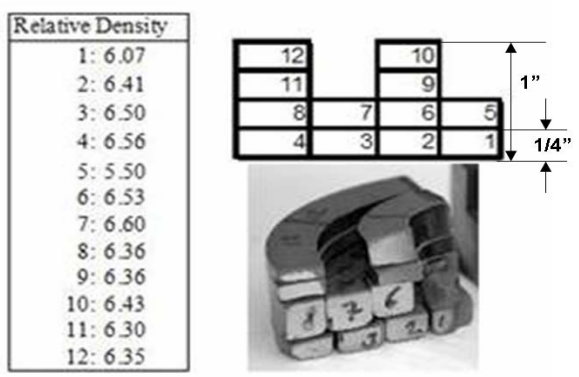

Figure 6. Average green-density map for the first press trial of the Cincinnati, Inc. sample part.

The green density for each piece was determined using the immersion density method (also called Archimedes' method) according to Metal Powder Industries Federation (MPIF) Standard 42: Method for Determination of Density of Compacted or Sintered Powder Metallurgy Products. By averaging the density measurements for the three parts, the green-density map for the

Cincinnati Inc. sample part of the first press trial was constructed (Figure 6).

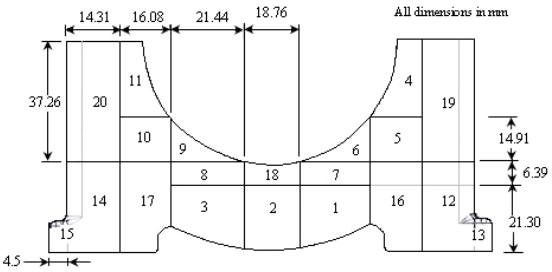

Figure 7a. MBC dimensions and location of the 20 samples.

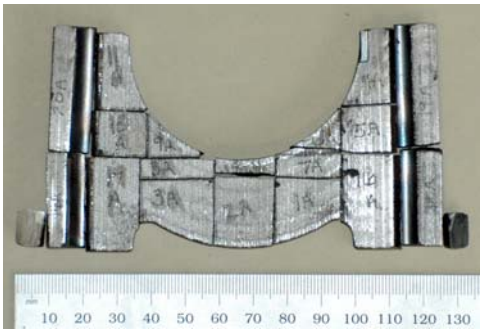

Figure 7b. Layer A of green MBC cut into 20 samples.

For the Metaldyne MBC, three different methods, image analysis, Archimedes' immersion and 2D X-Ray CT, were used to measure the green and sintered density. The same layering and sectioning of the MBC part was applied to all methods. Regarding the image analysis, a test procedure was developed specifically for the MBC. The MBC was sectioned into three layers of equal thickness. Each layer was further cut into 20 pieces, shown in Figures 7a and 7b.

In the image analysis procedure, the samples were mounted and then polished. Several images were captured for each of the 20 samples, using a Zeiss Axiovert 200MAT optical microscope with a motorized stage. A MATLAB program developed at CAVS was used as an image post-processor to overlay the porosity in red and output the total pore area of each image. The density of each sample was quantified using the void-area fraction, which is the ratio of void area to the representative sample area. In the 2D X-Ray CT technique, the X-ray image shows variations in photographic density between different parts of the object being scanned. In order to obtain density data, the gray-scale values of a CT image are correlated to known density values of different TRS samples using exactly the same scanning conditions. The gray-scale values in the CT are then converted to density values using a MATLAB image-processing program. This technique has the advantage of being a quick method to evaluate the relative density variations in the large P/M parts.

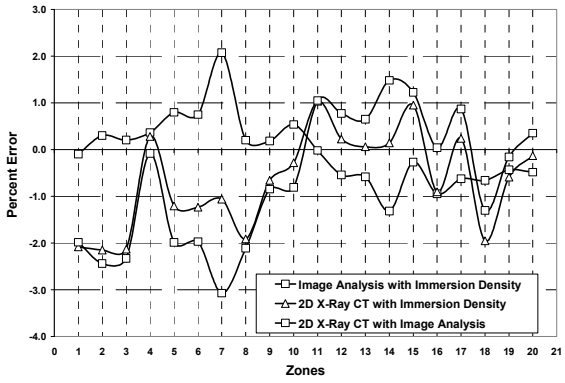

Figure 8. Percent error between the different density measurement methods for the layer A of the green MBC part.

Figure 8 shows the percent error between the three techniques. It is observed that the density measurement results from the immersion density and image analysis are very close. The percent error is given by

$$\%\ Error = \frac{D_1 - D_2}{D_2} \cdot 100 \qquad (1)$$

where D_1 and D_2 are the values of the two compared methods (the second density D_2 is assumed to be the "correct" value).

Dilatometry Test

The dilatometry test is a technique to measure the dimensional changes of a porous body continuously during sintering by using a probe or pushrod to measure the shrinkage or expansion of the sample *in situ*. Changes in the rate of shrinkage are linked to microstructural evolution and thermophysical events or chemical reactions [Blaine et al., 2005]. Dilatometry tests were performed on FC-0205 delubed compacts with a N_2 atmosphere. The compacts were heated at different constant heating rates (2°C/min, 5°C/min and 10°C/min) to 1120ºC (2048ºF)

with a holding time of 30 minutes. The cooling rate was 10°C/min. The observed variation in sintering shrinkage will be used to calibrate sintering parameters and to verify the predictive capability of the model (Figure 9). It is worthwhile to mention that the real sintering conditions are twice as fast as those shown in Figure 9.

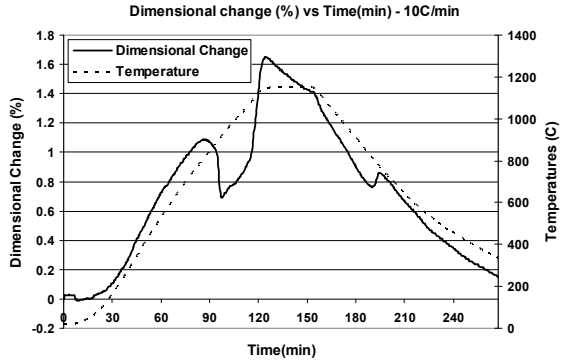

Figure 9. Dilatometer plots of axial shrinkage versus time for FC-0205 presintered compacts heated at a rate of 10°C/min to 1200°C in N_2 atmosphere.

To investigate the material grain-growth behavior, several sintering experiments on FC-0205 and 205Q powders were performed using three different heating rates and holding temperatures. The goal is to obtain the grain-growth rates graphically from the grain size against holding time plots for calibrating the grain-growth parameters.

Modeling

Compaction

The compaction model that was implemented in ABAQUS/Explicit was initially validated using literature data on Al-6061 Al powder. The FC-0205 parameters were calibrated using the p-q plot, which defines the evolution of the yield surface based on experimental data from Brazilian and compression tests, isostatic tests, and closed-die compaction tests.

The compaction was first validated using the FC-0205 parameters on cylindrical specimens by comparing the final average density from numerical results and experimental measurements. The model was then validated on more complex parts, such as the Cincinnati and MBC parts using, respectively, axisymmetric and hexahedral elements to represent the powder (Figure 10 and 11). To avoid numerical instabilities during the compaction simulation, two different numerical techniques were used. The Arbitrary Eulerian Lagrangian (ALE) adaptive meshing was applied to elements in order to control the mesh distortion. The no-separation relationship, which prevents the contact surfaces in interaction from separating once they have come into contact, was also applied to remove an unrealistic gap between the powder and the tool surfaces.

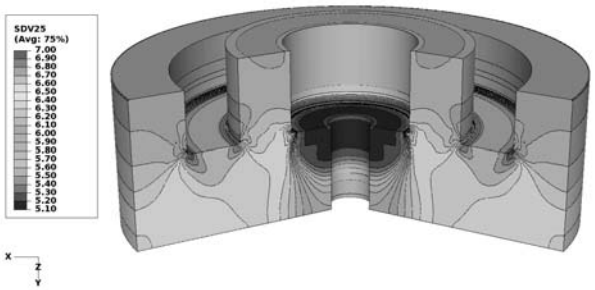

Figure 10. Density distribution (g/cc) in the Cincinnati part (axisymmetric model with swept display).

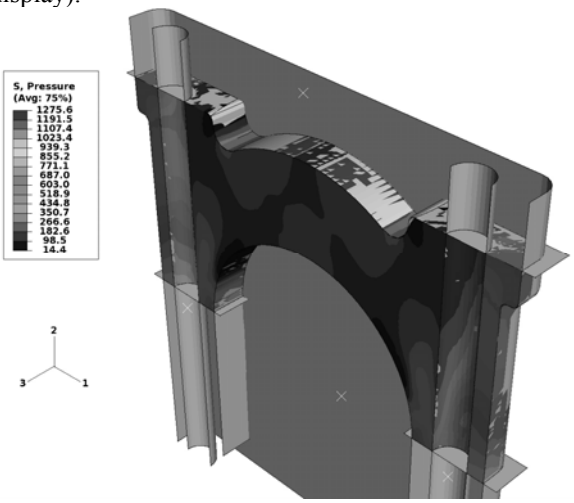

Figure 11. Pressure distribution (MPa) in the MBC part.

To validate the density distribution of the Cincinnati simulations, the density was averaged on several axisymmetric or hexahedral elements in volumes that correspond to the cut pieces for the immersion density method. Figure 12 shows the percent error of the average density from finite-element analysis (FEA) results compared with the immersion density values for the Cincinnati part. For the MBC simulation, CAVS is currently working with Metaldyne to determine the initial conditions and tool

motions in order to improve the simulation results (Figure 13).

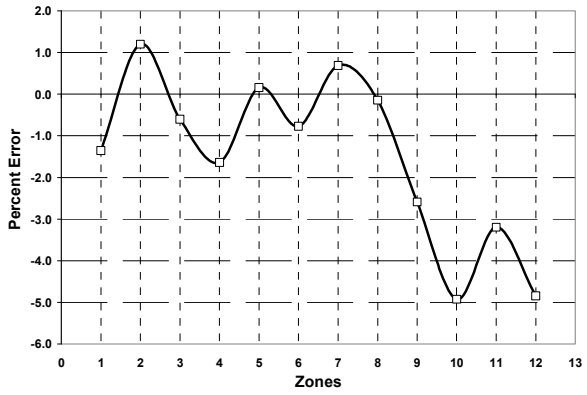

Figure 12. Percent error of the density values from finite-element analysis compared with density immersion measurement for the 12 pieces of the Cincinnati part.

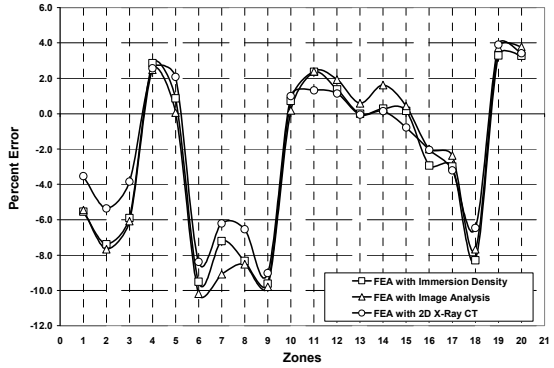

Figure 13. Percent error of the density values from FEA compared with different density measurement for the 20 pieces of the MBC part.

Sintering

To study the creep of powder due to diffusional mass transport on the interparticle contacts, a sintering model was implemented in the user-material subroutine UMAT of ABAQUS/Standard. This model is described by a macroscopic creep law that was initially proposed McMeeking and Kuhn [1992]. In the thermodynamic framework, to obtain the diffusional deformation rate as defined by McMeeking and Kuhn [1992], the following sintering dissipation potential was introduced:

$$F_{di} = -\frac{p}{K_d}\left(\frac{p}{2} + \sigma_s\right) + \frac{q^2}{6\mu_d}, \qquad (2)$$

where p and q are the first and second stress invariants, K_d and μ_d are shear and bulk viscosity, respectively, and σ_s is the sintering stress which arises from the surface tension forces of the pores. The densification rate is given by:

$$\underline{D}^{di} = -\frac{1}{3}\frac{p+\sigma_s}{K_d}\underline{I} + \frac{q}{3\mu_d}\underline{n}. \qquad (3)$$

where $\underline{I}$ and $\underline{n}$ are the unit tensor and plastic normal tensor. The stress-like term σ_s is the macroscopic manifestation of the driving forces for the processes of sintering. It is also called the sintering potential and is defined for different phases of the material [Kwon et al., 2004].

The viscosities μ_d and K_d are averages over the microstructure of the deformation processes within the particles and on interparticle boundaries [German, 1996].

The grain-growth evolution under pressureless sintering can be written as [Kwon et al., 2004]

$$\dot{G} = k'/G^2 \qquad (4)$$

where G is the grain size and k' is a material constant which can be determined from experimental data as a function of temperature.

The stress integration algorithm proposed by Govindarajan and Aravas [1994] was used to solve the sintering constitutive equations and compute the tangent consistent matrix.

The model was successfully tested using 17-4 PH stainless-steel parameters to evaluate the convergence efficiency and the robustness of the stress-integration algorithm. The next step will be to calibrate the FC-0205 and 205Q parameters using the dilatometry and void-growth data for complete validation of the sintering model.

Partnership with Metaldyne

Following the agreement between Metaldyne Sintered Component, Inc. and the Center for Powder Metal Technology (CPMT)/CAVS,

Metaldyne provided to CAVS the following items:

- Geometry of a GM MBC: part drawing, tool geometry in IGES format, and fill, mold and ejection position drawings.
- 205Q and 223 powder bucket of 50 lbs.
- 205Q and 223 green and sintered TRS bars of different densities
- 205Q tensile bars of densities ranging from 6.4 to 7.2 g/cc.
- 205Q material blanks of different thickness and densities to be machined into material samples for tension, compression, torsion and fatigue testing.
- 50 green and sintered MBC parts made from 223 powder.
- 100 green and 90 sintered MBC parts made from 205Q powder.

Performance Testing

Model-calibration testing has been performed on monotonic and fatigue specimens machined from 205Q material blanks provided by Metaldyne. Monotonic experiments were conducted to capture stress-state dependence, temperature dependence, and strain-rate dependence. The various stress states were compression, tension, and torsion. Temperature dependence was accomplished by performing the tests at both 293K and 593K, and strain rates at 0.0001/s and 2000/s for strain-rate dependency. To date, compression tests have been performed at both temperatures and strain rates. Tension has been tested at 0.0001/s and both temperatures. Torsion testing has been performed at 293K and 0.0001/s.

The test data obtained have been used to develop one set of constants for a microstructure-based ISV. A plot of low-density and high-density specimen experiments tested to date along with the model curves are shown in Figures 14 and 15, respectively.

Fatigue calibration experiments were performed on round specimens with the same two density levels as used in the monotonic experiments. Loading was applied under strain control with completely reversed strain amplitude.
Specimens were cyclically tested by first applying a strain in tension, then uniaxially reloading in compression. The strain amplitudes tested for the high-density specimens were: 0.4%, 0.3%, 0.2%, 0.175%, 0.15%, and 0.1%. The low-density strain levels were 0.3%, 0.2%, 0.15%, 0.125%, and 0.1%. A frequency of 2 Hz was used when testing at strain amplitudes of 0.15% and higher. For the lower strain amplitudes, 0.125% and 0.1%, a frequency of 3 Hz was utilized.

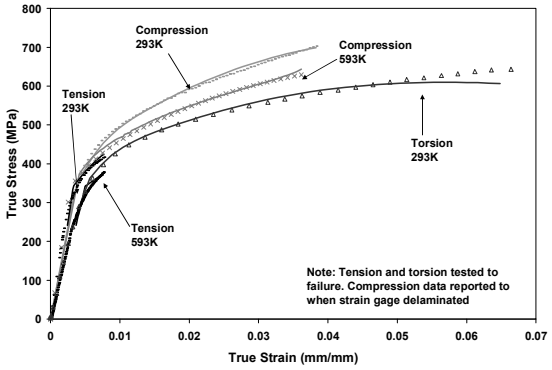

Figure 14. Low-density stress-strain showing the model (solid lines) plotted with the experimental data curves (dash lines).

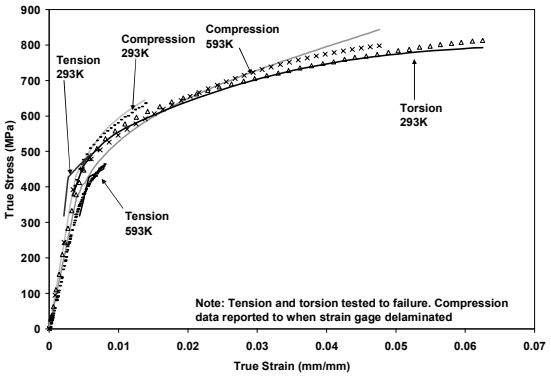

Figure 15. High-density stress-strain showing the model (solid lines) plotted with the experimental data curves (dash lines).

The fatigue experimental data were loaded into a microstructural-based ISV, multi-stage fatigue model. Figure 16 shows a strain-life plot of the experimental-data and model curve.

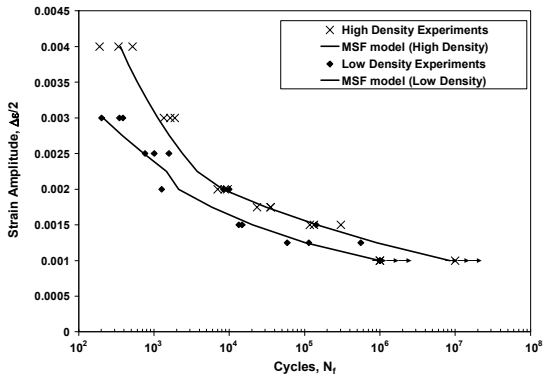

Figure 16. Strain-life fatigue experimental and multistage fatigue model comparison.

Conclusions

Determination of the microstructure-property relations and parameter calibration for the Powder-Metal Performance Modeling of Automotive Components project are almost completed except for the sintering-parameter calibration, which requires a more complicated procedure. The compaction model was validated with cylindrical and Cincinnati parts and partly with MBC parts; the numerical densities were in good agreement with the measured densities. The internal-state sintering and performance models have been developed and implemented. The ejection feature for the compaction model is being implemented and near completion. Therefore, having completed most of the material characterization and numerical developments, CAVS soon will be able to perform simulations of compaction and sintering for design, performance and mass optimization of the MBC. The final task will be the evaluation of lightweight materials in the MBC parts.

Publications

1. Allison P.G., Hammi Y. and Horstemeyer M.F., Determination of Microstructure-Property Relations for Performance and Design Optimization of the P/M Process", PowderMet 2007 conference, Denver, CO, May 13-16 2007, Vol. 1, Part 1.
2. Stone T.W., Jelinek B., Gullett P.M., Kim S.G., and Horstemeyer M.F., "MD Simulations of the Compressive Behavior of α-Fe and Fe-Cu Nanocrystalline Materials", PowderMet 2007 conference, Denver, CO, May 13-16 2007, Vol. 1, Part 1.

Acknowledgements

The authors would like to acknowledge funding from the Center for Advanced Vehicular Systems at Mississippi State University and from USAMP Advanced Materials Division (AMD). We thank Michael O'Neill, Ernie Bertolasio and Edmund Ilia from Metaldyne Sintered Components for all the information and material samples they provided us.

References

1. ABAQUS, User's Manual, Version 5.8, Hibbit, Karson & Sorensen, Inc., 2003.
2. Blaine, D., German, R., and Park, S., "Computer Modeling of Distortion and Densification during Liquid Phase Sintering of High-Performance Materials", Proceedings of the 2005 International Conference on Powder Metallurgy and Particulate Materials, Metal Powder Industries Federation, Princeton, NJ, 2005, 1.29-1.37.
3. Coube, O. and Riedel, H. "Numerical Simulation of Metal Powder Die Compaction with Special Consideration of Cracking", Powder Metallurgy, Vol. 43, No. 2, 2000, pp. 123–131.
4. German, R.M., Sintering Theory and Practice, Wiley and Sons, 1996.
5. Govindarajan, R.M., and Aravas, N., "Deformation processing of metal powders: Part II – Hot isostatic pressing", Int. J. Mech Sci. Vol. 36, No. 4, 1994, pp. 359-372.
6. Kwon, Y.S., Wu, Y., Suri, P. and German, R.M., "Simulation of the Sintering Densification and Shrinkage Behavior of Powder Injection Molded 17-4PH Stainless Steel," Metal. Mater. Trans., 2004, pp. 257–263.
7. McMeeking, R.M., and Kuhn, L.T., "A Diffusional Creep Law for Powder Compacts," Acta Metal. Mat., Vol. 40, 1992, pp. 961–969.
8. McIntire, P. (ed.), Nondestructive Testing Handbook, Volume 7, American Society for Nondestructive Testing, 1991, pp. 398-402.

9. Yu, C.J., Henry, R.J., Prucher, T., Parthasarathi, S., Jo J., 1992. "Reasonant frequency measurements for the determination of elastic properties of P/M components", Proceedings of the P/M'92 World Congress, Vol. 6, pp. 319–332.

[i] Denotes project 410 of the Automotive Materials Division (AMD) of the United States Automotive Materials Partnership (USAMP, www.uscar.org), one of the formal consortia of the United States Council for Automotive Research (USCAR) set up by Chrysler, Ford and General Motors (GM) to conduct joint, pre-competitive research and development.

D. Examining Fundamental Mechanisms of Tooling Wear for Powder Processing

Co-Principal Investigator: Seong Jin Park
Associate Research Professor
Center for Advanced Vehicular Systems (CAVS), 2215
Mississippi State University (MSST), P.O. Box 5405
Mississippi State, MS 39762-5405
(662) 325-8565; fax: (662) 324-4001; e-mail: sjpark@cavs.msstate.edu

Co-Principal Investigator: Randall German
Director and Professor
CAVS
MSST, P.O. Box 5405
Mississippi State, MS 39762-5405
(662) 325-5431; fax: (662) 323-3906; e-mail: german@cavs.msstate.edu

Co-Principal Investigator: Youssef Hammi
CAVS
MSST, P.O. Box 5405
Mississippi State, MS 39762-5405
(662) 325-5452; e-mail: yhammi@cavs.msstate.edu

Co-Principal Investigator: Paul T. Wang
Manager, Computational Manufacturing and Design
CAVS
MSST, P.O. Box 5405
Mississippi State, MS 39762-5405
(662) 325-2890; fax: (662) 325-5433; e-mail: pwang@cavs.msstate.edu

Technology Area Development Manager: Joseph A. Carpenter
(202) 586-1022; fax: (202) 586-1600; e-mail: joseph.carpenter@ee.doe.gov

Contract Monitor: Aaron Yocum
(304) 285-4852; fax: (304) 285-4403; e-mail: aaron.yocum@netl.doe.gov

---

Contractor: Mississippi State University (MSST)
Contract No.: 4000054701

Objective

- Develop an innovative design of tooling surfaces and novel lubricants for processing ferrous and lightweight materials.

Approach

- Productivity and performance of powder metallurgy (P/M) parts rely on the behavior of surface oxide which, by nature, is a dispersion-strengthened product. This work plans to use coated powders to provide an opportunity to control tool friction, surface reactions, and component strength. This research will apply new tools to the old problem of aluminum (Al) P/M. It relies on powder changes, alloying, and processing optimization to produce nearly full-density products with complex shapes and dimensional precision. The work is fundamentally new,

since very little efforts have been focused on moving forward the lightweight automotive components fabricated by P/M for meeting desirable property levels as comparable with traditional ferrous P/M. Significant progress is expected in the key areas such as the optimal particle size distribution, powder coatings, active lubricants, and computer simulations.

Accomplishments

- Developed a new methodology to quantify tool wear for die compaction in the mold using silicon rubber.
- Proposed a new integral equation to quantify tool wear from numerical simulation results.
- Characterized the effect of lubricant on tool wear.
- Obtained industry sponsor in-kind support including CetaTech, AMPAL, Gasbarre products, Arburg, and CM Furnaces.
- Published one journal paper and five conference papers related to this task.
- Produced one master degree through this task.

Future Direction

- Work with Oak Ridge National Laboratory (ORNL) wear test facility use through the High-Temperature Materials Laboratory (HTML)/ORNL user program.
- Developed full design and optimization algorithm.
- Evaluate mechanical performance including fatigue and high strain-rate experiment.

Introduction

P/M techniques are widely used to fabricate complex automotive components from ferrous powders. The energy efficiency and cost attributes of P/M are recognized by the domestic automotive industry. Al P/M emerged in the 1950s, but current tonnage in the USA is trivial. With the push for lighter-weight, higher-strength, more-durable structures, the barriers to Al P/M in domestic automobiles need to be addressed. Besides economics, the technical barriers are: tool wear, performance, and ductility at high strain rates (related to crashworthiness).

In this sense, the goal of this project is to examine fundamental mechanisms of wear in die compaction with priority and to synthesize new combinations or innovations in powders, lubricants, press operation, and compaction cycles to minimize tool wear with integration of experimentation and numerical simulation.

Current Progress Based on Schedule Planned

All subtasks are progressed well, as shown in the Table 1 below.

Table 1. The proposed project schedule with marks of progresses

Sub Task	Year 1				Year 2			
	Q1	Q2	Q3	Q4	Q1	Q2	Q3	Q4
5.1	100%							
5.2	100%							
5.3	100%							
5.4	90%							
5.5		100%						
5.6			100%					
5.7			40%					
5.8				30%				
5.9								

Summary of the Progress

This project comprises three research categories: die wear measurement, Al-alloy evaluation, and modeling and simulation for tool wear.

Die Wear Measurement

We proposed, established, and are developing a new methodology to quantify tool wear during die compaction (Figure 1a) through a nondestructive method using RepliSet (Figure 1b) and a TalySurf profilometer (Figure 1c).

Once the methodology was set up, we calibrated silicon-rubber technique and found that its resolution was ±0.5 μm. Now we are measuring tool wear with three die-tool materials and four different powders including die diameter, die

weight, surface roughness, and so on for quantifying tool wear. In addition, the microstructure was evaluated using scanning electron microscopy (SEM) as shown in Figure 2.

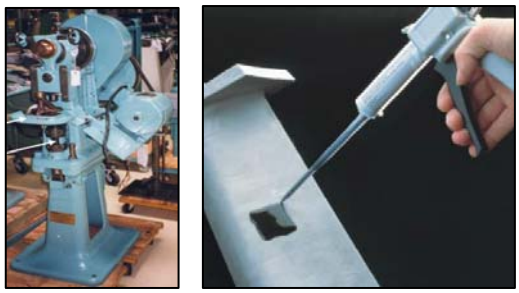

(a) (b)

(c)

Figure 1. Establishment of new methodology to quantify tool wear; (a) compaction machine with die for wear measurement, (b) RepliSet (silicon rubber and shot gun), and (c) TalySurf profilometer for surface measurement.

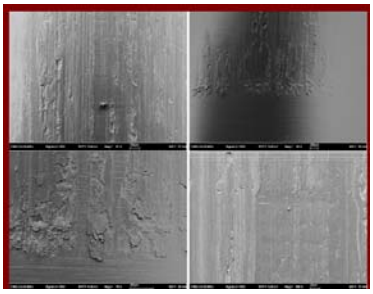

Figure 2. SEM image of silicon rubber surface to investigate ability of transcription of RepliSet.

Al-Alloys Evaluation

To obtain an Al alloy with excellent mechanical properties, we are evaluating nine different Al alloys with Mg, Cu, Si, SiC, and Ti. Especially, Al 6061 powder produced by rapid solidification, ATMIX, Japan, seemed to have a great potential so far. Our observation includes differential scanning calorimetry / thermogravimetric analysis (DSC/TGA) of mixed powder for phase transformation and melting; die- compaction and sintering behaviors through compressibility-curve and dilatometry tests; mechanical property measurements such as density, hardness with comparison (Figure 3a), and transverse rupture strength (TRS); and microstructure-evolution analysis using SEM pictures (Figure 3b). Furthermore, we just did the first trial of high-rate Hopkinson bar testing which is related to potential structural component analysis for crashworthiness.

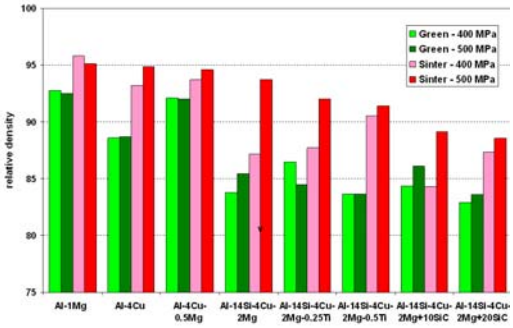

(a) Comparison of mechanical properties

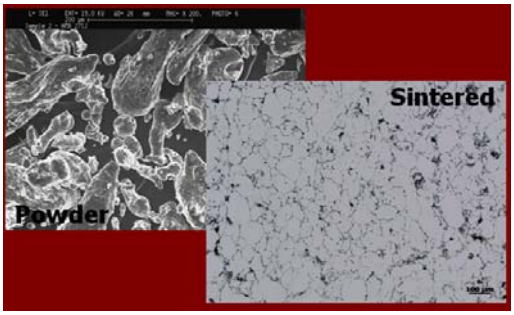

(b) SEM image of powder and sintered compact

Figure 3. Results of Al alloys evaluation.

Modeling and Simulation for Tool Wear

In order to take advantage of our simulation capability, we have proposed a new concept of wear work in integral form based on finite-element modeling (FEM) simulation results of die compaction and ejection as follows:

$$M = H\left(k_1 S_1 + k_2 S_2\right)W$$

and

$$W = \int_t \mu \int_A \sigma_n dA v dt$$

where M is the amount of tool wear, H is the Vickers harness number of tool material, k is the proportional constant, S is surface area of compact

contacted with die tool, subscript 1 is for Al powder and 2 is for hard additives such as alumina (Al_2O_3) or silicon carbide (SiC), W is the wear work, μ is the friction coefficient, σ_n is the normal stress to die tool surface, A is the surface area, v is the velocity of the powder compact, and t is the time. We applied this definition to developed FEM simulation tool for die compaction and ejection with experiment validation to investigate the effect of die compaction and ejection stage with different friction coefficient as shown in Figures 4 and 5.

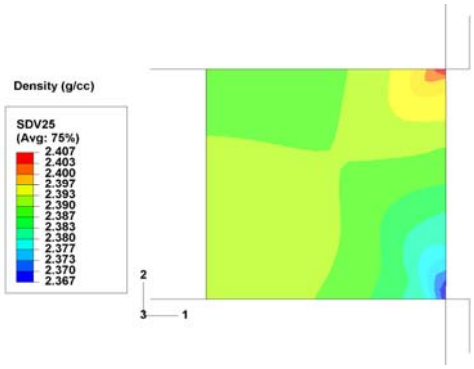

(a) density distribution

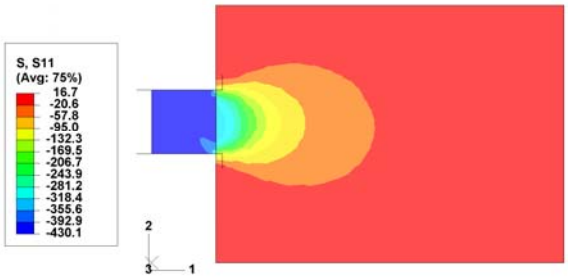

(b) stress distribution with die tool deformation

Figure 4. FEM simulation result.

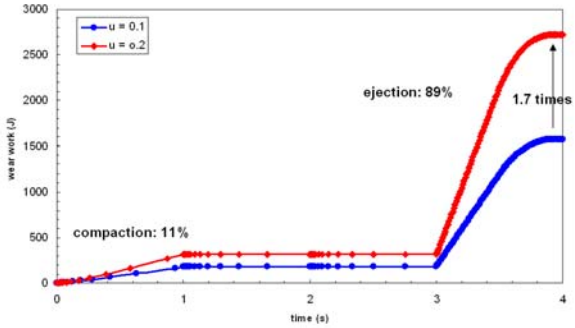

Figure 5. The effect of die compaction and ejection stage with different friction coefficient on tool wear.

We also investigated the effect of lubricant using FEM simulation. We used acrawax as the first trial with different amount of addition compared with results without lubricant, as shown in Figure 6, in term of compressibility and its effect on amount of tool wear.

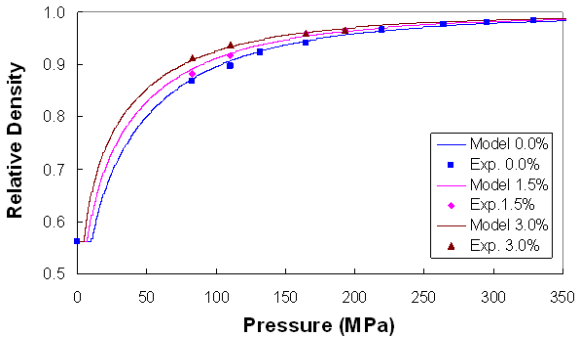

Figure 6. The effect of the amount of lubricant on compressibility of die compaction.

Conclusions

Last year, we produced one MS degree (James K. Thompson) through this project. In addition, we have accomplished the following technically:

- Developed a new, nondestructive methodology to quantify tool wear for die compaction in the mold using silicon rubber.
- Proposed a new integral equation to quantify tool wear from numerical simulation results.
- Characterized the effect of lubricant on tool wear.
- Published one journal paper and five conference papers related to this project.

Presentations/Publications/Patents

Journal Papers:

1. Suk Hwan Chung, Young-Sam Kwon, Seong Jin Park, and Randall M. German, "Sensitivity Analysis by the Adjoint Variable Method for Optimization of the Die Compaction Process in Particulate Materials Processing," Submitted for publication to ASME J. Eng. Mater. Tech., 2007.

Conference Presentations:

1. Arockiasamy Antonyraj, Seong Park, and Randall German, "Mechanical Properties of Various Aluminum Alloys by Powder Metallurgy," to be presented in TMS 2008, March 9-13, 2008: New Orleans, LA.
2. Seong Jin Park, Seong-Gon Kim, Mark Horstemeyer, and Randall M. German, "Multiscale Modeling in Powder Metallurgy: Atomistic, Discrete Element, and Finite Element Simulations," UKC (US – Korea Conference) 2007, August 9-12, 2007, Washington DC.
3. A. Antonyraj, Seong Jin Park, and Randall M .German, "Thermal Expansion and Viscoelastic Properties of Sintered Porous Ferrous Components," Proceedings of the 2007 International Conference on Powder Metallurgy & Particulate Materials (PowderMet 2007), complied by John Engquist and Thomas F. Murphy, Metal Powder Industries Federation and APMI International, Princeton, NJ, USA, Part 1, pp. 60-69, Denver, CO, USA, May 13-16, 2007.
4. James. K. Thompson, Seong Jin Park, Randall M. German, Fehim Findik, and Arockiasamy Antonyraj, "Novel Methodology to Quantify Tool Wear in Powder Metallurgy," Proceedings of the 2007 International Conference on Powder Metallurgy & Particulate Materials (PowderMet 2007), complied by John Engquist and Thomas F. Murphy, Metal Powder Industries Federation and APMI International, Princeton, NJ, USA, Part 1, pp. 50-59, Denver, CO, USA, May 13-16, 2007.
5. Fehim Findik, James K. Thompson, Arockiasamy Antonyraj, Seong Jin Park, and Randall M. German, "Mechanical and Physical Properties of Titanium and Silicon Carbide Containing Mixed Powder Sintered Aluminum," Proceedings of the 2007 International Conference on Powder Metallurgy & Particulate Materials (PowderMet 2007), complied by John Engquist and Thomas F. Murphy, Metal Powder Industries Federation and APMI International, Princeton, NJ, USA, Part 10, pp. 103-113, Denver, CO, USA, May 13-16, 2007.

5. AUTOMOTIVE METALS – STEEL

A. NSF Funding for the Development of 3rd Generation Advanced High-Strength Steels (AHSSs) (ASP 280[i])

Project Manager: Roger A. Heimbuch
Auto/Steel Partnership (A/SP)
2000 Town Center Drive, Suite 320
Southfield, Michigan 48075-1123
(248) 945-4770; fax: (248) 356-8511; e-mail: rheimbuch@a-sp.org

Chairman: Ronald Krupitzer
American Iron and Steel Institute (AISI)
2000 Town Center Drive, Suite 320
Southfield, Michigan 48075-1123
(248) 945-4761; fax: (248) 352-1740; e-mail: krupitzerr@autosteel.org

Technology Area Development Manager: Joseph A. Carpenter
(202) 586-1022; fax: (202) 586-1600; e-mail: Joseph.Carpenter@ee.doe.gov

Field Project Officer: Aaron D. Yocum
(304) 285-4852; fax: (304) 285-4403; e-mail: aaron.yocum@netl.doe.gov

Expert Technical Monitor: Philip S. Sklad
(865) 574-5069; fax: (865) 576-4963; e-mail: skladps@ornl.gov

---

Contractor: United States Automotive Materials Partnership (USAMP)[i]
Contract No.: DE-FC05-02OR22910 through the National Energy Technology Laboratory

---

Objectives

- Conduct the fundamental research required to develop 3rd Generation Advanced High-Strength Steels (AHSSs) that are higher in strength and more formable than currently available commercial grades of AHSSs with the potential of being more cost effective than stainless steels and twinning-induced plasticity (TWIP) steels.

Approach

- Conduct fundamental steel research at universities that can lead to the development of a cost-effective family of 3rd Generation AHSSs that can be applied for mass reduction in the auto body.
- Utilized National Science Foundation (NSF) processes to manage the research.
- Provide a portion of the funding (25%) through this project for fundamental research required to develop 3rd Generation AHSSs.
- Additional funding will be provided directly by the Department of Energy (DOE, 25%) and the NSF (50%).

Accomplishments

- NSF Advanced High-Strength Steel Workshop held October 22-23, 2006, Arlington, Virginia.
- NSF Advanced High-Strength Steel Proposal Panel Review held April 10-11, 2007, Arlington, Virginia. Eight proposals, from 30 submitted, were selected for funding using the NSF process and a budget allocation prepared by NSF. The research projects will be carried out over three years.
- NSF will notify the appropriate Principal Investigators (PIs) and universities of their grants and track and document the research projects following NSF standard practices.

Future Direction

- An industry-based steering committee is being formed to interface with the researchers.
- An annual progress review of 3rd Generation AHSS research is being planned which will include the NSF research, work from the Department of Energy (DOE) National Laboratories and other research programs. The intent is to share progress, identify gaps in the research program and identify areas where additional support would be valuable.

Introduction

One of the tasks of the ASP 240 Future Generation Passenger Compartment project (see 5.I) was to run the structural-optimization codes with unrestricted strength limitations to define the upper strength bound for auto-body steel for optimized mass reduction. Several areas of the body were found that would benefit from higher strength.

An additional 5 to 8% mass reduction is possible in those areas of the vehicle. Based on the specific areas of the body, estimates were made of the forming characteristic needed to make those types of parts. A window-of opportunity was defined ranging from 600 MPa/40% elongation to 1600 MPa/20% elongation for a cost-effective 3rd Generation AHSS family. It was recognized fundamental steel research would be required to develop steels in that property range. A collaborative effort by NSF, DOE, AISI and A/SP has been put together to fund eight university research proposals, using the NSF processes, to fund the supporting fundamental research to develop steels with the desired properties.

Objective

The objective of this project is to provide a portion of the funding (25%) for the fundamental research required to develop a cost effective family of 3rd Generation AHSSs that can ultimately be applied for mass reduction in the auto body. Additional funding will be provided directly by DOE (25%) and NSF (50%). The research will be done utilizing the processes of the NSF. If the research is successful, it will provide the basis for the commercial development of cost-effective 3rd Generation AHSSs by the A/SP steel members.

Project Status

A NSF Advanced High-Strength Steel Workshop was held October 22-23, 2006 in Arlington Virginia. As a result of that workshop, the NSF requested proposals for basic research to support the development of a family of 3rd Generation AHSS. A NSF AHSS Proposal Panel Review was held April 10-11, 2007, in Arlington, Virginia. Eight proposals, from 30 submitted, were selected for funding using the NSF process and a budget allocation was prepared by NSF. The research projects will be carried out over three years starting the academic year 2007-2008. The following table shows the PI, institutions and titles.

University	Professor	Topic
Carnegie Mellon University	Warren Garrison	AHSS through microstructure and mechanical properties
Case Western Reserve University	Gary Michal	AHSS through C partitioning
Catholic University of America	Abu Al-Rub Rashid	AHSS through particle size and interface effects
Colorado School of Mines (CSM), Ohio State University (OSU)	David Matlock (CSM) and Robert Wagoner (OSU)	Collaborative GOALI Project Formability and Springback of AHSS
Drexel University	Surya Kalidindi	FEM using crystal-plasticity simulation modeling tools
OSU	Ju Li	Multi-scale modeling of deformation for design of AHSS
University of Missouri-Rolla	David C. Van Aken	AHSS through nano-acicular duplex microstructures
Wayne State University	Susil K. Putatunda	High-strength, high-toughness bainitic steel

Conclusions

NSF is in the process of initiating the research contracts with the eight selected universities. Reporting of the research will follow the normal processes of NSF and brief summaries will appear in future editions of this annual report.

Future Work

An industry-based steering committee is being formed to interface with the researchers**.** An annual progress review of 3rd Generation AHSS research is being planned which will include the NSF research, work from the DOE National Laboratories and other research programs. The intent is to share progress, identify gaps in the research and identify areas where additional support would be valuable.

Acknowledgements

The support and guidance of Dr. Mary Lynn Realff of the NSF, Dr. Joseph Carpenter of the DOE and Ronald Krupitzer of the AISI in developing and implementing this research initiate is greatly appreciated. Dr. Joycelyn Harrison is the successor to Dr. Realff as NSF monitor of the grants.

References

The NSF Report, "Advanced High Strength Steel Workshop Oct.22-23, 2006, Arlington, Virginia" by Professor Robert Wagoner, Department of Material Science and Engineering, The Ohio State University, Columbus, OH.

[i] Denotes project 280 of the Auto/Steel Partnership (A/SP), the automotive-focus arm of the American Iron and Steel Institute (AISI). See www.a-sp.org. The A/SP co-funds projects with DOE through a Cooperative Agreement between DOE and the United States Automotive Materials Partnership (USAMP), one of the formal consortia of the United States Council for Automotive Research (USCAR) set up by Chrysler, Ford and General Motors to conduct joint, pre-competitive research and development. See www.uscar.org.

B. High-Strength Steel Joining Technologies (ASP 070[i])

Project Manager: Michael S. Bzdok
Auto/Steel Partnership (A/SP)
2000 Town Center, Suite 320
Southfield, MI 48075-1123
(248) 945-4778; fax: (248) 356-8511; e-mail: mbzdok@a-sp.org

Co-chair: John C. Bohr
General Motors Corporation (GM) – Controls, Robotics, and Welding
30300 Mound Road – Mail Code 480-109-164
Warren, MI 48090-9015
(810) 602-8276; fax: (586) 947-1039; e-mail: johnc.bohr@gm.com

Co-chair: Eric Pakalnins
Chrysler LLC
800 Chrysler Drive – CTC-CIMS 482-00-11
Auburn Hills, MI 48326-2757
(248) 576-7454; fax: (248) 576-7490; e-mail:ep18@chrysler.com

Technology Area Development Manager: Joseph A. Carpenter
(202) 586-1022; fax: (202) 586-1600; e-mail: joseph.carpenter@ee.doe.gov

Field Project Officer: Aaron D. Yocum
(304) 285-4852; fax (304) 285-4403; e-mail: aaron.yocum@netl.doe.gov

Expert Technical Monitor: Philip S. Sklad
(865) 574-5069; fax: (865) 576-4963; e-mail: skaldps@ornl.gov

---

Contractor: U.S. Automotive Materials Partnership (USAMP)[i]
Contract No.: DE-FC05-02OR22910 through the National Energy Technology Laboratory

---

Objective

- The objective of the High-Strength Steel Joining Technologies project team is to provide welding and joining expertise to the A/SP lightweighting projects to facilitate the increased use of advanced high-strength steels (AHSS). Additional project objectives include augmenting the technical knowledge pertaining to welding of AHSS through applied research and development of industry standards for quality acceptance and weldability testing of AHSS.

Approach

- Anticipate needs of the A/SP lightweighting projects and conduct applied research to address identified technology gaps.
- Determine welding parameters to produce quality welds, then statically and dynamically test welds produced at these parameters to quantify individual weld structural performance (see Figure 1). Tensile shear strength, impact energy and fatigue life are typically evaluated.
- Utilize commercially-available equipment or equipment typically found in existing manufacturing facilities for AHSS feasibility assessments. Utilize other, new technologies as necessary for lightweighting implementation.

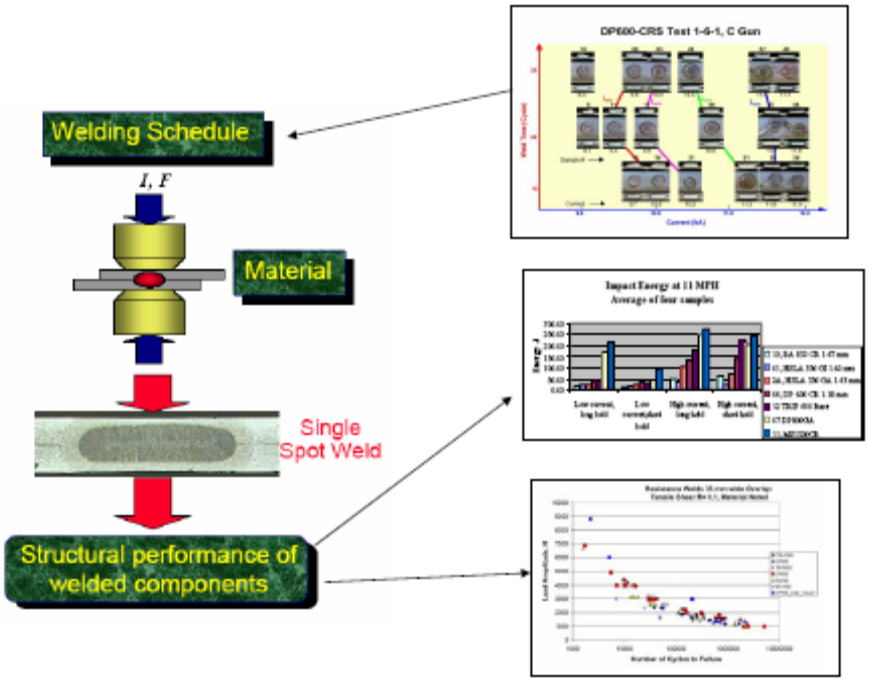

Figure 1. Resistance spot welding.

- Focus on materials classified as Group 3 and 4 (see Figure 2), as well as specific materials recommended by the A/SP Lightweight Structures Group.

Group: **Tensile Strength (MPa):**	**1. Low Strength** **< 350**	**2. Intermediate Strength** **350-500**	**3. High Strength** **> 500 - 800**	**4. Ultra High Strength** **> 800**
Typical Materials:	**Mild 140YS/270TS** **BH 180YS/300TS** **BH 210YS/320TS** **BH 240YS/340TS**	**BH 260YS/370TS** **HSLA 280YS/350TS** **HSLA 350YS/450TS** **DP 300YS/500TS**	**DP 350YS/600TS** **TRIP 350YS/600TS** **DP 500YS/800TS** **TRIP 500YS/800TS** **CP 700YS/800TS**	**DP 700YS/1000TS** **MS 950YS/1200TS** **MS 1150YS/1400TS** **MS 1250YS/1520TS** **HS 950YS/1300TS**
Note: Steels with a minimum tensile strength above 500 MPa (Groups 3 and 4) are generally considered Advanced High Strength Steels (AHSSs). Source: International Iron and Steel Institute (IISI), *Advanced High Strength Steel (AHSS) Application Guidelines, 6 June 2006*				

Figure 2. IISI steel classifications for welding.

- Investigate the use of process finite-element modeling to predict weld-quality characteristics and optimize weld-process parameters (see Figure 3). Utilize simulation for future projects to develop weld-process optimization and weldability assessments. Validate simulation results with experimental data.

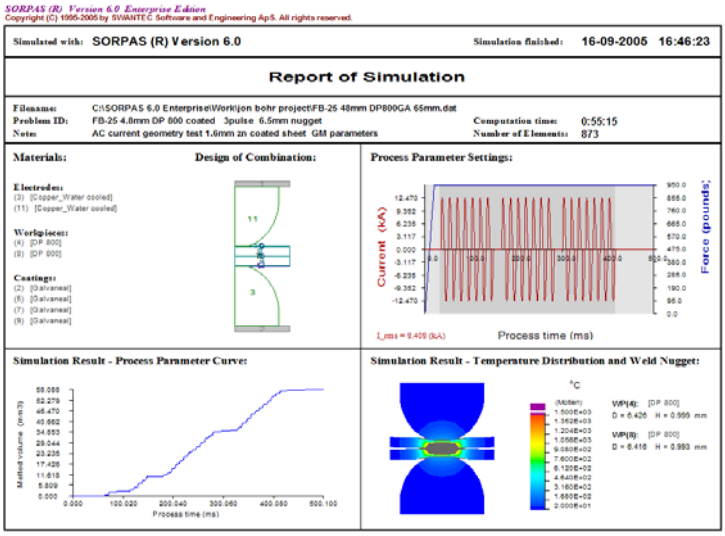

Figure 3. Process Simulation Report for resistance spot welding of DP780 Utilizing B-Nose Electrode and 3-Pulse Weld Schedule.

Accomplishments

- Produced and distributed public-project-result compact discs (CDs) and member-company toolkit CDs entitled "An Investigation of Resistance Welding Performance of Advanced High-Strength Steels," a Resistance Spot Weld (RSW) Design of Experiment (DoE) project (see Figure 4).
- Produced and distributed public-project-result CDs and member-company-toolkit CDs entitled "Advanced High-Strength Steel (AHSS) Weld Performance Study for Autobody Structural Components," a final project report of the Structural Weld Sub-Group (SWSG) study. Project included test matrix for evaluation of processes including metal inert gas (MIG), laser-assisted MIG, and plasma-assisted MIG (see Figure 4).
- Produced and distributed public-project-result CDs and member-company-toolkit CDs entitled "Impact Testing of Advanced High-Strength Steel (AHSS) Resistance Spot Welds at Various Temperatures," a study to quantify the effect of temperature on impact strength (see Figure 4).
- Produced and distributed public-project-result CDs and member-company-toolkit CDs entitled "Modeling Projection Welding of Fasteners to AHSS Sheet using Finite-Element Method," a study to model the projection welding of a hex-flanged weld nut using SORPAS with a cylindrical-block model.
- Produced and distributed public-project-result CDs and member-company-toolkit CDs entitled "Weld Lobe Development and Assessment of Weldability of Common Automotive Fasteners (Studs and Nuts) Using the Drawn Arc Welding Process" (see Figure 4). The purpose of this study was to determine the feasibility of welding studs to dual-phase (DP) and hot-stamped boron (HSB) steel, compare performances between cold-rolled steel and the above-mentioned steels, and develop a weld matrix for specific stud/material combinations (see Figure 5).

Figure 4. A/SP joining team project CDs.

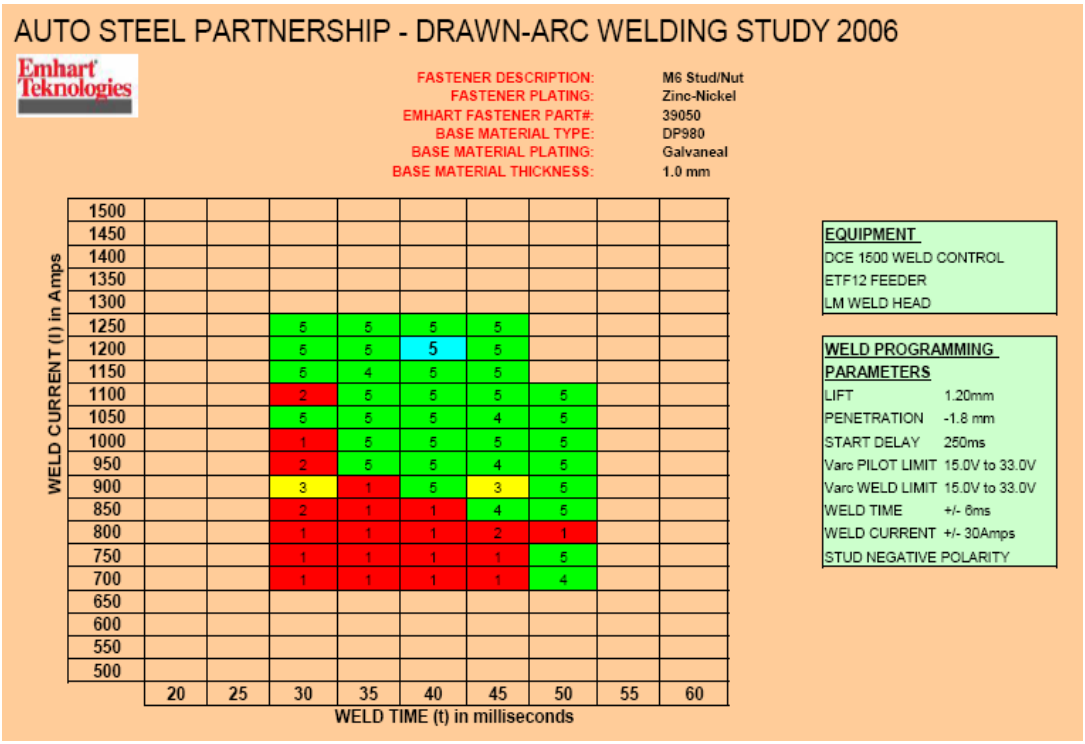

Figure 5. Drawn arc-weld matrix.

- Supported development of an automotive-industry AHSS resistance-weld-quality standard American Welding Society (AWS) D8.1M:2007 and provided technical support for development of an AHSS fracture-classification matrix for the standardization effort. The American National Standard Institute (ANSI) has completed the balloting process and was published in January 2007 (see Figure 6).

Figure 6. AWS/ANSI D8.1M:2007.

Future Direction

Future team activities include supporting welding development for the A/SP AHSS Application Guidelines Project Team and developing welding-parameter and joint-performance data for specific applications on AHSS automotive body prototypes. Future project work also includes:

- Complete development of a DoE methodology for material characterization and for assessing manufacturing feasibility of spot-welding AHSS.
- Develop software application to support common deployment and analysis of the AHSS Design of Experiment test method.
- Publish A/SP-recommended AHSS starting RSW schedules.
- Develop arc-weld procedures for various weld filler metals and AHSS joints, including determining the hot-cracking susceptibility and filler-metal compatibility of sheet AHSS materials.
- Create arc-weld design rules for the various lightweight chassis project teams' use.
- Complete a comprehensive study on Joint Efficiency that will allow joining-process comparisons for weld repair or substitution.

Introduction

The purpose of this project is to evaluate the weldability of the new AHSS currently being considered by the automotive companies as a solution to lightweighting without compromising cost or structural strength. The project intent is to evaluate various grades, thicknesses, and joining processes.

Initially, resistance welding was evaluated. Subsequent projects extended to metal inert gas (MIG), laser-assisted MIG, and plasma-assisted-MIG joining processes. Additional evaluations have included projection-nut welding and drawn-arc stud and nut welding to AHSS.

SWSG MIG/Laser Project

The arc-welding processes have historically been, and are today, commonly used in the manufacture of automotive structures. Recent increased usage of AHSS in automotive designs posed a desire to evaluate the application of arc-welding processes relative to the joining of AHSS.

This project establishes suitable welding parameters for AHSS material iterations (DP 600, DP 780, DP 800, DP 980 and high-strength low-alloy (HSLA) 350). Material section thicknesses ranged from 1.0 mm to 3.4 mm. Five arc-welding processes (Gas-Metal Arc Welding (GMAW)-Pulse/AC, GMAW-Pulse/DC, Laser-GMAW,

Laser, and Laser-Plasma) were examined in this operation.

Special consideration was given to the acceptance criteria for this project's welds. The standards of the three original equipment manufacturers (OEMs) were reviewed and a derivative acceptance standard was established for this study. Hardness/metallographic, impact, and yield/tensile properties related to the resulting weldments are presented as the results of this investigation.

A summary review of the results indicates:

- AHSS materials were successfully joined with the processes studied.
- Weld processes utilizing filler material demonstrated better results than processes with no filler material.
- Laser-welded lap joints generally failed in the weld metal, while GMAW fillet joints generally failed in the heat-affected zone (HAZ).
- Filler material/electrode strength had no direct effect on the weldment strength.
- Material strength and/or thickness gauge had no influence on laser-welded joint strength.
- Zinc-coated materials demonstrated high levels of porosity without a controlled/ engineered gap.

The project has been completed. The Project Team has produced and distributed public-project-result CDs and member-company-toolkit CDs entitled "Advanced High-Strength Steel (AHSS) Weld Performance Study for Autobody Structural Components."

Low-Temperature Impact Project

To date, performance data have only been reported under ambient-temperature conditions, and effects of extreme temperatures on impact of RSW of AHSS steels have not been considered. The objective of this study was focused on the impact performance through impact energy and peak load of various stack-up combinations of AHSS and mild steels at a large range of possible application temperatures. The conducted experiments provide a better understanding of the effects of extreme cold/hot weather conditions of RSW joints. The dynamic responses to low- and high-speed impact loading are investigated, which interact with the effects of stack-ups and temperature. The results show that impact energy and peak load are significantly different in magnitude, trend and scattering/variation. This study also shows that impact energy is more sensitive to material combinations than peak load.

The project has been completed. The Project Team has produced and distributed public-project-result CDs and member-company-toolkit CDs entitled "Impact Testing of Advanced High-Strength Steel (AHSS) Resistance Spot Welds at Various Temperatures."

Assessing Weldability of Projection-Welding Fasteners Using FEA

While the Joining Technology effort has been directed towards RSW, little focus has been directed toward projection-welding of traditional fasteners to AHSS sheet. Weld schedules and expected weld properties of projection-welded joints between fasteners and AHSS sheet are expected to differ from those in traditional material combinations. The highly-alloyed chemistry of AHSS and tailored material properties can result in undesirable properties after these materials are welded. Furthermore, the dissimilar-metal combination that is typical of projection welding of fasteners, adds complexity to the issue as a result of different base-metal properties and weld-metal dilution. In this sense, optimization of the weld process may be difficult as it requires an understanding of the effects of process parameters on the properties of the weld and surrounding base metal.

The projection-welding process of an M12/1.75/30 hex-flange 3-projection weld nut to 1.2-mm thick DP 780 hot-dip galvanized (HDG) AHSS sheet has been modeled using SORPAS.

The following conclusions have been found:

- A cylindrical-block model is best suited to this application. The axisymmetric geometry assumes one projection that encircles the entire nut resulting in a low

current density. The rectangular-block model results in excessive deformation in the nut body and requires reinforcement.

- The modeled results show strong correlation with experimental cross-sections.
- Increasing the weld current results in an increase in weld size.
- Increasing the weld force results in a decrease in weld size.
- Increasing the weld time to four cycles results in an increase in weld width, but has little effect on weld height.
- Increasing the weld time beyond four cycles has no effect on weld size.
- A peak in power during the first four cycles due to contact resistance causes rapid melting and collapse of the projection.
- Decreasing current density after collapse limits further nugget growth.
- Increasing the weld time results in an increase in HAZ size, but can also result in lower cooling rates.
- Modeling and experimental results indicate the projection-weld nut in this study to be weldable to DP 780 HDG sheet material under various conditions.

The project has been completed. The Project Team has produced and distributed public-project-result CDs and member-company-toolkit CDs entitled "Modeling Projection Welding of Fasteners to AHSS Sheet using Finite-Element Method."

Lightweight Rear Chassis Structures

The Lightweight Rear Chassis Structures team (see 5.J) of the A/SP needed assistance in welding a lightweight design from DP 600, 800, and 980 materials. After obtaining the various materials, the Joining Team proceeded to evaluate the weldability of these materials and to test weld the combinations prescribed for a rear-end structure. The Joining Team established the weld parameters and assisted the prototype source in making the structure. Weld parameters were delivered to the Lightweight Rear Chassis Structure team along with mechanical and chemical properties of the test materials.

Drawn-Arc Stud and Nut Welding to AHSS

Drawn-arc welding (DAW) is a well-established process for attaching studs to a variety of material type, thickness and coating combinations in automotive construction. The application of DAW is consistent with new automotive designs and manufacturing strategies that continually focus on ways to reduce costs. DAW provides a combination of short cycle time for stud attachment (high productivity) and adaptability to automation. Technological improvements in DAW equipment have resulted in increased application of the process.

The focus of this study was to determine whether drawn-arc stud welding can be performed on a consistent basis to new materials like DP steel and HSB steels. The approach of this study was to determine the feasibility of welding studs to DP and HSB steels, compare performances between cold-rolled steel and the above-mentioned steels, and develop a weld matrix for specific stud/material combinations.

Results indicate that the fasteners chosen for this study can be welded to the DP steel and HSB steel. Nut welding to HSB steel provided very interesting test results. Also, interesting to note was that certain geometries of a stud or nut are required to weld to HSB steel. These geometries also allow the automation of DAW process to be used for a variety of bracket configurations.

The project has been completed. The Project Team has produced and distributed public-project-result CDs and member-company-toolkit CDs entitled "Weld Lobe Development and Assessment of Weldability of Common Automotive Fasteners (Studs and Nuts) Using the Drawn Arc Welding Process."

Conclusions

Additional welding issues will be addressed during 2008 by the Joining Technologies Team funded by USAMP lightweighting initiatives and as member-company in-kind contributions.

Presentations and Publications

1. Donald F. Maatz, Jr., RoMan Engineering Services, "Advanced High-Strength Steel (AHSS) Weld Performance Study for Autobody Structural Components." Presented at the March 7, 2007 Great Designs in Steel Seminar in Livonia, Michigan. Paper presented at the MS&T'07 Conference at Cobo Center, Detroit, Michigan
2. Dr. Siva Ramasamy, Emhart Teknologies, "Drawn Arc Welding of Fasteners to Advanced High Strength Steels." Presented at the March 7, 2007 Great Designs in Steel Seminar in Livonia, Michigan
3. Dr. Siva Ramasamy, Emhart Teknologies, "Weld Lobe Development and Assessment of Weldability of Common Automotive Studs and Nuts with the Drawn Arc Welding Process." Paper presented at the MS&T'07 Conference at Cobo Center, Detroit, Michigan.

[i] Denotes project 070 of the Auto/Steel Partnership (A/SP), the automotive-focus arm of the American Iron and Steel Institute (AISI). See www.a-sp.org. The A/SP co-funds projects with DOE through a Cooperative Agreement between DOE and the United States Automotive Materials Partnership (USAMP), one of the formal consortia of the United States Council for Automotive Research (USCAR) set up by Chrysler, Ford and General Motors to conduct joint, pre-competitive research and development. See www.uscar.org.

C. Hydroform Materials and Lubricants (ASP 060[i])

Project Manager: Bart Clark
Auto/Steel Partnership (A/SP)
2000 Town Center, Suite 320
Southfield, Michigan 48075-1123
(248) 945-4776; fax: (248) 356-8511; e-mail: bclark@a-sp.org

Chairperson: Ronald Soldaat
Dofasco, Inc.
1330 Burlington Street East
P.O. Box 2460
Hamilton, Ontario, Canada L8N 3J5
(905) 548-7200; fax: (905) 548-4250; e-mail: Ronald_Soldaat@dofasco.ca

Technology Area Development Manager: Joseph A. Carpenter
(202) 586-1022; fax: (202) 586-1600; e-mail: joseph.carpenter@ee.doe.gov

Field Project Officer: Aaron D. Yocum
(304) 285-4852; fax: (304) 285-4403; e-mail: aaron.yocum@netl.gov

Expert Technical Monitor: Philip S. Sklad
(865) 574-5069; fax: (865) 576-4963; e-mail: skladps@ornl.gov

---

Contractor: United States Automotive Materials Partnership (USAMP)[i]
Contract No.: DE-FC05-02OR22910 through the National Energy Technology Laboratory

---

Objective

- Develop mechanical-test procedures and forming-limit diagrams for tubes.
- Improve the accuracy and confidence in finite-element modeling (FEM) of tubular hydroforming.
- Investigate the fabricating and performance characteristics of tailor-welded tubes (TWTs).
- Develop an understanding of steel and lubricant requirements for hydroforming using a combination of experiments and FEM.
- Support the work of other A/SP project teams when they investigate hydroformed structural components.
- Validate the performance benefits of hydroforming in automotive structures.

Approach

- The approach taken in this project is first to gain a basic understanding of the hydroforming process and potential issues, then apply the understanding to support other A/SP project teams in vehicle applications.
- The investigation encompasses various steel grades and gauges of steel tubing, including TWTs and advanced high-strength steel (AHSS), in free-expansion and corner-fill processes using several types of lubricants.
- The work has been divided into several phases.
  - Phase 1 – Investigate free-expansion and corner-fill characteristics.
  - Phase 2 – Investigate effects of pre-bending, lubricants and end-feeding on hydroforming limits.
  - Phase 3 – Investigate some of the pre-bending parameters for the hydroforming process.
  - Phase 4 – Investigate some of the bending parameters for AHSS tubing.

- Phase 5 – Determine the experimental forming limits of steel tubes.
- Phase 6 – Develop methods for empirical prediction of tube forming-limit diagrams and analysis of hydroforming data.
- Phase 7 – Investigate tubes made from tailor-welded blanks of varying grades and thicknesses.
- Phase 8 – Demonstrate the benefits of tube hydroforming through projects focused on real-world applications.

Note: Delays in obtaining sheet stock and tubes caused Phases 3 and 4 to follow Phases 5 and 6.

Accomplishments

During the report period (October 1, 2006 – September 30, 2007) the following were accomplished:

- Completed additional inside and outside corner-fill experiments with 90°-bent, interstitial-free (IF) and dual-phase (DP) 600 tubes with welded end caps to study the effect of elimination of tube end feed. Completed draft report.
- Completed experimental study on the hydroforming of TWTs fabricated from tailor-welded blanks of varying thicknesses of high-strength low-alloy (HSLA) 350 and DP 600 sheet steels. Tests included free-expansion and straight-tube corner-fill.
- In March 2005, the team was challenged to demonstrate the manufacturability of an AHSS hydroformed-TWT, lightweight, automotive front-rail. The team has taken on this challenge and accomplished the following to date:
  - Procured steels and tooling to fabricate tubes made from tailor-welded blanks with six different thicknesses/grades of high-strength steel.
  - Procured tooling to fabricate the front frame rail from the above tubes.
  - Soutec Soudronics in Switzerland fabricated the TWTs for the hydroforming process. Forming the TWTs, although eventually successful, proved to be very technologically challenging.
  - Procured special tooling dies for the hydroforming process
  - Began the process of bending the TWTs to fit the dies, which bending had been unsuccessful to date due to wrinkling and splitting.
- Developed a concept for a burst-testing-criteria fixture and identified a contractor to build it.
- Developed a proposal for a project concerning, “Investigation of Fabricating Dual Phase and TRIP Steel Tube from an ERW Production Line.” Project has been awarded to a contractor and the required sheet steels have been acquired.
- Developed a proposal for a project, “Stress and Strain Measurements under Non-Linear Loading through Tube Fracture for Improved Modeling and Prediction,” which involves controlled stress-path expansion of tubes. Quotes have been received in response to a request for quote (RFQ) and are in the process of being reviewed.

Future Direction

During fiscal year 2008, the Hydroforming Materials and Lubricant team plans to accomplish the following:

- Proceed with AHSS TWT bending trials for the front-rail project and gain an understanding of the effect of the process variables.
- Upon successful AHSS TWT trials, fabricate and determine the manufacturing parameters of a hydroformed front frame rail in support of the work performed by Lightweight Front Structures, ASP 110 (see annual report for fiscal year (FY) 2006). These rails will be further tested by the Strain Rate Characterization project Team, ASP 190 (see 5.G)
- Complete report for the hydroforming of HSLA 350 and DP 600 TWTs and make documentation available to A/SP member companies.
- Complete report on the hydroforming of DP 600 and IF Bent Tubes with Welded End Caps and make documentation available to A/SP member companies.

- Conduct the project, "Investigation of Fabricating Dual Phase and TRIP Steel Tube from an ERW Production Line."
- Conduct the project, "Stress and Strain Measurements under Non-Linear Loading through Tube Fracture for Improved Modeling and Prediction."

Introduction

Hydroformed steel tubes have been used in the automotive industry to form components that meet structural objectives, particularly strength and rigidity, at optimal mass. One of the most significant advantages of tubes is that they are monolithic closed sections and, as such, exhibit significantly greater stiffness in torsion than conventional open sections such as "C" and "hat" shapes. Eliminating the need for weld flanges, which are required to join two open members into a closed member, offers a potential for reducing vehicle mass. The use of hydroformed tubes is limited largely by lack of knowledge of the capabilities and parameters of hydroforming processes and the effects of those processes on the tubes.

This project was undertaken to investigate and quantify the capabilities and parameters of various hydroforming processes so that automotive designers and engineers can utilize a wider range of tube configurations and predict with reasonable accuracy the performance of hydroformed components. Hydroforming tubes made from high-strength and AHSS, and particularly tubes made from tailor-welded blanks, are of particular interest because of the potential reduction of mass associated with materials of higher strength and optimal thickness.

Discussion

The Hydroforming Process

Hydroforming is a process in which a tube is placed into a die shaped to develop the desired configuration of the tube. Water is introduced into the tube under very high pressures causing the tube to expand into the die. The tube ends can be held stationary or moved inward during the process to end-feed material into the die cavity. ---

The process has two distinct stages, shown in Figure 1. The first stage is free expansion (Figure 1a). It continues until the tube contacts the die wall (Figure 1b). In the second stage, corner filling, the tube is in contact with the surface of the die, which constrains subsequent deformation (Figure 1c). During this stage, the tube expands into the corners of the cavity, accomplishing corner fill. A tube that has been hydroformed is shown with the die in Figure 2. Note that the test was continued until the tube failed.

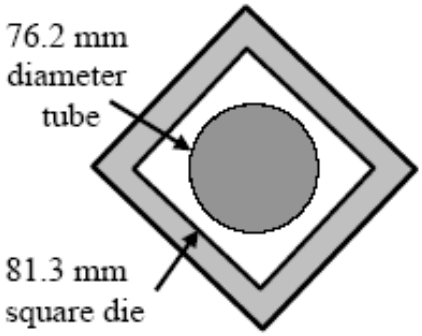

Figure 1a a) Free Expansion

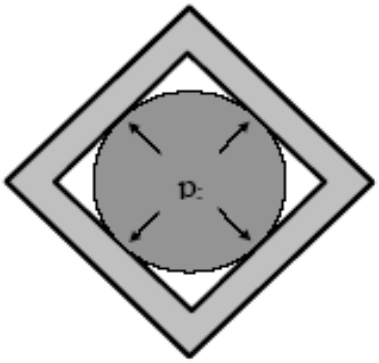

Figure 1b b) Contact with die wall

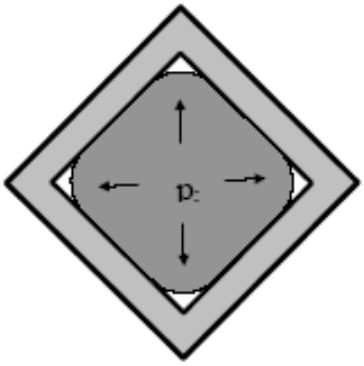

Figure 1c c) Corner filling

Figure 2. A hydroformed tube and die.

During corner fill, the tube slides against the die; therefore, friction between the tube and die affects the process, and the lubricant used in the process becomes a significant parameter.

Forming-Limit Diagrams (FLD)

During tube fabrication and during both stages of hydroforming, the tube undergoes plastic strain. The amount of plastic strain that can occur before the material fractures is predicted in stamping processes that utilize flat sheet steel by using a forming-limit diagram (FLD). The FLD is determined by the properties of the material. The hydroforming process is preceded by tube forming and sometimes pre-bending of the tube, both of which induce strains in the material and alter its properties. Before a FLD can be developed for the hydroforming process, the strain history – that is, the strain induced in the material prior to hydroforming – must be known.

An FLD is required for any successful computer simulation of hydroforming. Therefore, in addition to experiments with tube expansion to determine the effects of axial compression and tension in combination with internal pressurization, the effects of pre-bending and pre-forming on subsequent formability was addressed. Collected data were used to develop FLDs for tubular hydroforming of straight tubes. These data will be used to develop guidelines for optimizing bending operations.

Presently, the formability limits for pre-bent steel in tubular hydroforming are poorly understood. Accuracy needs to be addressed and improved to allow optimum application of tubular hydroforming in the lightweighting of vehicles.

Hydroforming Tailor-Welded Tubes

The Project Team began work on hydroforming TWTs. The work is being conducted on 76.2-mm (3") outside diameter (OD) tubes made from two material grades and two thicknesses. The test consists of five TWT configurations:

1) Baseline: 1.5-mm DP 600 single material tube
2) 1.5-mm DP 600 butt welded to 1.5-mm DP 600
3) 1.2-mm DP 600 butt welded to 1.5-mm DP 600
4) 1.5-mm HSLA 350 butt welded to 1.5-mm DP 600
5) 1.5-mm HSLA 350 butt welded to 1.2-mm DP 600

The blanks were butt welded before the tubes were formed. In all cases the tubes are 508-mm (20-inches) long.

The finished tubes were sent to the testing laboratory where they were analyzed. The laboratory found that tube concentricity was not adequate in some cases to allow conventional hydroforming, because it was not possible to maintain an adequate seal between the tube ends and the end caps, where water is introduced. At the suggestion of the laboratory and with the approval of the Hydroforming Team, the laboratory welded the end caps. Free expansion tests have been completed and the results are being analyzed.

Vehicle Front Structural Rail

In March, 2006, the Hydroforming Team began an initiative to fabricate a front structural rail, based on a design developed by the Lightweight Front Structures (LWFS) Team, ASP 110. LWFS had developed designs for a front rail for two vehicles. The first was the target vehicle. The second had 20% less mass than the target vehicle, which is a reasonable assumption based on anticipated secondary effects resulting in lower mass in systems such as suspension, powertrain and roof structure.

Two design concepts were developed for each vehicle and both concepts were optimized by using tailor-welded blanks. The first design concept in each case requires conventional stamping processes to form a "hat-shaped" member with a "top plate" spot-welded at the "hat" section flanges. The second concept utilizes a tailor-welded tube consisting of six different grades/gauges of steel. The TWT design did not address attachment to contiguous vehicle components.

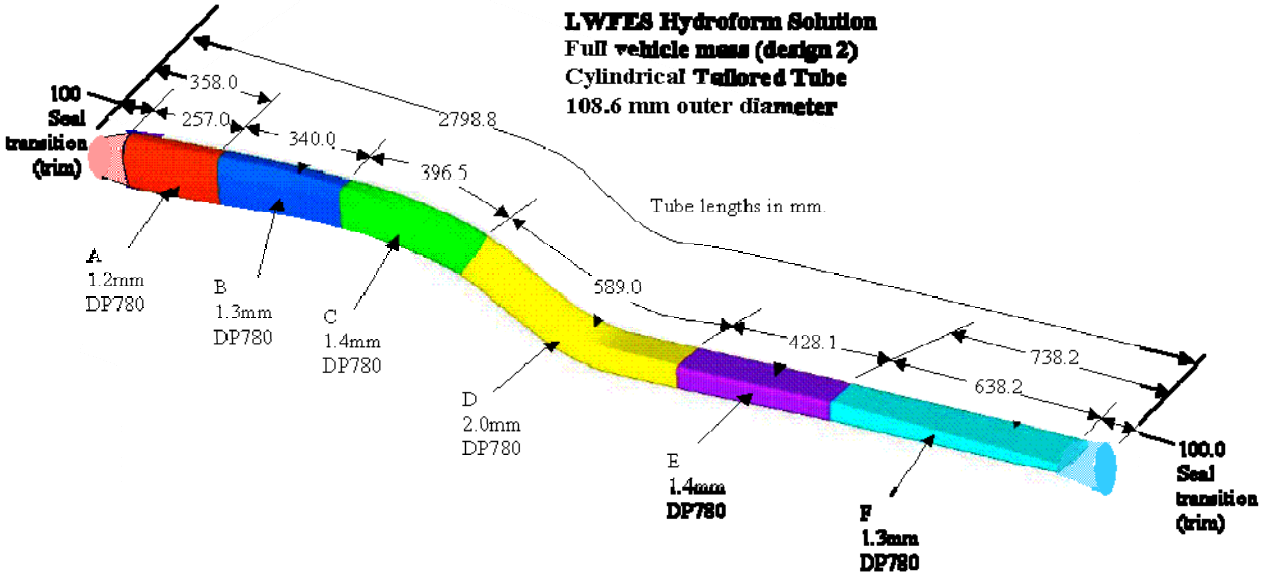

Figure 3. Hydroformed rail for full vehicle mass.

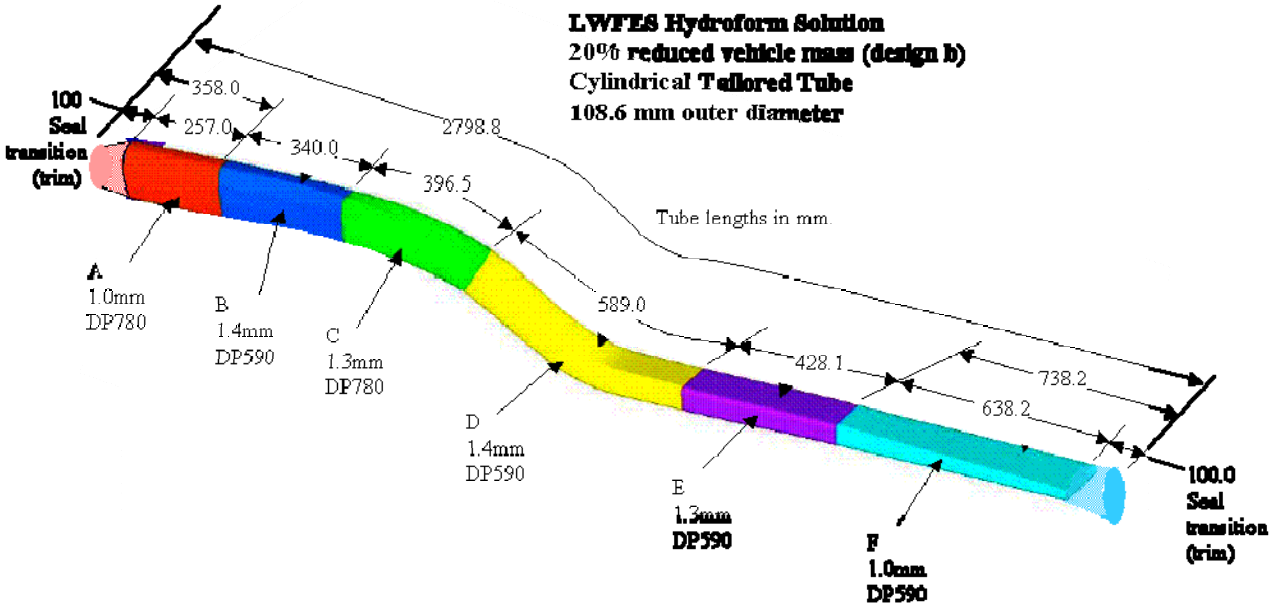

Figure 4. Hydroformed rail for 20% reduced vehicle mass.

The blank lineup for the rail in the target vehicle is shown in Figure 3 and the lineup for the rail in the vehicle with 20% reduced mass rail, in Figure 4. It is noteworthy that the rail for the full mass vehicle utilizes DP 780 steel in 1.2-mm to 2.0-mm thickness, while the rail for the 20% reduced mass vehicle utilizes both DP 780 and DP 590.

The Project Team agreed that the purpose of the front-rail initiative is a manufacturing-feasibility study. For this reason, no effort will be made to correct the hydroforming tools to bring the end product within dimensional-tolerance limits. Rather, the hydroforming supplier will be asked to utilize his experience to produce tubes as close as possible to dimensional tolerances, then perform comprehensive dimensional studies on the tubes to learn the effects of the fabrication process, such as springback and die release.

The Team selected a hydroforming supplier and a tube manufacturer, both of whom have state-of-the-art equipment and expertise, are willing to stretch their current technology and are willing to make significant in-kind contributions to the project.

The hydroforming tools have been procured, the tube-forming tools have been procured, and fabrication of the tubes has been completed. Work on the bending of the tubes is in progress.

Burst Criteria

The Hydroforming Team also recognized the need to develop burst criteria for hydroformed tubes. To date, a test fixture has been prescribed and a vendor has been selected to design and build the fixture. The second phase of this initiative will be the actual tests.

Future Work

During FY 2008, the Hydroforming Materials and Lubricants Team will pursue the following work:

- Gain an understanding of issues affecting bending of AHSS tailor-welded tubes.
- Manufacture front rails from TWTs to both designs (target vehicle and 20% reduced mass vehicle, Figures 3 and 4).
- Perform analyses on hydroformed rails.
- Complete the project on the hydroforming of DP 600 and IF Bent Tubes with Welded End Caps and make test documentation available to A/SP member companies.
- Conduct the project, "Investigation of Fabricating Dual Phase and TRIP Steel Tube from an ERW Production Line."
- Conduct the project, "Stress and Strain Measurements under Non-Linear Loading through Tube Fracture for Improved Modeling and Prediction."

Conclusions

Analysis of tests run during this reporting period indicates that:

- Tube bending can significantly limit subsequent tube formability and needs to be accounted for in part design.
- Tube-bending speed has only a minor effect on bending strains and subsequent hydroforming. Bending radius, however, has a large impact.
- Lubricant selection is important as it affects bending and hydroforming strains.
- Tube end feeding is very beneficial for achieving complex geometries.
- FLDs based on sheet-forming technology are useful for predicting necking strains in free-expansion hydroforming, but bursting in closed-die hydroforming requires further understanding.

Presentations and Publications

1. "Hydroforming Group," Auto/Steel Partnership Program Review, Department of Energy, September 21, 2005.
2. "Hydroforming Committee," A/SP SPARC financial planning review, July 18, 2006.
3. "Hydroforming Materials and Lubricants," Auto/Steel Partnership Department of Energy Peer Review meeting was conducted on Friday, December 1, 2006
4. "Influence of Lubricant in Bending & Hydroforming Evaluations" presentation by Jean Reid at ASTM D02 Petroleum Products and Lubricants Committee workshop/symposium on Tribological Challenges of Metal Deformation Fluids, Florida, June 17, 2007.

5. "Tube Hydroforming Phase V: Experimental Forming Limits of Steel Tubes" IRDI report, March 2007 (awaiting publication by A/SP Technology Transfer Team)
6. "Influence of Bending Parameters on the Hydroforming of IF and DP 600 Tubes" IRDI report, March 2007 (awaiting publication by A/SP Technology Transfer Team)
7. "Hydroforming Materials and Lubricants (ASP060) - Project Description Sheet, Statement of Project Objectives and Presentation," A/SP Project Review and Budget meeting, July 17, 2007.

[i] Denotes project 060 of the Auto/Steel Partnership (A/SP), the automotive-focus arm of the American Iron and Steel Institute (AISI). See www.a-sp.org. The A/SP co-funds projects with DOE through a Cooperative Agreement between DOE and the United States Automotive Materials Partnership (USAMP), one of the formal consortia of the United States Council for Automotive Research (USCAR), set up by Chrysler, Ford and General Motors to conduct joint, pre-competitive research and development. See www.uscar.org.

D. Sheet-Steel Fatigue Characteristics (ASP 160[i])

Project Manager: Bart Clark
Auto/Steel Partnership (A/SP)
2000 Town Center, Suite 320
Southfield, Michigan 48075-1123
(248) 945-4776; fax: (248) 356-8511; e-mail: bclark@a-sp.org

Chair: Raj Mohan Iyengar, Ph.D.
Severstal North America Inc
3001 Miller Road
P.O. Box 1631
Dearborn, MI 48121-1631
(313) 317-1303; fax (313) 337-9372; e-mail rmohan@severstalna.com

Technology Area Development Manager: Joseph A. Carpenter
(202) 586-1022; fax: (202) 586-1600; e-mail: joseph.carpenter@ee.doe.gov

Field Project Officer: Aaron D. Yocum
(304) 285-4852; Fax (304) 285-4403; e-mail: aaron.yocum@netl.doe.gov

Expert Technical Monitor: Philip S. Sklad
(865) 574-5069; fax: (865) 576-4963; e-mail: skladps@ornl.gov

---

Contractor: United States Automotive Materials Partnership (USAMP)[i]
Contract No.: DE-FC05-02OR22910 through the National Energy Technology Laboratory

---

Objectives

- Compile the test data generated in the previous phases of the project into a user-friendly database that can be used in all phases of design and structural analysis of sheet-steel vehicle bodies.
- Investigate the fatigue life of joints formed by spot welding, adhesive bonding and weld bonding (a combination of spot welding and adhesive bonding).
- Explore the fatigue response of advanced high-strength steels (AHSS) after being subjected to metal inert gas (MIG) and laser-welded joining and compare this behavior with that of standard automotive steels.
- Assist the Joining Technology team (see 5.B) in identifying the optimum welding parameters for laser- and MIG-welded joints, and develop a fatigue test program.

Approach

- Investigate the fatigue characteristics of resistance spot welding, a fusion process in which the metal pieces to be joined are melted and re-solidified via a brief high-voltage electrical pulse, forming an alloy with a distinctly different microstructure than that of the parent metals. At the intersection of the weld nugget, or button, and the faying surfaces, a crack-like discontinuity is formed which is often the site of initial crack growth. In addition, the weld nugget itself may contain discontinuities (such as porosity), which can also become sites at which fatigue cracks form. The amount and type of discontinuities and, thus, the fatigue properties can be affected to a considerable extent by the welding process. The microstructures of the joined metals are also changed in the area adjacent to the weld, which area is known as the heat-affected zone (HAZ).
- Investigate the fatigue characteristics of adhesive bonding, which substitutes an entirely different material in place of the weld to act as the load-bearing connection. The adhesive must adhere to the metals being joined and resist interfacial fatigue failure at the adhesive/metal interface and within itself (cohesive failure).

- Investigate the fatigue characteristics of weld bonding, which is a combination of adhesive bonding and spot welding.
- Investigate the previously unknown, or at best little known, factors that are expected either to improve impact durability or facilitate their modeling and simulation.
- Reduce the spot-weld, adhesive-bonded, and weld-bonded test data to a form that is useful to design engineers who perform vehicle structural analysis.
- Develop a test program to investigate the fatigue performance of gas metal arc welding (GMAW), a fusion welding process which results in continuous joints. However, under GMAW (or MIG), a third "filler" metal is introduced under an arc and shielding gas and, akin to spot-welding, alloys and microstructures are formed which are different from the metals being joined.
- Identify the parameters, including metal grades, metal thicknesses, coatings and joint configurations that impact the fatigue performance of GMAW welded joints.

Accomplishments

- Completed testing of spot welds in mild steel and ultra-high-strength boron steel and placed online the knowledge base developed from the results.
- Completed a detailed study of effect of geometric parameters on fatigue lives of spot-welded specimens.
- Developed a specification for fabricating MIG- and laser-weld specimens, submitted a request for quotation, selected a contactor and awarded a construction contract.
- Completed fatigue testing of MIG-welded specimens created by the Joining Technologies Team, ASP 070.
- Completed fabrication of test specimens for Phase 1A MIG-weld fatigue testing.
- Completed weld fatigue testing for single-lap-shear, MIG-welded test specimens.
- Initiated weld testing of double-lap-shear and perch-mount specimens.

Future Direction

- The project team will complete the Phase 1A of its own program of fatigue testing MIG welds.
- Specimen specifications for Phase 1B testing will be completed and Phase 1B will be initiated.
- Detailed analyses and interpretations of the test results will be conducted to develop appropriate parameters that capture the effect of weld and specimen geometry on fatigue performance.

Introduction

Future and near-future vehicle designs are faced with several stringent requirements that impose conflicting demands on the vehicle designers. Safety, particularly crash-energy management, must be improved while vehicle mass and cost are contained.

AHSSs, judiciously selected and applied, are currently the best candidates to achieve low-cost (compared with aluminum (Al), magnesium (Mg) and plastics), reliable materials for meeting these mandates. As structural components are optimized and thinner gauge, higher-strength materials are assessed, the fatigue lives of the areas where loads are transferred become increasingly important considerations. To assess the performance of a component in the design phase, the fatigue characteristics of not only the base material but the joints where loads are transferred, must be known. This project has essentially completed testing various grades of steel and steel coupons that have been spot welded, adhesively bonded and weld bonded. Testing of GMAW and laser-welded joints is under way.

Discussion

The effort to evaluate the fatigue characteristics of spot welds began in the 2002 fiscal year with presentations by key researchers on the current state of the work at Chrysler Corporation, Ford Motor Company, and General Motors Corporation. Based on these presentations, the Sheet-Steel Fatigue Project Team has produced results beneficial to all three companies. Early in the planning, the A/SP Joining Technologies Team was consulted, and that team prepared the samples that were tested. This interaction ensured that the samples were joined using consistent procedures that were properly controlled and in adherence to the best current practices in sheet-metal joining in the automotive industry.

The following fatigue test parameters were agreed upon and carried out:

- Two modes of testing: tensile shear (Figure 1) and coach-peel (Figure 2).
- A single thickness (1.6 mm) was selected to ensure that results were comparable between steel grades. A thinner gage (0.8 mm) was selected for a small satellite study (one AHSS and one high-strength low-alloy (HSLA)) on the effect of gage thickness on fatigue.
- Because no such data were available for AHSSs, several grades in this class were tested.
- Testing was done at two stress ratios, R, 0.1 and 0.3. The stress ratio R is defined as the ratio of the minimum stress to the maximum stress in the test cycle. Maximum and minimum values are algebraic, with tension designated as positive and compression negative.
- Eleven steel grades were tested.
- While the majority of testing was performed on spot-welded joints, the fatigue performance of adhesive-bonded and weld-bonded joints was explored in several tests series.

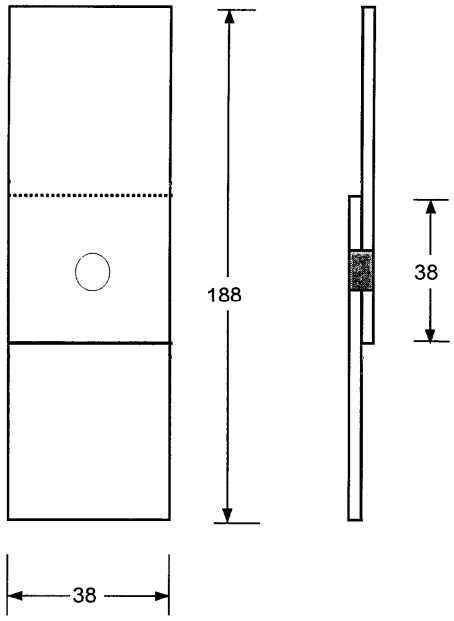

Figure 1. Spot-welded lap-shear test specimen.

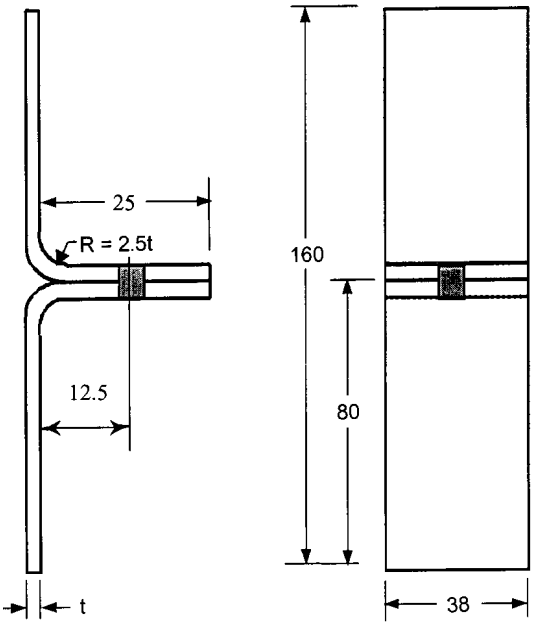

Figure 2. Coach-peel test specimen.

Two testing sources, of the nine invited to submit testing proposals, were selected to perform the fatigue experiments: The University of Missouri at Columbia, Missouri, and Westmoreland Mechanical Testing and Research, Inc. in Youngstown, Pennsylvania.

As the testing progressed and results were analyzed, the following tests were added for comparison purposes:

1. Testing at specified R ratios means that the maximum and minimum loads are constant throughout a given test. However, as the maximum load is increased to generate fatigue curve data, the minimum loads also increase. This process is valuable for establishing baseline data. However, in the real world, load amplitudes can be expected to be variable. For this reason, automotive-spectrum load tests, set to two different predetermined scalings, were run.
2. To investigate the effect of button size, fatigue studies were performed on specimens with a welding schedule that produced a smaller weld button.
3. At the request of the Joining Technologies Team, three test series were run using wide samples (125 mm vs. the standard 38 mm). The wider samples minimize rotation of the weld under load and allow negative R ratios to be explored.

GMAW Joints

GMAW welding is the second most common welding process used on vehicle structures, with the rate of applications increasing yearly. GMAW or MIG welds are used not only on body members and sub-frames in passenger cars, but also in frames for larger passenger vehicles, light trucks and sport-utility vehicles (SUVs). Therefore, the test samples will be made from two thickness groups: a thinner gage of 1.6 mm for body applications and a thicker gage of 3.4 mm for frame applications. These target thicknesses, primarily based on material availability, represent typical, as-welded material thicknesses found in body and frame applications, respectively.

Frame members do not generally require as much formability as do body members, and they offer excellent opportunities for mass reduction through downgaging. Therefore, tests on frame joints will ultimately employ higher-strength materials than those specific to body members, but often result in similar numbers of welds and amount of weld area.

The Team agreed to four specimen designs for testing. Each explores a different loading mode and reveals different information about the material/joint performance: butt weld (Figure 3), single-lap-shear (Figure 4), double-lap-shear (Figure 5), and perch mount (Figure 6).

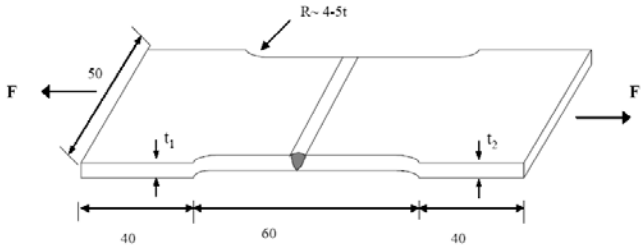

Figure 3. MIG butt-welded specimen.

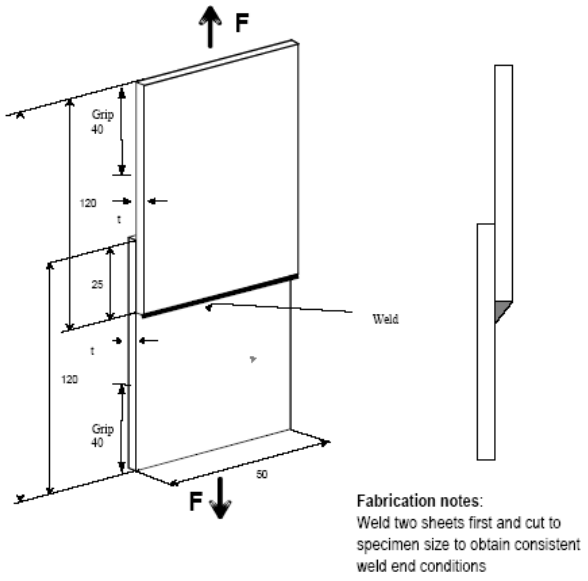

Figure 4. MIG-welded, single-lap-shear specimen.

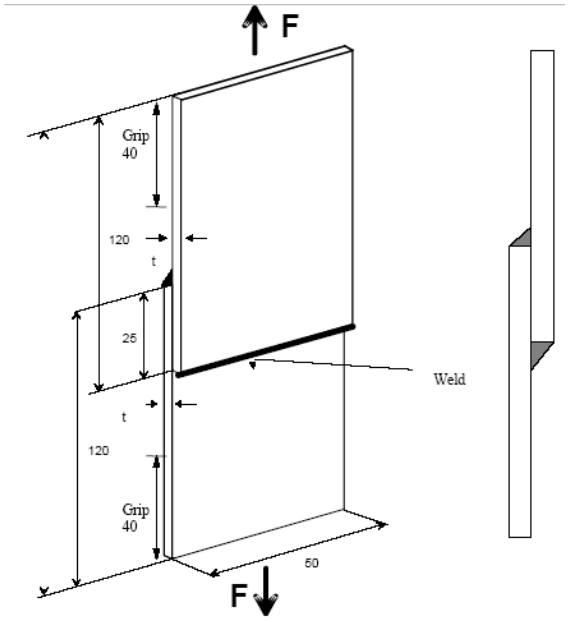

Figure 5. MIG-welded double-lap-shear specimen.

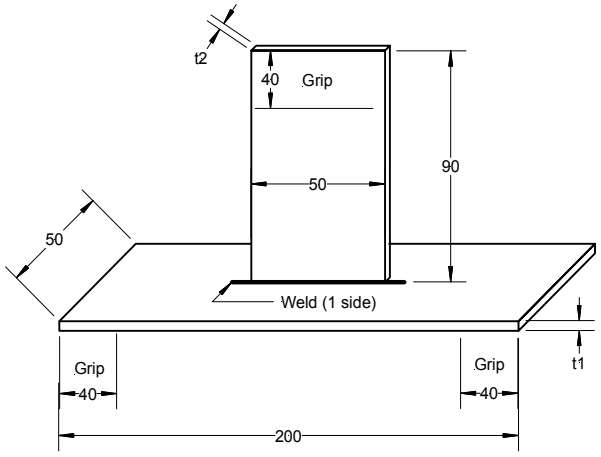

Figure 6. MIG welded perch mount specimen.

Results – Spot welds

Plotted in Figure 7 are all the tensile-shear and coach-peel fatigue results for all nominal 1.6-mm gage materials with 7-mm-diameter spot welds, conventional steels and AHSS included. Data labels ending in R0.1 indicate R=0.1 loading and data labels ending R0.3 indicate R=0.3 loading. Runouts are plotted but not otherwise indicated in this figure.

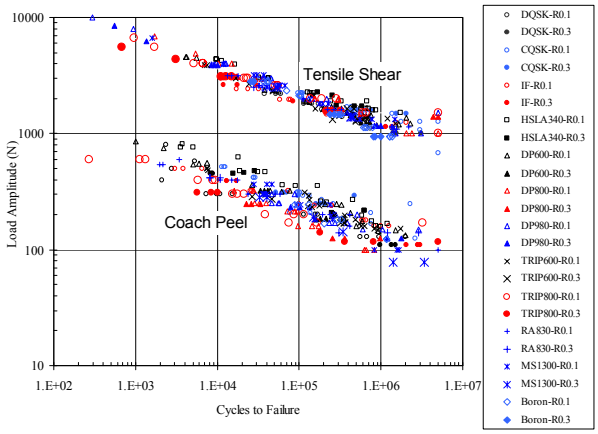

Figure 7. Fatigue results for all 1.6 mm thick, 7 mm diameter nugget spot-welded materials.

Two thicknesses of HSLA340 (1.0 mm and 1.78 mm) and two thicknesses (1.53 mm and 0.83 mm) of dual phase (DP 600) are compared in Figure 8. The nominal button size for all specimens was 7.0 mm and the welding parameters were held as similar as possible between the gages/grades without compromising strength. It was expected that the thinner gages would show shorter life because of the intrinsically higher stresses in the joint; this result was indeed found in both materials.

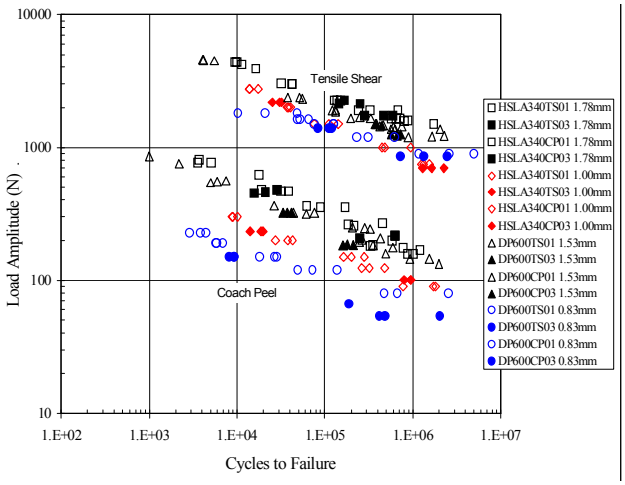

Figure 8. Effect of thickness on fatigue performance.

Results – Fusion Welds

Fatigue testing of specimens containing the fusion weld line within the width of the specimen was conducted to assist the Joining Technology team in identifying the optimum welding parameters for laser- and MIG-welded joints. The dimensions of

the specimens are shown in Figure 9a and 9b. The weld location was centered between the edges of the sample and the robot travel was 25 mm total. This produced a weld with a start and a stop within the gage section of each specimen. GMAW welding of the DP 780 AHSS was performed with 70 ksi and 90 ksi filler wires while GMAW welding of the DP 600 AHSS was performed with only 70 ksi filler wire. No filler was used with the laser welds.

The DP 600 results of the fatigue, shown in Figure 10a, indicate no significant difference in performance between the AC, DC or laser-assisted GMAW welding processes. Similarly, the performance of the DP 780 GMAW welds (Figure 10d) was not influenced by either the process type or the strength of the filler material used. Similar observations may be made concerning the laser processing presented in Figure 10b and 10c. The mean stress appears to be an insignificant factor in the fatigue performance of fusion-welded joints. This behavior can be seen in all of the graphs in Figure 10.

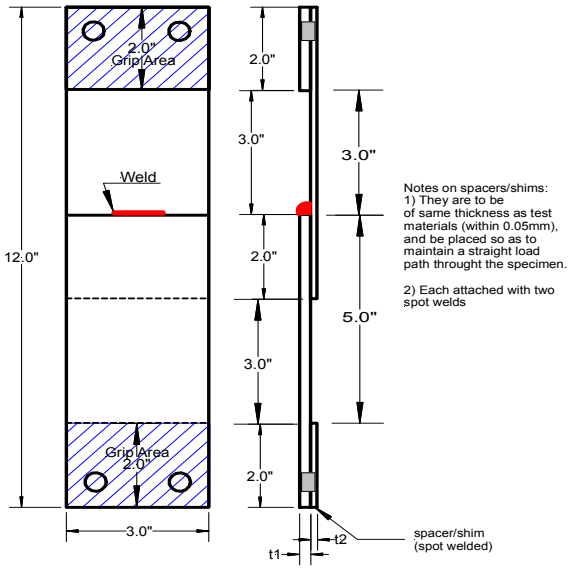

Figure 9a. Schematic of specimens for GMAW. Dimensions in mm.

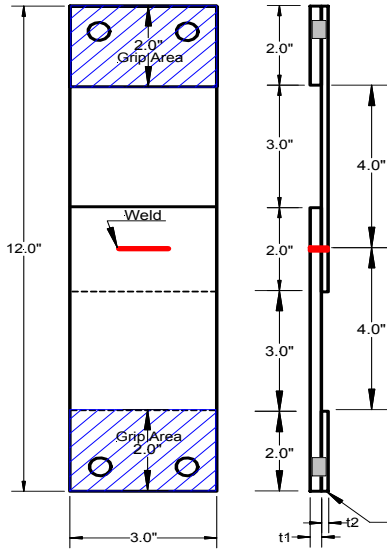

Figure 9b. Schematic of specimens for laser-weld fatigue tests. Dimensions in mm.

Conclusions

Analysis of test results indicates that, for the specimen geometries and steel grades selected for this study, the fatigue performance of a spot weld is independent of the base-metal strength. This finding supports the initial understanding that the melting and resolidifying processes associated with spot welding form new alloys and, thus, making the properties and coating of the material(s) being joined, and the welding parameters, insignificant contributors to fatigue performance.

Similarly, the results clearly indicate that, within either the GMAW- or laser-weld groups, the type of weld does not seem to influence the fatigue performance (e.g., for GMAW it does not matter if the weld is AC, DC, or laser-assisted).

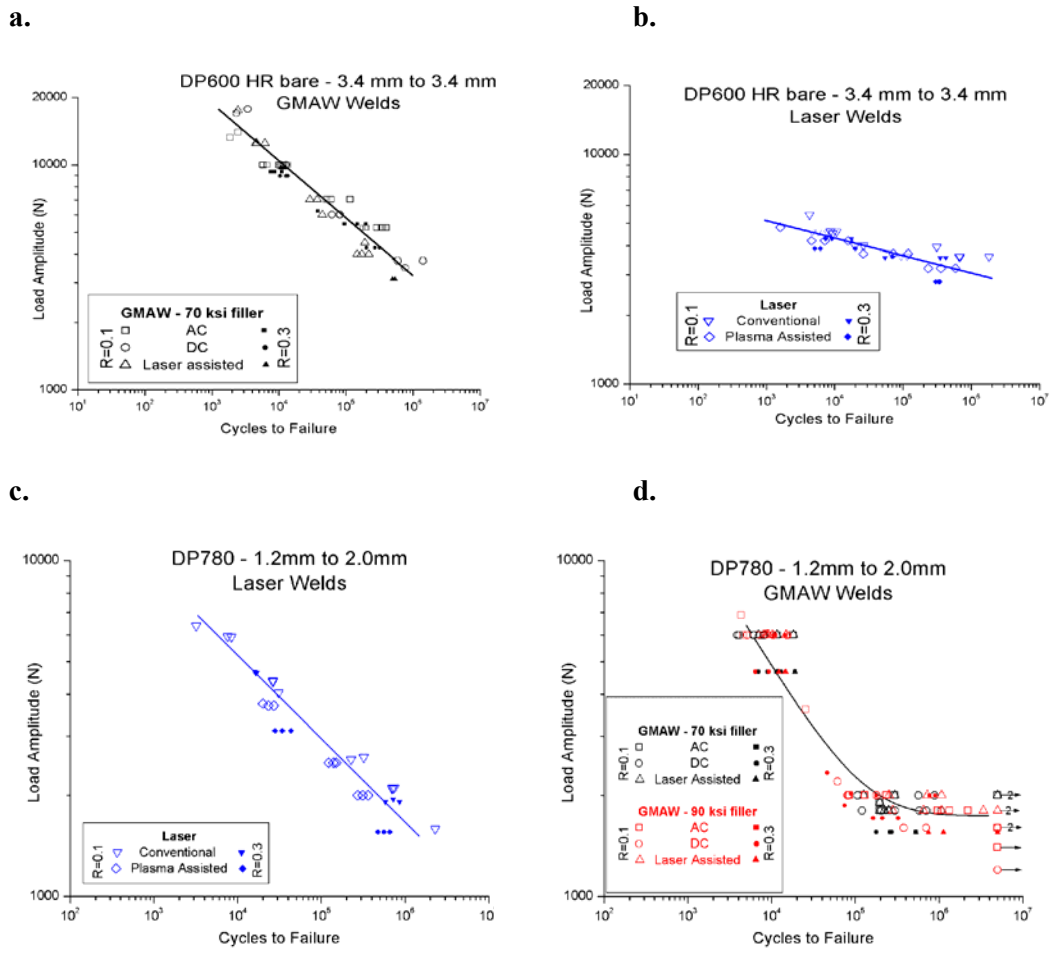

Figure 10. Fatigue-performance evaluation of GMAW and laser welds in two AHSSs: DP 600 hot-rolled, bare, and DP 780 coated. Specimens for DP600 are 3.4 mm to 3.4 mm while the specimens for DP 780 are 1.2 mm to 2.0 mm.

Presentations and Publications

1. "Sheet Steel Fatigue Group", Auto/Steel Partnership Program Review, Department of Energy, September 21, 2005.
2. "A/SP Sheet Steel Fatigue Committee", Joint Policy Board, Feb. 1, 2006.
3. J.J.F. Bonnen, Hari Agrawal, Mark A. Amaya, Raj Mohan Iyengar, HongTae Kang, A. K. Khosrovaneh, Todd M. Link, Hua Chu Shih, Matt Walp, Benda Yan, "Fatigue of Advanced High Strength Steel Spot Welds," 2006, Society of Automotive Engineers, SAE-2006-01-0978, pp. 19. *Republished in 2006 SAE Transactions.*
4. Kang, HongTae, "Evaluation of Spot Weld Fatigue Damage Parameters" 2006, Society of Automotive Engineers, SAE-2006-01-0978, pp. 19. *Republished in 2006 SAE Transactions.*
5. "Spot Welds, MIG Welds and their effect on the fatigue of AHSS steels," Mar. 10, 2006 (A/SP Frame group).
6. "Sheet Steel Fatigue Committee," A-S/P SPARC financial planning review, July 18, 2006.
7. "Spot Welds, MIG Welds and their effect on the fatigue of AHSS steels," Mar. 10, 2006 (Joining group).
8. "Fatigue of MIG Welds" AISI Wheel Task force meeting, Nov 18, 2005.
9. ASP Team Review, Dec. 15, 2005.
10. "Fatigue of AHSS SpotWelds," 2nd Annual Ford AHSS Conference, Oct. 18, 2005.

11. J.J.F. Bonnen and R. Mohan-Iyengar, "Fatigue of Spot Welds in Low-Carbon, High-Strength Low-Alloy, and Advanced High-Strength Steels and Fatigue of Fusion Welds in Advanced High-Strength Steels," 2006 Proceedings of the International Automotive Body Congress (IABC 2006), pp 12, 2006.
12. H.-T. Kang, J. J. F. Bonnen, and R. Mohan Iyengar, "Sources of Variability in the Fatigue Strength of Spot Welded Specimens," Proceedings of Materials Science & Technology Conference, Detroit, September 2007.
13. J. J. F. Bonnen and R. Mohan Iyengar, "Fatigue Performance of Conventional and Advanced High-Strength Steel Spot Welds," presented at the special symposium marking the 20th Anniversary of Auto-Steel Partnership, held as part of the Materials Science & Technology Conference, Detroit, September 2007.

[i] Denotes project 160 of the Auto/Steel Partnership (A/SP), the automotive-focus arm of the American Iron and Steel Institute (AISI). See www.a-sp.org. The A/SP co-funds projects with DOE through a Cooperative Agreement between DOE and the United States Automotive Materials Partnership (USAMP), one of the formal consortia of the United States Council for Automotive Research (USCAR), set up by Chrysler, Ford and General Motors (GM) to conduct joint, pre-competitive research and development. See www.uscar.org.

E. Tribology (ASP 230[i])

Project Manager: Pat V. Villano
Auto/Steel Partnership (A/SP)
2000 Town Center Drive, Suite 320
Southfield, Michigan 48075-1123
(248) 945-4780; fax: (248) 356-8511; e-mail: pvillano@a-sp.org

Project Chairman: David J. Meuleman
General Motors Corporation (GM)
Manufacturing Engineering
2000 Centerpointe Parkway
Mail Code 483-520-266
Pontiac, Michigan 48341
(248) 753-5334; fax: (248) 753-4810; e-mail:david.meuleman@gm.com

Technology Area Development Manager: Joseph A. Carpenter
(202) 586-1022; fax: (202) 586-1600; e-mail: joseph.carpenter@ee.doe.gov

Field Project Officer: Aaron D. Yocum
(304) 285-4852; fax (304) 285-4403; e-mail: aaron.yocum@netl.doe.gov

Expert Technical Monitor: Philip S. Sklad
(865) 574-5069; fax: (865) 576-4963; e-mail: skladps@ornl.gov

---

Contractor: United States Automotive Materials Partnership (USAMP)[i]
Contract No.: DE-FC05-02OR22910 through the National Energy Technology Laboratory

---

Objectives

- Identify the tribological factors that contribute to successful stamping of advanced high-strength steels (AHSSs). This includes the achievement of consistent, moderate coefficient of friction; minimized tool wear; and minimized galling/die pick-up.
- Identify the changes in the tribological system required by the use of galvanneal verses hot-dip-galvanized (HDG) coatings on AHSSs.
- Update the current A/SP lubricant testing procedure to accommodate the new AHSSs and the lubricants that can be used with them.

Approach

- Examine wear rates of different die materials, die-surface treatments and lubricants with AHSSs.
- Comparison of wear rates with different lubricants and die materials.
- Evaluation of methods of improving die life.
- Optimized lubricants/die combinations for AHSSs.
- Conduct a die-wear test and analysis consisting of seven individual One-Factor-at-a-Time (OFAT) tests totaling 550,000 pieces.
- Die-wear testing to include dual-phase (DP) 980, high-strength low-ally (HSLA), and DP 600 steels.

Accomplishments

- Completed Phase 1 report “Enhanced Stamping Performance of High Strength Steels with Tribology.”
- Completed Phase 2 report “Effect of Stroke Length and Penetration on Die Wear.”
- Completed Phase 3 report “Enhanced Stamping Performance of High Strength Steels with Tribology.”

- Completed Phase 4 Test work "Improve the Life of High Strength Steel Stamping Dies."
- Completed a Trim Die study to evaluate wear rates with American Iron and Steel Institute (AISI) A2 and AISI S7 when using AHSS and ultra-high-strength steel.

Future Direction

- Develop wear-rate model to predict die life.
- Gather wear test data to substantiate model.
- Correlate model with production data as AHSSs come into production.
- Conduct experiment using five commercially-available, trim-steel/coating combinations to be examined for wear resistance.

Introduction

OFAT Project

Based on Phase 4 test results, a new OFAT project was initiated where a selected number of variables were further tested. These included extended testing (to 100,000 strokes) of the best performing die-material/die-coating combination, testing of DP 780 and DP 980 steels and examination of weight loss in the draw beads as a measure of wear. Extreme wear of trim steels was also observed when trimming the DP 980 steel. An analysis of the data was conducted and we are waiting completion of the final report.

Final Phase 4 Improving the Life of High-Strength Steel Stamping Dies

All testing and analysis work has been completed; however, there is still ongoing work to be done to get the final report finished. The following are the conclusions from the study.

- Restraining force or stress is most influenced by sheet thickness and bead radius.
- Thinning strains confirm the stress factors.
- A significant interaction was found between base steel and thickness: the strain difference between the HSLA and DP 600 increases as sheet thickness increases.
- Wear-volume measurements show both abrasive and adhesive wear. The type of wear was generally related to the type of bead coating.
- In general, adhesion was heaviest with the galvanized sheet while abrasion was heaviest with the galvaneel sheet.
- The effect of wear on restraining force and thinning strain was not directly related to one type of wear, but more on the nature of the worn surface with pick-up generally increasing restraining force.
- Unexpectedly, abrasive wear did not, in many cases, lead to reduced restraining force rather than a restraining-force increase with increased abrasive wear.
- These results appear to be sensitive to bead material with the uncoated AISI D2 steel showing the strongest tendency for increased restraining force with increased abrasive wear.
- The effectiveness of the wax-based, dry-film lubricant (DFL) was less than expected, possibly due to melting.
- Run-in during the initial 4,000 strokes was plotted and shows a significant variation in restraining force during the run-in phase.
- The restraining force with the CrN-coated beads achieved stability much sooner than with the uncoated D2 beads.

The team is struggling over the best way to translate the results and still make the data available to the A/SP membership. Some of the results, however, were presented at the Great Designs in Steel Seminar that was held in March 2007.

Technical Papers for Publication

Six technical papers are being written from past work and are expected to be made available to various trade publications.

[i] Denotes project 230 of the Auto/Steel Partnership (A/SP), the automotive-focus arm of the American Iron and Steel Institute (AISI). See www.a-sp.org. The A/SP co-funds projects with DOE through a Cooperative Agreement between DOE and the United States Automotive Materials Partnership (USAMP), one of the formal consortia of the United States Council for Automotive Research (USCAR), set up by Chrysler, Ford and General Motors (GM) to conduct joint, pre-competitive research and development. See www.uscar.org.

F. High-Strength Steel Stamping Project (A/SP 050[i])

Project Manager: Michael S. Bzdok
Auto/Steel Partnership (A/SP)
2000 Town Center, Suite 320
Southfield, Michigan 48075-1123
(248) 945-4778; fax: (248) 356-8511; e-mail: mbzdokl@a-sp.org

Co-chair: James Fekete
General Motors Corporation
Body Manufacturing Engineering
2000 Centerpointe Parkway
Pontiac, Michigan 48341
(248) 753-5324; fax: (248) 753-4810; e-mail: jim.fekete@gm.com

Co-chair: Changqing Du
Chrysler LLC
800 Chrysler Drive
Auburn Hills, Michigan 48326
(248) 576-5197; fax: (248) 576-0230; e-mail: CD4@chrysler.com

Technology Area Development Manager: Joseph A. Carpenter
(202) 586-1022; fax: (202) 586-1600; e-mail: Joseph.Carpenter@ee.doe.gov

Field Project Officer: Aaron D. Yocum
(304) 285-4852; fax (304) 285-4403; e-mail: aaron.yocum@netl.doe.gov

Expert Technical Monitor: Philip S. Sklad
(865) 574-5069; fax: (865) 576-4963; e-mail: skladps@ornl.gov

---

Contractor: U.S. Automotive Materials Partnership (USAMP)[i]
Contract No.: DE-FC05-95OR22363 through the National Energy Technology Laboratory

---

Objectives

- Determine how to accurately predict and control the amount of springback and other deviations from the desired stamping geometry for parts made from advanced high strength steel (AHSS) prior to construction of production tooling.
- Develop part-design and manufacturing-process guidelines that can be recommended to automotive design and manufacturing engineers for the purpose of reducing springback and other part distortions.
- Investigate and analyze fractured materials for the purpose of understanding the fracture mechanism in terms of material properties and processing effects.

Approach

The approach of the High-Strength Steel (HSS) Stamping project is to:

- Predict AHSS stamping springback through finite-element analysis (FEA).
- Control AHSS stamping springback by developing knowledge of part-design geometries that affect flange springback and die processes that control springback.

- Develop predictive tools related to fracture in AHSS based upon an investigation and analysis of fractured material property microstructural characterization.

Accomplishments

The significant accomplishments of A/SP AHSS Stamping Group are as follows:

- Modified tooling for stretch-forming processes of AHSS auto-body structural components to neutralize the residual stresses that cause springback and sidewall curl. Predictable results have been shown for high-strength low-alloy (HSLA) 350 and dual-phase (DP) 600 MPa. The tooling was additionally modified for DP 780 MPa and DP 980 MPa. Panel measurements and data analysis have been reported upon. Identified additional processes to control springback, sidewall curl and panel twist.
- Modified panel geometry to show an alternative approach to control springback. Effective use of stiffening beads and other part-shape modifications and use of process variables are being recommended to product designers for control of twist, undercrown and springback based upon case studies of AHSS part developments.
- Utilized Multi-Process Master Shoe Die and Sub-Die inserts that are capable of a variety of part shapes and processes. The master shoe has a high-pressure hydraulic cushion that can be programmed for various process control features. Sub-die inserts for an Underbody Longitudinal Rail, a Cowl Cross Bar and a Body Center Pillar were modified and run in tryout. Completed detailed data analyses and developed part and process conclusions and recommendations based upon the analyses.
- Completed seven case studies of AHSS part developments by working through the original equipment manufacturers (OEMs). Applications guidelines studies were completed on a roof-rail reinforcement, three "B" pillar reinforcements, two "A" pillar reinforcements, and a rear rail.
- Initiated an investigation of shear fracture of AHSS with the Edison Welding Institute (EWI), in cooperation with the Ohio State University, to perform analyses directed at understanding the basic characteristics of fractures at a microstructural level.
- Initiated an investigation, at Wayne State University, of shear fracture in DP and transformation-induced plasticity (TRIP) steels that included: the key material parameters needed to predict fracture; fracture criteria based on these material parameters; and guidelines to develop predictive tools and develop standardized test for predicting failures in sheared edge stretching and breakage on a radius.
- Modified "15-Flange Die" for use in evaluating stretch-flanging capability of DP and other AHSS materials.

Future Direction

Partner companies have observed fractures in parts subjected to stretch flanging or stretching over a die radius. This phenomenon is not currently predictable. For this reason, the project team has solicited, received and evaluated proposals for work in the area of fracture analysis to support future formability analysis in dies. The project work has been awarded to the EWI and has started during the 2007 fiscal year. Focused project work is targeted at delivering:

- Key material parameters needed to predict fracture for the various conditions investigated.
- Fracture criteria based upon those key material parameters.
- Guidelines for development of predictive tools related to fracture.

The 15-Flange Die is to be utilized for further evaluation of stretch-flanging capability of AHSS including:

- Improved evaluation of microstructural effects.
- Include effect of shear-affected zone caused during trimming.
- Optimize process for best edge-stretch ability and maximum tool life.

Die trials with the new Multi-Process Die and programmable hydraulic cushion are continuing. This die is designed as a master die set and pressure system that will accept sub-die inserts to produce a variety of structural parts, such as underbody rails, cross bars and side-structure pillars. Additional, varied stamping processes for draw- or form-die actions can be developed with this tool.

Additional applications guidelines case studies are proposed to be completed at the rate of three per quarter by obtaining one study from each OEM per quarter and contracting additional case-study assistance.

Introduction

AHSS combining high strength and superior formability compared to the traditional HSLA steels are increasingly being used in automotive applications to deliver superior vehicle safety performance, while at the same time provide opportunities for mass reduction. AHSSs have high initial work-hardening rates as well as high tensile strengths. These characteristics, which make the material attractive to design engineers, also create challenges in the stamping and manufacturing processes, especially in terms of dimensional control. Stamped parts exhibit more springback after forming, compared to their lower-strength steel counterparts.

To address these issues, the A/SP initiated enabler projects, focusing on stamping and springback experiments using tools of production components, as well as understanding how best to simulate the forming processes using computer FEA models. To date, various classes of automotive parts have been studied, fabricated from AHSS with tensile strengths varying from 600 to 980 MPa.

Various process-control methods have also been investigated as means to control springback. So far, the method employed for controlling springback involves trial-and-error in the experiments, which is time consuming and costly. The need for accurate computer models for predicting springback is therefore apparent.

FEA has been widely used in the automotive industry for vehicle designs and manufacturing feasibility. Over a period of twenty years, a high level of confidence has been achieved using FEA to predict cracking and wrinkling in metal-forming processes. However, it remains a challenge to accurately predict springback, particularly for those parts with twists and sidewall curls. Numerous studies have been carried out to correlate computer prediction to experimental results. It has been shown that the material models, element formulations, friction and contact algorithms are important parameters affecting simulation accuracy. Other studies have also demonstrated the sensitivity of springback predictions to numerical parameters such as mesh size, number of through-thickness integration points, tooling traveling speed, contact-interface parameters, etc. During the last decade, FEA software developers and users have been investing much effort into the solution of springback-prediction problems. A steady improvement has been seen in the prediction capability and methodology.

In this study, experiments and computer simulations were conducted on an automotive rear rail. Various DP steels were used with tensile strength levels of 600, 780 and 980 MPa. Simulations were carried out using various numerical parameters (mass scaling, adaptive levels and mesh coarsening) in order to study their effects on the prediction accuracy. In the die-tryout experiments, various forming process variables were also investigated including pad forces, blank-hold forces and die configurations (drawing versus crash forming). Experimental results as well as the corresponding FEA simulation results were evaluated.

Discussion

The Project Group has focused on experimenting with a multi-process research die with sub-die inserts (Figure 1) to produce various automotive structural components by a variety of processes. This die has the necessary higher holding pressures and controlled processes required for working the higher-strength materials.

A programmable, hydraulic-pressure cushion is the main component of this system that provides the means of stretch forming the metal and controlling springback.

Sub-die inserts in the multi-process master shoe die enable stamping of underbody, cross-car and body-side structural components with a variety of stamping processes.

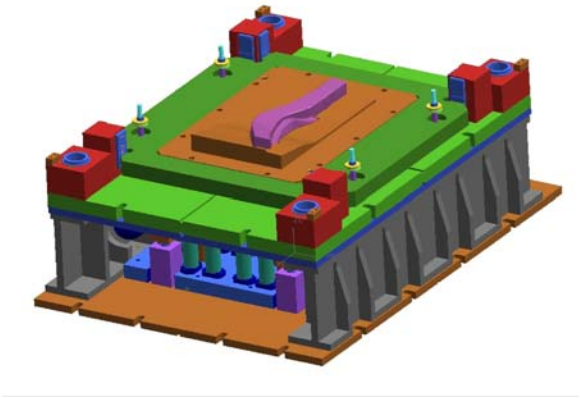

Figure 1. Lower half of multi-process die.

Sub-die inserts in the multi-process master shoe die enable stamping of underbody, cross-car and body-side structural components with a variety of stamping processes.

Rear Longitudinal Rail Sub-Dies

Tryout utilized three different stamping processes: draw action, with part on post or part on binder, and form die with upper pad. Materials included 1.6-mm and 2.2-mm DP 600 MPa steel and 1.6-mm DP 780 MPa and DP 980 MPa steel. Tryout resulted in identification of a forming process that lowered press forces and used material more efficiently (Figure 2). However, part dimensions were still outside acceptable ranges, so efforts with the higher-strength grades to improve the springback control with "shape set" features such as lock steps, added to the forming process.

Figure 2. Rail stampings by three processes.

Cowl Cross Member Sub-Die

A Cowl Cross Member sub-die is also part of the program. This stamping tryout also shows that the higher-strength steels are more easily formed than drawn for some panel configurations (Figure 3).

Figure 3. Cowl cross-bar processes.

The project examined die (forming) processes and material grades for their effect on part quality/dimensional accuracy and press-force/energy requirements.

Overall, the goal was to develop product/process-design guidelines for AHSS. The Cross Cowl Stamping trials covered the following materials: HSLA 350; DP 600; DP 780; and DP 980. The following three stamping configurations were examined: Cushion Draw with 340-mm-wide blank; Crash Form with 340-mm-wide blank; and Crash Form with 280-mm-wide blank.

The goal of the experiment was to form three parts for each material/stamping combination. Following stamping, each test part was scanned, laser trimmed, and re-scanned. Thus, only one set of parts were used for this study. Binder Force (cushion draw) and Pad Force (all forming processes) were established experimentally prior to conducting the trials and all trials were conducted under a single-press set-up.

Overall, satisfactory parts were stamped from all four materials and the three forming processes. Two areas were prone to wrinkles, the top surfaces near each end of the part. It is noted that production parts exhibit this same condition. Splits did occur with DP 980 but they were confined to an area off-part and could have been induced by holes laser cut for locating the blank.

The parts were examined through strain analyses, dimensional analyses (untrimmed and trimmed), and forming-tonnage requirements. Production drawn (toggle) and trimmed parts were included where appropriate comparisons could be constructed. Highlights of the analyses include:

- Surface strains were measured in four areas. Major- and minor-strain levels for DP 780 and DP 980 appear to be more uniform than HSLA 350 and DP 600.
- In the plan view, this part exhibits curvature on one side and is straight on the other side. The side with curvature had more side-wall curl but less opening angle (springback) than the straight side. For the respective side, there was more opening angle in the center, but curl increased towards the ends.
- The majority of springback is material related. Trimming had the second largest effect on overall springback followed by forming process and blank width.
    - The amount of springback increased parabolically with the material strength. For example, DP 980 had three times the springback of DP 600.
    - Trimming caused springback to increase by approximately 30%.
    - Drawing produced about 20% more springback than crash form.
    - Springback increased about 10% with the reduced blank size using the crash-form process.
- A typical increase in forming tonnage due to material grade was less than half the increase in tensile strength.

It is emphasized this part has open ends. Parts with closed ends create an entirely different forming condition and thus many of the aforementioned observations may not hold.

Body-Side Center-Pillar Sub-Die

A sub-die for a body-center pillar has also been completed and modified through tryout to optimize results (Figure 4).

Figure 4. Body-side center pillar.

This part is crucial to the body-side structure for meeting side-impact requirements. It is also typically difficult to stamp in medium-strength grades due to springback, twist and undercrown. The higher-strength grades increased the manufacturing difficulties.

During tryout, several features were added to the part to enable stamping in DP 780 material. Changes were made to the product shape to take up excess metal and features were added to stiffen the part. Split- and fracture-free stampings were then made from both DP 780 and DP 980 material. Parts have been scanned and dimensional analysis has been contracted.

Phase two of the project will complete the dimensional evaluation of both untrimmed and trimmed parts. Using this information and FEA analysis, computer-guided compensation will be used to re-cut the die to achieve dimensional accuracy of the part.

Summary

By recording the results of innovative forming processes, case studies for specific structural

parts have been presented, along with product-design and stamping-process guidelines for industry reference, when making product applications of the AHSS materials.

In addition, stamping-press tonnages are being recorded, along with impact loads, press-signature analysis and die-cushion-pressure requirements for the stamping industry's information. This will aid in better understanding the machine and equipment requirements for manufacturing components from this material.

Conclusions

Preliminary conclusions of the information indicate:

- Increases in material strength result in increases in forming-force requirements for typical automotive parts having open ends.
- Binder-force requirements can result in significant increases in forming force at ram positions relatively far from the bottom of the stroke. This effect far outweighs the material-property effects on press-force requirements.
- Active binders also result in significant increases in press-energy requirements. This has the potential to reduce throughput if the time required to recover the energy stored in the press flywheel exceeds the design stroke rate of the part.

Further stamping tryouts of DP 600, DP 780, and DP 980 will be conducted on typical automotive underbody, cross–car and side-structural members with new tooling and multiple processes. These materials, in lighter gauges than currently employed, will assist the weight-reduction and structural-performance goals of the Future Generation Passenger Compartment (see 5.I) and other lightweighting project groups in the A/SP.

Stamping experiments and LS-DYNA simulations were conducted on an AHSS automotive rear rail. The experimentally-obtained springback results were compared with those from the numerical simulation. The following conclusions are obtained:

- Both the experimental and the simulation results showed that the draw-form process produced more springback than the crash-form process; and the amount of springback increased with the material strength.
- The FEA predicted springback match to the experiments was seen to be dependent upon material strength. Reasonably good prediction accuracy was obtained for the DP 600 parts.
- The correlation between the predicted and the experimental results for DP 780 and DP 980 parts is not as good as that for DP 600 (Figure 5). Further study is needed to improve the predictability for higher-strength materials.

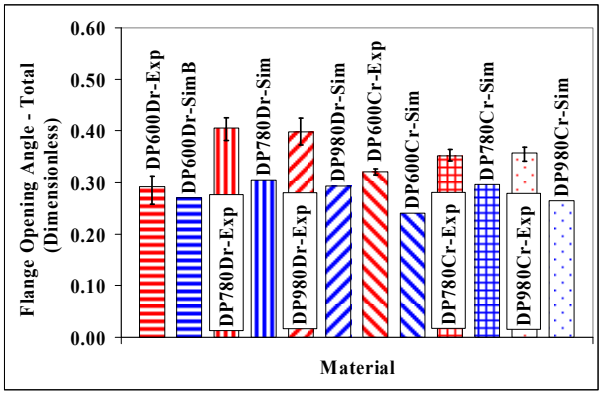

Figure 5. Correlation simulation vs. experimental.

- Increasing mass scaling and reduced adaptive levels will deteriorate the prediction accuracy. Mesh-coarsening prior springback analysis does not greatly affect the prediction results.

Presentations and Publications

1. C. Du, Chrysler LLC; X. M. Chen, United States Steel Corporation; T. Lim, Dofasco Inc., T. Chang, Severstal North America, P. Xiao and S.-D. Liu, Generalety, LLC, "Correlation of FEA Prediction and Experiments on Dual-Phase Steel Automotive Rails." Paper submitted to the Numiform 2007 Conference, Aveiro, Portugal. Paper presented at the MS&T'07 Conference at COBO Center, Detroit, Michigan.
2. James R. Fekete, General Motors Corporation and Stephen K. Kernosky, Ford Motor Company, "Characterization of Press Tonnage

Requirements during Stamping of Dual Phase Steel." Paper published at the 2007 SAE Congress in Detroit, Michigan.

[i] Denotes project 050 of the Auto/Steel Partnership (A/SP), the automotive-focus arm of the American Iron and Steel Institute. See www.a-sp.org. The A/SP co-funds projects with DOE through a Cooperative Agreement between DOE and the United States Automotive Materials Partnership (USAMP), one of the formal consortia of the United States Council for Automotive Research (USCAR, www.uscar.org), set up by Chrysler, Ford and General Motors to conduct joint pre-competitive research and development.

G. Strain-Rate Characterization (ASP 190[i])

Project Manager: Pat V. Villano
Auto/Steel Partnership (A/SP)
2000 Town Center Drive, Suite 320
Southfield, Michigan 48075-1123
(248) 945-4780; fax: (248) 356-8511; e-mail: pvillano@a-sp.org

Chairman: Kathy Wang
General Motors Corporation (GM)
2000 Centerpoint Parkway
Pontiac, Michigan 48341
(586)-986-1173; fax: 586-986-8722; e-mail: kathy.wang@gm.com

Lead Scientist: Srdjan Simunovic
Oak Ridge National Laboratory (ORNL)
Oak Ridge, TN 37831-6359
(865) 241-3863; fax: (865) 574-7463; e-mail: simunovics@ornl.gov

Technology Area Development Manager: Joseph A. Carpenter
(202) 586-1022; fax: (202) 586-1600; e-mail: Joseph.Carpenter@ee.doe.gov

Field Project Officer: Aaron D. Yocum
(304) 285-4852; fax: (304) 285-4403; e-mail: aaron.yocum@netl.doe.gov

Expert Technical Monitor: Philip S. Sklad
(865) 574-5069; fax: (865) 576-4963; e-mail: skladps@ornl.gov

---

Contractor: United States Automotive Materials Partnership (USAMP)[i]
Contract No.: DE-FC05-02OR22910 through the National Energy Technology Laboratory

---

Objectives

- Develop new experimental set-ups for characterization of crashworthiness and strain-rate sensitivity of advanced high strength steels (AHSSs) and AHSS structural designs.
- Replicate impact conditions that occur in automotive impact by simpler and more manageable experiments in order to generate meaningful data for computer modeling.

Accomplishments

- Developed experimental set-up procedures for new crashworthiness characterization test based on parallel-plates buckling, a procedure developed at the University of Dayton Research Institute (UDRI).
- Developed and conducted constant-velocity crash experiments on circular and octagonal tubes.
- Developed methods for strain-rate characterization in sub-Hopkinson velocity regime.
- Developed web-based database for display and analysis of impact experiments.

Future Direction

- Develop experiments to characterize fracture properties of advanced AHSS.
- Provide high-quality data for material and finite-element modeling (FEM) development.

Introduction

Crashworthiness characterization of AHSS requires testing of materials and structures under increased strain rates, large plastic strains, and large displacements that are characteristic of actual impact events. The AHSS characterization involves testing at several different length scales. The intrinsic material properties are investigated using the coupon-level specimens where the material is exposed to simple stress states that can be reduced to the equivalent stress and strain measures used in formulation of constitutive models. The coupon tests involve uniaxial tension and compression in plane-stress conditions. High-speed, hydraulic equipment is used to impose constant velocity in order to determine material response to different loading rates. At a higher length scale, the characteristic plastic-hinge mechanism responsible for crash-energy absorption in AHSS structures is investigated using the double-plate test. This test has shown that the strain-rate sensitivity of AHSS in bending under out-of-plane compression exhibit trends that cannot be fully explained using the plate-bending models derived from material behavior under uniaxial plane stress. At the component level, AHSS properties in tubular structures are investigated using specialized hydraulic equipment that allows constant crush speeds up to 8 m/s. In automotive design, the structural integrity of AHSS components is primarily provided by spot welds. The response of spot welds under different loading velocities and loading states have also been characterized in this project.

The above experiments provide high-quality data for development of material and structural FEM models for AHSS and, thereby, enable more accurate modeling and design of lightweight, crashworthy vehicles. The developed experiment technology is also directly relevant to other automotive materials as it provides a systematic approach to characterization and comparison of crashworthiness of new automotive materials.

Design of Experiments

The experiments conducted under this project have been compiled into interactive databases that are accessible over the World Wide Web. The portal page for the experiments is shown in Figure 1.

Figure 1. Web portal for AHSS experiments.

The experiments' data are integrated with the other project components. This provides mechanisms for data analysis and collaboration between project participants.

Strain-Rate Characterization in Sub-Hopkinson Regime

In support of the A/SP Strain Rate Characterization project, ORNL researchers are conducting high-rate experimental tests and analysis of base material specimens in uniaxial tension configuration (see 5.H). The objective of the test program is to provide the necessary experimental data in support of the A/SP efforts to determine high-strain-rate mechanical properties of AHSS. The test program consists of testing tensile specimens under strain rates of quasi-static, 0.1/s 1/s 10/s 100/s and maximum strain rates achievable in full open-loop configuration and the selected gage length. Among the unique features of the current approach is the ability to conduct tests across all speeds on the same apparatus and, thereby, eliminate variability associated with using different testing methods and actuators. The equipment allows for testing at speeds from quasi-static to 700 in/sec (18.5 m/s) over a range of 4 inches (100 mm) at maximum loads of 9000 lbf (40 KN). If an effective gage length for the chosen

specimen is known, equipment can run non-linear velocities in the drive file to achieve global strain control (engineering or true strain rate as desired). The test equipment is shown in Figure 2.

Figure 2. High-speed hydraulic tester. The test stage is elevated to allow for actuator acceleration to desired test speed.

The dynamic-testing procedures from recent studies sponsored by the International Iron and Steel Institute [1,2] and published literature [3,4] are followed and further enhanced using the new measurement techniques and synchronization. The multiple measurement methods of both forces and displacements allow for correlation of the results and verification of the method. Schematic representation of the test specimen and the measurement locations are shown in Figure 3.

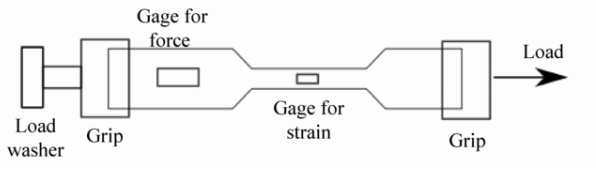

Figure 3. High strain-rate specimen design.

All the measurements are synchronized using the central trigger. High-speed video recording is used to provide detailed record of the test and to correlate optical measurement with the mechanical output data. An output of the program developed for optical measurement is shown in Figure 4. The measurement is based on the variations in color intensity along the prescribed scan lines. The distance between the found gage marks is shown in the images for increasing displacement.

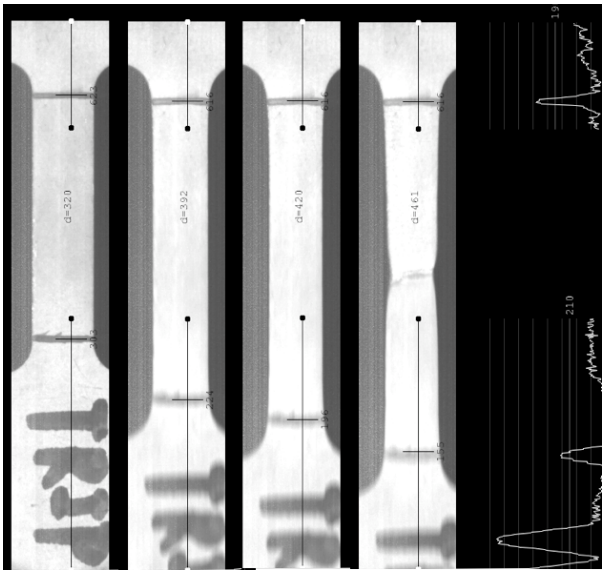

Figure 4. Optical strain-measurement output. Lines connecting black and white dots denote scan lines. Horizontal black lines denote found gage mark based on color intensity (shown on the right).

The multiple measurement methods of both forces and displacements allow for correlation of the results and verification of the method. All the measurements are synchronized using the central trigger. Web-based output for a transformation-induced plasticity (TRIP) 700 MPA specimen for 100/s rate is shown in Figure 5.

Component Crush Experiments

To improve experimental investigations of the material and structural behavior for automotive impact, the ORNL developed a new, integrated, virtual and physical test system for hydraulic, high-force, high-velocity crashworthiness experiments of automotive materials and structures. The system, a test machine for automotive crashworthiness (TMAC), permits controlled, progressive crush experiments at programmable velocity profiles and high force levels. The ability to control displacement (velocity) and the large lateral stiffness of the machine allows for strain history measurements that are not practical in inertia-based equipment. More details about the TMAC system can be found on http://www.ntrc.org. The TMAC system is shown in Figure 6. See also 12.B.

Figure 5. TRIP 700 test at 100 in/sec. Red (more varaiable) and yellow lines denote measurements from load washer and force strain-gage on specimen tab, respectively.

The component-level characterization of AHSS crashworthiness was examined using tube-crush tests of mild, high-strength low-alloy (HSLA) dual-phase (DP), bake-hardening and transformation-induced plasticity (TRIP) steels of various grades. The tests were run under constant crush velocities, 0.06 m/s, 0.6 m/s and 4 m/s. The crush data consist of time histories of force, displacement, strain measured in tube axial and hoop directions, and high-speed movies. Strain gages were positioned in regions where plastic folds form in order to investigate histories of strains and strain rates during crush in this crush-controlling region. An example of comparative effect of impact speed on the structural level of a spot-welded octagonal tube, representative of the latest vehicle front-end design, is shown in Figure 7.

Data from different sources are synchronized so that they can be used for detailed analysis of the crush progression. A synchronized frame with combined data from high-speed movie, impact force sensors and strain gages on the tube for a circular tube crush, is shown in Figure 8.

Figure 6. Test machine for automotive crashworthiness.

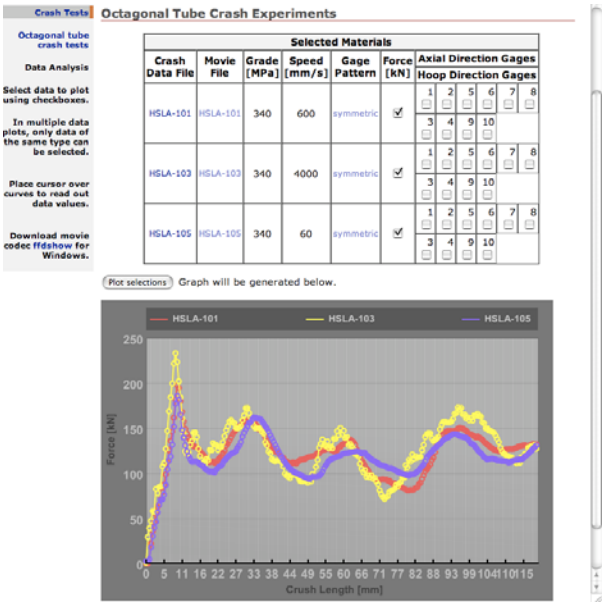

Figure 7. Force comparison for HSLA tubes for 0.06, 0.6 and 4 m/s crush. The data are selected from the Web database. Blue, red, and yellow lines denote crush tests at 0.06, 0.6 and 4m/s crush velocities, respectively.

Spot-Weld Experiments

Spot-welding is the principal method of joining steel sheets in today's automobiles. The spot welding of AHSS provides new challenges as it faces designers with new materials that draw their

performance from tightly-controlled microstructure that inevitably changes under thermo-mechanical effects of welding. In addition, the stronger materials usually stiffen the joint regions so that forces and shocks are more intensive than in conventional, mild-steel designs.

In order to investigate behavior of AHSS welds under impact loading and to provide data for the modeling project on AHSS spot welds, static and dynamic strength tests were performed for spot-welded specimens made of DP 780 and drawing-quality special-killed (DQSK) mild steels at the University of South Carolina. Lap-shear (LS) and cross-tension (CT) as well as a newly-designed, mixed-mode specimen were tested using a MTS hydraulic universal testing machine for static and drop-weight tower for dynamic tests. Three weld nugget sizes for each steel and specimen geometry (LS and CT) were made. In the mixed-mode test, only DP 780 of one weld size was tested. Load and displacement as functions of time and failure mode of the spot welds were recorded in the tests. The three nugget sizes were selected such that one is smaller, one is equal (medium) and one is larger than the weld nugget size determined from the formula, $d = 5\sqrt{t}$, where d is the diameter of the weld nugget and t the thickness of the sheet. In addition, a newly-designed, mixed-mode specimen and fixture were also tested which was made of DP 780 with weld nugget size of 5.9 mm, i.e., the large size. Force-versus-displacement curves were generated and the failure mode of each specimen was recorded from the tests. The test data are used in developing a dynamic-failure criterion of spot welds made of AHSS. The experimental data are collected into the project Web-based database. The front page for test selection for analysis is shown in Figure 9.

Data for various impact tests are shown in Figure 10. The implemented data-fitting options allow for reduction of test artifacts and comparison.

The test data show that: 1) the peak load (or the strength) increases with weld nugget size; 2) as the nugget diameter decreases, the specimens are more prone to interfacial mode of failure; 3) the peak load for LS specimen is higher than that for CT specimen under the same test conditions and weld configuration. It is observed that in mixed-mode tests when the loading angle is 90°, most specimens had the pull-out mode of failure while the interfacial-failure mode prevailed in the other two loading angles (0°, 30°).

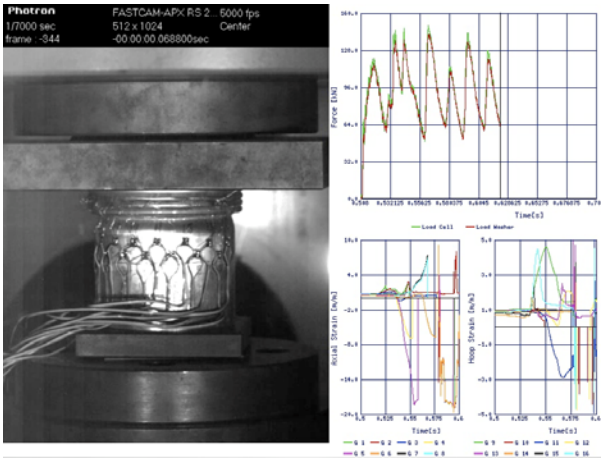

Figure 8. Synchronized data from crash test. Top graph shows force time history. Lower left and right graphs display strain-gage data in axial and hoop directions, respectively.

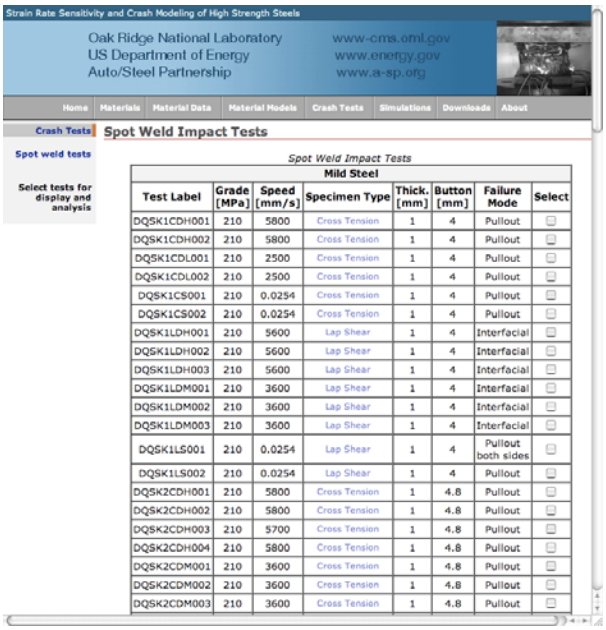

Test Label	Grade [MPa]	Speed [mm/s]	Specimen Type	Thick. [mm]	Button [mm]	Failure Mode	Select
DQSK1CDH001	210	5800	Cross Tension	1	4	Pullout	
DQSK1CDH002	210	5800	Cross Tension	1	4	Pullout	
DQSK1CDL001	210	2500	Cross Tension	1	4	Pullout	
DQSK1CDL002	210	2500	Cross Tension	1	4	Pullout	
DQSK1CS001	210	0.0254	Cross Tension	1	4	Pullout	
DQSK1CS002	210	0.0254	Cross Tension	1	4	Pullout	
DQSK1LDH001	210	5600	Lap Shear	1	4	Interfacial	
DQSK1LDH002	210	5600	Lap Shear	1	4	Interfacial	
DQSK1LDH003	210	5600	Lap Shear	1	4	Interfacial	
DQSK1LDM001	210	3600	Lap Shear	1	4	Interfacial	
DQSK1LDM002	210	3600	Lap Shear	1	4	Interfacial	
DQSK1LDM003	210	3600	Lap Shear	1	4	Interfacial	
DQSK1LS001	210	0.0254	Lap Shear	1	4	Pullout both sides	
DQSK1LS002	210	0.0254	Lap Shear	1	4	Pullout	
DQSK2CDH001	210	5800	Cross Tension	1	4.8	Pullout	
DQSK2CDH002	210	5800	Cross Tension	1	4.8	Pullout	
DQSK2CDH003	210	5700	Cross Tension	1	4.8	Pullout	
DQSK2CDH004	210	5800	Cross Tension	1	4.8	Pullout	
DQSK2CDM001	210	3600	Cross Tension	1	4.8	Pullout	
DQSK2CDM002	210	3600	Cross Tension	1	4.8	Pullout	
DQSK2CDM003	210	3600	Cross Tension	1	4.8	Pullout	

Figure 9. Spot-weld test database interface. The basic information for each test is shown in a table form and can be selected for further analysis.

Selected Materials								
Data File	Grade [MPa]	Speed [mm/s]	Test Type	Thck. [mm]	Btn. [mm]	Failure mode	Force [N]	Linear Fit Tolerance [N]
DP1CDH001	780	5700	Cross Tension	1.15	4.3	Interfacial	☐	Tol 100 ☐
DP1CDH002	780	5800	Cross Tension	1.15	4.3	Pullout	☑	Tol 1500 ☑
DP1CDM001	780	3500	Cross Tension	1.15	4.3	Interfacial	☐	Tol 100 ☐
DP1CS001	780	0.0254	Cross Tension	1.15	4.3	Interfacial	☑	Tol 100 ☐

Plot selections Graph will be generated below.

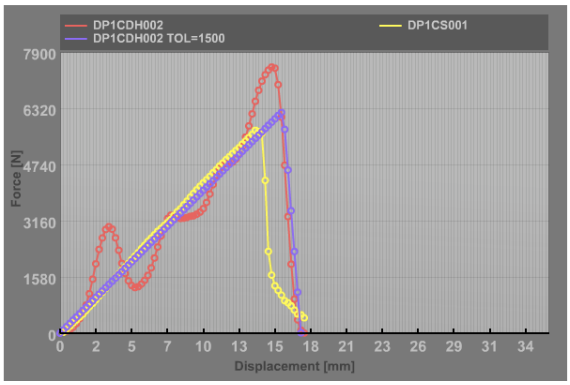

Figure 10. Force-displacement results for CT experiment. Yellow and red (more variable) curves denote tests at quasi-static and 5.7 m/s tests, respectively. Blue line denotes filtered data at high speed.

Conclusions

Several methods for characterization of AHSS crashworthiness have been developed. The material response at different length scales and under different deformation modes was investigated. The developed methods allow for accurate evaluation of crashworthiness properties, determination of material parameters to be used in computational modeling and design, and for development of modeling guidelines for AHSS materials and structures under impact loads.

Future Work

The future work on the project will focus on two topics:

1. Completing of base-material characterization tests.
2. Development of new coupon-level, crash-characterization experiments for AHSS fracture under impact.

Acknowledgements

Support from the Auto/Steel Partnership Strain Rate Characterization Team is acknowledged.

References

1. Recommendations for Dynamic Tensile Testing of Sheet Steels, International Iron and Steel Institute, 2005.
2. C. Wong, IISI-AutoCo Round-Robin Dynamic Tensile Testing Project, International Iron and Steel Institute, 2005.
3. D. Matlock, J. Speer, Constitutive Behavior of High Strength Multiphase Sheet Steels Under High Strain Rate Deformation, AISI/DOE Technology Roadmap Program, Report TRP 9904, 2005.
4. D.M. Bruce, "Dynamic Tensile Testing of Sheet Steels and Influence of Strain Rate on Strengthening Mechanisms in Sheet Steels", Ph.D. Thesis # MT-SRC-003-018, Colorado School of Mines, 2003.

[i] Denotes project 190 of the Auto/Steel Partnership (A/SP), the automotive-focus arm of the American Iron and Steel Institute (AISI). See www.a-sp.org. The A/SP co-funds projects with DOE through a Cooperative Agreement between DOE and the United States Automotive Materials Partnership (USAMP), one of the formal consortia of the United States Council for Automotive Research (USCAR, www.uscar.org.) set up by Chrysler, Ford and General Motors (GM) to conduct joint, pre-competitive research and development.

H. High Strain-Rate Deformation of Steel Structures

Principal Investigator: Srdjan Simunovic
Oak Ridge National Laboratory (ORNL)
P.O. Box 2008, MS6164
Oak Ridge, TN 37831-6164
(865) 241-3863; fax: (865) 241-0381; e-mail: simunovics@ornl.gov

Technology Area Development Manager: Joseph A. Carpenter
(202) 586-1022; fax: (202) 586-1600; e-mail: joseph.carpenter@ee.doe.gov

Expert Technical Monitor: Philip S. Sklad
(865) 574-5069; fax: (865) 576-4963; e-mail: skladps@ornl.gov

Contractor: ORNL
Contract No.: DE-AC05-00OR22725

Objective

- The objective of the project is to develop numerical-modeling guidelines in order to realistically assess the influence that the properties of strain-rate-dependent materials exert in crashworthiness computations. The dynamic-loading problems are modeled using diverse combinations of modeling approaches (sub-models) that are essential in describing strain-rate sensitivity in computational simulations. Sub-models examined include finite-element method (FEM) formulations, constitutive materials models, material properties under different strain-rates and loading conditions, contact conditions, etc, as well as material-property changes caused by component processing.

Accomplishments

- Investigated effects of stress transients for high-strength steel (HSS) and their effects on peak impact force.
- Developed experimental set-up for new crashworthiness characterization test based on parallel-plates buckling.
- Developed program for analysis of history of strain-rate calculations.
- Analyzed history of strain rates in unsymmetric crushing.
- Determined modeling effects on strain-rate history in unsymmetric crushing.
- Developed new constitutive models for HSS to account for strain-rate history and transients.
- Investigated forming and welding effects on steel tube crashworthiness.
- Developed model for tube roll-forming and validated it against manufacturing process.
- Developed modeling guidelines for modeling of tubular crush sections.

Future Direction

- Finding optimal formulations and approaches for modeling of spot-welded, polygonal advanced high-strength steel (AHSS) tubes.
- Development of models and experiments for damage and fracture of HSS in crash.

Introduction

The objective of the project is to develop numerical modeling guidelines for strain-rate-dependent materials in crashworthiness computations. The scope of the project is to study specific structural problems in automotive impact, develop new experimental and analytical techniques for characterization of strain-rate sensitivity of HSS and modeling of complex strain and strain-rate histories. The dynamic-loading problems are modeled using diverse combinations of modeling approaches (sub-models) that are essential in describing strain-rate sensitivity in computational simulations. Sub-models to be examined include finite-element formulations, constitutive materials models, contact conditions, etc. The trends, influences, and direct effects of employed modeling techniques will be identified and documented. The relative significance of employed sub-models is established, particularly in relation to the strain-rate effect resulting from the material constitutive models.

The research project is conducted as a team effort between the ORNL and the Auto/Steel Partnership Strain-rate Characterization Group (see 5.G). Recent results have been presented at the 2007 SAE World Congress and 2007 MS&T Conference.

Development of Crash Modeling Guidelines

Automotive structural components are primarily constructed of sheet metal. Under impact deformation, these components deform by formation of localized plastic zones that are responsible for dissipation of impact energy and containment of the deformation within the crash zones. The modeling of localized deformation and the response of metals under multiaxial states of stress and varying strain-rates are still far from being described by a unified theory. During multi-axial, large, plastic deformation, material undergoes significant changes of microstructure and texture that lead to changes in material properties on the macroscopic level. From a practical standpoint, the goal is that the selected material model is applicable to the range of loading and deformation for the problem at hand. In tubular crush devices that are used as energy absorbers in vehicles, metallic sheets are subjected to large, localized deformations that organize into global-collapse mechanisms. The standard practice for extracting strain-rate-relevant material parameters is to perform experiments with uniaxial-loading configurations. The ductility of uniaxial-tensile-loaded specimens is limited by the geometric instability. For automotive steel sheets, the magnitude of uniform plastic strains is limited to about 20%. However, the strains that are measured and modeled during tube crushing far exceed this limit. The physical reality of large deformations is not in question. The biaxial loading and bending provides additional stability that allows the utilization of a material's strain hardening, ductility and correspondingly large energy dissipation. The magnitude and distribution of plastic strains, large curvatures, and shifting of the neutral axis during fold formation clearly places the problem into the realm of large deformations.

Modeling of localized plastic deformation, plastic folds, is the area where material models and finite-element formulations are intrinsically linked. When shell elements are used to model tube crush, the issue of finite-element resolution comes down to the number and type of bi-linear shell elements that are used for modeling of a plastic fold. The experimentally-measured curvature of full plastic folds is of the order of the material thickness. For the fold representation to be accurate, the element length should approach the shell thickness. It is at this point that the assumptions of the standard shell theory are stretched beyond their limits and material models extrapolate far outside the experimentally-verified range. On the other end of the spectrum, when the finite-element resolution is fairly coarse (of the order of kinematic elements in analytical models), the material model extrapolation into large strains is not a concern because the strains get smeared over larger volumes and are within the range of uniaxial experimental data. However, the kinematics of the deformation are not met.

In both of the above FEM-meshing scenarios, in order to match the experimental results with models, material model parameters are commonly modified in engineering simulations. While the practice may be appalling to material scientists, the justification for modification in one case is to compensate for the inability to represent local deformations and, in the other, to account for the

significance of the large-strain region for which experimental data are not available. The flexibility of computer programs now even provides methods for definition of optimization problems where the material parameters are determined so that they result in the optimal match between simulations and experiments for crush measures such as impact-force history and deceleration. These approaches are linked to specific structural problems, FEM-mesh configurations and loading situations. A more rigorous approach is to make sure that the FEM element resolution and element formulations are sufficient for accurate kinematic representation of the problem and then focus on compatible material modeling approaches.

Impact Simulations

The current research develops modeling guidelines in combination with a detailed experimental program. The experiments and accompanying simulations are conducted at different length scales (coupon level, plastic-fold formation, progressive tube crush) in order to investigate different mechanisms and their collaborative effect. At the highest length scale, tubular specimens are progressively crushed in the specialized, velocity-controlled, high-speed, hydraulic, Test Machine for Automotive Crashworthiness (TMAC) at ORNL. The tests are performed on different AHSS materials and simulated using different modeling approaches and formulations. (See also 12.B.)

Figure 1 shows the comparison of a computer simulation with a crush experiment. The simulation employs a combination of strain-rate constitutive model derived from uniaxial-loading experiments and shell-element discretization of characteristic dimension proportional to two sheet thicknesses. The overlap of simulation and TMAC progressive crush is very close. The current combination of model formulations gives the best correlation with the experiments for other crush conditions as well. The detailed discretization is necessary to match the experimentally-observed deformation features and measured strain and strain-rate history across the plastic folds.

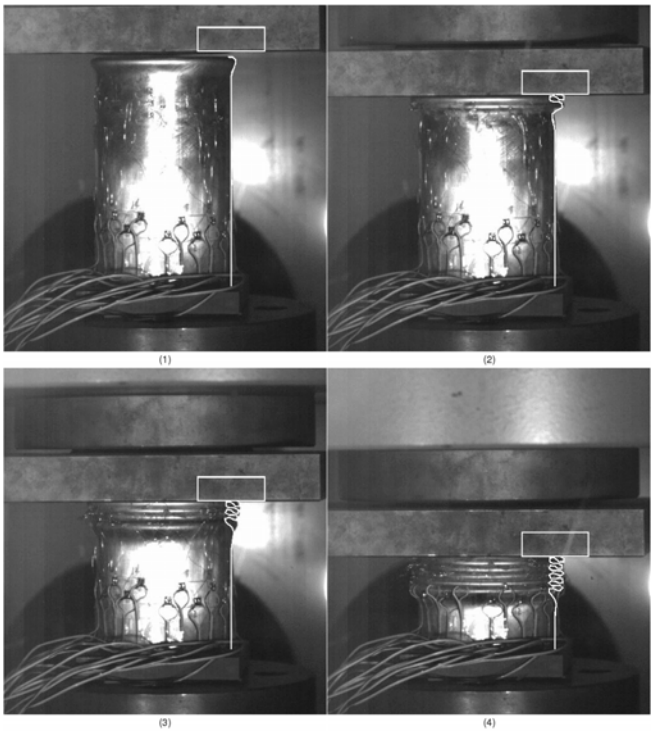

Figure 1. Comparison of experiment and simulation (white line) for 0.6 m/s crush of High-Strength Low-Alloy steel.

The comparison of simulated and measured impact force is shown in Figure 2. The discrepancy in the later part of the simulation is due to engagement of deceleration devices used to slow down the loading actuator.

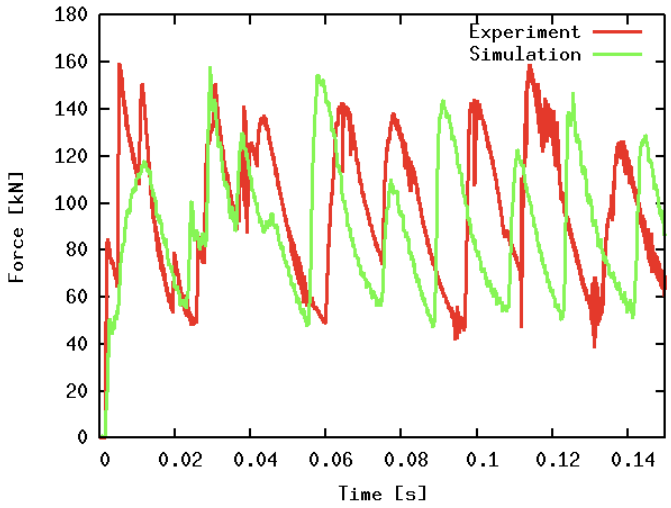

Figure 2. Comparison of simulation and experimentally-observed impact force.

Element formulation also has a significant effect on simulation accuracy. For a selected shell-element discretization, a combination of material

model and shell-element formulations is sought that gives a stable folding pattern representative of the experiment. To determine this combination, we simulate the circular tube impact first as a fully-axisymmetric problem using a narrow, 1-element-wide strip with circular-symmetry boundary condition. At this level, all shell-element formulations have equally accurate performance as the problem involves decoupled bending and in-plane components. This can be seen in Figure 3 where shell-element simulations using different formulations lined up.

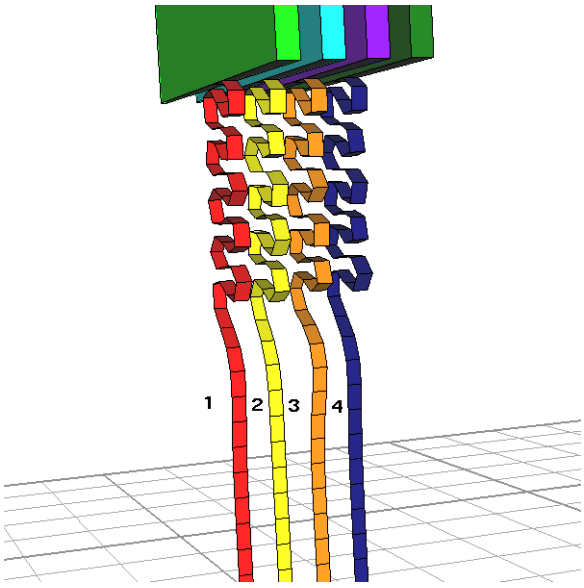

Figure 3. Results of axisymmetric problems using different shell formulations. The labels will be described in Figure 4.

As we increase the angle of the circular segment simulated, i.e., by attaching additional strips in the circumferential direction, we want to see if simulations with different shell-element formulations will remain axisymmetric as in experiments. As shown in Figure 4, only the formulation based on Bath-Dvorkin theory and on material model based on total strain-rate formulation (4) yields an axisymmetric mode as observed in experiments.

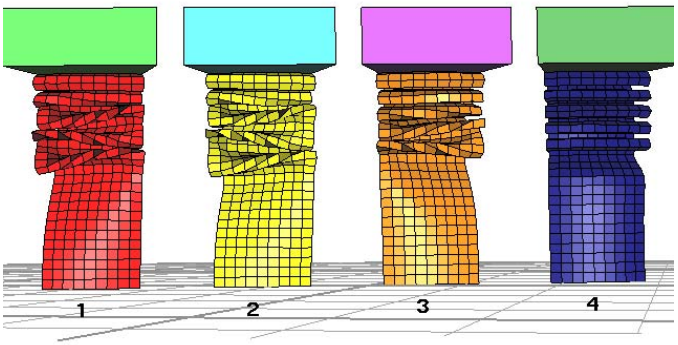

Figure 4. Shell-formulation stability analysis: 1) Belytshcko-Tsay shell formulation, strain-rate effect based on total strain-rate; 2) Belytshcko-Tsay shell, strain-rate effect based on plastic strain-rate; 3) Bathe-Dvorkin shell, strain-rate effect based on total strain-rate; 4) Bathe-Dvorkin shell, strain-rate effect based on plastic strain-rate.

Conclusions

An improvement in predictive capability of the crashworthiness models is linked to development of realistic material models and finite elements with better representation of complex strain and stress states in progressive crushing. Strain-rate sensitivity is an important component of the material models and needs to be incorporated in the crashworthiness models. The range of strains and strain rates calculated in the explicit FEM programs is of the order of 10 +3 /s, which provides a reasonable upper limit for the model. Strain-rate magnitudes of the order of 10 +2 /s are prevalent for shell-element sizes that are of the order of 2-4 tube shell thicknesses. The plastic rate for material modeling provides more realistically-feasible strain-rate histories. For modeling details of tube crushing, the FEM mesh discretization should be fine enough, as measured by the strain distribution, angle of shell directors, and resulting curvature, to model the crush fold formation. Simulation results indicate a close link between the strain-rate calculations and element type and discretization. Current technology can provide reasonable accuracy but at relatively high computational and technical cost due primarily to fine discretization. New, shell-element formulations are needed to model localized deformation at relatively high resolutions and improve modeling accuracy.

Future Work

The future work on the project will focus on two topics:

1. Finding optimal formulations and approaches for modeling of spot-welded polygonal AHSS tubes.
2. Development of models and experiments for damage and fracture of HSS in crash.

Acknowledgements

The research was performed at ORNL which is managed by UT-Battelle, LLC for the U.S. Department of Energy under contract DE-AC05-00OR22725. The tubes for the TMAC experiments were donated by the US Steel Corporation. The support of Auto/Steel Partnership Strain-Rate Characterization Team is acknowledged.

Presentations/Publications/Patents

1. S. Simunovic, J. M. Starbuck, P. V. K. Nukala; Characterization of strain and strain-rate histories in steel structures during impact; 2007 SAE World Congress, Detroit, 2007.
2. S. Simunovic, J. M. Starbuck, K. Wang, P. V. K. Nukala; Characterization of strain and strain-rate histories in HSS structures during progressive crush; MS&T Conference, Detroit, 2007.

I. Future Generation Passenger Compartment – Validation (ASP 241[i])

Project Manager: Pat J. Villano
Auto/Steel Partnership (A/SP)
2000 Town Center Drive, Suite 320
Southfield, Michigan 48075-1123
(248) 945-4780; fax: (248) 356-8511; e-mail: pvillano@a-sp.org

Co-Chairman: Joe Polewarczyk
General Motors Corporation (GM)
Body Systems & Closures
Engineering West
Mail Code 480-11-P64 Cube C1-1642
30200 Mound Road
Warren, Michigan 48092-2025
(586) 986-2157; fax: (586) 986-8592; e-mail: joseph.m.polewarczyk@gm.com

Co-Chairman: Jody R. Shaw
Manager, Automotive Marketing
United States Steel Corporation
5850 New King Court
Troy, Michigan 48098-2608
(248) 267-2608; fax: (248) 267-2581; e-mail: jrshaw@uss.com

Technology Area Development Manager: Joseph A. Carpenter
(202) 586-1022; fax: (202) 586-1600; e-mail: joseph.carpenter@ee.doe.gov

Field Project Officer: Aaron D. Yocum
(304) 285-4852; fax: (304) 285-4403; e-mail: aaron.yocum@netl.doe.gov

Expert Technical Monitor: Philip S. Sklad
(865) 574-5069; fax: (865) 576-4963; e-mail: skladps@ornl.gov

---

Contractor: United States Automotive Materials Partnership (USAMP)[i]
Contract No.: DE-FC05-02OR22910 through the National Energy Technology Laboratory

---

Objective

- Validate the greater-than-25% mass reduction demonstrated by Phase of 1 of the Future Generation Passenger Compartment (FGPC) project on a high-volume production vehicle while maintaining all.

Approach

The project is separated into five (5) phases:

- Phase 1 - Concept development,
- Phase 2a - Validation on a donated vehicle,
- Phase 2b – Development of advanced steels,
- Phase 2c – Concept development of large truck cab comprehending 2.5x roof-strength criteria,
- Phase 2d – Comprehend opportunities and influence of mass-compounding.

Accomplishments

Phase 1: Concept development

- On a concept vehicle, mass reduction of 30% has been achieved relative to current production vehicles while meeting all performance objectives.
- Robust solutions to a range of vehicle weights and bumper-height Insurance Institute for Highway Safety (IIHS) side impact are possible.
- Packaging of fuel-cell components is feasible within the constraints for the donor concept vehicle and can be designed for all structural criteria at equivalent structural mass of conventional powertrains.
- On small vehicles with B-pillars, the IIHS Side Impact and Side Pole Test performance criteria control the design, not the 2.5x roof-strength criteria. Large vehicles (sport-utility vehicles [SUVs] and trucks) will have more structure controlled by the 2.5x roof-strength criteria and the solution demonstrated in Phase 1 may not apply.
- Material properties that exceed the current advanced high-strength steel (AHSS) grades available can increase mass reduction of the passenger compartment from 30 percent to 36 to 38 percent.
- Mass-compounding effects have significant influence on the passenger-compartment structural mass.

Phase 2a: Validation of donor vehicle.

- Donor-vehicle model received and modified to apply results from Phase 1.
- Confirmations of the model and target settings were completed.
- Load-path optimization completed.
- Shape, gauge, and material optimization completed.
- Door shape and gauge completed.
- Mass-compounding effects have been quantified for modern vehicles and predict steel structures can achieve 50% FreedomCAR mass targets when all vehicle systems are resized accordingly.

Phase 2b: Development of advanced steels.
A separate project has been set up for the development of 3rd Generation AHSSs (ASP 280; see 5.A).
Eight research grants have been initiated at nine universities starting in the fall 2007.

Phase 2c: Concept development of a large truck cab comprehending 2.5x roof-strength criteria.
Study showed a hybrid solution of AHSS and composite reinforcements provided the most efficient solution.

Phase 2d: Comprehend opportunities for mass compounding:
Mass compounding effects have a significant influence on the passenger-compartment structural mass.

Future Direction

- Complete Phase 2a - Validation on a donated vehicle.
- Complete Phase 2b – Development of advanced steels.
- Complete Phase 2c – Validate Phase 1 results and correlate to the model that was developed.

Introduction

The FGPC project will incorporate current propulsion systems and fuel-cell technologies into concept architectures. This project will reduce passenger compartment mass by 25% or greater with cost parity relative to the FreedomCAR baseline while meeting the structural crash performance objectives for the IIHS side impact, anticipated future crash requirements for the Federal Motor Vehicle Safety Standard (FMVSS) pole-side impact test and FMVSS 2.5x vehicle

weight roof-strength test. Further, it will maintain performance in static and dynamic stiffness, durability and front- and rear-crash requirements and also comprehend packaging requirements for fuel cell powertrain. The study will address a 5-passenger, 4-door, sedan, donor-vehicle design and finally identify opportunities for steel properties that exceed the capability of existing automotive steel grades to improve lightweighting potential. The project is separated into five (5) phases: Phase 1 – Concept development; Phase 2a – Validation on a donated vehicle; Phase 2b – Development of advanced steels; Phase 2c – Concept development of large truck cab comprehending 2.5x roof-strength criteria; and Phase 2d – Comprehend opportunities and influence of mass-compounding;

Project Status

Phase 2a – FGPC Validation

A current production donor vehicle has been selected and work initiated in February 2007. The project has completed Task 1, which establishes performance baseline for the donor vehicle and sets performance targets for the project. Task 2, part 1 has also been completed. Initial investigations indicate that critical load paths identified in Phase 1 will be applicable to the Phase 2a donor vehicle. Task 2, part 2, shape optimization is progressing.

Phase 2b – Development of 3rd Generation AHSS

Work carried out under Phase 1 demonstrated the need for a new family of steels so additional mass savings could be realized. Following the National Science Foundation (NSF) processes, NSF, DOE and A/SP have jointly funded basic steel research to provide experimental and a theoretical foundation to develop 3rd Generation AHSS steels to further reduce vehicle mass. Eight (8) universities have been funded for three years to carry out the research work. (See 5.A.)

Phase 2c – Mass-Efficient Architecture for Roof Strength (MEARS)

Passenger-compartment concepts for large vehicles (trucks and SUVs), where structure is controlled by 2.5x roof strength, were completed in 2007. The project focused on three different concepts: stamping-intensive, termed Concept-1; hydroforming intensive, termed Concept-2; and stamped-with-structural-insert-intensive, termed Concept-3. These were developed in this study, with all three concepts using AHSSs. Extensive optimization was carried out for each concept using HEEDS software.

In the stamping-intensive design (Concept 1), structural changes including panel geometry, part thickness, and material grades were proposed. The major reinforcements in the A-Pillar, roof rail, and C-Pillar were proposed to be made from hot-stamped boron steel. The inner parts of these sections were proposed to be of dual-phase (DP) 600 and DP 800 steels. The body-side outer material was not changed, but its thickness was increased. The most mass-efficient design from several concepts was optimized as a final design for Concept 1.

In the hydroforming-intensive design (Concept 2), the reinforcements in the A-Pillar, roof rail, and C-Pillar were replaced with hydroformed tubes made from DP 780. Tubes were also investigated for the roof header and roof bow. A total of four concepts were proposed with different tube configurations, the most mass-efficient design being optimized to obtain the final design for Concept 2.

In the stamped configuration with structural inserts design (Concept 3), the thickness of major load-carrying members was reduced in the baseline model while materials were upgraded to AHSS to make the structure lighter and to take advantage of the stiffness provided by the lighter inserts. A total of four concepts were proposed with different types of inserts (i.e., Steel-Concepts 3A and 3B, Nylon-Concept 3B, and Beta Foam-Concept 3C). Optimization was not carried out for these basic-concept levels.

A comparative study of all concepts was done from the perspective of mass, cost, manufacturability, and repairability. The concept with the nylon inserts was selected as the final design. Further studies were carried out on the design to optimize the size of nylon inserts and the design of the sheet-metal parts. Formability studies were carried out on the major structural parts to ensure that there were no major issues.

Phase 2 has been approved and will focus on improving the modeling of the nylon inserts, adhesive materials, and validating the predictions with physical testing to validate the models performance.

Phase 2d – Quantification of Mass Compounding
Vehicle design engineers intuitively know that an unplanned mass increase in a component during vehicle design has a ripple effect throughout the vehicle: other components need to be resized increasing vehicle mass even more. The phrase *mass begets mass* describes this phenomenon. A more encouraging view of this behavior considers a reduction in the mass of a component enabled by new technology resulting in a greater mass-reduction ripple effect throughout the vehicle. Published data on this effect are sparse and based on 1975-1981 model years. The purpose of the project was to update the data using contemporary vehicles.

The secondary mass change is the additional mass reduction resulting from primary mass reduction by the implementation of mass-reduction technology. When all subsystems can be resized, the secondary mass savings are from 0.8 to 1.5 kg/kg (1.25 kg/kg is the estimate for the *all* vehicle group). When the powertrain has been fixed and is not available for resizing, the secondary mass savings is from 0.4 to 0.5 kg/kg (0.5 kg/kg is the estimate for the all vehicle group).

The initial study is complete for sedans and SUVs, with a deliverable of a report and a calculator for estimating secondary mass savings.

Conclusions

Phase 1 – FGPC
The optimization methods applied to this study achieved an 11% mass reduction of the modified parts of the body-in-white (BIW) and Door Impact Beams (Table 1), and 30% mass savings over a conventional in-class vehicle's BIW and instrument panel (IP) beam (Table 2. Table 3 is a comparison of an industry-standard vehicle's safety cage to FGPC, which shows a 31% mass reduction.

Phase 2a
There are no conclusions for this phase at this time.

Phase 2b
There are no conclusions for this phase at this time.

Phase 2c – Mass-Efficient Architecture for Roof Strength
The optimized vehicle architecture met the target for roof-structure deflection of less than 4.5 inches under a load of 3 times the vehicle weight with only an increase of 1.2 kg.

Phase 2d – Mass Compounding
When all subsystems can be resized, the secondary mass savings is from 0.8 to 1.5 kg/kg (1.25 kg/kg is the estimate for the *all* vehicle group). When the powertrain has been fixed and is not available for resizing, the secondary mass savings is from 0.4 to 0.5 kg/kg (0.5 kg/kg is the estimate for the all vehicle group).

The study indicates that optimized steel structures can meet the FreedomCAR mass-reduction targets when mass compounding is considered. Realizing this objective requires additional technology development and is challenged by mass increases resulting from increased safety requirements, alternative powertrains and additional passenger amenities.

Acknowledgements:

Shawn Morgans of Ford Motor Company is recognized for his leadership on the MEARS project team.

Presentations/Publications/Patents

There are no patents or publications associated with this project.
Phase 1
Results of FGPC have been presented at several automotive conferences and within individual member company forums.

Phase 2c – Mass-Efficient Architecture for Roof Strength

A roadshow with the results has been presented to one original equipment manufacturer (OEM) to date.

Phase 2d – Mass Compounding

Results of this study have been presented to engineers at automotive companies and steel partnerships, as well as the USAMP Steering Committee and the Multi-Material Vehicle (see 12.D) Task Force.

MODIFIED PARTS	BASELINE FGPC-BO* (kg)	FINAL FGPC-FCD* (kg)	MASS SAVINGS (kg)	CHANGE (%)
BIW	130.6	121.0	9.6	7
Doors	12.6	6.4	6.2	49
TOTAL	143.2	127.4	15.8	11

Table 1: Final Mass Summary For FGPC Project – Modified Parts Only

STRUCTURE	INDUSTRY STANDARD (kg)	FINAL FGPC-FCD (kg)	MASS SAVINGS (kg)	CHANGE (%)
BIW + IP BEAM	310.0	217.6	92.4	30

Table 2: Final Mass Summary For FGPC Project – Comparison to Industry Standard

STRUCTURE	INDUSTRY STANDARD (kg)	FINAL FGPC-FCD (kg)	MASS SAVINGS (kg)	CHANGE (%)
Passenger Compartment	246.8	169.3	77.5	31%

Table 3: Final Mass Summary For FGPC Project – Comparison to Industry Standard Passenger Compartment

* Before Optimization (BO)
* Final Concept Design (FCD)

[i] Denotes project 241 of the Auto/Steel Partnership (A/SP), the automotive-focus arm of the American Iron and Steel Institute (AISI). See www.a-sp.org. The A/SP co-funds projects with DOE through a Cooperative Agreement between DOE and the United States Automotive Materials Partnership (USAMP), one of the formal consortia of the United States Council for Automotive Research (USCAR) set up by Chrysler, Ford and General Motors (GM) to conduct joint, pre-competitive research and development. See www.uscar.org.

J. Lightweight Rear Chassis Structure (ASP 601[i])

Project Manager: Jim Cran
Auto/Steel Partnership (A/SP)
2000 Town Center, Suite 320
Southfield, MI 48075
(905) 385-8276; fax: (905)-383-3200; e-mail: jim.cran@sympatico.ca

Co-Chair: Jamal Alghanem
Chrysler LLC
800 Chrysler Drive
CIMS 484-36-02
Auburn Hills, MI 48326
(248) 576-1915; fax: (248) 576-2046; e-mail: ga5@chrysler.com

Co-Chair: Michael Gulas
Dofasco Inc.
P.O. Box 2460
1330 Burlington St .E. Hamilton, Ontario, Canada L8N 3J5
(905) 548-4719; fax: (905) 548-4250, e-mail:michael_gulas@dofasco.ca

Technology Area Development Manager: Joseph A. Carpenter
(202) 586-1022; fax: (202) 586-1600; e-mail: joseph.carpenter@ee.doe.gov

Field Project Officer: Aaron D. Yocum
(304) 285-4852; fax: (304) 285-4403; email: aaron.yocum@netl.doe.gov

Expert Technical Monitor: Philip S. Sklad
(865) 574-5069; fax: (865) 576-4963; e-mail: skladps@ornl.gov

---

Contractor: United States Automotive Materials Partnership (USAMP)[i]
Contract No.: DE-FC05-02OR22910 through the National Energy Technology Laboratory

---

Objectives

- Obtain a minimum mass reduction of 25% for a baseline passenger-car rear-chassis structure with no more than a 9% cost premium.
- Develop and document integrated solutions that balance the interaction of materials, manufacturing and cost. The solutions will focus on high-volume production (200,000 plus vehicles per year).
- Demonstrate the successful use of advanced high-strength steels (AHSSs) in a passenger-car, rear-chassis structure.
- Address corrosion and durability issues associated with reduced thickness AHSS.

Approach

- Phase 1: Material optimization. Through material substitution and minimal size and shape changes, the mass of the baseline chassis was reduced 15% noting limited reduction in stiffness. Prototypes have been fabricated and are being physically tested. The lessons-learned are being used in Phase 2. Phase 1 completion is scheduled for June of 2008.

- Phase 2: Design optimization. Through a clean-sheet redesign, the goal is to obtain a minimum mass reduction of 25% with no reduction in stiffness. From the cost perspective, the goal is to obtain no more than a 9% cost premium. A preliminary Phase 2 design has been prepared. Phase 2 completion is scheduled for September 2008.
- Phase 3: Communications. The goal is to transfer the technology developed in the project to original equipment manufacturer (OEM) and Tier 1 chassis-structure designers. Phase 3 completion is scheduled for March 2009.

Accomplishments

- Fabricated seven Phase-1 prototypes.
- Modal tested one Phase-1 prototype.
- Fatigue tested the brackets on three Phase-1 prototypes.
- Awarded a contract to Altair to evaluate analytical fatigue-resistance methods for chassis structures.
- Coated with Electropoli two baseline chassis structures and two Phase-1 prototypes for corrosion testing.
- Addressed AHSS availability, AHSS forming, and AHSS welding-technology gaps.

Future Direction

- Conduct sub-system fatigue testing on a Phase 1 prototype.
- Compare analytical fatigue results with laboratory fatigue results for the Phase 1 prototypes.
- Corrosion test the Phase-1 prototypes.
- Finalize the preliminary Phase-2 design.
- Undertake a cost study for the Phase-2 Final Design.
- Prepare final report for the project.
- Transfer the technology through road shows to A/SP member companies and key Tier 1 suppliers.

Introduction

There has been significant progress on Phase 1. Seven additional prototypes were fabricated. Three of the five technology gaps were addressed: AHSS availability, AHSS forming, and AHSS welding. Work on the remaining two—fatigue resistance and corrosion resistance—is well underway. Fatigue activity will be completed in the first quarter of 2008 and corrosion-resistance activity, due to the length of time required for physical testing, will be completed by June 2008.

The project was set back one year when it was discovered that the wrong loads were being used in the project. Fortunately, Phase 1 was not affected because loads were not used to design the Phase 1 prototypes. Rather, stresses under unit loads in the prototypes were compared to stresses under unit loads in the baseline. Unfortunately, the incorrect loads did impact the preliminary Phase-2 design.

The baseline was changed from the derivative of the current production chassis to the current production chassis itself (Figures 1 and 2). This change allows a better comparison with work completed to date. An analysis of the preliminary Phase-2 design using the correct loads showed that the preliminary Phase-2 design has less overstress than the current production chassis (the new baseline) when the actual materials used are accounted for. Thus, a request for quotation (RFQ) to finalize the preliminary Phase-2 design will be issued. The preliminary Phase-2 design is 12% lighter than the new baseline. However, it is believed that joint refinement and durability

analysis during final design will significantly increase this mass saving.

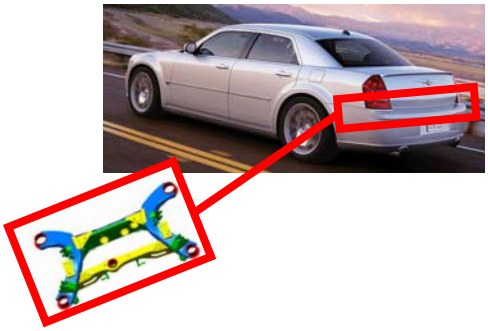

Figure 1. Donor vehicle and new baseline structure.

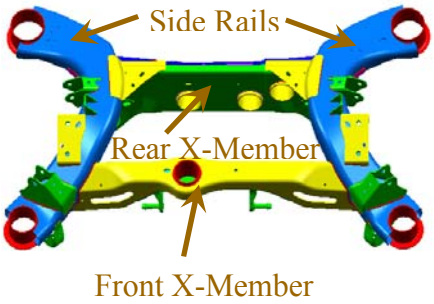

Figure 2. Baseline structure detail.

Phase-2 prototypes have been eliminated from the project. First, the technology gaps are being adequately addressed with the Phase-1 prototypes. Second, the Phase-2 design will be tested virtually. Third, if required, parts will be fabricated to check manufacturability. Fourth, if required, small specimens will be fabricated to address local issues.

The new completion date for the project is March 2009.

Phase 1: Materials Optimization

The project called for ten prototypes, three of which were fabricated in fiscal year (FY) 2006. The remaining seven were built during FY 2007. Prototypes 1 through 8 did not have gusset plates (as per the baseline chassis). They were allocated as follows: two for show pieces (Figure 3), one for modal testing (Figure 4), three for bracket fatigue testing (Figure 5) and two for corrosion testing. Prototypes 9 and 10 had gusset plates. They were allocated to sub-system fatigue testing.

Figure 3. Phase-1 prototype without gusset plates.

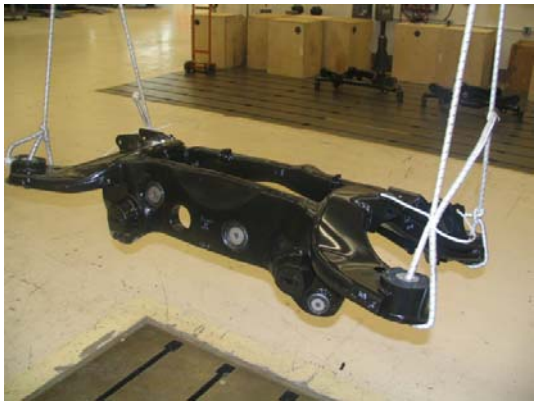

Figure 4. Modal test set-up.

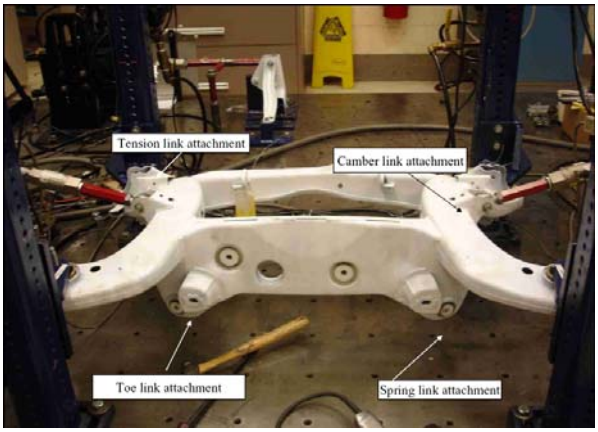

Figure 5. Bracket fatigue test.

Technology Gap Analysis – Availability of AHSS

The Team believes that the lack of a table showing the global availability of AHSS is hindering the use of AHSS for mass reduction in chassis structures. The Team pursued the development of a global table but discovered that the steel producers, for commercial reasons, do not want the availability of their AHSS in the public domain. Thus, the Team has reluctantly

agreed that it is unable to address this technology gap.

Forming of AHSS

Very little AHSS has been used in chassis structures. Thus, the Team wishes to assure itself there are no major forming issues associated with the use of AHSS thicker than that commonly used in body structures.

In the baseline chassis structure, the side rails are made from 240 MPa steel and the rear crossmember is made from 208 MPa steel. In the Phase 1 prototypes, dual phase (DP) 590 steel was used for both the side rails and the rear crossmember.

Experi-Metal, the prototype fabricator, experienced no difficulties in forming the side rails and rear crossmember from DP 590 steel.

In the baseline chassis structure, the front crossmember is made from 362 MPa steel, while transformation-induced plasticity (TRIP) 780 steel was used for it in the Phase-1 prototypes. Experi-Metal experienced splitting in the front crossmember flanges. Forming analysis conducted by United States Steel indicated that material having a hole expansion >54% is required to prevent the splitting. For the prototypes, Experi-Metal overdrew the flanges and cut off the excess flange depth.

Based on its experience with the Phase-1 prototypes, the Team has concluded that globally-available AHSS grades may be formed into satisfactory chassis structure parts.

Welding of AHSS

Heat-affected zone (HAZ) softening, which depends on steel chemistry, is more pronounced in higher-strength steels. This softening reduces joint efficiency and must be taken into account when designing a chassis structure.

To address the softening issue, in conjunction with A/SP's Joining Team (see 5.B), the requirements were defined for a set of design rules applicable to chassis structures. The Joining Team has awarded Applied Engineering and Technology a contract to prepare gas metal arc welding (GMAW) Weld Design Rules for all steel grades including AHSS. The Joining Team anticipates the Rules will be published by December 2007.

Oak Ridge National Laboratory (ORNL) is developing a model to predict the effects of welding on AHSS microstructure. The model predicts softening in the HAZ. The Chassis Team is interacting with ORNL to ensure a simplified model suitable for inclusion into automotive finite-element analysis (FEA) models is developed.

Corrosion Resistance

Downgaging with AHSS means thinner steel. In chassis structures, the thickness of the steel is used as the second line of defense against corrosion. Thus, there is concern thinner steel may cause corrosion problems.

The Team's Corrosion Working Group has concluded that the performance of E-Coat over parts made from galvanized steel is a known technology for chassis applications. Hence, it can be used to protect thin AHSS members (less than 2.0 mm) in chassis structures. However, the Group feels it is desirable to have an alternate corrosion-protection method. Thus, it is evaluating the Electropoli hot-dip-galvanizing method used in Europe to coat chassis structures after fabrication. Two baseline rear-chassis structures and two Phase-1 prototypes have been coated with Electropoli in France. One baseline structure with E-coat, one baseline structure with Electropoli and one Phase-1 prototype coated with Electropoli are being sectioned by Ford to evaluate coating coverage. One baseline structure with E-coat, one baseline structure with Electropoli and one Phase-1 prototype coated with Electropoli will be trailer tested by General Motors from November 2006 to May 2008.

Fatigue Resistance

Durability is a major criterion in chassis design. AHSS brings not only mass reduction but higher stresses, which may reduce fatigue resistance if not properly accommodated. The Team has addressed the fatigue issue with the A/SP Sheet Steel Fatigue (see 5.D) Team. There is ample

evidence that the fatigue strength of sheet steel is proportional to tensile strength. Thus, even though design stresses are higher in AHSS, the higher tensile strength of AHSS results in higher fatigue strength. The end result is the fatigue strength of AHSS material is not an issue. There is little data on the fatigue strength of metal inert gas (MIG) welded joints made with AHSS. However, fatigue experts agree that the fatigue strength of all MIG-welded joints depends on weld process and joint geometry, that is, the fatigue strength of MIG-welded sheet steel joints is independent of steel grade. To verify this conclusion, the Fatigue Team has launched a test program using DP 590, DP 780, DP 1000, and TRIP 780 AHSS joined by MIG and laser welds. The program should be completed in 2009.

The Team wants to compare the fatigue strength of the Phase-1 prototypes determined from the laboratory tests with the fatigue strength determined analytically. Altair was retained to construct as-built, computer-aided design (CAD) and finite-element (FE) models of the Phase-1 prototypes and to compare test and analytical results for the bracket fatigue tests, which have been completed. In addition, Altair is evaluating the use of FEsafe software with the BS 5400 module and the FEsafe software with the Verity module. The CAD and FE models have been constructed and Altair has concluded that the FEsafe and BS 5400 model predicted well fatigue life and fatigue-crack location. Altair will complete its assignment by December 2007.

Chrysler will start sub-system fatigue testing on a Phase-1 prototype early in 2008. It will use a half-rig test set-up and a standard Chrysler drive file. Chrysler will compare the physical test results with a CAE half-rig fatigue simulation.

Phase 2: Design Optimization

Martinrea prepared a preliminary Phase-2 design in FY 2006 (Figure 6). However, in order to properly incorporate the lessons learned from Phase 1 into Phase 2, work on Phase 2 was put on hold. When the Team discovered that the wrong loads were given to Martinrea for use in Phase 2, Martinrea was asked to determine the effect of the wrong loads on the preliminary design. The preliminary design is governed by stiffness and the Team believed the effect might be insignificant. Using linear static analysis and the correct loads, Martinrea found that the preliminary Phase-2 design has less overstress than the new baseline when the actual materials used for each are taken into account. Thus, the Team has agreed to finalize the Phase-2 preliminary design. The preliminary Phase-2 design is 12% lighter than the new baseline. However, the Team hopes to capitalize on additional mass reduction opportunities (e.g., improving the joints and additional durability analysis) during final design.

The original agreement with Martinrea to finalize the Phase-2 preliminary design did not include fatigue analysis or mass-compounding. Also, the Team has decided not to build Phase-2 prototypes because the technology gaps are being adequately addressed with the Phase-1 prototypes. Thus, support for a Phase-2 prototype build is no longer required from Martinrea. Lastly, Phase-2 work has been on hold for a year. To reflect the foregoing, the Team will issue a new RFQ to complete Phase 2.

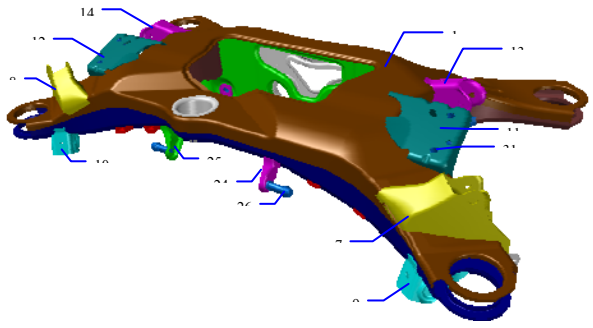

Figure 6. Phase-2 preliminary design.

Phase 3: Communications

Phase 3 communications activity is scheduled for January to March 2009.

Conclusions

Primarily due to design changes made to improve the Phase-1 prototypes, due to delays in obtaining test windows for prototype testing and due to the use of incorrect loads in Phase 2, it will take longer to complete the project than originally envisioned. The technology gaps that prevent

mass reduction in chassis structures through the use of AHSS are steadily being broken down. The Team is confident the project objectives will be accomplished and the results will facilitate the use of AHSS by chassis engineers to achieve mass reduction.

Presentations/Publications/Patents

To date, no presentations or publications have been placed into the public domain. The first ones planned are at the end of Phase 1.

---

[i] Denotes project 601 of the Auto/Steel Partnership (A/SP), the automotive-focus arm of the American Iron and Steel Institute (AISI). See www.a-sp.org. The A/SP co-funds projects with DOE through a Cooperative Agreement between DOE and the United States Automotive Materials Partnership (USAMP), one of the formal consortia of the United States Council for Automotive Research (USCAR), set up by Chrysler, Ford and General Motors (GM) to conduct joint, pre-competitive research and development. See www.uscar.org.

K. Characterization of Thermo-Mechanical Behaviors of Advanced High-Strength Steels (AHSS): Formability, Weldability and Performance Evaluations of AHSS Parts for Automotive Structures

Principal Investigator: Moe Khaleel
Pacific Northwest National Laboratory (PNNL)
P.O. Box 999
(509) 375-2438; fax: (509) 375-6605; e-mail: moe.khaleel@pnl.gov

Technology Area Development Manager: Joseph A. Carpenter
(202) 586-1022; fax: (202) 586-1600; e-mail: joseph.carpenter@ee.doe.gov

Expert Technical Monitor: Philip S. Sklad
(865) 574-5069; fax: (865) 576-4963; e-mail: skladps@ornl.gov

---

Contractor: PNNL
Contract No.: DE-AC06-76RL01830

Objective

- Investigate the formability of advanced high-strength steels (AHSS) with emphasis on loading temperature, loading paths and "secondary" deformation effects on part 'residual' strength and microstructure.
- Develop a fundamental understanding of transformation kinetics of AHSSs by analyzing the crystallographic and morphological features of the phase transformations subject to different thermal- and mechanical-loading paths from forming and welding.
- Provide performance data and constitutive models for formed AHSS parts.
- Investigate the weldability of AHSS under various welding processes and parameter conditions applicable to auto-production environment.
- Generate weld-performance data including static strength, formability, impact strength, and fatigue life as a function of welding processes and parameters.
- Investigate welding techniques for improved AHSS weld performance and benchmark the performance against the current welding practices for roll-formed and hydro-formed AHSS frame and underbody-structure applications.
- Develop design guidelines on AHSS to assist rapid structure design and prototyping.

Approach

- Investigate formability and weldability of AHSS. This task includes: forming under complex loading paths (uniaxial and biaxial); quantification of formability and weldability for various grades of AHSS based on their chemistries and corresponding thermal-mechanical process.
- Investigate the interdependency of manufacturing processes: weldability of a formed part and formability of a welded part.
- Develop transformation-kinetics model and macroscopic constitutive relationships for AHSS (dual-phase (DP), transformation-induced plasticity (TRIP) and complex phase (CP)).
    - Systematically evaluate the effects of various welding process and process parameters on the microstructure and property of welds. Welding processes include gas-metal arc welding, laser welding, hybrid laser-arc welding, and resistance spot welding. Metallurgical and process models will be used to analyze the

microstructure evolution. The properties will be measured as a function of geometry, composition, process and process parameters. A performance evaluation procedure will be developed that allows for quantifying the performance improvement, weight and cost savings associated with use of AHSS.

- Evaluate structural-performance evaluation of formed and welded parts made of AHSS. This task will provide the automotive design engineers with accurate material performance data for design verification of AHSS structural parts.

Recent Accomplishments

- Finished detailed microstructural characterizations of deformed TRIP-steel samples on grain-size distributions, texture evolution and transformation kinetics under different loading modes, loading temperatures and loading rates.
- Developed transformation-kinetics model for multiphase TRIP steel and implemented it in metal-forming simulations.
- Quantify the effects of phase transformation during forming operation and its influence on TRIP steel side-rail impact performance.
- Finished preliminary micromechanical studies on DP 980 focusing on the effects of martensite volume fraction and strength on the macroscopic stress versus strain relationships as well as failure modes of AHSSs.
- Finished preliminary micromechanics modeling of TRIP 800 considering austenitic phase transformation.

Future Direction

- Investigate effects of through-thickness microstructural inhomogeneity and banding on the forming/bending performance of DP 980.
- Conclude the feasibility of using neutron diffraction in quantifying the retained-austenite volume fraction.
- Micromechanics modeling of DP steel considering grain-boundary effects.
- Micromechanics modeling of TRIP steel considering phase transformation of individual grains.

Introduction

This project is a collaborative effort between PNNL, Oak Ridge National Laboratory (ORNL), and the United States Automotive Materials Partnership (USAMP) of the U.S. Council for Automotive Research (USCAR). The work began in October 2005.

Because of their excellent strength and formability combinations, more and more AHSSs are being used in vehicle-body structures to reduce vehicle weight and improve vehicle-crash performance. Currently, the technical barriers hindering wider applications of AHSS in the domestic auto industry include: 1) the fundamental behaviors of AHSS parts subject to different thermal- and mechanical-loading paths (forming and welding) are not fully understood and quantified; 2) the constitutive behaviors for the formed parts are not available to computer-aided engineering (CAE) engineers for rapid prototyping; and 3) welding-induced complex microstructures and the effects of different welding processes and welding parameters on weld performance are not well understood.

In order to address these technical barriers, PNNL's role in this project includes investigating the formability of AHSS, with emphases on loading temperature, loading paths and secondary deformation effects on part 'residual' strength and microstructure. The project also develops a fundamental understanding of transformation kinetics of AHSS steels by analyzing the crystallographic and morphological features of the phase transformations subject to different thermal and mechanical-loading paths from forming. The goal is to provide the automotive design engineers with accurate material-performance data and

constitutive models for design evaluations and verification of AHSS structural parts.

ORNL's focus is on the AHSS weld-performance evaluations and improvements. See 5.L.

TRIP Steels

Microstructure Characterizations of Deformed TRIP800 Steel Samples on Grain- Size Distributions, Texture Evolution and Transformation Kinetics Under Different Loading Modes, Loading Temperatures, and Loading Rates

Base material properties for TRIP 800 have been characterized under different original equipment manufacturer (OEM) manufacturing temperatures ranging from -40°C to 93°C under different strain rates. High strain-rate tensile tests under various temperatures were performed at ORNL's High-Temperature Materials Laboratory (HTML). It was previously reported that TRIP 800 has reduced ductility under dynamic loading compared to static loading.

In this reporting period, we studied the microstructure features and transformation kinetics under different loading conditions. For example, Figure 1 shows the electron backscatter diffraction (EBSD) map of as-received TRIP 800 with phase localization of ferrite (blue in color prints, dark background in black-and-white prints), austenite (red in color prints, dark gray in black-and-white prints) and zero-solution (green in color prints, light gray in black-and-white prints). Zero-solution zones can be ferritic grain boundaries, bainitic grains, martensitic grains, austenite with grain size smaller than 0.1μm, or zones with a high dislocation density. Results in Figure 1

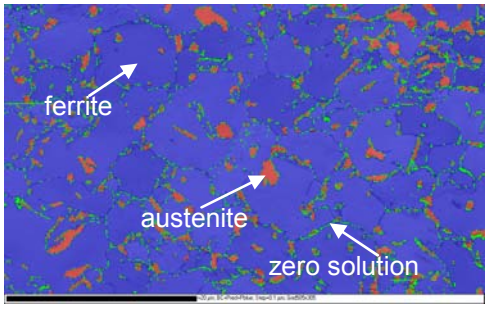

Figure 1. Phase map for as-received TRIP 800.

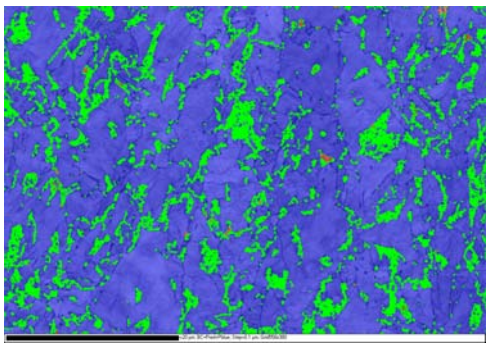

Figure 2. Phase map for deformed TRIP 800 under 256 in/sec loading rate and room temperature.

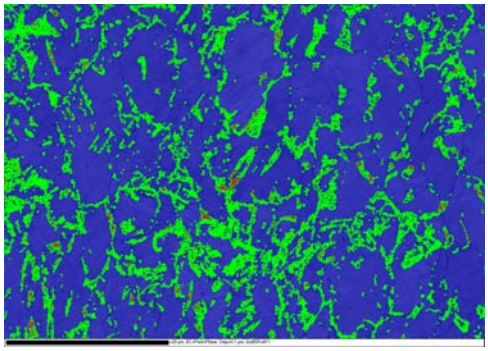

Figure 3. Phase map for deformed TRIP 800 under 640 in/sec loading rate and room temperature.

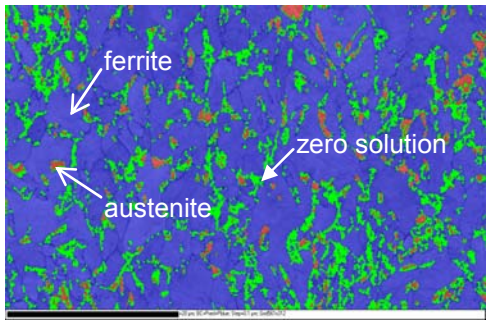

Figure 4. Phase map for deformed TRIP 800 under 256 in/sec loading rate and 93°C.

indicate that the microstructure of the "as-received" material consists of various phases with different grain sizes: the big grains are ferrite matrix and the small grains are essentially austenite, bainite or martensite. The average grain size for body-centered cubic (bcc) is close to 2 μm and for face-centered cubic (fcc) is 0.5 μm.

Figures 2 to 4 show the phase maps of deformed TRIP 800 samples under different deformation rate and temperatures. The results indicate that a slower austenite transformation rate occurs under higher loading temperature and higher loading rate. This explains the ductility reduction observed

under high-rate tensile test. Essentially, the heat generated by the sample's plastic deformation inhibits martensitic transformation during high-rate loading rendering the sample with higher amount of retained austenite in the deformed microstructure without the additional plasticity provided by the TRIP effect.

The influences of loading temperature and loading rate on transformation kinetics, hence, strength and ductility of TRIP steels, should, therefore, be carefully considered in applications of this type of steel for crash members in automotive structural components.

Finite-Element Forming Simulation with TRIP-Steel Transformation Kinetics

In this section, results of finite-element forming simulation are presented in which the phase transformation during forming is predicted for TRIP steels. The commercial finite-element package ABAQUS is used in the forming simulation and the material's constitutive relations are implemented in a user-defined material subroutine to interface with the main analysis engine.

First, steel with a fully-austenitic structure is used as the forming example. Assuming a friction coefficient of 0.2, Figure 5 shows the predicted martensite distribution in a typical automotive hat section after forming. Results in Figure 5 indicate that the side wall of the formed part has much higher martensite volume fraction than the two flanges and the bottom of the hat section. Therefore, in addition to the wall thinning induced by the forming process, inhomogeneous material properties will also need to be considered in evaluating the crash performance of the hat section during impact.

Figure 6 illustrates the effects of lubrication on forming-induced phase transformation. In this case, a perfectly-lubricated part is assumed and the friction coefficient between the part and the die/punch is set to be zero. Under this perfectly-lubricated condition, martensitic phase transformation occurs primarily at the bent corners of the hat section for the same amount of forming depth. Therefore, the corresponding points on the as-formed hat sections will have different mechanical properties depending on different forming-lubrication conditions. The effects of forming-induced phase transformation on the hat section impact performance will be discussed next.

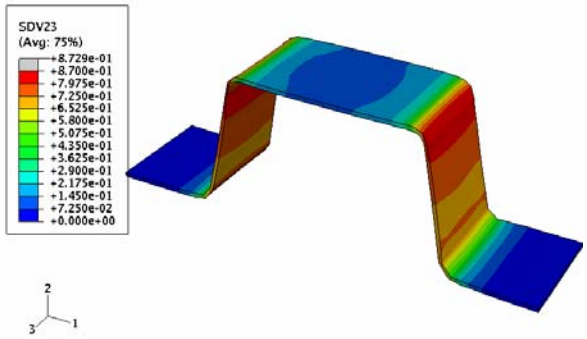

Figure 5. Distribution of martensite volume fraction after hat-section forming with friction coefficient = 0.2.

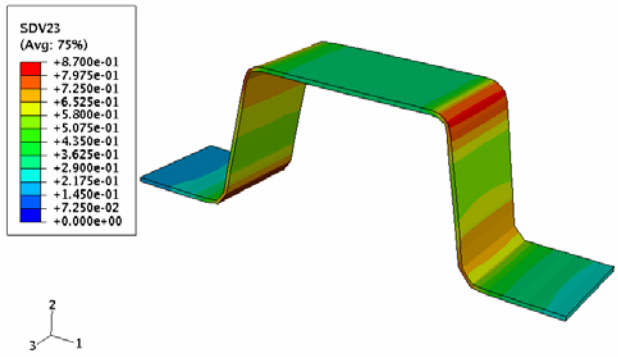

Figure 6. Distribution of martensite volume fraction after hat-section forming with friction coefficient = 0.

Effects of Phase Transformation During Forming Operation on Impact Performance of TRIP-Steel Side Rail

In this section, results of finite-element crash simulation are presented for a TRIP-steel side rail with and without considering the phase transformation during forming operations. The geometry for the two rails is the same with the same amount of wall thinning resulted from the forming operations. In the first case, a side rail with inhomogeneous material properties, as predicted by the forming simulation (friction coefficient = 0.2), is considered. In the second case, a side rail with uniform material property of austenite is considered. Figure 7 shows the evolution of von Mises stresses on the two side rails during crash simulation.

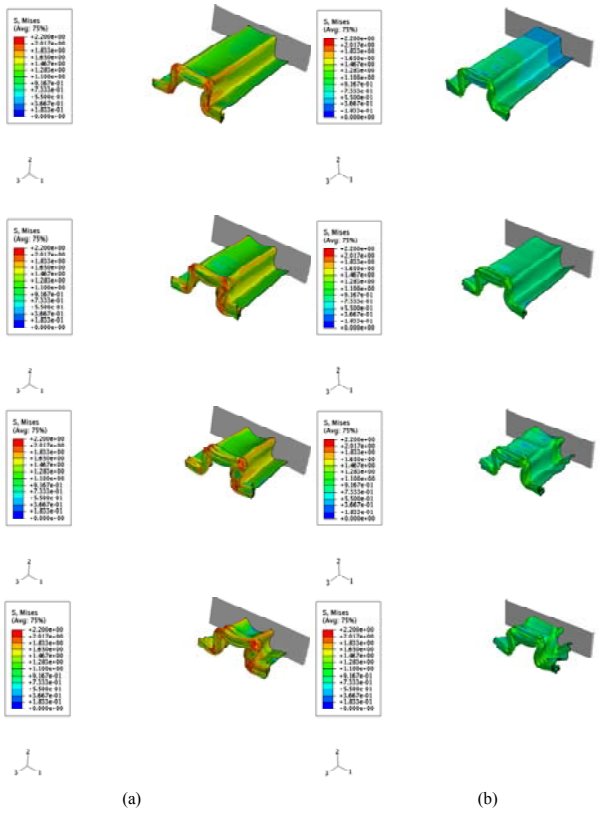

Figure 7. von Mises stress on deformed configurations during side-rail crash (a) with forming-induced phase transformation; (b) without forming-induced phase transformation.

For case (a), forming-induced martensite on the side wall of the hat section strengthens the side wall; therefore, much higher stress levels are predicted for case (a) than case (b). Figure 8 compares the energy absorption of the side rail versus time by considering and not considering the phase transformation strengthening resulted from forming operation. The results indicate that with the forming-induced phase transformation, higher energy absorption of the side rail can be achieved. On the other hand, if one only considers wall thinning from forming operations without considering phase transformation, the predicted hat-section energy-absorption level is much lower. Results here indicate that phase-transformation-induced strengthening should be considered by vehicle-structure engineers when TRIP steel is used as structural members.

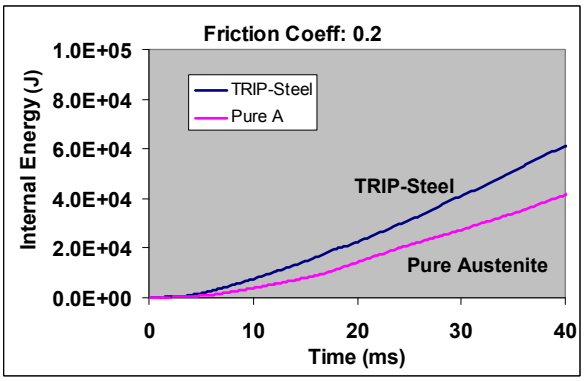

Figure 8. Effects of phase transformation on predicted side-rail energy absorption.

Dual Phase

Micromechanics Modeling for Dual-Phase Steel during Tensile Deformation

In previous studies, we have established the importance of various phase volume fractions on the macroscopic behaviors of the AHSS. In this section, we use micromechanics modeling approach to study the stress and strain partitions in the various phases of AHSS during deformation. The goal here is to gain a better understanding of the phase compatibility during deformation process for these steels and, therefore, to be able to predict the macroscopic strength and failure modes subjected to different loading conditions.

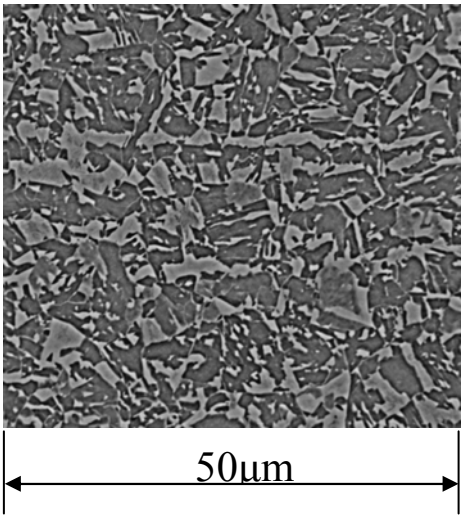

Figure 9. Typical microstructure used for micro-mechanics modeling of DP980.

Figure 9 shows the microstructure we started with for commercial DP 980 steel. The darker-color background represents the ferrite matrix and the brighter grains are the strengthening martensite phase. Figure 10 shows the finite-element mesh used for this representative volume element (RVE). In the micromechanics simulation, ferrite and martensite grains are given different material properties.

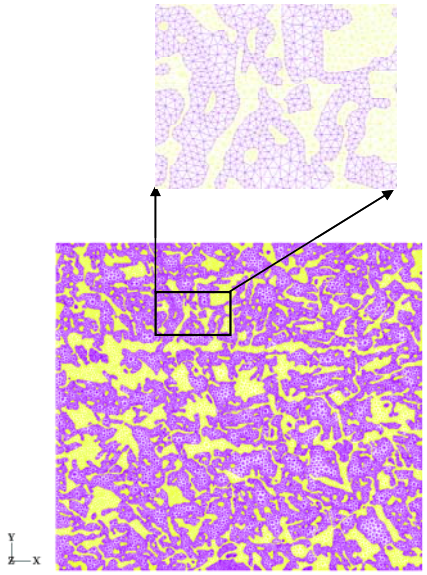

Figure 10. Finite-element discretization of the RVE.

The material properties for the individual ferrite and martensite phases are determined using the *in-situ* high-energy X-ray diffraction (HEXRD) method. The experiments were carried out at the 11-ID-C beamline of the Advanced Photon Source (APS) at Argonne National Laboratory (ANL). Figure 11 shows the measured lattice-strain partition among the different phases during the tension loading process. Based on the isotropic model, the three principal strain-tensor components, ε_{11}, ε_{22} and ε_{33}, were used to determine the stress-tensor components using Hooke's law:

$$\sigma_{ii} = E_{hkl}\left[\varepsilon_{ii} + \nu_{hkl}(\varepsilon_{11}+\varepsilon_{22}+\varepsilon_{33})/(1-2\nu_{hkl})\right]/(1+\nu) \qquad i = 1,2,3$$

where E_{hkl} is diffraction elastic constants and ν_{hkl} is the Poisson's ratio in the subset of grains with their *hkl* crystal planes normal to the diffraction vector, determined by the Kröner model for each phase.

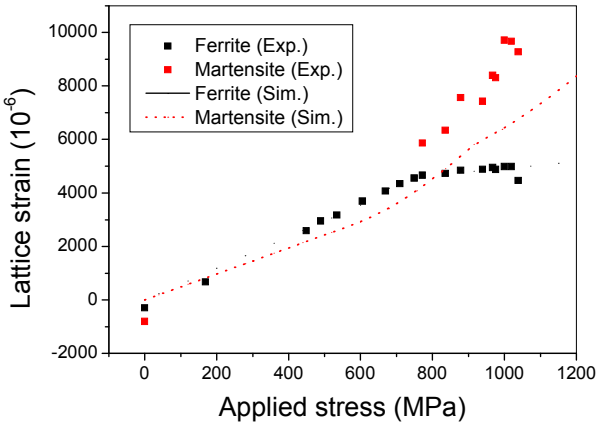

Figure 11. HEXRD-measured lattice strains along the loading direction for (200) reflections of ferrite and martensite during tensile loading.

The material properties used in the finite-element simulations are then:

$\sigma_y = 425 + 880\varepsilon_{ep}^{0.2}$ for ferrite and

$\sigma_y = 1130 + 1740\varepsilon_{ep}$ for martensite.

Note that no failure strain or ultimate elongation is specified for either phase. Finite-element analyses on the RVE level will be used to determine the macroscopic stress-versus-strain behaviors as well as the failure mode for this material subject to different loading and boundary conditions.

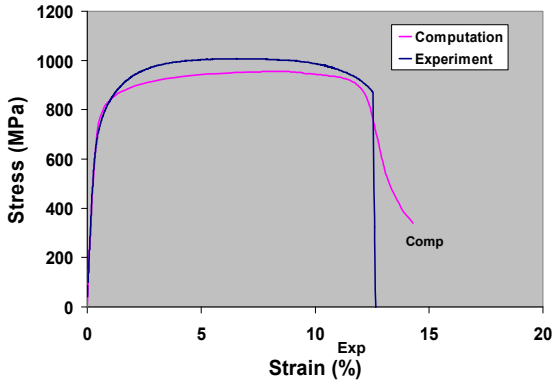

Figure 12. Predicted stress-versus-strain behavior for the RVE under plane-stress loading condition. The predicted failure mode under plane-stress loading condition is a macroscopic shear band.

Figure 12 compares the predicted and measured stress-versus-strain behaviors for this material under plane-stress loading condition. Overall

satisfactory results have been obtained comparing with experimental results with final elongation around 12.5%.

Figure 13 illustrates the predicted von Mises stress and equivalent plastic-strain contours for the RVE during tensile loading. Results in Figure 13 indicate that much higher stress is experienced in the martensitic grains than the ferrite matrix during deformation, therefore confirming the martensite strengthening theory we presented earlier. In contrast to the stress partitioning, the matrix ferrite grains experience much higher plastic strains than the martensite grains. The final failure mode predicted is the coalescence of regions with large plastic strains in the form of a macroscopic 45° shear band. This prediction is in qualitative agreement with experimental observations for DP 980 under quasi-static tensile loading conditions; see Figure 14.

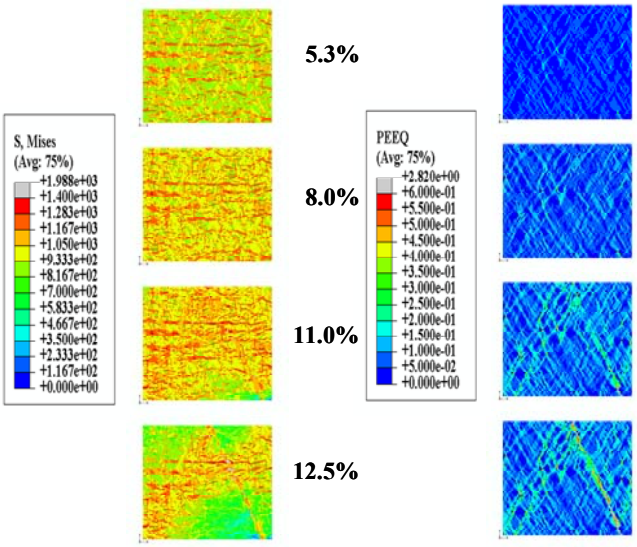

Figure 13. Predicted von Mises stress and equivalent plastic-strain contours for the RVE during tensile loading.

Future Direction

The next steps for our micromechanics modeling will be to include the grain-boundary effects and to consider the phase transformation of individual grains during deformation of TRIP steels. We are also planning on using ANL's APS facility in measuring the stress and strain partitioning in TRIP steels during deformation to validate the modeling results.

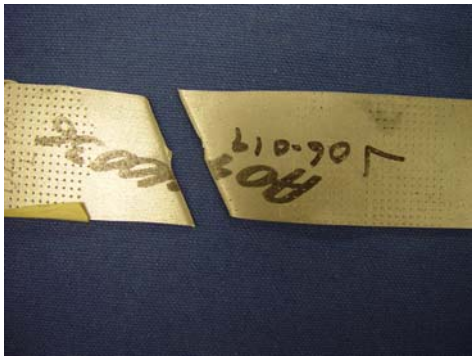

Figure 14. Experimentally-observed failure mode for DP 980 under quasi-static tensile loading.

Presentations/Publications/Patents

1. Sun, X, E.V. Stephens, and M.A. Khaleel. *Effects of Manufacturing Processes and In-Service Temperature Variations on the Properties of TRIP Steels.* SAE Paper No. 2007-01-0793. SAE World Congress 2007.
2. Liu, W.N., Choi, K.S., Sun, X., Khaleel, M.A., Ren Y. and Wang Y.D. *Modeling of Failure Modes Induced by Plastic Strain Localization in Dual Phase Steels.* To be presented at SAE2008 World Congress.
3. Liu, W.N., Choi, K.S., Sun, X., Khaleel, M.A. *Characterization of Thermo-Mechanical Behaviors of Advanced High Strength Steels (AHSS),* presented at 2007 USCAR AMD annual offsite review. PNNL-SA-57747.

L. Characterization of Thermo-Mechanical Behaviors of Advanced High-Strength Steels (AHSS): Weldability and Performance Evaluations of AHSS Parts for Automotive Structures

Principal Investigator: Zhili Feng
Oak Ridge National Laboratory (ORNL)
1 Bethel Valley Road, Oak Ridge, TN 37831
(865) 576-3797; fax: (865) 574-4928; e-mail: fengz@ornl.gov

Participants:
Stan A. David, ORNL
John Chiang, Ford Motor Company
Cindy Jiang, AET Integration, Inc
Min Kuo, ArcelorMittal Steel

Technology Area Development Manager: Joseph A. Carpenter
(202) 586-1022; fax: (202) 586-1600; e-mail: joseph.carpenter@ee.doe.gov

Expert Technical Monitor: Philip S. Sklad
(865) 574-5069; fax: (865) 574-6098; e-mail: skladps@ornl.gov

---

Contractor: ORNL
Contract No.: DE-AC05-00OR22725

Objective

- Develop fundamental understanding and predictive capability to quantify the effects of welding and service loading on the structural performance of welded AHSS auto-body structures.
- Investigate the weldability of AHSS under various welding-processes and -parameter conditions applicable to auto-production environment.
- Investigate welding techniques and practices to improve AHSS weld performance and benchmark the performance against the current welding practices.
- Generate weld-performance data including static strength, impact strength, and fatigue life as functions of welding processes/parameters and steel grade and chemistry.
- Develop design guidelines and computer-aided engineering (CAE) methodology to assist rapid structure design validation and prototyping of AHSS parts, to achieve maximum vehicle weight reduction through intelligent selection and utilization of AHSS based on the fitness-for-purpose principle.

Approach

- Conduct comparative welding experiments on various AHSSs including high-strength low-alloy (HSLA), dual-phase (DP), transformation-induced plasticity (TRIP), and boron steels to develop the correlation among the joint properties, welding process conditions, and steel chemistry.
- Characterize and rank the factors controlling the weld geometry, weld microstructures and weld joint performance.
- Develop an integrated, thermal-mechanical-metallurgical welding process and performance modeling methodology to accurately predict the microstructure and mechanical-property gradients in the weld region; use the experimental data to validate the integrated model.

Accomplishments

- Initial development of welding process model capable of simulating the microstructural changes and the softening in the heat-affected zone (HAZ) of AHSS welds.
- Determined the fundamental metallurgical mechanisms causing HAZ softening of the current generation of AHSS.
- Developed initial correlation between the structural performance (static, dynamic and fatigue) and the microstructural changes of AHSS welds.
- Revealed the stress partitioning among different phases in TRIP steel during deformation and the effect of austenite-to-martensite transformation on the deformation and work hardenability of TRIP steel via *in-situ* neutron-scattering experiment.
- Demonstrated considerable fatigue-life improvement by means of refining welding conditions (within industry's acceptable welding practices).
- Close interactions with the industry, including different Auto/Steel Partnership (A/SP) technical committees and the Big 3, to exchange research progress and collaborate with other related projects.

Future Direction

- Continue to identify key factors controlling the weld joint performance under static- and fatigue-loading conditions.
- Further investigate the weld joint performance under impact/crash-loading conditions.
- Investigate the structural performance of AHSS weld joints under complex loading conditions (component-level behavior)
- Complete development of integrated thermo-mechanical-metallurgical modeling framework for AHSS welded structures.
- Continue to investigate welding techniques and practices to improve weld performance.
- Develop design guideline and CAE analysis methodology to assist rapid design and prototyping of AHSS structures.

Introduction

This project is part of collaborative research by ORNL and Pacific Northwest National Laboratory (PNNL, see 5.K) on "Characterization of Thermo-Mechanical Behaviors of Advanced High-Stress Steels (AHSS)." This joint effort aims at developing fundamental understanding and predictive modeling capability to quantify the effects of auto-body manufacturing processes (forming, welding, paint baking, etc) and in-service conditions on the performance of auto-body structures made of AHSS. ORNL's research (designated as Task 2 in this project) focuses on welding of AHSS. In the late part of the program, the interdependency of manufacturing processes – weldability of a formed part and formability of a welded part – will be investigated.

Specific background of Task 2 as related to the mission of DOE Lightweighting Materials and the needs of automotive industry for accelerated use of AHSS for body-structure lightweighting has been given in a previous annual report and will not be repeated here.

Task 2 has a technical steering committee with representatives from Chrysler, Ford, General Motors, A/SP Joining Committee (see 5.B), and steel companies.

In fiscal year (FY) 2006, the first year of the program, the research focused on obtaining the baseline knowledge and understanding about the static strength and fatigue life of AHSS welds. To this end, we experimentally investigated a wide range of AHSS types and grades most interesting to the US automotive industry. It was found, for the steels and welding conditions investigated herein, that:

- The static tensile strength of a gas metal arc welding (GMAW) process weld increases as the base-metal-steel strength increases. However, the joint efficiency (the ratio of weld strength to the base-metal strength) under static-loading condition can be greatly influenced by the HAZ softening of an AHSS weld. Ultra AHSS such as martensitic and boron steels have most noticeable HAZ softening and, thereby, lower joint efficiency. The

lower-grade AHSS without HAZ softening maintain their high joint efficiency.

- Steel-grade dependency of weld fatigue life has been confirmed. The HAZ softening does not appear to be a major factor influencing the weld fatigue life.
- It is feasible to drastically improve the weld fatigue life of AHSS by manipulating welding-process conditions. The fundamental causes/mechanisms leading to the observed fatigue-life improvement re-quire further investigation.

In FY 2007, we began to focus on developing the fundamental understanding and predictive capability on the microstructural and property changes in the weld region of AHSS. Another major effort has been on investigating welding techniques to improve the weld durability (fatigue life) using a science-based approach. The experimental study on the welding effect expanded to the dynamic (impact) behavior of AHSS welds.

Steels and Welding

Based on the recommendations of Task 2 industrial technical steering committee, we have been focusing on welding of AHSS for chassis and underbody applications. The welding process was GMAW, the primary welding process for chassis and underbody structures. Five types of AHSS were selected in this study. They include dual-phase steels (DP 600, DP 780, DP 980), TRIP steels (TRIP 600, TRIP 780), martensitic steels (M130, M200), boron steel, and HSLA steel, with gauge thickness of 2-mm nominal. Details of the steels and welding conditions are provided in the FY 2006 annual report.

Improving Fatigue Life of AHSS Welds

In the past, the auto industry generally considered that the fatigue life of a weld joint is more or less independent of steel chemistry, and is dominated by the weld geometry (profile). Therefore, there is little room to improve the fatigue life of a steel weld from the welding perspective – the fatigue life of a steel weld will be primarily controlled by the load level (as indicated in the S-N curve). Such viewpoint stems from the experiences of conventional, low-strength, mild steels where the weld microstructure is not sensitive to welding. There have been very limited and systematic comparative studies on the fatigue behavior of different AHSS designed for automotive structural applications.

In FY 2006, we conducted a comparative study and found that there are noticeable differences in fatigue lives among different AHSS welds. Some of the higher-strength AHSSs studied such as boron steel had lower fatigue lives under the low-stress, high-cycle loading conditions ($> 10^5$ cycles) that are most relevant to the durability design of auto-body structures. In our FY 2006 study, all welds (of different AHSS) were made with the same set of welding parameters accepted by the industry for mild steels. This suggests that, in order to realize the benefits on the AHSS, different welding conditions would be required.

This year, we developed a new welding procedure that resulted in drastic improvement of the fatigue lives of AHSS welds. The new welding procedure involved adjusting different welding parameters to improve the weld profile, in particular the weld toe angle, to reduce the stress concentration at the weld toe. The adjustments of welding parameters developed in this study are readily transferable to a production environment. The welding speed (thus the productivity) is also within the range accepted by the industry. Figure 1 compares the different weld profiles produced using the baseline and improved welding conditions. The changes in weld profile resulted in a drastic increase in fatigue lives for AHSS, as shown in Figure 2. For comparison, the baseline fatigue lives of different AHSS welds made with the welding practice for mild steel are shown in Figure 3. An order-of-magnitude increase in fatigue lives has been achieved for DP and boron steels (relative to their respective baseline results).

The ability to improve the weld fatigue life of AHSS is significant. It addressed a critical concern in application of AHSS. The use of AHSS generally results in gage downsizing. This means that the AHSS structures will be subjected to higher fatigue stresses. If the fatigue life can not be improved through welding process innovations, the durability of the vehicle will suffer when mild steels are replaced with AHSS. Both A/SP Sheet Steel Fatigue Committee (see 5.D) and the Joining Technologies Committee (see 5.B) are interested in collaborating to further expand the study on this subject.

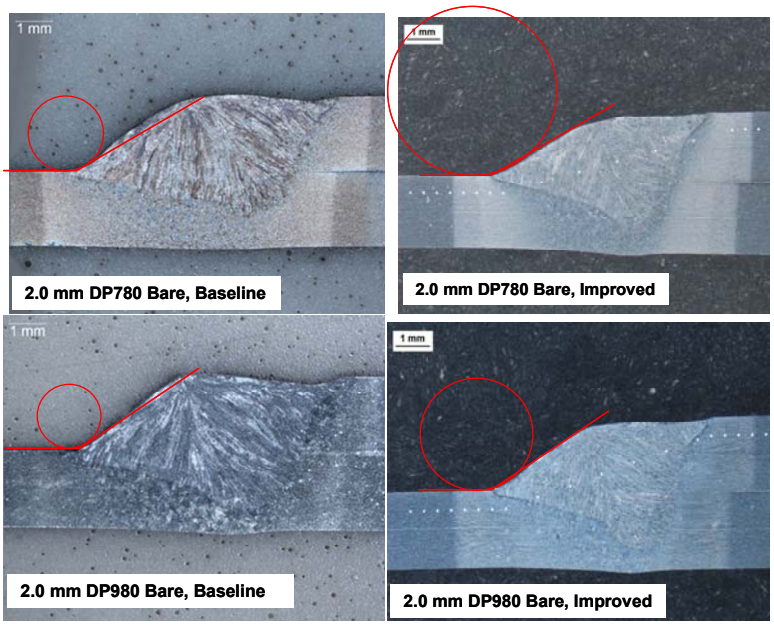

Figure 1. Weld-profile comparison between the baseline welding practice and the improved welding practice. The circles illustrate the changes in weld toe radius.

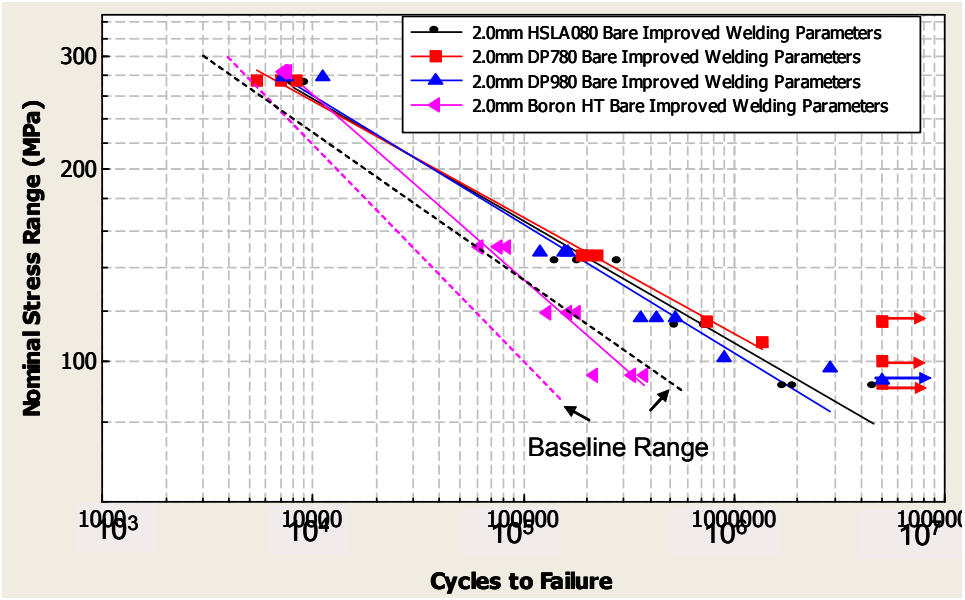

Figure 2. Improvement in fatigue life of AHSS welds by using AHSS-specific welding conditions.

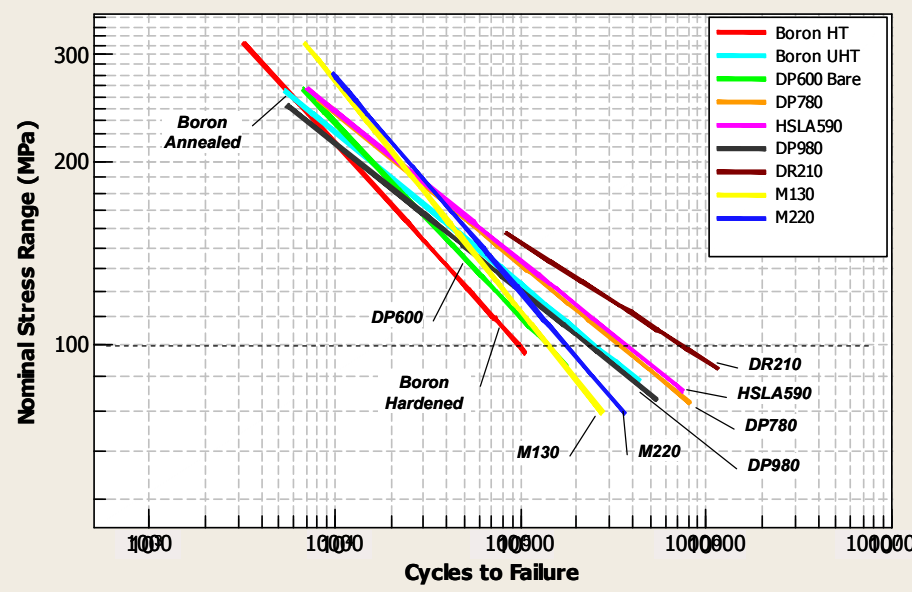

Figure 3. Comparison of fatigue S-N curves of different AHSS made under same welding conditions and having consistent weld profile. The regression curves are shown. R=0.1. Steel sheet thickness: 2 mm.

Predictive Models for Fatigue Life of GMAW Lap Joint of AHSS

In addition to the above experimental development of fatigue-life improvement of AHSS welds, we also completed the initial development of a weld fatigue-life prediction model that relates the fatigue life to the microstructure and geometry of AHSS weld joint. A summary of the model development is provided below.

We start with the local notch strain approach for welded joint [1,2]. In such an approach, the total fatigue life (N_t) of a welded joint consists of the crack-initiation part (N_i) and the subsequent cracking-propagation (to failure) part (N_p):

$$N_t = N_i + N_p$$

The propagation part can be estimated by the Paris law:

$$N_p = \frac{1}{C}\int_{a_i}^{a_c}\left(\frac{1}{\left(\Delta S\sqrt{\pi a}F(a)\right)}\right)da$$

Research in the past (for example, Lawrence et al. [1]) have shown that crack initiation is the dominant part in the total life of low-stress, high-cycle fatigue (i.e., in the stress range most relevant to auto-body durability design) in welded joints for high-strength steels and aluminum alloys. This differs from the case of mild construction steels where crack propagation takes up the majority in fatigue life of welded joints.

In this study, the Coffin-Manson equation is used for crack initiation life prediction:

$$N_i = \frac{1}{2}\left[\frac{2\left(\sigma_f^{'} - \sigma_m\right)}{K_f \Delta S}\right]^{-1/b}$$

$$K_f = 1 + \frac{K_t - 1}{1 + a_p/\rho}$$

$$b = -0.1667\log\left(2.1 + \frac{917}{S_u}\right)$$

$$\sigma_f^{'} = 0.95 S_u + 370 MPa$$

$$a_p = 1.187x10^5 / S_u^2$$

In the above equations, ΔS is the nominal stress range. σ_m is the mean stress. K_t is the stress concentration factor. K_f is the fatigue notch factor. ρ is the notch radius at the crack initiation site (weld toe or root in this study). Su is the local ultimate strength at the crack initiation site.

1 Lawrence F.V. 1973, "Estimation of fatigue crack propagation life in butt welds," *Welding Journal*, v53, 212s-220s.
2 Hou, C.Y. and Charng J.J. 1997, "Models for the estimation of weldment fatigue crack initiation life," *Int. J. Fatigue*, v19, 537-541.

The above equations relate the crack-initiation life to the three major factors governing the fatigue life of welded joint: (1) the stress state including the weld residual stress, (2) the local stress concentration due to weld geometry and discontinuity, and (3) the local material strength which is a function of the microstructure in the weld region.

The stress-concentration factors at the weld toe and weld root were determined using finite-element analysis. We analyzed the stress distributions for representative baseline and improved weld geometries under elastic deformation condition pertinent to the low-stress, high-cycle fatigue case. The actual weld profiles taken from weld cross-section metallographic pictures were used in building the finite-element mesh. The results are shown in Figure 4. The improved weld geometry reduces the stress concentration factor from 8.7 to 6.5 at the weld toe, and from 8.2 to 7.8 at the weld root.

Table 1 shows the drastic increase in the crack-initiation life of welded joint as result of reduction in fatigue notch factor, as determined from the fatigue-life prediction model described above. The improved weld geometry in our experiment would reduce the fatigue notch factor by about 20 to 30%. This translates into 5 to 10 times fatigue life improvement for mild steel (300 MPa ultimate strength). The improvement in fatigue life is even greater for AHSS, due to influence of material strength on crack initiation as indicated in the above equations. For example, fatigue life improvement for DP 780 is about 10 to 20 times. ***Thus, weld-geometry improvement can be particularly effective for higher-strength steels.*** The above analysis is supported by our experimental results, as shown in Figure 2 and Figure 3.

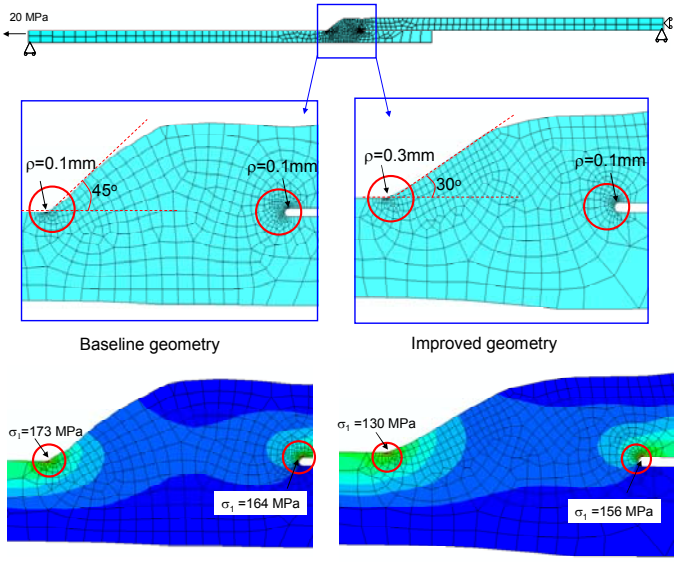

Figure 4. Finite-element analysis of local stress distributions around the weld toe and root region. The applied nominal stress is 20 MPa.

Table 1. Influence of fatigue notch factor on the crack-initiation life of a mild steel and a DP 780 steel.

Improvement in Kf	Improvement in Crack Initiation Life	
	Mild (300MPa)	DP780
5%	151%	176%
10%	223%	302%
20%	463%	829%
30%	906%	2098%
40%	1688%	4955%
50%	3014%	11032%

The fatigue-crack-initiation life-prediction model was further evaluated against the experimental testing data for a number of the steels and weld geometries studied in this project. The comparison and evaluation is summarized in Figure 5. Overall, the fatigue-life prediction model can capture the observed variations in fatigue lives due to steel grade, weld geometry and HAZ microstructure and local property variations of AHSS. However, the model underpredicts the experimentally-observed total fatigue lives as it does not contain the fatigue-crack-propagation part yet. The fatigue-crack-propagation life-prediction part of the model is being developed and verified.

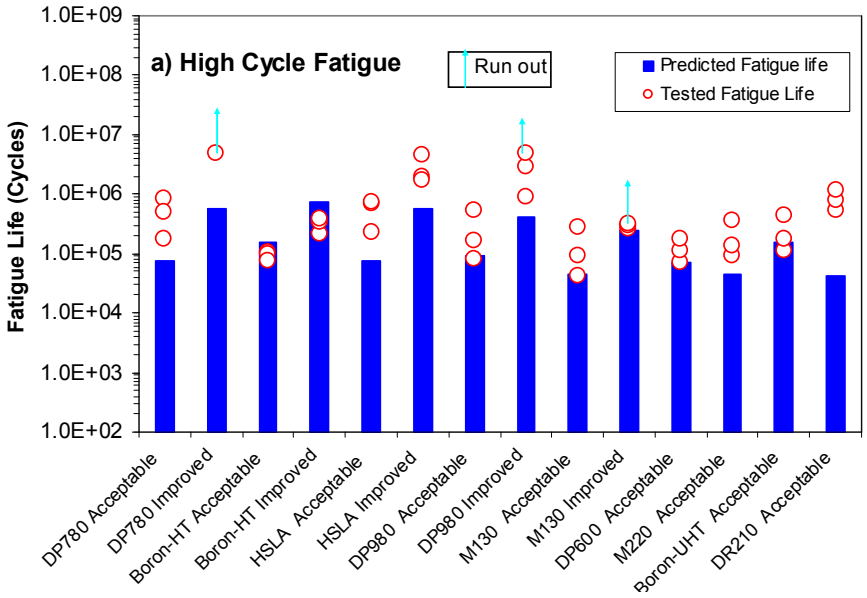

Figure 5. Comparison between experimental fatigue-life data and predicted fatigue crack initiation lives of GMAW lap joints for different grade steels and weld geometries [high-cycle fatigue case $N_f>10^5$].

Modeling of Weld Microstructure Changes and HAZ Softening

As evidenced in our FY 2006 work and others, AHSS exhibit considerable microstructure changes in the weld region. The microstructural changes can result in the HAZ softening which impairs the static (and possibly the impact/crash) strength of AHSS welded structures. A major objective of Task 2 is, then, to develop the predictive capability to quantitatively relate the microstructure and property changes to the steel chemistry and welding-process conditions and to integrate the weld model into CAE-based design and engineering methodology for use in the industry.

We have completed the initial development of a welding thermo-metallurgical model for AHSS GMAW welds. This model is capable of correctly predicting the microstructure changes and the HAZ softening for the AHSS studied so far. As an example, Figure 6 shows the comparison between the predicted microhardness distribution and the experimental mapping of the microhardness for a boron steel weld. As shown in the figure, the weld model is able to predict the minimum hardness location (away from the weld fusion line) and the overall distribution of the microhardness changes in the HAZ. Modeling approaches dealing with the weld metal are being developed.

By correlating the temperature and microstructure information obtained from the weld process simulation, it is possible to explain the observed HAZ softening in AHSS welds. The minimum hardness region in the HAZ (approximately 2 mm away from the weld fusion line in Figure 6 for boron steel) corresponds to the intercritical temperature range in the Fe-C phase diagram (i.e., between A1 and A3 in Figure 7).

During welding, the minimum-hardness region is heated into the intercritical temperature range in which two phases (austenite and ferrite) co-exist. On cooling, the austenite can decompose to hard, low-temperature phases such as martensite or bainite. On the other hand, the ferrite phase in the intercritical temperature range will stay untransformed on cooling as it is a stable phase at room temperature. The presence of the soft ferrite will result in reduced strength and hardness, thus the minimum hardness of the HAZ. Such explanation is consistent with the observations that the most-pronounced HAZ softening takes place in martensite and boron steels.

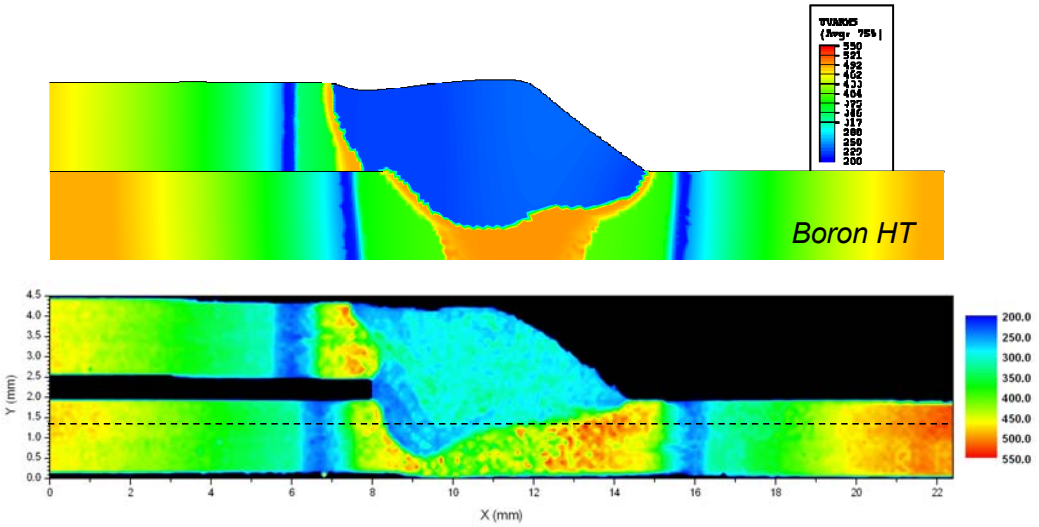

Figure 6. Comparison of predicted microhardness distribution (top) and experimental microhardness mapping (bottom). Boron steel is shown here. The model for the weld region is still under development.

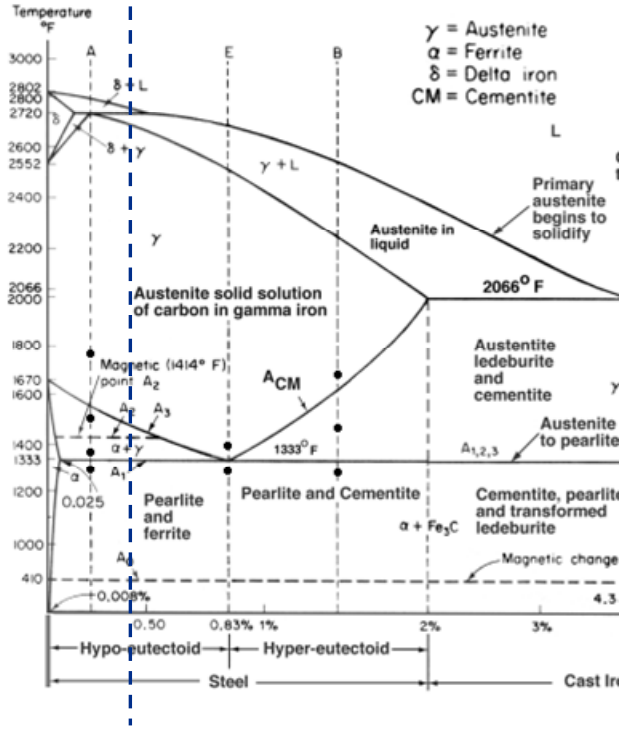

Figure 7. Fe-rich corner of Fe-C phase diagram.

The weld process model also reveals other mechanisms contributing to the HAZ softening of AHSS welds. Below the A1 temperature, the martensite in the base metal will undergo the tempering process, resulting in the observed gradual decrease in the hardness as the peak temperature approaching to A1. Above the A3, the steel will transform fully to austenite on heating. On cooling, whether the austenite will transform to martensite, bainite, or other hard phase depends on the hardenability of the steel (related to the steel chemistry). This explains the differences in the microstructure and microhardness in the near HAZ region (i.e., the region between the fusion line and the minimum-hardness region) of different AHSSs.

The above discussions on the fundamental metallurgical causes for the profound HAZ softening in AHSS are supported by the detailed microstructure-characterization analysis conducted in this study. A series of microstructure metallographic photos were systematically taken at different locations in the weld and HAZ region of a weld. The precise locations of these photos were determined by the distance from the fusion line and from the bottom surface of the sheet. With their locations being precisely known, these photos were then reconciled with the micro-hardness mapping results to yield the correlation between the microhardness and the underlining microstructures at various locations of the weld region. As example, Figure 8 and Figure 9 contrast the microstructures in different regions of a boron steel weld and a HSLA590 steel weld.

It is important to point out that the HAZ-softening phenomenon is an inherent characteristic for high-strength steels relying on allotropic phase transformation (i.e., decomposition of austenite to mixture of soft phases such as ferrite and hard phases such as martensite or bainite) to achieve a balance of strength and ductility. Such a phenomenon is not unique to automotive AHSS; it has also been observed in various high-strength steels such as low-carbon alloy steels such as X100 for natural-gas transmission pipelines and high-alloy steels such as 9Cr-1Mo steel for pressure vessels. On the other hand, the ferrite phase in the intercritical temperature range will stay untransformed on cooling as it is a stable phase at room temperature. The presence of the soft ferrite will result in reduced strength and hardness, thus the minimum hardness of the HAZ. Such explanation is consistent with the observations that the most-pronounced HAZ softening takes place in martensite and boron steels.

It is also important to point out that, while the HAZ softening is unavoidable in the current generation of AHSS, the degree of HAZ softening varies as a function of steel chemistry, base-metal microstructure, and welding process conditions. Various options can be explored to reduce the HAZ softening effect, from steel chemistry optimization, welding process selection, and effective structural design.

Other Progress

In-situ Neutron Diffraction Study of TRIP Steel.

In the past, the deformation behavior and the effects of phase transformation in TRIP steels have been studied post-mortem. Deformed samples are sectioned and examined using various metallographic techniques. The transformation-induced plasticity phenomenon is inferred from microstructure observations. What has been missing from these studies is the stress information within different phases that controls the transformation process in TRIP steels

In this project, we took the advantage of a neutron source to perform *in-situ* neutron experiments to study the phase-transformation kinetics in TRIP steels under loading. The goal was to determine the effect of deformation on austenite-to-martensite phase transformation in TRIP steels. Two TRIP steels, TRIP 590 and TRIP 780 were studied. By utilizing the unique time-of-the-flight feature of a pulsed neutron source, the lattice spacing changes of multiple crystallographic planes in two orthogonal directions were determined simultaneously. The *in-situ* measurement allowed for direct measurement of the phase-transformation process and the stress partitioning among different phases as the sample is being deformed. Figure 10 shows the changes in the lattice strains during the deformation process. The interplays between the austenite-to-martensite phase transformation and the deformation process are clearly revealed. Our *in-situ* neutron experiment, for the first time, provides direct and quantitative measurement of the TRIP behavior which can greatly assist and validate the constitutive model development effort at PNNL for forming simulation of TRIP steels.

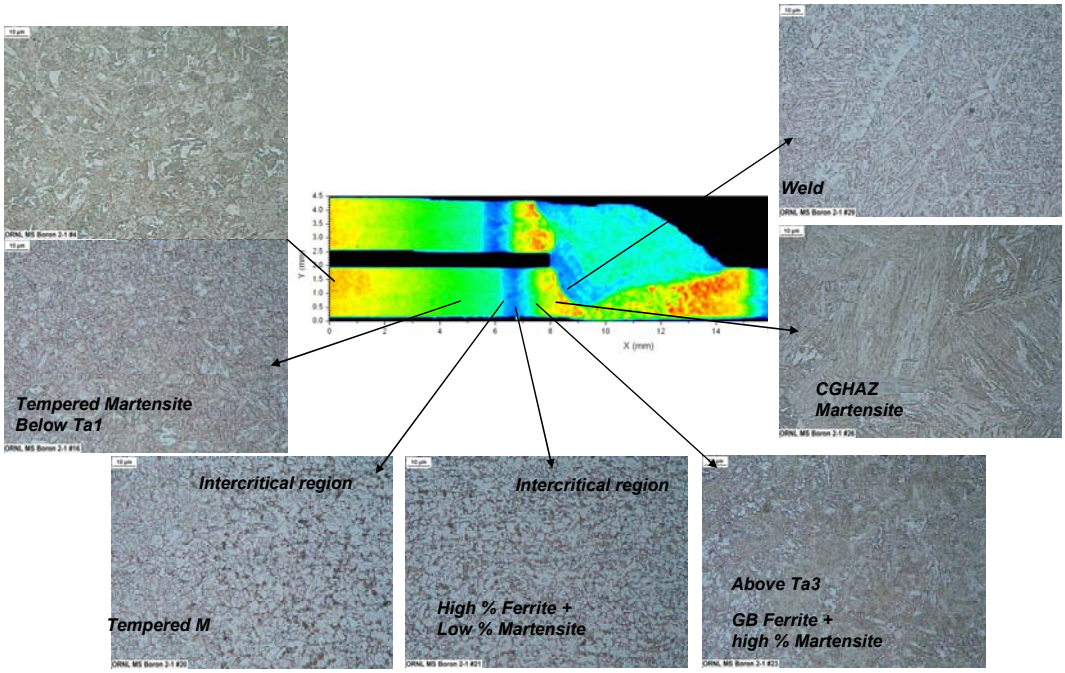

Figure 8. Microhardness distribution in a boron-steel weld and the corresponding microstructures in different locations in HAZ and weld. The drastic variations in microhardness result from considerable microstructure variations in different regions of HAZ. The lowest microhardness location corresponds to the intercritical region with high percentage of ferrite formed on heating and a low percentage of martensite transformed on cooling.

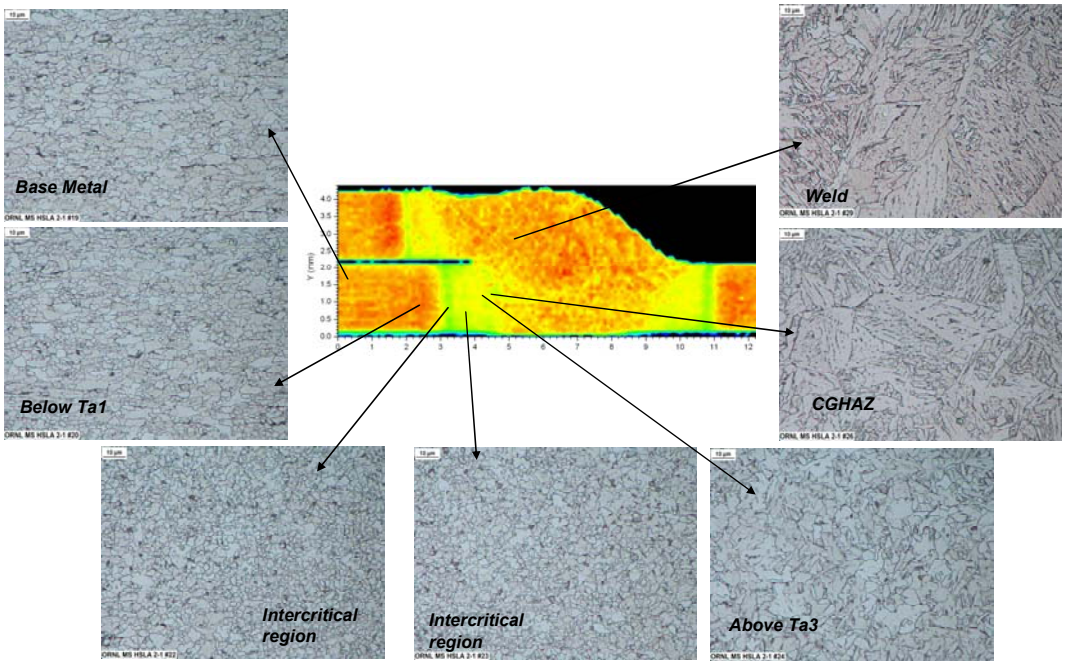

***Figure 9**. Microhardness distribution and the underlining microstructures in different part of HAZ of a HSLA590 steel.*

Interactions with the Auto and Steel Industry

The weldability task (Task 2) has received strong support from the industry from the start of the project. Since then, we have maintained active interactions with the auto and steel industry through the technical steering committee and A/SP. Such interactions have been mutually beneficial to the project and to the industry. We were invited to A/SP's Joining Technologies Team, Sheet Steel Fatigue Committee, and Lightweight Chassis Structures Team (see 5.J) to exchange research results. We also were invited to Ford, General Motors (GM) and Chrysler to discuss our research progress and understand the needs of the industry. Several collaborative efforts have come out of these interactions. For example, the Joining Technology Committee has decided to conduct a follow-on, static joint-strength-efficiency study to cover a wider range of steels, gage thickness and other welding processes. The Fatigue Committee is interested in incorporating our findings on fatigue-life improvement into their studies. Ford, GM, ArcelorMittal Steel and A/SP's joining and lightweight chassis design committees are looking into the feasibility of incorporating our weld microstructure model in some of their CAE design and research activities. We plan to maintain the strong interactions with the industry in this program.

Plan for FY 2008

The R&D activities in FY 2008 will be built on the strong progress of the project, focusing on completing the following tasks:

1) Complete the microstructure model development to include weld metal.
2) Initiate the integration of the welding process/microstructure model with mechanical-performance model that will enable simulation of the deformation and failure behavior of AHSS welds.
3) Continue on weld fatigue-life prediction model development.
4) Complete microstructure characterization of different AHSS welds to further validate the weld microstructure model.
5) Complete several topical reports on weld joint-efficiency study, microstructure characterization and weld-microstructure model development.

Presentations/Publications/Patents

1. Great Designs in Steel Seminar 2007, AISI, Livonia, MI, March 7, 2007
2. SAE World Congress & Exhibition, April 16-19, 2007, Detroit, MI (Invited Talk).

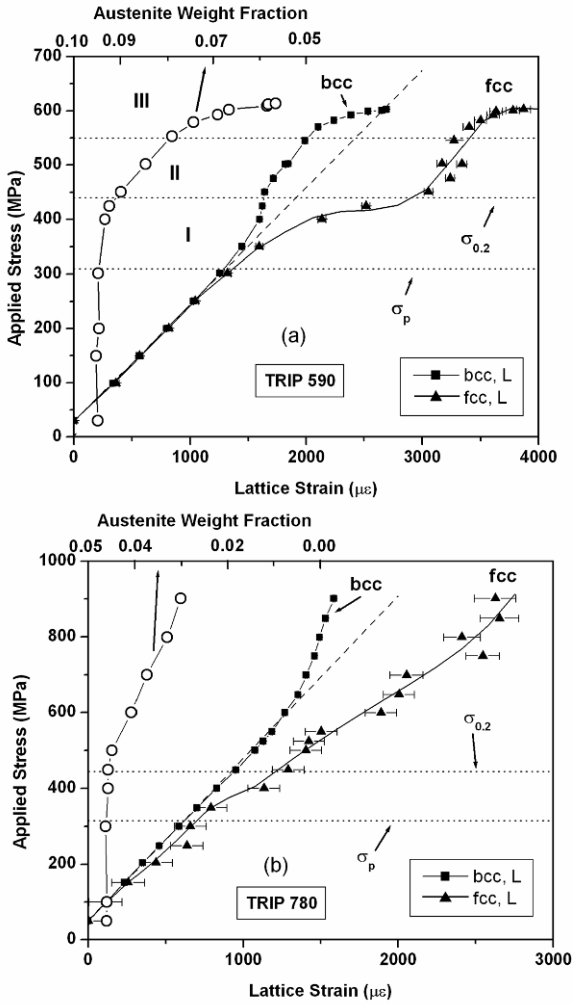

Figure 10. The lattice-strain evolution in the longitudinal direction of the face-centered cubic (fcc) phase and body-centered cubic (bcc) phases during the *in situ* neutron measurements in (a) TRIP 590 steel and (b) TRIP 780. The weight fraction of retained austenite (open symbols) was plotted to correlate to the lattice strain evolution. Note that bcc refers to the sum of ferrite and martensite phases, whose peaks overlap, after the martensitic transformation is induced. The weight fraction scale of (b) was adjusted to match that of (a), in order to illustrate the difference in phase transformation.

Acknowledgements

We would like to acknowledge the following individuals and A/SP committees who contributed to this project:

Chrysler: W. Marttila
Ford Motor: Paul Geck, J. Bonnen
General Motors: S. Gayden, J. Bohr, C. Chen
AK Steel: T. Montroy
Defasco: W. Bernert
Severstal N.A.: R. Mohan, Y.W. Wang
US Steel: M. F. Shi
A/SP Joining Technologies Team
A/SP Sheet Steel Fatigue Committee
A/SP Lightweight Chassis Structure Team

M. Materials Design for Steel Alloys

Co-Principal Investigator: Seong-Gon Kim
Assistant Professor
Physics and Astronomy
Hilbun Hall, Rm 237
Mississippi State University (MSST), P.O. Box 5405
Mississippi State, MS 39762-5405
(662) 325-8031; e-mail: kimsg@ccs.msstate.edu

Co-Principal Investigator: Mark F. Horstemeyer
Chair in Solid Mechanics & Professor, Mechanical Engineering
Center for Advanced Vehicle Systems (CAVS)
MSST
206 Carpenter Bldg., PO Box ME
Mississippi State, MS 39762
(662) 325-7308; fax: (662) 325-7223; e-mail: mfhorst@me.msstate.edu

Co-Principal Investigator: Randall German
Director and Professor
CAVS
MSST, P.O. Box 5405
Mississippi State, MS 39762-5405
(662)325-5431; (662)323-3906; fax: (662) 325-5433; e-mail: german@cavs.msstate.edu

Co-Principal Investigator: Hongjoo Rhee
Postdoctoral Associate
CAVS,
MSST, P.O. Box 5405
Mississippi State, MS 39762-5405
(662) 325-9221; e-mail: hrhee@cavs.msstate.edu

Co-Principal Investigator: Sungho Kim
Postdoctoral Associate
CAVS,
MSST, P.O. Box 5405
Mississippi State, MS 39762-5405
(662) 325-9241; e-mail: sk5@msstate.edu

Technology Area Development Manager: Joseph A. Carpenter
(202) 586-1022; fax: (202) 586-1600; e-mail: joseph.carpenter@ee.doe.gov

Contract Monitor: Aaron Yocum
(304) 285-4852; fax: (304) 285-4403; e-mail: aaron.yocum@netl.doe.gov

---

Contractor: MSST
Contract No.: 4000054701

Objective

- Design low-cost steel alloys with improved strength and formability for automotive applications.

Approach

We use a hierarchical, multiscale methodology to investigate the effect of nanoscale precipitates and additives to the overall strength and formability in steel-alloy design for automotive applications. Critical issues being addressed include: selection of key combination of precipitates and matrices, interaction of precipitate and matrix phases and, ultimately, composition-structure-property relationship. At the electronic level, quantum-mechanical, first-principles simulations based on Density Functional Theory (DFT) will be performed to investigate the interfacial interactions between matrix and the primary and the secondary precipitates. At the atomistic level, accurate atomistic simulations will be performed using efficient and reliable empirical interatomic potentials such as modified embedded-atom method (MEAM) or force-matching, embedded-atom-method (FMEAM) potentials. The interatomic potentials are constructed by optimizing the potential parameters to reproduce various experimental materials properties and atomic-force data from DFT calculations. Large-scale, atomistic simulations will be conducted to study the effects that size, shape, and volume fraction of different precipitates have on the thermo-mechanical properties of steel alloys. Many factors that govern the yield and hardening behavior of solids such as crack-tip propagation, dislocation nucleation, dislocation motion, and the interaction of dislocations with grain boundaries will be investigated through these simulations. Results will be used to guide quantitative alloy-composition designs to improve strength and formability of steel alloys.

- Construct and validate reliable interatomic potentials to model various phases of high-strength steel alloys.
- Obtain the electronic, structural and mechanical properties of the main phases of steel alloys.
- Investigate the effect of various precipitates present in modern high-strength steel alloys on their thermo-mechanical properties.
- Investigate the efficacy of novel additives to design new high-strength steel alloys with improved strength and ductility.
- Perform experiments to test new materials and validate the results.

Accomplishments

The first year objectives were met by accomplishing the followings:

- The DFT calculations were performed on iron (Fe) – carbon (C) alloy systems using the full spin-polarized, local-density approximations (LDA) to correctly account for the ferromagnetism in Fe atoms.
- Developed a new, multi-objective optimization (MOO) methodology as a robust procedure to construct reliable and transferable interatomic potentials for steel-alloy systems.
- Applied the MOO procedure to construct transferrable interatomic potential for Fe using the FMEAM.
- Applied the MOO procedure to construct transferrable interatomic potential for C using the FMEAM.
- Established a basic framework for the accelerated development of reliable and efficient interatomic potentials for other combination of alloy systems to perform large-scale, realistic atomistic simulations.
- Established a procedure to achieve a close integration with other tasks of the project. The task “Simulation-Based Design Optimization” (see 6.G) assists the present task in developing empirical interatomic potentials, which will be used by many other tasks including the present task and the task ”Examining Fundamental Mechanisms of Tooling Wear for Powder Processing” (see 4.D). The simulation results from the present task are then fed into the task “Multiscale Microstructure-Property Plasticity Considering Uncertainty” (see 6.J) for simulations in larger length scales.
- Established a close collaborative relationship with industrial partners including POSCO, SAC, Inc., and Wade Service.
- Submitted one paper on MOO methodology to Phys. Rev. B.
- One paper on the DFT calculations on cementite is in preparation.
- One paper on the development of FMEAM interatomic potential for Fe atoms is in preparation.
- One paper on the development of FMEAM interatomic potential for C atoms is in preparation.

Future Direction

- Develop interatomic empirical potentials for silicon (Si), nitrogen (N) and molybdenum (Mo) using the MOO procedure.
- Develop interatomic empirical potentials for various alloys involving Fe, C, Si, N, and Mo using the MOO procedure.
- Perform DFT simulations of ferrite-cementite interfaces (shear, debonding, etc).
- Perform large-scale, atomistic simulations of ferrite-cementite interfaces using empirical interatomic potentials.
- Perform DFT simulations of martensitic phase and Fe-Mo intermetallic compounds.
- Perform large-scale, atomistic simulations of martensitic phase and Fe-Mo intermetallic compounds.
- Obtain various high-strength steels and perform experiments on those materials to understand fundamental materials/mechanical properties and to provide information to design and simulation efforts.
- Validate numerical models using structure-property data obtained from experiments.

Introduction

The fabrication of desired automobile components is often the largest barrier to new materials, since automotive designs call for specific aerodynamic considerations. Despite their desirable material characteristics, high-strength steels have limited fabrication capability because they inherently resist deformation and wear the tooling. Therefore, we have the challenge and opportunities to perform compositional design of high-strength steel alloys in a manner that lowers mass, increases strength and retains workability, but generates required strength after the fabrication step.

Potential components for lightweighting and ultra-strength materials are the front end, powertrain, instrument panels, the chassis system, and car bodies including door panels, for example. We propose to perform compositional design of steel alloys to lower these barriers with a better understanding of the quantum-mechanical and atomistic structure of various constituent composite crystal structures and their interactions, the influence of alloying additions, and the effects of thermo-mechanical treatments on wrought materials during and after processing.

Ductility of materials can be improved by alloying and by the resulting activation of slip systems. We will investigate the origin of these alloying effects by using quantum-mechanical, first-principles methods such as DFT [Kresse96, Kohn65]. We will focus on the "gamma" surfaces (surface energy versus imposed shear) to understand the extent to which these effects are governed primarily by electronic structure or crystallography. Results will be integrated into thermo-dynamic-database extensions supporting quantitative alloy-composition designs to improve ductility.

Previous research on "triple-phase" sheet steels exploiting retained-austenite transformation plasticity for enhancement of sheet formability at high strength levels has identified the key role of austenite particle size and composition in optimizing transformation stability. We will investigate the control of austenite stability through isothermal bainitic transformation. The results will enable the prediction of new compositions and processing to increase austenite stability to a theoretically-predicted optimum and improve ultra-high-strength sheet-steel formability.

The use of precipitation reactions, such as Fe-Mo precipitates, is one of the ways to allow softer forming and high use strength. The other attractive option is to use laminates, such as Fe and aluminum (Al). Both Fe and Al are easily rolled into sheets and should have good roll bonding. After stamping, a thermal cycle could be used to induce diffusional alloying to produce FeAl, which is a ductile intermetallic. As the hard-soft laminates might prove optimal in toughness, it may not be necessary to fully homogenize the laminates. The low-density Al will reduce weight and the high-strength intermetallic will provide strength while the advantage of easy processing is retained by using laminated foils.

Experimental Approach

Figure 1 shows an overall flowchart of the project procedure along with proper technical approaches. First, reliable empirical interatomic potentials to model various phases of high-strength steel alloys are constructed and validated. Next, the structural, electronic, and mechanical properties of the main phases of advanced high-strength steel (AHSS) alloys are obtained by DFT and atomistic simulations. In order to design a novel AHSS alloy with improved strength and ductility, the effects of various phases, novel additives, heat treatment and manufacturing processes on the materials and mechanical properties of the AHSS are investigated by DFT and atomistic simulations. At this stage, various base alloys of interest with different intrinsic materials properties will be provided by industrial partners, such as POSCO and SAC, Inc. Various experiments on the base alloys will be carried out to understand fundamental materials/mechanical properties and the output will be provided for designing efforts. Such experiments include chemical analysis, microstructure observation, micro- and macro-mechanical tests. The overall chemical analysis of the base alloys will be performed by using a spectrometer. The quantitative and qualitative chemical compositions of each phase present in the alloys will be individually analyzed by an energy-dispersive x-ray (EDX) spectroscopy technique. Microstructures of the alloys will be investigated by an optical microscope (OM) and a scanning electron microscope (SEM). Conventional hardness tests will be conducted to gain overall properties of the alloys, while nano-indentation tests (NITs) will be performed to obtain micromechanical properties of various phases found in the alloys.

In order to obtain fundamental mechanical properties related to strength and ductility such as yield strength, elongation, tensile strength, work-hardening exponent (*n*-value), stress-strain relations and strain-rate effects, tensile tests will be carried out at various strain rates. The yield strength and tensile strength of the alloys are important because their relations are not only intrinsic materials properties but also general designation systems for high-strength steels. Such designation systems also classify different yield strength with equal tensile strength and vice versa, thereby, allowing some assessment of the stress-strain curves and amount of work hardening [IISI06]. The requirement of AHSS with improved formability and crash-energy absorption is strongly affected by the work hardening exponent (*n*) – the higher the *n*-value, the better stretch ability. Total elongation is also the traditional measure of the steel's general stretch ability over wide areas of the stamping. The modification of microstructure to create a novel AHSS for increased *n*-value, greater stretch ability, crash-energy absorption and higher total elongations is desired for application requirements demanded by the automotive industry. One of the critical problems to adapt high-strength steels to automotive is pure formability with increased strength. Therefore, the press formability will be investigated under different press modes. By utilizing the composition-structure-property relationship extracted by aforementioned experiments and various simulations, a novel AHSS will be designed. A small amount of sample will be manufactured and supplied by the industrial partners and model validation by various experiments will be carried out.

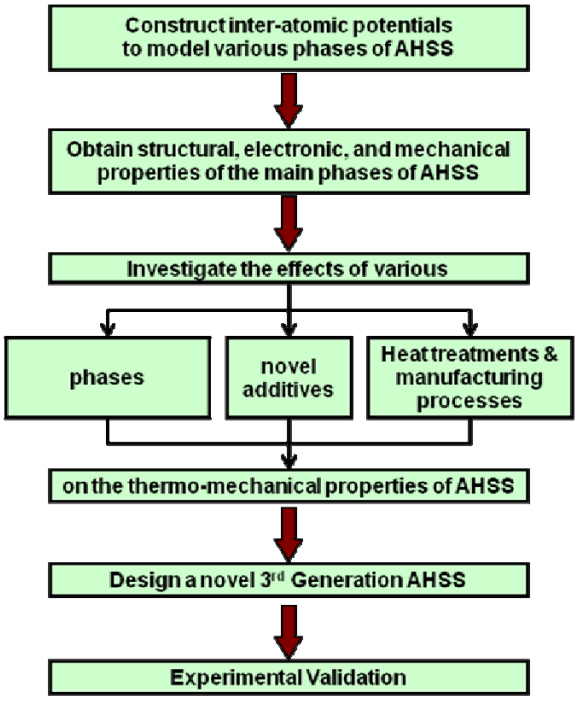

Figure 1. A flowchart showing the overall project procedure and technical approaches.

Computational Approach

We use a hierarchical, multiscale methodology to investigate the effect of nanoscale precipitates and additives to the overall strength and formability in steel-alloy design for automotive applications. In a hierarchical, multiscale framework, numerical methods are run independently at disparate length scales. Then, a bridging methodology such as statistical-analysis methods, homogenization techniques, or optimization methods are used to distinguish the pertinent cause-effect relations at the lower scale to determine the relevant effects for the next higher scale [E03]. One effective hierarchical method for multiscale bridging is the use of thermodynamically-constrained internal state variables (ISVs) that are physically based on microstructure-property relations [Coleman67, Rice71, Kestin70, Hasan95, Espinosa01, Gailly02]. We will adopt the strategy developed by Horstemeyer and his co-workers who used ISVs as a top-down hierarchical approach to bring the pertinent nanoscale, microscale, and mesoscale phenomena into the macroscale [Horst01, Horst03, Olson98, Olson00, Hao03, Hao04].

Critical issues being addressed include: selection of key combination of precipitates and matrices, interaction of precipitate and matrix phases and, ultimately, composition-structure-property relationship. At the electronic level, quantum-mechanical, first-principles simulations will be performed to investigate the interfacial interactions between matrix and the primary and the secondary precipitates. All first-principles, total-energy calculations and geometry optimizations are performed within the DFT [Kresse96, Kohn65] using Blöchl's all-electron projector augmented wave (PAW) method [Blochl94] as implemented by Kresse et al. [Kresse99]. For the treatment of electron exchange and correlation, we generally use the local density approximation (LDA) [Ceperley80, Perdew81] and sometimes the generalized gradient approximation (GGA) [Perdew96] depending on the accuracy required. The Kohn-Sham equations are solved using a preconditioned, band-by-band, conjugate-gradient (CG) minimization [Kresse93].

At the atomistic level, accurate atomistic simulations will be performed using efficient and reliable empirical interatomic potentials such as the MEAM [Baskes92, Daw84, Daw83] or FMEAM [Li03, Liu96] potentials. The interatomic potentials are constructed by optimizing the potential parameters to reproduce various experimental materials properties and atomic-force data from DFT calculations. Large-scale, atomistic simulations will be conducted to study the effect that size, shape, and volume fraction of different precipitates have on the thermo-mechanical properties of steel alloys. Many factors that govern the yield and hardening behavior of solids, such as, crack-tip propagation, dislocation nucleation, dislocation motion, and the interaction of dislocations with grain boundaries, will be investigated through these simulations. Results will be used to guide quantitative alloy composition designs to improve strength and formability of steel alloys.

FMEAM

In the FMEAM [Li03, Liu96], a force-matching method [Ercolessi94] is applied to the conventional embedded-atom method (EAM) [Daw84, Daw83]. Within the EAM approach, the total energy of the system can be written as

$$E = \sum_i E_i \tag{1}$$

where

$$E_i = \frac{1}{2}\sum_{j(\neq i)} V(r_{ij}) + F(n_i) \tag{2}$$

$V(r)$ is the pair interatomic potential, $F(n)$ is the embedding energy function, n_i is the total 'atomic density' at atom i from the surrounding atoms, and it is assumed that

$$n_i = \sum_{j(\neq i)} \rho(r_{ij}) \tag{3}$$

where $\rho(r)$ is the 'atomic density' around an isolated atom [Daw84].

Unlike the MEAM, the FMEAM approach does not use any analytic functional form for $\rho(r)$, $V(r)$, or $F(n)$. Instead, each of these functions is described as a set of control points, whose values are the parameters to be optimized. A cubic

spline function is used to interpolate the values between the control points. The control points are optimized by matching the forces of this potential to those of quantum-mechanical, *ab initio* calculations for a large set of different configurations. The potential parameters are simultaneously fit to several critical experimental data such as equilibrium lattice constant, cohesive energy, bulk modulus, and elastic constants.

MOO

A generic, MOO problem can be formulated as [Kim05, deWeck04]:

$$\begin{aligned} &\min\ \vec{J}(\vec{x}) \text{ s.t. } x \in S \\ &\text{where } \vec{J} = \left[J_1(\vec{x}) \cdots J_m(\vec{x})\right]^T \\ &\vec{x} = \left[x_1 \cdots x_n\right]^T \end{aligned} \tag{4}$$

Here, $\vec{J}$ is a column vector of *m* objectives, whereby $J_i \in \Re$. The individual objectives are dependent on a vector $\vec{x}$ of *n* design variables in the feasible domain *S*. The design variables are assumed to be continuous and vary independently. Typically, the feasible design domain is defined by the design constraints and the bounds on the design variables. The problem is to minimize all elements of the objective vector simultaneously. The most widely-used method for MOO is scalarization using the weighted-sum method. The method transforms the multiple objectives into an aggregated scalar objective function $\vec{J}$ that is the sum of each objective function J_i multiplied by a positive weighting factor w_i:

$$J(\vec{x}) = \sum_{i=1}^{m} w_i J_i(\vec{x}) \tag{5}$$

In this project, the overall goal is to develop FMEAM potentials for steel alloys. The individual objective functions are constructed from the normalized differences between the FMEAM-generated values and the target values:

$$J_i(\vec{x}) = \left[\frac{Q_i(x) - Q_i^0}{Q_i^*}\right]^2 \tag{6}$$

Here, Q_i is the physical quantity computed using the current FMEAM potential parameters and Q_i^0 is the target value to reproduce. The target values are usually experimental values, but the computed values from the first-principles method are chosen when the experimental data are not available. The normalization factor Q_i^* is a typical value for the given materials parameter and often $Q_i^* = Q_i^0$ is assumed. The overall objective function $J(\vec{x})$ can be minimized using usual multi-dimensional optimization routines. To avoid unnecessary complications, we use the *downhill simplex method,* [Press92] which requires only function evaluations, not derivatives.

Fe Interatomic Potential

The multi-objective optimization procedure was applied to develop a new interatomic potential for Fe based on FMEAM. We used the EAM potential by Chamati *et al.* [Chamati06] as the initial set of the parameters for our multi-objective optimization.

Figure 2 shows the cohesive energy of Fe atoms in a body-centered (bcc) crystal structure, its lowest-energy crystal structure, as a function of the nearest-neighbor distance. FMEAM potential calculations (blue open squares) are compared with DFT calculations (red open circles) and Rose equation-of-state (black line). The Rose equation-of-state is constructed from experimental data, namely optimum lattice constant, the cohesive energy, and the bulk modulus. Our results show that FMEAM potential for Fe reproduces experimental data extremely accurately over a wide range of separation distances. As it is generally accepted, DFT estimates the equilibrium bond length to be slightly smaller than the experimental value [Droogenbroeck04].

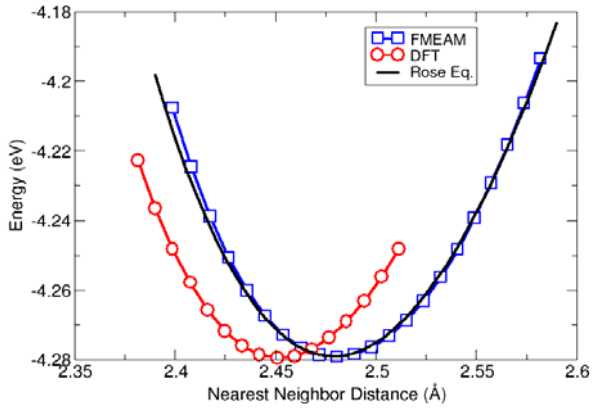

Figure 2. The cohesive energy of Fe atoms in a bcc crystal structure as a function of the nearest neighbor distance. FMEAM potential calculations (blue open squares) are compared with DFT calculations (red open circles), and Rose equation-of-state (black line) constructed from experimental data.

To validate the transferability of our new FMEAM potential, we calculated the cohesive energies of Fe atoms in other configurations such as face-centered cubic (fcc), and hexagonal close-packed (hcp) crystal structures as a function of the atomic volume. The results are summarized in Figure 3. Our results show that the new FMEAM potential for Fe atoms correctly predicts the order of stability among these common structures. In addition, the differences in equilibrium cohesive energies among these configurations are reasonably close to those of DFT calculations. However, FMEAM predicts the equilibrium atomic volumes for hcp and fcc to be similar to that of bcc while DFT predicts those values to be much smaller. Since other configurations are also relevant to various phases of steel alloys, we plan to further optimize the FMEAM potential for these configurations in the next year.

We also tested the transferability of the new FMEAM potential on a Fe dimer. Dimer interaction is an important indicator of the validity of empirical potentials because it is closely related to adsorption of atoms on surfaces, interfaces structures, and grain-boundary morphology and dynamics. As shown in Figure 4, our new FMEAM potential reproduces the total energy of a dimer reasonably well compared to more rigorous and time-consuming DFT calculations. The equilibrium bond length predicted by FMEAM potential is slightly larger than DFT's prediction. Also, the binding energy computed using the FMEAM potential is about 1.0 eV smaller than that of DFT calculations. Despite these minor discrepancies, these numbers represent an excellent validation result considering the fact that DFT calculations are known to underestimate the bond length and overestimate the binding energies compared to the experimental data [King94].

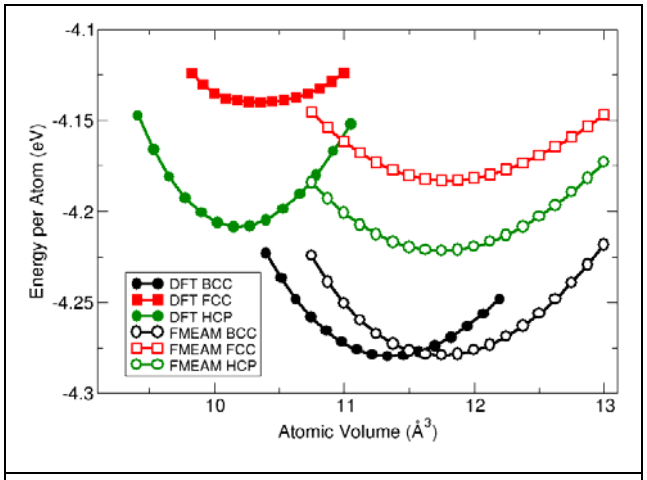

Figure 3. The cohesive energies of Fe atoms in bcc, fcc, and hcp crystal structures as a function of the atomic volume. The values reproduced with FMEAM potentials are compared with DFT calculations.

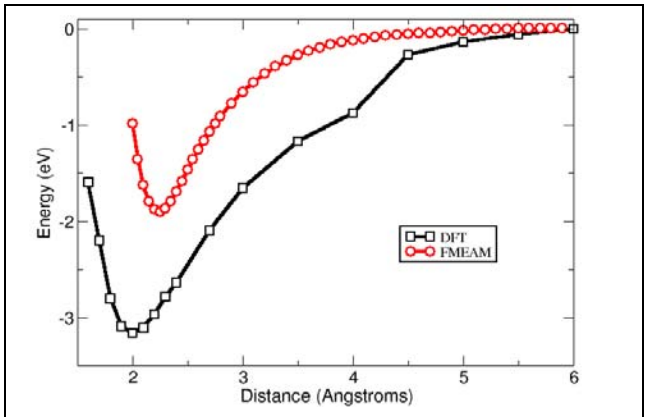

Figure 4. Total energy of a Fe dimer as a function of the separation distance. FMEAM potential calculations (red open circles) are compared with DFT calculations (black open squares).

C Interatomic Potential

The multi-objective optimization procedure was applied to develop a new interatomic potential for

C based on FMEAM. We used the MEAM potential by Lee [Lee06] as the initial set of the parameters for our multi-objective optimization. Figure 5 shows the cohesive energy of C atoms in a diamond structure as a function of the nearest-neighbor distance. The values obtained from FMEAM potential (black circles) are compared with the ones from DFT calculations (blue triangles). The Rose equation-of-state is constructed from experimental data, namely, optimum lattice constant, the cohesive energy, and the bulk modulus. Our results show that the energy values from FMEAM potential lie nearly on top of the Rose equation-of-state indicating that the new FMEAM potential for C atom works extremely well for C atoms in diamond lattice configuration, which is one of the most relevant structures for C in general.

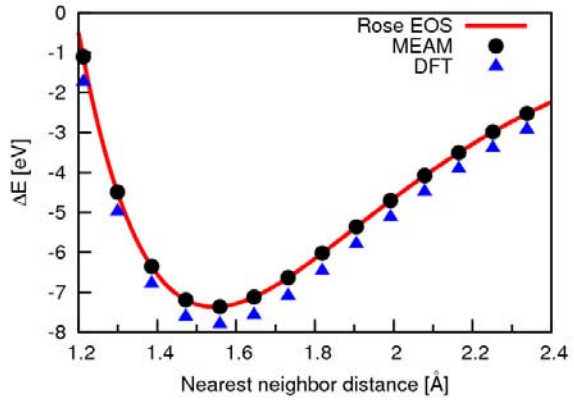

Figure 5. The cohesive energy of C atoms in diamond structure. The values obtained from FMEAM potential (black circles) are compared with the ones from DFT calculations (blue triangles) and the Rose equation-of-state constructed from experimental data.

Figure 6 shows the cohesive energies of C atoms in different configurations as a function of the atomic volume obtained from FMEAM potential calculations [Figure 6(a)] and DFT calculations [Figure 6(b)]. The plot shows that our FMEAM potential for C atoms correctly predicts that diamond structure is the lowest energy configuration. However, it fails to predict that the graphene sheet will have lower energy than cubic structure. Since graphene and graphite are also common and relevant structures for C atoms, we plan on improving this shortcoming in the next year.

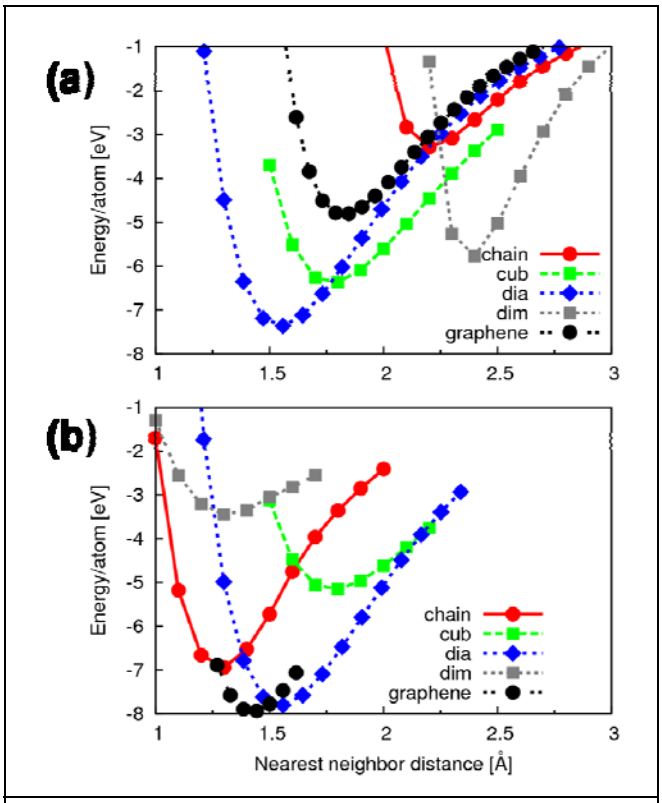

Figure 6. The cohesive energies of C atoms in different configurations as a function of the nearest-neighbor distance. (a) FMEAM potential calculations. (b) DFT calculations. The notations for configurations are: chain = linear chain, cub = cubic lattice, dia = diamond lattice, dim = dimer, grapheme = a single sheet of graphene.

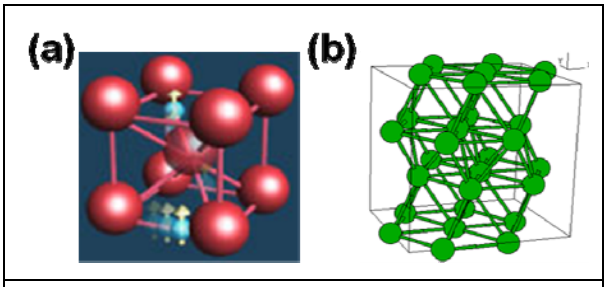

Figure 7. The crystal structure of Fe atoms. (a) bcc structure and (b) hcp structure.

Ferrite Phase

To establish the baseline of the simulations for the project, we performed the quantum-mechanical, first-principles calculations on the ferrite phase. Figure 7 shows the Fe atoms in bcc and hcp structures. It is well known that DFT total-energy calculation of Fe atoms using LDA to treat electron

exchange-correlation predicts the hcp nonmagnetic structure as the ground-state structure instead of the correct bcc ferromagnetic structure [Stixrude94]. We performed DFT calculations using different exchange-correlation functionals and pseudopotential models with and without spin polarization. Our results, summarized in Table 1, show that, when the full spin-polarized DFT calculations with the generalized gradient approximation (GGA) exchange-correlation energy were used, the correct ferromagnetic bcc structure is determined as the lowest-energy structure. We also found that the projector augmented wave (PAW) method is superior to the ultrasoft pseudopotential (US-PP) method as it gives much better energy differences between bcc FM and hcp NM structures. Our results also confirm previously reported calculations by Kresse *et al.* [Kresse99].

Table 1. Relative energy of Fe crystals in various crystal structures and magnetic states. Energy values are given in meV. PAW and US-PP denote the different methods to handle electron-ion interaction while LDA and GGA indicate the different methods to treat electron exchange-correlation:

	PAW[a]		US-PP[b]	
	LDA[c]	GGA[d]	LDA[c]	GGA[d]
bcc Fe NM	431	387	430	383
bcc Fe FM	151	**-66**	87	-238
fcc Fe NM	87	79	86	76
hcp Fe NM	0	0	0	0

[a]Projector augmented wave (PAW) method
[b]Ultrasoft pseudopotential (US-PP) method
[c]Local density approximation (LDA)
[d]Generalized gradient approximation (GGA)

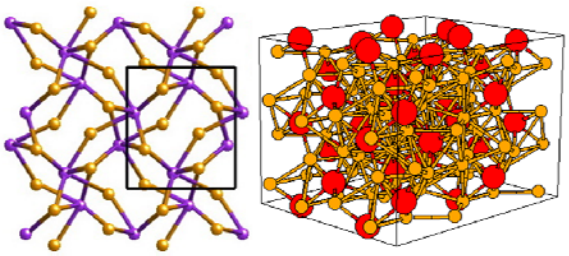

Figure 8. Two different views of the crystal structure of cementite. Gold spheres represent Fe atoms and red/purple spheres represent C atoms.

Table 2. Crystal structure parameters for cementite. *a*, *b*, and *c* are the lattice constants. *x*, *y*, and *z* are the relative coordinates for basis atoms.

	This work	Other[a]	Exp.[b]
a	5.03	5.06	5.09
b	6.72	6.74	6.74
c	4.47	4.51	4.53
C-x1	0.876	0.877	0.890
C-z1	0.438	0.440	0.450
Fe(I)-x2	0.035	0.038	0.036
Fe(I)-z2	0.837	0.837	0.850
Fe(II)-x3	0.176	0.176	0.186
Fe(II)-y3	0.068	0.068	0.063
Fe(II)-z3	0.332	0.332	0.328

[a]Chiou *et al.* [Chiou03]
[b]Fasiska *et al.* [Fasiska65]

Cementite Phase

The second main phase of the steel is the cementite (Fe_3C). We use the DFT method to investigate the materials properties of the cementite phase and its interactions with the ferrite phase. Figure 8 shows the structure of cementite phase which has the space group *Pnma* (No. 62) [Hahn83]. The unit cell contains four iron atoms in "first" positions [4 Fe(I)], eight iron atoms in "second" positions [8 Fe(II)], and four carbon atoms in large interstices [4 C], see Figure 8. The unit-cell structure of the cementite and the position of basis atoms are determined by the parameters listed in Table 2.

We performed DFT calculations to optimize the structure parameters listed in Table 2 simultaneously. The values obtained in the present work agree well with previously published results by Chiou *et al.* [Chiou03] and experimental values [Fasiska65]. Figure 9 shows the total energy of Fe_3C cementite as a function of the atomic volume. Our results indicate that the equilibrium volume for cementite is 151 $Å^3$ where the experimental value is 155 $Å^3$. Again, DFT calculations underestimate the equilibrium volume by 2.7%, confirming a well-known tendency of the DFT method

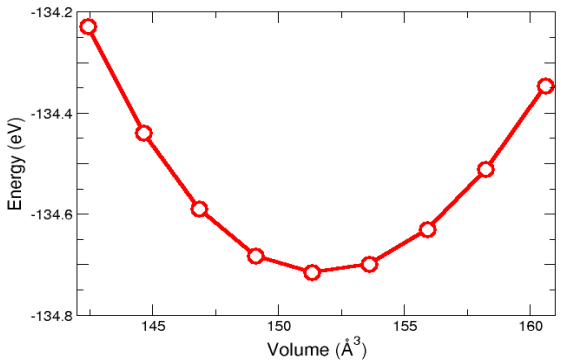

Figure 9. The total energy of cementite as a function of the atomic volume.

In the next year, we plan to perform large-scale, atomistic simulations of the interaction between the two main phases of steel, cementite and ferrite, using the FMEAM potentials developed in this project.

Conclusions

The goal of this project is to investigate the effect of nanoscale precipitates and novel additives to the overall strength and formability in steel-alloy systems. DFT calculations were performed on Fe-C alloy systems using the full spin-polarized LDAs to correctly account for the ferromagnetism in Fe atoms. We developed a new MOO methodology as a robust procedure to construct reliable and transferable interatomic potentials for steel-alloy systems. This MOO procedure was applied to construct transferrable interatomic potentials for Fe and C atoms using the FMEAM. We also established a basic framework for the accelerated development of reliable and efficient interatomic potentials for other combination of alloy systems to perform large-scale, realistic atomistic simulations. Full spin-polarized density-functional theory calculations have been performed on ferrite and cementite phases and compared with experiments.

This investigation should facilitate the design of a new generation of AHSSs by providing fundamental understanding of several critical issues that include the selection of key combinations of precipitates and matrices, interaction of precipitate and matrix phases and, ultimately, composition-structure-property relationship.

Presentations/Publications/Patents

1. Seong Jin Park, M.F. Horstemeyer, and Seong-Gon Kim, *"Atomistic Simulations for Steel Alloy Design"*, Colloquium at POSTECH, Pohang, KOREA, June 4, 2007.
2. Seong Jin Park, M.F. Horstemeyer, and Seong-Gon Kim, *"Atomistic Simulations for Steel Alloy Design"*, Seminar at Technical Research Laboratory of POSCO, Pohang, KOREA, June 5, 2007.

References

1. [Baskes92] M. I. Baskes, *"Modified embedded-atom potentials for cubic materials and impurities"*, Phys. Rev. B 46, 2727 (1992).
2. [Blochl94] P. E. Blöchl, Phys. Rev. B vol. 50, pp. 17953 (1994).
3. [Ceperley80] D. M. Ceperley and B. J. Alder, *"Ground State of the Electron Gas by a Stochastic Method"*, Phys. Rev. Lett. vol. 45, pp. 566—569 (1980).
4. [Chamati06] H. Chamati, N.I. Papanicolaou, Y. Mishin, D.A. Papaconstantopoulos, *"Embedded-atom potential for Fe and its application to self-diffusion on Fe (100)"*, Surf. Sci. vol. 600, pp. 1793—1803 (2006).
5. [Chiou03] W. C. Chiou, Jr., and E. A. Carter, *"Structure and stability of Fe3C-cementite surfaces from first principles,"* Surf. Sci. vol. 530, pp. 87—100 (2003).
6. [Coleman67] B. D. Coleman and M. E. Gurtin, *"Thermodynamics with internal state variables"*, J. Chem. Phys., vol. 47, 597—613 (1967).
7. [Daw83] M. S. Daw and M. I. Baskes, *"Semiempirical, Quantum Mechanical Calculation of Hydrogen Embrittlement in Metals"*, Phys. Rev. Lett. 50, 1285 (1983).
8. [Daw84] M. S. Daw and M. I. Baskes, *"Embedded-atom method: Derivation and application to impurities, surfaces, and other defects in metals"*, Phys. Rev. B 29, 6443 (1984).
9. [Droogenbroeck04] Joris Van Droogenbroeck, Karla Tersago, Christian Van Alsenoy and Frank Blockhuys, *"A systematic study of the effect of correlation, DFT functional and basis set on the structure of Roesky\u2019s ketone"*, Chem. Phys. Lett. vol. 399, pp. 516—521 (2004).

10. [deWeck04] O. L. de Weck, *"Multiobjective Optimization: History and Promise (The Third China-Japan-Korea Joint Symposium on Optimization of Structural and Mechanical Systems",* Kanazawa, Japan, (2004).
11. [E03] W. E and B. Engquist, *"Multiscale Modeling and Computation"*, Notices of the AMS, vol. 50, 1062-1070 (2003).
12. [Espinosa01] H. D. Espinosa, H. -C. Lu, P. D. Zavattieri, and S. Dwivedi, *"A 3-D Finite Deformation Anisotropic Visco-Plasticity Model for Fiber Composites,"* J. of Composite Materials, vol. 35, 369-410 (2001).
13. [Ercolessi94] F. Ercolessi and J.B. Adams, *"Interatomic potentials from first-principles calculations: the Force-Matching method"*, Europhys. Lett. vol. 26, pp. 583 (1994).
14. [Fasiska65] E. J. Fasiska and G. A. Jeffrey, *"On the cementite structure"*, Acta Cryst., vol. 19, 463—471 (1965).
15. [Gailly02] B. A. Gailly and H. D. Espinosa. *"Modelling of Failure Mode Transition in Ballistic Penetration with a Continuum Model Describing Microcracking and Flow of Pulverized Media*", Int. J. for Numerical Methods in Engineering, vol. 54, 365—398 (2002).
16. [Hahn83] T. Hahn (ed.), *International Tables for Crystallography*, vol. A, Reidel, Dordrecht (1983).
17. [Hao03] Su Hao, Brian Moran, Wing Kam Liu, and Gregory B. Olson, *"A hierarchical multi-physics model for design of high toughness steels"*, Journal of Computer-Aided Materials Design, vol. 10, 99—142 (2003).
18. [Hao04] Su Hao, Brian Moran, Wing Kam Liu, and Gregory B. Olson, *"Multi-scale constitutive model and computational framework for the design of ultra-high strength"*, Computer Methods in Applied Mechanics and Engineering, vol. 193, 1865—1908 (2004).
19. [Hasan95] O. A. Hasan and M. C. Boyce, "A Constitutive Model for the Nonlinear Viscoelastic Behavior of Glassy Polymers," Polymer Engng. and Sci., vol. 35, 331—344 (1995).
20. [Horst01] M. F. Horstemeyer, S. J. Plimpton, and M. I. Baskes. *"Size Scale and Strain Rate Effects on Yield and Plasticity of Metals"*, Acta Matallurgica, vol. 49, 4363—4374 (2001).
21. [Horst03] M. F. Horstemeyer and P. Wang. *"Cradle-to-grave simulation-based design incorporating multiscale microstructure-property modeling: Reinvigorating design with science"*, Journal of Computer-Aided Materials Design, vol. 10, 13—34 (2003).
22. [IISI06] *Advanced high strength steel (AHSS) application guidelines*, prepared by International Iron & Steel Institute, September 2006.
23. [Kim05] I. Y. Kim and O. L. de Weck, "Structural and Multidisciplinary Optimization", vol. 31, 105 (2005).
24. [King94] R. D. King-Smith and David Vanderbilt, *"First-principles investigation of ferroelectricity in perovskite compounds"*, Phys. Rev. B vol. 49, pp. 5828—5844 (1994).
25. [Kohn65] W. Kohn and L. J. Sham, "*Self-consistent Equations Including Exchange and Correlation Effects*", Phys. Rev. Vol. 140, pp. A1113—A1138 (1999).
26. [Kresse93] G. Kresse and J. Hafner, *"Ab initio molecular dynamics for liquid metals"*, Phys. Rev. B vol. 47, pp. 558 (1993).
27. [Kresse96] G. Kresse and J. Furthmüller, *"Efficient iterative schemes for ab initio total-energy calculations using a plane-wave basis set"*, Phys. Rev. B 54, 11169 (1996).
28. [Kresse99] G. Kresse and D. Joubert, "*From ultrasoft pseudopotentials to the projector augmented-wave method*," Phys. Rev. B vol. 59, pp. 1758 (1999).
29. [Kestin70] J. Kestin and J. R. Rice, *"Paradoxes in the application of thermodynamics to strained solids"*, in "A Critical Review of Thermodynamics", edited by E.G. Stuart, B. Gal-Or, and A. J. Brainard, Mono Book Corp., Baltimore, 275-298 (1970).
30. [Lee06] Byeong-Joo Lee, *"A modified embedded-atom method interatomic potential for the Fe—C system,"* Acta Materialia, vol. 54, pp. 701—711 (2006).
31. [Li03] Youhong Li, Donald J. Siegel, James B. Adams, and Xiang-Yang Liu, "*Embedded-atom-method tantalum potential developed by the force-matching method,*" Phys. Rev. B vol. 67, pp. 125101 (2003).
32. [Liu96] Xiang-Yang Liu, James B Adams, Furio Ercolessi and John A Moriarty, "*EAM potential for magnesium from quantum mechanical forces,*" Modelling Simul. Mater. Sci. Eng. vol. 4, pp. 293—303 (1996).
33. [Olson98] G. Olson. *"Systems design of hierarchically structured materials: Advanced*

steels", Journal of Computer-Aided Materials Design, vol. 4, 143—156 (1998).
34. [Olson00] G. Olson. *"New age of design"*, Journal of Computer-Aided Materials Design, vol. 7, 143--144 2000).
35. [Perdew81] J. P. Perdew and A. Zunger, *"Self-interaction correction to density-functional approximations for many-electron systems"*, Phys. Rev. B 23, 5048 (1981).
36. [Perdew96] J. P. Perdew, K. Burke, and M. Ernzerhof, *"Generalized Gradient Approximation Made Simple"*, Phys. Rev. Lett. vol. 77, pp. 3865 (1996).
37. [Press92] William H. Press and Brian P. Flannery and Saul A. Teukolsky and William T. Vetterling, *Numerical Recipes in C: The Art of Scientific Computing*, 2nd ed., Cambridge University Press, Cambridge (1992).
38. [Rice71] J.R. Rice, *"Inelastic constitutive relation for solids: An internal variable theory and. its application to metal plasticity"*, J. Mech. Phys. Solids, vol. 19, 433—455 (1971).
39. [Stixrude94] Lars Stixrude, R. E. Cohen, and D. J. Singh, "Iron at high pressure: Linearized-augmented-plane-wave computations in the generalized-gradient approximation", Phys. Rev. B vol. 50, pp. 6442—6445 (1994).

6. AUTOMOTIVE METALS – CROSS-CUTTING

A. Magnesium Research and Technology Development

Principal Investigator: Eric A. Nyberg
Pacific Northwest National Laboratory (PNNL)
P.O. Box 999, Richland, WA 99352
(509) 372-2510; fax (509) 376-1093; e-mail: Eric.Nyberg@pnl.gov

Technology Area Development Manager: Joseph A. Carpenter
(202) 586-1022; fax (202) 586-1600; e-mail; joseph.carpenter@ee.doe.gov

Expert Technical Monitor: Philip S. Sklad
(865) 574-5069: fax: (865) 576-4963; e-mail: skladps@ornl.gov

---

Contractor: PNNL
Contract No.: DE-AC06-76RL01830

Objective

- The Mg Research and Technology Development (MR&TD) project is aimed at increasing the use of the lightest structural metal, magnesium (Mg), in automotive applications.
- Increase awareness and familiarity of Mg as a viable option for automotive applications.
- Support the United States Automotive Materials Partnership's (USAMP) Mg Front End Research and Development (MFERD) project (see 6.C) in collaboration with China and Canada.
- Compile, document and evaluate state-of-the-art R&D in Mg research around the world as a resource to determine where U.S. government resources should be directed.

Approach

- Serve as the MFERD U.S. Project Technical Committee (PTC) Chairman, advising the U.S. Project Steering Committee (PSC) member of on-going activities by the PTC and project tasks.
- Assist in the coordination of U.S. MFERD project meetings and the international three-country meetings.
- Evaluate proposals and oversee the effectiveness of the nine tasks of the MFERD project.
- Conduct and report on the gaps in international research related to Mg R&D.
- Develop and maintain the Mg R&D Bibliographic Database located at Mg.pnl.gov.

Accomplishments

As the U.S. Project Technical Committee (PTC) chairperson, I assumed responsibility to serve as liaison between the project Task Leaders and the U.S. Project Steering Committee (PSC) representative, Dr. Joseph Carpenter, from the DOE Office of Vehicle Technologies (DOE-OVT). In this role, I performed the following activities:

- Coordinated and reviewed progress by the nine U.S. Task Leaders.
- Participated in quarterly international conference calls with other PTC members from China and Canada.
- Co-wrote the U.S. and International Semi-Annual and Annual MFERD Project Reports to DOE.
- Reviewed the U.S. Task Leaders' annual presentations held at United States Council for Automotive Research (USCAR) headquarters on 10/30/07.
- Organized the first annual Task Leaders' meeting which received favorable reviews by the participants and DOE.

- Co-authored a paper with other MFERD PTC members that will be presented at the TMS annual meeting in 2008.
- Developed and maintained a publicly-available database/bibliography on Mg R&D.
- Presented the opening plenary talk on Mg research in North America at the 2006 International Conference on *Mg and Its Alloys* in Dresden, Germany (November 2006).
- Co-authored a proposal for a North American Mg Network of Excellence with colleagues from Oak Ridge National Laboratory (ORNL, P. Sklad) and CANMET (J. Jackman).

Future Direction

- Primary future work on the MFERD project will be to evaluate progress of the MFERD tasks, participate in committee meetings, report results and make recommendations to the PSC.
- Develop resources that can be used at PNNL and ORNL in support of the MFERD project.
- Evaluate and propose Mg R&D activities that are unique and necessary.
- Serve as the TMS Mg Light Metals Committee Vice-Chairman and Symposium co-organizer.

Introduction

The primary purpose of this project is to support the Canada-China-U.S. collaborative project entitled "Mg Front End Research and Development" (MFERD; see 6.C). The goal of the MFERD project is to develop key enabling technologies for a lightweight, Mg, front-end body structure and other body applications. The MFERD project will develop enabling technologies in high-integrity casting, wrought-Mg processing, Mg and dissimilar-metal joining and corrosion, and generate scientific understanding in corrosion science, crash-energy management, fatigue, and noise, vibration and harshness (NVH) performance. The project will also provide a platform for Mg research collaboration in Canada, China, and the United States.

Background

The primary goal of the MFERD project is to develop key enabling technologies (body casting, extrusion, sheet & joining) and knowledge base (crashworthiness, NVH, durability, and corrosion) for primary (load-path) body applications of Mg alloys. The following are some specific objectives:

- Define materials and develop manufacturing processes for Mg body castings, extrusions, sheet, and joining technologies.
- Develop knowledge base and define Mg-body technical requirements in crashworthiness, NVH, durability, corrosion, and surface finishing.
- Enhance the infrastructure for integrated computational materials engineering for Mg applications, including alloy design/ development, process optimization, and component manufacturing (see 6.F to 6.G).
- A total life-cycle analysis showing the net benefit of vehicle lightweighting, using Mg vs. energy consumption, emission, and pollution in Mg production.
- High-quality professionals and students educated in materials science, engineering, and Mg research and development (R&D) infrastructure in Canada, China, and the United States.
- Establish automotive OEM / supplier / academia collaboration in Mg-body applications.

PNNL Approach to Supporting MFERD Project and Database Development

As the U.S. Project Technical Committee Chairman, I have participated in all project-related meetings since the initial three-country meeting held in Dearborn, MI in October 2005. The continuity and background developed because of this participation has made me uniquely qualified to advise the U.S. Project Steering Committee representative (Dr. Joseph A. Carpenter, Jr.) on the technical issues, task status, and cultural complexities that can and will develop as the project matures.

Other related activities include:

- Attended International Mg Workshop at Johns Hopkins University's *Center for Advanced Metallic and Ceramic Systems*, sponsored by the Army Research Laboratory (Baltimore, MD).
- Reviewed two international proposals: a Canadian proposal to develop a "*Center of Excellence*" on Mg research at the University of British Columbia and another for the Department of Manufacturing Engineering and Engineering Management at the City University in Hong Kong.

Conclusions

This technical-support project is aimed at effectively assisting in the management of the U.S. portion of the three-country MFERD project. To date, we have completed the first full year of the MFERD project and the annual report will be submitted by the end of the calendar year. Additionally, this project will serve as a resource for future funding decisions related to DOE-funded Mg projects.

Current and Future Work

Future work will be to evaluate progress of the tasks, participate in committee meetings, report results and make recommendations to the U.S. PSC Chairman.

Currently, we are in the midst of organizing plans for the 2nd Annual Task Leaders' meeting that will be held in China on April 2 and 3, 2008. This meeting will follow the joint PSC/PTC meeting. The U.S. and Canadian Task Leaders and PTC Chairmen plan to visit several facilities and organizations in China that are involved in the MFERD project.

Research opportunities inside and out of PNNL will be reviewed and proposed to DOE in consideration for future funding opportunities. Continue to manage the publicly-available Mg R&D Database.

Issue final version of the Mg Gap Analysis Report to the DOE Technology Area Development Manager, providing recommendations on critical areas of R&D funding that are not being adequately addressed.

Presentations

"*Mg Automotive R&D in North America*", J. Jackman, J. Carpenter, E. Nyberg, at the Intl. Conference on Mg Alloys and their Applications, Dresden, Germany, November 6, 2006.

B. Magnesium Front-End Design and Development (AMD 603[i])

Principal Investigator: Alan A. Luo
General Motors (GM) Research & Development Center
MC 480-106-212
30500 Mound Road
Warren, MI 48090-9055
(586) 986-8303; fax: (586) 986-9204, e-mail: alan.luo@gm.com

Program Technical Administrator: Robert C. McCune
Robert C. McCune and Associates, LLC
5451 S. Piccadilly Circle
West Bloomfield, MI, 48322-1446
(248) 661-0085; fax: (248) 661-8718; e-mail: robert.mccune@sbcglobal.net

Technology Area Development Manager: Joseph A. Carpenter
(202) 586-1022; fax: (202) 586-1600; e-mail: joseph.carpenter@ee.doe.gov

Field Project Officer: Aaron D. Yocum
(304) 285-4852; fax (304) 285-4403; email: aaron.yocum@netl.doe.gov

Expert Technical Monitor: Philip S. Sklad
(865) 574-5069; fax: (865) 576-4963; e-mail: skladps@ornl.gov

---

Contractor: United States Automotive Materials Partnership (USAMP)[i]
Contract No.: DE-FC05-02OR22910 through the National Energy Technology Laboratory

---

Objectives

The goal of the project is the engineering design/analysis and technical cost modeling for magnesium (Mg)-intensive, front-end structures for selected unibody and body-on-frame (BOF) vehicle architectures with the following design targets:

- Mass reduction: 60% (approx. 40 kg) lighter than comparator steel baseline structures and 35% (approx. 16 kg) lighter than aluminum (Al) structures for mid-size passenger cars at comparable strength and crashworthiness.
- Vehicle mass distribution: Shift the front-to-rear mass ratio by -1/+1 toward 50/50 for the rear-wheel drive, unibody donor architecture.
- Demonstration via technical cost modeling of a maximum of $8/kg (of mass saved) cost penalty (100,000 vehicles/year production volumes), via part consolidation using large Mg castings (e.g., dash panel, shotguns) and attractive pricing of Mg in world markets.
- Matched or improved key performance characteristics such as stiffness, durability and noise, vibration and harshness (NVH) of the Multi-Materials Vehicle (MMV, see 12.D) 'donor' vehicle as determined via simulation.

Approach

Task 1. Mg Front-End Design Deliverables: The Mg front-end design and analysis for the two selected vehicle architectures will consist of the following deliverables expected from the supplier with appropriate industry inputs:

- All computer-assisted design (CAD) and computer-assisted engineering (CAE) data.
- Bill-of-materials (materials properties and standards).

- Definition of interfaces to steel structure.
- Typical sections.
- Corrosion-prevention strategies and designs.
- Typical sections.
- Performance assessments:

  -- Frontal Crash: 35-miles-per-hour (mph), flat, frontal New Car Assessment Program (NCAP) and 40-mph Insurance Institute for Highway Safety (IIHS) Front Offset Deformable barrier (FODB).

  -- Stiffness (dynamic and static).

  -- Durability.
- Mass.
- Assembly.
- Impact on body-shop assembly.
- Assembly sequence.
- Paint-shop impact.
- Recycling strategies with attention to disassembly.
- Repair procedures, both in-plant and during use.

The design exercise will be staged to coincide with data being developed with regard to materials and processes as part of Mg Front-End Research and Development (AMD 604, see 6.C). The staging of the design project is summarized below:

A. Unibody Front-End Design Staging – Three Design Iterations

(1) First Design Iteration (6 months) based upon:
- Existing literature and USAMP material-property and performance data.
- Property data of experimental alloys provided by the USAMP team.
- Commercially-available manufacturing technologies, and
- Promising, non-commercial-scale, manufacturing processes selected by the USAMP team.

(2) Second Design Iteration (one year after the first iteration milestone) based upon:
- Materials-property data generated and/or validated in the AMD 604 project.
- Manufacturing processes developed and/or validated in the AMD 604 project, and
- Performance knowledge base (corrosion, crashworthiness, NVH, etc.) developed in the AMD 604 project.

(3) Third Design Iteration (one year after the second iteration milestone) based upon:
- Design optimization including part and function integration using all materials and manufacturing enabling technologies and performance knowledge base (corrosion, crashworthiness, NVH, etc.) developed in the AMD 604 project; and
- The manufacturing processes developed and/or validated in the AMD 604 project and the best practices and Mg technologies developed in the world-wide market.

B. Body-on-Frame Front-End Design Approach

- Utilize well-developed, Ford/USAMP designs for the Mg, upper-radiator support and Mg “shotgun” structure developed in collaboration with the Ultra Large Casting Project (see 3.C).
- The design effort in this project is focused on the attachment schemes at the A-pillar/shotgun interface and, additionally, the exploration of more part integration with the rest of the body structure.

- The BOF design is being carried out in parallel to the unibody design and is progressive in nature, incorporating the learning from the AMD 604 project and the new technologies developed in the industry during the project design phase (2.5 years).

Task 2. Technical Cost Modeling

The approach uses process-based, technical cost modeling [1] to provide the following deliverables for the two front-end designs (unibody and BOF):

- Determine primary Mg production costs, sustainability and market impact of the electrolytic vs. direct thermal-reduction (Pidgeon) processes.
- Provide a detailed cost analysis and report for all the components and assembly identified by Task 1 for both the unibody and BOF designs.
- Current steel designs for both the unibody and BOF are the comparators for weight and cost.
- The work is divided into two phases. Phase I includes a primary Mg production analysis and the component cost of individual parts for each design. Phase II includes the assembly of the components to each other and to the main body structure. Phase II will also incorporate any updates to Phase I determined by design changes or information gathered by AMD 604.
- This cost analysis includes surface finishing, machining or any other process each component requires to allow it to be attached or integrated with the rest of the front-end assembly. The overall cost of the assembly including components is provided for each design as compared to the steel baseline.

Accomplishments

- OEM project kickoff: November 1, 2006.
- Supplier kick-off and request for proposals: November 28, 2006.
- Selection of Cosma Engineering of Troy, MI, Task 1 (Design).
- Selection of Camanoe Associates of Cambridge, MA, Task 2 (Technical Cost Modeling).
- "Donor" vehicle baseline math data and vehicle design/performance targets provided to suppliers for design and cost modeling: GM, rear-wheel drive (RWD), unibody construction and Ford, BOF, pickup truck.
- Initial design for the unibody Mg front end was completed with stiffness and concept level crash assessments, as well as bill-of-materials.
- Specific progress against design and performance targets:

  -- (Unibody) part-count reduction: 50 pieces (29 Mg Front End vs. 79 steel baseline).

  -- Mass reduction: 37 kg (45%).

  -- Materials technologies: 15 castings, 3 extrusions, 9 formed sheets.

  -- Initial joining strategies developed.

  -- Crashworthiness (unibody): IIHS Deformable Barrier – maximum structural intrusions "acceptable" or "good" rating via simulation. NCAP, 35-mph, full frontal – deceleration pulse comparable to steel baseline.

  -- Modal analysis – full body-structure-only modes occur at higher frequencies than baseline.

  -- (BOF) – part count reduction: 7.

  -- Mass reduction (45%).
- Technical Cost Modeling: Detailed statement of work concluded; team kickoff; developed modeling framework and identified key variables.

Future Direction

- The design supplier (Cosma Engineering) will present its 1st total design iteration for review on December 10, 2007.

- The interim design reviews (four to date) have been used to track design progress and also to provide feedback to the designer with regard to materials and process feasibility or criticisms of the design itself. These design reviews are expected to continue as the next design iteration proceeds.
- The second design iteration calls for more incorporation of emerging Mg property data generated by the companion AMD 604.
- Materials performance, particularly the ductility and failure of cast metals, is expected to take on more significance due to the relatively large reliance on large castings for the initial design.
- Technical cost modeling will provide insight into the viability of the reliance on large castings.
- The anticipated manufacturing paradigm is also expected to have impacts on such areas as surface pretreatment and finishing, joining and corrosion protection.

Introduction

AMD 603, Mg Front-End Design and Development, is a complementary project to both the AMD 604 (Mg Front-End Research and Development) and the USAMP Multi-Materials Vehicle (MMV) projects. Whereas AMD 604 is predicated on development of enabling Mg technologies on an international scale, involving a wide range of suppliers and organizations, AMD 603 is confined to the OEM participants of USAMP (i.e., Chrysler, Ford and GM) and selected suppliers focused on design specifics and technical cost modeling.

The goal of AMD 603 is the engineering design and computer-aided analysis of Mg-intensive, front-end structures for both a RWD unibody and BOF vehicle architectures that are aimed at meeting defined targets for weight reduction, performance (including vehicle weight redistribution for the unibody design, durability, corrosion resistance, crashworthiness, NVH targets) and subassembly cost within defined parameters (i.e., a maximum cost penalty of $8 per kg of weight saved).

The OEM steering committee for the project determined that there would be two principal tasks: 1.) the actual physical design of the Mg-intensive structures envisioned, taking into account materials and their properties, assumptions regarding manufacturing and a virtual design permitting use of advanced CAE tools aimed at such requirements as crashworthiness, stiffness and NVH (noise, vibration and harshness), and 2.) Technical cost modeling to permit a better assessment of the costs of materials and mass production of the assemblies as designed. Definition of work statements and selection of suppliers for these tasks were the first items to be accomplished in the program.

The Statement of Work for Task 1 (Design) included assumptions declaring those elements of the design envelope and performance expectations provided by the OEM participants (e.g., GM and Ford designs for the candidate structures, based on present materials of use and manufacturing methods) and specific requirements as intended deliverables for the contract, summarized in the Approach section above.

The following sections describe, in greater detail, key technical accomplishments of the project occurring during fiscal year (FY) 2007.

Project Technical Structure, Launch and First-Year Achievements

The development of precise work statements for design and technical cost modeling were critical to the execution of the project, and were largely compiled before the project was unveiled to the supplier community in November, 2006. Four design and three cost-modeling proposals were received in response to the public announcement of the project and request for proposals. In early 2007, potential suppliers were interviewed. Cosma Engineering of Troy, MI was selected to conduct the design portion and Camanoe Associates of Cambridge, MA was selected to conduct the technical cost modeling. The donor vehicles, previously selected by the OEM team based on availability of design data and willingness of the respective OEMs to release such data for purposes of the project, are a GM RWD sedan for the unibody architecture and a full-size, Ford, pick-up truck for the BOF architecture. Relevant baseline CAD data and performance expectations were provided by the OEMs to Cosma at the outset. The

current Ford design utilizes a Mg radiator-support structure which has been described elsewhere [2]. Ultra-large Mg castings are also being evaluated for this vehicle structure as the subject of the USAMP AMD 406 project (Ultra-Large Castings, see 3.C).

The steel-baseline, unibody structure for the donor vehicle front end is illustrated in Figure 1 for purposes of showing the design envelope under consideration.

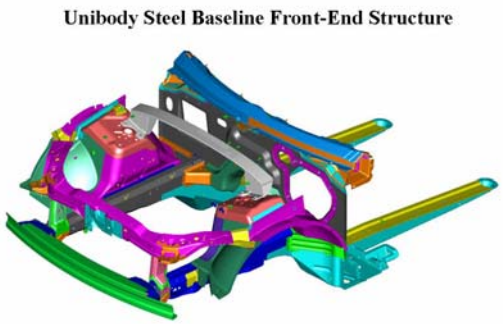

Figure 1. Unibody steel front-end baseline structure for GM donor vehicle.

Similarly, the baseline steel structure for the Ford donor vehicle is illustrated in Figure 2.

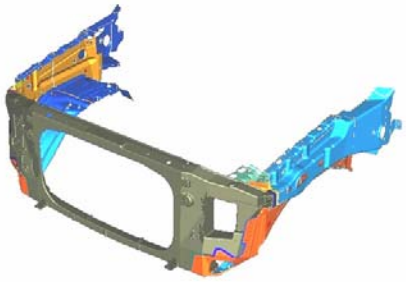

Figure 2. Baseline Ford BOF donor-vehicle steel structure with Mg radiator support.

The initial focus for the designers was the unibody structure, given that the BOF structure was more incremental in its development. The phasing of the design project called for an initial design to be completed six months after receipt of order. This design was to be predicated on "best available" materials properties and manufacturing methods as recommended by the project team. Ultimately, refinements and improvements in the design will occur as knowledge of material properties and manufacturing matures.

Nevertheless, the first unibody design iteration has yielded encouraging projections on most issues. The details are shown in the Accomplishments section above; however, in summary, the design yielded a reduction in part count from 79 to 29, with a weight reduction of 37 kg (45%). The Mg materials technologies utilized were: castings, 15; extrusions, 3; and formed sheet, 9. Other parts included isolators that were not Mg alloys.
Initial concept predictions came in the area of crashworthiness, where, after several iterations of design chiefly through alteration of cross-sectional thicknesses and shapes, it was found that if Mg of sufficient ductility and strength can be developed, then Mg unibody structures could be designed that meet acceptable structural performance for intrusion in IIHS, 40-mph, offset barrier and full-frontal impact at 35 mph. However, these initial results were based on Mg material performance of infinite ductility and no fracture in high-rate deformation (typically Mg does not behave with high ductility). Hence, the results are encouraging but not verified, and must be revisited as materials-property information is improved through the companion AMD 604 and AMD 702/703 projects (see 6.F). Further improvements are also expected as knowledge regarding joining, particularly employing structural adhesive bonding as a supplement to fasteners (e.g., self-piercing rivets), is developed.

The BOF structure has received considerable attention within USAMP as a candidate for a Mg-intensive front end, taking advantage of the large Mg radiator-support assembly already designed and in use by Ford. Attention has focused on integrating the inner fender or "shotgun" structures developed in USAMP AMD 406 (Ultra-Large Castings Project) [3], with attention given to assessing the capabilities of a number of advanced, high-integrity casting processes. Novel corrosion-protection schemes and parts-consolidation strategies are also under investigation. An example of a singe-piece, Mg alloy "shotgun" structure is shown in Figure 3.

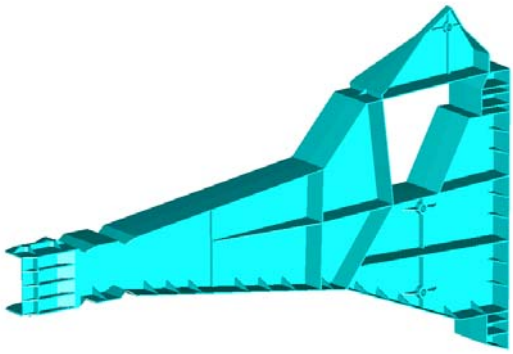

Figure 3. Structural Mg alloy "shotgun" structure designed for the Ford donor vehicle.

Support of the ongoing design activity on this type of structure by Cosma Engineering has, therefore, focused on methods of joining and structural adaptations to accommodate the types of mechanical fasteners envisioned. Successful implementation of the large castings and existing radiator support would effectively reduce the major portion of the front-end structure to three large Mg castings with associated joining hardware.

Conclusions

AMD 603 (Mg Front End Design and Development) was launched in late 2006, and in early 2007 enrolled suppliers for design/engineering and technical cost modeling. Results of the first design iteration, while encouraging, are constrained by limited understanding of the mechanical performance of candidate materials (chiefly Mg-alloy castings) under crash conditions, which are paramount in such a design exercise. Design targets for part-count reduction are similarly encouraging, and weight reduction, while appreciable (e.g., 45% relative to baseline steel), is expected to improve further as material properties are improved and physical designs are optimized.

Presentations/Publications

Mention of the AMD 603 Project has been included in the following reviews of the larger AMD 604 project:

1. A. Luo, E. Nyberg, K. Sadayappan and W. Shi, "Mg Front End Research & Development - A Canada-China-USA Collaborative Project", TMS Annual Meeting, Orlando, FL, USA, February 25 – March 1, 2007.
2. A. Luo, R. McCune, R. Beals, S. Logan, E, McCarty, J. Allison, M. Maj, D. Wagner, T. Lee, R. Osborne, L. Ouimet, J. Quinn and R. Verma, "The USAMP Mg Front End Program - Design and Enabling Technology Development", International Mg Association Mg in Automotive Seminar, Livonia, MI, USA, March 28, 2007.
3. A. Luo, R. McCune, R. Beals, S. Logan, E. McCarty, J. Allison, M. Maj, D. Wagner, T. Lee, R. Osborne, L. Ouimet, J. Quinn and R. Verma, "Mg Front End Development - USAMP Activities", Society of Automotive Engineers (SAE) 2007 Congress, Detroit, Michigan, USA, April 16-19, 2007.

References

1. R. Kirchain and F.R. Field III, "Process-Based Cost Modeling: Understanding the Economics of Technical Decisions," Encyclopedia of Materials Science and Engineering, 2001.
2. J. S. Balzer, P. K. Dellock, M. H. Maj, G. S. Cole, D. Reed, T. Davis, T. Lawson and G. Simonds, "Structural Mg Front End Support Assembly," SAE Paper No. 2003-01-0186 (2003).
3. U.S. Department of Energy, USAMP AMD 406 Annual Report (2007).

Acknowledgements

The success of this project is due to the dedicated efforts of team members at Ford, Chrysler, and General Motors, as well as the suppliers Cosma Engineering and Camanoe Associates. The continuing support of our respective organizations and the US Department of Energy is gratefully acknowledged.

[i] Denotes project 603 of the Automotive Materials Division (AMD) of the United States Automotive Materials Partnership (USAMP), one of the formal consortia of the United States Council for Automotive Research (USCAR) set up by Chrysler, Ford and General Motors (GM) to conduct joint, pre-competitive research and development. See www.uscar.org.

C. Magnesium Front-End Research and Development (AMD 604[i])

Principal Investigator: Alan A. Luo
General Motors (GM) Research & Development Center
MC 480-106-212
30500 Mound Road
Warren, MI 48090-9055
(586) 986-8303; fax: (586) 986-9204; e-mail: alan.luo@gm.com

Program Technical Administrator: Robert C. McCune
Robert C. McCune and Associates, LLC
5451 S. Piccadilly Circle
West Bloomfield, MI, 48322-1446
(248) 661-0085; fax: (248) 661-8718; e-mail: robert.mccune@sbcglobal.net

Technology Area Development Manager: Joseph A. Carpenter
(202) 586-1022; fax: (202) 586-1600; e-mail: joseph.carpenter@ee.doe.gov

Field Project Officer: Aaron D. Yocum
(304) 285-4852; fax (304) 285-4403; email: aaron.yocum@netl.doe.gov

Expert Technical Monitor: Philip S. Sklad
(865) 574-5069; fax: (865) 576-4963; e-mail: skladps@ornl.gov

---

Contractor: United States Automotive Materials Partnership (USAMP)[i]
Contract No.: DE-FC05-02OR22910 through the National Energy Technology Laboratory

---

Objective

The goal of this US-Canada-China collaborative project is the concurrent development of key enabling materials and manufacturing technologies and the accompanying performance knowledge base to permit design and implementation of magnesium (Mg)-intensive, automotive-body, front-end structures having greatly reduced mass, but with performance and cost comparable to sheet-steel baseline structures.

Two aspects of this project are unique within the USAMP:

- The focus is on entire "front-end" structures as the developmental object, in contrast to individual components, thereby offering critical, vehicle-level benefits in terms of mass distribution and performance while challenging the technical community to devise materials and manufacturing approaches to permit mass production of such structures at reasonable cost.

- Establishment of an international effort enlisting the best scientific and engineering expertise in Mg technology from the United States, Canada and China in a first-of-its-kind, global collaboration.

Approach

- Organization and Administration: Establishment of organizational and technical steering committees and systematic management of information and activities in a global environment.

- Partitioning of Projects: Separation of the design function into a separate USAMP project (AMD 603, see 6.B) as well as Integrated Computational Materials Engineering - ICME (AMD 702 and 703, see 6.F), to facilitate handling of original equipment manufacturer (OEM)-sensitive design data and to permit a broader, more uni-

versal approach to ICME. Further partitioning by subject-matter expertise and capabilities. The international project, additionally, has a task for life-cycle analysis, in which USAMP is not participating (see 12.A).

- Enabling Technologies: Assessment of the state-of-the-art and development of emerging technologies in primary forming, joining and finishing that would permit manufacture of the envisioned structures.

- Knowledge Base: Understand the current awareness and knowledge gaps with regard to materials and structural performance in the intended application, particularly with regard to crashworthiness, noise-vibration harshness (NVH), fatigue and durability, including corrosion.

- Technical Gateways: Provide for rigorous assessment of progress against pre-determined metrics at sub-levels of the project, assuring that functional targets are achieved or, alternatively, that further efforts are discontinued if required metrics cannot be achieved. Gateways exist for both the design stage and also for the enabling technologies, such that efforts for actual prototype build (Phase 2) only occur at successful accomplishment of Phase 1. Overall timing and conceptual flow for projects AMD 603 and AMD 604 are illustrated in Figure 1.

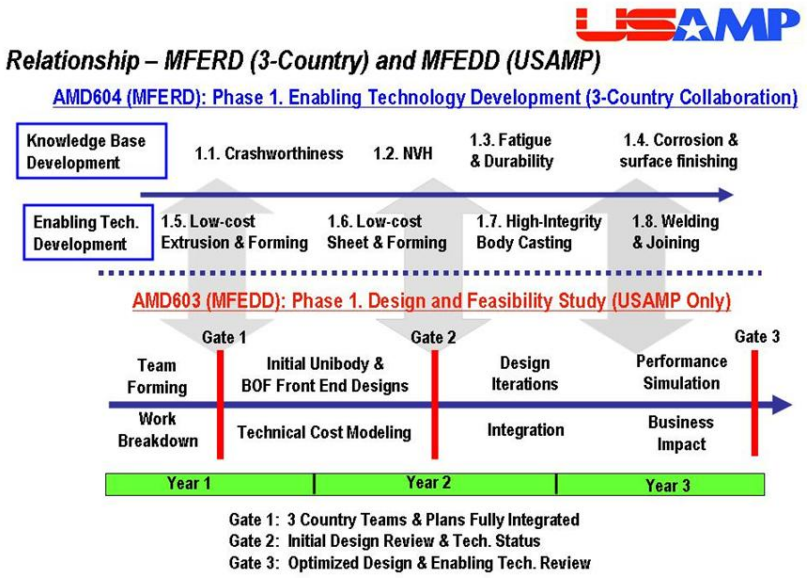

Figure 1. Schematization of AMD 603 and AMD 604 partitioning and technical gateways.

Accomplishments

The relationship between activities of the individual task areas and overall project objectives is summarized by the "fishbone" diagram shown in Figure 2. Targets for knowledge-based and enabling technologies are illustrated therein.

- OEM launch of AMD 604 by USAMP on November 1, 2006, followed by an OEM-supplier kickoff on November 28, 2006.
- Canadian program kickoff August 2006; China program kickoff December 2006.
- In calendar year (CY) 2007, the U.S. and International Task Teams conducted various organizational meetings and enlisted key supplier and funding organizations in their respective countries.
- Meetings of the Project Steering Committee (PSC), Project Technical Committee (PTC) and individual task representatives of the three countries were held on March 1 and 2, 2007 following the TMS Annual Meeting in Orlando, Florida. Follow-up sessions were also conducted in the Detroit area after this meeting.

- All international task teams have agreed on the technical agenda for the overall project and individual task areas including partitioning of the efforts, deliverables and timing.
- The PTC conducted meetings via teleconference on June 6, September 5 and December 18, 2007.
- The PTC and PSC have agreed upon April 2-4, 2008 as the time for the next three-country progress meeting to be held in Hangzhou, Peoples Republic of China (PRC).
- Project leadership received the AMD board of directors concurrence for meeting the goals of Gate 1 (project organization and setting of program metrics and timing).
- The first annual U.S. Project Review was held on October 30, 2007, for OEM and supplier participants.
- 31 Supplier companies have provided work plans and 19 purchase orders have been released.
- USAMP AMD 604 Task Area Highlights:
    - Task 1.1 Crashworthiness – Determination by partners of strain-rate regimes to be studied by each country and initial materials. LS-DYNA models are being fit to properties measured for AZ31 and AM30.
    - Task 1.2 Noise, Vibration and Harshness (NVH) – Delivery of flat Mg panels, actual-shape production parts, and base-line donor vehicle computer-aided design (CAD) data and NVH design and performance data from U.S. OEMs to Canadian and Chinese researchers to verify correlation of numerical simulation tools being developed.
    - Task 1.3 Fatigue and Durability – Fatigue efforts partitioned between three-country participants and also ICME (Mississippi State) contributors. AM30 extrusion material being prepared for round-robin testing.
    - Task 1.4 Corrosion and Surface Treatment – International work plan developed. U.S. team has enlisted suppliers for metal pre-treatment, anodizing, polymeric topcoat and analysis methods. Separate subteams were formed for fasteners, pre-treatment and testing.
    - Task 1.5 Extrusion - Extrusion alloys (AM30 and AZ61) selected and the property data provided to AMD 603 design team. Initial evaluation of microstructure, texture and mechanical properties of AM30 and AZ31 extruded sections conducted. Bending and warm-gas forming processes defined for Mg alloy extrusions.
    - Task 1.6 Sheet Forming – Exemplary sheet materials obtained from U.S. supplier (Mg Elektron), and Chinese supplier (Luoyang Copper). AZ31 sheet property data provided to AMD 603 design team. Initial evaluation of sheet microstructure and tensile and biaxial formability completed. The warm forming tools & process development, under the companion USAMP program AMD 602 (see 2.B), is on schedule, with the Deep Pan Die operational and successful demonstration of forming with direct-chill (DC) Mg sheet.
    - Task 1.7 High-Integrity Large Castings – International tasks defined and castings work initiated. For the U.S., a modified existing strut tower tool is being used in to develop the Super Vacuum Die Casting (SVDC) process for Mg. 100 SVDC castings have been produced in AZ91D. Casting-quality confirmation testing is underway. Castings to be free of cracks as determined by dye penetrant; porosity levels to be equal to or better than ASTM E-505 Level 1; and castings are to be heat treatable and weldable.
    - Task 1.8 Joining - Subteams established and suppliers engaged to pursue development of pretreatment, adhesive, self-piercing rivets (SPR), threaded mechanical fasteners and blind rivets. Pretreatment subtask began strength and corrosion assessment of baseline (untreated) and pre-treated substrates using two adhesives and eight pretreatments.

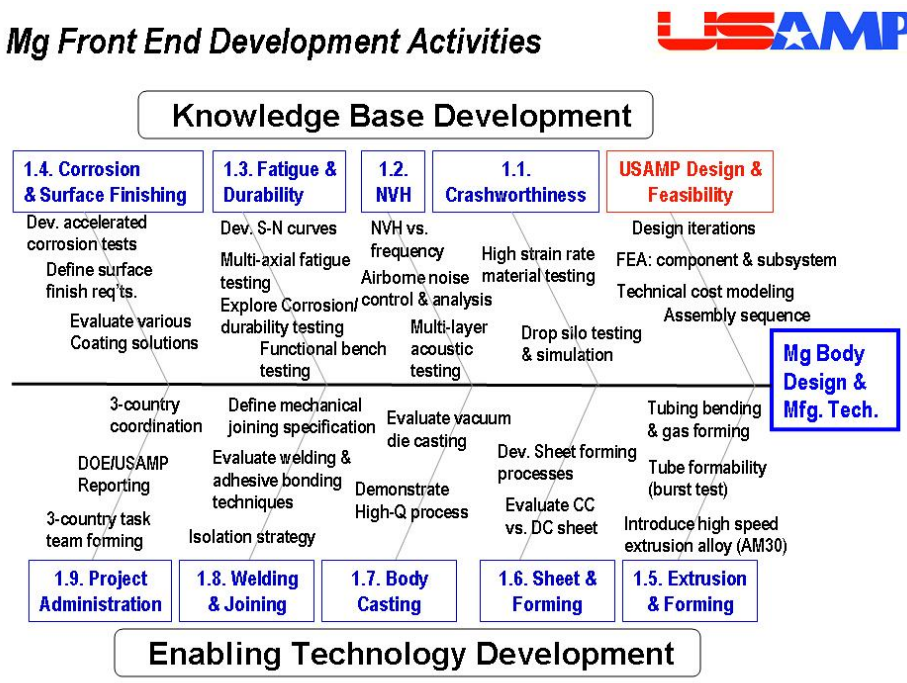

Figure 2. Mg front-end project/task structure fishbone diagram.

Future Direction

- Continuation of international discussions and progress reports via next annual meeting in Hangzhou, China (April 2008).
- Completion of requisite documentation for remainder of suppliers and issuance of USAMP purchase orders. Continue to book in-kind project contributions.
- U.S. Task Teams to provide updated physical property, material performance and manufacturing recommendations to AMD 603 Design Team.
- Information-sharing platform (web site) for international cooperation expected to become operational in calendar year (CY) 2008 upon resolution of all matters related to export-control regulations.
- 2008 Project Review to be held approximately end of October, 2008.

Introduction

Despite numerous advances in Mg manufacturing technologies, widespread and expanded use of Mg as a major automotive structural material has yet to be realized [1]. This is, in part, due to fundamental physical property limitations of Mg castings, which are the predominant form of usage, particularly with regard to deformation and fracture behaviors. Furthermore, technologies which permit the manufacture of extended structures by joining of individually-formed components are not well developed for Mg. Nevertheless, as a structural material, with high strength-to-weight values approaching or exceeding that of Al, Mg offers an attractive approach for achieving the FreedomCAR Materials goals of up to 50% weight reduction in comparison to mild steel baseline, with cost, durability and recyclability attributes that are comparable or better than other structural materials of consideration.

Project AMD 604 (Mg Front-End Research and Development – MFERD) has brought together a talented team of international scope (i.e., United States, China and Canada) to explore and develop certain "enabling" technologies which could, if successful, permit the integration of Mg-based subelements (e.g., castings, extrusions and formed sheet) into optimized assemblies for vehicle body-

structure applications. In this project the vehicle "front-end" structures for unibody and body-on-frame (BOF) architectures, serve as test beds by demonstrating significant levels of subassembly weight reduction and concomitant vehicle handling attributes, thereby, supporting the FreedomCAR goals for lightweighting materials.

The background for establishing this international effort has been previously reported [2,3]. The approach is aimed at bringing together those unique attributes from each nation, e.g., United States – product development, design and manufacturing; Canada – extractive metallurgy and manufacturing; and China – low-cost extraction, forming and component manufacturing processes, into a homologous project with the commonized technical focus of a useful and critical aspect of lightweight vehicle architecture.

The following sections describe key technical attributes of the project and accomplishments occurring during Federal fiscal year (FY) 2007.

2007 Progress and Accomplishments

Project Management and Organization: Although initial efforts began in the participant countries in late 2006, the first collective meeting occurred in March 2007 in Orlando, FL. While a draft work statement had served for organizational purposes, greater details were added at this meeting as well as a focus on the subject tasks as shown in Figure 2. The broader objectives for the project were cascaded into task-level deliverables that were discussed at a technical level among the experts present and formalized into work plans for each contributing country. A follow-up meeting was also held in southeast Michigan for purposes of continued discussions, particularly with the Chinese visitors and conducting tours of industrial and academic facilities.

Task 1.1 - Crashworthiness: Crashworthiness research includes material testing, failure characterization, computer-aided engineering (CAE) analyses and selected testing of a prototype section in crush (low loading rate) and crash (high loading rate) component tests. The strain rates for the material testing range from quasi-static (10^{-3} sec^{-1}), through the mid rates of 10 sec^{-1}, up to 1000 sec^{-1}, which is observed in the high-deformation areas during a high-speed crash. During 2007, initial testing began in the U.S., Canada and China. The LS-DYNA material models are being fit to the strain-rate and failure data for extrusion AM30 and AZ31 materials. A double top-hat section was chosen for future component testing to verify the CAE predictions.

Task 1.2 – NVH: NVH research focuses on sound transmission characteristics of Mg alloys to be used in dash panels. This research includes experimental analysis of Mg panels at 2-mm and 4-mm thickness and development of simulation tools that provide good correlation to the test panels for use in designing quiet Mg dash panels. The major accomplishments of this task for the first year have included: 1.) development of a working agreement between partner countries, 2.) delivery of flat Mg panels, actual-shape production parts, and baseline donor-vehicle CAD data and NVH design and performance data from U.S. OEMs to Canadian and Chinese researchers to verify correlation of numerical simulation tools being developed, and 3.) numerical studies of mid-to-high frequency airborne acoustic performance and modal analysis for flat panels were completed and experimental studies are underway to verify results of the computer simulations. Modifications will be made to the numerical simulation tools if the tested correlation is not good.

Task 1.3 - Fatigue and Durability: This task studies, improves and compares the fatigue-predictive capability for analyzing Mg-component and -subsystem behavior, by understanding the critical interactions of design, material and processing parameters that influence component microstructure and subsequent properties. Casting, extrusion and sheet products will be characterized sufficiently to establish links between microstructural features and fatigue behavior. Required monotonic and cyclic material properties for both multi-scale and traditional fatigue analysis methods were defined. Mississippi State University (MSST) via the AMD 702 (ICME) project and Canada's Ryerson University have completed limited monotonic and cyclic testing of extruded AZ31. The Joining (Task 1.8) Team has provided several joint configurations which will be empirically evaluated and CAE-analysis parameters developed to allow accurate simulations of the fatigue of joints. Both MSST multi-scale and tradi-

tional fatigue analysis methods will be used to analyze component structures when CAD data becomes available.

Task 1.4 - Corrosion and Surface Treatment: The U.S. Team agreed to divide the task into three initial subtasks: metal pre-treatment, fastener-related corrosion and testing methods. Chairpersons were identified and teams formed. Supplier companies have been enlisted to provide prototype pretreatments including conversion coatings, anodizing and various barrier-type layers. Suppliers of fastener coatings were also subscribed to the project and various laboratories have been selected to conduct specific evaluations of the intended sublayers. Since the metal pre-treatment will play a substantial role in the envisioned manufacturing process, it is also critical to understand the performance of the various metal pre-treatments with regard to the joining processes expected, particularly adhesive bonding. The Chinese efforts will incorporate two exemplary pre-treatments presently under development: 1) the micro-arc oxidation process developed at Xi'an University of Technology and 2) a phosphate-based conversion coating developed by the Institute for Metals Research. Canadian efforts will include a study of the cold-spray aluminizing process and also efforts directed to environmentally-assisted fracture (e.g., stress-corrosion cracking). A direct-current (DC) electrochemical technique for comparing the effectiveness of conversion-coating pretreatments is being developed by the Fontana Corrosion center of the Ohio State University.

Task 1.5 - Low-Cost Extrusion: Although initial conceptual designs for the front-end structures suggest a relatively small number of extrusions, these components are crucial insofar as providing among the higher specific strengths observed for structural Mg alloys and expectation of use in critical positions such as bumper beams and crush rails. The traditional limitation to greater use of Mg extrusions is the high cost of manufacturing, dictated in part by the size of the tooling required, and the relatively low rate of production due to the intrinsically poor formability of the material. Efforts underway include expanded use of modeling software such as DEFORM® to predict and optimize extrusion behavior for specific cross-sections. The Institute for Metal Forming of Lehigh University was selected to conduct modeling and microstructural evaluations of the extrusion process. The topic is similarly linked to AMD 702 (ICME) efforts at MSST to understand the influence of microstructure on the extrusion process. First-year results also include initial measurement of crystallographic textures of extruded shapes at key locations. A major U.S. supplier of extrusions, Timminco, has been enlisted to produce experimental shapes for the project.

Task 6 - Low-Cost Sheet and Forming: Mg Elektron of North America (MENA) was engaged as sheet supplier to AMD 604, and has to date provided 300 AZ31 sheet panels (20" x 48") in 2- and 4-mm thickness produced by the conventional DC process. This sheet material has been supplied to various task teams and partners for testing of crashworthiness, NVH, fatigue and joining. Additionally, DC sheet has been provided by the Luoyang Copper Company of China. Experimental low-cost, AZ31 sheet produced by twin-roll, continuous casting (CC) has been received from different suppliers by the companion USAMP program AMD 602 (see 2.B). Initial microstructure characterization of DC and CC sheet materials is completed. Tensile-testing protocol for warm-forming temperature range has been established and implemented at the University of Virginia. Initial tensile testing of two sheet materials is completed. Significant progress was made in establishing the biaxial testing protocol based on Marciniak flat-top punch test to provide intrinsic material formability without frictional effects. CANMET-Materials Technology Laboratory (MTL), Ottawa, has improved the test protocol and is currently evaluating different sheet materials. The initial emergent designs for the unibody front-end structure call for a number of components formed from Mg sheet.

The development of warm-forming tools and processes for making these parts is being carried out under the companion USAMP program AMD 602, and the complete progress is reported under that project. In summary, the tool and process development is proceeding as scheduled. The new Warm Forming Deep Pan Die is fully operational. Thermal modeling was used to optimize die design for temperature uniformity. Preliminary forming results show successful forming of deep pan with Mg sheet under a limited forming window. The

new press installation at Troy Tooling Technologies is on schedule.

Task 1.7 - High-Integrity Body Castings: One anticipated outcome of the companion design exercise is the strong reliance on a substantial number of Mg alloy castings which achieve the cost-lowering ability of part integration with, however, uncertainties due to the physical strength and crashworthiness aspects of cast Mg. These attributes are further compounded by concerns regarding the inhomogeneity of large castings, for a number of reasons. Fundamentally new approaches to overcoming the traditional limitations on large castings are being studied within AMD 406 (Ultra-large Castings, see 3.C). Results and technology from that project are tangential to the conduct of AMD 604. The principal target for improved large castings within AMD 604 is the study of vacuum-assisted processes which limit the gas incorporation in die-castings, thereby, permitting structures with more homogeneous and both greater intrinsic strength as well as fatigue strength governed, in part, by microporosity. Furthermore, through proper alloy selection and processing, such large castings are envisioned to be both heat-treatable and weldable, thereby further extending their utility.
In 2007, AMD 604 enlisted participation by Contech Corporation, which undertook the adaptation of high-vacuum processing to produce structural Mg castings of improved strength and integrity. Initial trial processes with alloy AZ91D, having anticipated good castability, were at least encouraging and initial strength measurements are underway at CANMET-MTL. The expected alloy of use for most structural die castings in AM60B and it is expected that castings of this material will be forthcoming in 2008. Gibbs Die Casting was also enlisted as a participant in 2007 and a second version of a higher-vacuum assist process will be the focus of their contribution. EKK, Inc. contributed computer analysis of metal flow in the Contech process during 2007. Such modeling is expected to improve the process capability and also lead to improved homogeneity of the castings.

Task 1.8 – Joining: Joining of Mg componentry produced by any of the basic forming processes under consideration into an integrated structure is essential to the success of the Mg front-end project. While resistance and fusion welding are essential to economic steel-body fabrication, there is simply no analog for the Mg structures envisioned. The basic partitioning of approaches on an international level places largely fusion-welding processes in China; laser, resistance and friction-stir processing in Canada; and SPRs, adhesive bonding, threaded fasteners and friction spot processing in the U.S. In 2007, specific efforts directed toward adhesive bonding, SPRs and threaded fasteners were initiated and subteams formed to conduct these efforts. The Henkel Corporation and Dow Automotive were enlisted to focus on adhesive bonding and, in Henkel's case, metal pre-treatment directed thereto. A liaison with USCAR's standing fastener committee was established and potential suppliers are under consideration. A parallel effort on specialized corrosion resistant coatings for steel fasteners is underway in Task 4. SPRs will undoubtedly require some form of heat application to the deforming Mg surrounding structure to resist mechanical, as well as corrosion break-down [4]. Initial investigations of the role of Mg pre-treatment on adhesive bond strength are underway, in collaboration with the University of Michigan at Dearborn.

Conclusions

AMD 604 concluded its first year of project work with advances in both the organizational aspects of the project as well as the accumulation of initial data and predictions at the various Task levels. The companion design project AMD 603 has provided insights into preferred technologies on which to focus and the AMD 604 project is expected, in short order, to provide AMD 603 with realistic material properties and manufacturing paradigms as they emerge, including surface treatments and joining methods. A major challenge for ICME will be in the area of extrusion modeling.

Presentations/Publications

1. A. Luo, E. Nyberg, K. Sadayappan and W. Shi, "Mg Front-End Research & Development - A Canada-China-USA Collaborative Project", TMS Annual Meeting, Orlando, FL, USA, February 25 – March 1, 2007.
2. A. Luo, R. McCune, R. Beals, S. Logan, E. McCarty, J. Allison, M. Maj, D. Wagner, T. Lee, R. Osborne, L. Ouimet, J. Quinn and R. Verma, "The USAMP Mg Front-End Program

- Design and Enabling Technology Development", International Mg Association Mg in Automotive Seminar, Livonia, MI, USA, March 28, 2007.
3. A. Luo, R. McCune, R. Beals, S. Logan, E. McCarty, J. Allison, M. Maj, D. Wagner, T. Lee, R. Osborne, L. Ouimet, J. Quinn and R. Verma, "Mg Front-End Development - USAMP Activities", Society of Automotive Engineers (SAE) 2007 Congress, Detroit, Michigan, USA, April 16-19, 2007.

References

1. USAMP, "Mg Vision 2020: A North American Automotive Strategic Vision for Mg," Nov. 1, 2006.
2. USAMP AMD604 DOE Annual Report, FY 2006. A. A. Luo, E. A. Nyberg, K. Sadayappan and W. Shi, "Mg Front-End Research & Development: A Canada-China-USA Collaboration," Mg Technology 2008 Symposium of TMS, Annual Meeting, March 9-13, New Orleans, LA (in press).
3. A. Luo, R. McCune, R. Beals, S. Logan, E. McCarty, J. Allison, M. Maj, D. Wagner, T. Lee, R. Osborne, L. Ouimet, J. Quinn and R. Verma, "Mg Front-End Development - USAMP Activities", Society of Automotive Engineers (SAE) 2007 Congress, Detroit, Michigan, USA, April 16-19, 2007.
4. Y. Durandet, W. Song, S. Blacket and M. Brant, "Spot Joining of Mg Using Thermally Enhanced Self-Piercing Riveting Technology," pp.141-146 in Proc. Third Int'l. Conf. on Light Metals Technology, Sept. 24-26, St. Sauveur, Quebec, CA.

Acknowledgments

The success of this project is due to the dedicated efforts of a large number of team members at Ford, Chrysler, and General Motors, the various supplier organizations listed below, as well as the international counterparts in Canada and China. The continuing support of our respective organizations and the U.S. Department of Energy is gratefully acknowledged.

[i] Denotes project 604 of the Automotive Materials Division (AMD) of the United States Automotive Materials Partnership (USAMP), one of the formal consortia of the United States Council for Automotive Research (USCAR), set up by Chrysler, Ford, and General Motors (GM) to conduct joint, pre-competitive research and development. See www.uscar.org.

D. Self-healing Coating Systems for Corrosion Control of Magnesium Alloys

Principal Investigator: Dr. Amit Singhal
Alternate POC: Dr. Ganesh Skandan, CEO
NEI Corporation
400 Apgar Drive, Suite E
Somerset, NJ 08873
(732) 868-3141; fax: (732) 868-3143; e-mail: asinghal@neicorporation.com; gskandan@neicorporation.com

Technology Area Development Manager: Joseph A. Carpenter
(202) 586-1022; fax: (202) 586-1600; e-mail: joseph.carpenter@ee.doe.gov

---

Contractor: NEI Corporation
Contract No. DE-FG02-06ER84563 Small Business Innovative Research (SBIR) and Small Business Technology Transfer (STTR) Program

---

Objective

- The goal of the Phase I project was to develop a chromate-free coating system for protection of magnesium (Mg) alloys, which includes both the primer and the pretreatment. Through a combination of novel pretreatment formulation and additives, both barrier and self-healing characteristics were imparted to the coating. Hybrid inorganic-organic pretreatments were synthesized and deposited on AZ31B alloy test coupons and corrosion inhibiting nanoscale additives were incorporated into a commercial epoxy primer formulation and their corrosion-inhibition characteristics were studied.

Approach

- Conducted literature review on the corrosion-inhibiting pretreatment and coating systems available for protecting Mg alloys. Zirconium-, phosphate-permanganate- and silane-based pretreatments provide good adhesion, but have poor barrier properties and are highly inefficient in inhibiting corrosion of Mg alloys.
- Surface preparation of Mg before coating was studied in detail since it has a substantial influence on the corrosion resistance properties of the coating system. The cleaning process adopted from American Society for Testing and Materials (ASTM) D 1732-03 was used to prepare AZ31B alloy before depositing the pretreatment (Task 1).
- A hybrid inorganic-organic pretreatment formulation was synthesized. The formulation had large concentration of adhesive functionalities and formed a highly corrosion-resistant thin film on the metal substrate. The chemistry of the formulation was developed during the Phase I program (Task 2).
- Nanoscale additives were incorporated into the pretreatment formulation as well as a commercial epoxy primer formulation and deposited on AZ31B alloy substrates.
- Salt-water immersion, electrochemical impedance spectroscopy, direct-current (DC) polarization and adhesion tests were conducted to study the barrier and adhesive properties of the pretreatment and the self-healing properties of the nanoscale corrosion inhibitors.
- Compared the electrochemical performance of the hybrid pretreatment with chromate (DOW 1) and commercial non-chrome pretreatments.

Accomplishments

- Demonstrated that by combining the attributes of nanoparticles and hybrid inorganic-organic coatings, pretreatment coatings with excellent barrier properties can be produced. The corrosion current density of the

nanoparticle-enabled, hybrid inorganic-organic pretreatment was 0.07 μA/cm^2, while it was as high as 10 μA/cm^2 for a commercial non-chrome pretreatment on the same type of Mg alloy, AZ31B (Figure 1).

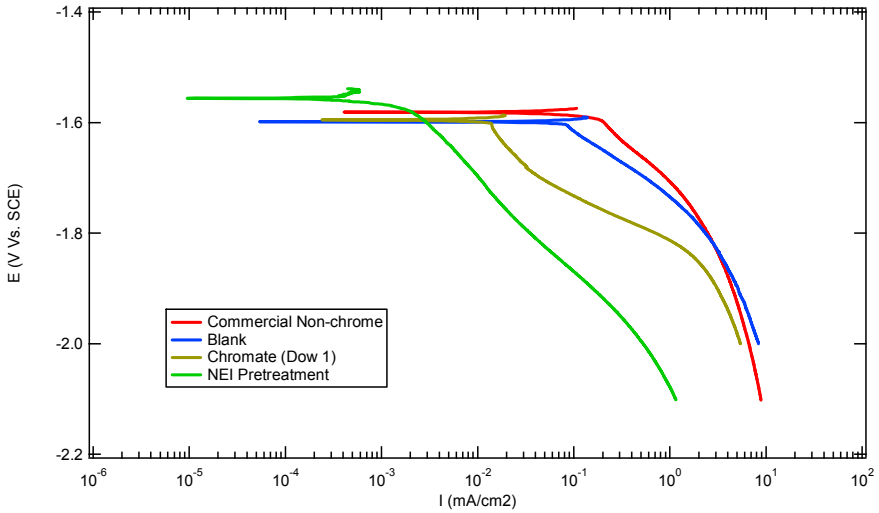

Figure 1. Cathodic polarization data of DOW 1 Chromate, a commercial non-chrome pretreatment, NEI pretreatment coatings, and uncoated AZ31B alloy. (Note that the chromate formulation was synthesized in-house following the DOW1 process).

- Observed that the corrosion current is also a function of the type of nanoscale additive. Adding about 1 wt% of Nanoparticle A in the hybrid inorganic-organic matrix does not reduce the corrosion current density. On the other hand, ~ 1 wt% of Nanoparticle B reduces the corrosion current density by an order of magnitude.

- The adhesion characteristics of the epoxy primer with the hybrid inorganic-organic pretreatment coating containing nanoscale additives are comparable to those of a commercial non-chrome as well as chromate coatings. Figure 2 shows dry and wet adhesion ASTM D4541 test data on different coatings.

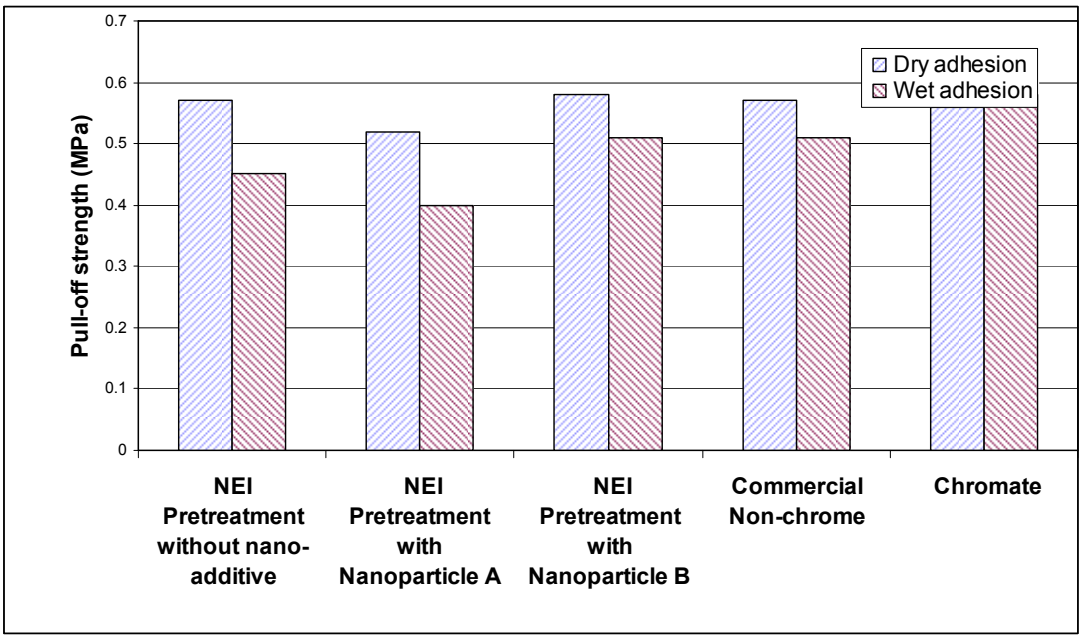

Figure 2. Adhesion strengths of an epoxy primer applied on NEI pretreatments with and without nanoscale additives, commercial non-chrome and a chromate pretreatment; before and after soaking the coated substrates in distilled water for 24 hrs.

- A commercial epoxy primer was applied on pretreated AZ31B panels. Intact primer/nanoparticle-enabled, hybrid inorganic-organic pretreatment coating exhibited higher corrosion resistance than the primer/commercial non-chrome and primer/chromate pretreatment coatings. Alternating-current (AC) impedance studies suggested that the initial low-frequency impedance of primer/NEI pretreatment containing nanoparticles was one order of magnitude higher than the control coatings. After two weeks of exposure, the low-frequency impedance of primer/ NEI's coating with nanoparticles was higher by nearly two orders of magnitude than that of primer/commercial non-chrome and comparable to primer/chromate coatings. Figure 3 compares the impedance values of the different coatings.

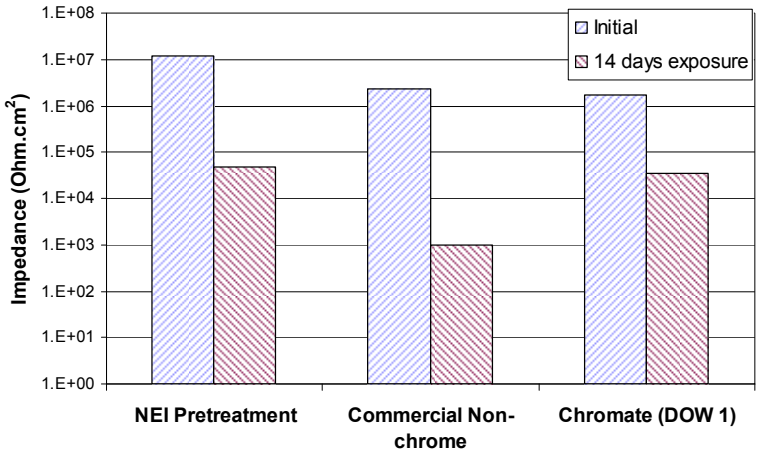

Figure 3. Low-frequency AC-impedance values of defect-free primer/pretreatment coatings for 14 days exposure to 3.5 % salt water.

- Began developing an understanding of the effect of different corrosion-inhibiting additives on the damage-responsive behavior (i.e., self-healing) of an epoxy primer coating that was applied on AZ31B panels treated with NEI's pretreatment. Defects were introduced in the coatings to expose the metal and the impedance values were measured after exposure to salt water for an hour (initial) and 11 days. Coatings containing corrosion-inhibiting nanoscale or micron-sized particles had impedance values more than an order of magnitude higher than primer coatings without additives (see Figure 4). Although we do not have any compositional evidence at this point, the increase in impedance supports the hypothesis of inhibitor particles leaching out at defect sites.

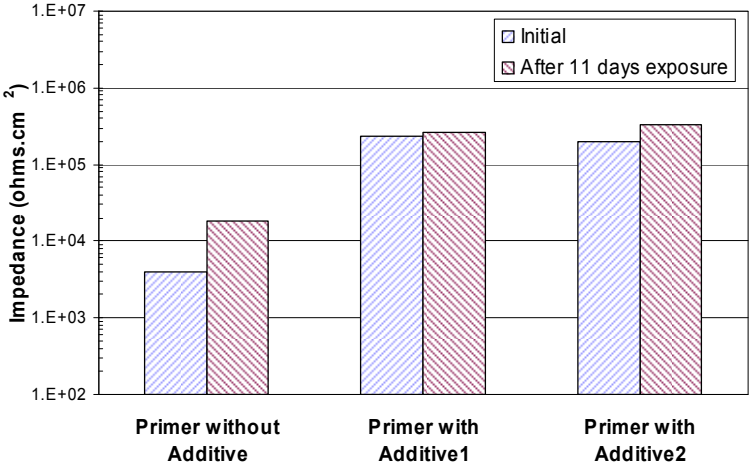

Figure 4. Comparison of low-frequency impedance after being exposed to 3.5 wt. % salt-water solution for 11 days for primers with intentionally-introduced defects.

As a result of the accomplishments of the Phase I program, we now have the opportunity to develop alternative coating architectures to impart corrosion resistance and self-healing characteristics to coatings on Mg alloys.

Nanoscale additives with the corrosion-inhibiting functionality can be added to either the pretreatment or the primer, or both.

Future Direction

- Recently, NEI Corporation has received a Phase I SBIR contract from the Department of Energy to start from July 2008 for development of chromate-free pretreatments/primer coatings systems for automotive Mg alloys. In this program, we will work towards developing a pretreatment formulation that has excellent adhesive properties and ability to exhibit damage-responsive corrosion inhibition similar to chromates. In a related program funded by the National Science Foundation, we are developing waterborne, self-healing coatings for Mg alloys.

Introduction

This Phase I project was completed in April 2007. Its goal was to demonstrate the feasibility of a non-chrome coating system, containing a pretreatment and primer that can inhibit corrosion through the use of nanoscale additives.

Task 1. Prepare Surface of AZ31B Alloys

Figure 5 shows the procedure for cleaning the panels before chemical treatment. The panels were ground with a # 320 SiC paper to remove the thick oxide layer formed on the surface. They were then immersed in n-hexane solvent and ultrasonicated for 2 minutes to remove dirt or grease from the surface. This was followed by etching the surface in an acetic acid/sodium nitrate solution for 60 seconds. This solution removed surface contamination, and a bright clean surface was obtained. The samples were rinsed in distilled water, dried and then immersed in an aqueous solution of hydrofluoric acid (HF) for surface activation. HF does not attack Mg to an appreciable extent but forms an insoluble, protective MgF_2 film. The samples were rinsed in water, dried and finally given a chemical pretreatment, followed by a spin-coating process for organic-inorganic hybrids and a dip-coating process for chromate conversion coating (DOW 1).

Task 2. Synthesize Hybrid Organic-Inorganic Pretreatment Formulation

The hybrid thin-film coating developed in the program was prepared from a hybrid inorganic-organic formulation. The pretreatment not only acts as an adhesive forming strong bonds with the metal surface, but also provides corrosion protection by forming a hard and insoluble barrier film.

Task 3. Synthesize Nanoscale Additives Functionalized with Corrosion-Inhibiting Ions

Nanoscale particles were functionalized and incorporated into the pretreatment formulation to enable them to inhibit corrosion of AZ31B alloy.

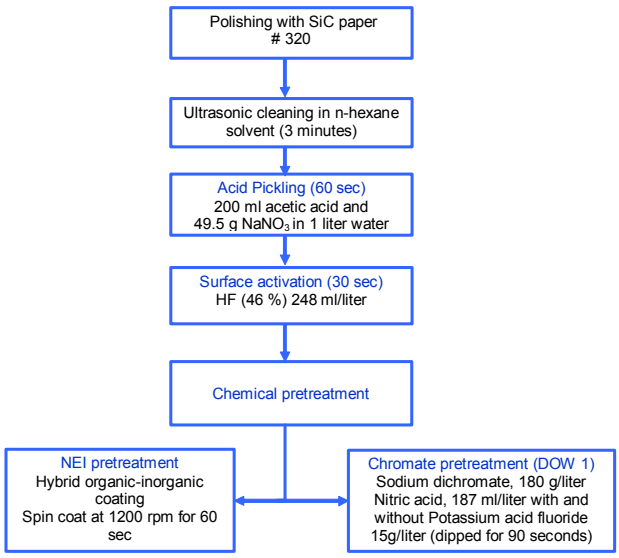

Figure 5. Surface preparation procedure of AZ31 B alloy before applying the pretreatment. (Chromate pretreatment was synthesized using the DOW 1 process).

Task 4. Perform Corrosion and Adhesion Tests on Pretreated Test Panels

Corrosion and adhesion performance tests on the pretreatment and the corrosion inhibiting nanoscale additives were performed by salt-water immersion, impedance measurements, DC polarization and pull-off adhesion tests. Additional characterization was done by

scanning electron microscopy (SEM).

Salt -Water Immersion

Figure 6 shows hybrid inorganic-organic pretreatments after 120 hours of 3.5 wt. % salt-water immersion. It is observed that the blank and commercially-pretreated AZ31B panels show general corrosion all over the surface. The chromate treatment made according to the DOW 1 process showed a lot of black corrosion products. These were chromium oxide/hydroxide formed on the surface that protects the metal from corrosion. NEI pretreatment, with and without nanoparticles, showed significantly less corrosion than the blank and commercial non-chrome pretreatment. Note that the addition of ~ 1 wt. % nanoscale particles to the NEI hybrid inorganic-organic pretreatment reduced the extent of pitting corrosion. These salt-water immersion results indicate that NEI pretreatments have considerably higher barrier and corrosion-resistance properties compared to a commercial non-chrome pretreatment. The addition of nanoscale additives further enhances the corrosion resistance of the pretreatment by reducing its porosity.

Scanning Electron Microscopy (SEM)

To understand the morphology of the commercial non-chrome and NEI pretreatment, high-resolution images using SEM were taken before and after 24 hours of salt-water immersion of the pretreated panels. As shown in Figure 7, the commercial non-chrome is not a homogeneous film. Upon exposure to 24 hours of 3.5 wt. % salt water, the treatment shows a mud-crack morphology, which also explains the general corrosion observed in the salt-water immersion test (Figure 6). NEI pretreatment shows some pores and defects which are the likely causes of pitting corrosion seen in the salt-water immersion test. The vertical lines are the polishing marks formed during the cleaning step that can be seen because of the sub-micron thickness of the pretreatment. Unlike the commercial non-chrome, NEI pretreatment does not crack and remains homogeneous upon exposure to salt water. Residual salt deposits can be seen on both the treatments (after exposure to salt water), since the panels were simply rinsed under tap water which may have not removed the salt completely.

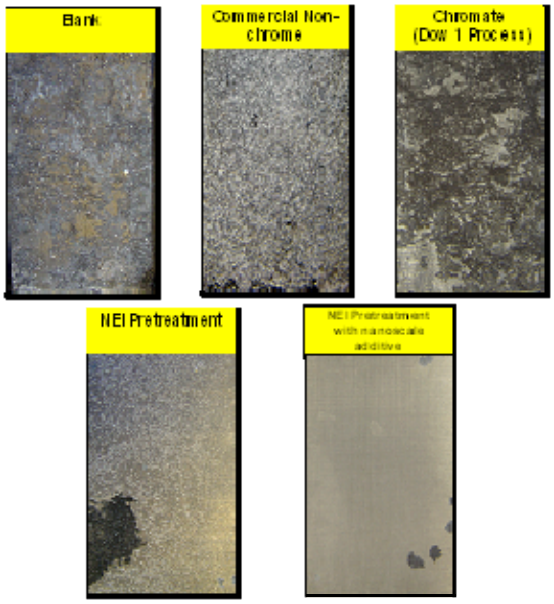

Figure 6. Pretreatments applied over AZ31 B after 120 hours of 3.5 % salt-water immersion.

Electrochemical Impedance Spectroscopy of Epoxy Primer Containing Corrosion-Inhibiting Additives

Artificial defects were introduced into the coatings and the inhibitive effect of the additives was analyzed by conducting impedance measurements over a period of 11 days. As shown in Figure 4, introduction of defects in the coating reduces the low-frequency impedance values. It is intriguing to see that the impedance values of coatings containing nanoscale particles are two orders of magnitude higher than the coating without additives. The coating without additive shows increase in impedance with time due to the formation of Mg $(OH)_2$ corrosion products. The above results are a clear indication that the addition of corrosion-inhibiting nanoscale additives has a positive effect on the corrosion performance of the commercial epoxy primer. Note that corrosion products at defect sites were visually observed for all the samples indicating that the inhibitors are not 100 % protective. More work needs to be done to improve the efficiency and quality of these materials.

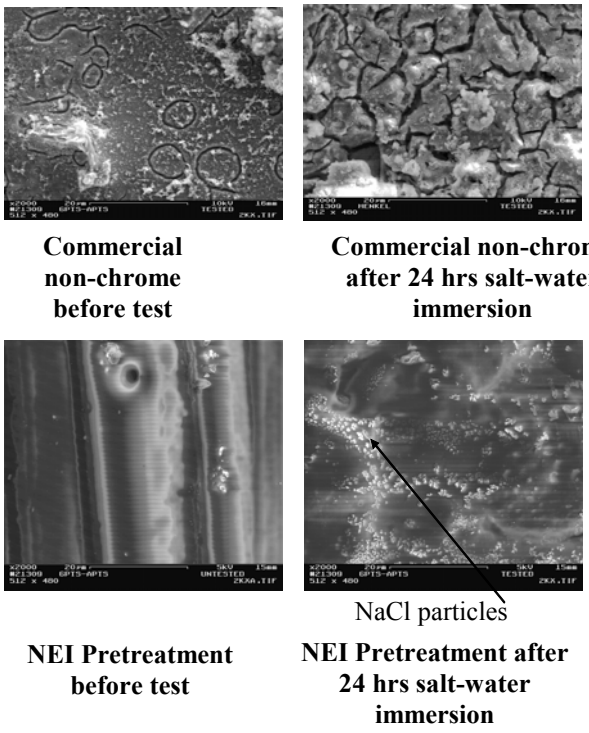

Figure 7. SEM pictures of NEI pretreatment and commercial non-chrome before and after 24 hours of 3.5 % salt-water exposure.

Adhesion of Pretreatment with Commercial Epoxy Primer

Dry and wet pull-off (ASTM D4541) was done on pretreatments under study. Wet adhesion was done after immersion of the coated panels in distilled water for 24 hours.

Figure 2 indicates that the dry adhesion values were similar for all pretreatments in the range of 0.52-0.58 MPa and, except for chromates; the wet-adhesion values were lower than the dry adhesion. For the commercial and NEI pretreatment containing nanoparticles, the wet-adhesion values were similar but 10 % lower than the dry adhesion. The wet adhesion for NEI pretreatment with and without additive was lower than the dry adhesion by 10 % and 21 %, respectively. This shows that the addition of nanoparticle B enhanced the barrier properties and decreased water penetration into the coating system. This is consistent with salt-water immersion results and cathodic polarization results, which showed that incorporation of nanoparticles enhanced the corrosion performance of NEI pretreatment. The chromate pretreatment made according to the DOW 1 process had the highest adhesion, which did not drop upon immersion in water indicating that the chromium (III) oxide/hydroxide protective film formed during the corrosion-inhibition process adheres strongly to the primer.

Acknowledgements

The author would like to acknowledge the Deportment of Energy, the sponsors of the project. We would like to thank Mr. Bob McCune for providing valuable insight into the Mg pretreatment processes and Mr. Sean Brossia of CC Technologies for conducting the electrochemical tests.

Conclusions

In Phase I, a thin, non-chromate pretreatment coating with excellent corrosion-protection ability was deposited on Mg alloy. The corrosion current of this pretreatment was at least two orders of magnitude lower than that of a commercially-available, non-chromate pretreatment. Further, it was observed that the corrosion-resistance behavior of the primer/pretreatment coating system was dependent upon the type of the corrosion-inhibitor additive in the primer coating.

Presentations/Publications/Patents

A provisional patent application has been filed with the US patent office. A full patent application will be filed soon.

E. Ferrate Conversion Coating for Corrosion Protection of High-Temperature Die-Cast Magnesium Alloys

Principal Investigator: Eric T. Clarke
Lynntech, Incorporated
7610 Eastmark Drive
College Station, Texas 77840
(979) 693-0017; fax: (979) 764-7479; e-mail: eric.clarke@lynntech.com

Technology Area Development Manager: Joseph A. Carpenter
(202) 586-1022; fax (202)586-1600; e-mail: joseph.carpenter@ee.doe.gov

---

Contractor: Lynntech, Incorporated
Contract No. DE-FG02-06ER84547 Small Business Innovative Research (SBIR) and Small Business Technology Transfer (STTR) Program

---

Objective

- Carry out a series of research studies to determine the optimum formulation for ferrate-based, corrosion-protection coatings on high-temperature diecast magnesium (Mg) alloys used in automotive powertrain applications to yield a corrosion-resistant coating comparable or better in quality than chromate-based coatings.
- Determine the corrosion resistance of the coating and its technical attributes including promotion of bonding with an organic sealant and the mechanical stability of the secondary organic coating.
- Investigate the mechanism of Mg corrosion process.

Approach

- Optimize the ferrate corrosion-protective coatings with respect to the concentration of ferrate anions and various additives and accelerators, as well as temperature, pH and time of treatment. Careful attention was given to the choice of acid-etch agents since mineral acids are known to accelerate mineralization of Mg with high rates of weight loss (Task 1).
- Expose Mg-alloy samples coated with ferrate to a 5% salt-spray corrosion resistance test and visually judge the relative extent of area covered by pit formation. Demonstrate a shift in corrosion current density (A/cm^2) using direct-current (DC) electrochemical polarization testing to show corrosion protection for the coated Mg alloy surface (Task 2).
- Evaluate adhesive properties of the secondary corrosion-protection coatings as they were supported by ferrate-based conversion coating. Adhesion evaluations were performed by cross-hatch tape test, impact-resistance test, and Taber abrasion-resistance test (Task 3).
- Characterize the chemical and metallurgical factors of corrosion for coated Mg-alloy samples using methods of scanning electron microscopy (SEM), X-ray absorption and Energy Dispersive Spectra (EDS), and high-resolution cross-sectional views of the ferrate conversion coating (Task 4).
- Assess the commercial manufacturing costs of ferrate production and document the completed project by compiling a final report inclusive of results and recommendations (Task 5).

Accomplishments

- The fiscal year (FY) 2007 Phase I accomplishments were as follows:

- Samples of Mg alloys (MRI 153M and 230D) were obtained from Dead Sea Mg, successfully sectioned, and coated at room temperature using the ferrate conversion-bath process.
- Performance of individual bath components and those in interaction with other components was evaluated in step-wise fashion using immersion conditions. A relative visual ranking system (Task 1) was used to identify useful trends of the conversion process.
- Improvements in surface sealing were noted (Task 1) when using calcium hydroxide primary sealant as compared to silicate sealant.
- Salt-fog-spray conditions (Task 2) were used to demonstrate superior corrosion protection for ferrate-converted Mg-alloy samples as compared to reference DOW 7 chromate conversion coatings, as well as for control samples prepared in the absence of ferrate.
- Similar salt-fog-spray testing of ferrate-converted Mg-alloy samples was successfully carried out for over 336 hours without formation of pits (Task 2) when the coatings were additionally sealed with a commercial varnish.
- Electrochemical-polarization tests (Task 2) were used to demonstrate a full order-of-magnitude reduction in corrosion current density (A/cm^2) for Mg alloys treated with ferrate relative to an untreated sample.
- Ferrate conversion of the Mg-alloy surfaces was shown to support the organic, varnish-type, secondary sealant film under high impact and load as demonstrated by standard mechanical testing (Task 3). Taber abrasion-resistance testing was used to show exceptional adhesion of the varnish to the converted Mg surfaces and set the stage for development of multi-layer coatings.
- Surface characterization was successfully carried out (Task 4) employing SEM methods and EDS methods. Pitted and non-pitted zones of treated Mg alloys were characterized. Non-pitted zones were clearly protected by calcium hydroxide films while pits were demonstrated to contain chlorine. Supplementary focused-ion-beam methods were used to view the coated Mg surfaces in cross-section and provide spectral analyses at higher resolution.
- Ferrate coating costs (Task 5) are projected to be affordable by original automotive parts manufacturers on the assumption that costs for scaled-up synthesis of ferrate will come down in a timely manner.
- A patent application for the ferrate conversion of Mg-alloy surfaces has been registered with the US Patent Office.

Future Direction

- The Phase I project is complete.

Introduction

The Mg Powertrain Cast Components project (see 3.B) is intended to supply lightweighting automotive Mg cast alloys to replace heavier aluminum (Al) parts in automotive manufacturing. Mg surfaces are highly reactive with respect to corrosion and must be protected by modification of their surface chemistry. Certain strong oxidizers such as ferrate, Fe(VI), are capable of modifying ("converting") the soft hydroxide film that forms on the surface of Mg to produce a harder and more protective film. Similar chromate formulations have been used successfully with Al (and other metals) to prepare surfaces for further finishing. The metallurgy of Al and Mg are similar in their oxide or hydroxide surface chemistry but differ in packing densities. The overall purpose of this study in corrosion protection of lightweighting automotive Mg diecast alloys is to evaluate the application of ferrate as an oxidizer of the soft Mg surface with respect to development of a widely-based industrial-coatings practice that protects bulk automotive Mg in a variety of structural applications and supports secondary protective films.

Immersion and salt-fog-spray corrosion testing was performed for converted alloy samples in stand-alone states and in combination with a secondary organic sealant, "RockHard" varnish. ("RockHard" varnish is produced by Indestructible Paint, Ltd., England.) Mechanical properties were determined for the varnish coating inclusive of

cross-hatch adhesion, impact resistance, and Taber abrasion resistance. Electrochemical polarizations demonstrated that the ferrate conversion coating contributed to lowering the corrosion current density at fixed potential. Electron micrographs show that converted surfaces sealed with calcium hydroxide were smooth and free of cracks. Projected costs indicate that ferrate conversion is as inexpensive as chromate without the burden of environmental risks and cleanup costs.

The results, as described below, clearly demonstrate the feasibility of a ferrate-based conversion coating for Mg. As demonstrated here, ferrate conversion coatings are at least as effective as chromate ones, without the environmental risks of chromates.

Task 1. Optimization of Ferrate Corrosion-Protective Coatings

Optimization of the corrosion-protection components in the ferrate formulations was performed with respect to the concentration of ferrate anions, the supplemental oxidant potassium permanganate and the second supplemental oxidant sodium nitrate. Hardeners such as phosphate or tungstate were optionally present in the bath. The pH of the ferrate solution was ~11.5, sufficient to stabilize the ferrate against spontaneous degradation to Fe (III). Solutions were filtered to remove impurities that remained from the ferrate production process carried out at Lynntech. Fresh ferrate solutions were replenished daily.

Samples of Mg alloys (MRI 153M and 230D) were obtained from Dead Sea Mg in the form of cast plates. Sample plates were cleaned by bead blasting to remove release-powder and dirt and then scrubbed with mild alkaline detergent to remove release-oils and grease smears. Samples were sectioned to form coupons, trued, and meticulously cleaned to remove contaminants that could have been transferred by the ensuing sanding and polishing steps. Oils and grease were removed in a manner consistent with industrial practices by employing dual washes in mineral spirit (petroleum ether) and acetone. Coupons were further degreased in an alkaline degreasing bath, rinsed, and de-oxidized using a weakly-acidic fluoride-containing bath. Immediately after stripping the surface hydroxides from the Mg samples, the coupons were rinsed and carried through a conversion and sealing sequence with the intention of replacing surface hydroxyls with iron oxometallate species as shown in Figure 1.

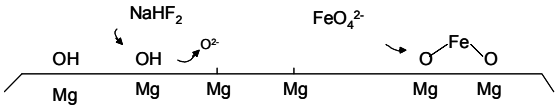

Figure 1. Schematic representation of ferrate (K_2FeO_4) conversion of Mg-alloy surface directly following cleaning and de-oxidation steps.

Results of the screenings are summarized in Figure 2 as they were obtained from a step-wise study with immersion in 5 % sodium chloride at room temperature. A relative visual ranking was used to help identify useful trends or components of the conversion process. Comparisons were made to control baths in the absence of ferrate and to reference chromate baths.

As seen in Figure 2, the common feature present in all of the combinations showing good or excellent performance is ferrate in the conversion coating and calcium hydroxide in the sealant layer. Also apparent is the fact that the ferrate conversion coatings have outperformed the chromate-based conversion coatings.

Chromate	Ferrate	Phosphate	Tungstate	Permanganate	Nitrate	Sealant: Silicate	Sealant: $Ca(OH)_2$	Protection Score
	*					*		Fair
	*	*				*		Poor
	*	*	*			*		Poor
	*			*		*		Poor
	*	*		*		*		Fair
	*	*	*	*			*	Poor
	*				*		*	Poor
	*	*			*	*		Fair
	*	*	*		*	*		Fair
	*			*	*		*	**Excellent**
	*	*		*	*		*	**Excellent**
	*	*	*	*	*		*	Poor
		*		*	*		*	Poor
		*		*		*		Fair
		*			*	*		Fair
*						*		Fair

Figure 2. Visual ranking chart for appearance of corroded coupons obtained by immersion in saline. Reference chromate was outperformed by ferrate in optimized baths.

Films obtained from boiling water or Mg hydroxide films produced in 0.01 M KOH baths were insufficient to protect Mg surfaces even with ferrate conversion treatment. Severe cleaning-bath conditions based on treatments in phosphoric acid or 10 % hydrofluoric acid were also screened out after it became apparent that these harsh condi-

tions produced rough or porous Mg-alloy surfaces. The most successful conversion baths contained components of ferrate, permanganate and nitrate.

Use of silicate as primary sealant (laid down on top of preexisting calcium hydroxide film) tends to mask the corrosion-protection results since the silicate eventually becomes opaque when exposed to sodium chloride. Use of calcium hydroxide alone may well be a better choice for primary sealant. Separate scores for corrosion-protection ranking were entered in the score chart on the basis of sealant selected. On occasion, an experiment was repeated to clarify results whenever a score could not be awarded. Worthy results obtained from the 48-hour immersion-screening process were selected for further study in long-term immersion tests or salt-fog-spray tests.

Task 2. Standard Corrosion-Resistance Testing

For purposes of salt-fog-spray corrosion testing, sample coupons of alloys MRI 153M and 230D converted with ferrate and, additionally, those coated with secondary organic sealant, "Rock-Hard" varnish, were exposed to a 5 % sodium chloride spray within a salt-fog chamber. Coupons not protected by a secondary coating of varnish were selected from the screening survey in Figure 2 and subjected to salt-fog or immersion tests for long durations, Figure 3. Silicate sealant did not perform as well as calcium hydroxide sealant under salt-fog conditions and tended to mask results obtained for the chromate reference coupons. The ferrate conversion process was superior to the reference chromate process (DOW 7) based on salt-fog-spray and immersion conditions. The appearance of the ferrate-treated specimens without an organic top-coat is better when calcium hydroxide was used as the primary sealant instead of silicate.

Figure 3. Ferrate with calcium hydroxide bath (two central samples) performed better under corrosive salt-fog conditions than silicate sealant (far left), or reference chromate treatment (far right).

The converted 230D alloys that were secondarily coated with varnish provided protection equal in level to their chromated counterparts, Figure 4.

Electrochemical-polarization testing for ferrate-coated Mg alloys provided additional corrosion-resistance information. A one order-of-magnitude reduction in corrosion current density (A/cm^2) was observed for Mg alloy MRI 153M coated with ferrate, relative to an untreated sample.

Figure 4. Secondary sealant (organic varnish) provides additional salt-fog corrosion protection. Ferrate conversion coating (left) as compared to reference chromate conversion (right).

Scans for corrosion current density and corrosion potentials were driven by CorrWare software relative to the open circuit potential (-1.5 volts) in a potential range that was selected to avoid evolution of hydrogen gas and oxygen gas (at cathodic potentials). The potentials were monitored by use of a silver/silver chloride reference electrode and a carbon working electrode, Figure 5.

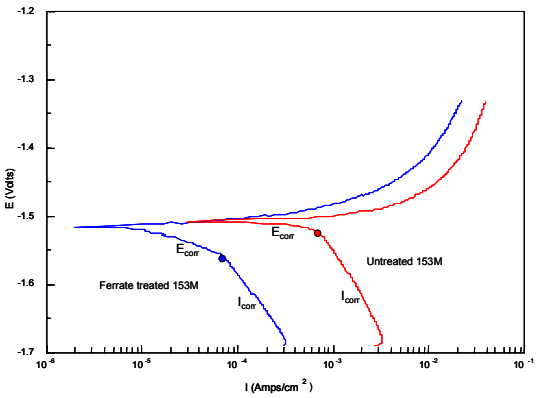

Figure 5. DC/Mg polarization of ferrate-converted Mg alloy demonstrates conclusively that ferrate is contributing to corrosion resistance for Mg.

Task 3. Mechanical Testing of Organic Varnish Coat

Adhesion of the ferrate conversion coating to the varnish secondary coating for Mg alloys was determined to fall within acceptable levels by non-specific cross-hatch tape tests and by impact-resistance tests. Excellent adhesion was determined by Taber abrasion-resistance testing (Figure 6) placing its hardness in a class comparable to polycarbonate.

Figure 6. Taber abrasion resistance for organic varnish applied to ferrate-coated Mg alloy.

Task 4. Surface Characterization of Ferrate Coatings

SEM micrographs with EDS were obtained for Mg-alloy samples coated with ferrate (and sealed with calcium hydroxide). For the SEM micrographs, the coated samples had been challenged by immersion in 5 % sodium chloride for up to three months to provide zones of pitting interspersed with pit-free zones in the coating surface. As viewed at 250X magnification, Figure 7, the pit-free zone is uniformly coated by calcium hydroxide and shows no evidence of cracking or damage. Pits (Figure 8) are sometimes observed as agglomerations of Mg hydroxide, or as dished-out areas with visible cracking.

The EDS data qualitatively reveal the presence of Mg, Al, silicon (Si), and calcium (Ca), together with other elements that are present at levels just above the baseline (Figure 9). A decrease in Al abundance (relative to Mg) may indicate that Al has preferentially dissolved away from corroded surfaces. The make-up of the corroded face more closely matches that of the untreated surface than the treated.

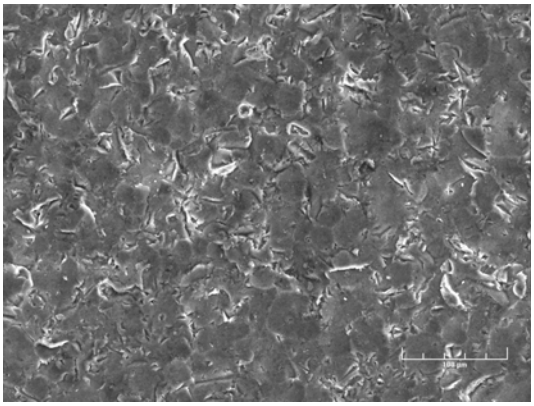

Figure 7. Unpitted zone of corroded ferrate-coated Mg alloy. Original magnification is 250X. Area of view was approximately 1 square millimeter (not to scale).

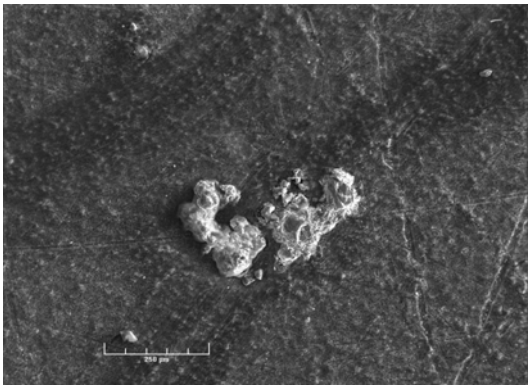

Figure 8. Surface pitting zone (agglomerations of 250 microns) for corroded Mg-alloy sample.

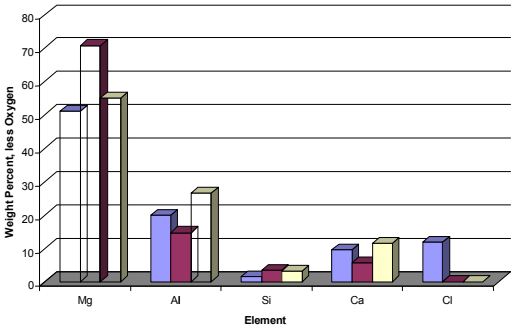

Figure 9. EDS spectral summary for ferrate-coated Mg surfaces. The distribution for each element is given in groups consisting of three different locations: pitted zones (left member of cluster), non-pitted zones (middle of cluster); and untreated zones (right member of cluster).

This indicates that the protective coating has been stripped away in this location by exposure to sodium chloride (or was never present, i.e., a defect

on the coating). The thickness of the calcium hydroxide sealant layer was 200 to 500 nm as determined by cross-sectional microscopic observations.

Conclusions

Ferrate-based conversion coatings of powertrain Mg alloys can be successfully used by original equipment manufacturers (OEMs) to provide corrosion protection to automotive Mg parts. Surface protection has been demonstrated for corrosive environments inclusive of moisture, air, and sodium chloride.

Presentations/Publications/Patents

A patent application has been filed with the U.S. Patent Office, entitled "Ferrate Conversion Coating for Mg Alloys that are used for Reduction of Vehicular Weight."

F. Integrated Computational Materials Engineering (AMD 702 and 703[i])

Principal Investigator: John E. Allison
Ford Motor Company Research and Innovation Center
Mail Drop 3182
2101 Village Road
Dearborn, MI 48124
(313) 845-7224; fax: (313) 323-1129, e-mail: jalliso2@ford.com

Program Technical Administrator: Robert C. McCune
Robert C. McCune and Associates, LLC
5451 S. Piccadilly Cir.
West Bloomfield, MI, 48322-1446
(248) 661-0085, fax: (248) 661-8718; email: robert.mccune@sbcglobal.net

Technology Area Development Manager: Joseph A. Carpenter
(202) 586-1022; fax: (202) 586-1600; e-mail: joseph.carpenter@ee.doe.gov

Field Project Officer: Aaron D. Yocum
(304) 285-4852; fax (304) 285-4403; email: aaron.yocum@netl.doe.gov

Expert Technical Monitor: Philip S. Sklad
(865) 574-5069; fax: (865) 576-4963; e-mail: skladps@ornl.gov

---

Contractor: United States Automotive Materials Partnership (USAMP)[i]
Contract No.: DE-FC05-02OR22910 through the National Energy Technology Laboratory

---

Objectives

The primary goal of this project is the development of an Integrated Computational Materials Engineering (ICME) infrastructure for magnesium (Mg) alloy development and Mg manufacturing process optimization. This is a key enabling technology for future Mg applications, including the Mg front-end architectures of companion programs AMD 603 Magnesium Front-End Design and Development (MFEDD) and AMD 604 Magnesium Front-End Research and Development (MFERD) (see 6.B and 6.C, respectively). The following are specific objectives:

- Establishment of an international ICME infrastructure (including contributor network, knowledge-base and cyberinfrastucture) for Mg alloys in automotive structural body applications, specifically:
  - Product and manufacturing-process optimization (processes include extrusion, sheet forming and high-pressure die casting).
  - Microstructural engineering.
  - Future alloy development.
- Development of a web-based cyberinfrastructure to serve as a hub for exchanging high-quality data and models between global collaborators in academia and industry.
- Use ICME infrastructure for MFERD Phase II product and process optimization.
- Attract materials researchers into the Mg field and leverage their efforts by providing a collaborative, virtual workplace for coupling high-quality data and models.
- Advance scientific understanding in various aspects of Mg cast and wrought alloys for structural body applications, including development of processing-structure-property relationships, corrosion science, crash-energy management, fatigue performance as well as design optimization.

- Incorporate the contributions of high-quality professionals and students educated in materials science and engineering in the U.S., Canada and China.

Approach

The project, while having a single unifying theme, is divided for contractual purposes into two separate projects within the Automotive Metals Division (AMD) of USAMP. AMD 703 is a 'traditional' USAMP project, funded by Lightweighting Materials of the Department of Energy (DOE), in which original equipment manufacturer (OEM) and supplier "in-kind" efforts provide cost matching for funds provided to universities and other suppliers in support of the project goals. In the project designated AMD 702, work conducted by USAMP OEM organizations will be provided on an "in-kind" basis in support of a separate DOE cooperative agreement with Mississippi State University (MSST), wherein ICME is one part of a broader research agenda. Although the project is structurally linked to AMD 604 which has Phase 1 duration of three years, the initial projected duration of the ICME Project is intended for five years. The plan of work is outlined as follows:

- Utilize the international framework of project AMD 604 (MFERD) as a platform for enlisting the work of scientists and engineers from Canada and China.
- Develop a web-based, electronic "community of practice" allowing development and integration of multi-scale, physics-based, open-source materials models for selected properties and processes.
- Establish and verify a web-accessible, "first-principles" and CALPHAD/diffusion infrastructure database. Using such database, assess the optimization process for the predominant wrought and cast Mg alloys and likely future variants (e.g., AZ and AM alloy base).
- Processing-structure-property (PSP) relationships. Establish physics-based and/or empirical relationships for microstructural evolution and similarly-based relationships between microstructures and mechanical response of materials under stress in tension, compression, fatigue and varying strain rates. This formalism would apply to:
  - Extruded Mg components.
  - Sheet Mg components.
  - High-integrity, high-pressure, die-cast Mg components.
- Establish and demonstrate capability for multi-attribute optimization. Demonstrate capability to optimize Mg alloys, processes and components for cost and performance on one or more extruded components. Extend such capability to MFERD Phase II efforts (should they occur).
- Coordination, information dissemination and reporting. Establish overall coordinated work structure between AMD 702 (ICME A), AMD 703 (ICME B), Canadian and Chinese suppliers, and MFERD.

Accomplishments

USAMP AMD 703, Integrated Computational Materials Engineering, and the companion project AMD 702, were approved on February 14, 2007 by the AMD Board of Directors and USAMP Steering Committee, and partitioned by accounting function as indicated previously. Accomplishments for the included time period of this report are summarized as follows:

- Identified and enlisted participant organizations.
- Developed detailed program plans and individual work statements for all participants including:
  - Three U.S. universities contributing to AMD 703 (Northwestern, Michigan and Virginia).
  - MSST (AMD 702).
  - Four companies or other organizations (e.g., Materials Genomics and The Minerals, Metals and Materials Society (TMS)).
- Legal agreement with MSST largely (approx. 90%) complete.
- USAMP purchase orders entered or completed for six organizations.

- Developed interdependent plans with Canadian and Chinese participants.
- Identified model Mg alloys for ICME developments.
- Secured materials for experimental work at various universities.

Future Direction

- Finalize legal agreement between USAMP and MSST.
- Assure implementation of all outstanding USAMP purchase agreements.
- Conduct ongoing international discussions as part of the MFERD Project meeting in China in 2008.
- Assist in populating the web-based "cyberinfrastructure" platform expected to be operational at MSST during 2008.
- Focus on Mg extrusion and low-cycle fatigue behavior as early targets in the U.S. program based on MFERD needs and suitability of available data.

Introduction

The availability of low-cost, widely-distributed, massive computational power as well as near-instant worldwide communication and information sharing via the internet has enabled previously intractable scientific and engineering problems to be addressed by extensive networks of participants working in parallel. While a well-known example of such a problem is perhaps the recent unraveling of the human genome, many fields of science and technology, including materials science, are confronted with similarly complex universal challenges, which could benefit from a similar approach.

One grand challenge in materials science is the unification of the relationships between structure and properties of materials over great ranges of length and time scales extending from the atomistic level to the engineering scale, and from the fempto second to years. Figure 1 illustrates an example of such scaling ranging from atomic structure to that of an automotive engine block. The classic approach of materials science has been one of reductionism, i.e., of continually improving the understanding of structure through refinement of measuring techniques to smaller levels and accompanying theoretical models for structure and behavior at the atomic and microstructural scales. In recent years, however, a movement has emerged within the materials community to integrate knowledge over the various length and time scales through appropriate methodologies to enable an "atoms-to-engines" paradigm to develop. The Journal of Metals has published several papers describing this approach [1-3]. Figure 2 illustrates the augmentation brought to the traditional materials science and engineering pyramid of design, material and manufacturing, through application of ICME principles.

ICME is expected to play a unique role in the companion Mg front-end program insofar as providing a cyberinfrastructure "platform" to facilitate the exchange of data and methodologies to permit a focused understanding of the various processing-structure-property (PSP) relationships critical to the simultaneous engineering and manufacturing understanding of the component technologies required for the Mg front end. Two aspects of this vision are noteworthy: 1) that the scope of the undertaking is limited to a single engineering material and 2) that, because processing/property and alloy characteristics are in a continuing and rapid state of development, the use of a tool such as ICME is very appropriate for the task at hand. Thus, while Mg, *per se*, is an older engineering material compared to nickel (Ni), titanium (Ti) and aluminum (Al) alloys, the Mg system is in its infancy from the perspective of alloy development and PSP relationships. Many recent worldwide advances in physical metallurgy, alloy development, processing and manufacturing (e.g., joining, surface treatment, etc.) make its consideration for a project such as AMD 604 very appealing and, furthermore, as a particularly valuable material in meeting the FreedomCAR goals of lightweighting, cost parity with existing materials and recyclability.

Project Launch and Technical Structure Status

During 2007, the USAMP launched project AMD 703 and simultaneously negotiated an agreement with MSST to provide automotive-industry "in-kind" support to their cooperative agreement with the U.S. DOE on this particular aspect of a broader research agenda. Work conducted by USAMP OEMs on this part of MSST's program will be recorded separately as AMD 702. Much of the work conducted in this fiscal year (2007), therefore, was in completing requisite USAMP formalities for project launch while simultaneously achieving agreement with the international partners contributing to AMD 604. While AMD 703 is a stand-alone USAMP project, its goals and objectives are additionally incorporated in the U.S.-Canada-China MFERD project. Additionally, individual tasks, including the physical establishment of a cyberinfra-structure, are to be conducted as part of MSST's cooperative agreement. (See 3.E and 6.G to 6.K.)

In support of the conduct of AMD 703, a number of supplier organizations have been enlisted in addition to the participation by the OEM companies, Chrysler, Ford and General Motors. The following paragraphs report the anticipated contributions of these organizations in summary form.

Northwestern University. Professor Christopher Wolverton leads this effort to develop first-principles atomistic models for the behavior of Mg

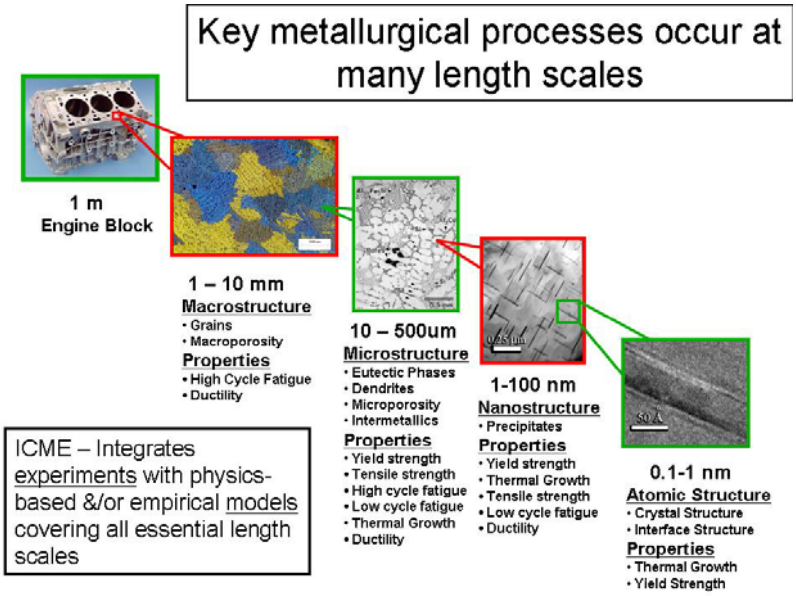

Figure 1. Atoms to engines paradigm for ICME as a unifying approach to material performance understandings beginning at the level of atomic and "nano" structural information and modeling.

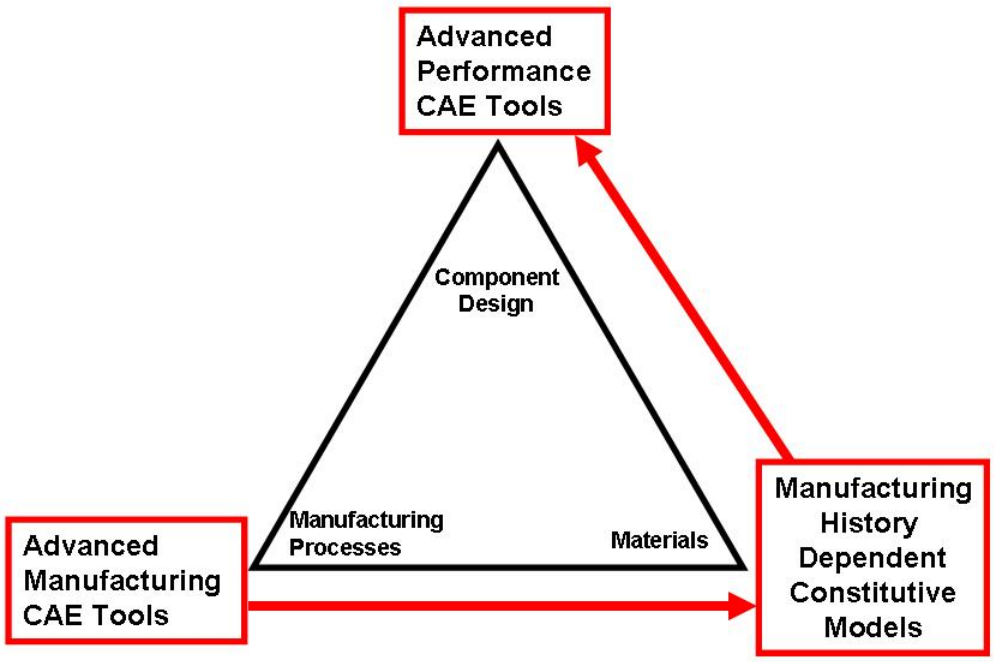

Figure 2. The ICME attributes applied to the traditional design, material and processing triangle of materials science and engineering.

and solute interactions using density functional theory (DFT). This effort will permit comparisons with more traditional phase diagram calculations, including computational methods, and measurements of both phase stability and transport properties including solute diffusion and second-phase formation.

The University of Virginia. Professor Sean Agnew will lead an effort to develop a better understanding of the role of crystal plasticity in the forming of Mg sheet, such model to include factors such as dynamic recrystallization and crystallographic textures occurring as a result of the sheet-forming processes under study. Additionally, constitutive equations and forming-limit diagrams for the thermally-enhanced deformation of Mg alloys critical to the MFERD program will be developed during the course of the project.

The University of Michigan. Professors J. Wayne Jones and Tresa Pollock will jointly conduct this project to understand and quantify the role of microstructures, as developed during the high-pressure die-casting of Mg alloys, on the subsequent yield strength and low-cycle fatigue properties of the base material and implications for the structural parts made in this fashion.

MaterialsGenome, Inc. Dr. Zi-Kui Liu, as a Professor at Pennsylvania State University, has developed computational methodologies for the determination of phase diagrams, will develop an interface that permits extensible materials thermodynamics databases to be organized and provided to third-party software programs that permit computerized calculation of alloy phase diagrams. It will provide an interface for linking the results of first-principles theory with phase-diagram calculations.

TMS. As a professional society, TMS is providing programming and a web-based portal to aid in the creation of a communications network among professionals dedicated to the subject matter of Mg science and technology and ICME.

Magma Foundry Technologies, Inc. As the supplier of the "MagmaSoft" computer program for the analysis of casting and solidification processes, Magma Foundry Technologies, Inc. will provide access and insights into application of this software for the particular purpose of "quality mapping" of castings such that projections of performance expectations based on physical models (e.g., porosity/fatigue strength) can be utilized for the structures of interest to the MFERD project. Such a capability fulfills the type of knowledge application to engineering articles envisioned by the ICME pyramid shown in Figure 2. Since many of the MFERD components are expected to be large, high-quality, Mg castings, this capability will be invaluable.

ThermoCalc Software, Inc. The use of computational methods to arrive at prediction of equilibrium phase diagrams and thermodynamic properties of alloys dates to the late 1970s. ThermoCalc is one of several software packages utilized for this purpose. The company has offered its assistance in the development of the appropriate user interfaces as proposed by MaterialsGenome, Inc. This assistance will be of value in establishing the broader links between software programs and user-populated databases within the ICME vision.

Conclusions

Integrated Computational Materials Engineering (AMD 703) was launched in early 2007 and will contain interfaces with both the AMD 604 (MFERD) project as an international focus and with the broad-based ICME effort underway through Mississippi State University. Proposals, including work plans from participating organizations have been developed and USAMP contracts have been either issued or are at various stages of the approval process. Additional "in-kind" support from candidate suppliers is welcomed and those discussions are continuing. The TMS "Magnesium" and "ICME" web portals are operational and the more specific "cyberinfrastructure" platform is expected to be finalized during fiscal year (FY) 2008. The U.S. and international teams have conducted organization meetings and technical progress by OEMs and suppliers is underway.

References

1. J. E. Allison, D. Backman and L. Christodoulou, "Integrated Computational Materials Engineering: A New Paradigm for the Materials Profession," Journal of Metals 58 [11], 25 (2006).
2. J. E. Allison, M. Li, C. Wolverton and X. SU, "Virtual Aluminum Castings: An Industrial Application of ICME," Journal of Metals 58 [11], 28 (2006).
3. D. G. Backman, D. Y. Wei, D.D. Whitis, M. Buczek, P. M. Finnegan and D. Gao, ICME at GE: Accelerating the Insertion of New Materials," Journal of Metals 58 [11], 36 (2006).

Acknowledgements

The success of this project is due to the dedicated efforts of team members at Ford, Chrysler, and General Motors, as well as the supplier organizations: The University of Michigan, The University of Virginia, Northwestern University, MaterialsGenome, Inc., Magma Foundry Technologies, Inc., ThermoCalc Software, Inc., and The Minerals, Metals and Materials Society. The project leadership also acknowledges the ongoing collaboration and discussions with colleagues at Mississippi State University. The continuing support of our respective organizations and the U.S. DOE is gratefully acknowledged.

[i] Denotes projects 702 and 703 of the Automotive Materials Division (AMD) of the United States Automotive Materials Partnership (USAMP), one of the formal consortia of the United States Council for Automotive Research (USCAR), set up by Chrysler, Ford and General Motors (GM) to conduct joint, pre-competitive research and development. See www.uscar.org.

G. Simulation-Based Design Optimization

Principal Investigator: Masoud Rais-Rohani
Department of Aerospace Engineering
Mississippi State University (MSST)
P.O. Drawer A, Mississippi State, MS 39762
(662) 325-7294; fax: (662) 325-7730; e-mail: masoud@ae.msstate.edu

Technology Area Development Manager: Joseph A. Carpenter
(202) 586-1022; fax: (202) 586-1600; e-mail: joseph.carpenter@ee.doe.gov

Contract Monitor: Aaron Yocum
(304) 285-4852; fax: (304) 285-4403; e-mail: aaron.yocum@netl.doe.gov

---

Contractor: MSST
Contract No.: 4000054701

Objective

- Develop single- and multilevel approaches for probabilistic modeling and reliability-based design optimization (RBDO) of automotive structural components and assemblies.
- Develop analytical or hybrid techniques for efficient uncertainty analysis and evaluation of component and system reliability within design optimization.
- Develop appropriate metamodels as low-cost surrogates for high-fidelity response simulations in RBDO of automotive structures.
- Develop techniques for the integration of multiscale material models in simulation-based design optimization of automotive structures related to the other tasks in the center.
- Apply the developed design methods and procedures to RBDO of automotive structural components and assemblies for the Magnesium Front-End Project (see 5.B and 5.C).

Approach

- Survey the capabilities of existing metamodeling techniques as low-cost surrogates for high-fidelity response simulations. Study the accuracy and efficiency of stand-alone and ensemble metamodels for estimation of nonlinear and noisy response functions.
- Use probabilistic modeling to describe various sources of uncertainty and their impacts on performance characteristics of a structural member or system. Investigate different approaches for RBDO of automotive structural components and assemblies. Develop RBDO formulations and solution techniques consistent with the variable nature of complexity of vehicle structures.
- Develop techniques for the integration of multiscale material models in simulation-based design optimization.
- Investigate new approaches to increase the efficiency and accuracy of structural reliability estimations. Develop analytical or hybrid techniques for evaluation of component and system reliability.
- Apply the developed design methods and procedures to RBDO of automotive structural components and assemblies.

Accomplishments

- Besides examining the performance of five different metamodeling techniques, a new technique based on optimum ensemble of metamodels was developed. Moreover, a framework for Flexible Advanced Metamodel Estimator (FAME) was established with the code currently under development by the Cyberinfrastructure project (see 6.K). (60% complete).

- Investigated a single-level RBDO methodology and its application to an automotive structural component (e.g., side rail). (50% complete).
- In collaboration with the Multiscale Microstructure-Property Plasticity Considering Uncertainty project (see 6.J), we initiated this objective ahead of the original schedule. Using the available ABAQUS UMAT subroutine for A356 cast aluminum (Al), we were able to integrate multiscale material modeling, uncertainty analysis, design optimization, and metamodeling technologies and demonstrate the new capability in design optimization of an automotive control arm. Also, in collaboration with the Materials Design for Steel Alloys project (see 5.M); we developed the approach and the associated codes for a multi-objective optimization procedure to develop modified-embedded-atom-method potentials with application to magnesium. (40% complete).
- Completed the evaluation of several methods for component-reliability analysis. Developed a new efficient method for analytical estimation of component reliability. (50% complete).

Future Direction

- Complete the multilevel approach for RBDO.
- Develop and test the performance of a new hybrid method for component and system reliability.
- Investigate a multi-attribute optimization problem which integrates product and process design into a single optimization problem.

Introduction

Simulation-based design optimization is an enabling technology that allows the design engineers to determine the best combination of product and process attributes to achieve the desired optimal performance and cost objectives while meeting the imposed design criteria. The tools necessary for design optimization of a complex system include simulation models and analysis codes that can describe the characteristics of the product and/or manufacturing process at each design point and numerical optimization techniques that can search the constrained, feasible-design space for an optimum design point. Gradient-based mathematical programming techniques are the most popular methods for the solution of general optimization problems. However, since most design optimization problems involve complex (often non-convex) design domains, gradient-based search techniques converge to a local optimum solution. Non-gradient (stochastic) search methods, on the other hand, are much less susceptible to local minimum entrapment, but they tend to be very computationally intensive and are often reserved for problems with a small number of design variables.

In this report, we will highlight our activities in different research areas under the general framework of simulation-based design optimization and describe our accomplishments as well as future direction to fulfill the remaining objectives.

Metamodeling

When response functions that appear in the objective or design constraint formulations are noisy or require computationally intensive simulations, optimizing the design becomes a very challenging task. In such conditions, surrogate mathematical models (metamodels) can offer a viable remedy.

Given the bounds on the individual input variables, a design-of-experiments (DoE) technique is used to identify the value that each input variable must take for a given experiment. By performing the computer experiments at the specified design points, a corresponding pool of response values (output) is generated. The matrix of input and output values is then used to fit or train a response surface model, which in turn can be used to estimate the value of response at any arbitrary point within the bounds of the input variables. This activity is generally known as design and analysis of computer experiments (DACE).

The common practice in the application of metamodeling techniques is to construct multiple metamodels based on a common training data set then to identify and use only the model considered the best while discarding the rest. This practice has some shortcomings as it does not take full

advantage of the resources devoted to constructing different metamodels, and it is based on the assumption that changes in the data set used to fit the metamodel will not jeopardize the accuracy of the selected model. It is possible to overcome these drawbacks and to improve the prediction accuracy of the model if the separate metamodels are combined together to form an ensemble.

As part of this research, we examined the performance of five different parametric and non-parametric metamodels for various linear, nonlinear, and noisy responses. The metamodeling techniques investigated included the global least-square method in the form of a quadratic polynomial regression (PR) [Myers and Montgomery 2002], radial basis functions (RBF) [Dyn et al. 1986; Mullur and Messac 2004], Kriging (KR) [Sacks et al. 1989; Martin and Simpson 2005; Simpson et al. 2001], Gaussian process (GP) [MacKay 1998; Rasmussen and Williams 2006; Wang et al. 2005], and support vector regression (SVR) [Clarke et al. 2005; Vapnik et al. 1997; Gunn 1997].

Furthermore, motivated by the previous research on committee of neural networks [Bishop 1995] and ensemble of surrogate models [Goel et al. 2007], we developed a more accurate ensemble methodology. This was done by modifying the general weighted average formulation and finding the optimum value for the weight factor associated with each metamodel such that a selected error metric is minimized. This methodology was successfully applied to different problems while considering different error metrics based on either the training points (i.e., cross validation errors) or a few validation points.

For evaluation of the stand-alone and ensemble of metamodels, we considered four mathematical functions (as benchmark problems) along with one car-crash example. The mathematical functions included three two-variable functions (i.e., Branin-Hoo, Camelback, and Goldstein-Price) along with the 3- and 6-variable Hartman function. In the crash problem, we considered the intrusion distance and average peak acceleration as responses of interest. We measured these responses at the driver seat, steering wheel, and the floor pan locations in a full-frontal and off-set-frontal impact simulations of a modified Partnership for a New Generation of Vehicles (PNGV) vehicle model. We used a total of nine input variables that defined the geometric shape and size of the side rails as well as the impact speed, offset distance, occupant mass, and a parameter quantifying the uncertainty in the stress-strain curve at different strain rates. All crash simulations were performed on a 32-processor IBM Linux Cluster using the nonlinear, finite-element analysis (FEA) code, LS-DYNA.

The flowchart in Figure 1 shows the steps taken in building the stand-alone and ensemble of metamodels using different techniques. In all the examples considered, the locations of the training points were obtained using the Latin Hypercube Sampling (LHS) method and maximin criterion.

The two error metrics considered are the generalized mean square error (GMSE) based on leave-one-out cross validation and the root mean square error (RMSE). Since for each metamodel, multiple replicates based on different training sets are developed, the mean value of GMSE or RMSE represent the criterion for establishing the accuracy of each model. Of the four different ensemble construction techniques identified in Figure 1, EP and EV have been developed under this research project.

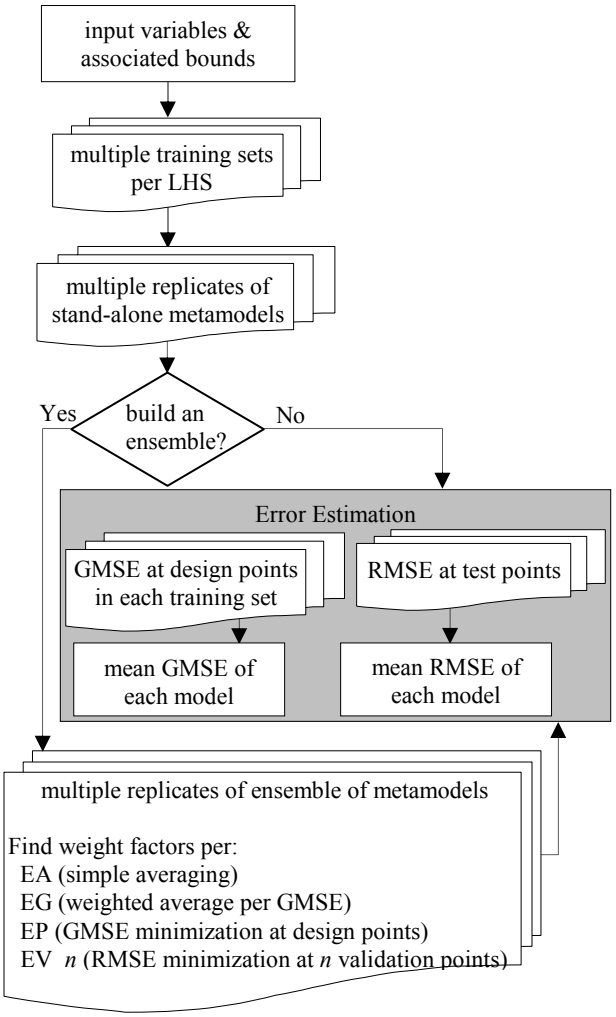

Figure 1. Flowchart of the procedure for metamodel development.

In all example problems, the best ensemble of metamodels outperformed the best stand-alone metamodel. Among the different ensemble techniques, EP proved to be the best when using GMSE as the error metric whereas EV_*n* and EG [Goel et al 2007] proved the best when using the RMSE.

The results for the full-frontal crash model are summarized in Tables 1 and 2 below. In both tables, the error for each response is normalized with respect to the stand-alone model having the lowest error among those in the same category. For example, for intrusion distance at the floor pan (ID_FP) area, GP had the lowest GMSE error among the stand-alone models whereas SVR had the greatest error (2.5 times greater than GP). Among the ensemble models, we found EP to be best overall in terms of GMSE and EV_*n* with *n* = 40 validation points to be the best with RMSE as the error metric.

Besides showing the advantage of EP and EV_*n* over other metamodels, another key finding was that a type of metamodel that accurately describes a response at one location may not necessarily show the same level of precision for the same response at another location. For example, in Table 1 for the average peak acceleration at the floor pan (A_FP), KR provides the most accurate stand-alone metamodel in terms of GMSE metric whereas, for acceleration at the driver seat (A_DS), it is the GP that is superior.

Table 1. Comparison of accuracies of stand-alone models for the full-frontal impact.

		Stand-Alone Model				
Response	Error metric	PR	RBF	KR	GP	SVR
ID_FP	GMSE	1.49	1.14	1.07	**1.00**	2.52
ID_FP	RMSE	1.44	**1.00**	1.15	1.71	2.88
ID_DS	GMSE	1.32	1.06	1.05	**1.00**	3.25
ID_DS	RMSE	1.79	**1.00**	1.39	1.30	4.82
ID_SW	GMSE	1.49	1.14	1.10	**1.00**	5.65
ID_SW	RMSE	1.99	**1.00**	1.85	1.75	11.25
A_FP	GMSE	1.50	1.09	**1.00**	1.10	1.04
A_FP	RMSE	1.36	**1.00**	1.64	1.59	2.03
A_DS	GMSE	1.40	1.03	1.07	**1.00**	1.09
A_DS	RMSE	1.28	**1.00**	1.41	1.15	1.87
A_SW	GMSE	1.16	**1.00**	1.00	1.24	1.39
A_SW	RMSE	1.70	**1.00**	1.07	1.42	2.31

Table 2. Comparison of accuracies of ensemble models for the full-frontal impact.

		Ensemble Model			
Response	Error metric	EA	EG	EP	EV_40
ID_FP	GMSE	1.13	1.05	**0.97**	1.10
ID_FP	RMSE	1.04	0.99	1.36	**0.91**
ID_DS	GMSE	1.16	1.02	**0.98**	1.02
ID_DS	RMSE	1.33	1.04	1.10	**0.94**
ID_SW	GMSE	1.50	1.05	**0.96**	1.13
ID_SW	RMSE	2.84	1.53	1.55	**1.00**
A_FP	GMSE	1.03	1.02	**0.98**	1.11
A_FP	RMSE	1.22	1.27	1.54	**0.99**
A_DS	GMSE	0.97	0.96	**0.95**	1.02
A_DS	RMSE	1.03	1.05	1.08	**0.87**
A_SW	GMSE	0.97	0.96	**0.94**	0.95
A_SW	RMSE	1.06	1.03	0.99	**0.93**

RBDO

Because of the presence of uncertainty in many aspects of product design (e.g., material characteristics, manufacturing process, operation environment, etc.), safety factors have traditionally been used to establish the design allowables. However, research shows that the use of safety factors in a deterministic design setting may not always provide the expected failure probability and that the resulting structural system may have inconsistent levels of reliability among its constituent members or modes of failure. Hence, a probabilistic approach is used to model the various sources of uncertainty and to keep track of their influences on the efficiency and robustness of the designed system.

In probabilistic design modeling, parameters that are subject to uncertainty are treated as random variables with properties (e.g., mean, standard deviation) defined by their corresponding probability distributions. Moreover, in the mathematical formulation of the design optimization problem, the objective and/or constraint functions that are influenced by uncertainty are formulated in terms of the probability of exceeding an allowable limit $P_f = P\left(G\left(\boldsymbol{X},\boldsymbol{Y}\right)<0\right)\le P_{all}$ or the corresponding reliability index $\beta = -\Phi^{-1}\left(P_f\right)$, where Φ is the cumulative distribution function of the standard normal variable.

This non-deterministic optimization approach, known as RBDO [Li and Yang 1994], has gained considerable popularity in recent years for design under uncertainty. Although the RBDO approach allows a more accurate assessment of the tradeoff between efficiency (e.g., cost, weight, performance) and safety, it is accompanied by the additional computational cost of the reliability analysis. Consequently, the solution to an RBDO problem tends to be more computationally intensive than one modeled using the traditional deterministic approach.

The RBDO formulation considered in this research is one of finding the optimal values of design variables defined by vector $\boldsymbol{Y}$ that would

$$\begin{aligned} &\text{minimize } f(\boldsymbol{Y}) \\ &\text{subject to } g_i^p(\boldsymbol{X},\boldsymbol{Y}) = 1 - \frac{\beta_i(\boldsymbol{X},\boldsymbol{Y})}{\beta_{\min}} \le 0;\ i = 1,N_p \\ &g_j^d(\boldsymbol{Y}) = \frac{R_{j_c}(\boldsymbol{Y})}{R_{j_{all}}} - 1 \le 0;\ j = 1,N_d \qquad (1) \\ &Y_k^l \le Y_k \le Y_k^u; \qquad k = 1,NDV \end{aligned}$$

where $f(\boldsymbol{Y})$ is the objective function, g_i^p designates a probabilistic constraint formulated in terms of the corresponding reliability index, β_i, and its target value, $\beta_{\min}$, and g_j^d represents a deterministic constraint that prevents the critical value of a response of interest, R_{j_c}, from exceeding its allowable value, $R_{j_{all}}$. In Eq. (1), N_p and N_d represent the numbers of probabilistic (reliability-based) and deterministic constraints, respectively, and $\boldsymbol{X}$ represents the vector of random variables in the problem.

The separation of design constraints into deterministic and probabilistic sets is meant to generalize the formulation and to help distinguish between responses that are impacted by uncertainty from those that are not. A contributing factor to the total cost of reliability analysis is the number of reliability-based constraints in the optimization problem.

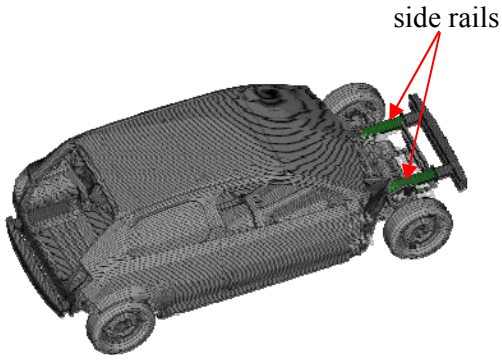

Figure 2. FE model of the vehicle.

The application problem we chose to investigate focuses on the steel side rails of a modified PNGV vehicle model as depicted in Figure 2. The selection of this particular vehicle model was to illustrate the methodology; newer vehicles and designs will be considered in the following year's work. The design criteria include limits on the intrusion distance and average peak acceleration

as measured at three remote sites (i.e., driver seat, steering wheel, and the floor pan) in the vehicle model under the full-frontal impact (FFI) and offset-frontal impact (OFI) scenarios.

Since the cross-sectional geometry of the rails can have a significant influence on their energy absorption, the selected geometric design variables permit the rail to acquire a non-prismatic shape. While the wall thickness is kept uniform, its magnitude can change during design optimization. The morphing of the cross-sectional shape requires the finite-element (FE) mesh to be modified during the design optimization. This is achieved by using the concept of geometric perturbation vectors according to the formula

$$\begin{Bmatrix} x_i^{(p)} \\ y_i^{(p)} \\ z_i^{(p)} \end{Bmatrix} = \begin{Bmatrix} x_i^{(o)} \\ y_i^{(o)} \\ z_i^{(o)} \end{Bmatrix} + \sum_{j=1}^{4} Y_j \begin{Bmatrix} x_i^{(j)} - x_i^{(o)} \\ y_i^{(j)} - y_i^{(o)} \\ z_i^{(j)} - z_i^{(o)} \end{Bmatrix} \qquad (2)$$

where subscript i identifies the FE node number whereas superscripts o and p refer to the original and perturbed mesh, respectively, and Y_j represents the value of the jth shape design variable.

Figure 3 shows the effect of the four shape-design variables in altering the shape of the rail on the right side of the vehicle with the one on the left side being the mirror image. Hence, depending on the optimal values of Y_1 through Y_4, the final shape of the side rail could be some combination of those shown in Figure 3.

Four elements of uncertainty are considered in this design. Here, we quantify the uncertainty in material constitutive relationship with the help of random variable, X_1. As indicated in Figure 4, X_1 defines the variability in the plastic region of the stress-strain curve at different strain rates. The markers in the graph show the range of variability in each curve within ± 3 standard deviations relative to the mean values defined by the curve itself. X_1 is assumed to have a lognormal probability distribution function with mean and coefficient of variation (COV) of 1.0 and 0.033, respectively. The second random variable, X_2 , defines the collision speed with the direction of impact always perpendicular to the barrier. X_2 has a mean value of

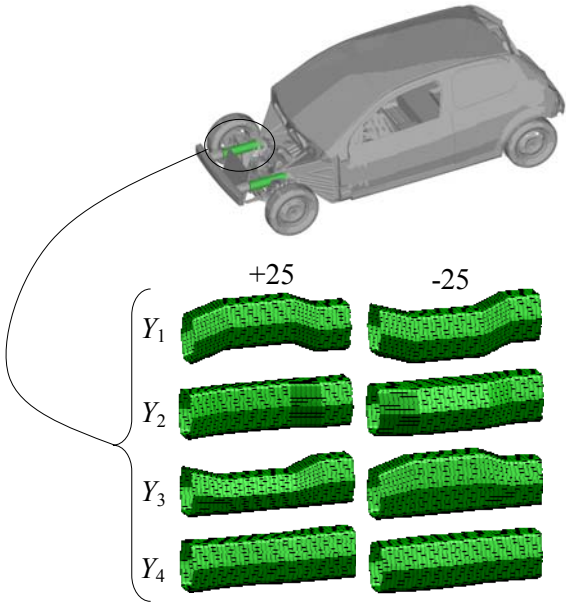

Figure 3. Perturbed geometry of the right side rail per upper and lower bounds in design variables Y_1 through Y_4.

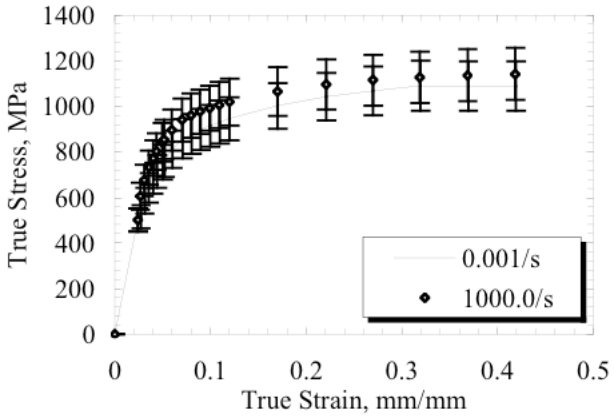

Figure 4. Band of uncertainty on the stress-strain curves at two different strain rates.

15.65 m/s (35 mph), COV of 0.067, and a normal distribution. In an OFI, only a fraction of the vehicle front end (e.g., 40%) comes in contact with the barrier. Here, the offset distance is also treated as a normal random variable, X_3 , with mean and COV of 40.0% and 0.167, respectively. The last random variable, X_4 , is chosen as that representing the mass of the occupant. It is also normally distributed with the mean of 136.2 kg and COV of 0.167.

In order to facilitate the integration of crash-response analysis and reliability assessment in RBDO of the side rails, we developed twelve separate metamodels that can describe the intrusion distances and average peak accelerations at three sites for the two different crash conditions. We also developed a metamodel for the mass of the side rails. The design and random variables were selected as the input variables. Based on previous experience and additional assessment, we chose to model the mass using an incomplete second-degree polynomial regression whereas the remaining 12 responses were all modeled using independent multiquadric radial basis functions.

We investigated a cadre of cases by selecting different responses as objective function and design constraints. For example, one case focused on minimizing mass while preventing all intrusion distances and accelerations from exceeding those in the baseline model whereas another considered minimizing the acceleration or intrusion distance at one location for one crash scenario while imposing upper limits on the remaining responses.

For the solution to the optimization problem in Eq. (1) we used the method of sequential quadratic programming with the reliability index analysis based on the modified advanced mean value method.

Generally, the tradeoff between performance (mass) and crashworthiness (safety) was observed in different cases. We found the constraining of responses at multiple sites imposed a far greater limit on the design of the side rail than those that simply constrained the responses at a single site. Also, the consideration of intrusion distance and acceleration under two different crash scenarios indicated the dominance of acceleration response over the intrusion distance as a design criterion.

We also investigated the influence of uncertainty on the optimum design by imposing reliability constraints on different responses while minimizing the mass of the side rail. Tables 3 and 4 give the summary of results for some of the RBDO cases we examined.
Different cases represent different constraint sets. The β_{min} value represents the largest attainable target reliability in each case. The differences in the β_{min} values give an indication of the severity of one set of design criteria compared to another. In cases 1 through 3, the intrusion distance responses are treated as probabilistic, measured in terms of the corresponding reliability index, whereas the average peak-acceleration responses are treated as deterministic.

Looking at case 1, for example, only the four responses at the driver-seat (DS) location are constrained. While the intrusion-distance constraints are probabilistic, those on average peak acceleration are treated as deterministic. Hence, the side-rail design is optimized for minimum mass solely based on the desirable characteristics at the DS location in FFI and OFI crash conditions without any consideration to responses at the other two sites. The target reliability, $\beta_{min} = 3.5$, is the largest bound that could be imposed in this problem without violating the bounds on the deterministic acceleration constraints at the same site. The optimum mass is found to be approximately 16% lighter than the baseline value. Among the unconstrained acceleration responses, only Acc_FP_F is worse (~10% higher) than that of the baseline model whereas the others are actually better. Moreover, among the unconstrained intrusion distance responses, Dis_FP_F and Dis_FP_O are better whereas Dis_SW_F and Dis_SW_O are much worse than those of the baseline model as evident by their large negative β values. At the optimal design point, the shape-design variables, Y_1 and Y_3 , are near their respective lower and upper bounds.

In cases 4 through 6, the average peak acceleration responses are treated as probabilistic, measured in terms of the corresponding reliability index, whereas the intrusion-distance responses are treated as deterministic.

In case 4, for instance, the four responses at the DS location are constrained. In comparison to the baseline model, Dis_FP_F, Dis_SW_F, and Dis_SW_O have higher values. Among the unconstrained acceleration responses, Acc_FP_O is worse while others are better than those in the baseline model. It is also interesting to note that design variables 1 and 2 are at their upper bounds.

With a β_{min} of 1.0, the optimum mass is about 18% less than the baseline value.

We also investigated the case where all twelve constraints are treated as probabilistic. In that case, the maximum-attainable β_{min} value was found to be 0.04 for a minimum side-rail mass of 2.277 lb. The optimal geometry for the side rail in cases 1 through 6 is depicted in Figure 5.

The inability to increase the target reliability value any higher than those specified in Tables 3 and 4 is mainly due to the conflicting behavior of response characteristics as a result of changes in the design variables [Rais-Rohani et al. 2006].

Table 3. Summary of RBDO results when two or more intrusion distance responses are treated as reliability-based constraints

Design Variable / Response	RBDO Solution		
	Case 1 β_{min} = 3.5	Case 2 β_{min} = 2.5	Case 3 β_{min} = 1.5
Y_1	-22.53	23.73	-2.90
Y_2	14.92	8.43	10.16
Y_3	25.0	-20.92	-13.70
Y_4	-4.28	19.54	-9.30
Y_5, mm	0.93	1.04	1.00
Opt. Mass, kg	1.95	2.49	2.41
β_Dis_FP_F	1.05	2.54[a]	1.50[a]
β_Dis_DS_F	3.50[a]	4.18	1.76[a]
β_Dis_SW_F	-5.54	-4.51	1.50[a]
Acc_FP_F, mm/s^2	447540	409410[a]	406090
Acc_DS_F, mm/s^2	667490[a]	749400	683710
Acc_SW_F, mm/s^2	429990	518630	573330
β_Dis_FP_O	0.94	2.56[a]	2.01[a]
β_Dis_DS_O	3.50[a]	2.20	1.50[a]
β_Dis_SW_O	-6.20	-2.13	1.50[a]
Acc_FP_O, mm/s^2	482710	503740[a]	528450
Acc_DS_O, mm/s^2	890820[a]	867420	103960
Acc_SW_O, mm/s^2	491840	499240	0 515940

Table 4. Summary of RBDO results when two or more peak acceleration responses are treated as reliability-based constraints.

Design Variable / Response	RBDO Solution		
	Case 4 β_{min} = 1.0	Case 5 β_{min} = 1.0	Case 6 β_{min} = 0.07
Y_1	25.00	-5.56	7.77
Y_2	25.00	8.83	4.19
Y_3	2.41	25.00	0.48
Y_4	-13.35	12.92	0.44
Y_5, mm	0.86	0.83	0.99
Opt. Mass, kg	1.91	1.68	2.29
Dis_FP_F, mm	63.1	60.5[a]	60.5[a]
Dis_DS_F, mm	42.3[a]	38.6	41.4[a]
Dis_SW_F, mm	10.5	13.7	9.1[a]
β_Acc_FP_F	0.22	0.99[a]	0.90[a]
β_Acc_DS_F	1.00[a]	-0.23	0.18[a]
β_Acc_SW_F	3.92	3.49	0.07[a]
Dis_FP_O, mm	67.4	67.7[a]	70.2[a]
Dis_DS_O, mm	45.2[a]	43.0	51.6[a]
Dis_SW_O, mm	7.8	9.3	6.1[a]
β_Acc_FP_O	-0.54	0.99[a]	0.07[a]
β_Acc_DS_O	1.00[a]	2.47	0.07[a]
β_Acc_SW_O	2.05	2.34	0.51[a]

[a]Response treated as a design constraint.

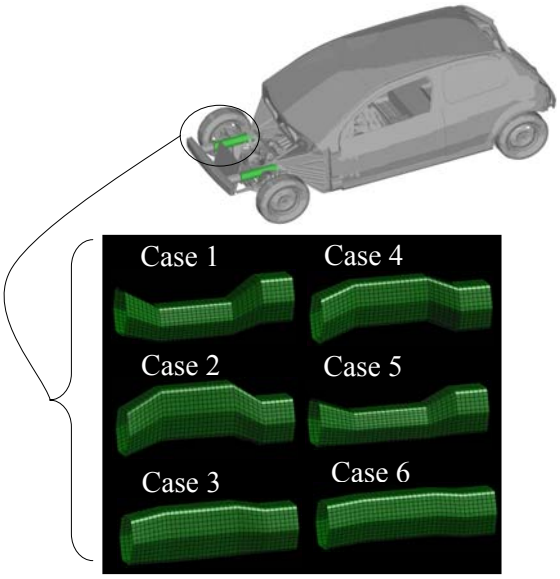

Figure 5. Optimal side-rail shapes.

Design with a Multiscale Material Model

Performance and failure of metallic components under static or dynamic loads are strongly influenced by the microstructural features (e.g., voids, cracks, and inclusion particles) of the material and their evolution during the manufacturing and in-service loading of the components. Likewise, the material microstructure characteristics depend on the type of metal, the process by which it is transformed into a product, and the environment in which the product is used.

An effective method to capture the microstructure-property relationships is by use of the internal state variable (ISV) evolution equations that are formulated at the macroscale level. The ISVs reflect the lower spatial size-scale microstructural rearrangements so that history effects can be properly modeled. With the help of such multiscale material models, it is possible to relate structural responses of interest, such as stress, strain, and toughness, to key material parameters such as particle size, interfacial strength, crack/void-density, and nearest-neighbor distance. In this study, the multiscale material model is based on the thermodynamically-constrained ISVs originally developed by Bammann et al. [1993] and later modified by Horstemeyer [2001].

Recently, Horstemeyer and colleagues [2005] investigated the effect of variability in microstructures and the boundary conditions that characterize the damage evolution using uncertainty-analysis methodology. In particular, void-nucleation, void-growth, and void-coalescence equations were evaluated and quantified in terms of sensitivity and uncertainty of various parameters in the constitutive equations. They found that a 1% uncertainty in the microstructural and boundary condition parameters results in 16% uncertainty in damage near failure, 5% uncertainty in failure strain, and 13% uncertainty in failure stress, thereby, revealing the need for incorporating uncertainties in the design process when a multiscale material model is used.

To study the influence of multiscale material modeling and associated uncertainties in an optimum design, we chose an automobile control arm as an application problem. The control arm is made of A356-T6 Al alloy, and it is manufactured using a die-cast process. This component has been selected because of the availability of data on its load-failure characteristics and the success of multiscale modeling in correctly predicting its failure mode. The two critical loading conditions considered in the design are (a) 0.8-g panic brake and (b) 0.8-g pothole strike, both of which are modeled using appropriate boundary conditions at the connection points.

Figure 6 shows the FE model of the control arm, which consists of 22,310 solid elements for 97,440 degrees of freedom. Nonlinear, static simulations of this high-fidelity model are performed using the FE code, ABAQUS implicit with multiscale-based material model incorporated using the user-defined material subroutine (UMAT).

The design optimization problem is set up similar to Eq. (1). The design variables controlling the geometry of the control arm are shown in Figure 6. These variables are used to control such features as wall thickness ($Y_1 - Y_9$), wall height (Y_{10}), and fillet radius ($Y_{11} - Y_{13}$). The arrows in Figure 6 also show the positive direction for each shape-design variable. For example, if Y_1 is positive, the corresponding wall thickness will decrease whereas, if it is negative, the wall will become thicker than that in the baseline model.

The thirty-eight constants that appear in the ISV model for an Al casting [Horstemeyer 2001] are used as random variables in the problem. They are assumed to be normally distributed with the COVs ranging from 0.05 to 0.25. In addition, there are four loading random variables that define the variability in the boundary conditions (i.e., displacements along x, y, z axes and rotation about the z axis) at the six connection points. The loading random variables are also assumed to be normally distributed with COV = 0.15.

To facilitate the integration of nonlinear FE simulation for damage evaluation with design optimization, we resorted to metamodeling. A total of six metamodeling techniques were considered in this study: Second-order response surface approximation (RS); Multiquadric RBF;

GP; KR; Feed-forward neural network (FFNN) [Smith 1993]; and SVR. All six techniques were programmed in MATLAB®.

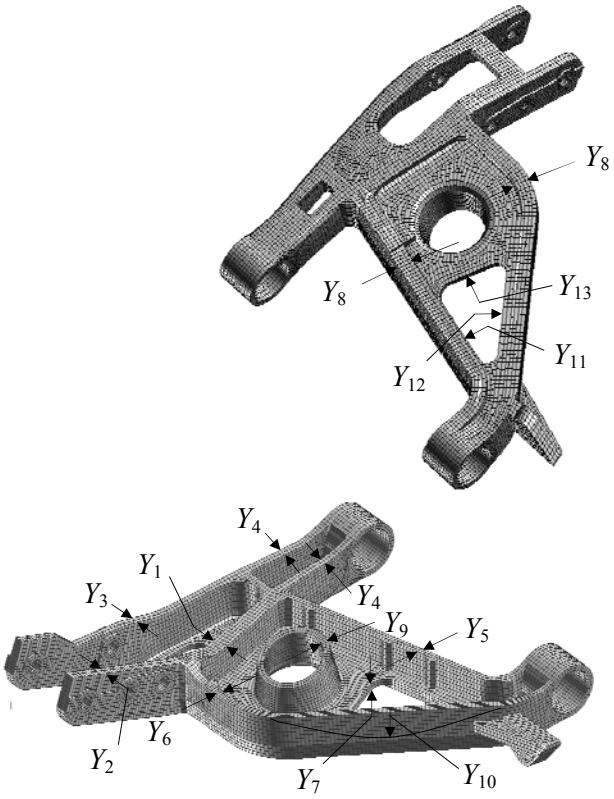

Figure 6. Description of shape-design variables.

We applied the maximin space filling technique proposed by Mourelatos et al. [2006] to generate an adequate number of training points for the metamodels as functions of the 13 design and 42 random variables. A preliminary investigation to identify and remove the subset of non-influential random variables proved inconclusive. Hence, all 42 random variables were retained.

In addition, we used variable transformation technique to increase the accuracy of metamodels, that is, instead of fitting each metamodel to damage response itself, which can vary in the range of 2.92×10^{-4} to 0.1 (three orders of magnitude variation), they were fitted to the logarithm of damage. We tested the accuracy of each metamodel for the damage response and found that the GP-based metamodel provided the most accurate predictions. High levels of noise and nonlinearity in the damage response were the main reason for GP being superior to other metamodels. These noise levels arose because of the heterogeneities arising from the microstructural differences throughout the mesh.

For von Mises stress, the GP-based metamodel again resulted in the most accurate prediction whereas, for weight, the second-order RS model was the most accurate, although the error in all weight-response metamodels was generally less than 0.2%.

Prior to solving the RBDO problem, a deterministic weight-minimization problem (case 1) was set up and solved with a design constraint imposed on the multiscale damage index. Starting with the baseline model as the initial design, the optimum design was found to be 25.3% lighter while satisfying the damage constraint. Almost all design variables were at their respective upper bounds which, in the case of wall thickness, they indicated a maximum size reduction. A post-optimization simulation of the control arm indicated that the actual value of damage was 0.0085, which was 15% less than the predicted value based on the corresponding metamodel. The ratio of the maximum von Mises stress in the optimum design to that of the baseline model was found to be 1.01 whereas the ratio for damage index was 0.112.

To investigate the influence of multiscale damage model on optimum design, we changed the design constraint from damage index to von Mises stress (case 2). Here, the upper limit on the von Mises stress was set equal to the largest value observed in case 1. Starting with the same initial design, the final weight was also found to be 25.3% lighter. This design was subsequently analyzed to find its damage index. Although this design first gave the appearance of being identical to that in case 1, it was found to have a damage index that was more than two times greater. Figure 7 provides the baseline and optimal designs together with their stress fringe plots and damage locations.

A reliability analysis on the optimum design in case 1 showed a damage reliability index of 6.48, which is already very high. However, to compare the solution with that of an RBDO problem, we set the target reliability to eight and minimized the

weight subject to a reliability-based constraint on damage.

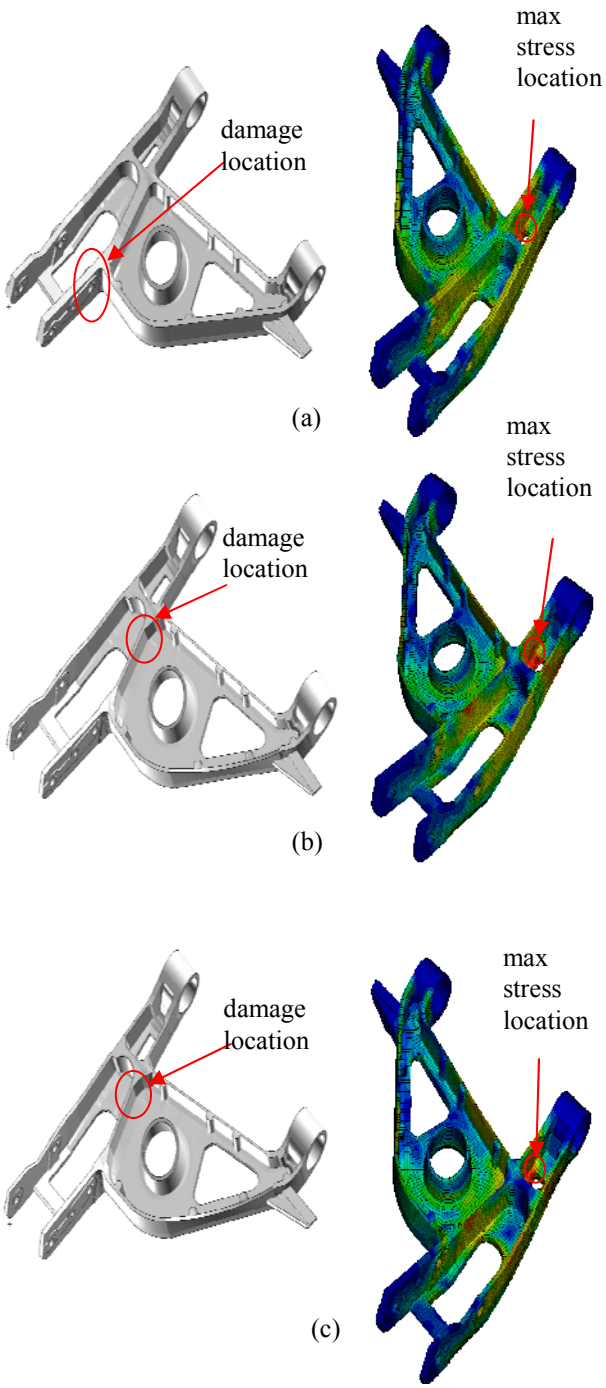

Figure 7. Comparison of (a) baseline and deterministic optimum designs using (b) multiscale and (c) plasticity models.

Not surprisingly, the optimal weight was found to be slightly heavier than in case 1. The geometry and stress plot of the reliability-based optimum design are shown in Figure 8.

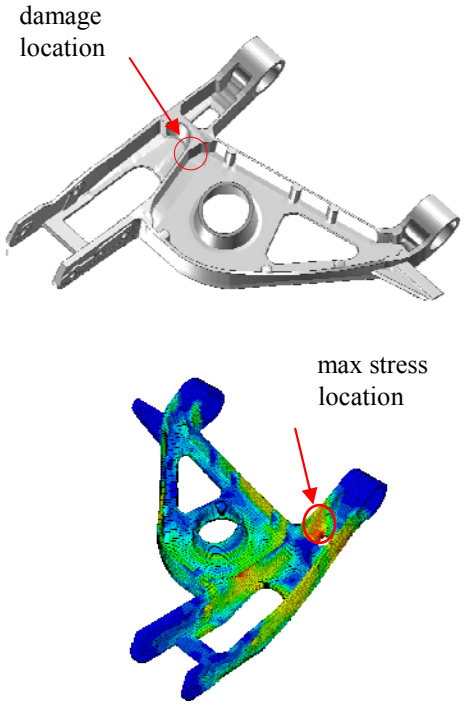

Figure 8. Optimum geometry and fringe plot of von Mises stress for the reliability-based optimum design.

A more detailed description of this study can be found in Solanki et al [2007]. In summary, we have, for the first time, documented a RDBO study that included microstructural heterogeneities in a FE simulation to predict the damage state under real-scenario design environments in order to redesign a component.

Structural Reliability

The reliability assessment of a structural component requires the evaluation of the failure probability of one or more possible failure modes. If the limit state or safety margin for a particular mode is defined by the function $G(\boldsymbol{X},\boldsymbol{Y})$, where $\boldsymbol{X}$ and $\boldsymbol{Y}$ denote the vectors of random and design variables, respectively, then safety is defined as $G(\boldsymbol{X},\boldsymbol{Y})>0$ and failure as $G(\boldsymbol{X},\boldsymbol{Y})\le 0$. The probability of failure is computed according to the multi-integral equation

$$P_f = P(G < 0) = \int_{G(\boldsymbol{X},\boldsymbol{Y})\le 0} f_X(\boldsymbol{X})d\boldsymbol{X} \quad (3)$$

where $f_X(\boldsymbol{X})$ is the joint probability density function of random variables. For most engineering problems, the analytical integration of Eq. (3) or the full distributional approach is not possible. Hence, numerical techniques such as Monte Carlo simulation, fast probability integration [Wu and Wirsching, 1987], or first- and second-order reliability methods (FORM, SORM) [Madsen et al. 1986] are often used for the evaluation of P_f or estimation of the corresponding reliability index, β. Although, depending upon the form of the limit state function and the number of random variables involved, the analytical methods tend to be less accurate than the simulation-based methods (e.g., Monte Carlo simulation, Adaptive Importance Sampling), they are more efficient especially when combined with optimization for RBDO of complex systems.

Here, we introduce a methodology for structural reliability analysis involving multidimensional and nonlinear performance functions. First, the first few statistical moments (usually the first four) of the performance function are estimated. Then, a probability distribution (preferably cumulative distribution function (CDF) or probability density function (PDF)) of the performance function is approximated with a flexible function. Finally, reliability is calculated using the approximate CDF or PDF. In this procedure, the accuracy of the reliability estimation depends on the accuracies of the estimated statistical moments and probability distribution.

Calculation of the statistical moments of a multidimensional performance function requires evaluation of multidimensional integrals. These integrals are usually simpler to compute than failure probability because the integration is not restricted to the failure domain; rather, it covers the entire random-variable space.

The dimension-reduction (DR) technique proposed by Rahman and Xu [2004] based on the additive decomposition of the response function is shown to be an efficient technique for calculating the moments of the performance function, especially when it is influenced by a moderate to large number of random variables. In DR, an N-dimensional integral of the response function is converted into N one-dimensional integrals. This approach has been successfully applied by others [Youn et al. 2006; Huang and Du 2006] in estimating statistical moments. Depending on the complexity of the response function, the one-dimensional integrals can be analytically or numerically evaluated using, for instance, the moment-based quadrature rule of Rahman and Xu [2004]. However, Youn et al. [2006] found that, for some nonlinear problems, the moment-based quadrature rule may lead to unstable moment predictions. They proposed to approximate the performance function using an approximate model (metamodel), which is then numerically integrated using one of several numerical methods.

After the statistical moments are estimated, the next step is to approximate the probability distribution of the performance function. Commonly-used distribution fitting approaches include the use of the Pearson or Johnson family of distributions, Saddlepoint approximations, and generalized lambda distributions.

The Pearson distribution has been shown to give unstable results near the boundaries of families in the skewness-kurtosis plane [Youn et al., 2006]; on the other hand, when only moment information is available, it is difficult to determine the parameters of the Johnson distribution [Johnson et al., 1995]. Furthermore, the numerical procedure followed in the Saddlepoint approximation is also prone to singularities [Huang and Du, 2006]. To avoid these difficulties, in this work we use the extended generalized lambda distribution (EGLD), which is based on the generalized lambda distribution (GLD) combined with the generalized beta distribution (GBD). After the moments of the performance function are calculated, the parameters of EGLD are computed via least -square regression. To demonstrate the performance and effectiveness of the proposed methodology for structural reliability analysis, two example problems were considered, the results for one of which are reported here.

We considered the vehicle side-impact problem [Youn et al. 2006] as one example. In this example, the crashworthiness of the vehicle is evaluated based on the velocity of the door at the B-pillar location. Youn et al. [2006] provided an explicit relationship for velocity, V_d in terms of seven random input parameters (X_1 through X_7) given as

$$V_d = 0.75 - 0.489X_1X_4 - 0.843X_2X_3 + 0.0432X_5X_6 - 0.0556X_5X_7 - 0.000786X_6^2$$

The statistical parameters of the random variables are taken from Youn et al. [2006]. Out of seven random variables, only two are normal, while the remaining ones follow beta or uniform distributions.

The reliability analysis results for this example are provided in Table 5. For evaluation of accuracy and efficiency, the proposed method (DR+EGLD) is compared with Monte Carlo simulation (MCS) and FORM. Clearly, the proposed method is very accurate as indicated by the proximity of the estimated reliability with that from MCS and is very efficient as noted by the number of function evaluations required.

Table 5. Summary of results for vehicle crash example.

Method	No. of Function Evaluations	Reliability
DR+EGLD	29	0.8071
MCS	1,000,000	0.8039
FORM	74	0.7344

The results of the example problems examined show that the methodology is computationally efficient as well as accurate for estimating the probability density functions of nonlinear performance functions and the calculation of structural reliability.

Conclusions

A summary of research progress under the general area of simulation-based design optimization was provided. Good progress has been made in the areas of reliability-based design optimization focusing on issues related to the integration of design optimization, reliability analysis, metamodeling, mesh morphing, and vehicle-crash simulations; metamodeling of nonlinear and noisy responses; design optimization using a multiscale material model; and an analytical method for accurate and efficient evaluation of structural reliability. Research activities have resulted in a number of technical papers and presentations.

Presentations/Publications/Patents

1. Rais-Rohani, M., Solanki, K., and Eamon, C., "Reliability-Based Optimization of Lightweight Automotive Structures for Crashworthiness," Proceedings of the 11th AIAA/ISSMO Multidisciplinary Analysis and Optimization Conference, Portsmouth, VA, Sep 6-8, 2006.
2. Rais-Rohani, M., "On Shape and Sizing Optimization of Automotive Structural Components for Crashworthiness," VR&D Optimization Users Meeting, Monterey, CA, Oct 30-31, 2006. (presentation only)
3. Rais-Rohani, M., "Reliability-based Design Optimization of Automotive Structures for Improved Crash Performance," TMS 2007 Annual Meeting, Orlando, FL, Feb 25 – Mar 1, 2007. (presentation only)
4. Solanki, K., Acar, E., Rais-Rohani, M., Eamon, C., Horstemeyer, M., "Reliability-Based Structural Optimization using a Multiscale Material Model," Proceedings of the 48th AIAA/ASME/ ASCE/AHS Structures, Structural Dynamics and Materials Conference, Honolulu, HI, Apr 23-26, 2007.

References

1. Bammann, D. J., Chiesa, M. L., Horstemeyer, M. F., and Weingarten, L. I., Failure in ductile materials using finite element methods, Structural Crashworthiness and Failure, edited by T. Wierzbicki and N. Jones, Elsevier Applied Science, The Universities Press (Belfast) Ltd., 1993.
2. Bishop, C.M., 1995, "Neural Networks for Pattern Recognition," Oxford University Press Inc., New York, NY, pp. 364-369.
3. Clarke, S.M., Griebsch, J.H., and Simpson, T.W., Analysis of Support Vector Regression for approximation of complex engineering

analyses, ASME Journal of Mechanical Design, Vol. 127, No. 11, 2005, pp. 1077-1087.
4. Dyn, N., Levin, D. and Rippa, S., Numerical procedures for surface fitting of scattered data by radial basis functions, SIAM Journal of Scientific and Statistical Computing, Vol. 7, No. 2, 1986, pp. 639-659.
5. Goel, T., Haftka, R.T., Shyy, W., and Queipo, N.V., "Ensemble of Surrogates," Structural and Multidisciplinary Optimization, Vol. 33, No. 3, 2007, pp. 199-216.
6. Gunn, S. R., Support Vector Machines for classification and regression, Technical Report, Image Speech and Intelligent Systems Research Group, University of Southampton, UK, 1997.
7. Horstemeyer, M.F., From Atoms to Autos, A new design paradigm using microstructure-property modeling, Part 1: monotonic loading conditions," Sandia National Laboratories, Sand2000-8662, March 2001.
8. Horstemeyer, M.F., Solanki, K. and Steele, W.G., Uncertainty methodologies to characterize a damage evolution model," Plasticity Conference, 2005.
9. Huang, B., and Du, X., "Uncertainty Analysis by Dimension Reduction Integration and Saddlepoint Approximations," Journal of Mechanical Design, ASME, Vol. 126, No. 1, 2006, pp. 26-33.
10. Johnson, N.L., Kotz, S., and Balakrishnan, N., "Continuous univariate distributions," Vol. 2, 2nd Edition. John Wiley, New York, 1995.
11. Li, W. and Yang, L, "An Effective Optimization Procedure Based on Structural Reliability," Computers and Structures, Vol. 52, No. 5, 1994, pp. 1061-1067.
12. MacKay, D.J.C., Introduction to Gaussian Processes, Neural Networks and Machine Learning, edited by C.M. Bishop, Vol. 168 of NATO ASI Series, Springer, Berlin, 1998, pp. 133-165.
13. Madsen, H. O., Krenk, S., and Lind, N. C., Methods of Structural Safety, Prentice Hall, Englewood Cliffs, NJ, 1986.
14. Martin, J.D., Simpson, T.W., Use of Kriging models to approximate deterministic computer models, AIAA Journal Vol. 43, No. 4, 2005, pp. 853-863.
15. Mourelatos, Z.P., Kuczera, R.C., and Latcha, M., An efficient Monte Carlo reliability analysis using global and local metamodels, Proceedings of 11th AIAA/ISSMO Multidisciplinary Analysis and Optimization Conference, Portsmouth, VA, 6-8 September 2006.
16. Mullur, A.A. and Messac, A., Extended radial basis functions: more flexible and effective metamodeling, Proceedings of 10th AIAA/ISSMO Symposium on Multidisciplinary Analysis and Optimization, August 30 – Sept 1, 2004, Albany, New York.
17. Myers, R.H., and Montgomery, D.C., Response surface methodology: process and product optimization using designed experiments, Wiley, New York, NY, 2002.
18. Rahman, S., and Xu, H., "A Univariate Dimension-Reduction Method for Multi-dimensional Integration in Stochastic Mechanics," Probabilistic Engineering Mechanics, Vol. 19, 2004, pp. 393-408.
19. Rais-Rohani, M., Solanki, K., and Eamon, C., "Reliability-Based Optimization of Lightweight Automotive Structures for Crashworthiness," Proceedings of the 11th AIAA/ISSMO Multidisciplinary Analysis and Optimization Conference, Portsmouth, VA, Sep 6-8, 2006.
20. Rasmussen, C.E., and Williams, C.K.I., Gaussian Processes for Machine Learning, The MIT Press, 2006.
21. Sacks, J., Welch, W. J., Mitchell, T. J. and Wynn, H. P., Design and analysis of computer experiments, Statistical Science, Vol. 4, No. 4, 1989, pp. 409-435.
22. Simpson, T.W., Mauery, T.M., Korte, J.J., and Mistree, F., 2001, Kriging models for global approximation in simulation-based multidisciplinary design optimization, AIAA Journal, Vol. 39, No. 12, pp. 2233-2241.
23. Smith, M., Neural Networks for statistical modeling, Von Nostrand Reinhold, New York, 1993.
24. Solanki, K., Acar, E., Rais-Rohani, M., Eamon, C., Horstemeyer, M., "Reliability-Based Structural Optimization using a Multiscale Material Model," Proceedings of the 48th AIAA/ASME/ ASCE/AHS Structures, Structural Dynamics and Materials Conference, Honolulu, HI, Apr 23-26, 2007.

25. Vapnik, V., Golowich, S., and Smola, A., Support Vector Method for function approximation, regression estimation, and signal processing, Advances in Neural Information Processing Systems, edited by Mozer, M., Jordan, M., and Petsche, T., MIT Press, Cambridge, MA, 1997, pp. 281-287.
26. Wang, L., Beeson, D., and Wiggs, G., Gaussian Process metamodels for efficient probabilistic design In complex engineering design spaces, ASME 2005 International Design Engineering Technical Conferences & Computers and Information in Engineering Conference, Long Beach, CA, September 2005.
27. Wu, Y.-T. ad Wirsching, P. H., "New Algorithm for Structural Reliability Estimation," ASCE Journal of Engineering Mechanics, Vol. 113, No. 9, 1987, pp. 1319-1336.
28. Youn, B.D., Xi, Z., Wells, L.J., and Wang, P., "Enhanced Dimension Reduction (EDR) Method for Sensitivity-Free Uncertainty Quantification," Proceedings of the 11th AIAA/ISSMO Multidisciplinary Analysis and Optimization Conference, Portsmouth, VA, Sep 6-8, 2006.

H. Fatigue of Lightweight Automotive Materials

James C. Newman, Jr.: Co-Principal Investigator
314C Walker Engineering Building
Mississippi Sate University (MSST)
P.O. Box A
Mississippi State, MS 39762
(662) 325-1521; fax: (662) 325-5433; e-mail: j.c.newman.jr@ae.msstate.edu

Yibin Anna Xue: Co-Principal Investigator
Assistant Research Professor, Center for Advanced Vehicular Systems (CAVS)
MSST
Mississippi State, MS 39762-5405
(662) 325-5450; fax: (662) 325-5433; e-mail: axue@cavs.msstate.edu

Mark F. Horstemeyer
CAVS Chair in Solid Mechanics & Professor, Mechanical Engineering
MSST
206 Carpenter Bldg., PO Box ME
Mississippi State, MS 39762
(662) 325-7308; fax: (662) 325-7223; e-mail: mfhorst@me.msstate.edu

Paul T. Wang
Manager, Computational Manufacturing and Design
CAVS
MSST, P.O. Box 5405
Mississippi State, MS 39762-5405
(662) 325-2890; fax: (662) 325-5433; e-mail: pwang@cavs.msstate.edu

Technology Area Development Manager: Joseph A. Carpenter
(202) 586-1022; fax: (202) 586-1600; e-mail: joseph.carpenter@ee.doe.gov

Contract Monitor: Aaron Yocum
(304) 285-4852; fax: (304) 285-4403; e-mail: aaron.yocum@netl.doe.gov

---

Contractor: MSST
Contract No.: 4000054701

Objective

- Our objective is to develop and experimentally validate prognostic tools for in-service life prediction and fatigue design of lightweight automotive materials and components. An extensive test program is being conducted on AZ31D Mg-alloy extrusions. Two fatigue models are being developed. The first is the multistage fatigue (MSF) model, which considers life to be composed of incubation, microstructurally and physically small-crack growth, and large-crack growth; and the second model, Small-Crack Theory, is based on small- and large-crack propagation alone, which assumes that micro-cracks (1 to 300-μm in size) initiate very early in the fatigue life from microstructural features (no incubation life).

Approach

- Develop methodologies for simulating microstructurally and physically small cracks in selected Mg alloys. Observation of the incubation lives for the selected Mg alloys, measurement and correlation of the growth of microstructurally and physically small cracks and large-crack behavior will be conducted for development of the physics-based models (Task 1).
- Perform literature survey on fatigue and small-crack behavior in Mg alloys; conduct fatigue and crack-growth tests on selected Mg alloys; conduct monotonic and cyclic stress-strain tests, uniaxial and multi-axial fatigue tests on AZ31; conduct "Round Robin" fatigue tests on AM30 Mg alloy under the leadership of General Motors (GM) for the United States Council for Automotive Research (USCAR); and use Mg fatigue data from the Fatigue and Durability Research Test 3 in the Mg-front-end project (5.C) to validate the models (Task 2).
- Perform *in-situ* scanning electron microscope (SEM) fatigue tests on selected alloy(s) to identify crack-initiation site(s) and metallurgical features. We will conduct in-situ studies on the fatigue and crack behavior of the selected Mg alloy (Task 3).
- Correlate the influence of grain boundaries, crack shapes and plasticity effects on the fatigue models. We will conduct microstructural studies on the influence of grain boundaries on crack growth and the effects of plastic deformations on the fatigue and fatigue-crack-growth behavior (Task 4 and collaboration with the optimization task in the Center for Virtual Manufacture and Design (CVMD).
- Experimentally validate the models with a selected material and non-proprietary, automotive component tested under in-service loading specified by sponsors (Task 5).

Accomplishments

- Conducted literature surveys on fatigue and small-crack growth in Mg alloys (Task 2).
- Developed a detailed statement of work (SOW) on "Development of Microstructure-Based Multistage Fatigue Models for Alloys Utilized in Automotive Mg Front End Project" (Task 2).
- Developed test matrix and test specimens for tensile and fatigue tests on the Mg alloys to determine material parameters for the MSF and Small-Crack Theory models (Task 2).
- Conducted MSF analyses of cast AZ91 material and components (Task 1).
- Conducted preliminary fatigue-crack-growth analyses and correlations of crack-growth rates for AZ91E to determine material parameters for Small-Crack Theory model (Task 1).
- Conducted fatigue analyses on unnotched strain-controlled tests on AZ91E coupons using Small-Crack Theory (Task 1).
- Acquired two AZ31D extrusions from General Motors (GM) (Task 2).
- Determined composition and particle morphology and distributions for AZ31D Mg alloy from GM (Task 2).
- Developed a detailed test plan for the tensile and fatigue specimens to be machined from AZ31D extrusions (Task 2).
- Initiated tensile testing on the extruded AZ31D alloy (Task 2).
- Submitted an abstract to TMS 2008 on fatigue of Mg AZ31 (Task 1).

Future Direction

- Evaluate and model fatigue behavior of self-piercing rivet (SPR) lap-joint configuration (May 2008).
  - Develop candidate SPR specimen.
  - Uniaxial tensile strain-life testing ($R > 0$).
  - Microstructural evaluations.

- Evaluate and model fatigue behavior of Mg AZ31D extrusions (August 2008).
  - Evaluate grain size, orientation and distribution for AZ31 Mg alloy.
  - Conduct fatigue-crack-growth tests on compact specimens made of AZ31 alloy.
  - Complete the monotonic and cyclic stress-strain tests on the AZ31 extrusion.
  - Conduct uniaxial strain-life test with mean stress effects (stress ratios R = -1 and R = 0.1).
  - Evaluate fractographs of fatigue specimens, identify incubation site(s), and fatigue stages.
  - *In-situ* SEM tests on AZ31 coupons to study fatigue incubation and crack-growth behavior (collaboration with Chinese partners).
  - Perform MSF analyses of the uniaxial, strain-controlled, fatigue tests on unnotched AZ31 coupons.
  - Perform Small-Crack Theory analyses of the uniaxial, strain-controlled, fatigue tests on unnotched AZ31 coupons.
- Fatigue components design (starting May 2008)
  - Obtain in-service spectrum loading sequence from the automotive industry.
  - Conduct MSF and Small-Crack Theory fatigue analyses under in-service, variable-amplitude loading.
- Publications and reports
  - Submit a paper on the fatigue analysis of the AZ91E alloy using Small-Crack Theory to International Journal of Fatigue (December 2007).
  - Complete a paper for MTS 2008 on fatigue of AZ31 (December 2007),
  - Complete a full report on fatigue analyses of AZ31D under constant- and variable-amplitude loading (August 2008).

Introduction

Prognostic tools for in-service life prediction of lightweight automotive materials and components are being developed and validated for Mg alloys. An extensive test program is being conducted on AZ31D Mg alloy from extrusions obtained from the automotive industry. Monotonic and cyclic stress-strain tests and fatigue tests under low- and high-cycle fatigue conditions are being conducted. Detailed observations of the fatigue-failure process will guide the development of the physics-based models. Two fatigue models are being developed using the extensive test program, a USCAR Round Robin, and other tests from the automotive consortium.

The first model is the MSF model, which considers life to be comprised of incubation, microstructurally and physically small-crack growth, and large-crack growth regimes. Material parameters in the MSF model will be evaluated from the extensive test program. The second model, Small-Crack Theory, based on small- and large-crack growth alone, assumes that microcracks (1 to 300-μm in size) initiate very early in the fatigue life from microstructural features (no incubation life). Fatigue-crack-growth tests will provide basic material properties from threshold to fracture and a crack-closure model will be used to correlate and predict the fatigue behavior. Both models will be validated by test coupons and automotive components.

MSF Model

The MSF approach [1] decomposes fatigue life into four consecutive stages (that we break down into three stages) based on the microstructural details of fatigue crack growth, similar to the approach summarized by Suresh [2], i.e.,

$$N_{\text{Total}} = N_{\text{Inc}} + N_{\text{MSC/PSC}} + N_{\text{LC}}, \quad (1)$$

where N_{Total} is the total fatigue life; N_{Inc} is the number of cycles to incubate a crack at a micronotch or a microscale discontinuity that nucleates crack-like damage and earlier crack propagation through the region of the micronotch root influence; N_{MSC} is the number of cycles

required for propagation of a microstructurally small crack (MSC) with the crack length, $a_i < a < k$ MS, with MS defined as a characterized microstructural length scale of interaction with microstructural features; N_{PSC} is the number of cycles required for propagation of a physically small crack (PSC), k MS $< a <$ O (10 MS), during the transition from MSC status to that of a dominant long crack (LC). Depending on the microstructural inclusion morphology, texture of the matrix and loading, the PSC regime may extend to 200 ~ 800 μm in the high-cycle fatigue (HCF) regime. In Equation (1), the MSC and PSC regimes are combined into one mathematical form. The number of cycles required for LC propagation is given by N_{LC}. In McDowell *et al*. [1], MS was defined as the dendrite cell size (DCS) for cast Al alloys, k on the order of 1-3 as the nondimensional factor that is representative of a saturation/percolation limit for the three-dimensional crack front encountering a set of microstructural obstacles to propagation. When considering the MSF model for the low-cycle fatigue (LCF) and HCF regimes of Mg alloys for automobile component applications [3], MS was also defined as the DCS; however, k was found to be higher in certain cases due to large gas pores (on the order of 10 μm) and the refined DCS (on the order of 5~10 μm) acted as a site of crack formation. For extruded Mg alloys, the MS will primarily represent the average grain size.

Figure 1 shows a schematic of three distinct regions of the constant-amplitude, completely-reversed uniaxial strain-life [4]. In this plot, the length scale, 'D' , pertains to the diameter of the inclusion, i.e., a typical particle or a gas pore for the case. The length scale, l , pertains to the size of the plastic zone at the micronotch root, defined as the scale over which the local plastic shear strain is greater than or equal to 0.01%. The constrained microplasticity regime is defined by the l/D ratio at which l/D is linearly varying with respect to the applied strain amplitude corresponding to the HCF regime. We can make the connection that macroscopic plasticity (hysteresis in the global stress-strain curve) is apparent when the local microplasticity develops past the constrained state – we define this as the domain of unconstrained microplasticity. Hence, we introduce a percolation limit for microplasticity through the microstructure as the transition away from the linearity. Eventually, as l/D approaches unity, the plasticity becomes extensive and the macroscopic state of cyclic plasticity, as measured in test specimens, is virtually indistinguishable from the connected microplasticity – we term this as the regime of limited plasticity corresponding to the LCF regime. Note that constrained microplasticity exists even below the macroscopic yield point, which leads to the formation and growth of fatigue cracks.

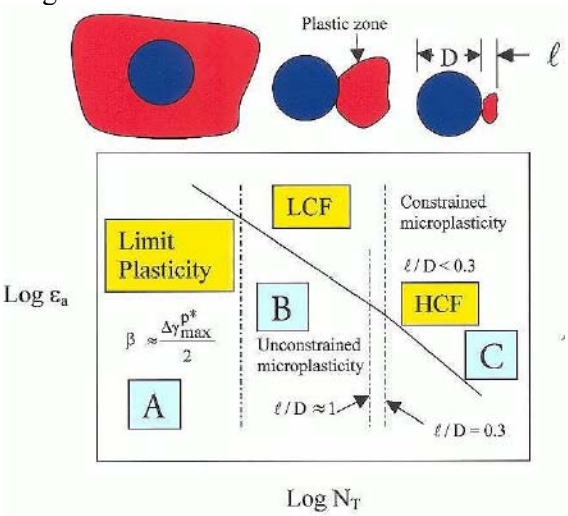

Figure 1. Regimes characterizing cyclic microplasticity at particles and casting pores: (A) elastic-plastic fracture mechanics (EPFM) crack-propagation-dominated, (B) transition regime, and (C) incubation-dominated ($l/D = 0.3$ is for A356 Al alloy).

Modifications of MSF Model for Cast Mg Alloys

Most of the fatigue damage formed at large casting pores near or at the edge of the specimens. Since the sizes of the casting pores dominated the fatigue life, the effect of the inclusion size was incorporated into the incubation model in a stronger fashion. The damage formation site often exhibited a region with relatively higher porosity when compared to the rest of the specimens. Therefore, the porosity affected fast-crack growth in the MSC/PSC regime and was incorporated into the crack-tip displacement.

The nonlocal maximum shear strain range at the micronotch, β, can be estimated using micro-mechanics analysis of a representative volume cell with a nonlocal averaging procedure [5],

$$\beta = \frac{\Delta\gamma^P_{\max}}{2} = Y\left[(\varepsilon_a - \bar{\varepsilon}_{th})\right]^q, \qquad \frac{l}{D} \le \eta_{\lim} \qquad (2a)$$

$$\beta = \frac{\Delta\gamma^P_{\max}}{2} = Y\left(1 + \xi\frac{l}{D}\right)\left[(\varepsilon_a - \varepsilon_{th})\right]^q, \ \eta_{\lim} < \frac{l}{D}, \qquad (2b)$$

where, Y, q, $\eta_{\lim}$ are material and microstructure-related parameters obtained using micro-mechanical simulations at inclusions. Parameter Y depends on the remote load ratio; based on finite-element analysis for A356 Al alloy, it was assumed

$Y = \left[y_1 + (1+R)y_2\right]\left(\frac{D}{D_0}\right)^{d'}$ with y_1 and y_2 as constants.

D_0 is the diameter of the pore in the specimen that caused fatigue failure and d' depicts the effect of pore size on the local plastic strain, which is taken as $0.1 < d' < 0.6$.

The crack-tip-opening displacement is related to the remote loading as,

$$\Delta CTD = f(\bar{\phi})g(\phi)C_{11}\left(\frac{DCS}{DCS_0}\right)^{0.1}\left[\frac{U\Delta\hat{\sigma}}{S_{ut}}\right]^{\zeta} a + C_1\left(\frac{\Delta\gamma^P{}_{\max}}{2}\bigg|_{macro}\right)^2 \qquad (3)$$

where C_1, C_{II} and ζ are material parameters to be determined based on fatigue-rack growth experiments in the MSC regime. The equivalent stress is defined as a linear combination of the von Mises stress and the maximum stress,

$\Delta\hat{\sigma} = \theta_1\left[\frac{3}{2}\frac{\sigma'_{ij}}{2}\frac{\sigma'_{ij}}{2}\right]^{0.5} + \theta_2\Delta\sigma_1$, with θ_1 and θ_2 as load-path-dependent and combined stress state-dependent parameters. Similar to MSF for A356 Al alloy, $\zeta = 4.2$ was found suitable for Mg alloy. Here, two porosity related functions are considered: (1) the variation of average porosity in the specimens: $f(\bar{\phi}) = 1 + \omega\left\{1 - \exp\left(-\frac{\bar{\phi}}{2\phi_{th}}\right)\right\}$, and the porosity threshold (considered as 0.0001); (2) the porosity in front of the microstructurally small crack that reduces the load- bearing capacity of the matrix,

$g(\phi) = (1-\phi)^{-\lambda}$ and $0 < \lambda < 1$.

The MSF model correlations were based on the crack-like damage initiating at casting pores of 25 microns in diameter. The endurance limit for AZ91D was determined as 55 MPa, which is one-third of the cyclic yield strength.

MSF Model Correlations for an AZ91 Cast Mg Alloy

Two types of specimens were prepared: as-cast and cut from a cast automotive component. The general static and fatigue strain-life, stress-life, and cyclic hardening properties were obtained by Westmoreland Testing and Research. Figure 2 shows strain versus fatigue life under R=-1 strain-controlled, constant-amplitude tests at room temperature and in lab air. Multistage fatigue models were correlated based on the static, cyclic and strain-life test results.

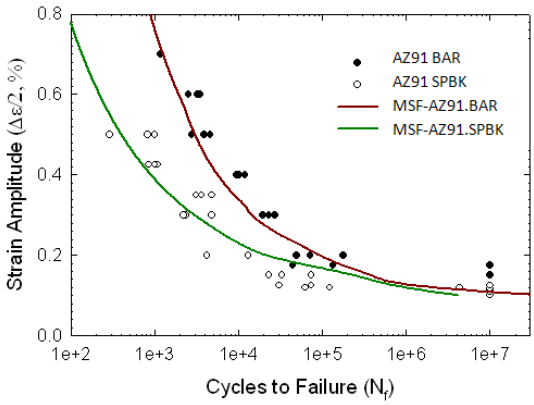

Figure 2. Strain-life test and calculated results on cast bars (BAR) and machined from a support bracket (SPBK) under R=-1 strain control at room temperature and lab air.

Evaluation of an AZ31 Extruded Mg Alloy

Extruded Mg AZ31 alloy was provided in an extruded engineering piece shown in Figure 3. Surfaces representing various features in the extrusion pieces were cut and polished/etched to reveal the extrusion metallurgical features. After mechanical polishing, the inclusion particles were first examined using an optical microscope. Figure 4 shows the optical micrographs of typical surfaces perpendicular to the extrusion direction and to the normal direction. Digitized-image analysis will be implemented to quantify the variations in inclusion-particle distributions and distinguish the variations among different

surfaces. Then, the surface will be etched using an acetic-picral solution. The grain structure and morphology will be revealed in the optical micrographs.

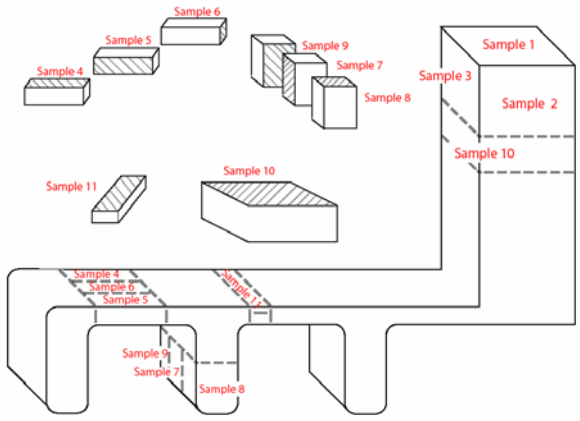

Figure 3. Sketch of extruded AZ31 Mg alloy and surfaces prepared to evaluate various extrusion-specific microstructural features.

Static Tensile Properties of an AZ31 Extruded Mg Alloy

Quasi-static, uniaxial tensile tests were performed at the strain rate of 10^{-3}/s on the specimens along the extrusion and transverse directions. Figure 5 shows the true stress-strain curves of the AZ31 Mg alloy along extrusion direction at room temperature and 100°C and along the transverse direction at room temperatures, respectively. Strong anisotropic yield strength and hardening behavior are demonstrated for the extruded AZ31 Mg alloy.

FASTRAN and Small-Crack Theory

For a number of engineered materials, the fatigue process has been shown to be dominated by "crack propagation" from metallurgical features or discontinuities such as voids, inclusion-particle clusters and grain-boundary locations. These materials were 2024 and 7075 (bare and clad) Al alloys, 2090 Al-lithium alloy, 4340 steel and titanium (Ti)-6Al-4 vanadium (V) titanium engine disc forgings [6-8]. Thus, the fatigue life is primarily composed of the cyclic life for microstructurally and physically small cracks and large-crack behavior. For these materials, observations of the fatigue process indicated that microcracks are present when the material is processed or they crack very early from microscale plasticity at local discontinuities.

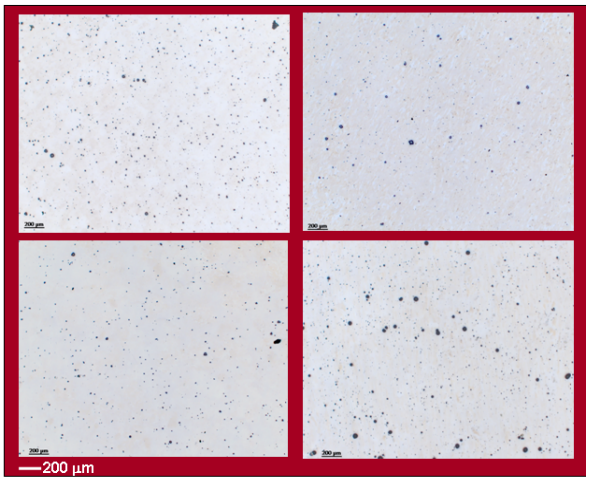

Figure 4. The optical micrographs of typical surfaces of extruded AZ31 Mg alloy. LD, TD, and ND are the extrusion, transverse, and normal direction of the processing coordinate, respectively. LD_TD and TD_ND are the planes formed by the two directions, respectively.

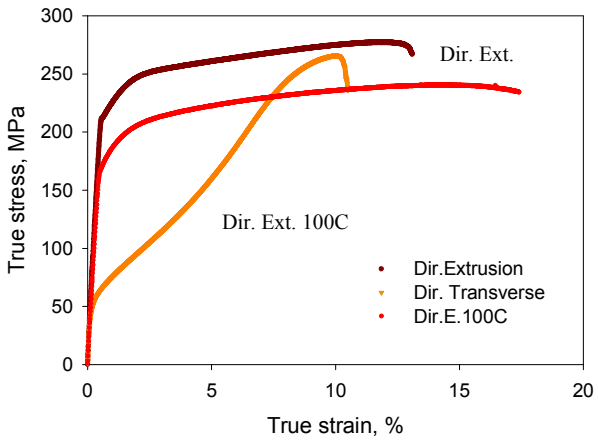

Figure 5. Stress-strain curve of AZ31 Mg alloy under uniaxial tension at room temperature and 100°C along extrusion and transverse directions.

For the 2024 and 7075 alloys, the initial flaw sizes have ranged from 6 to 20 µm [6 and 8]. The 4340 steels have exhibited 8 to 30 µm flaws from calcium-aluminate and manganese-sulfide particles [9]. Initial flaw sizes in the Al alloys and steels were determined by measuring the inclusion particle sizes that precipitated fatigue failures. The Ti alloy forgings had 2 to 20 µm flaws, but these were determined by an equivalent-initial-flaw-size

(EIFS) procedure. In the EIFS procedure, nonlinear fracture mechanics and fatigue-crack growth-rate (small and large crack) properties were used to determine the particular flaw size to fit the stress (S) versus number of cycles-to-failure (N) S-N behavior.

Small-Crack Theory, which assumes an initial flaw size from 1 to 30 μm for various materials, has been used with the fatigue-rack growth-rate properties and a crack-closure model [10] to predict or calculate the S-N curves under both constant and variable amplitude loading. In the Small-Crack Theory approach, no distinction is made between microstructurally- and physically-small cracks. They are both considered "small" cracks and the influences of microstructure are in the measured crack growth-rate data. Small-crack growth behavior is achieved by continuum-mechanics analyses using monotonic and cyclic plasticity and the crack-closure transients under the prescribed load histories.

One of the objectives of the current project is to determine whether Mg alloys have similar initial flaw sizes in their microstructure that precipitate fatigue failure from crack propagation alone. In an effort to address the feasibility of using Small-Crack Theory to calculate fatigue lives on a Mg alloy, fatigue strain, ε, versus N data were recently obtained at MSST for AZ91D (B. Jordon, MSST, private communication, 2007).

Fatigue-Crack Growth

Fatigue-crack growth-rate (dc/dN, change in crack length, c, with change in cycles, N) data on a AZ91E Mg alloy have been obtained from Dr. Andy Newman, U.S. Army at NASA Langley Research Center. These data were determined from compact tension specimens under two stress ratios ($R = P_{min}/P_{max} = 0.1$ and 0.7), and these data are shown as symbols in Figure 6. The crack-growth-rate data were measured from threshold to near fracture and the fracture toughness was estimated to be about 15 ksi-in$^{1/2}$. Cracks in the high stress-ratio tests have fully-open cracks (no crack-closure). Thus, these data are used to establish the effective stress-intensity factor against rate (ΔK_{eff}-rate) baseline curve for the material and test conditions (room temperature and lab air). (The ΔK_{eff}-rate baseline curve is used in the FASTRAN model [10] to predict small- and large-crack growth under constant and variable amplitude loading.) Because the high-R tests fracture at lower values of ΔK than low-R tests, i.e., $\Delta K_c = K_c (1-R)$, the low-R test results are also used to estimate the ΔK_{eff}-rate curve at high rates.

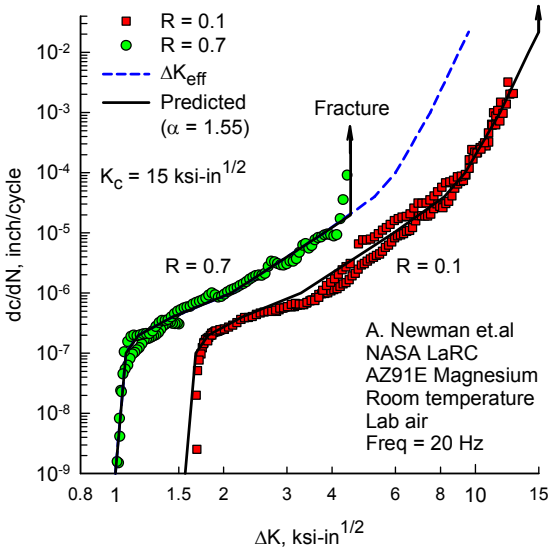

Figure 6. Fatigue-crack growth-rate data on AZ91E Mg alloy.

For high rates, an iterative procedure is used because the curves are a function of the crack-front constraint factor, α. For these data, α was found to be 1.55, which is lower than expected. Increased crack-closure effects due to crack-surface roughness may have caused the lower value. The solid (black) curves are the predicted curves from the FASTRAN model.

Strain-Life Tests on Mg Alloy

Fatigue data were obtained from Jordon at MSST for the Mg alloy AZ91D. Fatigue test (ε-N) data generated on $K_T = 1$ bar specimens under fully-reversed loading are shown in Figure 7 (diamond symbols). The data from Figure 2 are also included for comparison. Jordon's data also included the full-strain- and load-against-cyclic history on eight specimens. The bar specimens were 0.12 inches thick by 0.25 inches wide and tested at three strain levels (0.002, 0.003 and 0.0035). These data fell in between the fatigue data shown in Figure 2.

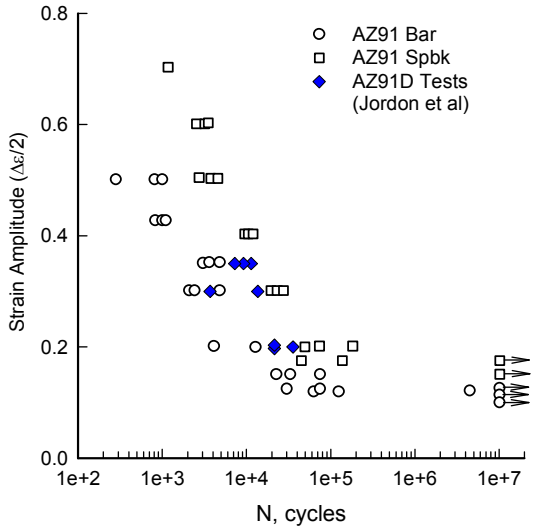

Figure 7. Strain against cycles-to-failure on AZ91 Mg alloys.

The cyclic strain and load histories were available on all LCF specimens (LCF-3 to 10) as shown in Figure 9. A rapid (vertical) drop off of stresses indicated failure of the specimens as illustrated in Figure 8. Based on the measurements, the applied strains were very accurately maintained during the duration of the tests. Figure 8 shows the applied stress (maximum and minimum) for test specimen LCF-3. The maximum applied stress was nearly constant (S_{max} ~ 20.5 ksi) during the duration of the test, but showed a slight reduction near the end of life due to cracking. But the minimum applied stress showed more variation (–18 to –22 ksi). The reason for this behavior was unknown but could be related to the tensile and compressive stress-strain curves being different (as shown in Figure 5), cyclic strain hardening, or variations in the stress-strain response from different sections of the Mg material.

Fatigue-Life Calculations on Mg Alloy

The FASTRAN life-prediction code was used to calculate the fatigue lives on the AZ91D alloy specimens using crack propagation from an EIFS. The effective stress-intensity factor against crack-growth- rate curve had previously been obtained on an AZ91E alloy from NASA Langley. The significance of the Mg alloy treatment, D or E, could not be addressed.

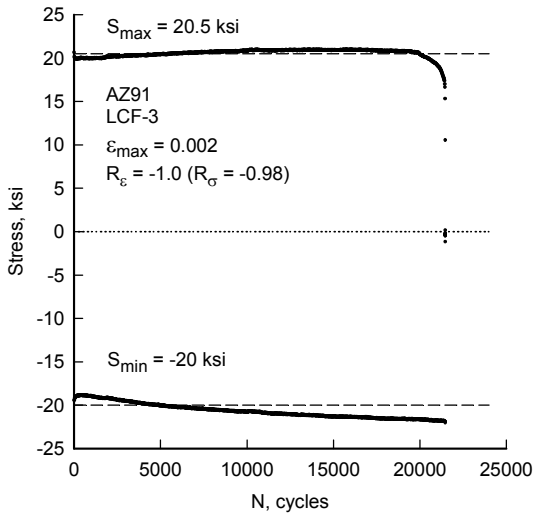

Figure 8. Applied stress against cycles for LCF-3.

Since the FASTRAN code is based on the "applied stress" instead of applied strain, either an average stress history or the variations in both minimum and maximum stresses would have to be considered in the fatigue-life analyses. For simplicity, an average stress history (S_{max}, S_{min}) was selected for each specimen and these values were used in the fatigue-life analyses. Some typical results are shown in Figure 8, which shows the maximum and minimum stresses applied to LCF-3 as a function of cycles. This test had a stress ratio R_σ (S_{min}/S_{max}) of –0.98. The rapid (vertical) drop off of stress indicated failure of the specimen at 21,500 cycles. While the cyclic strains were very accurately maintained during the duration of the test, the stresses showed some variations. The range of stress ratios from the eight tests was from –0.98 to –0.42.

The maximum applied stress against cyclic life (S-N) for the AZ91 alloy is shown in Figure 9. As noted, the applied stress ratio (R_σ) varied. Thus, calculations have been made at –1 and –0.4. A trial-and-error procedure was used to find the EIFS to fit the test data. The EIFS was found to be a 0.012-inch (305-μm) semi-circular surface flaw. The R = –1 curve agrees well with five of the eight specimens. The R = –0.4 curve agrees well with specimen LCF-5, which had an applied stress ratio of –0.42. But, the results for test specimens LCF-3 and 4 showed that the calculated curves were very conservative.

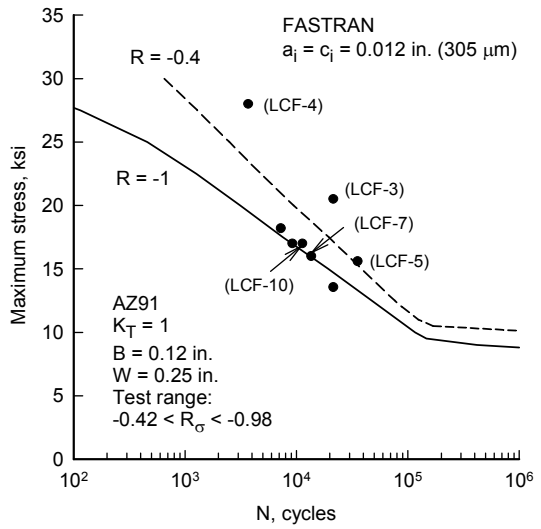

Figure 9. Stress against cycles-to-failure on AZ91 Mg alloy.

A typical fatigue surface from the AZ91 alloy is shown in Figure 10. The initiation site appeared to be a large void (620-μm deep by 250-μm wide) located near the edge of the specimen. Using Murakami's area rule, a 280-μm semi-circular surface crack would have the same area. Thus, the assumed 305-μm radius surface flaw was very close to the void area.

Most of the calculations fell within ± 30%, but calculations made on specimens LCF-3 and 4 were very conservative (factor-of-10) and the calculation on specimen LCF-6 was un-conservative by over a factor-of-2. A determination of the distribution of void sizes in the AZ91 alloy would be useful. Specimens LCF-3 and 4 could have had smaller voids that precipitated failure due to the very small specimen tested. FASTRAN could be used with the distribution of voids to make an upper and lower bound estimate for the fatigue scatter.

The MSF and FASTRAN calculations represented the AZ91 Mg alloy very well, in that the fatigue lives on six of eight tests were accurately calculated. However, these tests were basically LCF results. Whether Small-Crack Theory will work well on the Mg alloys for HCF is yet to be studied. In the past, the fatigue-crack-growth thresholds and the initial flaw sizes have correlated very well with the endurance limits on the materials previously studied with Small-Crack Theory. Thus, Small-Crack Theory has worked well for HCF conditions on Al alloys, Ti alloys and steels. The key for any physics-based model is to observe the fatigue process very early in life to assess the state of damage or cracking.

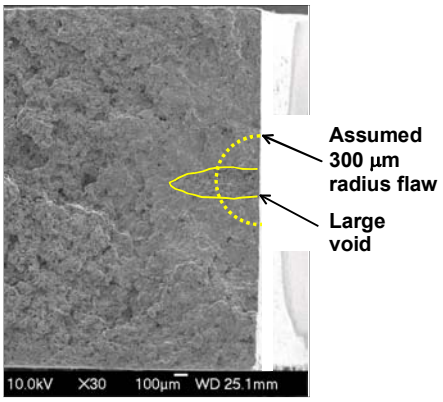

Figure 10. Initiation site at large void and assumed EIFS in AZ91 alloy.

Conclusions

Preliminary studies on the AZ91 alloy have been used to exercise the two fatigue models: (1) the MSF model and (2) Small-Crack Theory using a crack-closure model. The initial evaluations were made under fully-reversed fatigue-loading conditions. The MSF model accounted for the influence of the manufacturing process on the strain-life behavior. The Small-Crack Theory model used fatigue crack growth properties and a 300-μm semicircular flaw to calculate the fatigue lives under the strain-controlled loading conditions.

Two AZ31D Mg extrusions from the automotive industry are being machined into a wide range of tensile and fatigue specimens to generate the mechanical properties for calibration of the two fatigue models.

Presentations/Publications/Patents

Xue, Y., Lugocamarena, M., Horstemeyer, M.F. and Newman, J.C., Jr., "Multistage Fatigue Model for an Extruded AZ31 Mg Alloy," TMS 2008 (accepted for presentation).

References

1. McDowell, D.L., Gall, K., Horstemeyer, M.F. and Fan, J., "Microstructure-based fatigue modeling of cast A356-T6 alloy," Engineering Fracture Mechanics, 70 (2003), 49-80.Suresh, S., Fatigue of Materials, 2nd Edition, Cambridge University Press, p. 543, 2003.
2. Xue, Y., Horstemeyer, M.F., McDowell, D.L., El Kadiri, H. and Fan, J., Microstructure-based multistage fatigue modeling of cast AE44 Mg alloys, *International Journal of Fatigue* 2007; 29:666-76.
3. Horstemeyer, M.F., Fan, J., and McDowell, D.L., "From Atoms to Autos: Part 2 Fatigue Modeling," Sandia National Laboratories Report, SAND2001-8661.
4. Xue, Y., Burton, C.L., Horstemeyer, M.F. and McDowell, D.L., Multistage Fatigue Modeling of Cast A356-T6 and A380-F Aluminum Alloys, *Metallurgical & Materials*, Trans. B (in press).
5. Newman, J.C., Jr. and Edwards, P.R., Short-Crack Growth Behaviour in an Aluminum Alloy - an AGARD Cooperative Test Programme, AGARD R-732, 1988.
6. Short-Crack Growth Behaviour in Various Aircraft Materials, AGARD R-767, P.R. Edwards and J.C. Newman, Jr., editors, 1990.
7. Newman, J.C., Jr., Wu, X., Venneri, S. and Li, C., "Small-Crack Effects in High-Strength Aluminum Alloys," NASA RP-1309, May 1994.
8. Swain, M.H., Everett, R.A., Jr., Newman, J.C., Jr. and Phillips, E., "The Growth of Short Cracks in 4340 Steel and Aluminum-Lithium 2090," AGARD R-767, 1990, pp. 7.1-7.30.
9. Newman, J.C., Jr., "A Crack-Closure Model for Predicting Fatigue Crack Growth Under Aircraft Spectrum Loading," ASTM STP-748, 1981, pp. 53-84.

I. Materials Design for Magnesium Alloys

Seong-Gon Kim: Co-Principal Investigator
Assistant Professor
Physics and Astronomy
Hilbun Hall, Rm 237
Mississippi State University (MSST), P.O. Box 5405
Mississippi State, MS 39762-5405
(662) 325-8031; fax: (662) 325-8898; e-mail: kimsg@ccs.msstate.edu

Mark F. Horstemeyer: Principal Investigator
Center for Advanced Vehicular Systems (CAVS) Chair in Solid Mechanics & Professor, Mechanical Engineering
MSST
206 Carpenter Bldg., PO Box ME
Mississippi State, MS 39762
(662) 325-7308; fax: (662) 325-7223; e-mail: mfhorst@me.msstate.edu

Randall German: Co-Principal Investigator
Professor and Director CAVS
MSST, P.O. Box 5405
Mississippi State, MS 39762-5405
(662) 325-5431; fax: (662) 325-5433; e-mail: german@cavs.msstate.edu

Hongjoo Rhee: *Co-Principal Investigator*
Postdoctoral Associate
CAVS
MSST, P.O. Box 5405
Mississippi State, MS 39762-5405
(662) 325-9221; fax: (662) 325-5433; e-mail: hrhee@cavs.msstate.edu

Sungho Kim: Postdoctoral Associate
CAVS, CAVS 2182-C
MSST
Mississippi State, MS 39762-5405
(662) 325-9241; fax: (662) 325-5433; e-mail: sk5@msstate.edu

Greg Olson: Co-Principal Investigator
Winson-Cook Chaired Professor in Engineering Design
The Steel Research Group at Northwestern
Northwestern University
Department of Mechanical Engineering
2145 Sheridan Road
Evanston, Illinois 60208-3111
(847) 491-2847; fax: (847) 491-7820; e-mail: g-olson@northwestern.edu

Qingyou Han: Co-Principal Investigator
Purdue University
Mechanical Engineering Technology Department
401 North Grant Street
Knoy Hall - Room 107
West Lafayette, IN 47907-2021
(765) 494-7528; fax: (765) 494-6219; e-mail: hanq@purdue.edu

Joseph A. Carpenter: Technology Area Development Manager
(202) 586-1022; fax: (202) 586-1600; e-mail: joseph.carpenter@ee.doe.gov

Expert Technical Monitor: Philip S. Sklad
(865) 574-5069; fax: (865) 574-6098; e-mail: skladps@ornl.gov

Contractor: MSST
Contract No.: 4000054701

Objective

- Design low-cost magnesium (Mg) alloys with improved castability, ductility, and high-temperature creep-deformation mechanisms for automotive applications.

Approach

- In support of the collaborative materials-design effort proposed here aimed at lightweight components for automotive applications, a systems approach to materials design [Olson98] will be applied. Working within a multiscale hierarchy of microstructural subsystems governing desired property combinations for structural performance, key microstructural elements will be identified for the calibration, application, and validation of process/structure and structure/property design models defining key theoretical parameters and critical experiments enabling parametric design of novel alloy compositions.

- We will use quantum mechanical, first-principles methods such as Density Functional Theory (DFT) [Kresse96, Kohn65] to elucidate the origin of the alloying effects. A fundamental understanding of solidification, dislocation, creep, fatigue, crack nucleation and failure of Mg-based alloy systems also requires accurate atomistic modeling of nanoscale systems containing up to hundreds of thousand atoms. We will perform large- scale atomistic simulations using efficient and reliable empirical interatomic potential methods such as the modified embedded-atom method (MEAM) [Baskes92, Daw84, Daw83] and force-matching-embedded-atom-method (FMEAM) potentials.

- Various state-of-the-art experimental techniques will also be employed in this project. Scanning electron microscopy (SEM) and transmission electron microscopy (TEM) will be used to obtain microscale as well as nanoscale structural information of Mg alloys. The structure and energies of dislocation cores and planar defects, including stacking faults and twin boundaries, determine the mechanical behavior of the Mg alloys. Electron backscatter diffraction (EBSD) and X-ray diffraction (XRD) measurements will be used to keep track of texture evolution during deformation. An *in-situ* chemical analysis and mapping of alloying elements can be used to keep track of these elements. Three-dimensional atom probe (3DAP) is capable of resolving the chemical identity and position of individual atoms in 3D with atomic resolution in the z-direction and sub-nanometer resolution in the lateral direction. Furthermore, fundamental thermo-mechanical experiments to measure creep resistance and ductility will be carried out under various loading conditions. Experimental failure analysis will be performed to understand the microstructure-driven mechanism of plasticity and damage growth under monotonic and cyclic loadings. X-ray computed tomography (CT) will be used to quantify in three-dimensions, morphological and topological evolutions of voids and relevant microstructural features to material damage. A depth-sensoring microindenter and a nanoindenter will also be used to evaluate the micromechanical properties of each microstructural phase present in the Mg alloys. These measurements will be used to validate and, in turn, guide the computational material design of new Mg alloys.

- Construct and validate reliable interatomic potentials to model various phases of Mg-based alloys.
- Obtain the electronic, structural and mechanical properties of the Mg alloys.
- Investigate the effect of various additives on the thermo-mechanical properties of Mg alloys;

- Develop rigorous models for investigating the effect of various fabrication processes on the thermo-mechanical properties of the Mg alloys;
- Perform experiments to validate new design models.

Accomplishments

The first-year objectives were met by accomplishing the following:

- Mg alloys AM50B, AM60B, and AE44 have been cast at ORNL by Qingyou Han (now at Purdue) as the base alloys for the project.
- The nanostructure of an experimental, low-melting-point Mg- 7 zinc (Zn) - 3Al prototype alloy was characterized by 3D atom-probe microanalysis in a local-electrode atom probe (LEAP) after aging at 150^{o}C for 100 hours (hrs) to peak hardness corresponding to a yield strength of 190 MPa. The strengthening phase composition was consistent with the ternary Phi phase, including metastable compositions. The equivalent sphere diameter of the precipitates at peak strengthening is measured as 20-50 nm, providing an important strength- model calibration for materials design. The experimental results are available as a preprint:

  Shengjun Zhang and Gregory B. Olson, 3D-atom probe investigation of strengthening precipitates in a Mg-7Zn-3Al alloy, preprint.
- The MEAM potentials for Mg-Al alloys have been developed. We improved upon the potentials previously published [Baskes92, Lee03] to achieve better agreement with experiments and first-principles method based on quantum mechanical, density functional theory (DFT). The potential parameters and validation data have been published in:

  B. Jelinek, J. Houze, Sungho Kim, M. F. Horstemeyer, M. I. Baskes, Seong-Gon Kim, "Modified embedded-atom method interatomic potentials for the Mg-Al alloy system", Phys. Rev. B, vol. 75, pp. 054106 (2007).
- A multi-objective optimization methodology to construct empirical interatomic potentials with minimal manual fitting has been developed and applied to construct a new MEAM interatomic potential for Mg. This new methodology is designed to optimally reproduce multiple target values that consist of several essential materials properties obtained from experiments and first-principles calculations based on DFT. The optimized target quantities include elastic constants, cohesive energies, surface energies, vacancy formation energies, and the forces on atoms in a variety of structures. The new procedure has been applied successfully to develop a new MEAM potential for Mg. The accuracy of the new potential is assessed by computing several material properties of Mg and comparing them with those obtained from other potentials previously published. We found that the present MEAM potential yields a significantly better overall agreement with DFT calculations and experiments. The new methodology and its application to Mg potential along with its validation data have been submitted to a peer-reviewed journal for publication:

  J. Houze, Sungho Kim, Amitava Moitra, B. Jelinek, Sebastien Groh, M. F. Horstemeyer, Erdem Acar, Masoud Rais-Rohani, Seong-Gon Kim, "A multi-objective optimization procedure to develop modified-embedded-atom-method potentials: an application to magnesium", submitted to Phys. Rev. B, http://arxiv.org/abs/0708.0075

Future Direction

- Develop new MEAM potentials for Mg – oxygen (O) and Al-O alloy systems to study the effect of oxygen in Mg-Al-based alloys.
- Validate Mg-O and Al-O MEAM potentials with DFT calculations.
- Perform large-scale molecular dynamics simulations to study the effect of additive elements on material properties of Mg-based alloys.
- Carry out microstructure and mechanical properties characterization of the base-alloys (AM50B, AM60B, and AE44) to understand fundamental materials and mechanical properties.
- Available thermodynamic databases and literature on precipitation-strengthening phases will be reviewed in support of theoretical feasibility assessment of microstructural strategies for castable alloys with creep resistance at 150 ^{o}C. Candidate alloy systems will be identified for further 3D atom-probe microanalytical studies.

Introduction

Mg alloys are currently used in relatively small quantities for automotive components, generally limited to die castings. Two main barriers to wider impact of Mg alloys to automotive industry are poor creep resistance at temperatures above 150 °C for powertrain applications and poor ductility for structural body parts, engine components, engine cradle and control arms.

To achieve the goal of improving the fuel efficiency of the cars built in the future, the automobile industry needs to have Mg-alloy, light-weight, high-strength materials with better materials properties. We need to perform compositional design of Mg-based alloys in a manner that increases creep resistance and ductility while keeping production cost low.

The future state of this technology will be the development of Mg-based alloys that have lower mass densities and increased strength compared to Al-based alloys, and have better creep resistance than that of AE44-grade Mg alloy and cost comparable to that of AZ19D-grade Mg alloy. The new Mg-based alloys should also exhibit sufficiently high ductility to allow conventional fabrication processes to be used, but generate adequate strength after the fabrication process.

Approach

In support of the collaborative materials design effort proposed here aimed at lightweight components for automotive applications, a systems approach to materials design [Olson98] will be applied. Working within a multiscale hierarchy of microstructural subsystems governing desired property combinations for structural performance, key microstructural elements will be identified for the calibration, application, and validation of process/structure and structure/property design models defining key theoretical parameters and critical experiments enabling parametric design of novel alloy compositions.

Figure 1 shows an overall flowchart of the project procedure along with proper technical approaches. First, reliable, empirical interatomic potentials to model various phases of Mg-based alloys are constructed and validated. Next, the structural, electronic, and mechanical properties of the main phases of Mg-based alloys are obtained by DFT and atomistic simulations. In order to design a novel Mg-based alloy with improved castability and ductility, the effects of various phases, novel additives, and precipitates on the materials and mechanical properties of the Mg-based alloys are investigated by DFT and atomistic simulations. At this stage, various base alloys of interest with

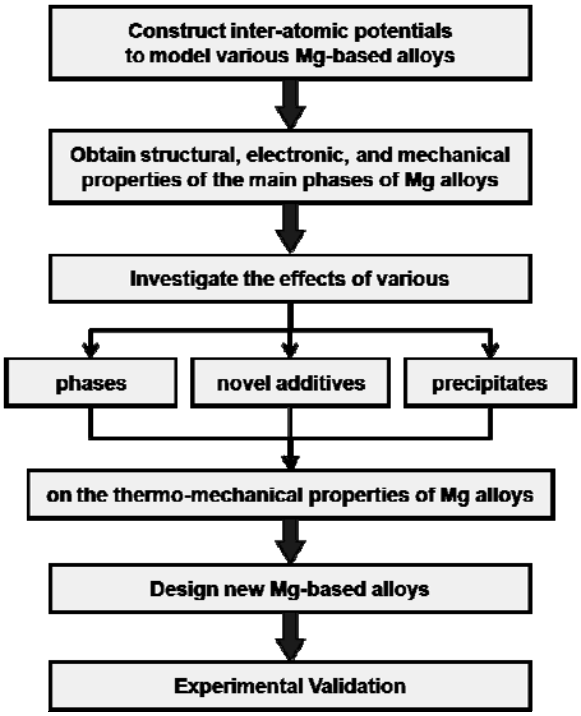

Figure 1. Overall flowchart of the project procedure along with proper technical approaches.

different intrinsic materials properties will be provided by collaborators at ORNL. Various experiments on the base alloys will be carried out to understand fundamental materials/mechanical properties and the output will be provided for materials-designing efforts. Such experiments include chemical analysis, microstructure observation, and micro- and macro-mechanical tests.

Computational Approach

We use a hierarchical, multiscale methodology to investigate the effect of nanoscale precipitates and additives to the overall strength and ductility in Mg-based alloy design for automotive applications. In a hierarchical multiscale framework, numerical methods are run independently at dispa-

rate length scales. Then, a bridging methodology such as statistical analysis methods, homogenization techniques, or optimization methods are used to distinguish the pertinent cause-effect relations at the lower scale to determine the relevant effects for the next higher scale [E03]. One effective hierarchical method for multiscale bridging is the use of thermodynamically-constrained internal state variables (ISVs) that are physically based on microstructure-property relations [Coleman67, Rice71, Kestin70, Hasan95, Espinosa01, Gailly02]. We will adopt the strategy developed by Horstemeyer and his co-workers who used ISVs as a top-down hierarchical approach to bring the pertinent nanoscale, microscale, and mesoscale phenomena into the macroscale [Horst01, Horst03, Olson98, Olson00, Hao03, Hao04].

At the electronic level, quantum-mechanical, first-principles simulations are performed to investigate the interfacial interactions between matrix and the primary and the secondary precipitates. All first-principles, total-energy calculations and geometry optimizations are performed within the DFT [Kresse96, Kohn65] using Blöchl's all-electron projector augmented wave (PAW) method [Blochl94] as implemented by Kresse et al. [Kresse99]. For the treatment of electron exchange and correlation, we generally use the local-density approximation (LDA) [Ceperley80, Perdew81] and sometimes the generalized gradient approximation (GGA) [Perdew96] depending on the accuracy required. The Kohn-Sham equations are solved using a preconditioned band-by-band conjugate-gradient (CG) minimization [Kresse93].

At the atomistic level, accurate atomistic simulations will be performed using efficient and reliable empirical interatomic potentials such as the MEAM or FMEAM [Li03, Liu96] potentials. The interatomic potentials are constructed by optimizing the potential parameters to reproduce various experimental materials properties and atomic force data from DFT calculations. Large-scale atomistic simulations will be conducted to study the effect that size, shape, and volume fraction of different precipitates have on the thermo-mechanical properties of Mg-based alloys. Many factors that govern the yield and hardening behavior of solids, such as crack-tip propagation, dislocation nucleation, dislocation motion, and the interaction of dislocations with grain boundaries, will be investigated through these simulations. Results will be used to guide quantitative alloy composition designs to improve castability and creep resistance of Mg alloys.

Experimental Approach

Various state-of-the-art experimental techniques will be employed in this project. The overall chemical analysis of the base-alloys of interest will be performed by using a spectrometer. Microstructures of the alloys will be investigated by an optical microscope (OM) and a SEM. SEM and TEM will be used to obtain microscale as well as nanoscale structural information of Mg alloys. The structure and energies of dislocation cores and planar defects, including stacking faults and twin boundaries, determine the mechanical behavior of Mg alloys. EBSD and XRD measurements will be used to keep track of texture evolution during deformation. The quantitative as well as qualitative chemical compositions of each phase present in the alloys will be individually analyzed by an energy-dispersive x-ray (EDX) spectroscopy technique. An *in-situ* chemical analysis and mapping of alloying elements can be used to keep track of these elements. 3DAP is capable of resolving the chemical identity and position of individual atoms in 3D with atomic resolution in the z-direction and sub-nanometer resolution in the lateral direction. Conventional hardness tests will be conducted to gain overall properties of the alloys, while depth-sensoring microindentation and nanoindentation tests (NITs) will be performed to obtain micro-mechanical properties of each microstructural phase present in Mg alloys. These measurements will be used to validate and, in turn, guide the computational material design of new Mg alloys. Furthermore, fundamental thermo-mechanical experiments to evaluate creep resistance and ductility will be carried out under various conditions. In order to obtain fundamental mechanical properties and attain proper stress levels for creep tests, tensile tests will be carried out at elevated and room temperatures. The creep behaviors of the base alloys will be extensively investigated to determine better ways for developing novel Mg alloys with improved creep resistance. The creep specimens will be machined from the as-cast condition and the density of the samples will be measured prior to and after the creep tests.

An X-ray computed tomography (CT) will be used before and after the creep tests to quantify the 3D morphological and topological evolutions of voids and microstructural features relevant to material damage. Experimental failure analysis will be performed to understand the microstructure-driven mechanism of plasticity and damage growth under monotonic and cyclic loadings.

By utilizing the composition-structure-property relationship extracted by aforementioned experiments and various simulations, a novel Mg alloy with improved creep resistance and ductility will be designed. A small amount of sample will then be manufactured and supplied by the industrial partners and the model validation by various experiments, including creep tests, will be carried out.

Empirical Interatomic Potentials

To meet the industrial demand for high-strength, lightweight Mg alloys, it is essential to obtain detailed understanding of the effect of individual alloying elements on the properties of Mg alloys. The alloying elements can form interstitial or substitutional defects, or can precipitate into small particles creating complex interface structures. The interactions between these alloying elements need to be investigated using atomistic simulation techniques such as molecular dynamics (MD) or Monte Carlo simulations. These atomistic simulations require accurate atomic interaction potentials to compute the total energy of the system. First-principles calculations certainly can provide the most reliable interatomic potentials. However, realistic simulations of alloy systems often require a number of atoms that renders these methods impractical – they either require too much computer memory or take too long to be completed in a reasonable amount of time. One alternative is to use empirical interatomic potentials that can be evaluated efficiently, so that the atomistic approaches that use them can, in certain cases, handle systems with more than a million atoms.

There are two additional essential features that are expected from a useful empirical approach besides its efficiency: reliability and flexibility. A reliable interatomic potential would accurately reproduce various fundamental physical properties of the relevant element or alloy, such as elastic, structural, and thermal properties. Reliability also includes transferability. A transferable interatomic potential would perform reasonably well even under circumstances that were not used during its construction phase. A flexible empirical approach can represent interaction potentials among a wide variety of elements and their alloys using a common mathematical formalism.

Within the embedded-atom method (EAM) [Daw84, Daw83] approach, the total energy of the system can be written as

$$E = \sum_i E_i \tag{1}$$

where

$$E_i = \frac{1}{2}\sum_{j(\neq i)} V(r_{ij}) + F(n_i) \tag{2}$$

$V(r)$ is the pair interatomic potential, $F(n)$ is the embedding energy function, n_i is the total 'atomic density' at atom i from the surrounding atoms, and it is assumed that

$$n_i = \sum_{j(\neq i)} \rho(r_{ij}) \tag{3}$$

where $\rho(r)$ is the 'atomic density' around an isolated atom, and *r* is the interatomic distance [Daw84]. The EAM was able to reproduce physical properties of many metals and impurities. The EAM was applied to hydrogen embrittlement in nickel [Daw83], and to nickel and palladium with hydrogen [Daw84].

Baskes *et al.* [Baskes87] proposed the MEAM, which is an extension of EAM to include angular forces. The MEAM potential proposed was the first empirical interatomic potential method to use a single formalism for face-centered cubic (fcc), body-centered cubic (bcc), hexagonal close-packed (hcp), diamond-structured materials and even gaseous elements, in good agreement with experiments or first-principles calculations [Baskes87, Baskes89, Baskes92, Baskes94]. Cherne *et al.* made a careful comparison of MEAM and EAM calculations in a liquid nickel system [Cherne01].

In the FMEAM, a force-matching method [Ercolessi94] is applied to the conventional EAM. Unlike the MEAM, however, the FMEAM approach does not use any analytic functional form for $\rho(r)$, $V(r)$, or $F(n)$. Instead, each of these functions is described as a set of control points whose values are the parameters to be optimized. A cubic spline function is used to interpolate the values between the control points. The control points are optimized by matching the forces of this potential to those of quantum mechanical, *ab initio* calculations for a large set of different configurations. The potential parameters are simultaneously fit to several critical experimental data such as equilibrium lattice constant, cohesive energy, bulk modulus, and elastic constants.

Multi-objective Optimization

A generic, multi-objective optimization (MOO) problem can be formulated as [Kim05, deWeck04]:

$$\begin{aligned} &\min\ \vec{J}(\vec{x})\ \text{s.t.}\ x \in S \\ &\text{where}\ \vec{J} = \left[J_1(\vec{x}) \cdots J_m(\vec{x})\right]^T \\ &\vec{x} = \left[x_1 \cdots x_n\right]^T \end{aligned} \tag{4}$$

Here, $\vec{J}$ is a column vector of *m* objectives, whereby $J_i \in \Re$ (a real number). The individual objectives are dependent on a vector $\vec{x}$ of *n* design variables in the feasible domain *S*. The design variables are assumed to be continuous and vary independently. Typically, the feasible-design domain is defined by the design constraints and the bounds on the design variables. The problem is to minimize all elements of the objective vector simultaneously. The most widely used method for MOO is scalarization using the weighted-sum method. The method transforms the multiple objectives into an aggregated scalar objective function $\vec{J}$ that is the sum of each objective function J_i multiplied by a positive weighting factor w_i:

$$J(\vec{x}) = \sum_{i=1}^{m} w_i J_i(\vec{x}) \tag{5}$$

In this project, the overall goal is to develop FMEAM potentials for Mg-based alloys. The individual objective functions are constructed from the normalized differences between the FMEAM-generated values and the target values:

$$J_i(\vec{x}) = \left[\frac{Q_i(x) - Q_i^0}{Q_i^*}\right]^2 \tag{6}$$

Here, Q_i is the physical quantity computed using the current FMEAM-potential parameters and Q_i^0 is the target value to reproduce. The target values are usually experimental values, but the computed values from the first-principles method are chosen when the experimental data are not available. The normalization factor Q_i^* is a typical value for the given materials parameter and often $Q_i^* = Q_i^0$ is assumed. The overall objective function $J(\vec{x})$ can be minimized using usual multi-dimensional optimization routines. To avoid unnecessary complications, we use the *downhill simplex method* [Press92], which requires only function evaluations, not derivatives.

Mg Interatomic Potential

The MOO procedure was applied to develop a new interatomic potential for Mg based on MEAM. We used the previously published MEAM potential by Baskes [Baskes92] as the initial set of the parameters for our MOO.

Figure 2 shows the cohesive energy of Mg atoms in the hcp structure, its lowest-energy crystal structure, as a function of the lattice constant. MEAM-potential calculations (open circles) are compared with the Rose equation-of-state (solid curve). The Rose equation-of-state is constructed from experimental data—optimum lattice constant, the cohesive energy, and the bulk modulus. Our results show that MEAM potential for Mg reproduces experimental data extremely accurately over a wide range of lattice constants.

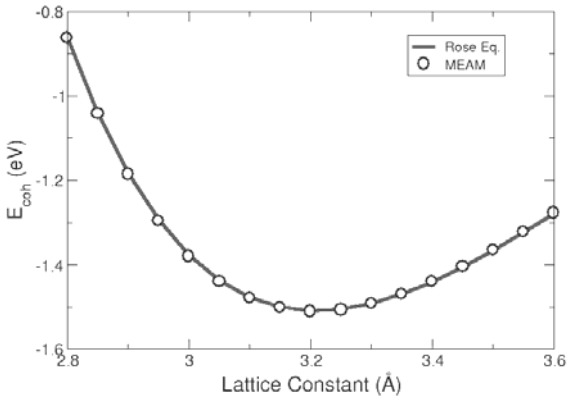

Figure 2. The cohesive energy of Mg atoms in the hcp cubic crystal structures as a function of the lattice constant *a* (open circles), compared with the Rose equation (solid curve).

To validate the transferability of our new MEAM potential, we calculated the cohesive energies of Mg atoms in three common configurations, namely, hcp, fcc, and bcc crystal structures, as a function of the atomic volume. The results are summarized in Figure 3. Our results show that the new MEAM potential for Mg atoms correctly predicts the order of stability among these common structures. In addition, the differences in equilibrium cohesive energies among these configurations are reasonably close to those of DFT calculations.

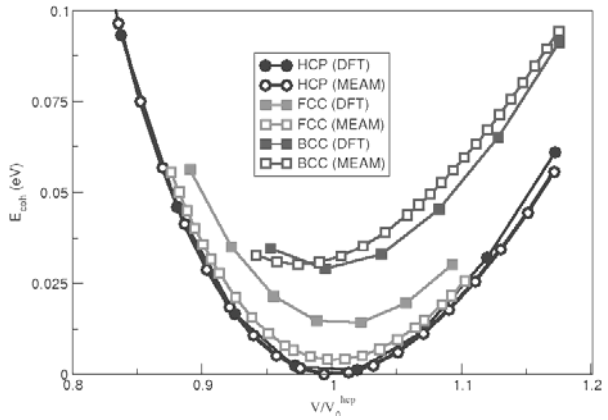

Figure 3. The cohesive energies of Mg atoms in hcp, fcc, and bcc crystal structures as a function of the atomic volume. The values reproduced with MEAM potentials are compared with DFT calculations. Volumes are scaled by the equilibrium atomic volume of the hcp structure.

Semi-infinite surface is one of the simplest forms of defects. To test the transferability of Mg MEAM potential, surface-formation energies for several different surfaces are computed. Surface-formation energy per unit surface area, E_{surf}, is defined as

$$E_{surf} = (E_{tot} - N\varepsilon)/A, \quad (7)$$

where E_{tot} is the total energy of the structure with a surface, N is the number of atoms in the structure, ε is the total energy per atom in the bulk, and A is the surface area. Table 1 shows the surface formation energies of many different surfaces constructed from hcp Mg crystals. Results from the present MEAM potentials are in good agreement with the DFT calculations, representing a significant improvement over two of the previously published MEAM potential by Hu *et al.* [Hu01] and EAM potentials by Liu *et al.* [Liu97].

Table 1. Surface-formation energies for hcp Mg. The units are mJ/m^2. The second column indicates if the structure was relaxed. Comparisons with DFT calculations and other previously developed MEAM potentials are also given**.**

Surface	Relax	DFT	MEAM[a]	MEAM[b]	EAM[c]
(0001)	No	638	604		500
(0001)	Yes	637	595	310	499
(1010)	No	855	642		517
(1010)	Yes	846	523	316	515

[a]The present MEAM potential [Jelinek07]
[b]MEAM potential by Hu *et al.* [Hu01]
[c]EAM potential by Liu *et al.* [Liu97]

Stacking fault is another kind of structure that occurs frequently in real materials and provides a good test environment for empirical potentials. Stacking-fault energy per unit area is defined by

$$E_{sf} = (E_{tot} - N\varepsilon)/A, \quad (8)$$

where E_{tot} is the total energy of the structure with a stacking fault, N is the number of atoms in the system, ε is the total energy per atom in the bulk, and A is the surface area that is perpendicular to the stacking fault. Four stacking-fault types from the calculation of Chetty and Weinert [Chetty97] were examined. Total-energy calculations for I_1, I_2, T_2, and E stacking-fault types were per-

formed using both DFT and MEAM calculations. The results are compared in Table 2. The present

Table 2. Stacking-fault energies for hcp Mg. Results from the present MEAM and DFT calculations are compared. Stacking-fault energies per unit area are given in mJ/m^2. Comparisons with other previously-developed empirical potentials are also given.

Fault	**MEAM**[a]	EAM[b]	MEAM[c]	DFT[d]	DFT[e]
I_1	**7**	27	4	18	21
I_2	**15**	54	8	37	44
T_2	**15**	54		45	51
E	**22**	81	12	61	68

[a]The present MEAM potential [Jelinek07]
[b]EAM potential by Liu *et al.* [Liu97]
[c]MEAM potential by Hu *et al.* [Hu01]
[d]DFT calculations from the present work [Jelinek07]
[d]DFT calculations by Chetty *et al.* [Chetty97]

MEAM potential shows a substantial improvement over the previously published MEAM potential by Hu *et al.* [Hu01]. The stacking-fault energies are consistently underestimated by the present MEAM potentials compared to the results of the DFT calculations, while the results by the EAM potential Liu *et al.* [Liu97] are consistently overestimated.

Recently, we developed another empirical interatomic potential for Mg atoms based on FMEAM instead of MEAM. This new potential is very similar to our previous MEAM potential [Jelinek07] in its performance, but has superior thermal properties during MD simulations. To demonstrate one of its thermal properties, we calculated the melting temperatures of pure Mg crystals. We followed a single-phase method as described by Kim and Tománek [Kim94], in which the temperature is increased at a constant rate and the internal energy of the system is monitored. Figure 4 shows the internal energies of Mg crystal in hcp structure as a function of temperature. The plot was obtained from the ensemble average of five hcp structures containing 448 Mg atoms. The initial velocity vectors were set randomly according to the Maxwell-Boltzmann velocity distribution at T = 100 K. The temperature of the system was controlled by using a Nosé-Hoover thermostat [Nose84, Hoover83]. It is clearly seen from Figure 4 that the internal-energy curve makes an

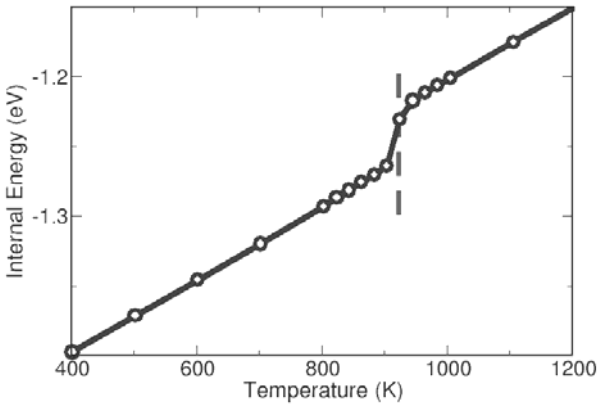

Figure 4. The internal energies of Mg crystal in hcp structure as a function of temperature. The energies are obtained from the ensemble average of the MD simulations of five structures containing 448 Mg atoms. The vertical dashed line indicates the experimental melting temperature 923 K.

abrupt transition from one linear region to another, marking the melting point. Using this method, we obtained 920 K as the melting temperature of Mg crystals. This result is in good agreement with the experimental value of 923 K. Our result represents a substantial improvement in accuracy from 745 K obtained from a previously-published EAM potential [Liu96] or 780 K from a MEAM potential [Jelinek07].

Al Interatomic Potential

We applied the MOO procedure to develop a new interatomic potential for Al based on the MEAM. We used the previously published Al MEAM potentials by Baskes [Baskes92] as the initial set of the parameters for our MOO procedure.

To test the validity of this new Al MEAM potential, we computed the atomic energy of Al atoms in four common configurations, namely fcc, hcp, bcc, and simple cubic (sc) crystal structures, as a function of the atomic volume. The results are summarized in Figure 5. As expected, the curve for the fcc structure produced by the MEAM potential retraces the results of DFT calculations nearly perfectly since fcc was used as the reference structure during the potential construction process. The agreement between the MEAM potential and DFT for the hcp structure is also remarkable. The most important result, however, is the fact that the new MEAM potential correctly identified fcc as the most stable structure for Al.

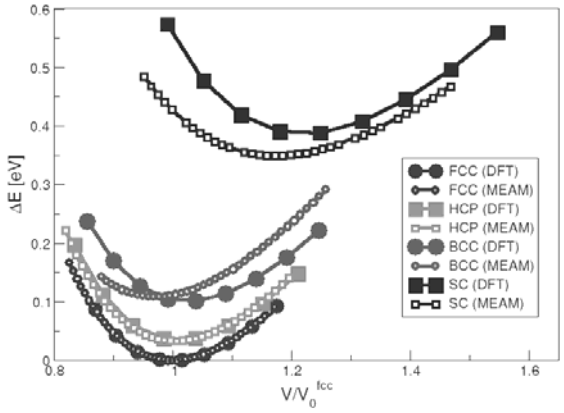

Figure 5. Atomic energies (total energies per atom) as a function of the atomic volume (volume per atom) for Al atoms in fcc, hcp, bcc, and simple cubic (sc) crystal structures. The energies are measured from the equilibrium atomic energy of fcc structure. Volumes are scaled by the equilibrium atomic volume of the fcc structure.

Furthermore, the sequence of the structures is correctly predicted in the order of stability by the Al MEAM potential. The relative cohesive energies, with respect to the one for the fcc structure, are also in good agreement with the DFT calculations, although the result for the simple cubic structure is slightly underestimated.

The relative equilibrium atomic volumes, with respect to the one for the fcc structure, are also well reproduced. We point out that the equilibrium atomic volume for fcc Al, obtained by the MEAM potential (16.61 $Å^3$), is slightly different from the one predicted by DFT (15.76 $Å^3$). This is due to the fact that the MEAM parameters are fitted to reproduce the experimental volume, while DFT within LDA tends to underestimate the equilibrium lattice constants by roughly 1% [Droogenbroeck04, King94].

As another test for the transferability of the Al MEAM potential, surface formation energies for several different surfaces are computed. Table 3 shows the surface formation energies of many different surfaces constructed from fcc Al crystals. Results from the present MEAM potentials are in good agreement with the DFT calculations, representing a significant improvement over two of the previously published MEAM potential by Lee *et al.* [Lee03] and EAM potentials by Liu *et al.* [Liu97].

Table 3. Surface-formation energies for fcc Al. The units are mJ/m^2. The second column indicates if the structure was relaxed. Comparisons with DFT calculations and other previously-developed MEAM potentials are also given.

Surface	Relax	DFT	MEAM[a]	MEAM[b]
(111)	No	992	737	
(111)	Yes	988	731	629
(110)	No	1371	1068	
(110)	Yes	1349	1035	948
(100)	No	1213	1025	
(100)	Yes	1212	1025	

[a]The present MEAM potential [Jelinek07]
[b]MEAM potential by Lee *et al.* [Lee03]
[c]EAM potential by Liu *et al.* [Liu97]

Stacking fault is another kind of structure that occurs frequently in real materials and provides a good test environment for empirical potentials. Three stacking-fault types from the calculation of Chetty and Weinert [Chetty97] were examined. Total energy calculations for I, E, and T stacking-fault types were performed using both DFT and MEAM calculations. The results are compared in Table 4. For the case of stacking fault type *I*, our MEAM result is in good agreement

Table 4. Stacking-fault energies for fcc Al. Results from the present MEAM and DFT calculations are compared. Stacking-fault energies per unit area are given in mJ/m^2. Comparisons with other previously-developed empirical potentials are also given.

Fault	Relaxed	**MEAM[a]**	EAM[b]	DFT[c]	Expt.[d]
I	No	**150**	169	136	
I	Yes	**146**	142	133	140-160
E	No	**150**	169	135	
E	Yes	**148**	154	133	
T	No	**75**	84	62	
T	Yes	**74**	77	61	

[a]The present MEAM potential [Jelinek07]
[b]EAM potential by Liu *et al.* [Liu97]
[c]DFT calculations from the present work [Jelinek07]
[d]Experimental results by Hirth *et al.* [Hirth82]

with the available experimental value even though our DFT result is lower than the experimental value. In all cases considered, the present MEAM potential shows better overall agreement with DFT calculations compared with the EAM potential by Liu *et al.* [Liu97].

Mg-Al Alloy Interatomic Potential

Based on interatomic potentials for Mg and Al atoms, we developed a new interatomic potential for Mg-Al alloy system based on the MEAM by applying the MOO procedure. We used the previously-published MEAM potentials for Mg-Al alloys by Baskes [Baskes92] as the initial set of the parameters for our MOO procedure.

To test the validity of this new MEAM potential for Mg-Al alloy system, we computed the heat of formation per atom for different configurations. In order to compare Mg-Al alloy systems with different stoichiometric coefficients, we define the heat of formation per atom as

$$H_f = \frac{E_{tot} - N_{Mg}\varepsilon_{Mg} - N_{Al}\varepsilon_{Al}}{N_{Mg} + N_{Al}}, \qquad (9)$$

where E_{tot} is the total energy of the system, N_{Mg} and N_{Al} are the numbers of Mg and Al atoms in the system, and ε_{Mg} and ε_{Al} are the total energies per atom for Mg and Al in their ideal bulk structures, respectively. Figure 6 shows the heat of formation per atom H_f for the *B*1, *B*2, and *B*3 structures compared with the results from the DFT calculations. The *B*1 (cubic rocksalt) structure was used as the reference structure for the Mg-Al alloy MEAM potential. Figure 6 shows that the sequence of the structures in the order of stability is predicted correctly by the MEAM potential for the Mg-Al alloy system. The relative cohesive energies, with respect to the one for the reference structure, are also in good agreement with the DFT calculations. The equilibrium atomic volume and bulk modulus of Mg-Al in the *B*1 structure are reproduced almost exactly.

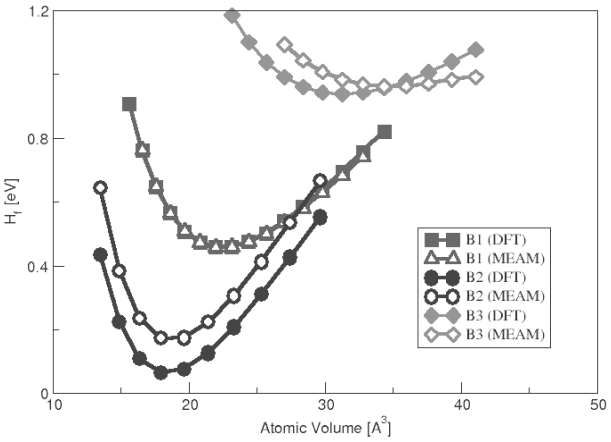

Figure 6. The heat of formation per atom for Mg-Al alloys in the *B*1, *B*2, and *B*3 crystal structures.

To further demonstrate the validity of our potentials, we computed the heat of formation per atom for many intermetallic phases of Mg-Al alloys. The total energy values in Eq. (9) of *B*1, *B*2, *B*3, *C*1, *C*3, *C*9, *C*15, *D*03, *D*09, *A*15, *L*12, and *A*12 structures were evaluated at the optimal atomic volume for each structure. The results from the MEAM calculations, compared with the ones from the DFT calculations, are summarized in Figure 7. Although the Mg and Al atoms in these intermetallic phases are in a chemical environment very different from the one in the reference structure (*B*1), the agreement between MEAM and DFT is quite satisfactory. In most cases, MEAM preserves the order of stability predicted by DFT.

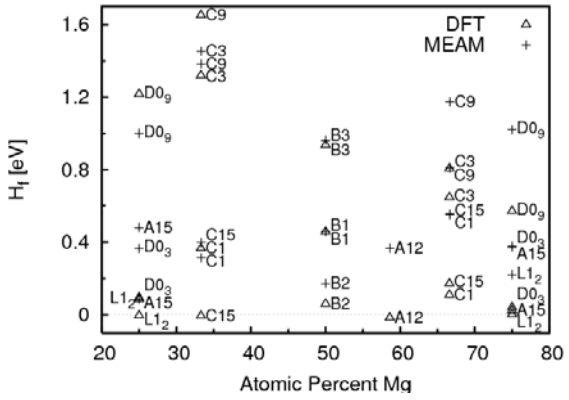

Figure 7. The heat of formation per atom for Mg-Al alloys in various intermetallic phases with different stoichiometric coefficients. The results obtained from the Mg-Al MEAM potentials are compared with the DFT calculations. The structure names are written next to the symbols (open triangles for DFT and crosses for MEAM).

The differences in the heat of formation per atom from MEAM and DFT are less than 0.5 eV at most. However, we note that the MEAM failed to predict that the formation of one of the experimentally-observed Mg-Al alloy structures [Singh03, Okamoto98], $\gamma(Mg_{17}Al_{12})$, denoted as the *A*12 structure in Figure 7, as an exothermic process. In comparison, our DFT calculation correctly predicted the H_f for this structure to be a negative value (−0.017 eV).

Precipitates in a Mg-7Zn-3Al alloy

While typical Mg-Al-Zn casting alloys such as AZ91 are Al-rich, Zn-rich alloys associated with the Zn-rich lower ternary eutectic can provide low-melting compositions with the potential for greater precipitation strengthening. A previous study demonstrated that a MgZnAl aged to peak hardness at 150°C for 100 hrs could reach a yield strength of 190 MPa [Shiao06].

While details of precipitation strengthening in MgAlZn alloys are not well known, the precipitation strengthening in binary MgZn alloys has been well studied. The precipitation sequence in Mg-Zn is well documented starting from Guinier-Preston (GP) zone formation, followed by the formation of β_1' and β_2' metastable precipitates before reaching the formation of equilibrium β phase [Sturkey59, Gallot64, Wei95]. In the present work, the precipitates in a Mg–7Zn–3Al (in wt. %) alloy aged to peak hardness at 150°C have been characterized by 3DAP microanalysis as the basis for calibration of precipitation-strengthening models for alloys design.

3D LEAP Tomography

A ZA73 alloy (Mg–7Zn–3Al) was induction melted under an Ar atmosphere and cast into ingots. The samples were encapsulated together in a pyrex tube in vacuum to prevent oxidation of the Mg and then backfilled with argon to prevent vaporization of the Zn. These samples were heated in a furnace at a solution treatment temperature of 358 °C for 24 hours and then quenched in oil to retain a super-saturated solid solution. Samples were then encapsulated individually and aged in a furnace for 100 hours at 150 °C corresponding to the peak hardness conditions identified in a previous study [Shiao06].

Square bars having a dimension of 0.5 mm × 0.5 mm × 12 mm were cut from the bulk specimens and electropolished to make sharp needle specimens for atom probe analysis. The electropolishing electrolyte was 2% perchloric acid + 2-butoxy ethanol (2% $HClO_4$ + $CH_3(CH_2)_3O(CH_2)_2OH$) and the voltage was initially set at 30 V and reduced to 10 V when pulsing. The sharpened specimens were rinsed in ethanol after electroplishing.

In order to analyze the microstructure of these nanoscale precipitates, 3DAP tomography was employed. Atom-probe tomography utilizes a combination of time-of-flight mass spectrometry and point-projection microscopy to chemically identify and locate individual atoms within a bulk sample. Atom-probe specimens are needles or tips sharpened to less than 100 nm in diameter. A positive voltage pulse is applied to the sharpened tip, causing field evaporation of positively-charged metal ions that are subsequently drawn to a detector plate along a voltage differential. The chemical identity of each ion is revealed through the mass-to-charge ratio as determined by the time-of-flight between the applied pulse and point of detection. The x and y coordinate of each ion within the sample is then determined from the point of impact on the two-dimensional (2D) detector, and the depth (or z coordinate) is determined by the sequence number or absolute time of impact.

For this research, a new generation atom probe is employed termed a local-electrode atom probe (LEAP™). The LEAP improves upon conventional 3DAP by generating the electric field through a localized extraction electrode. Due to the close proximity of the electrode to the specimen tip, the voltage requirements for field evaporation are much smaller and can be pulsed at much higher frequencies (2×10^5 Hz), significantly raising the data-collection rate. The electrode also serves to shield evaporated ions from the effect of the cycling electric field near the specimen tip, providing for increased mass resolution (greater than 1/500 full-width at half-maximum (FWHM)) at large fields-of-view up to 40. The practical result of these improvements is the ability to

reconstruct significant volumes of material (>10^6 nm^3) in a matter of hours instead of days, making the LEAP comparable to other conventional forms of microscopy used to study the nanoscale. The LEAP tomograph at the Northwestern University Center for Atom Probe Tomography (NUCAPT) was employed in this study.

Atom-probe tomography was performed using a LEAP™ 3000 tomograph manufactured by Imago Scientific Instruments Corporation in Madison, WI. Analyses were performed after cooling specimens to a temperature of 40 K to minimize atomic motion while under ultra-high vacuum (residual pressure <10^{-8} Pa). Field evaporation of atoms from the specimen tip was achieved through applied high-voltage pulses at a frequency of 200 kHz. Voltage is applied to the specimen tip through a standing direct-current (DC) voltage with voltage pulses applied through the extraction electrode at a pulse-to-DC voltage ratio of 15%. The voltage levels required for field evaporation are dependent on the radius of curvature of each specimen tip, with the standing DC voltage ranging from 500 V for very sharp tips (diameter < 10 nm) to 15,000 V for larger tips (~ 100 nm diameter). Steady field evaporation rates of 400-10,000 atoms/second were maintained through software-controlled manipulation of the voltage levels, with applied voltage steadily increased to account for tip blunting with continued specimen evaporation.

An alternative mode of operation of pulsed-laser evaporation reduces the frequency of nanowire fracture by eliminating the voltage pulses in favor of more localized laser excitation, which does not produce a repetitive stress on the sample. The precise mechanisms by which the laser promotes ion evaporation are still being debated, but it seems clear that local heating on very short (picosecond) timescales promotes thermally-assisted field evaporation. In addition to reducing specimen fracture, laser pulsing generally produces sharper mass spectra and fewer unidentified peaks. Both voltage-pulse and laser-pulse modes of field evaporation were applied in this study.

Reconstruction and quantitative analysis of collected data sets were performed with the IVAS 3.0 software from Imago Scientific Instruments.

The volume of the analyzed material (v_{total}) was calculated from the total number of ions in the reconstruction (n) using

$$v_{total} = \frac{n\Omega}{f} \qquad (10)$$

where the average atomic volume, Ω, is set equal to that of bcc Fe (1.18×10^{-2} nm^3) and the overall detection and reconstruction efficiency (f) is estimated at 0.6. Standard deviations (σ) of measured compositions through the LEAP analysis were calculated using Eq. (10) [Miller00]:

$$\sigma_c = \sqrt{c(1-c)/N} \qquad (11)$$

where c is the measured composition of the particular element, N is the total number of atoms detected. To quantify the two precipitate dispersions, two tools are used in the IVAS software: isoconcentration surfaces and 1D composition profiles. Isoconcentration surfaces are essentially 3D compositional contour maps, where a threshold composition is selected for one or a combination of elements and a surface is drawn connecting the selected concentration. 1D compositional profiles were generated through a cylindrical selection volume 1 nm in diameter at various lengths. Composition profiles are generated by counting the number and type of each atom contained within the cylinder over increments 0.1-nm thick.

Results and Discussion

Figure 8 displays LEAP tomographic reconstructions for the ZA73 alloy aged at 423 K for 100 hours using the voltage mode. Compared

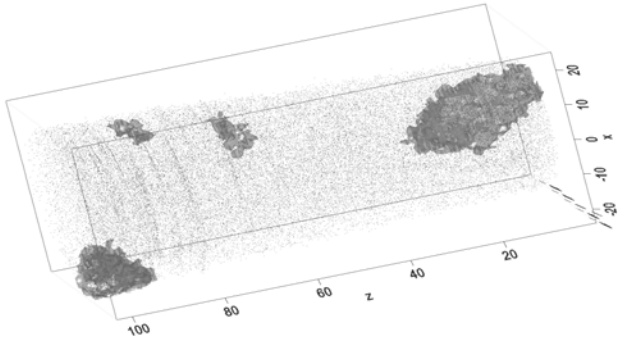

Figure 8. LEAP tomographic reconstructions of 5 % Zn isoconcentration surfaces for the ZA73 alloy aged at 423 K for 100 hours using the voltage mode.

with the bulk alloy composition, a good agreement has been obtained in the Zn content. However, a small discrepancy exists in the Al content.

A proximity histogram (proxigram) showing the concentration of Mg, Zn, Al and Ca as a function of radial distance from the precipitate interface is also presented in Figure 9. It is apparent that both Zn and Al partition to the precipitates. The Zn and Al contents are very low in the matrix. The approximate chemical compositions of the matrix and the precipitates can be read in this proximity diagram. The average chemical compositions of the matrix and the precipitates are reported in Table 5.

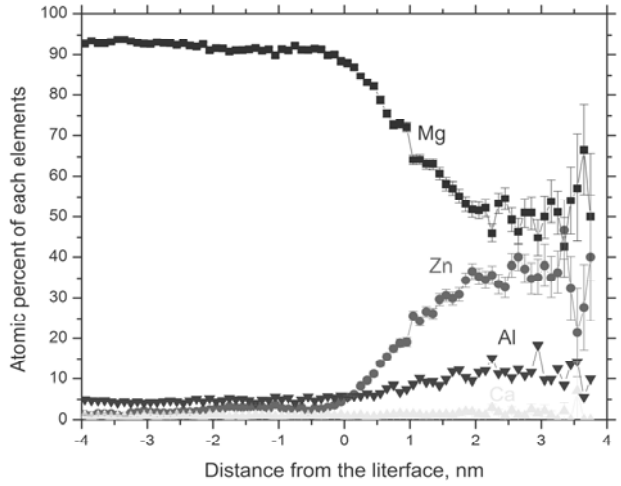

Figure 9. Proximity histogram for the LEAP tomographic reconstructions displayed in Figure 8 showing the average concentration of Mg, Al, Zn and Ca as a function of distance from the Mg-Zn-Al ternary heterophase interface, as defined by a 5 at. % Zn isoconcentration surface. Concentration error bars are calculated as $\sigma_c = \sqrt{c(1-c)/N}$, where N is the total number of atoms detected.

Table 5. Composition of the matrix and the precipitates in ZA73 alloy as measured by LEAP spectrometry (voltage mode) and by calculations using Thermo-Calc and COST2 database.

at %	Matrix			Precipitates		
Elements	Mg	Zn	Al	Mg	Zn	Al
LEAP	95.06	1.08	4.50	51.79	38.08	10.13
Thermo-Calc	96.97	1.63	1.40	37.46	47.47	15.07

Figure 10 displays LEAP tomographic reconstructions for a second equivalent specimen using the laser mode. Compared with Thermo-Calc predictions, good agreement has been obtained in the Zn content. However, a small discrepancy exists in the Al content. The specimen composition is distinctly different from the first specimen, consistent with the expected inhomogeneity of the cast alloy.

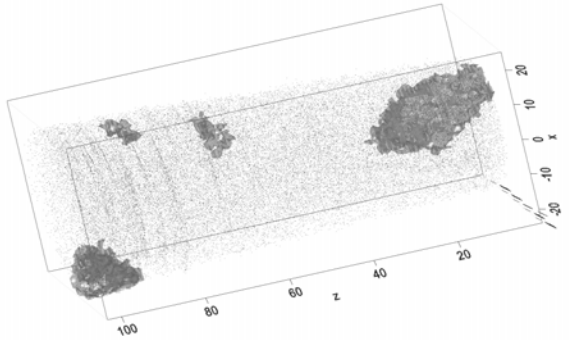

Figure 10. LEAP tomographic reconstructions of 5 % Zn isoconcentration surfaces for the ZA73 alloy aged at 423 K for 100 hours using the laser mode.

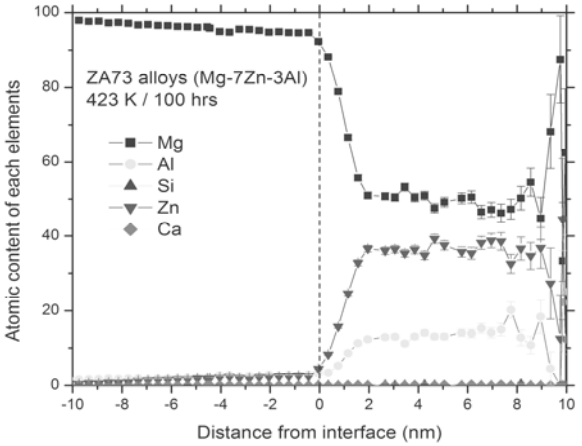

Figure 11. Proximity histogram for the LEAP tomographic reconstructions displayed in Figure 10 showing the average concentration of Mg, Al, Zn and Ca as a function of distance from the Mg-Zn-Al ternary heterophase interface, as defined by a 5 at. % Zn isoconcentration surface. Concentration error bars are calculated as $\sigma_c = \sqrt{c(1-c)/N}$, where N is the total number of atoms detected.

A proxigram showing the concentration of Mg, Zn, Al and Ca as a function of radial distance from the precipitate interface is also presented in Figure 11. It is again apparent that both Zn and Al partition to the precipitates, while the Zn and Al contents are very low in the matrix. The average chemical compositions of the matrix and the precipitates are reported in Table 6.

Table 6. Composition of the matrix and the precipitates in ZA73 alloy as measured by LEAP spectrometry (laser mode) and by calculations using Thermo-Calc and COST2 database.

at. %	Methods	Mg	Zn	Al	Ca
Matrix	LEAP	98.25	0.54	1.16	0.04
	Thermo-Calc	98.52	0.57	0.91	--
Precipitate	LEAP	54.80	32.39	12.75	0.055
	Thermo-Calc	54.55	23.85	21.61	--

The Thermo-Calc calculation shows that hcp and φ phases ($Mg_6(Zn, Al)_5$) are in equilibrium. The calculated isopleth section of Mg-3Al-Zn alloy with the different Zn content and isothermal sections of the Mg-Al-Zn system at 423 K are shown in Figures 12, 13, 14 and 15.

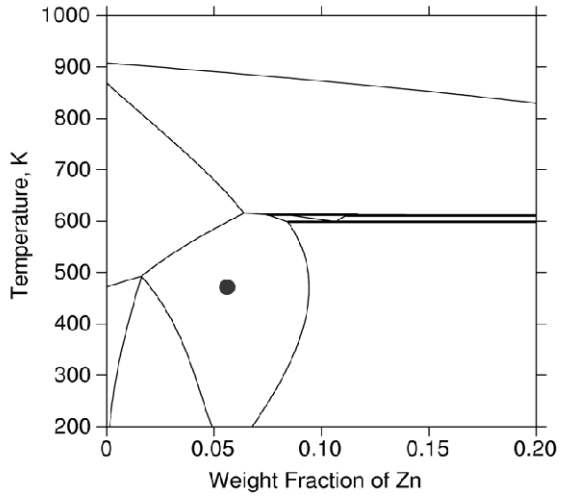

Figure 12. Calculated isopleth section of Mg-3Al-Zn alloy with varying Zn content. The dark dot is the chemical composition point of ZA73 alloy at aging temperature of 423 K.

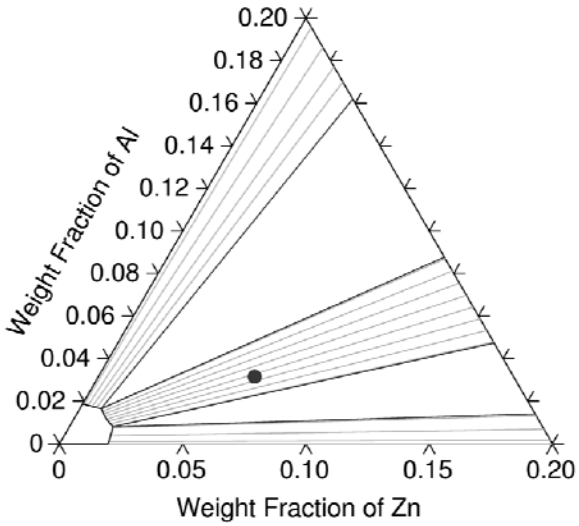

Figure 13. The enlarged view of the Zn-rich corner at 423 K. The light-grey lines are the tie lines which indicate the two phases' regions. The dark dot is the chemical composition point of the ZA73 alloy.

Combining the results using voltage mode and the laser mode, the equivalent sphere diameter of precipitates is 20 – 50 nm at peak hardness, providing calibration for precipitation-strengthening models.

Figure 14 shows the enlarged view of the Zn-rich corner at 423 K represented in mole fractions with

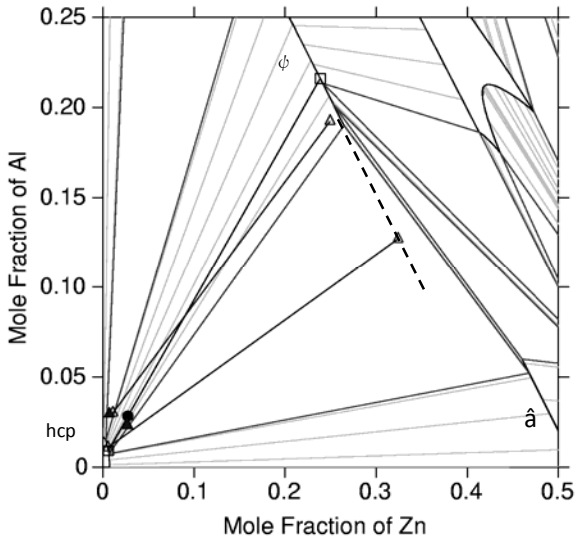

Figure 14. The enlarged view of the Zn-rich corner at 423 K represented in mole fraction. The light-grey lines are the predicted tie lines which indicate the two phases regions. The darker lines are the tie-lines measured by LEAP. The tie-line via voltage mode connects to the extended φ phase. The tie-line via laser mode is in the stable hcp + φ two phase region.

the darker tie-lines detected by LEAP. The tie-line of the sample analyzed via voltage mode connects to the extended φ phase. The tie-line of the sample analyzed via laser mode is in the stable hcp + φ two-phase region.

Figure 15 displays the calculated metastable two-phase region between the hcp and φ phase at 423 K, with light-grey tie-lines to show their directions. The trends are similar to the experimental tie-lines of Figure 14.

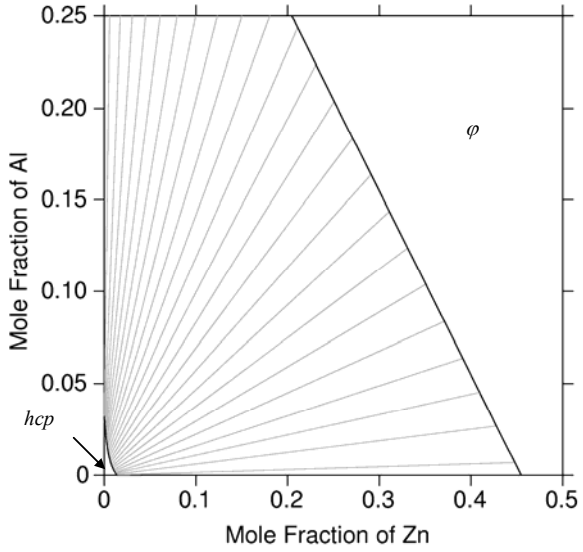

Figure 15. Calculated metastable isothermal section at 423 K between hcp and φ phase. The light-grey lines are the calculated tie lines showing directions similar to the data of Figure 14.

Conclusions

One of the main goals of this project is to understand the effect of nanoscale precipitates and novel additives to the overall strength and ductility in Mg alloy systems. We developed a new MOO methodology as a robust procedure to construct reliable and transferable interatomic potentials for Mg-based alloy systems. This MOO procedure was applied to construct transferrable interatomic potentials for Mg and Al atoms using the FMEAM. We also established a basic framework for the accelerated development of reliable and efficient interatomic potentials for other combinations of alloy systems to perform large-scale, realistic atomistic simulations.

The nanostructure of strengthening precipitates in a Mg-7Zn-3Al aged to peak hardness at 423 K for 100 hrs was investigated. The chemical compositions of the alloys as well as the matrix and the precipitates were measured by LEAP spectrometry and compared with the results calculated by the Thermo-Calc software based on the COST2 database. Ternary nano-sized precipitates have been found. The precipitates have compositions consistent with the ternary φ phase including its metastable extension. The precipitate size at peak hardness corresponds to an equivalent sphere diameter of 20 – 50 nm.

This investigation should facilitate the design of a new generation of Mg-based alloys with improved castability and high-temperature creep resistance by providing fundamental understanding of several critical issues that include the selection of key combination of precipitates and matrices, interaction of precipitate and matrix phases and, ultimately, composition-structure-property relationship.

Presentations/Publications/Patents

1. Bohumir Jelinek, Sungho Kim, Jeffery Houze, Seong-Gon Kim, M. F. Horstemeyer, and M. I. Baskes, *"Development and testing of MEAM Potentials for Al-Mg Alloys"*, APS 2006 SESAPS Meeting, Williamsburg, VA, November 2006.
2. B. Jelinek, J. Houze, Sungho Kim, M. F. Horstemeyer, M. I. Baskes, and Seong-Gon Kim, *"Modified embedded-atom method interatomic potentials for the Mg-Al alloy system"*, Phys. Rev. B, 75, 054106 (2007).
3. J. Houze, Sungho Kim, Amitava Moitra, B. Jelinek, Sebastien Groh, M. F. Horstemeyer, Erdem Acar, Masoud Rais-Rohani, Seong-Gon Kim, *"A multi-objective optimization procedure to develop modified-embedded-atom-method potentials: an application to magnesium",* submitted to Phys. Rev. B., arXiv:0708.0075.
4. Shengjun Zhang and Gregory B. Olson*, "3D-atom probe investigation of strengthening precipitates in a Mg-7Zn-3Al alloy",* preprint.
5. S. Groh, B. Jelinek, J. Houze, Seong-Gon Kim, M. F. Horstemeyer, *"Mobility of <a> dislocations in Mg and Mg/Al alloys by molecular dynamic simulations"*, submitted to Computational Materials Science.

References

1. [Baskes87] M. I. Baskes, *"Application of the Embedded-Atom Method to Covalent Materials: A Semiempirical Potential for Silicon"*, Phys. Rev. Lett. 59, 2666 (1987).
2. [Baskes89] M. I. Baskes, J. S. Nelson, and A. F. Wright, *"Semiempirical modified embedded-atom potentials for silicon and germanium"*, Phys. Rev. B 40, 6085 (1989).
3. [Baskes92] M. I. Baskes, *"Modified embedded-atom potentials for cubic materials and impurities"*, Phys. Rev. B 46, 2727 (1992).
4. [Baskes94] M. I. Baskes, J. E. Angelo and C. L. Bisson, *"Atomistic calculations of composite interfaces"*, Modell. Simul. Mater. Sci. Eng. 2, 505 (1994).
5. [Blochl94] P. E. Blöchl, *"Projector augmented-wave method"*, Phys. Rev. B 50, 17953 (1994).
6. [Ceperley80] D. M. Ceperley and B. J. Alder, *"Ground State of the Electron Gas by a Stochastic Method"*, Phys. Rev. Lett. 45, 566 (1980).
7. [Cherne01] F. J. Cherne, M. I. Baskes, and P. A. Deymier, *"Properties of liquid nickel: A critical comparison of EAM and MEAM calculations"*, Phys. Rev. B 65, 024209 (2001).
8. [Chetty97] N. Chetty and W. Weinert, *"Stacking faults in magnesium"*, Phys. Rev. B 56, 10844 (1997).
9. [Coleman67] B. D. Coleman and M. E. Gurtin, *"Thermodynamics with internal state variables"*, J. Chem. Phys. 47, 597 (1967).
10. [Daw83] M. S. Daw and M. I. Baskes, *"Semiempirical, Quantum Mechanical Calculation of Hydrogen Embrittlement in Metals"*, Phys. Rev. Lett. 50, 1285 (1983).
11. [Daw84] M. S. Daw and M. I. Baskes, *"Embedded-atom method: Derivation and application to impurities, surfaces, and other defects in metals"*, Phys. Rev. B 29, 6443 (1984).
12. [Droogenbroeck04] Joris Van Droogenbroeck, Karla Tersago, Christian Van Alsenoy and Frank Blockhuys, *"A systematic study of the effect of correlation, DFT functional and basis set on the structure of Roesky's ketone"*, Chem. Phys. Lett. 399, 516 (2004).
13. [deWeck04] O. L. de Weck, *"Multiobjective Optimization: History and Promise (The Third China-Japan-Korea Joint Symposium on Optimization of Structural and Mechanical Systems",* Kanazawa, Japan, (2004).
14. [E03] W. E and B. Engquist, *"Multiscale Modeling and Computation"*, Notices of the AMS 50, 1062 (2003).
15. [Espinosa01] H. D. Espinosa, H. -C. Lu, P. D. Zavattieri, and S. Dwivedi, *"A 3-D Finite Deformation Anisotropic Visco-Plasticity Model for Fiber Composites,"* J. of Composite Materials 35, 369 (2001).
16. [Ercolessi94] F. Ercolessi and J.B. Adams, *"Interatomic potentials from first-principles calculations: the Force-Matching method"*, Europhys. Lett. 26, 583 (1994).
17. [Gailly02] B. A. Gailly and H. D. Espinosa. *"Modelling of Failure Mode Transition in Ballistic Penetration with a Continuum Model Describing Microcracking and Flow of Pulverized Media*", Int. J. for Numerical Methods in Engineering, 54, 365 (2002).
18. [Gallot64] J. Gallot and R. Graf, Comptes. Rendus. Acda. Sci. 258, 2818 (1964).
19. [Hao03] Su Hao, Brian Moran, Wing Kam Liu, and Gregory B. Olson, *"A hierarchical multi-physics model for design of high toughness steels"*, Journal of Computer-Aided Materials Design, 10, 99 (2003).
20. [Hao04] Su Hao, Brian Moran, Wing Kam Liu, and Gregory B. Olson, *"Multi-scale constitutive model and computational framework for the design of ultra-high strength"*, Computer Methods in Applied Mechanics and Engineering 193, 1865 (2004).
21. [Hasan95] O. A. Hasan and M. C. Boyce, *"A Constitutive Model for the Nonlinear Viscoelastic Behavior of Glassy Polymers,"* Polymer Engng. and Sci. 35, 331 (1995)/.
22. [Hirth82] J. P. Hirth and J. Lothe, *"Theory of Dislocations,"* John Wiley and Sons Inc, New York (1982).
23. [Horst01] M. F. Horstemeyer, S. J. Plimpton, and M. I. Baskes. *"Size Scale and Strain Rate Effects on Yield and Plasticity of Metals"*, Acta Matallurgica 49, 4363 (2001).
24. Horst03] M. F. Horstemeyer and P. Wang. *"Cradle-to-grave simulation-based design incorporating multiscale microstructure-property modeling: Reinvigorating design with science"*, Journal of Computer-Aided Materials Design 10, 13 (2003).

25. [Hoover83] William G. Hoover, *"Canonical dynamics: Equilibrium phase-space distributions"*, Phys. Rev. A 31, 1695 (1983).
26. [Hu01] Wangyu Hu, Bangwei Zhang, Baiyun Huang, Fei Gao and David J Bacon. *"Analytic modified embedded atom potentials for HCP metals"*, J. Phys.: Condens. Matter 13, 1193 (2001).
27. [Jelinek07] B. Jelinek, J. Houze, Sungho Kim, M. F. Horstemeyer, M. I. Baskes, and Seong-Gon Kim, *"Modified embedded-atom method interatomic potentials for the Mg-Al alloy system"*, Phys. Rev. B 75, 054106 (2007).
28. [Kim94] S. G. Kim and D. Tománek, *"Melting the fullerenes: A molecular dynamics study"*, Phys. Rev. Lett. 72, 2418 (1994).
29. [Kim05] I. Y. Kim and O. L. de Weck, Structural and Multidisciplinary Optimization 31, 105 (2005).
30. [King94] R. D. King-Smith and David Vanderbilt, *"First-principles investigation of ferroelectricity in perovskite compounds"*, Phys. Rev. B 49, 5828 (1994).
31. [Kohn65] W. Kohn and L. J. Sham, "*Self-consistent Equations Including Exchange and Correlation Effects*", Phys. Rev. 140, A1113 (1965).
32. [Kresse93] G. Kresse and J. Hafner, *"Ab initio molecular dynamics for liquid metals"*, Phys. Rev. B 47, 558 (1993).
33. [Kresse96] G. Kresse and J. Furthmüller, *"Efficient iterative schemes for ab initio total-energy calculations using a plane-wave basis set"*, Phys. Rev. B 54, 11169 (1996).
34. [Kresse99] G. Kresse and D. Joubert, "*From ultrasoft pseudopotentials to the projector augmented-wave method*," Phys. Rev. B 59, 1758 (1999).
35. [Kestin70] J. Kestin and J. R. Rice, *"Paradoxes in the application of thermodynamics to strained solids"*, in "A Critical Review of Thermodynamics", edited by E.G. Stuart, B. Gal-Or, and A. J. Brainard, Mono Book Corp., Baltimore, 275 (1970).
36. [Lee03] Byeong-Joo Lee, Jae-Hyeok Shim, and M. I. Baskes, *"Semiempirical atomic potentials for the fcc metals Cu, Ag, Au, Ni, Pd, Pt, Al, and Pb based on first and second nearest-neighbor modified embedded atom method",* Phys. Rev. B 68, 144112 (2003).
37. [Lee06] Byeong-Joo Lee, *"A modified embedded-atom method interatomic potential for the Fe—C system,"* Acta Materialia 54, 7011 (2006).
38. [Li03] Youhong Li, Donald J. Siegel, James B. Adams, and Xiang-Yang Liu, *"Embedded-atom-method tantalum potential developed by the force-matching method",* Phys. Rev. B 67, 125101 (2003).
39. [Liu96] Xiang-Yang Liu, James B Adams, Furio Ercolessi and John A Moriarty, "*EAM potential for magnesium from quantum mechanical forces,*" Modell. Simul. Mater. Sci. Eng. 4, 293 (1996).
40. [Liu97] X.-Y. Liu, P. P. Ohotnicky, J. B. Adams, C. Lane Rohrer, and R. W. Hyland, Jr., *"Anisotropic surface segregation in Al-Mg alloys"*, Surf. Sci. 373, 357 (1997).
41. [Miller00] M. K. Miller, *"Atom probe tomography: analysis at the atomic level,"* Kluwer Academic/ Plenum Publishers, New York, (2000).
42. [Nose84] Shuichi Nosé, *"A unified formulation of the constant temperature molecular dynamics methods"*, J. Chem. Phys. 81, 511 (1984).
43. [Okamoto98] H. Okamoto, *"Al-Mg (Aluminum--Magnesium)",* J. Phase Eq. 19, 598 (1998).
44. [Olson98] G. Olson. *"Systems design of hierarchically structured materials: Advanced steels",* Journal of Computer-Aided Materials Design 4, 143 (1998).
45. [Olson00] G. Olson. *"New age of design"*, Journal of Computer-Aided Materials Design 7, 143 (2000).
46. [Perdew81] J. P. Perdew and A. Zunger, *"Self-interaction correction to density-functional approximations for many-electron systems"*, Phys. Rev. B 23, 5048 (1981).
47. [Perdew96] J. P. Perdew, K. Burke, and M. Ernzerhof, *"Generalized Gradient Approximation Made Simple"*, Phys. Rev. Lett. 77, 3865 (1996).
48. [Press92] William H. Press, Brian P. Flannery, Saul A. Teukolsky, and William T. Vetterling, *Numerical Recipes in C: The Art of Scientific Computing*, 2nd ed., Cambridge University Press, Cambridge (1992).
49. [Rice71] J.R. Rice, *"Inelastic constitutive relation for solids: An internal variable theory*

and. its application to metal plasticity", J. Mech. Phys. Solids 19, 433 (1971).
50. [Shiao06] C. Shiao, *"Design of a Self-Healing Alloy for the Application of Unmanned Aerial Vehicles"*, Senior Project Report, Northwestern University (2006).
51. [Singh03] D. Singh, C. Suryanarayana, L. Mertus, and Chen R.-H., *"Extended homogeneity range of intermetallic phases in mechanically alloyed Mg-Al alloys,"* Intermetallics 11, 373 (2003).
52. [Sturkey59] L. Sturkey and J. B. Clark, Journal of the Institute of Metals 88, 177 (1959).
53. [Wei95] L. Y. Wei, G. L. Dunlop and H. Westengen, Metall. Mater. Trans. A-Phys. Metall. Mater. Sci. 26, 1705 (1995).

J. Multiscale Microstructure-Property Plasticity Considering Uncertainty

Mark F. Horstemeyer: Principal Investigator
Chair in Solid Mechanics & Professor, Mechanical Engineering
Center for Advanced Vehicular Systems (CAVS)
Mississippi State University (MSST)
206 Carpenter Bldg., PO Box ME
Mississippi State, MS 39762
(662) 325-7308; fax: (662) 325-7223; e-mail: mfhorst@me.msstate.edu

D. J. Bammann: Co-Principal Investigator
Professor, Mechanical Engineering
MSST
210 Carpenter Bldg.
Mississippi State, MS 39762
(662) 325-3260; Home: (662) 294-2585; fax: (662) 325-5433; *e-mail: bammann@cavs.msstate.edu*

E. B. Marin: Co-Principal Investigator
Senior Structural Analyst
CAVS
MSST
200 Research Blvd.
Mississippi State, MS 39762
(662) 325-6696; fax: (662) 325- 5433; e-mail: ebmarin@cavs.msstate.edu

Kiran Solanki: Research Associate II
CAVS
MSST
200 Research Blvd.
Mississippi State, MS 39762
(662) 325-5454; fax: (662) 325-5433; e-mail: kns3@cavs.msstate.edu

Sebastien Groh: Postdoctoral Fellow
CAVS
MSST
200 Research Blvd.
Mississippi State, MS 39762
(662) 325-5431; fax: (662) 325- 5433; e-mail: groh@cavs.msstate.edu

Technology Area Development Manager: Joseph A. Carpenter
(202) 586-1022; fax: (202) 586-1600; e-mail: joseph.carpenter@ee.doe.gov

Contract Monitor: Aaron Yocum
(304) 285-4852; fax: (304) 285-4403; e-mail: aaron.yocum@netl.doe.gov

---

Contractor: MSST
Contract No.: 4000054701

Objective

- Develop a multiscale, nested, internal state variable (ISV) modeling methodology that includes statistical variations from the material microstructure for lightweighting designs made of various structural alloys.

Approach

- The approach is to quantify structure-property relations through multiscale modeling and multiscale experiments so the macroscale ISVs can capture the lower length-scale effects. Once the cause-effect relations are quantified for various engineering metal alloys, then statistical methods can be used in the context of the ISVs and used for constitutive models in finite-element analysis (FEA). As such, the FEA can be used for a simulation-based design methodology as manufacturing processes and in-service life are accurately modeled.

Accomplishments

- We have made progress at all scales of simulations and have applied the current nested ISVs into a macroscale finite-element code. We have introduced a crystal-plasticity code that can include different volume fractions of hexagonal close-packed (hcp) magnesium (Mg) with different volume fractions of face-centered cubic (fcc) aluminum (Al) in order to evaluate the plastic deformation of different alloying solutions. With the macroscale ISV theory, we have conducted some materials-processing studies that capture the structure-property relations in the model-correlation and model-validation stages for hydroforming and rolling of various metals. In doing so, we show the importance of the deformation history. In these simulations we are working with other projects at MSST: "Simulation-Based Design Optimization" (see 6.G), "Material Design for Steel Alloys" (atomistic simulations, see 5.M), "Cyberinfrastructure" (see 6.K), and "Mission Eggcellence – K-12 Outreach Program" (see 12.E). These projects are also sponsored by DOE. Finally, we have started the inclusion of the statistical variations and uncertainty within the macroscale ISV model.

Future Direction

- In the next year, we will conclude these studies that we have started and start bridging the different length-scale studies and the different manufacturing histories and in-service life histories.

Introduction

Several sections will show the multiscale modeling and the macroscale modeling of the history of the materials-processing steps for several processes and materials.

Mesoscale Crystal-Plasticity Simulations of Mg-Al Alloys

Renewed interest has been shown in Mg alloys as methods of forming and working have improved and the need for lighter-weight components has increased. Al is one of the most common alloying elements used to improve the properties of Mg. In this regard, particular reference can be made to the Al-zinc (Zn) ternary systems (AZ alloys) where the Al content is important. These alloys are widely used in industrial applications, with major commercial grades being AZ31 (3% Al), AZ61 (6% Al) and AZ91 (9% Al). In general, the addition of Al atoms to pure Mg leads to the formation of solid solutions and/or new second phases, with the particular microstructure formed being strongly influenced by the concentration of Al atoms as well as the heat-treatment conditions (temperature and cooling rate) employed to produce the alloy. Equilibrium (stable) or metastable structures can be obtained in this process and which can be analyzed with the help of phase diagrams.

In this work, a crystal-plasticity (mesoscale) model is used to examine the deformation behavior of Mg alloys with varying amounts of Al. For this study, it is assumed that the Mg-Al alloy has a hypothetical microstructure where the Al impurity atoms have formed a dispersed second phase (fcc grains) in the Mg matrix (hcp grains). The study of this system using a crystal-plasticity approach allows a more-accurate representation of the microstructure as discrete grains and their crystallographic properties (slip systems); and, some aspects of phase distribution can be explicitly modeled. This is particularly beneficial

in this case as the differences in texture evolution and grain interaction due to the presence of the Al can be observed. The tests will begin to show how properties of the two phases combine to form the macroscopic properties of the alloy and how the individual properties of each separate phase change due to the presence of the other phase.

Modeling Procedure

The model used is a crystal elasto-viscoplastic model based upon a previous rigid viscoplastic formulation (Marin and Dawson, 1998). The kinematics of the model assume that crystallographic slip is the dominant mechanism of deformation. The model does not incorporate twinning behavior although it has been shown to have a profound effect on Mg behavior. Implementation of twinning to more accurately capture the deformation process is planned for next year. The current model was implemented as a user material routine in *ABAQUS*. Meshes were created to show the change in stress-strain response when varying the number of Al grains present in the Mg alloys. Each case used a cube of 25x25x25 elements with each of the 15,625 elements representing a single grain. For these simulations, eight-node brick elements with reduced integration were selected. The percentages of Al grains tested were 0%, 3%, 6%, 9%, 12%, and 15% with the remaining grains being Mg. The Al grains were assigned randomly as can be observed in the models shown in Figure 1.

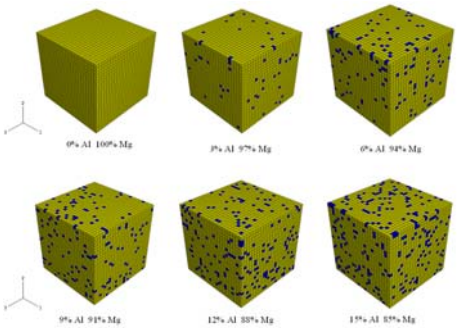

Figure 1. Models showing composition of Al and Mg.

For each of the models. the Euler angles of the grains were assigned randomly so that no initial texture was present. The models were loaded in plane-strain compression at a constant strain rate of 10^{-3} by fixing the faces normal to the 1 direction, the rear face normal to the 3 direction, and the bottom face normal to the 2 direction. Displacement loading was specified on the top face in the -2 direction and the left-front face in the 3 direction. The elastic constants used for the Al were taken from (Dawson, Boyce, MacEwen, and Rogge, 2001). The material parameters for the crystal-plasticity model for Al were taken from (Marin and Dawson, 1998). The elastic constants for the Mg were taken from (Kocks, Tome, and Wenk, 1998). The material parameters for the Mg were determined by fitting published experimental compression data of pure untextured Mg from (Agnew, Yoo, and Tome, 2001). The deformed meshes are shown in Figure 2. The stress-strain responses of the cases are shown in Figure 3.

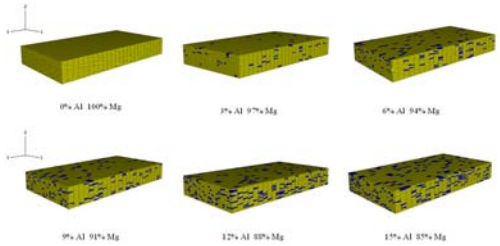

Figure 2. Models after plane-strain compression.

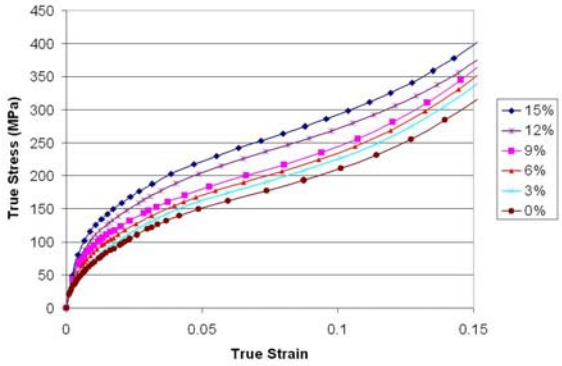

Figure 3. Stress-strain response of Mg alloys containing varying percentages of Al.

Summary and Future Work

The inhomogenous deformation of the models is apparent in Figure 2 as the grains all deformed differently from one another. The considerable difference in shape of the final deformed grains is due to the crystal anisotropic properties, the difference in crystallographic orientation between neighboring grains, and the presence of grains of two distinct phases. Figure 3 shows that the

strength of the alloy increases as the amount of Al increases. This demonstrates the usefulness of alloying in improving the properties of Mg as the 15%-Al Mg alloy is considerably stronger than the pure Mg. The curves also seem to indicate a rule of mixtures as the strength increases by an amount consistent with the increase in Al. The results are encouraging and suggest that more information may be gathered through crystal-plasticity testing of this type.

Future plans include the representation of twinning behavior in the crystal-plasticity model and examination of the texture evolution of the fcc and hcp phases. The evaluation and incorporation of lower length-scale hardening rules are planned from the use of atomistic simulations and dislocation dynamics. Experiments are also planned to help quantify the evoluation to texture, twinning, and dislocation activity upon various stress states.

Modeling the Hydroforming Process of T-Shape Copper (Cu) Tube Fittings

Tube hydroforming is an important forming technology used in the automotive industry. Although steel has been typically used in the majority of automotive applications, Al hydroforming has started to have its place in this area, in particular, for the production of lightweight automotive structures.

In this section, we present a summary of the macroscale ISV modeling and simulation work that has been performed in tube hydroforming using some aspects of the technology being developed in this program. Although the material used in this work is Cu and the application is plumbing, the established methodology and models can be extended to other materials and application areas. The specific work concerns the numerical analysis of the hydroforming process of Cu tube fittings used by a local manufacturing company (Mueller Industries, Inc.).

This study involves constructing a finite- element (FE) model of the process, performing mechanical and microstructural characterization analyses on the tube's material, using a multiscale constitutive model to represent the material response during the process, validating the hydroforming model, and performing the statistical analysis of the forming process to determine the most important parameters of the process. Through this numerical study, the manufacturer should be able to learn more about the process behavior and, hence, establish guidelines to better plan/improve its hydroforming process.

A synopsis of the Mueller hydroforming process is presented in Figure 4. A Cu blank with a previous deformation history (extruded, drawn, annealed) is being formed by a simultaneous application of axial velocity and internal pressure loads.

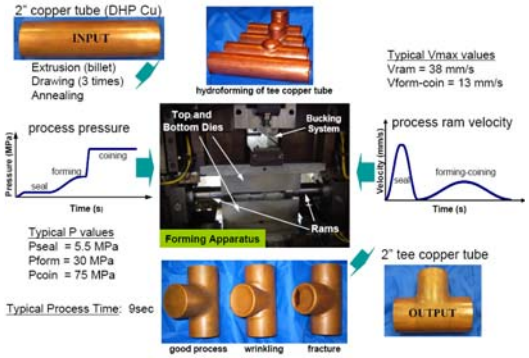

Figure 4. Mueller's hydroforming process for 2" T-shape Cu tube fittings.

In general, modeling the hydroforming process should account for the six components of the system: two rams, top and bottom die, Cu blank, and the bucking plate; see Figure 5. However, due to symmetry, only one quarter model can be used. The three-dimensional FE mesh of the hydroforming components (die, bucking plate, ram and Cu billet) is also presented in Figure 5. In this FE model, all components are represented as rigid bodies except the Cu blank, which is deformable.

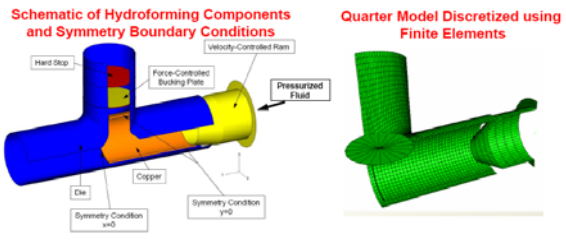

Figure 5. Hydroforming components and finite-element mesh of quarter model.

Characterization studies have been performed on the tube's material (Deoxidized High Phosphorus (DHP) Copper - DHP Cu) to understand the effect of the deformation history on the material microstructure as well as to obtain experimental data to calibrate the multiscale ISV model. Figure 6 presents a summary of these studies: the stress-strain response, the grain structure and the deformation texture.

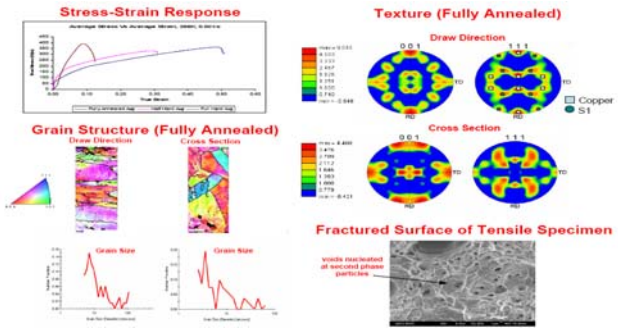

Figure 6. Mechanical and microstructural characterization of Mueller's Cu Tube.

The ISV material model (Bammann, 1990; Bammann et al. 1993, Horstemeyer et al. (2000a, 2001), based upon a hierarchical, multiscale methodology, has been calibrated with the experimental data presented above. The corresponding experimental and computed responses as well as the the geometry of the tensile specimen (physical sample and FE model) are presented in Figure 7.

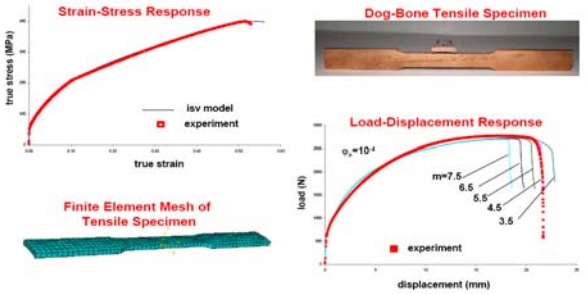

Figure 7. Calibration of the plasticity and damage parameters of the ISV model using experimental data. The geometry of the dog-bone tensile specimen is also shown.

A validation study was performed with the constructed FE model of the hydroforming process and the calibrated multiscale ISV material model. The material model was implemented in ABAQUS through a user material routine.

Figure 8 depicts the formation of the T-shape fitting during the hydroforming process as predicted by the numerical model. The process curves for the ram velocity and fluid pressure used in the simulation are shown at the top of the figure. These curves have vertical markers indicating the times at which the snapshots of the deforming tube have been extracted from the simulation, so that one can relate the progression of the forming process with the different stages (sealing, forming, coining) defined by the processing variables.

The validation of the numerical model was accomplished by comparing the material flow patterns and tube geometry between simulated and manufactured T-shape tube fittings. The experimental flow patterns were obtained from a Cu blank etched with straight lines before being hydroformed. The resulting flow patterns are presented in Figure 9 together with the predicted ones from the simulations. Clearly, the flow lines match well. The same figure also presents a comparison of the thickness profiles between the predicted and manufactured T-shape fittings. Again, the results from the FE model agree well with the experimental ones.

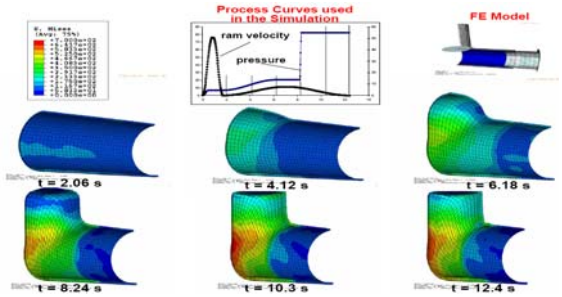

Figure 8. Snapshots showing the formation of the T-shape fitting during the hydroforming simulation.

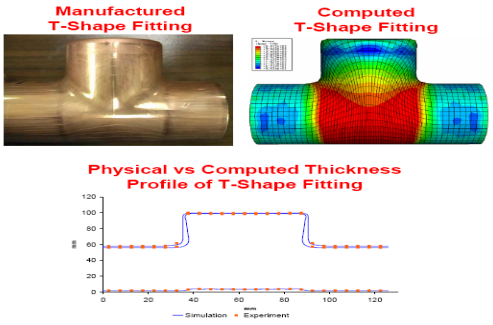

Figure 9. Comparison of flow patterns and thickness profiles between manufactured and simulated T-shape fittings.

The validated numerical model was used in a statistical study of the hydroforming process using numerical experiments designed based on a design and analysis of computer experiments (DACE) methodology. The numerical experiments have been performed in two phases: a screening analysis using a fractional factorial design and a full study employing a full factorial design. The screening study is mainly focused on computing the "main effects" of an initial set of design variables in order to rank their effect on the outcome of the process. In DACE, an outcome is typically a chosen "metric" that characterizes the response of a system (hydroforming process). Based on this preliminary ranking, one can then select a few of the most important variables to perform the full study of the process, study that involves not only main effects but also interaction effects. With this last analysis, one can then suggest recommendations regarding the main process parameters that should be carefully controlled/set to improve the outcome of the hydroforming process.

The set of design variables selected for the screening study together with their range of possible values (design space) are displayed in Figure 10. As shown in the figure, some of these variables define specific features of the velocity and pressure curves and, hence, they control the profile of the processing curves. To select the combination of parameter values to use in the numerical simulations, we have used a 1/32, two-level, fractional factorial design (sampling procedure) to build the matrix of numerical experiments (design matrix with 32 simulation runs). The main effects of these design variables have been quantified using a number of performance metrics which included measures of product quality (thickness of the Cu fitting at different locations) and mechanical rupture (von Mises stress, stress triaxiality, effective plastic strain). The computed values of the metrics have been analyzed using statistical tools widely employed in DACE approaches: main-effect plots, normal probability plots and analysis of variance (ANOVA).

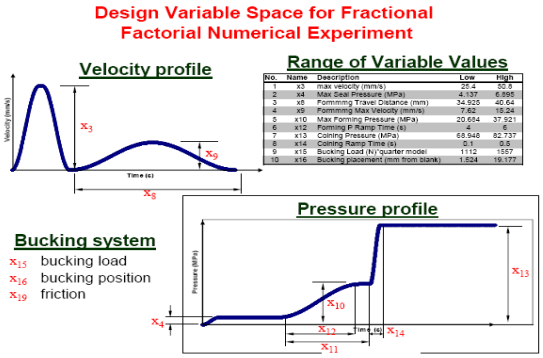

Figure 10. Design variables selected for screening study of hydroforming process.

The results of the screening study have indicated that five parameters are the most influential in the hydroforming process. These parameters are listed in Figure 11, where the column denoted "occurrences" lists the number of times the parameter shows up as an influential factor for a particular metric. At this point, discussions were held with the process experts from Mueller to get their input regarding the results of the study. These discussions have produced a reduced and modified set of design parameters which are also listed in Figure 11. Based on this, a full study has been performed using a two-level, full factorial design which involved 16 numerical experiments. The experimental matrix for this design is presented in Figure 11 as well.

Influential Design Parameters from Screening Study

Variable	Description	Occurances
x4	Maximum Sealing Pressure	2
x8	Forming Travel distance	9
x9	Forming Maximum Velocity	5
x10	Forming Pressure	13
x14	Coining Ramp Time	1

Design Parameters for Final Study

Variable	Description
x4	Maximum Sealing Pressure
x9	Forming Maximum Velocity
x10	Forming Pressure
x12	Forming Pressure Ramp Time

Design Matrix for Two-Level Full Factorial Numerical Experiment

Sim No.	1	2	3	4	5	6	7	8	9	10	11	12	13	14	15	16
x4	1	2	1	2	1	2	1	2	1	2	1	2	1	2	1	2
x9	1	1	2	2	1	1	2	2	1	1	2	2	1	1	2	2
x10	1	1	1	1	2	2	2	2	1	1	1	1	2	2	2	2
x12	1	1	1	1	1	1	1	1	2	2	2	2	2	2	2	2

1: low value of parameter, 2: high value of parameter

Figure 11. Influential design parameters used in a full numerical experiment of the hydroforming process.

The T-shape tube fitting geometries obtained from the final 16 simulation runs are presented in Figure 12. Note that the simulations predict that wrinkling of the Cu tube happens for some combinations of the design parameters. An analysis of the computed performance metrics mentioned above has also been carried out using the following statistical tools: ANOVA, normal-

probability plots, Paretto charts, main-effects plots, and two-way and three-way interaction plots. A sample of the results from this statistical study is shown in Figure 13, which depicts the analysis of the maximum value for the von Mises stress (a metric for mechanical rupture) using some of the statistical tools referred above. A main conclusion of this full-factorial numerical study is that, for the range of parameter values used, the hydroforming process is mainly driven by major interactions among the most important process parameters and, hence, these interaction effects should be considered when selecting/setting the process curves for the hydroforming process.

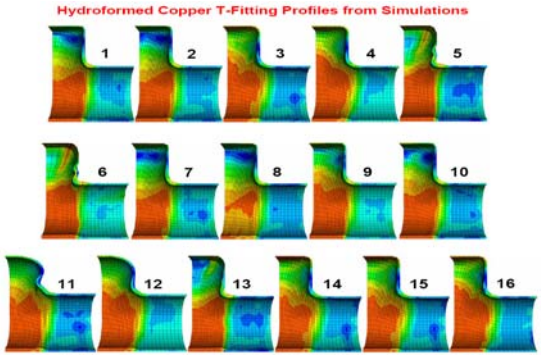

Figure 12. Simulation results from final DACE study of hydroforming process.

Based on this study, a number of suggestions have been proposed for Mueller to better control its hydroforming process and avoid typical process failures such as bursting and wrinkling. It is important to mention here that this study has also shown that using FE simulations together with a DACE methodology is a powerful tool to understand the process-product relationship of complex industrial forming processes.

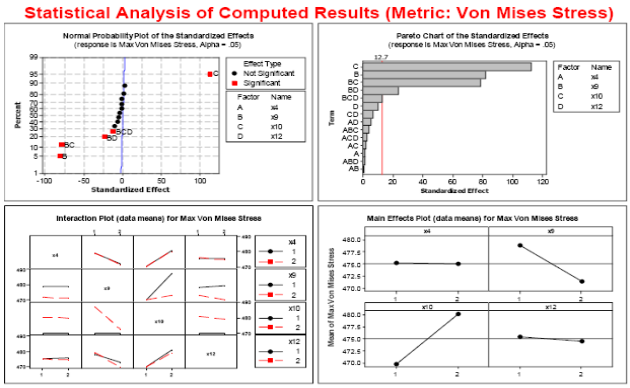

Figure 13. Statistical analysis from final DACE study: metric "von Mises stress".

Rolling History Microstructure-Property Relations of a Rolled 6022 Al Alloy

This section covers microstructure analyses and mechanical properties of 6022 Al alloy at various stages of the rolling process. The history effect reflected from these stages will provide a database for advanced material modeling. The rolling steps comprise reductions of a 6-inch slab to a 3-inch slab to a 1/8-inch sheet, an annealing process of the 1/8-inch sheet, and finally a reduction to the 1/32-inch finish-gauge sheet. The microstructural content was obtained through scanning electron microscope (SEM) analyses, optical microscopy (OM) analyses, and X-ray tomography. Research results obtained here should be useful for the improvement of manufacturability of 6022 Al-alloy closure panels applied in the automotive industry.

The 6022 Al alloy was developed by Alcoa in the late 1980's primarily for automotive closure-panel applications. The automotive body panels are fabricated using a stamping process of thin-gauge Al sheets. The 6022 Al alloy displayed enhancements in formability and hemming performance, superior surface quality, and excellent paint-bake response which are vital for performance in the stamping process. The 6022 Al alloy also displayed improved corrosion resistance over other commercially-available alloys (Kamat et al., 2002).

Experimental Procedure

The 6022 Al-alloy material was provided by Alcoa Inc. at various stages of the manufactured rolling process.

Microstructure Analysis

The strengthening of Al-Mg-Si alloys is based on a precipitation hardening process. According to Miao et. al. (Miao and Laughlin, 1999), the precipitation sequence for the 6022 Al alloy is defined as:

α (sss) $\rightarrow$ *GP* zones $\rightarrow$ needle–like β''

$\rightarrow$ rod-like β' + lath-like precipitates $\rightarrow \beta$ + Si

where α (sss) is the supersaturated solid solution. GP (Guinier-Preston) zones are generally considered spherical clusters with unknown structure. The β'' are fine, needle-shaped zones along $<100>_{Al}$ with a monoclinic structure, and β' are rod-shaped precipitates along $<100>_{Al}$ with a hexagonal crystal structure. The β are usually Mg_2Si platelets.

The microstructural analysis was conducted on material samples taken from the various stages of the manufacturing rolling process. The samples were mounted using a cold-mounting epoxy and polished using Struers automatic polishing equipment and procedures. The specimens were analyzed with a JEOL field-emission SEM with attached x-ray-electron diffraction spectroscopy (X-EDS) spectrometers and a Zeiss high-power microscope. The material matrix and second-phase precipitate compositions were determined through energy-dispersive x-ray (EDX) evaluation. X-ray scans of the material were conducted using a Phoenix dual-tube Xtome machine to determine any porosity present throughout the thickness of the material.

The SEM images and EDX evaluations of the material reveal a supersaturated solid solution matrix with second-phase particles and inclusions in the samples taken from the 6-inch to 1/8-inch hot-rolled material as seen in Figure 14. The 1/8-inch sheet is put through an annealing process where the Mg_2Si precipitates are formed as seen in Figure 15. These Mg_2Si precipitates are then flattened, as seen in Figure 16, during the cold-rolling process used to produce the final gauge thickness of the material. The X-ray scans revealed the presence of microporosity located at the center of the thickness in the 6-inch material.

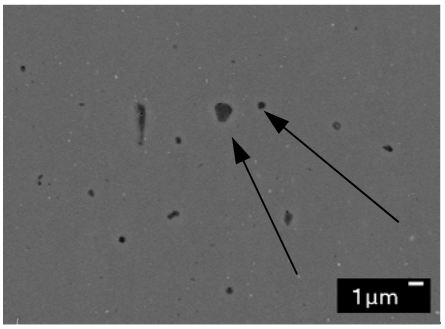

Figure 14. SEM image at 1000X magnification of a Al 6022 sample taken from the 1/8-inch sheet (before annealing) material. The black spots are Mg_2Si precipitates.

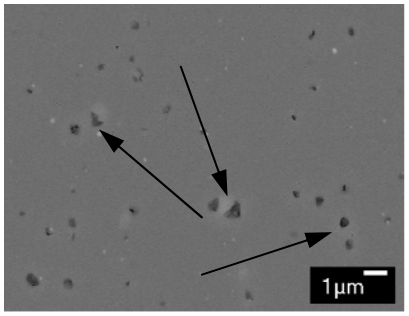

Figure 15. SEM image at 1400X magnification of a Al 6022 sample taken from the 1/8-inch sheet (after annealing) material. The increase in Mg_2Si precipitates after the annealing process can be seen.

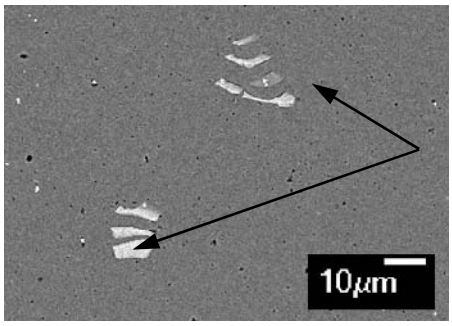

Figure 16. SEM image at 400x magnification of an Al 6022 sample taken from the 1/32-inch sheet material. The flattening of the second-phase particles can be seen as noted by the arrows.

Mechanical Testing

Mechanical tests were performed on specimens oriented in the rolling direction, long transverse direction, and short transverse direction for each stage of the manufacturing rolling process.

Tensile specimens were fabricated using a computerized numerical control (CNC) milling machine according to American Society for

Testing and Materials (ASTM) E8 subsize specimen standards. Tensile specimens were tested using an Instron 5882 electromechanical machine at ambient temperature with a constant strain rate of 0.0001 sec^{-1}. A clip-on style extensometer was used for measurement and control of the strain.

Results

The tensile test results, shown in Figure 17, of the specimens oriented in the rolling direction (L direction) showed a slight decrease in strength and ductility during the hot-rolling reduction process from the 6-inch slab to the 3-inch slab. An increase in strength and a decrease in ductility were observed in the 1/8-inch hot-rolled sheet. After the annealing process, a decrease in strength and increase in ductility were observed in the 1/8-inch sheet. An increase in strength and decrease in ductility were observed in the 1/32-inch finish-gauge sheet.

The tensile-test results, shown in Figure 18, of specimens oriented in the long transverse direction (T-direction) showed observations similar to the rolling direction results. The exception was an increase in ductility during the hot-rolling reduction process from the 6-inch slab to the 3-inch slab.

Tensile-test specimens oriented in the short transverse direction (S-direction) could only be extracted from the 6-inch slab. These tests showed similar strength values in all directions. Only slight differences in ductility were observed as shown in Figure 19. However, significant differences can be seen in the 1/32-inch sheet tensile test results in the different orientations as seen in Figure 18.

Using the BCJ (Bammann, Chiesa, and Johnson, 1996) ISV model to fit the experimental data, parameters can be found that describe the material response at the various stages of the rolling process. Figure 20 shows a comparison of the model fit using these parameters and the experimental data from the tensile tests.

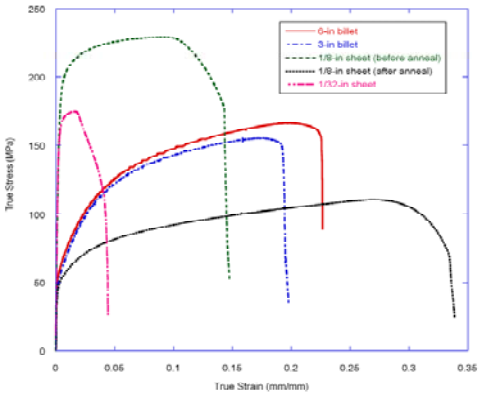

Figure 17. True-stress versus true-strain curves from tensile tests performed at ambient temperature for Al 6022 specimens taken from the various rolling stages oriented in the rolling direction (L direction).

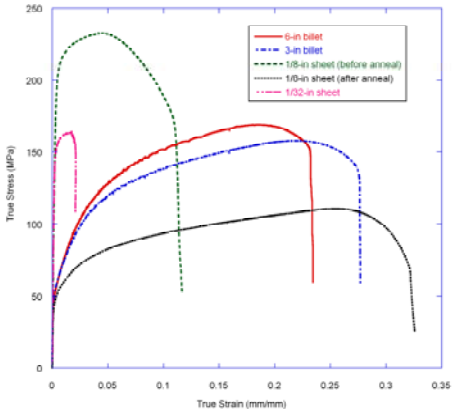

Figure 18. True-stress versus true-strain curves from tensile tests performed at ambient temperature for Al 6022 specimens taken from the various rolling stages oriented in the long transverse direction (T direction).

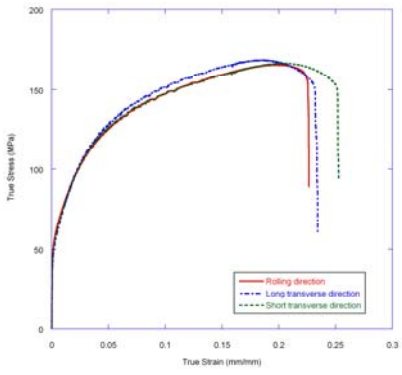

Figure 19. True-stress versus true-strain curves from tensile tests performed at ambient temperature for Al 6022 specimens taken from the 1/32-inch sheet oriented in different directions.

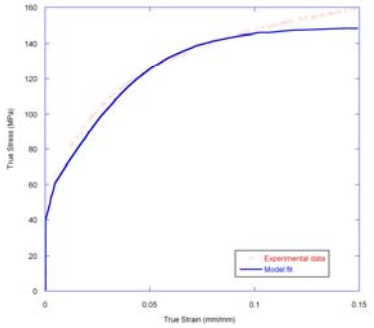

Figure 20. True-stress versus true-strain curves from tensile tests performed at ambient temperature for Al 6022 specimens taken from the 1/32-inch sheet oriented in different directions.

Summary

We investigated the material behavior of Al 6022 alloy throughout various stages of the rolling process. The preliminary structure-property relationship indicates that the mechanical properties are strongly related to the microstructural state of the material at each stage. In the initial stages of the rolling process, texturing effects are negligible. However, in the later stages texturing effects can be seen with the differences in the strength and ductility for different orientations of the specimens. For the heat-treatable 6022 Al alloy, it follows the anticipated microstructure development during anneal process.

This effort will enable us to develop a comprehensive ISV model of the material response during the rolling process.

Future Work

Further work on the grain distribution, size, and orientation gradients from the center of the bulk material to the rolling surface of the initial manufacturing stages will be investigated. Additional mechanical tests will be conducted, such as compression and torsion, at additional strain rates and temperatures. Parameters will be determined for implementation into a FE code for simulations of material responses during the various stages of the rolling manufacturing process.

Microstructural-Property Characterization of a Dodge Neon Passenger Car

Passenger-vehicle occupant safety and crashworthiness are essential attributes in today's automotive industry. In this study, a detailed FE model of a 1996 Plymouth/Dodge Neon was used (originally developed at the Federal Highway Administration/National Highway Transportation Safety Administration (FHWA/NHTSA) National Crash Analysis Center and later modified at CAVS) to perform crashworthiness simulations under different impact scenarios. Based on the initial crashworthiness simulations, the ten most energy-absorbing components were selected to develop their microstructure-property relationships. Test specimens were extracted from the as-built vehicle. Microstructural analyses were conducted to characterize grain sizes and their distribution for each component. Mechanical tests, including tension and hardness tests, were performed. Different microstructure-property relations, mechanical properties and microstructural spatial clustering were found for each component. The research objective of this work is to perform material characterizations of critical Dodge Neon components for material response refinement in crashworthiness simulations to improve occupant safety.

Introduction

Crashworthiness simulations using full-scale FE vehicle models are becoming an increasingly important part of vehicle design to decrease vehicle weight and yet increase the performance and safety under different crash scenarios. Lightweighting and safety improvement have been critical issues for both the automobile and its related manufacturing industries. According to NHTSA, there were over six million vehicle crashes in the United States in the year 2004, which claimed the lives of more than 40,000 people. A detailed FE model of a 1996 Plymouth/Dodge Neon was developed at the FHWA/NHTSA National Crash Analysis Center as part of the Partnership for a New Generation of Vehicles (PNGV) program. Crashworthiness simulations were conducted on the NHTSA FE model for different impact crash scenarios and the top ten energy-absorbing components of the

vehicle were determined. Material for the specimens was extracted from the as-built vehicle.

Microstructural analyses of the vehicle components were conducted (at MSST) to obtain the average grain size and distribution for each component. Mechanical tests were conducted. Hardness tests were performed to determine the Vickers hardness and Young's Modulus of each component. Tension tests were performed at two different strain rates at ambient temperature conditions to determine elastic-plastic responses. The results are presented in the following sections.

Experimental Procedure

The microstructural analysis was performed using the AxioVisio Grains software developed by Zeiss. The grain size and distribution were obtained using the ASTM 112-96, which defines the ASTM grain size number, G, and assigns to each G a number of grains per unit area, average grain area and average diameter. The microhardness tests were carried out using a Hysitron TriboIndenter. Nine indentations were performed in every sample using a Berkovich tip, to obtain the load-displacement curves.

The uniaxial-tension tests were performed on material extracted from the vehicle components. These tests were conducted under constant strain-rate conditions using an extensometer for feedback control. The tension tests were conducted at two different strain rates, $0.01s^{-1}$ and $0.0001s^{-1}$, on material from the front bumper, trunk lid and rear floorboard components. The $0.0001s^{-1}$ strain-rate tension tests were carried out on an Instron Model 5869 electromechanical machine using an Epsilon extensometer. The $0.01s^{-1}$ strain-rate tension tests were conducted on a hydraulic MTS Model 810 machine. Specimen width and thickness were measured before the tension tests. All of the tests were performed at ambient temperature.

From the microhardness test, the Young's modulus and yield stress values can be obtained using the following equations (Triboindenter User Manual, 2005):

$$\frac{1}{E_r} = \left(\frac{1-\upsilon^2}{E}\right)_{material} + \left(\frac{1-\upsilon^2}{E}\right)_{indenter} \quad (1)$$

$$HV = 3.03 \cdot \sigma_y \quad (2)$$

where υ is the poisson's ratio, E is the elastic modulus (E_r is the reduced elastic modulus), σ_y is the yield strength, and HV denotes the Vickers Hardness (Vickers Pyramid Number).

The yield stress was also obtained from the tension tests using the offset method in the ASTM standard. (ASTM Standards, 2000).

Results

The Dodge Neon front bumper was the most critical component in the frontal-impact crash scenarios. The microstructure of the front-bumper material can be observed in Figure 21 and Table 1 shows the chemical composition.

Table 1. Chemical composition of the front bumper material.

Fe	C	Mn	Nb	V	Al	Others
98.3	0.078	1.2	0.103	0.063	0.048	0.218

This composition indicates that the material is a microalloyed steel, specifically niobium high-strength low-alloy (HSLA) steel.

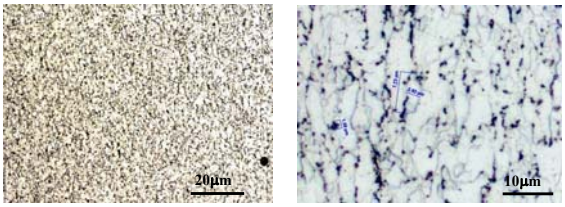

Figure 21. Photomicrographs of the front-bumper material.

All of the microstructures observed were predominantly ferritic. The samples observed presented a mixed microstructure with fine grains having an average diameter range from 2 to 7 µm, and bigger grains with an average diameter from 15 to 25 µm. The grain boundaries are irregular and the grains are elongated in the rolling direction. A darker phase, or precipitates, can be observed in the grain boundaries and some in the ferrite grains. We presumed that this phase is composed of niobium carbide. The precipitates are distributed unevenly with some grain boundaries free of precipitates.

Figure 22 shows the grain-size distribution for each sample. The grain-size mean value is G-11. Using the ASTM 112-96 standard, the mean area is 63 μm^2 and the grains per unit area at 1x is 15872 grains/mm^2. In the positions where the samples were extracted, the material displays little variation in the Vickers hardness values shown in Figure 23, indicating a homogeneous material. The mean Vickers hardness value is 265.4±14.1 HV. The mean yield point and Young's Modulus were calculated at 858.4±45.8 MPa and 181.6±20.1 GPa, respectively, using equations 1 and 2.

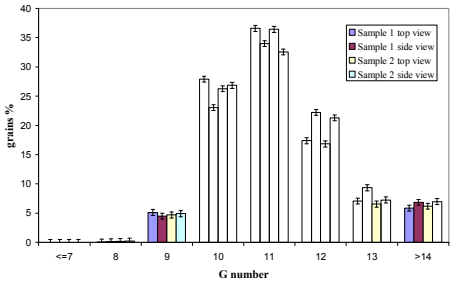

Figure 22. Grain-size distribution of the front bumper.

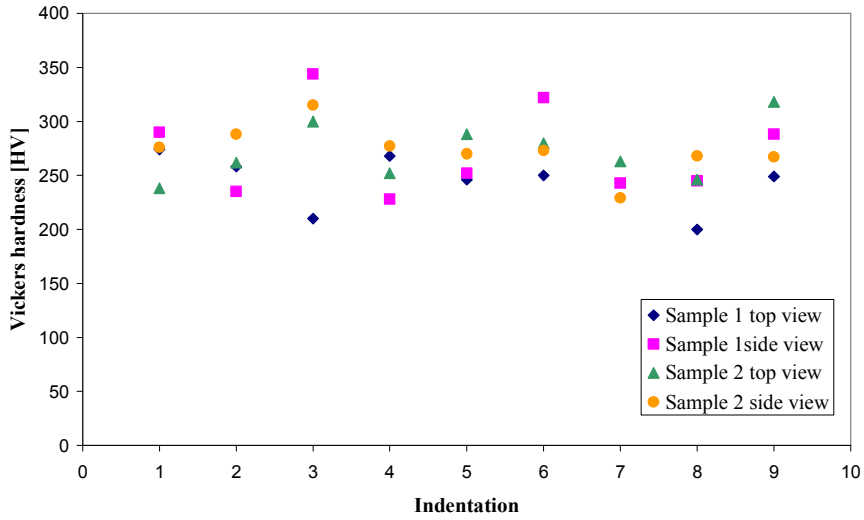

Figure 23. Vickers hardness for the front bumper.

Table 2. Front-bumper properties summary.

	Mean Values			
	Microhardness	*Tension 0.01 /s*	*Tension 0.0001 /s*	*Handbook values plain carbon steel*
Young's Modulus [GPa]	181.6±20.1	166.5±38.8	145.4±20.6	197-206
Yield Point [MPa]	858.4±45.8	511.6±192.1	486.5±193.4	206-275
Ultimate Strength [MPa]	-	601.8±13.2	579.7±39.3	340-450
Vickers Hardness [HV]	265.4±14.1	-	-	130

The summary of the properties obtained for the front-bumper material is shown in Table 2. The stress-strain curves for this material are shown in Figure 24.

We observed that the yield stress increases when the strain rate is higher. These yield-stress values are higher compared to the average values of plain-carbon steels. The Young's modulus is close to the average value for most steels.

Summary

Uncertainty related to microstructure was quantified based on the microstructure-characterization techniques. Different microstructure-property relations for each component were found.

Differences in the microstructural spatial clustering were observed. The chemical composition and optical microscope images of each component show that the material is different for every vehicle part. Therefore, the use of similar stress-strain-stress curves and material properties on a model used in crashworthiness simulations, can affect the results obtained.

Strain-rate dependency was observed in the stress-strain curves on each component tested. This dependence can be noticed in the yield stress and ultimate stress values, since they are lower for the 0.0001/s strain rate for every component.

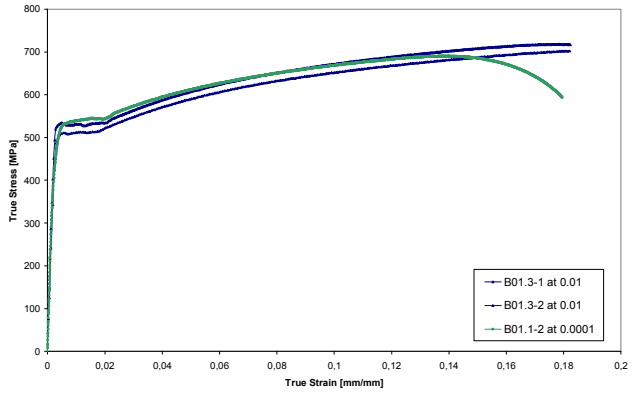

Figure 24. True-stress/true-strain curves of the front bumper.

More vehicle components were determined to be critical during the crash scenarios. To obtain better and more accurate results in crash simulations and to improve passenger safety, the actual material properties of these components should be used in the model. The microstructure characterization of these components is still being determined.

The Associated Sensitivities and Uncertainties of a Multiscale ISV Model with Damage Evolution Arising from Structure-Property Relations

In this section, we analyze the effects of uncertainties pertaining to structure-property relations of an ISV plasticity-damage model that predicts failure. In particular, the microstructural spatial variabilities, the constitutive model-parameter sensitivities, and boundary-condition uncertainties on the damage evolution and final failure using both cast- and wrought-Al alloys are examined. The cast material used in this study is A356 and wrought is Al 6022. The uncertainty analyses are performed using traditional methods like propagation rule and Monte Carlo (MC) techniques and then compared with uncertainty analysis performed by blending a dimension reduction (DR) method and a distribution fitting technique. We first calculate the first four statistical moments of damage using a DR method that reduces the multidimensional integrals (needed in calculating the statistical moments) to a series of single-dimension integrals. Then, we estimate the probability distribution of damage using an extended generalized lambda distribution. We investigated the efficiency and accuracy of this uncertainty analysis methodology on an engineering problem and found very good agreement between the uncertainty predictions of this methodology between different techniques. Finally, we applied the uncertainty analysis methodology for predicting the damage uncertainty. The scatter in damage (that is, the coefficient of variation of damage) increased as the strain increased, even though the uncertainties in the material-plasticity and microstructure parameters remain constant (Figure 30). For A356, the mathematical sensitivity analysis related to damage uncertainty is consistent with the physical nature of the damage progression. At the very beginning, the initial porosity and void nucleation are shown to drive the damage evolution. Then, void coalescence becomes the dominant mechanism. Near failure, one of the macroscale structural properties (fracture toughness)

dominates the damage-evolution process as illustrated by the sensitivity/uncertainty analysis.

Introduction

Improving structural safety requires not only understanding the history of a material through its manufacturing process and in-service life, but also assessing the correlation between the various physical scales present, from the atomic level interactions to the microstructural composition and to the macroscale behavior. With the help of such multiscale material models, it will be possible to relate structural responses of interest such as stress, strain, and toughness, to key material parameters at each length scale, such as particle size, interfacial strength and spacing. The works on multiscale modeling include those of Horstemeyer et al. (2000b, 2001, 2003; Ganapathysubramanian and Zabaras (2004), and Shilkrot et al. (2004). For a summary of recent progress in multiscale material modeling and simulations, the reader is referred to Graham-Brady et al. (2006).

In this work, we utilize the damage-evolution model developed by one of the authors (Horstemeyer et al., 2000a; 2000c; 2001) since we had good access to experimental and computational details. Horstemeyer (2001) has employed successfully a multiscale analysis for automotive structural components made of A356 cast Al. More recently, Horstemeyer et al. (2005) investigated the effect of variability in microstructures and the boundary conditions that characterize the damage evolution using first-order Taylor series (FOTS) uncertainty analysis. In particular, void-nucleation, void-growth, and void-coalescence equations were evaluated and quantified in terms of sensitivity and uncertainty of various parameters in the constitutive equations. However, uncertainty analysis using a FOTS expansion is amenable to errors, especially for nonlinear response functions (like damage). Therefore, the current work extends the work of Horstemeyer et al. (2005) in that we perform a more accurate uncertainty analysis using a DR technique proposed by Rahman and Xu (2004).

In general, modeling uncertainty exists due to numerical accuracy and simplifying assumptions and to variations in design conditions, input parameters, and other components of a model. Most of the literature on modeling uncertainty has addressed the effect of input-parameter uncertainty. Some recent work has addressed the area of verification and validation (V&V) in an attempt to estimate the other components of model uncertainty. The basis for modeling uncertainty was adapted from the widely-used experimental uncertainty analysis. The experimental uncertainty-analysis references for this study all use the same basic methodology. The worldwide standard for this experimental uncertainty analysis is authored by the International Organization for Standardization (ISO, (1995)).

In the traditional form of uncertainty analyses we incorporated propagation rule (FOTS expansion) and MC techniques. In propagation technique, the uncertainty in damage is given as (Coleman and Steele (1999))

$$U_\phi = \sqrt{\sum_{i=1}^{j}\left[\left(\frac{d\phi}{d\eta}\frac{\partial\eta}{\partial x_i}+\frac{d\phi}{dV_v}\frac{\partial V_v}{\partial x_i}+\frac{d\phi}{dC}\frac{\partial C}{\partial x_i}\right)U_{x_i}\right]^2} \quad (3)$$

where x_i are boundary condition and microstructure parameters, U_{x_i} is the uncertainty for each parameter, and $\eta, V_v, and\ C$ are nucleation, void-growth and coalescence, respectively. To measure the influences of different parameters, two main uncertainty definitions were used:

- Uncertainty magnification factor (UMF_i)

$$UMF_i = \frac{x_i}{\phi}\frac{\partial\varphi}{\partial x_i} \quad (4)$$

- Uncertainty percentage contribution (UPC_i)

$$UPC_i = \left(\left(\frac{x_i}{\phi}\frac{\partial\varphi}{\partial x_i}\right)^2\left(\frac{U_{x_i}}{x_i}\right)^2 \Big/ \frac{U_\phi{}^2}{\phi}\right)100 \quad (5)$$

The overall procedure of uncertainty analysis using uncertainty analysis using dimension reduction and distribution fitting (UDRDF) can be outlined as depicted in Figure 25. First, the physically-motivated damage calculations are performed at some selected points in the random variable space. Next, the first four statistical moments of the performance function are estimated using DR. Then, the probability distribution of the damage is approximated with EGLD (extended generalized lambda distribution). The accuracy of this analysis

is highly dependent on the accuracies of moment estimation and distribution correlation.

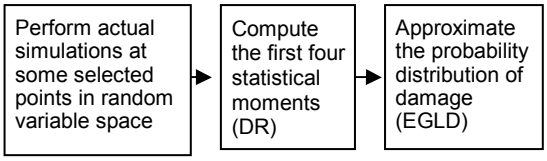

Figure 25. Procedure for UDRDF.

The main contribution of this report is to incorporate different uncertainty analysis techniques in the context of constitutive modeling to illustrate the effects of microstructural variations, along with uncertainties in the loading and boundary conditions, to assess the uncertainty in damage, which is calculated using a multiscale ISV material model. In addition, we aim to quantify the influence of uncertainty of various parameters in the constitutive equations.

Multiscale Microstructure-Property Relationships

The multiscale microstructure-property relationship modeling framework (Horstemeyer (2001), Bammann et al. (1993)) used here accounts for stress-state-dependent damage evolution. The pertinent equations in this model are denoted by the rate of change of the observable (temperature, stress state, and rate of deformation) and the ISVs. For the sake of clarity, a listing of these equations and their relation to the multiscale analysis within the context of FE methodology is briefly described here with additional details provided in (Horstemeyer (2001)).

The frame-indifferent co-rotational rate of the Cauchy stress, $\overset{\circ}{\underline{\sigma}}$, is expressed as

$$\overset{\circ}{\underline{\sigma}} = \lambda(1-\phi)tr\left(\underline{D}^e\right)\underline{I} + 2\mu(1-\phi)\underline{D}^e - \left(\frac{\dot{\phi}}{1-\phi}\right)\underline{\sigma} \qquad (6)$$

where $\underline{\sigma}$ is the Cauchy stress, ϕ is the damage fraction of material within a continuum element (an ISV that represents the damage state) with $\dot{\phi}$ representing its material time derivative, λ and μ are the Lamé elastic constants, $\underline{D}^e$ is the elastic rate of deformation tensor, and $\underline{I}$ is the second-order identity tensor. The underscore symbol in all the equations indicates a second-rank tensor.

The plastic rate of deformation tensor or the deviatoric inelastic flow rule, $\underline{D}^p$, encompasses the regimes of creep and plasticity and is determined as

$$\underline{D}^p = f(T)\sinh\left\{\frac{\left\|\underline{\sigma}'-\underline{\alpha}\right\| - \left[R+Y(T)\right](1-\phi)}{V(T)(1-\phi)}\right\}\frac{\underline{\sigma}'-\underline{\alpha}}{\left\|\underline{\sigma}'-\underline{\alpha}\right\|} \qquad (7)$$

where $\underline{\sigma}'$ is the deviatoric part of stress tensor, T is temperature in Kelvin, $\underline{\alpha}$ is the kinematic hardening (an ISV reflecting the effect of anisotropic dislocation density), and R is the isotropic hardening (an ISV reflecting the effect of global dislocation density). The function $V(T)$ determines the magnitude of rate dependence on yielding, $f(T)$ determines when the rate dependence affects initial yielding, and $Y(T)$ is the rate-independent yield stress. Functions $V(T)$, $Y(T)$, and $f(T)$ are related to yielding with Arrhenius-type temperature dependence and are given as:

$$V(T) = C_1 e^{\left(-C2/T\right)};\ Y(T) = C_3 e^{\left(C4/T\right)};\ f(T) = C_5 e^{\left(-C6/T\right)} \qquad (8)$$

where C_1 through C_6 are the yield-stress-related material parameters that are obtained from isothermal compression tests with variations in temperature and strain rate.

The co-rotational rate of the kinematic hardening, $\overset{o}{\underline{\alpha}}$, and the material time derivative of isotropic hardening, $\dot{R}$, are expressed in a hardening-recovery format as

$$\overset{o}{\underline{\alpha}} = \left\{h(T)\underline{D}^p - \left[\sqrt{\frac{2}{3}}r_d(T)\left\|\underline{D}^p\right\| + r_s(T)\right]\|\underline{\alpha}\|\underline{\alpha}\right\}\left[\frac{DCS_0}{DCS}\right]^z \qquad (9)$$

$$\dot{R} = \left\{H(T)\underline{D}^p - \left[\sqrt{\frac{2}{3}}R_d(T)\left\|\underline{D}^p\right\| + R_s(T)\right]R^2\right\}\left[\frac{DCS_0}{DCS}\right]^z \qquad (10)$$

where DCS_0, DCS, and z parameters capture the microstructure effect of grain size. The dislocation populations and morphology within crystallographic materials exhibit two types of recovery. In Eqs. 9 and 10, $r_d(T)$ and $R_d(T)$ are scalar functions of temperature that describe

dynamic recovery, $r_s(T)$ and $R_s(T)$ are scalar functions that describe thermal (static) recovery, whereas $h(T)$ and $H(T)$ represent anisotropic and isotropic hardening modulus, respectively. These functions are calculated as

$$r_d(T)=C_7\left[1+C_a\left(\frac{4}{27}-\frac{J_3'^2}{J_2'^3}\right)-C_b\left(\frac{J_3'}{J_2'}\right)^{3/2}\right]e^{\left(-C_8/T\right)},$$
$$R_d(T)=C_{13}\left[1+C_a\left(\frac{4}{27}-\frac{J_3'^2}{J_2'^3}\right)-C_b\left(\frac{J_3'}{J_2'}\right)^{3/2}\right]e^{\left(-C_{14}/T\right)} \quad (11)$$

$$r_s(T)=C_{11}e^{\left(-C_{12}/T\right)},\quad R_s(T)=C_{17}e^{\left(-C_{18}/T\right)} \quad (12)$$

$$h(T)=C_9\left[1+C_a\left(\frac{4}{27}-\frac{J_3'^2}{J_2'^3}\right)+C_b\left(\frac{J_3'}{J_2'}\right)^{3/2}\right]e^{\left(-C_8/T\right)}-C_{10}T,$$
$$H(T)=C_{15}\left[1+C_{22}\left(\frac{4}{27}-\frac{J_3'^2}{J_2'^3}\right)+C_b\left(\frac{J_3'}{J_2'}\right)^{3/2}\right]e^{\left(-C_8/T\right)}-C_{16}T \quad (13)$$

where $J_2'=\frac{1}{2}\left(\underline{\sigma}'-\underline{\alpha}\right)^2$, $J_3'=\frac{1}{3}\left(\underline{\sigma}'-\underline{\alpha}\right)^3$, C_7 through C_{12} are the material-plasticity parameters related to kinematic hardening and recovery terms, C_{13} through C_{18} are the material-plasticity parameters related to isotropic hardening and recovery terms, whereas C_a and C_b are the material plasticity parameters related to dynamic recovery and anisotropic hardening terms, respectively. Constants C_1 through C_{18} are determined from macroscale experiments at different temperatures and strain rates.

The two components of damage-progression mechanism are void nucleation and growth from silicon particles and pores. In this regard, the material time derivative of damage, $\dot{\phi}$, is expressed as

$$\dot{\phi}=\left(\dot{\phi}_{particles}+\dot{\phi}_{pores}\right)c+\left(\phi_{particles}+\phi_{pores}\right)\dot{c} \quad (14)$$

where $\phi_{particles}$ represents void growth from particle debonding and fracture, ϕ_{pores} represents void growth from pores, with $\dot{\phi}_{particles}$ and $\dot{\phi}_{pores}$ representing their respective time derivatives; parameter *c* represents the void coalescence that is indicative of pore-pore and silicon (Si)-pore interactions with $\dot{c}$ as its time derivative. The particle- and pore-based void growth rate and the void-coalescence rate equations are given as

$$\dot{\phi}_{particles}=\dot{\eta}v+\eta\dot{v} \quad (15)$$

$$\dot{\phi}_{pores}=\left[\frac{1}{(1-\phi_{pores})^m}-(1-\phi_{pores})\right]\sinh\left[\frac{2\left(2^{V(T)/Y(T)}-1\right)}{\left(2^{V(T)/Y(T)}+1\right)}\frac{\sigma_H}{\sigma_{vm}}\right]\left\|\underline{D}^p\right\| \quad (16)$$

$$\dot{c}=\left[Cd_1+Cd_2\left(\eta\dot{v}+\dot{\eta}v\right)\right]e^{(C_{CT}T)}\left(DCS_0/DCS\right)^z \quad (17)$$

where *v* is the void growth, η is the void nucleation, whereas σ_H and σ_{vm} are the hydrostatic and von Mises stresses, respectively. The parameters Cd_1 and Cd_2 are related to first and second normalized nearest-neighbor distance parameters, respectively, and C_{CT} is the void-coalescence temperature-dependent parameter. The void nucleation rate and void growth rate are given as

$$\dot{\eta}=\left\|\underline{D}^p\right\|\frac{C_{coeff}d^{1/2}}{K_{IC}f^{1/3}}\eta\left[a\left(\frac{4}{27}-\frac{J_3^{\,2}}{J_2^{\,3}}\right)+b\frac{J_3}{J_2^{3/2}}+c\left\|\frac{I_1}{\sqrt{J_2}}\right\|\right]e^{\left(-C_{\eta T}/T\right)} \quad (18)$$

$$\dot{v}=\frac{\sqrt{3}R_0}{2(1-m)}\left[\sinh\left(\sqrt{3}(1-m)\frac{\sqrt{2}I_1}{3\sqrt{J_2}}\right)\right]\left\|\underline{D}^P\right\| \quad (19)$$

where C_{coeff} is a material constant that scales the response as a function of initial conditions, *d* is the particle size, K_{IC} is the fracture toughness, *f* is the volume fraction of second-phase particles, $C_{\eta T}$ is the void-nucleation temperature-dependent parameter, I_1, J_2, and J_3 are the independent stress invariants, *m* is the void growth constant, R_0 is the initial void radius, whereas material constants *a*, *b*, and *c* are the void-nucleation constants that are determined from different stress states (i.e., *a* is found from a torsion test while *b* and *c* are determined from tension and compression tests, with all three having units of stress).

The time integral form of Eq. (14) is used as damage and, along with von Mises stress, represents the failure responses of interest. Based on this ISV model, failure is assumed to occur when $\phi\rightarrow 1.0$ within a finite element. For all practical purposes, material failure can be assumed at a much smaller value (percolation limit) of ϕ as damage increases very rapidly to 1.0 shortly after ϕ reaches a small percentage. The mechanical properties of a material depend upon the amount and type of microdefects within its structure. Deformation changes these microdefects and, when the number of microdefects accumulates, damage is said to have grown. By including

damage state ϕ as an ISV, different forms of damage rules can be incorporated easily into the constitutive framework.
In summary, α, R, σ, ϕ, c, v, and η in Eqs. 6 through 19 represent the ISVs in this multiscale material model.

Material Microstructure Characterizations and Their Uncertainties

The microstructure of a typical metallic material contains a large number of microdefects such as microcracks, dislocations, pores, and particles. Some of these defects are induced during the manufacturing process and are present before the material is subjected to mechanical loads and thermal fields. In general, these defects are small and are distributed throughout most of the volume.

We are focusing on cast and wrought Al alloys. In the cast A356-T6 Al alloy, the microstructure of this material consists of the primary (Al–1.6wt.%Si) and eutectic (Al–12.6wt.%Si) phases. In the eutectic regions, large Si particles and clusters form a dendritic substructure while the Si remains solutionized in the primary phase. The microstructural alterations have a strong influence on the monotonic mechanical properties of Al castings through changes in void nucleation, growth, and coalescence characteristics.
An optical microscope image of the cast Al alloy, as shown in Figure 26, suggests that the material is more isotropic in nature. The secondary constituent particles within the matrix range from 3 to 6 μm, with the Si particles ranging from 3 to 5 μm, with an average size of 4 μm and particle volume fraction of approximately 7% (5.25% to 8.75%).

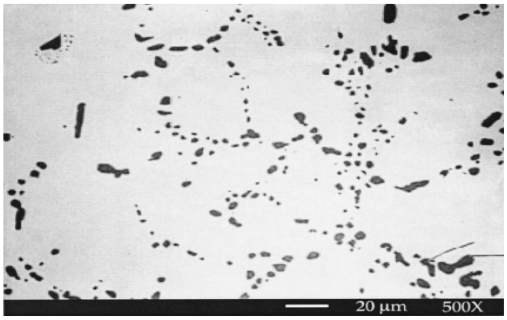

Figure 26. Optical micrograph A356 cast Al alloy which shows second-phase particles.

The microstructural analysis was conducted on a material sample taken at 6*in* slab-thickness stage of the manufacturing rolling process, as shown in Figure 27, using EBSD and image analyses software, and suggests that the material is more anisotropic in nature.

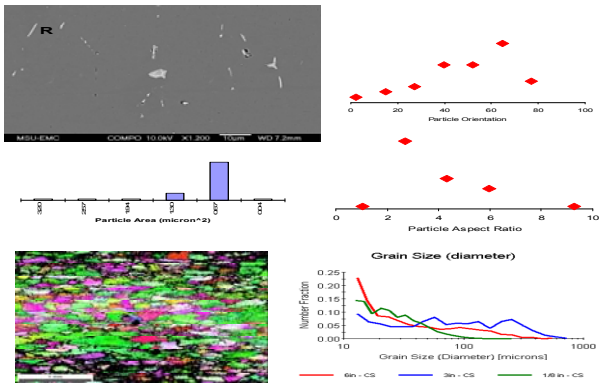

Figure 27. Microstructure clustering of wrought Al 6022 (SEM and electron backscatter diffraction (EBSD), experimental microstructure uncertainty quantification).

In this study for wrought Al alloy, we consider various stages of the rolling process, to understand the influences of manufacturing history and their subsequent effects on uncertainty analysis. (see Figure 28).

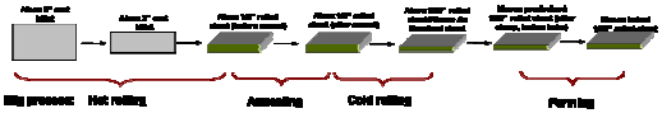

Figure 28. Various rolling stages of wrought 6022 Al alloy to quantify manufacturing history effect.

Recently, Horstemeyer et al. (2005) investigated the effect of variability in microstructures and the boundary conditions that characterize the damage evolution using uncertainty-analysis methodology. In particular, void-nucleation, void-growth, and void-coalescence equations were evaluated and quantified in terms of sensitivity and uncertainty of various parameters in the constitutive equations. They found that a 1% uncertainty in the microstructural and boundary-condition parameters results in 16% uncertainty in damage near failure, 5% uncertainty in failure strain, and 13% uncertainty in failure stress, thereby revealing the need for incorporating uncertainties in the design process when multiscale material model is used.

Table 3a. Microstructure-property (elastic-plastic) model constants for A356-T6.

ID #	Constants (Units)	Mean	ID #	Constants (Units)	Mean
1	G (MPa)	25920	13	C_{10} (°K)	10.94
2	A	1.0	14	C_{11} (sec/MPa)	0.01369
3	K (MPa)	67630	15	C_{12} (°K)	2000
-	B	0.0	16	C_{13} (1/MPa)	0.0000165
4	melt temp (°K)	5556	17	C_{14} (°K)	-1000
5	C_1 (MPa)	53.09	18	C_{15} (MPa)	2818
6	C_2 (°K)	945.3	19	C_{16} (°K)	4.622
7	C_3 (MPa)	155.9	-	C_{17} (sec/MPa)	0.0
8	C_4 (°K)	110.5	20	C_{18} (°K)	235.4
9	C_5 (1/MPa)	0.00001	21	C_a	-7.0
-	C_6 (°K)	0.0	22	C_b	-0.3776
10	C_7 (1/MPa)	0.00087	23	init.temp (°K) heat gen.	297
11	C_8 (°K)	-1877	-	Coeff.	0.0
12	C_9 (MPa)	4820			

Uncertainties in the microstructure-property relationships and multiscale ISV material model are incorporated. The effect of variability in microstructures and boundary conditions that characterize the damage evolution is investigated using uncertainty-analysis methodology. A nonlinear regression algorithm developed previously (Horstemeyer (2001)), was used to fit the plasticity model constants for both wrought and cast Al alloys (the A356-T6 Al alloy, as shown in Tables 3a and 3b). The experimental uncertainty, U_E, is calculated based on systematic and random uncertainties in the measured quantities such as force, strain, and specimen sizes (Eqns. 19 and 20).

$$U_E = \sqrt{U_r^2 + U_s^2} \tag{19}$$

where U_r is random uncertainty and U_s is systematic uncertainty.

The random uncertainty, U_r, in experimentally measured quantities, r_i (force and strain), for M different tests is given by

$$U_r = 2\sqrt{\frac{1}{M-1}\sum_{i=1}^{M}(r_i - r_{i\,mean})^2} \tag{20}$$

where r_{imean} is mean of experimentally-measured quantities (force and stain).

The systematic uncertainty in experimentally measured quantities, r_i (force and strain), for M different tests is given by

$$U_s = r_i\sqrt{U_L^2 + U_{daq}^2} \tag{21}$$

where U_L is uncertainty in load cell or extensometer or strain gauges and U_{daq} is uncertainty in data acquisition.

Quantitative fractographic measurements were used to quantify the variability in microstructure spatial clustering, as shown in Figure 27. A typical optical montage used in quantitative fractographic measurement is shown in Figure 26. The experimental uncertainties related to stress-strain responses are propagated through model correlation routine using propagation law (Eqns. 19 to 21) to predict uncertainty related to material-plasticity parameters as defined by Eqns. 6 to 11.

Table 3b. Microstructure-property (damage) model constants for A356-T6 Al alloys.

ID #	Constants (Units)	Mean
24	M	0.3
25	R_o (mm)	0.0002
26	A	615369
27	B	58630
28	C	30011
29	C_{coeff}	90.6
30	K_{ic} MPa(m$^{1/2}$)	17.3
31	d (mm)	0.000004
32	F	0.07
33	cd1	1.0
-	cd2	0.0
34	DCS0 (mm)	20
35	DCS (mm)	20
36	Z	0.0509
37	initial void volume fraction	0.0001
38	$C_{\eta T}$	0.6
-	C_{CT}	0.0

Uncertainty Analysis of Damage Evolution

In this section, we first apply the DR+EGLD uncertainty-analysis methodology to characterize the uncertainty in damage at different strain values for cast Al alloy. Then, we present a sensitivity and uncertainty analysis of damage related to different input parameters.

We consider uniaxial tensile loading of an A356 Al alloy at strain rate of 10^{-3} 1/sec. The probability distributions of the damage (integration of Eq. 14) at different part of the strain-damage response (see

Figure 29) are provided in Figure 30. The scatter of damage (the coefficient of variation of the damage, C_ϕ) increases along with the mean value of the damage as the strain value increases. The comparison of the probability distribution functions (PDFs) obtained through DR+EGLD and MC simulations (MCS) of sample size 10,000 are also shown in Figure 30, indicating a good agreement between the results of DR+EGLD and MCS considering these analyses were performed independently.

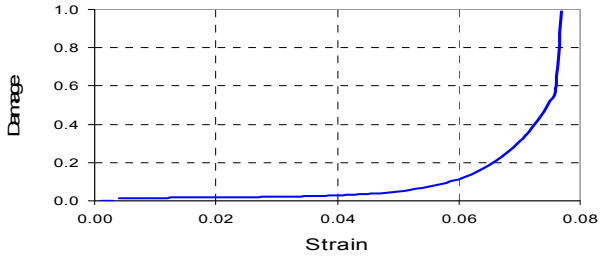

Figure 29. Strain versus damage curve for A356 Al alloy.

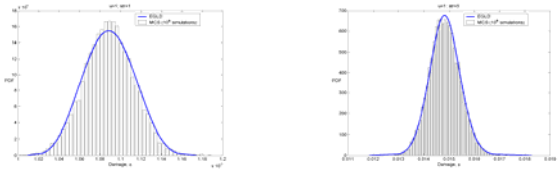

(a) strain = 0.001; C_ϕ = 0.022 (b) strain = 0.005; C_ϕ = 0.040

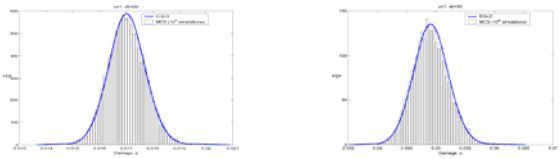

(c) strain = 0.02; Cϕ = 0.040 (d) strain = 0.05; C_ϕ = 0.061

Figure 30. PDFs of damage at different applied strain levels (0.001, 0.005, 0.02, and 0.05) obtained through DR+EGLD and MCSs (with sample size of 10,000).

We also compare uncertainty-analysis results of DR with FOTS uncertainty analysis results. Table 4 shows that the DR uncertainty predictions are better (1% difference at 5% strain) than FOTS uncertainty predictions (4% difference at 5% strain) when compared to MCSs (with sample size of 10,000).

Table 4. Uncertainty analysis results obtained through FOTS expansion, DR (with 4N+1 points), and MCS.

	Standard deviation of damage			
	Strain = 0.001	**Strain = 0.005**	**Strain = 0.02**	**Strain = 0.05**
FOTS	2.43×10^{-7}	6.00×10^{-4}	7.29×10^{-4}	3.09×10^{-3}
DR	2.43×10^{-7}	5.92×10^{-4}	6.93×10^{-4}	3.00×10^{-3}
MCS (10^4 simulations)	2.43×10^{-7}	5.98×10^{-4}	6.87×10^{-4}	2.97×10^{-3}

Results

Uncertainty Characterization of Wrought Al Alloy

In this section, we apply uncertainty analysis methodology to characterize the uncertainty in various rolling stages of manufacturing process. Figure 31 shows comparisons between experimental data to the model along the longitudinal direction for various rolling stages. The uncertainties in experimental data were calculated using Eqs. 19 to 21.

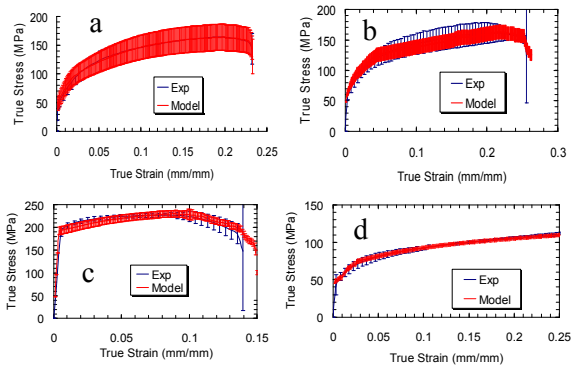

Figure 31. Comparison between experiment and model for a) 6-in. rolled sheet, b) 3-in rolled sheet, c) 1/8 in before annealing, and d) 1/8 in after annealing.

Experimental uncertainties were then propagated through a model correlation routine to estimate uncertainty in model. Figure 31 shows good comparison between model and experimental uncertainties for various rolling stages. The variations of uncertainty from one stage to another were due to variations in microstructural clustering. These results indicate the physical nature of uncertainty analyses, which are

associated with material history and inherent heterogeneities.

Sensitivity of Uncertainty of Damage at Different Strain Values Using the Cast Al Alloy.

In this section we calculate the sensitivity of uncertainty of damage to multiscale material parameters. We measure the sensitivity of damage, S_i, to an input random variable, X_i, by using

$$S_i = \frac{\partial C_\phi}{\partial C_i} \frac{C_i}{C_\phi} \qquad (22)$$

where C_i is the coefficient of variation of X_i. Sensitivities of uncertainty of damage to the uncertainties of the multiscale material parameters are depicted in Figure 32. For instance, Figure 32 (a) shows that, at the very beginning of the damage evolution, the initial radius of spherical void, d, (31st random variable) and nucleation coefficient (35th random variable) are the most influential parameters. Figure 32 (b-c), on the other hand, shows that, as damage progresses, the initial temperature (28th random variable), coalescence temperature dependence term (46th random variable), coalescence factor cd1 (39th random variable) and initial void volume fraction (44th random variable) are more important. Finally, Figure 32 (d) displays the effect of parameters on the last stages of damage progression. We see that the most influential terms can be ordered according to their importance as the fracture toughness (36th random variable), initial temperature (28th random variable) and coalescence temperature dependence (46th random variable), respectively.

The sensitivity plots in Figure 32 are also consistent with the physics of the damage progression. At the very beginning, the void nucleates and grows. Then, voids combine with each other and coalescence becomes the main driver. Near failure, macroscopic properties such as fracture toughness, K_{IC}, determines the damage evolution process.

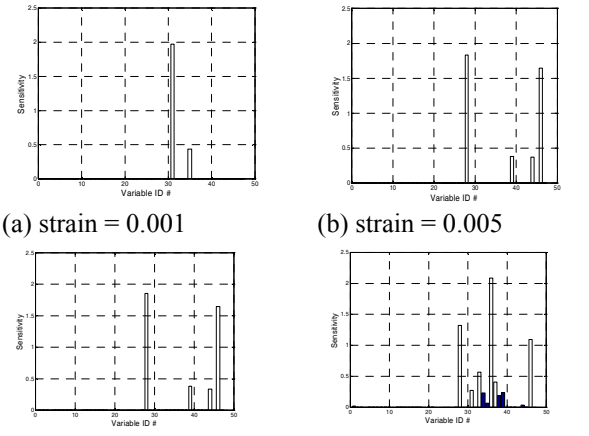

(a) strain = 0.001 (b) strain = 0.005

(c) strain = 0.01 (d) strain = 0.05

Figure 32. Sensitivity of uncertainty of damage to the uncertainties of the multiscale material parameters.

Summary

The specific conclusions are:

1. The scatter in damage (that is, the coefficient of variation of damage) increases as the strain values increase even though the uncertainties in the input variables remain fixed.
2. The sensitivities of the uncertainty of damage to the uncertainties of the input random variables were found to be dependent on the strain values. As the strain value changed (that is, as the damage evolved), the importance of the random variables changed. This correlates exactly with the physical basis of the damage formulation.
3. As such, the sensitivities were found to be consistent with the physics of the damage progression. At the very beginning, the void nucleation properties drive the damage evolution. Then, voids combine with each other and coalescence becomes the main driver during the intermediate and later stages of deformation. At final fracture, macroscopic properties such as fracture toughness, K_{IC}, became dominant.
4. We compared the uncertainty-analysis results obtained through FOTS expansion and DR with those of the MCS and found that DR uncertainty predictions were better than FOTS-series predictions.

Presentations/Publications/Patents

1. Hammi, Y., Horstemeyer, M.F., "A Physically Motivated Anisotropic Tensorial Representation of Damage with Separate Functions for Void Nucleation, Growth, and Coalescence," Int. J. Plast., Vol. 23, pp. 1641-1678, 2007.
2. Querin, J.A., Schneider, J.A., Horstemeyer, M.F., "Analysis of micro void formation at grain boundary triple points in monotonically strained AA6022-T43 sheet metal," Materials Science and Engineering A, v 463, n 1-2, p 101-106, 2007.
3. Potirniche, G., Horstemeyer, M.F., Ling, X.W., "An internal state variable damage model in crystal plasticity," Mechanics of Materials, v 39, n 10, p 941-952, 2007.
4. Jordon, J.B., Horstemeyer, M.F., Solanki, K., Xue, Y., "Damage and stress state influence on the Bauschinger effect in aluminum alloys", Mechanics of Material, Vol. 39, pp. 920-931, 2007.
5. Anurag, S., Guo, Y., Horstemeyer, M.F., "The Effect of Materials Testing Mode on Dynamic Mechanical Behavior Modeling and Hard Machining Simulation," Proc. 2007 Int. Manufacturing Science and Engineering Conference, MSEC2007-31087, Oct 2007, Atlanta, GA.
6. Solanki, K, Horstemeyer, M.F., "A Physically Motivated Uncertainty-Based Higher Order Plasticity and Damage Model," MCMAT2007-30120, ASME Applied Mechanics and Materials Conference, University of Texas at Austin, June 3-7, 2007.
7. Horstemeyer, M.F., Solanki, K., "Internal State Variable Modeling of Structure-Property Relationships in Deformed Microstructures," The Minerals, Metals, and Materials Society, 2007 TMS Annual Meeting & Exhibition, Orlando, Florida, 25 Feb - 1 March 2007.

References

1. Agnew, S. R., Yoo, M. H., and Tome, C. N. (2001) "Application of texture simulation to understanding mechanical behavior of Mg and solid solution alloys containing Li or Y", Acta. Mater., 49, 4277-4289.
2. ASTM Standards, "Section 3: Metals Test Methods and Analytical Procedures", Vol. 03.01, American Society of Testing and Materials, West Conshohocken, PA, 2000.
3. Bammann, D. J., (1990), "Modeling Temperature and Strain Rate Dependent Large Deformation of Metals," Applied Mechanics Reviews, Vol. 43, No. 5, S312-S319.
4. Bammann, D. J., Chiesa, M. L., Horstemeyer, M. F., and Weingarten, L. I., (1993), "Failure in Ductile Materials Using Finite Element Methods," Structural Crashworthiness and Failure, edited by T. Wierzbicki and N. Jones, Elsevier Applied Science, The Universities Press (Belfast) Ltd.
5. Bammann, D. J., Chiesa, M. L., and Johnson, G. C., (1996), "Modeling large deformation and failure in manufacturing processes," Theoretical and Applied Mechanics, ed. T. Tatsumi, E. Wannabe, and T. Kambe (Elsevier, Amsterdam), 359-376.
6. Baskes, M.I., (1992), Phys. Rev. B 46, 2727.
7. Coleman, H. W., and Steele, W. G., (1999), "Experimentation and Uncertainty Analysis for Engineers", 2nd Edition, John Wiley, New York, NY.
8. Dawson, P., Boyce, D., MacEwen, S., and Rogge, R. (2001) "On the influence of crystal elastic moduli on computed lattice strains in AA-5182 following plastic straining," Mat. Sci. Engrg., A313, 123-144.
9. Ganapathysubramanian, S and Zabaras, N., (2004), "Design across length scales: A reduced-order model of polycrystal plasticity for the control of microstructure-sensitive material properties," Computer Methods in Applied Mechanics and Engineering, Vol. 193, pp. 5017-5034.
10. Graham-Brady, L. L., Arwade, S. R., Corr, D. J., Gutierrez, M. A., Breysse, D., Grigoriu, M., and Zabaras, N., (2006), "Probability and Materials: from Nano- to Macro-Scale: A Summary," Probabilistic Engineering Mechanics, Vol. 21, pp. 193-199.
11. Horstemeyer, M. F. and Ramaswamy, S., (2000a), "On Factors Affecting Localization and Void Growth in Ductile Metals: A Parametric Study," Int. J. Damage Mech., Vol. 9, pp. 6-28.
12. Horstemeyer, M. F., Lathrop, J., Gokhale, A. M., and Dighe, M., (2000b), "Modeling Stress

State Dependent Damage Evolution in a Cast Al-Si-Mg Aluminum Alloy," Theoretical and Applied Fracture Mechanics, Vol. 33, pp. 31-47.
13. Horstemeyer, M. F., Matalanis, M. M., Sieber, A.M., and Botos, M.L., (2000c), "Micromechanical Finite Element Calculations of Temperature and Void Configuration Effects on Void Growth and Coalescence," Int J. Plasticity, Vol. 16.
14. Horstemeyer, M. F., (2001), "From Atoms to Autos A New Design Paradigm Using Microstructure-Property Modeling, Part 1: Monotonic Loading Conditions," Sandia National Laboratories, Sand2000-8662, Livermore, CA.
15. Horstemeyer, M. F., Wang, P., (2003), "Cradle-to-Grave simulation-Based Design Incorporating Multiscale Microstructure-Property Modeling: Reinvigorating Design with Science," J. Computer-Aided Materials Design, Vol. 10, pp. 13-34.
16. Horstemeyer, M.F., Gall, K. A., Dolan, K., Haskins, J., Gokhale, A.M., and Dighe, M.D., (2003) "Numerical, Experimental, and Image Analyses of Damage Progression in Cast A356 Aluminum Notch Tensile Bars," Theoretical and Applied Fracture Mechanics. Vol. 39, n 1, p 23-45.
17. Horstemeyer, M. F., Negrete, M., and Ramaswamy, S., (2003), "Using a Micromechanical Finite Element Parametric Study to Motivate a Phenomenological Macroscale Model For Void/Crack Nucleation in Aluminum with a Hard Second Phase," Mechanics of Materials, Vol. 35, pp. 675-687.
18. Horstemeyer, M.F., Solanki, K. and Steele, W.G., (2005) "Uncertainty Methodologies to Characterize a Damage Evolution Model," Proceeding of International Plasticity Conference, Hawaii.
19. ISO, (1995), International Organization for Standardization, Guide to the Expression of Uncertainty in Measurement, ISO, Geneva.
20. Kamat, R.G., Butler, Jr., J. F., Murtha, S. J., and Bovard, F., S., (2002), "Alloy 6022-T4E29 For Automotive Sheet Applications," Materials Science Forum, 396-402, 1591-1596.
21. Kamat, M. Z., and Kassner, M. E., (2002), "Tensile and Fatigue Properties of Aluminum Alloy Sheet 6022," Journal of Materials Engineering and Performance, Vol. 11, 166-168.
22. Kocks, U. F., Tome, C. N., and Wenk, H. R. (1998) "Texture and Anisotropy", Cambridge University Press, 1st edition.
23. Marin, E. B. and Dawson, P. R., (1998) "On modelling the elasto-viscoplastic response of metals using polycrystal plasticity." Comput. Methods Appl. Mech. Engrg., Vol. 165, 1-21.
24. Miao. W. F., and Laughlin, D. E., (1999), "Precipitation Hardening in Aluminum Alloy 6022," Scripta Materialia, Vol. 40, 873-878.
25. Rahman, S., and Xu, H., (2004), "A Univariate Dimension-Reduction Method for Multi-dimensional Integration in Stochastic Mechanics," Probabilistic Engineering Mechanics, Vol. 19, pp. 393-408.
26. Shilkrot, L. E., Miller, R. E., and Curtin, W. E., (2004), "Multiscale Plasticity Modeling: Coupled Atomistics and Discrete Dislocation Mechanics," Journal of the Mechanics and Physics of Solids, Vol. 52, pp. 755-787.
27. Triboindenter User Manual, NRL-M-023 v. 5.0, Hysitron Inc., Minneapolis, 2005.

K. Cyberinfrastructure

Co-Principal Investigator: Tomasz Haupt
Center for Advanced Vehicular Systems
Mississippi State University (MSST)
PO Box 5405, Mississippi State, MS 39762
(662) 325-4524, fax: (662)325-5433, haupt@cavs.msstate.edu

Technology Area Development Manager: Joseph A. Carpenter
(202) 586-1022; fax: (202) 586-1600; e-mail: joseph.carpenter@ee.doe.gov

Contract Monitor: Aaron Yocum
(304) 285-4852; fax: (304) 285-4403; e-mail: aaron.yocum@netl.doe.gov

---

Contractor: MSST
Contract No.: 4000054701

Objective

- Design and develop cyberinfrastructure to exploit the recent transformative research in material science involving multiscale physics-based predictive modeling, multiscale experiments and design.

- This project is aligned with the United States Automotive Materials Partnership (USAMP) Integrated Computational Materials Engineering (ICME, see 6.F) effort for the Mg international pilot project (see 6.C).

Approach

- The development of the cyberinfrastructure to support the capabilities described above will leverage tools, technologies, and software approaches developed by other large-scale, scientific cyberinfrastructures, in particular GEONGrid (http://www.geongrid.org/) and NEESit (http://it.nees.org/). Much of the foundation of the infrastructure is common across domains (security, grid integration, etc) and can serve to bootstrap this project to delivering an initial working solution in a relatively short time frame. Some initial customization will be needed to support the unique aspects of this project, but we have the experience and contact with the other projects to ensure those are relatively quick. After the initial system is developed, we expect many of the advanced capabilities of the system to require additional software development or customization and entirely new development to support additional features. Hence, we will proceed with a two-stage development model: phase one to initially leverage existing software and tools to bring up a working software infrastructure, then phase two to evaluate and further develop missing or insufficient software as needed to support the project requirements.

- The user will access the engineering virtual organization (EVO) services through a grid portal. The grid portal will manage the user credentials and user sessions, and will host portlets implementing rich graphical user interfaces (GUI) for services rendered by the infrastructure (database queries, remote job submission, etc.). The GUI will be implemented using the combination of Java Applets, Java Script and Asynchronous JavaScript and eXtensible Markup Language (XML) (AJAX). In addition, the portal will enable accessing the services from grid-enabled stand-alone applications. Finally, the software integration will be accomplished applying Java Business Integration (JBI) approach using an open-source service bus implementation.

Accomplishments

- **Task 1**: Identify, acquire and deploy servers supporting simple object access protocol (SOAP), Web Service Description Language (WSDL) and integrating Message Oriented Middleware. This task has been completed. We selected and installed: Globus Toolkit 4 grid computing (remote access to resources, security); Apache/Tomcat Web Server with support for J2EE (Java 2 Platform, Enterprise Edition), GridSphere (portlet container), JBoss (Enterprise JavaBeans container), Axis (SOAP and WSDL container), ServiceMix (JBI – Service Bus), and Microsoft's Share Point Server for the deployment of USAMP community portal.

- **Task 2:** Create a virtual organization encompassing all partners involved in the project research and implement authentication, authorization, and auditing mechanisms according to policies negotiated with the system administrators. This task has been modified. At this phase of the project, there is no need for resource sharing (e.g., running jobs on machines outside MSST campus or allowing non-MSST employees or students to run jobs on MSST systems). On the other hand, the USAMP project mandates the development of an electronic "community of practice" web-site that allows development and integration of multiscale, physics-based material models for selected properties and processes. To this end, we deployed the Share Point Server configured to be accessible from any place in the world with all necessary security setting protecting against misuse and cyber-vandalism. The portal has been made available to selected test users participating in the USAMP Mg project. Eventually, the server will provide a single point of access to all services rendered by the cyberinfrastructure, through the contents aggregation.

- **Task 3:** Develop and deploy services for secure access to remote resources (job submission to high performance platforms, job monitoring, access to file systems and databases). Most of the services have been developed and utilized in Task 5. This present Task 3 is essentially completed; however, the developments in Task 5 to 7 may require some additional customization and/or hardening of the implementation.

- **Task 4:** Develop support for service orchestration and workflows. The service orchestration is achieved by employing the Service Bus and used in Task 5. The interfaces for composing workflows remain to be implemented. This means that Task 4 is 50% completed.

- **Task 5:** Develop specific services supporting design optimizations (design-of-experiment (DoE)), metamodels, optimization, input/output (I/O) for ABAQUS and other finite-element analysis (FEA) codes from multiscale and multiscale simulations (bridges from Tasks 1 and 2). This task actually comprises three tasks: online repository of material properties, support for design optimizations and support for multiscale simulations. This builds on the results of activities within Tasks 1, 3, and 4, and is the subject for the integration effort in Tasks 2 and 7. The preliminary version of the repository (including the capability to generate mechanical material properties using internal state variables – DMGfit – see Figure 1) has been developed and made available for testing by engineering students at MSST (presented at 7th international conference on Grid Computing, Barcelona'06, and International Conference on Grid Computing and Applications, Las Vegas 2007). For design optimization, we have implemented support for the creation of metamodels: DoE, automatic-creation ABAQUS and LS-DYNA input decks with the value of design variables according to DoE results, running FEA codes on remote, high-performance resources, collecting the output files, and extracting the responses to build a metamodel (presented at e-Science'06 conference, Amsterdam, NL). In parallel, in collaboration with Project 4, we are developing a Flexible Advanced Metamodeling Estimator (FAME) for automatic generation of best metamodel-based surrogate model (c.f. 4.3). The support for multiscale simulations has been postponed to the later phases of the project.

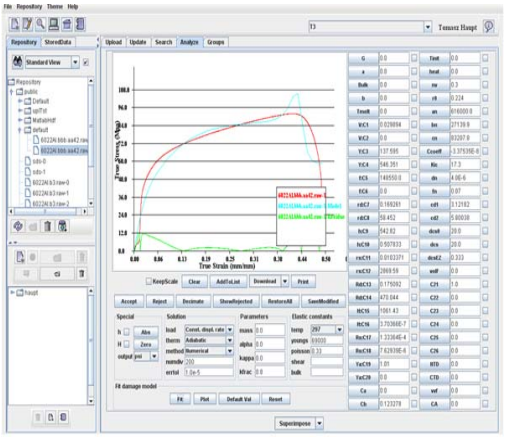

Figure 1. Repository of Material Properties - a snapshot of the web-based user interface.

- **Task 6:** Develop a resource-management system for multiscale simulations. We have developed an overlay

scheduler to support adaptive multiscale simulations (presented at The Minerals, Metals and Materials Society (TMS) 2006 conference).

- **Task 7:** Integrate all components into a single system (cyberinfrastructure). Verify and validate the system by running design optimization and multiscale cases. Improve the GUIs, performance and robustness. These activities are about to be initiated.

Future Direction

- During the first year, the basic infrastructure has been created that forms a solid foundation for creating the cyberinfrastructure for EVOs. Furthermore, preliminary implementation of vital components has been done, in particular support for design optimizations and service-based repository of material properties. During year two, the production version of these components needs to be developed and deployed. This involves thorough tests and validation and gathering feedback for early users. The components need to be integrated into a single versatile and expandable system accessible by the Grid Portal. The final integration is the subject of Task 7, which will dominate the activities in year two.

- The system at the end of year two will provide the basic collaborative system enabling design optimization and multiscale experiments and simulations. This base system will be further expanded adding new software components and the implementation will be brought to the next level to support autonomous execution of complex computational workflows, including self-optimizations (scheduling in high-performance, heterogeneous, distributed environments and adaptive resource management), self-healing (fault-tolerance through monitoring of resource availability, fault detection, and conditional workflows), self-protection (context-sensitive security), and self-configuration (automatic detection of new hardware, software, and data components).

- The specific activities for the year two include:
    - **Repository of Material Properties:** The preliminary implementation requires further optimizations (both back-end services and GUIs, as well as systematic validation. The repository is already on-line ready for the early users, and we are in the process of collecting the users' feedback. Currently, it provides support for fitting parameters to the Bammann-Chiesa-Johnson (BCJ) plasticity model (see 6.J) and to the damage model. Additional models and more material properties are being prepared for the integration (optical properties, fatigue, etc).
    - **Support for Design Optimizations:** Currently, two approaches have been adopted. In the early stages of this project we have created grid-enabled system that automates performing design optimizations and concurrent execution of FEA models on remote, high-performance systems. The second approach is to develop a system for adaptive metamodeling (FAME). The next step is to merge the two approaches into a single system with user-friendly interfaces and develop flexible resource-management techniques to minimize the turnaround time for generation metamodels. In the later phases, the subsystem for design optimizations will be integrated with the subsystem for multiscale simulations.
    - **Support for Multiscale Simulations:** We have developed an overlay scheduler to manage an adaptive tree of processes spawned while performing multiscale simulations. Further development of the support for multiscale simulations has been postponed. The concurrent developments of multiple system components jeopardize timely completion of the tasks and the multiscale simulations are the least mature for automation and integration (as opposed to repository of material properties and support for design optimizations).
    - **Portal for the Virtual Organization:** The USAMP ICME for the Mg international pilot project redefined our initial requirements for creation of the Virtual Organization. The new requirements call for the deployment of a collaborative portal based on Microsoft's SharePoint server. This portal will enable sharing documents and management of the tasks and projects between the participants of the ICME Mg project. In the next step, the support for sharing data will be added and, finally, all capabilities of the cyberinfrastructure under development at MSST will be made available through this portal.

Introduction

The objective of this project, Cyberinfrastructure, is the establishment of an EVO to exploit the recent transformative research in material science involving multiscale, physics-based predictive modeling, multiscale experiments and design, in conjunction with robust design and manufacturing process optimizations with uncertainty and cyberinfrastructure development (Figure 2). The information, data, and software tools generated by the virtual organization will enable closing the significant knowledge gaps in a unifying, physics-based modeling theme that captures a broad range of materials, admits structure-property relations, can be used in simulation-based design, can be implementable into finite-element codes, can be experimentally validated, can capture history effects, and can morph into a metamodel for rapid use prognostics. The knowledge and data will come from many sources across organizational boundaries (distributed databases of geometries, material properties, manufacturing processes, experimental results coming from different labs, etc.) allowing experts from different disciplines (such as bio-inspired material models, models at different length scales, metamodeling and optimizations) to work together toward the common goal.

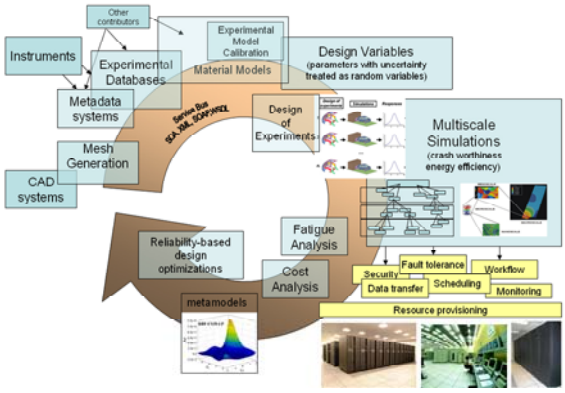

Figure 2. The vision - the cyberinfrastructure will integrate distributed databases of engineering knowledge and computational workflows for multi-objective, multiscale, design optimizations under uncertainty.

The implementation will follow Service-Oriented Architecture paradigm. The user will access the EVO services through a grid Portal. The grid portal is implemented using GridSphere – a robust and widely used implementation of the JSR-168 Portlets specification. The grid portal will manage the user credentials and user sessions, and will host portlets implementing rich GUIs for services rendered by the infrastructure (database queries, remote-job submission, telepresence, etc.). The GUI is being implemented using the combination of Java Applets, Java Script and AJAX. In addition, the Portal will enable accessing the services from Grid-enabled stand-alone applications. For example, modules for MATLAB and ABAQUS are planned to allow these applications to access the material- properties databases directly from the native GUI (MATLAB, ABAQUS, respectively) and submit jobs to remote, high-performance platforms.

The Portlets will delegate the actual processing of the user requests to services implemented in Java. The services will form a façade for the Grid fabric services such as Globus grid resource allocation management (GRAM) — remote-ob submission, direct-access interface system (DAIS) – remote-database access, and gridFTP (file transfer and remote file system access) as well as Data Turbine (telepresence). The overall architecture of the proposed cyberinfrastructure for engineering Virtual Organization is shown in Figure 3.

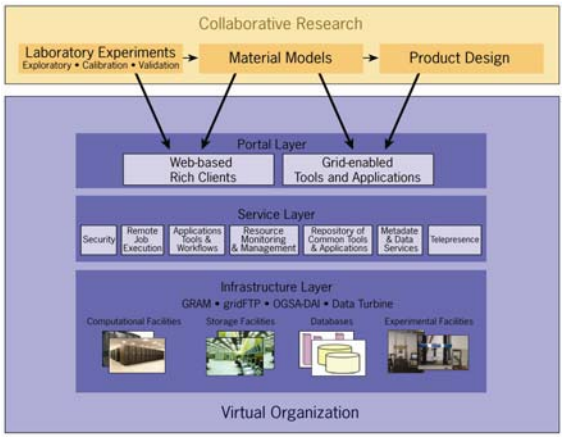

Figure 3. Architecture for EVO.

Finally, the software integration will be accomplished applying JBI approach using an open-source Service Bus implementation, as shown in Figure 4.

Figure 4. Horizontal software-integration bases on the service-bus concept (as opposed to currently-used centralized, "hub and spoke" architectures leading to vertical silos and stovepipes.

Repository of Material Properties

Introduction

The goal for this repository is threefold. Firstly, the repository provides the support for *ad-hoc* collaborations that require sharing restricted-access data between members of dynamically-created groups. Secondly, the repository supports creating different views on the storage by virtual gathering metadata records in hierarchical collections mimicking a tree of folders. Finally, the repository supports data transformations on-the-fly taking the advantages of the flexibility of the enterprise service bus (ESB)-based architecture.

The system is designed to support sharing thousands of data sets of a small to moderate size (gigabytes) per group. The number of the data sets mandates a support for metadata describing these data sets thus allowing for queries. The manner how the data is described, that is, the metadata schema, may vary from group to group and, in addition, it may change in time adapting to the evolving user needs. Therefore, it is necessary to introduce a very flexible metadata system without compromising the performance of queries. The data may be stored at different locations that support different mechanisms or interfaces for data access. Finally, strong authentication and group-based authorization mechanisms are required.

The metadata catalog and the storage are deliberately organized independently from each other. The storage is implemented as a flat collection of files and the physical location of a particular file is determined by the storage. The user can access it only by its logical name. The resolution from the logical name to the physical location is performed dynamically by an independent service – the replica locator. The metadata catalog is conceptually implemented as a single "business" structured query language (SQL) table. The columns of the table represent the attributes of the metadata, with the logical name of the file as one of the attributes. The user may query the catalog to retrieve a set of logical names of files that match the selection criteria constructed as Boolean expressions involving the values of the metadata attributes – equivalent of SQL queries. In addition, the metadata system supports capturing the parent-child relationships between the metadata entries adding to the flexibility creating different views on the catalog and, consequently, allows the user to customize the interfaces for the data selection.

The data stored in the repository are meant to be consumed by the user applications (as input files). It is well known fact that hardly ever any two applications accept the data in the same format. It is thus imperative that the repository provides support for data transformations. The transformation can be simple such as format translations (e.g., the parameters of a stress-strain curve need to be formatted differently for ABACUS and LS-DYNA finite-analysis simulations) or may involve more complex processing such as performing model fits.

The repository is implemented as an aggregate of independent services: metadata service, replica locator, data storage and authorization service, and transformation services, all integrated using Apache's ServiceMix - an Open Source implementation of an Enterprise Service Bus compliant to the JBI specification.

Model of the Repository

Each entry in the repository (a file, a database record or other data item) is associated with a metadata record (a variable-length vector of attributes name-value pairs that describes the properties of the entry). The attributes capture the properties of the resource; both generic properties (such as ownership of the data, time of creation and data format) and application-specific, user-defined attributes that facilitate queries. The

details of that flexible metadata support that allows the evolution of the metadata schemas without risking loosing the integrity of the data is described elsewhere. Notably, the metadata records do not capture the physical location of the resources.

Each metadata record is uniquely identified by a uniform resource identifier (URI). The relationship between the metadata record URI and the uniform resource locator (URL) of the corresponding repository entry (or its replicas) are maintained by a replica locator. Consequently, the repository is implemented as three independent services: metadata service, replica-locator service, and storage services.

Creating the repository as an aggregate of three independent services, as shown in Figure 5, has clear advantages. The separation of concerns simplifies the implementation and enables reusing existing components, if required. For example, depending on the characteristics of the data sets to be maintained by the repository, the storage service can be implemented as a simple file system accessible through a secure file-transfer protocol such as gridFTP, or it can be implemented on top of a relational database system. If mass-storage and high-performance protocols are needed, a heavy-duty system such as SDSC Storage Resource Broker (SRB) can be used as the storage service instead. Other advantages, including the support for *ad-hoc* collaborations and creating different views are discussed below.

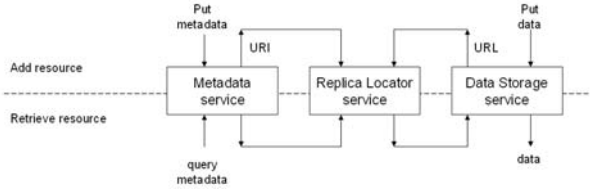

Figure 5. High-level model of the repository.

To add a data resource to the repository, the user puts a metadata record to the metadata service which returns URI of the resource and puts the file to the data storage which returns URL. The URI-URL pair is then put to the replica locator. To retrieve a data resource, the user queries the metadata repository to obtain the URI of the resource (or uses cached URI). The URI is resolved to URL by the replica locator. The URL is used to retrieve the corresponding data resource.

The repository is designed to facilitate *ad-hoc* collaborations that require sharing of restricted-access data between members of dynamically-created groups. To achieve this functionality, the repository must provide support for creating and managing groups of users and provide access-control mechanisms that allow or deny the access to data resources based on the user's membership in a group.

Support for *Ad-Hoc* Collaborations

The repository access-control mechanisms are based on privileges assigned to groups to perform specified operations on the entries. Each entry is associated with one or more groups by setting permission flags which specify permissions for the group members to perform operations on the resources. The user may be a member of a several groups, with each group having different privileges, that is, rights to perform specific operations on the same resource. For example, let the resource permission flags be set to grant members of group A read access to a file and deny members of group B privileges to the same file. To download the file from the repository, the user must prove that he or she belongs to group A; and, to delete the file from the repository, she must prove that she is a member of group B. If she is a member of both groups, she will be allowed to read and/or delete the file.

The current authorization frameworks are not applicable to a distributed repository where trust relationship between services is required, with one service providing authorization necessary for the next service. The solution adopted here extends the Virtual Organization Membership Service (VOMS) architecture. The authorization is group-based with Group Membership Authorization Service (GMAS) responsible for maintaining the user the membership in a group. Each user is authorized to create a new group and the group moderator (by default the creator) can add and remove group members. The user can then securely share data with the other members of the group in a distributed repository, as shown in Figure 6.

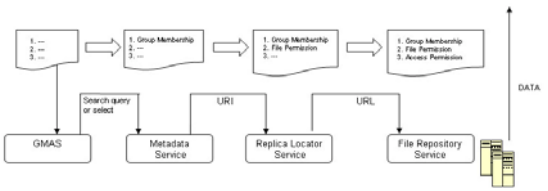

Figure 6. Starting with GMAS issuing a Security Access Markup Language (SAML) assertion about the user's membership in a group, and then collecting SAML assertions from the component services (Metadata and Replica Locator) the user assembles a complete assertion document that allows it to retrieve data from a data service.

Since the metadata service effectively acts as an index of all data entries anyway, it is natural that the resource permission flags are maintained as a part of the metadata record. It has an additional advantage of providing access control not only to the data entries but also to metadata records. Controlling the access to metadata is important since the metadata records may reveal too much information on the contents of the data and, in addition, the very existence of the data may be confidential.

Custom Views on the Repository Contents

The metadata catalog is conceptually implemented as a single "business" SQL table. The user may query the catalog to retrieve a set of logical names of files that match the selection criteria constructed as Boolean expressions involving the values of the metadata attributes – equivalent of SQL queries. In addition, the metadata system supports capturing the parent-child relationships between the metadata entries. Since the organization of the metadata is independent from the organization of the file repository, it is possible to create different views on the catalog and, consequently, allows the user to customize the interfaces for the data selection.

In particular, two categories of the interfaces can be created: folder-based and attribute based. Assume that the user is collecting data from an instrument measuring the mechanical properties of a material sample. The user may want to make several measurements, experimenting with different instrument settings, making measurements at different conditions (temperature, sample orientation, etc.), or using different samples of the same material. It is very likely that the user introduces some conventions for naming the resulting files and it might be convenient to organize the files in a tree of folders. To achieve that, the interface provides controls for creating and managing folders. However, the folders are "virtual". Instead, the metadata attributes are set to capture the intended parent-child relationship that can be displayed as a tree of files and folders making it easy for the user to find the results. Another user, however, might be interested is seeing all results for a given material obtained at a specific conditions, regardless of the who, when, and where of the measurement (subject to access control). In such a case, the attributes describing the parent-child relationship are simply ignored and a different tree is presented to the user. The data are sorted by materials, by sample types, by experiment types, etc., in the order specified by the user.

Data Service Facade

Construction of the repository from the independent services has many advantages. On the other hand, it is difficult for the end user (or the user agent) to use such a distributed system. Many conceptually-simple operations, such as retrieving a file, require making multiple requests to different services. The above mentioned flexibility of the system adds to the complexity of using the repository: the user must not only know the right order of service invocations, but also needs to know interfaces of the particular services and the communication protocols used by these services. Furthermore, since all services act independently from each other, maintaining repository consistency becomes difficult (e.g., each metadata record corresponds to at least one data resource and each data resource has associated metadata records).

To ease these difficulties, all constituent services of the repository are hidden from the user behind a facade which is the middle-tier service that orchestrates the services and exposing a simple, intuitive interface for the end user. Now, given the URI of the resource (from querying the metadata service or otherwise), there is a single method of the facade to retrieve the file. The invocation of this method results in all actions needed to get the authorization assertions, resolving URI to the

physical locations and returning the data stream. To achieve that, the facade employs the business delegate pattern that delegates the actual implementations of the back-end service clients to service providers which understand the transport and assertion requirements of the corresponding services. In addition, the provider-based architecture makes it easy to retarget the repository to a different implementation of any of the constituent services – it requires just replacing the service provider without the need for modifications of the facade interface. The business logic of the facade also enforces the integrity of the repository. For example, a request to remove a data resource from the storage automatically triggers appropriate actions of replica-locator and metadata services initiated by the facade.

Data Transformations

Hardly ever any two applications accept the data in the same format. It is thus imperative that the repository provides support for data transformations. There are two basic types of data transformations. One type facilitates relatively simple operations such as format translations or processing data headers that can be performed on-the-fly. The other type supports the processing of large files or making complex transformations. These transformations are delegated to high-performance platforms. The data transformations are independent from the metadata catalog or file repository services, and need to be implemented as independent services (the loose-coupling principle) and invoked either prior to the data uploading or after retrieving the data from the file repository, but before returning the data to the end user.

As proof-of-concept, several data transformations have been developed. Among the purposes of the material properties repository is the collection of data coming from measurement of stress-strain curves. The data coming from different instruments are, very expectably, in different formats. A transformation service hides these differences from the instrument operator who uploads the data to the repository. The service creates a metadata record by combining the information from the header automatically generated by the instrument from the system (e.g., time and the operator id), and the data typed in by the operator (the instrument has no way to know what material and in what manufacturing stage, e.g., after rolling or stamping, is being measured) and, then, from the measured values of the displacements and loads calculates the true stress and strain values. Once this "transformation" is complete, the metadata and data pair are uploaded to the repository. When retrieving the data from the repository, the user may specify the desired format, e.g., raw data, data formatted to match the syntax of the ABAQUS FEA package, or others. Such format translation is delegated to another transformation service that is invoked automatically after retrieving the data from the repository and before sending the data to the user. The National Aeronautics and Space Administration (NASA) Rapid Prototyping Capabilities project has different requirements. An example of a data transformation is the generation of a time series of selected observables for a selected geographical region. It involves retrieving a set of satellite images for the specified time period, re-projecting them so that an x-y pixel represents the same spatial location on each image, and then filtering out "noise" pixel (e.g., cloud cover), and finally filling the gaps resulting form the noise elimination by comparing images at adjacent time frames. These operations involve significant central processing unit (CPU) power and, since most of the procedure is embarrassingly parallel, it is desirable to perform it on a high-performance cluster.

Integration of Data Repository Services Using the ESB

The primary functionality of the service bus is routing messages between services associated with it. There are two base types of associations. The service can be plugged into the bus container as so-called service engine to be directly invoked through a Java message service (JMS). Alternatively, a service may be deployed in a separate container and be invoked through web-service interface (WSDL). The web service invocation is facilitated by a binding service bus component.

The incoming requests, generated by a web portal or a stand-alone client, are accepted by a custom-developed, hypertext transfer protocol (HTTP) input component. The input component effectively acts as a service broker forwarding the requests to the target services that generates the actual responses to the client requests. To make it possible, the client's request must provide a signature of the target service. In order to invoke the service (i.e., to forward the request) the signature must be resolved into the service endpoint reference (EPR). To this end, the broker uses a service directory--another custom service engine. The service signature is a collection of the service attributes. In the simplest case, it could be just the service name. The service WSDL interface could serve as the service signature; however, for this data repository, most of the transformation services implement the same WSDL interface making it easy to "bind" the actual transformation late, depending on the context of the request. The EPR may refer to an "atomic" service (either a service engine or a binding component) or refer to an orchestrating service (e.g., a Business Process Execution Language (BPEL) engine, or a service facade) that aggregates several services in order to generate the final response the client requested.

Architecture of the Repository

The architecture of the repository is shown in Figure 7. The clients, implemented as Java applets or stand-alone applications implemented in Java, Python, or otherwise, communicate with the ESB through HTTP/HTTPS. The Input Component/Service Broker accepts three types of requests: metadata query, data upload (that may or may not involve the data transformations), and data download (that may or may not involve the data transformations). The metadata query allows the user to search the metadata catalog to locate the data set of interest, create custom views on the data repository, as well as uploading and downloading of data are orchestrated by the data-repository facade, as described above. Consequently, the client requests to perform these operations are simply forwarded by the service broker to the façade service engine. The data facade invokes the constituent service services as needed through the binding components.

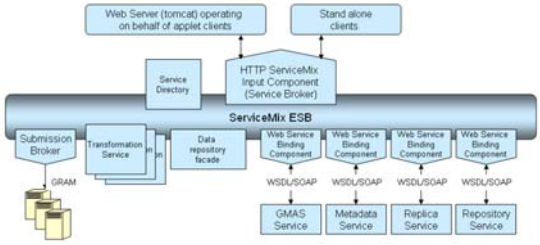

Figure 7. Architecture of the data repository integrated by ESB.

The data transformations, on the other hand, are bound dynamically. If the repository operation requires a transformation, the name of the transformation is passed as the request argument. The broker resolves the transformation name into the service EPR using the service directory, and invokes the service before or after invoking the data-facade services, depending whether data are uploaded to or downloaded from the repository, respectively. Simple transformations are implemented as ESB service engines, while complex transformations are executed by the submission broker – a binding ESB component. The submission broker is responsible for setting the run-time environment (setting the environmental variable, creating a working directory, etc.), staging in data, executing and monitoring jobs on remote systems, and finally passing the results to the requested destination (typically through a third-party data transfer). Since all transformations implement the same WSDL interface (the transformation-specific parameters are grouped as a single array of strings), the dynamic binding allows seamless adding or replacing existing transformations.

Summary and Future Work

The system has been internally deployed at MSST as is subjected to test users. The feedback from the early users will guide us in improvements of the User Interfaces, improvements in the system functionality, and hardening the implementation. Once tested and validated, it will serve the ICME Mg project. In addition, we plan adding new transformations for extracting more material properties including optical properties.

Support for Design Optimizations

Simulation-Based Design Optimizations

Simulation-based design optimization is playing an increasingly important role in engineering-product development. It enables engineers to make optimal product design and manufacturing-process decisions, reduce or eliminate the need for physical prototyping, and increase the quality of manufactured products. This importance is also evident in the development and marketing of several commercial optimization software tools (e.g., DOT, iSIGHT) that can be interfaced with computer-aided design/computer-aided engineering (CAD/CAE) and engineering simulation programs to accommodate a paperless product-design activity.

The rapid development of computer technology and commercial simulation tools has enabled engineers to solve more complex problems and obtain more details to enhance knowledge. For example, it is now possible to perform full-scale, finite-element (FE) simulations of vehicle crashes with commercial FE codes and parallel computers. However, the increased complexity has significantly increased the computational cost that, in turn, prevents engineers from combining the simulation tool with an optimization method, which is an iterative procedure and requires hundreds or even thousands of simulations to perform one design. To alleviate the high computational cost of full-scale simulations, yet maintain the level of complexity, the metamodeling approach has been widely adopted in simulation-based design optimization.

In the metamodeling approach, the expensive simulation tool is replaced with a surrogate approximation model (metamodel) that is in explicit form and efficient to evaluate. The metamodel is created from the results of some predefined simulations determined by DoE methods. Figure 8 illustrates the procedure of simulation-based design optimization using DoE and metamodeling. There are four major components in this procedure: DoE, simulation, metamodeling, and optimization--which serve as four independent functional blocks.

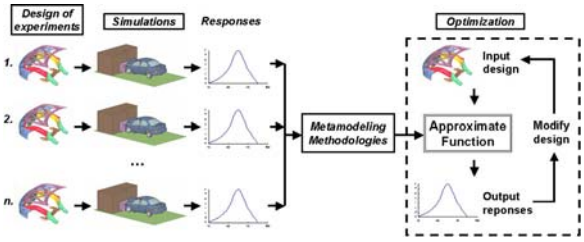

Figure 8. Workflow for simulation-based optimization using DoE and metamodeling.

Since a limited number of simulations are used in creating the metamodel, the model accuracy will depend on how well the selected designs represent the design space. To this end, the DoE methods such as factorial design, central composite design, Taguchi orthogonal array, and Latin hypercube sampling, are typically used to create the samples and referred to as the response surface methodology (RSM). For high-order, nonlinear responses, other metamodeling methods using high-order, nonlinear functions, particularly the radial basis functions (RBF), work best.

With the created metamodels representing responses within the design space, the optimization can be carried out using existing optimization methods such as gradient-based or direct-search algorithms. As pointed out by the no-free-lunch theory, there is no single optimization method that is good for all types of problems. Therefore, it is preferred to apply different optimization methods at this stage to obtain the best solution.

The Need for Cyberinfrastructure

The complexity of the new generation of simulation codes demands the employment of high-performance computing platforms, even when employing the metamodeling approach. However, the reduction of the computational costs down to an affordable amount is achieved at the price of a very tedious and error-prone manual effort by the designer to submit, monitor and coordinate hundreds of jobs in heterogeneous, distributed environments. Performing simulation-based optimization is not only a time consuming but it also requires the designer to learn the arcana of ever-changing information-technologies (IT) such as operating systems, batch systems, storage systems, networking, and security. To reduce the time and cost associated with the design, it is thus

imperative to provide a cyberinfrastructure that effectively and efficiently manages high-performance computing resources. Furthermore, the infrastructure should provide mechanisms of resource discovery (hardware, software and data) and seamlessly integrate simulation programs (including multiscale simulations), CAD/CAE tools and various functional components such as DoE, metamodeling, and design optimization.

Functional Requirements

Figure 9 summarizes the required minimum functionality of the system needed to automate the optimization process. Conceptually, the system comprises three major components: a GUI, execution environment, and data repositories.

The GUI provides means for defining the optimization problem and specifying the optimization workflow. The GUI also embeds clients to a grid infrastructure that provides access to grid resources including remote-data repositories (such as product geometries and material properties) and execution environment for submitting, controlling, and monitoring the workflow.

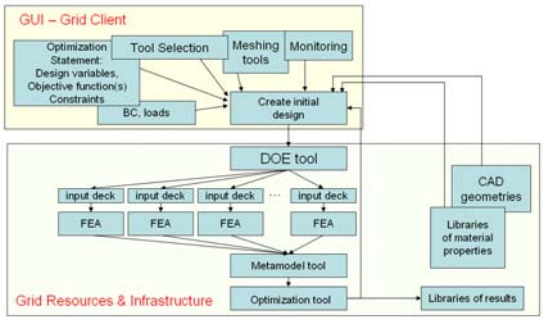

Figure 9. Functionality of the simulation-based optimization system.

Defining the Optimization Process

The starting point for the design optimization process is the specification of the initial design. This involves the creation of the geometry of the initial design (usually imported from CAD), specification of material properties (taken from the material properties databases), as well as the definition of boundary conditions, loads, and constraints. The optimization problem is then defined by a vector of design variables $\mathbf{x}$, one or more objective functions $f(\mathbf{x})$ and set of constraints $g(\mathbf{x}) \leq 0$, $h(\mathbf{x}) = 0$.

To solve the stated problem, computational tools needs to be selected. The first tool to be selected is a simulation code to perform FEA. There are many commercial packages available for that purpose such as ABAQUS, LS-DYNA, or PAM-CRASH, each optimized for a particular class of problems. Once the FEA tool is selected, the initial design must be expressed in terms of an input deck formatted for the selected tool.

To finish setting up the optimization workflow, the DoE tool, the metamodeling tool, and optimization tool need to be selected. Typically, each such tool requires the selection of a particular method and its parameters.

For design optimizations of complex systems, it is vital to provide the capability of selecting the best tool (or the best method) for the problem at hand, including a support for "plugging in" new tools as needed. Such flexibility can be achieved by using the horizontal integration approach, as opposed to vertical stovepipes. Horizontal integration means the adoption of uniform management interfaces so that the large numbers of resources (such as software and hardware), distributed over what used to be distinct silos, can be allocated, used, monitored, and managed in a common and automated manner.

Optimization Process Workflow

Once the optimization process is defined, it is submitted for execution. The DoE module generates sets of values of the design variables that are used for automatic generation of FEA input decks, one for each set of design variables' values. The input decks are then staged at remote computational servers and used to run the FEA analysis. Since there are no data dependencies between different FEA runs, all of them can be run concurrently if enough computational resources are available. Once all instances of the simulation code are completed, their outputs are parsed to extract the value of the responses which, in turn, are used to create the metamodel that is the input for the optimization module.

To increase the engineer's productivity, it is imperative that, once the optimization problem is interactively defined through the GUI, the optimization workflow runs asynchronously, automatically and autonomously. It should run asynchronously to let the engineer perform other tasks while waiting for the optimization results, as simulating complex systems can take hours or days to complete. The workflow can be asynchronous only if the complete process is automated (generation of input data sets for all software components in the workflow, setting the run environment, staging files in and out, generation of batch scripts, allocating the resources, etc.), and autonomous (self-optimizing, adapting to changes in the resource availability and capable of recovering from failures).

Cyberinfrastructure

The design-optimization process requires horizontal software integration with loosely-coupled components. The loose coupling is enabled by web services or any service-oriented architecture (SOA), such as Open Grid Services Architecture (OGSA) - based grid infrastructure. Loosely-coupled services, even if they use incompatible system technologies, can be joined together on demand to create composite services; however, participants must establish a shared semantic framework to ensure messages retain a consistent meaning across participating services. Furthermore, the grid infrastructure establishes a separation between the service provider and the consumer and provides the ability to negotiate a desired quality of service from the provider. All these properties are needed for asynchronous and autonomous execution, making the grid infrastructure a good choice for the implementation of the cyberinfrastructure for the optimization workflow. The architecture of the system is shown in Figure 10.

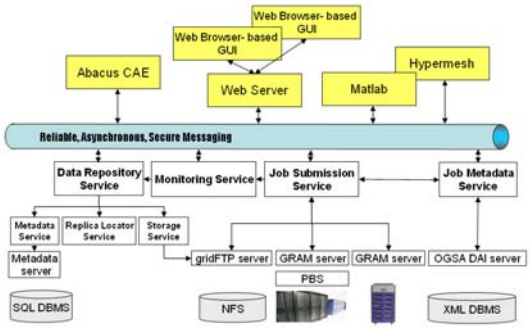

Figure 10. Cyberinfrastructure for horizontal integration.

Horizontal Integration

The first step towards horizontal integration is the decoupling of the user applications, such as design-optimization process, from the hardware. A workload manager would use common grid infrastructure mechanisms (OGSA services) to discover available resources and deploy application components onto these resources. As load increases, new resources could be automatically (and temporarily) allocated to, and used by, the application. In other words, the grid resources—compute servers, file systems, databases—need to be provisioned on demand by making them available as services. Following the loose-coupling strategy, it is not important what technology is used to implement these services. The system described here employs GRAM, OGSA-DAI, and gridFTP services included in Globus Toolkit 4 (GT4), and WSDL-based (Axis) Metadata Service developed at MSST and described in detail elsewhere. The rationale for this particular choice is the ease of availability. The GRAM service provides access to the remote compute servers (or resource-management systems such as PBS), gridFTP is used for file transfers effectively providing access to remote file systems, while OGSA-DAI and the Metadata Service provide access to remote databases.

The next layer of the infrastructure supporting horizontal integration comprises services for deploying application components onto selected resources, job monitoring and data access. Higher-level services, including resource discovery, brokerage, workflow enacting, adaptive scheduling and self-management, belong here, too. They will be added in the forthcoming phase

of this project; at present, this functionality is delegated to the clients.

Job Submission

Deploying application components onto computational resources is the responsibility of the Job Submission Service (JSS). The needed flexibility for submitting a particular application component on a selected hardware is achieved by employing a Job Descriptor (JD). The descriptor is an XML document that provides a "recipe" on how to run the component on target machines where the component is installed. The JSDL-like schema captures all information necessary to automatically generate a run script, a batch script, and/or Globus GRAM RSL string.

The JDs for all the application components needed for the design optimization process are maintained in an XML database deployed as a Grid Service (OGSA-DAI), referred to as Job Metadata Service (JMS). Each application component, such as FEA code, is uniquely identified by a URI. The URI for the selected component can be obtained from the Job Metadata Service itself by querying the database by application name and/or other application signature attributes.

The support for the selection of the tools is implemented by embedding the Job Metadata Service client in the GUI and hiding the syntax for queries from the end user. Adding new tools to the system is simply a matter of adding new JDs to the repository, assuming that the code is already installed, and that the user has authorization to use those systems.

To submit a job, the client needs to retrieve the corresponding JD from the Job Metadata Service and customize it for a particular run. This involves the selection of the target system from the list embedded in the JD itself and replacing the default values of job attributes (such as location of the input deck and other data files) by the actual ones. The updated JD is then sent as a payload of the request to the JSS. The JSS parses the JD and follows the recipe it contains. Typically, these are the operations that need to be performed: staging the input files (using gridFTP); if necessary, creation and staging execution scripts; creating the run environment (such as creating a working directory for the job); creating the RSL string; submitting the job request to the Globus GRAM server; creating a job entry in the job database (explained in the Job Monitoring section below); and, finally, registering itself for GRAM notifications. As the job executes, JSS forwards the notifications to the JMS, and when the job completes, it stages it out to the location prescribed in the JD using gridFTP.

The customization of a JD can be performed in separate steps (with a JD file passed from one service to another). For example, the location of the input files for FEA can be provided by the input deck creation tool, while the selection of the target system can be determined by a resource scheduler. The former creates a new input desk for each set of design variables' values as returned by the DoE module, and the scheduler is responsible for selecting resources so that all FEA simulations complete roughly at the same time. Such separation of concerns is an important element of the horizontal integration and the reusability of services. The DoE is independent of the choice of the FEA tool, input deck is FEA-specific (e.g., an ABAQUS input is formatted differently than LS-DYNA one), and the scheduler is a generic Grid service. In the current implementation, however, the customization of the JD is performed by the JSS client embedded in the GUI. This will change in the next release of the system.

Job Monitoring

All jobs submitted within the optimization process are run asynchronously and, therefore, there is a need to monitor their status. Resource Management Systems, such as PBS, provide this functionality for all pending and executing jobs. However, once the job completes, the information about it disappears. To remedy this, an independent Job Monitoring Service (JMS) is provided that persistently maintains information on all submitted jobs in a database. The job entry in the database is kept until the user explicitly deletes it.

Results produced by individual jobs are used to create a metamodel and, therefore, they are not of

direct interest for the user – as long as the optimization process proceeds as expected. If a failure should occur (for example, the FEA analysis produces results different than anticipated), the user must be provided with the means to identify the problem. Therefore, the JSS provides not only the information on the current status of the job (pending, running, completed) but also the complete provenance of the job (input deck, run scripts, etc.), and it provides the access to its output files. For example, the ASCII log file can be opened at the user workstation without the user explicitly transferring it, and binary data files can be downloaded for analysis using ABAQUS CAE by a single mouse click.

The JMS, which is a WSDL-based grid service, uses the data service (described below) to maintain the information about the jobs. The changes in job status reported by the GRAM server are forwarded to JMS by the JSS. File transfers, if requested by the user, are seamlessly made using gridFTP.

Data

The data, in particular input and output data sets that needs to be examined or shared between the users, are maintained by the data service (described in details elsewhere), composed of three independent services: Metadata Service, Replica Locator Service and Storage Service. The metadata (an XML-encoded, variable-length vector of attribute name-value pairs) allows for efficient queries and generation of multiple views on the data collections to fit the user's needs, regardless how the files are actually stored. It is implemented on top of J2EE and SQL Database Management System (DBMS). The storage service uses a Unix file system with gridFTP for file transfers. The replica locator provides the mapping between the logical file name (URI) and the physical file (URL). The Data Service is a WSDL service that act as a facade orchestrating the three constituent services.

GUI

The user interactions with the system logically split into two independent subjects:

- the specification of the optimization process, including the selection of the tools (DoE, FEA, metamodeling and optimizations) together with capabilities for monitoring of the process status, and
- the specification of the initial design, including the product's geometry and its discretization, materials, loads, and constraints.

The process definition and monitoring requires embedding clients of the grid services, as described in Section "Horizontal Integration" above. Many different technologies can be used to develop this part of the user interface, e.g., a Java applet or extensions to existing stand-alone applications such as MathWorks' MATLAB™.

On the other hand, there are many state-of-the-art commercial and community tools available for specifying the initial design, such as Hypermesh, or vendor-provided GUIs for specific FEA packages, such as ABAQUS CAE™.

Since for the first demonstration problems an Abaqus input deck needs to be generated, it is natural to extend the ABAQUS CAE as the complete, stand-alone GUI for specifying the product design-optimization process. ABAQUS CAE interface has an open architecture with a published application program interface (API), and it is implemented in Python.

Thanks to the open architecture, ABAQUS CAE can be extended by providing new GUI elements and modules in Python, including modules that act as Grid services' clients. A similar approach – embedding the Grid clients into an existing standalone application – can be applied to other products used in the engineering practice, notably MATLAB.

The extensions needed to adopt the ABAQUS CAE as the GUI fall into two categories: GUI components and modules. The new GUI components, invoked through extensions to the existing menus, include forms to specify definition of design variables, constraints and objective functions as well as setting the parameters of DoE, metamodeling and optimization modules. Other GUI components allow control of the JSSs and display the status of all remotely run jobs.

In addition to new GUI element, six new modules have been added:

1. ABAQUS **input deck parser**. The initial product design is created using ABAQUS CAE tools, and the process results in generating the ABAQUS input deck that drives the FEA analysis of that initial design. The parsers extract variables defined in the input deck. This information is used for selecting the design variables (not all variables needed to simulate the design are subject to the optimization process), define objective functions and constraints (these are typically functions of the design variables).
2. **DoE module** does not require much CPU and, therefore, can be run inside the ABAQUS CAE environment. It is adopted from the HIPPO package (an Object-Oriented Framework for General Purpose Design Optimization by H. Wang) by rewriting it in Python.
3. **Input deck generator** replaces the value of design variables specified in the initial design by those generated by the DoE module.
4. **Metamodel creator**, using the native ABAQUS CAE Python libraries, parses the outputs of Abacus FEA simulations to extract the responses and creates the input data set to create the metamodel by launching a separate process outside the ABAQUS CAE environment.
5. **JSS client** delegates computations to remote, high-performance computers (including all necessary file transfers)
6. **JMS client** accesses the status of remotely-executed jobs.

Summary and Future Work

The developed cyberinfrastructure comprises a collection of Grid services that automates creation, submission and monitoring of jobs. In addition, support is provided for accessing information needed to identify the reasons of failures, should any occur. The front end of the system extends the commercial tool (ABAQUS CAE), that is, it augments the state-of-art user graphical interface for defining a FEA problem with GUI components for specifying the optimization problem and providing access to remote resources. The access to remote resources is achieved by embedding clients of grid services in the ABAQUS CAE. The next phases of the project include integrating this infrastructure with FAME and thorough test and validation of the system.

Support for Multiscale Simulations

We have developed an overlay scheduler to manage an adaptive tree of processes spawned while performing multiscale simulations. Further development of the support for multiscale simulations has been postponed. The concurrent developments of multiple system components jeopardize timely completion of the tasks, and the multiscale simulations are the least mature for automation and integration (as opposed to repository of material properties and support for design optimizations).

Portal for the Virtual Organization

The USAMP ICME for Mg international pilot project redefined our initial requirements for creation of the Virtual Organization. The new requirements call for the deployment of a collaborative portal based on Microsoft's' SharePoint server. This portal will enable sharing documents and management of the tasks and projects between the participants of the ICME Mg project. In the next step, the support for sharing data will be added and, finally, all capabilities of the cyberinfrastructure under development at MSST will be made available through this portal.

Conclusions

The creation of the cyberinfrastructure is on schedule, in spite of changes in the requirements. Of particular importance is the establishment of tight connections between this project and the ICME Mg project.

Presentations/Publications/Patents

1. T. Haupt, "Cyberinfrastructure for multiscale Simulations", *2007 TMS Annual Meeting*, Orlando, FL, Feb 25-March 1, 2007.
2. T. Haupt, A. Voruganti, A. Kalyanasundaram, I Zhuk. "Grid-Based System for Product Design Optimization", *2nd IEEE International Conference on e-Science and*

Grid Computing, Amsterdam, the Netherlands.
3. T. Haupt, A. Kalyanasundaram, I. Zhuk "Architecture for a Secure Distributed Repository", *7th IEEE/ACM International Conference on Grid Computing*, Barcelona, Spain: IEEE/ACM Press, 170-177.
4. T. Haupt, A. Kalyanasundaram, G. Singh, I. Zhuk, "Data Repository for Ad-Hoc Collaborations Horizontally Integrated with Transformation Services", *The 2007 International Conference on Grid Computing and Applications,* Las Vegas, NV, June 25-28, 2007.

7. LOW-COST CARBON FIBER

A. Low-Cost Carbon Fiber from Renewable Resources

Project Contact: F. S. Baker, N. C. Gallego, A. K. Naskar, D. A. Baker
Oak Ridge National Laboratory (ORNL)
P.O. Box 2008
Oak Ridge, TN 37831-6087
(865) 241-1127; fax: (865) 576-8424; e-mail: bakerfs@ornl.gov

Technology Area Development Manager: Joseph A. Carpenter
(202) 586-1022; fax: (202) 586-1600; e-mail: joseph.carpenter@ee.doe.gov

Expert Technical Monitor: Philip S. Sklad
(865) 574-5069; fax: (865) 574-6098; e-mail: skladps@ornl.gov

---

Contractor: ORNL
Contract No.: DE-AC05-00OR22725

Objective

- Carbon-fiber resin composite materials could substantially reduce the weight of passenger vehicles, increase vehicle fuel economy, and result in lower CO_2 emissions. Carbon fiber have the potential for substantial weight saving in vehicles because of their remarkable high strength, high modulus, and low density; each 10% reduction in vehicle weight would translate into an increase in vehicle fuel economy of about 6%, with concomitant reduction in emissions. To place the potential increase in fuel economy into perspective, body-in-white (BIW) modeling indicates that over 60% of the steel in a vehicle could be replaced with carbon-fiber composite materials without impacting vehicle crashworthiness. However, carbon-fiber is currently too expensive for large-scale automotive use, which necessitates a large reduction in cost of appropriate-strength fiber from about $20/lb to about $5/lb. The cost of the precursor material currently accounts for about 50% of the cost of manufacturing carbon fibers and, therefore, emphasis in the ORNL research work is being placed on the development of processes utilizing low-cost precursor materials, notably textile-grade polyacrylonitrile (PAN) and lignin, a renewable resource material. The goal of this project is to identify at least one precursor formulation, comprising both renewable and recycled materials, which could be used to produce industrial-grade carbon fiber at a cost in the range of $3-5 per pound. In addition to precursor, cost savings will also be achieved through advanced processing techniques, including plasma oxidation (see 7.D), carbonization (see 7.E) and graphitization of the precursor fiber, to obtain more efficient utilization of energy resources.

Approach

- Derive the fundamental data required to establish melt-spinning conditions for the continuous production of lignin-based carbon fiber meeting target properties.
- Using research and pilot-scale carbon-fiber production lines, construct the technical database necessary to facilitate commercial production of lignin-based carbon fiber, including knowledge in the following respects:
  - Isolation and purification of lignin to obtain appropriate precursor properties for carbon-fiber production.
  - Melt-spinning technology, including extruder and spinneret configuration, spinning conditions, co-polymers, and plasticizing agents.
  - Thermal processing of precursor fiber into carbon fiber.
  - Advanced processing of lignin-based carbon fiber.
  - Mechanical properties of lignin-based carbon fibers.
  - Surface treatment and sizing technology for relevant resin systems.

  - Economics of lignin purification and processing of precursor fiber into finished carbon fiber.
- Development of intellectual property for the production of lignin-based carbon fibers.

Accomplishments

- Proof-of-concept demonstration of the melt-spinning of lignin precursor fiber, utilizing lignin materials isolated from the Kraft chemical pulping of hardwood (for paper production) and the Organosolv pulping of hardwood (for lignin production), respectively.
- Proof-of-concept demonstration of the thermal processing of lignin-based precursor fiber into carbon fiber.
- Demonstration of melt-spinning of 28-filament lignin fiber tow from Kraft hardwood lignin (in collaboration with the University of Tennessee); melt-spinning not sustainable for any significant length of time because of impurities in the lignin.
- Development of a laboratory-scale procedure for purification of Kraft hardwood lignin to target specifications; production of 14 lb of purified lignin for melt-spinning studies through repetitive lab-scale runs.
- Proof-of-concept demonstration of melt-spinning of purified Kraft hardwood lignin fiber using polyethylene terephthalate (PET) as a copolymer to plasticize the purified lignin.
- Demonstration of the lab-scale production of (single) carbon fiber meeting 60% of the target engineering properties; thermal processing temperature limited to maximum 1200°C, too low for structure development.
- Development and demonstration of a scaleable procedure for purifying Kraft hardwood lignin to target specifications using an organic solvent-extraction approach; production of multi-kg batches of the purified lignin for melt-spinning studies.
- Construction, installation, and commissioning of custom-designed, multifilament melt-spinning equipment in ORNL research facility for low-cost carbon-fiber (LCCF) research.
- Demonstration of continuous melt-spinning and winding of 12-filament tow from the solvent-extracted lignin (SEL) over a sustained period of time (5 hours) without interruption; establishment of the relationship between winding speed (drawdown ratio) and filament diameter; demonstration of production of 10-micron-diameter, defect-free, lignin precursor fiber; spinning of target-diameter fiber at almost 70% of the preliminary target speed of 600 meters/minute.
- Proof-of-concept demonstration of cross-linking (stabilization) of SEL fiber through ultraviolet (UV)-irradiation at ambient temperature.

Future Direction

- Development of a technically- and economically-viable process for the commercial production of industrial-quality carbon fiber from lignin feedstock. Key tasks will include:
  - Identification of sources of lignin suitable for carbon-fiber production and establishment of conditions for purification of lignin to the desired specifications (as needed for specific sources of lignin).
  - Procurement of a large batch (100 lb +) of purified lignin from at least one source for carbon-fiber process development work.
  - Selection of appropriate copolymers and/or plasticizing agents as needed to facilitate melt-spinning of precursor fibers from specific sources of lignin.
  - Design of extruder and spinneret die to obtain high spinning speed of target-diameter fiber with good internal structure.
  - Development of techniques for spooling and rewinding of lignin-based precursor fiber tow.
  - Establishment of conditions for continuous melt-spinning of lignin fiber tow at speeds of at least twice the preliminary target of 600 meter/minute.
  - Establishment of conditions for batch-scale thermal processing of lignin-based precursor fiber into carbon fiber meeting target engineering properties

  - Establishment of conditions for continuous thermal processing of lignin-based precursor fiber tow into carbon fiber.
  - Identification of methods for surface treatment of lignin-based carbon fibers to enhance compatibility with relevant resin systems.
  - Production of a suitable quantity of finished, lignin-based carbon fiber for composite testing by the Automotive Composites Consortium (ACC).
- Collaboration with industrial, government, and academic partners to:
  - Clearly establish sources of lignin suitable for carbon-fiber production, including lignin derived from the production of ethanol fuel from biomass resources; e.g., waste wood and switchgrass.
  - Resolve any outstanding issues regarding the isolation and purification of lignin from different sources.
  - Address knowledge gaps with respect to the use of recycled polymers as alloying agents for melt-spinning of lignin-based precursor fibers.
  - Complete identification of melt-spinning conditions and fiber-winding technology for continuous production of lignin-based precursor fiber tow.
  - Demonstrate carbon-fiber production from lignin-based, multifilament tow using a pilot-scale process line.
  - Achieve target engineering properties of lignin-based composite materials incorporating lignin-based carbon fibers (with the ACC).
  - License and transfer lignin-based carbon-fiber production technology to industry.

Introduction

The Department of Energy (DOE) FreedomCAR-funded work at ORNL is directed to the development of processes for the low-cost production of carbon fibers, including the use of advanced processing techniques such as plasma oxidation, carbonization, and 'graphitization' of the precursor fiber. The objective of the FreedomCAR project is to develop more energy-efficient, cost-effective processes for production of carbon fibers for use in composite materials for vehicles, which would substantially reduce vehicle weight, increase vehicle fuel economy, and result in lower CO2 emissions. For example, each 10% reduction in vehicle weight would translate into an increase in vehicle fuel economy of about 6%, with concomitant reduction in emissions. Carbon fibers have the potential for substantial weight saving in vehicles because of their remarkable high strength, high modulus, and low density.

To place the potential increase in fuel economy into perspective, BIW modeling indicates that over 60% of the steel in a vehicle could be replaced with carbon-fiber composite materials without impacting vehicle crashworthiness. However, carbon fiber is currently too expensive for large-scale automotive use, which necessitates a large reduction in cost of appropriate-strength fiber from about $20/lb to about $5/lb, and the supply is far too limited to meet the projected demand for automotive use. The cost of the precursor material currently accounts for about 50% of the cost of manufacturing carbon fibers; therefore, emphasis in the ORNL research work is being placed on the development of processes utilizing low-cost precursor materials, notably textile-grade PAN and lignin, a renewable resource material.

Lignin has a significant potential cost advantage over even textile-grade PAN as a precursor material for low-cost carbon-fiber production. Whereas the cost of PAN is almost directly proportional to the cost of oil, the cost of lignin is largely independent of oil price, and essentially is based on its fuel value of about 5¢/lb. On the downside, however, relatively little is known about how to transform lignin into a carbon fiber. Furthermore, as currently isolated from the chemical pulping of wood for paper production (using either the Kraft or soda processes), the lignin by-product is not suitable for carbon-fiber production and requires purification before it can be properly used for this purpose, which increases its cost but not prohibitively.

Currently, chemical pulping of wood is the only immediate source of lignin in the USA, but as

biomass refineries come on-stream, the lignin by-product from cellulosic ethanol fuel production will represent a valuable resource material for carbon-fiber production. Work on biomass lignins produced from the Oganosolv pulping of wood, the first step in cellulosic ethanol production, has already demonstrated that such lignins are readily melt-spinnable as isolated and are of a much higher purity level than lignins derived from the chemical pulping of wood for paper production.

Lignin is one of the main components of all vascular plants and the second most abundant polymer in nature (after cellulose). It is an amorphous, polyphenolic material arising from the enzymatic dehydrogenative polymerization of three phenyl propanoid monomers, namely, coniferyl alcohol, sinapyl alcohol, and *p*-coumaryl alcohol. The biosynthesis process leads to the formation of a complex, three-dimensional polymer that lacks the ordered, repeating units found in other natural polymers such as cellulose and proteins. Lignin plays a significant role in the carbon cycle, sequestering atmospheric carbon into the living tissues of woody perennial plants. It fills the spaces in the cell wall between cellulose, hemicellulose, and pectin components of wood. It is covalently bound to hemicellulose and thereby crosslinks different plant polysaccharides, conferring mechanical strength to the cell wall and thereby to the plant as a whole.

An example of the complex structure of lignin is shown in Figure 1 for lignin isolated from beech hardwood. Hardwood lignin is composed of coniferyl alcohol and sinapyl alcohol units in varying ratios, whereas softwood lignin predominantly comprises coniferyl alcohol (> 90%) and a small proportion of *p*-coumaryl alcohol. Because it is almost impossible, certainly very difficult, to isolate lignin from wood without degradation, the true molecular weight of native lignin is a subject of debate. However, the weight-average molecular weight of softwood lignin isolated by mechanical milling of the wood (low-degradation process) is about 20,000. Milled hardwood lignin exhibits significantly lower molecular weights. These and other differences between the chemistries of hardwood and softwood lignins influence the utilization of lignin for carbon-fiber production.

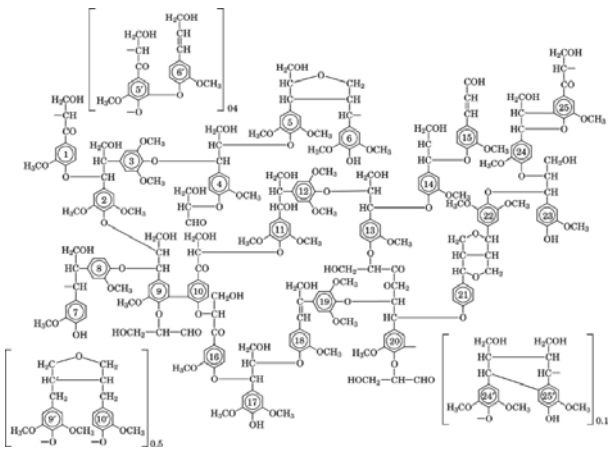

H. H. Nimz, *Angew. Chem. Int. Ed.*, **13**, 313 (1974)

Figure 1. Chemical structure of hardwood lignin.

Depending on species, lignin comprises about 15-25 wt% of wood, compared to about 38-48 wt% cellulose (on a dry-wood basis); switchgrass has a similar content of lignin. Thus, wood and switchgrass contain significant amounts of lignin (about half of the proportion of cellulose), which if utilized for the production of value-added products, such as carbon-fiber, could effectively offset the high cost of producing cellulosic ethanol from biomass (a relatively small proportion of the lignin would be used as a fuel in the ethanol-production process). Furthermore, utilization of the lignin by-product for carbon-fiber production (and other value-added chemicals) would result in real benefits in the contexts of increased energy efficiency, reduced environmental pollution, and enhancement of national security interests (e.g., reducing dependence on imported fossil fuels).

Worldwide, over 200 million metric tons of lignin passes through pulp mills annually, of which about 1.2 million tons are isolated for the production of lignin-based products. Lignin is not a waste product of the pulp-and-paper industry, but a co-product that is utilized in modern, highly-integrated pulping operations as a fuel (and reducing agent) in the pulping chemicals recovery process (it has about 70% of the calorific value of #2 fuel oil). In fact, many modern mills have co-generation facilities to produce electrical energy for sale to utility companies.

Lignin is already utilized in transportation applications on a large scale, for example, as

emulsifying agents for asphalt road surfaces. Similarly, it is used as a dispersing agent for cement and concrete mixes, much of which is utilized in the construction of roads. Lignin is used as an "expander" (of active species surface area) in the negative plates of lead-acid batteries, the large majority of which are used for starting, lighting, and engine ignition (SLI) functions on vehicles. Lignin derivatives are used as economical adhesives for carbon black, 70% of the world production of which is used in the compounding of rubber for vehicle tires. Other large-scale uses include textile dye dispersants; oil-drilling muds; pesticide surfactants; sequestrants for micronutrients (agricultural and forestry uses); water treatment for boilers and cooling systems; and binders for plywood, particle board, fiberglass insulation, and animal feed.

Use of Lignin for LCCF Production

The majority (> 90%) of carbon fiber is currently produced from PAN precursor fiber, which is made using a wet (solvent-based) process. This first unit operation of carbon-fiber production is one of the most intensive operations of the overall process, involving many stages of washing to remove residual traces of solvent which would otherwise adversely impact carbon-fiber properties, especially of the high-end and expensive-grade fibers for aerospace applications (upwards of $150/lb). The associated solvent-recovery and purification operations also add to the complexity and cost of PAN precursor fiber production. Melt-spinning of a precursor fiber is much preferred over the wet-spinning process, but currently is only utilized in the spinning of pitch-based carbon-fibers, which account for a relatively small proportion of worldwide carbon-fiber production. PAN cannot be melt spun, at least as formulated to achieve the engineering requirements of PAN-based carbon-fibers, because it rapidly decomposes close to its melting point.

Certain types of lignin, notably hardwood-derived, can be melt-spun providing that the contaminants in lignin isolated from the "black liquor" in chemical pulping operations can be substantially reduced to acceptable levels. Impurities include non-melting particulates (clays and sand, which block the very fine holes in the spinneret), inorganic salts (e.g., sodium sulfate), rosin, and residual carbohydrates (both in the form of fibers and bound to the lignin). The contaminated hardwood lignin could be melt- spun in principle, but the spinning operation could not be maintained for any useful length of time to produce continuous fibers before the spinneret was blocked. Also, the contaminants in the spun fibers degrade the engineering properties of the carbon-fiber subsequently produced from the small quantities of lignin fiber. Nevertheless, the demonstration that even single carbon fibers could be produced from lignin was an encouraging development and represented a milestone achievement in the project.

A dedicated effort in earlier carbon-fiber project work at ORNL led to the development of laboratory-scale techniques to purify Kraft lignins to the targeted levels. Ironically, purification of the lignin, notably hardwood lignin, rendered the lignin non-melt-spinnable because the melting point of the lignin was raised above its decomposition temperature. Chemically-pulped lignin is a heterogeneous material that includes a wide range of molecular weights, etc., and it is the presence of some of the lowest molecular weight fractions that appears to impart melt-spinnability to the hardwood lignin as a whole. Unfortunately, the lower molecular weight lignin fractions, which in essence serve as plasticizing or alloying agents for the higher molecular weight fractions, were selectively removed during the purification process.

Thus, solutions to this unexpected challenge had to be found, which included the development of alternative methods of purifying the lignin to retain its desirable properties for melt-spinning. This was tackled on several fronts, including the funding of fundamental work at Pacific Northwest National Laboratory (PNNL) and the collaborative efforts of several large paper manufacturers, notably MeadWestvaco (MWV, Charleston, SC), the only current producer of Kraft lignin-based products worldwide. At the same time, work was also implemented to identify suitable plasticizing agents for purified lignins, including softwood lignin that, because of its chemistry, is not readily melt-spinnable. These efforts led to the development of a radically different process for purifying lignins, both hardwood and softwood and, more significantly, the first demonstration (in fiscal year [FY] 2007) of continuous and

uninterrupted spinning of multi-filament lignin fiber 'tow' over a period of many hours.

To support the efforts on the lignin-based carbon-fiber project, melt-spinning equipment was custom designed and built for the project, and installed at ORNL. The equipment, shown in Figure 2, is the main workhorse for establishing appropriate process conditions for melt-spinning of lignin fiber tows and for producing precursor fiber for thermal processing into carbon-fiber. The equipment includes a draw frame which permits fibers to be tensioned and hot-stretched through a series of rollers to both obtain the desired filament diameter and to help align the molecular structure of the precursor fiber to facilitate development of the desired engineering properties during the subsequent processing to carbon fiber.

Before attempts are made to melt-spin a lignin material on this equipment, however, it is characterized with respect to its rheological properties, most notably its viscosity and thermal stability at temperatures close to its melting point (above and below). Thermal-analysis measurements are carried out to determine the glass transition temperature (T_g) and melting point of the lignin, as well as the temperature range for carbonization of the lignin and yield of carbon, a very important factor with respect to the economics of carbon-fiber production. When an acceptable understanding of the fundamental properties of a candidate lignin material has been obtained, it is examined for melt-spinnability on small, single-fiber spinning equipment. If a candidate lignin shows promise for fiber spinning, it is examined on the larger and more effort-intensive, multi-filament spinning equipment. It is on this equipment that the process boundary limits will be defined for a given lignin and larger quantities of precursor fiber produced for processing into carbon fiber.

Figure 2. Multi-filament melt-spinning equipment

Lignin Purification and Fiber Spinning

As noted earlier, a laboratory-scale process was developed at ORNL to purify Kraft hardwood lignin to the required level. However, the laboratory process was not readily scaleable to either pilot-scale or commercial production and, therefore, a joint program of work was implemented by PNNL and MWV to develop an economically-viable process for lignin purification (based on the ORNL findings). As laid out in the timeline and tasks for the project, PNNL would focus on the use of combinatorial chemistry techniques to examine the key variables of the proposed process to establish appropriate processing conditions, MWV would scale-up the PNNL findings to produce larger samples of purified lignin for melt-spinning studies and perform the economic analysis of the proposed process, and ORNL would carry out the melt-spinning studies.

The first approach to lignin purification at PNNL using an aqueous method proved to be problematic, and MWV was unable to scale-up the process and furnish the purified lignin needed by ORNL to move its lignin-based carbon-fiber efforts forward. To overcome this hurdle in the short-term, MWV agreed to re-examine an alternative approach to the purification of Kraft lignin that had been investigated by the company (Westvaco) several years earlier, namely, extraction of the lignin with organic solvents to dissolve the lignin components away from the

insoluble salts, carbohydrates, and other impurities, which essentially is the opposite approach to the aqueous method.

Early in the fourth quarter of FY 2007, a small sample of the SEL was received from MWV. The rheometry measurements made on the material indicated that it exhibited the desired viscosity-temperature-time relationships and that it should be readily melt-spinnable. Examples of the rheometry test data are shown in Figure 3, in which the stability of the MWV SEL product is exemplified by the horizontal line for the plot (circular symbols) of transient viscosity as a function of holding time at a given temperature. In contrast, undesirable rheometry data are exemplified by the upper plot (square symbols) for the MWV hardwood lignin ("PC-1369") as-received, which exhibits an unstable (rising) viscosity as a function of residence time; it was this hardwood lignin material that was solvent-extracted to produce the SEL product.

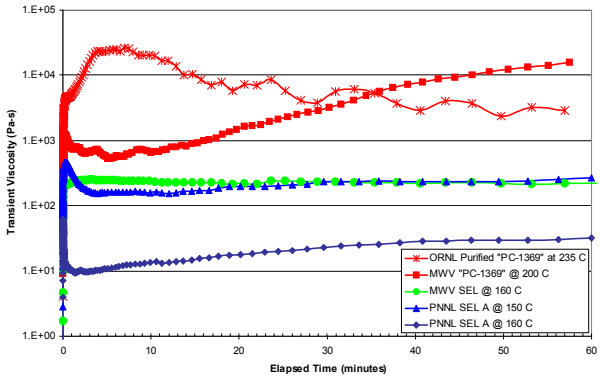

Figure 3. Viscosity of hardwood lignin as a function of time (at a given temperature).

The suitability of the MWV SEL product for melt-spinning was confirmed through single-fiber melt-spinning tests, during which lignin fiber was continually spun onto small spools; in fact, the lignin was the most readily melt-spinnable of all the lignin materials examined in the ORNL work to that date. On the basis of these positive findings, MWV committed to the production of kilogram quantities of the purified lignin for testing at ORNL on the multi-filament spinning equipment.

The first 'large' batch of MWV solvent-extracted (organic-purified) lignin was melt spun in early August 2007, with very positive results. Once steady-state conditions were established in the extruder, metering pump, and spinneret, 12-filament fiber was continuously spun over several hours without interruption (other than to change take-up spools) and without the need for addition of alloying or plasticizing agents. An example of a spool of the lignin fiber is shown in Figure 4. Emphasis in this first run was placed on establishing the relationship between fiber winding speed and filament diameter, the results of which are summarized in Figure 5.

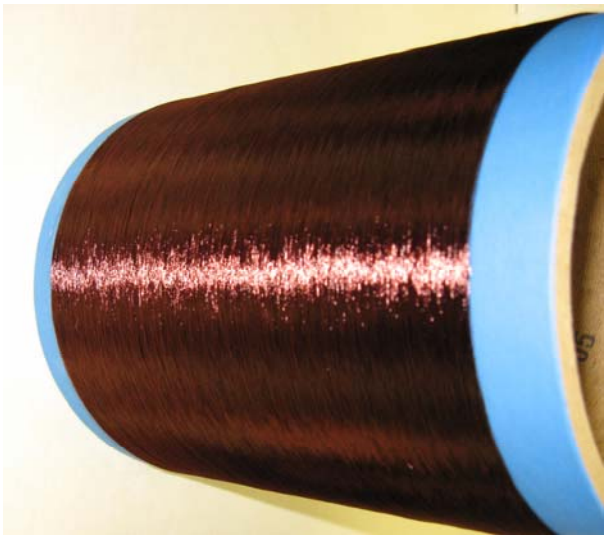

Figure 4. Lignin fiber tow comprising twelve filaments, each 11 micron in diameter.

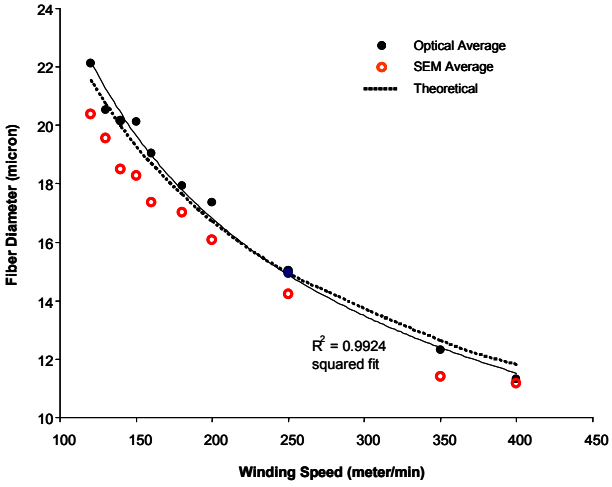

Figure 5. Lignin filament diameter as a function of winding speed.

The maximum fiber-winding speed achieved in this first multifilament spinning run was 400 meters/minute (m/min), i.e., 67% of the preliminary target speed of 600 m/min. This was a significant, first-time accomplishment. In fact, it was apparent that fiber-winding speed could have been increased to at least the preliminary target industrial rate of 600 m/min, but the subsequent increase in draw-down ratio would have resulted in filament diameters substantially below the target of 10 micron (µm), i.e., entering the upper end of the region of filament diameters that present a potential respiratory hazard. In the interest of safety, this particular study of spinning speed was terminated after five hours of continuous spinning when the lignin filament approached a visually-estimated diameter of 10 µm; optical microscopy and scanning electron microscopy (SEM) measurements of filament diameter were made after the fact.

Representative SEM images of lignin filaments, about 15 µm in diameter, are shown in Figure 6. The SEM images revealed that, regardless of filament diameter, the filaments exhibited very uniform diameters, smooth outer surface, and a cross-section structure that was totally devoid of air-entrapment, impurity particles, or other observable defects that could impact the engineering properties of carbon fiber subsequently produced from the precursor fiber. SEM magnifications as high as 20,000x were made, confirming the structural uniformity of the lignin fibers.

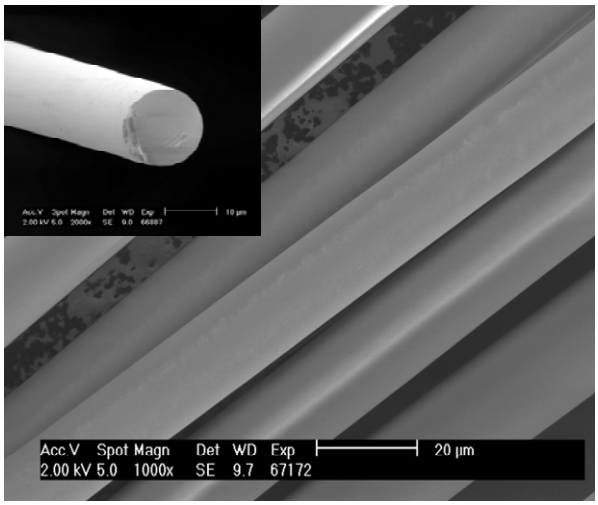

Figure 6. SEM Images of lignin precursor fibers.

The next study of spinning speed will target at least a two-fold increase in spinning speed (1000 m/min), increasing mass throughput in the melt extruder and spinneret such that the target filament diameter can be achieved at high spinning speed without exceeding the maximum draw-down ratio of 15:1 for the 12-filament die. Spinning of 24-filament lignin fiber tow will also be evaluated.

The first of the samples expected from the PNNL/MWV lignin-purification program arrived from PNNL in mid-September, too late to make a significant impact on our efforts in FY 2007. Nevertheless, based on the initial evaluation of the first PNNL lignin, it proved to be readily melt-spinnable without an additive. In fact, its thermal and rheological characteristics were very similar to those of the MWV solvent-extracted lignin that melt-spun so well. The similarity of the MWV SEL product and the first PNNL material is exemplified by the rheometry data shown in Figure 3, in which the viscosity data for the PNNL lignin are represented by triangle symbols, which are almost directly superimposed on the plot for the MWV SEL product (circular symbols).

PNNL subsequently confirmed that its first sample of purified lignin was not only produced from the same "PC-1369" hardwood lignin (i.e., not from black liquor, *per se*), but also was purified by a solvent-extraction approach (not aqueous). Thus, given these commonalities, it is not surprising that the MWV and PNNL purified hardwood lignin samples exhibited similar viscosity characteristics and were each readily melt-spinnable without the need for a plasticizing additive. Apparently, PNNL has refined its solvent extraction procedure to produce a higher melting point material (a desirable feature), which will be sampled to ORNL in the near future for evaluation.

In the meantime, PNNL also scaled-up production of an aqueous-purified hardwood lignin, an approach that, as mentioned earlier, had been problematic through most of the year. A (1 lb) sample of the aqueous-purified lignin, produced from the same "PC-1369" batch of hardwood lignin, was received in the first quarter of FY 2008 (11/9/07). The initial tests indicate that its melting point is approximately 220°C. However, the rheometer tests indicate that it is not sufficiently

stable at this temperature and begins to decompose within a short time span.

Single-fiber tests confirmed that the first sample of the PNNL aqueous-purified lignin was not melt-spinnable without the aid of a plasticizing agent. Further testes indicated that it may be melt-spinnable when blended with a solvent-extracted lignin, e.g., either the MWV or PNNL SEL products. These preliminary findings on the PNNL sample of aqueous-purified lignin are consistent with earlier findings on the same batch of hardwood lignin purified by ORNL using a similar aqueous approach.

The aqueous approach yields a clean lignin that more than meets the purity specifications and also exhibits a melting point (at least a "softening point") at a desirable temperature (around 230°C). However, the purified hardwood lignins produced to date through use of an aqueous procedure are not melt-spinnable without a plasticizing agent. Nevertheless, it is a positive development that hardwood lignin purified through an aqueous procedure can be melt spun by inclusion of a minor proportion of a readily-spinnable, solvent-extracted lignin. The positive attributes of each are reinforced and the negative aspects essentially eliminated.

Apart from its good purity, a positive attribute of the aqueous-purified hardwood lignin is high carbon yield. This is highlighted in Figure 7 (A), in which thermogravimetric analysis (TGA) data are shown for ORNL aqueous-purified hardwood lignin together with the corresponding data for the unpurified lignin as-received. TGA data for an unpurified softwood lignin are included for the purpose of comparison. In this figure, carbon yields obtained at 950°C are compared on a dry basis (adjusted for the initial moisture content of the starting material). The beneficial effect of purifying the hardwood lignin using an aqueous procedure is discerned from the fact that carbon yield increased from 40.9% to 48.2%. The theoretical carbon content of hardwood lignin is about 55-60% (Table 1). For comparison, the yield of carbon obtained from carbon-fiber (CF) grade PAN under the same TGA conditions was 45.2 % (Figure 7 B). The negative attribute of the aqueous-purified lignin is that it is not melt-spinnable without the addition of a plasticizing agent.

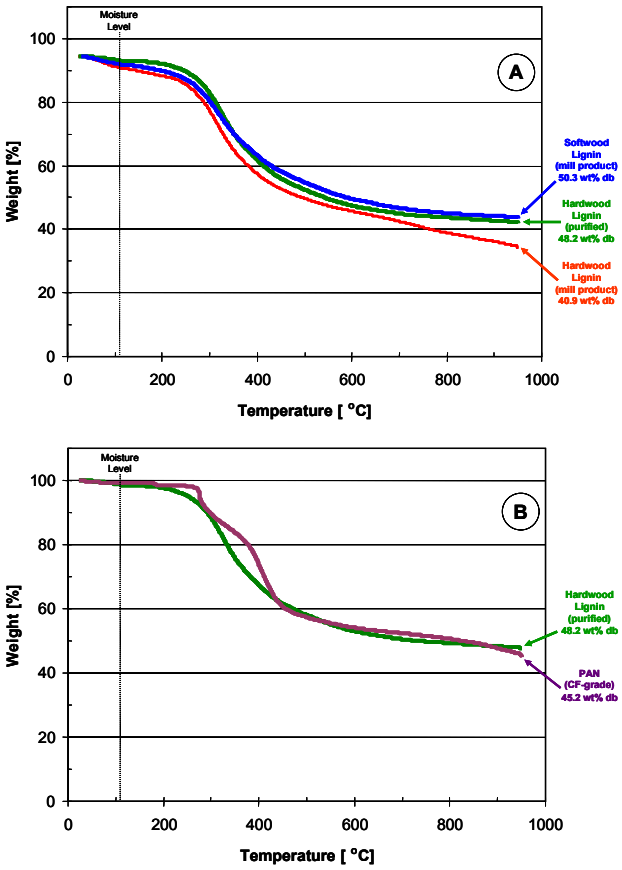

Figure 7. TGA data for lignins (A) and PAN (B).

Conversely, the positive attribute (in addition to high purity) of the organic-purified, solvent-extracted lignin is the fact that it is very readily melt-spinnable, and can also be used as a plasticizing agent for non-melt-spinnable lignins. The negative aspect of the SEL is relatively low carbon yield. This is apparent from the TGA data shown in Figure 8 for SEL samples. As-received, the SEL powder exhibited a carbon yield of 36.6% at 950°C. Encouragingly, though, when the SEL powder was oxidized with air, *in situ* at 300°C in the TGA instrument, the carbon yield increased to a respectable 50.6%. This demonstrated that the SEL material is cross-linkable, i.e., there is no thermodynamic barrier to stabilizing the solvent-extracted lignin or to achieving high carbon yield from the material. However, the temperature (300°C) at which the SEL powder was oxidized to obtain a meaningful rate of cross-linking was about twice that of the melting point of the lignin (about 140°C), and therefore impractical with respect to the production of carbon-fibers from the SEL material.

Table 1. Carbon Contents of Lignin and PAN

Precursor Material	Theoretical C-content	ORNL TGA Measurement
Hardwood Lignin Mill product	50-55	40.9
Hardwood Lignin Aqueous-purified	55-60	48.2
Softwood Lignin Mill product	55-60	50.3
Softwood Lignin Aqueous-purified	60-65	*55* ?
PAN CF-grade	68	45.2

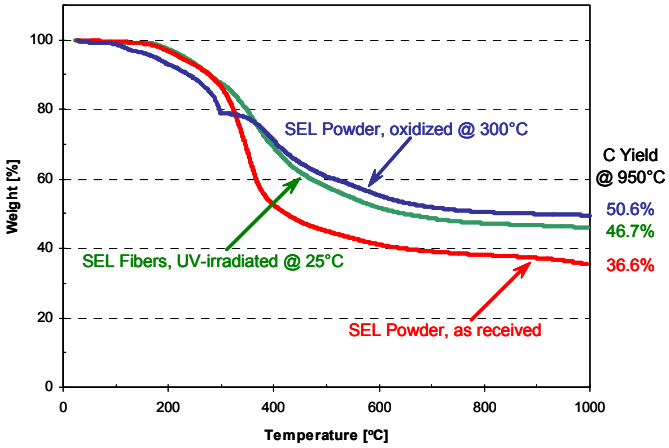

Figure 8. TGA data for fibers produced from MWV solvent-extracted hardwood lignin (SEL).

Thus, for solvent-extracted lignins to be of practical use with respect to the production of carbon fibers, a viable, alternative approach to stabilization of SEL materials must be identified. Very recent preliminary data in this context are summarized in Figure 8, in which the TGA data for SEL fibers irradiated with ultraviolet (UV) light at ambient temperature (25°C) in air are shown. Melt-spun fibers obtained from the multi-filament spinning run discussed above were UV-irradiated for different lengths of time; the data shown in Figure 8 are those for SEL fibers irradiated for 16 minutes. The carbon yield at the reference temperature of 950°C was 46.7%, indicating that the SEL lignin had cross-linked (oxidized) under the treatment conditions.

Although this is a very preliminary finding and must be confirmed through more detailed work, it nevertheless is encouraging that a relatively simple UV treatment of a lignin material will facilitate stabilization of the material in fiber form.

Based on the data obtained to date with respect to the purification and subsequent melt-spinnability of Kraft hardwood lignin, general conclusions can be drawn, namely, aqueous purification procedures are based on the separation of water-soluble contaminants and lignin (alike) at high pH and the subsequent separation of the contaminants and lignin through selective precipitation of the different species upon careful reduction of solution pH. The purified lignin so obtained is a higher molecular-weight material in which the lower molecular-weight lignin fractions are retained in solution with the salt and other mineral impurities. The lower molecular-weight lignin fractions appear to be the "plasticizing" agent for the lignin as a whole, and their elimination from the hardwood lignin renders the purified lignin non-melt-spinnable.

In marked contrast, organic solvent extraction of lignin purifies the lignin by dissolving the lignin away from the contaminants (mineral and carbohydrate). However, lower molecular weight lignin fractions are preferentially dissolved over higher molecular-weight fractions, at least under the organic solvents and process conditions examined to date. Thus, the organic-purified lignin contains a large proportion of the low molecular-weight lignin fractions that are plasticizing agents for the lignin as a whole, thereby retaining the melt-spinnability characteristics in the purified lignin. However, because of their lower molecular weight, these fractions depress the average molecular weight of the purified lignin, which is reflected by a melting point too low to permit stabilization of the subsequent fiber at an acceptable rate through conventional thermal-processing techniques alone.

Summary of Progress on the Lignin Project in FY 2007

Progress made on the lignin project over the past year (FY 2007) included:

- For the first time, multi-filament lignin tow was successfully melt-spun continuously

(without disruption) over an extended period of time (5-hours). The fiber exhibited excellent structural characteristics.
- The relationship between fiber winding speed and filament diameter was established (for a given set of melt-extrusion conditions).
- Target-diameter fiber (10 μm) was produced at 67% of the initial goal for spinning speed (600 m/minute), with indications that spinning speed can be readily increased several-fold.
- Preliminary data obtained indicate that melt-spun lignin fibers can be quickly stabilized through UV irradiation in air at 25°C.
- Demonstration that hardwood lignin purified using organic solvent-extraction procedures are readily melt-spinnable into the target-diameter filaments. Also, that they be used as plasticizing agents for hardwood lignin purified using aqueous procedures, the products from which are not melt-spinnable.
- Derivation of a better understanding of the factors that influence the melt-spinnability of lignin materials, what must be done to purify lignin to the target level and, at the same time, retain the melt-spinnability characteristic of hardwood lignin as produced in a pulp mill.
- Identification of commercial sources of lignin materials other than MeadWestvaco.

Lignin Sources for Continued Development Work

Following the merger of Mead and Westvaco in 2002, the business direction of the new corporation has been towards packaging and land development and away from the production of paper and specialty chemicals. Many of the new corporation's pulp-and-paper operations have been sold, and divestiture of its specialty-chemicals business, which is largely based on the isolation of tall oil, fatty acid, and lignin by-products from pulping operations (in Charleston, SC), is possibly part of MWV's long-term business strategy. Thus, even before the company's decision towards the end of FY 2007 to terminate all its long-term research efforts, including its support of the low-cost carbon-fiber project (LCCF), it was clear that an alternative industrial partner would need to be found.

Kruger Wayagamack, Inc., Quebec, Canada, is a large Canadian-based pulp-and-paper producer that also utilizes the Kraft process for the pulping of wood (predominantly softwood in Canada). Almost two years ago, Kruger made it clear that it was interested in isolating lignin to debottle its recovery-constrained mills and increase pulp production. To increase small profit margins and stave off competition from China, many pulp-and-paper companies wish to increase pulp production and throughput of paper in their mills, but are largely unable to do so because the mills concerned are not able to also increase recovery of the pulping chemicals (new recovery boilers are very capital-intensive). Thus, some mills are seeking to isolate lignin from the black liquor, largely for the purpose of using it as a fuel in other operations but also a potential source of valued-added products. Kruger, for example, is initially targeting the production of fire logs, an application that has a value of about 20¢/lb of lignin. At a potential price of 50¢/lb, sale of lignin for low-cost carbon-fiber production is of substantial interest to Kruger.

Kruger has licensed the "LignoBoost" lignin-isolation technology from STFI-Packforsk, a Swedish research company. As a point of information, the LignoBoost process was developed to produce a lignin-based biofuel.

Kruger senior management has recently given the formal go-ahead for mill trials, a significant financial commitment. As part of this effort, the company is constructing a pilot-scale lignin-isolation plant with a capacity of 100 kg/day, which is expected to be on-stream within 4-6 months. Thus, we have another pulp-and-paper manufacturer on-board that is willing to take over from MeadWestvaco and furnish ORNL with Kraft lignin for the LCCF efforts. Needless to say, this will not be without its own challenges, not the least of which is that we must demonstrate melt-spinning of multi-filament tow from the lignin, which is softwood based. However, we have learned a great deal about spinning lignin materials over the past year, which will help us to move forward with the new source of lignin as a precursor material for carbon-fiber production.

We have already demonstrated that the first Kruger lignin material is melt-spinnable with a plasticizing additive, namely, the solvent-extracted hardwood lignin discussed above. Furthermore,

based on an analysis of the first lab-scale sample received from the company, the purity of the Kruger lignin is close to the desired specifications and certainly much better than that of the commercial Kraft lignin products from MWV with which we have worked to date. Refinement of the isolation procedure (e.g., through incorporation of additional washing stages) could result in a lignin material meeting the purity specifications *without* the need for subsequent purification.

Weyerhaeuser Company, WA
Weyerhaeuser has recently indicated that it is willing to provide its lignin to the FreedomCAR program for multi-filament melt-spinning evaluation and carbon-fiber production. Access by the FreedomCAR program to Weyerhaeuser lignin is considered to be an important element of future efforts on the FreedomCAR LCCF program.

Lignol Innovations Ltd., British Columbia, Canada
Lignol Innovations, a wholly owned subsidiary of the Lignol Energy Corporation, is building biorefineries in Canada for the production of ethanol fuel and other products from lignocellulosic biomass, notably waste wood. Lignol has improved on the process originally developed by General Electric (GE) and further refined by Repap Enterprises, Inc., from which the "Allcell" lignin product was produced. It has been known since the earliest days of the LCCF project at ORNL that the Allcell lignin product (derived from hardwood) is relatively pure as-isolated and is readily melt-spinnable. However, the Allcell product was unable to compete with commercial lignin products produced from conventional chemical pulping, and Repap consequently ceased business operations. With the greatly increased emphasis on the production of cellulosic ethanol, however, there is renewed interest in finding markets for the lignin by-products from cellulosic ethanol operations, and Lignol Innovations regards LCCF production as an attractive potential market for its lignin product.

Other Biomass-Derived Lignins
Biomass-derived lignins will become increasingly available from other cellulosic ethanol programs around the world, most notably from the joint venture by the University of Tennessee (UT) Knoxville and ORNL. We anticipate getting in on the ground floor of the new UT/ORNL program with respect to evaluating the lignin produced in this particular biomass-to-ethanol research work. The economics of any biomass-to-ethanol process will partially depend on what one does with the lignin "by-product" from the process, which could account for upwards of 35% of the mass input of the biomass. Certainly, it will not be acceptable either environmentally or economically to landfill the lignin, and burning it for energy is worth only about 5¢/lb, even based on today's oil prices.

Solvent-Extracted Lignins
Recapping, both the MWV and PNNL solvent-extracted hardwood lignin materials exhibited excellent melt-spinnability characteristics, especially the former. The downside to these particular solvent-extracted lignin materials is their low melting point of about 140°C, which is fine from a melt-spinning standpoint but is too low to stabilize spun fiber at an acceptable rate using conventional thermal-processing techniques. Nevertheless, it was demonstrated that the MWV solvent-extracted lignin will readily cross-link at temperatures above its melting point, resulting in a substantial increase in carbon yield from 37 to 51%. It was also demonstrated that UV irradiation of the MWV solvent-extracted lignin fiber at ambient temperature (25°C) over a short period of time (16 minutes) resulted in a similar, substantial increase in carbon yield, indicating the potential for UV stabilization of fibers produced from such lignins. Furthermore, both the MWV and PNNL solvent-extracted lignins were useful plasticizing agents for other, non-melt-spinnable lignins, including those purified using an aqueous procedure.

Thus, some efforts will be continued to exploit the beneficial characteristics of lignins purified using a solvent-extraction process, particularly if it is demonstrated that, through refinement of the procedure, the melting point of such lignins can be raised to near the desired level of about 250°C. However, efforts at ORNL in this respect will be limited to evaluation of solvent-extracted lignins, i.e., the work will not encompass lignin purification, *per se*.

Approximately 5 tons of the "PC-1369" hardwood lignin produced by MWV in support of the LCCF project at ORNL is available for sale. If new

findings are developed that indicate that the molecular-weight and melting-point properties of a solvent-extracted lignin could be enhanced through refinement of the solvent extraction procedure (e.g., choice of solvents), then it would be appropriate to consider funding a solvent-extraction purification run by the toll processor identified by MWV for this purpose. Furthermore, it would be advantageous to have solvent-extracted lignin on-hand for use as a plasticizing agent for other purified lignins that are not readily melt-spinnable (about 2 kg of SEL is currently on-hand for this purpose).

Kraft lignin exhibits antioxidant properties because it is a radical scavenger (e.g., has been tested for the treatment of certain cancers). It readily absorbs UV radiation and, as noted above, UV irradiation may be a viable route to stabilizing solvent-extracted lignins as currently produced. In addition, though, an evaluation should be made of whether the SEL material could be satisfactorily stabilized using other advanced processing techniques, including plasma treatment or incorporation of a catalyst to promote oxidative stabilization of the spun fibers at temperatures below their melting point of about 140°C.

PNNL-Produced Lignin Materials

PNNL has overcome the difficulties encountered in the early part of the PNNL/MWV program to purify hardwood lignin using an aqueous procedure and has produced purified material for evaluation. Similarly, PNNL has refined its organic solvent-extraction procedure to produce a purified hardwood lignin of higher molecular weight and melting point. Both of these hardwood-lignin materials should be evaluated for melt-spinnability and production of multi-filament tow. However, PNNL is not in a position to furnish the kg-quantities of purified lignin required for multifilament melt-spinning; someone else must scale-up the PNNL process.

Project Deliverables

By the end of this multi-year program, production of carbon fibers suitable for transportation use, from one or more economically-feasible, renewable resource materials, will have been demonstrated and the transfer of production technologies and related intellectual property to industry implemented.

Presentations/Publications/Patents (FY 2007)

1. Frederick S. Baker*, Nidia C. Gallego, Felix L. Paulauskas, and Amit K. Naskar, "Lignin-based Carbon-fibers: A Route to Energy Independence in the USA," Invited Keynote Lecture, *CARBON 2007 Conference*, Seattle, WA, July 15-20, 2007.
2. Frederick S. Baker*, Nidia C. Gallego, Felix L. Paulauskas, and Amit K. Naskar, "Production of Low-cost Carbon-fibers from Renewable Resource Materials for More Energy-efficient Vehicles and Reduced Environmental Pollution," Invited Lecture, *Carbons for Energy Storage and Environment Protection, CESEP'07 Conference*, Krakow, Poland, September 2-6, 2007.
3. C. Dave Warren*, C. Cliff Eberle, Felix L. Paulauskas, Fred S. Baker, Amit Naskar, and Alan Wheatley, "FreedomCAR and Low-cost Carbon-fiber for Automotive Applications," *7th International Congress on Materials for Lean Weight Vehicles*, University of Warwick, Warwick, England, September 26-27, 2007.

* = Presenter

B. Improved Lignin Purification/Recovery Process for Carbon-Fiber Applications

Co-Principal Investigator: James F. White
Pacific Northwest National Laboratory (PNNL)
902 Battelle Blvd., Richland, WA 99352
(509) 372-5053; fax: (509) 372-6507; e-mail: jim.white@pnl.gov

Co-Principal Investigator: Bert DelliColli (retired)
Co-Principal Investigator: David Knox (current)
Affiliation: MeadWestvaco Corporation
Address: P.O. Box 118005, Charleston, S.C. 29423
(843)-740-2304; fax: 843-746-8165; e-mail: david.knox@meadwestvaco.com

Technology Area Development Manager: Joseph A. Carpenter
(202) 586-1022; fax: (202) 586-1600; e-mail: joseph.carpenter@ee.doe.gov

Expert Technical Monitor: Philip S. Sklad
(865) 574-5069; fax: (865) 576-4963; e-mail: skladps@ornl.gov

---

Contractor: PNNL
Contract No.: DE-AC06-76RL01830

Objective

- The project objective is to develop an economically-viable and technically-sound process for the purification of lignin to make it acceptable as a raw material for the manufacture of low-cost carbon fiber (CF).
- Lightweighting the USA car and light-truck fleet for better fuel efficiency is a current DOE objective. The substitution of stamped steel panels and other body and interior parts with strong, yet lightweight and resilient carbon-fiber-reinforced plastic (FRP) parts can contribute significantly to this objective. Unfortunately, current processes for manufacture of CF are costly and produce CF at well above the established target cost of under $5.00/lb needed for vehicle lightweighting.
- A considerable portion of the cost of current CF is borne by the expensive synthetic polymers that are the normal raw materials. Lignin, as a byproduct of the pulp-and-paper industry, is an attractive alternate and potentially low-cost raw material for CF. Unfortunately, today's standard means of recovering lignin from paper-mill streams is not able to yield lignin with the levels of acceptable purity and physical properties for fast and economically-viable melt-spinning and eventual conversion to CF.
- This project is tasked with developing and demonstrating at the lab-scale effective means to isolate, recover and purify pulp-mill-derived lignin with properties acceptable for its use as a raw material for CF. Initially, this effort is focused on hardwood lignin from Kraft black liquor and eventually will be extended to softwood lignin from Kraft black liquor. The purity targets that have been set for lignin by prior CF work at ORNL (see 7.A) serve as a guideline. However, we will also use a preliminary test for melt-spinnability (via a fiber-draw test) as a guideline for determining early-success potential. We will also examine other physical properties including melt index (MI) and dynamic viscosity. These physical properties are also expected to be a key to a material's ability to be processed economically into CF whose properties are acceptable for use in CF-reinforced car and truck parts.
- The focus in fiscal year (FY) 2007 was on hardwood lignin from Kraft black liquor. Eventually, the focus will extend to softwood lignin from Kraft black liquor. We are using a dynamic mechanical analyzer (DMA), and thermogravimetric analysis, differential scanning calorimetric (TGA-DSC) analysis for preliminary physical property evaluations.

Approach

- Evaluate the MeadWestvaco (MWV) concept of differential removal of impurities and lignin precipitation as a process route to achieving the desired level of lignin purity and properties for CF application.
- Evaluate post-pulping processes to remove carbohydrate from lignin using appropriate, representative Kraft black liquor(s).
- Screen and determine optimal process variables for the selected process.
- Scale selected process and the optimized conditions to 300 cc and/or to 1-liter batch levels or larger as appropriate, to verify process and determine overall material balance and perform preliminary assessment of adaptability to a continuous process.

Accomplishments

- Purchased MI instrument for lignin product characterization. Set up instrument and accomplished operator training and baselining with commercial polymers.
- Successfully addressed environmental, health and safety (EH&S) issues. This included standard operating procedures and safety reviews of instrumentation and autoclave equipment and approved procedures for disposal of waste and recycle materials.
- Developed approved material-handling, characterization and processing procedures.
- Developed procedures for TGA, differential thermal analysis (DTA) and DSC of samples to determine moisture, ash and melting-range behavior.
- Samples, which appear via these preliminary tests to represent potential candidate purification technologies, were scaled and sent to Clemson University and/or Oak Ridge National Laboratory (ORNL) for melt-spinning trials.
- Established and validated a preliminary "fiber-draw" test to assess the ability of lignin samples to be successfully melt-spun.
- Determined that existing PNNL DMA instrumentation can adequately measure lignin sample melt viscosity under shear, another property that is deemed key to predicting its ability to be melt-spun into fiber.
- Begun combinatorial, high-throughput experiments with well-per-plate format to assess post-pulping processes. Selected several leads for further evaluation.
- Performed a preliminary evaluation of the MWV differential process for lignin clean-up.
- Performed an evaluation of % loading and methods of incorporation for one recommended type of plasticizer / rheology control agent, to aid in lignin melt-spinning. Selected an appropriate loading and incorporation method. (Prior efforts by others have suggested that lignin must be plasticized in order to be effectively melt-spun.)
- Via the cooperative research and development agreement (CRADA) partner, established a technical-service type arrangement with a USA university to perform single-fiber melt-spin tests on samples that appear successful in preliminary testing.

Future Direction

- Development of technology capable of delivering hardwood lignin to the desired purity level.
- Selection of one of three best-apparent technologies for hardwood-lignin recovery and scaling these to a level suitable for validation and to provide sufficient material for single-fiber melt-spin tests at a university.
- Extension of hardwood-lignin recovery methods to the development of technology capable of delivering softwood lignin to the desired purity level.
- Selection of one of three best-apparent technologies for softwood-lignin recovery and scaling these to a level suitable for validation and to provide sufficient material for single-fiber melt-spin tests at a university.
- Delivery of 5 kilograms of the desired purified lignin for melt-spinning evaluations.

Introduction

CF derived from lignin-based feedstock offers the potential for meeting the aggressive cost goals established by FreedomCAR for structural applications CF. However, the critical requirement for successful development of a lignin-based CF is the ability to purify the lignin feedstock effectively so that it can be melt-spun and processed at attractive rates into a viable CF having the required physical and mechanical properties. Effective purification of lignin requires the removal of insoluble particulates, salts and undesirable carbohydrate fragments, which adversely affect the melt-spinning and overall fiber processing. In order to meet current cost targets it is essential that a practical purification process be compatible with current Kraft pulping operations as Kraft lignin is the largest practical source of lignin for the near future. It is also essential that the general lignin purification scheme be easily adaptable to both hardwood and softwood lignin. Longer term, the process must also be able to handle lignin from other renewable sources and processes other than those based on Kraft-type technology.
MWV, the project's cost-sharing CRADA partner, has developed a relatively untested and unrefined concept for lignin purification/recovery that has potential to meet the required purity levels in a cost-effective, environmentally-suitable manner. In addition, the MWV process concept is compatible with existing pulp-plant layout and function, which is a key requirement for early implementation of high-purity lignin for CF.

The most deleterious lignin components are perceived to be easily volatilized, lignin-bound carbohydrate fragments, along with inorganic salts, insoluble and non-melting materials. MWV's conceptual process is expected to remove these undesirable components very early in the lignin-recovery process and also can be retrofitted into a conventional pulp-mill design. Early experimental evidence suggests that this concept, although simple, is likely to be more complex and difficult to accomplish successfully than initially believed.

Approach

The overall project approach is multifold, including use of high-throughput, combinatorial methods at PNNL for fast screening and discovery. Bench-scale experiments at 300 cc to 1-liter levels to validate, verify and refine leads, found via high-throughput methods, are also planned. Scale-up to pilot-size and beyond as appropriate will also be conducted to provide confidence in the process and to provide material for single- and multiple-fiber melt-spinning evaluation and also carbonization tests. Initially, the project plan involved various tasks properly described as preparatory, including acquisitions, personnel training and items related to EH&S. This was followed by experimental recovery of lignin via various physical means and also experimental evaluations of a variety of chemical treatments. Ultrafiltration of the black liquor (BL) was also briefly examined.

Fundamentally, we are starting with lignin at the black-liquor stage, that is, when it is closest to the form in which it is first removed from the wood. Prior CF development work with lignin has used material that had already been recovered, isolated, subjected to some degree of purification and dried. Since lignin can have significant reactivity before and during drying, we think that beginning at the BL stage allows us to intercept lignin and process it more effectively before undesirable and irreversible changes take place.

Results

Early accomplishments include the acquisition, set-up, personnel training, a safety review and standard operating procedures (SOP) approvals of a Tinius-Olsen Melt Index testing machine. We have evaluated and validated this instrument with several commercial polymers with known ability to be melt-spun and blown into films.

We have also set-up and validated a preliminary test to very simply evaluate a new material's potential ability for melt-spinning. This preliminary test, known as the "fiber-draw" test is modeled closely after a test designed and successfully used by some staff at Clemson University for determining if a given sample is likely to be suitable for melt-spinning. The "fiber-draw" test apparatus is contained inside a nitrogen

(N)-filled glove box as lignin is often perceived to be reactive with air. The test is quite simple in concept. A sample is placed in a small aluminum pan on a hot plate whose surface temperature may be accurately controlled and changed. As the sample temperature is raised by increasing the hot plate's surface temperature, a visual indication of possible melting or softening can be observed. When melting or softening behavior is seen, a sharp-pointed pin is touched to the sample and slowly removed. If a long, uniform, thin fiber can be drawn from the sample as the pin is removed while the sample transitions through a melting or softening stage, then the sample is considered to have good potential for melt-spinning. Figure 1 shows the "fiber draw" behavior of M-50 pitch, a material known to have good melt-spinning behavior. Note the relatively nice looking, long fibers drawn from the melted pitch contained in the pan.

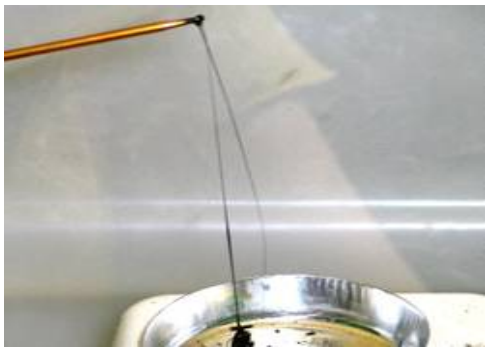

Figure 1. M-50 pitch fiber-draw test.

Other early activities included staff training on a TGA-DSC apparatus used to determine melting points or melting ranges and also weight loss vs. temperature in inert or air atmosphere.

Experimental work for recovering lignin from hardwood BL is using a commercial BL obtained from the MWV Kraft pulp mill in Charleston, SC. We found that most particulate matter and the tall oils could be removed in a single centrifuging step after appropriate pH adjustments. The liquid remaining after this treatment contained about 14% lignin along with dissolved inorganic salts and other organics. Simple precipitation of this lignin followed by washing to remove the inorganic salts and soluble organics followed by vacuum drying, did not yield a particularly good fiber draw test (see Figure 2). The "clumps" and "nodules" on the drawn fibers are indicative of poor melt-spin behavior and are consistent with earlier work which established the need to plasticize the lignin prior to melt-spinning, regardless of its purity.

Figure 2.
Precipitated lignin.

Figure 3.
PC-1369 lignin.

Figure 4. Fiber draw test.
Experimental combi lignin.

As a comparison, Figure 3 shows the fiber-draw test result with unprocessed PC-1369, which is a commercial grade of hardwood lignin shown in past ORNL studies not to be suitable for melt-spinning. The PC-1369 and also the lignins shown in Figures 2 and 4 contain the preferred plasticizer/rheology control agent; but, note the very severe degree of clumping and poor fiber formation in Figure 3 which suggests quite poor melt-spin behavior for PC-1369.

However, Figure 4 shows a fiber-draw test that appears positive for a lignin sample that was obtained from high-throughput screens to evaluate various other BL pretreatments before precipitation, washing and vacuum drying. An approach such as this in combination with a suitable plasticizer is expected to ultimately produce the desired result, an easily melt-spinnable, lignin-based precursor to CF.

These results appear to be worth following up. Thus, a series of follow-up tests is planned for next quarter at both the 20 mls combi level and at a larger bench-scale. Note that high-throughput combinatorial screens are performed in the PNNL

combi system using a 6-well plate. The capacity of each well is about 20 mls. Only a few grams of lignin can be recovered from these screens, about enough to do only TGA-DSC and a fiber draw test.

Conclusions

Experimental results suggest that the conceptual MWV differential recovery / purification process is not acceptable for hardwood-black-liquor-derived lignin.
PNNL combinatorial, bench-level scaling studies and corresponding fiber draw tests have suggested that both organic and completely aqueous post-pulping process schemes, may provide alternatives that have promise for leading to a lignin product acceptable for melt-spinning. Currently, however, only organic-based processes are able to yield a melt-spinnable lignin. Further evaluation is required to validate all-aqueous schemes. All schemes contemplated thus far should be easily integrated into a typical Kraft pulp mill.

Presentations/Publications/Patents

None in FY 2007.

C. Advanced Stabilization of PAN Fiber Precursor

Principal Investigator: Felix L. Paulauskas
Oak Ridge National Laboratory (ORNL)
PO Box 2008, Oak Ridge, TN 37831-6053
(865) 576-3785; fax: (865) 574-8257; e-mail: paulauskasfl@ornl.gov

Project Manager, Composites: C. David Warren
ORNL
P.O. Box 2008, Oak Ridge, TN 37831-6065
(865) 574-9693; fax: (865) 574-6098; e-mail: warrencd@ornl.gov

Technology Area Development Manager: Joseph A. Carpenter
(202) 586-1022; fax: (202) 586-1600; e-mail: joseph.carpenter@ee.doe.gov

Expert Technical Monitor: Philip S. Sklad
(865) 574-5069; fax: (865) 574-6098; e-mail: skladps@ornl.gov

Principal Team Members:
Christopher J. Janke, ORNL
Amit K. Naskar, ORNL
Cliff Eberle, ORNL
Truman Bonds, Atmospheric Glow Technologies
Daniel Sherman, Atmospheric Glow Technologies
Professor Amod Ogale, Clemson University
Professor Roberto Benson, University of Tennessee
Marshall Cleland, IBA-RDI
Rick Galloway, IBA-RDI

Contractor: ORNL
Contract No.: DE-AC05-00OR22725

Objectives

- Develop an improved technique for stabilizing carbon-fiber (CF) precursor with increased line speed and reduced CF cost.
- Verify that finished fiber properties satisfy automotive and heavy-vehicle manufacturers' requirements.
- Conduct a preliminary evaluation of the cost impact of the new stabilization technique.
- Integrate the stabilization module into an advanced technology pilot-line.

Approach

- Investigate thermochemical, ultraviolet (UV), and electron-beam (EB) processing stabilization routes.
- Select one of the aforementioned stabilization routes for detailed equipment and process development.
- Conduct parametric studies to correlate processing parameters and fiber properties.
- Determine process parameters that minimize residence time.
- Characterize fibers to confirm that they satisfy program requirements.

Accomplishments

- Discovered how to stabilize virgin precursor fibers via plasma-assisted thermochemical route.
- Thermochemically stabilized virgin precursor fibers in less than half of conventional stabilization residence time.
- UV-stabilized virgin precursor fibers in less than half of conventional stabilization residence time.
- Investigated various EB-stabilization irradiation parametric effects on plasma oxidation.
- Plasma-oxidized precursor fibers after they were UV-stabilized.
- Selected plasma stabilization as the primary route for implementation at a conversion factory and EB stabilization as the primary route for implementation at a precursor factory.

Future Direction

- Develop advanced thermochemical stabilization for implementation at a conversion factory.
- Develop e-beam stabilization for implementation at a precursor factory.
- Conduct parametric studies and fiber characterization to better understand process effects and to quantify fiber properties.
- Commence scaling the advanced-stabilization equipment and process.

Introduction

The purpose of this project is to investigate and develop a technique to rapidly and inexpensively stabilize a polyacrylonitrile (PAN) precursor. New processing techniques are being developed for the purpose of reducing the cost of CF conversion. Previous and ongoing research at ORNL has demonstrated that plasma processing shows great promise for inexpensively and rapidly oxidizing, carbonizing, and graphitizing polymer precursors to convert them to CFs. The precursor needs to be lightly stabilized, or cross-linked, before it can be subjected to plasma oxidation. Stabilization and oxidation together are estimated to represent ~ 18% of the cost of commercial grade carbon fiber.[i] A rapid, inexpensive and robust stabilization technique is needed to complement the aforementioned advanced-process modules and enable the development of an integrated, advanced-technology conversion line that converts polymer precursor fibers into CFs at significantly lower cost than conventional conversion technology.

This project, therefore, intends to develop an advanced-stabilization module that integrates with other advanced fiber processing modules to produce inexpensive CF with properties suitable for use by the automotive industry. Critical technical criteria include: 1) ≥ 25 Msi tensile modulus and ≥ 1.0% ultimate strain in the finished fiber; 2) uniform properties along the length of the fiber tow; 3) repeatable and controllable processing; and 4) significant unit cost reduction compared with conventional processing.

Project Deliverable

At the end of this project, the project team will have demonstrated satisfactory PAN precursor fiber stabilization with residence time well below that typical of conventional CF conversion lines. The project deliverable is a process specification that will enable the commencement of scaling experiments aimed at development of a subscale, multiple large-tow, advanced-technology pilot-line.

Technical Approach

The researchers are investigating three prospective PAN precursor fiber stabilization routes: electron beam processing, thermochemical processing, and UV processing. All three routes are based on discoveries previously made in other carbon-fiber projects, and each appears to offer certain advantages. After experimental concept investigation, the researchers will select the most promising route for detailed process development, with the principal criteria for selection being mechanical properties and finished fiber cost. The preferred

route will then undergo detailed parametric studies to characterize the process and develop the processing recipe.

Progress

Detailed design and process data are not disclosed in this report due to export-control restrictions. They are periodically reported to the program managers and partners in compliance with the export-control restrictions. Material properties and residence times can be disclosed, and example data are shown in Table 1.

EB Processing

EB stabilization was demonstrated in fiscal year (FY) 2006, showing very high throughput (line-speed) potential. The electron irradiation step is completed in seconds, but early experiments have required a few-minute thermal post-treatment to render the precursor fibers stable in the plasma-generated, oxidative environment. Current efforts are focused on understanding and resolving the cause of the unstable behavior when exposed to the plasma-generated, reactive, oxidative species. Electron spin resonance data indicate that irradiation generates free radicals, which are thought to cause the unstable behavior. Efforts to resolve the free radical problem are underway. FY 2007 irradiation experiments were conducted to study the effect of various irradiation parameters.

EB-stabilized precursor has been converted to finished fibers by a range of process combinations. The results, which are compared in Figure 1, include both previously-reported and new data. All of the conversions, even by fully-conventional means, were conducted at low carbonization temperature and without the benefit of fiber tensioning, tow spreading, or controlled stretching in any of the conversion stages; hence, the fiber mechanicals are expected to be low compared to those of corresponding commercial fibers. Most specimens exhibit a tensile modulus exceeding the 25 Msi requirement. The strain is generally somewhat below the 1% requirement. It is noteworthy that the EB-stabilized samples, even those that were subsequently plasma oxidized, exhibit mechanicals that are not far below those of the thermally-converted fibers. This gives us confidence that the property targets are well within reach. New equipment for carbonizing fiber quantities at correct temperature and tension recently became operational and will be utilized in future testing.

Thermochemical Processing

Stabilization was originally found to be needed before plasma oxidation, because virgin precursor could not withstand the reactive oxidative species generated by plasma. When virgin precursor was exposed to the plasma-generated chemistry, significant exothermic heating occurred fairly rapidly, resulting in interfilamentary adhesion and tow rigidity. While it was necessary to investigate other stabilization routes, the quest to discover a way to stabilize the precursor fibers using plasma chemistry has continued. One obvious advantage of this route is that it would integrate seamlessly with the plasma-oxidation module (see 7.D), becoming essentially a single module for both stabilization and oxidation, and being directly analogous to the conventional conversion modules.

A non-plasma, thermochemical stabilization processing concept was developed in FY 2006, but the residence time was still longer than desired. Investigation of plasma-based thermochemical stabilization has continued. In FY 2007, *the research team was finally able to demonstrate plasma-based stabilization.* Serendipitously, this discovery was prompted by observations made on the results of EB and UV stabilization. In its current development status, plasma stabilization seamlessly integrates with plasma oxidation and requires less than one-third of the conventional stabilization residence time.

UV Processing

UV processing potentially offers the combination of high line speeds with low capital cost. The chemistry is generally similar to that of EB, but very often UV requires a photoinitiator that would not be needed for EB cross-linking. One of the major challenges is whether UV radiation can deliver uniform cross-linking throughout the bulk volume of individual filaments as well as throughout the tow, with acceptable residence time. The UV processing development is being conducted at Clemson University with ORNL providing technical consultation and direction.

Table 1. Example data from various stabilization routes with Hexcel 3k PAN precursor. For multiple-step experiments, steps are tabulated in the order of completion.

Experiment	Process	Density, g/cc		Residence time, min	
		Before	After	Pass	Total
Thermal Stabilization, Thermal Oxidation	Thermal 1st Pass	1.19	1.33 - 1.34	26	53
	Thermal 2nd Pass	1.33 - 1.34	1.37 - 1.38	27	
Thermal Stabilization, Plasma Oxidation	Thermal stabilization	1.19	1.22 - 1.23	23	49
	Plasma oxidation	1.22 - 1.23	1.35 - 1.36	26	
UV Stabilization, Plasma Oxidation	UV stabilization	1.19	~ 1.20	2.25	28
	Plasma oxidation	~ 1.20	1.34 - 1.35	26	
	UV stabilization	1.19	~ 1.20	4.5	31
	Plasma oxidation	~ 1.20	1.35 - 1.36	26	
	UV stabilization	1.19	~ 1.20	6.75	33
	Plasma oxidation	~ 1.20	1.33 - 1.34	26	
	UV stabilization	1.19	~ 1.20	10	36
	Plasma oxidation	~ 1.20	1.33 - 1.34	26	
EB Stabilization, Plasma Oxidation	EB Protocol 1	1.19	~ 1.19	0.1	53
	Thermal anneal	~ 1.19	1.23 - 1.24	26	
	Plasma oxidation	1.23 - 1.24	1.36 - 1.37	27	
	EB Protocol 2	1.19	~ 1.19	0.3	53
	Thermal anneal	~ 1.19	1.27 - 1.28	26	
	Plasma oxidation	1.27 - 1.28	1.36 - 1.37	27	
	EB Protocol 3	1.19	~ 1.19	0.3	53
	Thermal anneal	~ 1.19	1.28 - 1.29	26	
	Plasma oxidation	1.28 - 1.29	1.37 - 1.38	27	
Plasma Stabilization, Plasma Oxidation	Plasma single pass	1.19	1.33- 1.34	26	26
	Plasma 1st pass	1.19	1.33- 1.34	26	53
	Plasma 2nd pass	1.33- 1.34	1.37 - 1.38	27	
	Plasma 1st pass	1.19	1.33- 1.34	26	106
	Plasma 2nd pass	1.33- 1.34	1.37 - 1.38	27	
	Plasma 3rd pass	1.37 - 1.38	> 1.40*	26	
	Plasma 4th pass	> 1.40*	> 1.40*	27	

* 1.40 g/cc is the maximum measurable density by the instrument used for these experiments

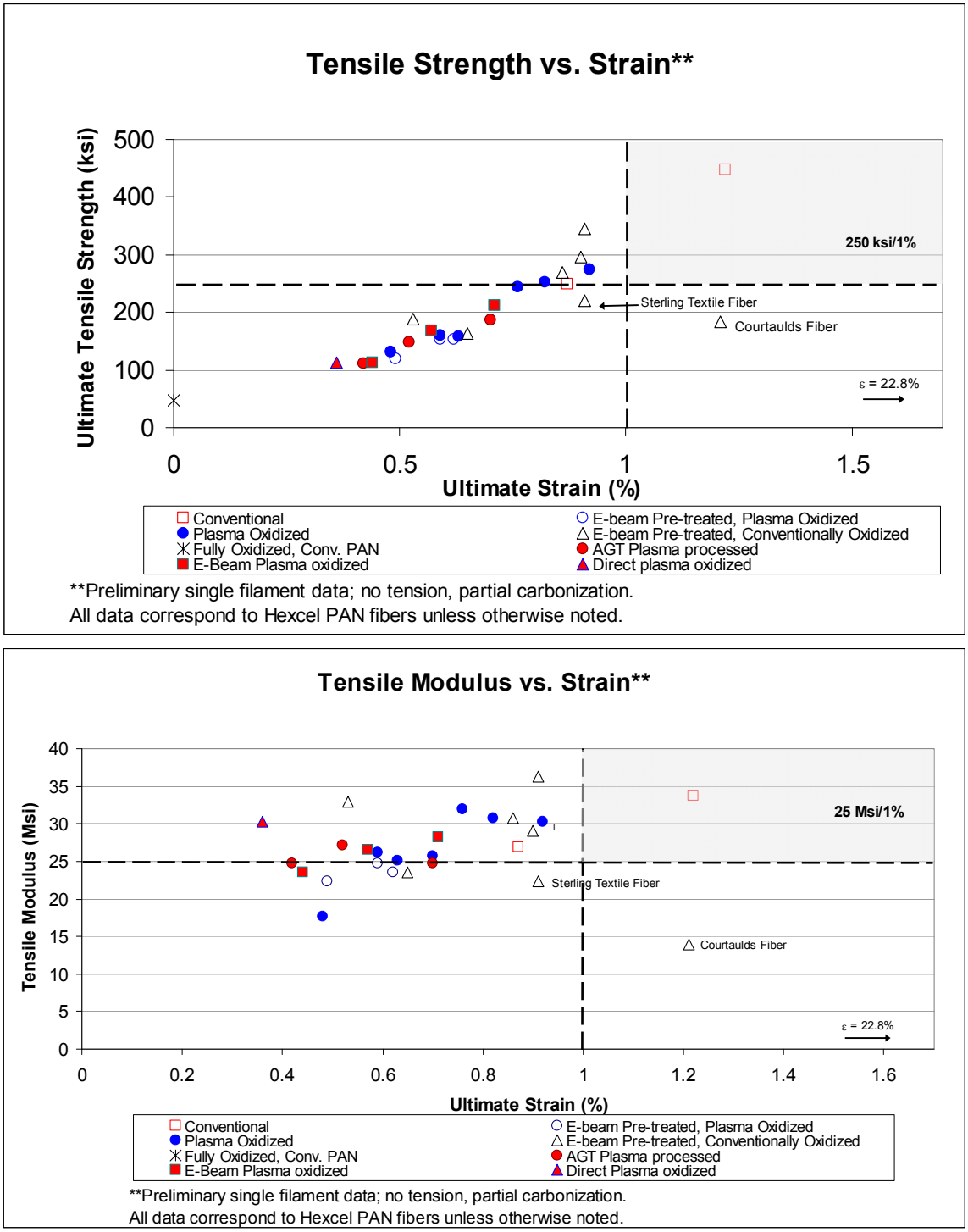

Figure 1. Mechanical properties of fiber specimens (tested by single-filament tensile strength method) converted by various routes. Conventional data points were thermally shocked and thermally ramped, respectively.

During FY 2007, effects of UV exposure were investigated in greater detail. As expected, increasing UV exposure produces increased cross-linking. The differential scanning calorimeter (DSC) thermogram is shown in Figure 2. In the latter half of FY 2007, continuous UV processing capability was developed. Uniform treatment throughout the tow is a problem, as illustrated in Figure 3, which shows DSC thermograms for UV-stabilized fibers taken from different parts of the same tow. The uniformity challenge has not been resolved to date, and we have not yet conceived a satisfactory approach to achieve uniform tow treatment with UV.

Stabilization Route Selection

A major FY 2007 milestone was to select one stabilization route for continued development.

The advanced stabilization project was started in late FY 2005 because we were then unable to achieve plasma stabilization, and at least light cross-linking was needed before plasma oxidation. In FY 2007, we finally discovered a plasma-stabilization recipe that delivers the necessary cross-linking without damaging the precursor fibers. Plasma stabilization seamlessly integrates with plasma oxidation and offers the same advantages as plasma oxidation. It is prudent to minimize the number of distinct technologies employed in the conversion line. Plasma stabilization was therefore selected as the primary stabilization route for further development.

EB stabilization offers, by far, the highest throughput per unit area of footprint. EB economies of scale are problematic in a conversion factory, but are well matched to implementation at a precursor factory, which typically runs at line speeds of order 100 m/min with factory capacities of order 100M lb/yr. There are scenarios where the precursor may be at least partially cross-linked in the precursor factory or a toll processing facility before shipment to the conversion factory. We are confident that with further development, we can resolve the free-radical problem and perhaps even learn to use it to advantage. E-beam stabilization was selected as the stabilization route for this scenario.

UV stabilization offers the potential for high line speeds at low capital cost. However, UV is fundamentally a surface phenomenon. We have observed that it cross-links the tow surface, but must depend on thermal or other means to cross-link the tow's interior. This can be readily overcome in laboratory experiments by tow spreading or other means to ensure that all fibers are irradiated. However, we think this is a fundamental limitation that is unlikely to be resolved at the production-scale within the program schedule. We are also concerned about the size and performance stability (UV lamp performance degrades significantly with time) of a UV-stabilization module. For these reasons, we have elected to discontinue the development of the UV-stabilization route.

Future Direction

We will focus our primary efforts on the development of plasma stabilization, its integration with plasma oxidation, and scaling of the plasma stabilization/oxidation technique. We will also continue development of EB stabilization as an option that can be implemented at the precursor factory or a toll-processing facility upstream of the conversion factory.

Patents and Publications

There was no new patent or publication activity during this period.

Education

Educational institutions participating in this project include Clemson University and the University of Tennessee. Clemson chemical engineering graduate students are conducting UV-processing studies under the direction of Professor Amod Ogale. UT materials science graduate students are providing characterization support to the project under the guidance of Professor Roberto Benson.

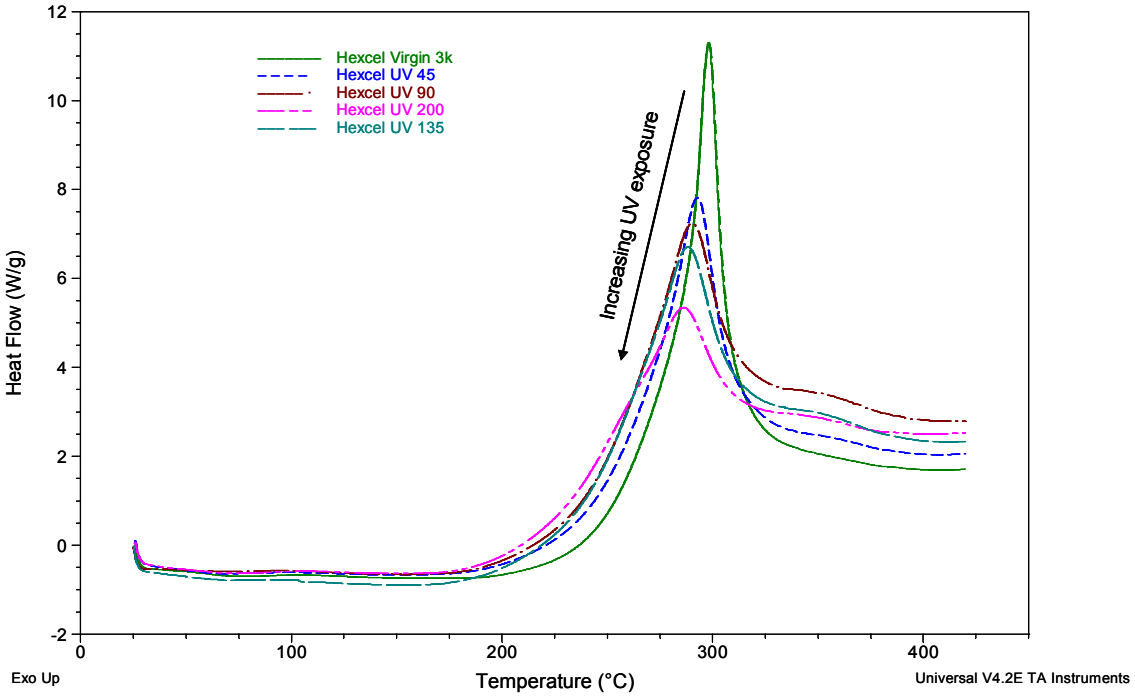

Figure 2. DSC thermogram of UV stabilized fibers showing the effect of increasing UV exposure.

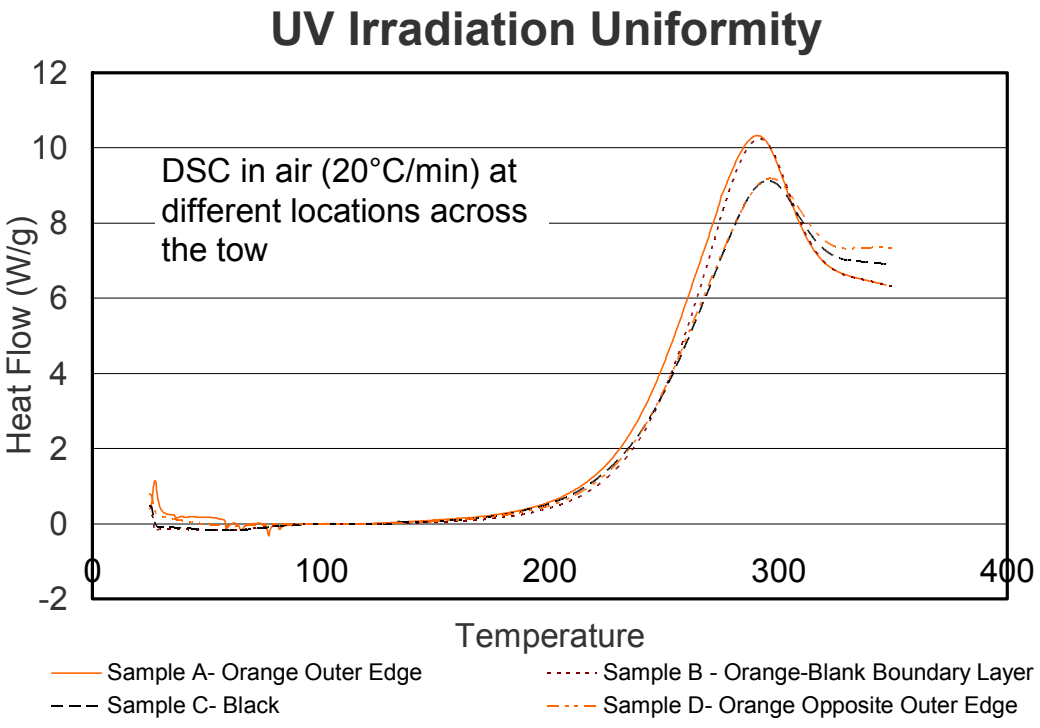

Figure 3. DSC thermograms from different parts of the same UV-stabilized tow sample.

Partners

ORNL gratefully acknowledges the following partners that have made valuable contributions to this project:

- Atmospheric Glow Technologies – plasma equipment design and processing (subcontract)
- Automotive Composites Consortium – programmatic and technical direction (complimentary)
- Clemson University – UV process development (subcontract)
- Hexcel Corporation – raw materials and technical consultation (complimentary)
- Radiation Dynamics Inc. – irradiation analysis, protocols, and beam time (complimentary)
- Toho Tenax America – raw materials and technical consultation (complimentary)
- University of Tennessee – characterization (subcontract)

Conclusions

Three prospective processing routes to lightly stabilize polymer precursors in an advanced carbon-fiber conversion line have been investigated. They are thermochemical, ultraviolet, and electron-beam processing. Thermochemical (plasma) stabilization has been selected as the stabilization route for use in a conversion factory. Electron-beam stabilization will be carried as an option for high throughput cross-linking upstream of the conversion factory.

---

[i] S. M. Cohn and S. Das, "A Cost Assessment of Conventional PAN Carbon Fiber Production Technology." Energy Division, Oak Ridge National Laboratory, TN (1998).

D. Advanced Oxidation of PAN Fiber Precursor

Principal Investigator: Felix L. Paulauskas
Oak Ridge National Laboratory (ORNL)
Oak Ridge, TN 37831-8048
(865) 576-3785; fax: (865) 574-8257; e-mail: paulauskasfl@ornl.gov

Project Manager, Composites: C. David Warren
ORNL
P.O. Box 2008, Oak Ridge, TN 37831-6065
(865) 574-9693; fax: (865) 576-4963; e-mail: warrencd@ornl.gov

Technology Area Development Manager: Joseph A. Carpenter
(202) 586-1022; fax: (202) 586-1600; e-mail: joseph.carpenter@ee.doe.gov

Expert Technical Monitor: Philip S. Sklad
(865) 574-5069; fax: (865) 574-6098; e-mail: skladps@ornl.gov

Participants:
Amit K. Naskar, Kenneth D. Yarborough, ORNL
Professor Joseph Spruiell, University of Tennessee
Daniel Sherman, Truman Bonds, Atmospheric Glow Technologies

Contractor: ORNL
Contract No.: DE-AC05-00OR22725

Objectives

- Develop an improved technique for oxidizing carbon-fiber (CF) precursor with reduced residence time, CF cost, and equipment footprint.
- Verify that finished fiber properties satisfy automotive requirements.
- Provide data for the preliminary evaluation of the cost impact of the new oxidation technique.
- Investigate interfaces and compatibility with other advanced conversion processes.

Approach

- Develop a process for polyacrylonitrile (PAN) precursor oxidation using atmospheric-pressure plasma.
- Develop fiber-handling protocols for continuous processing.
- Conduct parametric studies and perform diagnostics to correlate processing parameters and fiber properties.
- Characterize fibers to confirm that they satisfy program requirements.

Accomplishments

- Developed stable protocol for stabilization and oxidation of 3k virgin PAN precursor tow with atmospheric-pressure plasma in < 1/3 of conventional residence time.
- Demonstrated 0.3 m/min plasma-stabilization/oxidation line-speed using a continuous, single-pass process.
- Demonstrated 4-hour continuous reactor operating time.
- Demonstrated the capability to plasma oxidize 100+ m continuous length of 3k tow. Delivered 100 m of plasma oxidized, spooled 3k tow to each Automotive Composites Consortium (ACC) original equipment manufacturer (OEM).

- Carbonized fibers after plasma oxidation and measured mechanical properties.
- Upgraded the six-tube reactor with improved flow control, process monitoring, and data acquisition.
- Instrumented the six-tube reactor with gas monitors and analyzed gas composition at various locations as a function of process parameters.
- Commenced construction of a next-generation, single-cavity (multiple-pass), multiple-tow reactor that was ~ 60% complete at fiscal year end.
- Successfully oxidized fibers that were stabilized by different routes.

Future Direction

- Continue refining and scaling the reactor design and processing protocols to achieve high-speed, multiple-large-tow, semi-continuous (multiple-pass) plasma-oxidation process.
- Integrate plasma stabilization and plasma oxidation into a single conversion module.
- Acquire and implement new diagnostic tools. Conduct parametric studies and fiber characterization to better understand process effects and the processing window and to quantify fiber properties.
- Conduct rate-effect studies and update cost analysis.
- Investigate oxidation of alternative precursors.
- Investigate interface with microwave-assisted plasma (MAP) carbonization process and integrate into an advanced-technology pilot-line.

Introduction

The purpose of this project is to investigate and develop a plasma processing technique to rapidly and inexpensively oxidize polyacrylonitrile (PAN) precursor fibers. Conventional oxidation is a slow thermal process that typically consumes over 80% of the processing time in a conventional CF conversion line. A rapid oxidation process could dramatically increase the conversion-line throughput and appreciably lower the fiber cost. A related project has already demonstrated the potential for greatly increasing line speed in the carbonization and graphitization stages and rapid stabilization techniques are being developed, but the oxidation time must be greatly reduced to effect fast conversion. This project intends to develop plasma-oxidation technology that integrates with other advanced fiber-conversion processes to produce inexpensive CF with properties suitable for use by the automotive industry. Critical technical criteria include: 1) ≥ 25 Msi tensile modulus and ≥ 1.0% ultimate strain in the finished fiber; 2) uniform properties over the length of the fiber tow; 3) repeatable and controllable processing; 4) and significant unit cost reduction compared with conventional processing.

Project Deliverable

At the end of this project, the researchers will have developed an advanced oxidation process with residence time much less than that typical of conventional CF conversion lines. The advanced oxidation process will be sufficiently well understood and documented that the team can commence scaling it to develop a multiple, large-tow, oxidation module for an advanced-technology pilot-line.

Technical Approach

The researchers are investigating PAN precursor fiber oxidation using non-equilibrium, non-thermal plasma at atmospheric pressure. Plasma processing is thought to enhance oxygen diffusion and chemistry in the PAN oxidation process. Atmospheric-pressure plasma provides better control over the thermal environment and reaction rates than evacuated plasma, in addition to eliminating the sealing problems accompanying evacuated plasma processing. Various fiber characterization tools and instruments are used to conduct parametric studies and physical, mechanical, and morphological evaluations of the fibers to optimize the process.

Atmospheric-Pressure Plasma Processing Results

Exposure to plasma products at or near atmospheric pressure provides superior thermal control because the gas flow convectively heats or cools the fibers. This is deemed particularly important to avoid fiber melting from exothermic reactions. However, the short mean- free-path and lifespan of the chemically-reactive species at atmospheric pressure presents another set of challenges principally associated with finding a process recipe that delivers high process stability and short residence times.

In ORNL's conventional pilot-line, which represents the baseline process, PAN stabilization and oxidation occur in four successive furnaces in air, at temperatures increasing from about 200 to 250°C. Although there is not a precise transition from stabilization to oxidation, in general, one can consider stabilization to occur in the first furnace and (chemical) oxidation in the last three. So, in this project the researchers are working to reproduce the conversion advancement from the last three furnaces. The advancement from the first furnace is being addressed in the parallel advanced stabilization project. (See 7.C.)

At the end of fiscal year (FY) 2007, ~3X reduction in oxidation residence time and 0.3 m/min, single-pass line-speed was achieved in a six-zone reactor. Thus, the current tow speed in atmospheric plasma oxidation processing is more than twice the speed that was achieved at the end of FY 2006. Initial single-fiber mechanical data were generated, with results that fall short of property requirements but are encouraging at this stage of the development program.

During the first half of FY 2007, single fibers were carbonized after various combinations of stabilization and plasma oxidation and their mechanical properties measured. The results are shown in Figure 1, and do not differ substantially from previously reported results except that there are data from new combinations of stabilization and oxidation parameters. Despite the lack of fiber tension, tow-spreading, or controlled stretching during conversion and the low-temperature carbonization, plasma-oxidized fibers were generally about 25 Msi tensile modulus (25 Msi requirement) and ≥ 0.5% ultimate tensile strain (1.0% requirement). These values exceed expectations at this stage of the investigation and inspire confidence that the required properties will be exceeded.

PAN fiber tows with different stabilization histories were plasma oxidized and subsequently carbonized. Based on the mechanical properties of the final carbonized fibers, researchers were able to evaluate effectiveness of different stabilization routes. It was observed that under similar oxidation protocols, ultraviolet (UV)-stabilization resulted in weaker CFs with significant variation in the properties. It is thought that poor penetration of UV radiation through the bundle of filaments (masking effect) caused such variation. However, untreated PAN and electron-beam (EB) pretreated fibers after plasma oxidation and subsequent carbonization produced carbonized filaments with moderate properties.

Significant equipment and process modifications were made during this reporting period. The reactor system was redesigned and reconfigured with additional gas-flow control ports and process monitoring ports. Additionally, new process-monitoring equipment, specifically for monitoring concentrations of certain critical gas species, was purchased and installed. The data acquisition system was upgraded. Also, the fiber-transport system was upgraded to enable multi-pass operation for achieving higher line speeds, as well as single- or multi-pass processing of long tows. At the end of the reporting period, the researchers had demonstrated plasma oxidation in ~ 1/3 of conventional residence time (unchanged from the previous reporting period), with a multi-pass line speed of 0.3 m/min (up from 0.15 m/min previously), and four hours of continuous reactor operation (up from approximately one hour). The length of fibers processed was extended to continuous lengths which were terminal only to the required sample size. Semi-continuous, multi-pass oxidation was conducted to obtain spools of continuous tow > 100 m length. 100+ m of plasma-oxidized, spooled 3k tow was delivered to each ACC OEM.

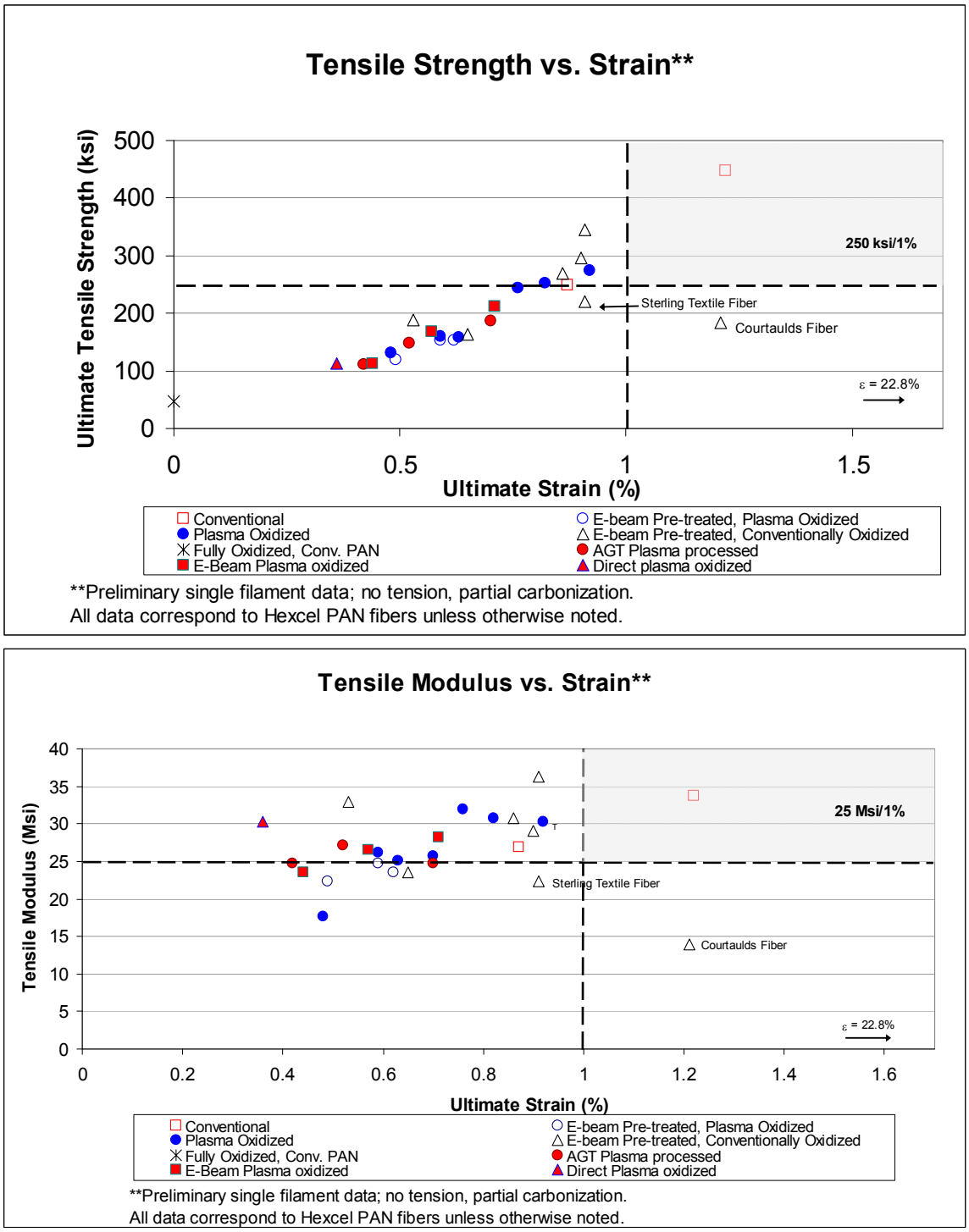

Figure 1. Mechanical properties of carbon fibers stabilized and oxidized by various routes, then conventionally carbonized at low temperature. There was no tensioning, controlled stretching, or tow-spreading during conversion. Conventional data points are for thermally-shocked and thermally-ramped heating protocols.

For the evaluation of composition, stability and consistency of the resulting atmospheric plasma, feed-gas analysis on heated tubes without fibers or reactive species (plasma) was conducted at several weekly intervals in the last half of FY 2007. The gas composition was found to be consistent throughout the temperature conditions tested.

A next-generation, single-cavity (multiple pass), multiple-tow reactor module was designed and partially constructed to ~ 60% completion at FY end. This reactor will be completed and used for scaling investigations starting in FY 2008.

For patent protection and export control reasons, equipment and process parameters are not published, but they are periodically disclosed to the relevant program managers in oral briefings.

Future Direction

During FY 2008, the project focus will shift from parametric studies with improved diagnostics to scaling to large multiple tows. The researchers will also carbonize plasma-oxidized fiber under more rigorous conditions (tension and temperature) using the new precursor evaluation system to validate its mechanical properties. We plan to complete the basic process development to the point that we can commence plasma-oxidation process and equipment-scaling investigations in FY 2008.

Patents and Publications

One invention disclosure was submitted on the development of PAN composition for accelerated stabilization and plasma oxidation.

Education

The materials characterization has been conducted in partnership with the University of Tennessee's (UT's) materials science department. UT graduate students were engaged to provide characterization support to the project.

Partners

ORNL gratefully acknowledges contributions to this project by Hexcel and TohoTenax America. Both have generously provided raw materials and offered technical consultation. Additionally, technical and programmatic consultation has been provided by the ACC.

Conclusions

Plasma oxidation of PAN fibers continues to progress toward the goal of reducing the cost of carbon-fiber manufacture. To date, the researchers have reduced oxidation residence time by ~ 3X compared to conventional oxidation, achieved 0.3 m/min line speed in a six-zone, multi-pass reactor configuration, and demonstrated four hours of continuous reactor operation. Plasma-oxidized fibers were carbonized and the mechanical properties checked, with good results considering the level of rigor applied and the current stage of process development. Continuous PAN 3k tow of >100 m length were plasma-oxidized in the reactor and 100 m spools of plasma oxidized 3k tow were delivered to each ACC OEM. Reactor system upgrades and new diagnostic capabilities made during this reporting period have enabled continued discovery and process improvements. Significant scaling experiments will commence in FY 2008.

E. Carbon-Fiber Systems Integration

Principal Investigator: Felix L. Paulauskas
Oak Ridge National Laboratory (ORNL)
P.O. Box 2008, Oak Ridge, TN 37831-8048
(865) 576-3785; fax: (865) 574-8257; e-mail: paulauskasfl@ornl.gov

Project Manager, Composites: C. David Warren
ORNL
P.O. Box 2008, Oak Ridge, TN 37831-6065
(865) 574-9693; fax: (865) 576-4963; e-mail: warrencd@ornl.gov

Technology Area Development Manager: Joseph A. Carpenter
(202) 586-1022; fax: (202) 586-1600; e-mail: joseph.carpenter@ee.doe.gov

Expert Technical Monitor: Philip S. Sklad
(865) 574-5069; fax: (865) 574-6098; e-mail: skladps@ornl.gov

Principal Team Members:
Timothy S. Bigelow, Cliff Eberle, Stanley C. Forrester, Amit K. Naskar, C. David Warren, Kenneth D. Yarborough, ORNL
Mohamed Abdallah, MGA Advanced Composites and Engineering
Ana Paula Vidigal, Paolo Correira, José Contreiras, FISIPE SA

Contractor: ORNL
Contract No.: DE-AC05-00OR22725

Objectives

- Develop a sub-scale, modular test facility for demonstrating advanced carbon-fiber (CF) conversion technology.
- Integrate advanced-technology conversion modules into a functional and reliable system.
- Validate system process models and system inputs into cost analyses.
- Provide a capability for developing and testing conversion protocols for new polymer precursors.
- Provide the capability to produce small quantities of finished CF.
- Demonstrate advanced conversion technology to prospective commercialization partners.

Approach

- Procure and install a sub-scale, conventional CF pilot-line.
- Construct a prototypical, advanced-technology CF line using equipment and process specifications developed in other CF-conversion projects.
- Locate the advanced-technology and conventional lines adjacent to each other, highly instrument them for process characterization, and equip them with versatile fiber-transport equipment.
- Develop a small tube-furnace system for developing and evaluating conversion processes for prospective precursor fibers available in quantities of a few grams or less.

Accomplishments

- Continued making upgrades and performance improvements to the conventional pilot-line. Completed installation of carbon-proofing enclosures and modification of gas-supply and exhaust ducting to enable continuous operation. Implemented fully-programmable, automatic control. Partially completed implementation of a web-interfaced monitoring capability.
- Completed and approved safety basis for permanent, continuous operation of conventional pilot-line (previously approved on a run-by-run basis) and precursor-evaluation system.
- Initiated work on full-scale development of textile polyacrylonitrile (PAN) precursor.
- Completed a technical evaluation of the pilot-line and laboratory capabilities of Portuguese textile-PAN-fiber manufacturer FISIPE SA and entered into a partnership with them to scale-up and commercialize textile-PAN precursor technology.
- Down-selected a preferred textile-PAN/vinyl acetate (VA) chemical composition from among numerous candidate chemical compositions.
- Procured, installed, commissioned, and commenced operating a precursor-evaluation system.

Future Direction

- Defer further funding of the integration project until stabilization and oxidation modules are scaled sufficiently to construct and operate laboratory-scale pilot equipment.
- Redirect integration funding to new projects to support full-scale development of textile PAN precursor, maintenance and operation of equipment for delivering material samples to the Automotive Composites Consortium (ACC), and performing proof-of-concept investigations.
- Resume integration project when the various conversion technologies are more mature and sufficiently scaled to plug into a laboratory-scale, advanced-technology pilot-line.

Introduction

The purpose of this project is to integrate advanced CF technology developed in the Low-Cost Carbon Fiber (LCCF) initiative under Lightweighting Materials. The project encompasses the acquisition and operation of conventional conversion technology for benchmarking and validation; integration of advanced-technology conversion modules into a functional system; and developing and/or evaluating conversion protocols for prospective precursors.

A small pilot facility will be designed specifically for processing tows of commercial-grade (large-tow) fiber but will be sufficiently versatile that it can potentially process some higher-strength fibers. It will be designed to process a variety of polymer precursors. It may be adaptable to pitch precursors (this would require equipment and process modifications), but that is not a project requirement.

The heart of the pilot-scale conversion facility will be two adjacent, sub-scale, CF-conversion lines. One line will be based on conventional pre-treatment, conversion, and post-treatment processes and the other will embody advanced-technology processes. The facility will be highly instrumented for characterizing fiber properties and process parameters. It will also be highly modular and be equipped with versatile tow-transport equipment so that tows can be routed through any combination of conventional and advanced- technology conversion, pre-treatment, or post-treatment modules. The systems-integration line will be capable of running a single tow or any number of tows up to its maximum capacity which will be at least five 50k tows. The integration line may eventually be mated with upstream or downstream processes. The facility is shown schematically in Figure 1. Essential advanced-technology modules are stabilization, oxidation, and carbonization. Optional advanced-technology modules include graphitization, surface treatment, advanced instrumentation and control, and downstream processing. The integration line will use conventional pre-treatment, sizing, and fiber-transport equipment.

New precursor development projects initially produce much smaller quantities of precursor fibers than are required by the aforementioned pilot-lines. Therefore, a precursor-evaluation system has been assembled for evaluating small quantities of prospective precursors and developing their conversion protocols.

It has become apparent that it will be multiple years before advanced stabilization and oxidation technologies are ready for integration. Therefore, the integration project will be temporarily halted after fiscal year (FY) 2007, to be resumed when those technologies are ready for integration. Beginning in FY 2008, the integration funding will be redirected to commercialization of textile-PAN precursor and operational support for the precursor-evaluation system. The commercialization of textile-PAN precursor received very significant effort this year and that progress is reported herein.

Project Deliverables

At the end of this project, advanced-technology modules will have been assembled into a functional, prototypical CF-conversion line with 5 – 10 large-tow capacity and alternative precursor-conversion protocols will have been developed and/or evaluated. The following tasks will have been completed:

- Confirm that advanced-technology conversion modules work together as a functional system.
- Determine interfaces to optimize system cost and performance.
- Determine and/or characterize system processing envelope, utility requirements, effluent streams, etc.
- Demonstrate system process control, stability, repeatability, scalability, safety, and reliability/availability/maintainability.
- Investigate system fault tolerance and response.
- Evaluate alternative precursor fibers and develop conversion protocols for selected precursors.
- Scale alternative precursor tow sizes and validate their conversion at the pilot-scale.
- Validate that program cost and technical targets were achieved.

Completion of these tasks should sufficiently demonstrate the advanced technology's value, robustness, and scalability to convince an industrial partner to commercialize it.

Current Status

Conventional Pilot-Line

In FY 2007, we completed critical upgrades to the conventional pilot-line. The most important of these were the addition of carbon-proofing enclosures around the take-up winders and sizing module to prevent the generation of airborne carbon particulate that might compromise the operation of nearby high-voltage equipment. Also, the gas supply was changed from compressed-gas bottles, requiring frequent bottle changes, to a large dewar that will support many days of continuous operation. Figure 2 shows the conventional pilot line installed at ORNL.

The previous owner of the pilot-line did not find it necessary to automate its operation. They run a 24/7 production facility, so it is quite simple for production operators to make manual adjustments to the pilot-line during its startup, operation, and shutdown. By contrast, ORNL research is a single-shift operation. Therefore, automation is necessary to enable safe and effective, single-shift operation. In FY 2007, we developed fully-programmable, automatic-control capabilities that will enable safe, unattended system warm-up and standby, enabling us to conduct experiments in a single-shift operation. We also partially completed the implementation of a web-interfaced monitoring system that will allow us to monitor warm-up and cool-down from our office or home computers via a web interface.

Advanced-Technology Pilot-Line

The microwave-assisted plasma (MAP) carbonization module is the base module for the advanced-technology integration line. Other modules will later be added to it. It is now in place and operational.

During this period, MAP-carbonized tow and plaques were made and delivered to the ACC for independent evaluation of mechanical properties. High-speed winders and tensioners are needed to support operation at the bandwidth (number of tows) and range of speeds targeted for the conventional and advanced-technology lines.

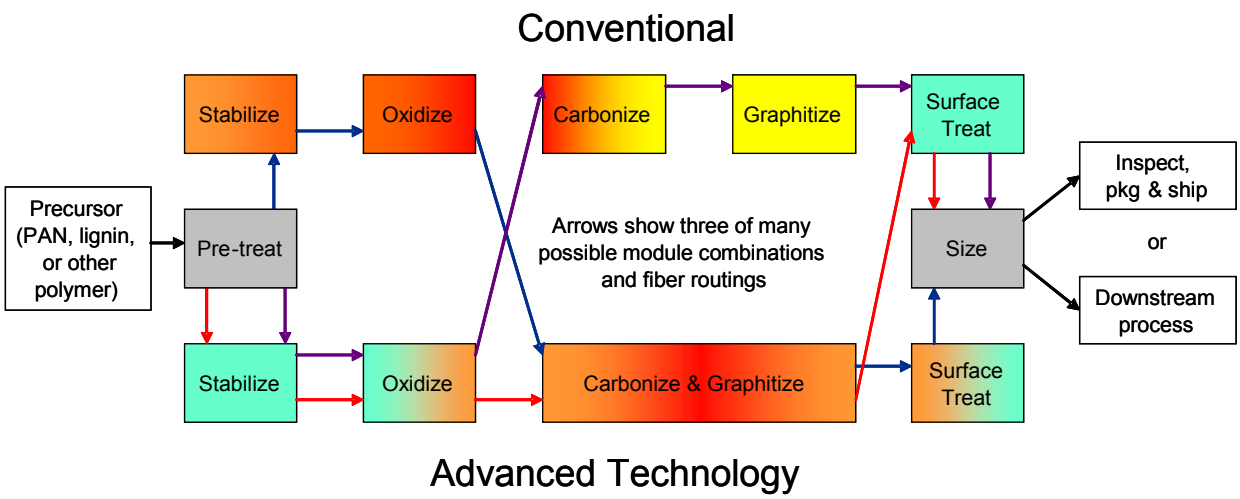

Figure 1. Schematic of carbon-fiber pilot-lines.

Figure 2. Conventional pilot-line installation at ORNL.

Acquisition was planned to commence in FY 2006; however, budget reprioritization delayed acquisition
by a year. Winder specifications were developed in FY

2006 and reviewed in early FY 2007. The winder package procurement was released in the third quarter of FY 2007, satisfying a project milestone. The winder package should be received in FY 2008, quarter 2. We also commenced fabrication and installation of an improved MAP cooling system in FY 2007.

Because the stabilization and oxidation modules still require significant development before they are ready to integrate to the MAP carbonization module, advanced-technology integration will be deferred indefinitely and its budget will be redirected to other low-cost CF activities.

Precursor-Evaluation System

Due to its size, the aforementioned pilot facility requires ≥ 1k tows at least 50-m long. The tensioning system is designed for large tows and is, therefore, not sufficiently precise to accurately tension small tows and is likely to break tows smaller than about 1k. Startup time for the conventional pilot-line graphitization furnace is at least 10 hours, so restringing and restarting after tow breakage requires many hours. This is incompatible with the need for inexpensive, fast- turnaround precursor evaluations. New precursor-development projects need many intermittent trials on very small tows, as they usually extrude one or a few filaments in short lengths for initial testing. The conventional pilot-line is not amenable to this kind of operation; therefore, a precursor-evaluation system based on compact tube furnaces and precision tensioners was commissioned for evaluating prospective precursors and developing their conversion protocols. The precursor-evaluation system has rapid start-up/shutdown capabilities and is capable of heat-treating short lengths of single filaments or a single tow from a few filaments up to large tow size. Controlled tension can be applied to tows larger than approximately 10 - 20 filaments. Tows too small for controlled tensioning can be “restrained” to provide some tension. Short fiber lengths can be readily transported through the system on trays or similar compact carriers.

The precursor-evaluation system design commenced in FY 2006. In FY 2007, we completed the design, procured and installed the furnaces and transport equipment, commissioned the system, and began operations. Figure 3 shows some of the tube furnaces awaiting installation.

Figure 3. Continuous stabilization/oxidation (in furnace at right) and low-temperature carbonization (in furnace at left) of conventional 3k PAN precursor tow in precursor-evaluation system.

Textile-PAN Precursor Scale-Up

Our evolving understanding of the probable costs and risks of various candidate precursors, coupled with the emergence of new partnership opportunities and the continued capacity constraints in the CF market, prompted us to revisit the textile-PAN technology that was mothballed in 2004. Therefore, in the first half of FY 2007, we began preliminary planning to scale-up the textile-PAN precursor technology that was originally developed by Hexcel under the LCCF initiative, and in the last half of FY 2007 we worked aggressively toward textile-PAN scale-up. We have established a highly-interactive and mutually-beneficial partnership with Portuguese textile fiber manufacturer FISIPE SA, and are in serious discussions with two other prospective commercialization partners. FISIPE has installed a chemical-treatment unit in their pilot-line. ORNL has conducted extensive characterization of precursor chemical composition and extruded filaments generated by FISIPE, as well as conversion trials on filaments and tows generated by FISIPE from selected precursor chemical compositions. An example differential scanning calorimeter (DSC) characterization is shown in Figure 4. We have selected a preferred chemical composition that is the baseline for future work. At FY's end, FISIPE was making multiple spools of chemically-treated 26k tow at 1 – 2 kg of fiber per spool. This fiber will then be used for conversion trials on ORNL's precursor-evaluation system and pilot-line.

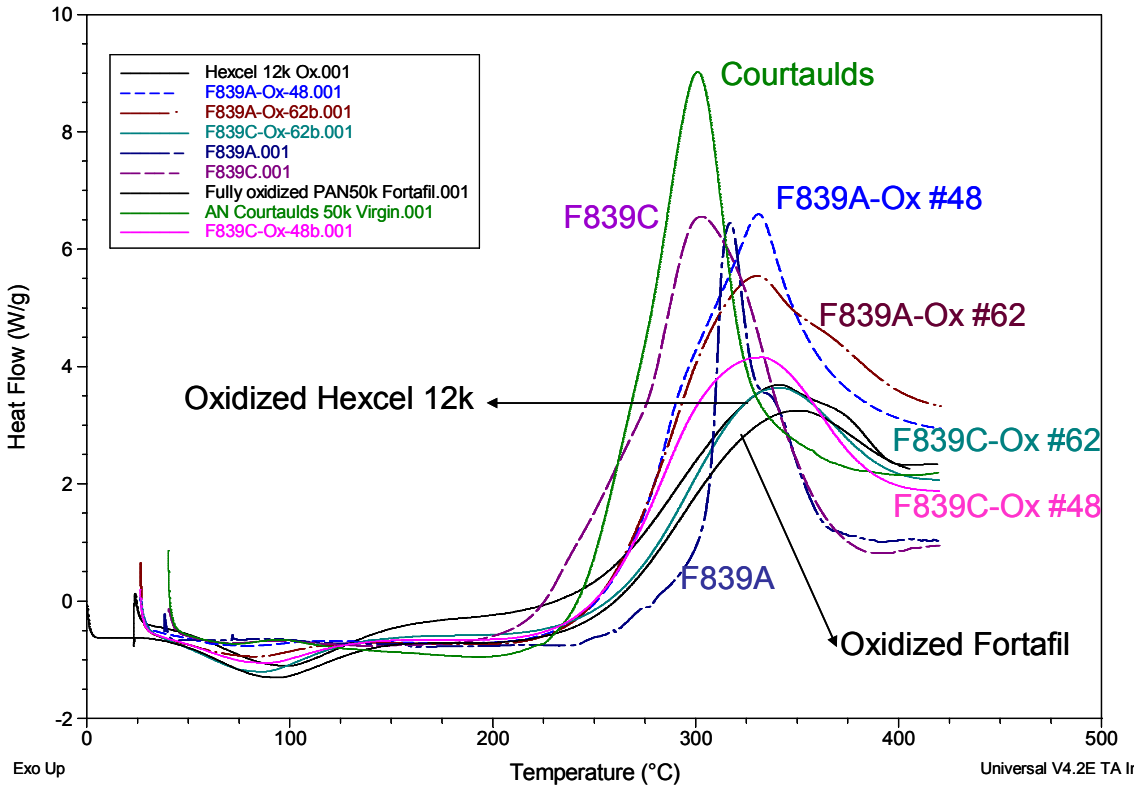

Figure 4. DSC characterization of various oxidized textile-PAN precursor compositions and comparison to oxidized commercial precursors.

Future Direction

The integration project will be deferred until stabilization and/or oxidation modules are ready to integrate into an advanced-technology pilot-line. The integration budget will be reallocated to support textile PAN-precursor scale-up, materials sampling, proof-of-concept investigations, and/or other LCCF work.

Conclusions

Several pilot-line modifications were completed, and the development of a web-based monitoring capability is almost complete. A precursor-evaluation system was installed and commissioned, and is already being gainfully utilized. Further integration of an advanced-technology pilot-line will be deferred until stabilization and oxidation modules are more mature. Full-scale development of textile-PAN precursor was initiated and is now well underway.

Presentations/Patents/Publications

None.

8. POLYMER COMPOSITES R&D

A. Automotive Composites Consortium Focal Project 4 (ACC 007[i])

Principal Investigators: Libby Berger
General Motors Corporation
Research & Development
MC 480-106-710
30500 Mound Road
Warren, MI 48090-9055
(586) 986-1177; fax: (586) 986-1207; e-mail:libby.berger@gm.com

John Jaranson
Ford Motor Company
Vehicle Design R&A
2101 Village Road MD 3137
Dearborn, MI 48121
(313) 390-5842; fax:(313) 337-5581; e-mail: jjaranso@ford.com

Field Project Manager, Composites: C. David Warren
Oak Ridge National Laboratory (ORNL)
P.O. Box 2009, Oak Ridge, TN 37831-8050
(865) 574-9693; fax: (865) 574-0740; e-mail: warrencd@ornl.gov

Technology Development Manager: Joseph Carpenter
(202) 586-1022; fax: (202) 586-1600; e-mail: joseph.carpenter@ee.doe.gov

Field Project Officer: Aaron D. Yocum
(304) 285-4852; fax: (304) 285-4403; e-mail: aaron.yocum@netl.doe.gov

Expert Technical Monitor: Philip S. Sklad
(865) 574-5069; fax: (865) 576-4963; e-mail: skladps@ornl.gov

---

Contractor: U.S. Automotive Materials Partnership (USAMP)
Contract No.: DE-FC-59OR22545 through the DOE National Energy Technology Laboratory

---

Objectives

- Guide, focus, and showcase the technology research of the four Automotive Composites Consortium (ACC) working groups (Materials, Processing, Joining, and Energy Management).
- Design and fabricate structural automotive components with reduced mass and cost, and with equivalent or superior performance to existing components.
- Develop new composite materials and processes for the manufacture of these high-volume components.

Approach

- Design, analyze, and fabricate a structural composite underbody and assemble it into a donor-vehicle structure, focusing on:
  - A 2 ½-minute cycle time (at 100,000 units per annum (upa), 2-shift operation).

  - Methods of joining and assembly of the underbody to the vehicle.
  - Processes for fabricating localized areas of oriented reinforcement within the time window.
- Design, analyze, and fabricate a second-row composite seat (with and without an integrated restraint system (SIR and STD, respectively)) which will combine the functions of a seat and a load floor.

Accomplishments

- Selected glass-fabric sheet molding compound (SMC) with a high-elongation core as our material and process system (MPS) based on mass and cost considerations, demonstrated manufacturing feasibility, and measured initial material properties for this system.
- Developed design methodologies to achieve acceptable performance for Full Frontal, Frontal Offset Deformable Barrier, Side, and Rear Offset Impact, and completed computer-aided engineering (CAE) stiffness, crash-performance, and mass assessments.
- Completed a CAE study on weld-bond modeling and a performance-sensitivity study.
- Completed a technical cost model for the selected MPS.
- Achieved a seat design that meets load requirements for front impact (Federal Motor Vehicle Safety Standard (FMVSS) 2076/210) with a cushion that is 30% lighter and a seat back that is 16% lighter than the comparator average.

Future Direction

- Begin Phase 2, the detailed design of the underbody, including manufacturing and assembly, for the composite underbody.
- Concept development of the weld-bonded joint, including detailed design, analysis, and test validation.
- Further manufacturing demonstration of the selected MPS, with cycle-time analysis, and determination of durability and high strain-rate properties.
- Continued investigation of nondestructive evaluation (NDE) techniques for manufacturing quality and durability.
- Complete additional load-case CAE analysis to confirm composite seat design.
- Complete cost model and analysis of the ACC seat and the Ecole Polytechnic Federale de Lausanne (EPFL) thermoplastic programmable powdered preform process (TPP4) seat.

Introduction

This project encompasses two components, a composite underbody and a lightweight composite seat, with unique goals with respect to vehicle volume per annum (VPA), physical size, materials, and technology development. They both require structural performance with reduced mass and acceptable cost, and with equivalent or superior performance to existing components.

Structural Composite Underbody

The structural composite underbody is targeted to be part of the USAMP Multi-Material Vehicle (MMV) project (see 12.D), and will follow the MMV vehicle technical specifications. The primary research outcomes of this project are:

- A 2 ½-minute cycle time (100,000 upa, 2-shift operation).
- Developing methods of joining and assembly of the underbody to the vehicle.
- Processes for fabricating localized areas of oriented reinforcement within the time window.

Phase 1 of this project was the selection of the materials and processes for the underbody which involves:

- The development of a design concept, including a means of joining and assembly.
- The preliminary design of the concept using three material and process systems,
- The selection of an MPS based on
  - Manufacturing considerations

    - 2 ½ minute cycle time
    - Joining and assembly feasibility
    - Technical feasibility
  - Compatibility with MMV goals
  - Technical cost model analysis

Phase 2 will be full design, incorporating other components of the MMV, based on a Large Rear-Drive Vehicle (LRDV).

Phase 3 will be fabrication of the underbody and assembly to the donor-vehicle structure.

In Phase 1, a preliminary composite underbody design was developed to replace the steel assembly from a production steel LRDV donor vehicle. The preliminary design takes into account three proposed MPS candidates, general vehicle packaging, assembly and joining requirements. The vehicle-level stiffness performance with the composite underbody is required to have equivalent performance to the LRDV, while crash performance is required to meet applicable government and industry requirements.

The deliverable for this phase is the selection of a material and process system, based on a concept design that is suitable for predicting preliminary CAE-based structural performance and mass reduction, conducting technical cost modeling, and further Phase 2 detail design and development.

One concern which has been raised about structural applications of composites is how to ensure quality, both after initial manufacture and through day-to-day durability degradation or low-energy crash events. At what point are they no longer capable of carrying crash loads? This will require development of NDE techniques that are low cost, robust, and easy to use. Examples of techniques which we will be evaluating for further development are thermal wave imaging, embedded microspheres encapsulating a fluorescent die, embedded fiber-optic mesh, and "coin tap" techniques.

Composite Design Concept

Multimatic, the design and analysis supplier for this Phase, examined the benchmark steel vehicle underbody (see Figure 1) to determine the basic construction, attachment requirements, parts count, material selection and gage.

The basic philosophy for designing the preliminary composite design was to:

- Integrate as many components as possible
- Increase section sizes where possible
- Avoid large structural cores
- Consider metallic components for hardpoints and welded attachments
- Optimize material selection based on performance / mass / cost trade-off.

Based on an evaluation of the donor-vehicle design, two composite concepts were proposed for further evaluation (see Figure 2). The first concept was a single-piece molded floor with ribs for maximum manufacturing efficiency, and the second concept was a bonded assembly for maximum structural efficiency.

The team selected the ribbed concept as the primary design direction due to the program cycle time requirements and the desire for minimum cost. The development of this concept is the subject of this report.

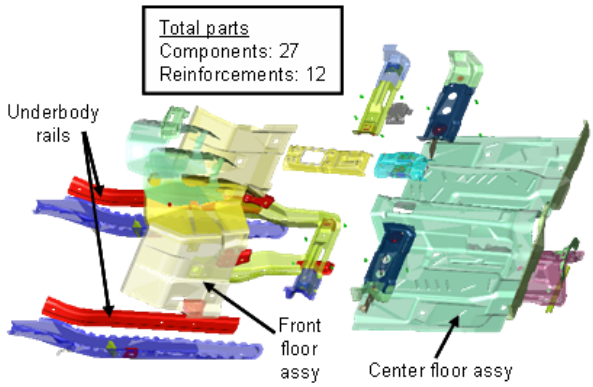

Figure 1. Exploded view of the benchmark steel underbody assembly.

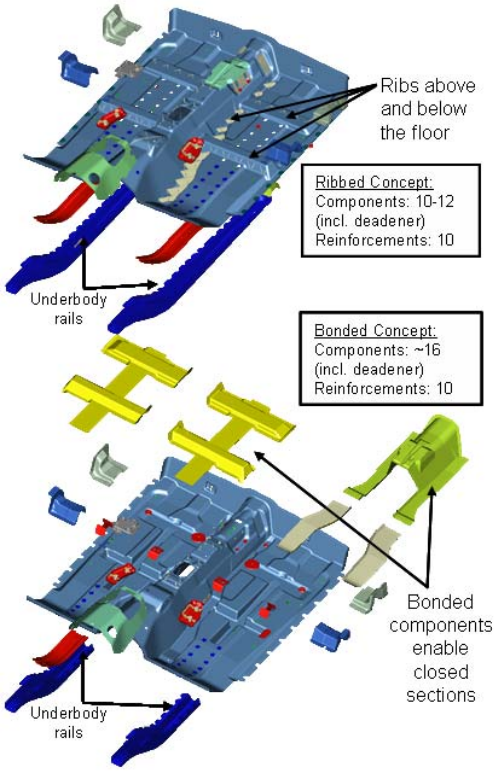

Figure 2. Ribbed and bonded design concepts.

Vehicle Assembly / Joining

Traditional composite structures are often manufactured as bonded assemblies to meet structural requirements. In optimal, lightweight, multi-material designs, structural bonding provides enhanced seam integrity, gap-bridging or tolerance functions and galvanic separation. In the high-volume automotive environment, cycle time, body-shop assembly process compatibility, and structural performance are all key requirements, and welding is a primary joining technique. The combination of welding and bonding, weld-bonding, is currently being implemented in OEM body designs and assembly plants as a means of increasing stiffness, reducing mass, and improving durability. Weld-bonding is currently envisioned as the primary joining process to meet the complex automotive requirements for the composite underbody. Specifically, the concept is either to embed or otherwise attach metallic inserts or doublers to the composite to enable spot welding to the surrounding steel structure as well as to attach the structural underbody rails to the composite floor (see Figure 3). The joints would be bonded prior to spot welding. Not only would this provide compatibility with current body-shop welding processes for installing the underbody itself, but the spot welds would also serve as peel stoppers in the adhesive joints, provide fixturing during adhesive cure, and enhance overall joint durability and robustness.

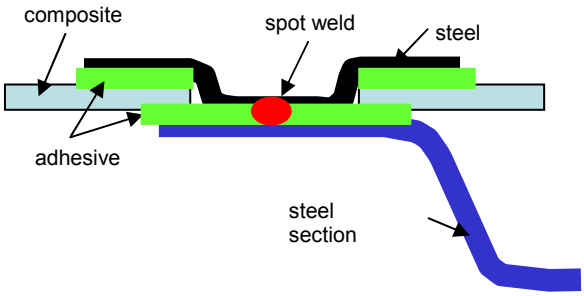

Figure 3. Weld-bonding concept for steel bonded to composite, using a metal doubler.

Computer-Aided Design (CAD) Model

A three-dimensional (3-D) CAD model of the preliminary ribbed design concept was developed to assess structural performance using CAE methods. The model represents the proposed joining concept and component integration. Material thickness and selection are MPS-specific and will be discussed in the following sections.

CAE Performance Assessment

The model was integrated into the full-vehicle noise-vibration-harshness (NVH) (NASTRAN) and crash models (LS-DYNA) for the donor vehicle.

The structural performance of the composite underbody was assessed as an integral part of the full LRDV vehicle. For Phase 1, the following key development load cases were considered:

- Body-in-White (BIW) static torsional and bending stiffness and modal response
- New Car Assessment Program (NCAP) 35-mph Full Frontal Impact
- EuroNCAP/ Insurance Institute for Highway Safety (IIHS) 40-mph Frontal Offset Deformable Barrier (ODB)
- Federal Motor Vehicle Safety Standard (FMVSS) 214 33.5-mph Side Impact
- FMVSS301 50-mph Rear Offset Impact

Material Properties

For the initial design assessments, the ACC-provided surrogate static room-temperature material properties which were used to represent candidate material systems pending the availability of physical test data from molding trials. The primary materials under consideration were fiberglass composites, either randomly oriented or with fabric. Randomly-oriented and fabric-carbon-fiber composites were evaluated to gain insight into maximum potential mass savings. Surrogate material property data were selected based on fiber volumes that could be reasonably achieved for the target MPSs. During the latter stages of Phase 1, the tensile and compressive properties were updated for some candidate materials as preliminary test data became available. Four composite material reinforcement systems were evaluated: (a) random fiberglass with a core, (b) glass fabric, (c) glass fabric with a core, and (d) carbon fiber with a core, where the core is a low-density/high strain-to-failure composite. In these evaluations, processing was not considered.

Global Stiffness Performance

Several vehicle-level stiffness and modal studies were conducted before selecting the ribbed design concept direction. Random fiberglass composite material properties were applied to the geometry of the benchmark steel model to evaluate the effect on the global BIW performance. These studies concluded that global vehicle stiffness is relatively insensitive to the floor stiffness as long as a minimum threshold stiffness is achieved. Assessments of the final four composite material system selections confirmed that the static torsional BIW stiffness increased by up to 4.6%, and the static bending stiffness decreased by up to 2.6% relative to the baseline vehicle. The first bending and torsional modes were within 0.05 Hz of the baseline vehicle.

However, once the first vehicle crash simulations were run, it was found that the requirements to meet crash performance overshadowed the requirements for the vehicle-level stiffness performance. Hence, the effort to develop feasible composite designs to meet crash requirements was prioritized.

Vehicle Crash Performance

Based on the results for the preliminary composite underbody stiffness model and the CAD model for the ribbed composite design concept, an initial LS-DYNA crash model was developed. The composite materials were represented by the MAT58 material model which requires orthotropic stiffness and strength properties, as well as several parameters that govern the post-failure material response. The required parameters were selected based on the surrogate material data, engineering judgment, and several model sensitivity studies. Further material development and test correlation will be needed for the selected materials in Phase 2.

Initial vehicle-level crash simulations indicated that the most severe loading case for the underbody floor structure was the EuroNCAP/IIHS 40-mph Frontal ODB case. The initial studies indicated that the thicknesses required to meet global stiffness were insufficient for maintaining integrity of the structure during crash. To achieve acceptable crash performance, the most mass-effective methods were:

- Optimizing the local material thickness and orientation to keep the strain levels sufficiently low to avoid net section material failure, while allowing localized failure
- Adding a low-density, high strain-to-failure core material such as high-modulus polypropylene (HMPP) to the laminate with a thickness of up to 2.5 mm in strategic regions of the floor
- Allowing the driveshaft to telescope an additional 70 mm
- Reducing the thickness of the carry-over steel underbody rail components
- Reducing the ribbing height and deleting ribbing in some locations.

Using the above methods and an iterative design process, acceptable Frontal ODB crash performance was achieved for the composite under-bodied LRDV with all-composite material systems that were considered. Acceptable performance was defined as the absence of any net section failures, with a small amount of localized material damage deemed acceptable.

Upon meeting the crash performance requirements for the frontal ODB case, the four materials systems were evaluated for all four crash-load cases outlined above. Some additional adjustment to the lay-ups was required to meet the full frontal impact and to account for the as-tested material properties before achieving acceptable performance.

By the end of the Phase 1, a total of 225 crash simulations (165 Frontal ODB, 19 full-frontal, 26 side-impact, and 15 rear-impact crash) and 44 global-stiffness analyses were conducted to arrive at a feasible lower mass solution for each material system design.

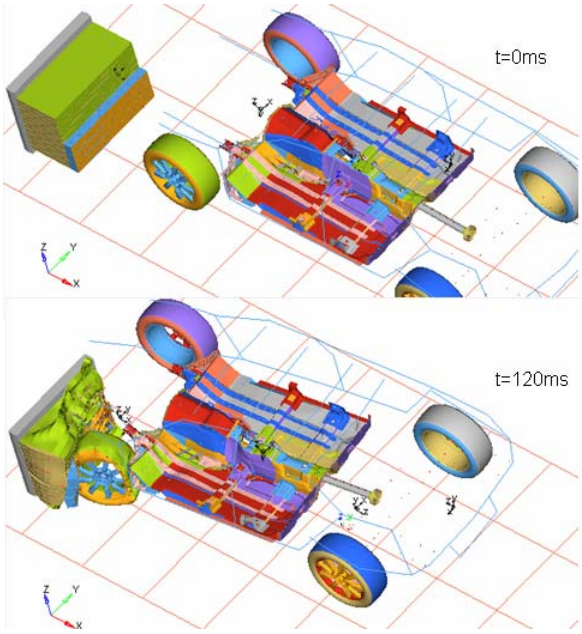

Figure 4. Front OBD – Predicted deformed shape for proposed composite underbody.

A Frontal ODB crash model setup and representative deformations for a fiberglass-fabric composite design are shown in Figure 4. Note that full vehicle crash models were used in the simulations but only the floor structure, wheels, and a wire frame representing the vehicle outline are shown in the figure. As can be seen in the figure, the offset barrier imparts a severe compressive and shearing load in the vehicle which results in local damage and intrusion in the floor structure. A corresponding representative damage plot is shown in Figure 5. The red areas in the damage plot indicate regions of localized material damage due to impact. The crash pulses for the composite underbody designs were found to be compatible with typical occupant restraint systems.

Thickness and Mass

A representative map of the material thicknesses and orientations required to achieve acceptable crash performance for a representative all-fiberglass-fabric underbody design proposal is illustrated in Figure 6. The total material thickness, the core thickness, and fiberglass-fabric composite thicknesses are indicated in the figure. The total material thickness for the final four MPS designs ranges from 1.6 mm to 8.1 mm.
The mass for all the material system designs are compared to the benchmark steel structure mass in Table 1.

Table 1. Representative underbody and mass breakdown.

Trial	Description	Total (Floor & Rails)			Floor Only			Rails Only		
		Mass*	Reduction		Mass	Reduction		Mass	Reduction	
		kg	kg	%	kg	kg	%	kg	kg	%
1098	Baseline steel	68.5	0.0	0%	44.9	0.0	0%	23.6	0.0	0%
1190	Fiberglass random, 2.5mm core, reduced rail thickness, telescoping driveshaft	61.2	-7.3	-11%	39.6	-5.3	-12%	21.6	-2.0	-9%
1175	Fiberglass fabric, reduced rail thickness, telescoping driveshaft	55.9	-12.6	-18%	35.6	-9.3	-21%	20.3	-3.3	-14%
1177	Fiberglass fabric, 1.0mm core, reduced rail thickness, telescoping driveshaft	53.6	-14.9	-22%	33.3	-11.6	-26%	20.3	-3.3	-14%
1188	Carbon fabric, 1.0mm core, reduced rail thickness, telescoping driveshaft	52.0	-16.5	-24%	31.7	-13.2	-29%	20.3	-3.3	-14%
	*Note: includes 14.1 kg of non-composite mass									

The results indicate a total mass reduction potential of 7.3 to 16.5 kg vs. the total 68.5 kg baseline steel structure mass, which includes a secondary 2.0 to 3.3 kg mass reduction as a result of a gage reduction in the carry-over design steel underbody rails. Considering only the floor (not accounting for the reduction in the rails) gives a mass reduction of 5.3 to 13.2 kg, or up to 29%.

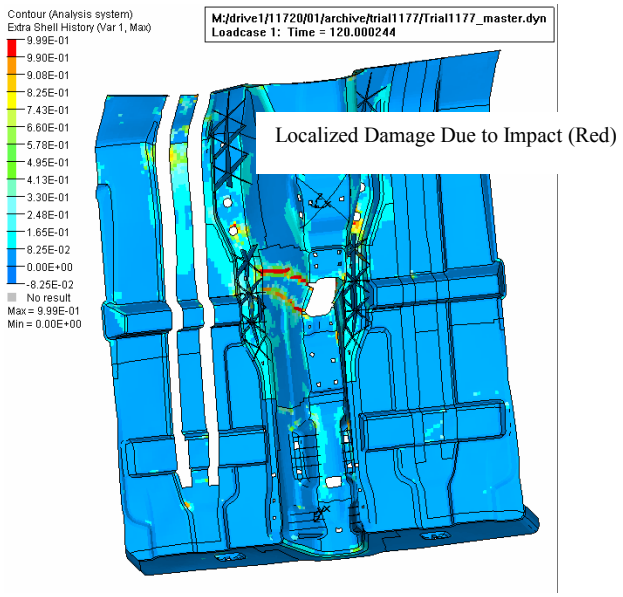

Figure 5. Front ODB – Representative predicted damage contours for proposed composite underbody.

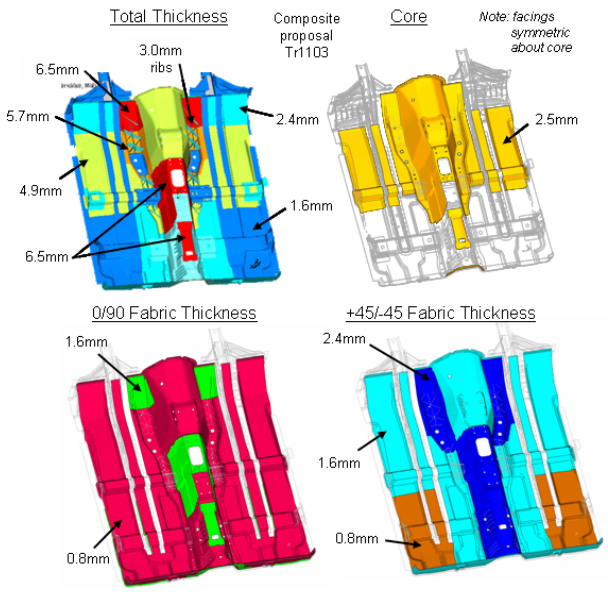

Figure 6. Representative thickness map for composite underbody.

Figure 7 illustrates the predicted mass reduction and compares the four material system designs (white bars) based on meeting the requirements for the four crash cases with revised material properties to the results of the initial predictions based only on the frontal ODB case (shaded bars). As can be seen in the figure, a large range of potential mass reduction is possible depending on the selected material system. The arrows in the figure indicate the change in mass for comparable material system designs.

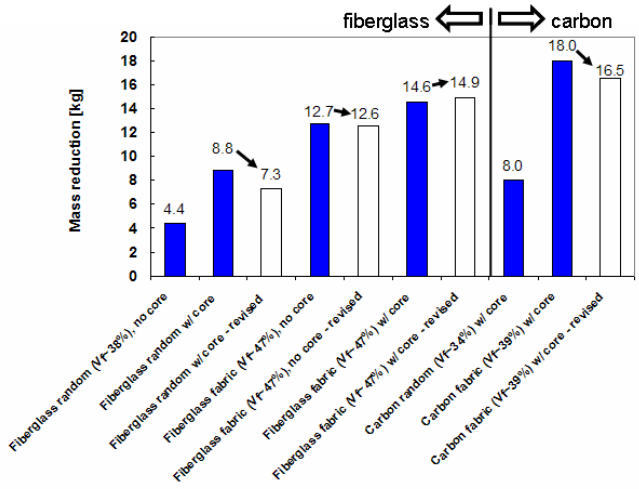

Figure 7. Predicted mass reduction vs. material system.

It is clear from the studies conducted to date, that mass reduction and part thickness are related to the strength of the materials investigated, where higher strength leads to lower mass and part thickness. Although not directly discussed here, materials with higher strength and also higher strain-to-failure properties would further reduce mass and thickness.

Weld-Bond Studies

A weld-bond coupon was designed to evaluate the tensile structural joint performance using several finite-element (FE) modeling methods. The analysis results indicated that physical test data would be required to determine several key modeling parameters. Further, sensitivity studies (see Figure 8) were conducted to establish how various joint and material parameters influence the joint strength. Relative to the nominal configuration, it was found that key joint parameters are the bond-line length, adhesive strength, and metal substrate strength. These results will be used to guide physical testing planned for Phase 2.

Material and Process Systems

Three MPSs have been evaluated for this project, based on manufacturing considerations, ability to deliver mass savings, and cost as predicted by

technical cost modeling. The three MPSs initially selected for evaluation were long-fiber injection (LFI), nylon Direct Long Fiber Thermoplastic (DLFT), and sheet molding compound (SMC). Each of these systems has the potential for a combination of fabric and random fibers, as well as either glass or carbon reinforcement. In the processing trials; however, carbon fiber was not evaluated due to cost targets, a lack of available material, and a lack of dedicated processing equipment.

LFI

The LFI process is currently in production with several relatively large composite components such as heavy truck panels and personal watercraft hulls. The LFI process as developed by Bayer utilizes robotic heads to chop glass into an open mold. As the glass is chopped, it is sprayed with a

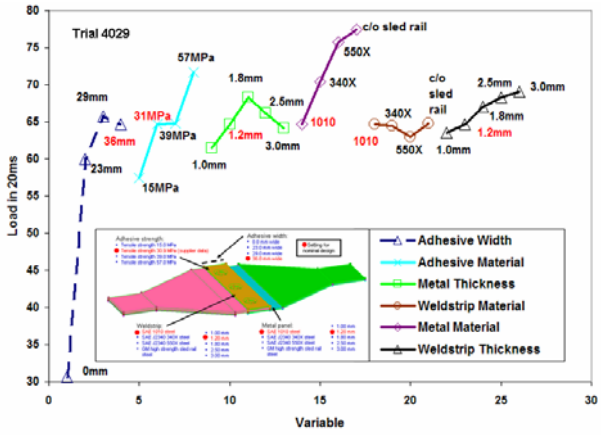

Figure 8. Weld-bond sensitivity study.

urethane resin. Bayer recommended a structural polyurethane (PU) system, Baydur 426, with a chop-and-spray LFI process. The molded samples are made with glass rovings that are dispensed from a reel and cut to any length before processing. PU and glass roving are introduced into the open mold simultaneously, with the chopped glass fiber being externally added to the PU spray jet. The molding is then cured in the closed mold. Bayer has successfully combined chopped LFI with sprayed continuous-filament mats (CFM). Our needs in this project would require replacing this CFM with glass fabric, and combining this with chopped LFI.

Introducing a glass fabric to the process is new, with trials being conducted in June 2007 and again in November 2007, at Bayer's development lab in Pittsburgh. Plaques were successfully molded at glass loading of 45, 50, 55 and 60% glass by weight. Bayer also prepared plaques containing a CFM at 45, 50, 55 and 60% by weight. However, we have been unable to mold with glass fabric.

Benefits for the LFI process:

- Easy mold access to apply local reinforcements
- Low press tonnage, allowing for a large platen size, which can easily accommodate the composite underbody assembly
- Potentially fast cycle time using a carousel and rapid-heating tooling

Concerns for the LFI process:

- Incorporating the fabric, which is needed for acceptable material properties
- Ability of the urethane to withstand temperature requirements of the assembly process
- Lack of existing infrastructure

Nylon DLFT

Nylon DLFT is a derivative of the more traditional polypropylene resin-based DLFT process. In initial trials with Nylon® 6 at 50% glass, significant glass damming in the processing was seen, and the strengths of the tested plaques were very low. Subsequent trials varied the resin and glass formulations with glass volumes ranging from 40-50% by weight. Despite better processing, improved glass flow, the addition of glass fabric and a high modulus polypropylene core, the material strength continues to be very low.

Benefits for the nylon DLFT process:

- Reduced cycle time
- Recyclable

Concerns for the nylon DLFT process:

- Limited mold access to apply local reinforcements

- Material properties- including incorporating the fabric, which is needed for acceptable material properties
- Ability of the nylon to withstand temperature requirements of the assembly process
- Press tonnage
- Capital investment

Due to the nature of the DLFT process, adding glass fabric or a polypropylene core to the charge has proven to be very difficult. The fabric and core must be heated to ensure the nylon DLFT does not cool prior to being compressed in the mold. This requires additional heating elements and increases capital costs as well as complicating the manufacturing process. While the nylon DLFT was processed at 600°F, the polypropylene core had to be processed at 325°F to prevent it from melting. How the two materials interact upon contact when building the charge is still under investigation, but there is concern that the polypropylene core rapidly cools the DLFT while the core is heated past its melting point and loses the strain properties for which it is intended.

SMC

The third MPS system investigated is SMC. Polywheels currently compounds an unsaturated polyester-modified vinyl-ster blend SMC in glass contents ranging from 27% to 55% glass by weight. For this project, additional material strength and strain are required, demanding higher glass content and reinforcement fabrics be added. The glass content of the SMC was increased in increments of 5% until visible non-wetting conditions of the glass occurred at 70%. Further development led to a reduction of the glass content to 57% to improve process capability on the compounding line. Additional material testing is in process to determine if the additional chopped-glass content is beneficial enough to justify the increased complexity involved in compounding a higher glass-content SMC.

Plaque molding trials in April 2007 demonstrated that additional reinforcement via glass fabrics can be incorporated into the SMC, utilizing both a uni-directional glass fabric (FGI W1300) and a bi-directional glass fabric (FGI 1854). These plaques showed a significant improvement in material properties. The bi-directional fabric proved to be the most useful for the underbody in various dynamic-impact scenarios and, therefore, became the primary reinforcement selection. To improve the strain rate of the SMC in order to retain floor integrity during a dynamic impact and to further reduce mass of the system, fabrication of plaques with a highly elastic material sandwiched within the SMC as a thin core was also investigated using a HMPP material as mentioned earlier. In the initial trials, the fabric and core were placed within the charges as dry material. This caused issues with wet-out and trapped air within the plaques, causing blisters and inconsistent material properties.

Subsequent trials in October utilized pre-compounded, bi-directional glass fabric which improved material handling as well as reduced wet-out issues. The core was also pre-compounded for the October trials, but it proved to be less effective—the core became even more difficult to cut, and initial material tests have not shown the increased strain-to-failure performance improvement seen in the earlier trial.

Filling ribs with the high glass-content, chopped-glass SMC has also been successfully demonstrated. Using the bi-directional glass fabric as a base layer and chopped glass to fill the ribs, ribbed plaques consistently filled as long as the ribs were well lubricated. Burn-off tests to determine the glass content in the ribs will be conducted, but evidence while molding suggests that the ribs will be structurally effective with glass reinforcement.

Benefits for the SMC process:

- Best composite material properties among MPSs evaluated
- Relatively easy mold access to apply local reinforcements
- Capable of surviving the elevated temperatures of Electro coat painter operation (ELPO) and paint cure
- Relatively low capital investment, as there is extensive SMC infrastructure within the automotive industry

Concerns for the SMC process:

- Material properties--Can we develop a composite material with enough tensile and shear strength and strain-to-failure performance to meet crash requirements?
- Achieving 2 ½ minute cycle time
- Press tonnage

Material Testing Results

Figures 9 through 11 show examples of the properties of some of the tested materials. The plaque testing has shown that the addition of woven compounded material increases the tensile modulus of the SMC material. Stress and strain values also show a significant increase.

Table 2 shows an evaluation of the possible mass saved for the reinforcement systems in SMC, as compared to the cost. For the glass-fiber materials, the glass fabric with HMPP core saves 14.6 kg, for a cost of $96 per part. The carbon comparisons show a larger mass save of 18.0 kg, but at a cost of $350. Compared to fiberglass, the incremental cost per kg of mass saved of the carbon fiber is about $75, which is considered to be high.

A fabric HMPP material was added to the SMC as a core, to increase elongation to ultimate failure, as well as to increase thickness using a lower density material. The strength properties and elongation of the material increased compared to the SMC. HMPP does have increased elongation properties, which would help to avoid net section failures in the underbody. More development and testing will be done in order to realize the potential mass and elongation benefits of this material in the underbody design. We are currently evaluating issues with the performance of HMPP at high temperatures.

Nylon DLFT material was molded into plaques and tested. The glass content which was easily molded into the DLFT was 40%, compared to the 57% SMC by weight. Increasing the glass content above 40% caused the plaques to have dry fibers. The tests showed a significant decrease in properties compared to the SMC and the SMC with woven glass mats.

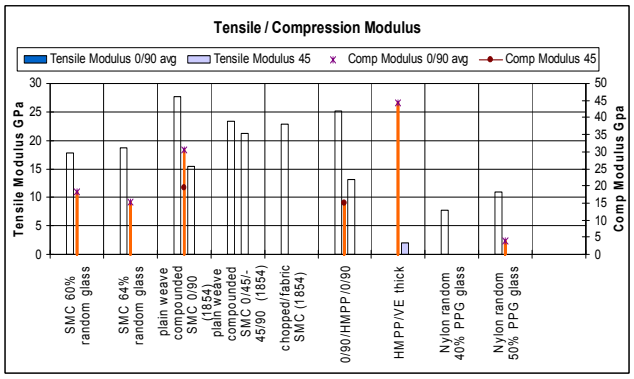

Figure 9. Tension- and compression-modulus values for a range of plaques molded and tested as part of this program.

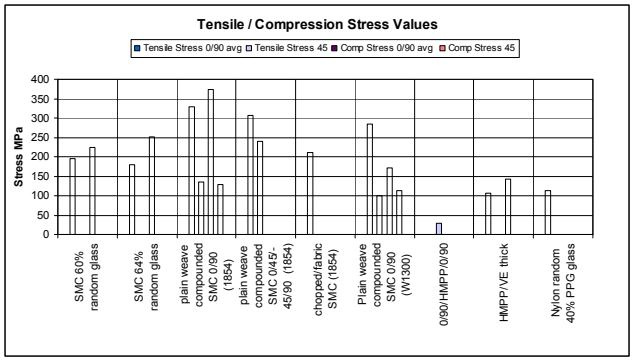

Figure 10. Tension- and compression-strength values for a range of plaques molded and tested as part of this program.

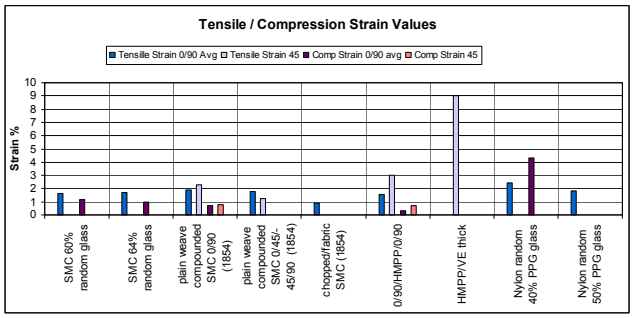

Figure 11. Tension- and compression strain-to-break values for a range of plaques molded and tested as part of this program.

Technical Cost Model

In order to aid in the selection of the MPS, we contracted with IBIS Associates to do a technical cost model for the underbody, comparing the three processes discussed above and incorporating six reinforcement scenarios for each MPS:

- All random fiberglass
- Random fiberglass with HMPP core

- All fiberglass fabric
- Fiberglass fabric with HMPP core
- Random carbon fiber with HMPP core
- Carbon-fiber fabric with HMPP core

This gives a total of eighteen different scenarios. The purpose of this cost model was to compare these systems to each other, not to get an absolute cost for the production of the underbody, nor to compare them to the steel underbody.

Table 2. Mass savings for SMC materials systems and costs/parts from the technical cost model.

		Mass Savings (kg, including rails)	Cost (per part)
Glass	Random no core	4.4	$104
	Random with core	8.8	$97
	Fabric no core	12.7	103
	Fabric with core	14.6	96
Carbon	Random no core		
	Random with core	8.0	368
	Fabric no core	17.6	
	Fabric with core	18.0	350

The result of this study was that the LFI and SMC processes were almost identical in their costs. The DLFT process is more expensive, based on the higher cost of the nylon. However, if a lower-cost nylon can be used (which may be an issue because of temperature requirements), the DLFT is also cost competitive.

IBIS concluded that the competitive position of the target processes will be determined by their respective material performance within each of the component designs. Material requirements will then drive the process rate and investment assumptions outlined in this study. Thus, each scenario's design-material performance will determine its respective mass and part cost.

Selection of MPS

Based on the molding trials, in which SMC is the only one of the processes that successfully incorporated the glass fabric as well as the HMPP core, the material properties, and the technical cost model, we have selected SMC with glass fabric and a HMPP core as our primary MPS. Our future processing, material evaluation, and design efforts will focus on this material. However, both LFI and nylon DLFT show possible unique advantages, so we will continue to follow up on these processes.

Non-Destructive Evaluation (NDE)

The objective of NDE is to evaluate the composite structure during manufacturing operations, final inspection, after durability runs and post-crash analysis. We are currently using NDE techniques to evaluate the panels we have molded as part of the MPS selection process. We have used ultrasound and thermal wave imaging to investigate delamination in the glass SMC/HMPP panels, and have been able to image blisters and delaminations. Plans are underway to use vibro-thermography and pulse-echo ultrasound to evaluate weld-bonded joints, to use fluorescing dye penetrant to investigate damage in panels subjected to impact loads, and to determine the feasibility of conductivity methods for evaluating damaged SMC panels modified to be conductive. NDE surface analysis techniques using optical methods are under investigation for their applicability.

Underbody Summary

Phase 1 of the Composite Underbody Project has been completed, with glass-fabric SMC, and a high-elongation core being selected as our material and process system. A composite underbody design concept was selected based on the potential to reduce cycle time and cost. Studies of global BIW stiffness and crash performance indicated that the dominant design load case was EuroNCAP/IIHS 40-mph Frontal ODB crash. Using this MPS, acceptable crash performance was predicted to occur with only localized material damage and low levels of dash-panel intrusion. A large range of potential mass reduction was predicted when considering all four crash cases, with a minimum reduction of 7.3 kg with random fiberglass and a maximum reduction of 16.5 kg with carbon-fiber-fabric composites. Initial manufacturing feasibility for the glass-fabric SMC system has been demonstrated with good initial material properties, and more extensive molding and testing trials are underway. Phase 2, the detailed design of the underbody, including manufacturing and assembly, is beginning. Investigations into NDE techniques to

determine manufacturing quality and durability are underway.

Lightweight, Low-Cost Composite Seat

The primary objective of the project is to develop materials, processes and designs to yield a light-weight, low-cost composite seat structure. Second-row outboard stand-alone seats are the target applications for the composite-seat project with volumes up to 340,000 upa. Only the back frame, cushion frame, and the pivoting recline/ folding joint will be included in the scope of the effort. The project will investigate predominately glass-fiber-reinforced composites due to cost considerations, but will consider local reinforcement with carbon fiber and other materials including metal reinforcements in order to achieve a 30% weight save versus the components being replaced. Both thermoset- and thermoplastic-matrix material will be included. A design achieving a 50% weight savings utilizing carbon-fiber-reinforced composites is also being developed.

Results from the comparator seat teardowns and testing have been used to develop weight targets for the composite seats. These can be seen in Table 3.

CAE Analysis

Following topology optimization done by Altair Engineering on the available design space for both the seat back and seat pan, initial CAE models of the STD and SIR seat were developed. Linear static analysis was performed initially using the several load cases in order to compare the concept seat to the comparator seats and to provide basic sizing of the sections.

Following that initial FE modeling, a more complex, non-linear model of both the STD and SIR seats was developed. The initial load cases evaluated using these non-linear models have been the FMVSS 207/210 load case for front impact on the SIR seat and a 20-g rear impact for the STD seat. Cargo-retention loading has also been investigated. Several iterations of material and design changes have been performed using these models to date and this work is continuing.

These analyses have resulted in design changes and iterations of both the composite-seat components and the steel hinges and reinforcements. The current seat design meets the 120% loading requirements with only some minor local issues that are being addressed.

Weight Status

The seat design is currently at its 30% target weight for the cushion pan. Additional optimization of the thickness of the seat back is required to meet its weight target. The details of the weight status can also be seen in Table 3 below. The current design of the seat can be seen in Figures 12 and 13 for the standard version of the seat.

Table 3. Composite seat weight status.

Focal Project 4 Composite Seat	Weights (kg)						
	Complete Seat	Riser	Headrest	Soft Trim	Hardware	Cushion Str	Back Str
Comparators							
DCX Stow N Go (non-SIR)	33.02	15.34	0.89	3.59	6.79	4.62	1.79
Ford LR3 (non-SIR)	23.65	8.79	0.63	2.78	3.36	4.28	3.81
GM GMT900 (non-SIR)	22.41	9.29	0.69	3.37	2.29	3.47	3.30
Average (no DCX)	23.03	9.04	0.66	3.08	2.83	3.88	3.56
Targets - 30% Weight Save	**20.46**	**8.80**	**0.63**	**3.00**	**2.83**	2.71	2.49
Current Design Status							
Composite Std Seat	20.52	8.80	0.63	2.78	2.63	2.70	2.98
%Weight Save	11%	3%	5%	10%	7%	30%	16%
Weight Save (kg)	2.5	0.2	0.0	0.3	0.2	1.2	0.6
Composite SIR Seat	22.30	8.80	0.63	2.78	3.59	2.89	3.10

Specifc Gravity Assumptions		
	Steel	7.8
	Carbon/Nylon	1.3

Material Assumptions

The composite seat will be comprised of nylon 6 reinforced with chopped carbon fiber for the bulk of the molded composite part. Local continuous carbon-fiber/nylon 6 inserts will reinforce the edges of the cushion pan and the seat back. These inserts will be symmetrical laminates of 0° and 90° tapes. The location and shape of the inserts is illustrated in Figure 13. The composite parts will be compression molded using DLFT-compounded material. The inserts will be preformed from blanked, pre-laminated sheet stock and heated prior to being placed in the main molding tool. Robotic transfer will be necessary to meet the cycle times for the insert transfer. The process schematic is illustrated in Figure 14.

Figure 12. ACC standard seat design.

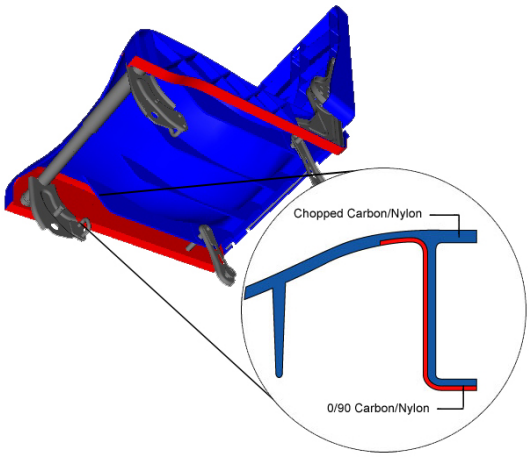

Figure 13. Typical section – cushion.

Cost Modeling

Work continues with EPFL on developing a cost model for the composite seat. EPFL has designed a version of the seat back that utilizes the TPP4 process and materials. This design will be used for comparison to the compression-molded DLFT version of the seat being developed by the ACC. Preliminary estimates show a comparable weight savings using the TPP4 process and materials and there is potential for additional cost savings with the TPP4 seat.

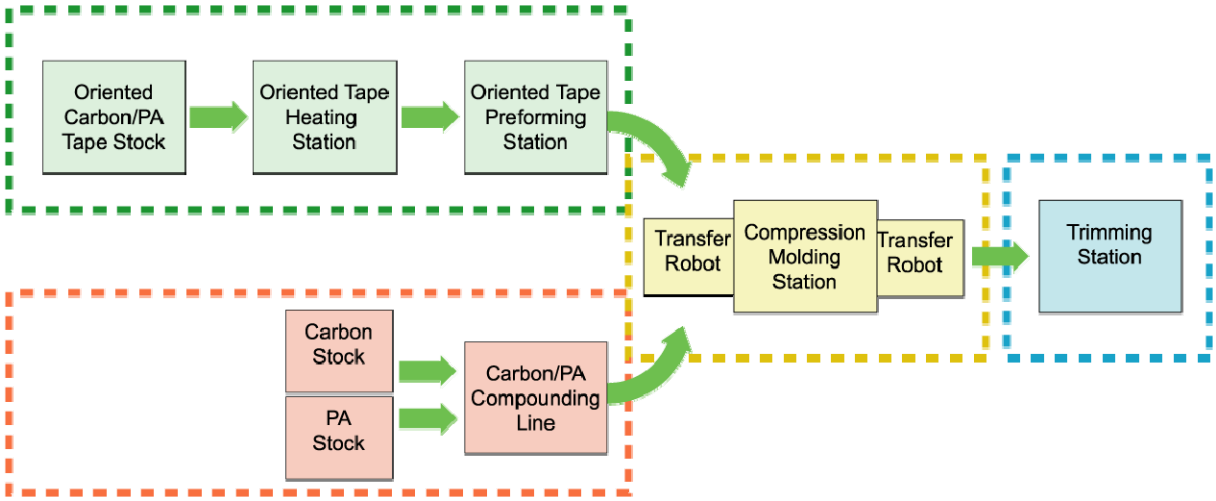

Figure 14. Seat Molding Process Schematic.

Additional trim parts and reinforcements may be necessary for the TPP4 seat and a full cost analysis to get to an equivalent seat in terms of performance and fit and finish needs to be completed. Currently the ACC Seat Team has provided EPFL with cost-model input for the design, materials, and processes for the ACC seat design.

---

[i] Denotes project 007 of the Automotive Composites Consortium (ACC), one of the formal consortia of the United States Council for Automotive Research (USCAR, see www.uscar.org) set up by Chrysler, Ford and General Motors to conduct joint, pre-competitive research and development.

B. Development of Manufacturing Methods for Fiber Preforms (ACC 040[i])

Principal Investigator: Patrick Blanchard
Ford Motor Company, Research and Innovation Center
P.O. Box 2053, MD 3135 RIC, Dearborn, MI 48121-2053
(313) 390-6230; fax: (313) 390-0514; e-mail: pblanch3@ford.com

Principal Investigator: Jeff Dahl
Ford Motor Company, Research and Innovation Center
P.O. Box 2053, MD 3135 RIC, Dearborn, MI 48121-2053
(313) 845-1039; fax: (313) 390-0514; e-mail: jdahl@ford.com

Project Manager: C. David Warren
Oak Ridge National Laboratory (ORNL)
P.O. Box 2009, Oak Ridge, TN 37831-8050
(865) 574-9693; fax: (865) 576-4963; e-mail: warrencd@ornl.gov

Technology Area Development Manager: Joseph A. Carpenter
(202) 586-1022; fax: (202) 586-1600; e-mail: Joseph.Carpenter@ee.doe.gov

Field Project Officer: Aaron D. Yocum
(304) 285-4852; fax: (304) 285-4403; e-mail: aaron.yocum@netl.doe.gov

Expert Technical Monitor: Philip S. Sklad
(865) 574-5069; fax: (865) 576-4963; e-mail: skladps@ornl.gov

---

Contractor: U.S. Automotive Materials Partnership (USAMP)
Contract No.: DE-FC05-95OR22910 through the DOE National Energy Technology Laboratory

---

Objective

- Develop and demonstrate new fiber-preforming processes to decrease cost, increase manufacturing rates and improve reproducibility of large preforms/blanks for composite manufacturing.
- Develop the thermoplastic programmable powdered preform process (TP-P4) concept as a high- volume, composite manufacturing process for thermoplastic composite materials.
- Demonstrate a new method to provide robust corrosion protection for magnesium (Mg) structural members by encapsulating them in polymer.

Approach

- Investigate materials, process equipment, and tooling technology to further reduce the cost and enhance the quality of chopped-fiber preforms.
- Explore the extension of automated-preforming technology to make preforms with a thermoplastic matrix.
- Investigate heating methods for thermoplastic composite blanks manufactured using the TP-P4 process.
- Perform cost analysis of the TP-P4 to determine the economic benefits versus competing process technology.
- Adopting the multi-material approach, use research conducted in the Ultra-Large Casting of Al and Mg (ULC, AMD 406; see 3.C) project as a platform for new research in the Automotive Composites Consortium (ACC). Totally encapsulate Mg structural casting in a polymer to demonstrate robust corrosion prevention while providing more opportunity for parts consolidation. The process of focus will be the Powder Impression Molding (PIM) process, with investigation of other potential encapsulation processes such as Magna Advanced Technologies' Self Aligning and Actuating Mold (SAAM) process (which utilizes low-pressure, compression-molded sheet molding compound (SMC)) and possibly injection molding.

Accomplishments

- Completed processing studies to establish feasibility of the TP-P4 process.
- Finite-element analyses (FEA) of a "shotgun" design and material specifications development have been initiated.

Future Direction

- Extend the capability of TP-P4 deposition equipment to achieve adequate throughput of chopped fiber blanks.
- Continue cost modeling of process concepts to determine business rationale for migration of process technology to original equipment manufacturer (OEM) supply base.
- Perform application studies to expose outstanding processing hurdles that may become obstacles to future technology implementation.
- Perform extended FEA of the shotgun design using multiple materials and reinforcements.
- Investigate other possible materials and processes to lower costs and weight of the component.

Thermoplastic P4 (TP-P4)

Introduction

This work has focused on the development of a thermoplastic-focused derivative of the programmable powdered perform process (P4), TP-P4. This fully-automated deposition process deposits commodity-grade, commingled yarns of polypropylene and glass onto a screen to produce blanks for subsequent compression molding. Previously, experimental studies were performed at the National Composite Center (NCC) in Kettering, Ohio. However, most of the technical development is now being pursued through collaborative use of the P4 cell at ORNL. (See related 8.C.) Extensive experimental investigations have also been conducted in collaboration with the Polymers Laboratory (LTC) at the Swiss Federal Institute of Technology (EPFL) in Switzerland.

During this reporting period, investigations were conducted in the following process areas.

- TP-P4 chopper-gun deposition speeds.
- Preconsolidation and preheating methods for TP-P4 blanks.
- Polymer degradation vs. heating time.
- Hot flow compression molding of TP-P4 blanks.

TP-P4 Chopper-Gun Trials

Previous cost-modeling studies [1,2] performed in 2006 showed that deposition time had an important effect on part cost. A range of values was considered in the cost study, which for one robot ranged from 7.5 kg/min to 12.2 kg/min. For example, comparing the slowest one-cell variant to the fastest two-cell variant, the deposition cell cost/part was decreased from $3.70 to $2.50 per part. Hence, work has focused on the following deposition aspects:

- Improve chopper deposition rates.
- Evaluate a single-motor chopper-gun design for chopping Twintex roving.

Based upon trials at the NCC and ORNL, several factors were found to limit the deposition rates. These included fiber jamming due to fiber fuzz, linear velocity of the fiber rovings and practical limitations on robot acceleration and deceleration. However, modification of the roller pressure, gap and tensioning systems enabled throughput rates of 3200 g/min and 4200 g/min to be achieved for 25-mm and 75-mm long fibers, respectively.

To achieve the higher throughputs needed, the deposition rate of the chopper head needs to be increased and should, hence, be redesigned specifically for Twintex materials. The bounds cost modeled previously were 7.5 kg/min with 11 ends to 12.2 kg/min with 22 ends. Key challenges that remain include reducing downtime due to fiber jamming and improvement in the durability of chopper-gun contact surfaces. As a first step towards this, an alternative glass-fiber chopper head was purchased. Initial trials with this chopper system would suggest that 6 kg/min is feasible with 3 ends of material and without the fiber jamming observed with the current chopper design. A revised design would still be required to incorporate an increase in the number of ends.

Preconsolidation and Preheating Methods

After deposition, a heat-set cycle is used (as in the original P4 process) to partially melt the polypropylene and, hence, stabilize the preform for subsequent handling. Without this step, the preform does not have any mechanical integrity. The heat-set stage consisted of blowing hot air through the preform, which was located between perforated matched tools. The hot-air cycle could also be followed by a cool-air cycle.

The baseline process, as shown in Figure 1, used an additional preconsolidation stage after the deposition process. Studies of the preconsolidation stage have been reported previously. Figure 1 shows that this added an extra $2/part, and a resulting action for this experimental work was to investigate if the preconsolidation stage could be removed, that is, is the heat-setting operation alone sufficient to achieve sufficient mechanical handling integrity of the preformed blank?

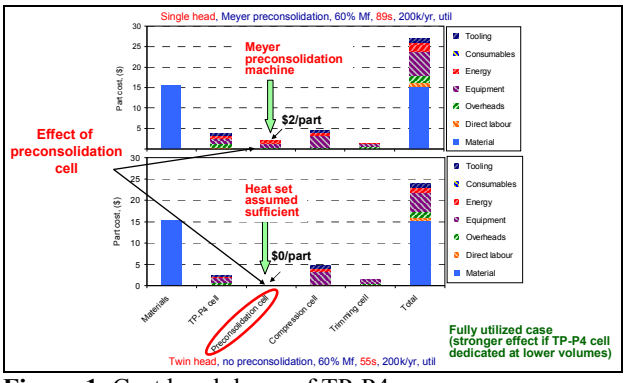

Figure 1. Cost breakdown of TP-P4 process.

The feasibility of eliminating the lamination operation is driven largely by practical limitations of heating thick glass-fiber/polypropylene blanks. The low thermal conductivity often results in surface degradation of the polymer constituent before the blank mid-plane temperature reaches target. This problem is amplified as heat-set blanks are typically over five times the thickness of those laminated. Therefore, heating trials were performed using a forced-hot-air oven to determine whether adequate heating rates could be achieved. A summary of the results is shown in Figure 2.

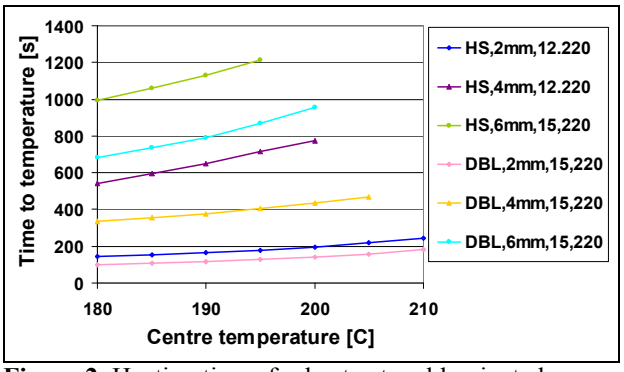

Figure 2. Heating times for heat-set and laminated blanks (of molded thickness 2-6 mm).

Increasing blank thickness resulted in a corresponding increase in heating times. This is most noticeable for heat-set blanks of 6 mm (final molded part thickness). Heating times of over 20 minutes were recorded, with target temperatures above 200°C not possible. Therefore, laminated blanks would be recommended for this thickness. On the contrary, 2-mm blanks showed minor differences in heating times between those that were laminated and those which were heat set. This would suggest that use of 2-mm blanks could eliminate the requirement for the lamination step. However, it should be noted that reducing blank thickness would result in an increase in cycle time for the deposition cell as more blanks would be required for subsequent molding.

Polymer Degradation Studies

In order to determine how temperature and time-at-temperature affected degradation of the TP-P4 polypropylene matrix, measurements of polymer molecular weight were performed. Following deposition of the rovings in the TP-P4 cell, degradation is a function of the subsequent thermal history, including the heat-set phase, the optional double-belt lamination process. Finally, any heating prior to molding will also have an impact. In comparison with heat-set material, double-belt lamination can reduce the heating time needed for the material to reach a temperature suitable for press forming, but also adds an additional thermal process. The study compared degradation of the TP-P4 after compression molding for both heat-set and double-belt laminated material to see the combined degradation effects.

Figure 3 shows a summary chart for polymer molecular weight for a range of heating conditions. 2-mm blanks, whether laminated or heat set, showed few signs of degradation at any temperature. However, increasing thickness to 4 mm and 6 mm showed a significant drop in molecular weight for heat-set samples alone. This reinforces the argument that the lamination process can only be eliminated provided the TP-P4 blank thickness is limited to 2 mm or less.

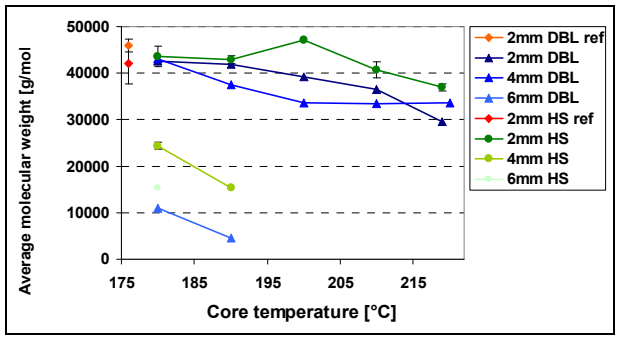

Figure 3. Effect of heating time and target temperature on polymer molecular weight.

Hot Flow Compression Molding

A design-of-experiments approach was used in order to find the necessary press requirements to promote in-plane and out-of-plane flow of TP-P4 blanks. This included the use of a 250-mm x 250-mm, deep-rib tool to establish the appropriate processing parameters. An example of a completely-filled part is seen in Figure 4. Optimum conditions appeared to be a molding pressure of 250 bar, fiber length of 25 mm, and a compression velocity of 100 mm/s. Note that the latter is a 100% increase in compression velocity compared to standard molding presses. This is largely due to the high glass mass fraction of the blank, 60% wt, vs. standard glass-mat thermo-plastic (GMT, 40 wt%). Nevertheless, the TP-P4 blanks were able to flow into the 77-mm ribs which would indicate capability for component geometries featuring similar rib depths.

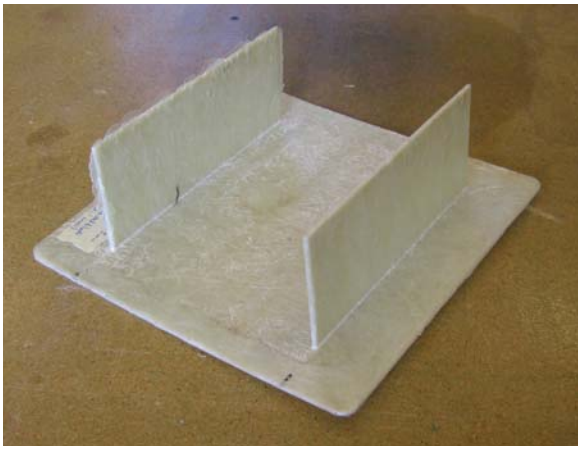

Figure 4. Molded TP-P4 blank using a deep-rib compression-molding tool.

Conclusions and Future Work

Based upon cost and process investigations conducted in 2007, future developments will focus on the development of the high-throughput chopper gun. Once a robust system is in place, a target component will be selected to identify other processing obstacles that may exist.

Powder Impression Molding (PIM)

Introduction

This effort has focused on the development of a fully-encapsulated Mg shotgun utilizing the Powder Impression Molding (PIM) process. The PIM process is based on the licensed technology from 3DM Worldwide and locally at VP Tech in Auburn Hills, MI.

An initial concept was designed based on the USAMP ULC project (AMD 406) in which additional features such as battery tray, washer-fluid reservoir and splash shield were combined into a single molded piece. The shotgun casting consists of a highly-ribbed structure and incorporates hood hinge pivots and front bolster attachments (Figure 5).

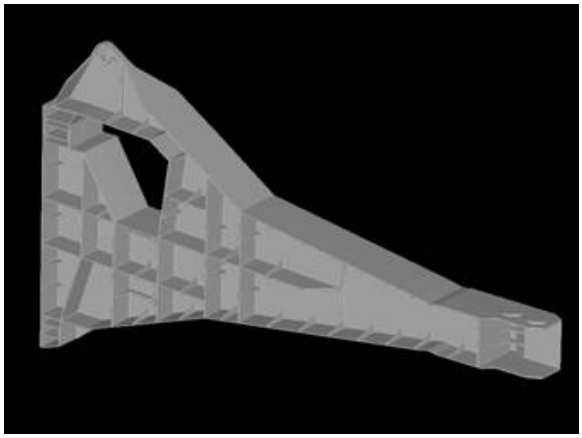

Figure 5. AMD 406 Mg shotgun.

The new process makes use of thermoplastics (primarily polypropylene) to encapsulate a component in foam with a dense (void-free) outer layer. Preliminary investigations were conducted on a cross member to determine the feasibility of the process. The sections that follow describe the results from these studies.

Equipment Capability

The PIM process was developed to manufacture polymer-based composite components by heating a two-piece metal tool and applying powdered polymer material to form a melted skin conforming to the cavity of the mold. The mold halves are brought together after the skins are formed and may include layers of filler or reinforcement materials as well as expandable foam.

Basic Process Principles

The key process parameters are time and mold temperature. The combination of dwell time at a specific mold temperature determines the plastic skin thickness, typically 1 mm or greater. The two mold halves with independently-formed skins are placed together like a sandwich after introducing the desired amount of expandable filler foam material, as well as desired fillers or reinforcements, and held together for a pre-determined time while heated again.

The PIM process is generally carried out at relatively low temperatures, i.e., slightly higher than that of the melting point of the plastic, polymer-based, particulate material being contacted with the heated mold. Because of the low-temperature and low-pressure application, the molds do not degrade as they do in injection molding and thus offer long life cycles. The preferred mold material is aluminum (Al) because of its uniform heat distribution characteristics, machinability and relatively long molding cycle life.

Material

The PIM process was designed to accommodate all thermoplastic materials as long as they can be produced in powder form. The foam is usually of the same material as the skin, except for adding a foaming agent.

Design / Tooling

The process is based upon open cope-and-drag tooling configurations thus allowing for complex shape designs with parting lines. The ability to insert filler material and/or reinforcement materials provides for additional product design flexibility. Size of molds can range from very small geometric objects to large shipping-container mold segments. Tooling material is typically cast or slab Al machined to the desired cavity geometry.

Previous Mg Encapsulation Work

Testing was performed on an encapsulated Mg cross member with favorable results. The Mg cross member was manufactured by machining a billet piece of Mg into a frame cross member typical of those found on frame-based pick-up trucks and sport-utility vehicles (SUVs) (Figure 6). The cross member was encapsulated using the PIM process at VP Tech. Al inserts were molded in place, in lieu of separate isolators to inhibit galvanic corrosion (Figure 7).

The encapsulated cross member was tested according to Ford APG and APGE corrosion test specifications and incurred no detrimental effects. The cross member was also gravelo-meter tested to assess the effects of stone impact, at various temperatures, again incurring no detrimental effects.

Figure 6. Machined Mg cross members.

Figure 7. Encapsulated Mg cross members.

Ongoing Work

A purchase order has been released to Global Tech (licensor of 3DM's PIM technology) to complete deliverables in task 1 (Table 1) of the statement of work. The deliverables include

1) report on previous work completed.
2) completed concept design (Figure 8).
3) comprehensive cost model (Figure 9).

Table 1. Deliverables for Task #1.

Deliverable	Description	Cost ($US)
1	Report on encapsulation work done to date.	35k
2	Complete concept design tailored for the PIM process.	
3	Preliminary cost model based on the PIM process.	
4	FEA analysis of the battery tray area, according to Ford test specs.	9.7k

To date, two of the deliverables have been met (#2 & #3). Red Cedar Technology was consulted regarding finite-element analysis (FEA) of the battery-tray area, to supplement the original deliverables. The FEA concentrates on the battery-tray area to test the feasibility of using the PIM materials without any additional reinforcement except for the designed rib features. A quote was finalized and another purchase order has been released to start the FEA.

Upon completion of the FEA of the battery-tray area, a decision will be made either to proceed to Task #2, fabrication of tooling, or make appropriate design changes involving the possibility of selectively embedding reinforcement in the battery tray.

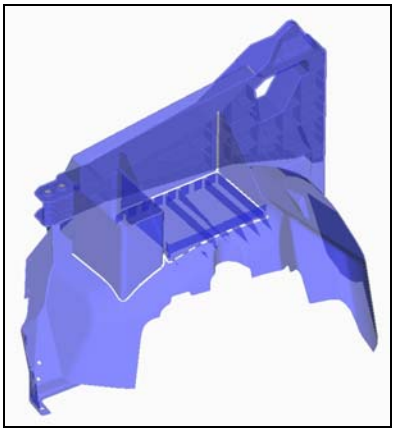

Figure 8. Encapsulated Mg shotgun, showing integrated battery tray, washer-fluid reservoir and splash shield.

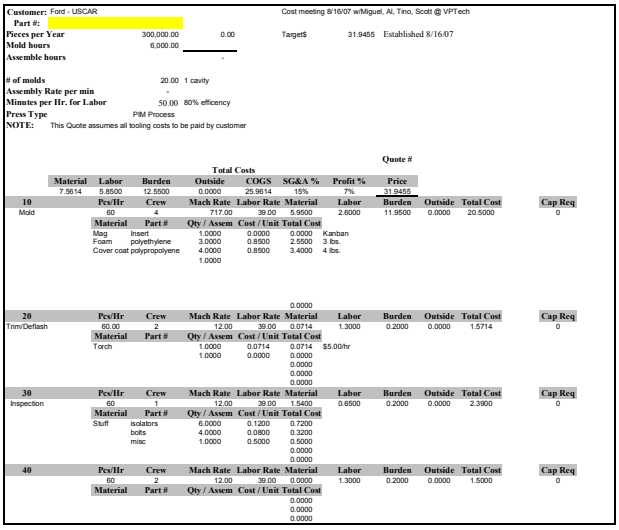

Customer: Ford - USCAR — Cost meeting 8/16/07 w/Miguel, Al, Tino, Scott @ VPTech
Part #:
Pieces per Year 300,000.00 0.00 Target$ 31.9455 Established 8/16/07
Mold hours 6,000.00
Assemble hours -
# of molds 20.00 1 cavity
Assembly Rate per min -
Minutes per Hr. for Labor 50.00 80% efficency
Press Type PIM Process
NOTE: This Quote assumes all tooling costs to be paid by customer

Quote #

Total Costs

Material	Labor	Burden	Outside	COGS	SG&A %	Profit %	Price
7.5614	5.8500	12.5500	0.0000	25.9614	15%	7%	31.9455

	Pcs/Hr	Crew	Mach Rate	Labor Rate	Material	Labor	Burden	Outside	Total Cost	Cap Req
10	60	4	717.00	39.00	5.9500	2.6000	11.9500	0.0000	20.5000	0
Mold										

Material	Part #	Qty / Assem	Cost / Unit	Total Cost	
Mag	Insert	1.0000	0.0000	0.0000	Kanban
Foam	polyethylene	3.0000	0.8500	2.5500	3 lbs.
Cover coat	polypropolyene	4.0000	0.8500	3.4000	4 lbs.
		1.0000			
				0.0000	

	Pcs/Hr	Crew	Mach Rate	Labor Rate	Material	Labor	Burden	Outside	Total Cost	Cap Req
20	60.00	2	12.00	39.00	0.0714	1.3000	0.2000	0.0000	1.5714	0
Trim/Deflash										

Material	Part #	Qty / Assem	Cost / Unit	Total Cost	
Torch		1.0000	0.0714	0.0714	$5.00/hr
		1.0000	0.0000	0.0000	
				0.0000	
				0.0000	
				0.0000	
				0.0000	

	Pcs/Hr	Crew	Mach Rate	Labor Rate	Material	Labor	Burden	Outside	Total Cost	Cap Req
30	60	1	12.00	39.00	1.5400	0.6500	0.2000	0.0000	2.3900	0
Inspection										

Material	Part #	Qty / Assem	Cost / Unit	Total Cost
Stuff	isolators	6.0000	0.1200	0.7200
	bolts	4.0000	0.0800	0.3200
	misc	1.0000	0.5000	0.5000
				0.0000
				0.0000

	Pcs/Hr	Crew	Mach Rate	Labor Rate	Material	Labor	Burden	Outside	Total Cost	Cap Req
40	60	2	12.00	39.00	0.0000	1.3000	0.2000	0.0000	1.5000	0

Material	Part #	Qty / Assem	Cost / Unit	Total Cost
				0.0000
				0.0000
				0.0000

Figure 9. Cost model summary for 300k pieces per year.

Preliminary tests have also been performed on PIM plaques to mimic battery loading at elevated temperatures. Two PIM plaques (nominally 25.4-mm thick) were placed into an oven at 50°C. One plaque was supported by two steel blocks (approximately 25-mm thick) along its length (Figure 10) and the other along its width (Figure 11). A reference measurement was taken near the center of the plaque and approximately

18.6 kg of weight was placed on top of the plaque, relatively centered, to mimic the loading of a typical battery. The oven was then ramped up to 105°C and the maximum deflection of the plaque was recorded over time.

Figure 10. PIM plaque supported along its length (approx. 412.8 mm apart).

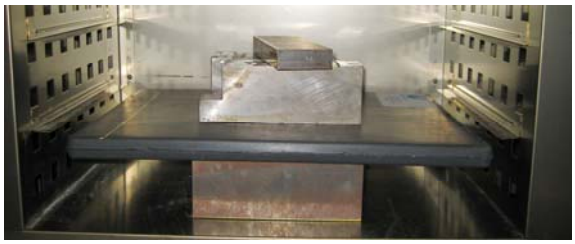

Figure 11. PIM plaque supported along its width (approx. 263.5 mm apart).

Of the plaques tested to date, a maximum deflection of 12.55 mm was observed for the plaque that was supported along its length. For the two plaques that were supported along their widths, a maximum deflection of 2.20 mm was observed (Figure 12).

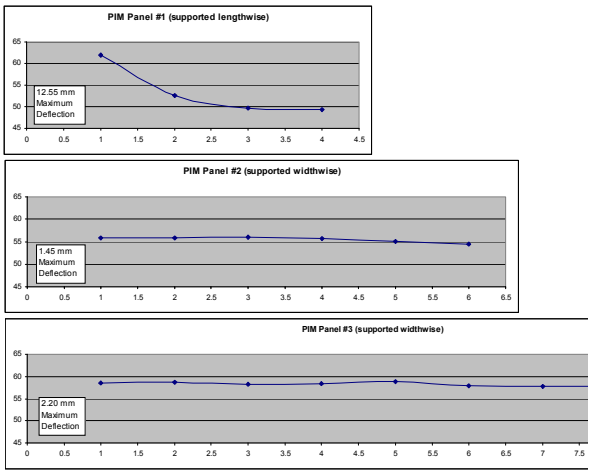

Figure 12. Recorded deflections over time for lengthwise-supported and widthwise-supported PIM plaques. (Same scales utilized.)

Ultimately, the battery tray will have to pass specified durability tests. Red Cedar Tech is currently employing Ford Motor Company specifications for FEA. Further material testing will commence upon receipt of the all deliverables from Task 1 and upon favorable results from the FEA of the battery-tray area.

References

1. M.D. Wakeman, G. Francois, J-A.E. Manson, "USCAR: Cost Modeling of Thermoplastic P4 Process Technology progress report 1", April 2006, EPFL, Lausanne, Switzerland.
2. M.D. Wakeman, G. Francois, J-A.E. Manson, "USCAR: Cost Modeling of Thermoplastic P4 Process Technology progress report 2", September 2006, EPFL, Lausanne, Switzerland

[i] Denotes project 040 of the Automotive Composites Consortium (ACC), one of the formal consortia of the United States Council for Automotive Research (USCAR, www.uscar.org) set up by Chrysler, Ford and General Motors to conduct joint, pre-competitive research and development.

C. Development of Next-Generation Programmable Preforming Process

Principal Investigator: Robert E. Norris, Jr.
Oak Ridge National Laboratory (ORNL)
P.O. Box 2008, Oak Ridge, TN 37831-6053
(865) 576-1179; fax (865)-574-8257; e-mail: norrisrejr@ornl.gov

Field Project Manager, Composites: C. David Warren
ORNL
P.O. Box 2008, Oak Ridge, TN 37831-6065
(865) 574-9693; fax: (865) 576-4963; e-mail: warrencd@ornl.gov

Technology Area Development Manager: Joseph A. Carpenter
(202) 586-1022; fax: (202) 586-1600; e-mail: joseph.carpenter@ee.doe.gov

Expert Technical Monitor: Philip S. Sklad
(865) 574-5069; fax: (865) 574-6098; e-mail: skladps@ornl.gov

---

Contractor: ORNL
Contract No.: DE-AC05-00OR22725

Objectives

- Develop the next-generation of low-cost fiber preforming technologies based on programmable, robotic-controlled, directed-chopped-fiber processes for the application of:
  - low-cost carbon fiber
  - reinforced thermoplastics
  - hybrid glass-carbon
- Develop supporting technologies required to successfully implement the process technology including:
  - preform characterization (e.g., permeability, areal density uniformity)
  - preform process modeling for process-effects analysis
- Conduct parametric process studies to investigate fundamental process effects and establish process-property relationships.
- Conduct requisite molding investigations—experimentally and through modeling—to elucidate relationship between preform characteristics and moldability.

Approach

- Establish a base-research, programmable, robotic preforming system for which advanced capabilities (e.g., new chopper designs) can be developed and evaluated.
- Establish a highly instrumented and controlled, research molding capability to isolate and investigate the effects of process variables on moldability and mechanical properties.
- Develop new severing technology to facilitate the implementation of low-cost carbon-reinforced thermoplastics and hybrid glass-carbon products.
- Benchmark and implement process modeling into experimental work to guide parameter selection and to provide tools for longer-term implementation of preforming and related technologies.

Accomplishments

- Demonstrated successful chopping of small quantities of Direct Re-Enforcement Fabrication Technology (DRIFT) material (reinforcing fibers pre-impregnated with polypropylene) and molded a thin demonstration article.
- Based on the above accomplishment, worked with Polycomp to modify the product form and preformed and molded several 24-in x 24-in panels for demonstration and testing.
- Worked with the Automotive Composites Consortium (ACC) and Ecole Polytechnic Federal de Lausanne (EPFL) to provide a substantial number of panels using TwinTex commingled glass and polypropylene fibers for evaluation of technical and economic feasibility for automotive applications.
- Purchased evaluation quantities of latest commercially-available industrial grades of carbon fiber and initiated experimental work with hybrid blends at various ratios of carbon and glass reinforcement to evaluate potential advantages of combining these materials to achieve performance and/or economic benefits.
- Currently evaluating feasibility of *in-situ* blending reinforcing fiber with thermoplastic matrix fiber at the preforming machine versus buying materials commingled by reinforcement fiber manufacturers such as the TwinTex product. Since the variety of forms of commingled materials is extremely limited, this allows evaluation of materials not available at all in commingled form and in a much broader array of blending alternatives. Although the focus of this approach is to facilitate evaluation of alternative material combinations especially looking at hybrids, *in-situ* blending may prove economically attractive as well.
- Completed integration of injection/compression press and general-purpose mold with associated heating system and instrumentation and initiated molding of test panels.
- Transferred the ACC Wolfangel high-speed prototype chopper to ORNL and initiated modifications to enable control of chopper to simulate robotic preforming operations at speeds exceeding those of the current chopper system.
- Initiated complementary investigation of cutting tribology issues to determine if alternative materials and techniques might improve variations of current severing technologies.
- Continued experimentation to demonstrate feasibility of laser-severing technology concentrating on improved optics to facilitate more focused delivery of the beam energy to the cutting region in order to validate earlier estimated requirements. Initiated effort to model the laser-delivery system and associated energy distribution.
- Previously-developed general modeling approach was modified to improve the flexure model for fiber deformation and to separate modules to improve speed and reduce code size.

Future Direction

- Continue preforming studies with various product forms incorporating reinforcement and thermoplastic matrix materials “co-processed” through the preforming machine including forms with low-cost carbon fiber as available. Near-term focus is hybrid blends of glass and industrial grades of carbon fiber.
- Advance bench-top studies of advanced severing technology to determine technical and economic feasibility of developing new techniques (e.g., laser-severing) or substantially improved equipment (e.g., higher-speed choppers, improved blade materials, etc.) that can be practically adapted and implemented for this application within one to three years.
- Evaluate preform process models relative to physical preform characteristics and expand model capability as resources permit.
- Evaluate programmatic benefits versus costs and risks of refurbishing an existing injection machine or acquiring a rebuilt unit for structural reaction injection molding (SRIM) to complement current focus on other molding technologies and implement if justified. This equipment will be critical for evaluation of any materials in liquid-molding processes and will be useful in evaluating a variety of material forms including hybrid blends, natural-fiber preforms and early evaluation of low cost carbon fiber.

- Continue developing and implementing tools for more effective characterization of process variable and effects on final products. Conduct permeability measurements on preforms made by simulated split-tow products of varying tow-size and construct and test through-thickness permeability rig as funding and other resources permit.

Introduction

Polymer-matrix composite materials offer a number of benefits in lightweighting of automotive and heavy vehicles, including greater stiffness and strength per unit weight than conventional materials, easier formability, less corrosion susceptibility, the ability to tailor properties to specific load requirements, and enhanced noise and vibration damping. However, widespread implementation of carbon-fiber composites, which offer among the greatest mass savings potential, requires lower-cost materials and manufacturing processes than are currently available. Advanced preforming processes offer opportunities to facilitate the widespread use of carbon composites.

Robotic-controlled, programmable, directed-fiber preforming processes have demonstrated exceptional value for rapidly preforming large, glass-reinforced, automotive composite structures. Due to their unique features and flexibility, and to their inherent low scrap rate, they are among the most viable candidate processes for making affordable carbon-fiber preforms for a variety of structural automotive components. The ACC has implemented the Programmable Powdered Preform Process (P4) with glass fibers very successfully in its truck box program—Focal Project 2 (FP2). Prototype B-pillars were also successfully fabricated from both carbon- and glass-fiber reinforcement and tested as part of the ACC's Focal Project 3. Original-equipment manufacturers (OEMs) have transferred the technology to commercial applications such as the General Motors (GM) Silverado pickup box and the Aston Martin Vanquish body-side.

Analyses have indicated a potential for greater than 60% mass savings for a carbon-fiber-intensive body-in-white under the assumption of a thickness design constraint of 1.5 mm. The analyses also indicate the potential of saving an additional 15% if the thickness constraint is reduced to 1 mm. Unfortunately, evidence suggests that 1.5 mm may be a practical limit for liquid molding. However, thermoplastics preforms, in which the matrix and fiber are both deposited in the preforming step, offer a potential path to obtaining thinner sections and, consequently, additional mass savings as well as greater potential for recyclability. Hybrid-fiber preforms that can effectively take advantage of concurrently utilizing carbon and glass fibers offer another potential benefit in terms of economics and property enhancement and may be a good route for actually introducing more carbon fiber at somewhat lower quantities than necessary for all-carbon components in automotive applications.

Preforming Developmental Approach

The objective of this project is to advance directed-fiber preforming processes to effect a further reduction in vehicle mass—relative to conventional glass-fiber composites—while maintaining the economical advantages of net-shape preforming. The project is pursuing three focus areas corresponding to three materials systems: reinforced thermoplastics, carbon fiber, and hybrid glass-carbon fiber. Each focus area consists of four main tasks concentrating on: 1) materials developments, including introduction and evaluation of alternative and/or new fiber product forms and binders; 2) machine developments, particularly new severing technology; 3) process developments, for example, to control areal density uniformity and preform anisotropy; and 4) development of supporting technologies such as modeling and preform characterization techniques. Furthermore, this project will undertake to develop sufficient understanding of fundamental aspects of the process and their effect on preform quality and mechanical properties in the molded part. As such, this project will support, augment, and facilitate the current and future research activities undertaken in related ACC projects.
A research-focused preforming system has been installed in the polymer-composites laboratories at the ORNL to serve as the base for hardware and

associated technology developments. A number of combinations of reinforcing fibers, binders and/or matrix fibers have been obtained to establish materials baselines for comparison with and advancement of previous P4 work conducted by the ACC. This machine is currently being used to build preforms for evaluation utilizing the TwinTex product (glass fiber commingled with thermoplastic fiber to serve as the matrix), glass impregnated with thermoplastic resin utilizing the DRIFT process, and various forms of carbon and glass reinforcement in alternate independent as well as hybrid forms. Although the near-term focus is on demonstrating advances with glass fiber and existing industrial grades of carbon fiber, the longer-term goal is to establish the ground-work for introduction of large-scale implementation of low-cost carbon fiber for significant impact in automotive lightweighting.

Preform Materials and Processing

The ACC Materials and Processing working groups had initiated work with EPFL to study processing effects and material properties of commingled glass and thermoplastic fibers leading to cost-model comparisons of various thermoplastic composite processes. Focus of this work has been on the TwinTex materials produced by Saint-Gobain Vetrotex incorporating glass and polypropylene fibers, while the basic evaluation process can be extended to a variety of materials and processes based on this concept. After up-front trials in preparation, ORNL hosted representatives of EPFL for extensive fabrication of panels supporting the ACC/EPFL-requested experimental matrix. Initial efforts focused on establishing a preferred baseline fabrication process and experiments were conducted to compare temperature data at various locations in order to define data-capture plans.

With support of EPFL and an ACC representative, approximately 200 sample panels were fabricated using various fiber lengths (25-75 mm) and preform thickness (2-4 mm) along with variations in preforming compaction station time (10-60s) and air-temperature variables (180-240^{o}C). Panels were trimmed and shipped to EPFL for molding trials and final analysis. Results so far have helped to establish initial thickness limits for processing at 3 mm without additional heat stabilization modification to the materials. (ORNL and the ACC have separately discussed with Vetrotex adding improved heat-stabilization capability to the TwinTex. ORNL and Vetrotex have tentatively planned specific evaluation trials, but these trials have been on hold pending resolution of the sale of this business unit.) Material properties from the ORNL panels processed by EPFL are competitive with similar materials and, in some cases, significantly improved. Overall economics for this process were shown by EPFL analysis to approach targets as chopping speeds improve, leading to additional near-term focus on demonstrating the technical and economic feasibility of higher-speed chopping processes.

As another portion of the current focus on thermoplastics, ORNL has been working with Polycomp (inventor of DRIFT) and Fiberform (a key licensee) to evaluate the possibility of chopping the DRIFT product form in the ORNL preforming machine as well as providing one route to evaluating the DRIFT material in general. In fiscal year (FY) 2006, Polycomp made sample quantities of glass-impregnated polypropylene using a 2400 tex glass tow which had been processed into a ribbon about 0.2-in wide and .035-in thick. As expected, the ribbon handled more like a solid strip of plastic than a pliable fibrous tow and did not cut as easily as a glass tow. In initial trials, ORNL was able to get some of the material through the chopper, but with only very small amounts cut before beginning to break blades in the chopper.

Polycomp agreed to make some modified samples in FY 2007 in order to get a thinner ribbon using a smaller glass tow size at about 1150 tex, which is essentially the size of glass tow utilized in the current TwinTex product. The samples were actually made at a weight ratio of 65% glass to 35% polypropylene, which yields a product comparable to the 60/40 TwinTex ratio. Polycomp made two variations of these samples – one at about 5/16-inch width and the other at about 3/16-inch width. ORNL was able to cut both tow sizes, having more success with the 5/16-inch width (nominally about .008-in in thickness) than the 3/16-inch width (at about .015-inch thickness). Although there was not enough material for extensive trials, there was enough combined material to conduct several experiments to

establish cutting parameters. The balance of the materials was used to spray up and compact a small amount of material that was subsequently molded in a lab press into a very thin section solely for demonstration purposes.

Based on the success with the small amount of sample materials, ORNL subsequently procured 250 lbs of the DRIFT materials in the 5/16-inch width to do more process development and material evaluation. Initial work established a basic processing envelope including both preforming and molding adequate for being able to fabricate evaluation panels as shown in Figure 1. A panel has been provided to the ACC Materials Group to begin assessing the properties of molded DRIFT materials after preforming. Once initial property data are received in FY 2008, plans are to focus effort on developing more optimum processing techniques taking into account material forms and chopper configurations that might be economically feasible for implementation.

ORNL has initiated a more in-depth study of mechanical chopping in FY 2007 to correlate chopping of various composite material forms versus alternative chopping parameters, configurations, and equipment forms and materials including evaluation of the high-speed Wolfangel chopper recently procured by the ACC. With a better understanding of this background and related equipment experience, we will be able to better address alternative means for processing the DRIFT materials form.

Longer-term, ORNL and Polycomp are continuing the ongoing discussion concerning consideration of putting a prototype DRIFT line at the end of a Low Cost Carbon Fiber pilot line to evaluate and demonstrate technical and economic potential for various automotive applications of the DRIFT process. As improvements are achieved in chopping and molding of the DRIFT material and progress is demonstrated in continuous manufacturing of low-cost carbon fiber, more definitive work plans will be developed for

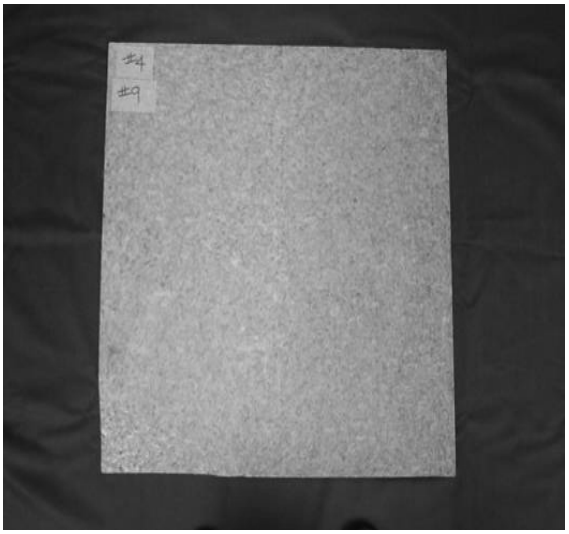

Figure 1. Panel preformed and molded by ORNL from DRIFT.

collaboration in both broad application of DRIFT with carbon fiber as well as more specifically with utilization in performing equipment. Objectives would include optimizing the fiber types, percentages, and types of polymer systems to achieve needed levels of mechanical performance and appearance. Important process characteristics, such as low warpage and reduced material system cost, will be explored. Test specimens and components will both be tested for characterization and durability for use in structural and semi-structural applications.

Since it is believed that hybrid-fiber preforms can effectively take advantage of concurrently utilizing carbon and glass fibers and offer potential benefits in terms of economics and property enhancement, ORNL has obtained standard lower-cost carbon-fiber alternatives from Zoltek and Toho to evaluate in conjunction with glass-fiber reinforcement previous acquired from Owens Corning. ORNL also procured polypropylene fiber to serve as the composite matrix from Fiber Science to use in initial trials to evaluate and demonstrate *in-situ* blending at the preforming machine. Due to current product availability typically only in very small tow sizes and desire to enhance intermixing of fibers and maintain capability to adjust the mix ratios to a large degree, the polypropylene was combined by the vendor to a larger tow size that was still about $1/6^{th}$ the size of the smaller glass and carbon tows on hand. Currently, the only packaging found

immediately available was outside pull for this product. These limitations necessitated use of a multiple-position creel to facilitate processing and mitigate entanglement (Figure 2). Further combining of packages at ORNL also served to minimize spatial requirements as more polypropylene is added to the blend ratios. During the initial preparation for the hybrid experiments, a limited amount of time was spent evaluating

Figure 2. Multi-package creel for *in-situ* blending experiments.

potential for use of the high-speed photographic equipment from the nearby Test Machine for Automotive Crashworthiness test system. (See 12.B) It appears this equipment will be beneficial in evaluating degree of intermixing in at least the glass and carbon or carbon and polypropylene mixtures, although it may be difficult to distinguish polypropylene from glass without additional study.

Although the initial work is utilizing polypropylene for demonstration purposes, the concept should also be applicable for other thermoplastic materials including polyethylene terepthalate (PET), nylon, and others. It is believed that regardless of whether the *in-situ* blending proves adequate for high-quality thermoplastic matrix parts, the technology being developed could prove advantageous in blending glass and carbon reinforcement to a level adequate for utilization of hybrid reinforcement and may be a good route for actually introducing more carbon fiber at somewhat lower quantities than necessary for all-carbon components in automotive applications.

Establishment of Molding Capability for Composites Evaluation

Key to being able to demonstrate the advances achieved in preforming technology is the ability to demonstrate that these advances translate into improvements in actual representative composites. The best way to effect this demonstration is through adequate evaluation of the preform itself as well as full consolidation of the preform and resin in a composite in the manner in which this would be accomplished in actual composite manufacturing.

Previously, ORNL staff worked with members of the ACC's Processing Group to quantify process-equipment requirements so that an appropriately-equipped research press and general-purpose research mold could be procured and installed at ORNL to support programmatic needs. The intelligent-leveling press was specified to accommodate various molds and molding processes and to be instrumented above routine standards in order to provide more process details in experimental research. Nominal pressing capacity is 750 tons. The general purpose plaque mold is specified for instrumented experiments using SRIM, compression molding of reinforced thermoplastics, and sheet molding compound (SMC) processes. This equipment will allow ORNL to demonstrate preform advances while further investigating advances in the various molding processes themselves.

In order to complete capability for basic molding operations, a dual-zone Sterling heat-transfer system was procured and installed at ORNL. Due to the differences in mass of the sections, dual-zone heating is necessary to be able to balance the temperature of the top and bottom sections of the mold to achieve uniform temperatures and is also useful in controlling the mold clearances and shear edges as the sections slide together and separate in operation. Also during this period, mold instrumentation was completed and integrated into the press data-acquisition system. In order to conduct initial materials evaluation experiments and establish detailed requirements

for more optimum charge heating and transfer of the charge to the press, a screen and aluminum (Al) plate are being used in various configurations in molding experiments. Currently, an existing laboratory oven is being utilized for charge heating, but the oven is not designed for rapid material insertion, charge heating, and material removal and is located further away from the press than would be optimally employed for routine manufacturing operations, especially when molding relatively-thin sections that would rapidly dissipate heat. The Al plate is used to convey the charge from the oven to the press and has raised sections on three sides for rigidity and to somewhat impede air flow across the charge surface while allowing ease of transfer of the charge from the fourth side. The screen is used to allow air flow across the surface of the charge and, when employed on the top surface of the charge, can be used to mitigate "lofting" of the preform while heating. Initial experiments do indicate that the plate helps to retain enough heat during transfer to still have flow in the molding operation, but more experimentation in FY 2008 will help to define adequacy of this approach versus utility and requirements for a dedicated oven in close proximity to the press and mold.

Although originally a portion of the press and mold procurement process, procurement of an SRIM machine was deferred due to higher than expected bid costs during the formal procurement period and somewhat less recent focus on development and demonstration of the SRIM process. Programmatic benefits for utilizing an existing, older-model SRIM machine having capacities close to those identified as targets for the procurement process are being evaluated versus costs and risks for possible refurbishment and/or upgrade of this machine or trade-in for a rebuilt unit with capabilities comparable to the targeted parameters. In current planning, it is thought that this equipment will be critical for evaluation of any materials in liquid-molding processes since this capability is being down-scoped at other program facilities and will be very useful in evaluating a variety of material forms including hybrid blends, natural-fiber preforms, and early evaluation of low-cost carbon fiber. This decision has been deferred again until budget and program direction are better defined.

Fiber-Severing Technology

Due to significant differences in the physical properties of various reinforcement fibers as well as their available product forms, chopping technology that has been successful for glass-fibers systems has demonstrated less-satisfactory results for the carbon-fiber products that are currently available. It is expected that similar results will occur for reinforced thermoplastics and hybrid glass-carbon products. Accordingly, consideration is given in this project to identifying alternative severing technology. A literature and patent search was previously undertaken to assess promising technologies for bench-top investigation. Possibilities identified include mechanical-based, laser-based, CO_2 pellet, liquid nitrogen, water-jet, and ultrasonic. Based on the information available in the literature and consideration of project-team experience in related activities, laser-based choppers appeared to offer the most promise for development and eventual deployment.

Calculations based on the enthalpy of vaporization of carbon indicated that a neodymium: yttrium-aluminum-garnet (YAG) laser system should be able to comfortably deliver the energy required to sever a large carbon-fiber tow (roughly 50,000 filaments) at about 1,000 cuts per second, which would represent a tow traveling at close to the maximum velocity as would be encountered in the ORNL chopper and chopped at a rate sufficient to yield a 0.5-inch cut length. However, in initial experiments at or close to these conditions, we were unsuccessful in getting the necessary power delivered into the entire fiber bundle to effect severing. It appeared that the surface of the outer fiber was ionizing and preventing further energy deposition and penetration into the bundle. In follow-up work conducted using a continuous-wave CO_2 laser as well as an excimer laser and a more tunable (and slower pulse-rate) neodymium: YAG laser, severing of carbon fiber was demonstrated, although none were accomplished at the rates representative of the most aggressive cases thought possible with the original neodymium: YAG laser.

During FY 2007, work was continued with various smaller cross-sectional tow sizes and the

more tunable neodymium: YAG laser. New optic configurations were introduced and evaluated with each iteration targeting a more compact and "efficient" energy-deposition line. A recently-evaluated aspheric lens clearly reduced the spherical aberrations noticed in prior attempts to form a much better line-focus. However, the performance of this configuration in actual cutting was less successful than expected. Essentially, those conditions that produced cuts in the original configuration were now only producing partial cuts. Taking a closer look at several burn patterns as a function of energy and working distance, it was noticed that, at higher energies, the line was much broader than had been hoped and the line was very sensitive to working distance because the numerical aperture (NA) of the new design was much larger than the original configuration (depth of focus is inversely proportional to NA). In terms of cutting, the first observation says that, despite what the simulation showed, the new optics were still not getting all the photons into the smallest possible line. This is most likely due to the fact that the real collimated beam departs significantly from the beam profile assumed in most ray tracers. The second observation is that this system develops a tight focus over a very narrow range of displacements which, in this case, is unfortunately corresponding to some fraction of the thickness of the fiber bundle.

Subsequent work compared the newer beam-line to the former utilizing systematic burns repeated with swapped optics. This repeated experimentation did not illuminate any specific new issues that had been overlooked in introducing the new optics. Since it is still believed that the key immediate issue remains the delivery optics, effort was initiated late in FY 2007 to identify capability to more effectively model optics configurations during FY 2008 to determine what is really practical in terms of the desired processing speeds and physical limitation likely to exist in a production environment. If it appears success can be achieved with improved optics alone or in combination with other alternative systems, these results will be utilized to define the more detailed laser-parameter and control requirements in order to be able cleanly sever a moving carbon-fiber tow at the speeds required for utilization in the P4 system. Initial work will continue to be done in static tests to determine beam width, power levels versus time, and other necessary information before moving to low-speed tests and then tests at speeds more representative of actual fiber deposition rates. With the concept demonstrated, plans would then be to scale up the hardware for on-machine experimentation and demonstration. In addition to severing carbon fiber, future work will address other reinforcing fibers, as well as fibers used as binders, and blends of reinforcing and binder fibers.

As previously mentioned, ORNL has initiated a more detailed study of mechanical chopping for various materials forms and techniques along with the above plans to continue evaluation of the potential for laser-severing. It also had been mentioned earlier that effort is underway to more fully evaluate the Wolfangel chopper at ORNL and to evaluate modifications to the chopper equipment including cutting wheels and blades for both units. Near-term plans for the Wolfangel chopper include very extensive cutting of a large amount of TwinTex material up to a simulated work-week to establish speed and durability of the chopper in its current configuration, as well as potential for scale-up to even higher speeds that may be required for process economics. These trials should afford a good opportunity to evaluate several blade options and possibly other options as well as establishing solid data for the baseline configuration. Effort has been initiated to characterize the metallurgy of the current cutting blade materials and identify candidate replacement materials, coatings, surface treatments, or cutter designs. Initial work has shown that the commercially-available blades currently supplied by Aplicator may be supplied with edge chips (Figure 3) at sizes on the order of fiber diameter, which at a minimum could lead to incomplete fiber cutting.

Sources for other commercial blades and coatings are being surveyed and samples of the most promising materials are being obtained for further evaluation. Current alternatives include the low-temperature carburization process developed by Swagelok (this recently won the 2006 ASM engineering materials award) and the C3I coating

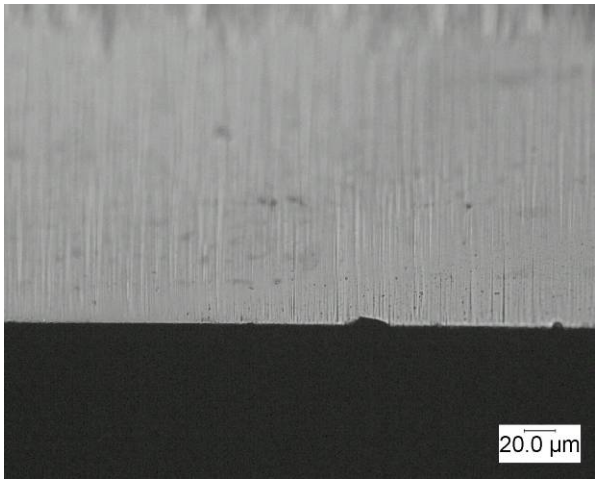

Figure 3. Commercially-supplied blade with edge chip.

process (this won a 2006 R&D 100 award). Both can be used on the existing material. Tungsten carbide blades have also been obtained. Based on test data and other input, recommendations will be developed for enhancing the durability of cutter assemblies. This may include changing to more durable materials, changing the surface finish, changing design of the cutters or holders, and applying coatings or surface treatments to existing or alternative materials.

With a better understanding of chopping mechanics and developing experience with varying blade designs, blade materials, and cutting mechanisms, we will be able to better address a variety of cutting issues associated with carbon fibers specifically as well as with other materials and material blends including somewhat unique products such as the DRIFT materials.

Modeling of Fiber Deposition

A C-based program continues to be developed to analyze the effect of process variables on preform characteristics. The program can be used to evaluate preforms in terms of measures such as fiber run length, fiber connectivity, distribution of voids, etc. When correlated with permeability data and areal density measurements, the program will provide an understanding of the effect of process variables on resulting preforms and their "moldability."

Advancements to the program have included continued enhancement of the previously-developed general modeling approach by addition or improvement of many of the capabilities such that it can simulate a variety of fiber-deposition patterns, orientations, fiber types, layers, network densities, and thicknesses. The program models statistical material properties such as distribution of contacts, voids, segment lengths, fiber undulation, layers, etc. in a full three-dimensional fiber network structure.

A very-much-improved flexure model for fiber deformation has been completed and integrated into the Simulator code. Although not quite as fast as earlier deflection models employed, the new one produces much more realistic fiber conformations than any of the earlier versions and can be extended to include physical effects that would have been impossible for earlier versions to handle.

The full Simulator code has been divided into two separate, stand-alone systems. The first of these eliminates the Void Search and Void Analysis routines, but includes all functions required for managing lay-up growth and for performing various analyses of a completed lay-up. Upon completion of a lay-up, all data relevant to a user-selected "sampling slice" are written to files for further analysis and for support of the now stand-alone Void Analysis code. Several factors motivated the decision to partition the code. Code size was certainly one of these. More important, however, was the desire to be able to develop and store a lay-up upon which a variety of Void Search and Void Analysis experiments could be performed.

The stand-alone Void Search module resulting from the division noted above has been very much refined relative to earlier versions and is now both considerably faster and much more accurate in its delineation of the Void spaces in a lay-up. Void Analysis capabilities are likewise enhanced. For instance, using the stand-alone Void code, the same lay-up (as represented by the data stored with the intermediate "sample slice" file noted above) can be searched many times for Voids, each time using a different probe sphere size. Extraction of information relevant to resin flow, etc. is thus considerably simplified.

Near-term plans include the development of capability to simulate fiber lay-ups made of multiple fiber types deposited concurrently, with emphasis on on-line and off-line commingling for different deposition scenarios. Plans also include development of methods for evaluation of manufacturing feasibility of the above lay-ups. Work is underway to improve availability of the code for more wide-spread evaluation, likely on a work-station platform.

Summary and Conclusions

This project is continuing to build on past development and application of directed-fiber preforming processes, namely, those of the baseline P4, to extend the process to new material systems. Developments are expected to facilitate the use of lower-cost carbon fiber, reinforced thermoplastics, and glass-carbon hybrid materials as effectively as is the current state-of-the-art with glass. Utilizing these materials is expected to lead to further reductions in vehicle mass in a more cost-competitive scenario than is currently possible.

A research-focused preforming system installed in the polymer-composites laboratories at ORNL is currently being used to build preforms for evaluation utilizing various forms of glass fiber commingled with thermoplastic fiber to serve as the composite matrix and glass fiber pre-impregnated with thermoplastic resin utilizing the DRIFT process. Evaluation of a large number of ORNL-fabricated preforms from off-the-shelf commingled TwinTex by EPFL and the ACC has been both technically and economically encouraging, while data have not yet been received on the DRIFT forms. With the acquisition of polypropylene fiber and establishment of means to combine a number of tows *in-situ*, the focus is being expanded to include evaluation of current commercially-available industrial grades of carbon fiber and hybrid blends of carbon fiber and glass fiber along with various blends of thermoplastic fiber.

Also during FY 2007, a heat-transfer system for the complementary advanced research press and general purpose plaque mold was procured, installed, and integrated with instrumentation providing the requisite equipment necessary to demonstrate the advances achieved in preforming technology through composite manufacturing. Use of this system is expanding in evaluating DRIFT and hybrid material variations produced in preforming experiments.

Severing investigations are being conducted in two areas looking at both mechanical-chopping and laser-severing alternatives. The mechanical investigations are looking at blade materials and coatings to also include various cutter configurations. In laser-severing, the optics delivery system is being modeled to determine if there is a practical route to effective laser-energy deposition applicable to this project's requirements.

Modeling of the fiber-deposition process continues through the development of an in-house code. Work is underway to incorporate capability to simulate lay-ups made with multiple fiber types and to provide availability of at least a portion of the model to operate on a more accessible work-station platform.

Collectively, the technologies under development in this project will advance low-cost processing on two fronts. First, it will provide the opportunity to employ additional materials in the net-shape preforming process, which is expected to lead to additional mass reduction and/or better performance. Second, it will provide the requisite tools to evaluate the effect of process parameters on the utility and performance of preforms and molded parts.

D. Low-Cost Carbon-Fiber Composites for Lightweight Vehicle Parts

Principal Investigator: Mark A. Janney
Materials Innovation Technologies, LLC
320 Rutledge Road, Fletcher, NC 28732
(828) 651-9646; fax 828-651-9648; e-mail: mjanney@emergingmit.com

Technology Area Development Manager: Joseph A. Carpenter
(202) 586-1022; fax: (202) 586-1600; e-mail: joseph.carpenter@ee.doe.gov

Contractor: Materials Innovation Technologies, LLC
Contract No.: DE-FG02-05ER84327 (Small Business Innovative Research (SBIR) and Small Business Technology Transfer (STTR) Program

Objectives

- Develop at pilot-scale the Three Dimensional Engineered Preform (3-DEP) process, a slurry-based, low-cost, high-volume production process for making net-shape, carbon-fiber preforms for use in polymer-composite automobile parts.
- Optimize 3-DEP tooling development and evaluate how it influences fiber placement in the preform.
- Optimize carbon-fiber slurry development and determine how it affects preform properties.
- Develop process capabilities to include material handling, preform molding, preform drying, and reducing preform variability.
- Demonstrate the utility of 3-DEP preforms to make an in-production, thermoset composite, automotive component using production tooling (Corvette wheelhouse support).
- Build a process cost model for composites made using 3-DEP preforms.
- Write training and quality manuals.

Approach

- Investigate effects of processing parameters on properties of flat-plate parts and Corvette wheelhouse-support parts in the 3-DEP machine.
- Examine effects of (1) fiber flow within the tank and (2) 3-DEP forming-head motion to produce uniform preforms.
- Demonstrate ability to control part weight during a 3-DEP production run.
- Demonstrate ability to control within-part areal weight distribution (i.e., fiber areal density).
- Collaborate with a current Tier 1 automotive supplier to demonstrate the applicability of 3-DEP preforms in an existing production process.

Accomplishments

- Made 14 x 14-inch flat preforms in 1/4-inch, 1/2-inch, and 1-inch chopped carbon fiber with part-to-part coefficient of variation (COV) between 1 and 4%.
- Made complex shape preforms (Corvette wheelhouse support) in 1-inch carbon fiber with part-to-part COV of 2-4%.
- Made both flat preforms and Corvette preforms having within-part COVs ≤ 3.5 %.
- Demonstrated that carbon-fiber Corvette preforms could be molded into composite parts on production molding equipment using a standard production polyester resin.
- Demonstrated that plaques molded from 3-DEP flat preforms had mechanical properties acceptable for automotive semi-structural applications.
- Demonstrated the ability to make molded plaques with fiber loadings up to 30 vol %.

- Demonstrated that 3-DEP works well with reclaimed/recycled carbon fiber.

Future Direction

- Develop preforming technology to achieve higher fiber loading (>50 vol %) in molded composites.
- Extend the capability of the technology to make large parts up to 6 feet x 6 feet (e.g., hood inners, trunk liners).
- Combine 3-DEP preforms with continuous-fiber face sheets to make true structural composites.
- Identify opportunities within the automotive, industrial, and aerospace communities to commercialize the 3-DEP technology.
- Expand our forming capabilities to other fiber-reinforced composites including fiberglass, aramid, natural fibers, and hybrids of these.

Introduction

This work is being conducted under an SBIR Phase II project. The goal of the project is to develop at pilot-scale a potentially low-cost, high-volume production process for making net-shape, carbon-fiber composites for use in polymer-composite automobile parts. The main technical focus of the project is making components and optimizing their manufacture using the 3-DEP fiber-forming process. 3-DEP is an advanced slurry molding process which produces a homogeneous fiber distribution within parts, and consistent part weight and dimensions from part-to-part. Making a consistent preform is key to making consistent parts. A more detailed account of the 3-DEP process, including a short video, can be found at http://www.emergingmit.com/Presentations.html.

The overall objective of the project is to complete the development of the technology started in the Phase I SBIR project by focusing on a complex-shaped component that will be commercially viable. The part chosen for the Phase II project is the front wheelhouse lower support for the Corvette, Figure 1.

This part is currently manufactured by our partner in the project, the Molded Fiber Glass Companies (MFG) of Ashtabula, Ohio. MFG has been supplying Corvette with fiberglass-reinforced polymer parts since the car was introduced in 1953. MFG currently manufactures ~60,000 of the front wheelhouse lower supports per year in fiberglass. The average thickness of these parts is 2.5-3 mm; the glass fiber content is 24% by volume and the part weighs about 0.75 lb. It is about 12 inches wide by 4 inches tall.

Figure 1. Corvette wheelhouse lower support demonstration part molded at MFG using a carbon-fiber preform made by the 3-DEP process.

The front wheelhouse lower support was chosen as a demonstration part because:

a). It is a very complex shape with multiple curvatures, deep draws, nearly-vertical walls, and sharp-edge and corner features. It is one of the most challenging parts MFG molds by the preform process. If this part can be produced using preforms made by the 3-DEP process, then there are a number of related automotive parts (e.g., hoods, trunks, floors, doors) that can also be readily produced.

b). It is currently made in commercial quantities (60,000 per year) in fiberglass giving a body of production and technical data to which we can compare our new process.

c). It is a structural part but not a safety-critical one. Also, it does not require a "Class-A" surface finish (such as an exterior body panel

would require), which would add another level of difficulty to its production.

d). The impregnation/compression molding tool is available at MFG, eliminating an expensive capital expenditure for new tooling.

At the completion of Phase II, we will have a process producing trial parts for evaluation by an automobile manufacturer, General Motors (GM).

Specifically, the technical objectives of our Phase II project are to:

1). Develop at pilot-scale the 3-DEP process, a slurry-based, low-cost, high-volume production process for making net-shape, carbon-fiber preforms for use in polymer-composite automobile parts.

2). Optimize 3-DEP tooling development and how it influences fiber placement in the preform.

3). Optimize carbon-fiber slurry development and how it affects preform properties.

4). Develop process capabilities to include material handling, preform molding, preform drying, and reducing preform variability.

5). Demonstrate the utility of 3-DEP preforms to make a thermoset composite, in-production automotive component using production tooling (Corvette wheelhouse support).

6). Build a process cost model for composites made using 3-DEP preforms.

7). Write training and quality manuals for the 3-DEP process.

Progress to date has been excellent. We have conducted twelve runs of carbon-fiber preforms. The tests comprised between 16 and 40 parts each; we ran 14 x 14-inch flat plaques and the Corvette wheelhouse part. The part-to-part COV was between 0.8 % and 4.9 % depending on the part being formed, the mass of the part, and the fiber length. The within-part COV for flat plaques in 1-inch-long carbon fiber was ≤ 3.5%. This is considered good repeatability by automotive standards.

We have made substantial modifications to the 3-DEP lab-scale machine that should allow us to achieve forming consistency from part to part and within-part that are acceptable to the automotive community. We have also demonstrated the ability to make preform molds that will produce good quality parts in a cost-effective manner. Twenty-five carbon-fiber preforms of the Corvette lower wheelhouse support and twelve 14 x 14 inch flat preforms were sent to MFG in 2007 for molding in polyester. Preliminary molding trials have been favorable.

Task 1 - Design and Construction of the Forming Tool and Vacuum Box

Our objective is to design a low-cost tooling system for the wet-forming and drying operations, Figure 2.

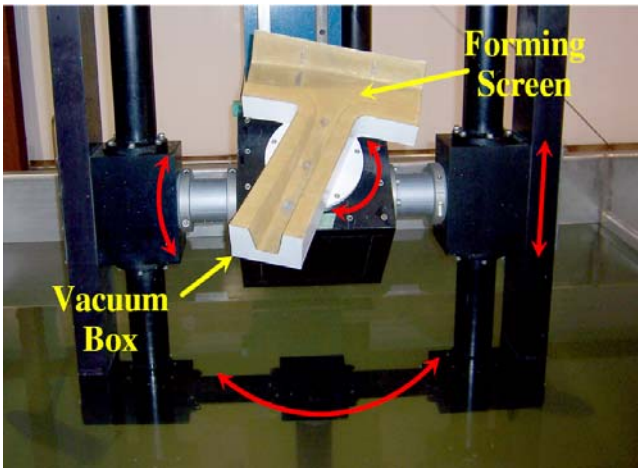

Figure 2. 3-DEP forming head with B-pillar forming tool.

We have considered three approaches:

- An all stainless steel or brass, heavy production tooling system.
  This approach was the lowest risk, but highest cost. The risk was low because it employs technology that has been used for more than 30 years in the speaker-cone industry. The cost is high because it requires complex sheet-metal forming processing to form the perforated stainless steel sheet into the complex shape of the demonstration part, the Corvette wheelhouse support.

- A low-cost, composite prototype tooling system.
  This approach has the advantage that a tool can be formed directly from an existing part. The tool was made in just a few days, rather than the several weeks required for the

stainless-steel tool. The trade-off was that the tool is not as robust as an all-metal tool.

- A semi-composite tools design that is more robust but yet low in cost.
  This approach delivered a combination of properties of the metal and composite tools. It was manufactured fairly quickly, like the composite tool, but was nearly as robust as the stainless-steel tool. This is the approach we think will be most valuable as production tooling as we go forward with the 3-DEP commercialization process.

We have shown proof of concept on all three tooling systems and now have moved on to study how the fibers form against these tools as they are deposited from the suspension.

Task 2 - Fiber and Suspension Issues

A new computer-programmable agitation system has been designed and built for the gimbaled molding machine. This new agitator system allows us to make changes during the formation cycle, which is reducing some of the variations we had previously seen in the suspension. The new agitation system is also a much more robust design that will be suitable for use in the next-generation preforming machine. Our current, lab-scale machine has a suspension tank with a 2000 gallon capacity. The next-generation machine will have a suspension tank capacity of about 50,000 gallons.

Task 3 - Motion Program for Vacuum Forming Parts

We have conducted numerous trials to determine what the capability of the 3-DEP machine is relative to making 14 x 14-inch flat plaques and the Corvette lower wheelhouse support part in carbon fiber. We have used 1-inch, 1/2-inch and 1/4-inch-long fibers in our studies. The binder fibers, which bind the carbon fiber together in the dry state, are either cotton linter or acrylic fiber, which have found extensive use in the speaker-cone industry.

Figures 3-5 show overviews of the Corvette wheelhouse support preform in 1-inch and ¼ -inch carbon fiber along with a set of 25 1-inch carbon-

Figure 3. Top and bottom view of Corvette lower wheelhouse support preform in 1-inch chopped carbon fiber. As-formed, no trimming was done.

fiber preforms that were sent to MFG for initial compression molding trials using their production equipment. The dried preforms are quite robust. The parts shown in Figure 5 were shipped by ground transport to MFG for molding and all parts survived the trip intact and ready to be molded.

A close-up of the fibers in a preform is given in Figure 6. This shows that the architecture of the carbon-fiber preforms is a combination of individual fibers and some fiber bundles. We have

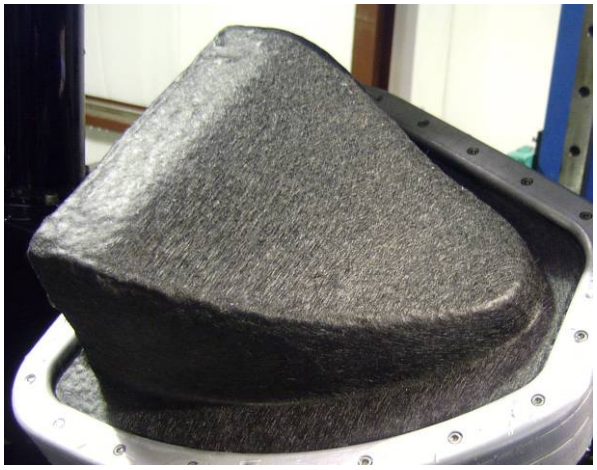

Figure 4. Corvette lower wheelhouse support; ¼- inch chopped carbon fiber; part still mounted on the forming tool. Note improved surface finish of 1/4-inch compared with 1-inch chopped fiber in Figure 3.

Figure 5. Corvette wheelhouse support preforms were shipped to MFG for molding in polyester.

not measured the orientation distribution of the fibers in the preforms (it was not a defined task in this project); however, the distribution appears to be fairly random based on observations of many different areas in numerous preforms.

Machine Variables

We have identified forty-two variables in this new wet-molded preforming process and now have computer-programmable control of twenty-two of them with the remaining twenty manually controllable.

By proper selection of machine variables, we have been able to fine-tune our preforming process.

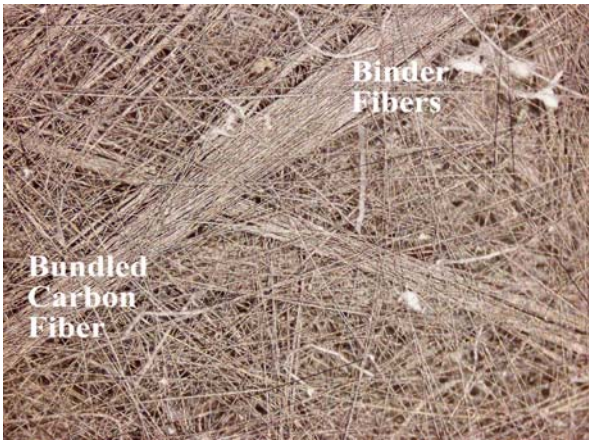

Figure 6. Photomicrograph (20X original magnification) of carbon-fiber preform showing individual carbon fibers, some bundled carbon fibers, and binder fibers.

Figure 7 shows run charts for the Corvette part and for 14 x 14-inch flat plaques from our initial trials in April 2007 and for trials in June 2007.

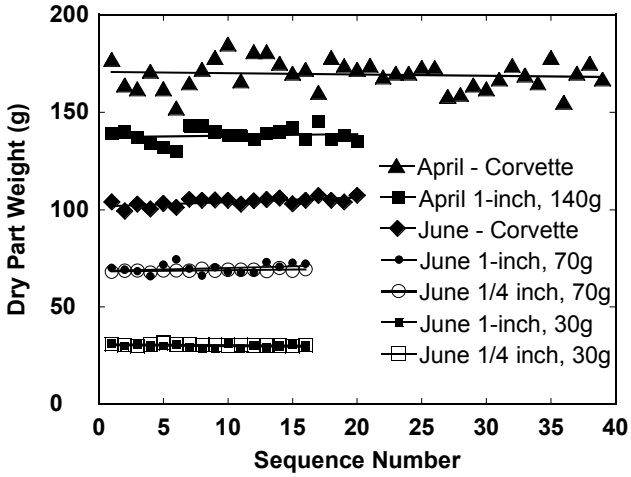

Figure 7. Control charts (part weight vs. sequence number) for 3-DEP preforms (flat and Corvette) made from 1/4- and 1-inch carbon fiber. Similar results were obtained for 1/2-inch carbon fiber.

Table 1 summarizes the mean part weight and part-to-part COV for each run. The April Corvette parts exhibited a very respectable COV of 4.4%; engineers at GM informed us that a COV <10% would be acceptable. The April flat preforms exhibit a good COV (2.7%) but show evidence of "chasing weight" during the run, which necessitated making manual adjustments to the machine settings (at part 7 and part 13). In contrast, the Corvette parts made in June (after running several 3-DEP experiments to optimize

uniformity of the Corvette preform) show extremely good part-to-part COV (2%). The flat plaque COVs for short (1/4-inch) fibers were even smaller, ~ 1%.

Table 1. Summary Data for 3-DEP Parts.

Part	Fiber Length (inch)	Part Mass Mean (g)	Part Mass COV (%)	Number of Parts
April 2007 Corvette	**1**	**169**	**4.4**	**40**
Flat plaque	**1**	**138**	**2.7**	**20**
June 2007 Corvette	**1**	**104**	**2.0**	**20**
Flat plaque	**1**	**69.5**	**3.5**	**16**
Flat plaque	**1**	**49.1**	**4.9**	**16**
Flat plaque	**1**	**29.9**	**3.3**	**16**
Flat plaque	**0.25**	**68.8**	**0.8**	**16**
Flat plaque	**0.25**	**50.3**	**0.9**	**16**
Flat plaque	**0.25**	**30.6**	**1.3**	**16**

In addition to the part-to-part variation, we are also interested in within-part variability of the basis weight. Figure 8 shows a Corvette preform and a flat preform that were sampled for basis-weight variation using a 3-inch diameter punch. The basis weights for the two preforms were similar (852 vs. 857 g/m^2). The within-part basis-weight COVs were also similar at 3.5 and 3.6 %. What this means is that the uniformity of a preform manufactured by the 3-DEP process is not sensitive to the part geometry. This is a very exciting result given the complex geometry of the Corvette wheelhouse support.

Finally, it should be noted that forming time for parts using the 3-DEP process is not a function of the geometric complexity of the part. The Corvette part and the flat preform shown in Figure 8 were made in a similar amount of time.

Task 4 - Drying the Preform

We are starting to investigate combining the step of "de-watering" the preform with the step of transferring the preform to a separate drying station. ("Dewatering" the preform is the initial drying step and uses a high volumetric flow of air through the preform to reduce the water content from 30 wt % to about 10 wt %.) The transfer system design draws the remaining molding water from the preform as it transfers the preform to the drying station where the remaining moisture can be driven away with heat and possibly pressure.

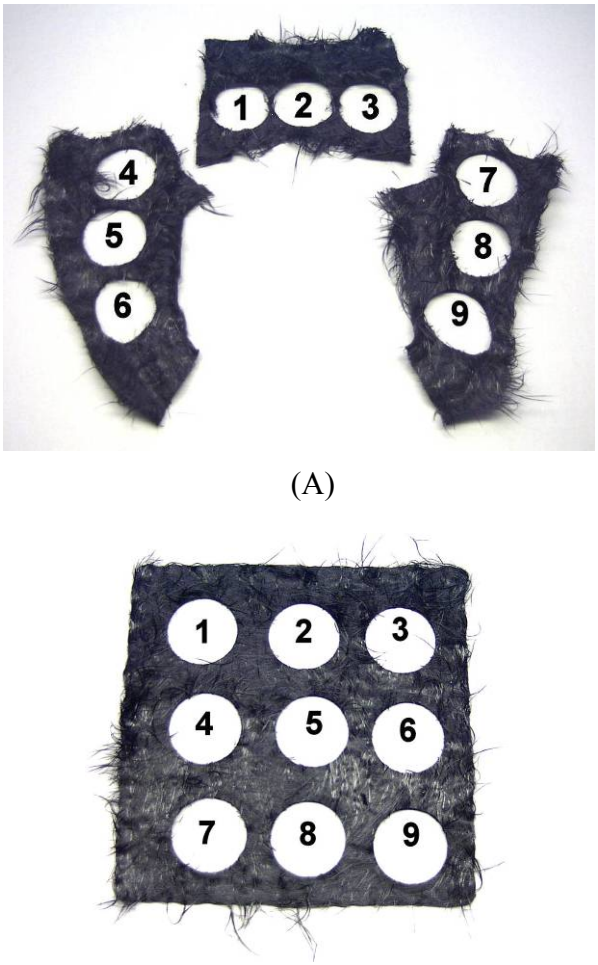

Figure 8. Basis-weight sampling using a 3-inch diameter punch was conducted on a flattened Corvette preform (A) and a flat preform (B).

The design goal is to minimize the number of tools required in the preform drying operation to support a three-minute production cycle.

Task 5 - Fiber and Suspension Issues

All of our work to date has been conducted using ¼-, ½-, and 1-inch polyacrylonitrile (PAN)-derived carbon fibers with cotton linter or acrylic fiber as the binder fiber. We are starting to look at a variety of additional binder fibers to help increase dry strength.

Figure 9 shows three flat-plaques that were made using ¼, ½ and 1 inch fibers. Clearly, the ¼-inch fiber creates the most loft and the1-inch fiber creates the least. It is believed that similar changes in loft can be affected by the proper selection of binder fiber.

Task 6 - Properties of Molded Flat Plaques

We have collected some preliminary physical property data for flat plaques, Table 2. The plaques were molded at MFG using 1-inch carbon-fiber flat preforms and an unfilled production polyester resin. The strength and stiffness were reasonable given the low fiber content of the plaques (17 vol %).

Task 7 - Reclaimed Carbon-Fiber Processing

The following task is not a part of the DOE SBIR Phase II project. It is included because of the wide interest in how one might use reclaimed carbon fiber.

There is a strong interest in the reclamation of carbon fibers from retired aircraft and other carbon fiber-intensive products. In the reclamation process, used composite materials are roughly chopped and processed to free the fibers from the epoxy matrix using thermal or chemical processes. After the fibers have been freed from the matrix, the resulting product has been shown to have individual fiber properties very close to those of the virgin material.

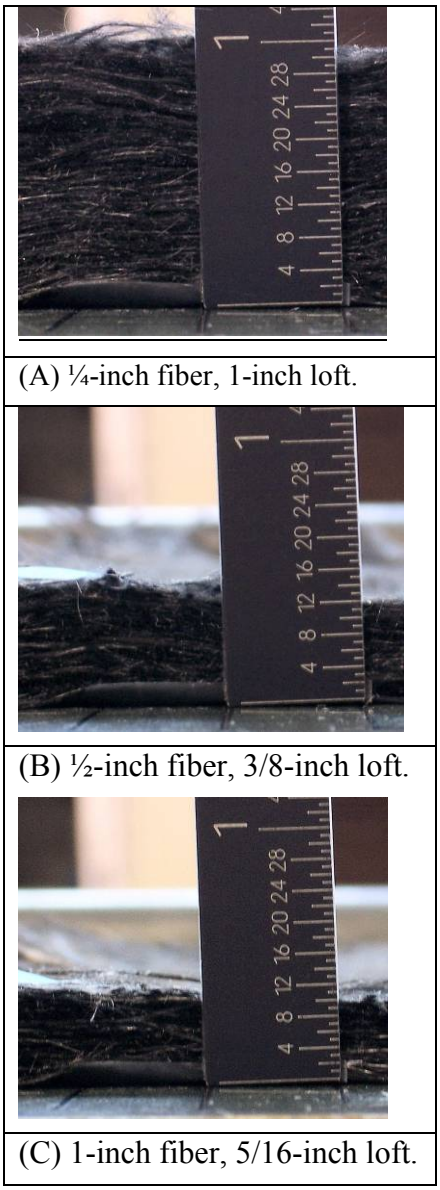

(A) ¼-inch fiber, 1-inch loft.

(B) ½-inch fiber, 3/8-inch loft.

(C) 1-inch fiber, 5/16-inch loft.

Figure 9. Preform loft decreased as fiber length was increased from ¼-inch to 1 inch. Side view of dry preforms.

Table 2. Mechanical properties of flat test panel fabricated at MFG, 17 vol % fiber, polyester resin.

Property	ASTM Method	N	Mean	Unit	COV (%)
Tensile Strength	D-638	6	156 23	MPa kpsi	12.8
Tensile Modulus	D-638	6	16.8 2.4	GPa Mpsi	9.1
Flexural Strength	D-790	6	264 38	MPa kpsi	9.1
Flexural Modulus	D-790	6	13.3 1.9	GPa Mpsi	14.7
Un-notched Izod	D-4812	6	370	J/m	24.3
Density	D-792	5	1.29	g/cm3	1.6
Water Absorption	D-570	5	0.72	wt %	8.3

The reclaimed carbon fibers were supplied to MIT-LLC by Boeing Corp. The material was taken from an F-18 stabilator. The composite material had been roughly chopped before the fiber-reclaiming process was applied. It contained a large quantity of impurities (metal particles, wire, support structures, aluminum honeycomb materials). The carbon fiber was variable in type, length and configuration. Unidirectional fiber, woven carbon fabric, and lose carbon fibers were present. The fibers ranged in length from <1" to >4." After inspection of the pyrolyzed fiber, it was determined that it needed to be thoroughly cleaned prior to use in the 3-DEP process.

The cleaned and length-reduced fibers were used in the 3-DEP process to evaluate the potential of the process to manufacture useful preforms. In the process, standard machine settings and fiber loading rates were used. No issues were found in dispersing the fibers in the system on in generating a uniform suspension. Six flat-panel preforms and six Corvette wheelhouse fiber preforms were manufactured from the reclaimed fibers; panels were also formed from virgin fiber. Figures 10a and 10b show Corvette wheelhouse preforms manufactured from recycled and virgin chopped carbon fibers. The shorter average fiber length in the reclaimed fiber accounts for the smaller amount of "fuzz" around the edges of the reclaimed preform (cf., Figures 3 and 4) as compared with the virgin fiber preform.

Figure 10a. Corvette preform from reclaimed carbon fiber.

Figure 10b. Corvette preform from virgin carbon fiber.

The Corvette wheelhouse parts were successfully molded with polyester resin at MFG. To make a composite part, the top and bottom of a preform were coated with unfilled polyester resin. The part was then placed on the bottom tool, the mold was closed, and the part was densified and cured. No issues were encountered in molding parts by this method. The preforms showed excellent resin penetration during molding and the product showed excellent stiffness after molding.

Summary and Conclusions

The key to the 3-DEP process is the ability to handle chopped-fiber reinforcements in a high-volume, cost-effective process while enhancing the quality and the functionality of the component. Typical forming times are 1 to 2 minutes. Neither the time required to make a preform, nor the

uniformity of fiber distribution with a preform, are sensitive to the geometric complexity of a part.

This has significant implications for making composite parts for automotive applications since those parts often contain deep draws, narrow channels, combined vertical and horizontal surfaces, sharp corners and edges, etc. Uniformity of parts is high; COVs of part-to-part weight and weight distribution a part are ~3%. Preforms are truly net-shape with almost no scrap.

The 3-DEP process brings to materials forming an exciting, innovative way to make composites. 3-DEP has the potential to radically change the way preforms and the composites made from them of are fabricated and used.

Presentations/Publications/Patents

1. Mark A. Janney, "Forming Natural Fiber Composites by the 3-DEP Process: An Initial Study," presented at the Automotive Composites Consortium Annual Meeting, September 25, 2007, Dearborn, MI.
2. M. Janney, E. Geiger, Jr., and N. Baitcher, "Fabrication of Chopped Fiber Preforms by the 3-DEP Process," Proceedings of COMPOSITES & POLYCON 2007, ACMA, October 17-19, 2007, Tampa, FL.
3. Mark A. Janney and David P. Haack, "Fabrication of Net-Shape, Chopped Fiber Preforms by the 3-DEP Process," presented at Carbon Fiber 2007, December 5-7, 2007, Washington, D.C. Online at http://www.emergingmit.com/Presentations.html.

E. High-Volume Processing of Composites (ACC 115[i])

Principal Investigator: Gerard Olszewski
Chrysler LLC, Materials Engineering
CIMS 429-50-00, 2301 Featherstone Road, Auburn Hills, MI 48326
(248) 512-8531; fax (248) 512-7915; e-mail: go5@chrysler.com

Technology Area Development Manager: Joseph A. Carpenter
(202) 586-1022; fax: (202) 586-1600; e-mail: joseph.carpenter@ee.doe.gov

Field Project Officer: Aaron D. Yocum
(304) 285-4852; fax: (304) 285-4403; e-mail: aaron.yocum@netl.doe.gov

Expert Technical Monitor: Philip S. Sklad
(865) 574-5069; fax: (865) 576-4963; e-mail: skladps@ornl.gov

---

Contractor: United Sates Automotive Materials Partnership (USAMP)
Contract No.: DE-FC-59OR22545 through the DOE National Energy Technology Laboratory

---

Objective

- Develop and demonstrate high-volume manufacturing (molding) processes to produce lightweight composite automotive components.
- Expand the scope of the Automotive Composites Consortium (ACC) composite projects into the thermoplastic and natural-fiber areas.
- Develop, build, and demonstrate an economical, lab-scale, automated fiber-retting process and apparatus suitable to bast-based fibers including hemp, kenaf, and flax.
- Develop, build, and demonstrate a lab-scale, natural-fiber preform and compression-molding process, and produce panels to develop a mechanical and thermal natural-fiber polymer-composite database.

Approach

- Develop and study high-volume composite manufacturing processes within approved research programs.
- Work with a Tier 1 automotive composites supplier to investigate and develop an improved carbon-fiber sheet molding compound (SMC) material amenable to cost-effective, high-volume applications.
- Acquire tooling necessary for the support of the ACC 115 research programs.
- Continue development of a tool to quantify the severity of bondline read-through (BLRT).
- Conduct several lab-scale process trials of fiber preparation-retting processes enabling the development of the most appropriate process and instrumentation.
- Develop, design and construct a lab-scale, non-aqueous, fiber-preform manufacture apparatus.
- Conduct full mechanical, thermal, and environmental characterization of natural-fiber-reinforced panels.

Accomplishments

- Provided process support for Automotive Composites Consortium Focal Project 4 (ACC 007, see 8.A).
- Proposed upgrading an existing SMC compounder at a Tier 1 supplier, Continental Structural Plastics (CSP), to acquire carbon-fiber capability. Secured DOE and ACC funding to accomplish that. Purchase orders are being issued.

- Injection-molding and compression-molding plaque tools completed and starting work on thermoplastic and thermoset characterization database and supporting Development of Manufacturing Methods for Fiber Preforms (ACC 040, see 8.B) and ACC 007 investigations.
- Continued work on BLRT by the molding, bonding, and analysis of plaques to develop base-line measurement of bondline read-through.
- Initiated efforts with Pacific Northwest National Laboratory (PNNL, viz., James Holbery, Kevin Simmons, Dan Howe) for retting, preforming, and manufacture of natural-fiber-reinforced composites (See 8.F).

Future Direction

- High-volume processing of lightweight structural thermoplastic composites.
- Oak Ridge National Laboratory (ORNL will continue researching optimization of the Direct Reinforced Fabrication Technology (DRIFT®) material-processing envelope.
- Carbon-fiber SMC materials for structural automotive applications:
- Continue working with fiber and resin suppliers through the Tier 1 supplier (CSP) to develop a superior material with improved manufacturability within cost and supply constraints.
- Demonstrate material on potential applications.
- Natural-fiber reinforcements and soy-based polymers:
- Optimize fiber surface treatments and polymer systems to minimize the moisture absorption of natural-fiber composite systems.
- Characterization results will be used to refine testing methods for determining durability properties of natural fiber composite systems.
- Provide process support to ACC 007.
- Utilize the injection- and compression-molding plaque tools to manufacture composite plaques for material characterization and development of a thermoplastic reference database.

Introduction

The purpose of this project is to develop the high-volume, composite-molding technologies germane to automotive production. The direction of the project ACC 115 is to collaborate with suppliers to develop low-cost, high-volume molding processes compatible with the material- property and processing requirements of the automotive industry.

Five processing investigations are under way: 1.) DRIFT®, a patented pultrusion process, is being studied for its ability to support the project objectives and its compatibility. This work is being conducted at ORNL; 2) BLRT, continued with studies of plaques molded with specific bond-area variations to assess the ability of the ONDULO system to identify and quantify the surface distortions; 3) A program has been initiated to upgrade an existing SMC compounder at a Tier 1 supplier to produce carbon-fiber-SMC compounding capability; 4) The creation and use of specialized tools for both injection and compression molding, highly instrumented and capable of producing test specimens of advanced composites; and, finally, 5) To develop a critical capability in the area of natural-fiber retting, preform and composite manufacture to enable the large-scale insertion of natural-fiber reinforcement into the automotive industry.

DRIFT®

As part of the current focus on thermoplastics, ORNL has been working with PolyComp (inventor of DRIFT®) and Fiberform (a key licensee) to evaluate possibility of chopping the DRIFT® product form in the ORNL preforming machine as one means of evaluating the DRIFT® material in general. In fiscal year (FY) 2006, PolyComp made sample quantities of glass-impregnated polypropylene using a 2400 tex glass tow which had been processed into a ribbon about 0.2-inch wide and 0.035-in thick. As expected, the ribbon handled more like a solid strip of plastic than a pliable fibrous tow and did not cut as easily as a glass tow. In initial trials, ORNL was able to get some of the material through the chopper,

but with only very small amounts cut before beginning to break blades in the chopper.

PolyComp agreed to make some modified samples in FY 2007 in order to get a thinner ribbon using a smaller glass tow size at about 1150 tex, which is essentially the size of glass tow utilized in the current TWINTEX® product. The samples were actually made at a weight ratio of 65% glass to 35% polypropylene, which yields a product comparable to the 60/40 TWINTEX® ratio. PolyComp made two variations of these samples – one at about 5/16-inch width and the other at about 3/16-inch width. ORNL was able to cut both tow sizes, having more success with the 5/16-inch width (nominally about .008-inch thick) than the 3/16-inch width (at about .015-inch thick). Although there was not enough material for extensive trials, there was enough combined material to conduct several experiments to establish cutting parameters. The balance of the materials was used to spray-up and compact a small amount of material that was subsequently molded into a very thin section solely for demonstration purposes in a lab press.

Based on the success with the small amount of sample materials, ORNL subsequently procured 250 lbs of the DRIFT® materials in the 5/16-inch width to do more process development and material evaluation. (See 8.C) Initial work established a basic processing envelope, including both preforming and molding, adequate for being able to fabricate evaluation panels. A panel has been provided to the ACC Materials Group to begin assessing the properties of molded DRIFT® materials after preforming. Once initial property data are received in FY 2008, plans are to focus effort on developing more optimum processing techniques taking into account material forms and chopper configurations that might be economically feasible for implementation.

Bondline Read-Through

Phase 1

Development of a tool to quantify the severity of BLRT continued. In FY 2006, the Joining team manufactured seventy-two panels that exhibited varying levels of BLRT. Thirty-six panels from this set and twelve white-painted panels from a previous Ford study were imaged using the ONDULO technology this year.

The BLRT "signatures" seen in the ONDULO images demonstrated that the source of the variation seen in the jury visual assessment may simply have been a result of differing perceptions of the relative severity of the different "types" of read-through by different jurors. The team also found that severity rankings based on visual assessments of filtered ONDULO curvature maps are unreliable. Consequently, the team determined that panel severity must be judged via visual assessment of the panels.

Visuol Technologies generated numerous algorithm candidates to quantify the severity of the defects. A critical step in post-processing of the curvature data is the selection of the type and wavelength of the filter. Once the data are filtered, pixels with small curvature amplitude are removed from the curvature map. The remaining pixels are then aggregated into continuous "identified defects." Finally, defects with a small average curvature are deleted. The severity of each remaining defect is quantified by multiplying the square of the average amplitude times the size of the defect. The severity scores for all the defects on a panel are added to generate a final overall severity rating. This algorithm was found to correlate well to visual assessment of the panels.

Since the team is interested in understanding the relationship between adhesive geometry and BLRT severity, the team made two panels using drops of adhesive. When those panels were imaged, one curvature map clearly showed oval defects. Further refinement of the algorithm was required to achieve a set of parameters that are applicable to both continuous beads as well as drops. The team also manufactured and painted a set of twelve panels bonded with drops of adhesive. These panels were made using the same conditions as the painted panels made with continuous beads. Unfortunately, the BLRT visible on these panels was less severe than on the equivalent continuous bead panels, so these were not particularly useful in the algorithm development.

The ACC Joining Working Group purchased an ONDULO system for our use this year. Four members of the team have been trained to use the system. Learning to use the system has given the team a much better understanding of the potential sources of variation in the data. Two gage repeatability and reproducibility tools for the system will be completed in FY 2008. The first will evaluate the repeatability and reproducibility of the measurements when the system is not moved between measurements. The second will evaluate the repeatability and reproducibility of the measurements when the system is moved between measurements.

Phase 2

To conclusively determine what factors contribute to BLRT, the manufacturing process used to build prototype assemblies must eliminate as many sources of manufacturing noise as possible. Consequently, several pieces of equipment were built to mold the panels that will be used in this work and to facilitate the bonding operation. A compression-molding tool for molding inner panels was completed by JATCO Machine & Tool Co., Inc. in early FY 2007.

A matched metal bonding fixture, small bonding press, and small cooling fixture were built by R/PC Alliance. The bonding fixture and press will be used to control the stress created between the panels, the bondline thickness, and the panel heating conditions during bonding. The cooling fixture will be used to create a repeatable amount of warpage in the inner panels. The "outer panels" in these assemblies are flat plaques. Some of the outer panels in the first experiment will be steel panels, so the team obtained twenty-five 24"x24" sheets of electrogalvanized, bake-hardened 210 steel from Mittal Steel. These sheets were then e-coated by Ford Motor Company in preparation for bonding. The SMC outer panels will be molded using the existing ACC compression-molding plaque tool. Many other groups within the ACC also used this tool this year. Since the tool was not designed to produce Class "A" panels, the other groups used this tool first. It was then sent back to the tool shop to have the top surface brought up to a Class "A" finish. This has delayed completion of the first experiment until the first quarter of FY 2008.

Tooling

More trials were held at Husky in Novi, MI for the injection-molding tool. The intent of the trials was to see the effect of various gating scenarios on glass-reinforced polypropylene (PP) material. The material for this trial was a Ticona Celstran PP-GF40-03 which is a 40% long-glass-filled PP. The new gate configurations included an insert to shut off the edge gate for a truly balanced center fill. Parts were made at thicknesses of 3.0 mm and 5.0 mm. All previous tool problems that were fixed from the trial in Mexico were validated. During this trial, a liquid-crystal polymer was molded at the 2.0-mm thickness to see if the tool was indeed capable of making parts this thin. The parts were filled from the center gate only at a mold temperature of 190^{o}F which is the maximum Husky will go with the rubber hoses on their machine. The parts were full shots and measurements were taken to confirm that 2.0 mm is possible.

Further improvements/refinements to the tool ancillaries are necessary. These include a trim fixture for edge de-gating, a set of tools for thickness changes and parts measurement and a tool case to ship everything in. As part of this, a data acquisition system (DAS) is currently being specified. This will include everything to take data from the tool sensors and thermocouples and from the injection-molding machine. This DAS will coordinate all molding data in a manner that aligns to Materials Property Database for direct insertion.

Once everything is purchased, fixed and proven-out, a trial will be run for PNNL with long-fiber materials for the long-fiber prediction-modeling project (See 8.J).

The compression tool was also used at various molding trials at Polywheels, Bayer Material Science and Meridian. Polywheels molded both SMC and nylon 6. The nylon was processed with glass on their direct long fiber thermoplastic (DLFT) line. Various reinforcement mats, both glass and thermoplastic, were compounded/ molded with these materials in different configurations/lay-ups. Bayer molded plaques using the Kraus-Maffei Long Fiber Injection - Polyurethane (LFI-PUR) system along with the Hennecke Composite Spray Molding (CSM)

system. The plaques were glass-mat reinforced with Bayer Baydur 426 polyurethane.

Meridian molded class "A" panels for the BLRT experiments for the Joining Group.

Carbon-Fiber SMC

The objectives of this work are to develop high-performance, cost-effective, carbon-fiber-SMC materials and associated processing techniques for high-volume automotive components. The technical emphasis is to optimize properties, improve consistency of the properties, and to optimize the manufacturability of the compound. The project assumptions are that the material could be used for all current structural and Class-A SMC applications, that the current SMC compounding, molding processes and equipment can be utilized, and that the thickness of the new materials will be in the range of 1.0 to 3.0 mm. In addition to the technical issues and constraints, business challenges have been addressed by working with CSP to leverage their production knowledge of what it takes to develop a marketable system. Zoltek, a low-cost carbon-fiber manufacturer, has agreed to work with CSP, supplying appropriate carbon fibers and developmental sizing systems suitable for automotive resin systems.

Upgrading the CSP SMC compounder to provide carbon-fiber-compounding capability was proposed, justified, and approved. DOE and ACC funding was secured to initiate the effort and the purchase orders are being generated.

Conclusions

ACC 115 explores different approaches to the high-volume processing of composites. Five processing programs are in progress, each with the objective of researching ways to save weight in automobiles, at the volumes unique to the industry. Carbon-fiber-SMC research is progressing slowly against constraints of cost and supply. DRIFT® work continues; basic characterization is in progress and applications will be considered. Acquisition of new equipment specifically owned by ACC will speed research by eliminating time needed to move tools between suppliers, and will also provide the benefit of reducing variation in the test results. The natural-fiber efforts, begun on July 1, 2007, are underway with the initial focus on developing a fiber-preparation/ mechanical retting process for industrial scale. At this time, PNNL has investigated several concepts and will be finalizing the design in the next quarter. In parallel, fiber-structure analysis and composite processing has begun, green fiber has been contracted to be planted and harvested for this project in Mississippi, and relationships have been developed with the following partners:

- Ashland Chemical
- AOC resins
- TimTek Inc.
- Material Innovation Technologies
- Kengro, Inc.
- Stemergy, Inc.
- Mississippi State University

[i] Denotes project 115 of the Automotive Composites Consortium (ACC), one of the formal consortia of the United States Council for Automotive Research (USCAR) set up by Chrysler, Ford and General Motors to conduct joint, pre-competitive research and development.

F. Natural-Fiber Composite Retting, Preform, Manufacture and Molding (RPM2)

Principal Investigators: James Holbery, Kevin Simmons, Dan Howe
Pacific Northwest National Laboratory (PNNL)
P.O. Box 999
Richland, Washington 99354
(509) 375-3686; fax: (509) 375-2379; e-mail: james.holbery@pnl.gov

Technology Area Development Manager: Joseph A. Carpenter
(202) 586-1022; fax: (202) 586-1600; e-mail: joseph.carpenter@ee.doe.gov

---

Contractor: PNNL
Contract No.: Prime Contract No. DE-AC06-76RLO 1830

Objective:

- To develop, build, and demonstrate an economical, lab-scale, automated fiber retting process and apparatus suitable to bast-based fibers including hemp, kenaf, and flax;
- To develop and demonstrate a thermoset polymer preform compression molding process and produce panels to develop a mechanical and thermal natural-fiber polymer-composite database.

Approach:

- Explore existing and new fiber-preparation approaches including decordication techniques, high-speed fiber separation, steam explosion, chemical treatment, and modified extrusion methods.
- Develop the fundamental understanding of bast-fiber structure that will provide direction for fiber separation.
- Conduct several lab-scale process trials of fiber preparation-retting processes enabling the development of the most appropriate process and instrumentation.
- Develop a non-aqueous natural-fiber preforming process capable of integrating surface modification and hybrid fiber, preform geometries.
- Design and construct a lab-scale, non-aqueous, fiber preform manufacturing apparatus.
- Explore alternative material forms including, sheet-molding compounds (SMCs) from natural-fiber and hybrid reinforcements.
- Conduct full mechanical, thermal, and environmental characterization of manufactured panels.

Accomplishments:

- Conducted fiber structural tests on kenaf and hemp samples.
- Explored chemical methods to break down pectin bonding – work currently underway.
- Conducted preliminary fiber surface analysis.
- Conducted fiber calandering on kenaf fibers; subsequently molded panels of clean fiber.
- Established relationships with U.S. kenaf farm, Kengro Inc.; planted, harvested, and delivered one ton of green kenaf.
- Investigated several forms of decordication-fiber preparation including previously-developed systems derived from the wood products and cotton industries.

- Developed three designs that integrate existing processes – now exploring small-scale decordication and fiber-preparation tests to determine validity of the methods.
- Initiated research to develop a fundamental understanding of bast-fiber structure that will provide direction for fiber separation.
- Developed relationships with resin suppliers including AOC, Reichold, and Ashland Chemical; with processing companies including Material Innovat ion Technologies, TimTek, Inc., and Canadian hemp supplier, Stemergy.

Future Direction:

- To build a small-scale bast-fiber processing cell to conduct accelerated fiber separation techniques.
- Explore further environmentally-friendly fiber-retting technologies.
- Integrate fiber-decordication, fiber-separation, and fiber-preparation-retting techniques into a lab-scale fiber-preparation unit.
- Deliver process and lab-scale unit to our customer in FY 2008.
- Explore non-aqueous, natural-fiber preforming processes capable of scaling to industrial volumes.
- Develop natural-fiber SMC and hybrid-fiber architectures; produce panels and characterize in mechanical, thermal, and environmental tests.

Introduction

The objective of this project is to develop a critical capability in the area of natural-fiber retting, preform manufacture, and composite manufacture to enable the large-scale insertion of natural-fiber reinforcement into the automotive industry. The benefits of natural-fiber-reinforced composites are well known, including lightweight, energy savings, cost reduction, carbon capture, recycling, and the environmental benefits from using renewable resources. However, several technical milestones must be met before the full confidence of the engineering, manufacturing, and commercial sectors will embrace natural-fiber reinforcement as a viable replacement for glass fiber. In the proposed research and development effort, three critical barriers restricting natural-fiber usage in automotive manufacture are addressed: (1) to develop an inexpensive, rapid, and environmentally-friendly mechanical process to remove natural fibers from plant stalks; (2) to develop a rapid, cost-effective method to create natural-fiber preforms suitable for infusion of a thermoset polymer matrix; and (3) to develop a natural-fiber polymer-composite molding process adaptable to hybrid fiber composites and ester, soy, and urethane resin.

(A parallel, complementary effort is covered in Report 8.G.)

Natural fibers can be harvested annually, or for kenaf, jute, and hemp, may be planted and harvested two to three times annually. Kenaf, cultivated in the U.S. for a variety of uses, including oil-spill absorbent, can grow to a height of four meters in four months, and can yield two or three harvests a year. Jute, grown in China, India, and Bangladesh, can be grown in four to six months. Agronomically, jute and kenaf have advantages because of their resistance to climatic extremes, pests, and diseases.

Once bast fiber is harvested, it must go through a process to separate the fiber from the woody stem by removing the non-fibrous cementing materials that hold the fibers together, without damaging the fiber cellulose. It is advantageous to use retted fibers in polymer-composite applications, as it has been shown that unretted fiber tissue may change, or degrade, over a time scale of months or years after it has been embedded in a polymer resin, seriously affecting the useful life of the composite.

Essentially, retting is a process to moisten or soak the fiber to soften and separate the fibers by partial rotting and can take up to two weeks or longer. The following retting processes are the most

prominent in use today, and each has certain advantages and disadvantages:

- Dew retting occurs when the stalks are left in the field so that rain, dew, or irrigation is used to keep the stems moist. This may take up to 6 weeks and produces a coarse fiber with a light brown color.

- Water retting occurs when stems are bundled and then submerged in water so that bacteria break down pectin. This takes 7-10 days and produces a quality fiber.

- Warm-water retting occurs when bundles are soaked for 24 hours after which the water is replaced. Heat is then applied to warm the batch for the next two or three days. This results in a uniform, clean fiber.

- Chemical retting occurs when chemicals (usually alkali solutions) are used to dissolve the pectin, allowing the components to be separated from the decorticated stalk. This shortens the time to as little as 48 hours, though it affects several fiber properties including a loss in tenacity, color, and luster, as compared to the bacterially-retted fibers.

Once retted fiber has been produced, the fibers can be modified by a variety of physical and chemical methods, to correct fiber deficiencies; fibers can be treated to promote bonding and adhesion, dimensional stability, and thermoplasticity. Surface modification of natural fibers can be employed to optimize properties of the fiber-matrix interface and integrated within the fiber preform manufacturing process, to produce a preform that may be stored for long periods of time before composite manufacture without a loss of properties, or more importantly, excessive moisture uptake with compromised composite interfacial properties.

When considering natural fibers as engineering materials, several factors must be considered, particularly, their hygroscopic nature. Physical and chemical methods have been used to optimize the interfacial characteristics and improve the properties of natural-fiber polymer composites, although high moisture absorption and low microbial resistance are disadvantages, compounded by the fact that their hydrophilic behavior adversely affects the properties of the fibers and their composites. One outcome is that lignocellulosic-based fibers change dimensions with changing moisture content because the cell-wall polymers contain hydroxyl and other oxygen-containing groups that attract moisture through hydrogen bonding. High water and moisture absorption of the fiber causes swelling and a plasticizing effect, resulting in dimensional instability and poor mechanical properties.

A primary consideration in bonding cellulose-based fibers to a surface polymer is the moisture present in the fiber during the reaction. It is costly to dry natural fibers to less than 2-3 percent moisture, but the -OH group in water is more reactive than the -OH group available in the lignocellulosic components, rendering hydrolysis faster than substitution. The most favorable condition for surface reaction is one that requires a trace of moisture and the rate of hydrolysis that is relatively slow. Three factors determine the rate at which moisture is removed from lignocellulosic materials: temperature, relative humidity, and air velocity. The ability to control and minimize energy input during this process is one opportunity foreseen within processing natural-fiber materials. The ability to eliminate water absorption during service of natural-fiber-based composite components is an enabling technology within automotive natural-fiber-reinforced hardware development; this is particularly true where a Class A finish is required.

Fiber Preparation - Retting

PNNL began this effort by contacting Kengro, Inc. in Charleston, MS to contract 0.5 acres (approximately 1500 lbs.) of kenaf to be grown and cut green, to be used in developing the fiber-preparation process. Fiber was planted in mid-July, and cut on November 7, 2007. PNNL personnel traveled to MS in July, 2007, to meet with Kengro, the USDA-ARS cotton research facility in Stoneville, MS, and Mississippi State University (MSST). In addition, to begin the research effort the following fibers were procured for research purposes: (1) fresh-water-retted kenaf from Bangladesh; (2) un-retted fiber from Kafus, Inc., Raymondville, TX; (3) industrial hemp from Stemergy, Ontario, Canada; and (4) chemically-

modified kenaf from Prof. Brian Baldwin, Agriculture Department, MSST.

PNNL personnel have thus far investigated the following processing approaches:

- Decordication (removal of kenaf core) using parallel rollers, both at MSST (Prof. Dan Seale's laboratory with a patented process from TimTek Corporation) and at PNNL with parallel rolling device. Progress has been made; we have just received fiber and are working on techniques to rapidly achieve decordication.

- Chemical retting: PNNL has developed a process to achieve kenaf chemical retting. This includes using a combination of sodium hydroxide and hydrochloric acid treatments; we are now attempting to develop a continuous flow process that utilizes near 100% of the constituents.

- Water retting: PNNL is exploring a combination warm water-steam retting approach, which shows promise.

- PNNL has produced a lab-scale carding roller to align bast fiber for preform or SMC manufacture. The simple design allows fiber to be processed in very small quantities, removing the fiber fines and unwanted core from the fiber (Figure 1).

Figure 1. Manually-operated fiber carding device (top), fiber fines and unwanted remnants removed from the process (bottom).

Bast-Fiber Structure

The structure of several bast fibers has been explored to determine the composition and to assist future process development. This is important because process changes affect fiber structure, which in turn affects fiber behavior, and most importantly for this effort, the separation of fiber from core, and fiber-fiber interaction, enabling fiber separation for follow on steps (i.e., preform manufacture).

Three techniques have been undertaken: fiber structure analysis, using TAPPI (previously "the Technical Association of the Pulp and Paper Industry, now just "TAPPI") specification 222 and others, to determine cellulose, hemi-cellulose, lignin, and extractive content, Fourier transform infrared (FTIR) analysis and x-ray photoelectron spectroscopy (XPS) analysis. Fiber structure analysis results for two trial runs each of MS kenaf (Kengro, Inc.), hemp (Stemergy, Ontario, Canada), TX kenaf (Raymondville, TX), and water-retted kenaf (Golden Tiger Fiber, Bangladesh) have been run. The cellulose and hemi-cellulose are still being analyzed. Results for the lignin content indicate that, surprisingly, water-retted kenaf contains the highest total (Table 1). This is a very curious result, as neither the MS nor TX kenaf had been processed.

The results of the extractive, ash, and lignin content (cellulose and hemi-cellulose will be completed as soon as the high-performance liquid chromatograph (HPLC) at PNNL is operational – within two weeks) indicate distinct differences in the fiber structures.

Table 1. Results of two samples each of lignin content from MS kenaf (Kengro, Inc.), hemp (Stemergy, Ontario, Canada), TX kenaf (Raymondville, TX), and water-retted kenaf (Golden Tiger Fiber, Bangladesh).

Type	Dry Wt. Total 1	Dry Wt. Total 2	Avg. Dry Wt.	Sample (ex free, dry basis)	%lignin
MS Kenaf	34.4852	34.4857	34.4855	0.1882	6.88%
MS Kenaf	35.7119	35.7104	35.7112	0.1896	8.62%
Hemp	35.8981	35.8995	35.8988	0.1939	7.68%
Hemp	34.4496	34.4534	34.4515	0.1904	8.56%
TX Kenaf	35.8253	35.8219	35.8236	0.1903	9.51%
TX Kenaf	35.7241	35.7235	35.7238	0.1899	7.21%
Water Ret Kenaf	37.7416	37.7407	37.7412	0.1893	13.39%
Water Ret Kenaf	34.1437	34.1445	34.1441	0.1904	11.40%

Table 2 shows the averaged data of two samples each that have been tested and characterized. Note that the water-retted fiber has no extractives; this is a critical finding, as the extractives can cause long-term degradation to fiber-polymer interfacial bonding. Also, note the lignin content of the water-retted fiber; this can be important for many reasons, including extraction for process fuel, which can be of economic benefit. Ash content, usually due to the quality of the soil, is highest in Texas kenaf, which could be due to a high mineral content.

Table 2. Results of extractive, ash, and lignin content of MS kenaf (Kengro, Inc.), hemp (Stemergy, Ontario, Canada), TX kenaf (Raymondville, TX), and water-retted kenaf (Golden Tiger Fiber, Bangladesh). Note cellulose and hemi-cellulose data still under analysis.

Type	Avg. % Extractive	Avg. % Ash	Avg. % Lignin	Total
MS Kenaf	0.1467%	1.39%	7.75%	9.2883%
Ontario Hemp	0.5921%	2.42%	8.12%	11.1387%
TX Kenaf	0.2716%	4.35%	8.36%	12.9874%
Water Ret Kenaf	0	1.24%	12.39%	13.6327%

XPS has been conducted on several samples to obtain binding energies of different fiber structures. Figure 2 provides a comparison of hemp, chemically-retted kenaf, unretted kenaf, and water-retted kenaf.

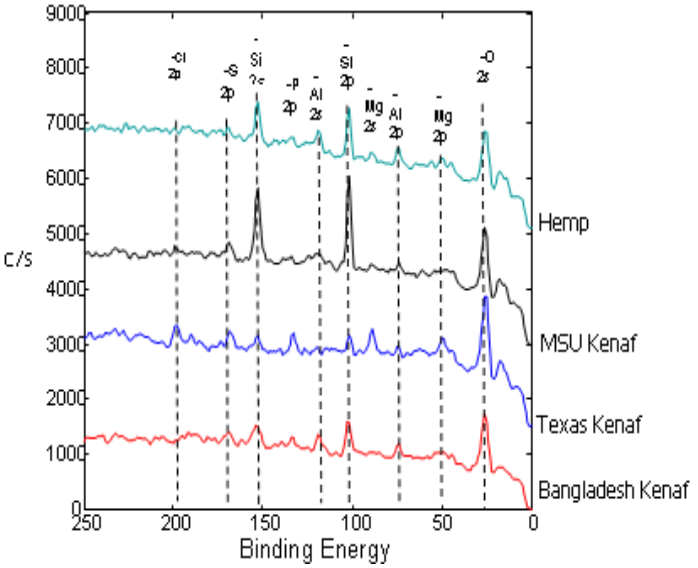

Figure 2. Wide-scan XPS spectra 0-1350 eV comparison of hemp (top), chemically-retted kenaf (second from top), Texas kenaf –unretted (second from bottom), and water-retted kenaf (bottom).

The plot in Figure 2 does not provide a great deal of information. Further analysis of 0-250 eV in Figure 3 indicates Si, Mg, Al, and P peaks that vary with fiber type. A full analysis of the XPS data is presented in Table 3 below.

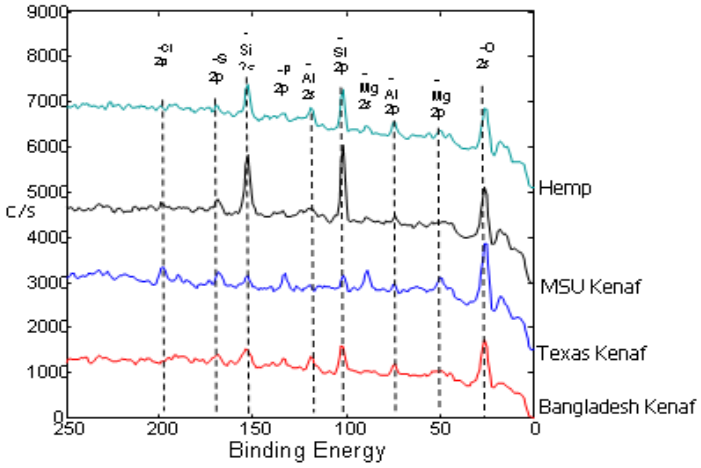

Figure 3. XPS spectra 0-250 eV comparison of hemp (top - Stemergy, Ontario, Canada), chemically-retted kenaf (second from top; - MS), kenaf –unretted (second from bottom – Raymondville, TX), and water-retted kenaf (bottom - Golden Tiger Fiber, Bangladesh). Note Si peaks in the hemp and chemically-retted fibers at 153 eV.

FTIR analysis has been initiated on the fibers, but at this time, the data are inconclusive. For example, Figure 4 illustrates plots of the fiber and their spectral differences. While distinct bond differences exist, particularly at wave numbers 1300-1800, PNNL is now using a software package to analyze the data further.

Scanning electron microscopy (SEM) has been employed to characterize the fiber surface of several fibers.

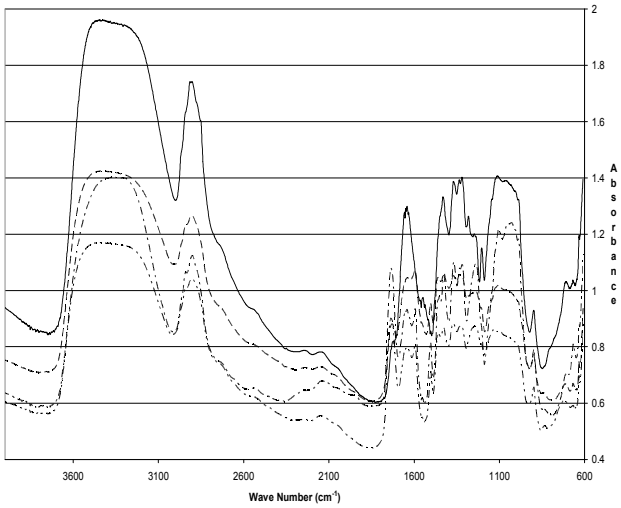

Figure 4. FTIR plot of fiber surfaces. Straight line is hemp, long-short-short long is chemically-treated MS kenaf, long-long is Texas kenaf, and long-short-long is water-retted kenaf from Golden Tiger, Bangladesh.

Table 3. Atomic concentrations from the wide-scan XPS spectra. This provides a baseline understanding for further process development and fiber modification.

File name	Sample description	C1s	N1s	O1s	Mg1s	Al2p	Si2p	P2p	S2p	Cl2p	Ca2p
09190701.spe	59755-4-B1 XPS fibers	67.7	2.3	28.4	0.0	0.3	0.6	0.1	0.1	0.0	0.5
09190705.spe	59755-4-B1 XPS fibers	67.5	2.8	28.0	0.2	0.2	0.6	0.1	0.1	0.0	0.5
Average of both data sets	**Kenaf – Golden Tiger, Bangledesh Enzyme Field Retted**	67.6	2.6	28.2	0.1	0.3	0.6	0.1	0.1	0.0	0.5
09190702.spe	59755-4-B2 XPS fibers	67.7	3.4	27.0	0.3	0.2	0.3	0.1	0.1	0.1	0.9
09190706.spe	59755-4-B2 XPS fibers	68.5	2.9	27.1	0.2	0.0	0.2	0.1	0.1	0.1	0.8
Average of both data sets	**Kenaf – Kafus, Raymondville, TX**	68.1	3.1	27.0	0.2	0.1	0.2	0.1	0.1	0.1	0.9
09190703.spe	59755-4-B3 XPS fibers	75.9	1.0	21.4	0.0	0.1	1.2	0.0	0.1	0.0	0.3
09190707.spe	59755-4-B3 XPS fibers	83.9	0.8	13.5	0.0	0.1	1.2	0.0	0.1	0.0	0.3
Average of both data sets	**Kenaf – MS \ Chemically Retted**	79.9	0.9	17.4	0.0	0.1	**1.2**	0.0	0.1	0.0	0.3
09190704.spe	59755-4-B4 XPS fibers	73.9	2.1	22.4	0.1	0.3	0.8	0.1	0.1	0.0	0.4
09190708.spe	59755-4-B4 XPS fibers	72.7	2.1	24.0	0.1	0.2	0.5	0.1	0.0	0.0	0.4
Average of both data sets	**Hemp-Stemergy, Ontario, Canada**	73.3	2.1	23.2	0.1	0.2	**0.6**	0.1	0.0	0.0	0.4

The images at 10,000x are not all that different, as shown in Figure 5.

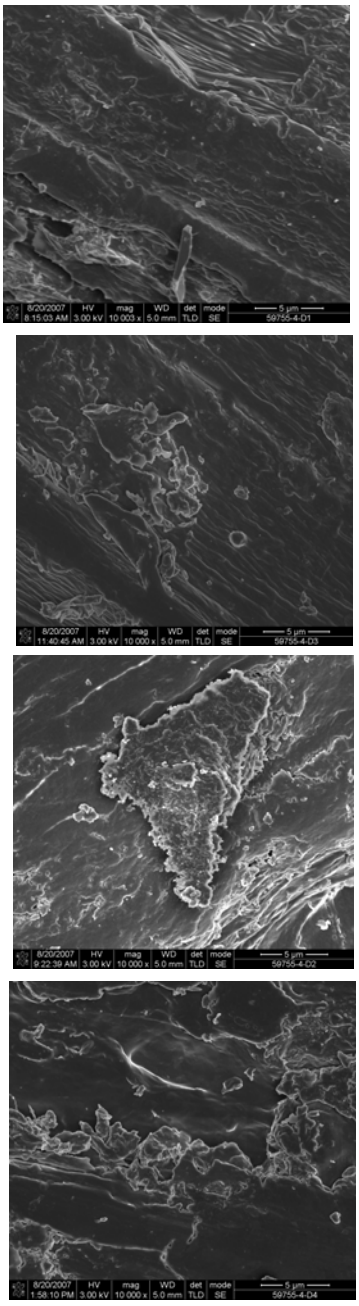

Figure 5. SEM image (10,000x) of fiber surface of fiber surface of water-retted fiber (top - Golden Tiger, Bangladesh), unretted fiber (2nd - Texas kenaf), chemically-retted fiber (3d - MS kenaf), and hemp (4th - Stemergy, Ontario Canada).

However, at 25,000x, distinct differences appear, particularly the surface of the chemically-retted fiber (Figure 6).

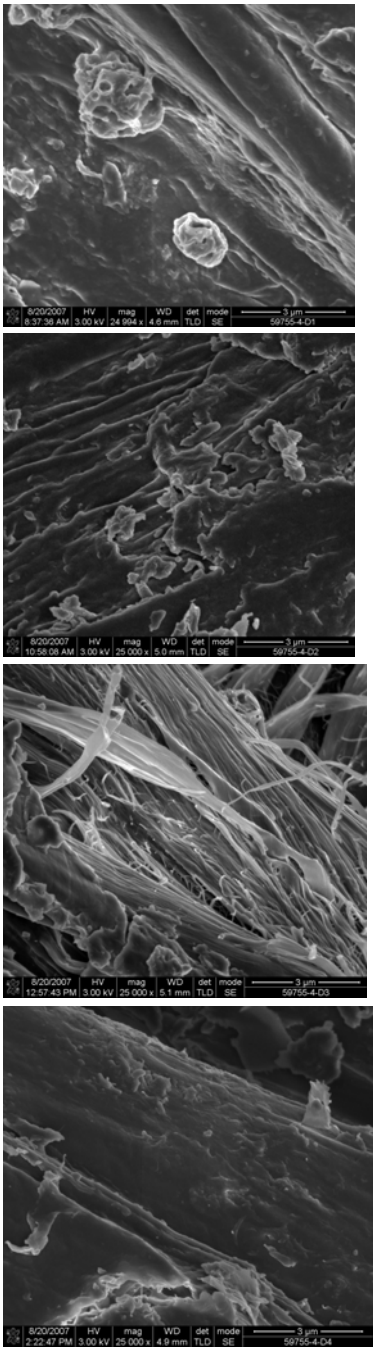

Figure 6. SEM image (25,000x) of fiber surface of fiber surface of water-retted fiber (top - Golden Tiger, Bangladesh), unretted fiber (2nd - Texas kenaf), chemically-retted fiber (3rd - MS kenaf), and hemp (4th - Stemergy, Ontario Canada).

Preform Processing

The goal of this task is to develop a preforming process to produce natural-fiber-reinforced preforms of a variety of geometries without an

aqueous solution. This task will begin in the second year of the project and has not been undertaken.

Composite Manufacture & Characterization

This task has begun, as it is believed that the program must produce and test full-scale test coupons, as the program progresses, to determine the effectiveness of the fiber-preparation processes. Using the carding machine described previously, PNNL has molded several panels from kenaf preforms (Figure 7).

Figure 7. Preform prior to molding with polyester resin, preform in the press (middle) and after molding (bottom).

As we begin to produce fibers emanating from the processes we are developing, full characterization will take place using PNNL personnel and outside vendors, as necessary. We will focus on mechanical, thermal, and environmental properties. These tests are outlined in the following paragraphs. A schedule is not presented at this time. While this task is to be the focus of year 3 of the project, it will be ongoing with full completion and focus in year 3.

Mechanical Properties

Tensile properties will be tested per American Society for Testing and Materials (ASTM) D 3039, and flexural properties per ASTM D 790. Compression testing will be conducted on composites per ASTM D 695. In addition, short-beam shear will be tested to determine the interlaminar bonding of the composite per ASTM D 2344.

Moisture Absorption

Treated and untreated samples will be characterized for moisture absorption per ASTM D 5229M. Samples first dried by heating will be weighed (W1) and then soaked in a bath of deionized water, at room temperature, for a prescribed time (W2). Water absorption (WA) will be determined by the following:

$$\mathrm{WA}(\%) = \left(\frac{W_2 - W_1}{W_1} \right) \bullet 100$$

Thickness swelling (TS) will be calculated on the fibers as follows:

$$TS(\%) = \frac{(t_c - t_o)}{t_o} \bullet 100$$

where t_c is the thickness of the sample after immersion and t_o is the thickness of the sample before immersion.

PNNL has constructed a special accelerated moisture-uptake system capable of infusing composites with moisture at 60°C and 85% relative humidity (RH) at pressures up to 10 bar. This has proven to be a successful process for accelerating long-term moisture-uptake testing on carbon epoxy composites; it may be utilized as needed in this program (Figure 8).

Figure 8. Picture of the PNNL accelerated composite moisture-uptake experimental set-up consisting of two pressure vessels, data logger, etc.

TGA/DSC Characterization

Thermogravimetric analyses (TGA) and differential scanning calorimetry (DSC) are useful methods to determine the glass transition, extent of cure, moisture uptake, and thermal stability of virgin fibers, treated fibers, and polymer fiber composites. Our intent will be to utilize TGA and DSC to measure the properties of the composites, and to probe the process parameters, to achieve an optimum process for both the polyester and virgin fibers.

DMA Testing

Dynamic mechanical analysis (DMA) will be utilized to measure the viscoelastic response of selected composites.

Conclusions

This program, begun on July 1, 2007, is underway with the initial focus on developing a fiber-preparation mechanical-retting process for industrial scale. At this time, PNNL has investigated several concepts and will be finalizing the design in the next quarter. In parallel, fiber-structure analysis and composite processing has begun, green fiber has been contracted to be planted and harvested for this project in Mississippi, and relationships have been developed with the following partners:

- Ashland Chemical
- AOC resins
- TimTek Inc.
- Material Innovation Technologies.
- Kengro, Inc.
- Stemergy, Inc.
- Mississippi State University

Presentations/Publications/Patents

1. Presentation to the Auto Composite Consortium, Sept. 26, 2007, Detroit MI.
2. Presentation to Mississippi State University, July 15, 2007, Starkville MS.

G. Natural-Fiber Composites for Structural Component Design

Jilei Zhang: Co-Principal Investigator
Associate Professor, FWRC – Forest Products
Franklin Center, Rm 113
Mississippi State University (MSST)
Mississippi State, MS 39762
(662) 325-9413; fax: 662-325-8126; email: jzhang@cfr.msstate.edu

Yibin Anna Xue: Co-Principal Investigator
Assistant Research Professor, Center for Advanced Vehicular Systems (CAVS)
MSST
Mississippi State, MS 39762-5405
(662) 325-5450; fax: (662) 325-5433; e-mail: axue@cavs.msstate.edu

R. Daniel Seale
College of Forest Resources
MSST
Mississippi State, MS 39762
662-325-3072; fax: 662-325-8126; email: dseale@cfr.msstate.edu

Sheldon Q. Shi, Co-Principal Investigator
Assistant Professor, FWRC – Forest Products
Franklin Center, Rm 222
MSST
Mississippi State, MS 39762
662-325-3110; fax: 662-325-8126; e-mail: sshi@cfr.msstate.edu

Thomas Lacy
316C Walker Engineering Building
P. O. Box A
Mississippi State, MS 39762
(662) 325-2754; e-mail: lacy@ae.msstate.edu

Steven Elder: Co-Principal Investigator
Associate Professor, Ag & Bio Engineering
Ag & Bio Engineering Bldg, Rm 214
MSST
Mississippi State, MS 39762
(662) 325-9107; e-mail: selder@abe.msstate.edu

L. Catherine Brinson
Department of Materials Science and Engineering
Northwestern University
2220 Campus Drive, Evanston, IL 60208-3108;
(847) 491-3537; fax: (847) 491-7820; e-mail: cbrinson@northwestern.edu

Ray Boeman
Oak Ridge National Laboratory (ORNL)
P.O. Box 2008, MS-6472
Oak Ridge, TN 37831-6472
(865) 946-1203; fax: (865) 946-1214; e-mail: boemanrg@ornl.gov

Cliff Eberle
ORNL
P.O. Box 2008,
Oak Ridge, TN 37831-6053
(865) 574-0302; fax: (865) 574-8257; e-mail: eberlecc@ornl.gov

C. David Warren
ORNL
P.O. Box 2008
Oak Ridge, TN 37831-6065
(865) 574-9693; fax: (865) 574-6098; e-mail: warrencd@ornl.gov

Technology Area Development Manager: Joseph A. Carpenter
(202) 586-1022; fax: (202) 586-1600; e-mail: joseph.carpenter@ee.doe.gov

Expert Technical Monitor: Philip S. Sklad
(865) 574-5069; fax: (865) 574-6098; e-mail: skladps@ornl.gov

---

Contractor: MSST
Contract No.: 4000054701

Objective

- Obtain material data of several biomaterials (e.g., kenaf) to study microstructural characteristics, fabrication methods (i.e., retting, formatting), and mechanical properties (i.e., polymer resin/fiber compatibility) for use in automotive structural design.

Approach

- For automotive exterior applications, natural-fiber-reinforced, polymer-based composites are developed according to the following steps: 1) evaluating current fiber-retting technologies and recommending solutions aimed at cost reduction of fiber-retting process; 2) evaluating two-dimensional (2D) fiber-mat format and other fiber-feeding systems with the aim of developing a natural-fiber format and formatting method for ready feeding into a sheet molding compound (SMC) line; 3) enhancing composite mechanical properties through dispersing nano-phase additives, improving interfacial bond strength, and developing mechanical models.

Accomplishments

Fabrication methods:

- A new chemical-retting technique was developed with the aim of improvement of fiber quality and cost reduction of the fiber-retting process.

Micro-structural characteristics and mechanical properties:

- An inorganic nano-particle impregnation technique was developed with the aim of reducing defects in the natural-fiber polymer-composite processing and enhancing mechanical properties through filling voids on fiber-cell-wall structures and surface modification.
- Tensile behaviors of different kenaf-bast-fiber forms (yarns, slivers and bundles) were measured. Effects of kenaf-fiber orientation on mechanical properties of kenaf-fiber/polymer composites and effects of weight fraction of kenaf fibers in the polypropylene (PP) matrix on thermal properties of the composite, and interaction between the fibers and PP matrix, were experimentally investigated and analyzed.

- A simple, rate-dependent model was proposed for kenaf fibers. Effects of moisture content, fiber volume fraction, and distribution pattern on the elastic modulus of woodfiber-reinforced composites were simulated and quantified using micromechanical approaches.

Future Direction

- Fabrication methods - Continue the current effort of evaluation of retting technologies with the aim of recommending a cost-effective retting process. Develop a natural-fiber format and formatting method for ready feeding to a SMC process.
- Mechanical properties and enhancement - Continue the research efforts to understand and improve interfacial bonding between natural fiber and polymer matrix and study processing and environmental variables (such as moisture and heat) effects on composite properties through conducting experimental and simulation work. Disperse nano-phase additives into traditional natural-fiber/polymer-based composites with the aim to improve material properties.

Statistical Evaluations of Tensile Properties of Kenaf Fibers and Composites

Team Members: Yibin Xue, Yicheng Du, Steve Elder, Devin Sham, Mark Horstemeyer, Jilei Zhang

Introduction

Plant-bast fibers such as kenaf, hemp, and flax have low density and high specific strength and are of utmost interest in applications striving for lightweight and high strength. Bast-fiber-reinforced, polymer-based composites have been developed successfully as of automotive interior panels. The quality of fibers, the formats of fibers and the interfacial bonding with polymer matrices are extremely important for advanced applications that require high strength such as automotive sub-structural exterior components.

Since the 1990s, various aspects related to kenaf-fiber production, fabrication, and composites have been investigated at MSST. These are cultural and biological factors, harvesting and processing, chemical and physical properties, woven and non-woven products, pulp and paper products, and composites [1]. Injection-molded, 40 wt% kenaf-fiber and PP composites were found to have comparable tensile moduli to the glass-fiber-reinforced PP (8.3 MPa vs. 9 MPa) [2]. Due to the lower density of kenaf fibers, the specific tensile modulus is greater than glass-fiber composites by a ratio of 7.8:7.3. To the writers' best knowledge, no systematic evaluations and fabrications have been conducted to explore advanced applications of kenaf-fiber-reinforced plastic composites in the US research community until now. Currently, we are seeking implementation of kenaf-fiber-reinforced plastic composites for automobile exterior components or semi-structural applications. *Understanding the fundamental mechanical properties of kenaf-fiber bundles, which is in a natural form of kenaf, as composites is necessary before they can be processed with plastics.* Kenaf-bast-fiber bundles (KBFBs) are composed of many semi-unidirectionally-aligned kenaf fibers of length from 1.6 to 5 mm and diameter range from 16 to 23 micrometers (μm) and are bonded with lignin and pectin [3]. In this report, the KBFB test samples were selected to be at least four times the maximum length of a single kenaf fiber. The tensile behaviors of KBFBs were evaluated at two loading rates. Kenaf-bundle-reinforced epoxy in sliver and yarn forms were also evaluated in a similar approach.

Experimental

Materials

Two forms of kenaf-fiber-related products were evaluated: KBFBs obtained directly from kenaf stems, as shown in Figure 1, and kenaf-bast-fiber, unidirectionally-reinforced epoxy strands (sliver and yarn), as shown in Figure 2. Both KBFB sliver and yarn are composed of 50 weight percent of KBFB and 50 weight percent epoxy, in which the strands were twisted with KBFBs along the fiber longitudinal direction. The yarns have a spiraling angle of 20° while slivers have a very small spiraling angle of 8°.

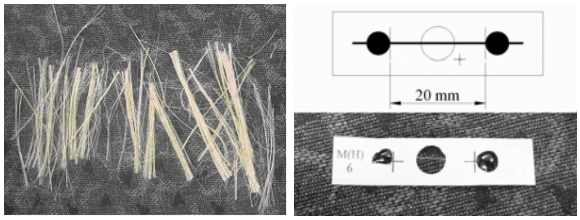

a) b)

Figure 1. KBFBs cut from the kenaf plant stem a) and the dimension of KBFB samples and test frame b).

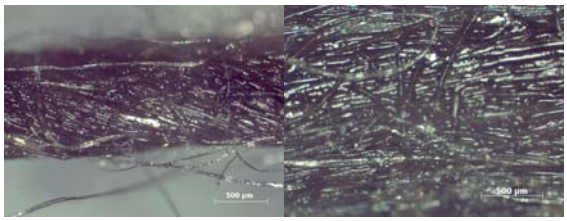

a) b)

Figure 2. Optical micrographs of KBFB-reinforced epoxy strands: a) yarns and b) slivers.

The cross-sectional area of the sliver was about six times larger than the cross-sectional area of the yarn. Both kenaf fibers and composite strands were conditioned in an environment with an ambient temperature of 23ºC and a relative humidity of 30-40% for over 48 hours prior to tests. The moisture content (MC) of the KBFB was around 8.5% based on this conditioning.

Test Setup and Sample Preparations

Uniaxial-tension properties of KBFB were evaluated according to ASTM Standard C 1557 – 03 for a standard test method for tensile strength and Young's modulus of fibers [4]. KBFBs were extracted from three locations along the full plant-size fiber bundles. Top and bottom KBFBs were taken from within 10 cm at both ends; middle KBFBs were from right at the middle of the kenaf stalk. KBFBs were cut to 30 mm in length with the top and bottom KBFBs having 30 replicates, respectively, and the middle KBFB having 45 replicates. Observed under an optical microscope, all short KBFB samples have no obvious defects. Figure 1 shows KBFBs as-cut and KBFBs mounted on a paper card as a frame for the grip and test assembly. Yarns and slivers were cut to 70 mm in length and their optical micrographs are shown in Figure 2.

The cross-section of the KBFBs was assumed to be elliptical in shape with the area of the cross-section, A, calculated using, $A = \pi ab/4$, where a and b are the diameters along the major and minor axes of the ellipse, respectively. The major and minor diameters of KBFBs and yarn were measured directly from optical images obtained using an optical microscope (Nikon Eclipse E 600). A fast-cure epoxy was used to bond the KBFB to the paper card.

Tests for KBFBs were performed on a stepper-motor-driven micromechanical testing system (Model: Mach-1 V500cs). The instrument has a maximum loading capacity of 10 N and a precision of 0.1 gram (g.) Precision of displacement control is about 0.5 μm. Displacement-controlled loading was applied at a speed of 25 μm/s, which is equivalent to a strain rate of 0.0125/s when the nominal length of the specimens is 20 mm. A lower loading-rate condition was applied to specimens from the middle part of the plant at a loading speed of 2.5 μm/s (0.00125/s). Specimens were gripped at the paper tabs. After being mounted on the grips, the tabs were disconnected using scissors. A 0.5-g preload was applied to avoid slack in the fiber. The tests were conducted under displacement control. Both forces and displacements were recorded at the frequency of 20 Hz. Stress was calculated using load and the averaged cross-sectional area. Strain was calculated using displacement and the nominal gauge length. The slope of the best-fit line through a subjectively-chosen linear portion of the stress-strain curve was considered to be the Young's modulus.

The cross-section of the yarns was measured in the same manner as the KBFBs. Compared to KBFBs and yarns; a sliver has a relatively larger, flat cross-sectional area. Therefore, the area of sliver was considered to be rectangular and the width and thickness were measured using a caliper. Both slivers and yarns were tested on an Instron (Model 1011) universal testing machine. A 500-N load cell was used. Nominal gauge length was about 50 mm. Only one loading rate was applied to yarns. Load for slivers was applied at three different speeds: 3 mm/min (equivalent strain rate at 0.001/s), 15 mm/min (0.005/s), and 60 mm/min (0.02/s). The accuracy of load and displacement was approximately 0.5% of indicated values.

Mechanisms of tensile failure were evaluated by examining the fracture surface of the samples using a field-emission gun scanning electron microscope (FEG-SEM) with the fracture surface sputter-coated with gold.

Results and Discussions

Tensile Properties of KBFBs from Different Locations Along the Kenaf Stalk--Test Results

Figure 3 shows randomly-selected stress-strain curves of KBFBs from three different parts of the kenaf stalk. The scatter in measurements is significant due to the large variation of natural-fiber constituents and distribution, such as the scatter in the diameter and length of a single kenaf fiber.

Table 1 lists the Young's modulus, tensile strength, and failure strain of KBFBs obtained from the tests shown in Figure 3. KBFBs from the middle of the plant had the highest Young's moduli and higher tensile strengths compared to those from the other two parts along the stem. The fiber length, in general, is shorter at the bottom of the stalk and longer at the top of the plant, and the increase in fiber length from the bottom to the top plant was not linear but S-shaped [5]. This might contribute to the bottom KBFBs having the lower Young's moduli and tensile strengths.

Table 1. Mean comparisons of KBFBs' Young's moduli, tensile strengths, and failure strains obtained from three different parts along the stem under uniaxial tension at the loading rate of 0.0125/s.

	Young's Modulus(GPa)			Tensile Strength (MPa)			Failure Strain (%)		
	Mean	Std Dev	COV(%)	Mean	Std Dev	COV(%)	Mean	Std Dev	COV(%)
Top	13.05 (B)	4.78	36.6	199.45 (A, B)	109.26	54.8	1.80 (A)	1.04	57.8
Middle	20.19 (A)	6.50	32.2	260.87 (A)	151.47	58.1	1.57 (A)	1.07	68.1
Bottom	12.81 (B)	3.94	30.8	156.36 (B)	73.06	46.7	1.59 (A)	1.20	75.9

Note: Values with the same capital letter are not statistically significant at 5-percent significance level. COV = coefficient of variance.

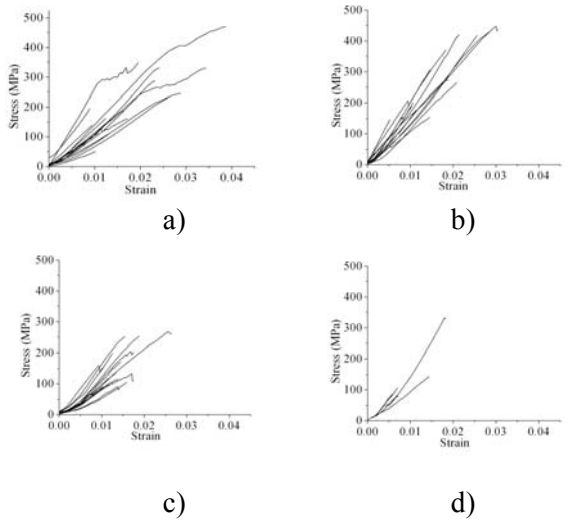

Figure 3 Stress-strain plot of top, middle, and bottom KBFBs at the loading rate of $0.0125s^{-1}$ at: a) top, b) middle, and c) bottom of the kenaf plant, respectively, and d) at the loading rate of $0.00125s^{-1}$ on the middle section of kenaf plant only.

In optical observations, KBFBs from the top appear slim, soft, full of branches, and uniform in area; middle KBFBs, to the contrary, were uniform and branchless. This might be the reason why the top KBFBs did not have the higher tensile properties.

Statistical Distribution of Tensile Properties

Figure 4 presents histograms of the tensile strength and failure strain of KBFBs from three different parts of the kenaf stalk. Most of them showed a right-skewness. Kohji Suzuki et al. [6] found that, at the same loading rate, the distribution of tensile strength was well described by the two-parameter Weibull distribution. Weibull-distribution parameters were calculated and statistical evaluations of the tensile properties of KBFBs are presented in Table 2. The accuracy of this set of Weibull evaluations is limited by a small sample size, as illustrated in histograms of the distributions shown in Figure 4. The mean and COV of tensile strength are similar to those obtained by assuming a normal distribution. Meanwhile, the histogram of failure-strain distributions also shows a right-skewness and does not obey normal distributions.

Table 2. Weibull measures of KBFBs' tensile strengths obtained from three different parts along the stem under uniaxial tension at the loading rate of 0.0125/s.

		Top	Middle	Bottom
		Tensile Strength	Tensile Strength	Tensile Strength
		MPa	MPa	MPa
Parameter Estimates	λ	1.993	1.763	2.334
	κ	226.182	292.330	176.670
Mean		200.46	260.24	156.54
Std Dev		105.10	152.42	71.24
COV (%)		52.4	58.6	45.5

Failure Mechanisms

The SEM micrographs display two possible failure modes in the KBFBs, as shown in Figure 5: fiber pullout from the bundle (a and c) and fiber fracture (b and d). Accompanying fiber pullout from the bundle, a large region of fiber separation exists at the interfaces. On the possibly broken-fiber section, there is only a slight hint of fibrous debonding. Figure 5(a) also shows a coexistence of debonding and fiber failure.

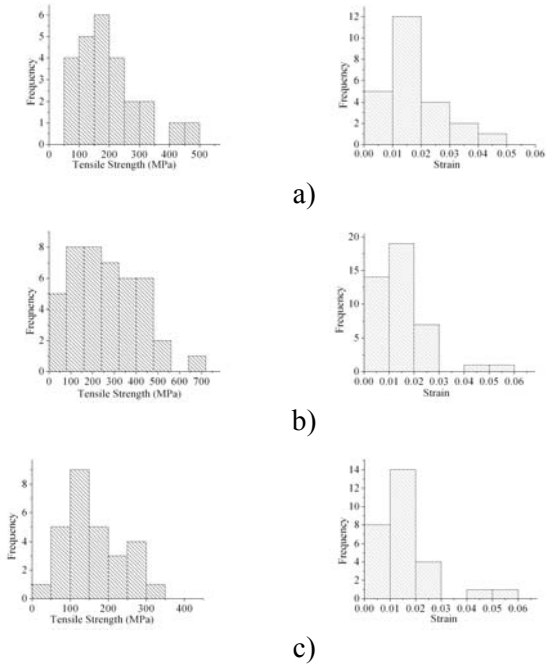

Figure 4. Histograms of failure strain and tensile strength for KBFBs from three different parts along the stalk (0.0125/s): a) top, b) middle, and c) bottom of the kenaf plant.

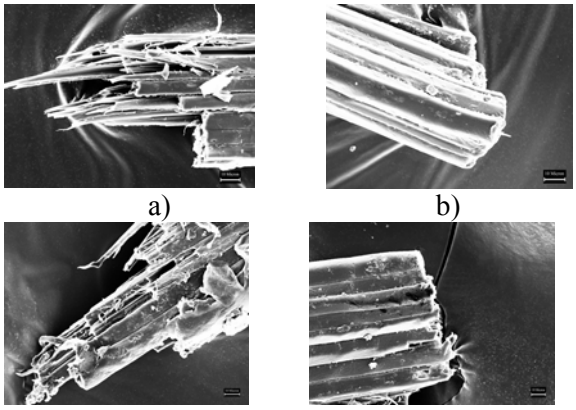

Figure 5. SEM micrographs of fracture surfaces of KBFBs.

Tensile Properties of Kenaf-Reinforced Epoxy

Test Results

Figure 6 shows typical stress-strain curves of yarns and slivers under uniaxial tension. It should be noted that a flat region appeared in the stress-strain curve where stress had no significant increase when strain increased.

For yarns, the flat regions appeared when the stress went up to around 100 MPa; for slivers, flat regions were found when the stress was just about 20 MPa. This probably was ascribed to the earlier failure of a weak region in the composites. Young's moduli were presented for the two regions before and after the appearance of the flat region: 1st stage, the modulus calculated from the linear region on the stress-strain curve before the flat region occurred; 2nd stage, modulus obtained after the flat region occurred.

Table 3 summarizes the test results for both yarns and slivers. Yarns demonstrated higher Young's moduli and tensile strengths than slivers. However, they are both relatively low when compared to KBFBs (sliver is about 1/3 and yarn is about 0.8 of that of KBFB). Meanwhile, the variations of yarns and slivers were both lower than those of KBFBs with respect to Young's modulus and tensile strength.

Table 3. Summary table of Young's moduli and tensile strengths of epoxy-reinforced kenaf, performed at three different test strain rates.

Sliver (0.001/s)				
	Young's Modulus (GPa)		Tensile Strength	Maximum Strain
	1st Stage	2nd Stage	(MPa)	(%)
Mean	4.47	4.5	115	3.46
Std Dev	0.84	0.66	26.98	0.94
COV (%)	19	15	23	27
Sliver (0.005/s)				
	Young's Modulus (GPa)		Tensile Strength	Maximum Strain
	1st Stage	2nd Stage	(MPa)	(%)
Mean	5.59	5.12	103.9	2.28
Std Dev	1.48	0.49	16.3	0.25
COV (%)	26	10	16	11
Sliver (0.02/s)				
	Young's Modulus (GPa)		Tensile Strength	Maximum Strain
	1st Stage	2nd Stage	(MPa)	(%)
Mean	3.7	5.2	98.7	2.82
Std Dev	0.74	0.38	5.98	0.35
COV (%)	20	7	6	12
Yarn (0.001/s)				
	Young's Modulus (GPa)		Tensile Strength	Maximum Strain
	1st Stage	2nd Stage	(MPa)	(%)
Mean	10.69	8.37	249.5	3.45
Std Dev	2.68	1.25	39.75	0.37
COV (%)	25	15	16	11

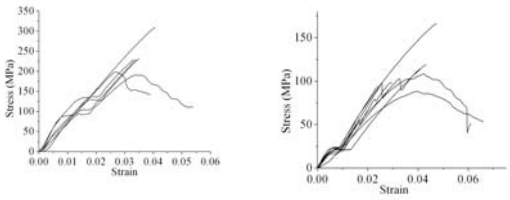

a) b)

Figure 6. Stress-strain plots for slivers and yarns under displacement-control uniaxial tension with a strain rate of 0.001/s: a) sliver and b) on yarn.

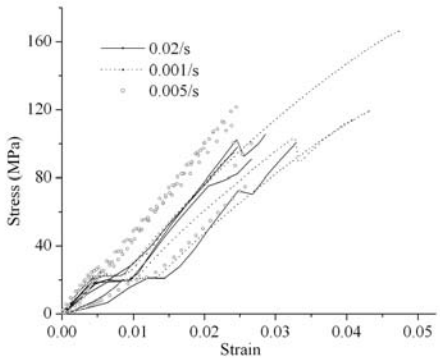

Figure 7. Stress-strain curves of kenaf slivers under displacement-controlled uniaxial loading at the strain rate of 0.001, 0.005, and 0.02/s.

When the loading rate increases, slivers demonstrated a slightly different tensile behavior, as shown in Figure 7. The sliver had relatively lower failure strength at a higher strain rate while the flat region occurred at almost the same stress level. A larger sample set will be evaluated for statistical analysis of the rate-dependent properties of slivers.

Modeling of Rate-Dependent Tensile Behavior

A standard linear model for viscoelastic behavior of solid materials, which effectively combines the Maxwell Model, $\dot{\varepsilon} = \frac{\sigma}{\eta} + \frac{\dot{\sigma}}{E}$, and a Hookean spring in parallel, is used in this study. This model can also be treated as a modification of the Kevin-Voigt model of Newtonian damper and Hookean elastic spring in parallel,

$\sigma = E\varepsilon + \eta\dot{\varepsilon}$, i.e.,

$$\sigma = \sigma^e + \sigma^v = E_\infty \varepsilon + \eta\dot{\alpha} \qquad (1a)$$

$$\sigma = \sigma^e + \sigma^v = E_\infty \varepsilon + E(\varepsilon - \alpha) \qquad (1b)$$

where the total stress is decomposed into an elastic and a viscous component that are determined using an elastic spring constant, E_∞ and a linear viscosity constant, η, which can be extended to an internal state variable shown in Equation (1a) [7]. (See "Nom-enclature" at the end of theis section to identify other symbols.) The viscous stress can also be represented as an inelastic strain in the dashpot, at the extended time interval (-∞,T] shown in Equation (1b). However, the time dependence of inelastic strain in Equation

(1) makes it almost impossible to be directly quantified using tensile tests. For the purpose of demonstrating the loading-rate dependency of the material, a simplification has been proposed by assuming a rate-dependent elastic behavior of the tensile modulus in a form of

$$E = E_0\left(1+\lambda_1 \ln\frac{\dot{\varepsilon}}{\dot{\varepsilon}_0}\right), \qquad (2a)$$

which is also applied to the proportional stress, or "yield strength," or flow stress, when considering viscoplasticity or nonlinear viscoelasticity,

$$\sigma_Y = \sigma_{Y0}\left(1+\lambda_2 \ln\frac{\dot{\varepsilon}}{\dot{\varepsilon}_0}\right) \qquad (2b)$$

where, E_0, σ_{Y0} and $\dot{\varepsilon}_0$ can be treated as reference tensile modulus, reference yield strength, and reference strain rate, respectively. Two parameters, $\lambda_{1,2}$, in Equation (2) are similar to other strain-rate dependent coefficients, which can be obtained using experimental results in Table 3 as

$$\lambda_{1,2} \propto \frac{\partial\left(E,\sigma_y\right)}{\partial \ln \dot{\varepsilon}}. \qquad (3)$$

It should be noted that Equation (2b) and subsequent strain-rate dependent coefficients in Equation (3) may depend on the flow rules introduced to evaluate the nonlinear viscous behaviors of materials. Figure 8 shows the experimental data and model correlations of strain-rate dependency of tensile modulus and "yield" strength of KBFB-epoxy slivers with the loading strain rate ranging from 0.001 to 0.02. It is interesting that the yield strength of the sliver decreases as the loading strain rate increases, which is different from most observations of other short-fiber-reinforced composites.

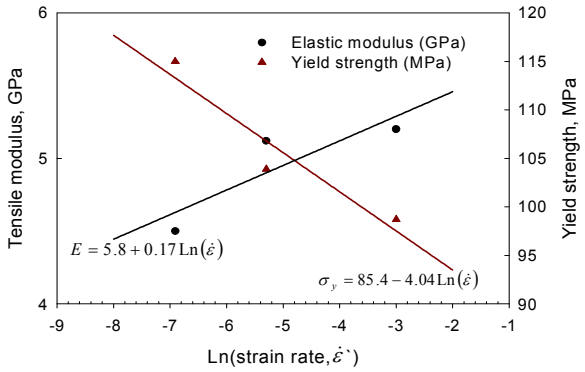

Figure 8. The experimental data and model correlations of strain-rate dependency of tensile modulus and "yield" strength of KBFB-epoxy slivers.

References

1. Kenaf Properties, processing and products, ed. By Terry Sellers, Jr., Nancy A. Reichert, Mississippi State University, 1999.
2. R. M. Roger, A. Sanadi, R. Jacobson, D. Caulfield, Properties of Kenaf/Polypropylene Composites, In: Kenaf Properties, processing and products, ed. By Terry Sellers, Jr., Nancy A. Reichert, Mississippi State University, pp. 381-92, 1999.
3. M. J. Kocurek et al. Secondary Fibers and Nonwood Pulping, The Pulp and Paper Manufacture Series, Vol. 3, 1987.
4. American Society for Testing and Materials. 2003. Standard Test Method for Tensile Strength and Young's Modulus of Fibers. ASTM C 1557-03. ASTM, West Conshohocken, PA.
5. James S. Han et al. Validity of plant fiber length measurement – a review of fiber length measurement based on kenaf as a model, Kenaf properties, In: Processing and products, pp.149 – 167, 1999.
6. Kohji Suzuki, Isao Kimpara, Hiroshi Saito, Kunio funami, Cross-sectional area measurement and monofilament strength test of kenaf bast fibers, Journal of the Society of Materials Science, Japan. Vol. 54, No. 8, pp. 887-894, 2005.
7. J. C. Simo and TJR Hughes, Computational Inelasticity, Interdisciplinary Applied Mathematics, Mechanics, and Materials, Springer, 1997.

Acknowledgement

The authors would like to express appreciation for the support of the U.S. Department of Energy and the Center for Advanced Vehicular Systems at Mississippi State University. We would also express special thanks to Mr. David Baker for his support on micrographs using scanning electron microscope. We would also express special gratitude to Mr. Hugh McKee, the president of Bast Fibers LLC, for his consistent support on Kenaf bast fiber and composites.

Presentations/Publications/Patents

1. Publications - Xue Y., Y. Du, S. Elder, K. Wang, and J. Zhang. 2007. Multiscale Experiments and Modeling of Kenaf Fiber Bundles and Composites. Submitted for publication in the Composites Part B: engineering.
2. Presentation - Xue, Y., Y. Du, S. Elder, D. Sham, M. Horstemeyer, and J. Zhang. Statistical tensile properties of Kenaf fibers and its composites. The 9th International Conference on Wood & Biofiber Plastic Composites, May 21-23, 2007, Madison, WI.

Nomenclature

$\dot{\varepsilon}$	=	Strain Rate
$\dot{\varepsilon}_0$	=	Reference Strain Rate
σ	=	Total Stress
$\dot{\sigma}$	=	Stress Rate
η	=	Linear Viscosity Constant
$-\infty$	=	Extended Time Interval
E'	=	Storage Modulus
σ^e	=	Elastic Component
σ^v	=	Viscous Component
E_∞	=	Elastic Spring Constant
E	=	Tensile Modulus
E_0	=	Reference Tensile Modulus
σ_Y	=	Yield Strength
σ_{Y0}	=	Reference Yield Strength
$\lambda_{1,2}$	=	Strain-rate Dependent Coefficients

Chemical Retting for Stem-Length Natural Bast Fibers: Fiber Characteristics

Team Members: Sangyeob Lee, Sheldon Q. Shi, and Mark F. Horstemeyer

Introduction

Kenaf is a seasonal fiber crop, grown in large amounts every year in the United States. In Mississippi, for example, kenaf fiber production is about 3,600 tons per year (Columbus 2006). Kenaf-bast fiber is an excellent cellulose resource for fiber-based products such as newsprint, bond paper, and corrugated liner board. Extracting the kenaf fibers has less environmental impact because less chemical is required for the process than for wood sources. Short-bast-fiber retting has been developed for the pulp-and-paper applications (Ramaswamy et al. 1994, Hesch 2002, Kawahara et al. 2005). A limited number of studies have been conducted to generate long bast fibers used in the natural-fiber polymer composite (NPC) area. Other limited uses of the kenaf bast fibers include automobile dashboards, carpet padding, corrugated medium, and textiles (Ramaswamy et al. 1995, Webber et al. 2002).

The overall objectives of this study are threefold: investigate a chemical-retting technique, characterize fiber properties, and develop inorganic nanoparticle impregnation technology to produce natural-fiber cell-wall structures. *We focus on investigating a chemical-retting technique first*, followed by developing inorganic nanoparticle impregnation technology for the micropore cellular structure of natural fibers using the ionic salts for making NPC. We also examine the framework of compatible nanoparticle loading and nanoparticle sizes as a function of increased attraction force at the fiber and polyolefin interphase.

Experimental

Materials

For the retting study, kenaf stems (*Hibiscus cannabinus*, L.) were harvested from MSST north farm in January 2007 (Courtesy of Dr. Dan Seale). Bast and core were separated and bast was cut into 5.1-cm lengths from the top, middle and

bottom sections of the stems. The bast was conditioned in an environment with an ambient temperature of 22ºC and a relative humidity of 50% until the MC reached an equilibrium of 8%. Retting chemicals sodium hydroxide (NaOH), hydrogen peroxide (H_2O_2) and acetic acid (CH_3COOH) were purchased from Fisher Scientific, Inc.

Chemical Retting of Kenaf Stem

Table 4 shows the chemical-retting conditions used in this study. Top and bottom sections were taken from within 10 cm at both ends; the middle section was removed from the exact middle of the kenaf stalk. Each section was cut into 25.4-mm lengths and 30 grams of samples were weighed out. Each section was pre-soaked in 80°C water for 24 hours. The pre-soaked kenaf sections were washed and dewatered by gravity. The dewatered sections were retted with 1%, 5%, and 8% sodium hydroxide for an hour at 60 °C. Washed chemically-retted kenaf bundles were neutralized with 5% acetic acid. The excessive chemicals were washed out and the kenaf fiber bundles were dried by air. The dried fiber bundles were characterized using field-emission scanning electron microscopy (FESEM: JSM-6500F) for surface morphology and atomic force microscopy (AFM- Nanoscope IIIa from Digital Instruments) for the surface roughness. Kenaf single fibers were also prepared using a fiber-maceration method (H_2O_2) to address single-fiber dimensions in each section using an image-analysis system (Spot Insight camera and UTHSCSA Image tool Ver. 3.0).

Table 4. Conditions for Chemical Retting

Kenaf Stem	51 mm Length
Sample Collect Location	Top, Middle and Bottom
Pre-soaking	H_2O
Pre-soaking Temperature & Time	80°C for 24 hours
Kenaf/H_2O Ratios for Pre-soaking	1:20
NaOH Concentration	1%, 5% and 8%
Liquid Ratios (Kenaf: NaOH)	1:30
Reagent Chemicals	Acetic Acid (CH_3COOH)
Reaction Temp.	60°C
Reaction Time	1 Hour

Results and Discussions

Characteristics of Chemically-Retted Kenaf-Fiber Bundles

Table 5 shows the chemical composition of kenaf harvested from the MSST north farm. Chemically-retted bast fibers have three principal chemical components such as α-cellulose (46%), hemicelluloses (30%), and lignin (19%) with minor components (5 to 6%) called fats, waxes, inorganic matter, nitrogenous matter, and pigments. The lignin and the hemicelluloses can be almost completely removed by dilute alkali. Due to the chemical treatment, the α-cellulose remained as a final insoluble residue in a fiber form. The chemical compositions of hemicellulose and lignin, compared with published values, were slightly lower and resulted in decreased α-cellulose contents. However, the cellulose content is still equal or higher than fiber sources coming from wood materials. Bast fibers contain a higher cellulose content which contributes to their strength properties. The fibers also have less lignin to support their structural stand. Therefore, the fibers should require fewer chemicals to separate fiber bundles or single fibers. The hemicellulose and lignin contents relate directly to the void spaces of the cell-wall structure and lower amorphous regions. All percentages refer to the weight fraction of oven-dried initial samples.

Table 6 shows fiber dimension and surface roughness of chemically-retted kenaf-fiber bundles as an addition to the single-fiber characteristics. The highest yield was obtained from the top section of the kenaf stem and this section provided longer and more slender fibers than fibers extracted from other sections. Fiber dimensions of stem bast fibers contributed to extreme aspect ratios (length to width). Increased sodium hydroxide contents from 1 to 8% altered fiber surfaces. Sampling locations in the kenaf stem also dictate the smoothness of the surface of chemically-retted fibers. The top section produced rough surfaces of bast fibers, caused by remaining hemicellulose and lignin. Due to the relatively high cellulose contents, the mechanical and physical properties of the kenaf fibers are higher than or equal to those of wood fibers. The cell-wall structure of kenaf-fibers is similar to that of the wood fibers.

Table 5. Chemical Composition of Kenaf- Bast Fibers Harvested from MSST North Farm.

Characteristics	
Moisture content (wt. %)	7.40
Ash (wt. %)*	5.07
Klason Lignin (wt. %)**	19.10
Holocellulose (wt. %)***	75.83
α- cellulose****	45.95
Hemicellulose (by subtraction)	29.88

* TAPPI standard 211-om93 (TAPPI 1993).
** Institute of paper chemistry, Appleton, Wisconsin 428, 1951.
*** Wise, L.E., M. Murphy, and A.A. D'Addieco, Paper Trade J. 122(2):35 (1946).
**** Zellcheming Merkblatt IV/29A

Figure 9 shows topographical and morphological images of fibers treated with different chemical concentrations. The scanning electron microscopy (SEM) images show the changes of surface morphology through sodium hydroxide extraction at different levels of chemical concentrations. A higher chemical concentration provides a smoother fiber surface with less deposited materials on the surface of natural fibers. Bacterially-retted fiber shows similar surface roughness and deposited-material conditions somewhere between 1% and 5% diluted sodium hydroxide levels. This result indicates that a smooth surface was produced under the 8% concentration and may provide a better opportunity for the inorganic nano-particle impregnation method to produce porous structures of natural fibers.

Table 6. Physical Characteristics of Chemically- Retted Kenaf Fiber Bundles.

	Fiber Yield	Length*	Diameter*	Root Mean Squire (RMS) Surface Roughness					
				1% NaOH		5% NaOH		8% NaOH	
	(%)	(mm)	(μm)	2.5 μ Scan	1 μ Scan	2.5 μ Scan	1 μ Scan	2.5 μ Scan	1 μ Scan
Top	73 (2.0)	2.72 (0.50)	12.6 (2.1)	159.8 (69.7)	78.4 (36.5)	77.1 (15.8)	44.7 (15.3)	73.4 (18.3)	35.4 (16.5)
Middle	66.3 (2.3)	2.49 (0.42)	14.1 (1.9)	117.3 (32.9)	70.3 (28.6)	86.3 (25.1)	43.8 (18.9)	55.2 (17.8)	29.6 (13.7)
Bottom	59.4 (1.7)	2.57 (0.31)	13.6 (1.5)	99.1 (35.1)	45.5 (23.9)	68.8 (12.1)	36.7 (18.4)	66.9 (19.2)	38.6 (18.4)

*= Measurement from single fibers (Averages of 25 Single Fibers), ()= Standard Deviation

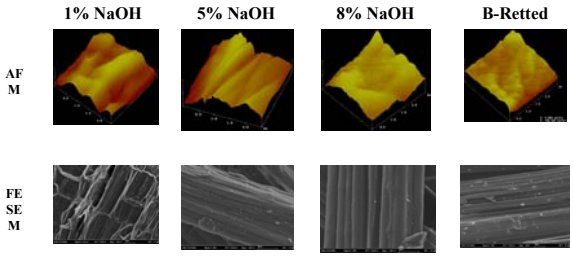

Figure 9. Surface topography and morphology of chemically-retted kenaf-fiber bundles with 1%, 5% and 8% sodium hydroxide concentrations at middle sections. Bacterially-retted images (right) are used for comparison.

Conclusions

Chemically-retted kenaf-bast fibers and their characteristics were evaluated to explore practical applications of such methods to the compressed polymer composite. Relatively higher α-cellulose content (45.95%) was obtained from the kenaf harvested from the MSST north farm. The physical appearance of chemically-retted fiber bundles was quantified as follows: an average 2.6 mm in fiber length and 13.3 μm in diameter with 66% fiber yield. Sodium hydroxide concentrations at 5 to 8% provided smoother surfaces and less deposited materials compared with the 1% NaOH extraction and bacterially-retted fibers. This result was also confirmed by the surface topography and morphology. Uniform root mean square (RMS) roughness and clean surface were obtained from increased NaOH concentration.

References

1. Columbus, E.P. 2006. Telecommunication. (Dec. 14. 2006).
2. Hesch, R. 2002. Device and method for producing a fiber composite. US Pat. 6,460,224. (Oct. 8, 2002).
3. Kawahara, Y., T. Keiichi, R. Endo, M. Shioya, Y. Sugimura, T. Furusawa. 2005. Chemically retted kenaf fibers. Sen'i Gakkaishi, 61(4):115-117.
4. Ramaswamy, G.N., C.G. Ruff, and C.R. Boyd. 1994. Effect of bacterial and chemical retting on kenaf fiber quality. Textile Res. J. 64(5):305-308.
5. Ramaswamy, G.N., and S. Craft. 1995. Uniformity and softness of kenaf fibers for textile products. Textile Res. J. 65(12):765-770.
6. Technical Association of Pulp and Paper Industry (TAPPI). 1993. Ash in wood, pulp, paper and paperboard: combustion at 525°C, TAPPI T 211 om-93. TAPPI Press, Atlanta, GA.
7. Webber, C.L., V.K. Bledsoe, R.E. Bledsoe. 2002. Kenaf production: fiber, feed, and seed. J. Janick and A. Whipkey. Eds. ASHS Press, Alexandria, VA.

Acknowledgement

The authors would like to express appreciation for the support of the US Department of Energy and the Center for Advanced Vehicular Systems at Mississippi State University. We would also express special thanks to Dr. Leslie H. Groom and Dr. Thomas Elder, USDA-Forest Service Southern Research Station, Pineville, LA for Instrumental Support. The authors would like to thank Dr. El Barbary M. Hassan, Bio-oil Group, Forest Products Dept, Starkville, MS for Instrumental Support.

Presentations/Publications/Patents

1. Publication - Lee, S., S.Q. Shi, and M. Horstemeyer. 2007. Morphology and mechanical properties of chemical retted natural bast fibers. ***Paper in preparation.***
2. Publication - S.Q. Shi, S. Lee and M. Horstemeyer. 2007. Natural Fiber Retting and Inorganic Nanoparticle Impregnation Treatment for Natural Fiber/Polymer Composites. 22nd Annual American Society for Composites. University of Washington, Seattle, WA.
3. Presentation - Kenaf Bast Fiber Retting and Inorganic Nanoparticle Impregnation Treatment for Natural Fiber/Polymer Composites. 22nd Annual American Society for Composites Tech. Conf. Univ. of Washington Seattle, Washington, USA. Sept. 17–19, 2007.
4. Presentation - Chemical retting for stem-length natural bast fibers: fiber morphology and mechanical properties. 61st International Convention, Forest Products Society, Knoxville, Tennessee, USA. June 10-13, 2007.

Multifunctional Nanoparticles at the Hydrophilic and Hydrophobic Interface

Team Members: Sangyeob Lee, Sheldon Q. Shi, and H. Michael Barnes

Introduction

The cell-wall structure of natural fibers contains many micropores. One of the events occurring in fiber processing is that lignin and hemicellulose of natural fibers are usually removed during chemical treatments or pulping, which creates additional micropores (Allan et al. 1992a). The presence of these micropores in the cell wall could cause manufacturing defects in composites, such as interfacial failure and air pockets. To reduce the air-pocket defect, one can incorporate a vacuum-assist system in the natural-fiber polymer-composite (NPC) processing to reduce air bubbles to some extent. Another effective way is to introduce nano-particles into the micropores of the fiber cell-wall structure through an impregnation process to fill those voids.

Compatibility between the hydrophilic natural fibers and the hydrophobic polyolefins has been a major issue for the NPC (Lee 2002, Ma *et al.* 2005). Lee *et al.* (2006) indicated that the deposited nano-scale particles on a natural-fiber surface may serve as heterogeneous nucleation sites to initiate crystalline orientation of a molten-polymer matrix. These results suggested that nanoparticles might control the heterogeneous nucleation of a semicrystalline polymer on the natural-fiber surface. The natural fiber itself

cannot initiate nuclei due to extremely unbalanced free energy between the cellulosic fibers and molten polyolefin matrices (Mullin 1993, Gasser *et al*. 2001, Lee *et al*. 2006). Therefore, the nanoparticle impregnation would not only fill the micropores of the fiber-cell-wall structure by minimizing air-bubble defects of the NPC, but would also introduce nanoparticles onto the fiber surfaces to serve as attraction-force manipulators to polymer matrices for improving the compatibility between fiber and polymer interfaces.

Calcium carbonate is a versatile additive for use in the pulp/paper and plastic industries for elastomeric applications to obtain a hydrophobic surface-coating (Khrenov *et al.* 2005). It has a regular and controlled crystalline shape (orthorhombic) and a 0.05 to 2.5-µm particle size (Allan and Carroll 1994, Kuang *et al.* 2002, Yan *et al.* 2005). A smaller particle size can be obtained from ionic-salt impregnation to build a crystal form of calcium carbonate (Choi 1995). Chemical-impregnation technology has well been developed and applied in pulp-and-paper and surface-coating industries (Allan *et al.* 1991, Allan *et al.* 1992a and 1992b, Lee *et al.* 1999, Koepenick 2000, Lork 2004, Kuusipalo *et al.* 2005). However, in the pulp-and-paper applications, the amount of inorganic-compound loading is limited to 7% due to the concerns of surface-printing ability and paper strength (Kocman and Bruno 1995, Li *et al.* 2002, Perng and Wang 2004, Kralj *et al.* 2004, Frederick *et al.* 2004, Sancaktar and Walker 2004, Yan *et al.* 2005). For NPC applications, the amount of inorganic nanoparticle loading in the natural fibers could be increased, thus improving the attractive forces in the composites. The nanoparticle sizes and their distribution presented in the impregnated natural fibers may have a significant impact on the NPC properties. It has been shown that the inorganic nanoparticle size can be controlled by the reaction time and the ionic salt ratio (Choi 1995, Gasser *et al.* 2001).

The objective of this present study is to develop inorganic nanoparticle impregnation techniques for the natural-fiber cell-wall structures in order to reduce the NPC processing defects and enhance the mechanical properties.

Experimental

Materials

In the inorganic nanoparticle impregnation experiments, Kraft wood-pulp fibers (southern pine-*Pinus* spp.) were obtained from a local pulp company. They were collected from a bleached pulp stream and kept in a wet condition (150% MC) to obtain optimum nano-void openings. The fibers were stored at a temperature of 4ºC until ready for further experiments. Primary (Na_2CO_3) and secondary ionic ($CaCl_2$) salts were purchased from Fisher Scientific Inc.

Experimental Procedures

Figure 10 shows a simplified flow chart for the inorganic nanoparticle impregnation using two steps of the ionic-salt treatment under heat and pressurized-chamber conditions. Micropore impregnation of ionic salts was effected with never-dried Kraft pulp fibers in a pressurized reactor. The primary salt, Na_2CO_3, and secondary ionic salt, $CaCl_2$, were impregnated into micropores of the natural-fiber cell wall consecutively to obtain nanoparticles (< 100 nm). The nanoparticle sizes were controlled by the reaction time and molar fraction of ionic salts. The chemical reaction is described as follows:

$$CaCl_2 \cdot H_2O + Na_2CO_3 \xrightarrow{H_2O} CaCO_3 + 2NaCl + 2H_2O$$

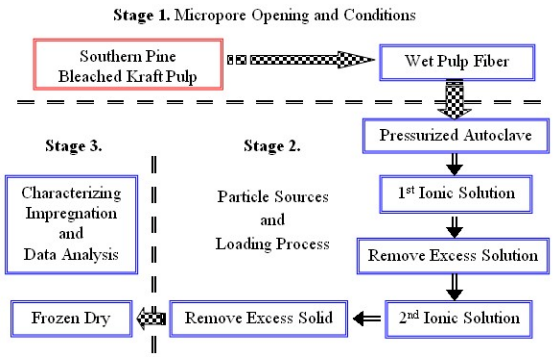

Figure 10. Inorganic nanoparticle impregnation using two steps of the ionic salt treatment under heated and pressurized chamber conditions.

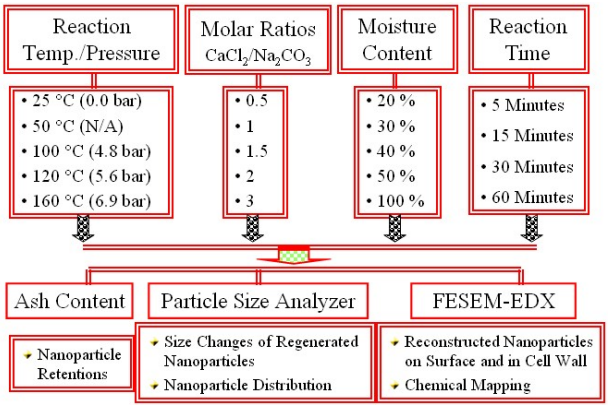

Figure 11. Experimental variables for the inorganic nanoparticle impregnation into the cell-wall structure of natural fibers.

For this study, parameters (Figure 11) were selected to optimize inorganic nanoparticle loading into the porous structures of natural fibers. The parameters investigated included reaction temperature, molar ratios of two ionic salts, moisture content of natural fibers, and reaction time. The experimental process was to optimize the process to get the best impregnation conditions. The MCs (oven-dry-basis (ODB)) of 20, 30, 40, 50, 100% and molar ratio of 1 were chosen to see the effect of MC. From the result, 20% and 30% MC were selected. Molar ratios of 0.5, 1, 1.5, 2, and 3 with the two MCs were evaluated by ash contents of pulp fibers impregnated with $CaCO_3$. After the previous steps, reaction temperature and time factors were recorded without Kraft pulp with primary (Na_2CO_3) and secondary ionic salt ($CaCl_2$). Temperatures of 25, 50, 100, 120 and 160°C were evaluated with a fixed molar ratio of 1 and MC of 30%. The effect was evaluated with particle size analysis and SEM to address how the temperatures influence the nanoparticle formation and sizes. Two molar ratios, 0.5 and 1, MC of 30%, and a temperature of 25°C were selected to evaluate reaction times of 5, 15, 30 and 60 minutes between primary and secondary ionic salts after the primary ionic salt was diluted for 15 minutes. The selected parameters such as molar ratio of 1, MC of 30%, temperatures of 25 and 160°C, and reaction time of 15 minutes were directly applied to impregnate nanoparticles into the cell wall structure of kenaf fibers. SEM-energy dispersive x-ray (EDX) was used to evaluate the Ca++ ion mapping and chemical-element analysis.

A 1-L pressurized reactor (Parr Instrumental Co.) with Model 4843 controller was employed to affect the inorganic-nanoparticle-impregnation process. In a typical experiment, bleached commercial pulp fibers (0.5% ash content, 91% MC (ODB)) were introduced into the pressure vessel along with the primary ionic solution. The vessel was sealed and pressurized to the level shown in Figure 11 for the reaction temperature used. The solution was constantly stirred at 100 rpm. Pressure was maintained for 15 minutes followed by venting to atmospheric pressure and removal of the reacted fiber. After washing out the excess primary solution, the fiber was reintroduced into the reaction vessel with the secondary ionic salt and the process was repeated. The inorganic-nanoparticle-impregnated fibers were dried and evaluated in terms of nanoparticle-size distribution, surface morphology, and chemical loading of the inner cell-wall structure of the natural fibers. The treated fibers were freeze-dried under vacuum for 12 hours and stored in a vacuum desiccator. A muffle furnace was used to measure ash contents (T 211 om-93) for each treatment condition.

A particle size analyzer (Microtrac UPA 250) with Microtrac V.9.1.17 software was used to determine inorganic-nanoparticle growth and distribution. The micro- to nano-scales of particles were detected by a dynamic-light-scattering detector (0.003 to 6.541 micron capability) for 180 seconds. Nanoparticle samples were treated with sonic waves for three minutes to increase the detector sensitivity. Deionized water was used as a carrier. The morphology and chemical-mapping analysis using field-emission scanning electron microscopy (FESEM: JSM-6500F and EDX: Oxford Instruments INCA Energy with X-ray Elemental Analysis) were used to investigate the inorganic nanoparticle distribution in the cell wall and surface morphology. Mounted fibers were coated with an approximately 15-nm thin gold layer using an ion sputter. Images were generated at 5 kV and 10,000x.

Results and Discussion

Effect of Reaction Temperature

Figure 12 shows the effect of reaction temperature on the inorganic nanoparticle formation and growth in the reaction chamber. The nanoparticle sizes were from 138 nm to 2,000 nm. The crystal size was decreased with an increased reaction time. Also, the longer the reaction time, the more uniform the particle size distribution is. Nano-scale crystal formation on the surface of micro-scale inorganic particles was observed at a relatively lower temperature under 50°C. When the reaction temperature reached 160°C, the reaction-chamber pressure was 6.9 bar; the pressure might play a role in inorganic-nanoparticle formation and growth during the reaction of two ionic salts.

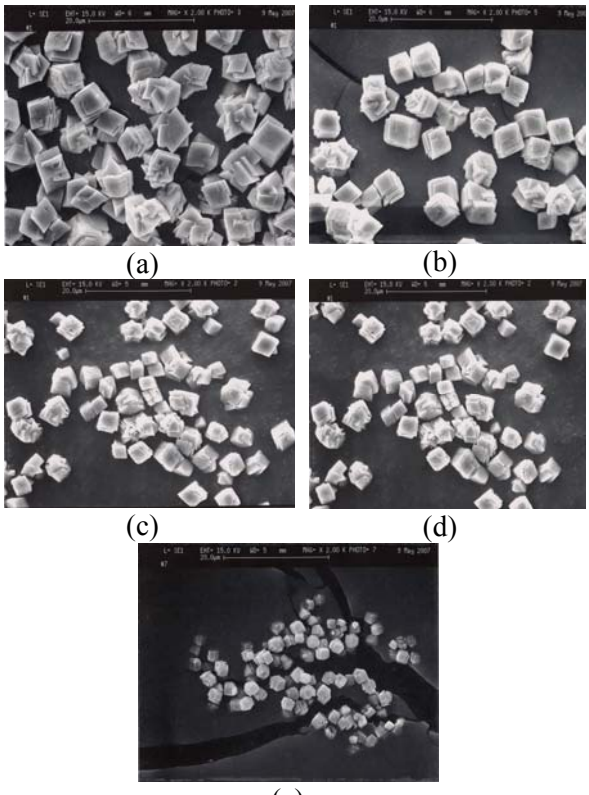

Figure 12. Inorganic-nanoparticle formation and growth of consecutively-reacted ionic salts with reaction time applied in the reaction chamber at 2000 x. (a) 25 °C, (b) 50 °C, (c) 100 °C, (d) 120 °C, and (e) 160 °C.

The optimum reaction time was 15 minutes after the secondary ionic salt was introduced into the reaction chamber. The reaction time was evaluated at a temperature of 25 °C with two types of molar ratios of sodium carbonate and calcium chloride. The longer reaction time contributed to the growth of $CaCO_3$ crystal structures. The molar ratios of $CaCl_2/Na_2CO_3$ of 1 and 2 provided relatively low average particle size. The ratio 2 showed a wide distribution from 45 nm to 6 μm, while the ratio 1 showed a relatively uniform distribution.

Moisture Content of Kraft Pulp

Figure 13 shows the effect of fiber MC on the nanoparticle loading for the fiber-cell-wall impregnation. It shows that the fiber-saturation point (FSP) of the bleached Kraft fibers at about 30% MC is a critical point to impregnate the fillers into their cell-wall structure. When the MC is less than FSP (i.e., MC<30%), cellular structures of natural-fiber cell wall may play an important role. It also influences the dispersing characteristics of ionic salts into the porous structure of the cell wall. Below FSP, the microfibrils are closer and fewer micropores are available to be impregnated with inorganic fillers (Choi 1995, Kocman and Bruno 1996). It should also be noted that the dry fibers are not compatible with the impregnation of inorganic compounds due to the collapsing cellular structure of fiber cell walls. It is difficult to recover their structure with swelling agents (Allan 1992, Choi 1995). In this impregnation study, we targeted 10 to 15 % inorganic nanoparticle loading in order to keep both the fiber strength properties and the void-filling requirement. Since the inorganic nanoparticle loading is higher than the target (10 to 15%), all of the wet-fiber conditions can be acceptable for the nanoparticle loading, except that the MC remains below FSP.

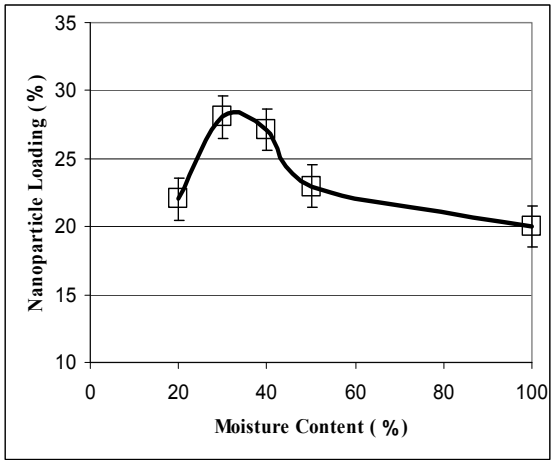

Figure 13. Moisture contents of Kraft fiber on a wood cell wall loaded with $CaCO_3$ particles.

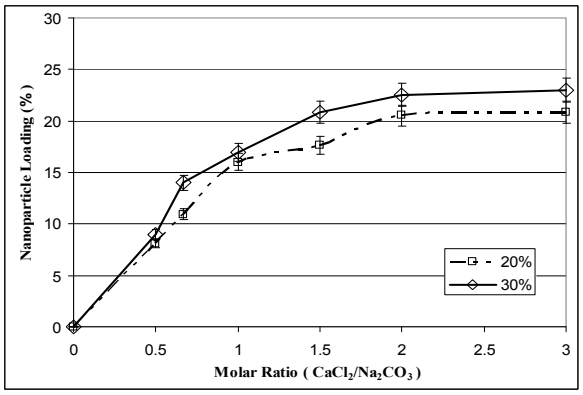

Figure 14. The effects of molar ratios of calcium chloride and sodium carbonate on cell-wall loading (CWL) of wood fibers at 25ºC for 30 minutes.

Effect of Molar Ratios of Ionic Salts

Figure 14 shows that the increase of concentration of calcium chloride ($CaCl_2$) and a greater molar ratio (calcium chloride to sodium carbonate =$CaCl_2/Na_2CO_3$) level will increase the precipitation level of calcium carbonate ($CaCO_3$). Additional findings suggest that longer reaction times and higher ionic-salt ratios will result in a large $CaCO_3$ crystal structure (up to > 1 μm in diameter). The desirable particle sizes for the nanoparticle impregnation are in the range of 10 nm up to 200 nm. This can be achieved by controlling the reaction time and calcium chloride contents in the ionic-salt ratio. The effect of molar ratios ($CaCl_2/Na_2CO_3$ =1) of ionic salts addressed 16 % to 17% cell-wall loading (CWL) capability.

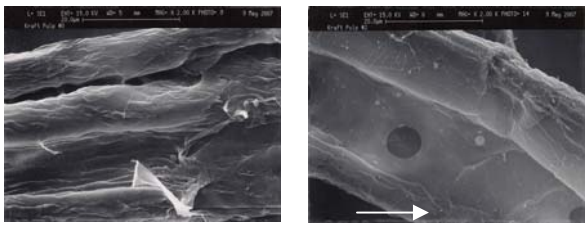

(a) (b)

Figure 15. Surface nanoparticles formed by excessive ionic salts. (a) before ionic treatment and (b) after ionic treatment.

Reconstructed Nanoparticles and $CaCO_3$ Precipitation

Figures 15 and 16 show the FESEM images and the EDX analysis before and after inorganic-nanoparticle impregnation. The morphological images show that the deposited materials remain on the surface. The deposited materials may consist of lignin and hemicellulose materials as well as the particles from natural fiber itself. The bright particles shown in Figure 15 (b) indicate that the inorganic crystal is formed on the surface and grown with excessive ionic salts. The residual ionic salts generally allow forming larger crystals of the calcium carbonate than the crystals formed in the inner cell wall. Because the largest voids are generally around 1,000 Å, the inorganic nanoparticles loaded inner cell wall may be less than the largest voids. The evidence of calcium carbonate impregnation as a filler of the nano-scale porous structure in the natural-fiber cell wall is shown in Figure 16. The dots (Figure 16 (a)) indicate Ca^{++} ion distribution inner cell- wall structures. The dots also indicate that impregnated inorganic nanoparticles ($CaCO_3$) are uniformly distributed through the natural-fiber cell wall. The EDX analysis (Figure 16 (b)) shows higher quantities of Ca^{++} ions with residual sodium and chloride ions.

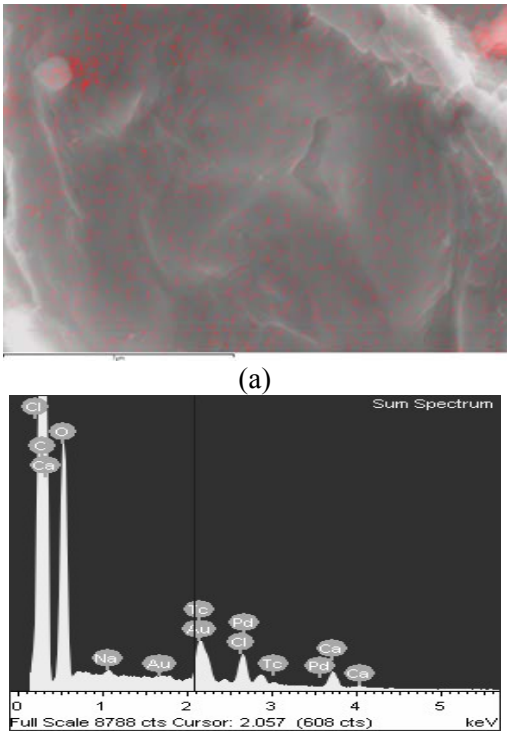

Figure 16. Chemical mapping of Ca^{++} ion in cross-section using SEM-EDX in the cell-wall structure of natural fibers. (a) Ca^{++} ion mapping, and (b) chemical-element analysis.

Conclusions

Through the impregnation process developed in this study, inorganic nanoparticles were observed in the micropore structure of the cell wall. These nanoparticles may serve as void fillers and potentially provide nucleation sites for the semi-crystalline polymers. The longer the reaction time, the smaller the reconstructed nanoparticle size and the more uniform is the nanoparticle size distribution. Parameters for the inorganic nanoparticle impregnation using ionic salts to the natural-fiber cell-wall structures were evaluated to optimize the attraction force at the fiber and polyolefin interphase. The inorganic nanoparticle precipitation increases with the increase of $CaCl_2/Na_2CO_3$ molar ratio. To reach an optimal loading condition, the process should keep the reaction time shorter, the reaction temperatures higher (120 to 160°C) with applied pressure, the reconstructed nanoparticle size smaller, and the nanoparticle distribution uniform. An optimum MC for the inorganic nanoparticle loading is at FSP, about 30% . Under the optimum conditions, Ca^{++} ions were observed in the cell wall of the fiber cross-section. During the course of developing impregnation processes, inorganic nanoparticles were observed in the micropore structure of the cell wall. These nanoparticles may serve as void fillers in the micropores of the natural fibers and potentially provide nuclear sites for semi-crystalline polymers.

References

1. Allan, G.G., Y.C. Ko, and P. Ritzenthaler. 1991. The microporosity of pulp. Tappi J. 74(3): 205.
2. Allan, G.G. 1992. Cell wall loading of never-dried pulp fibers. U.S. pat. 5,096,539 (Mar. 17, 1992).
3. Allan, G.G., A.R. Negri, and P. Ritzenthaler. 1992a. The microporosity of pulp; the properties of paper made from pulp fibers internally filled with calcium carbonate. Tappi J. 75(3):239-244.
4. Allan, G.G., J.P. Carroll, A.R. Negri, M. Raghuraman, P. Ritzenthaler, and A. Yahiaoui. 1992b. The microporosity of pulp; the precipitation of inorganic fillers within the micropores of the cell wall. Tappi J. 75(1):175-178.
5. Allan, G.G. and J.P. Carroll. 1994. Composition and methods for filling dried cellulosic fibers with an inorganic filler. U.S. pat. 5,275,699 (Jan. 4, 1994).
6. Choi Y.D. 1995. Impregnation behavior of $CaCO_3$, KCl and K_2SO_4 into micropore of pulp fiber. MS thesis, Yeungnam Univ., Kyungsan, Korea. 41p.
7. Frederick, W.J., B. Shi, D.D. Euhus, and R.W. Rousseau. 2004. Crystallization and control of sodium salt scales in black liquor concentrators. Tappi J. 3(6):7-13.
8. Gasser, U., E.R. Weeks, A. Schofield, P.N. Pusey, and D.A. Weitz1. 2001. Real-space imaging of nucleation and growth in colloidal crystallization. Science. 292:258-262.
9. Khrenov, V., M. Klapper, M. Koch, and K. Müllen. 2005. Surface functionalized ZnO particles designed for the use in transparent nanocomposites. Macromol. Chem. Phys. 206(1):95–101.
10. Kocman, V. and P. Bruno. 1995. Accurate determination of six common fillers in fine papers, newsprint, and recycled stock by X-

ray fluorescence spectrometry. Tappi J. 78(4): 129-134.

11. Kocman, V. and P.J. Bruno. 1996. Thermal stability of paper fillers: A strong case for a low temperature paper ashing. Tappi J. 79(3): 303-306.
12. Koepenick M. 2000. Nanoparticle prospects and perspectives. TAPPI J. 83(5): 45-47.
13. Kralj, D., J. Kontrec, L. Brečević, G. Falini, and V. Nöthig-Laslo. 2004. Effect of inorganic anions on the morphology and structure of magnesium calcite. Chem. Eur. J. 10:1647-1656.
14. Kuang, D., A. Xu, Y. Fang, H. Ou, and H. Liu. 2002. Preparation of inorganic salts ($CaCO_3$, $BaCO_3$, $CaSO_4$) nanowires in the Triton X-100/cyclohexane/water reverse micelles. J. Crystal Growth 244:379–383.
15. Kuusipalo, J., M. Kaunisto, A. Laine, and M. Kellomäki. 2005. Chitosan as a coating additive in paper and paperboard. Tappi J. 4(8):17-21.
16. Lee, S.Y., J. Lee, and S. Yang. 1999. Preparation of silica-based hybrid materials coated on polypropylene film. J. Materi. Sci. 34:1233-1241.
17. Lee, S.Y. 2002. Transcrystallization behavior and interfacial strength of a semicrystalline polymer combined with thermomechanical pulp (TMP) fiber. M.S. Thesis. Univ. of Idaho, Moscow, ID. 72 p.
18. Lee, S.Y., T.F. Shupe, L.H. Groom, and C.Y. Hse. 2006. Heterogeneous nucleation of a semicrystalline polymer on fiber surfaces. In: Recent developments in the particleboard, fiberboard, and molded wood products industry. Shupe, T.F. ed. Forest Products Society. Madison, WI. pp. 99-105.
19. Li, L., A. Collis, and R. Pelton. 2002. A new analysis of filler effects on paper strength. JPPS. 28(8):267-273.
20. Lork, A. 2004. Silicone resin emulsion coatings: the strength profile of the silicone resin network in paint microstructures. Surface Coatings Inter. Part B: Coatings Transa. 87(B1):1–6.
21. Ma, C., M. Rong, M. Zhang, and K. Friedrich. 2005. Irradiation-induced surface graft polymerization onto calcium carbonate nanoparticles and its toughening effects on polypropylene composites. Polym. Engin. Sci. 45(4):529-538.
22. Mullin, J.W. 1993. Crystallization, 3rd Edit. Butterworth-Heinemann Ltd. Oxford, England. 527p.
23. Perng, Y. and E. Wang. 2004. Development of a functional filler: swelling sericite. Tappi J. 3(6):26-31.
24. Sancaktar, E., and E. Walker. 2004. Effects of calcium carbonate, talc, mica, and glass-fiber fillers on the ultrasonic weld strength of polypropylene. J. Appli. Polym. Sci. 94:1986–1998.
25. Yan, Z., Q. Liu, Y. Deng, and A. Ragauskas. 2005. Improvement of paper strength with starch modified clay. J. Appl. Polym. Sci. 97: 44–50.

Acknowledgement

The authors would like to express appreciation for the support of the US Department of Energy and the Center for Advanced Vehicular Systems at Mississippi State University. The authors would like to thank Dr. James Rawlins and his research group, Thames-Rawlins Polymer Research, Shelby Freland Thames Polymer Science Research Center, University of Southern Mississippi, Hattiesburg, MS for instrumental support.

Presentations/Publications/Patents

1. Publication - Lee, S**.,** S.Q. Shi, and H.M. Barnes. 2007. Inorganic nanoparticle impregnation into micropore cellular structure as void filler and interfacial compatibilizer. ***Paper in preparation.***
2. Publication - Lee, S., S.Q. Shi, and H.M. Barnes. 2007. Multifunctional Nanoparticles at the Hydrophilic and Hydrophobic Interface. In Advanced Biomass Science and Technology for Bio-Based Products. International Rattan and Bamboo Center, Beijing, China. ***In press.***
3. Publication - S.Q. Shi, S. Lee and M. Horstemeyer. 2007. Natural Fiber Retting and Inorganic Nanoparticle Impregnation Treatment for Natural Fiber/Polymer Composites. 22nd Annual American Society for Composites. University of Washington, Seattle, WA..

4. Presentation - Kenaf Bast Fiber Retting and Inorganic Nanoparticle Impregnation Treatment for Natural Fiber/Polymer Composites. 22nd Annual American Society for Composites Tech. Conf. Univ. of Washington Seattle, Washington, USA. Sept. 17–19, 2007.
5. Presentation - Inorganic nanoparticle impregnation into micropore cellular structure: void filler and interfacial compatibilizer. 2007 Intern. Conf. on Nanotechnology for the Forest Products Industry. Knoxville, Tennessee, USA. June 13–15, 2007.
6. Presentation - Multifunctional Nanoparticles at the Hydrophilic and Hydrophobic Interface. Advanced Biomass Science and Technology for Bio-Based Products. International Rattan and Bamboo Center. Beijing, China. May 23–25, 2007.

Unidirectional Natural-Fiber Polyolefin Laminates: Thermal and Mechanical Properties

Team Members: Sangyeob Lee, Sheldon Q. Shi, and Yibin Xue

Introduction

Natural-fiber (mainly woodfiber) polyolefin composites (NPC) have been a natural choice for both non-structural and structural applications such as decking, doors, window frames, flooring, fencing, walls, furniture, automobiles and electronic products (Clemons 2002, Serizawa *et al.* 2006). However, due to their shorter fiber length, their reinforcement potential is limited in terms of the strength properties of the composites (Feng *et al.* 2001, Arzondo *et al.* 2004, Bledzki *et al.* 2004, Serizawa *et al.* 2006). Increasing the length of the natural fiber is one of the alternatives to improve natural-fiber reinforcement. Agricultural bast fibers from jute, hemp, sisal and kenaf can be good candidates because of relatively high cellulose content and enhanced fiber properties (Karnani *et al.* 1997, Rana *et al.* 1998, Eichhorn *et al.* 2001, Sanadi *et al.* 2002, Joseph *et al.* 1993, 2003, Tajvidi *et al.* 2005). Long kenaf (*Hibiscus cannabinus* L.) bast-fiber bundles are traditionally used to make ropes, mats, carpets, paper, and other products (Sellers and Reichert 1999). In recent years, there has been an increasing interest in finding new applications of natural bast fibers in making fiber-reinforced polymer composites for automobile parts to replace synthetic fibers made of glass and carbon.

The objectives of this study are threefold: evaluate kenaf-bast-fiber characteristics, investigate the effect of fiber orientation on the mechanical properties of laminates, and address the thermal and interfacial characteristics at the kenaf fiber and polymer interface.

Materials and Experimental Procedures

Materials

For this study, stem-length kenaf fibers (*Hibiscus cannabinus*, L.) were obtained from an international trading company in February 2007. The fibers were bacterially-retted, stem-length kenaf fibers. The bast was conditioned in an environment with an ambient temperature of 22ºC and a relative humidity of 50% until the MC reached an equilibrium of 8%. The stem-length fibers were macerated to evaluate single-fiber characteristics. For the kenaf maceration, hydrogen peroxide (H_2O_2) was purchased from Fisher Scientific Inc. Polypropylene film (CO-EX), as a polymer matrix, was provided from Plastic Suppliers, Inc. Dallas, TX.

Laminate Fabrication

Figure 17 shows the fabrication procedure of kenaf and polypropylene (PP) film laminates for this study. Stem-length, bacterially-retted fibers were cut into 7-inch lengths and combed to separate the kenaf fibers into separate fiber bundles. A total of thirteen layers (six layers of kenaf fiber and seven layers of PP films) of laminates were fabricated to evaluate the effect of fiber orientation angles (0°, 45° and 90°) and material formulations (kenaf/PP= 30/70, 40/60 and 50/50). A laboratory hot press (6 × 6-inches) was used to press the laminates under 100 psi at 200 °C for 2½-minutes pressing time. The compressed laminates were cooled down at a rate of $25°C \cdot min^{-1}$ as a super-cooling condition. The compressed samples were stored at an ambient temperature of 22ºC for 24 hours before cutting samples for mechanical tests. The kenaf-fiber bundles were also cut into 2-inch lengths of each

top, middle, and bottom to characterize fiber properties such as single-fiber length, diameter, surface topography and surface roughness.

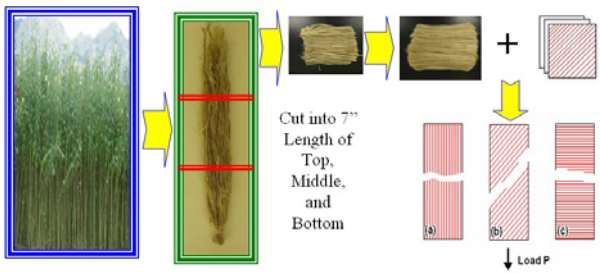

Figure 17. Thirteen layers of laminate fabrication to evaluate the effect of oriented angles.

Instruments and Data Collection

The fiber-bundle strength tests were carried out to address the strength properties at the top, middle and bottom using Mach1V500 (CS instrument Inc.). Loading capacity for this tester was 0-10 N with precision of 0.1 g at 0.5-µm displacement. Before and after the test, the fiber-bundle images were generated using Spot Insight Camera (Advanced V 4.6, Diagnostic Instrument Inc.) as an image-capture system and UTHSCSA Image Tool® V.3.0 for image analysis. Using the image analysis, fiber length and diameters of bast-fibers data were collected to characterize regional differences of kenaf fibers from the top, middle, and bottom sections.

An AFM (Nanoscope IIIa -Digital Instruments) and an SEM (Zeiss SupraTM 40 – Gemini®) were used for the surface topography and morphology of top, middle and bottom bast fibers. The AFM used the tapping mode and two scanning areas, 2.5 × 2.5 µm and 1× 1 µm, to evaluate topographical and RMS surface roughness differences at the top, middle, and bottom section of whole-length bast-fiber bundles. An environmental SEM was also used to address morphological characteristics of the fracture surfaces at 100 and 500 magnifications at 15 kV.

Mechanical test data for kenaf fiber and PP film laminates were evaluated by an Instron 5869 with 5 kN load cell. The cross-head speed was 0.25 in.·min.$^{-1}$ for tensile strength and 0.125 in.·min.$^{-1}$ flexural (modulus of elasticity, MOE, and modulus of rupture, MOR) tests based on ASTM D638-03. Laminate failure was also observed in samples made from fiber-orientation angles of 0°, 45°, 90° and random.

Thermal analysis was carried out by using a thermogravimetric analyzer - differential scanning calorimeter (TGA-DSC) 150 (Setsys Evolution 1750 TGA-DSC) with Fourier transform infrared (FTIR) and gas chromatograph-mass spectrometer (GC-MS, Setaram Instrumentation). The experiment followed standard procedures of ASTM E793-01 and E794-01. Thermal characteristics such as peak, onset temperature, and heat flow were collected with 5°C·min^{-1} heating and cooling rate from -25 to 200°C and 200 to 50°C, respectively

Results

Results are briefly displayed here. Detailed discussion will be furnished in the next report.

Table 7. Kenaf-fiber bundles and single-fiber properties.

	Young's Modulus* (GPa)	Tensile Strength* (MPa)	Length*** (mm)	Diameter*** (µm)	Surface Roughness (RMS)	
					2.5 µ Scan	1 µ Scan
Top	12.1 (2.0)**	0.20 (0.05)	2.50 (0.72)	12.0 (1.5)	119.5 (114.1)	47.5 (29.9)
Middle	18.5 (3.4)	0.26 (0.10)	2.62 (0.58)	11.7 (1.3)	57.5 (19.1)	30.9 (15.8)
Bottom	13.5 (3.0)	0.17 (0.41)	2.79 (0.52)	12.3 (1.1)	54.6 (25.2)	26.1 (11.5)

* = Averages of 25 fiber bundles.
** = Standard deviation.
*** = Measurement from single fibers.
RMS = Root mean square.

Fiber strength and physical properties are fundamental elements to predict and design composite properties. Table 7 shows the mechanical strength, surface roughness and fiber dimensions of the bacterially-retted, stem-length kenaf fibers. The fibers were from the top (2 inch from top), middle and bottom (2 inch from bottom) of the stem-length kenaf fibers. The highest Young's moduli and higher tensile strengths were obtained from fiber bundles from middle fibers compared to those from the other two sections. However, fiber-bundle strength may not be appropriate to address or design the final polymer-composite properties. Both fiber length and diameters were close to published values and the collected data were under the variation ranges, while mean fiber lengths were increased from top

to bottom section. The surface roughness of the bundle fibers showed smother surface of fibers from the top to bottom section. In general, the bottom section of kenaf stems contained higher lignin content to support stem structure. In contrast, top fibers contained juvenile fibers with lower fiber length. Therefore, fiber bundles from the middle section might have the better Young's modulus and tensile strength.

Figure 18 shows morphological and topographical images at top, middle and bottom sections of kenaf bast fiber bundles generated by stem-length bacterial retting. The SEM images were generated with 100x magnification and showed a general appearance of surfaces with relative smoothness. The images also showed deposited particles on the surface of the bacterially-retted kenaf fibers regardless of the fiber sections. The deposited materials might be fractures of the kenaf fibers generated during the retting process. The topographic images also showed similar appearances of surfaces due to the different Z height of the surface. The high Z height from the middle section was 190 nm and represented as the smoothest surface. However, surface roughness analysis on each scan area showed the differences were under variation ranges of sample measurements while the Table 7 showed a trend of the reduced mean surface roughness from the top to bottom section.

Effects of Fiber Orientation and Material Types on the Mechanical Properties

Figure 19 shows that MOE increased as the kenaf-fiber contents in the laminates increased when the fibers were highly oriented to fiber direction. In contrast, the 40% the kenaf-fiber content provided higher strength than its other mixing formulations. Modulus and strength decreased as the fiber angle increased. The 45^{o} and 90^{o} angles of fiber orientation provided a lesser contribution to the flexural modulus and strength of kenaf-fibers/PP film laminates regardless of fiber amounts in the laminate system. The fiber-orientation angles played an important role on the mechanical-property enhancement. The strength of kenaf fibers contributed to an enhanced strength of the natural-fiber-reinforced composites. This result also can be explained by less matrix and lack of interfacial compatibility between surface of natural kenaf fibers and the polyolefin matrix.

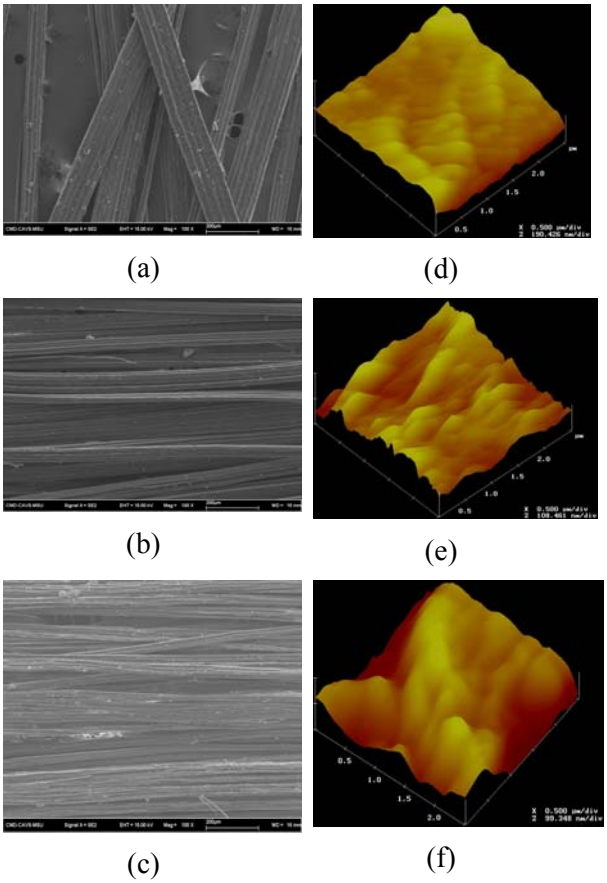

Figure 18. Morphological (a= Top, b= Middle, and c= Bottom) and topographical (d= Top, e= Middle, and f= Bottom) images of kenaf bast-fiber bundles produced by bacterial retting.

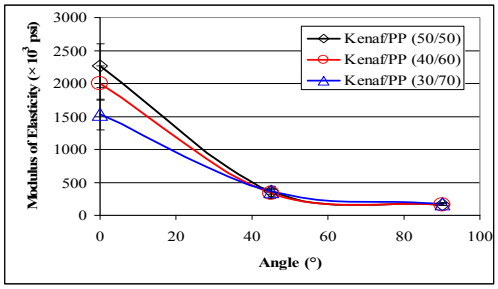

(a)

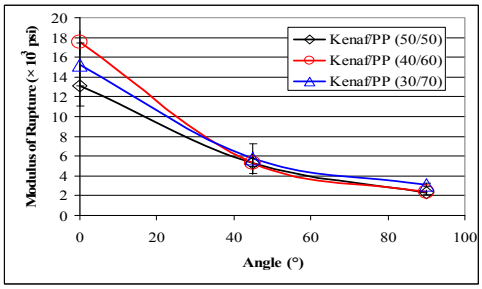

(b)

Figure 19. Flexural modulus and strength of kenaf fiber and PP laminates as function of the different fiber orientation with three different kenaf and PP formulations. (a= Modulus of Elasticity, b= Modulus of Rupture).

Figure 20 shows flexural modulus and strength of kenaf fiber and polypropylene laminates as functions of fabrication types. The different fiber orientation data were collected with 40% kenaf-reinforced PP film laminates. Pure PP matrix, wood flour and 90° fiber orientation showed a poor performance on the mechanical properties. Sheet molding compound (SMC) contained 25% fiberglass provided by Meridian Automotive Systems Inc. Even though the matrix was polypropylene, randomly-oriented kenaf-fiber reinforcement provided an equal or higher enhancement of NPC compared to fiberglass reinforcement in polyvinyl ester resin. The differences between the two matrices were behaviors during the mechanical failure of composites. SMC products showed linear behavior to failure, while NPC behavior was linear to curvilinear during the mechanical test.

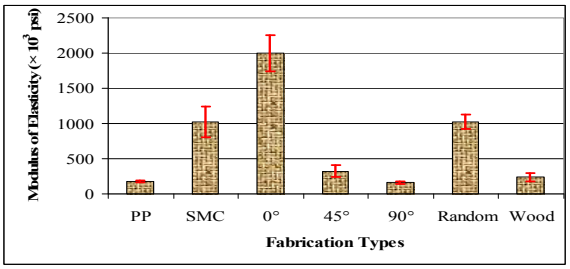

(a)

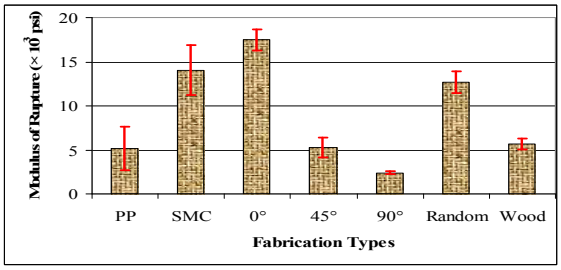

(b)

Figure 20. Flexural modulus and strength of kenaf fiber and PP laminates as function of the different fiber orientation with three different kenaf and PP formulations. (a= Modulus of Elasticity, b= Modulus of Rupture).

Figure 21 shows tensile strength of kenaf fiber and PP film laminates. The results of NPCs were obtained with composites fabricated with 40% kenaf fibers and 60% PP film. The tensile strength properties showed similar trends compared to flexural modulus and strength. The highest tensile strength was obtained with the 50% kenaf content in the polymer composite system with 0° fiber orientation. From the mechanical test results, it is encouraging to see that the randomly-oriented kenaf-fiber reinforcement has potential to provide equivalent properties to the fiberglass/polyvinyl ester composites with the current lab compression-molding process.

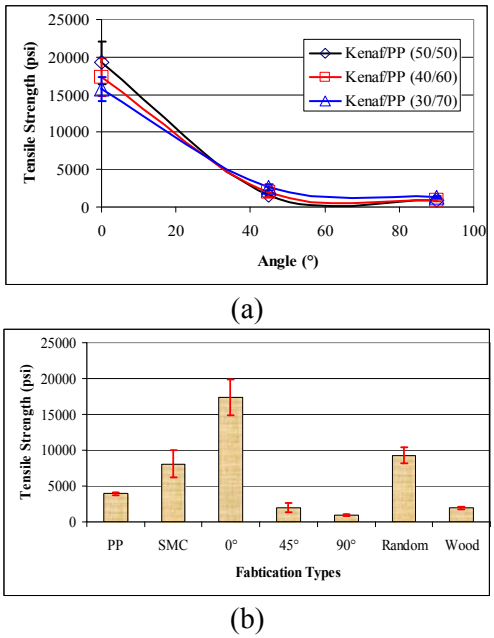

Figure 21. Tensile strength of kenaf fiber and polypropylene laminates. (a= tensile strength at the different fiber orientation, b= comparisons between fabrication types --- fiber and matrix ratio = 40% kenaf/60% PP).

Thermal Properties of kenaf/PP Formulations

Thermal characteristics of the prepared kenaf and PP formulations were evaluated by TGA-DSC. Results are summarized in Table 8. Polymer melting and maximum crystallization points with the addition of kenaf fibers initiated earlier than the pure PP formulation. Increased crystallization peak temperatures were observed when the fibers were incorporated in the polymer matrices. This increment could be more sensible when the fibers are chemically and physically modified. Thus, the fiber reinforcement influenced thermal histories of the PP polymer such as increased heat flow and delayed polymer relaxation. The thermal property changes resulted in higher enthalpy in both melting and crystallization. The increased heat of fusion and earlier induction of PP crystallization can be explained by the increased nucleation ability and crystallinity of the polymer matrices on the surface of retted kenaf fibers.

Table 8. Thermal characteristics of kenaf fiber and polypropylene formulations.

	Heating			Cooling		
	Onset Temp. °C	Peak Temp. °C	Enthalpy µV·s/mg	Onset Temp. °C	Peak Temp. °C	Enthalpy µV·s/mg
PP only	153.0	166.3	24.5	122.3	116.9	25.5
Kenaf/PP (50/50)	154.9	165.3	37.9	127.1	120.9	42.2
Kenaf/PP (40/60)	154.2	165.0	37.7	126.7	120.0	35.2
Kenaf/PP (30/70)	153.1	164.9	53.1	127.1	120.5	57.9

Fractural Morphology at the Interface

A SEM examination of fracture surfaces at the thermoplastic and kenaf fiber interface is shown in Figure 22. The figure clearly shows that there was relatively uniform fiber distribution in the PP matrix and polymer melt flow among the reinforced kenaf fibers. As the fiber content increases, the concentration of fibers is also increased. The figure also suggested that the fracture process appeared to have been dominated by a shear failure mode. Here, a considerable number of fibers and matrix exposure without bonding are in evidence to indicate a poor interaction between both materials. Fracture surfaces of the kenaf-fiber/polypropylene composites revealed inter-laminar crack propagation at the hydrophobic and hydrophilic interface. The kenaf fibers oriented along the fiber direction (Figure 22 (a)) were pulled out from the brittle matrix.

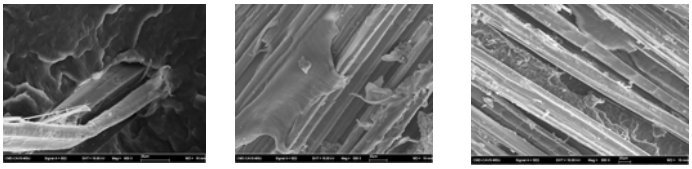

(a) (b) (c)

Figure 22. Fractural morphology of kenaf bast fibers and polypropylene laminates. (fiber orientation angles of a= 0°, b= 45°, and c= 90°).

The other two orientations clearly showed interfacial failure and separation at the interface. The fiber bundles oriented as 45° angles were covered by the molten PP polymer matrix, and failure occurred at the interface with stretched matrix under shear loads. Most failure at the interface and matrix itself were observed with the fiber oriented perpendicular to the fiber direction. Therefore, fracture macrographs indicated a weak interaction and incompatibility at the fibers and PP matrix interface.

Conclusions

This study investigated the effect of fiber orientation on the mechanical properties of laminates, kenaf-bast-fiber characteristics, and thermal/interfacial characteristics at the kenaf-fiber and polymer interface. Fibers from the middle section of the kenaf stem showed relatively smooth surfaces and strengths comparable to those of fibers from other sections. The mechanical properties (MOE, MOR and tensile strength (TS)) were increased as the fiber orientation angle decreased. Randomly-oriented kenaf-fiber reinforcement provided equal (random fiber orientation) or better (0° fiber orientation) property enhancement to fiberglass reinforcement into polyvinyl ester resin. Thermal properties were also altered with the presence of different weight fractions of kenaf fibers in the PP matrix. Fracture macrographs indicated a week interaction between the fibers and PP matrix.

References

1. Arzondo, L.M., A. Vazquez, J.M. Carella, and J.M. Pastor. 2004. A low-cost, low-fiber-breakage, injection molding process for long sisal fiber reinforced polypropylene. Polym Eng Sci 44(9):1766-1772.
2. Bledzki, A.K., H.P. Fink, and K. Specht. 2004. Unidirectional hemp and flax EP- and PP-composites: influence of defined fiber treatments. J. Appl. Polym. Sci. 93(5):2150-2156.
3. Clemons, C. 2002. Wood plastic composites in the Unite States; the interfacing of two industries Forest Products J. 52(6):10-18.
4. Eichhorn, S.J., C.A. Baillie, N. Zafeiropoulos, L.Y. Mwaikambo, M.P. Ansell, A. Dufresne, K. M. Entwistle, P.J. Herrera-Franco, G.C. Escamilla, L. Groom, M. Hughes, C. Hill, T.G. Rials, and P.M. Wild. 2001. Review current international research into cellulosic fibres and composites, J. Mater. Sci. 36:2107–2131.
5. Feng, B., D.M. Cao, W.J. Meng, J. Xu, R.C. Tittsworth, L.E. Rehn, P.M. Baldo, and G.L. Doll. 2001. Characterization of microstructure and mechanical behavior of sputter deposited Ti-containing amorphous carbon coatings. Surface Coatings Tech. 148(2-3):153-162.
6. Joseph, K., S. Thomas, C. Pavithran, and M. Brahmakumar. 1993. Tensile properties of short sisal fiber-reinforced polyethylene composites. J. Appl. Polym. Sci. 47:1731-1739.
7. Joseph, P.V., K. Joseph, S. Thomas, C.K.S. Pillai, V.S. Prasad, G. Groeninckx, and M. Sarkissova. 2003. The thermal and crystallisation studies of short sisal fibre reinforced polypropylene composites. Composites: Part A. 34:253–266.
8. Karnani, R., M. Krishnan, R. Narayan. 1997. Biofiber-reinforced polypropylene composites. Polym. Engin. Sci. 37(2):476-483.
9. Rana, A.K., A. Mandal, B.C. Mitra, R. Jacobson, R. Rowell, and A.N. Banerjee. 1998. Short jute fiber-reinforced

polypropylene composites: effect of compatibilizer. J. Appl. Polym. Sci. 69:329-338.
10. Sellers, T. and N.A. Reichert. 1999. Kenaf Properties, Processing and Products. Mississippi State University, Ag & Bio Engineering, Starkville. 532 p.
11. Sanadi, A.R., J.F. Hunt, D.F. Caulfield, G. Kovacsvolgyi, and B. Destree. 2002. High fiber-low matrix composites: kenaf fiber/polypropylene. In: 6th Intern. Conf. on woodfiber-plastic composites. Madison, Wisconsin. pp.121-124.
12. Serizawa, S., K. Inoue, M. Iji. 2006. Kenaf-fiber-reinforced poly (lactic acid) used for electronic products. J. Appl. Polym. Sci. 100:618–624.
13. Tajvidi, M., R.H. Falk, and J.C. Hermanson. 2005. Time-temperature superposition principle applied to a kenaf-fiber/high-density polyethylene composite. J. Appl. Polym. Sci. 97:1995-2004.

Acknowledgement

The authors would like to thank Dr. Leslie H. Groom and Dr. Thomas Elder, USDA-Forest Service Southern Research Station, Pineville, LA for Instrumental Support.

Presentations/Publications/Patents

1. Publication - Lee, S., S.Q. Shi, and Y. Xue. 2007. Thermal and mechanical properties of unidirectional natural fiber-polyolefin laminates. ***Paper in preparation.***
2. Presentation - Unidirectional natural fiber-polyolefin laminates: thermal and mechanical properties. 61st International Convention, Forest Products Society, Knoxville, Tennessee, USA. June 10-13, 2007.
3. Presentation - Unidirectional natural fiber-polyolefin laminates: thermal and mechanical properties. 9th International Conference on Wood and Biofiber Plastic Composites. Monona Terrace Community and Convention Center. Madison,Wisconsin, USA. May 21-23, 2007.

Micromechanical Simulation on Hygro-Mechanical Properties of Woodfiber-Reinforced Plastic Composites

Team Members: Kungpeng Wang, Yibin Xue, Hongwu Zhang, Mark Horstemeyer

Introduction

Woodfiber-reinforced composites (WRCs) have received considerable attention in the forest-product industry for engineering applications like automotive panels. They show many potential merits such as increased durability of woods, low maintenance during service, low cost, and ease of fabrication using traditional plastic/composite processing techniques (Rowell et al. 1998, Rowell 1998). To assess its potential as an engineering structure, a better understanding of the mechanical performance of woodfiber-reinforced composites is vital. Woodfiber, as a kind of natural material, is sensitive to changes of environment such as moisture; therefore, understanding the influence of MC on woodfiber composites is critical. The aim of this work is to predict the elastic properties of woodfiber-reinforced composites using micromechanical approaches in which fiber volume fraction (FVF), fiber distribution, and MC are incorporated.

Micromechanical simulations can be used to obtain an overall behavior of woodfiber composites when the properties of constituents are known (woodfiber and matrix). Typical simulations are conducted based on a representative volume element (RVE) or a unit cell (Aboudi 1991, Nemat-Nasser and Hori 1993). Some empirical and semi-analytical methods have been developed to predict the effective material properties of composites (Xue et al. 2007), and were applied to specific cases. Knowing the limit of analytical methods and the recent advances of computational efficiency, numerical methods such as finite-element modeling (FEM) have been utilized to predict the mechanical performance of composites.

In the micromechanical approach to predict the effective elastic properties of woodfiber-reinforced composites, one of the key issues is the selection of a proper size of RVE necessary to

capture all prominent features of the entire composite of interest. Drugan and Willis (Drugan and Willis 1996) stated that the minimum size of a RVE is the smallest volume element of the composite that is at least twice the diameter of the reinforcement. They also indicated that the maximum error is about five percent in elastic constants obtained from this minimum RVE size.

The mechanical response of a composite material can be effectively simulated by applying periodic boundary conditions to a single RVE (Segurado and Llorca 2002). When periodic boundary conditions are applied to a macroscopic composite, deformation within each RVE is identical and deformation along each RVE boundary/edge is compatible.

In the present research work, woodfiber-reinforced composite is considered as a short-fiber composite. In order to investigate the mechanical performance of woodfiber composites, two three-dimensional micromechanical models with imposed periodic boundary conditions are established: 1) using single-fiber RVE to predict the effective elastic properties of composites and the effect of moisture content (MC) and 2) using two-fiber RVE to calculate the influence of the woodfiber arrangement on the effective material properties of composites.

Woodfiber-Reinforced Composite

Generally, woodfiber-reinforced composite is composed of cellulose-like fibers of wood, bamboo or straw and plastics such as a high-density polyethylene (HDPE) or polyvinylchloride (PVC). The effective properties of woodfiber composite can be expressed as linear-elastic orthotropic, assuming homogeneity in the medium,

$$\bar{\sigma}_{ij} = D_{ijkl}\bar{\varepsilon}_{kl} \quad (4)$$

in which the volume average of the local or microscopic stress σ_{ij} and strain ε_{ij} can be expressed as

$$\bar{\sigma}_{ij} = \frac{1}{V}\int_{\Omega}\sigma_{ij}d\Omega, \quad \bar{\varepsilon}_{ij} = \frac{1}{V}\int_{\Omega}\varepsilon_{ij}d\Omega \quad (5)$$

where Ω denotes the domain of the RVE and V is the volume of RVE. The superscript bar denotes the volume average of a quantity, e.g., macroscopic or effective quantity.

Material Properties of Constituents of Woodfiber-Reinforced Composite

Elastic Properties of Woodfiber

It is well known that woodfiber is, in general, elastic and orthotropic in the longitudinal, radial and tangential directions of wood and has nine independent elastic constants, which can be denoted as elastic moduli (E_L, E_R, E_T), shear moduli (G_L, G_R, G_T) and Poisson's ratios (ν_{LR}, ν_{LT} and ν_{RT}), in which L denotes the longitudinal direction parallel to the fibers, T means tangential to the growth rings in the cut section and R, radial, perpendicular to the growth rings in the cross-section. Woodfiber, hydrophilic in nature, is prompted to absorb and desorb water when the environmental moisture contents (MCs) change. The elastic properties of wood are affected adversely by MC. In this research, Sikta spruce is chosen as the woodfiber whose properties are shown as a function of moisture contents in Table 9.

Table 9. The material properties of Skita spruce at various moisture content (Carrington 1922).

MC (%)	1	5	10	15
E_L (MPa)	13556.0	13591.0	13282.0	12742.0
E_R (MPa)	822.6	832.2	743.6	605.3
E_T (MPa)	504.7	463.8	411.0	344.5
G_{LR} (MPa)	699.7	734.7	706.9	655.3
G_{LT} (MPa)	614.2	613.0	575.4	514.9
G_{RT} (MPa)	23.8	22.7	20.8	18.7
v_{LR}	0.363	0.355	0.344	0.329
v_{LT}	0.507	0.517	0.558	0.616
v_{RT}	0.501	0.483	0.516	0.574

It is worth noting that, for simplicity, the influence of the growth ring's direction is neglected. The local cylindrical coordinates of woodfiber, T, R and L, convert to the global coordinates, 1, 2 and 3 in the present work.

Material Properties of Matrix

HDPE, of relatively high strength and easy machinability, is used as the matrix. HDPE is considered to be isotropic. The elastic properties of HDPE are Young's modulus, $E = 641\text{MPa}$, and Poisson's ratio, $\nu = 0.41$ (Li 2001).

In the woodfiber-reinforced composites evaluated, the orthotropic fibers are embedded unidirectionally in an isotropic matrix. The resulting composite is also an orthotropic material, whose properties can be calculated by the method as described in the next section.

Numerical Solution with FEM

Representative Volume Element (RVE)

One of the most powerful tools used to speed up the modeling process, both the composite discretization and the computer simulation of composites in real conditions, is the homogenization method (Aboudi 1991, Nemat-Nasser and Hori 1993). The main idea of the method is to find a globally-homogeneous medium equivalent to the original composite, where the strain energy stored in both systems is approximately the same. In general, the object under consideration is regarded as a large-scale/macroscopic structure. The common approach to modeling the macroscopic properties of three-dimensional (3D) woodfiber-reinforced composites is to create a RVE that captures the major features of the underlying microstructure. Woodfiber composite can be considered as a short-fiber composite, which is composed of short fragments of woodfibers and a polymer-matrix material. Schematic views of unidirectional-woodfiber composite (a) and the RVE (b), that is selected as the simplest form of (a), are illustrated in Figure 23.

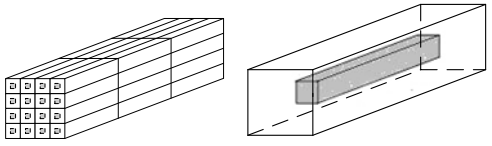

(a) (b)

Figure 23. (a)The microstructure of periodic woodfiber-reinforced composite; (b) A RVE for (a), where □ - matrix, ▢ - woodfiber.

In this work, a static analysis of periodic structures with perfectly-bonded condition between woodfibers and matrix is performed. Assuming symmetric boundary conditions exist, a regular woodfiber-reinforced composite will be analyzed by using a RVE approach, imposed with periodic boundary conditions.

Periodic Boundary Condition

Composite materials can be represented as an array of periodic RVEs, which are the smallest volume that contains sufficient information of geometrical and material parameters at the microscopic level. To obtain the effective properties of composites, periodic boundary conditions must be applied to the RVE to ensure that deformation-compatible results and that stress and strain are correctly computed. Thus, displacements that need to be applied to a uniform strain field in a corresponding homogeneous composite are given by the equation below (Suquet 1987)

$$u_i = \varepsilon_{ij}^0 x_j \qquad i, j = 1,2,3 \tag{6}$$

where u_i is the prescribed displacement at some large distance, x_j is a position vector from a reference point to a point on the boundary, and ε_{ij}^0 is the applied average strain in the composite array.

Finite-Element Modeling

In this work, all calculations were conducted using the ABAQUS FEM package. To obtain homogenized effective properties, the periodic boundary conditions, Equation (6), were applied to all the six faces of the RVE by coupling opposite nodes on opposite boundaries. To utilize these periodic boundary conditions by ABAQUS FEM, meshes on the opposite boundary surfaces must be the same. On each nodal pair, a constraint condition (periodic boundary condition) was imposed on its displacements. Because numerous constraints should be applied on the opposite boundary surfaces, it was very difficult to implement constraints in ABAQUS manually. A FORTRAN program, which generated all required constraint conditions automatically, was developed. Element C3D8R in ABAQUS was used.

Numerical Results and Discussion

Effect of Fiber Volume Fraction (FVF) on the Effective Elastic Properties of Composites

Primary interest to material designers and engineers is the effect of FVF on the effective material properties. To investigate that, a RVE, as shown in Figure 24, was developed, which includes a single woodfiber of an elongated cubic shape, $f_1 \times f_2 \times f_3 = 1 \times 1 \times 10\,\text{mm}^3$ and the RVE size is $L_1 \times L_2 \times L_3 = (f_1 + 2d) \times (f_2 + 2d) \times (f_3 + 2d)$ in which *d* can be considered as a parameter to determine the FVF. Table 10 gives the relation between FVF and *d*. The material properties of woodfiber were chosen at 5% MC as shown in Table 9. Appling the periodic boundary conditions stated previously, the effective material moduli of the RVE could be obtained, as illustrated in Figure 25 (a-c), in which the effective material properties of composites at 0% and 100% FVF correspond to the material properties of HDPE and woodfiber, respectively.

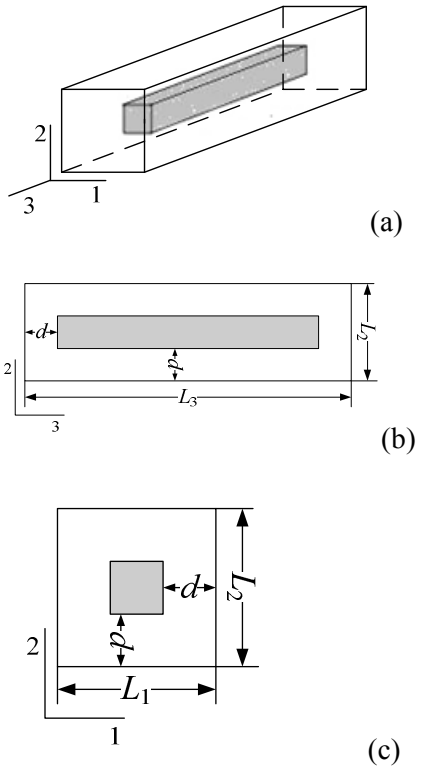

Figure 24. (a) The sketch of RVE for predicting the effective material properties of woodfiber composite; (b) The projection at Plane 2-3; (c) The projection at Plane 1-3.

Table 10. The relation between fiber volume fraction and *d*.

d (mm)	FVF (%)
1.0	9.26
0.5	22.73
0.2	49.06
0.1	68.08
0.0	100.00

With the increase of FVF, the effective material properties of woodfiber-reinforced composites trend to the material properties of woodfiber. It clearly shows the effect of the change in FVF on the effective material properties of composites, and woodfiber as an inclusion changes the properties of composites greatly.

The approach used in this work has been used successfully in (Berger et al. 2005) for predicting the effective material properties of long-fiber, unidirectional composite. Because the aspect ratio of woodfiber is relatively high, we expect the material properties of this composite to be similar to the properties of long-fiber composites. The material properties of a long-fiber composite, made of the same matrix and woodfiber, are illustrated in Figure 25 to validate this approach. It shows good agreements between the analytical long-fiber properties and the finite element analysis (FEA) simulation results. Therefore, the approach presented is suitable for predicting the material properties of short-fiber composites, i.e., woodfiber-reinforced composites.

Effect of Moisture Content on the Effective Elastic Properties of Composites

Woodfiber is sensitive to the variation of MC. The changes of effective elastic coefficients of woodfiber-reinforced composites by MC are calculated in this section. Since FVFs in the range of 50% to 70% are of great interest to the composite designers, the same RVE with d=0.2 mm (FVF=49.06%), as used in the previous section, was chosen for investigating the influence of moisture content. Due to hydrophobicity of the matrix, HDPE, the elastic properties of HDPE are assumed not to be affected by its MC. Since the woodfibers are surrounded with the matrix, HDPE, its MC would not go beyond its FSP. Therefore, only Fick's-law diffusion was

considered in the moisture-diffusion study. The elastic properties of woodfiber at 1%, 5%, 10% and 15% MC, as listed in Table 9, were used in this present research. Following the method described previously above, the effective elastic moduli of woodfiber-reinforced composite, as a function of MC, were obtained and shown in Figure 26 (a-c).

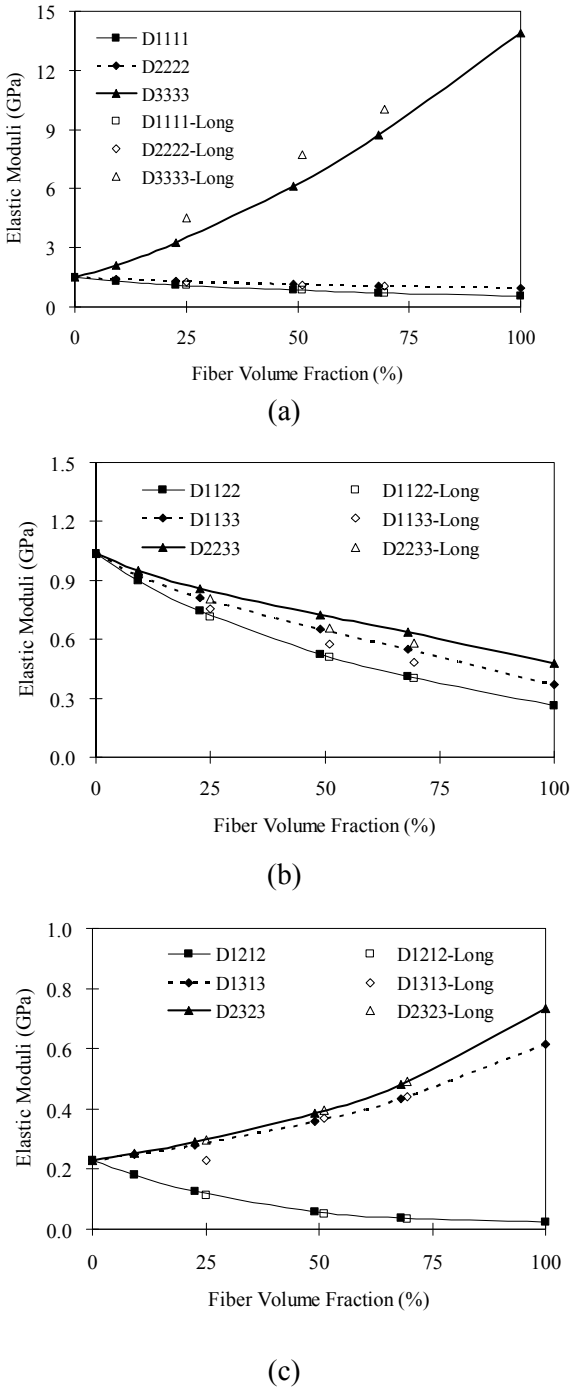

Figure 25. Effective material moduli of WPCs as a function of FVF.

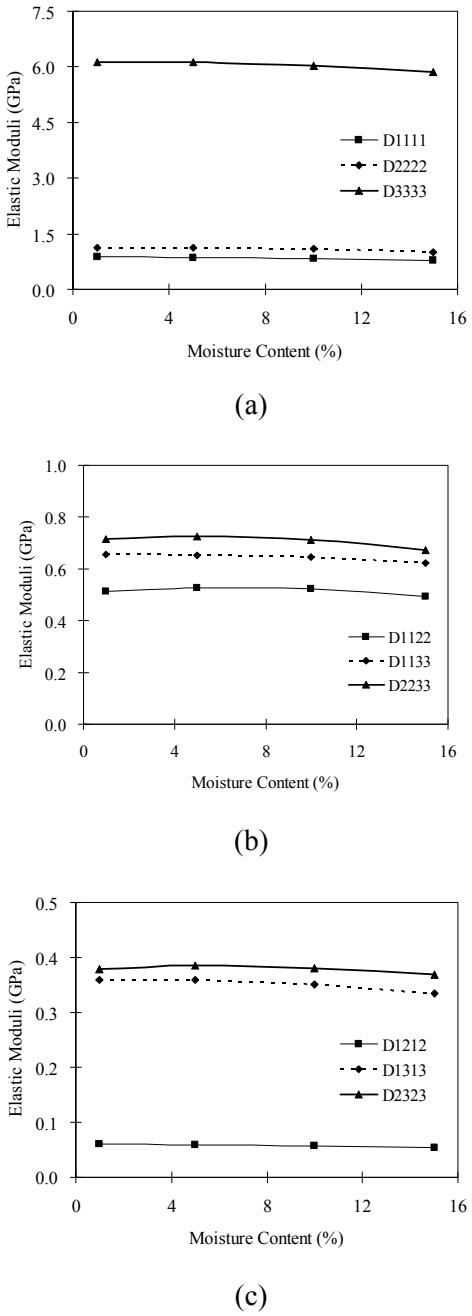

Figure 26. Effective material moduli of a WPC with 50 % fiber volume fraction as a function of moisture content.

As shown in Figure 26, the strength of woodfiber-reinforced composite is weakened slightly with the increase of woodfiber MC; the woodfiber-reinforced composites are relatively insensitive to moisture.

Effect of Woodfiber Arrangement on the Effective Elastic Properties of Composites

Woodfiber-reinforced composite, as one kind of short-fiber-reinforced composite, could have complex interactions between fibers. The effect of woodfiber arrangement on the effective material properties of composites is very important to the composite designer. In the past, most common models used were with square fiber arrangement, hexagonal fiber arrangement and random fiber distributions. In this work, an offset model was proposed based on the model with square fiber arrangement, as shown in Figure 23 (a). As shown in Figure 27 (a), the RVE included two complete fibers paralleled along the direction of the 2-axis in the Cartesian coordinate. The offsets might occur in the longitudinal direction (the 3-direction) or transverse direction (the 1-direction) as illustrated in Figure 27 (b-c). The material properties of matrix and woodfiber given previously above were used here. The RVE size was defined by three constants: $L_1 = f_1 + 2d$, $L_2 = 2L_1$, and $L_3 = f_3 + 2d$, in which *d* is a parameter to control FVF. To express the influence of fiber offsets clearly, relations between the deviation of effective moduli and the offset ratio were obtained, in which the offset ratio was defined as the ratio between the offset quantity, W_3 or W_1, and a length of composite RVE, L_3 or L_1, and the deviation of effective moduli were normalized with respect with the quantities of the zero offset. In this section, d=0.2 mm (FVF=49.06%).

Figure 28 and Figure 29 (a-c) illustrate the effective material properties of composites as a function of transverse and longitudinal offsets. The influence of offset on material properties of composites, no matter whether it is in transverse or longitudinal direction, is within 15%. Because the aspect ratio of woodfiber is fixed, the influence of longitudinal offset is relatively smaller than the effect of transverse offset on the effective material properties of woodfiber-reinforced composites.

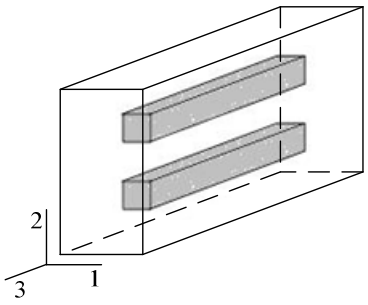

(a)

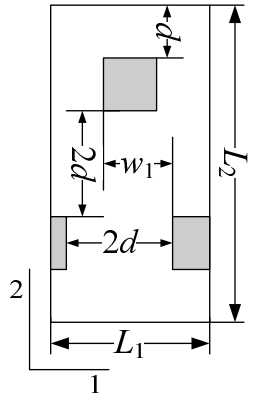

(b)

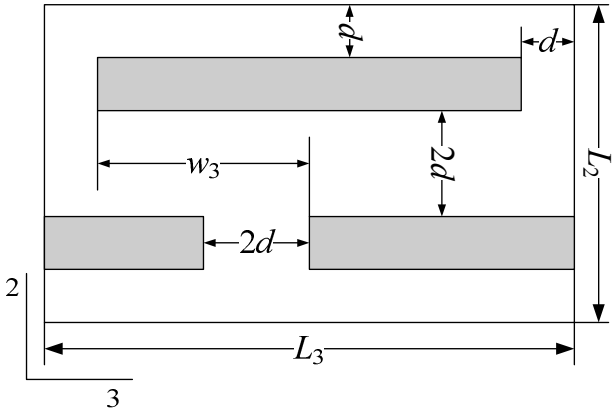

(c)

Figure 27. (a) A sketch of RVE for evaluating the influence of woodfiber arrangement. (b) The projection at Plane 1-2. (c) The projection at Plane 2-3.

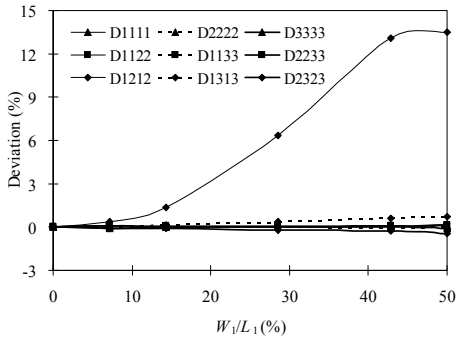

Figure 28. The deviation of effective material moduli of a WPC with 50 % FVF as a result of the fiber offset along the transverse direction. There is almost no significant dependency except D_{1212}.

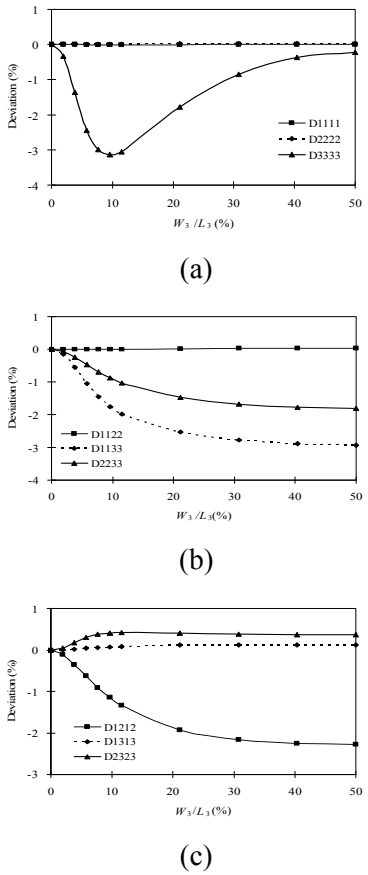

Figure 29. The deviation of effective material moduli of a WPC with 50 % fiber volume fraction as a result of the fiber offset along the longitudinal direction, which demonstrated significant dependency on the fiber offset distance.

Conclusions

A numerical approach for predicting the effective elastic properties of unidirectional woodfiber-reinforced composites has been developed using micromechanical simulations. The effective orthotropic coefficients of woodfiber composites were calculated by imposing periodic boundary conditions on a RVE. It is observed that FVF affects the effective material properties of woodfiber-reinforced composites strongly, while the effect of moisture content has slight impact on the effective properties of woodfiber composites. In the short-woodfiber-reinforced plastic composite, the interactions between fibers are more complex than long-fiber composites. The woodfiber arrangement will affect the effective properties of woodfiber composites: when the aspect ratio of woodfiber is relatively large, the influence of transverse offset on the effective elastic properties of composites is relatively larger than the longitudinal offset.

References

1. Aboudi, J. 1991. Mechanics of Composite Materials. A Unified Micromechanical Approach. Elsevier Science Publishers. Amsterdam.
2. Berger, H., Kari, S., and Gabbert, U. 2005. An analytical and numerical approach for calculating effective material coefficients of piezoelectric fiber composites. International Journal of Solids and Structures. 42(21-22): 5692-5714.
3. Carrington, H. 1922. The elastic constants of spruce as affected by moisture content. Aeron. J. 26:462-471.
4. Drugan, W., and J. Willis. 1996. A micro mechanics-based non local constitutive equation and estimates of representative volume element size for elastic composites. Journal of the Mechanics and Physics of Solids. 44: 497-524.
5. Li, R. 2001. Effect of flake distribution on elastic properties of flake composites. Journal of Composite Materials. 35: 1529-52
6. Nemat-Nasser, S., and M. Hori. 1993. Micromechanics: Overall Properties of Heterogeneous Materials. Elsevier Science Publishers. Amsterdam.

7. Rowell, R.M., D.F. Caulfield, and G. Chen. 1998. Recent advances in agro-fiber/thermoplastic composites. *In*: Proceedings of the second international symposium on natural polymers and composites, Atibaia, Brazil. pp. 11–20.
8. (not called) Rowell, R.M. 1998. Economic opportunities in natural fiber–thermoplastic composites. *In*:. Science and technology of polymers and advanced materials. Plenum Publishing Corp., New York. pp. 869–72.
9. Segurado, J., and J. Llorca. 2002. A numerical approximation to the elastic properties of sphere-reinforced composites. Journal of the Mechanics and Physics of Solids. 50:2107-2121.
10. Suquet, P. 1987. *In*: Homogenisation Techniques for Composite Media. Springer-Verlag. Berlin. pp. 194-275.
11. Xue, Y., Veazie, D.R., Glinsey, C., Horstemeyer, M.F., Rowell, R.M. 2007, Environmental Effects on the Mechanical and Thermomechanical Properties of Aspen Fiber-Polypropylene Composites, Composites B: Engineering, 38:152-58.

Acknowledgement

The Mississippi State University authors would like to express appreciation for the support of the US Department of Energy and the Center for Advanced Vehicular Systems at Mississippi State University.

Presentations/Publications/Patents

1. Presentation - X Kungpeng Wang, Yibin Xue, Hongwu Zhang, and Mark Horstemeyer. Micromechanical Simulation on Hygro-Mechanical Properties of Woodfiber-Reinforced Plastic Composites. The 9th International Conference on Wood & Biofiber Plastic Composites, May 21-23, 2007, Madison, WI.

H. Interphase Analysis and Control in Fiber Reinforced Thermoplastic Composites

Principal Investigator: Jon J. Kellar
Department of Materials and Metallurgical Engineering
South Dakota School of Mines and Technology
501 E. St. Joseph Street
Rapid City, SD 57701-3901
605-394-2343, 605-394-3369, jon.kellar@sdsmt.edu

Technology Area Development Manager: Joseph A. Carpenter
(202) 586-1022; fax: (202) 586-1600; e-mail: joseph.carpenter@ee.doe.gov

Field Project Officer: Aaron D. Yocum
(304) 285-4852; fax: (304) 285-4403; e-mail: aaron.yocum@netl.doe.gov

Expert Technical Monitor: Philip S. Sklad
(865) 574-5069; fax: (865) 576-4963; e-mail: skladps@ornl.gov

---

Contractor: South Dakota School of Mines and Technology
Contract No.: DE-FG02-04ER46117

Objectives

- Develop the science underlying the formation and effects of transcrystalline regions in carbon fiber reinforced thermoplastic matrix composite systems.
- Exploit the understanding developed from the research described above to allow controlled tailoring of the interphase transcrystallinity for specific applications.
- Analyze processing parameters in new thermoplastic matrix composite technologies, specifically the DRIFT (**D**irect **Rei**nforcement **F**abrication **T**echnology, Southern Research Institute/University of Alabama-Birmingham) and the P4 (**P**rogrammable **P**owered **P**reform **P**rocess, Department of Energy (DOE)/Oak Ridge National Laboratories (ORNL)) processes.
- Generate composites with tailored interphases for specific applications of laminates produced by the DRIFT and P4 processes in the FreedomCAR and other DOE initiatives in lighter weight vehicles.

Approach

- Choose matrix materials relevant to the FreedomCAR and DOE automotive lightweight materials initiatives.
- Characterize the chosen matrix materials with respect to mechanical properties and crystallinity.
- Determine the thermodynamic and practical adhesion between the chosen matrix materials and carbon fibers. The carbon fibers will be both sized and unsized.
- Identify and control the presence and size of transcrystalline regions in the matrix material adjacent the carbon fibers.
- Manufacture laminates using the DRIFT and P4 processes having controlled transcrystalline regions.
- Perform mechanical testing, including tensile testing, impact testing and indentation testing of the laminates having controlled interphases.

Accomplishments

- Finalized design and build of a compact, laboratory-scale DRIFT machine.
- Completed an operator's manual for the DRIFT machine.
- Conducted preliminary testing with the DRIFT machine for the following fiber/matrix systems: E-glass/polypropylene (PP), Kevlar®/nylon, pitch/PP, PAN/PP.
- Batch samples (pitch/PP, PAN/PP) for detailed analysis were produced.
- Samples were examined using optical and scanning electron microscopy (SEM).
- SDSM&T research team held two Access Grid meetings with Mr. Robert Norris from ORNL.

Future Direction

- Manufacture tape laminates with fibers other than unidirectional carbon fibers. This will include Kevlar® and glass fibers and multi-directional fabrics.
- Manufacture tapes suitable for use, after further preparation, in the P4 process at ORNL.
- Optimize the manufacture of composite tapes with PAN carbon fibers in a manner to improve fiber dispersion.

Introduction

Over the past decade considerable effort has been expended to develop a new generation of vehicles that are lighter and more fuel-efficient than today's vehicles. In addition, these vehicles should retain crashworthiness and be of relatively low cost. Targets include reduction in overall weight of approximately 40%, primarily achieved through lighter body and chassis materials. Polymer matrix composites (PMCs) have reached this target with a potential weight savings of 70%. At the current time, PMC technology has, in general, been deemed too costly, as carbon fiber based PMCs can cost ten times as much as steel parts. Some of this increased cost is due to the high price of carbon fibers and some due to limitations in the manufacturing process. Many of the problems in the manufacturing process are caused or exacerbated by lack of fundamental scientific knowledge of the interactions between the fibers and matrix materials.

This research is of significance to the DOE Automotive Lightweighting Materials Program in that it will help develop the necessary science base to allow more complete exploitation of PMCs having thermoplastic matrices. Traditionally, these materials have trailed the use of PMCs having thermosetting matrices, because of processability issues stemming from the low viscosity and wetting of the thermoplastic matrix material. In addition, thermoplastic matrices are generally less strong and less stiff than thermoset matrices. This liability is further compounded by the fact that most fiber reinforcements associated with thermoplastic matrix PMCs are of fairly short length, mainly because of the processing limitations mentioned earlier. This latter aspect is relevant because short fiber reinforcements do not carry load as well as long or continuous fiber reinforcements. From the automotive perspective, short fiber reinforced PMCs are therefore most utilized in non-structural components. Further comparisons between thermoplastic and thermoset matrix PMCs are warranted here to highlight the focus of this research project, namely the role of the interface / interphase region between the fiber and the matrix.

The development of the interphase in thermoplastic PMCs is quite different from that of thermosetting matrices, which tend to be amorphous in nature. Rather, in thermoplastic PMCs, the interphase development is generally due to nucleation and growth of crystallites from the fiber surface rather than actual chemical reactions within the interphase. The interphases formed in these systems are termed transcrystalline regions, reflecting their dependence upon the thermoplastic crystallinity. There has been much speculation in the literature as to the cause for the formation of the transcrystalline region and its role in bulk composite properties. Several conclusions can be reached. First, the transcrystalline region can grow in size to tens of microns, depending upon such parameters as fiber type, morphology and fiber surface treatments such as sizings. Second, the transcrystalline region can significantly affect properties such as the strength and impact

resistance. Also, in some cases different types of transcrystalline interphases may be formed. For instance, both α and β transcrystalline regions were produced around natural fibers in polypropylene matrix composites. These regions could be altered by inclusion of maleic anhydride in the polypropylene or on the fiber.

With respect to these novel processing routes, two examples are of particular interest to this research. The first is a low-cost process to produce continuous reinforcing fibers with thermoplastic matrices, called the **D**irect **Rei**nforcement **F**abrication **T**echnology (DRIFT) developed by the Southern Research Institute (SRI) and now located at the University of Alabama-Birmingham (UAB). PMCs produced by this continuous fiber technology could serve as metal-replacements in structural applications, specifically for the automotive industry. Keys to optimal utilization of the DRIFT process are fiber wetting, and ultimately adhesion, of the thermoplastic matrix. Traditionally, sizings are applied to the fibers to help prevent abrasive damage, and assist with lubrication. A major component of the sizing is a coupling agent that aids in wetting, adhesion and hydrothermal stability of the composite. Research conducted in this program will utilize thermoplastic matrix PMCs produced by UAB or in-house using the DRIFT process. The second novel processing route of interest is the **P**rogrammable **P**owered **P**reform **P**rocess (P4). While the P4 technology does allow control over fiber length, its main potential benefit is its ability to circumvent previous PMC process limitations through robotic control. To our knowledge, no fundamental analysis of PMC interphases formed by the P4 technology has been undertaken.

This research program builds upon a multi-disciplinary effort with a strong background in interphase analysis and control in thermosetting PMC systems, and applies this experience to new thermoplastic matrix PMC systems critical to the future success of the Lightweight Materials Program. The research investigates model systems deemed of interest by members of the Automotive Composites Consortium (ACC) as well as samples at the forefront of PMC process development (DRIFT and P4 technologies). Finally, the research investigates, based upon the fundamental understanding of the interphases created during the fabrication of thermoplastic PMCs, the role the interphase play in key bulk properties of interest to the automotive industry.

Project Deliverables

This research will provide a better understanding of the science, particularly with respect to adhesion, of thermoplastic matrices with fiber reinforcements. The adhesion data will be used to identify processing parameters for thermoplastic matrix composites to tailor transcrystalline interphase formation. Transcrystalline interphases are often quite large (>10 microns) and can be stronger and stiffer than the matrix material or tougher and with greater work of fracture than the matrix. In addition, this work will produce composite samples using new processing technologies and the scientific knowledge gained with respect to adhesion and interphase formation. These test protocols are important to possible end uses for the tailored PMCs in automotive applications.

Accomplishments

Research accomplishments during the past year occurred primarily in the effect of transcrystallinity on composite performance area; specifically, the manufacture and testing of specimens using a custom designed mini-DRIFT machine. Progress in this area is described below.

Research on the effect of transcrystallinity on composite performance has centered on developing a miniature DRIFT machine. The goal of this mini-DRIFT research was to develop a system for producing lab-scale thermoplastic composite prepreg samples using the DRIFT process. The DRIFT process is a procedure for making continuous-fiber prepreg materials. In the process a continuous-fiber reinforcement material is drawn through a molten resin after being heated beyond the temperature of the resin. While in the resin, a shear is applied to the reinforcement material leaving substantially no voids in the prepreg material (Patent Number: 5,911,932). One of the goals of this aspect of this research is to control and monitor operating parameters and their effects on fiber wetting and material properties. The parameters to be

controlled include: fiber draw speed, fiber tension, fiber preheat temperature, resin temperature, and prepreg cooling. Two primary areas with respect to the mini-DRIFT machine were completed. One area investigated was the manufacture of the mini-DRIFT machine and the second area investigated was assessment of the product quality of the mini-DRIFT manufactured composite materials.

Mini-DRIFT Manufacture

There were three primary goals identified for this phase of the work:

1. Make the DRIFT process less "art" and more "science".
2. Make the machine of smaller scale for research purposes.
3. Allow for system adjustability for experimentation.

These goals resulted in a set of requirements for the mini-DRIFT machine. These requirements were:

1. System variables should be accurately monitored and controlled.
2. Based on available lab space, the machine should have a footprint of approximately 4 feet by 8 feet.
3. Allow for up to 20K fiber tows.
4. The machine should have the ability to heat the fibers up to ~450 ºC.
5. Allow for system flexibility and adjustment through replaceable die heads, moveable/ replaceable shear pins, and sufficient temperature operating range.

The design and manufacturing of the mini-DRIFT machine culminated in early 2008. There were five primary components to the design:

1. Extruder
2. Impregnation Tool/Tool Heating
3. Fiber Puller/Fiber Feed
4. Fiber Heating
5. Chiller

The design process for these components is described in detail in the Master of Science thesis of Mr. R.D. McGlothlen (see Reference 1). The extruder chosen was one already located at the site where the mini-DRIFT machine would be located. This extruder was a Haake PolyLab extruder as shown in Figure 1. This extruder has a maximum operating temperature of 450 ºC and maximum through- put of 5 kg/hr. Both of these meet or exceed the requirements for the DRIFT design.

The impregnation tool was designed after visiting an operating DRIFT machine at the University of Alabama-Birmingham and was made to fit the Haake extruder. Figure 2 show the impregnation tool with front face removed. The pins over which the fibers travel are adjustable to accommodate different fiber types. The tool is able to be completely taken apart for cleaning and for use of different fiber entrance and exit plates for tows of differing sizes. In addition, the tool was designed with a cartridge heating system using four heaters with temperature feedback provided by a thermocouple inserted into the center of the tool. This design feature allows the tool to be kept at the processing temperature of the molten thermoplastic material dispensed into the tool from the extruder.

The third portion of the mini-DRIFT machine is the fiber puller and feed assembly. The fiber puller chosen is shown in Figure 3 and consists mainly of pulling the fibers through two motorized, rubber-surfaced drums. The drums have an aluminum core coated in 60A durometer polyurethane. The coating provides a firm grip on the material being processed, but prevents the material from being damaged. One drum was fixed in position and the other was attached to an adjustable lever arm to allow for adjustment of the gripping force on the fibers. The stationary wheel was attached to a keyed shaft driven by a motor through a belt and pulley system to reduce the motor speed. The motor was controlled by a Genesis variable-frequency-drive, which allowed accurate control of the motor speed. The frame for the puller was constructed of 2 in. x 2 in. x 1/8 in. angle iron and bolted to the top of the steel cart on which the mini-DRIFT machine was mounted to keep from moving. The puller speed can be varied between 0.55 and 33 m/minute.
A brake system for the fiber feeding was also needed. The final brake design can accommodate fibers on any size spool. The final design involved

attaching an adjustable magnetic brake to the end of a keyed shaft. The magnetic brake unit purchased was Precision Tork™ model MC5 capable of being adjusted from 0-25 in.-lb of torque. The actual force applied by the brake unit depends on the radius of the fiber spool. With the goal of great flexibility, the brake unit was modified to accept fibers regardless of their storage system. The system was retrofitted with drums similar to the puller unit and an adjustable upper arm. Fibers were routed to the drums through a system of guides. The guide configuration used depended on the dispensing system of the fibers and was left to the discretion of the researcher. The frame for the unit was also constructed from 2 in. x 2 in. x 1/8 in. angle iron and bolted to the lower shelf of one of the carts to conserve space and to minimize fiber exposure. Fibers were routed through the system through a series of guides. Figure 4 shows the final brake design.

The next portion of the system to be designed was the fiber heating section. This variable is one of the key to the DRIFT process. The final design consisted of a tube furnace that allowed the fibers to be heated as they passed through the furnace to the opening of the impregnation tool. A Lindberg Mini-Mite tube furnace was purchased for this task and can be seen in Figure 5. The furnace has a single heating zone with a maximum operating temperature of 1100 °C and a single set point digital controller. An 18 in. long by 1 in. outer diameter alumina process-tube was placed inside the furnace. The length of the tube purchased was chosen so that the tube could extend beyond the furnace and be butted up to the impregnation tool to insulate the fibers as they passed from the furnace to the impregnation tool. The fiber guide system for the machine ensured that the fibers do not touch the walls of the process tube.

The final portion of the mini-DRIFT machine to be designed was the chiller system. The chiller system chosen is shown in Figure 6. The chiller uses two stainless steel drums with water circulating internally acting as a coolant. Water is passed through the drums through swivel joints on the ends of either drum. The drums are supported by bearings bolted to adjustable platforms, allowing the configuration of the drums to be changed for routing purposes. The system was initially cooled using only tap water. The system could also utilize a re-circulating water cooler for greater system control, although that was not done here

Figure 7 shows the assembled system used for assessment of product quality. This system meets all the requirements specified earlier.

Figure 1. Haake PolyLab extruder.

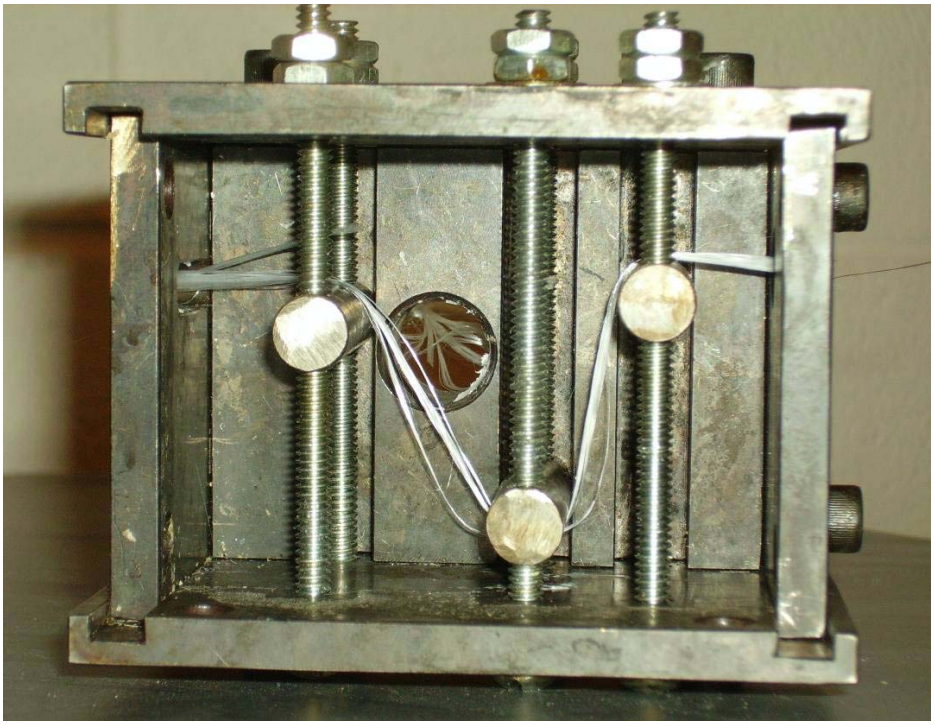

Figure 2. Impregnation tool with side plate removed showing fiber routing.

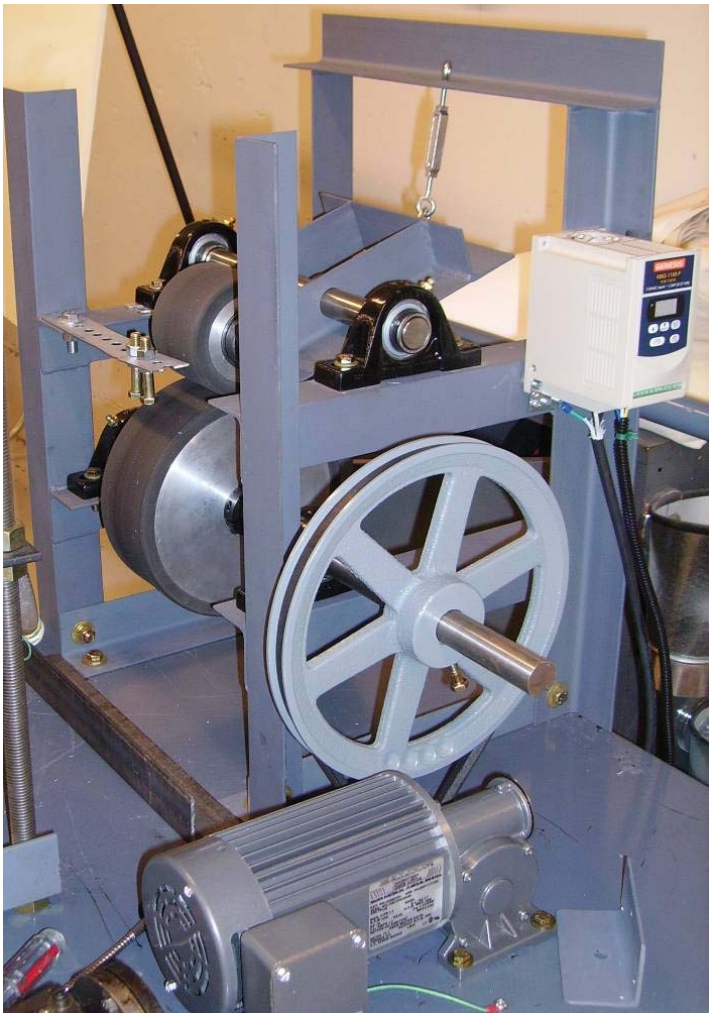

Figure 3. Completed puller system.

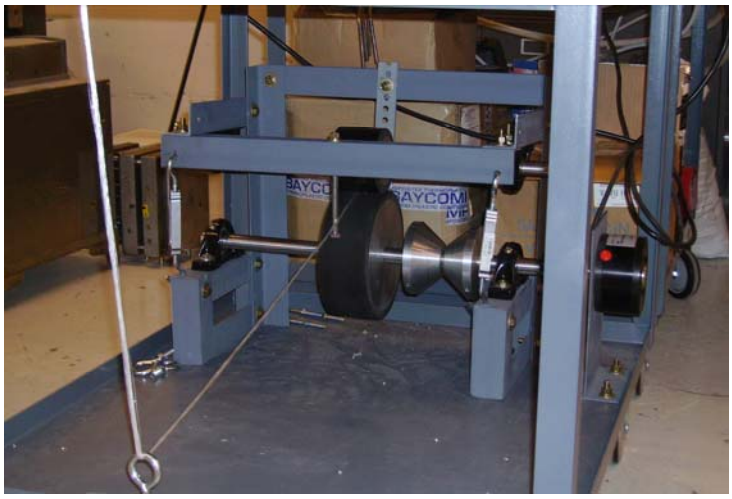

Figure 4. Final brake design.

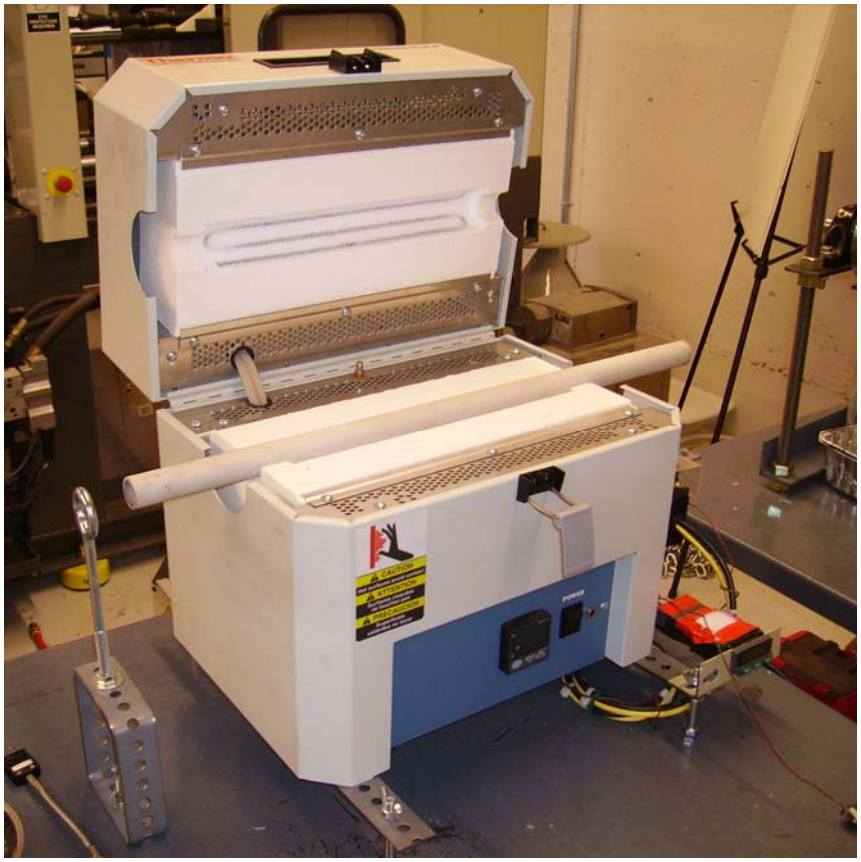

Figure 5. Tube furnace with its top open showing the process tube.

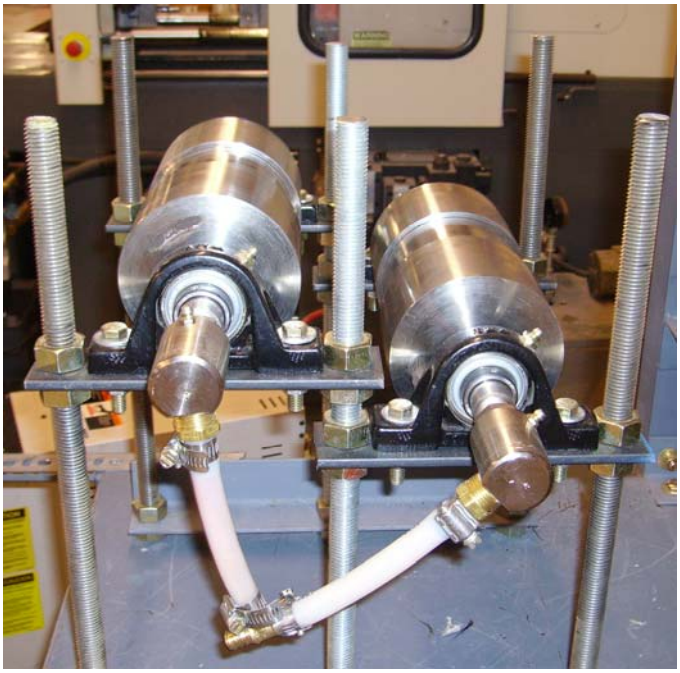

Figure 6. Chiller system.

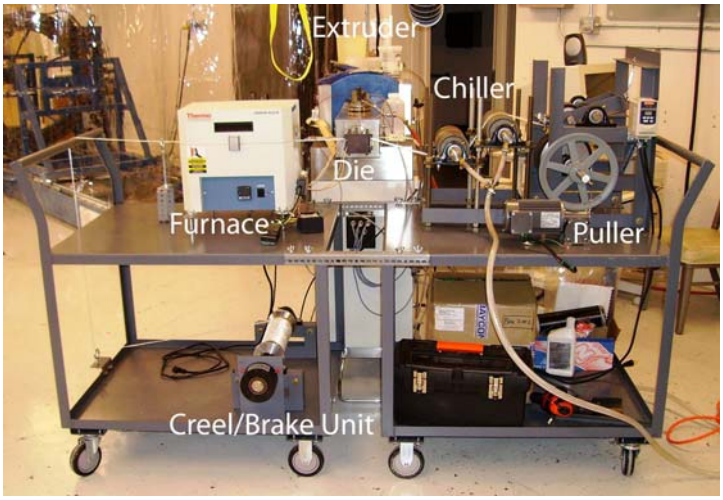

Figure 7. Completed miniature DRIFT system.

Assessment of Product Quality

The product quality of tapes manufactured by the mini-DRIFT machine described previously was accomplished by two primary methods, tensile testing of the tapes produced and microscopic analysis of the materials. In microscopic analysis, fiber dispersion was examined through both optical and scanning electron microscopic (SEM) techniques, while wetting was primarily examined by SEM. Composite samples were made with polypropylene as the polymer matrix. Both pitch and PAN carbon fibers were used as reinforcement. Tensile testing and microscopic examination of these two composites systems were then compared to each other. In addition, the effect of fiber preheat temperature was also examined.

Tensile Testing

Tapes were manufactured using both PAN and pitch-based carbon fiber reinforcement in polypropylene matrix, and mechanical performance assessed by tensile testing. Tensile tests were conducted following the guidelines set forth in ASTM D 3039/ ASTM D 3039M with the exception that the samples produced did not meet dimensional tolerance requirements. As such, the measurement and calculation methods used came from the standard. Figure 8 shows a stress-strain curve resulting from tensile testing. From this data, the modulus of elasticity, the maximum tensile strength, the elongation at break and the modulus of resilience were determined as per ASTM D3039M. The stress-strain curve in Figure 8 shows that the composite is brittle, as little deviation from linearity is observed. At least five samples were tested for every fiber/matrix and processing temperature combination to help to understand the variability of the manufacturing process. The results are shown in Figures 9-12. In general, the PAN-fiber composites showed better properties, as expected. There does not to be a large difference in the properties of either composite system as the fiber pre-heat temperature increased. The mean behavior at room temperature is often slightly less than the properties found when the fibers are preheated, but this was within the 10-15% variation between samples. Complete description and results of all testing are given in Reference 1.

The tensile strength was examined further by comparing the measured value to the value calculated from the rule of mixtures. At all fiber preheating temperatures and fiber types, the measured strength was 66-75% of the theoretical value. This decrease is likely due to damage to the fibers during processing. However, little of this decrease is due to preheating the fiber.

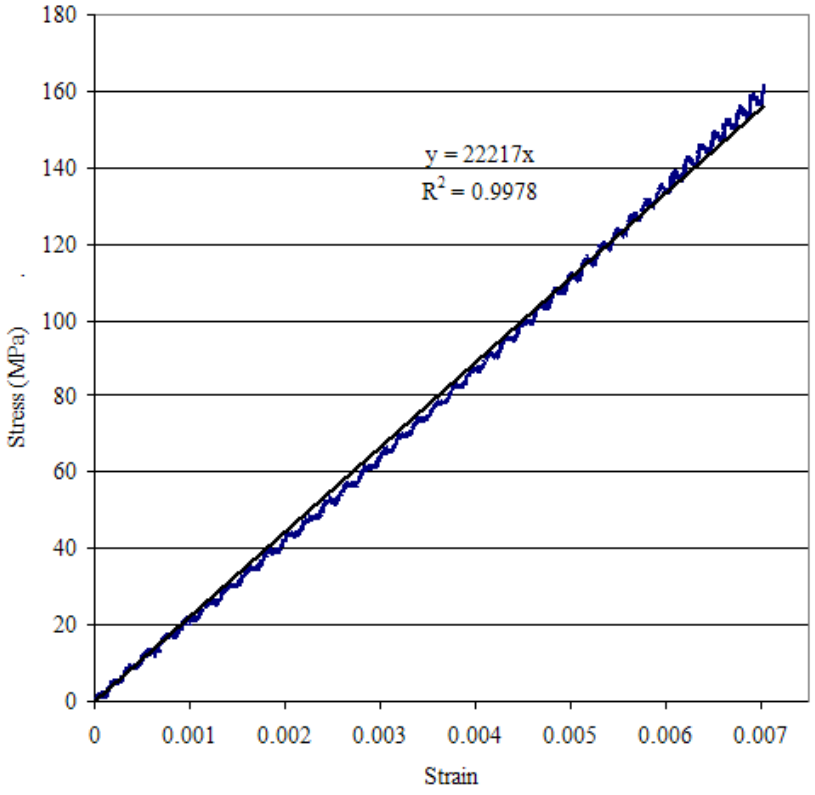

Figure 8. Example pitch 225 °C sample stress-strain plot as a function of fiber pre-heat temperature.

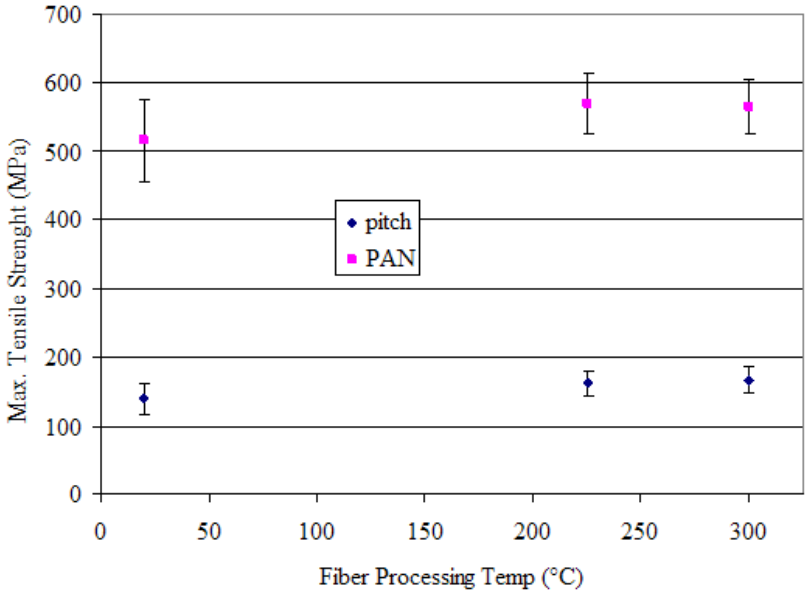

Figure 9. Maximum tensile strength for each sample set as a function of fiber pre-heat temperature.

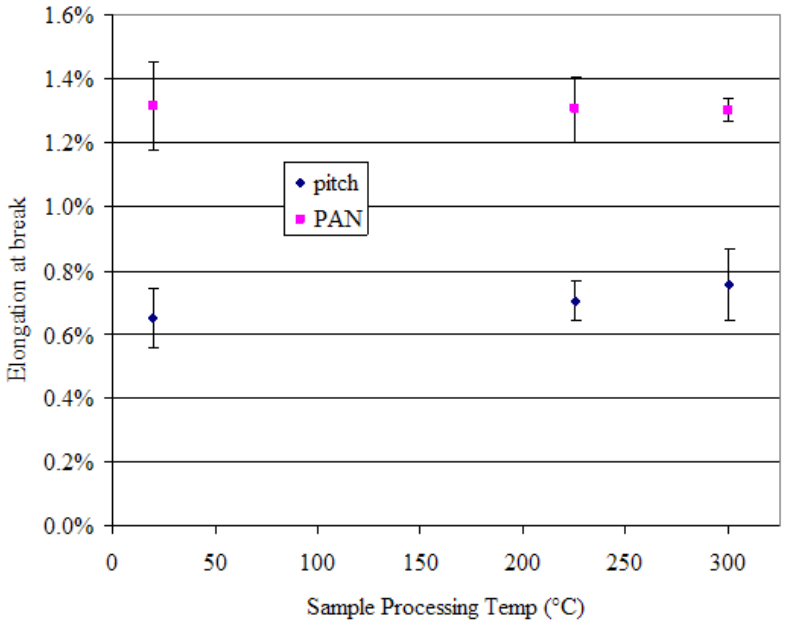

Figure 10. Elongation at break as a function of fiber pre-heat temperature.

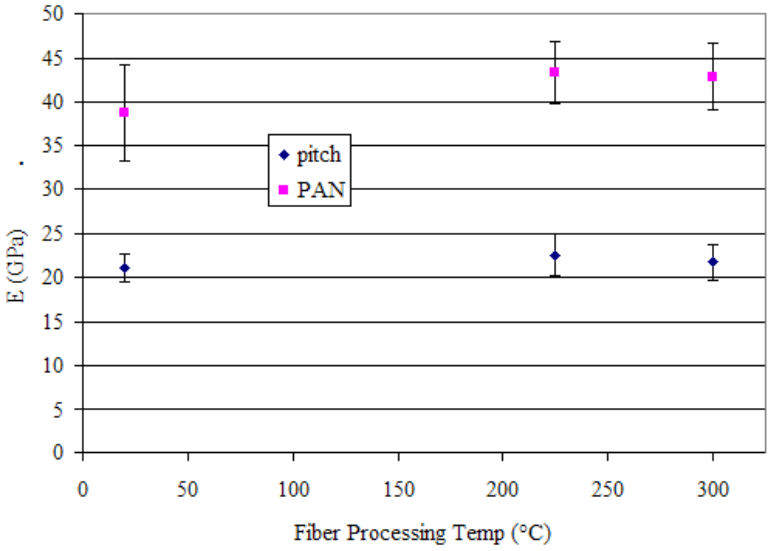

Figure 11. Elastic modulus as a function of fiber pre-heat temperature.

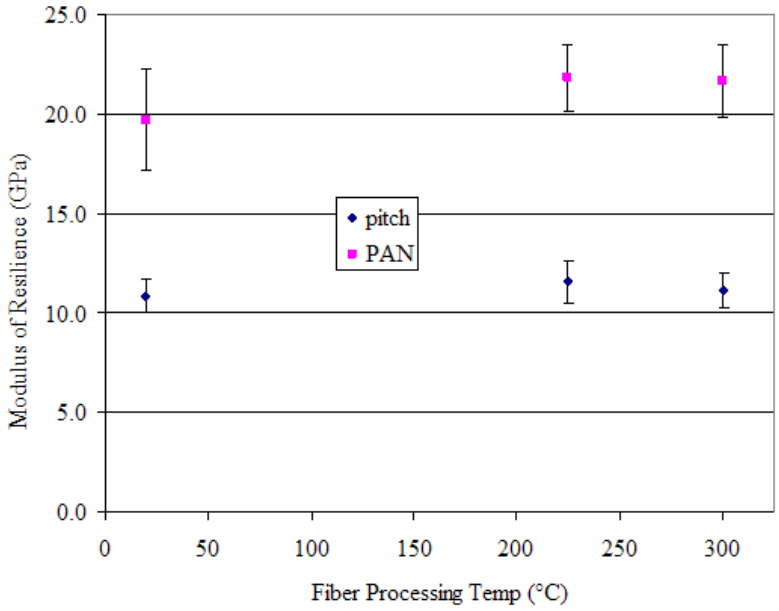

Figure 12. Modulus of resilience as a function of fiber pre-heat temperature.

Optical Microscopy

Next, tape samples were embedded in an epoxy matrix, sectioned, polished to 0.3 μm with alumina polishing compound, then viewed with a VanGuard microscope having 4x, 10x, 40x, and 80x lenses using a Steindorff digital camera having 10x magnification yielding magnifications between 40x and 800x. The overall fiber dispersion of tapes of each type (pitch and PAN) and fiber pre-heating (25, 250, 300 ºC) was determined by optical microscopy at 40x. Full descriptions of all images are given in Reference 1. Figure 13 shows a typical tape with pitch fibers, Figure 14 for PAN fibers. All tapes showed that the edges had more fibers than the center region, as can be seen in Figures 13 and 14. In addition, the center regions had large regions of nearly pure matrix. These pure matrix regions were usually above/below a row of fibers, and in some cases between concentrations of fiber. Higher magnifications were used to examine the wetting and dispersion more closely. Figures 15 (100x) and 16 (400x) show examples of the optical micrographs collected. In Figure 15, the pitch fibers are observed to be larger in diameter than the PAN fibers. Also, a few extremely large diameter pitch fibers can be seen, as can fibers that are similar to pies with a missing piece. In both composite systems, the fibers appear reasonably well wet by the polymer, although some of the pitch fiber composites show more voids in the polymer matrix. The PAN fiber composites were also examined at high magnification, 800x (Figure 17). The PAN fibers appear to be well dispersed and wet. In addition, the PAN fibers are observed to have a very consistent diameter.

The observations from these samples highlight the need for more investigation into the mechanisms involved in dispersing the fibers in the matrix in order to create a more uniform composite.

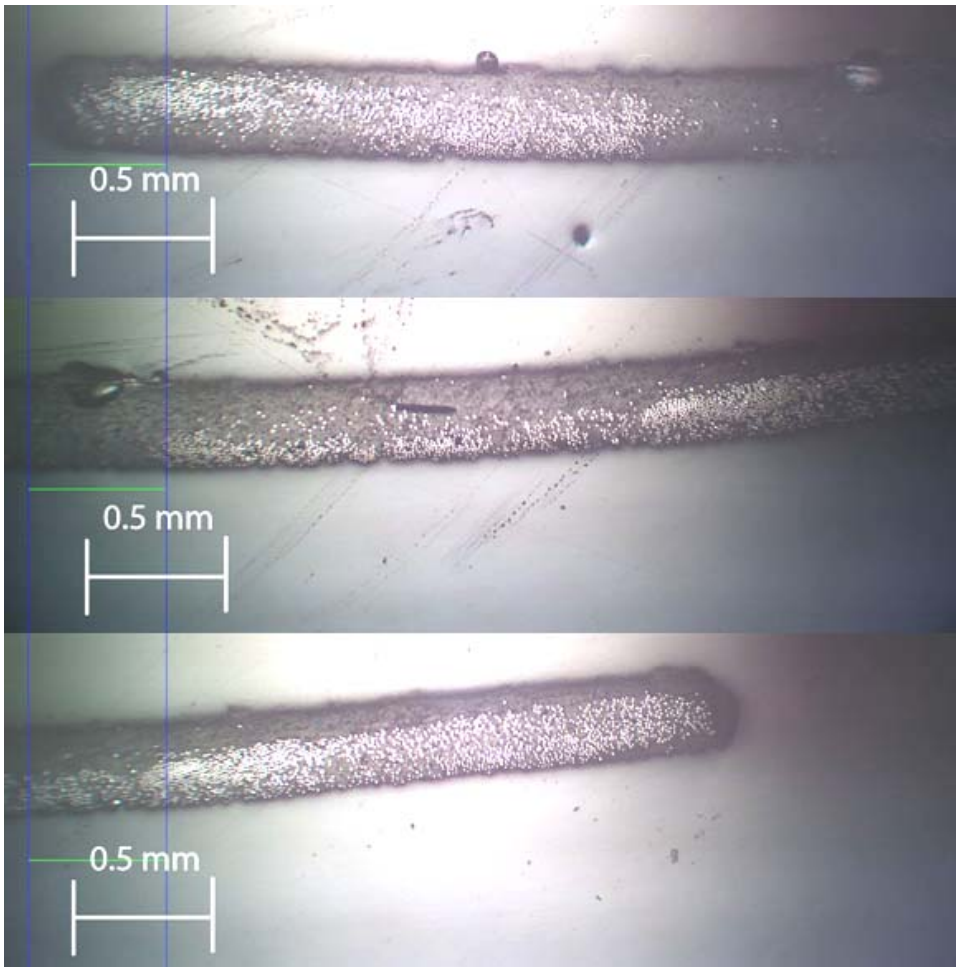

Figure 13. Images showing full width of room temperature preheat pitch sample (40x).

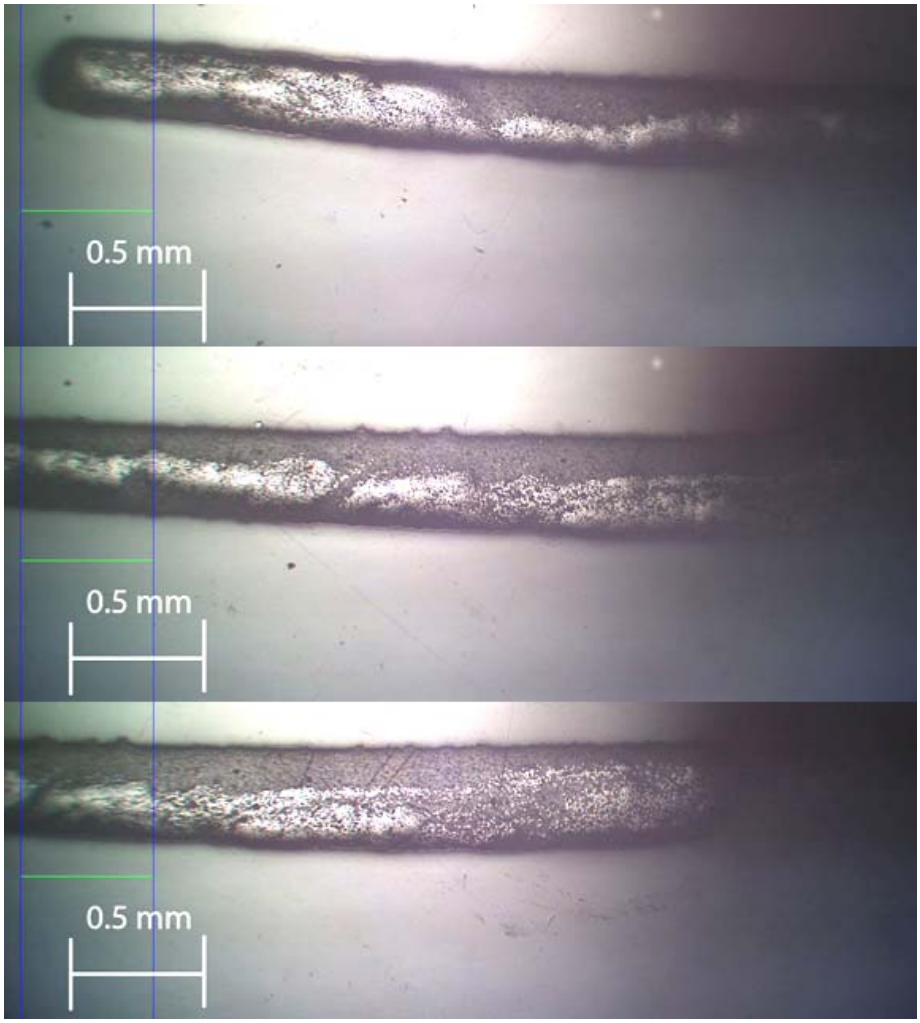

Figure 14. Images showing full width of room temperature preheat PAN sample (40x).

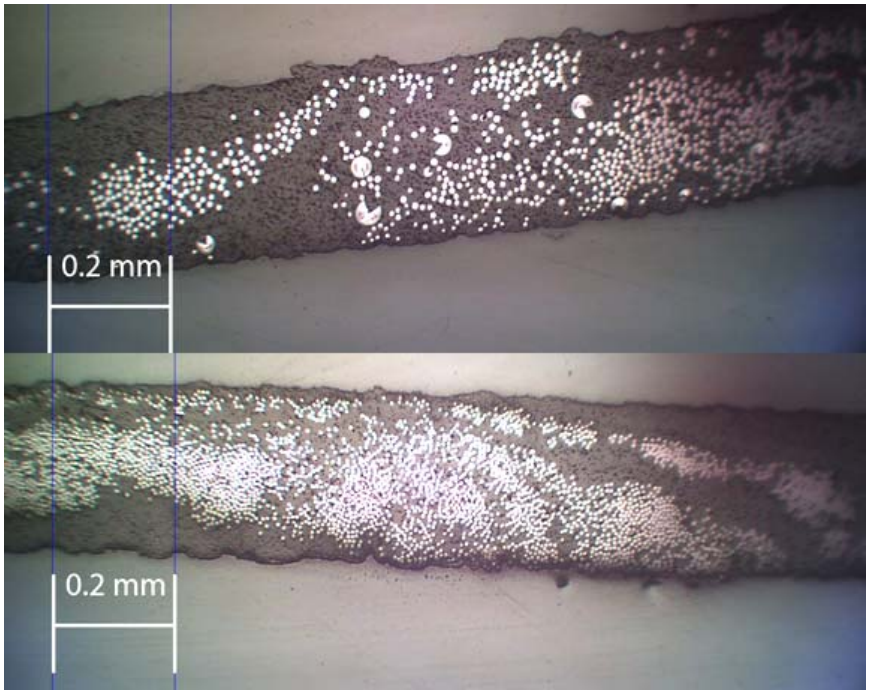

Figure 15. Comparison of pitch (top) and PAN (bottom) fiber composites at 100x.

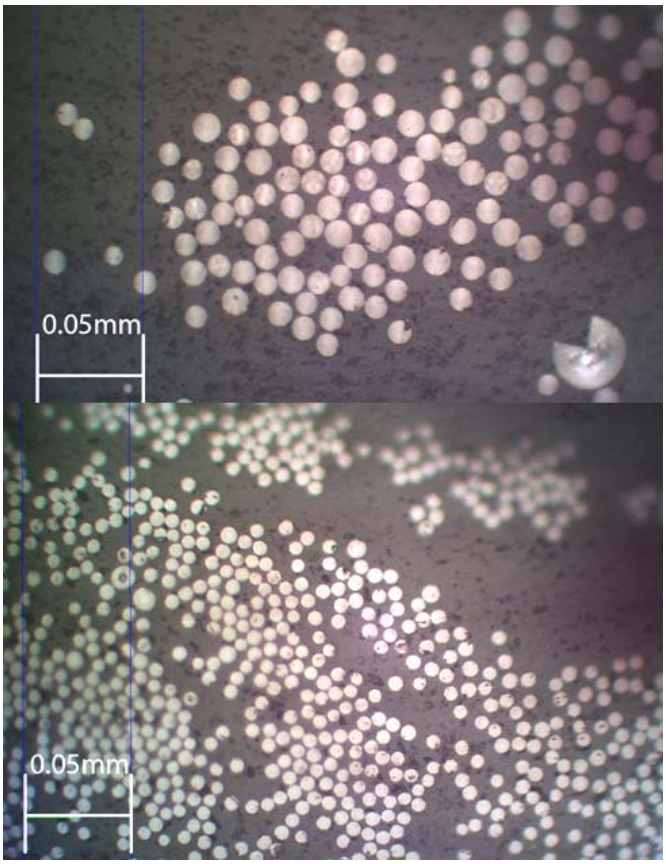

Figure 16. Comparison of pitch (top) and PAN (bottom) fiber composites at 400x.

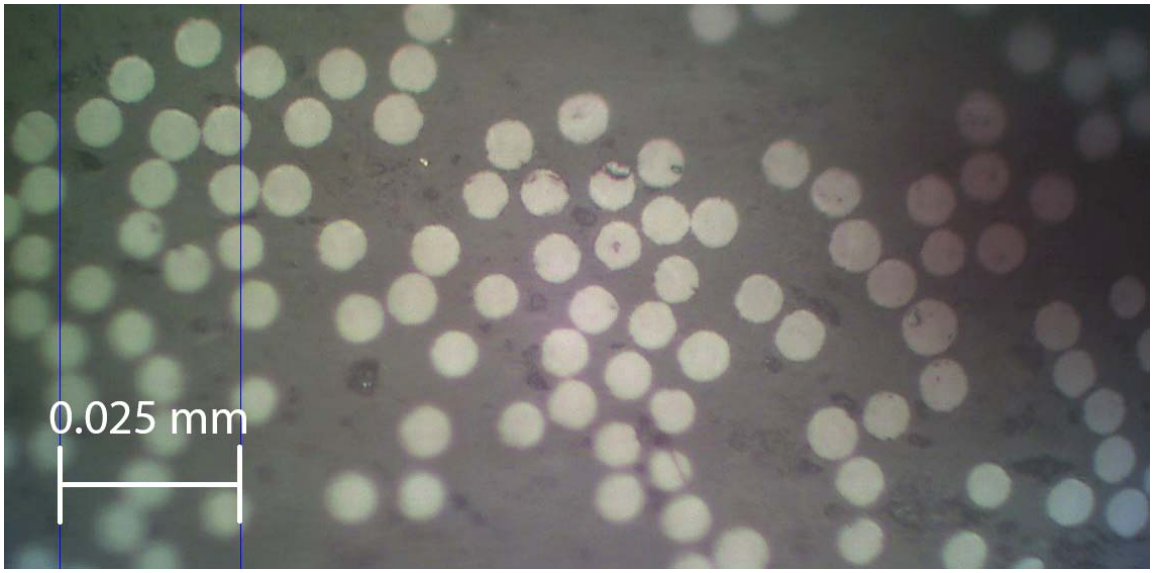

Figure 17. PAN fiber composite at 800x.

Scanning Electron Microscopy

Fractured tensile samples were viewed on the scanning electron microscope (SEM). The SEM used was a Carl Zeiss Supra 40VP field emission scanning electron microscope. Samples were gold coated to give images a greater depth of focus. All images were taken at 10 kV excitation energy. SEM images were taken of the fractured surface of tested tensile samples. In many cases, the SEM images confirmed what was observed by optical microscopy. Full description of all images is given in Reference 1. From Figure 18 it can be noted that the room temperature preheat fibers are concentrated towards the top of the sample while the 225 ºC preheat fibers were more evenly distributed through the thickness. Fiber pullout is also shown by the holes in the matrices. A higher magnification image of an area showing a block of matrix with fibers is shown in Figure 19. The fibers appear to be well wet by the matrix.

By comparison PAN fiber composites exhibited much longer fiber pullout lengths as shown in Figure 20. Because of this, examining the regions between the fibers was more difficult. However, Figure 21 shows a close-up of one region exhibiting considerable matrix existing between the pulled-out fibers.

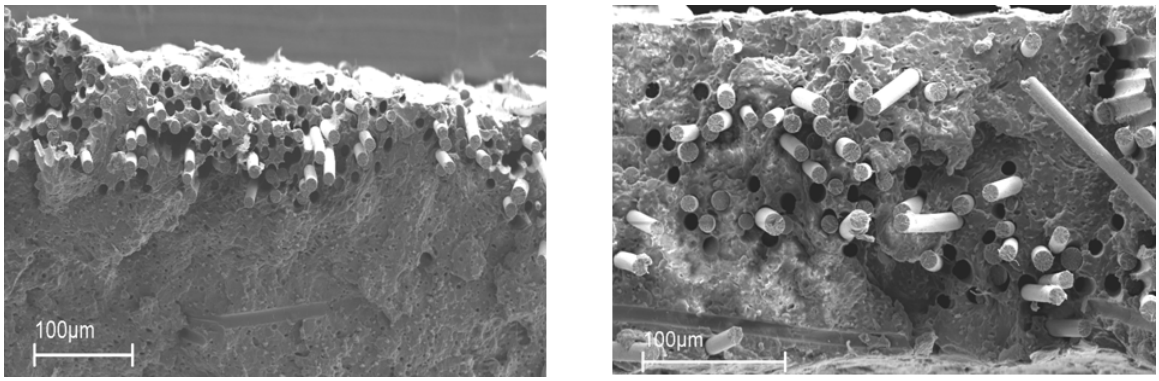

(a) (b)

Figure 18. Fracture surface SEM micrographs of through thickness of pitch fiber composites with room temperature (a) and 225 ºC (b) preheat.

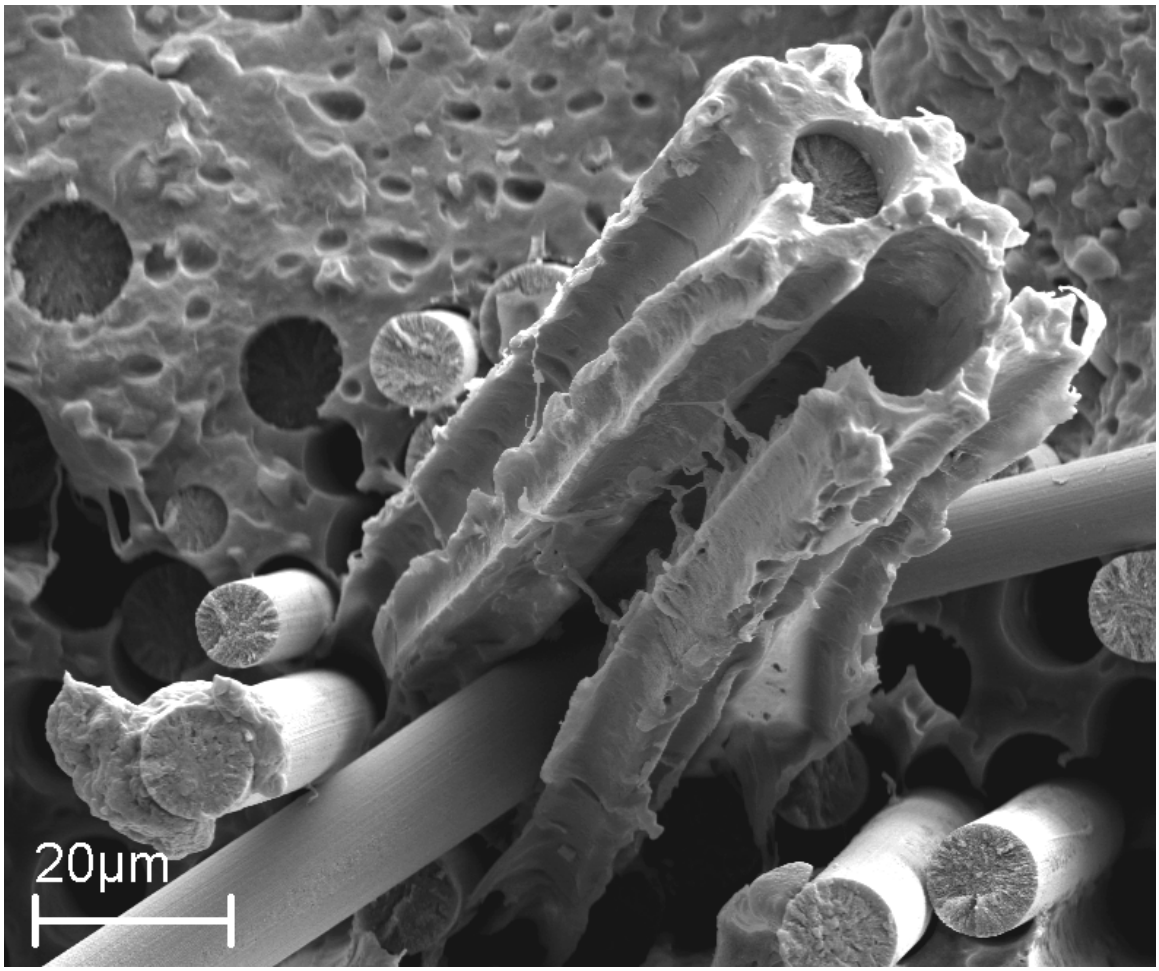

Figure 19. Close-up of fiber pullout on the fracture surface of a pitch composite.

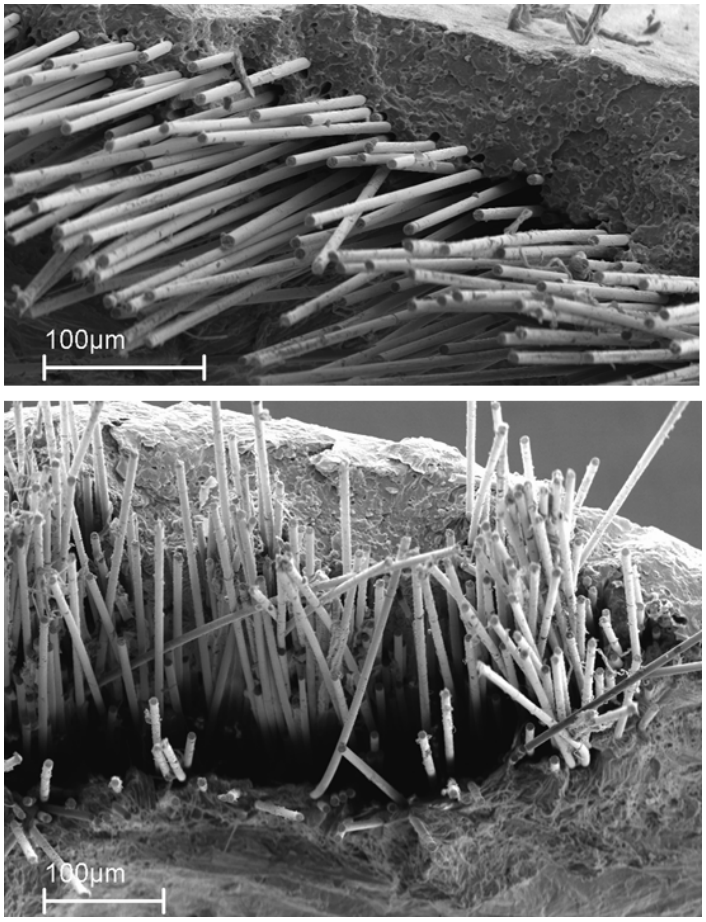

Figure 20. Fracture surface of PAN fiber composites with 225 ºC (top) and 300 ºC (bottom) fiber preheat.

Figure 21. Close-up of fiber pullout on the fracture surface of a PAN composite.

Conclusions

Highlights of the 2007-8 research include:

1. Finished design and manufacture of a miniature-DRIFT process laminate machine, including a detailed manual.
2. Experimentally tested the laminates resulting from conclusion 1 via tensile testing
3. Optical microscopy revealed good fiber wetting for both types of fibers tested with polypropylene.
4. Optical microscopy revealed that, especially in the center, fibers tended to clump together and were not evenly distributed throughout the thickness of the tape.
5. Scanning electron microscopy revealed that the fracture surfaces showed fiber pull-out and good wetting of the fibers.

Reference

1. McGlothlen, R. G., "Design and Testing of a Compact DRIFT Machine for Manufacturing of Continuous Fiber Thermoplastic Composites", Masters of Science Thesis, South Dakota School of Mines and Technology, 2008.

Presentations/Publications/Patents

1. McGlothlen, R. G., "Design and Testing of a Compact DRIFT Machine for Manufacturing of Continuous Fiber Thermoplastic Composites", Masters of Science Thesis, South Dakota School of Mines and Technology, 2008.
2. Robinson, L., Cross, W.M., Kjerengtroen, L. and Kellar, J., "Thermoplastic Melting and Wetting Behavior on Carbon Fibers", Joint ND/SD EPSCoR Conference, Sept. 2007, Fargo, ND.

I. Composite Crash-Energy Management (ACC 100[i])

Principal Investigator: Mark E. Botkin
General Motors Corporation
30500 Mound Rd
Warren, MI 48090
(586) 986-0510; fax: (586) 986-0446, e-mail:mark.e.botkin@gm.com

Technology Area Development Manager: Joseph A. Carpenter
(202) 586-1022; fax: (202) 586-1600; e-mail: joseph.carpenter@ee.doe.gov

Field Project Officer: Aaron D. Yocum
(304) 285-4852; fax: (304) 285-4403; e-mail: aaron.yocum@netl.doe.gov

Expert Technical Monitor: Philip S. Sklad
(865) 574-5069; fax: (865) 576-4963; e-mail: skladps@ornl.gov

---

Contractor: United States Automotive Materials Partnership (USAMP)
Contract No.: DE-FC05-02OR22910 through the DOE National Energy Technology Laboratory

---

Objective

- Experimentally determine the effects of material, design, environment, and loading on macroscopic crash performance to guide the design and the development of predictive tools.
- Determine the key mechanisms responsible for crash-energy absorption and examine microstructural behavior during crash to direct the development of material models.
- Develop analytical methods for predicting energy absorption and crash behavior of components and structures.
- Conduct experiments to validate analytical tools and design practices.
- Develop and demonstrate crash design guidelines and practices.
- Develop and support design concepts for application in demonstration projects.

Approach

- Conduct experimental projects to increase understanding of the global and macro influences of major variables on crash performance.
- Use the data from these experiments to create crash intuition, guidelines, and rules-of-thumb and data for the validation of analysis developments.
- Conduct microscopic experimental characterization to define the mechanisms that occur during and as a result of the crash process.
- Develop and validate analytical design tools to predict structural crash performance based on both phenomenological and micro-mechanical approaches to material and crash-mechanism modeling.

Accomplishments

- Development of a new random-fiber composite (RaFC) geometry-generation algorithm (High Fiber Volume Fraction Sequential Inclusion - HFVFSI) capable of achieving high fiber volume fractions comparable with those envisioned for practical applications (~35%).

- Generation of an automated finite-element modeling (FEM) analysis procedure using the commercial software package ABAQUS®, to statistically investigate the influence of the representative volume element (RVE) size on the elastic properties of the homogeneous random carbon-fiber (CF) material.
- Validation of the FEM results through comparison with analytical and semi-analytical approaches for random CF material.
- A first-level, multi-scale, crush-prediction software tool has been completed and delivered to the Automotive Composites Consortium (ACC). Quasi-static test results for both round and square tubes of 30^o, 45^o, and 60^o tubes have been compared to analysis simulations.

Future Direction

- Continue the development of geometry-generation algorithms and software implementation to achieve high fiber volume fractions. A user-friendly, completely-automated, software environment is necessary for rapid geometry generation for material design and analysis.
- Perform FEM-based analysis to evaluate the equivalent homogeneous material elastic properties, in conjunction with determination of minimum RVE size, for carbon-fiber RaFCs and elliptical fiber cross-sections.
- Conduct micro-scale experimental work and develop the corresponding internal state variables (ISVs) for the developed RVE.
- Develop specific material modeling subroutine for ABAQUS® for RVE implementation and consequent macro-structure damage analysis of random CF.
- Account for the rate-sensitivity effects, and calibrate the rate sensitivity model to the available test data in multi-scale modeling of braids.
- Study the effects on damage & failure characteristics of "size" of specimen/structural dimensions relative to the size of the damage zone and/or microstructure.
- Study the effects of temperature during processing on resin properties.
- Test random CF tubes for the purpose of validation of the random CF crush prediction project.

Introduction

The purpose of the Composite Crash-Energy Management project is to develop and demonstrate the technologies required to apply production-feasible structural composites in automotive crash and energy-management applications. Efforts within the project are intended to understand the mechanisms of polymer-composite crash, develop analytical tools for use in vehicle design, and build a knowledge base for the vehicular application of lightweight polymer composites. The efforts relate to materials, molding and assembly processes and design configurations that are useful in realistic applications. Design-analysis methods will be developed that can be used at several different steps in the design process. These steps require different levels of precision and speed-of-use, and the appropriate tools are expected to include both micro-mechanical and phenomenological approaches.

Crashworthiness Assessment of Tubular RaFC Structures Based on Micro and Interfacial Mechanics

The goal of this work is to create a novel Hierarchical, Micro Experimental and Computational Characterization (HiMECC) algorithm for RaFCs. This will be realized through the following deliverables: (1) Develop computational tools for RaFC micro-scale material characterization and damage modeling;
(2) Conduct experimental work to determine required material parameters and validate numerical analysis tools; (3) Determine key mechanisms responsible for macro-scale failure; and (4) Develop and demonstrate crash design guidelines and practices.
To date, the following tasks have been completed:
1. Development of a random-geometry-generation algorithm and software implementation based on the Random Sequential Adsorption (RSA) approach.
2. Generation of RaFC geometries for materials with up to 20% volume fraction using the RSA algorithm.
3. Development of a procedure for numerical determination of the elastic constants for the equivalent homogeneous material.
4. Generation of an automated FEM analysis procedure using the commercial software package ABAQUS®, to statistically investigate the influence of the RVE size on the elastic properties of the homogeneous material.

5. Validation of the FEM results through comparison with analytical and semi-analytical approaches.
6. Development of a new RaFC geometry-generation algorithm (High Fiber Volume Fraction Sequential Inclusion - HFVFSI) capable of achieving high fiber volume fractions comparable with those envisioned for practical applications (~35%). The new algorithm accounts for fiber bundle curvatures occurring during the manufacturing process, as well as for arbitrary bundle cross-sections. The curved bundle geometry is implemented using spline modeling, with three-dimensional (3D) bundle-intersection checks carried out by employing convex optimization algorithms.
7. Optical investigation of E-glass and carbon-fiber RaFC samples for geometry characterization (Figures 1 and 2).
8. Generation of RaFC geometries for materials with up to 36.7% volume fraction (Figure 3). Validation of the FEM results for large fiber volume fractions through comparison with analytical and semi-analytical approaches.

Figure 1. Optical characterization of RaFC samples – in-plane view.
Left: E-Glass-fiber sample; Right: Carbon-fiber sample.

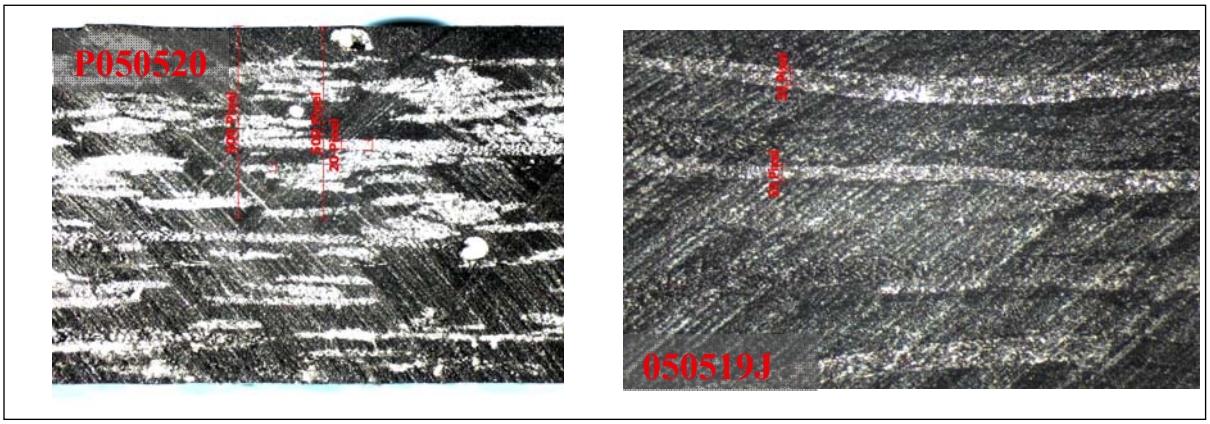

Figure 2. Optical characterization of RaFC samples – through thickness view.
Left: E-Glass fiber sample; Right: Carbon-fiber sample.

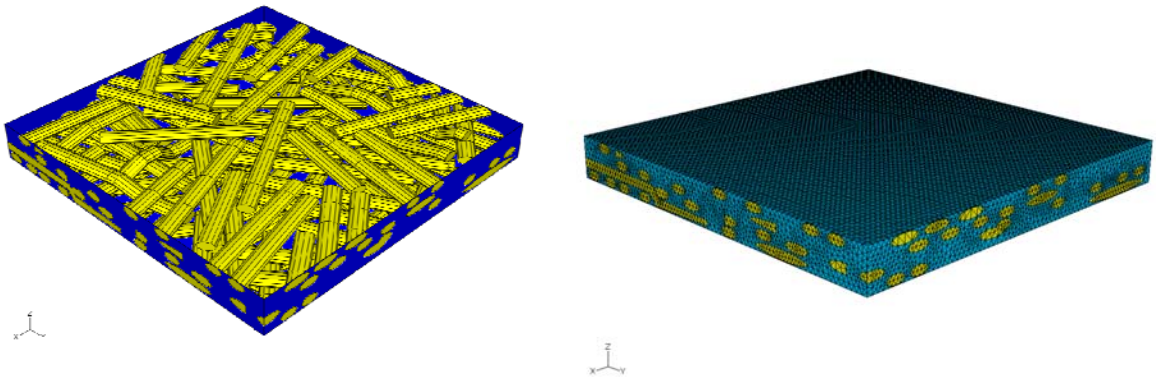

Figure 3. HFVFSI-algorithm-generated RVE of 36.7% volume fraction random composite (eliptical cross-section bundles).

Multi-scale Design System

Over the past year, we developed a Multi-scale Design System (MDS) and validated it on circular and square tube crush simulation with different (30^o, 45^o, 60^o) braid angles. Size effects and the influence of tow buckling were studied and implemented into the model. A multi-step calibration (parameter identification) scheme was developed and implemented. A comprehensive user manual for multiscale design system and a complete set of demonstration movies have been developed for the MDS.

The MDS consists of the state-of-the-art, multi-scale analysis tools integrated with the commercial finite-element analysis (FEA) engine (ABAQUS) and optimization package for model calibration (or parameter identification) and validation. The MDS, schematically illustrated in Figure 4, consists of:

a. Mathematical upscaling: derivation of coarse-scale equations from fine-scale equations. This is accomplished using mathematical homogenization theory.

b. Computational upscaling: reducing the complexity of solving a fine-scale problem to a manageable size for available computational resources.

c. Parameter identification: solving an inverse problem for constitutive parameters (interfaces, fibers/tows, matrix) by minimizing the error between experimental data at coupon and fine-scale levels hosted in the Experimental Depository.

d. Graphic User Interface (GUI) based on ABAQUS/CAE. The GUI, which serves as the front-end for the analysis, is implemented via Python codes taking advantage of ABAQUS/GUI toolkit.

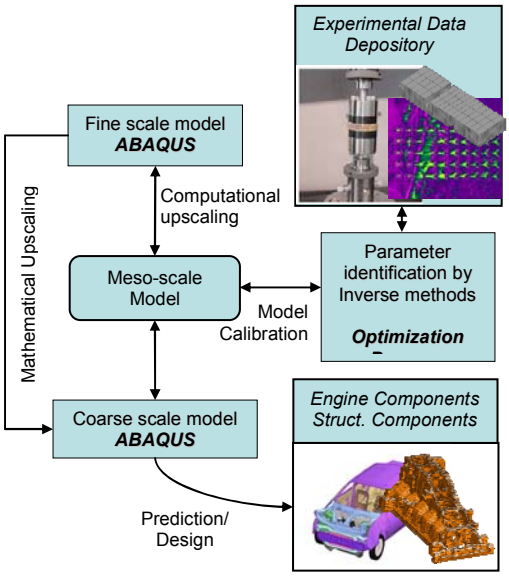

Figure 4. MDS developed at Rensselaer.

Figure 5 depicts braid architectures considered in our studies.

For all tube-crush simulations we considered quasistatic loading (load rate = 0.5 in/min), initiator plug with 5/16-inch fillet radius, two layers of braided composite, and quarter-tube

models. For circular tubes, the inner diameter is 2.35 in. as illustrated in Figure 6.

Figure 7 compares the multi-scale simulations and experimental results for the 45° braid architecture shown in Figure 5. An excellent agreement with the experiment can be observed.

Figure 8 compares the multi-scale simulations and experimental results for the 30° braid architecture shown in Figure 5. This time, the agreement with experiment is not as good. Possibly, this can be attributed to the fact that, so far, we have not incorporated rate effects and interface failure into the model. This is also true for the calibration phase.

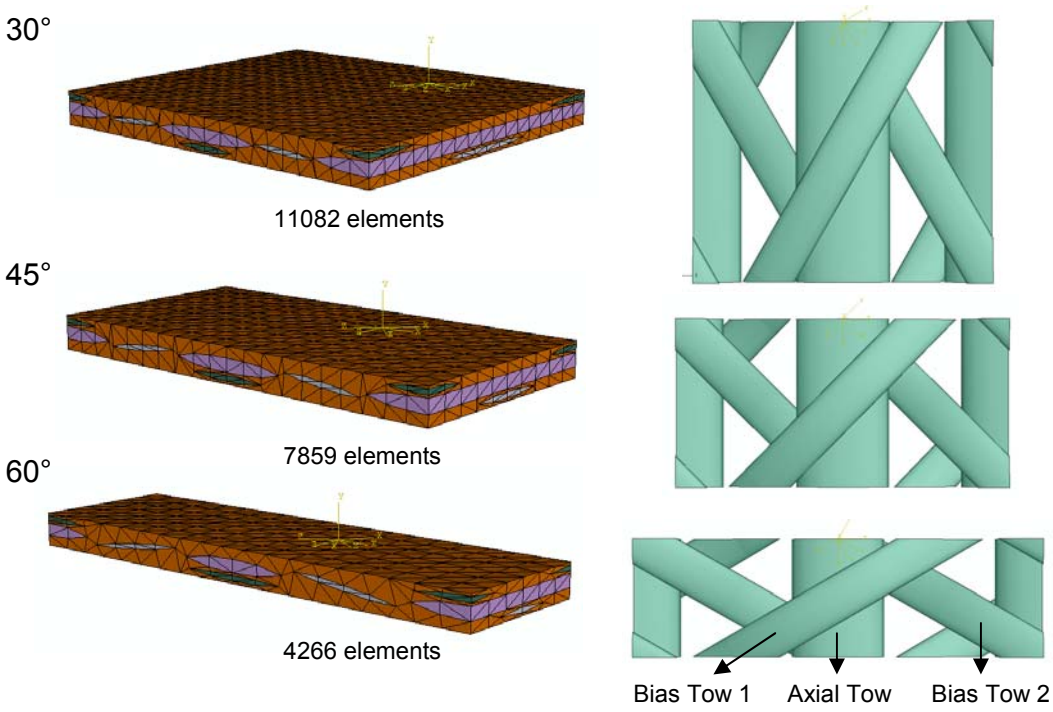

Figure 5. Braid architectures considered in simulations.

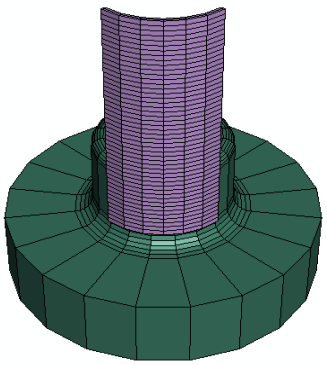

Figure 6. Circular tube model.

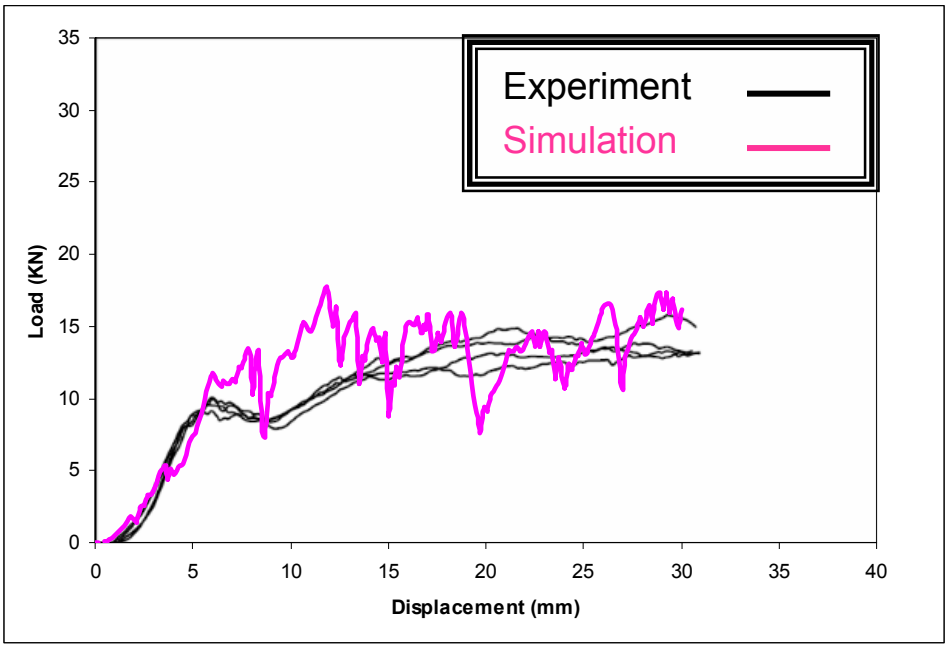

Figure 7. Comparison of the multi-scale simulation and experimental results for circular tube made of 45° braid architecture in quasistatic loading.

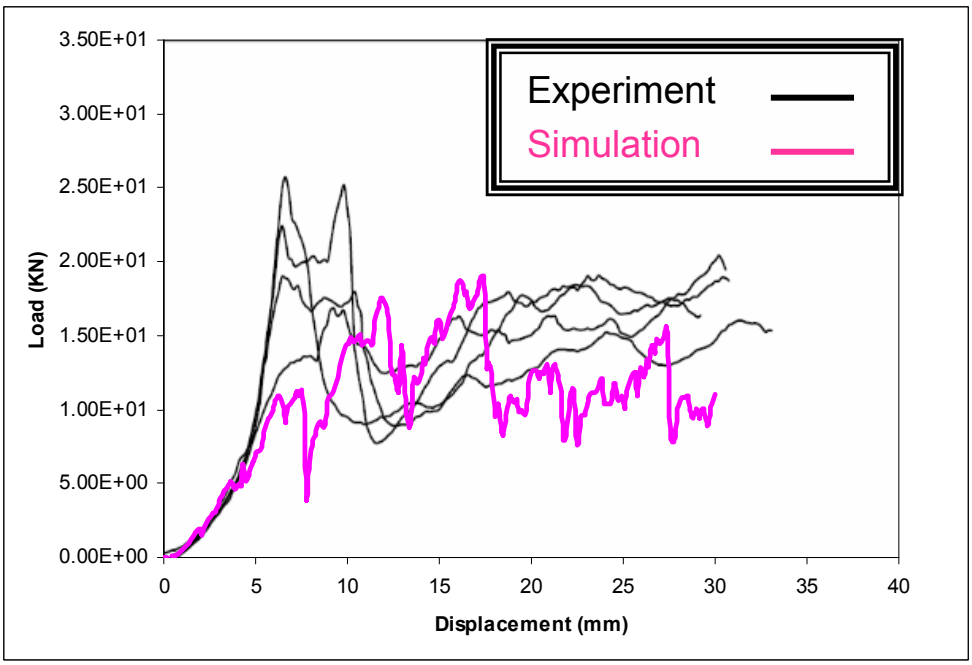

Figure 8. Comparison of the multi-scale simulation and experimental results for circular tube made of 30° braid architecture in quasistatic loading.

Figure 9 compares the multi-scale simulations and experimental results for the 60° braid architecture shown in Figure 5. Again, an excellent agreement with the experiment can be observed.

Next, we studied the mesh-size effect, that is, the influence of mesh size on simulation results.

Figure 10 summarizes the findings of these studies. Interestingly, the model shows very little if any influence to the mesh size. For coarser meshes, the oscillations are higher, which is due to the fact that when element is removed, the load is reduced. The larger element is eroded, the larger jump is expected.

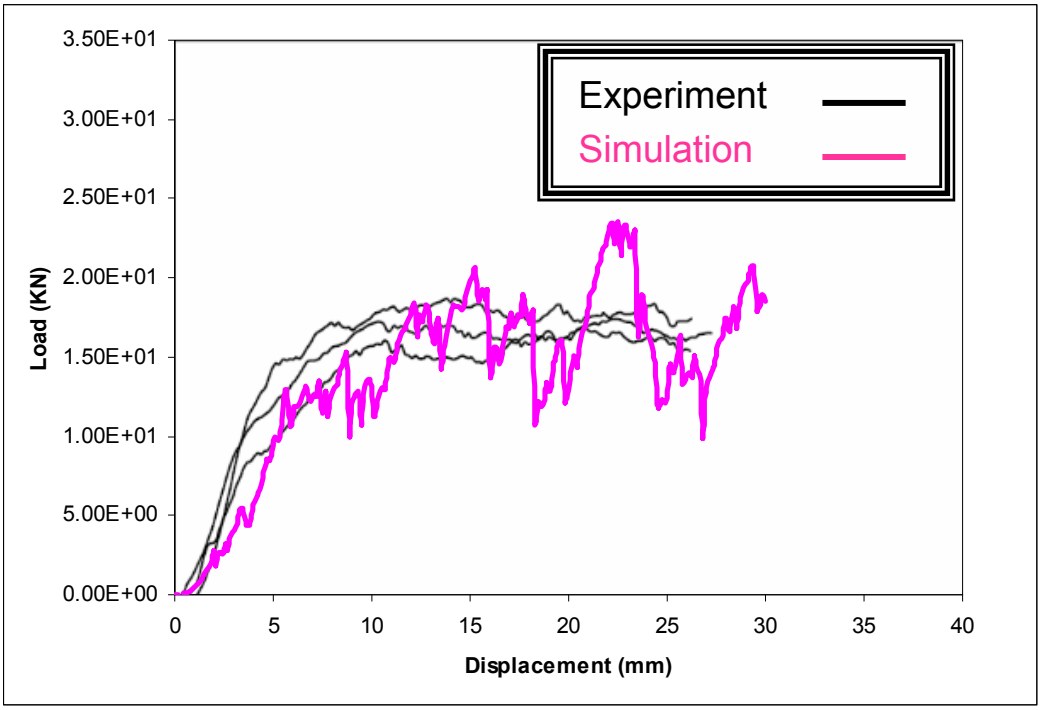

Figure 9. Comparison of the multi-scale simulation and experimental results for circular tube made of 60° braid architecture in quasistatic loading.

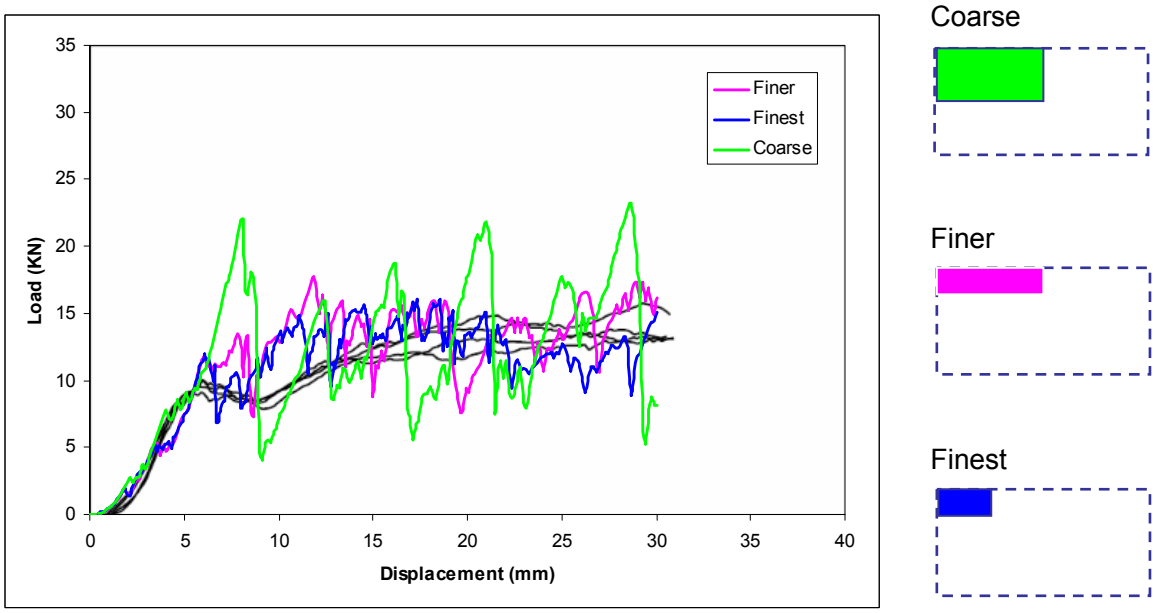

Figure 10. Size effect studies for three different mesh sizes shown on the right.

Next, we conducted crush simulations of square tube as shown in Figure 11. The inner dimensions of the tube were 2 in. x 2 in. and inner corner radius of 0.33 in. An initiator plug with ¼-inch fillet radius was considered.

Figure 12 compares the multi-scale simulation and experimental results for the 45° braid architecture shown in Figure 5.

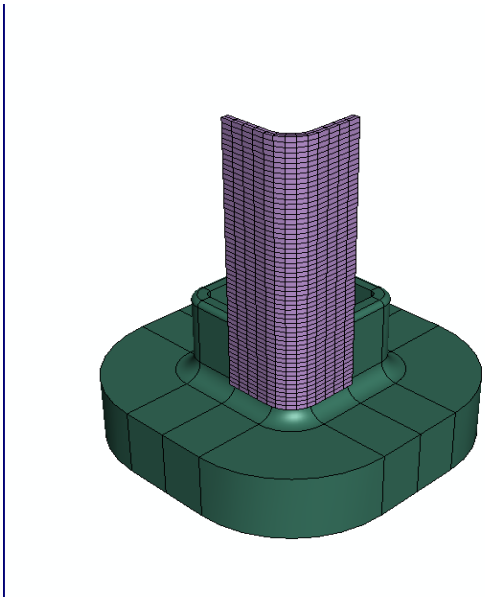

Figure 11. Square tube model.

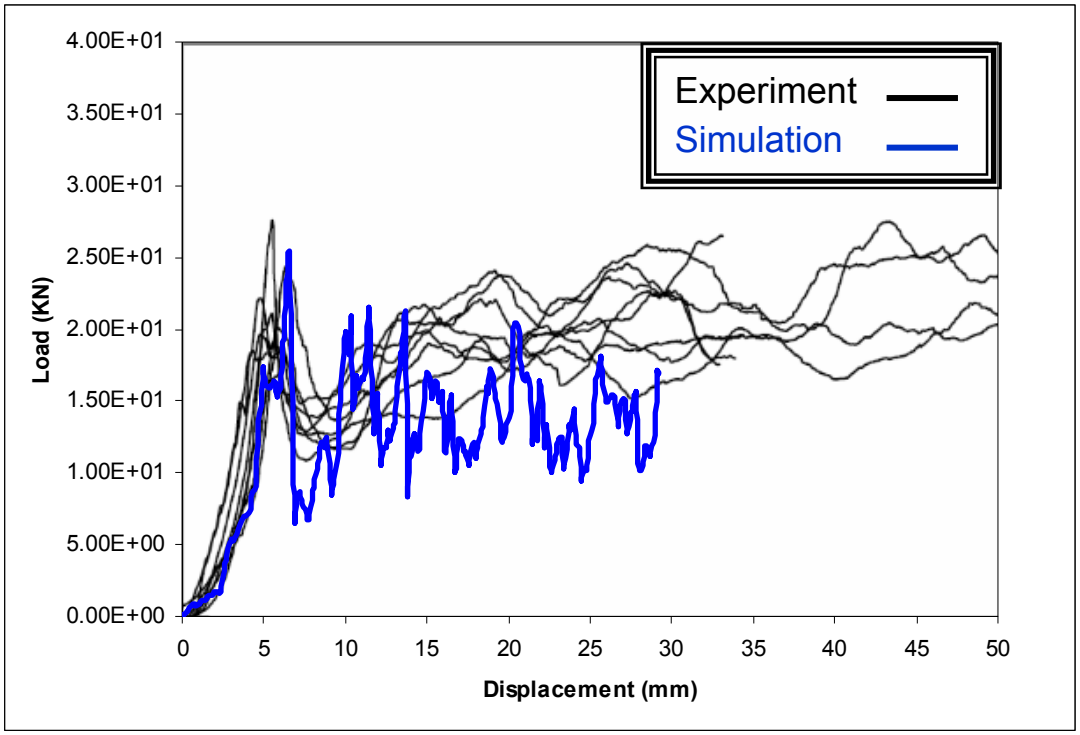

Figure 12. Comparison of multi-scale simulation and experimental results for square tube made of 45° braid architecture in quasistatic loading.

Figure 13 compares the multi-scale simulation and experimental results for the 30° braid architecture shown in Figure 5.

Figure 14 compares the multi-scale simulation and experimental results for the 60° braid architecture shown in Figure 5.

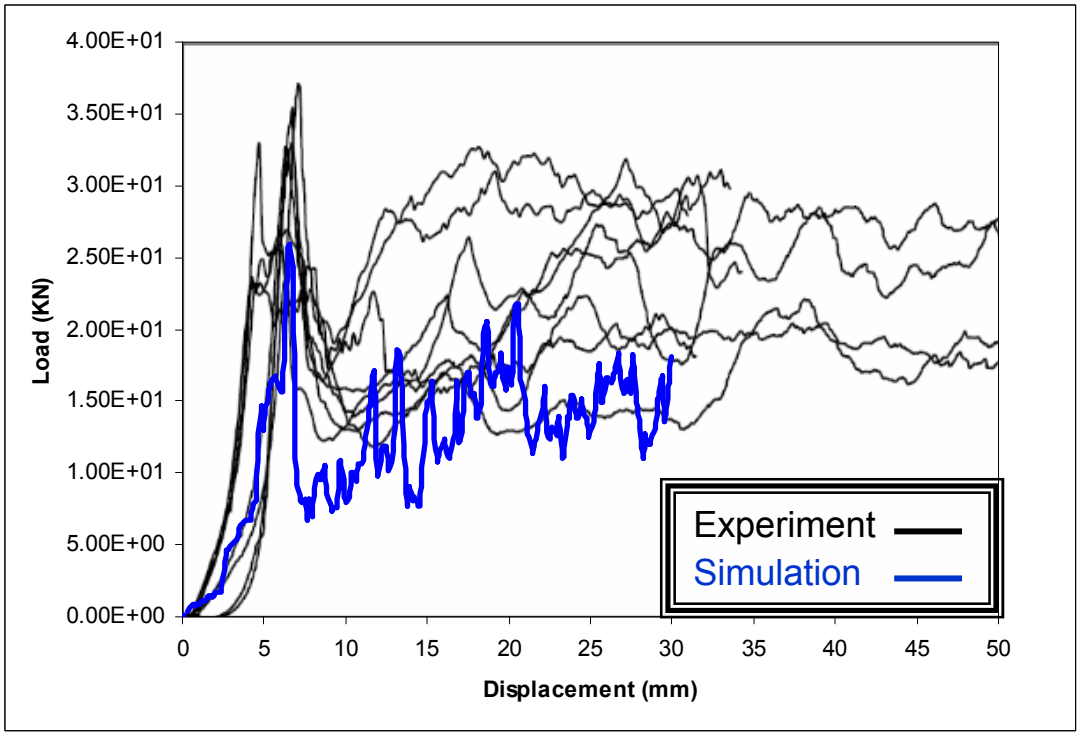

Figure 13. Comparison of multi-scale simulation and experimental results for square tube made of 30° braid architecture in quasistatic loading.

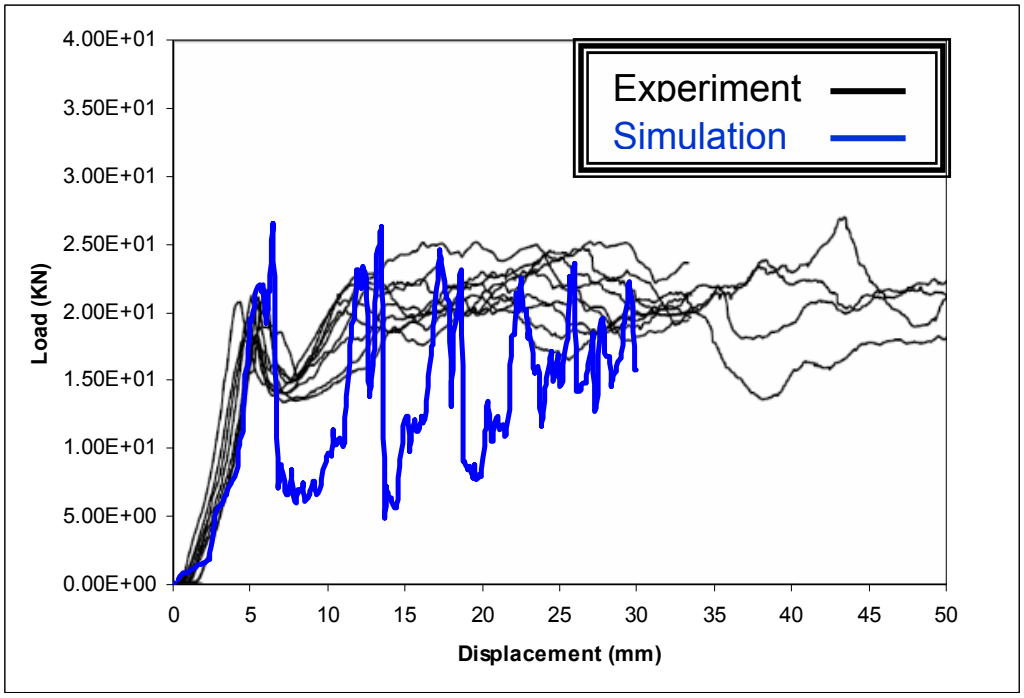

Figure 14. Comparison of multiscale simulation and experimental results for square tube made of 60 braid architecture in quasistatic loading.

These results demonstrate the need for considering interface failure. Note that implementation of interface failure will affect the calibrated properties of microconstituents. This is because the failure properties of microconstituents were calibrated to fit the coupon data.

Size Effects in Textile Composites

This new effort is focused on developing a qualitative and quantitative understanding of the important topic of meso-to-macro size effects in structures made of textile-composite, quasi-brittle materials. Such an understanding plays a role in the accurate modeling and characterization of structural crashworthiness and energy absorption in components made of lightweight, quasi-brittle materials (such as textile composites). Obtaining an understanding and useful insights of size effects, along with verifiable experimental evidence and clarification of the implications of the size effects for computational FEM of structures made of two-dimensionally triaxially-braided composites (2DTBC), is the major goal of the project.

It is important at this point to clarify what is meant by "size" and what are the "effects". "Size" refers to the size of specimen/structural dimensions relative to the size of the damage zone and/or micro-structure. "Effects" refer to those effects on damage and failure characteristics, nominal strength, and post-peak regime in materials exhibiting such strength–size dependence.

This new effort is motivated by the following fundamental question: What is the relationship between the measurements of energy released and dissipated (i.e., fracture properties and material nonlinearities) carried out in the laboratory at the coupon level of a 2DTBC, and their manifestations at the structural level in a real crash setting of a structure made of the same 2DTBC. That is, do the measured overall material/ structural properties change when different size specimens are tested? It is important to note that the issue of concern in this topic (i.e., specimen-size effects on measured material properties) does not stem from the well-known statistical distribution of micro-flaws in a material based on Weibull theory, but rather from an energetic consideration driven by the relatively-recent findings that quasi-brittle materials exhibit size effects because their fracture process-zone is not negligible (in size) compared with structural dimensions.

This new effort is divided into two parts and led by two collaborating universities. The work involves extensive experimental testing (including the design and construction of a new resign transfer molding (RTM) tool to test large braided-carbon plaques) and advanced state-of-the-art computational modeling and validation. The work is focused on one matrix/resin system and three carbon-fiber-braid architectures. At the end of this two-year effort, the sponsor will receive all information related to tests, material characterizations, and results, as well as all modeling assumptions, FEMs and external/user modules, validation results and recommendations according to the detailed deliverable and requirements stated in the detailed proposal.

Presentations/Publications/Patents

1. Pan, Y., A.A. Pelegri, L. Iorga (2007), Analysis of 3D random chopped fiber reinforced composite using the finite element method, Journal of Computational Material Science (under review.)
2. Iorga, L., Y. Pan, A. A. Pelegri (2007), Comparison of stiffness prediction approaches for random fiber composites, ASME Applied Mechanics and Materials Conference, McMAT 2007, June 3-7, 2007.
3. Pan, Y., A.A. Pelegri, L. Iorga (2007), The Elastic Properties of 3-D Random Chopped-Fiber Reinforced Composite, ASME Applied Mechanics and Materials Conference, McMAT 2007, June 3-7, 2007.
4. Pan, Y., L. Iorga, A. A. Pelegri (2007), Modeling of 3-D Random Chopped Fiber Composites with Curved Non-Circular Fibers, ASME International Mechanical Engineering Congress and Exhibition, IMECE 2007, November 11-15, 2007
5. Iorga, L., Y. Pan, A. A. Pelegri (2007), Material characterization of random fiber composites in the elastic domain, ASME International Mechanical Engineering Congress and Exhibition, IMECE 2007, November 11-15, 2007.

[i] Denotes project 100 of the Automotive Composites Consortium (ACC), one of the formal consortia of the United States Council for Automotive Research (USCAR, www.uscar.org) set up by Chrysler, Ford and General Motors to conduct joint, pre-competitive research and development.

J. Engineering Property Prediction Tools for Tailored Polymer Composite Structures

Principal Investigator: Ba Nghiep Nguyen
Pacific Northwest National Laboratory (PNNL)
902 Battelle Boulevard, P.O. Box 999, MS: K5-22, Richland, WA 99354
(509) 375 3634; fax: 509-375 6736; e-mail: Ba.Nguyen@pnl.gov

Co-Principal Investigator: Vlastimil Kunc
Oak Ridge National Laboratory (ORNL)
P.O. Box 2009, Oak Ridge, TN 37831
(86) 574 8010; fax: 865-574-0740; e-mail: kuncv@ornl.gov

Technology Area Development Manager: Joseph A. Carpenter
(202) 586-1022; fax: (202) 586-1600; e-mail: joseph.carpenter@ee.doe.gov

Expert Technical Monitor: Philip S. Sklad
(865) 574-5069; fax: (865) 574-6098; e-mail: skladps@ornl.gov

---

Contractor: PNNL, ORNL
Contract No.: DE-AC06-76RL01830, DE-AC05-00OR22725

Objective

- Enable the optimum design of lightweight automotive structural components using long-fiber-reinforced injection-molded thermoplastic composites (LFTs).

Approach

Phase I: Technical feasibility assessment

- Perform a technical assessment of current process models and computational methods for short-fiber polymer injection-molded composites in order to determine their accuracy, limitations and potential applications to LFTs.
- Identify the research directions needed to develop process and constitutive models for LFTs.
- Understand and examine the LFT emerging microstructure, characterization techniques and material processing.
- Characterize fiber orientation in LFT samples.
- Examine the molding behaviors of glass and carbon fibers.

Phase II: Research and development

Develop an integrated approach that links process to structural modeling allowing the optimum design of LFT composite structures. This work includes:

- development of process models for LFTs that allow simulations of LFT structures in order to predict flow-induced fiber orientation and other microstructural features,
- development and implementation of LFT constitutive models for structural finite-element analyses that make use of the composite microstructure predicted by process modeling. These constitutive models will predict the composite thermoelastic properties and its nonlinear behaviors due to damage, fatigue, creep and impact,
- development of characterization methods for LFT materials,
- injection-molding of larger samples and complex geometries,
- experimental testing to determine the model parameters and to validate the process and constitutive models.

Accomplishments

- A fiber-orientation model for LFTs was developed. This model is defined as the *anisotropic rotary diffusion* (ARD) model that extends the Folgar-Tucker model to LFTs.
- Computational models developed in fiscal year (FY) 2006 were applied to compute the elastic properties and coefficients of thermal expansion (CTEs) of LFT samples.
- Models were developed to predict the reduction of the elastic moduli as a function of fiber curvature and fiber/matrix debonding.
- A homogenized elastic-plastic model for LFTs was developed and implemented into ABAQUS.
- A failure criterion was implemented in the homogenized elastic-plastic model to predict strength of LFTs.
- A method for correcting the raw fiber-length distribution (FLD) was developed, and the Weibull's distribution was used to represent the corrected FLD. FLD effect on the elastic properties was studied.
- A cooperative research and development agreement (CRADA) with Moldflow, Inc. was signed which has brought Moldflow, Inc. to the project.
- PNNL built the tooling for injection-molding glass/polypropylene (PP) ISO-plaques using the same molding parameters as Delphi, and also optimized parameters.
- Experimental methods for measuring fiber length in LFTs were developed at ORNL and successfully applied to characterize FLD in LFT samples.
- FLDs and elastic moduli were measured for all material configurations.
- Mechanical tests were performed to obtain stress-strain responses of LFT samples.
- Procedure for obtaining high-quality tomography reconstruction of glass-fiber LFTs was developed, enabling measurement of orientation and curvature of individual filaments.
- Matched individual filaments from optical microscopy and tomography reconstruction for samples.
- Testing equipment capable of operating within the X-ray micro-tomography unit was developed.
- LFT specimens were tested and progressive damage was observed using coupled testing tomography.

Future Direction

- Further develop process and property prediction models for LFTs. Collaborate with Moldflow to analyze simple and larger injection-molded geometries.
- Develop a creep model for LFTs and enhance the homogenized elastic-plastic model to include progressive damage.
- Utilize previously-developed measurement techniques to determine fiber orientation and fiber length in newly-molded parts. Generate extensive set of experimental results supporting development of non-linear and time-dependent material models.
- Further develop advanced material microstructure characterization tools to establish fiber curvature and other fiber-network parameters. Advance understanding of processes active in LFTs subjected to load by observing deformations and damage in loaded samples in three dimensions.
- Procure materials and subsequently mold test samples with selected Tier 1 molder.

Introduction

During fiscal year (FY) 2007, we focused our modeling efforts on validating the thermoelastic property predictions for LFTs against the experimental results. In parallel, a fiber-orientation model for these materials was developed that incorporates an ARD term to capture fiber orientation in LFTs. Preliminary predictions by the ARD model agreed with the experimental results for LFTs. Concentrated long fibers induce fiber curvature that reduces the composite properties. A micromechanical model based on the Eshelby-Mori-Tanaka (EMT) approach was then developed to compute the composite elastic properties as a function of fiber curvature. Fiber/matrix debonding was also investigated. This problem was modeled by a modified EMT formulation that accounts for imperfect fiber/matrix interfaces. Finally, a homogenized elastic-plastic model for LFTs and a failure criterion were developed and implemented in ABAQUS allowing the simulations of LFT stress-strain responses until failure.

Property prediction requires fiber-orientation- and length-distribution data. By manual measurement, it was verified that the Leeds' system [1] could be used to measure fiber orientation in LFTs. Therefore, fiber orientation results determined by

the Leeds' system were used in the computation. In the meantime, measurement methods were developed to systematically characterize fiber-length distributions (FLDs) in LFTs. Also, a method was developed to correct the raw FLD data. A tensile-testing machine within a tomography unit was designed and developed allowing us to observe the LFT microstructure and its evolution during loading. Finally, mechanical testing was performed to determine the material stress-strain responses until failure allowing the validation of the elastic-plastic model and strength prediction.

Prediction of the LFT Thermoelastic Properties

Computation of the LFT Thermoelastic Properties

These computations contain three steps [2-3]. First, the elastic stiffness and CTEs of a reference unidirectional (UD) composite are determined using the EMT model [4-5]. The reference composite contains the same fiber-volume fraction and length distribution as the actual composite. Next, the stiffness and CTEs of the actual composite are determined from the solutions for the reference composite that are averaged over all possible orientations using the orientation averaging method [6-7]. Finally, the overall stiffness and CTEs of the composite specimen can be determined considering the specimen as being formed by a stacking sequence of composite layers. The lamination theory is then applied to calculate the composite overall properties formed by this stacking sequence.

Figure 1 presents the corrected FLD expressed in terms of weight of fibers versus fiber length for an LFT glass/PP ISO-plaque, while Figure 2 shows the measured and predicted fiber-orientation tensor components, A_{11} and A_{22}. These distributions were used in the computation of the through-thickness elastic properties and CTEs for this specimen (Figures 3, 4 and 5). The *z*-coordinates normalized by the specimen thickness, *h* are used in Figs 2-5. Table 1 presents the longitudinal ($\overline{E}_{11}$) and in-plane transverse ($\overline{E}_{22}$) moduli for this plaque. The moduli predicted based on both the experimental fiber-orientation distribution (FOD) and corrected FLD agree well with the experimental results. However, the computation using the FOD predicted by the current fiber orientation model (*reduced strain closure* (RSC) model [8]) under-predicts the modulus $\overline{E}_{22}$. This is because the RSC model under-predicts A_{22}. The use of the Weibull's FLD and experimental FOD also has provided good predictions (Table 1).

Effect of fiber curvature

The effect of fiber curvature on the elastic properties was studied using a unit-cell homogenization approach and micromechanical modeling [9]. The first approach used a unit cell with a fiber or fiber bundle. Appropriate boundary conditions were prescribed to extract the elastic stiffness components. The second approach made use of the EMT model in which fiber curvature was accounted for through the variation of fiber orientation within a prescribed range that corresponds to a given degree of fiber curvature. Figure 6 presents the predicted variations of the normalized elastic moduli as a function of the fiber curvature represented by the end-angle θ. These results show that curved fibers significantly affect the composite properties since they lead to a significant reduction of modulus E_{11} while relatively small increase in E_{22} is achieved. The 1-direction is parallel to the segment joining the fiber ends. The 2-direction is in the plane containing the curved fiber.

	Prediction (1) MPa	Prediction (2) MPa	Prediction (3) MPa	Experiment MPa
$\overline{E}_{11}$	6017	5361	6001	6063
$\overline{E}_{22}$	6935	6377	6916	7211

Table 1. Predicted and measured elastic moduli $\overline{E}_{11}$ and $\overline{E}_{22}$ for an LFT glass/PP ISO-plaque – Use of (1) experimental FOD and corrected FLD – (2) predicted FOD (RSC model) and corrected FLD – (3) experimental FOD and Weibull's FLD.

Effect of Fiber/Matrix Debonding

It has been observed that in some of our tested specimens, the modulus values were significantly lower than expected. One of the reasons for lower properties is fiber/matrix debonding. This defect was modeled using the modified EMT formulation

proposed in [10]. To include some initial fiber/matrix debonding due to processing, it was assumed that debonding manifests as fiber/matrix sliding without separation. This assumption leads to the following expression for the fiber/matrix interface compliance tensor, η_{ij} :

$$\eta_{ij} = \beta(\delta_{ij} - n_i n_j) \qquad (1)$$

where β is a parameter that expresses the debonding intensity, and δ_{ij} is the identity tensor. n_i and n_j are the components of the unit normal vector at the fiber/matrix interface. $\beta = 0$ represents the perfect fiber/matrix interface while $\beta \to \infty$ corresponds to free fiber/matrix sliding. Eq. (1) was then introduced into the modified EMT formulation to compute the stiffness matrix of the reference UD composite. Finally, the stiffness matrix of the as-formed composite containing debonded fiber/matrix interfaces is obtained from the solution for the reference composite that is averaged over all possible orientations using the orientation averaging method [6-7]. The elastic properties predicted for an LFT glass/PP center-gated disk are shown in Table 2. Accounting for fiber/matrix debonding has improved the elastic property prediction for this material.

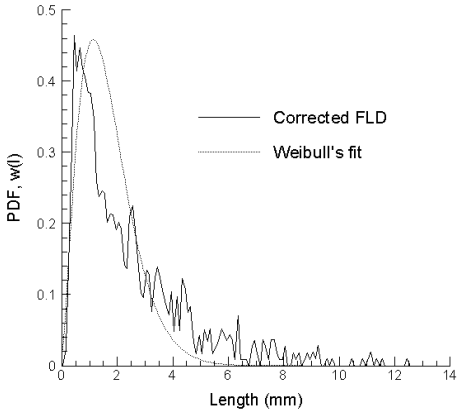

Figure 1. Corrected FLD in terms of probability density function (PDF) for weight of fibers for a glass/PP ISO-plaque - Weibull's distribution was used to fit the corrected FLD data.

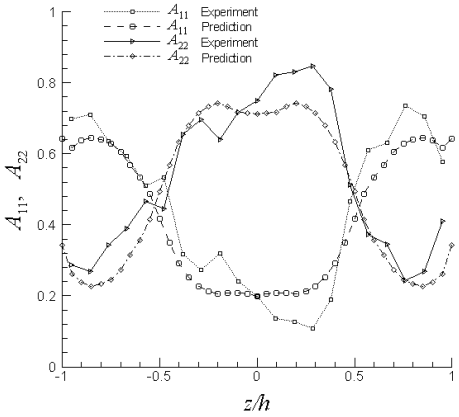

Figure 2. Predicted and measured fiber orientation tensor components A_{11} and A_{22} for a glass/PP ISO-plaque. The prediction was achieved by the RSC model.

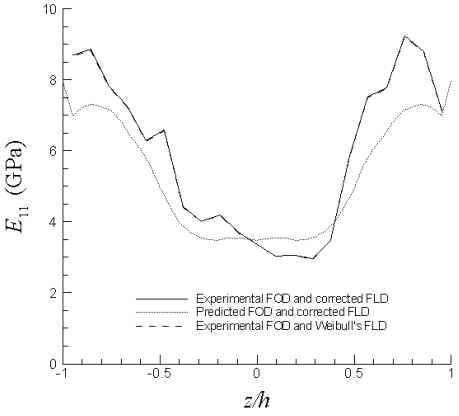

Figure 3. Predicted thru-thickness variations of the elastic modulus E_{11} for a glass/PP ISO-plaque. The 1-direction is the plaque longitudinal direction.

	Prediction (no debonding) MPa	Prediction (debonding, β=20) MPa	Experiment MPa
$\overline{E}_{11}$	5543	4833	4737
$\overline{E}_{22}$	7703	7246	6840

Table 2. Predicted and measured elastic moduli $\overline{E}_{11}$ and $\overline{E}_{22}$ for an LFT glass/PP center-gated disk.

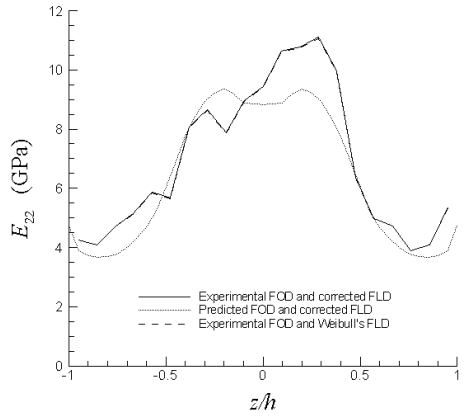

Figure 4. Predicted thru-thickness variations of the elastic modulus E_{22} for a glass/PP ISO-plaque. The 2-direction is the plaque in-plane transverse direction.

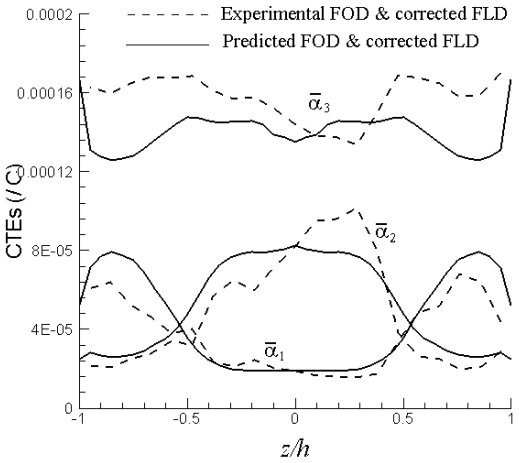

Figure 5. Predicted CTEs ($\bar{\alpha}_1, \bar{\alpha}_2$, and $\bar{\alpha}_3$) for a glass/PP ISO-plaque.

An Elastic-Plastic and Strength-Prediction Model for LFTs

Thermoplastic composites exhibit nonlinear stress-strain responses that are caused by the elastic-plastic behavior of the thermoplastic resin and progressive damage due to matrix cracking, fiber/matrix debonding, fiber pull-out and fiber breakage. An elastic-plastic model for LFTs was developed that accounts for *elastic fibers* embedded in an *isotropic elastic-plastic matrix* obeying the deformation theory of plasticity [11] and the Ramberg-Osgood relation given by [12]:

$$\varepsilon_{\mathrm{m}}^{\mathrm{eq}} = \frac{\sigma_{\mathrm{m}}^{\mathrm{eq}}}{E_{\mathrm{m}}} + \left(\frac{\sigma_0}{E_{\mathrm{m}}}\right)\left(\frac{\sigma_{\mathrm{m}}^{\mathrm{eq}}}{\sigma_0}\right)^n \qquad (2)$$

where $\sigma_{\mathrm{m}}^{\mathrm{eq}}$ and $\varepsilon_{\mathrm{m}}^{\mathrm{eq}}$ are the matrix equivalent stress and strain. E_{m} is the matrix elastic modulus, and σ_0 and n are the reference stress and hardening exponent, respectively. An *incremental* EMT approach was formulated to compute the composite (overall) stress increment resulting from the composite strain increment and the material nonlinearity. The composite overall response is computed incrementally. The incremental EMT procedure is as follows. First, the matrix tangent modulus is computed from the matrix elastic and plastic moduli using the Ramberg-Osgood relation. This allows the computation of the composite instantaneous stiffness tensor by the standard EMT model and fiber-orientation averaging technique. Next, the matrix-strain increment resulting from the overall strain increment is calculated (using the fiber and matrix-strain-concentration tensors) to compute the matrix stress increment. The matrix-stress is then updated to calculate the matrix equivalent stress using the deformation theory of plasticity.

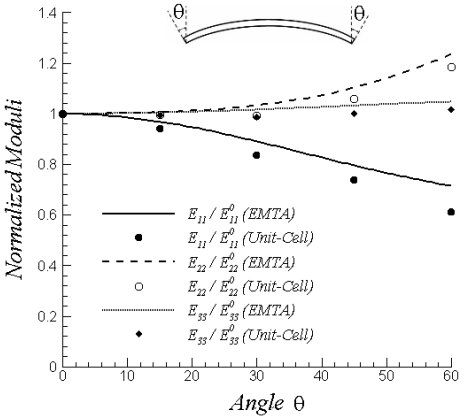

Figure 6. Variation of the normalized moduli with the end-angle θ representing fiber curvature. The values of the moduli for straight fibers (θ =0) were used for the normalization. EMTA stands for the Eshelby-Mori-Tanaka approach.

Finally, the matrix equivalent plastic strain is updated using Eq. (2) and is saved to start the next increment. Also, the composite overall stress is updated. At each increment, potential failure of the composite is predicted using the Van Hattum-Bernado model [13]. This model expresses the Tsai-Wu failure criterion in terms of matrix and fiber strengths based on the Kelly-Tyson model [14] and fiber-orientation tensors to account for the fiber-orientation effect on the composite strength.

The elastic-plastic and strength-prediction model was implemented into the ABAQUS finite-element code by means of user subroutines. Fiber-orientation data from process modeling or measurement were imported into an ABAQUS analysis via a utility subroutine of this code. In addition, FOD is represented by the Weibull's distribution in terms of weight of fibers versus fiber length. Figures 7 and 8 show the tensile longitudinal and in-plane transverse responses predicted by this model for a LFT glass/PP ISO-plaque. Measured FOD was used in the computation. On these figures are also presented the experimental results for this specimen. It has been found that the model predicts well the longitudinal stress-strain behavior up to a certain loading level (about 2/3 of the experimental strength). After that, the experimental curves become more nonlinear than the predicted one. In fact, progressive damage became more and more important about the end of the loading leading to pronounced nonlinearity observed in the experimental curves. Progressive damage is being studied, and the effect on the composite response will be discussed in our next report.

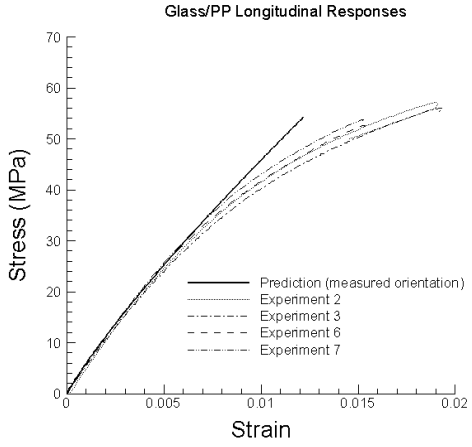

Figure 7. Predicted and experimental longitudinal stress/strain responses for a glass/PP ISO-plaque.

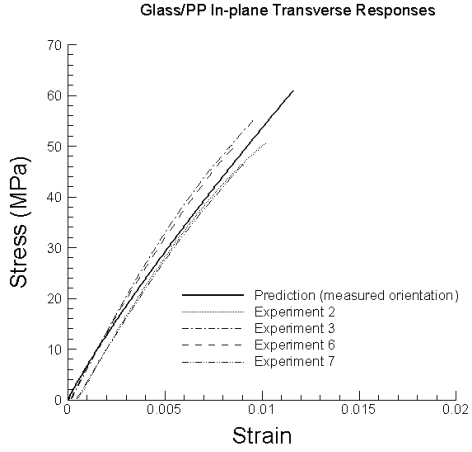

Figure 8. Predicted and experimental in-plane transverse stress/strain responses for a glass/PP ISO-plaque.

A Fiber Orientation Model for LFTs

Previously, an assessment of process models showed that using a large value of the interaction coefficient C_I in the RSC model allowed a correct prediction of the flow-direction component, A_{11} of the second-order fiber-orientation tensor [2, 15]. However, the thickness-direction component A_{33} was then over-predicted, resulting in the under-prediction of the cross-flow component A_{22}. Thus, it was necessary to develop a better fiber-orientation model for LFTs. The Folgar-Tucker model accounted for fiber-fiber interactions through the isotropic rotary diffusion governed by C_I [16-17]. It was hypothesized that accounting for such interactions with ARD would allow us to better capture the FOD in LFTs. Such a model then replaces the scalar C_I with a tensorial description **C** for the fiber-fiber interactions.

Phan-Thien and Fan [18] proposed a fiber-orientation model using ARD. However, the Phan-Thien/Fan model's diffusion term failed to return the fibers to an isotropic orientation at steady state, a necessary condition of any diffusion model. To correct the Phan-Thien/Fan model, an expression for rotary diffusion was developed that was defined on the surface of the unit sphere traced by all orientations of the unit vector **p** [19]. The expression for the ARD model to properly match the LFT fiber orientation data is:

$$\dot{\mathbf{A}} = (\mathbf{W}.\mathbf{A} - \mathbf{A}.\mathbf{W}) + \xi(\mathbf{D}.\mathbf{A} + \mathbf{A}.\mathbf{D} - 2\overline{\overline{\mathbf{A}}}:\mathbf{D}) + \dot{\gamma}(2\mathbf{C} - 2(\mathrm{tr}\mathbf{C})\mathbf{A} - 5(\mathbf{C}.\mathbf{A} + \mathbf{A}.\mathbf{C}) + 10\overline{\overline{\mathbf{A}}}:\mathbf{C}) \quad (3)$$

where **A** and $\overline{\overline{\mathbf{A}}}$ are the second- and fourth-order orientation tensors, respectively. $\dot{\mathbf{A}} = D\mathbf{A}/Dt$ with t being the time. **W** is the vorticity tensor, and **D** is

the rate of the deformation tensor. $\dot{\gamma}$ is the scalar magnitude of **D**, and ξ is the shape parameter (ξ=1 for any fiber). Tensor **C** is constructed from the **A** and **D** tensors as:

$$\mathbf{C} = b_1\mathbf{I} + b_2\mathbf{A} + b_3\mathbf{A}^2 + b_4\frac{\mathbf{D}}{\dot{\gamma}} + b_5\frac{\mathbf{D}^2}{\dot{\gamma}^2} \qquad (4)$$

where b_i (i=1,..,5) are the scalar constants. A systematic method of selecting b_i was developed in [18] to ensure stable and valid orientation solutions. To properly match experimental orientation data, one may need to slow the predicted orientation dynamics of a given model. For instance, the RSC model [8] can objectively slow the orientation dynamics of the Folgar-Tucker model. Treating the ARD model similarly, the ARD-RSC model is obtained as:

$$\begin{aligned}\dot{\mathbf{A}}^{\mathrm{ARD-RSC}} &= (\mathbf{W}.\mathbf{A} - \mathbf{A}.\mathbf{W}) \\ &+ \xi(\mathbf{D}.\mathbf{A} + \mathbf{A}.\mathbf{D} - 2[\overline{\overline{\mathbf{A}}} + (1-\kappa)(\overline{\overline{\mathbf{L}}} - \overline{\overline{\mathbf{M}}} : \overline{\overline{\mathbf{A}}})] : \mathbf{D}) \\ &+ \dot{\gamma}(2[\mathbf{C} - (1-\kappa)\overline{\overline{\mathbf{M}}} : \mathbf{C}] - 2\kappa(\mathrm{tr}\mathbf{C})\mathbf{A} \\ &- 5(\mathbf{C}.\mathbf{A} + \mathbf{A}.\mathbf{C}) + 10[\overline{\overline{\mathbf{A}}} + (1-\kappa)(\overline{\overline{\mathbf{L}}} - \overline{\overline{\mathbf{M}}} : \overline{\overline{\mathbf{A}}})] : \mathbf{C})\end{aligned} \qquad (5)$$

where **C** is given by Eq. (4). $\overline{\overline{\mathbf{L}}}$ and $\overline{\overline{\mathbf{M}}}$ are the fourth-order tensors that are defined in terms of the eigenvalues and eigenvectors of **A**. κ (<1) is a scalar parameter which controls the rate of orientation dynamics. With κ = 1/30 and b_1 = 7.848×10^{-4}, $b_2 = 2.357 \times 10^{-2}$, $b_3 = 1.0 \times 10^{-2}$, $b_4 = 1.168 \times 10^{-5}$, and $b_5 = -3.0 \times 10^{-3}$], an excellent fit to all the experimental orientation data was obtained for the LFT glass/PP ISO-plaque (Figs 9 and 10).

Experimental Characterization of Fiber Length Distribution

Techniques developed for sample and fiber separation for FLD measurement were described in our previous reports. Figure 11 shows FLD measurement results for the glass/PP and carbon/PP center-gated disks. Results for slow and fast cavity mold filling speeds are presented. The results indicate that slow cavity-filling speed results in greater retention of longer fibers, whereas fast mold-filling speed induces greater fiber-length attrition. This result was expected.

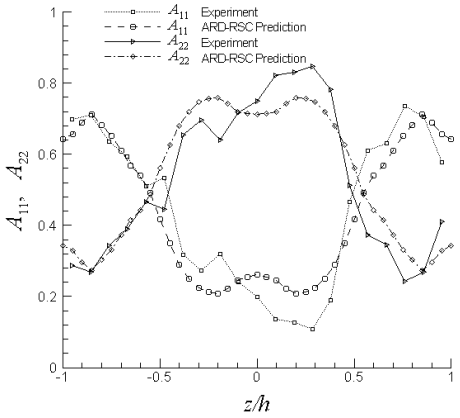

Figure 9. Predicted (by the ARD-RSC model) and measured fiber-orientation tensor components A_{11} and A_{22} for a glass/PP ISO-plaque.

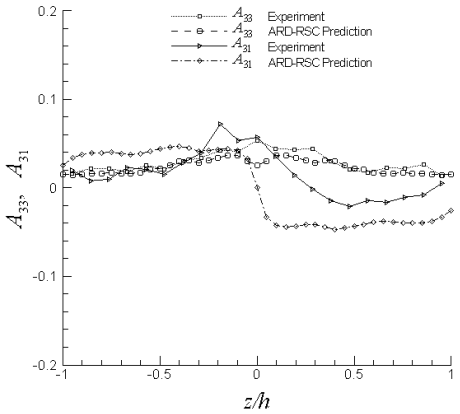

Figure 10. Predicted (by the ARD-RSC model) and measured fiber-orientation tensor components A_{33} and A_{31} for a glass/PP ISO-plaque.

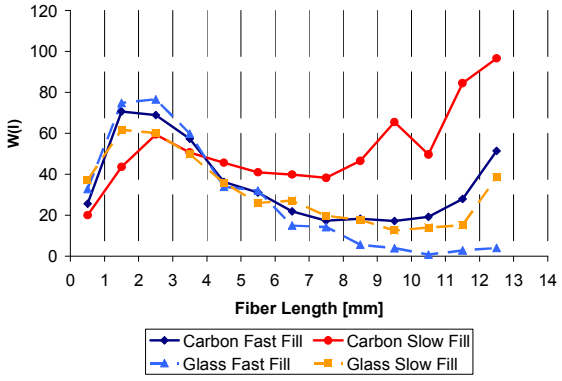

Figure 11. Measured weighted FLDs for disk specimens.

Figure 11 also indicates greater retention of long fibers in carbon/PP samples. This result was not expected due to the perceived brittleness of carbon

fibers. Greater retention of fiber length can be caused by higher strength of carbon filaments used in the material and/or by smaller diameter of carbon fibers in comparison with glass fibers. If one assumes that screw action, shear flow and fiber-fiber interactions subject filaments to bending, fibers with smaller diameter would experience lower stress compared to fibers with larger diameter at identical displacement.

Results presented in Figure 11 were measured manually using ImageJ [20] software and the sample population was 2000 fibers. The number of fragments below 0.3 mm in size was estimated, and correction for preferential selection of longer fibers was applied before using these measurements in calculations referenced above. Measurements on a limited number of identical samples were performed separately by ORNL and PNNL to validate the measurement techniques and the results matched each other very closely. Development of automated software, which would measure most of the fiber lengths automatically and which would separate problematic regions for manual measurement, yielded mixed results due to very short fragments being present in realistic samples. While the software measured a large number of fiber lengths, the number of fibers left over for manual measurement was still too large for a realistic sample size.

Mechanical Testing

Mechanical tests were performed to determine elastic properties in flow and cross-flow directions. Most of the tests were performed to increase the number of replicate data points for samples molded at Delphi. A limited number of carbon/PP ISO plaques molded at PNNL were also evaluated. Measurement averages performed on three or more replicates are presented in Table 3. Carbon/PP samples molded at PNNL exhibited poor fiber/matrix adhesion resulting in soft failure at lower than expected loads. This behavior was previously observed in the carbon/PP center-gated disks molded by Delphi and indicates the need to optimize carbon-fiber sizing for the given thermoplastic matrix. Neat PP samples exhibited strong strain-rate dependency indicated in Figure 12.

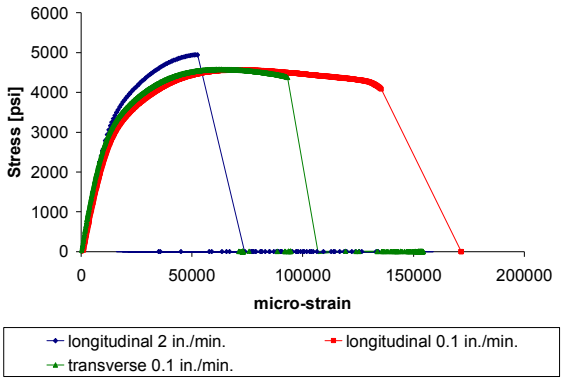

Figure 12. Stress-strain behavior of samples obtained from neat PP ISO plaques indicating strain-rate dependence.

These results were obtained from dog-bone specimens designed to eliminate grip failures and to accommodate existing plaque sizes. Identical specimen dimensions were subsequently used to obtain stress-strain behavior of LFT glass/PP samples. These tests provided consistent stress-strain curves as indicated in Figure 13. Measurements were performed for the entire set of glass-filled ISO plaques and for comparison with the elastic-plastic predictions (see Figures 7-8).

	AS3D	**AF3D**	**AS3I**	**AF3I**
$\overline{E}_{11}$ (MPa)	5305	4905	6370	6063
$\overline{E}_{22}$ (MPa)	7521	7698	7213	7211
	BS3D	**BF3D**	**PP31C**	
$\overline{E}_{11}$ (MPa)	7821	7256	10070	
$\overline{E}_{22}$ (MPa)	12031	10161	9486	

Table 3. Experimentally-measured stiffness values for glass/PP and carbon/PP disk and ISO specimens.

AS3D: 3-mm slow-fill glass/PP center-gated disk
AF3D: 3-mm fast-fill glass/PP center-gated disk
AS3I: 3-mm slow-fill glass/PP ISO-plaque
AF3I: 3-mm fast-fill glass/PP ISO-plaque
BS3D: 3-mm slow-fill carbon/PP center-gated disk
BF3D: 3-mm fast-fill carbon/PP center-gated disk
PP31C: 3-mm fast-fill carbon/PP ISO-plaque

Advanced Characterization of Fiber Architecture

Description of fiber architecture was so far confined to FODs and FLDs. Properties of LFTs

are strongly influenced by these distributions; however, it became apparent through observation and through analytical work that these measures do not describe fiber architecture of LFTs with the

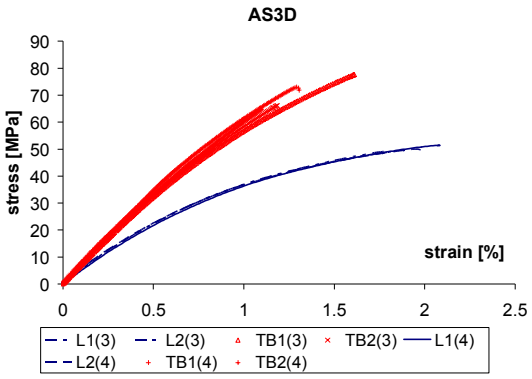

Figure 13. Four replicates of stress-strain curves for longitudinal (L) and transverse (TB) specimens show consistent measurements of material properties obtained from dog-bone specimens.

same fidelity as for short-fiber-reinforced thermoplastics. Fiber curvature and the nature of fiber entanglement appear to have significant influence on properties of LFTs. X-ray micro-tomography can be used to evaluate the fiber network inside a small LFT sample. Tomography reconstruction must be of high quality for fiber surface and fiber ends to be clearly distinguishable. This required reduction of specimen size to approximately 0.5 mm x 0.5 mm and long exposure time. After reducing the size of the specimens used for fiber-orientation measurement by the Leeds' system, it was possible to match individual filaments in the micrograph of Leeds' samples and in the tomography reconstruction. Filaments identified on the polished surface were subsequently tracked below the surface to establish their curvature and depth below the surface. Figure 14 shows section of a micrograph of an AS3D Leeds' sample and corresponding section of tomography reconstruction showing behavior of filaments below the polished surface. Tracking of filaments has been performed manually; however, techniques to accomplish this using software are being investigated.

Design of Testing Equipment for X-Ray Micro-Tomography Unit

The micro-tomography unit located at ORNL is being used to evaluate the microstructure of LFTs. These investigations have shown significant fiber curvature being present in the samples. Fiber curvature may influence elastic properties, as discussed in the previous section, and it likely influences non-linear and ultimate properties of the material. A testing machine capable of operating within the tomography unit was designed in order to evaluate the effect of fiber curvature as well as the presence of short fiber fragments and non-uniform fiber distribution on the strain state of a sample subjected to mechanical loading. Solid modeling and finite-element analysis were used to ensure load capacity of 300 lbf and 150° of unobstructed view necessary for full three-dimensional (3D) reconstruction of fiber-reinforced sample loaded to failure (Figure 15).

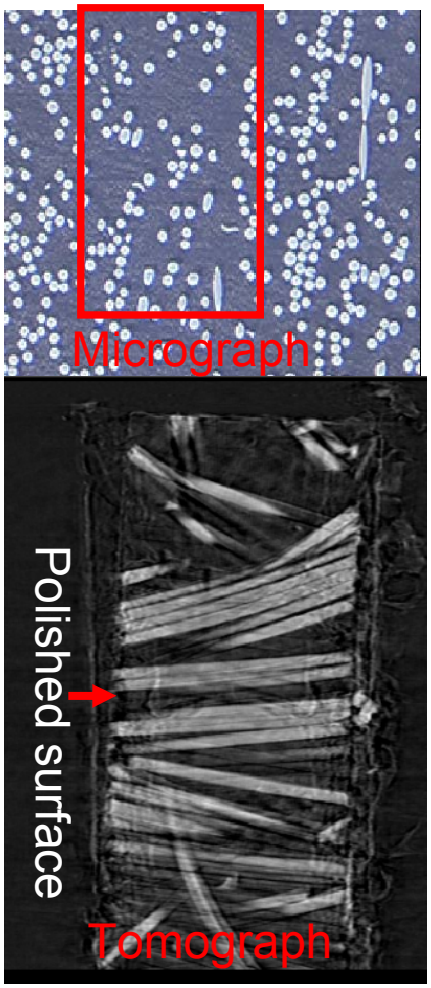

Figure 14. AS3D micrograph and corresponding section of tomography reconstruction.

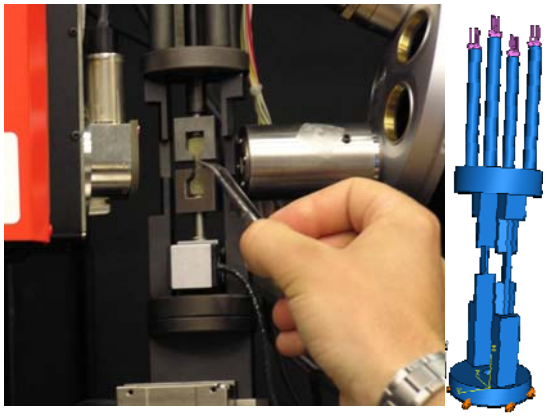

Figure 15. Testing machine within X-ray micro-tomography unit and corresponding solid model.

First, it has been proven that it was possible to obtain 3-D reconstruction of LFT sample subjected to load. Even though the specimen may relax significantly during imaging necessary for full reconstruction, individual filaments can be clearly distinguished. Post-failure investigations confirm previous observations of fiber bridging across initial crack opening. Figure 16 shows reconstruction of fiber architecture after failure and its section showing a region in which fibers still bridge from one crack surface to another.

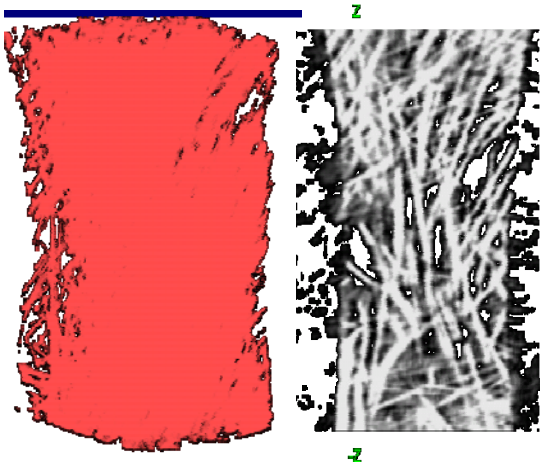

Figure 16. Tomography reconstruction and its section showing fiber bridging in LFTs after initial failure.

It was still necessary to apply load, albeit low in magnitude, to pull out or break these remaining fibers. Observations performed with this new tool should allow better identification of damage processes active within material under load. Understanding these processes will enable us to develop better predictive tools for LFTs.

Conclusions

Computational tools were developed to successfully predict the thermoelastic properties of LFTs. In addition, fiber curvature and fiber/matrix debonding were modeled and their effects on the LFT elastic properties were determined. An elastic-plastic model associated with a failure criterion was developed and implemented in ABAQUS to predict the stress-strain responses of LFTs until failure. The elastic-plastic responses agreed fairly well with the experimental results.

A fiber-orientation model for LFTs was developed that replaces the isotropic rotary diffusion term in the Folgar-Tucker model by an anisotropic rotary tensorial expression. The ARD model can provide more accurate predictions of fiber orientation in LFTs.

Methods have been established to efficiently measure fiber-length distributions in LFTs for property predictions. These methods have been applied to obtain FLDs in LFT samples. Also, it has been found that the correction of the FLD raw data is necessary for more accurate property predictions. The Weibull's distribution can accurately represent the actual distribution for weight of fiber lengths. Fiber curvature has been observed in LFT samples using X-ray micro-tomography, and the effect of fiber curvature on the composite elastic properties has been investigated and modeled.

Finally, testing equipment for the X-ray micro-tomography unit has been designed to allow observing the microstructure of LFT samples. The developed methodology is very promising for characterizing the composite microstructure that is needed in the analysis of the LFT nonlinear behavior due to damage.

References

[1] P.J. Hine, N. Davidson, R. A. Duckett, A. R. Clarke, I. M. Ward (1996). "Hydrostatically Extruded Glass-Fiber-Reinforced Polyoxy-methylene. I: The development of Fiber and Matrix Orientation." *Polym. Compo.*, 17:720-729.

[2] B.N. Nguyen, J.D. Holbery, V. Kunc (2006). "Engineering Property Prediction Tools for Tailored Polymer Composite Structures." In:

Automotive Lightweighting Materials, DOE Office of FreedomCAR and Vehicle Technologies, *FY 2006 Progress Report*.

[3] B.N. Nguyen, V. Kunc, B.J. Frame, J.H. Phelps, C.L. Tucker III, S.K. Bapanapalli, J.D. Holbery, M.T. Smith (2007). "Fiber Length and Orientation in Long-Fiber Injection-Molded Thermoplastics – Part I: Modeling of Microstructure and Elastic Properties." *J. Comp. Mater.* (submitted).

[4] J.D. Eshelby (1957). "The Determination of The Elastic Field of An Ellipsoidal Inclusion and Related Problems." *Proc. Royal Soc. London*, A 241:376-396.

[5] T. Mori, K. Tanaka (1973). "Average Stress in Matrix and Average Elastic Energy of Materials with Misfitting Inclusions." *Acta Metall.*, 21:571-574.

[6] S.G. Advani and C.L. Tucker III (1987). "The Use of Tensors to Describe and Predict Fiber Orientation in Short-Fiber Composites." *J. Rheol.*, 31 (8):751-784.

[7] C. Camacho, C.L. Tucker III, S. Yalvac, R.L. McGee (1990). "Stiffness and Thermal Expansion Predictions for Hybrid Short-Fiber Composites." *Polym. Compos.*, 11:229-239.

[8] C.L. Tucker III, J. Wang, and J.F. O'Gara (2007). "Method and Article of Manufacture for Determining a Rate of Change of Orientation of A Plurality of Fibers Disposed in A Fluid. U. S. Patent No. 7,266,469. See also Wang J., O'Gara J. F., and Tucker III, C. L. (2007). "An Objective Model for Slow Orientation Kinetics in Concentrated Fiber Suspensions: Theory and Rheological Evidence." *J. Rheol.* (submitted).

[9] S.K. Bapanapalli, B.N. Nguyen (2007). "Prediction of Elastic Properties for Curved Fiber Polymer Composites." *Polym. Compos. (in press).*

[10] J. Qu (1993). "The Effect of Slightly Weakened Interfaces on the Overall Elastic Properties of Composite Materials," *Mech. Mater*." 14:269-281.

[11] A.S. Khan, S. Huang (1995). "Continuum Theory of Plasticity." Wiley InterScience, New York.

[12] J. Aboudi (1991). "Mechanics of Composite Materials." Elsevier Science Publishers, Amtersdam, The Netherlands.

[13] F.W.J. Van Hattum, C.A. Bernado (1999). "A Model to Predict the Strength of Short Fiber Composites." *Polym. Compos.*, 20(4):524-533.

[14] A. Kelly, W.R. Tysons (1965). "Tensile Properties of Fibre-Reinforced Metals: Copper/Tungsten and Copper/Molybdenum." *J. Mech. Phys. Solids*, 13:329-350.

[15] J.H. Phelps and C.L. Tucker III (2006). "Assessing Fiber Orientation Prediction Capability for Long-Fiber Thermoplastic Composites." Technical Report submitted to PNNL, University of Illinois at Urbana-Champaign, IL 61801.

[16] R.S. Bay, C.L. Tucker III (1992). "Fiber Orientation in Simple Injection Moldings. Part I: Theory and Numerical Methods." *Polym. Compos.*, 13: 317-331.

[17] F. Folgar, C.L. Tucker III (1984). "Orientation Behavior of Fibers in Concentrated Suspensions."*J. Reinf. Plast. Comp.*, 3: 98-119.

[18] N. Phan-Thien, X.-J. Fan, R. I. Tanner, and R. Zheng (2002). "Folgar-Tucker Constant for A Fibre Suspension in A Newtonian Fluid. *J. Non-Newt. Fluid Mech.*, 103:251-260.

[19] Phelps, J.H., Tucker III, C.L. (2006). "The Anisotropic Rotary Diffusion Model for Fiber Orientation." Technical Report submitted to PNNL, University of Illinois at Urbana-Champaign, Urbana, IL 61801.

[20] Rasband, W.S., ImageJ, U. S. National Institutes of Health, Bethesda, Maryland, USA, http://rsb.info.nih.gov/ij/, 1997-2005.

Presentations/Publications/Patents

[1] G. Velez-Garcia, V. Kunc (2006). "Experimental Methods to Evaluate Fiber Length and Orientation Distribution of Long Glass Fibers in Injection Molded Thermoplastics." Presented at Fiber Society Conference, Knoxville, TN, October 10-12, 2006.

[2] S.K. Bapanapalli, B.N. Nguyen (2007). "Prediction of Elastic Properties for Curved Fiber Polymer Composites." *Polym. Compos.* (*in press*).

[3] B.N. Nguyen, V. Kunc, B.J. Frame, J.H. Phelps, C.L. Tucker III, S.K. Bapanapalli, J.D. Holbery, M.T. Smith (2007). "Fiber Length and Orientation in Long-Fiber Injection-Molded Thermoplastics - Part I: Modeling of Microstructure and Elastic Properties." *J. Comp. Mater*. (submitted).

[4] B.N. Nguyen, V. Kunc, B.J. Frame, J.H. Phelps, C.L. Tucker III, S.K. Bapanapalli, J.D. Holbery, M.T. Smith (2007). "From Process Modeling to Elastic Property Prediction for Long-Fiber Injection-Molded Thermoplastics." Proc. 7th Annual SPE Automotive Composites Conference & Exposition, Detroit, Sep. 11-13, 2007

[5] V. Kunc V, B.J. Frame, B.N. Nguyen, C.L. Tucker III, G. Velez-Garcia (2007). "Fiber Length Distribution Measurement for Long Glass and Carbon Fiber Reinforced Injection Molded Thermoplastics." Proc. 7th Annual SPE Automotive Composites Conference & Exposition, Detroit, 11-13, 2007.

[6] B.N. Nguyen, V. Kunc, M.T. Smith (2007). "Prediction of Elastic Properties for Long-Fiber Thermoplastic Injection-Molded Composites." Presented at the 2007 ASME Applied Mechanics and Materials Conference (McMat 2007), Austin, TX, June 3-7, 2007.

K. Predictive Modeling of the Structure and Properties of Polymer-Matrix Composites: NSF/DOE Grant Projects

Principal Investigator: BN Nguyen
Pacific Northwest National Laboratory (PNNL)
P.O. Box 999, Richland, WA 99352
(509) 375-3634, e-mail: ba.nguyen@pnl.gov

Principal Investigator: Vlastimil Kunc
Oak Ridge National Laboratory (ORNL)
One Bethel Valley Road, Oak Ridge, TN 37831-6053
(865) 574-8010, e-mail: kuncv@ornl.gov

DOE Technology Area Development Manager: Joseph A. Carpenter
(202) 586-1022; fax: (202) 586-1600; e-mail: joseph.carpenter@ee.doe.gov

National Science Foundation (NSF) Grant Monitor: Joycelyn S. Harrison
(703) 292-7088; e-mail: j-harris@nsf.gov

Contractor: PNNL
Contract No.: DE-AC06-76RL01830

Objective

- The objective of these six projects, jointly funded by NSF and DOE and administered by NSF as grants, is to perform fundamental development of modeling, simulation and processing of polymer composite materials. These projects support the DOE-funded "Engineering Property Prediction Tools for Tailored Polymer Composite Structures" project being conducted jointly by ORNL and PNNL (see 8.J). The NSF/DOE-funded projects are intended to investigate alternate modeling and processing approaches that can contribute to more fundamental understanding of the mathematical and physical behavior of fiber-reinforced polymer composites. The following sections provide a high-level summary of the grant objectives and work progress during 2007. Each of the projects was extensively outlined in the Automotive Lightweighting Materials annual progress report for fiscal year (FY) 2006 and detailed reports providing significantly higher levels of detail for the work accomplished during FY 2007 are available through NSF. The publications listed at the end of each section also provide more details.

Comparative Determinations of Orientation in Injection-Molded Thermotropic Liquid-Crystalline Copolyester (TLCP) Plaques

Wesley R. Burghardt, Ph.D.
Department of Chemical & Biological Engineering
Northwestern University
2145 Sheridan Road, Room E136
Evanston, IL 60208
(847) 467-1401; fax: (847) 491-3728;
e-mail: w-burghardt@northwestern.edu

NSF Award ID: 0521823

Research and Education Activities

During 9/1/06 thru 8/31/07, we made considerable progress on both experimental and simulations aspects of this project.

On the experimental side, the new graduate student working on this project (Mr. Fang) led a synchrotron run at the Advanced Photon Source to implement refinements in our *in situ* injection-molding experiment. New capabilities were added to monitor time-dependent changes in the pressure of the molding machine, pneumatic supply, and temperature within the mold. Acquisition of these

signals was coordinated with collection of x-ray scattering data, in order to allow closer coordination between the time-resolved structural data and the actual stages of mold filling. In addition, a second mold geometry (T-shaped plaque) was fabricated and tested, in order to see how variations of mold geometry influence orientation development. A second synchrotron run was performed in summer 2007 in order to obtain high quality *ex situ* scattering data on the same plaques produced during the time-resolved *in situ* experiments. Analysis of these data is still pending; this is a necessary step to fully interpret the *in situ* data. Dr. Bubeck (collaborator from Michigan Molecular Institute (MMI)) participated in each of these experiments. Finally, Mr. Fang has continued involvement with the surface orientation studies led by MMI.

Significant progress has also been made in adapting process-simulation software to simulate orientation distributions in complex processing flows of thermotropic liquid-crystal polymers (TLCPs). This approach relies on a strong analogy between the Larson-Doi polydomain model for liquid crystalline polymers, and the Folgar-Tucker fiber-orientation model that is widely used in composites processing. Mr. Fang has nearly completed an extensive set of simulations of isothermal, complex-channel flows, allowing detailed testing of the performance of this modeling approach against extensive x-ray scattering data previously collected in our flow experiments using x-ray scattering in a unique channel-flow extrusion die. Future efforts will concentrate on extending the simulation effort to *ex situ* and *in situ* data from injection molding.

Beyond the primary purpose of the project as the focal point in Mr. Fang's graduate education, results were also disseminated to the broader community via two conference presentations during 2006-07 (Society of Rheology and American Institute of Chemical Engineers), both focusing on our new *in situ* injection-molding capabilities.

Findings

Refinements to the *in situ* molding apparatus will allow for more meaningful analysis and presentation of data relative to events during the injection-molding cycle. Detailed conclusions from the latest experiments are still pending, awaiting completion of analysis of data from our most recent experiments.

Our first extensive series of simulations have demonstrated that the Larson-Doi polydomain model (and the simulation strategy drawing upon the Folgar-Tucker analogy) are quite capable of predicting many subtle details of how orientation develops in complex flows of liquid-crystalline polymers. This is the first time such simulations have been performed.

Journal Publications

- Rendon, S.; Burghardt, W. R.; Bubeck, R.A., "Orientation Dynamics in Commercial Thermotropic Liquid Crystalline Polymers in Transient Shear Flows", Rheologica Acta, (2007).
- Rendon, S.; Bubeck, R. A.; Thomas, L. S.; Burghardt, W.R.; Hexemer, A.; Fischer, D. A., "Interrogation of 'Surface', 'Skin' and 'Core' Orientation in Thermotropic Liquid Crystalline Copolyester Moldings by Near-Edge X-ray Absorption Fine Structure and Wide-Angle X-ray Scattering", Journal of Applied Polymer Science, (2007).

A Hierarchical, Structure-Oriented and Stochastic Approach to Model Liquid Molding Processes

Thanasis D. Papathanasiou
Department of Chemical Engineering
University of South Carolina
Columbia, SC 29208
(803) 777-7219; fax: (803) 777-6245;
e-mail: papathan@engr.sc.edu

NSF Award ID: 0522221

Research and Education Activities

Our research activities in the previous year were focused on the following:

(1) Continued to develop microstructure-generation codes and to test/propose metrics that quantify microstructural features such as fiber clustering. A Monte-Carlo method was implemented using a Lennard-Jones inter-fiber potential and microstructures exhibiting various degrees of clustering were generated.

(2) Continued to investigate the effects of microstructure on the permeability of unidirectional fibrous media, using in-house two-dimensional (2D) and parallel-boundary-element codes. Specifically, the effects of non-uniform inter-tow and intra-tow fiber packing and random fiber clustering were studied.

(3) Started to implement a parallel-boundary-element code for solving three-dimensional Stokes flow problems.

(4) Started to implement the Fast Multipole Boundary Element Method (FMBEM). The FMBEM for solving 2D potential flow problems has been applied to study the barrier-improvement factor in flake-filled membranes.

In the same period we attended:

(1) A Workshop titled 'A short course on the Fast Multipole Boundary Element Method', Los Angeles, California, USA. July 22, 2006.

(2) The annual SPE Conference ANTEC 2007, Cincinnati, Ohio, USA. May 7-11, 2007.

Findings

Further details on our activities are included in the full NSF report. Principal technical focus and findings include:

(1) Computation of the effects of microstructure on the permeability of unidirectional fibrous media was performed. Specifically, the effects of non-uniform inter-tow and intra-tow fiber packing and random fiber clustering were studied.

(2) Quantification of fiber clustering was performed using a metric derived from Ripley's K-function.

(3) Benchmarking of the performance of a parallel-boundary-element code for solving three-dimensional Stokes flow problems was completed using two different matrix assembly parallelization strategies.
(4) Use of a Fast Multipole Boundary Element Method code to investigate the effect of internal structure on the mass flux across random arrays of impermeable flakes was completed.

Journal Publications

1. Chen X. and T.D. Papathanasiou, 'The transverse permeability of disordered fiber arrays: A statistical correlation in terms of the mean interfiber spacing', Transport in Porous Media, accepted, 3/2007.
2. Chen X. and T.D. Papathanasiou, 'Micro-Scale Modeling of Axial Flow through Unidirectional Disordered Fiber Arrays', Composites Science and Technology, 67 (2007) 1286-1293
3. Xiaoming Chen and T.D. Papathanasiou, "The transverse permeability of disordered fiber arrays: A statistical correlation in terms of the mean interfiber spacing", Transport in Porous Media, accepted 3/2007
4. X.Chen and T.D.Papathanasiou, "Permeability of Flake-filled Barrier Membranes: A Numerical Evaluation", SPE ANTEC-2007 Proceedings, paper # 0621, p. 621, (2007). Published.

Linking Process-Induced Properties to Thermoplastic-Matrix Woven-Fabric Composites

Principal Investigator: James A. Sherwood
Department of Mechanical Engineering
University of Massachusetts Lowell
One University Avenue
Lowell, MA 01854
(978) 934-3313; fax: (978) 945-5701;
e-mail: James_Sherwood@uml.edu

NSF Award ID: 033126

Research and Education Activities

The major research activities have been in the area of studying the friction between a woven, commingled glass-polypropylene fabric and the steel tool for thermoforming processes. Additional research has been conducted in the area of material modeling techniques using classical mechanics of materials approaches and the finite-element method (FEM).

Findings

According to a parametric study conducted using a finite-element model of the thermostamping process with the empirical friction model developed in this research, increasing the velocity of the punch increased the reaction force on the punch more than increasing the binder force. Thus, it is important to incorporate a friction model based on changing processing parameters into predictive

numerical simulations. Otherwise, the reaction force on the punch could be greatly over-predicted or under-predicted.

A normalization method was proposed for the picture-frame tests. It was found that using this normalization method, the test data obtained using different sizes of picture frames and specimens could be normalized so that they were comparable.

A finite-element model composed of a combination of shell and truss elements could be used to build a model for woven-fabric composites. The shell elements can represent the interactions among tows and the truss elements can represent the tows. The hybrid finite-element model could be used to simulate the picture-frame test, bias-extension test and the thermostamping process. The results, including the reaction force and the distributions of stress and strain in the stamped part, could be used to predict and to optimize the real manufacturing process.

A user-defined subroutine containing the friction model resulting from this research was developed for use with ABAQUS implicit finite-element modeling software. This friction model is for use with glass-polypropylene woven-fabric composites in contact with a steel tool during thermoforming processes. Two user-defined subroutines containing the material models resulting from this research were developed for use with ABAQUS implicit finite-element modeling software. These material models are for use with glass-polypropylene woven-fabric composites during thermoforming processes. Currently, these numerical tools are being shared with our research partners at Northwestern University to advance the research supported by this grant. ABAQUS, Inc. has expressed interest in incorporating this friction subroutine into future releases of their finite element package. It will be available on the website (http://m-5.uml.edu/acmtrl).

Related Journal Publications

There were no publications on this project to-date. The following references are provided for information:

1. Gorczyca, J., Sherwood, J. and Chen, J., "Friction between the Tool and the Fabric During the Thermostamping of Woven Co-Mingled Glass-Polypropylene Composite Fabrics", Proceedings for the 18th Annual American Society for Composites Conference, p. 1, vol. CD, (2003).
2. Gorczyca, J., Sherwood, J., Lu, L. and Chen, J., "Friction and Shear in Thermostamping of Composites - Part I", Journal of Composite Materials, p. 1911, vol. 38, (2004).
3. Gorczyca, J., Sherwood, J. and Chen, J., "Friction Model for use with a Commingled Fiberglass-Polypropylene Plain-Weave Fabric and the Metal Tool during Thermostamping", European Finite Element Revue, p. 729, vol. 14, (2005).
4. Composite Fabrics: FEA with User-Defined Subroutines in ABAQUS/Standard", Proceedings for the 19th Annual American Society for Composites Conference, p. 1, vol. CD, (2004).
5. Li, X., Sherwood, J., Liu, L. and Chen, J., "A material model for woven commingled glass-polypropylene composite fabrics using a hybrid finite element approach", International Journal of Material Product & Technology, p. 59, vol. 21, (2004).
6. Li, X., Sherwood, J. Lu, L., Chen, J., "Material Model and Finite Element Model for Woven Commingled Glass-Polypropylene Composite Fabrics", Proceedings for the 18th Annual American Society for Composites Conference, p. 1, vol. CD, (2003). Published,
7. Lu Liu, Julie Chen, Xiang Li, James Sherwood, "Two-Dimensional Macro-Mechanics Shear Models of Woven Fabrics", Composites Part A, p. 105, vol. 36, (2005). Published,
8. Lu Liu, Julie Chen, Jennifer Gorczyca, James Sherwood, "Modeling of Friction and shear in thermo-stamping process - Part II", Journal of Composite Materials, p. 1931, vol. 38, (2004).
9. Lu Liu, Julie Chen, James Sherwood, "Material Modeling and Benchmark Testing of Woven-Fabric Composites in the Thermo-Stamping Process", 7th ESAForm Conference paper, p. 357, vol. 7, (2004).
10. Lu Liu, Julie Chen, James Sherwood, "Analytical Model of Shear of 4-harness Satin Weave Fabrics", 8th Numiform Conference paper, p. 338, vol. CP712, (2004).
11. Lu Liu, Julie Chen, James Sherwood, "Parametric Study of Commingled Glass/Polypropylene Woven Fabrics during Shear", Proceedings of the 19th annual

American Society for Composites conference, p. 1, vol. CD, (2004).
12. Peng XQ, Cao J, Chen J, Xue P, Lussier D, Liu L, "Experimental and numerical analysis on normalization of picture frame tests for composite materials", Composites Science Technology, p. 11, vol. 64, (2004).
13. Li, X., Sherwood, J., Liu, L., and Chen, J., "Hybrid Finite Element Model of Woven-Fabric Composite", Proceedings of the 19th Annual American Society for Composites, p. 1, vol. CD, (2004).
14. J.L. Gorczyca, J.A. Sherwood, J. Chen, "Friction at the Tool-Fabric Interface during the Thermostamping of Woven Commingled Glass-Polypropylrnr Composite Fabrics", Proceedings of the 7th Esaform Conference on Material Forming, p. 337, vol. 7, (2004).
15. X. Li, J.A. Sherwood, L.Liu, J. Chen, "Simulation of Double-Dome Stamping of Twill Woven Fabric Composites", Proceedings of the 8th Esaform Conference on Material Forming, p. 1003, vol. II, (2005).
16. X. Li, J. Sherwood, J. Gorczyca, J. Chen, L. Liu, "A Study of the Thermostamping Process for a Woven-Fabric Composite", Third M.I.T. Conference on Computational Fluid and Solid Mechanics, p. 229, (2005).
17. L. Liu, J. Chen, "A solid mechanics shear model of commiingled glass/polypropylene woven fabrics", Third M.I.T. Conference on Computational Fluid and Solid Mechanics, p. 237, (2005).
18. Gorczyca, J., Sherwood, J. and Chen, J., "Development of a Friction Model for Use in the Thermostamping of Commingled Glass-Polypropylene Woven Fabrics", Composites Part A, p. 393, vol. 38, (2007).
19. Xiang Li, James A. Sherwood, Lu Liu, and Julie Chen, "Simulation of Double Dome Stamping of Twill Woven Fabric Composites", Proceedings of the 8th ESAForm Conference on Material Forming, Cluj, Romania, p. 1, vol. 8th, (2005).

Incorporating Higher Order Tensors in the Computation of Polymer Composite Mechanical Properties

Principal Investigator (PI): Douglas E. Smith
University of Missouri at Columbia
E2411 Lafferre Hall/MAE Dept., Columbia, MO 65211
(573) 884-6552; fax: (573) 884-5090; e-mail: smithdoug@missouri.edu

NSF Award ID: 0522694

Research and Education Activities

The objective of this research is to develop a predictive capability that evaluates the mechanical properties of short- and long-fiber-reinforced polymer composites from higher-order orientation tensors. The approach is to develop an automated three-dimensional finite-element procedure for predicting the effective mechanical properties of a fiber suspension from its orientation distribution and the mechanical properties of the constituent materials. The work also includes measuring fiber orientations with micro-computerized tomography (CT) imaging techniques and developing a computational approach for generating fiber samples numerically from polymer melt flow simulation results. As part of this research, a Monte-Carlo simulation procedure will be used to assess the statistical nature of the predicted properties and the simulation methodology will be demonstrated on industrially-relevant products.

Fiber-reinforced polymer composites are the material of choice in numerous engineering applications due, in part, to their superior strength-to-weight ratio. This is especially true for long- and short-fiber composite products, which also benefit from extremely versatile manufacturing methods such as injection molding. As a result, there continues to be a major effort to incorporate more fiber-reinforced polymers in commercial products, particularly in the US automotive industry where future vehicles must have reduced weight, emissions, and fuel consumption. Indeed, a specific objective of the FreedomCAR program at the US Department of Energy, a co-sponsor and collaborator of this research, is to reduce the weight of an automotive structure by 50% for the same cost and durability as seen in today's products. The research also includes the development of educational visualization tools that will provide a clearer understanding of fiber suspension mechanics for future engineering students.

Previous work in the areas of numerical methods, composite mechanics, and fiber-orientation analysis will serve as a basis for further development. The focus here is to:

1) Develop a model for predicting mechanical properties from higher-order orientation tensors derived from flow simulations or measurements that is not limited by the material symmetry requirements imposed by current models.

2) Develop an automated, three-dimensional voxel-based, finite-element modeling technique that may be used to predict the effective mechanical properties of a fiber suspension.

3) Integrate micro-CT-derived fiber-orientation states to illustrate the applicability of the proposed approach on production hardware to be obtained from Visteon Corporation.

4) Statistically assess mechanical-property calculations to address sampling issues associated with using the proposed averaging techniques.

5) Demonstrate the proposed methodology on an industrially-relevant polymer composite product where flow-simulation software is to be provided from Moldflow Corporation.

6) Develop techniques for visualizing discrete fibers and fiber suspensions in reinforced polymer composites to provide students at the graduate and undergraduate levels, as well as other composite materials researchers, insight into the microstructure of polymer composites.

Project activities that have been performed to date are as follows (note that this project is in year 2 having started September 2005):

1) Literature review and collection of related information and theory.

2) Development of a Monte-Carlo simulation method for evaluating the statistical nature of elastic mechanical properties of short-fiber composites that is based on sample fiber sets defined by orientation-distribution functions in homogeneous and non-homogeneous flow fields.

3) Derivation of elastic mechanical properties from fiber-orientation tensors that is based on the expected values of the compliance tensor for random individual fibers.

4) Derivation of the statistical nature, including the mean and standard deviation, of the elastic mechanical properties from fiber-orientation tensors and fiber-distribution functions.

5) Development of a voxel-based, finite-element procedure for evaluating the mechanical properties of a set of short fibers in a polymer matrix. This includes the development of a representative volume element and the appropriate boundary conditions.

6) Verification of voxel-based, finite-element approach for single fibers within a polymer matrix.

7) Development of a program for defining the spatial location and orientation of a set of fibers from fiber size and aspect ratio, and a fiber-orientation distribution function.

8) Development of a new fiber-interaction model that simulates fiber/fiber collisions in a manner that is suitable for use in an injection-molding simulation program.

9) Development of a composite materials-based model for the fibrous annulus of the human intervetral disk.

Findings

The most significant finding in the research conducted to date under this award deals with the relationship between fiber-orientation tensors and the resulting elastic mechanical properties of short-fiber composites. Nearly two decades ago, Advani and Tucker presented an equation for computing a stiffness (or compliance) tensor from a 4^{th}-order fiber-orientation tensor and the constitutive properties of the fiber and matrix. This earlier work used the unidirectional elastic properties of several single fibers, each having a pre-selected orientation, to arrive at the final result which was given with little derivation. In our work, a rigorous derivation has been developed to evaluate the same results from the statistical expectation of single-fiber mechanical properties where the distribution of fibers is defined by the fiber-orientation distribution function. Unidirectional properties of single fibers are rotated into a

common reference frame where the rotation tensor is defined by directions that follow the orientation distribution function itself. As a result, we are now able to compute mechanical properties from either orientation tensors or fiber-orientation distribution functions. We have also been able to show that orientation tensors having an order higher than four do not contribute to the expectation value when the commonly used Fourier basis functions are employed. This derivation reduces to the Advani and Tucker form when it is assumed that fibers do not interact under stress and strain in the final composite.

Using a similar derivation technique, we have also derived, for the first time, a means to quantify the statistical variability in the elastic properties of a short-fiber composite. This work provides the variance of a characteristic volume of fibers from the fiber-orientation distribution function or higher-order tensors. It is shown that the variance requires orientation tensors through 8th order when orientation tensors are used in place of an actual distribution function.

In addition, a Monte-Carlo simulation method has been developed to assess the statistical nature of short-fiber composites that may be described by fiber-orientation distribution functions. In this work, sample sets of fibers are defined by a representative cell size, fiber size, and volume fraction. For each sample set, elastic mechanical properties are computed from the calculations described above. The results of numerous sample sets are then combined to obtain the mean and standard deviation of the predicted elastic properties. The calculations have been performed for selected fiber-orientation distribution functions, as well as those that are computed from simple homogeneous and non-homogeneous flows. Results have validated those derived from the orientation function expectation described above. We have also compared the results of these calculations when various closure approximations are employed.

Work continues on the development of a voxel-based, finite-element implementation to compute the elastic mechanical properties for both short- and long-fiber composites. The current approach divides a representative volume element into cube-shaped finite elements. The number of elements and number of degrees of freedom are significantly reduced by increasing the element size while adding additional integration points to capture the spatial variation in mechanical properties. The model is being developed in the general purpose finite-element program ABAQUS where the user-defined element subroutine is employed to add this additional capability. The representative volume element includes the appropriate periodic boundary conditions so that the results are representative of a larger domain. Verification simulations are underway at this time where preliminary results show that we can reproduce elastic moduli consistent with classical theories for isotropic materials. Numerous 2D and three-dimensional (3D) examples from the literature are being used to validate this new modeling approach. Anisotropic results suggest a modification of the multi-Gauss point approach will be required to obtain the correct properties.

The Monte-Carlo simulation program described above is being enhanced for use with our voxel-based, finite element model. A molecular-dynamics simulation is being used to adjust the position of fibers so that they do not overlap in space and maintaining a predefined orientation distribution function. Preliminary results look positive; however, development continues in order to use this approach to fulfill the objectives of this research project.

Our new fiber-interaction model has been implemented in a program that evaluates fiber-orientation tensors for fiber distributions in an arbitrary flow. Limits on the parameters contained in the model have been established and limitations of the approach have been identified. Fiber-orientation predictions have been compared with test data obtained from PNNL. Results show a significant improvement in elongational flows, but much less effect in shear-dominated flows. Further development is needed to obtain an improved accuracy in shear flows.

As part of the REU supplement to this grant, an undergraduate student is developing a finite- element modeling approach for representing the fibrous annulus as a long-fiber composite material. All previous approaches 'stitch' in bar elements within a matrix of solid bricks to represent the fibers. This earlier approach is tedious and is only

appropriate for simple geometries. Our approach rotates a transversely-isotropic elasticity tensor defined by the matrix and fiber properties into the direction of the disk fibers. As a result, each element has its own fiber orientation and elastic properties. This approach will make it possible to model the actual disk geometry which is far more complex than that used in earlier analyses. Our approach is made possible by leveraging the short- and long-fiber composites work described above.

The US Department of Energy FreedomCAR program is providing partial support for this project through NSF DMI. They are also making available computational resources and data from their testing that is related the goals and tasks of this research. A project kick-off meeting was held in August 2005 to initiate the collaborative effort.

As part of this collaboration, information on research progress is exchanged between the PI and personnel at PNNL, which includes reports, journal articles, test data and PowerPoint presentations. PNNL has also made available computer facilities where future Monte Carlo simulations will be run.

Journal Publications

1. D.A. Jack and D.E. Smith, "Material Property Predictions for Short-Fiber Polymer Composites: Part 1, Analytical Forms for Expectation and Variance from Orientation Tensors", Journal of Composite Materials, Submitted.
2. D.A. Jack and D.E. Smith, "Material Property Predictions for Short-Fiber Polymer Composites: Part 2, Validation of Analytical Expectation and Variance with the Method of Monte Carlo", Journal of Composite Materials, Submitted
3. David A. Jack and Douglas E. Smith, "The Effect of Fiber Orientation Closure Approximation on Mechanical Property Prediction", Composites Part A., p. 975, vol. 38, (2007).

Simulation of Compression-Resin Transfer-Molding Process for Manufacturing Net-Shape Structures.

Principal Investigator: Suresh G. Advani

Department of Mechanical Engineering
University of Delaware
Newark, DE 19716
(302) 831-8975; fax: (302)-831-8525;
e-mail: advani@me.udel.edu

NSF Award ID: 0521789

All liquid composite molding (LCM) processes require one to place a fibrous preform inside the mold. The mold is sealed and a liquid resin is injected to saturate the preform. The fibers in the preform and the preform itself are usually stationary but in some variations they may undergo small (and slow) deformation during the injection process. Next, the resin is allowed to cure and the part is removed. Two commonly used techniques in this process are resin-transfer molding (RTM) and vacuum-assisted resin-transfer molding (VARTM).

The subject of this work, compression resin-transfer molding (CRTM) differs from the other LCM processes by injecting the resin before the mold is fully closed and preform compacted. The gap between preform and mold surface serves for uniform resin distribution over the part surface. Following mold closure and preform compaction then distributes the resin through the preform thickness.

This process offers the potential to manufacture moderately-sized structures in a few minutes while preserving the advantages of RTM, net-shape manufacturing of complex curvatures with Class A surface finish.

In all LCM variations, the flow of the resin through the preform is important. If particular sections of the preform remain dry after the injection is complete, the resulting void will seriously compromise the part properties. The cost of trial-and-error part design created a need for the simulation of the filling process using science-based process model. For conventional RTM processes, many reliable computer simulation tools have been established and validated with experiments. However, for the other LCM variations the modeling tools are scarce and RTM tools are usually adapted, though the results are sometimes not quite satisfactory.

The resin flow in CRTM process is more complex than in any other LCM variation. It exhibits three distinct stages. All of the phases can be modeled as flow through porous media under different boundary and initial conditions. The three stages are

1. Resin injection into the narrow gap between the mold platen and the fiber preform in the mold.
2. Closing of the gap while squeezing the resin into preform without direct contact between movable tool part and the perform.
3. Compaction of the preform by the mold platen along with continuing resin impregnation.

Research and Education Activities

We extended, streamlined and analyzed the existing approach to model CRTM and enhanced its capabilities by fully modeling preform deformation. The scheme was successfully utilized to analyze the process and to identify significant process parameters. However, low computational performance continues to be an issue. To address this concern, extended problem descriptions which include fiber tow saturation and preform deformation were developed. As the material description necessary to utilize either of these models far exceeds the usual level of characterization in LCM, preform materials of suitable types were characterized. On the educational side, the process model was introduced in an undergraduate course on Introduction to Principles of Composites Manufacturing (MEEG 655).

Findings

The current approach that combined the RTM governing equation with an iterative process clearly showed that the resulting pressure was very different. An existing RTM simulation package was utilized to model the CRTM process with limited success and some parametric studies were performed. The preform displacement was added into the model and a 2D version, more suitable for process study, was developed. This model provided tools for extensive analysis of parameters influencing the process. New governing relations for the general LCM was implemented in a full, finite-element-based numerical scheme. The scheme is currently being tested. Methodology was developed to test preform materials in order to obtain the full set of material data necessary for modeling. Several materials, including the programmable powdered perform process (P4, see 8.C) preform, were characterized to obtain wet and dry deformation behavior and permeability/deformation relations.

Journal Publications

None.

Simulation of Injection Molding of Thermoplastics Reinforced with Short and Long Fibers

Principal Investigator: Donald G. Baird
Department of Chemical Engineering
Virginia Polytechnic Inst & St U
Blacksburg, VA 24061
(540) 231-5998; fax: (540) 231-2732;
email:dbaird@vt.edu

NSF Award ID: 0521918

A procedure for identifying the appropriate rheological experiments to determine a unique set of rheological parameters in a constitutive equation for polymers, containing long glass fibers was developed. Furthermore, the equations of motion coupled, with this constitutive equation, have been used to formulate a simulation of injection molding in which flow and fiber orientation are coupled. This has been done initially assuming Hele-Shaw flow but is presently being extended to general flow including the advancing front. Appropriate rheological tests were developed which provide the necessary material parameters needed in the numerical simulation.

Research and Education Activities

The goal of this work is to improve on current predictions of fiber orientation in polymer matrices using a constitutive relation in which fiber orientation is coupled with the flow and not post-calculated. The major research and education activities are:

1. To develop rheological techniques for handling fluids containing high aspect-ratio fibers and to connect the rheological behavior to fiber orientation. Studies have been carried out to determine the impact of fiber concentration, aspect ratio, orientation distribution and suspending medium viscoelasticity on the rheology of short- and long-glass-fiber composite fluids.

2. To teach numerical methods suitable for handling the flow of complex fluids. A finite-element simulation was developed as discussed below.
3. Numerical schemes which give conversion at high Deborah numbers were addressed. A code for a discontinuous Galerkin finite-element method has been written that can handle multiple viscoelastic constitutive equations. Simulations have been carried out for shear/extensional rheometrical flows and 2D injection-molding flows with the Hele-Shaw approximation.
4. Rheometry in conventional rheometers is difficult especially for long-fiber systems. A sliding-plate rheometer was designed and built for studying the rheology and flow of long-glass fiber composites.
5. Methods for investigating fiber orientation during flow were investigated. Center-gated samples were injection molded and analyzed for fiber orientation at ORNL.

Findings

1. Rheological Characterization Technique (short fibers): Developed a novel rheological technique that addresses problems associated with the non-homogeneous shear field found in parallel-plate rotational rheometers and boundary interactions in cone-and-plate rheometers.
2. Rheological Characterization Technique (long fibers): The mechanical components (currently unable to purchase the electrical components) of a sliding-plate rheometer have been designed and fabricated primarily for the purpose of performing unbiased and reproducible rheological experiments on long-glass-fiber-filled polymeric fluids that are otherwise impossible to perform on rotational rheometers. In addition, the rheometer will be used in tracking the transient evolution of long-fiber orientation upon startup and cessation of shear flow.
3. Rheology: Rheological characterization of the short-glass-fiber composites was performed, including intermittent stress growth/relaxation tests to elucidate the stress contribution of the fiber, matrix, and flow field on the transient evolution of fiber orientation. Rheological characterization of the long-glass-fiber composite has been deemed impossible without the completion of the sliding-plate rheometer.
4. Model (short fibers): A constitutive relation has been developed that incorporates stress contributions from the fiber and the viscoelastic suspending medium and includes the ideas of non-affine motion. Model predictions show good agreement compared to rheological experiments and preliminary results for the experimentally-determined fiber orientation.
5. Fiber-Orientation Measurements: We have determined an approach to characterizing the 3D fiber orientation within composite parts using confocal laser microscopy. We have initiated the characterization of fiber orientation in both rheometrical flows and complex flow geometries.
6. Model (long fibers): Various approaches to modeling flexible fibers have been investigated. These approaches include modifying current theory for rigid fibers to include a 'flexibility parameter', track individual fibers using Hinch's infinitely- flexible fiber theory or constitutive equations resulting from bead-rod theory.
7. Simulations: Developed a Galerkin/discontinuous Galerkin finite-element simulation package to simulate the filling stage of injection molding. The features of this simulation package are: use of multiple constitutive equations, compare with Hele-Shaw approximation for end-gate plaque and ceter-gated disk, and combined front tracking/ALE technique for advancing front simulations.

Training and Development

The students involved in this project are learning:

1) how constitutive relations for polymers containing high aspect-ratio fibers are developed; 2) how to design rheological tests for assessing the parameters in the models; 3) how to develop finite-element code for complex fluids in which structure and flow are coupled; 4) the importance of coupling simulations with the measurement of fiber orientation.

Journal Publications

1. PR. Eberle, D. G Baird, and P Wapperom, "Modeling the Transient Rheology of a Polypropylene Melt Reinforced with Long

and Short Glass Fibers", SPE Technical Papers, p. 1257, vol. 52, (2006). Published.
2. D. Baird and A. Eberle, "Modeling The Rheology And Orientation Distribution Of Short Glass Fibers Suspended In Polymeric Fluids: Simple Shear Flow", Proceedings of the 65th Annual Technical Conference, p. 2823, vol. 65, (2007). Published.
3. P. E. Eberle, D. G. Baird, and P. Wapperom, "The Rheological Properties of Non-Newtonian Fluids Containing Glass Fibers: A Review of Literature", Ind. Eng. Chem. Res. Submitted.

L. Structural Nanocomposite Design

Co-Principal Investigator: Thomas E. Lacy
Associate Professor, Aerospace Engineering
Mississippi State University (MSST)
316c Walker Bldg., P.O. Box A
Mississippi State, MS 39762
(662) 325-2754; fax: (662) 325-7730; e-mail: lacy@ae.msstate.edu

Co-Principal Investigator: Yuanxin Zhou
Assistant Professor, Tuskegee Center for Advanced Materials (T-CAM), Department of Mechanical Engineering
Tuskegee University (TU)
Tuskegee AL 36088
(334) 724-4222; fax: 334-727-8801; e-mail: yzhou@tuskegee.edu

Co-Principal Investigator: Shaik Jeelani
Director, Center for Advanced Materials (CAVS)
Vice President, Research and Sponsored Programs
Tuskegee University (TU)
Tuskegee AL 36088
(334) 727-8970; fax: (334) 724-4224; e-mail: jeelanis@tuskegee.edu

Technology Area Development Manager: Joseph A. Carpenter
(202) 586-1022; fax: (202) 586-1600; e-mail: joseph.carpenter@ee.doe.gov

Contract Monitor: Aaron Yocum
(304) 285-4852; fax: (304) 285-4403; e-mail: aaron.yocum@netl.doe.gov

---

Contractor: MSST
Contract No.: 4000054701

Objective

- Design low-cost nanoreinforced composite systems for automotive structural applications.

Approach

A multiscale design methodology is being employed to investigate the effects of nanoreinforcements on the mechanical properties of fiber-reinforced composites for automotive structural applications. Critical issues being addressed include: selection of key combinations of fibers (glass, carbon, natural, etc.), matrix materials (thermoset, thermoplastic), and relatively cost-effective nanoreinforcements (vapor-grown carbon nanofibers, nanoclay particles, etc.); fabrication of fine-scale and coupon-scale material samples for static and dynamic testing; and development of a multiscale materials modeling strategy for assessing high-performance nanocomposites that accounts for the influence of material-processing parameters on mechanical properties of the material under static and dynamic loads. This effort involves completion of five primary objectives.

- Determine appropriate composite fiber-matrix systems and identify and prioritize candidate nanoreinforcements for evaluation.
- Investigate the effects of different mixtures of nanoreinforced fibers/polymer matrices from a manufacturing and cost perspective.
- Quantify nanoreinforced structure-property relations experimentally.
- Study material failure modes and energy-absorption characteristics under different loading conditions.

- Development of a multiscale materials model based upon micromechanics models and experiments for nanocomposites.

Accomplishments

- Selected readily-available, low-cost thermoset (polyester) and thermoplastic (polypropylene) resins as the primary matrix materials in this investigation; other polymer resins (*e.g.*, epoxy) may be considered as part of supplemental investigations associated with this work.
- Selected Applied Science, Inc. PR-24 carbon nanofibers (CNFs) as the primary nanoreinforcement for use in the initial examination.
- Selected E-glass unidirectional- and woven-fabric plies as the primary traditional continuous-fiber reinforcement phase in this investigation because of their widespread use in automotive applications.
- Fabricated nanophased resin test specimens comprised of a thermoset polyester resin and varying weight fractions of CNFs using a combination of mechanical mixing, sonication, addition of catalyst, dessication and cure.
- Evaluated the dispersion of nanoreinforcements within polymer resins using scanning electron microscopy (SEM).
- Established a method for functionalizing CNFs in order to enhance dispersion in and interaction with the polyester matrix, as well as to minimize CNF agglomeration.
- Established vacuum-assisted resin transfer molding (VARTM) as a viable, inexpensive technique to fabricate continuous-fiber E-glass laminates with nanophased thermoset resins.
- Fabricated nanophased thermoplastic resins (*e.g.*, CNF/ polypropylene) using well-established extruding, grinding and hot-press techniques.
- Performed three-point bend experiments for two-phase (nanoreinforced) resin test specimens comprised of polyester reinforcement with varying weight fractions of CNFs (0.0%, 0.5%, 1.0%, 1.5%, 2.0%, 3.0%).
- Established a student exchange between MSST and T-CAM, where two MSST minority undergraduate students fabricated CNF/polyester three-point bend test specimens and compression-test specimens using T-CAM experimental facilities.
- Used SEM to assess damage morphology and failure mechanisms for nanophased resins.
- Initiated development of a multiscale materials modeling strategy that employs a combination of micromechanics models, three-dimensional (3D) finite elements (ABAQUS, GENOA), and validation experiments for nanocomposites.
- Established a partnership with AlphaStar, Inc. for the modeling of nanocomposites using the finite-element code GENOA.
- Submitted and published one refereed journal article.
- Submitted one conference paper for presentation.

Future Direction

- Continue ongoing dynamic mechanical analysis (DMA) and thermo-gravimetric analysis (TGA) testing of CNF/ polyester resins to assess the thermal properties of nanophased polymer resins.
- Conduct structure-property tests for three-phase composite systems (nanophased resin, E-glass plies) in order to assess the mechanical behavior and failure of the structural nanocomposites.
- Determine weight fractions of nanoreinforcements that lead to optimal nanophased resin and structural nanocomposite properties.
- Determine material failure modes and energy-absorption characteristics for structural nanocomposites subjected to static and dynamic loading conditions. Perform flexure, tension, fatigue, fracture, and dynamic tests of structural nanocomposites.
- Validate micromechanical model for determining effective properties of nanophased resins using structure-property data.
- Incorporate effective nanophased resin properties from micromechanical models into 3D finite-element models of three-phase composites. Validate numerical models using structure-property data.

Introduction

A multiscale design methodology is being employed to investigate the effects of nanoreinforcements on the mechanical properties of fiber-reinforced composites for automotive structural applications. Critical issues being addressed include: selection of key combinations of fibers (glass, carbon, natural, etc.), matrix materials (thermoset, thermoplastic), and relatively cost-effective nanoreinforcements (vapor-grown carbon nanofibers, nanoclay particles, etc.); fabrication of fine-scale and coupon-scale material samples for static and dynamic testing; and development of a multiscale materials modeling strategy for assessing high-performance nanocomposites that accounts for the influence of material processing parameters on mechanical properties of the material under static and dynamic loads. A literature review of recent experimental and modeling activities related to nanoreinforced composites, particularly those involving glass fibers coupled with thermoset resins (e.g., vinyl ester, polyester, as well as epoxy), was performed (cf., Odegard, et al., 2001; Ghoniem, et al, 2003; Thostenson, et al., 2004; Buryachenko, et al., 2005; Gates, et al., 2005; Odegard, et al., 2005; Valavala and Odegard, 2005; Hussein, et al., 2006; Liu and Brinson, 2006; Fischer, et al., 2007). Such material systems are of particular interest to the Automobile Composites Consortium (ACC). A dialogue has been initiated with the ACC in order to solicit guidance and feedback on relevant aspects of the research, including identification of additional industry partners to participate in cost-share relationships with MSST, T-CAM, and the Department of Energy (DOE). A summary of year one accomplishments is included in the following discussion.

Determination of Composite Fiber-Matrix Systems and Nanoreinforcements

Because of their widespread use and relatively low cost, one commercially-available thermoset resin (U.S. Composites, Inc. polyester) and one thermoplastic resin (polypropylene) were selected as the primary matrix materials in this investigation; other polymer resins (e.g., epoxy) are being considered as part of supplemental investigations associated with this work (*cf.*, Zhou, *et al.*, 2007). Applied Science, Inc. PR-24 carbon nanofibers (CNFs) (typical diameters, 60-200 *nm*; typical lengths, 20-100 μm) were selected as the primary nanoreinforcement for use in this examination. CNFs are relatively inexpensive and possess excellent mechanical properties. Because of prevalent use in automotive applications, E-glass unidirectional- and woven-fabric plies are being used as the primary traditional continuous-fiber reinforcement phase in this investigation.

Investigation of the Effects of Different Mixtures of Nanoreinforced Fibers/Polymer Matrices on Manufacturing

In year one, nanophased resin test specimens comprised of a thermoset polyester resin and varying weight fractions of CNFs were fabricated using a combination of mechanical mixing, sonication, addition of catalyst, dessication, and cure; Figure 1 shows a flowchart of the fabrication process used to develop the two-phase resin system. The resin used in this study is commercially-available stand polyester from US Composite, Inc. The weight fractions of CNFs were varied between 0-4% in order to identify an optimal combination that gives the best thermal and mechanical properties. In general, precalculated amounts of carbon nanofibers and liquid polyester (Part A) were mixed together in a beaker using high-intensity ultrasonic irradiation (Ti-horn, 20 kHz Sonics Vibra Cell, Sonics Mandmaterials, Inc., USA) for 30 minutes on pulse mode (50 seconds on/25 seconds off). The beaker containing a given mixture was submerged in an ice bath to avoid a temperature rise during the sonication process. Once the irradiation was complete, a catalyst (part B in Figure 1) was mixed with the modified polyester using a high-speed mechanical stirrer for roughly 10 minutes. The ratio of part A to part B was 100:1. The rigorous mixing of part A and part B typically produces highly reactive, volatile vapor bubbles at initial stages of the reaction, which could lead to detrimental void formation in the final product (two-phase resin). A high vacuum was applied for 30 minutes to the solution using a Brand Tech Vacuum system to completely remove any bubbles; the mixture was then transferred into plastic- and Teflon-coated metal molds and kept for 24 hours at room temperature. The cured material was demolded and trimmed and test samples were

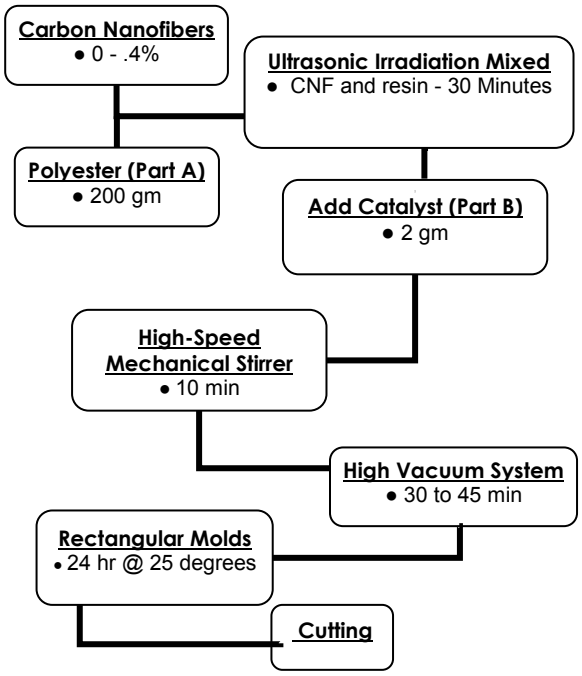

Figure 1. Manufacturing of nanophased resin samples.

machined for thermal and mechanical characterization.

The dispersion of nanoreinforcements within the polyester resin was evaluated using scanning electron microscopy (SEM). SEM images of the failure surfaces associated with three-point bend specimens suggest that agglomeration of CNFs during fabrication and processing is a concern. As a consequence, current efforts are aimed at functionalizing CNFs in order to enhance dispersion in and interaction with the polyester matrix.

Nanophased thermoplastic resins (e.g., CNF/polypropylene) have been fabricated using well-established extruding, grinding, and hot-press techniques (*cf.*, Zhou, *et al.*, TBD). Supplemental investigations of low-cost fabrication/ processing techniques will continue into year two of the project.

VARTM has been established as a viable technique to fabricate continuous-fiber E-glass laminates with nanophased thermoset resins involving a variety of different nanoreinforcements (*cf.*, Chisholm, *et al.*, 2005; Chowdhury, *et al.*, 2006, Zhou, *et al.*, 2006). VARTM may be used to produce high-quality composite parts and is an attractive alternative to autoclave processing.

Experimental Structure-Property Relations for Nanoreinforced Materials

In accordance with American Society for Testing and Materials (ASTM) D790-86, three-point bend experiments were performed for two-phase (nanoreinforced) resin test specimens comprised of polyester reinforced with vapor-grown CNFs. Test samples were cut from larger panels using a Felker diamond-coated steel saw. Six different weight fractions of CNFs (0.0%, 0.5%, 1.0%, 1.5%, 2.0%, 3.0%) were initially considered in order to identify an optimal combination that gives the best thermal and mechanical properties. Three replicates were tested for each weight fraction, for a total of 18 flexural tests. As part of a student exchange associated with this work, two MSST minority undergraduate students fabricated CNF/polyester three-point bend test specimens and compression test specimens using T-CAM experimental facilities.

Preliminary flexural data from these tests contained some surprising results: both the flexural modulus and strength for the three-point bend specimens generally *decreased* with increasing CNF content. This is in contrast to earlier results obtained by T-CAM for CNF-reinforced epoxy, where the inclusion of CNFs resulted in an increase in mechanical properties. Additional experimental investigations will be performed in order to more fully assess the mechanical and thermal performance of CNF/polyester resins. These include an ongoing assessment of the dispersion/agglomeration of CNFs in the resin, consideration of lower weight fractions of CNF reinforcement (*e.g.*, 0.1%, 0.2%, 0.3%, 0.4%), as well as functionalization of the CNFs. In order to enhance the adhesion between the CNFs and polyester resin, MSST will chemically treat CNFs to induce an oxide layer on the fiber surface. Such modified fibers will be used in upcoming mechanical and thermal tests performed at T-CAM. In addition, a lower-viscosity polyester resin is also being considered for use in this study.

Figure 2 contains SEM images of the fracture surface from a three-point bend specimen comprised

of neat polyester (0% weight fraction CNFs) at different magnifications. As seen in Figure 2a, the neat resin exhibits a relatively smooth fracture surface; an initial crack occurred the near the tensile edge of specimen. The higher magnification fractographic image shown in Figure 2b shows striated features typical of brittle fracture behavior, thus accounting for the generally low fracture toughness of the unfilled polyester.

Figure 3 contains SEM images of the fracture surface from a three-point bend specimen comprised of 0.5% CNF/polyester at different magnifications. In contrast with results obtained for the neat resin, the initial crack did not occur at the tensile edge of the specimen. As can be seen in Figure 3a, failure initiation occurred in the interior of the specimen in the vicinity of a large particle that appears to be an agglomeration of several CNFs. Apparently, the crack initiation was caused by the stress concentration due to the agglomerated particle. Figure 3b shows a higher-magnification SEM image of the fracture surface somewhat removed from the agglomerated particle. Note that the fracture surface is substantially rougher than that for the neat polyester (*cf.*, Figure 2b). This suggests that *well distributed* CNFs have the potential to inhibit crack propagation and increase fracture toughness of the resin. Figure 2c contains a high-resolution SEM image that clearly shows a number of dispersed individual CNFs emanating from the fracture surface. Of course, in order to fully realize the potential of nanoreinforced resins, the CNFs must be processed in manner that will minimize agglomeration and the associated stress concentrations. CNF functionalization and surface treatment are being investigated in order to optimize surface chemistry, enhance interaction/bonding between the polymer matrices (*e.g.*, polypropylene, polyester) and CNFs, and to ensure proper dispersion during mixing/ sonication of nanophased materials. This issue will be addressed in upcoming experimental activities associated with this work.

Based upon flexural stiffness/strength data, in conjunction with SEM images of the failure surfaces (*cf.*, Figures 2-3), proper dispersion of CNFs is a crucial aspect in the development of nanophased resins with superior mechanical properties. Initial test results suggest that improper dispersion of the nanophase can result in a decrease in mechanical test results suggest that improper dispersion of the strength. Of course, in order to fully realize the potential of nanoreinforced resins, the CNFs must be processed in a manner that will minimize agglomeration and the associated stress concentrations. As mentioned previously, functionalization of CNFs is being performed in order to address this issue. Initial experimental results suggest that *well distributed* CNFs have the potential to inhibit crack propagation and increase fracture toughness of the resin. Dynamic mechanical analysis (DMA) and thermo-gravimetric analysis (TGA) testing of CNF/polyester resins are currently being performed to assess the thermal properties of nanophased thermoset resins. Similar tests will be performed for nanophased thermoplastics.

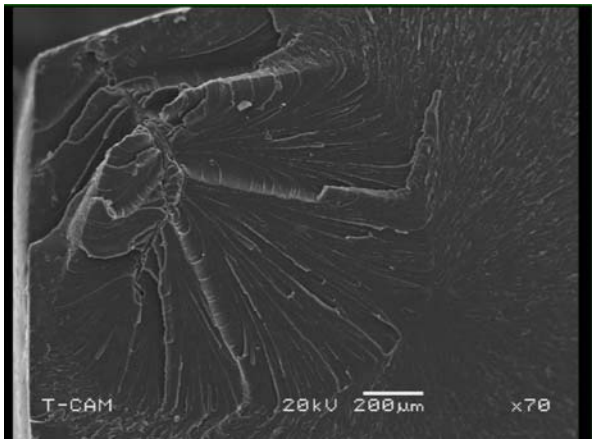

a)

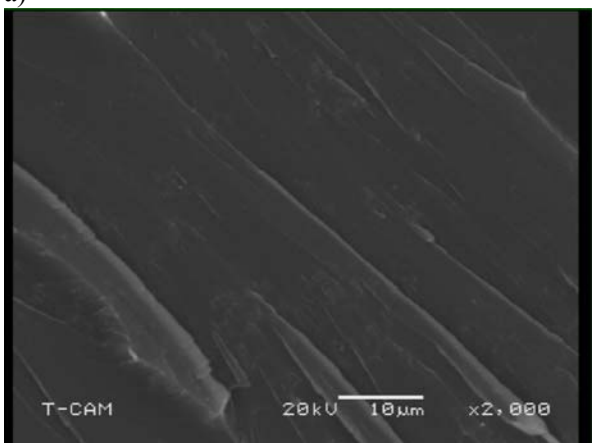

b)

Figure 2. SEM images of fracture surface for three-point bend specimen comprised of neat polyester. a) Crack near free surface of specimen and b) higher resolution image of fracture surface typical of brittle fracture.

Structure-property tests are being developed for three-phase composite systems (nanophased resin, E-glass plies) in order to assess the mechanical behavior and failure of the structural nanocomposites. These activities will continue into year two of the project.

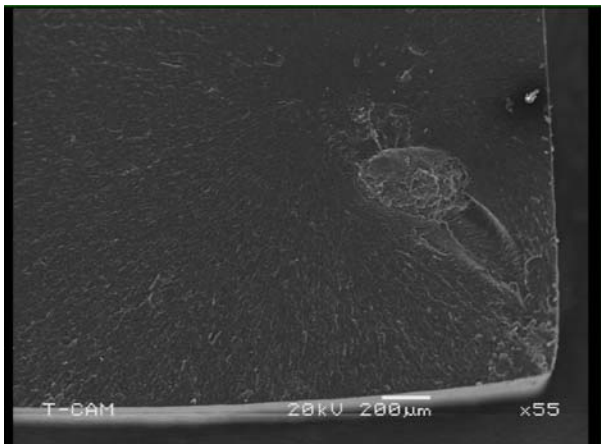

a)

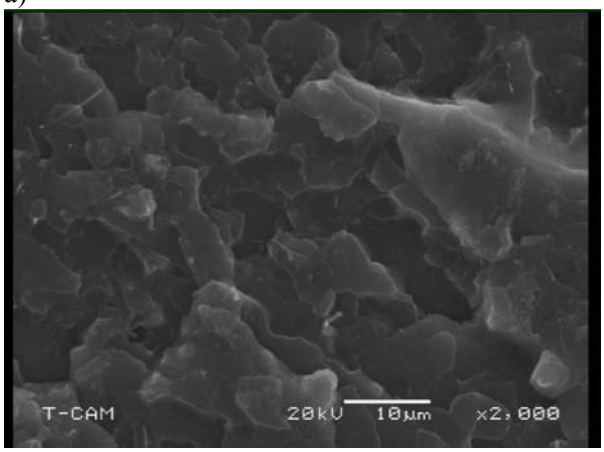

b)

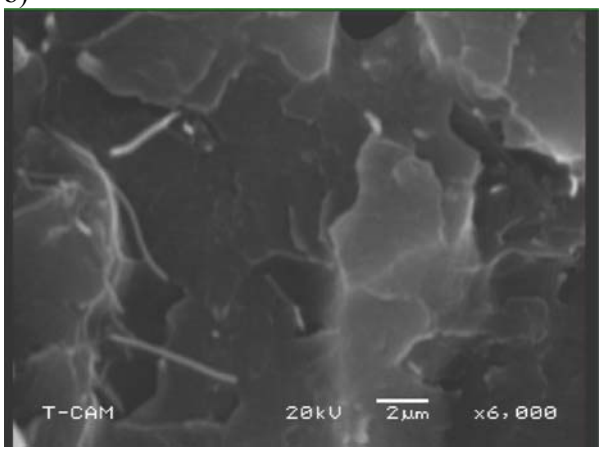

c)

Figure 3. SEM image of fracture surface for 0.5% CNF/polyester three-point bend specimen. a) Crack near agglomerated particle, b) typical fracture surface and c) CNFs bridging the fracture surface.

Assessment of Nanocomposite Material Failure Modes and Energy-Absorption Characteristics under Different Loading Conditions

Once optimal levels of CNFs have been determined for the candidate thermoset and thermoplastic resins, the static and dynamic failure behavior of test specimens comprised of three-phase composites will be investigated using a number of standard tests, with emphasis on energy absorption/crash applications. The goal of this work is to establish relationships between composite processing, constituent morphology, properties and macroscale performance. The effects of nanoreinforcements on macroscale physical properties (stiffness, toughness, energy absorption, *etc.*) will be examined using a combination of three-point bend tests (ASTM D790), tensile tests D3039), fatigue tests, crush tests, fracture tests, Hopkinson bar tests, and other experiments involving specimen geometries and lay-ups of interest to the ACC. A combination of visual inspection, light microscopy, SEM and transmission electron microscopy (TEM) will be used to assess damage development and failure of structural nanocomposite specimens.

Similar studies of carbon fiber/CNF-reinforced epoxy composite systems suggested that inclusion of relatively small amounts of CNFs can lead to a marked improvement in macroscale performance (*cf.*, Zhou, *et al.*, 2006). For example, Figures 4a and 4b contain SEM images of the tensile failure surfaces for continuous carbon fibers reinforced with neat epoxy and CNF-reinforced epoxy, respectively. As can be seen from the figure, use of a nanophased resin appears to dramatically improve the quality of the fiber/matrix interface. The motivation for this work is to fabricate cost-effective nanoreinforced composite materials suitable for automobile primary structural applications. The majority of these activities will be performed in year two of this project.

Development of Multiscale Materials Model Based upon Micromechanics and Experiments for Nanocomposites

Materials property data obtained from structure-property tests are being used in the development and validation of representative volume element (RVE)-based micromechanical models of the two-phase (nanoreinforced) resins. The multiscale modeling methodology developed in this work involves both nanoscale and mesoscale homogenizations. The former is required to establish effective properties of the nanoreinforced matrix (here the characteristic size of a typical nanoreinforcement may be several orders of magnitude smaller than a typical glass-fiber diameter). One key issue is the establishment of an empirically-validated material model (and appropriate homogenization technique) for predicting effective properties of the two-phase matrix; a variety of methods (molecular dynamics, finite elements, etc.) are currently being considered.

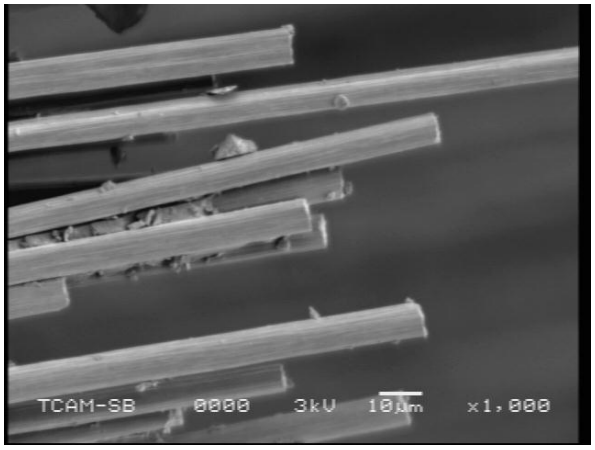

a)

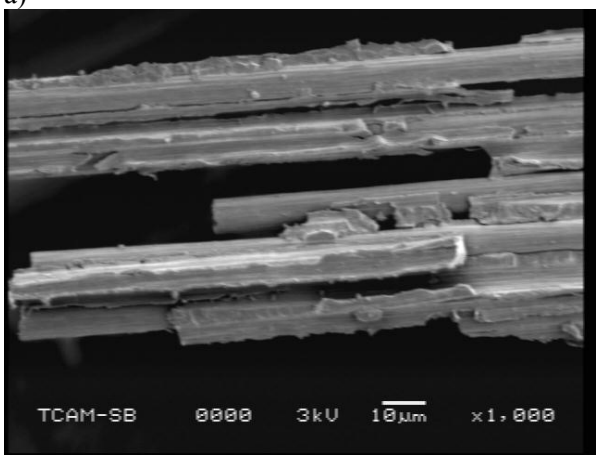

b)

Figure 4. SEM image of continuous-carbon-fiber composite with a) neat epoxy resin and b) CNF/epoxy resin.

Three-dimensional finite-element (FE) models of two-phase resin systems are being developed to establish effective properties of the nanoreinforced matrix. Effective nanophase resin properties obtained from FE simulations are being compared to those obtained using analytic micromechanics solutions (e.g., Mori-Tanaka method and similar effective medium idealizations; *cf.*, Mura, 1991; Nemat-Nasser and Hori, 1993). Effective property data from these simulations, as well as from bulk structure property tests performed by T-CAM, will be employed in a RVE-based FE model of the fiber system/ enhanced resin subjected to both load control and displacement control boundary conditions. Standard homogenization techniques (*cf.*, Mura, 1991; Nemat-Nasser and Hori, 1993) will be employed to determine the effective properties of the three-phase composite systems (i.e., nanophased polymer matrix, traditional continuous-fiber system architectures), with an initial focus on E-glass plain-weave woven-fabric laminates. Modeling and simulation activities will continue into the second year of the project.

Conclusions

The goal of this investigation is to exploit expertise in polymer chemistry, composite materials processing, and computational solid mechanics to design, synthesize, test and analyze cost-effective multiscale engineered nanocomposites for automobile primary structural applications. One key challenge is to establish empirically-validated, multiscale methodologies, based on the morphologies and geometries of real heterogeneous materials, to obtain structure-property relationships over a wide range of length scales.

A crucial aspect of the work is that structure-property relations will be experimentally validated using a combination of fine-scale and macroscale tests. This study should facilitate the development of engineered multiscale materials design by providing insight into relationships between nanomaterial fabrication/processing, chemical and physical characteristics, and interaction and evolution of structure across disparate spatial scales that leads to improved macroscale performance

Presentations/Publications/Patents

1. Zhou, Y., Akanda, S.R., Jeelani, S., and Lacy, T.E., "Nonlinear Constitutive Equation for Vapor-Grown Carbon Nanofiber-Reinforced SC-15 Epoxy at Different Strain Rate," accepted for publication in *Materials Science & Engineering A*, 2007.
2. Zhou, Y., Jeelani, S., and Lacy, T.E., "Strain Rate Dependent Behavior of Carbon Nanofibers Filled Polypropylene," abstract submitted for presentation at the 49th AIAA/ ASME/ ASCE/ AHS/ ASC Structures, Structural Dynamics, and Materials Conference, Schaumberg, IL, April 7-10, 2008.

References

1. Buryachenko, V.A., Roy, A., Lafdi, K., Anderson, K.L., and Chellapilla, S., 2005, "Multi-scale mechanics of nanocomposites including interface: Experimental and numerical investigation," *Composites Science and Technology*, **65**, 2435–2465.
2. Chisholm, N., Mahfuz, H., Rangari, V.K., Ashfaq, A., Jeelani, S., 2005, "Fabrication and mechanical characterization of carbon/SiC-epoxy nanocomposites," *Composite Structures*, 67, 115–124.
3. Chowdhury, F.H., Hosur, M.V., Jeelani, S., 2006, "Studies on the flexural and thermomechanical properties of woven carbon/nanoclay-epoxy laminates," *Materials Science and Engineering A*, 421, 298–306.
4. Fisher, F.T., Bradshaw, R.D., and Brinson, L.C., "Fiber waviness in nanotube-reinforced polymer composites: I. Modulus predictions using effective nanotube properties," submitted to *Composites Science and Technology,* 2007.
5. Gates, T.S., Odegard, G.M., Frankland, S.J.V., and Clancy, T.C., 2005, " Computational materials: Multi-scale modeling and simulation of nanostructured materials, *Composites Science and Technology*, **65**, 2416-2434.
6. Ghoniem, N.M., Busso, E.P., Kioussis, N., Huang, H., 2003, "Multiscale modelling of nanomechanics and micromechanics: an over-

view," *Philosophical Magazine*, **83(31–34)**, 3475–3528.
7. Hussain, A., Hojjati, M., Okamoto, M., and Gorga, R.E., 2006, "Review Article: Polymer-Matrix Nanocomposites, Processing, Manufacturing, and Application: An Overview," *Journal of Composite Materials*, **40(17)**, 1511-1575.
8. Liu, H., and Brinson, L.C., 2006, "A hybrid numerical-analytical method for modeling the viscoelastic properties of polymer nanocomposites," *Journal of Applied Mechanics*, **73,** 758-768.
9. Mura, T., 1991, Micromechanics of Defects in Solids, Second Edition, M. Nijhoff Publ., The Hague.
10. Nemat-Nasser, S., and Hori, M., 1993, Micromechanics: Overall Properties of Heterogeneous Materials, North-Holland, Amsterdam.
11. Odegard, G.M., Gates, T.S., Nicholson, L.M., and Wise, K.E., 2001, "Equivalent-Continuum Modeling of Nano-Structured Materials," **NASA/TM 210863**, 1-30.
12. Odegard, G.M., Clancy, T.C., and Gates, T.S., 2005, "Modeling of the mechanical properties of nanoparticle/polymer composites," *Polymer*, **46**, 553–562.
13. Thostenson, E.T., Li, C., and Chou, T.-W., 2004, "Nanocomposites in context," *Composites Science and Technology*, **65**, 491–516.
14. Valavala, P.K., and Odegard, G.M., 2005, "Modeling techniques for determination of mechanical of polymer nanocomposites," *Review Advance Material Science*, **9**, 34-44.
15. Zhou, Y., Pervin, F., Rangari, V., Jeelani, S., 2006, "Fabrication and evaluation of carbon nano fiber filled carbon/epoxy composite," *Materials Science and Engineering A*, 426, 221–228.
16. Zhou, Y., Akanda, S.R., Jeelani, S., and Lacy, T.E., "Nonlinear Constitutive Equation for Vapor-Grown Carbon Nanofiber-Reinforced SC-15 Epoxy at Different Strain Rate," accepted for publication in *Materials Science & Engineering A*, 2007.
17. Zhou, Y., S.R., Jeelani, S., and Lacy, T.E., "Strain Rate Dependent Behavior of Carbon Nanofibers Filled Polypropylene," abstract submitted for presentation at the 49th AIAA/ ASME/ ASCE/ AHS/ ASC Structures, Structural Dynamics, and Materials Conference, Schaumberg, IL, April 7-10, 2008.

9. JOINING

A. Forming Limits of Weld Metal in Aluminum Alloys and Advanced High-Strength Steels

Principal Investigator: Richard W. Davies
Pacific Northwest National Laboratory (PNNL)
P.O. Box 999, Richland, WA 99352-0999
(509) 375-6474; fax: (509) 375-5994; e-mail: rich.davies@pnl.gov

Technology Area Development Manager: Joseph A. Carpenter
(202) 586-1022; fax: (202) 586-1600; e-mail: joseph.carpenter@ee.doe.gov

Expert Technical Monitor: Philip S. Sklad
(865) 574-5069; fax: (865) 576-4963; e-mail: skladps@ornl.gov

Participants:
Elizabeth V. Stephens and Glenn J. Grant, PNNL
General Motors, Chrysler, Ford, US Steel, Alcoa

Contractor: PNNL
Contract No.: DE-AC06-76RL01830

Objective

- Develop, validate, and disseminate a combined experimental and numerical method to statistically describe and systematically quantify the forming limits of welded aluminum (Al) alloys and advanced high-strength steels (AHSSs).

Approach

- Develop a standard tool for weld-process development that will systematically quantify failure probabilities during forming.
- Provide accurate and standardized methods of experimentally characterizing weld-metal formability using unique, but simple, test methods available on the shop floor.
- Provide predictive models for more accurate forming simulations of tailor-welded blanks (TWBs) and hydroforming operations. Predict parts-per-thousand failure rates during production from finite-element analysis (FEA).
- Characterize static/fatigue properties and forming behavior of several weld populations and correlate with statistically-based tool.

Accomplishments

- Completed uniaxial experiments of friction-stir welded (FSW) AA5182-O material population.
- Increased focus on biaxial forming experiments of FSW AA5182-O to 6111-T4 material population.
- Completed coordinate transformations (utilizing digital-imaging correlation) of full-dome biaxial tests of laser-welded (LW) DP 600 and AA5182-6111 welded alloy populations to improve accuracy of strain results input into the model.
- Completed all biaxial experiments for each welded alloy population.
- Completed the combined forming-limit prediction for DP 600, AA5182-6111, and AA5182 welded alloys.

- Participated in the Minerals, Metals, and Materials Society (TMS) 2007 Annual Meeting and presented two presentations related to project work.
- Participated in Materials Science and Technology (MS&T) 2007 Conference and Exhibition and presented one presentation related to project work.

Future Direction

- Quantify the combined forming-limit diagram (FLD) using the statistical approach for each welded alloy population.
- With original equipment manufacturer (OEM) participation, validate the experimental and numerical methodology with any existing TWB applications in production.
- Complete all final work and submit journal articles detailing work and findings.
- Conduct final project presentation summarizing results with Industrial Team Advisory Committee.

Introduction

This work is a collaborative effort between PNNL, the United States (U.S.) Automotive Materials Partnership (USAMP) team of the U. S. Council for Automotive Research (USCAR), U.S. Steel, Olympic Controls, and Alcoa. This project will develop, validate, and disseminate combined experimental and numerical methods that systematically quantify the forming limits of weld materials in Al alloys and AHSSs through a combination of experimental and deformation-modeling analysis. This work will enable high-volume, robust deployment of TWB, seam-welded tubes and tailor-welded tubes in emerging materials. Figure 1 is a schematic of the project.

The deformation of weld materials and their limits of formability are important aspects to both TWB and hydroforming technologies. The conventional, low-carbon steels used in automotive applications are easily fusion welded using conventional technologies and suffer no appreciable strength degradation near the weld. Al alloys are more difficult to weld than low-carbon steels due to high conductivity and reflectivity and low molten viscosity. Al also has a high propensity for porosity to form during fusion welding as well as hot cracking and heat-affected zone (HAZ) related issues in heat-treatable Al alloys. Many of the AHSSs that are finding increasing application in the automotive industry suffer from degradation of strength in the HAZ. Furthermore, nearly all

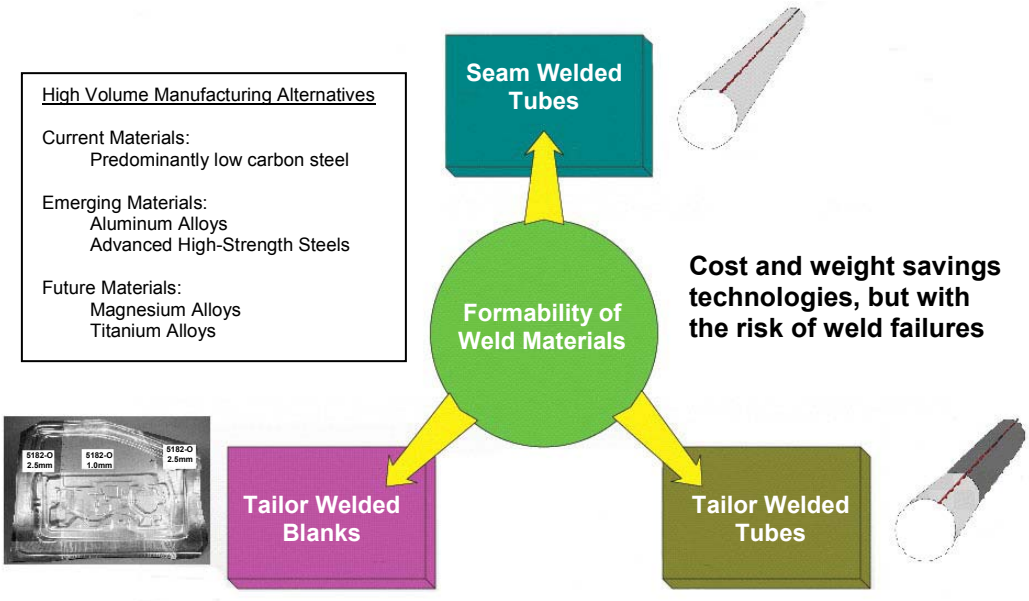

Figure 1. A schematic of the formability of weld materials project.

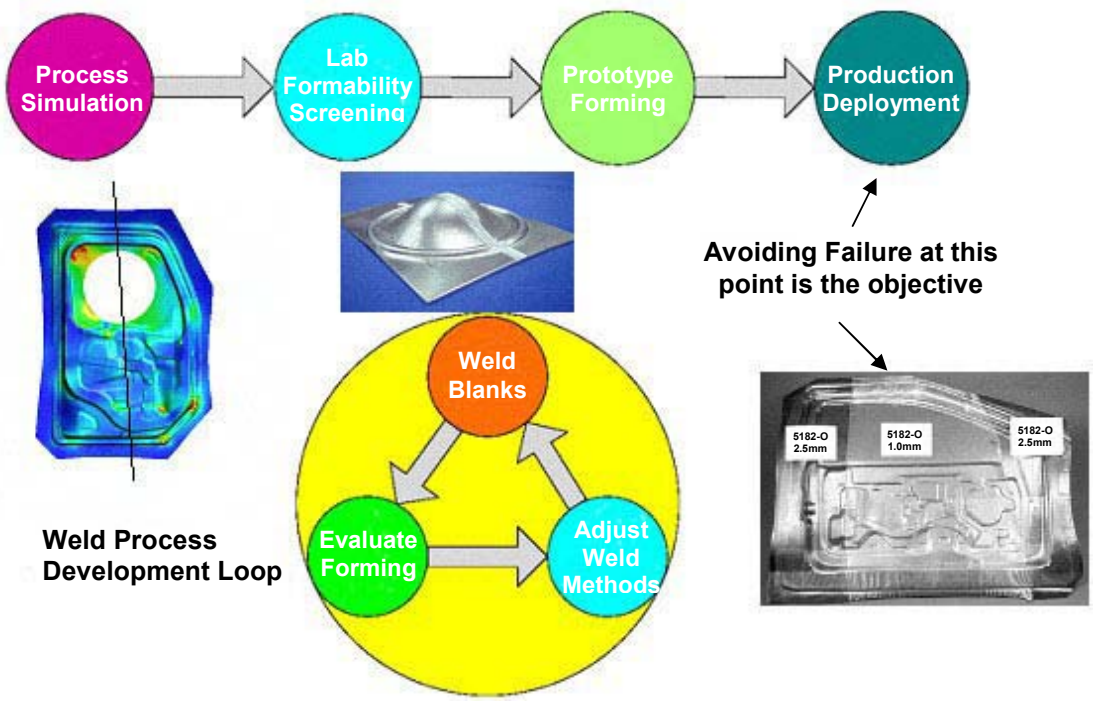

Figure 2. A schematic of the typical manufacturing process development.

fusion welds suffer from irregular geometries and elevated levels of surface roughness compared to the parent materials, which aspects also influence formability and component performance.

This project will focus on developing a generalized numerical method to predict material forming limits in weld materials and verifying deformation and forming-limit predictions. The approach will rely on developing standardized test methods for weld-material populations to establish a statistical description of material imperfection and mechanical properties in their weld region, and developing statistically-based, forming-limit diagrams or continuum damage models that predict material failure in the weld region.

The project will include numerical-model development, validation, and supporting experiments. A number of candidate weld methods will be examined in combination with selected Al alloys and AHSSs. The project materials will include 5000 series and 6000 series Al alloys and relevant high-strength steel alloys including high-strength low-alloy (HSLA), transformation-induced plasticity (TRIP) and dual-phase (DP) steels. The selection of sheet materials and welding methods will be coordinated with the participating OEMs and will be representative of high-volume, commercially-viable materials and processing technologies.

The deliverables will include a standard procedure for weld-material evaluation coupled with a numerical approach for establishing weld-region forming limits. The results will also allow evaluation and development of candidate weld processes and the interaction between materials and weld parameters. The overall objective is to develop test methods and experimental results to enable widespread deployment of weight-optimized TWB and tube hydroforming and to avoid weld failures during production. Figure 2 is a schematic of the typical manufacturing process development.

Experimental Characterization

This year, an increased focus on biaxial experiments occurred. Currently, the experimental characterization has focused on incorporating biaxial limited-dome-height (LDH) tests to FSW AA5182-O to AA5182-O alloys. Biaxial testing continued for the FSW AA5182-O to AA6111-T4 alloys and DP 600 laser-welded alloys. The

following details progress to date with greater emphasis on the 5182 welded alloy population. In the uniaxial experiments of 5182 FSW specimens, twenty-nine of the thirty longitudinal specimens failed in the thin sheet-grip region and all thirty transverse specimens also failed in the thin sheet-grip region. The TWB thickness combination for this population is 2 mm to 1 mm. Figure 3 illustrates the failure observed in both a longitudinal and a transverse specimen.

Miniature tensile tests performed on specimens removed from the weld and weld region indicated the weld material to be just as ductile and strong as the parent sheet. Figure 4 compares the stress-strain response observed in the parent sheet and weld material. Minimal mechanical property gradients across the weld and weld region were observed. This led to implementing a new test approach involving biaxial LDH tests to further characterize the 5182 FSW TWBs.

Biaxial LDH tests were performed on the 5182 welded alloys. Both full domes, 4-inch-wide domes, and 1.5-inch-wide domes were tested, with a minimum of five specimens tested for each condition. Smaller width domes were implemented to obtain uniaxial strain data since the smaller the width of the dome, the closer the behavior is to uniaxial. Full-dome tests were also conducted on the parent sheet material for the TWB combination. Digital-imaging correlation (DIC) was used to evaluate the specimens.

For the 5182 welded specimens, all full-dome biaxial tests failed in the thin sheet (Fig. 5). Testing then continued with the 4-inch-wide specimens; however, failures in the lock bead region of the thin sheet were observed when the same test conditions as in the full-dome-height tests were used. Figure 6 illustrates the failure observed. Failure in the lock bead is typically indicative of too large of a clamp load. When the clamp load was reduced, failures in the lock bead still occurred regardless of the pressure used even when excessive draw took place. An acceptable clamp load was ultimately found and much effort and care was put forth in specimen preparation and shimming of the specimen to reduce excessive failures in the lock bead.

Fourteen 4-inch-width specimens were tested at the same test conditions and six of the fourteen specimens failed in the weld transverse to the weld. Failure in the lock bead prevented the other specimens from reaching full height. Figure 7 illustrates the DIC strain data for a 4-inch width specimen.

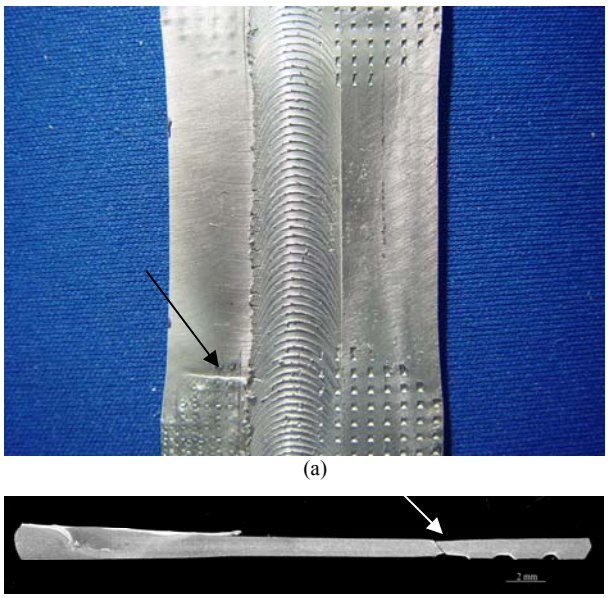

(a)

(b)

Figure 3. An illustration of the failure observed in the grip region of the 5182 welded alloy uniaxial speicmens. Image (a) is a longitudinal specimen and (b) is a cross-section of a transverse specimen.

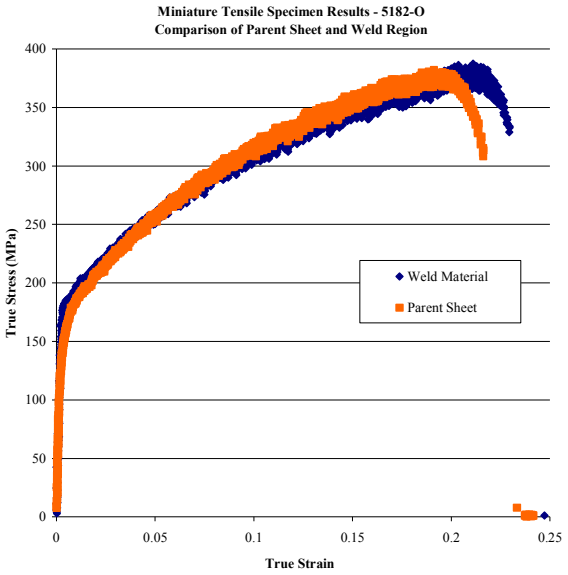

Figure 4. The stress-strain curves of the parent material and weld material of the 5182 TWB.

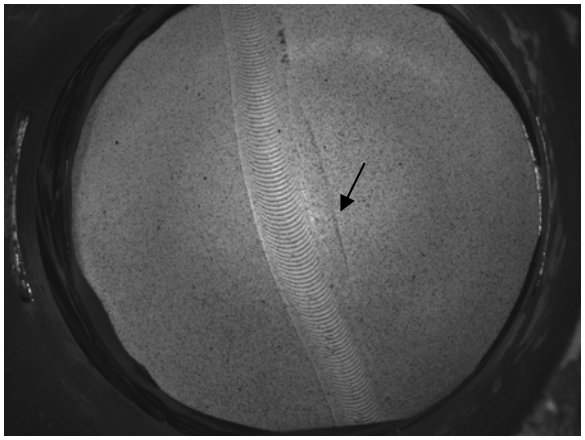

Figure 5. Photo representative of failure observed in the thin sheet of full-dome LDH tests of the 5182 TWB welded alloy.

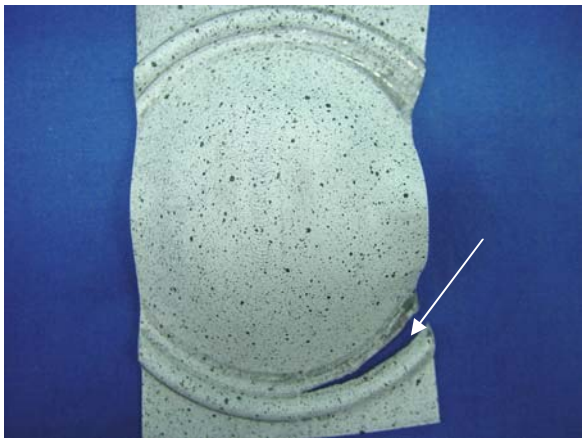

Figure 6. Photo representative of failures observed in the lock bead region of 4-inch and 1.5-inch LDH specimens.

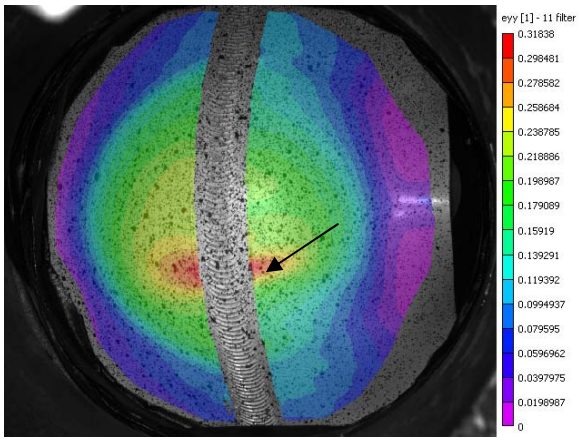

Figure 7. An illustration of the DIC strain data just prior to fracture on a 4-inch-width 5182 welded dome-eight specimen. Fracture occurred in the red region.

LDH tests of the 1.5- inch-width FSW 5812 specimens were not successful. All specimens tested failed in the lock-bead region of the thin sheet. Failure still occurred in the lock-bead region when a low clamp load was used that allowed excessive draw-in. When a monolithic, 1-mm-thick, 1.5-inch-width 5182 specimen was tested, failure was still observed in the lock-bead region. Modifications to the lock-bead radius may be needed to prohibit failure in the lock-bead region.

Due to the high quality of the weld, further analysis of the strain data is needed to determine how the biaxial results compare to the monolithic 5182 FLD. This will help determine whether further biaxial testing is viable.

Marciniak-Kuczynski (M-K) Method to Predict Formability

Previously, FLDs for the DP 600 and 5182-6111 TWBs were generated using a M-K method approach. The M-K model can track the development of plastic strains in the monolithic sheet and the weld materials under applied external loading. The model also tracks the evolution of imperfections and predicts localization and failure of the specimens. Theoretical FLDs are generated based on uniaxial tensile results and statistical probability. The level of imperfection, f, that must exist in the specimens in order to describe the formability for each of the thirty longitudinal specimens, is determined. A Weibull probability distribution is then applied to describe the longitudinal specimen imperfections and the predicted FLD for the TWBs is generated.

Previously, the 5182-6111 full-dome biaxial test experiments were compared to the theoretical FLD generated. Discrepancies of the model and biaxial experiments were observed, so all test results were combined in a FLD where the strain longitudinal to the weld and the strain transverse to the weld were plotted. The FLD of the parent sheet material (from literature) was also plotted. Figure 8 shows that there is a region in the FLD where the weld will always fail and a region where the sheet will fail. In between is a “gray area” where either the weld or HAZ of the thin-sheet 6111 material will dictate the failure.

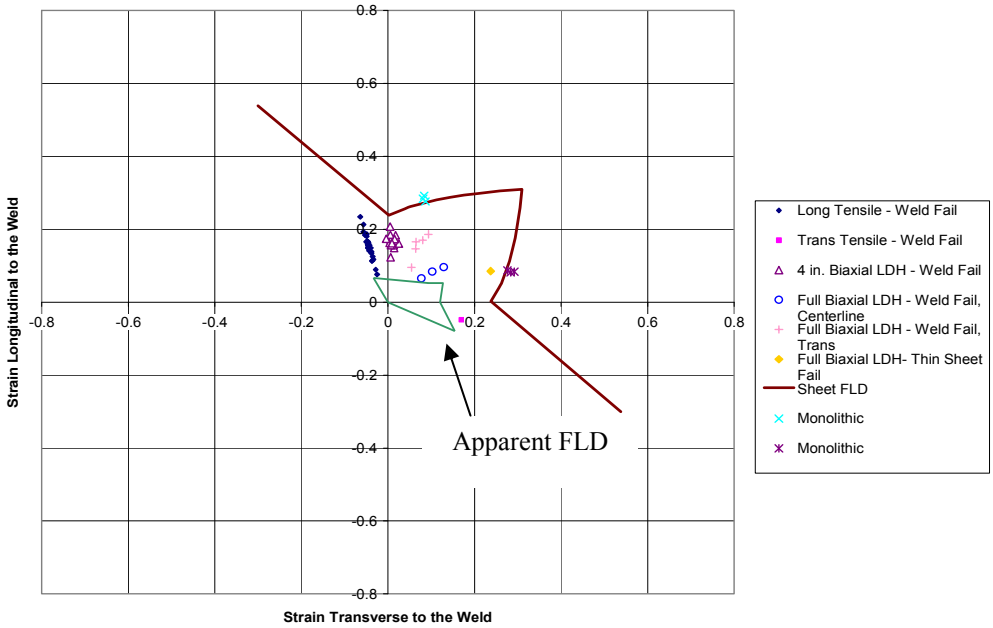

Figure 8. 5182-6111 friction-stir-welded materials combined test results demonstrating apparent FLD for the welded alloy population. The FLD for 6111 monolithic sheet is also shown.

Additional LDH tests were completed to further investigate how the FLDs would be suppressed in these "gray areas." Nine full-dome-width specimen tests and fifteen 4-inch-width specimen tests were completed. Three different failure modes were observed among the full-width specimens and all 4-inch-width specimens failed in the weld, transverse to the weld. Figure 8 demonstrates where the apparent FLD would be for this population. Further modification to the forming-limit prediction is still needed.

Conclusions

From this investigation, the following conclusions were derived:

- Due to the high quality of the weld, obtaining failures in the 5182 FSW alloys through biaxial testing proved to be difficult.
- Further analysis of the FSW 5182 strain data is needed to determine how the biaxial test results compare to the monolithic 5182 FLD to determine the viability of additional biaxial testing.
- Further investigation of a combined forming limit prediction of DP 600 and AA5182-6111 welded alloys is needed where the combined FLD is quantified using the statistical approach.

Presentations

1. *"Characterization and Formability of 5182-6111 TWBs"* presented at Materials Science & Technology 2007 Conference and Exhibition, Detroit, MI, September 17, 2007.
2. "*Forming Limits of Friction Stir Welded 5182-6111 TWBs*" presented at TMS 2007 Annual Meeting, Orlando, FL, and March 1, 2007.
3. *"Determining Aluminum Alloy Strain Localization under Biaxial Loading Using In-Situ Optical Strain Imaging"* presented at TMS 2007 Annual Meeting, Orlando, FL, March 1, 2007.
4. *"Forming Limits of Weld Material in Aluminum Alloys and High-Strength Steels"* presented to Industrial Team Advisory Committee, Detroit, MI, December 2006
5. *"Forming Limits of Weld Material in Aluminum Alloys and High-Strength Steels"* presented at USAMP AMD Offsite Annual Review Meeting, Detroit, MI, October 2006.

B. Impact Modeling and Characterization of Spot Welds

Principal Investigator: Zhili Feng
Oak Ridge National Laboratory (ORNL)
1 Bethel Valley Road, Oak Ridge, TN 37831
(865) 576-3797; fax: (865) 574-4928; e-mail: fengz@ornl.gov

Principal Investigator: Srjdan Simunovic
ORNL
1 Bethel Valley Road, Oak Ridge, TN 37831
(865) 241-3863; fax: (865) 574-7463; e-mail: simunovics@ornl.gov

Principal Investigator: Bill Chao
University of South Carolina
Columbus, SC 29208
(803) 777-5869; fax: (803) 777-0106; e-mail: chao@sc.edu

Technology Area Development Manager: Joseph A. Carpenter
(202) 586-1022; fax: (202) 586-1600; e-mail: joseph.carpenter@ee.doe.gov

Expert Technical Monitor: Philip S. Sklad
(865) 574-5069; fax: (865) 574-6098; e-mail: skladps@ornl.gov

---

Contractor: ORNL
Contract No.: DE-AC05-00OR22725

Objective

- Develop a new, robust Spot-Weld Element (SWE) for modeling various modes of spot-weld failure as a function of impact, welding conditions and materials while maintaining the current computational efficiency and ease-to-use.
- Develop the implementation procedure to incorporate SWE in crash-simulation finite-element analysis (FEA) codes used by the automotive crash modelers.
- Generate a companion experimental database on the performance of advanced high-strength steel (AHSS) spot-weld behavior under various loading conditions and deformation rates to support and validate the modeling approach.

Approach

- A new SWE and associated constitutive models.
- Modeling and characterization of weld microstructure and property.
- Deformation and failure-behavior testing under different dynamic-loading conditions.

Accomplishments

- Completed welding and welding-coupon preparation for dynamic testing.
- Completed static testing and dynamic testing.
- Initial correlation between failure load, failure mode and weld conditions under both static- and impact-loading conditions.
- Completed weld-quality assessment and microstructure characterization.
- Initial weld-element analytical formulation.

Future Direction

- Complete welding-process simulation of spot welds to provide detailed weld-property and attribute information for SWE development.
- Complete weld-failure criterion development.
- Complete development of SWE to demonstrate its basic characteristics meeting the intended modeling requirements.
- Deliver initial version of the SWE and its implementation procedure.

Introduction

A primary premise that drives increased use of AHSS in auto body structures is the drastic improvement in crash performance while reducing the weight. Resistance spot welding (RSW) is, by far, the most common joining process used in automotive manufacturing. Typically, there are thousands of spot welds in a vehicle. Because the separation of spot welds can affect the crash response of a welded structural component, the static and dynamic behaviors of the spot welds have been critically important considerations in vehicle design and manufacturing.

RSW of AHSS presents unique technical challenges for automotive structure applications. Due to their high carbon and alloying-element contents, AHSSs are considerably more sensitive to the thermal cycle of welding than the conventional steels used in auto body structures. The higher-grade AHSSs (e.g., dual-phase (DP) 800/1000, transformation-induced plasticity (TRIP), boron) are more difficult to weld and more susceptible to forming brittle microstructures and solidification-induced defects in the weld region. In addition, heat- affected zone (HAZ) softening can occur. Therefore, RSW of AHSS can exhibit very different structural performance characteristics than of conventional steels. For example, AHSS spot welds can fail under different failure modes (button pullout, interfacial, or mixed). In addition, impact experiments on joints and structural components (top-hat, double-hat sections) have shown that RSWs have different response under static and dynamic loads. The spot-welded structural performance among different AHSS can be drastically different and highly dependent on the grades and types of AHSS. Furthermore, there can be considerable variations in microstructure and properties in the weld region for a given type and grade of AHSS made by different steel producers due to the differences in steel chemistry and processing routes employed.

In recent years, computer-aided engineering (CAE)-based simulation of dynamic-impact behavior of auto body structure during crash has become an indispensable tool that enables rapid and cost-effective design and engineering of crash-resistance auto-body structures. Currently, the behavior of spot welds in finite-element modeling (FEM) impact simulations is usually modeled with a kinematics representation of the joint and the associated constitutive model describing the material-related response of the joint. Currently, the kinematics of the joint are treated as a point connection by means of flexible or rigid (i.e., constrained) links. The sophistication of these beam-link models is limited and can practically involve only force-based laws. One of the principal problems with beam-based kinematics models is that the stress and strain distributions in the weld area are not accurately represented. On the other hand, the maximum shear stress in the weld nugget could be the primary stress component causing the interfacial failure of RSW. For RSW in *conventional* steel structures, the dominant failure mode is the button pull-out and the inadequate calculation of the shear stress may not be a major concern in impact simulation of vehicles. For AHSS RSW, accurate determination of the shear stress may be critical because of the reported interfacial failure or mixed interfacial plus pull-out failure mode. In addition, the multiple failure modes and the changes in failure modes under different loading conditions require development of more versatile failure criteria based on the fracture- and damage-mechanics principles than the resultant force-based ones. From the structural stiffness perspective, the bar-and-beam models typically yield acceptable accuracy under tension, out-of-plane torsion and bending loads. However, the stiffness models are highly inaccurate for in-plane torsion and shear.

This program aims at developing a novel and robust spot-weld modeling approach supported by

experimental data that can be implemented in crash-simulation FEA codes used by the automotive crash modelers. The research tasks include: (1) developing a new, robust, spot-weld finite-element formulation and implementation procedure for modeling various modes of spot-weld failure as a function of impact, welding conditions and materials while maintaining the current computational efficiency; (2) performing coupon-level, dynamic testing to generate the experiment database of spot-weld performance under different loading modes and strain rates during impact; (3) developing failure criterion which can adequately deal with the failure mode changes usually encountered during dynamic loading of a spot weld; and (4) validation of the new crash-modeling approach by component-level crash testing.
This report covers the progress for the first 10 months of the program (December 2006 to September 2007).

Material Selection and Fabrication of Welds

Two steels, DP 780 and draw-quality special-killed (DQSK), were selected by the A/SP Strain Rate Characterization Project Team (see 5.G) for initial development in this project. A third steel, either Boron or DP 980, was considered in the later part of the project. The DP 780 steel had a nominal thickness of 1.15 mm. The nominal thickness of DQSK mild steel was 1.0 mm.

The selection of welding conditions considered the effect of weld-nugget size on failure mode during testing. Three target weld nugget sizes were chosen as the weld matrix for model development:

- Minimum nugget size per industry specification (provided by A/SP Joining Technologies Team): $4\sqrt{t}$ (where t = sheet thickness).
- Maximum nugget size attainable without expulsion: $5.5\sqrt{t}$.
- Medium nugget size = (min+max)/2.

The welding conditions were adjusted to produce the different sized welds.

Table ***1*** summarizes the welds and the associated welding conditions. The weld-nugget size (as determined by peel test) ranged from 4 to 6 mm.

Table 1. Summary of welding conditions and weld nugget sizes.

Weld Schedule Data									
Test	Material	Gauge	Coating	Specified Weld Size	Weld Size Range	Electrode Cap	Weld Force	Weld Current*	Weld Time
3806r1	DP780	1.15 mm	Galv'nel	4.3	4.1 – 4.5	A1 - 4.2	500	6.6	8
3806r2	DP780	1.15 mm	Galv'nel	5.1	4.9 – 5.3	A2 - 5.0	650	6.7	12
3806r3	DP780	1.15 mm	Galv'nel	5.9	5.7 – 6.1	A3 - 5.8	750	8.0	16
3806r4	Mild	1.00 mm	HDG	4.0	3.8 – 4.2	A4 - 3.9	400	7.7	8
3806r5	Mild	1.00 mm	HDG	4.8	4.6 – 5.0	A5 - 4.7	400	8.4	11
3806r6	Mild	1.00 mm	HDG	5.5	5.3 – 5.7	A6 - 5.4	550	9.7	15

Microstructure Characterization

Figure 1 shows the appearance of spot welds made under different welding conditions. There are drastic differences in weld microstructure between DP 780 welds and DQSK (mild steel) welds. More detailed microstructure characterizations are under way.

It is **also** important to point out the solidification shrinkage void at the center of DP 780 welds made to the minimum nugget size. The solidification-shrinkage-induced void was observed on replicate weld samples. Such defects may have contributed to the interfacial failure during quasi-static and impact testing.

Figure 2 shows the microhardness distributions of DP 780 and DQSK spot welds. Due to symmetry, only the top half of the spot weld was measured. The overall microhardness distributions of different-sized welds of the same steel made with different welding conditions are similar, with slightly higher hardness for the smaller welds. However, DP 780 exhibits very different microhardness and strength distribution from the DQSK steel. These differences will need to be considered in the formulation of the SWE.

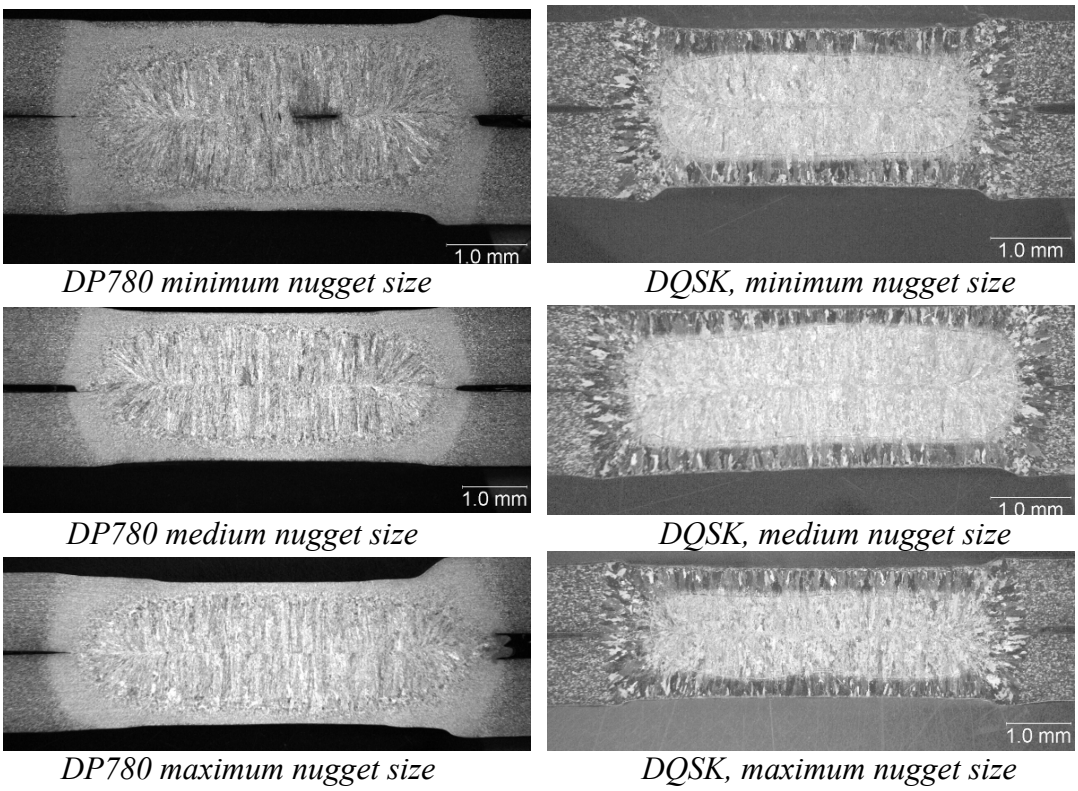

Figure 1. Weld nugget appearance of DP 780 and DQSK welds. Solidification void was observed in DP 780 welds.

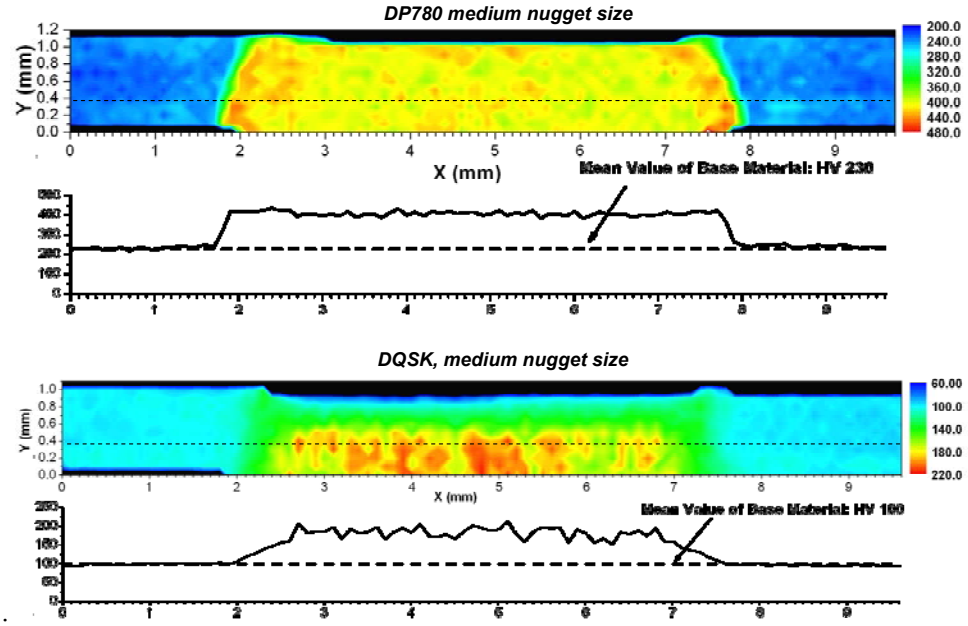

Figure 2. Microhardness mapping of spot welds. Only upper half of the spot weld is measured. The line plots show the hardness variations alone the dashed lines in the hardness mappings.

Impact and Static Test of Spot Welds

Both dynamic and static testing of the spot welds, in lap-shear, cross-tension, and mixed torsion/tension loading configurations, were performed. The test matrix included the followings:

- Two steels: DQSK, and DP 780.
- Three weld-nugget sizes: minimum specified, maximum without expulsion, and medium.
- Five loading modes: cross-tension, lap-shear, three combinations of torsion and tension at 0, 30 and 90 degrees.
- Four loading velocities: quasi-static, 2.6 m/s (5.8 mph), 3.6 m/s (8.1 mph), and 5.8 m/s (12.5 mph).

Standard lap-shear and cross-tension weld coupons were used in this study. The dimensions of the lap-shear coupon were 2-in. wide and 6-in. long, with the spot weld at the center of 2-in. overlap. The cross-tension coupons were also 2-in. wide and 6-in. long. A specially-designed coupon configuration was used for the mixed torsion and tension loading-mode testing. Figure 3 shows the mixed-load coupon design and the experimental set-up.

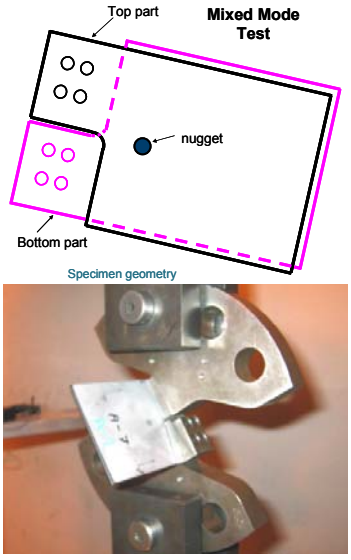

Figure 3. Mixed torsion/tension load weld coupon design and the experimental setup for mixed torsion/tension loading at 30 degrees.

Table 2 summarizes the failure modes observed during the lap-shear and cross-tension test for different loading rates and weld button sizes. For mild steel (DQSK), the failure mode is clearly related to the loading mode. All interfacial failure occurred under shear loading mode. For DP 780, interfacial failure is also associated to the shear loading, except for the minimum button-size case where a solidification-shrinkage void was observed. The weld size also has a pronounced effect; interfacial failure occurred when the weld is at the minimum or medium button size.

Table 2. Failure modes of spot welds in lap-shear and cross-section tests.

Material	Weld Button Size (mm)	Load Mode	Loading speed (mph)	Failure mode
DP780	4.3	CT	Static	Interfacial
DP780	4.3	CT	8.1	Interfacial
DP780	4.3	CT	12.5	Interfacial
DP780	5.1	CT	Static	Pullout
DP780	5.1	CT	5.8	Pullout
DP780	5.1	CT	8.1	Pullout
DP780	5.1	CT	12.5	Pullout
DP780	5.9	CT	Static	Pullout
DP780	5.9	CT	8.1	Pullout
DP780	5.9	CT	12.5	Pullout
DP780	4.3	LS	Static	Interfacial/Pullout
DP780	4.3	LS	8.1	Pullout
DP780	4.3	LS	12.5	Interfacial/Pullout
DP780	5.1	LS	Static	Pullout
DP780	5.1	LS	8.1	Pullout
DP780	5.1	LS	12.5	Interfacial/Pullout
DP780	5.9	LS	Static	Pullout
DP780	5.9	LS	8.1	Pullout
DP780	5.9	LS	12.5	Pullout
Material	**Weld Button Size (mm)**	**Load Mode**	**Loading speed (mph)**	**Failure mode**
DQSK	4	CT	Static	Pullout
DQSK	4	CT	5.8	Pullout
DQSK	4	CT	12.5	Pullout
DQSK	4.8	CT	Static	Pullout
DQSK	4.8	CT	8.1	Pullout
DQSK	4.8	CT	12.5	Pullout
DQSK	5.5	CT	Static	Pullout
DQSK	5.5	CT	5.8	Pullout
DQSK	5.5	CT	8.1	Pullout
DQSK	5.5	CT	12.5	Pullout
DQSK	4	LS	Static	Pullout
DQSK	4	LS	8.1	Interfacial
DQSK	4	LS	12.5	Interfacial
DQSK	4.8	LS	Static	Pullout
DQSK	4.8	LS	8.1	Interfacial/Pullout
DQSK	4.8	LS	12.5	Interfacial/Pullout
DQSK	5.5	LS	Static	Pullout
DQSK	5.5	LS	8.1	Pullout
DQSK	5.5	LS	12.5	Pullout

No inter facial failure was observed at the maximum weld size produced in this study. Increases in loading rate tend to promote the interfacial failure for lap-shear loading condition.

The effect of weld-button size on the failure load of spot welds is provided in Figure 4. The data

presented include all the loading rates under lap-shear and cross-tension. Clearly, failure strength is proportional to the weld size. DP 780 has much higher failure strength than DQSK. The effect of the loading rate (impact velocity) is shown in Figure 5. For comparison between different steel grades, the failure load is normalized to that under the static-loading case. The effect of loading rate (strain-rate sensitivity) was clearly observed. Overall, the failure strength generally increases as the strain rate increases. However, the degree of strain rate sensitivity is rather complicated – it appeared to be strongly related to the steel grade and the loading mode. Further data analysis is under way to quantify the effect of strain-rate sensitivity.

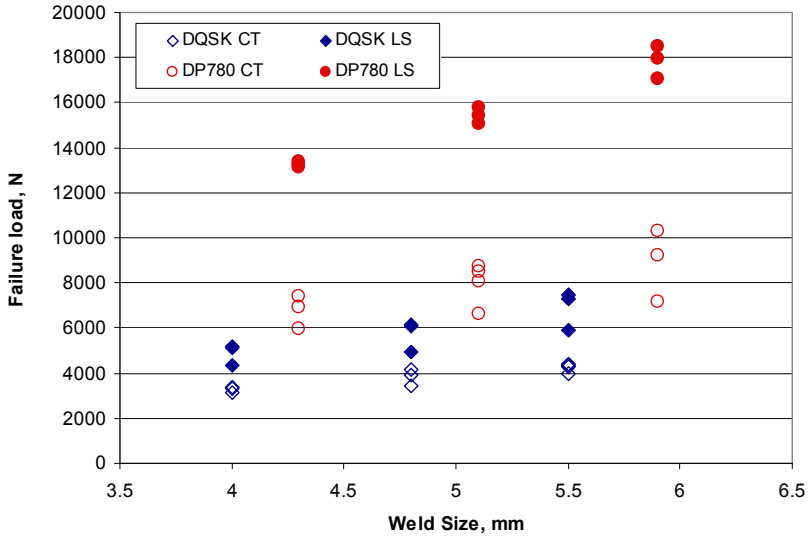

Figure 4. Effect of weld size on the failure load of spot welds.

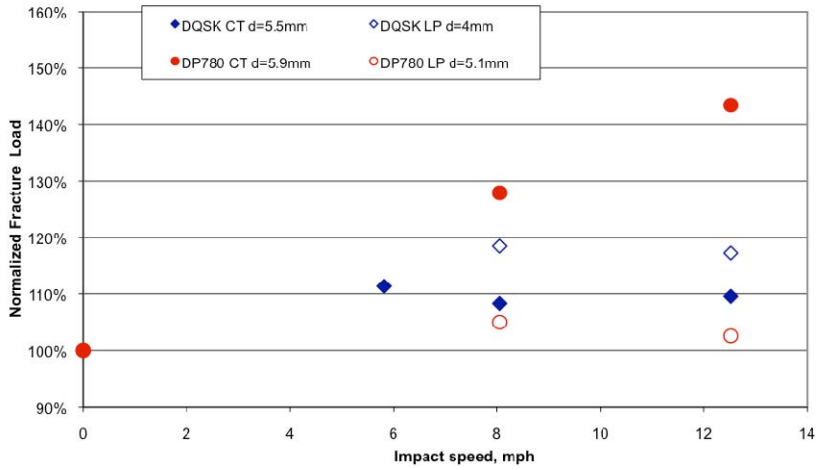

Figure 5. Percentage change of failure load as function of loading rate (impact speed).

Development of Spot Weld Element

A new FEM element formulation, the SWE, based on constraints between thick shell element for modeling of sheets and solid elements for model ing of spot-weld zone, has been developed. Shell degree of freedoms (DoF) are coupled with solid Element DoF using constraints that are connecting shell-element displacements and rotations of its mid-surface with displacements in the solid element. The objective is to provide a better model

for transfer of loads through the spot weld. The better description of the forces and deformations in the spot weld will allow for utilization of more accurate failure criteria based on stresses in the HAZ and the weld nugget.

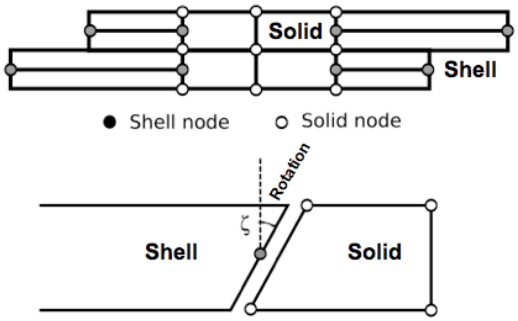

Figure 6. Spot-weld zone representation using shell and solid elements.

Two formulations are being explored. The first formulation depicted in Figure 6 is based on coupling rotational and displacement degrees of freedom between the shell (sheet metal) and the solid (spot-weld nugget). The second formulation (Figure 7) uses thick shell elements in the HAZ to better couple through-thickness stresses.

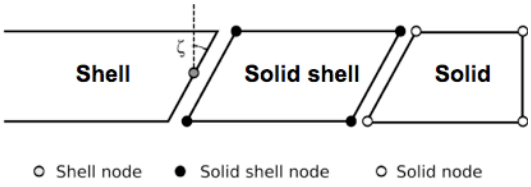

Figure 7. Spot-weld model using tick shells for HAZ.

The analytical expressions defining the mapping of DoF between the elements have been developed. Current shell-element discretization for crash-model sizes are often of the same order as weld diameter and it is, therefore, feasible to introduce a new modeling entity of the RSW dimensions.

The solid elements use eight nodes which provide sufficient flexibility for representation of the stress and strain fields within the RSW zone. Stress distribution in solid elements and element geometry can be used to introduce fracture toughness of the interfacial region in the failure criteria. Mesh refinement of the weld zone is straightforward and non-conformal meshes can also be explored. It is expected that the constitutive models to be used in a SWE will be based on strain-rate sensitive, elasto-plastic fracture- and damage-mechanics models. The actual material models will need to be first evaluated in the context of RSW as such efforts have not been reported in the open literature. The coupling of the constitutive model to the SWE will require more sophisticated element failure and removal strategy than is currently available in commercial software.

Initial simulations using the above formulations were performed on lap-shear, cross-tension and mixed-mode specimens (Figure 8 to Figure 10, respectively).

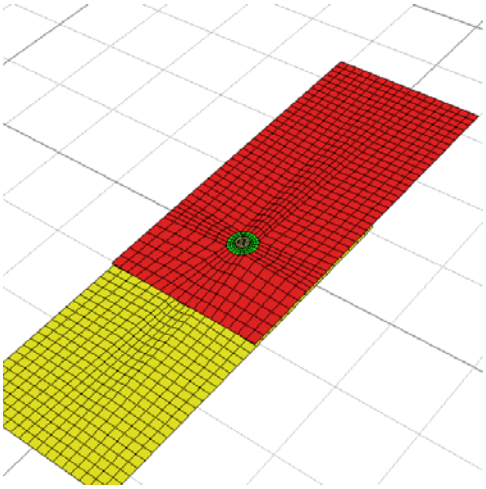

Figure 8. Lap-shear spot-weld model.

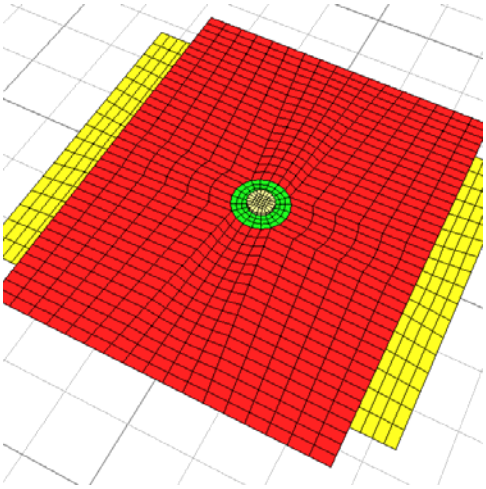

Figure 9. Cross-tension spot-weld model.

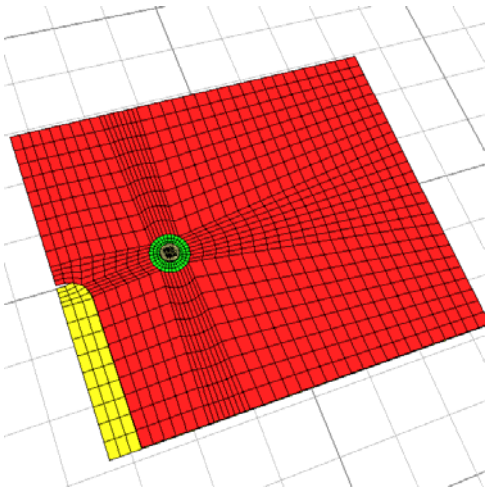

Figure 10. Mixed-mode spot-weld model.

Models are using very fine finite-element meshes in order to remove artifacts due to mesh sensitivity, and the final models will employ much coarser discretization. Simulation results are compared with the experiments to develop failure criteria for the spot welds. The deformations prior to the spot-weld failure are in good agreement with the experiments. Various failure criteria are currently being explored for inclusion into the overall spot-weld model.

Plan for FY2008

- Complete welding-process simulation of spot welds to provide detailed weld- property and attribute information for SWE development.
- Complete weld-failure criterion development.
- Complete development of SWE to demonstrate its basic characteristics meeting the intended modeling requirements.

C. Friction-Stir Spot Welding of Advanced High-Strength Steels

Principal Investigator: Michael L. Santella
Oak Ridge National Laboratory (ORNL)
1 Bethel Valley Road, Oak Ridge, TN 37831-6096
(865) 574-4805; fax: (865) 574-4928; e-mail: santellaml@ornl.gov

Principal Investigator: Glenn J. Grant
Pacific Northwest National Laboratory (PNNL)
902 Battelle Boulevard, P.O. Box 999, Richland, WA 99352
(509) 375-6890; fax: (509) 376-6034; e-mail: Glenn.Grant@pnl.gov

Principal Investigator: Yuri Hovanski
PNNL
902 Battelle Boulevard, P.O. Box 999, Richland, WA 99352
(509) 375-3940; fax (509) 376-6034; e-mail: Yuri.Hovanski@pnl.gov

Technology Area Development Manager: Joseph A. Carpenter
(202) 586-1022; fax: (202) 586-1600; e-mail: joseph.carpenter@ee.doe.gov

Expert Technical Monitor: Philip S. Sklad
(865) 574-5069; fax: (865) 576-4963; e-mail: skladps@ornl.gov

Expert Technical Monitor: Mark Smith
(509) 375-4478; fax: (509) 375-4448; e-mail: mark.smith@pnl.gov

---

Contractor: ORNL and PNNL
Contract Nos.: DE-AC05-00OR22725 and DE-AC06-76RLO1830, respectively

---

Objective

- The primary objective of this project is to develop friction-stir spot welding (FSSW) as a superior method to join advanced high strength steels (AHSS).
- Phase 1 activities will address the critical questions of whether there are tool materials available that have potential for reasonable life and whether FSSWs made in high-strength steels are feasible and can develop similar or better mechanical performance than welds made by conventional processes like resistance spot welding (RSW).
- Phase 2 activities will seek to increase joint strength through a more thorough investigation into weld-process parameters and tool design. This will be accomplished both explicitly using new tools and refined operating parameters and by means of modeling both the process and fundamental conditions applicable to FSSW.

Approach

- The project is in collaboration between ORNL and PNNL, and includes an advisory committee with representatives from Chrysler, Ford, General Motors (GM), two automotive-steel suppliers, and a friction-stir-welding tool supplier.
- Lap joints are made and used to correlate tensile shear strength with processing parameters and microstructures.

- Tool durability is evaluated by measuring tool wear after and during test programs and by characterizing the tool strength with changing welding conditions.
- Process modeling will be developed to help define optimum processing conditions and tool geometries.

Accomplishments

- Test programs fabricating spot welds in dual phase (DP) 780 and hot-stamped boron steel (HSBS) were initiated; a wide range of weld parameters were investigated.
- Fabricated coupons were subjected to metallographic examination, hardness testing, and lap-shear tests.
- Metallurgically-bonded areas in the weld nuggets were measured, characterized, and found to be smaller than expected; therefore, tools were redesigned to more effectively bond AHSS via FSSW.
- Initially, two tool materials (tungsten 25% rhenium [W25Re] and polycrystalline cubic boron nitride [PCBN]) and three tool geometries were investigated.
- Trials showed that tool wear in PCBN was low, but tool wear in W25Re was high.
- Mechanical testing of Phase 1 lap-shear coupons in DP 780 and HSBS indicate that, while overall strengths for certain weld parameters are in the range of acceptable values defined by the Draft American Welding Society (AWS) specification for RSW of steel, the specific strength of nearly any condition exceeds the minimum stress condition.
- Mechanical testing of FSSWs joined via Phase 2 tools produced dramatic increases in lap-shear strength when compared to the results from FSSWs produced with Phase 1 tools.
- Testing with Phase 2 tools further established the significant relationships between tool design, process parameters and weld material.
- Numerous evaluations of Phase 2 tools were made in both HSBS and DP 780, producing lap-shear strengths greatly exceeding the AWS D8.1M RSW minimum standard.
- Two new tool materials, silicon nitride (Si_3N_4) and titanium diboride (TiB_2) were used to produce several tools that are currently being evaluated.

Future Direction

- Further develop a process model linking factors critical to industrial implementation including total spot cycle time, tool wear and weld performance with changes in process parameters, tool materials and tool design.
- Evaluate the effects of steel corrosion coatings (hot-dipped galvanized and galvaneal) on the FSSW lap-shear strength.
- Produce a statistical evaluation of FSSW strength in both lap-shear and cross-tension.
- Establish the framework of a design database for spot friction-welded structures.

Introduction

The technology for implementing FSSW of aluminum (Al) in automotive manufacturing environments exists. C-gun-type FSSW heads have been developed and adapted to robotic systems that are now commercially available for FSSW of Al alloys. This project addresses the questions of whether the FSSW process is viable for joining AHSS and whether FSSW has advantages over conventional processes like RSW. Preliminary work on FSSW of AHSS suggested that several features of the process (fine-grained microstructure in the nuggets of AHSS, potentially higher-strength joints and higher energy absorption in crash, low energy consumption and environmental emission during manufacturing) may give FSSW cost and energy-saving advantages over RSW. In addition, the process may be viable for high-strength,

lightweighting alloys that currently have joining problems using conventional techniques (DP 1000, martensitic steels such as HSBS, etc.).

Important questions remain about effective, economical application of FSSW to AHSS. Critical questions being addressed in this study include:

- Are tool materials available that have potential for reasonable life?
- Are joint strengths comparable or better than conventional processes?
- Are manufacturing issues appropriate (cycle time, tool wear, process robustness and sensitivity to production variation)?
- Do FSSW joints have any advantage for nondestructive evaluation (NDE), or for real-time process control over RSW?
- Are total life-cycle costs appropriate?
- Can the process be modeled and predictive tools developed to aid designers?

If the effectiveness of FSSW for joining AHSS is established, it could accelerate the insertion of these high-strength, lightweighting alloys into automotive body construction to help meet FreedomCAR goals.

Approach

The primary objective of this project is to characterize the responses of AHSSs to FSSW. The project is organized into two phases. Phase 1 activities addressed the critical questions of whether there are tool materials available that have potential for reasonable life and whether FSSWs made in high-strength steels could develop strengths comparable to those made by conventional processes like RSW. Phase 2 objectives focus on the factors crucial to industrial implementation of FSSW; therefore, the second phase of the project concentrates on evaluation of several specific targets including cycle time, tool durability, process robustness, and repeatability.

The Phase 1 results, combined with the initial work under Phase 2, highlight two important challenges: the development of robust tool materials and the development of weld parameters needed to achieve consistently-high joint strengths. Presently, PCBN is the most durable, effective material from which to make stir tools for welding of steels. PCBN is relatively expensive. It is also difficult to machine into the needed shapes and it is not widely available for purchase. These characteristics significantly complicate modifying tool designs, but such modification is a critical element of maximizing joint strengths. In addition, the intrinsic durability of PCBN is not well characterized. There is considerable interest in identifying and evaluating alternatives to PCBN, particularly any that would reduce tool costs and improve durability.

A second set of challenges, framed by prior work, relates to developing consistently-high joint strengths. Joint strengths are being obtained which compare favorably with minimum values specified in industry standards for spot welds, such as AWS D8.1M. However, the consistency of obtaining these strength levels must be improved. In addition, welding times must be minimized. These conditions can be met by increasing the bonded area of FSSWs. Clearly, both sets of issues, those related to tooling and those related to joint strength, are interrelated.

Besides addressing the issues discussed above, Phase 2 intends to encompass developing a more detailed process model which includes weld-performance prediction, evaluating joint microstructures and mechanical properties, assessing the potential for in-process NDE, and establishing the framework of a design database for spot friction-welded structures. The project is a 50/50 collaboration between ORNL and PNNL, and it includes an advisory committee with representatives from Chrysler, Ford, GM, Mittal Steel Corp., and Gestamp US Hardtech, Inc.

Materials and Experimental Details

Presently, two uncoated high-strength steels are being used for the FSSW studies: the DP 780 and a HSBS (sourced from a Swedish supplier, the parent of US Hardtech). The DP 780 is 1.5-mm-thick sheet; the thickness of the HSBS sheet is 1.4 mm.

The FSSW performed during Phase 1, as well as during the initial portion of Phase 2, were done

nearly exclusively with PCBN tools. However, during the Phase 2 program, several new tool materials are being evaluated including Si_3N_4, TiB_2 and a new W-based cermet alloy. These materials are currently under investigation as lower-cost alternatives for FSSW tool materials.

All spot welds were made in displacement-control mode by varying the parameters of tool plunge depth and tool-plunging rate. In addition to these control parameters, a number of other process variables are typically recorded for each weld, including weld time, spindle torque, normal force, and temperature, on the back side of the two-sheet stack-ups. This additional information is archived for future use and analysis.

Joint strength is being evaluated by tension testing lap joints to determine their shear-tension strengths. Strengths are being correlated with processing parameters and microstructures. Micro-hardness mapping is also being used to assess the characteristics and properties of the joints.

Results and Discussion

Previously-reported results confirmed that FSSW has the potential to produce joints that meet strength minimums specified by AWS D8.1 for RSWs. However, the initial results also showed that developing high joint strength was related to producing large bonded areas in the FSSWs. It was further deduced that obtaining large bonded areas depended directly on weld parameters, primarily plunge depth, for a particular tool tip length. The results also illuminated the need for carefully matching tool designs to the sheet thicknesses being welded.

Based on the results from the initial work, four new PCBN tools (BN97, BN98, BN99 and BN46) were designed with the intent of increasing the overall bonded area of the FSSWs. Pin lengths were shortened on the BN97, BN98, and BN99 tools to force their shoulders to engage deeper into the top sheet of two-sheet stack-ups. The pin geometries were also altered to enhance the stirring action of the tools. Additionally, one tool, BN46, was designed with a convex shoulder and short, threaded pin with the intent of stirring and bonding larger regions in shorter weld times. Photographs of these four tools are presented in Figure 1.

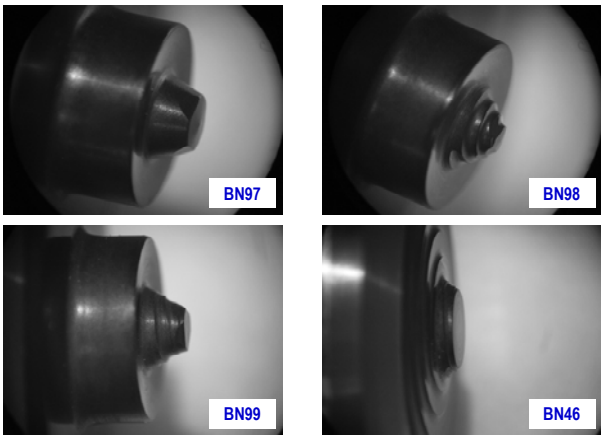

Figure 1. Initial Phase-2 Tools.

The effects of small modifications to tools design are illustrated by the shear-tension strength plots shown in Figure 2. The top plot is of the strength data obtained for DP 780 joints made with the BN77 tool from Phase 1 using plunge depths of 2.7-2.9 mm. The bottom plot shows the strengths measured for joints made with the same plunge depths using the BN99 tool. The solid line in both plots represents a minimum strength for RSWs in 1.5-mm-thick DP 780. Using the BN77 tool, only 2 of 21 specimens exceed the AWS D8.1 minimum. In contrast, 10 of 16 specimens exceeded this limit using the BN99 tool.

Further evaluation of Phase-2 tooling provided greater insight into the affect of tool geometry on weld performance. All four tools showed a marked increase in joint strength, in both DP 780 and HSBS, compared to their Phase-1 counterparts; however, specific performance varied dramatically based on weld material, surface preparation, and weld parameters. Figure 3 shows charts of joint strengths in both AHSS for a FSSW made at 800 rotations per minute (RPM) in 10-second duration. Such data demonstrate the effective differences of tool performance under similar operating conditions in various materials.

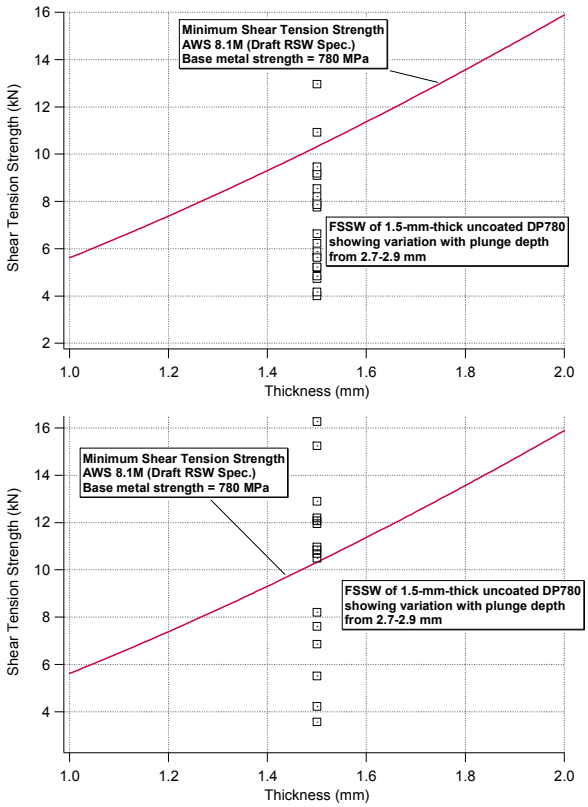

Figure 2. Shear-tension strengths for joints made to plunge depths of 2.7-2.9 mm with (top) BN77 tool (Phase 1), and (bottom) BN99 tool.

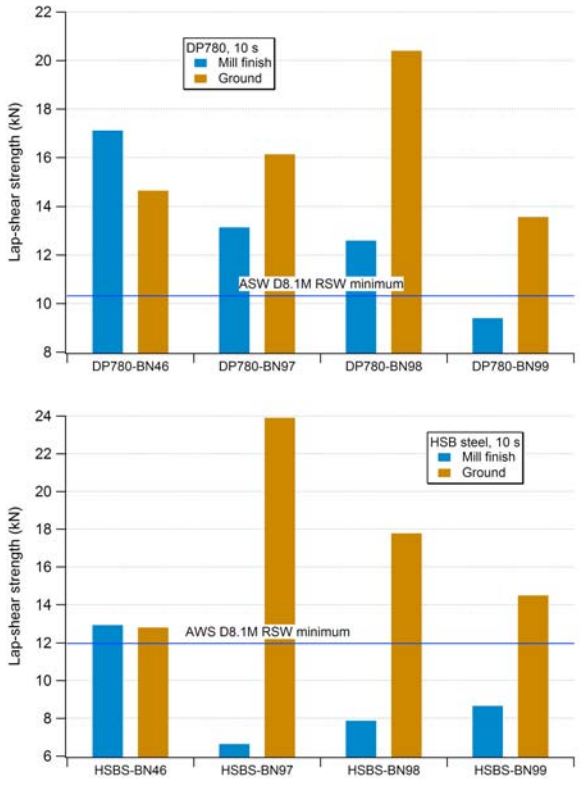

Figure 3. Shear-tension strengths for joints made to plunge a depth of 2.9 mm at 800 RPM in 10 seconds. FSSWs with all four Phase 2 tools in DP 780 (top) and HSBS (bottom).

As performance of the three pin tools (BN97, BN98 and BN99) greatly varied with surface preparation, all data presented in Figure 3 are displayed for joints made in both surface-ground and mill-finish surfaces. The BN46 showed less variability associated with surface preparation and achieved joint strengths above the AWS D 8.1 minimum standard for both DP 780 and HSBS.

An example of the associated microstructure formed using this less-conventional FSSW tool is illustrated in Figure 4. This optical micrograph shows a FSSW made in DP 780 with the BN46 tool. The overall effect of this tool design was to produce a wider, shallower pin cavity. For this particular weld, the plunge depth was actually less than the 1.5-mm thickness of the DP 780 sheets. The overall effect of this approach was to produce what appears to be a much larger bonded area between the two individual sheets than is typical of more conventionally-shaped tools like BN97, BN98, and BN99.

Figure 4. Optical micrograph of FSSW made in DP 790 using the BN46 stir tool.

A sense about the possible differences in properties between FSSWs and RSWs is illustrated in Figure 5. The top two images in this figure are optical micrographs showing a FSSW (upper image) and a RSW (lower image) made in DP 780. The bottom two images are representations of the joint made using data from micro-hardness mapping. Identical scaling was used in both the hardness images with the colors indicating the variations in micro-hardness across the welds. The hardness images confirm that both welds are harder than the DP 780 base metal. However, the weld nugget of the RSW is about

25% higher than that of the stir zone of the FSSW. Additionally, the heat-affected zone (HAZ) of the FSSW is much wider than that of the RSW. These characteristics of the FSSW will influence their overall mechanical behavior and will be addressed in continuing efforts.

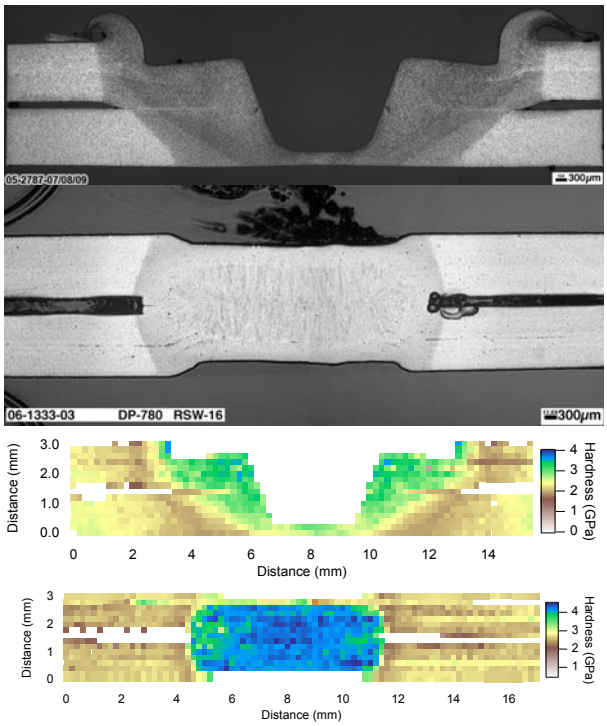

Figure 5. Top two images show optical micrographs of DP 780 FSSW (upper) and RSW (lower). The bottom two images are representations of each weld formed from micro-hardness test data.

Conclusions

During this reporting period, four new PCBN stir tools were designed and produced. Numerous testing conditions were found which produced spot welds that exceed industry-specified minimum strengths for 1.5-mm-thick DP 780 steel and 1.4-mm-thick HSBS.

One of the four new stir tools is a new approach in FSSW tool design. Examination of initial FSSWs made with this tool (BN46) on both AHSSs suggest that it is capable of producing larger bonded areas than those achieved with more conventional pin tool designs. This tool also showed less variability in joint strength with changes in surface preparation than the other Phase-2 tools.

Metallographic examinations showed that in DP 780 the weld-zone hardness of a RSW was about 25% higher than that of a FSSW. Both weld zones had higher hardness than the DP 780 base material. The HAZ of the FSSW was also significantly wider (> 3 mm) than that of the RSW (~ 2 mm). The implications of these differences will be addressed in the continuing testing program.

Finally, several new tool materials were selected for evaluation, including Si_3N_4, TiB_2 and a tungsten-based cermet that does not use the conventional cobalt binder. These tool materials are currently being evaluated and will continue to be investigated during the upcoming year.

Presentations/Publications/Patents

1. Y. Hovanski, M.L. Santella and G.J. Grant. Friction Stir Spot Welding of Hot-Stamped Boron Steel. Scripta Materialia, 57 (2007) 873-876.
2. Y. Hovanski, M.L. Santella and G.J. Grant. Friction stir spot welding of advanced high strength steels. Presentation at MS&T Sept. 2007.
3. Grant GJ, Y Hovanski, and M Santella. 2007. "Friction Stir Spot Welding of Advanced High Strength Steels for Automotive Applications." In: International Symposium on Friction-based Spot Welding Processes, eds. A.M da Silva, J.F.dos Santos, G. Amancio, International Institute of Welding, GKSS Forschungszentrum, Geesthacht, Germany, 2007, pp. 107-148.

D. Thermal-Drilling Application Development

Co-Principal Investigator: P. J. Blau
Oak Ridge National Laboratory (ORNL)
P.O. Box 2008, Oak Ridge, TN 37831-6063
(865) 574-5377; fax: (865) 574-6918; e-mail:blaupj@ornl.gov

Co-Principal Investigator D. M. Paxton
Pacific Northwest National Laboratory (PNNL)
P.O. Box 999/K2-03,Richland, WA 99352
(509) 375-2620; fax: (509) 375-2186; e-mail:dean.paxton@pnl.gov

Participants:
This project is being conducted as a partnership with the United States Automotive Materials Partnership (USAMP), Automotive Metals Division (AMD), with participation that includes the following representatives:

Bill Charron, Ford Motor Company
Larry Krawczak, Chrysler Corporation
Ron Strong, General Motors (GM) Corporation

Technology Development Area Manager: Joseph A. Carpenter
(202) 586-1022; fax: (202) 586-1600; e-mail: joseph.carpenter@ee.doe.gov

Expert Technical Monitor: Philip S. Sklad
(865) 574-5069; fax: (865) 574-6098; e-mail: skladps@ornl.gov

---

Contractor: ORNL and PNNL
Contract No.: DE-AC05-00OR22725 and DE-AC06-76RLO1830, respectively

---

Objectives

- Determine the feasibility of using thermal drilling (ThD) to form fastener holes in high-strength steels and light-weight alloys in the form of castings, hydroformed parts, and sheet stock.
- Determine suitable ThD parameters for selected alloys if they prove to be amenable to the process.
- Thermally drill and tap fastener holes, measure their dimensions, and conduct clamp-load tests to compare the properties of ThD holes to traditionally-produced fastener holes.
- Develop a better fundamental understanding of the ThD process.

Approach

- Alloys for ThD tests were selected and provided by the USAMP project team. ThD bits were purchased or provided as in-kind contributions from tool suppliers.
- ORNL conducted ThD and tapping experiments on the selected alloys, noting which performed best. Hole dimensions and microstructures were documented.
- Where possible, methods were developed to correct any observed hole defects. These included the use of pre-heating and pilot holes. Needs for future process development were documented.
- Maximum fastener clamp loads were measured at PNNL and related to ThD parameters.

Accomplishments

- Established the feasibility of ThD four high-strength steels and six non-ferrous alloys (Al and Mg-based).
- Developed a method of using pilot holes prior to ThD to avoid 'flower-petal' defects in Al alloys.
- Demonstrated that hydroformed high-strength-steel sections were highly suitable for ThD.
- Compiled a list of ThD process parameters for the selected alloys and included it in the final report.
- With one exception, demonstrated that steels were found to be generally more suitable for thermal drilling than the non-ferrous Al and Mg alloys. In fact, ThD and tapped holes in steel sheet thicker than 2.0 mm were so strong that the fastener broke rather than stripping the threads.
- Clamp-load testing was completed on all alloys that could be thermally drilled satisfactorily.
- A comprehensive final report was prepared, submitted to the USAMP team for review, and published.

Future Directions

- Contingent on new funding, optimize ThD on hydroformed steels to produce demonstration articles.
- Investigate new tool-bit designs and establish the feasibility of ThD multiple layers.
- Improve the ThD process to enable better quality results on non-ferrous alloys.

Introduction

The research on this project concluded in mid - fiscal year (FY) 2007 and the major findings will be presented in a final report currently under internal review. The concluding summary is repeated here.

Thermal drilling (ThD), also known as 'friction drilling,' is related to other joining and surface-conditioning processes like friction-stir welding and friction-stir processing that utilize frictional heat generated between a rotating tool and a metal part. In ThD, a conically-tipped tool (usually metal-bonded tungsten carbide) spins against the surface of the part to be drilled, generating heat and softening the surface. It penetrates and then perforates the workpiece, as shown in Figure 1. Softened material is extruded to form a bush on the exit side of the workpiece. A small boss may also be formed on the entrance side, under the shoulder portion of the tool. Another version of the tool has a cutter to remove the boss.

ThD is currently used in the manufacture of tubular hospital furniture and certain niche applications, but has not been adopted in the automotive industry where it has significant potential to enable more extensive use of lightweight, high-strength alloys.

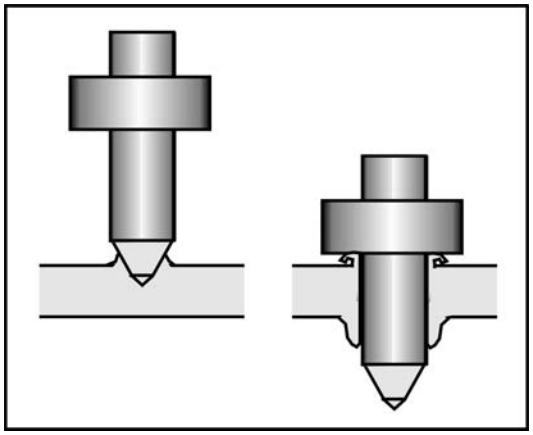

Figure 1. Schematic representation of ThD. The spinning tool penetrates the workpiece (left) to form a boss on the inlet side and a bush on the exit side (right).

Advantages of ThD include the following:

- Unlike traditional drilling, ThD creates no chips.
- ThD does not require drilling fluid that must be handled and disposed of.
- By forming an extruded bush, ThD thickens the effective tappable thickness of thin workpieces like sheet stock and thin-walled castings, so that weld nuts (with their added weight and assembly operations) may not be needed.
- ThD may enable designs that would be impossible due to the need to install nuts or get at the exit side of the hole.

- ThD could simplify manufacture of chassis components from lightweight materials.

The goal of this project was to demonstrate the feasibility of using ThD on selected ferrous and non-ferrous alloys of interest to the automotive industry and to acquire clamp-load data to measure the fastener holding capabilities of ThD and tapped alloys. These alloys are listed in Table 1. Thickness ranged from about 1.12 to 4.1 mm depending on the materials provided and their form.

Table 1. Materials provided for thermal drilling studies.

Alloy	Form
Al A380	Die casting
Al A319-T5	Die casting
Mg AZ91	Die casting
Mg AM60	Die casting
Mg AE44	Die casting
Mg AM50	Die casting
DP 600 HSS	Sheet
DP 780 HSS	Sheet
DP 780 HSS	Hydro-formed tube
HSLA50 HSS	Sheet
TRIP 800 HSS	Sheet

Technical Approach

The technical approach drew on the strengths of USAMP team members and national laboratories. It consisted of a drilling feasibility study at ORNL that established the ThD parameters that would produce acceptable holes (demonstrated, but not optimized) and clamp-load testing of fasteners in ThD and tapped holes at PNNL. ORNL also made measurements of hole dimensions for the range of drilling conditions that were investigated.

The ThD process variables included the following: (a) hole diameter (drill-bit diameter), (b) drill length, (c) spindle speed, (d) in-feed rate, (e) stock thickness, (f) use of drilling paste, (g) use of pre-heating or pilot holes, (h) use several types of bits, and (i) use of thread-cutting or thread-forming taps. Additional details of the task plan were provided in prior project reports and will be in the final report.

Results

A qualitative assessment of thermal drillability was made based largely on visual observations of the quality of the bushes created using bits for M6-sized holes. Table 2 summarizes these assessments. The designation codes were:

- **Poor** (***P***) – not suitable (distorted or torn bushes)
- **Marginal** (***M***) – might work but requires additional studies and process enhancements
- **Special Procedures** (***SP***) – satisfactory results are obtained when using special procedures like pilot holes or drilling paste.
- **Good** (***G***) – expected to work well, especially by optimizing standard process parameters like spindle speed and in-feed rate.

Most steels were rated *G*, but the *P* rating for TRIP 800 was based on the formation of flower-petal-like features at the exit sides of the holes.

Table 2. Assessment of ThD Response of Selected Alloys.

Alloy	Form and Stock Thickness (mm) (Note 1)	'Thermal Drillability' Rating
Al A380	DC (4.1)	*S P*
Al A319-T5	DC (4.1)	*S P*
Mg AZ91	DC (1.5, 3.0)	*M*
Mg AM60	DC (3.0)	*M*
Mg AE44	DC (3.0)	*M*
Mg AM50	DC (3.0)	*M*
DP 600 steel	Sh (1.2 – 2.2)	*G*
DP 780 steel	Sh (1.15 – 2.0)	*G*
Hydro-formed DP 780	HF (~ 2.5)	*G*
HSLA50 steel	Sh (1.14)	*G*
TRIP 800 steel	Sh (1.0)	*P*

Note 1) DC = die-cast, Sh = rolled sheet or plate

Spindle speeds and down-feed rates for the M6 hole-sized ThD tools are summarized in Table 3. It should be noted that the reported speeds and down-feeds were not optimized in this concept feasibility effort, but rather they were experimentally found to produce satisfactory holes for subsequent tapping and clamp-load testing.

Table 3. ThD Conditions for Alloys Used in this Project (M6 fastener holes).

Alloy	Spindle Speed (rpm)	Down-feed (in/min)
DP 600 steel	2500-4000	0.50
DP 780 steel	2000	0.75-1.00
HSLA50 steel	2000	0.50
Al A380*	10,000	2.5
Al A319-T5*	10,000	2.5
Mg AZ91D*	2,500	2.0
Mg AM60	8,000	2.0
Mg AE44*	8,000	2.0
Mg AM50	8,000	2.0

* Pilot holes were used.

Fastener Testing at PNNL

Torque-tension testing was performed at PNNL using the methods described in previous project reports.

The two primary factors that influence the clamp load at failure and the mode of failure are the thread-engagement depth of the fastener and the strength of the materials to be joined. For steel samples greater than 2-mm thick with either ThD and tapped holes and using the baseline design of 5- and 8-mm weld nuts and M6 machine screws, the failure mode was always to break the fastener and the clamp load at failure was 16-18 kN, as is shown in Figure 2. Similar performance was observed for ThD and tapped holes in DP 780 hydroformed tubes. Neither the type of steel nor the ThD process variables appeared to have an effect on the magnitude of clamp load.

For conventionally-drilled or thermally-drilled holes in steel plate with thicknesses of 1.5 mm or less, the failure mode was always stripping of the threads. Thermally drilled holes in 1.2 mm plates still generated nearly 14-16 kN in clamp load before stripping, whereas convention-ally drilled holes in the same thickness plate generated less than half that amount at ~7 kN.

For the lightweight aluminum and magnesium alloys, torque-tension testing of thermally drilled and tapped holes produced stripped threads at clamp loads of 6-8 kN. Further research is needed to optimize the microstructure and processing of lightweight alloys to achieve higher clamp loads.

Future Work

This project ended at the end of March 2007. Several car companies are considering the implementation of this novel production technology under internal sponsorship. Future R&D work is needed in several areas identified in the final report, particularly for non-ferrous alloys, but no follow-on effort has yet been identified.

Conclusions

The feasibility of thermally drilling a variety of ferrous and non-ferrous alloys, in various thicknesses, has been determined but not optimized. The success of this work was due in part to effective collaboration among USAMP team members and by the ability to draw upon prior work at the University of Michigan and ORNL. The following conclusions were reached:

1. High-strength steels, such as DP 600, DP 780, and HSLA50, seemed well suited for ThD, but TRIP 800 was not.
2. Thread-forming fasteners offer opportunities to make the best use of ThD technology and should be a focus for future work.
3. The formation of extended bushes by ThD can increase the tappable hole length in steel sheet products by as much as 300%.
4. ThD conditions must be developed for the specific material being drilled and cannot be generalized for all metals and alloys within a particular class (e.g., “steels”).
5. Maximum clamp-load data for thermally-drilled and tapped steel stock over 2.0-mm thick were encouraging and suggest the potential for using this method in assembling high-strength steel automotive components including hydroformed sections.
6. Additional research on the processing method is needed to improve the ThD results for aluminum and magnesium alloys which tend to have lower than desired maximum clamp loads.

A more extensive set of conclusions and a list of subjects for future research in thermal drilling are presented in the final report which is undergoing review.

Publications

1. P. J. Blau, B. C. Jolly, J. Qu, and D. M. Paxton (2007) *Feasibility of Thermally Drilling Automotive Alloy Sheet, Castings, and Hydroformed Shapes*, Final Project Report, to be published as an Oak Ridge National Laboratory Tech Report, 53 pp (under review).

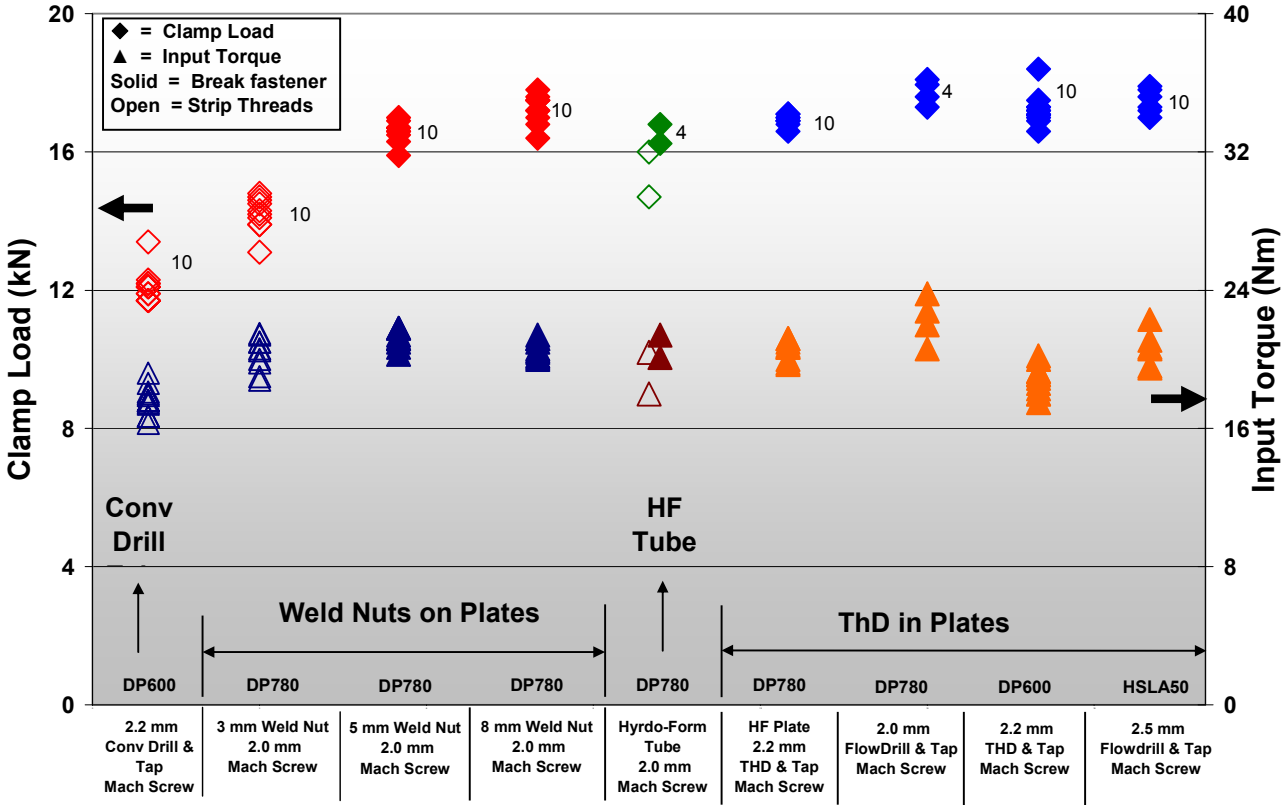

Figure 2. Torque-tension test results for ~2 mm thick steel samples with a variety of hole types and M6 machine screws with Magni 565 coating.

E. Weld-Element and Joining-Process Technology Development

Co-Principal Investigator: Douglas J. Bammann
Professor, Mechanical Engineering
Mississippi State University (MSST)
210 Carpenter Bldg.
Mississippi State, MS 39762
(662) 325-3260; Home: (662) 294-2585; e-mail: djb215@me.msstate.edu

Co-Principal Investigator: Sergio Felicelli
Associate Professor
MSST
Mechanical Engineering
Carpenter Engineering Bldg, Rm 210
Mississippi State, MS 39762
(662) 325-1201; e-mail: felicelli@me.msstate.edu

Postdoctoral Associate: Liang Wang
Center for Advanced Vehicular Systems (CAVS), 2182-B
MSST, P.O. Box 5405
Mississippi State, MS 39762-5405
(662) 325-9235; Home: (662) 325-5421; e-mail: liangw@cavs.msstate.edu

Co-Principal Investigator: Wing Kam Liu
Walter P. Murphy Professor of Mechanical Engineering
Director of the NSF Summer Institute on Nano Mechanics and Materials
Robert R. McCormick School of Engineering and Applied Science
Northwestern University (NU)
Department of Mechanical Engineering
2145 Sheridan Road
Evanston, Illinois 60208-3111
(847) 491-7094; fax: (847) 491-3915; e-mail: w-liu@northwestern.edu

Co-Principal Investigator: Ted Belyteschko
McCormick Professor of Computational Mechanics
Walter P. Murphy Professor of Computational Mechanics
Departments of Civil and Mechanical Engineering
Robert R. McCormick School of Engineering and Applied Science
NU
2145 Sheridan Road
Evanston, Illinois 60208-3111
(847) 491-7270; fax: (847) 491-3915; e-mail: tedbelytschko@northwestern.edu

Co-Principal Investigator: Michael Santella
Oak Ridge National Laboratory (ORNL)
1 Bethel Valley Road, Oak Ridge, TN 37831-6096
(865) 574-4805; fax: (865) 574-4928; e-mail: santellaml@ornl.gov

Co-Principal Investigator: Zhili Feng
ORNL
1 Bethel Valley Road, Oak Ridge, TN 37831
(865) 576-3797; fax: (865) 574-4928; e-mail: fengz@ornl.gov

Co-Principal Investigator: Srdjan Simunovic
ORNL
1 Bethel Valley Road, Oak Ridge TN 37831-6359
(865) 241-3863, fax: (865) 241-0381; e-mail: simunovics@ornl.gov

Technology Area Development Manager: Joseph A. Carpenter
(202) 586-1022; fax: (202) 586-1600; e-mail: joseph.carpenter@ee.doe.gov

Field Technical Monitor: Philip S. Sklad
(865) 574-5069; fax: (865) 574-6098; e-mail: skladps@ornl.gov

---

Contractor: MSST
Contract No.: 4000054701

Objective

- Develop the next generation of weld-element technology and joining-process technology (i.e., spot welding, ultrasonic welding) and assess the applicability of new technology for impact simulations and process optimization using lightweight alloys.

Approach

- Currently, weld-element performance and failure is based on a simple beam model in which the weld is modeled as a single element between two welded sheets and failure is postulated to occur when the tension or a moment exceed a certain specified threshold. This type of model does not reflect the thermo-mechanical details of the welding process and, consequently is unable to address variations in strength due to differences in weld-process parameters and the metallurgy of the materials being joined.
- To develop the next generation of weld-analysis technology in which details of the welding process and the metallurgy of the parent material are reflected in the behavior of the weld element, the physics of the resistance-welding process must be modeled in detail. The nature of the solidification process within the weld will be studied. The computed thermal history induced during the welding process will be used to predict microstructural evolution within the weld and adjacent material, thereby allowing prediction of the large mechanical-property gradients associated with the weld. The evolution of damage in the weld under subsequent high strain-rate loading will be studied with strain-rate-dependent constitutive models.
- The development of an ultrasonic welding process has remained largely empirical because the process is extremely complex due to friction-induced deformation and heat generation. We plan to assess the feasibility of developing a weld-element technology and a three-dimensional (3D) process model which will enable a better design of the ultrasonic welding process.

Accomplishments

- A thermo-metallurgical-mechanical model was developed to predict the temperature distribution, solid-phase transformation, and residual stress during the spot-welding process with the commercial finite element software SYSWELD. The TRIP model was reviewed and summarized.

Future Direction

- A comprehensive review of the weld elements for all types of welding procedures – year 1 (MSST).
- The detailed finite-element model (FEM) will first be developed and used to predict the strength of a spot weld under high strain-rate loading; recent development of weld-simulation technology at ORNL will be utilized by MSST team to expedite the weld-element development – year 1 (MSST, ORNL).

- For validation, experiments will be performed to measure the strength of spot-welded coupons under various high strain-rate loadings – years 1 and 2 (ORNL, MSST).
- Following this development and validation of the detailed FEM, a simple weld element will be developed which approximates the mechanical response of the detailed model under high strain-rate loading – year 2 (MSST, ORNL, NU).
- A neural network will potentially be employed within the weld-element development process in conjunction with physics-based, structure-property relations – year 2 (MSST).
- Pilot-scale, high strain-rates tests of large spot-welded components using ORNL high-rate tester to compare with modeling results – year 2 (ORNL, MSST).
- Assess the feasibility of modeling ultrasonic welding process and developing FEM element technology – year 2 (ORNL, MSST, NU). Note: ORNL's effort on this task is planned to be covered under related funding from a DOE program.

Introduction

Resistance spot welding (RSW) is a common joining process used in automotive manufacturing, with thousands of spot welds in a single vehicle. When simulating the behavior of a vehicle under crash conditions, the mechanical behavior of the spot welds under dynamic loading must be incorporated. Currently, spot welds are simulated using a weld element based on a simple beam theory; a next- generation, spot-weld element is needed in which details of the welding process and the metallurgy of the parent material are reflected. A FEM was developed to predict the process-properties relations in the RSW, which model will be implemented in the Spot Weld Element formulation.

Finite Element Modeling

A 3D FEM was developed to simulate the spot-welding process using the commercial code SYSWELD. The model was used to predict the temperature distribution, molten zone, volume fraction of each phase, and residual stress for two-sheet spot welding. Electrical-thermal, thermal-metallurgical, and thermo-metallurgical-mechanical analyses were considered in this model.

Electrical-Thermal Model

In RSW, the heat is generated within the material being joined by the resistance to the passage of a high current through the metal parts which are held under a pre-set pressure. Considering the Joule effect as an internal heat source, the electrical-thermal governing equation is presented as

$$\rho\frac{\partial H}{\partial t} - div(\lambda \cdot \mathbf{grad}T) - \mathbf{grad}V \cdot \sigma \cdot \mathbf{grad}V - Q = 0 \quad (1)$$

The electrical phenomena in the computational domain are assumed to be governed by the electrokinetic model for a frequency close to 50 Hz:

$$div(\sigma \cdot \mathbf{grad}V) = 0 \quad (2)$$

where T, V are the temperature and the scalar electrical potential, respectively. ρ, λ, H, and σ represent the density, the thermal conductivity, the enthalpy, and the electrical conductivity of the medium. The full coupling between electrical and thermal phenomena can be governed by the term $\mathbf{grad}V \cdot \sigma \cdot \mathbf{grad}V$ in the heat equation.

Thermal-Metallurgical Model

In this model, the metallurgical transformations are temperature dependent and accompanied by latent heat effects which modify temperature distribution. The thermal properties depend on the temperature and material phase. Based on the thermal history at each point in the resistance spot welding process, the phase transformations that may occur in the material are predicted using the semi-empirical models presented below. Different metallurgical phases, austenite, ferrite, bainite and martensite, are taken into account for this study. For the martensitic transformation, the Koistinen-Marburger law is used [Koistinen, 1959]:

$$p_m(T) = \overline{p}_m(1 - \exp(-b(M_s - T)))$$
$$\text{for} \quad T \le M_s \quad (3)$$

where $\overline{p}_m$ represents the volume fraction of martensite obtained at an infinite low temperature ($\overline{p}_m$ is frequently assimilated to 1). M_s is the martensite start temperature and b is the evolution coefficient of the transformation process, taken as 0.015 in this model [ASM, 2005].

For the phase transformations involving diffusion in steels (austenitic, ferritic, and bainitic transformations), under isothermal conditions, the Johnson-Mehl-Avrami law is used [SYSWELD, 2005]:

$$p(T,t) = \overline{p}(T)\left(1 - \exp\left(-\left(\frac{t}{\tau_R(T)}\right)^{n(T)}\right)\right) \qquad (4)$$

where $\overline{p}$ represents the phase proportion obtained after an infinite time at temperature T, τ_R is the delay time, and n is the exponent associated with the reaction rate. The parameters of the Johnson-Mehl-Avrami model were extracted from the continuous cooling transformation (CCT) diagram according to the cooling rate and were inserted in the FE code in a tabular form.

Thermometallurgical-Mechanical Model

Several types of interactions between thermal and mechanical analyses are considered including the thermal strains, the volume changes due to the transformations, the influence of the phases on the behavior law, and the plasticity induced by metallurgical transformations. In this study, flat-tip electrodes are used and the mechanical analysis can be uncoupled from the thermometallurgical analysis. The mechanical contact area is equal to the electrothermal contact area, which is assumed to be constant.

The total strain rate is partitioned as follows:

$$\dot{\varepsilon} = \dot{\varepsilon}_e + \dot{\varepsilon}_p + \dot{\varepsilon}_{tp} + \dot{\varepsilon}_{th} \qquad (5)$$

where $\dot{\varepsilon}_e$, $\dot{\varepsilon}_p$, $\dot{\varepsilon}_{tp}$, and $\dot{\varepsilon}_{th}$ are elastic strain rate, plastic strain rate, transformation plasticity, and thermal and metallurgical strain rate, respectively.

Results and Discussions

Two 0.01-mm, zinc-coated, low-carbon steel sheets are utilized in this study. The thickness of each sheet is 0.7 mm. The electrode radius is 3 mm. The current frequency is 50 Hz and the current intensity is 9.2 kA during 20 periods starting at 0.1 s. The force is 3100N during 30 periods staring at 0.1 s.

The temperature contour at the end of the current application (t = 0.3 s) in Figure 1 shows the molten zone. The molten-zone size is determined by the melting temperature (1450 °C). The effect of the current intensity on the temperature distributions has been investigated.

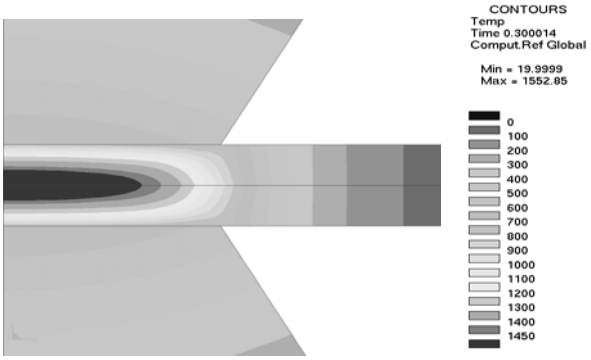

Figure 1. Temperature contour at the end of the current application (t = 0.3 s).

Figure 2 shows the temperature profiles at different locations along the interface between the two sheets with the current intensities of 9.2 kA and 12 kA. It can be seen that the local maximum temperature occurs on the left side of the interface between the two sheets and decreases along the interface. The maximum temperature is about 1500 °C for 9.2 kA, but it can reach 2200 °C for 12 kA on the left side of the interface. The molten zone increases with increasing current intensity.

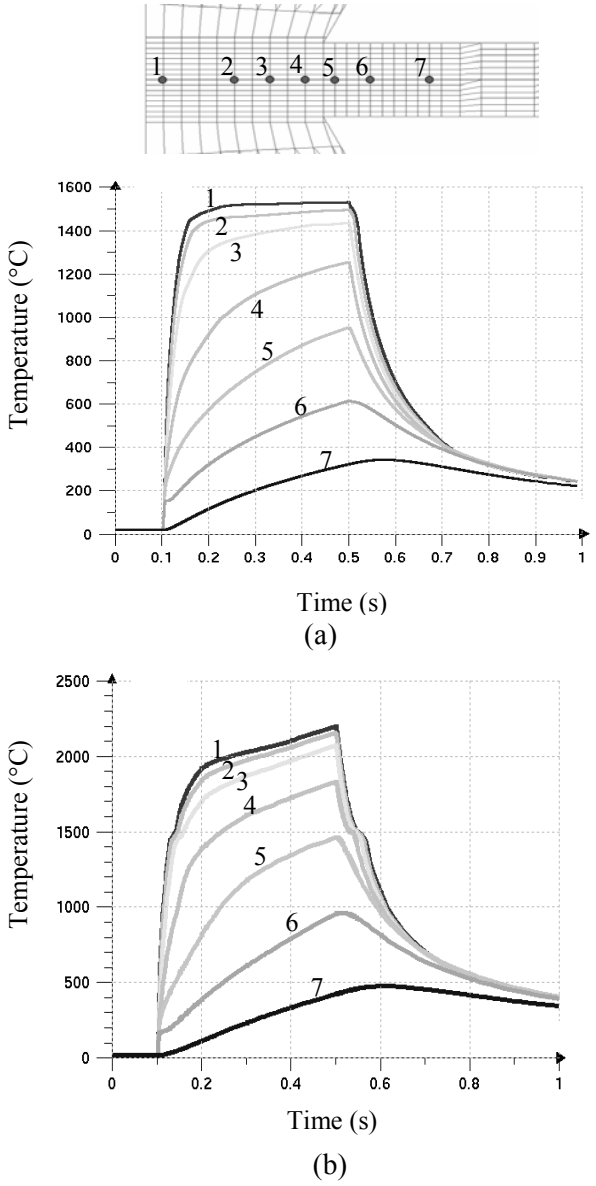

Figure 2. Temperature curves at different locations along the interface between two sheets at (a) 9.2 kA; (b) 12 kA.

Figure 3 shows the contours of ferritic and martensitic phase proportions at the end of the welding process. There are three types of zones. In the molten zone and around it, there is martensitic phase because it has been completely transformed. In a second zone, there is a mixture of the ferritic and martensitic phase. In the external zone, ferrite remains in the initial proportions since the base material was not heat affected.

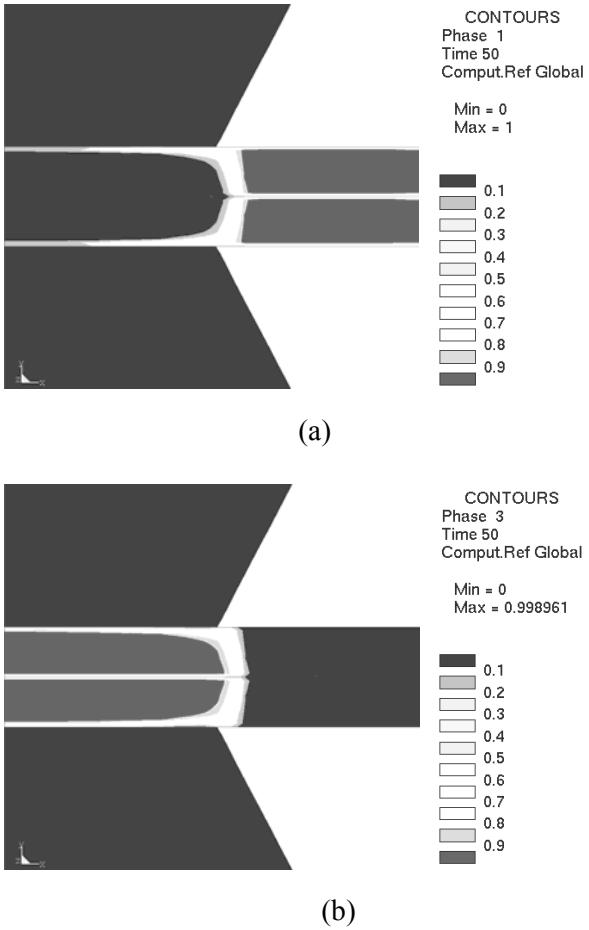

Figure 3. Volume fraction of (a) ferritic and (b) martensitic phase at the end of welding (t = 50 s).

The residual stresses, including Von Mises stress, in-plane stress (σ_{11}), and the stress perpendicular to the interface (σ_{33}), due to the welding process of the two sheets are presented in Figure 4. The most significant stresses are placed where the phases are the mixture of the ferritic and martensitic phases.

TRIP Model

As illustrated above, the model employed in SYSWELD can predict the residual stresses in resistance spot welding. However, in the presence of a deviatoric stress field, the weaker phase undergoes an additional deviatoric straining imposed upon it by the stronger phase. This transformation-induced plasticity (TRIP) can have substantial effects on residual stresses and

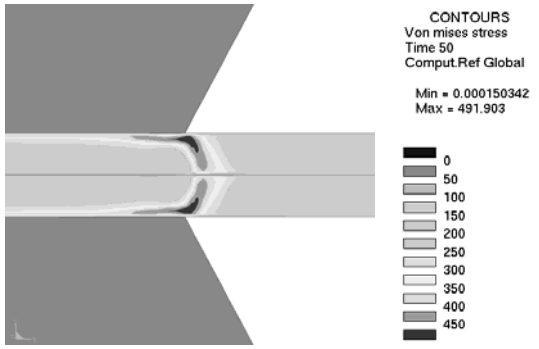

(a)

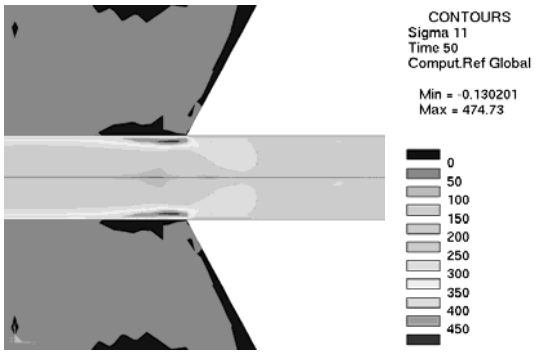

(b)

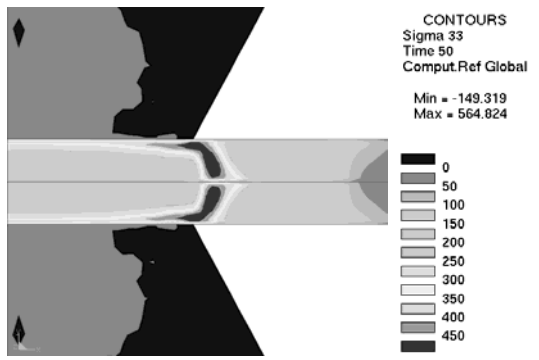

(c)

Figure 4. Residual stress distributions at the end of welding. (a) Von Mises stress, (b) $\sigma 11$, (c) $\sigma 33$.

distortions. Rather than utilizing existing empirical models to describe the TRIP effect, such as those employed in SYSWELD, we extend a single-phase, rate- and temperature-dependent, internal state variable model to describe multiple phases.

The model to be utilized in the description of the material response during the spot-welding process is an extension of a multiphase model developed previously to predict distortions and residual stresses in the heat-treatment and quenching process [Bammann, 1996]. To simplify the description, we consider only a two-phase model, although the following is easily generalized to five or more phases. We begin by including two features at the microscopic level that have direct effects on the macroscopic response for materials susceptible to phase transformations during rapid cooling. The volume difference associated with the phase change imparts a purely dilatational deformation. The volumetric strain associated with the phase change is included directly in the flow rule, while the TRIP effect is included by the introduction of interface stresses between the phases – the harder phase exerting a forward stress on the softer phase and a backward stress for the softer phase upon the harder one. An overview of this approach for two phases follows.

Internal state variable models have been utilized previously to describe the response of single-phase metals over large strain-rate and temperature ranges. These models have been formulated in a manner consistent with the kinematics of large-deformation, elastic-plastic response and are discussed elsewhere [Bammann, 1990]. For multiphase materials, additional complications arise in predicting the material response. In particular, the effects of phase-transformation-induced plastic strain must be included. As steel is cooled from above the austenization temperature, a solid-state phase transformation occurs, the detailed nature of which phase forms depending upon the temperature and the cooling rate. Although we consider only martensite here, the model is easily generalized to consider additional product phases. The martensite occupies approximately 4% more volume than the austenite from which it transforms. The yield strength of martensite can also be an order of magnitude higher than that for austenite. As the austenite transforms to martensite, a volumetric strain develops in the austenite owing to the volume mismatch and difference in strength. In the presence of any deviatoric far-field stress, this will be accompanied by a deviatoric component of strain. Since the martensite is much stronger, this results in a forward stress, $\pi^{(1)}$, in the austenite, resulting in an apparent softening of the material.

Similarly, a backward stress, $\pi^{(2)}$, is created in the martensite. This stress field is a true, tensorial backstress that must be subtracted from the applied stress to get the glide resistance to macroscopic plastic flow. To first order, it is proportional to the volume fraction of hard particles and has its microscopic origins in the TRIP mechanism [Kocks, 1987]. Introducing such a backstress in the yield condition and flow rule provides a natural way to model the apparent yield drop and additional plasticity characteristic of TRIP.

To generalize the state-variable model for multiphase materials, we assume that each point of the continuum can be occupied simultaneously by all phases. Each phase is modeled by the appropriate state-variable model for that phase with rate and temperature dependence as described in [Bammann, 1990]. The material response can then be modeled with as much complexity or simplicity as required, since the model reduces to rate-independent, bilinear response with an appropriate choice of parameters. We denote the current configuration deviatoric Cauchy stress in the austenite and martensite by $\sigma'^{(1)}$ and $\sigma'^{(2)}$, respectively. We assume a classic volume-fraction-weighted rule of mixtures, such that the total Cauchy stress, σ', is given by

$$\sigma' = \Phi\sigma'^{(2)} + (1-\Phi)\sigma'^{(1)} \tag{6}$$

We assume a hypoelastic relation for each phase that is consistent with an assumption of linear elasticity giving

$$\overset{\circ}{\sigma}'^{(i)} = 2\mu D'^{(i)}_e + \frac{\dot{\mu}}{\mu}\sigma'^{(i)} \tag{7}$$

where $D'^{(i)}_e$ is the elastic symmetric part of the deviatoric velocity gradient, and μ is the temperature-dependent shear modulus, assumed to be the same for both phases. Elastic-deformation rates are defined as the difference between the total deformation rate and the sum of the thermal, $D'^{(i)}_{th}$, and the inelastic, $D'^{(i)}_p$, contributions in each phase

$$D'^{(i)}_e = D' - D'^{(i)}_p - D'^{(i)}_{th} \tag{8}$$

Here, $\circ$ denotes the convective derivative of the Cauchy stress defined by

$$\overset{\circ}{\sigma}^{(i)} = \dot{\sigma}^{(i)} - W^{(i)}_e\sigma^{(i)} + \sigma^{(i)}W^{(i)}_e \tag{9}$$

where $W^{(i)}_e$ is the skew part of the elastic velocity gradient for each respective phase given by

$$W^{(i)}_e = W - W^{(i)}_p \tag{10}$$

For the present purposes, we choose a Jaumann derivative and all $W_p = 0$. Defining, $\pi^{(2)}$ and $\pi^{(1)}$ as the backward and forward long-range stresses in the martensite and austenite, respectively,

$$\pi^{(2)} = \frac{-(1-\Phi)}{\Phi}\pi^{(1)} \tag{11}$$

This type of approach was taken by Freed, Raj and Walker [Freed, 1992] in modeling the hard and soft regions of a polycrystalline material as first proposed by Kocks [Kocks, 1987].

Approximating compatibility of the hard and soft regions using the self-consistent scheme of Budiansky and Wu [Budiansky, 1962], they found that the total and local deviatoric strain fields must satisfy

$$\varepsilon'^{(i)} = \varepsilon' + \left(\frac{\beta}{1-\beta}\right)\frac{\pi^{(j)}}{2\mu} \tag{12}$$

where i, j=1,2 and i is not equal to j. Here, β is the Eshelby shape factor for a spherical inclusion. We will make a simplifying Taylor-like assumption and assume that the strains in each field are identical. In an effort to relieve this assumption, a numerical micromechanical simulation of the deformation partitioning will be the subject of a future work.

In addition to the long-range forward and backward internal stress fields which act between the phases, we assume the existence of two short-range internal stress fields, $\alpha^{(i)}$ and $\kappa^{(i)}$, which

act locally within each phase. We then define the net stress acting in each phase as

$$\xi^{(i)} = \sigma'^{(i)} - \alpha^{(i)} - \kappa^{(i)} - \pi^{(i)} \tag{13}$$

Now, we impose specific assumptions concerning the directionality of the stresses $\pi^{(i)}$ and $\kappa^{(i)}$. In particular, we postulate that they act in the direction of the Cauchy stress minus the short-range stress, $\alpha^{(i)}$, in each phase,

$$\pi^{(i)} = \pi^{(i)} \frac{\sigma'^{(i)} - \alpha^{(i)}}{\left|\sigma'^{(i)} - \alpha^{(i)}\right|} \quad \kappa^{(i)} = \kappa^{(i)} \frac{\sigma'^{(i)} - \alpha^{(i)}}{\left|\sigma'^{(i)} - \alpha^{(i)}\right|} \tag{14}$$

The effective stresses acting to cause plastic flow in each phase are then given by

$$\left|\xi^{(i)}\right| = \left|\sigma'^{(i)} - \alpha^{(i)}\right| - \kappa^{(i)} - \pi^{(i)} \tag{15}$$

where $\kappa^{(i)}$ are the scalar internal variables acting in each phase as discussed above. The plastic flow rule is chosen to have a strong nonlinear dependence upon the deviatoric stress

$$D_P^{(i)} = f^{(i)}(\theta)\sinh\left\{\frac{\xi^{(i)} - Y^{(i)}(\theta)}{V^{(i)}(\theta)(1+N(c))}\right\}\frac{\sigma'^{(i)} - \alpha^{(i)}}{\left|\sigma'^{(i)} - \alpha^{(i)}\right|} \tag{16}$$

where $f(\theta)$ and $V(\theta)$ describe a rate dependence of the yield stress at constant temperature and N(c) describes the yield increase with increasing carbon content, c. Tensor variables, $\alpha^{(i)}$, and scalar variables, $\kappa^{(i)}$, have been introduced to describe the deformed state of each phase as described previously for a single phase material [Kocks, 1987]. The evolution of these variables is defined for phase (i) by

$$\begin{aligned}\dot{\kappa}^{(i)} &= H^{(i)}(\theta,c)\left|D_P^{(i)}\right| - \left\{R_S^{(i)}(\theta) + R_D^{(i)}(\theta)\left|D_P^{(i)}\right|\right\}\kappa^{(i)}\left|\kappa^{(i)}\right| \\ \dot{\alpha}^{(i)} &= h^{(i)}(\theta,c)D_P^{(i)} - \left\{r_S^{(i)}(\theta) + r_D^{(i)}(\theta)\left|D_P^{(i)}\right|\right\}\alpha^{(i)}\left|\alpha^{(i)}\right|\end{aligned} \tag{17}$$

The fit to the carbon-dependent data reported by Sjöström [Sjöström, 1982] is shown in Figure 5. Finally, we adopt the simplest evolution equation for the long-range internal stress that is, to first order, proportional to volume fraction, but vanishes as the austenite transforms entirely to martensite

$$\dot{\pi} = C\frac{\Delta V}{V}\left\{\dot{\Phi} - 2\Phi\dot{\Phi}\right\} \tag{18}$$

Here, a simple exponential kinetics are used as described in [Lusk, 1995]

$$\dot{\Phi} = \tilde{k}\exp\left(\lambda_j\left\{\eta - \eta_M\right\}^2\right)\dot{\eta};\ j = 1,2 \tag{19}$$

where η is the driving force for transformation,

$$\eta = k(M_s - \theta) \tag{20}$$

and M_s is the martensite start temperature. Here, λ_{12} and η_M are prescribed by the rate kinetics [Oddy, 1990].

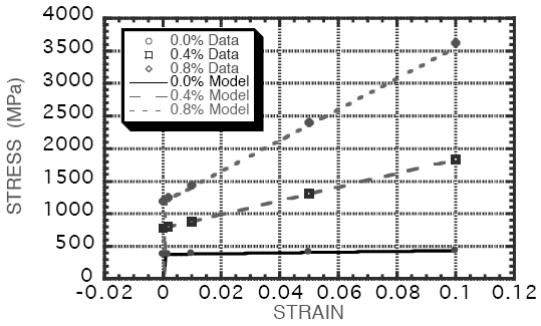

Figure 5. Stress-strain curves to fit the carbon dependent data [Sjöström, 1982].

This model has been extended successfully to account for five phases and utilized in finite-element description of the quenching of a gear blank. In this analysis, a fundamental balance principle was used to model phase-transformation kinetics at a volume-fraction level for a broad range of industrial steels. This micro balance provides differential equations for transformation kinetics which couple naturally to the differential equations governing the mechanical and thermal aspects of a given process [Fried, 1994, Fried, 1993]. Avrami-type kinetics, as well as the Koistinen-Marburger equation, have been shown to result from special classes of energy and mobility functions [Lusk, 1995]. An illustrative example using a 5140 alloy demonstrates how Time-Temperature-Transformation (TTT) and

Continuous Cooling Transformation (CCT) curves can be generated using a particularly simple energy function. The formulation of this theory is discussed in [Lusk, 1995] for a single product phase, and in modeling the possibly competitive development of ferrite, pearlite, bainite and martensite. This model will be applied to the spot-weld problem. Extensions to the model will include more accurate distributions of the strain among the phases using a combination of statistical mechanics and self-consistent scheme. Also, more physical descriptions of the flow rule and state variable evolution for the non-austenite phases will be addressed.

Conclusions

A finite-element model was developed to predict the thermal behavior, molten zone, solid phase transformation and the residual stress during the resistance spot welding. The calculation was performed with the commercial software SYSWELD. Preliminary study on the effects of process parameter (current intensity) on the temperature distribution and molten zone was performed. The results show that SYSWELD is an effective tool to perform numerical modeling in the resistance spot welding process in order to determine the process-properties relations.

A framework of phase-transformation kinetics based on TRIP concepts was presented. This will enhance the development of welding-modeling work with robust materials models for weld and weld-effective zones, in which critical experiments will be guided by the needs of models rather than by empirical approaches.

Presentations/Publications/Patents

None.

References

1. [Koistinen, 1959] D. P. Koistinen and R. E. Marburger, A General Equation Prescribing the Extent of Austenite-Martensite Transformation in Pure Fe-C Alloys and Plain Carbon Steels, Acta Metall., vol. 7, pp. 417–426, 1959.
2. [ASM, 2005] ASM Handbook, Welding, Brazing, and Soldering, Vol. 6, ASM International, Material Park, OH, 2005, 438.
3. [SYSWELD, 2005] SYSWELD 2005 Reference Manual, ESI Group, 2005.
4. [Bammann, 1996] Bammann, D. J., Prantil, V. C., Kumar, A., Lathrop, J., Mosher, D., Callabresi, M., Lusk, M., Krauss, G., Jou, H. J., Elliott, W., Ludtka, G., Dowling, W., Nikkel, D., Lowe, T., Shick, D., "Development of a Carburizing and Quenching Simulation Tool: A Material Model for Carburizing Steels Undergoing Phase Transformations," *2nd Int. Conf. on Quenching and the Control of Distortion*, Cleveland, OH, 1996.
5. [Bammann, 1990] D. J. Bammann, "Modeling Temperature and Strain Rate Dependent Large of Metals," *Applied Mechanics Reviews*, Vol. 43, No. 5, Part 2, May, 1990.
6. [Kocks, 1987] U. F. Kocks, "Constitutive Behavior Based on Crystal Plasticity," *Unified Constitutive Equations for Creep and Plasticity*, ed. A. Miller (London: Elsevier Applied Science, 1987), 1-88.
7. [Freed, 1992] A. D. Freed, S. V. Raj, and K. P. Walker, "Three-Dimensional Deformation Analysis of Two-Phase Dislocation Substructures," *Metallurgica et. Materialia*, 27 (1992), 233-238.
8. [Budiansky, 1962] B. Budiansky and T. T. Wu, "Theoretical Prediction of Plastic Strains of Polycrystals," *Proc. Fourth U. S. Cong. Appl. Mech.*, Vol. 2, (New York, NY: American Society of Mechanical Engineers, 1962), 1175-1185
9. [Sjöström, 1982] S. Sjöström, "The Calculation of Quench Stresses in Steel," (*Ph.D. Thesis, Linkoping University, Sweden, 1982)*.
10. [Lusk, 1995] Lusk, M., Krauss, G., and H.-J. Jou, *Journal de Physique IV*, C8 (1995) 279-284.
11. [Oddy, 1990] A.S. Oddy, J.A. Goldak, and J.M.J. McDill, "Numerical Analysis of Transformation Plasticity in 3D Finite Element Analysis of Welds," *Eur. J. Mech., A/Solids*, 9 (3) (1990), 253-263.

12. [Fried, 1994] Fried, E. and Gurtin, M., *Phys. D*, 72 (1994) 287-308.
13. [Fried, 1993] Fried, E. and Gurtin, M., *Phys. D*, 68 (1993) 326-343.

10. NONDESTRUCTIVE EVALUATION

A. Nondestructive Evaluation (NDE) Inspection of Resistance Spot Welds in Automotive Structures Using an Ultrasonic Phased Array

Principal Investigator: Deborah Hopkins, Ph.D.
Lawrence Berkeley National Laboratory (LBNL)
1 Cyclotron Road, MS 46A-1123, Berkeley, CA 94720
(510) 486-4922; fax: (510) 486-4711; e-mail: dlhopkins@lbl.gov

Technology Area Development Manager: Joseph Carpenter
(202) 586-1022; fax: (202) 586-1600; e-mail: joseph.carpenter@ee.doe.gov

Expert Technical Monitor: Philip S. Sklad
(865) 574-5069; fax: (865) 576-4963; e-mail: skladps@ornl.gov

---

Contractor: LBNL
Contract No.: DE-AC03-765F0095

Objective

- Develop a cost-effective, ultrasonic phased-array system that is sufficiently fast to inspect and accurately analyze spot welds in a few seconds, that is also robust enough to be used in manufacturing environments.

Approach

- Work in conjunction with the U.S. Automotive Materials Partnership's (USAMP) AMD 409 project to set technical specifications, define the technical approach and evaluate results.
- Develop a spot-weld inspection system based on state-of-the-art ultrasonic phased-array technology that can be used by operators with minimal training.
- Develop the hardware and software necessary to allow resistance spot welds (RSWs) to be ultrasonically imaged and automatically assessed in a few seconds.
- Design and fabricate a fully-integrated prototype system that is as lightweight, portable and ergonomic as possible, that is also rugged enough for use in a production facility and flexible enough to ensure access to welds on complex components.
- Conduct validation experiments to demonstrate the prototype system's ability to characterize welds with sufficient accuracy and repeatability.
- For mild and low-carbon steel, develop a fundamental understanding of the relationships among micro-structure, weld strength, the size of the weld nugget and weld button, and ultrasonic transmission across the welding interface. Determine how these relationships are affected by surface coatings, unequal-thickness stackups, teardown methods and differences in alloys.

Accomplishments

- Designed and fabricated a portable, integrated probe housing that maintains the phased-array probe in water, contains a miniature mechanical system that allows linear translation of the probe, and provides an outer membrane that confines the water column while also providing acoustic coupling to the part under inspection. Identified and tested commercially-available coupling materials that allow satisfactory signals to be obtained outside of a water tank.

- Demonstrated the ability to acquire more than 4,000 signals per weld and analyze the resulting data in a few seconds to render an estimate of weld quality. Demonstrated good correlation between ultrasonic measurements and metallographic images.
- Developed signal and image-processing algorithms that allow dimensional analysis of welds. Demonstrated the ability to accurately predict the size of weld buttons from the ultrasonic data, and the repeatability of the predictions. Developed a method to accurately quantify the uncertainty in the predictions at the size threshold that separates satisfactory from undersized welds. This value is the upper 95% confidence interval at the threshold, and ranges between 0.4 and 0.8 mm depending on the stackup (relative sheet thicknesses and material properties) and whether or not indentation variables are used in the prediction model.
- Developed a better understanding of how metallurgy, coatings, and stackup affect creation of welds, weld strength and transmission of ultrasonic energy across the welding interface.

Future Direction

- Complete a comprehensive report detailing the work and conclusions drawn from the research performed to date to determine the technical feasibility of using ultrasonic phased arrays for inspection of RSWs in steel.
- Using the hardware and software developed for inspection of spot welds in mild steel, develop inspection protocols for welds in other automotive materials such as Al and advanced high-strength steel (AHSS).

Introduction

In previous work, a prototype ultrasonic phased-array inspection system was designed and built for inspection of RSWs. The system integrates a commercial phased-array probe and controller with custom hardware and software to provide high-resolution images of the welds. The portable probe housing maintains the phased array in water, contains a miniature mechanical system that allows linear translation of the probe, and provides an outer membrane that confines the water column while also providing acoustic coupling to the part under inspection (Figure 1). Close to 4,000 signals per weld are acquired and analyzed in a few seconds to render an estimate of weld quality and size. The prototype system has been used to conduct measurements on both production parts and test coupons provided by industry partners.

The work performed during fiscal year (FY) 2007 had three main thrusts: 1) improving models used to predict the size of weld buttons from the ultrasonic data, evaluating the prediction uncertainty of these models, and assessing the repeatability and reproducibility of measurements made with the prototype spot-weld inspection system; 2) understanding the mechanics and metallurgy of weld formation in coated steel (mild and interstitial free) to better understand the relationship between the microstructure in the weld zone and the transmission of ultrasonic energy across the welding interface; and 3) understanding the stackup dependence in ultrasonic measurements.

Measurements and Signal Processing

The results presented here were obtained using an 80-element, 17-MHz, linear phased-array probe with curved elements that create a natural focal length of 37 mm. Electronic focusing is used in the direction perpendicular to the mechanical focusing to achieve a relatively small focal spot that is scanned through the weld. The miniature mechanical scanner integrated into the probe housing is used to translate the probe in the direction perpendicular to the electronic scan to create two-dimensional images of the weld.

The ultrasonic signals are analyzed in the frequency domain, where the relative magnitude of the peaks in the power spectrum is indicative of the amount of energy reflected at the interface between the welded sheets. For a satisfactory weld, most of the ultrasonic energy propagates through the weld resulting in a peak that corresponds to the travel path through both sheets. For discrepant welds, where most of the energy is reflected at the interface between the two sheets, there is a peak in the spectrum that corresponds to a travel path equal to twice the thickness of the upper sheet. For each of the 3,900 signals that comprise each weld image, the ratio of the peaks in the power spectrum is calculated. The signals are amplified by the material attenuation rate to make data obtained for different thickness sheets more comparable. The resulting amplified frequency ratio (AFR) images are displayed in the following figures. Weak signals, that cannot be analyzed, are also displayed and serve two functions. The first is to provide in-

formation on the quality of the data and the second is to provide diagnostic feedback (large areas of weak signals surrounding the weld are indicative of a burnt weld). In sizing the weld and analyzing quality, the best results are achieved by extracting several diagnostic features from the data. The contiguous area over which there is transmission across the interface (above a threshold) is calculated, and the frequency ratio is integrated over this area to obtain the integrated amplified frequency ratio (IAFR). The surface indentation caused by the welding electrode on the measurement surface is also calculated and the depth, shape, and inclination of the indentation provide useful process feedback.

Figure 1. Integrated probe being used to inspect welds on a truck door.

Results of Mechanical Testing

In one of the two studies described here, eight spot-welded test coupons were created in each of 15 weld groups by the Ford Motor Co. For seven of the groups, the coupons consisted of equal-thickness (1 mm) sheets of galvanized steel, and for the other eight groups the test specimens were composed of unequal-thickness sheets (1.0:1.45 mm). Within each group, welding parameters were held constant, and between groups they were varied to create a range of weld qualities from very weak welds to burnt welds. After ultrasonic measurements were performed, three welds from each group were subjected to lap-shear tests, two were subjected to coach-peel tests, two were sectioned and etched for metallographic analysis, and one was left undamaged to be available for future work. For the welds subjected to destructive testing, the resulting weld buttons (if any) were measured. The size of the button is sensitive to the way the load is applied, so button measures from different tests are not directly comparable. AFR ultrasonic images along with the force-displacement curves obtained for the same welds are shown in Figure 2 for four welds subjected to lap-shear testing, and in Figure 3 for four welds subjected to coach-peel testing. The strength measures derived from the curves are the peak load attained and the total area under the curve. The average button diameters and ultrasonic IAFR values for the same welds are listed in Table 1. The lap-shear and coach-peel results differ in both the peak loads and post-peak behavior, but in both cases the force-displacement curves show a progression in mechanical behavior.

The weakest welds pull apart under almost no load (e.g., weld E6). For somewhat stronger welds, the force-displacement curves indicate little if any strength after the peak load (e.g., weld M1). Even though neither weld M1 nor L1 pulled a button in lap shear, suggesting interfacial failure, the force-displacement curves show a transition toward more ductile behavior for weld L1 (Figure 2). The ultrasonic IAFR values are similar for the two welds (Table 1), but what is visible in the AFR images is a transition from dispersed areas of transmission across the interface to a more uniform contiguous area of high transmission. Weld O1 is a borderline-good weld, and while there is not much increase in peak load compared to the weaker welds, the weld demonstrates increased ductility and a substantially higher IAFR value. The fourth weld in the series (H1) is a satisfactory weld that sustained a higher peak load, with much more area under the force-displacement curve and a high IAFR value compared to the smaller welds.

For the welds tested in coach peel (Figure 3), the button pulls out of the parent material of one of the sheets. Weld E6 was very weak, and the AFR image shows that fusion initiated along a ring. Weld D6 is an undersized weld, with a force-displacement curve that is characteristic of undersized and satisfactory welds. Weld G8 is a large weld and A7 is a burnt weld; in both cases, there is a transition from ductile to more brittle behavior as evidenced by the relatively sharp peaks in the force-displacement curves. The black pixels evi-

dent in the AFR images outside of the welded region for these two welds indicate weak signals that suggest interfacial bonding characteristic of very large and burnt welds. Burnt welds are easily identified from the ultrasonic data, not only because of the weak signals, but also because of large transmissive areas, high IAFR values and excessively- deep surface indentations.

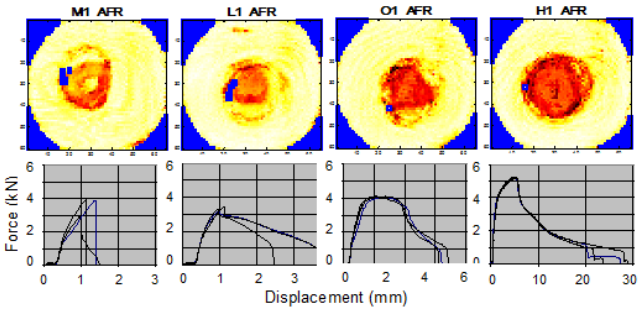

Figure 2. AFR ultrasonic images (top row) and the corresponding force-versus-displacement curves for all welds in the same group for four welds subjected to lap-shear strength testing (note that the x-axis scales differ). The button dimensions and IAFR values obtained for the same welds are reported in Table 1.

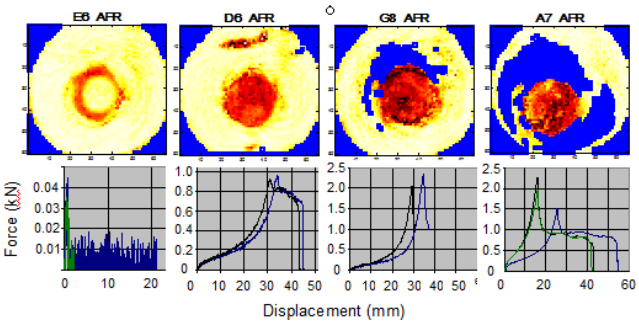

Figure 3. AFR ultrasonic images (top row) and the corresponding force-versus-displacement curves for all welds in the same group for four welds subjected to coach-peel strength testing (note that the axes scales differ). The large dark areas in the AFR images for G8 and A7 are indicative of burnt welds. The button dimensions and IAFR values obtained for the same welds are reported in Table 1.

Table 1. Button sizes and ultrasonic IAFR values for welds tested in lap shear and coach peel.

Lap-shear strength tests (sheet-metal stackup 1.0:1.45mm)				
	Weld M1	Weld L1	Weld O1	Weld H1
Ave. button diameter	No button	No button	3.3 mm	5.5 mm
Ultrasonic IAFR	353	348	718	1119
Coach-peel strength tests (sheet-metal stackup 1.0:1.0mm)				
	Weld E6	Weld D6	Weld G8	Weld A7
Ave. button diameter	No button	3.6 mm	6.2 mm	8.0 mm
Ultrasonic IAFR	243	925	1346	4604

Comparison of Ultrasonic and Metallographic Images

For the Ford study, two welds from each of the 15 groups were sectioned in the plane of the sheet metal to create planar sections at the welding interface that were subsequently polished and etched with picral to reveal the microstructure. These metallographic maps are particularly useful because they are in the same plane as the images created from the ultrasonic measurements (see Figure 4). For those welds that were sectioned, the size of the weld nugget was measured in the images and compared to the ultrasonic data. The dimensioned box in the metallographic image in Figure 4 is the heat-affected zone (HAZ). The weld nugget is the smaller circular region, which has a finer grain structure than the HAZ. The sheet metal used for the Ford samples had a very low carbon content, and the result is ferrite grain growth in the outermost region of the HAZ. As shown in the figure, the area over which there is ultrasonic transmission across the welding interface corresponds very closely to the HAZ.

For the second study discussed here, test coupons were made by General Motors (GM). In this case, the samples were made with three different sheet-metal stackups: thin-thin (sheet thickness equal to 0.8 mm); thick-thick (sheet thickness equal to 1.8 mm); and thin-thick. The thin sheets were interstitial-free (IF) low-carbon steel, and the thick sheets were mild steel. For each of the three stackups, there were five target weld classes: stick, small, undersized, minimum acceptable, and large. Following ultrasonic inspection of the welds, the samples were peeled apart to determine the weld quality as indicated by the size of the weld button.

Each of the samples was then sectioned vertically with respect to the welding interface, polished and etched with picral to reveal the weld nugget and the microstructure in and around the welds.

Micrographs for the thin-thin stackup are shown in Figure 5 for four welds targeted to be undersized.

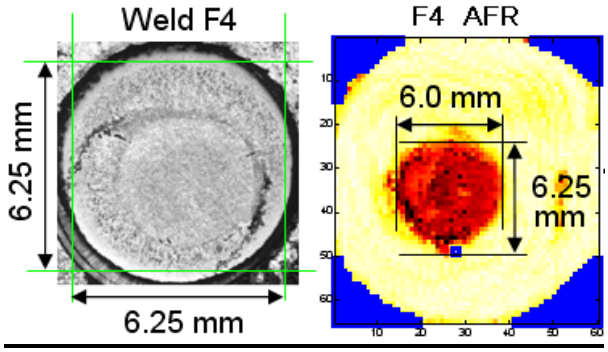

Figure 4. Metallographic planar section of a satisfactory weld (left-hand image) and the ultrasonic AFR image for the same weld (right-hand image).

The cross-sections were taken through the weld buttons, which in this case all pulled out of the upper sheet. The upper dimensions in the images are of the buttons. The smaller dimension in each of the images corresponds to the weld nugget (martensite), which is easy to see because of the thin white outline. The line is the result of carbon segregation that occurs during the first phase of solidification, during which carbon migrates into the melt zone. The picral etch is sensitive to carbon content, and thus marks the carbon-depleted line. The whitish area surrounding the nugget is a two-phase (ferrite and austenite) region of the HAZ. In the first image (weld 16), it is possible to see long ferrite grains in the outer area of the HAZ that show up relatively dark compared to the two-phase zone and the parent material. These long grains are characteristic of IF steel and do not usually occur in mild steel.

Three of the four welds were sectioned along the short axis of the samples, as indicated by the rectangles in the upper-left corner of the micrographs. The images for these welds (welds 16, 18 and 19) show relatively small nuggets and buttons. The weld sectioned in the perpendicular direction (weld 17) has a larger button and nugget, and a more typical image for an undersized weld. Recall that all four welds were made under identical conditions with the same welding parameters, suggesting something in the setup that created misshapen welds. The corresponding ultrasonic AFR images are also shown in the figure. The approximate positions of the cross-sections are indicated by the long black lines. Consistent with the micrographs, the AFR images show a large band of reflectivity at the top of the images indicating a lack of fusion. The size of the buttons compared to the nuggets for welds 16, 18 and 19 show that there is a relatively-strong, solid-state bond at the interface outside of the nugget. For welds 16, 18 and 19, where there is a large difference in size between the button and nugget, the micrographs show that the zone of high ultrasonic transmission corresponds very closely to the dimension that includes the nugget and the strong interfacial bond surrounding the nugget.

An important objective of this year's work was to better understand the relationship between the ultrasonic signals and the interfacial solid-state bonds that vary in strength from extremely weak to very strong. Micrographs and the corresponding AFR images are shown in Figure 6 for large welds in thin-thin (left-hand side) and thick-thick stackups (right-hand side). The images indicate that the signals are sensitive, at least in some cases, to conditions that affect the strength of interfacial bonds. The micrograph for weld 69 in the thin-thin stackup shows an annular weld. Because the strength of the weld is relatively insensitive to the quality of the weld in the center, these "donut" welds are considered satisfactory. In this case, the ultrasonic signals suggest that the interfacial bond in the center is very strong, transmitting the acoustic energy as well as the surrounding nugget material. In contrast, the micrograph for weld 62 in the thick-thick stackup indicates that the nugget had a plane of weakness on the left-hand side, probably resulting from porosity and voids in the nugget on the left-hand side). The corresponding ultrasonic AFR image indicates that the signals were sensitive to the weakness in the nugget. The zone of high ultrasonic transmission corresponds to the button diameter, which does not include the section of the nugget that failed.

Stackup Dependency

The modeling results in the next section show that the relationship between the weld button and ultrasonic variables varies depending on the sheet-metal stackup. One objective of this year's work

was to better understand this dependency. The most difficult sample set analyzed to date is the GM thin-thick stackup (0.8:1.8mm). Figure 7 shows metallographic images, photographs of the buttons and the corresponding ultrasonic AFR images for five welds from this group. In all cases, the nuggets formed in the thick sheet at the

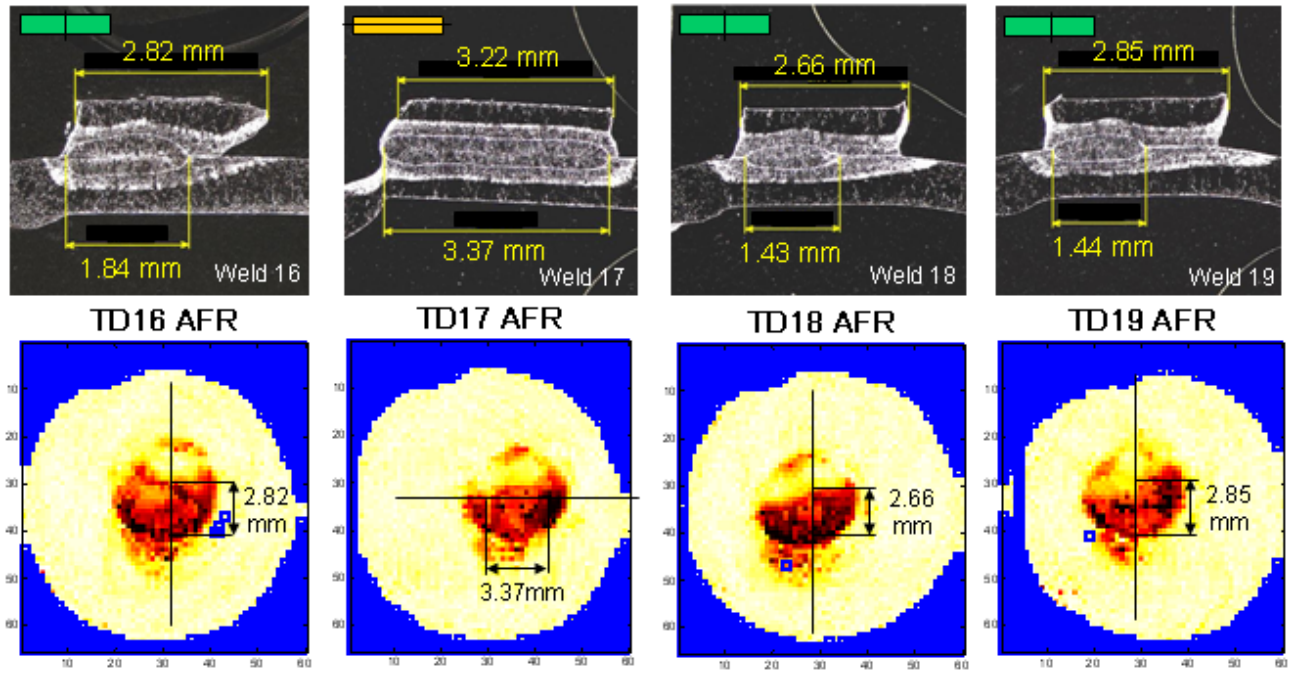

Figure 5. Micrographs and ultrasonic AFR images for four undersized welds. The rectangles in the upper-left corner of the micrographs (top view) and the black lines in the AFR images indicate the approximate location of the cross section.

geometric center of the stackup. Note that there is very little if any penetration of the weld nugget across the welding interface except for the largest welds. Nonetheless, the undersized and minimum-acceptable welds pulled relatively large buttons, and the AFR images for all but the weakest of these welds show transmission of the ultrasonic energy over a large area indicating a strong solid-state bond at the interface. As explained by Dr. Jerry Gould of the Edison Welding Institute, for coated steels, the melting and expulsion of the zinc coating leaves behind clean surfaces relatively free of oxides, thereby facilitating creation of the solid-state bonds. The fact that the nugget initiates at the geometric center of the stackup strongly indicates that these solid-state bonds conduct heat, eliminating the resistance at the welding interface. The lack of penetration of the nuggets across the faying surface is attributed to two factors. Given that the nugget initiates at the center of the stackup, the large difference in thickness (0.8 versus 1.8mm) between the two sheets requires a large nugget to even reach the welding interface. The second factor that inhibits penetration of the nugget across the interface is the difference in material properties between the sheets. The thin, IF-steel sheet is twice as conductive as the thick, mild-steel sheet. In essence, the stackup can be described as a conductor sitting on top of an insulator. This difference in conductivity is thought to foster creation of very strong solid-state bonds. The ultrasonic AFR images for these welds show that there was substantial transmission of acoustic energy across the welding interface for all welds regardless of target quality, supporting the hypothesis that the stackup geometry and difference in conductivity resulted in strong solid-state bonds that formed in conjunction with the weld nugget. Also note the voids visible in the nuggets for the three largest welds. These voids are also visible in the AFR images. At higher magnification, it is also possible to see porosity and cracking in the nuggets. In general, the presence of voids in the nugget increases with increasing sheet thickness.

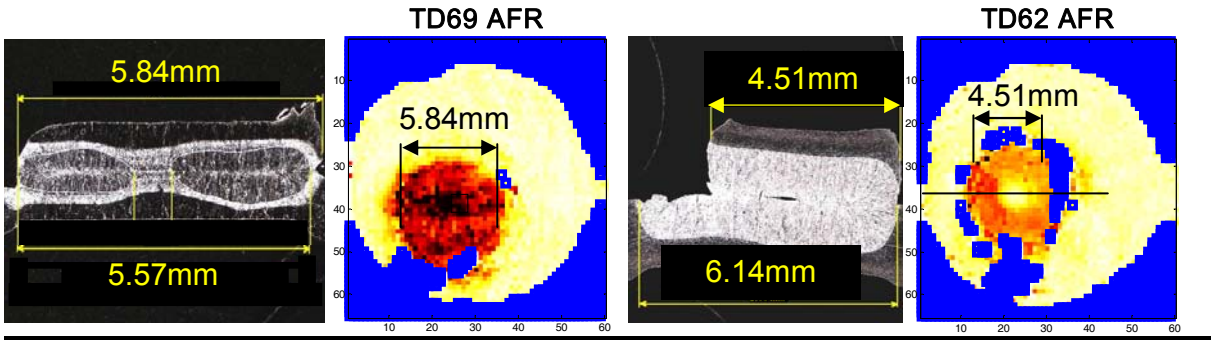

Figure 6. Micrographs and ultrasonic AFR mages for two large welds for thin-thin (left-hand side) and thick-thick stackups (right-hand side). The black lines in the AFR images indicate the approximate location of the cross section.

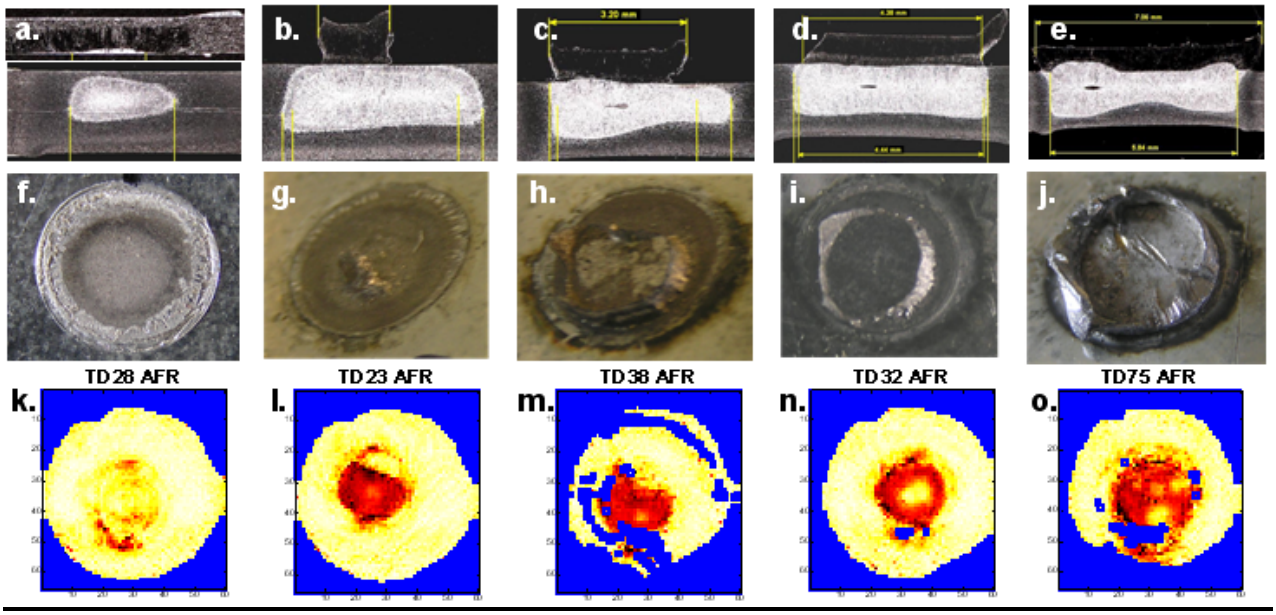

Figure 7. Metallographic cross-sections, pictures of weld buttons and ultrasonic AFR images for five welds in the thick-thick stackup with targeted qualities: stick, small, undersized, minimum acceptable, and large.

Prediction of Weld Size

To predict weld size, several step-wise regression models were estimated. The dependent variable in the regressions is based on the measurements of the weld button or, in the case of the welds sectioned by Ford, the size of the nugget identified in the metallographic image. For the step-wise technique used, variables are introduced sequentially based on a selection criterion that estimates their contribution to prediction performance. The candidate variables are all derived from the ultrasonic signals: the area over which there is transmission across the interface (TA); the IAFR, the average indentation depth (ID) and indentation area (IA).

Ideally, the variables included in the models and their order of inclusion would be identical regardless of material thickness and stackup. The Ford models are more similar to each other than the GM models both in the ultrasonic variables included and in the R^2 values obtained. The Ford data also show less stackup dependence and little is gained from using the indentation information. In contrast, there is a strong stackup dependence in the GM data and, in some cases, adding the indentation variables substantially improves the model fits. As described above, the stackup dependence in the GM data is attributed to the greater difference in relative thickness in the thin-thick stackup for the GM samples and the difference in material

properties between the IF and mild steel used in the GM coupons. The regressions were run for the data broken out by stackup, and also for the data pooled across stackups. The best results are obtained using linear regression with quadratic terms, although for the Ford data, the results were nearly identical using only linear terms.

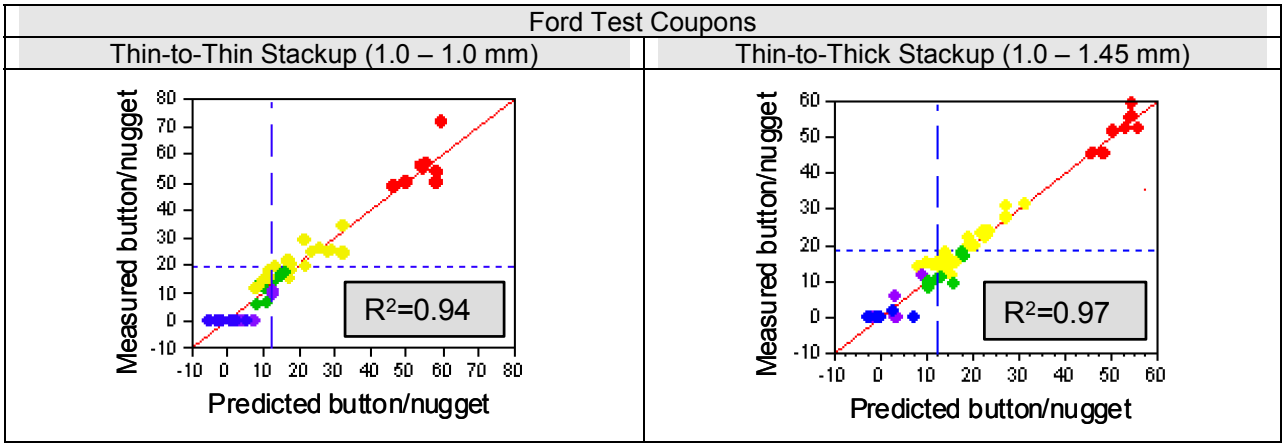

Figure 8. Measured versus predicted button areas for the full model using IAFR, TA, ID, and IA. As shown in the figures, the R^2 values for the full model are 0.94 and 0.97 for the thin-thin and thin-thick stackups, respectively. The corresponding values for the restricted model that excludes the indentation variables are 0.94 and 0.95, respectively.

One of the outputs of the regressions is the R^2 value, which is a measure of the goodness-of-fit of the model ranging between 0 and 1 (a perfect fit). In all cases, the R^2 values indicate excellent model fits. For the Ford data broken out by stackup, the R^2 values (adjusted for the number of variables in the model) are 0.94 and 0.97 for the models using indentation information (Figure 8), and 0.94 to 0.95 when the indentation variables are excluded. For the GM data by stackup, the adjusted R^2 values range from 0.96 to 0.98 for the models using indentation information (Figure 9), and from 0.90 to 0.96 when the indentation variables are excluded. For the Ford data pooled across stackups, the R^2 values are 0.96 and 0.93 for the models with and without indentation variables, respectively. The corresponding numbers for the GM data are 0.92 and 0.81.

To help evaluate the performance of the models, the prediction error at the size threshold that separates undersized from satisfactory welds was calculated based on the width of the confidence interval for the prediction equation at the threshold. This calculation answers the question as to how much larger than the threshold the welds have to be made or measured to ensure with 95% confidence that all welds predicted to be satisfactory are in reality larger than the threshold. This value ranges between 0.8 and 1.2 mm for the Ford data, and 0.4 and 0.8 mm for the GM data, for all stackups and both models (using indentation data and excluding it). The larger margin for the Ford data is not surprising given that the measured data was obtained using three different teardown methods.

Repeatability and Reproducibility

The GM welds were measured by three operators, from both the front and back sides of the samples. An additional set of measurements was made by Operator 1 from the top side in a water tank. The ultrasonic AFR images obtained by Operator 1 for four welds are displayed in Figure 10. In general, there is excellent qualitative agreement among the AFR images for repeat measurements. For example, the images for weld 28 (top row, first four images), is one of only two welds in this dataset that shows the ultrasonic signature that has in the past been associated with cold welds. The ability to reliably identify these welds is critical, since they are very weak. A quantitative evaluation of repeatability is only preliminary because of the small sample, but shows good repeatability of both predictions of weld quality and of the ultrasonic variables input into the prediction equations. AFR

images obtained by the three operators for weld 40 are shown in Figure 11, along with the images obtained by Operator 1 in a water tank. Again there is in general good qualitative agreement among the images.

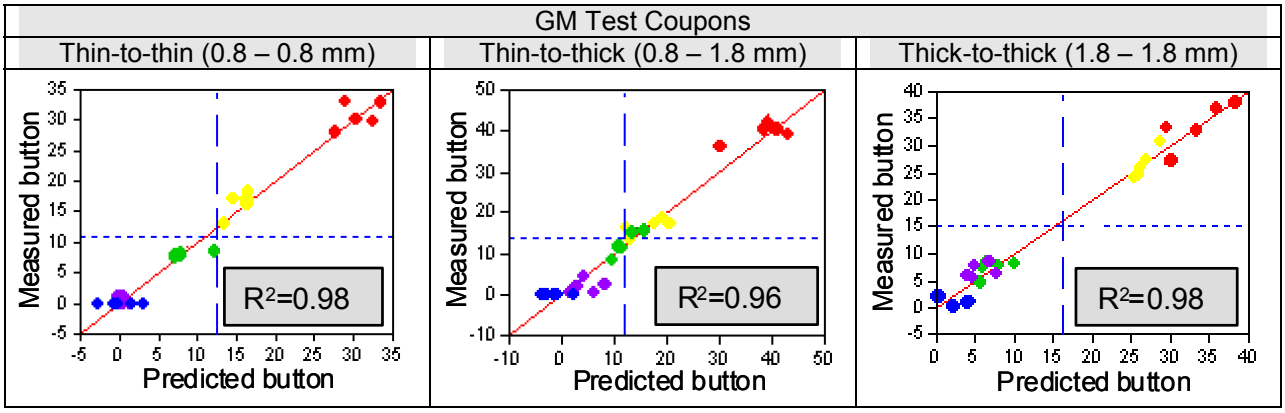

Figure 9. Measured versus predicted button areas for the full model using IAFR, TA, ID, and IA. The R^2 values for the full model are 0.98, 0.96 and 0.98 for the thin-thin, thin-thick and thick-thick stackups, respectively. The corresponding values for the restricted model that excludes the indentation variables are 0.96, 0.95, and 0.90, respectively.

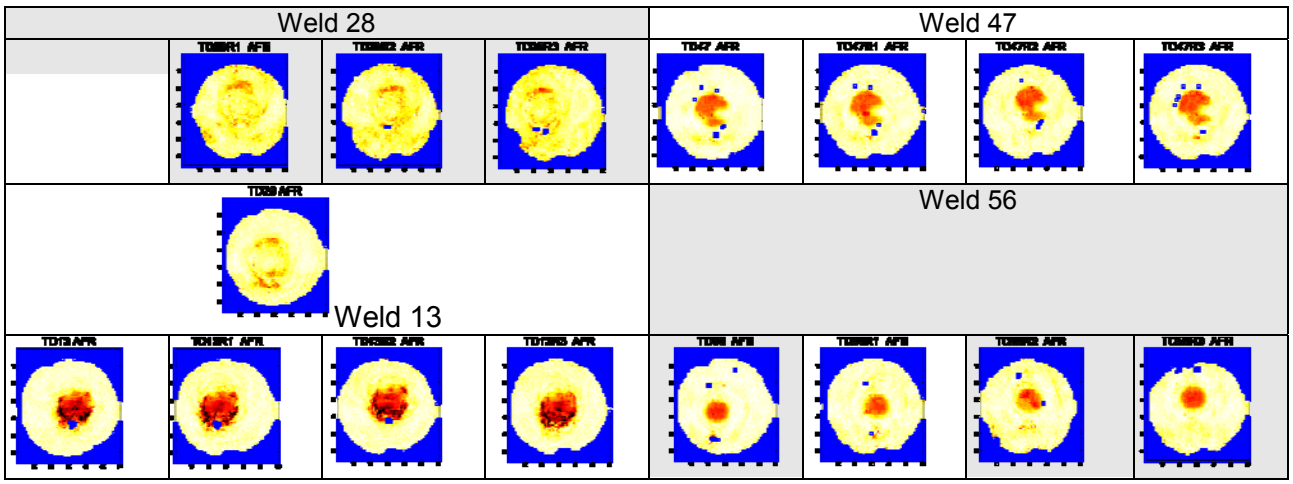

Figure 10. AFR images for the repeat measurements made by Operator 1 on four welds.

Exceptions occur in those cases where there are many weak signals, which can indicate a coupling problem. Also encouraging is the good agreement between the measurements made in the water tank and those made with the portable probe unit. The variability of the predictions made by Operators 2 and 3 is larger than that for Operator 1. Variability is greatest for Operator 2, who did not attempt to orient the probe to maximize the signal amplitude.

Conclusions

The relationships among weld strength, the size of the weld nugget and button, and ultrasonic data are complex, and depend on the sheet-metal stackup and material properties. Metallographic images are invaluable in helping to understand these relationships and their dependence on microstructure.

Force-displacement curves obtained during strength testing show a transition from brittle behavior for the weakest welds, to ductile behavior for satisfactory welds, back to more brittle-like behavior for burnt welds. Ultrasonics can identify the weakest welds and burnt welds, and can also provide information on weld shape, voids, cracks, and surface indentation, all of which are useful feedback to the welding process.

For coated steels, the melting and expulsion of zinc acts to clean the welding interface, fostering the creation of solid-state bonds. These bonds form either as a precursor to nugget formation in the case of equal-thickness sheets, or in conjunction with nugget formation in unequal-thickness sheets. The strength of solid-state bonds varies from weak to very strong. Unequal-thickness stackups and welds in dissimilar materials contribute to creation of strong solid-state bonds. All but the weakest of these welds and bonds transmit acoustic energy across the interface between the welded sheets. It has also been shown that solid-state bonds can pull a button. The existence of these bonds is, therefore, a complication for both destructive and nondestructive testing. At least in some cases, ultrasonic signals are sensitive to the strength of the solid-state bond.

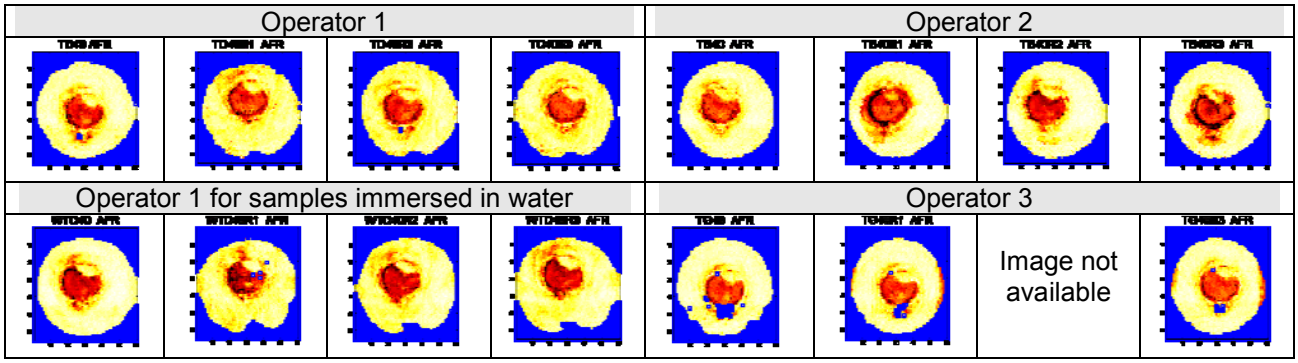

Figure 11. AFR images for repeat measurements made by three operators on weld 40, and a fourth set of measurements made on the same weld by Operator 1 for test coupons immersed in a water tank.

The best results for sizing welds is obtained using the IAFR along with other diagnostic variables extracted from the ultrasonic signals. The repeatability and reproducibility results for the GM data are encouraging, but preliminary because of the relatively small number of repeat measurements. Future work would benefit from using experimental designs that would allow gage repeatability and reproducibility (R&R) to be assessed according to industry protocols.

Measurements performed on hundreds of welds strongly indicates that sizing and assessing weld quality are more complex than simply identifying and measuring the zone of ultrasonic transmission across the welding interface. Understanding how the acoustic signals are affected by the microstructure in the weld zone is, therefore, key for determining both the capabilities and limitations of ultrasonic weld characterization.

Comparison of the results obtained using the prototype system with a coupling membrane to data obtained from measurements made by immersing the coupons in a water tank indicates that the membrane is not introducing significant error into the measurements. This result supports the feasibility of applying phased-array technology in production. Experiments to date also show that acceptable measurements can be made using inexpensive, off-the-shelf membrane materials, and that these materials are very durable, results that further improve the feasibility of using the technology in plants.

Presentations

1. D. Hopkins and W.B. Davis, “Ultrasonic Phased-Array Signal Processing for Resistance-Spot-Weld Inspection,” Automotive Industry Advancements with NDT, American Society for Nondestructive Testing, May 2007, Dearborn, MI.
2. D. Hopkins, “Development of an Ultrasonic Phased-Array System for Nondestructive Evaluation of Resistance Spot Welds,” United States Automotive Materials Partnership (USAMP) — Automotive Materials Division (AMD) Joining Offsite, November 2007, Southfield, MI.
3. W.B. Davis, "Predicting Spot Weld Button Area with an Ultrasonic Phased Array," 34th Annual Review of Progress in Quantitative Nondestructive Evaluation, August 2007, Golden, CO.

4. D. Hopkins, “Use of Metallographic Analysis and Strength Testing to Improve Ultrasonic Phased-Array Evaluation of Resistance Spot Welds,” 34th Annual Review of Progress in Quantitative Nondestructive Evaluation, August 2007, Golden, CO.
5. D. Hopkins, “Reliability in High-Volume Manufacturing — An Automotive Perspective,” American Society for Nondestructive Testing Fall Conference, November 2007, Las Vegas, NV.

Publications

1. W.B. Davis, "Predicting Spot Weld Button Area with an Ultrasonic Phased Array," To appear in *Proc. 34th Annual Review of Progress in Quantitative Nondestructive Evaluation*, 2008.
2. D. Hopkins, “Use of Metallographic Analysis and Strength Testing to Improve Ultrasonic Phased-Array Evaluation of Resistance Spot Welds,” To appear in *Proc. 34th Annual Review of Progress in Quantitative Nondestructive Evaluation*, 2008.
3. D. Hopkins and USAMP NDE Steering Committee, “Reliability in High-Volume Manufacturing — An Automotive Perspective,” feature article in *Materials Evaluation*, American Society for Nondestructive Testing, December 2007.

B. Nondestructive Inspection of Adhesive Metal/Metal Bonds (NDE 601[i])

Principal Investigator: David G. Moore
Sandia National Laboratories (SNL)
P.O. Box 5800, MS 0863
Albuquerque, NM 87185
(505) 844-7095; fax: (505) 844-9068; e-mail: dgmoore@sandia.gov

Principal Investigator: Joseph DiMambro
SNL
P.O. Box 5800, MS 0340
Albuquerque, NM 87185
(505) 284-8914; fax: (505) 844-7011; e-mail: jdimamb@sandia.gov

Principal Investigator: Cameron J. Dasch
General Motors Research & Development
30500 Mound Road, Warren MI 48090
(586) 986-0588, fax: (586) 986-3091; e-mail: cameron.j.dasch@gm.com

Technology Area Development Manager: Joseph A. Carpenter
(202) 586-1022; fax: (202) 586-1600; e-mail: joseph.carpenter@ee.doe.gov

Field Project Officer: Aaron D. Yocum
(304) 285-4852; fax: (304) 285-4403; e-mail: aaron.yocum@netl.doe.gov

Expert Technical Monitor: Philip S. Sklad
(865) 574-5069; fax: (865) 576-4963; e-mail: skladps@ornl.gov

---

Contractor: U.S. Automotive Materials Partnership (USAMP)
Contract No.: DE-FC26-02OR22910 through the DOE National Energy Technology Laboratory

---

Objective

- The goal of this project is to identify and develop a nondestructive inspection (NDI) method(s) for adhesive-bond evaluation to be used in an automotive manufacturing environment that would foster increased confidence and use in adhesive joining. The primary objective is to identify and validate an NDI method(s) which can: 1) measure the adhesive area, 2) measure adhesive thickness, and 3) detect weak metal-to-adhesive bonds (intimate contact but which have reduced strength). Wider use of adhesive joining could result in reduced vehicle weight, increased body stiffness, and improved crashworthiness. Adhesives are also seen as a critical enabler for the joining of dissimilar materials in order to avoid corrosion from dissimilar metals.

Approach

- There are five major attributes which contribute to the strength of an adhesive bond on a metal flange: the width of the adhesive area, the adhesive thickness, the location of the bead relative to the edges of the flange, the state of cure, and the quality of the adhesion. The general approach is to develop a suite of inspection techniques that can be used on the manufacturing floor which allow all the required adhesive characteristics to be measured nondestructively. The chosen methods must be a single-side inspection that can follow a flange, navigate large changes in geometry and have spatial resolution near 1 mm. To accomplish this, there is a two-step validation process: first, successfully inspect the flat, adhesively-bonded specimens representative of automobile flanges and second, deploy the inspection method on production car bodies. The flat specimens vary in adhesive, adherent type and thickness, stackup (2-3 layers), cure state, and surface contaminants. These conditions bound the processing parameters for the adhesive assembly process. A through-transmission ultrasound inspection is

performed to characterize the flat specimens and is considered a "gold standard" reference inspection method. Selected samples are also peel tested to measure bond strengths. Multiple automotive bodies-in-white (BIWs) containing a number of adhesive joints were produced by the original equipment manufacturers (OEMs) to determine whether complex geometries provide any inspection impediments and to develop body-inspection strategies. Three promising, single-sided inspection technologies for bond area, location, and thickness were studied this year. They were phased-array ultrasonics, laser ultrasonics, and pulsed thermography.

Accomplishments

- Rapid progress in this first year has produced a novel, ultrasonic phased-array imaging system that has been validated and already applied to production vehicles to answer real engineering questions. This pulse/echo system uses a custom, high-frequency, linear array in a novel probe carrier designed by the project team to scan along an adhesive bead. The system includes a position encoder and portable, closed-loop, water-circulation system. These features allow images of adhesive bonds, registered to markers on the body, to be made on the production floor. The validation included a large test suite of weld-bonded steel and aluminum (Al) coupons and a production body subsystem with embedded defects. This system surpassed the design requirements for off-line inspections and can scan at over 5 meters per minute with 1-mm resolution.
- The project team is currently working on a second-generation ultrasonic array system design that will be more adaptable to the complex geometries found on production vehicles. It will be able to inspect regions with stronger radii of curvature, smaller flange widths, and smaller confinements. This will allow a very high fraction of the bonded area on BIW's to be inspected.
- A new wedge-peel destructive test was developed to provide a high-resolution measurement of the bond strength along an adhesive bead. This uses a standard impact wedge in a fixture designed by the team. This method allows larger engineering joints up to 0.6-m long to be measured quantitatively. This method was combined with ultrasonic thickness maps to determine adhesive strength laws.
- The NDI assessment of the pulsed thermography was completed based on the inspection performance on the test coupons. Both steel and Al adhesively-bonded coupons were verified by comparing inspection results to the destructive findings.
- A reproducible procedure for constructing an intimate-but-weak ("kissing") bond samples using a grease contaminate was established. Samples with reduced shear strength were made and evaluated with an ultrasonic inspection. The resulting images could be correlated to the subsequent strength measurements.

Future Direction

- In the coming year, the second-generation ultrasonic array system will be built and evaluated, especially on the BIW structures. A major emphasis of this development will include advanced signal analysis to determine reliably the bead thickness and quality of all adhesive/adherent interfaces. These developments are geared to improve inspectibility, reduce overall system cost, increase reliability and to reach a production-ready system. The second year will also begin the process of identifying methods to detect weak bonds. These are likely to include vibrothermography, angle-beam ultrasonic spectroscopy, nonlinear ultrasonics, and laser shock peening. A mid-year report will be written addressing the advantages and disadvantages of each technique. The third year is focused on productionizing a weak-bond detection method.

Introduction

Adhesive bonding is increasing every year as automotive manufacturers strive to make bodies stiffer and stronger. Recent applications see as much as 100 meters of adhesive per vehicle being used. Adhesive joining is already widely used in automotive production today for improving body stiffness and durability, but is increasingly being used for impact performance. Current manufacturing processes for adhesive joints rely primarily on quality control of the adhesive preparation and application. Controls include machine-vision technologies to verify the applied adhesive bead before the mating piece is joined. However, there is no method currently available to test the overall quality of the final assembled joints other than destructive testing. Adhesive joining is seen as a major weight-saving technology. When adhesives are used in combination with spot welds or rivets, the

resulting joints are much stiffer and stronger. Almost a doubling of shear strength has been produced in weld-bonded joints when compared with spot welds alone. Moreover, by enabling dissimilar materials to be used in close proximity to each other, assemblies can be constructed with optimized, lightweight materials such as magnesium (Mg) and Al.

A major strategy of this project is to leverage the decades of development in the aerospace sector devoted to the NDI of adhesive joints. NDI is now commonly used in aerospace manufacturing of adhesive joints, especially for composite panel joining. Entire load-bearing structures are inspected. Portable NDI methods are also used in routine, in-service aircraft inspections.

Within the automotive prototype development sector, increased inspection capability is needed. The major area of need is within the body shop before the adhesive is cured. This is the most likely place in the manufacturing steps where discrepant joints would be repaired. Additionally, inspections are also needed at the end-of-line to ensure the quality of the entire assembled, cured, and painted product. NDI inspections are also seen as a major cost savings for accelerating engineering and environmental testing, ramp-up to production, and monitoring the long-term performance of the joints.

Coupon Preparation and Characterization

Several sets of flat, adhesively-bonded specimens, representative of automobile flanges, have been generated by the automotive OEMs and adhesive suppliers to test the feasibility of NDI techniques to assess bond area and bond-line thickness. The specimens include mild steel bonded to Al and mild steel with several production adhesives. A range of adhesive production variables, thickness under compression, and both cured and uncured conditions are embedded in the samples. These variables were designed into the specimens to include as many production processes as possible. These coupon sets allowed for parallel nondestructive and destructive testing to occur within the project.

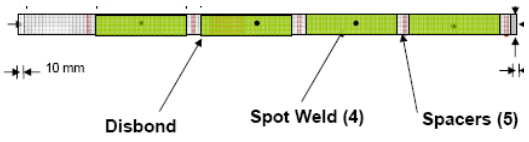

Figure 1. Joint layout prior to assembly.

An example of the coupons prior to assembly is shown in Figure 1 showing the wire spacers used to control the adhesive thickness, intentional skips, and a section of Teflon tape to simulate a kissing bond. Most of the specimens have also been spot welded using typical production welders and standard welding parameters.

All the manufactured test specimens were nondestructively inspected using high-frequency, immersion, ultrasonic through-transmission inspection method (UT-TT). The transmitted signal strength allows the areas where all interfaces in the stack are in contact with each other to be imaged (Figure 2a). Using the experimentally-measured speed of sound for each adhesive in its state-of-cure, a map of the adhesive thickness is simultaneously measured (Figure 2b). Using image analysis, the bead width and average bead thickness at each flange location can be determined. These data provide the reference for the evaluation of the other inspections.

a) Ultrasonic Transmission Intensity

b) Ultrasonic Thickness Measurement

Figure 2. Ultrasonic characterization of a 600-mm long weld-bonded coupon.

A new, wedge-peel destructive test was also developed. This method uses an instrumented load frame to pull a standard wedge (ISO11343) through the adhesive bond. This produces a load-vs.-displacement curve. This method was selected after evaluating three alternative peel methods including the standard floating-roller peel, a multi-roller peel test, and a thin-slicer peel test. As seen in Figure 3, the load-versus-displacement curves have been combined with the ultrasonic bead-width and average bead-thickness measurements to determine strength laws.

The combination of nondestructive imaging with destructive tests has driven our emphasis on bead-width measurement and minimum bead-thickness detection.

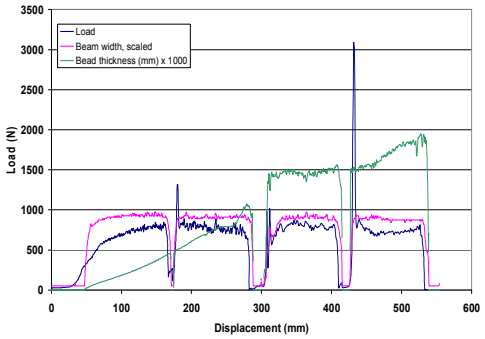

Figure 3. Wedge-peel strength measurements compared with ultrasonic bead-width and thickness measurements.

Ultrasonic Pulse/Echo Imaging

Ultrasonic pulse/echo imaging has been a standard inspection tool for adhesive inspections for many decades. A short ultrasonic pulse is launched through the outer adherent and the train of echoes from the various adhesive-adherent interfaces is detected. Typically, the ultrasonic beam is raster-scanned over the bond area and variations of the interface reflectivity are used to determine the joint condition. The primary barriers to introducing this to the plant floor have been the complex joint geometries and the difficulty of analyzing the ultrasonic echoes. This year, three different pulse/echo inspections have been used in this project. Traditional raster scans in an immersion tank have been used to obtain high-quality data on flat samples for signal-analysis development. For a manufacturing tool, both a phased-array scanner and a laser-ultrasonic scanner have been under development.

Phased-array (PA) probes are comprised of many small piezoelectric elements embedded into a polymer base material. Each ultrasonic element is individually wired, allowing individual delays (phasing) to be applied to each element. This delay allows the ultrasonic beam to be steered and focused and for the reflected signals from each element to be coherently added. Linear arrays with 16 to 128 elements are commonly available, but square and circular arrays have been made for special applications. This technology also has the ability to introduce both longitudinal and shear waves simultaneously into a specimen.

A phased-array holder/scanner was designed by SNL and the United Sates Council for Automotive Research (USCAR) Design Team [1]. The probe holder has been designed specifically to rapidly inspect long and narrow flanges that may be flat or have tight radii of curvatures. The unit uses a high-frequency linear array that spans the flange width and produces a focused ultrasonic beam that is rapidly scanned electronically at up to 10,000 points per second. This probe is manually scanned along the flange or inspection area. The probe holder incorporates a position encoder so that a two-dimensional (2D) image is obtained. Figures 4 and 5 show the version 1 prototype probe and the water delivery system.

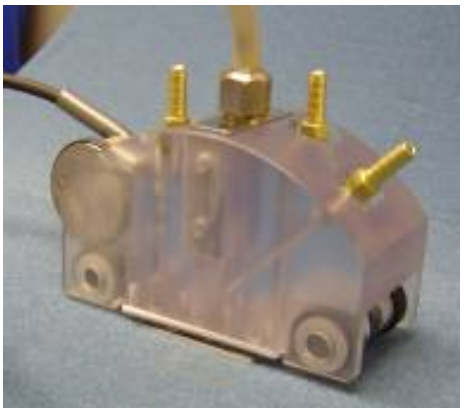

Figure 4. High-frequency phased array embedded in a custom probe holder (Version 1).

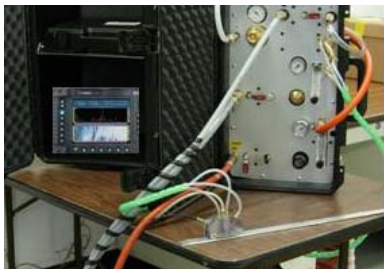

Figure 5. Phased-array probe holder on a test coupon.

The holder uses a closed-loop water-circulation system to maintain a water column between the array and the flange surface. Two angled inlet ports supply water to the array while the two vertical ports vacuum excess water from the part. The closed-loop circulation system was designed and built to include a filtered water supply,

returnpump and coupling gages in a self-contained shipping case.

The system has been validated in a C-scan mode using simple time-gating in order to inspect the first adherent/adhesive interface. This provides a rapid, high-resolution scan of the adhesive-bead position and area. The system can scan at up to 10 meters per minute with 1-mm resolution. This is more than enough to inspect 100 meters of adhesive in an off-line, two-hour inspection window. The system performance was validated on flat test specimens and large BIW samples. Images demonstrating the high-resolution performance are shown in Figures 6 and 7. The PA resolution is comparable to an ultrasonic inspection using an immersion tank, i.e., about 1 mm.

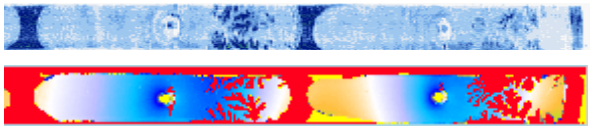

Figure 6. Phased-array image (top) of a 300-mm x 25-mm section of a coupon compared to the UT-TT reference thickness map (bottom). Note: spring-back feathering.

Deployment of the PA Probe on BIW Test Samples

After tests of embedded discrepancies such as shown in Figure 7, the scanner was deployed on BIW vehicles (Figure 8). This shows multiple adhesive maps taken of the adhesives beads between the roof-bows and the roof. This is shown for illustrative purposes since features can be readily identified. The PA and scanner have now been demonstrated on a variety of different bodies and joint designs.

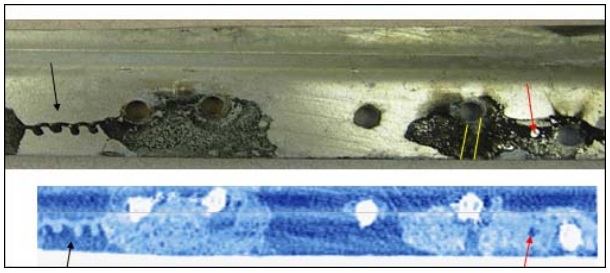

Figure 7. Section from a vehicle (30 mm x 100 mm) with embedded skips. Top image is after peeling; lower PA image is before. The spot welds are readily identifiable.

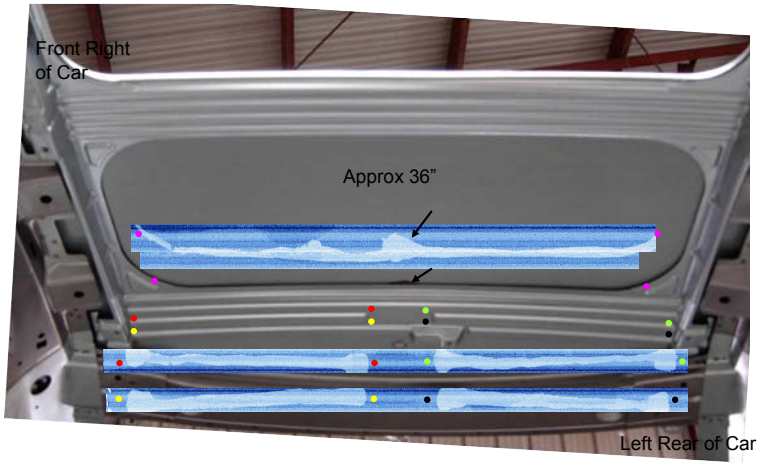

Figure 8. Maps of the adhesive area on a roof bow using the PA probe holder. The colored PA images were obtained on the roof and are superimposed on a picture of the roof bow taken from the vehicle interior.

While already of engineering usefulness, the amplitude C-scans are incomplete. They only register the location of adhesive on the outer adherent. Only with signal analysis can the other interfaces and the thickness be imaged.

The C-scan images are easily interpreted and oriented relative to features on the surface. Furthermore, they can be obtained with simple controllers without signal processing similar images on coupons have been obtained with laser ultrasonics (LU). The primary advantage of using LU is not requiring a water delivery system. However, the production scan rates are currently much lower.

Preliminary Pulse/Echo Signal Analysis

The short burst of high-frequency sound waves travel through the material with some loss of energy and is reflected at any interface. The reflected signal is captured and then analyzed to define the presence and location of reflected surfaces. Variations in reflectivity or scattering can be used as the basis of flaw detection. Transit times of the echoes can be used to assess bond-line thickness. SNL contracted with the Lawrence Livermore National Laboratory (LLNL) to determine if there was any unique signal processing and analysis that could determine adhesive thickness. The LLNL algorithm processes an ultrasonic echo that has many cycles and yields an output that is narrower with respect to time. The ideal output is to reduce multiple complex echoes to a series of delta functions. This

would allow small echoes from secondary adhesive interfaces to be resolved. This LLNL algorithm has been used successfully on single interfaces, but not on layered structures with multiple echoes. Figure 9 displays the "golden standard" data to the LLNL algorithm and shows that adhesive thickness is not resolved. There is no uniformity in the data.

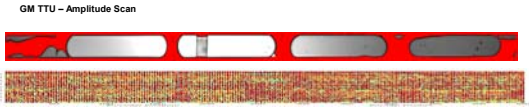

Figure 9. Comparison of through-transmission ultrasonics (TTU) data to the LLNL algorithm.

PA Signal-Analysis and Data Processing

A second, more successful, algorithm repeatedly subtracts a model waveform from a data waveform in a least-square fashion to remove the primary echoes from the first interface. The subtraction attempts to extract the relatively weak echoes associated with the secondary interfaces. Particular care was given to develop an algorithm that uses as few computations as possible and being applied thousands of times in only a few seconds.

The algorithm assumes the primary echoes have a single reflectivity, a fixed round-trip delay time, and minimal frequency dispersion. With these assumptions made, two signals are considered. The first is called the "model" signal, which is the waveform acquired when it is known that no adhesive is present (Figure 10). The second is called the "data" signal, which is associated with adhesive present (Figure 11).

These example signals are from the PA system. The overlapping signals represent the peak values of multiple echoes from model and data waveforms. When adhesive is present, peak values are reduced due to the lower reflectivity. Secondary echoes are typically 10-25% of the peak echoes depending on the adherent.

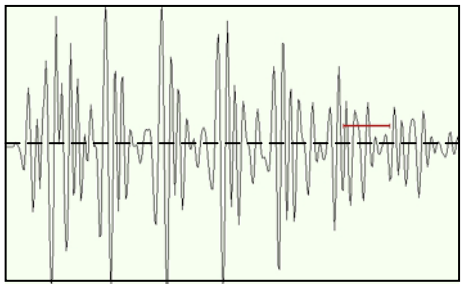

Figure 10. Representative pulse/echo signals on a test specimen – no adhesive present.

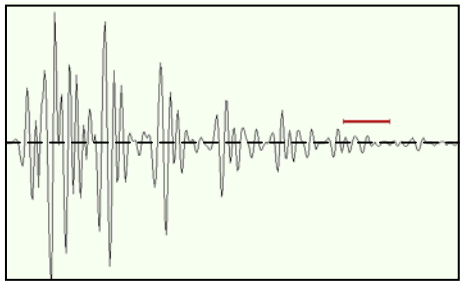

Figure 11. Representative pulse/echo signals on a test specimen – adhesive present.

Finally, the third year of the project will analyze all the inspection data to determine if any data fusion (combining inspection data from two types of inspections) will be achievable.

Completed Assessment of Pulsed Thermography

This technology uses thermal gradients to analyze the physical characteristics of a structure for internal non-uniformity. Flash lamps heat the surface of the structure and the heat diffusion is measured by imaging the surface temperature with a fast-cycle-time infrared camera. Areas that appear hotter or cooler may indicate the presence of a flaw beneath the surface (heat diffusion into deeper layers). By analyzing the time-history of the infrared signal, subtle variations can be enhanced in the image. By plotting the log of temperature versus log of time, quantitative adhesive bond-line thickness measurements were obtained (Figure 12). Additional information about this inspection technique and sample preparation can be found in the first year reports [2, 3].

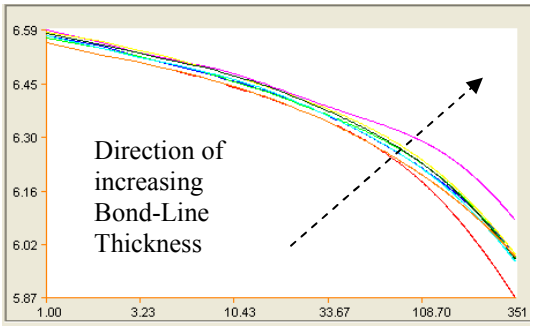

Figure 12. Log of temperature vs. log of time depicts thickness variations on an uncured steel stackup.

While SNL was conducting pulsed-thermography inspections on BIW vehicles, similar inspections on the flat, adhesively-bonded specimens were being conducted concurrently at Thermal Wave Imaging Incorporated. Unfortunately, the high optical reflectivity and low infrared emissivity of Al and steel typically prohibit a successful pulsed-thermography inspection without adding a black paint to the inspection surface.

New Mexico State University (NMSU) was sent infrared (IR) data files to analyze. C-scans optimized for adhesive/no adhesive contrast were processed to extract relative intensity of the pixels along a data line as seen in Figure 13. The spot welds, adhesive and skips can be distinguished in the data. Unfortunately, adhesive thickness could not be easily extracted without reanalyzing the entire time-history datasets.

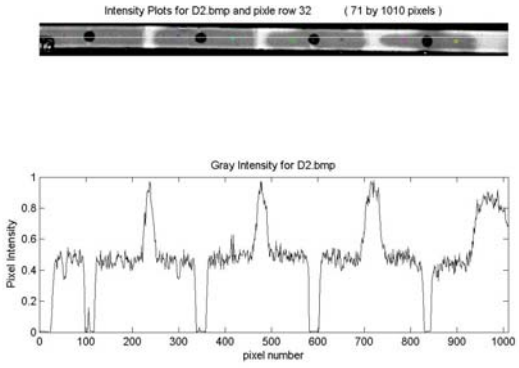

Figure 13. Pixel intensity versus pixel number along the mid-line of an uncured steel stackup.

Inspection of Uncured Adhesives

To date, there has been no difficulty imaging uncured coupons. While the uncured adhesives have a significantly lower speed of sound and are more attenuative, this has not presented a problem so far. In Figure 14, results from the reference UT-TT measurements are shown in comparison with the pulsed-thermography and phased-array pulse/echo measurements. While the thermography results have poorer contrast, the skips, welds, and bead-spread are discernable.

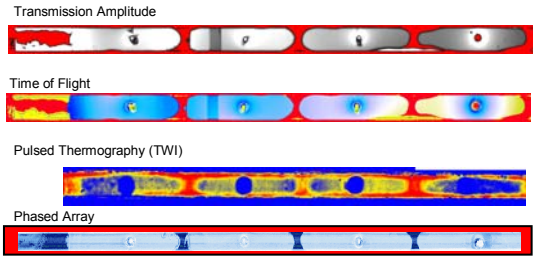

Figure 14. Comparisons of three inspection methods on an uncured-adhesive coupon.

Weak (Kissing) Bond Samples

A procedure to make weak bond samples reproducibly was developed. These used a bearing grease as a model surface contaminate. Figure 15 shows the range of lap-shear strengths obtainable for different thicknesses of grease. These adhesives are designed to work on greasy surfaces and major contamination is needed to affect the strength. These samples were also ultrasonically imaged. The ultrasonic data could be processed to predict the strength with good confidence.

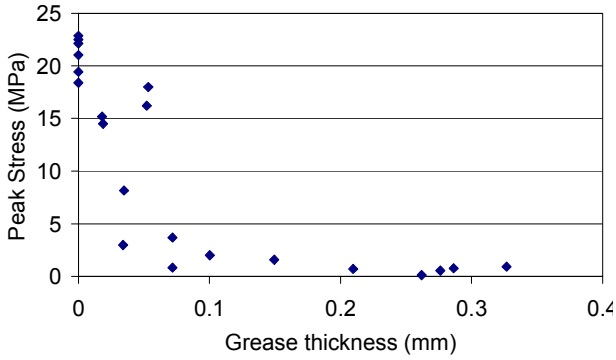

Figure 15. Weak bond shear-strength as a function of grease-contaminate thickness.

Conclusions

Good progress was made on the project objectives during this first full year. An effective inspection tool for off-line inspections was designed, verified, and tested on production vehicles. While this ultrasonic array system is currently only able to inspect the wet-out on the outer skin, the system performance appears to be adequate to allow the adhesive thickness and second interface inspection of 2-layer stickups as signal processing improves. A second-generation version of this ultrasonic array scanner is under development to improve the performance on curved surfaces. A new, high-resolution, wedge-peel test was developed and used to obtain strength scaling laws. Finally, promising results were obtained on the weak-bond samples in the presence of a grease-contaminate.

Acknowledgements

This project team consisted of members from the automobile industries, federal research laboratories and universities. The team members were: Ciji Nelson, Kirk Rackow, Steve Younghouse, Kim Lazarz, Dan Ondrus, Dave Biernet, Jessica Schroeder, John Fickes, Ray Bis, Mike Golden, Dave White, Rajat Agarwal, Bill Brown, Kent Wen and Marvin Klein. We also would like to thank IOS and Olympus NDT for their input and Metal Steel and Novellis for supplying metal blanks.

References

1. Disclosure of Technical Advance Dated February 20, 2007, "*Probe Deployment Device for Optimal Ultrasonic Wave Transmission and Area Scan Inspections*", Joseph DiMambro, Dennis Roach, Kirk Rackow, Ciji Nelson, Sandia National Laboratories and Cameron Dasch General Motor Corporation.
2. NDE601-FY2006 Annual Progress Report for DOE ALM, Joseph DiMambro and Dennis P. Roach Sandia National Laboratories, Cameron J. Dasch General Motors Research & Development, December 15, 2006.
3. "Preliminary Report of Sample Preparation and Ultrasonic Through-Transmission Images of Flat, Mild Steel Coupons for USCAR /USAMP Project NDE 601 – NDI of Adhesive Metal Bonds", *C. J. Dasch, A. Terry, W. Brown, R. Bis, D. White, and D. Sigler*, January 31, 2007.

Presentation/Publications/Patents

1. "Preliminary Report of Sample Preparation and Ultrasonic Through-Transmission Images of Flat, Aluminum Coupons for USCAR /USAMP Project NDE 601 – NDI of Adhesive Metal Bonds", *C. J. Dasch, A. Terry, W. Brown, R. Bis, D. White, and D. Sigler*, February 14, 2007.
2. "Automotive Lightweight Materials: the Roles for NDE in Bringing New Materials into Production", *C. J. Dasch*, Plenary Lecture, Conference on Quantitative Nondestructive Evaluations, Golden, CO, July 2007.
3. "Nondestructive Inspection of Adhesive Bonds in Automotive Metal/Metal Joints (NDE 601)", C. J. Dasch, USAMP Off-site Review, Oct. 25, 2007.
4. "Correlating Adhesive Bond Strength with Non-Destructive Test Methods", K. Lazarz, C. Dasch, R. Agarwal, to be presented at the Annual Meeting of the Adhesion Society, Austin TX, Feb. 2008.

[i] Denotes project 601 of the Nondestructive Evaluation Working group of the United States Automotive Materials Partnership (USAMP), one of the formal consortia of the United States Council for Automotive Research (USCAR, www.uscar.org) set up by Chrysler, Ford and General Motors to conduct joint, pre-competitive research and development.

C. Laser-Ultrasonic Inspection of Adhesive Bonds Used in Automotive Body Assembly

Principal Investigator: Marvin Klein
Intelligent Optical Systems
2520 West 237th Street
Torrance, CA 90505
(424) 263-6361, fax: (310) 530-7417; e-mail: mklein@intopsys.com

Technology Area Development Manager: Joseph A. Carpenter
(202) 586-1022; fax: (202) 586-1600; e-mail: joseph.carpenter@ee.doe.gov

Contractor: Intelligent Optical Systems
Contract No.: DE-FG02-06ER84545 Small Business Innovative Research (SBIR) and Small Business Technology Transfer (STTR) Program

Objective

- Adhesive bonding is widely used in automotive production, especially for body assembly. It is critical to be able to measure the strength of adhesive bonds during manufacture in a nondestructive, effective and rapid manner. There is no current means for inspecting these bonds in real time. The specific inspection requirement is to (1) map the adhesive spread, (2) measure the thickness over the full area, and (3) measure the bond strength. All inspections must be performed from one side and must be able to function on contoured surfaces with ~1 mm resolution. The ideal tool must be able to perform the above measurements simultaneously (i.e., in one pass across the bond). In this project we have applied the technique of laser ultrasonics to the adhesive-inspection requirements described above. The specific goals of this project are to determine the best inspection configuration and signal-processing approach, followed by the development and demonstration of a prototype inspection system.

Approach

- The technology which we will apply to this inspection requirement is laser ultrasonics, in which a pulsed laser beam is directed to the surface to generate ultrasonic waves in the sample, and a continuous-wave laser receiver is used to detect the waves after they interrogate the required sub-surface feature and return to the surface. Laser-based ultrasonic inspection has a number of benefits over transducer-based ultrasonic inspection, including 1) lack of physical contact with the workpiece; 2) high spatial resolution obtained using focused laser beams; 3) high scan rate associated with rapid beam scanning, and (4) high bandwidth, thereby improving the measurement accuracy.

- This project is closely coordinated Sandia National Laboratories' phased-array project, "Nondestructive Inspection of Adhesive Metal/Metal Bonds," funded by DOE and managed by the USCAR Nondestructive Evaluation (NDE) Working Group. (See 10.B) That USCAR-managed project has produced a large number of adhesive-bonded specimens. The flat specimens vary in adhesive, adherent type and thickness, stackup (2-3 layers), cure state, and surface contaminants. These conditions bound the processing parameters for the adhesive assembly process. These specimens have been used to optimize the beam configuration and signal-processing techniques. The remaining portion of our project is devoted to the development and demonstration of a prototype scanning inspection system that can be scaled to a measurement speed of 1 meter/minute.

Accomplishments

- In 2007, we completed a 6-month SBIR Phase I project, as well as three months of a 24-month SBIR Phase II project that started during the year. During the course of this effort, we tested six of the USCAR specimens, thereby enabling us to determine the configuration of both laser beams (separation, size, shape, energy) that provides the best signal-to-noise. We also investigated several algorithms for processing the raw signals to

provide mapping and thickness, and selected one of these for further development. We developed a specification for a scanning prototype system and began the associated hardware development.

Future Direction

- In 2008 we will complete the signal processing algorithm development and continue to develop prototype system hardware. The major elements of the hardware development will include implementation of robot scanning, along with associated control software. A measurement head that provides the required beam configuration at the workpiece surface will also be designed and tested.

Introduction

Adhesive bonding is widely used in automotive production, especially for body assembly. The most common use is the lap joining of two or three sheet-metal panels. Adhesive bonding adds strength, and thus allows the use of lighter components at equal performance. Adhesive bonding allows the joining of dissimilar materials such as aluminum (Al) and steel. Modern adhesives (especially epoxy resins) have excellent fatigue and thermal shock resistance and less critical design tolerances because of their gap-filling capabilities. Their service range extends from space environments to high temperatures. It is critical to be able to measure the strength of these bonds during manufacture in a nondestructive, effective, and rapid manner.

The most important manufacturing issues that can influence the strength of an adhesive bond are the maintenance of the proper fit-up and proper surface preparation. While adhesive bonds are tolerant of some range of gap between the panels, if the gap is too large, the adhesive will not cover the required area, and the intrinsic strength of the adhesive itself is reduced. If surface contamination (e.g., oil, grease, surface oxides, corrosion, water infiltration) is present, the bond adhesion will be reduced. In the limit of very low adhesion, weak bonds may have intimate contact, but little or no bond strength ("kissing").

The corresponding requirements for nondestructive evaluation of adhesive bonds fall into three areas: (1) mapping of the adhesive coverage, (2) measurement of adhesive thickness, and (3) measurement of the adhesion of each metal/adhesive bond.

All inspections must be performed from one side and must be able to function on contoured surfaces. The ideal tool must be able to perform the above measurements simultaneously (i.e., in one pass across the bond).

At the current time, nondestructive inspection is not performed during the bonding process. The only quality control techniques now implemented are careful process control, machine-vision inspection of the adhesive bead before joining, and selective destructive evaluation. A nondestructive technique for in-line measurement of adhesive integrity would reduce scrap and warranty costs, and thus allow wider use of adhesive joining.

Laser ultrasonics offer an attractive approach for nondestructive evaluation over a broad range of applications. The full complement of ultrasonic waves (longitudinal, shear, Lamb and Rayleigh) can be produced with known directionality. The pulses are high in bandwidth, thereby providing the high depth resolution required for thin sheets and bonds. The spot sizes on the part can be much less than 1 mm in diameter, thereby providing high spatial resolution.

The objective of this project is to develop a real-time system for inspection of adhesive panels during auto body assembly (see Figure 1). This system will incorporate a fiber-delivered robotic measurement head containing a scanning mirror that will be able to scan narrow sections of adhesive very rapidly.

Samples Provided

General Motors and the USCAR project were kind enough to provide a number of samples for testing. As shown in Figure 2, Samples A1 (uncured) and A3 (cured) consist of a two-sheet stackup with three adhesive joints distributed along the length of the samples, each joint having a spot weld near the center. The middle adhesive joint also contained a section of Teflon tape to simulate a kissing bond. The adhesive is Dow Betamate

1480, a crash-stable epoxy with a longitudinal wave velocity of 2.2 mm/μs in the cured state.

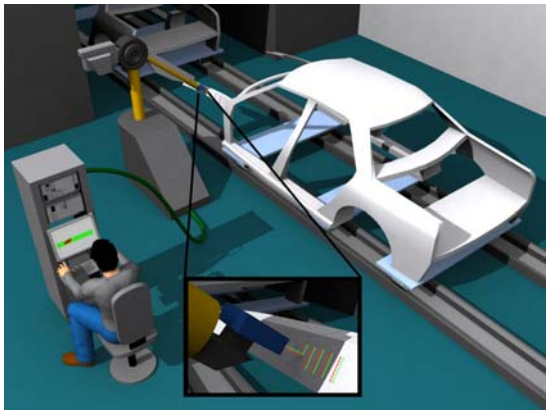

Figure 1. Depiction of robot-driven inspection system performing a two-dimensional scan of an adhesive-bonded auto body panel.

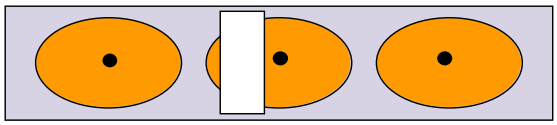

Figure 2. Schematic layout of Samples A1 and A3, showing the thickness for each sheet.

Sample Scans

Typical maps or C-scans of the center portion of Sample A3 are shown in Figure 3. The amplitude map captures the adhesive spatial coverage and detects the presence of the (unbonded) section of Teflon tape. The time-of-flight map contains grey-scale variation that is indicative of the varying thickness of the adhesive. In this latter map, the areas with no ultrasonic arrivals (no adhesive or Teflon tape) appear with random amplitude, as the software is processing only noise.

The maps in Figure 3 were taken with 3-mm steps to speed the data acquisition. An amplitude zoom scan of the left portion of Figure 3 with 1-mm step size is shown in Figure 4. The edges of the adhesive are now resolved to a level required for factory implementation.

All subsequent measurements were performed with both beams on the same side (pitch-catch configuration) and spaced 1-2 mm apart. In this configuration, multiple echoes are expected from both the A and B interfaces (with A the adhesive

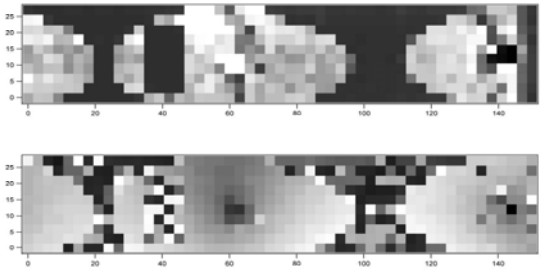

Figure 3. Through-transmission C-scans of Sample A3 based on amplitude (top) and time-of-flight (bottom). Step size=3 mm.

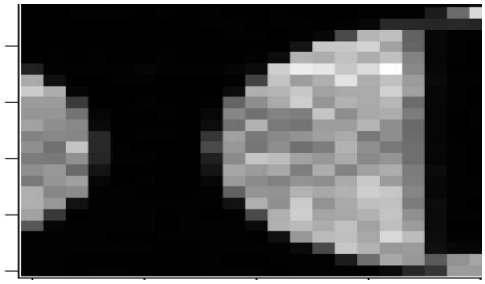

Figure 4. Zoom image of left portion of Figure 3 (top). Step size=1 mm.

interface closest to the measurement head and B the adhesive interface furthest away from the measurement head). The value of the reflectivity at these interfaces is dependent on the impedance values of each material. Specifically, the reflectivity of a steel/adhesive interface (~0.9 in amplitude) is smaller than that of a steel/air interface (very close to 1.0). This difference is not large, but it is sufficient to yield a measurable difference in the amplitude of the interface echoes. We also expect that phase changes could alter the shape of the arrivals. We wish to use these characteristic changes as a means of mapping the adhesive.

In Figure 5, we show a B-scan on sample F14 in which the beams pass over a gap in the adhesive between position x=-9 mm and x=+9 mm. A B-scan is a grey-scale plot of the detected signal at a series of one-dimensional (1D) positions along the sample. Our beam configuration produces very strong multiple reflections in the front sheet. As indicated above, the reflection coefficient from the back surface of the front sheet is slightly larger when adhesive is absent than it is when adhesive is present. Thus, the reflected wave amplitude is larger over the gap, and the difference from the adhesive areas increases with each reflection. This

effect is clearly visible in Figure 5. The clarity of this difference is directly associated with the optimized beam configuration that we have determined. In spite of the clear amplitude difference in Figure 5, it is risky to rely on amplitude as an indicator of the spread of adhesive, as many other experimental factors can change the amplitude and possibly give a false positive indication. The next section discusses an alternative and preferred approach to mapping the adhesive.

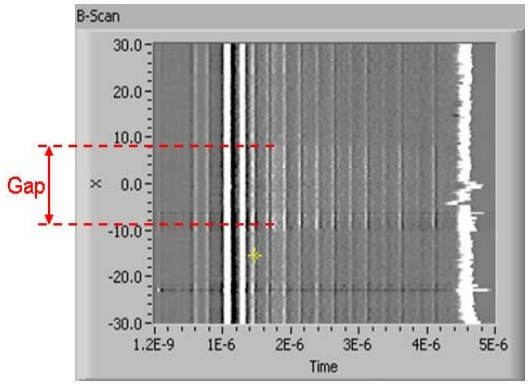

Figure 5. B-scan across 60 mm on Sample F14.

Signal-Processing Development

The objective of our signal-processing development is to amplify the features in the signals which allow direct measurement of the adhesive spread with requiring a direct measurement of signal amplitude. Specifically, we wish to identify the transition regions at the edges of the adhesive. We have applied a number of digital signal-processing techniques to enhance the edge signals in our scans. In Figure 6, we show an example of a processed B-scan using the data plotted in Figure 5. Now the transition regions are identified as changes in sign of the backwall echoes are small shifts in the arrival times. These features are not dependent on variations in the amplitude of the echoes and are thus much more robust for automated processing.

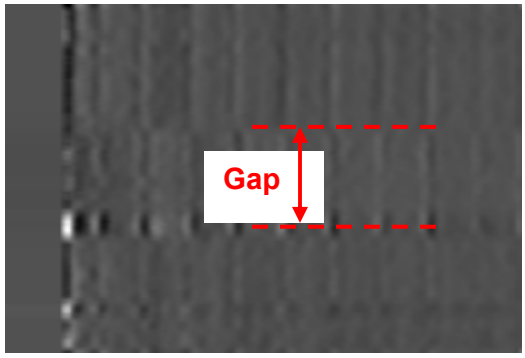

Figure 6. Processed and expanded B-scan using the data shown in Figure 5. Based on the time scale in Figure 5, the time span in Figure 6 extends from 1.5 to 4 microseconds.

Scanning-Head Development

The scanning head has two main components: the measurement head, and the generation laser-coupling module. The measurement head is diagrammed in Figure 7. The generation beam is delivered through a fiber bundle, while the probe beam is delivered through a conventional fiber. The beams are combined at a dichroic beam combiner and then focused onto the adhesive panel surface. The beams are separated on the surface by a few millimeters. The return probe light from the surface is collected and delivered to the signal fiber for later processing. The measurement head has been designed for ease in assembly and alignment.

In Figure 8 we show a top view photo of the assembled head.

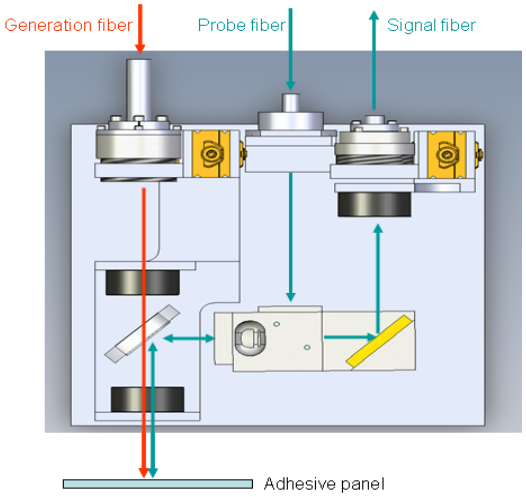

Figure 7. Schematic drawing of measurement head.

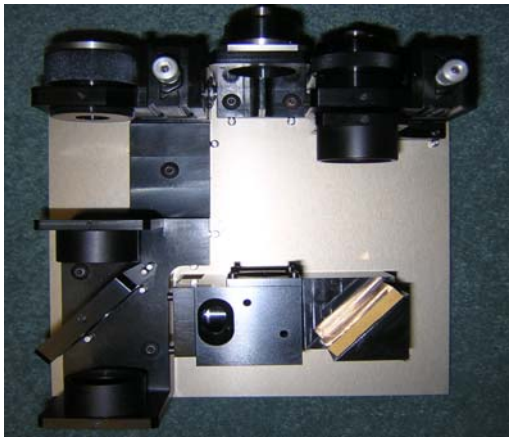

Figure 8. Top view photo of assembled head with cover removed.

The generation laser pulses can easily damage a fiber if not controlled carefully. In order to eliminate the risk of damage, we use a fiber bundle to deliver this beam to the measurement head. A proprietary optical module is used to couple the generation laser beam into the fiber bundle.

Conclusions

In 2007, we completed an SBIR Phase I project and started a Phase II project. Good progress was made on the overall project objectives.

We have successfully applied laser ultrasonics to the requirement for evaluating adhesive bonds used in auto body assembly. Techniques have been developed to map the adhesive spread and measure the thickness. The signal processing efforts have indicated a pathway for processing the raw data in real time. We have designed prototype scanning hardware that will be robot-mounted for automated measurements. Continued work in 2008 will be required to refine the signal processing and test/improve the measurement hardware.

Presentations/Publications/Patents

None.

D. In-Line Resistance Spot Welding (RSW) Evaluation System for Lightweight Materials

Project Leader: William Charron
Ford Motor Company
6100 Mercury Drive, Dearborn, MI. 48126
(313) 805-6628; e-mail: wcharron@ford.com

Principal Investigator: Xin Sun
Pacific Northwest National Laboratory (PNNL)
P.O. Box 999/K2-03, Richland, WA 99352
(509)375-6489; fax: (509) 375-2604; e-mail: xin.sun@pnl.gov

Project Technical Administrator: Todd Cleaver
Tech Knowledge
(734) 675-5562; fax: (734) 675-5562; email:toddcleaver@wowway.com

Technology Area Development Manager: Joseph A. Carpenter
(202) 586-1022; fax: (202) 587-1600; e-mail: joseph.carpenter@ee.doe.gov

Expert Technical Monitor: Philip S. Sklad
(865) 574-5069; fax: (865) 576-4963; e-mail: skladps@ornl.gov

Participants:
This project is being conducted as a partnership with the Automotive Metals Division (AMD) of the U.S. Automotive Materials Partnership (USAMP) with participation that includes (but is not limited to) the following automotive company representatives:
Bill Charron, Ford Motor Company
Dan Cerjanec, Chrysler Corporation
John Bohr, General Motors Corporation

Contractor: PNNL
Contract No.: DE-AC06-76RL01830

Objectives

- Assess the current state-of-the-art for in-line resistance spot welding (RSW) control and evaluation systems and determine their potential for application to direct weld control for lightweight sheet materials.
- Determine feasibility of the most promising control technologies to overcome the primary technical hurdle, accurate identification of key weld characteristics and all weld defects that occur in the production process (during nugget formation or immediately thereafter).
- Assess the control technologies for probability to meet performance, business, and retrofit/integration targets.

Approach

- Develop assessment criteria and performance targets for weld quality, cost, and retrofit/integration potential. A team of original equipment manufacturer (OEM) welding experts will participate in this task and establish a test protocol for an “apples-to-apples” comparison of systems which will be used to assess evaluation systems currently available for testing.

- Suppliers/developers of in-line RSW control and evaluation systems will be invited to participate and subject their systems to the proposed assessment.
- Samples of the full range of potential defects will be made for control systems that require them. Each system will process selected lightweight sheet materials and thickness combinations.
- Data and system outputs will be captured, evaluated, measured, and assessed against the criteria/targets established by the team and identification and recommended next development steps (if any) will be reported.

Recent Accomplishments

- Developed business-issues questionnaire for in-line adaptive and post-weld audit systems.
- Developed test protocol for in-line adaptive and post-weld audit systems.
- Identified the materials needs and material availability.
- Identified the full list of potential system suppliers.
- Invited potential system suppliers to participate in testing and complete the business-issues questionnaire.

Future Direction

- Project terminated.

Introduction

Aluminum (Al) and advanced high strength steel (AHSS) sheet materials represent substantial opportunities to save weight and improve fuel efficiency. Robust spot-weld control and quality assessments are significant hurdles in the accomplishment of widespread implementation of these materials. This project assesses the current state-of-the-art for in-line RSW control and evaluation systems and determines their potential for application to direct weld control for lightweight sheet materials.

No economically-reliable method exists today to inspect RSWs at production rates. The currently accepted practices make use of labor-intensive, manual teardown inspection processes, performed every shift to determine weld quality off-line. In addition, in-line manual pry checking is performed on selected joints. Pry-testing and teardowns do not allow plant management and engineers to collect inspection data that allow them to identify trends and potential problems or make pre-emptive adjustments to the weld systems prior to defect identification. And, these practices result in significant cost, quality, productivity, and safety/health issues and always occur many cycles after the welds have taken place.

Furthermore, these inspection techniques are not viable options for advanced, lightweight, thinner-gage AHSS and Al materials. As the industry moves toward body structures with more AHSS and Al, the post-mortem teardown inspection processes for weld integrity will be less reliable and more difficult and costly, potentially discouraging the implementation of these materials. The pry-test procedure may not work at all with AHSS materials or damage the material as is the case with Al sheet. Clearly, a new method is required to assure that high-quality welds have occurred.

Several OEMs and suppliers have attempted to develop technologies (ultrasonics, infrared [IR] thermography, artificial intelligence, etc.) to resolve these problems. However, concept feasibility has not been demonstrated for many of these developments and even fewer have been evaluated in OEM test facilities or on production lines. The lack of comparable measurables for these systems hampers a clear understanding of the technical hurdles to be overcome (if any) before any systems can be deployed with any confidence. In the final analysis, widespread usage of this technology in the domestic automobile industry will depend on the ability to 1) identify all weld defects (during nugget formation or immediately thereafter); 2) develop robust control

algorithms; 3) retrofit/integrate into existing weld controllers; and 4) provide affordable technology. The objectives of the current concept-feasibility study are: 1) determine feasibility of the most promising control technologies to overcome the primary technical hurdle, i.e., *accurate identification of key weld characteristics and all weld defects that occur in the production process* (during nugget formation or immediately thereafter) and 2) assess the control technologies for probability of meeting performance, business, and retrofit/integration targets. Upon successful completion of this project, a follow-on effort may be proposed to resolve identified technical hurdles of the most promising control systems.

This effort is an essential first step in understanding what control and assessment technologies/ approaches are appropriate for maturation and application in spot-welding lightweight materials. This work will lead to better understanding of the welding process resulting in improved consistency, optimization and control. And, it may offer the potential to reduce the number of welds and associated manufacturing costs and facilities. In summary, development of in-line evaluation and control techniques is an enabling technology for greater use of lightweight materials such as AHSSs and Al, in the automotive industry where systems to assure product quality are essential for industry and consumer acceptance of new materials and manufacturing methods. This project, a collaboration between USAMP AMD and PNNL, started in December of 2006.

Development of Business-Issues Matrices for In-line Adaptive and Post-Weld Audit Systems

During the first quarter of the project, the project team met regularly and developed the business-issues matrices and technology-issues matrices for both the in-line adaptive and post-weld audit systems (Refs 1-2).

For example, the business issues matrix for the in-line adaptive systems include scores for 19 (nineteen) categories including the individual system's stage of technology, product capital cost, process time per weld, etc. See Table 1. These scores will help OEMs in understanding and building a case for business-related concerns to measure/evaluate impact to incumbent operations that may affect implementation and adoption of the technologies.

Supplier/system name	Input			Comments
Stage of technology		1-5	1 being at research level	5 being commercial ly available
Product capital cost ($)/system			From supplier	Best-faith-estimate based on purchase of 20 units
Process time/weld			Measured	
Product life cycle (years)			From supplier	
Warrantee coverage (years)			From supplier	
Maintenance frequency (#/shift)			From supplier	What & how often
Calibration frequency (days)			From supplier	
Cost and time to calibrate			From supplier	
Non-contact or contact		1 or 0	1 for non-contact	0 for contact
Portability (weight in lb.)		1 or 0	1 portable	0 non - portable
Personnel training cost				
Operator skill level		3 = non-skille d	2 = skilled	1 = technician 0 = engineer
Programming cost and set up time to launch			From supplier	
Safety and ergonomics		1-5		
Roster of current applications				
References for each application locations				
List robot your system HAS interfaced with				
List robot your system CAN interface with				
Adaptive to servo guns?				

Table 1. Business-isues matrix for in-line adaptive systems

The potential supplier list for the in-line adaptive system included nine commercial suppliers, the three OEMs and DOE's Oak Ridge National Laboratory [ORNL] and Lawrence Berkley National Laboratory [LBNL].

The materials considered include:
a. Bare mild steel
b. Hot-dip (HD) galvanized mild steel
c. Galvanneal mild steel
d. Coated high-strength low-alloy (HSLA)
e. Bare transformation-induced plasticity (TRIP)
f. HD galvanized TRIP
g. Galvanneal TRIP 800 or coated dual phase (DP) 800
h. Boron steel
i. Al alloy xxxx (TBD)

Development of Test Protocol for In-line Adaptive and Post Weld Audit Systems

Weld sample fabrication protocols have been established for the two different types of systems due to the intrinsic difference in inspection and control philosophy.

Audit Systems

For the audit systems, a two-step procedure is used in which the first step involves sample fabrication and the second step is actual inspection. Sample-fabrication process will generate the desired fusion-zone size distribution as well as the desired types of weld defects in order to test the capabilities of the inspection systems.

The ground rules for the inspection procedure are then developed for all the participating systems:
- All participants/system suppliers will be provided representative training sets for machine set up.
- All participants/system suppliers will be evaluating the same welds, both on the coupon level and on the component level, i.e., a production door or other selected production part.
- After all the samples are evaluated by all the system suppliers, X-ray, peel tests and metallographic cross sectioning will be performed to quantify various weld attributes.
- For each supplier system, the following measurements will be recorded and compared with actual destructive measurements:
  - Maximum fusion-zone diameter
  - Minimum fusion-zone diameter
  - Fusion zone penetration
  - Weld indentation
  - Amount of weld porosity
  - Amount of weld cracks

Table 2 shows the weld-quality quantification Table A for each weld population and system supplier. Consolidated data for each supplier for all the weld populations will then be captured in Table 3 for overall system evaluations.

In-Line Adaptive Systems

The control capability of in-line adaptive systems will be examined under both perfect and imperfect welding conditions. The imperfect welding conditions include:
a. Electrode wear/mushrooming
b. Gap
c. Edge weld
d. Shunting
e. Sealant

In order to efficiently examine the capability of weld-quality control systems under these different welding conditions, a coupled welding procedure is developed in which 554 welds are made for each weld population. Out of the 554 welds, 72 will be cross sectioned, 72 will be peeled. All the rest of the welds are performed to simulate electrode wear conditions. For details, please refer to the testing procedures listed in Ref. 2.

Ground rules for sample fabrication procedures for the in-line adaptive systems are determined; once the system is set-up for one population, no adjustments are allowed while making all the 554 welds for that population. Details follow the document from AMD 303.

All the system measurements will be compared with destructive weld attributes measurements such as metallographic cross-sectioning and peel tests. For each supplier, the following parameters will be compared for each weld between the specified value and the actual destructively tested value:
- Maximum fusion-zone diameter – target values per American Welding Society (AWS) D8.1M or AWS D8.2M (Refs. 3-4)
- Minimum fusion-zone diameter -- target values per American Welding Society (AWS) D8.1M or AWS D8.2 (Refs. 3-4)
- Fusion-zone penetration – Target minimum values to be determined

- Weld indentation – Target allowable values to be determined
- Expulsion
- Weld porosity
- Weld cracking

Supplier/System Name:																		
Weld population ID:																		
Weld No.	Max fusion-zone diameter (mm)			Min fusion-zone diameter (mm)			Weld indentation (mm)			Weld penetration (mm)			Weld porosity definition (%)			Weld cracking definition (%)		
	System measured	Destructive test	Deviation from NDE to actual destructive measurement α (mm)	System measured	Destructive test	Deviation from NDE to actual destructive measurement β (mm)	System measured	Destructive test	Deviation from NDE to actual destructive measurement γ (mm)	System measured	Destructive test	Deviation from NDE to actual destructive measurement ζ (mm)	System measured	Destructive test	Deviation from NDE to actual destructive measurement ψ (%)	System measured	Destructive test	Deviation from NDE to actual destructive measurement η (%)
1																		
2																		
…																		
20																		
Average deviation																		

Table 2. Weld-quality quantification Table A for audit system.

Supplier/System name:									
Can max and min fusion zone diameters be measured?	1 or 0: Yes- 1, No- 0								
Can weld penetration be measured?	1 or 0: Yes- 1, No- 0								
Can weld indentation be measured?	1 or 0: Yes- 1, No- 0								
Can weld porosity be measured?	1 or 0: Yes- 1, No- 0								
Can weld cracking be measured?	1 or 0: Yes- 1, No- 0								
Deviations (α-η) from Table A or correlations (χ) from Table B			α	β	γ	ζ	ψ	η	χ
System measurement accuracy	TRIP or DP	2-t stack							
	Boron steel	2-t stack							
	aluminum alloy	2-t stack							

Table 3. Weld-quality quantification Table B for audit system.

For each weld population, Table 4 will be filled out for systems that are able to control the above seven parameters. For systems that do not control certain attributes, that column will be keyed in as 'NA'. The numerical results from Table 4 will then be used as inputs for each row in Table 5 to consolidate the results for each supplier.

The weld acceptance criteria documented in the new AWS standards (Refs. 3-4) are used to define the attributes for acceptable welds. All the suppliers in the adaptive-controls category are subjected to the same testing and evaluation conditions.

Identification of Materials Availability

Initial material-availability search has been conducted inside other project teams within USCAR, Auto Steel Partnership (A/SP) and among OEM and suppliers. Corresponding material needs have been calculated and the weld population definitions have also been drafted.

Sources for all the materials needed for the project have been identified. These sources include: Chrysler, General Motors, A/SP Inventory, and steel suppliers.

Project Execution

After the business-issues questionnaires and test protocols for both the in-line adaptive and post-weld audit systems were developed, they were sent to 15 system suppliers with an invitation to participate. The survey used the commercial website called 'Survey Monkey.' Because of sensitivity of data requested, individual questionnaires were held in confidence and not shared with competitors. The questionnaires surveyed the following topics on individual systems:

- Calibration
- Maintenance
- Training
- Launch
- Cost
- Development Needs
- Cycle Time
- Commercial Availability
- Portability
- Robot Interface

Supplier/System Name:															
Weld population ID:															
Weld measurements	Max fusion-zone diameter (mm)			Min fusion-zone diameter (mm)			Weld indentation (mm)			Weld penetration (mm)			Porosity	Expulsion	Cracking
	Specified/ requirement	Destructive test	Deviation from actual measurement to requirement α *(mm)	Specified/ requirement	Destructive test	Deviation from actual measurement to requirement β *(mm)	Specified/ requirement	Destructive test	Deviation from actual measurement to requirement γ (mm)	Specified/ requirement	Destructive test	Deviation from actual measurement to requirement ζ *(mm)	No- 0 Yes- 1	No- 0 Yes- 1	No- 0 Yes- 1
1															
2															
3															
…															
9															
Average deviation															

Table 4. Weld-quality quantification Table A for RSW adaptive systems.

Supplier/System name:							
Control accuracy (α-ψ) from Table A	α	β	γ	ζ	χ	η	ψ
Electrode wear							
Gap							
Edge weld							
Shunting							
Sealant							

Table 5. Weld-quality quantification Table B for RSW adaptive systems.

Although the initial responses at the project kick-off meeting were overwhelmingly enthusiastic from many suppliers, the feedback to the business-issues questionnaire and testing was sparse. Only four suppliers submitted the questionnaires. Only two suppliers volunteered to participate in the testing of their systems. The remaining suppliers declined to participate.

Both infrared (IR) thermography technology suppliers submitted questionnaires and identified potential technology needs. These needs were identified as measurement accuracy of cracks, porosity and indentation.

Because of the lack of participation from various system suppliers in this stage of the project, the project team concluded that it was no longer possible to meet the project objectives and timeline for deliverables outlined in the Statement of Work (SOW) and decided to stop all development work.

The team then proceeded with project closure tasks and notified AMD and USAMP of team decision.

Conclusions

Technology questions and concerns still remain regarding the feasibility of control technologies to accurately identify key weld characteristics and defects that occur in the production process during nugget formation or immediately thereafter. Furthermore, no viable technologies exist for the inspection and control of RSW for advanced, lightweight, thinner gage, AHSS and Al materials. As a result, as the industry moves toward body structures with more AHSS and Al, the post-mortem teardown inspection processes for weld integrity will be less reliable and more difficult and costly, potentially discouraging the implementation of these materials.

The only technical needs identified in the project for further development consideration were in IR-thermography technology.

References

1. RSW Audit System Evaluation Matrix and Testing Procedure (DRAFT), AMD 605 document, February 2007.
2. RSW Inline Adaptive System Evaluation Matrix and Testing Procedure (DRAFT), AMD 605 document, April 2007.
3. Specification for Automotive Weld Quality – Resistance Spot Welding of Steel, AWS D8.1M-E1-DS1, An American National Standard, American Welding Society, 2007.
4. Specification for Automotive Weld Quality – Resistance Spot Welding of Aluminum, AWS D8.2M, An American National Standard, American Welding Society, 2006.

11. RECYCLING

A. Recycling Assessments and Planning

Principal Investigator: Edward J. Daniels
Argonne National Laboratory (ANL)
9700 S. Cass Ave., Argonne, IL 60439
(630) 252-5279; fax: (630) 252-1342; e-mail: edaniels@anl.gov

Technology Area Development Manager: Joseph A. Carpenter
(202) 586-1022; fax: (202) 586-1600; e-mail: joseph.carpenter@ee.doe.gov

Expert Technical Monitor: Philip S. Sklad
(865) 574-5069; fax: (865) 576-4963; e-mail: skladps@ornl.gov

Participants:
This project is conducted as part of a Cooperative Research and Development Agreement (CRADA) among ANL, the Vehicle Recycling Partnership (VRP) of the United States Council for Automotive Research (USCAR), and the American Chemistry Council-Plastics Division (ACC-PD, formerly the American Plastics Council (APC)).

CRADA Partner Principal Investigators:
Claudia Duranceau, VRP, Ford Motor Co., (313) 390-0504; e-mail: cdurance@ford.com
Nakia Simon, VRP, Chrysler Corp., (248) 576-1869; e-mail: nls8@daimlerchrysler.com
Candace Wheeler, VRP, General Motors Corp., (586) 986-1674; e-mail: candace.s.wheeler@gm.com
James Kolb, American Chemistry Council-Plastics Division, (248) 244-8920; e-mail: james_kolb@americanchemistry.com.

Contractor: ANL
Contract No.: W-31-109-Eng-38

Objectives

- Eliminate any real or perceived recycling barriers that might preclude the use of advanced automotive materials.
- Enable the optimum recycling of all automotive materials, current and future, thereby obviating the need for legislative recycling mandates.
- Assess the critical needs for cost-effective recycling of automotive materials and components.
- Establish research priorities to enable cost-effective recycling of advanced automotive materials and components.
- Communicate a collaborative industry/government approach to issues related to the recycling of automotive materials.
- Coordinate research with other agencies and stakeholders in the United States, Europe, and Asia.

Approach

- Consult with automotive manufacturers and recycling industries, USCAR and its affiliates, national laboratories, universities, and other relevant organizations to assess critical recycling needs/barriers.

- Develop a recycling research plan that will serve as a "working document" to guide the U.S. Department of Energy (DOE) in establishing priority goals, with an initial emphasis on lightweighting body and chassis materials.
- Establish an outreach/communication function to enable cooperation amongst, and leveraging of resources with, all stakeholders and the international community.
- Assist DOE in establishing advanced recycling research and development (R&D) initiatives and provide technical oversight to ensure that priority objectives/goals are accomplished.

Accomplishments During this Reporting Period (10/1/06-9/30/07)

- Conducted by-monthly progress reviews with CRADA team.
- Identified new lightweighting materials being considered for vehicles of the future.
- Continued gap analysis with CRADA team.
- Prepared and presented several papers outlining the industry/government collaboration at national and international conferences.
- The CRADA team received the Society of Plastics Engineers (SPE), Environmental Division, Global Plastics Environmental Conference (GPEC) "Enabling Technologies in Processes & Procedures" 2007 Award. The award is in recognition of the work of the CRADA team in the development of enabling processes and procedures to facilitate the recovery and recycling of automotive plastics from end-of-life vehicles (ELVs).
- Continued liaison with the Institute of Scrap Recycling Industries (ISRI), the Automotive Recycling Association (ARA) and individual shredders.
- The American Chemistry Council-Plastics Division's Operating Committee visited the Argonne pilot-plant.

Prior Accomplishments

Fiscal Year (FY) 2006

- Conducted quarterly progress reviews with CRADA team.
- Conducted annual project review and gap analysis with CRADA team.
- Developed CRADA Team presentation Brochure (was prepared by Energetics) and One-Pager.
- Launched US ELV CRADA Team Website (http://www.transportation.anl.gov/materials/crada_recycling.html). It includes an overview of the CRADA Team activities, downloadable CRADA Team brochures, a bibliography of recycle literature, presentations, and annual reports of the team.
- Presented papers outlining the industry/government collaboration at international conferences.
- The CRADA team held a media event for America Recycles Day. Press releases and related news stories are accessible through the CRADA team website.
- Continued liaison with the Institute of Scrap Recycling Industries (ISRI) and the Automotive Recycling Association (ARA) and held several meetings with the CRADA partners and representatives of ISRI and ARA.

FY 2005

- Conducted quarterly progress reviews with CRADA team.
- Conducted annual project review and gap analysis with CRADA team.
- Conducted one-day, peer-review progress review. It was attended by experts in the field, in addition to the CRADA partners.
- Conducted one-day Roadmap workshop to update the 2001 Roadmap for Recycling End-of-Life Vehicles (ELVs) of the Future.
- Continued liaison with ISRI and held several meetings with the CRADA partners and representatives of ISRI.

FY 2004

- Conducted quarterly progress reviews with CRADA team.
- Conducted annual project review and gap analysis with CRADA team.
- Held a CRADA announcement event at ANL on December 2, 2004. The event was attended by representatives of the press, industry, and government.
- Established liaison with ISRI and held several meetings with the CRADA partners and representatives of ISRI.

FY 2003

- Developed 5-year project plan.
- Negotiated a CRADA with the VRP, the APC, and ANL as partners. Effort under the CRADA was initiated in August 2003.

Future Direction

- Continue development and management of the R&D plan with the CRADA partners consistent with the recommendations of the updated Roadmap. As appropriate, new recycle R&D needs that are identified will be incorporated into the plan and projects for conducting the requisite R&D will be developed.
- Continue gap analysis with the CRADA partners.
- Conduct scheduled progress reviews.
- Maintain and update the US ELV CRADA team website.
- Continue ongoing efforts toward the milestones and objectives of the CRADA statement-of-work.
- Continue outreach efforts to broaden the basis for cooperation among stakeholders.
- Continue ongoing project efforts to assist DOE in preparation of planning documents, priority recycling R&D needs, proposal reviews, and related tasks.
- Identify research needs for recycling new lightweighting materials.
- Update the ELV Roadmap as necessary.
- Continue to prepare and publish papers.

Summary

The objective of this project is to establish priorities and develop cost-effective recycling technologies and strategies in support of the U.S. Department of Energy (DOE) Vehicle Technologies Program's (VTP's) long-term objectives and goals. The major goals of this research are to: 1) enable the optimum recycling of all automotive materials; 2) ensure that advanced automotive materials that improve the life-cycle energy use of vehicles are not precluded from use as a result of a perception that those materials are not recyclable; and 3) enable market-driven vehicle recycling.

Today, cars that reach the end of their useful service life in the United States are profitably processed for materials and parts recovery by an existing recycling infrastructure. That infrastructure includes automotive dismantlers, automotive remanufacturers and scrap processors (shredders). The dismantlers recover useable parts for repair and reuse. The dismantlers also recover some of the automotive fluids including the refrigerants and the engine oil. The refrigerants can be purified and reused. Facilities for recycling engine oil also exist. The oil can be used as an energy source or it could be refined and used to make new engine oil. Remanufacturers remanufacture a full range of components including starters, alternators, transmissions and engines to replace defective parts. The scrap processors recover ferrous and non-ferrous metals from the remaining auto "hulk."
The recyclability of the plastics and elastomers of the ELVs is limited at present by the lack of 1) commercially-proven technologies to identify and cost-effectively separate materials and

components, and 2) profitable post-use markets. The presence of polychlorinated biphenyls (PCBs) on the plastics severely limits their end use. During the next 20 years, both the number and complexity of ELVs are expected to increase, posing significant challenges to the existing recycling infrastructure. The automobile of the future will use significantly greater amounts of lightweight materials (e.g., ultra-light steels, aluminum [Al], magnesium [Mg], titanium [Ti], plastics, and composites) and more sophisticated/complex components, such as fuel cell stacks, hydrogen storage systems, and electronic controls.

Roadmap Recommendations

A workshop to update the original roadmap, which was published in 2001, was held on September 14, 2005, at ANL. Representatives from DOE, key stakeholders, universities and other experts attended the meeting. The workshop evaluated the original Roadmap and its recommendations. The following were identified as some of the factors that can affect the recyclability of future shredder residue:

- Vehicles containing new materials of construction for lightweighting (composites, lightweight steel, Al alloys, Mg, and Ti);
- Catalysts for better environmental control; and
- Vehicles powered by fuel cells, electric batteries, hydrogen, and hybrids.

The key recommendations from the original roadmap, which was developed with input from key stakeholders to guide DOE's recycle research, were:

- Come together as a unified recycling community to cost-share in the development of required new technology.
- Incorporate reuse, remanufacturing, and recycling into the design phase for vehicles whenever possible.
- Recycle as early in the recycling stream as possible, while relying on the market to optimize the value and amount recycled at each step.
- Maintain a flexible recycling process that can adapt to diverse model lines fabricated with different techniques and materials from various suppliers.
- Develop automated ways to recover bulk materials.
- Emphasize R&D on post-shred material identification, sorting, and product recovery.
- Focus R&D efforts on materials not recycled today by sorters (e.g., post-shred plastics, glass, rubber, fluids, and textiles).
- Develop uses for recovered materials (whether in the same or different applications) and testing specifications.
- Encourage investment in the infrastructure needed to achieve the recyclability goal. Build on the existing infrastructure.
- Develop a means to prevent the entry of PCBs and other hazardous materials into the recycling stream and promote acceptable limits in shredder residues.
- Consider the recycling requirements of new technologies entering fleets as early as possible.

The Five-Year R&D Plan

On the basis of the roadmap and continuing discussions with key stakeholders, a five-year research plan was prepared. The plan includes three focus areas, as discussed below.

Area 1. Baseline Technology Assessment and Infrastructure Analysis

The focus of the work under this activity is to develop the tools and document the information necessary to make effective decisions relative to technology needs to facilitate sustainable future vehicle recycling and to make effective decisions regarding the allocation of R&D resources. (See 11.B)

Area 2. Materials Recovery Technology Development and Demonstration

Research to be conducted in this area will initially focus on addressing technology needs for post-shred materials recovery, including mechanical recycling and conversion to fuels and chemicals. (See 11.E) Projects that enhance pre-shred recovery—including disassembly for materials recovery and direct reuse and remanufacturing of components—will also be considered. In the long term, such components as fuel cells, advanced batteries, and onboard hydrogen reformers are more likely to enter the recycle stream through

pre-shred recovery for remanufacturing, repair, and materials recovery. Research will be undertaken to determine the technology needs to ensure the recyclability of these advanced automotive components.

Area 3. Recovered Materials Performance and Market Evaluation

Understanding and enhancing recovered materials performance is an essential ingredient to a successful recycling program. This is especially true in automotive systems when the materials and components that are recovered have been in use for an average of from 10–15 years. Area 3 includes projects to quantify the relative performance of recovered materials vis-à-vis new or virgin materials; research on compatibilization of recovered polymers to improve performance properties (see 11.D); development of technologies to upgrade the recovered materials, such as separation of fibers from polymeric substrates; and development of applications for other recovered materials, such as rubber and glass.

CRADA Projects

A CRADA among ANL, the VRP, USCAR, and the APC (now the ACC-PD) has been structured to provide a core team of expertise and the resources to enable the optimum recycling of all automotive materials.

The CRADA team's R&D agenda focuses on the following key objectives:

- Develop and demonstrate sustainable technologies and processes for ELV recycling.
- Demonstrate the feasibility of resource recovery from shredder residue, including materials recovery for reuse in automotive and other applications, chemical conversion of residue to fuels and chemicals, and energy recovery.
- Develop viable strategies for the control and minimization or the elimination of substances of concern. (See 11.C)
- Benchmark recycling technology and provide data to stakeholders.
- Stimulate markets for reprocessed materials to support economic collection, processing, and transportation.
- Transfer technology to commercial practice.

This project provides for the overall management of the CRADA team activities and for communication and advocacy with other organizations. The other major projects that have been initiated under the CRADA include the following:

- Baseline Assessment of Recycling Systems and Technology.
- Post-Shred Materials Recovery Technology Development and Demonstration.
- Development of Technology for Removal of PCBs and Other Substances of Concern from Shredder Residue.
- Compatibilization/Compounding Evaluation of Recovered Polymers.

The objectives and progress on these projects are discussed in their respective sections of this report (see 11.B, 11.E, 11.C and 11.D, respectively). Effort under the CRADA was initiated in the fourth quarter of FY 2003.

Outreach Efforts

While the CRADA team provides a core of expertise, cooperation with other organizations is key to achieving the overall program objectives. In the United States, a market-driven recycling infrastructure is in place. The CRADA team is actively pursuing cooperation with the organizations and companies that are a part of that infrastructure. Cooperation with other stakeholders is also essential.

The CRADA team received the SPE, Environmental Division, GPEC Enabling Technologies in Processes & Procedures" 2007 Award. The award is given in recognition of the work of the CRADA team in the development of enabling processes and procedures to facilitate the recovery and recycling of automotive plastics from ELVs.

Many shredders, polymer recyclers, and the ACC-PD's operating committee visited Argonne's automotive recycling pilot-plant and discussed plastics-recycling activities.

A website was launched in March of 2006 to provide for better communication and networking with stakeholders and other research teams: (http://www.transportation.anl.gov/materials/crada

_recycling.html). The website provides an update of the CRADA progress and provides access to relevant information and publications including a bibliography of mechanical, thermo-chemical conversion, and energy-recovery technologies for recycling automotive materials.

The CRADA team held a media event at Argonne for "America Recycles Day." It was attended by a number of media organizations. Articles featuring the work done by the CRADA team were written by the media members who attended. CRADA team members were interviewed by several radio stations after the media event.

Several presentations and publications were made to further communicate with interested parties, including a paper entitled, "Market Driven Technology Development for Sustainable End-of-Life Vehicle Recycling: A Perspective from the United States." This was presented by Edward Daniels at the 6th International Automobile Recycling Congress, Amsterdam, Netherlands, March 15-17, 2006. A joint DOE, USCAR, and APC paper on "Market Driven Recycling in North America" was presented as the keynote paper at the 2004 International Car Recycle Congress in Washington, D.C.

Several meetings with representatives of ISRI and ARA and with shredder operators were held to brief them on the CRADA objectives and projects and to elicit their participation.

To further communicate the U.S. approach to ELV recycling, a one-page CRADA summary and a CRADA brochure have been prepared and it is available at the CRADA website.

As previously mentioned, a review of the projects and ongoing efforts of the CRADA team was held on September 13, 2005, and a workshop was also held on September 14, 2005 to review and update the ELV Roadmap.

Publications

1. *The R&D of the FreedomCAR Materials Program*, Carpenter, J. A., Jr., E. J. Daniels, P. S. Sklad, C. D. Warren and M. T. Smith, Proc. Of the International Auto Body Congress, Novi, MI, September 19, 2006.
2. *Market Driven Technology Development for Sustainable End-of-Life Vehicle Recycling: A Perspective from the United States*, Daniels, E. J., Jody, B. J., Pomykala, J. A. Jr., and Spangenberger, J. S., presented at the 6th International Automobile Recycling Congress, Amsterdam, Netherlands, March 15-17, 2006.
3. *Industry and Government Collaboration to Facilitate Sustainable End-of-Life Vehicle Recycling*, Daniels, E. J., 2005 ASME International Mechanical Engineering Congress & Exposition, BRTD-4: Sustainability Applications in Product Design and Manufacture, Orlando, Florida, November 5-11, 2005.
4. *Market Driven Automotive Recycling in North America*, Duranceau, C., presented at the Institute of Scrap Recycling Industries Shredder Meeting, Dallas, TX (Oct. 30, 2004).
5. *Sustainable End-of-Life Vehicle Recycling: R&D Collaboration between Industry and the U.S. DOE*, Daniels, E. J., Carpenter, J. A. Jr., Duranceau, C., Fisher, M., Wheeler, C., and Winslow, G., JOM, The Mineral, Metals & Materials Society, vol. 56, no 8, pp 28-32 (Aug. 2004).
6. *Market Driven Automotive Recycling in North America*, Duranceau, C., USCAR, Carpenter, J., U.S. DOE, Fisher, M., American Plastics Council, keynote at the 2004 International Car Recycling Workshop, May 19, 2004, Washington D.C.
7. *Automotive Materials Recycling: A Status Report of U.S. DOE and Industry Collaboration*, Daniels, E. J., Ecomaterials and Ecoprocesses, Proc. of the International Symposium on Ecomaterials and Ecoprocesses, August 24-27, 2003, Vancouver, BC, Canada, pp 389-402.
8. *Effects of Transportation on the Ecosystem*, Carpenter, J.A., Jr., Ecomaterials and Ecoprocesses, Proc. of the International Symposium on Ecomaterials and Ecoprocesses, August 24-27, 2003, Vancouver, BC, Canada, pp 13-22.
9. *Automotive Technology: Looking Forward*, Sullivan, R., D. Hamilton and J.A. Carpenter, Jr., Ecomaterials and Ecoprocesses, Proc. of the International Symposium on Ecomaterials and Ecoprocesses, August 24-27, 2003, Vancouver, BC, Canada, pp 49-67.

10. *A Roadmap for Recycling End-of-Life Vehicles of the Future*, prepared by Energetics for the U.S. Department of Energy, Office of Advanced Automotive Technologies (May 2001).

B. Baseline Assessment of Recycling Systems and Technology

Principal Investigator: Edward J. Daniels
Argonne National Laboratory (ANL)
9700 S. Cass Ave., Argonne, IL 60439
(630) 252-5279; fax: (630) 252-1342; e-mail: edaniels@anl.gov

Technology Area Development Manager: Joseph A. Carpenter
(202) 586-1022; fax: (202) 586-1600; e-mail: joseph.carpenter@ee.doe.gov

Expert Technical Monitor: Philip S. Sklad
(865) 574-5069; fax: (865) 576-4963; e-mail: skladps@ornl.gov

Participants
This project is conducted as part of a Cooperative Research and Development Agreement (CRADA) among ANL, the Vehicle Recycling Partnership (VRP) of the United States Council for Automotive Research (USCAR), and the American Chemistry Council-Plastics Division (ACC-PD, formerly the American Plastics Council (APC)).

CRADA Partner Principal Investigators
Claudia Duranceau, VRP, Ford Motor Co., (313) 390-0504, e-mail: cdurance@ford.com
Nakia Simon, VRP, Chrysler Corp., (248) 576-1869; e-mail: nls8@daimlerchrysler.com
Candace Wheeler, VRP, General Motors Corp., (586) 986-1674, e-mail: candace.s.wheeler@gm.com
James Kolb, American Chemistry Council-Plastics Division, (248) 244-8920; e-mail: james_kolb@americanchemistry.com.

Contractor: ANL
Contract No.: W-31-109-Eng-38

Objective

- Establish the baseline or state-of-the-art for automotive materials recovery/recycling technology.

Approach

- Review the state-of-the-art of worldwide automotive-materials recovery/recycling technologies.
- Develop technology profiles of emerging automotive materials recycling technologies.
- Review international, federal, and state regulatory information regarding vehicle recyclability, substances of concern, and recycle laws and mandates.
- Conduct life-cycle studies to quantify the environmental burdens and benefits associated with various end-of-life recycling technologies.
- Conduct reference-case end-of-life recyclability studies.

Accomplishments during this Reporting Period (10/1/06-9/30/07)

- Updated the database of recycle technologies.
- Initiated the life-cycle study of current shredding operations.
- Prepared and published the document reviewing technologies and the state-of-the-art for recycling shredder residue.

Prior Accomplishments

FY 2006

- Completed compilation of recycle bibliography, structured as a pull-down PDF file, posted on US ELV CRADA Team website http://www.es.anl.gov/Energy_Systems/CRADA_Team_Link/Index.html.
- Completed Changing World Technologies (CWT) life-cycle case study.
- Completed life-cycle study of ANL process technology.
- Completed second draft of state-of-the-art assessment in recycling of vehicles and automotive materials.

FY 2005

- Conducted a literature search that identified mechanical, thermo-chemical conversion, and energy-recovery technologies and completed first draft of state-of-the-art assessment.
- Completed Salyp life-cycle case study, initiated CWT life-cycle case study.

FY 2004

- Compiled and structured recycle bibliography.
- Characterized North American recycle infrastructure.
- Conducted a review of U.S. regulatory issues.
- Initiated life-cycle studies of end-of-life recycle technologies (Salyp case study) .
- Completed reference recyclability calculations for reference cases and three lightweight alternatives: lightweight steel, composite materials, and aluminum (Al).

Future Direction

The focus of this task in FY 2008 will be on:

- Updating the database of recycle technologies.
- Update the document reviewing technologies for recycling shredder residue.
- Complete the life-cycle study of current shredding operations.

Summary

The objectives of this project are to benchmark the automotive materials recycling industry and to compile information in an accessible format regarding the status of existing and emerging recycling technology and research.

The focus of the work under this activity is (1) to develop the tools and document the information necessary to make effective decisions relative to technology needs to facilitate sustainable future vehicle recycling and (2) to make effective decisions regarding allocation of R&D resources.

The state-of-the-art of worldwide automotive-materials recovery/recycling technologies and associated resource-recovery infrastructures has been reviewed to identify technology gaps and needs and to identify differences in automotive recycling strategies among North America, Europe, and Asia. Technologies that are included in this review include, but are not limited to, post-shred materials-recovery technologies, pre-shred materials-recovery technologies, materials-identification technologies, automated-dismantling technologies, technologies for the recycling of specific components of vehicles (such as bumpers), and thermochemical-conversion technologies.

Life-cycle analyses of alternative recycle technologies have also been conducted to identify differences between technologies, such as mechanical recycling vis-à-vis thermochemical recycling, relative to energy and environmental benefits.

Regulations at the international, federal, and state levels are examined to identify the impact that proposed and existing regulations may have regarding recycling of automotive materials.

Reference-case recyclability calculations are made to quantify the expected recyclability of alternative vehicle designs.

Infrastructure

The North American recycling infrastructure has been characterized and a representative figure was shown in previous annual reports.

Technology Profiles

The recent literature has been reviewed, and summaries and profiles of available and emerging recycle technologies have been compiled into a draft working document that will be updated annually as new information becomes available.

A bibliography of abstracts of papers that discuss automotive recycling issues has been compiled (Table 1). The bibliography is organized in fifteen sections.

The bibliography was compiled from an extensive literature search, which included reviewing the following sources:

1. Society of Automotive Engineers (International) World Congresses from 1997 to 2007
2. Environmental Sustainability Conference and Exhibition, 2001
3. SPE:
   - ARC Conference from 1998 to 2000
   - GPEC Conference from 2002-2007
4. Other conference proceedings:
   - International Automobile Recycling Congress from 2001 to 2006
   - TMS Fourth International Symposium of Recycling of Metals and Engineered Materials, 2000.
   - Ecomaterials and Ecoprocesses, The Conference of Metallurgists, COM 2003

The bibliography has been posted on the US ELV CRADA Team website: http://www.es.anl.gov/Energy_Systems/CRADA_Team_Link/Index.html

More references will be added to the bibliography as they become available.

Table 1. Citations included in the recycling bibliography.

Bibliography Section	Number of Citations
Recycling infrastructure	20
Design for recycling	5
Legal and regulatory issues	23
Life-cycle analysis	12
Research programs	11
Substances of concern	5
Disassembly technologies and case studies	12
Reuse of automotive parts and subassemblies	1
Remanufacturing	0
Mechanical-separation technology	20
Thermochemical-conversion technology	14
Energy-recovery technology	11
Advanced materials recycle technology	9
Other technology	40
Case studies of materials recycled for auto applications	23
Total citations	206

Recycling Technologies: State-of-the-Art

The final document has been published and has been posted on the US ELV CRADA Team website: http://www.es.anl.gov/Energy_Systems/CRADA_Team_Link/Index.html.

Because post-shred residue contains residue from shredded white goods and other obsolete items in addition to vehicles, these were also discussed in the document.

Regulatory Situation

The European Union has issued End-of-Life Vehicle (ELV) Recycle Directives. The enforcement of these directives is, however, the responsibility of each member state. Although the United States has not developed a federal policy or mandate, regulations at the federal and state level can impact the technology needs for recycling automotive materials. For example, U.S. Environ-

mental Protection Agency (EPA) regulations regarding polychlorinated biphenyl (PCB) limits the concentration of PCBs on recycled materials to below the detectable limit (i.e., 2 ppm). State regulations regarding other substances of concern (SOCs), such as mercury and polybrominated diphenyl ethers (PBDEs), can also impede materials recycling.

Life-Cycle Studies

The objective is to use life-cycle analysis to assess the environmental impacts of various mechanical-separation technologies and alternative end-of-life recycling technologies. This information will then be used to create a flexible, computerized, life-cycle inventory model, which is process-specific and yet can be modified to include additional recycling technologies and various material inputs. Life-cycle involves assessing all of the upstream burdens associated with the production of the materials and energies used in the process, including the transport of all materials to the facility.

PE Europe GmbH, a company that is experienced in conducting life-cycle assessments and in model development using its own GaBi (Ganzheitliche Bilanzerung) software, was contracted to perform these analyses. Three analyses have been completed for: 1) Salyp NV's mechanical-separation process; 2) CWT's thermal-conversion process; and 3) ANL mechanical and froth-flotation process. A fourth, life-cycle study of current shredding operations has been initiated. Data for the study are still being collected with the assistance of ISRI.

PE Europe has developed a flexible end-of-life model which was used to compare the two different approaches to recycling shredder-residue. The model allows the user to run simulations on shredder-residue separation within different boundary conditions. The following boundary conditions can be modified: 1) shredder-residue composition, 2) location of the facility, 3) type and distance of transportation, 4) market values for the separated fractions, 5) new potential applications for separated fractions, and 6) utilization ratio of the facility.

Salyp's separation process combined equipment developed by ANL and several others to create a facility that separates shredder residue into discrete fractions of metals, foam, mixed plastics, and fiber-rich and fines streams. On the other hand, the CWT process converts organic materials into hydrocarbon fuels and other potential products.

Data were collected for each of the three processes, including all energy, water, and material inputs, plus data on emissions to air and water, wastes, and products produced. The three sets of data were entered into the GaBi software to create a flexible model of the process.

In the case of the Salyp separation process, three different scenarios for handling the various materials recovered from shredder residue were determined. These scenarios included using specific material fractions as fuel for cement kilns (energy recovery), as well as using mixed plastics to replace such products as wood pallets and polypropylene (PP) pellets (material substitution). The various scenarios were assessed by using a variety of impact categories, including primary energy demand and CO_2 emissions. In the case of primary energy demand, all scenarios showed a net credit in total energy use. For the three scenarios studied, substituting recovered polypropylene/ polyethylene (PP/PE) in a new PP application had the greatest benefit. However, if the mixed plastic stream was used to replace wood (e.g., decking material, park benches, wood pallets, etc.), the benefits to primary energy demand were less than if the recovered materials were simply used for energy recovery. In terms of CO_2 emissions, the PP application again showed the greatest benefit. Substituting PP for wood applications was next with a lower benefit, while the energy-recovery scenario showed an increase in CO_2 emissions.

In the case of the CWT process, two basic scenarios were assessed. They involved using the light hydrocarbon oil generated by the process for fuel oil used in power plants to generate electricity and substituting light hydrocarbon oil for diesel oil (both with and without an added hot-oil processing step). While the oil product generated is more refined than an actual crude oil, it would require additional steps before it could be considered a true diesel oil. Therefore, reality is probably located somewhere between scenarios 1 and 2. In

this study, the impact on primary energy demand resulted in a benefit in all cases. The benefits in the diesel substitution case were slightly greater than in the fuel-oil case. In the case of CO_2 emissions, all scenarios again showed an overall benefit. However, the diesel substitution case had a greater benefit than the fuel-oil substitution case.

Life-cycle analysis of the ANL process considered both the mechanical separation of the shredder residue to produce a polymer concentrate and recover residual metals, followed by froth-flotation to separate plastics from the polymer concentrate for recycling as plastics (material substitution). The analysis concluded both the mechanical and the froth-flotation processes resulted in environmental benefits, Figure 1. The environmental benefits of the ANL process were also compared with those of Salyp (Table 2) and CWT processes (Table 3). The environmental benefits are higher for the ANL process compared to the Salyp process except for the acidification potential and higher for the ANL process compared to the CWT process except for the impact category EP and NO_x emissions. Energy-wise the ANL process was the most advantageous. Interestingly, the best results can be obtained by combining both (ANL and CWT) processes, where organic fractions separated by ANL which do not meet the requirements for material substitution (such as mixed plastics and rubber by-products) are processed by CWT for fuel production.

Recyclability Studies

Recyclability studies were conducted to examine the effect of using automotive lightweighting material on recyclability. A Toyota Prius hybrid was selected as a reference case. This vehicle is a second-generation hybrid with a gas/electric powertrain. Evaluating the recyclability of this vehicle and its new technology will be a step in identifying changes that will impact end-of-life recycling of vehicles of the future.

In collaboration with Johnson Controls, Inc. (JCI), the VRP dismantled the vehicle according to VRP procedures to single-material components and entered data for each part into a database. A material list that identified the breakdown of materials into separate classifications (such as ferrous and nonferrous metals, as well as composite materials and plastics) was prepared.

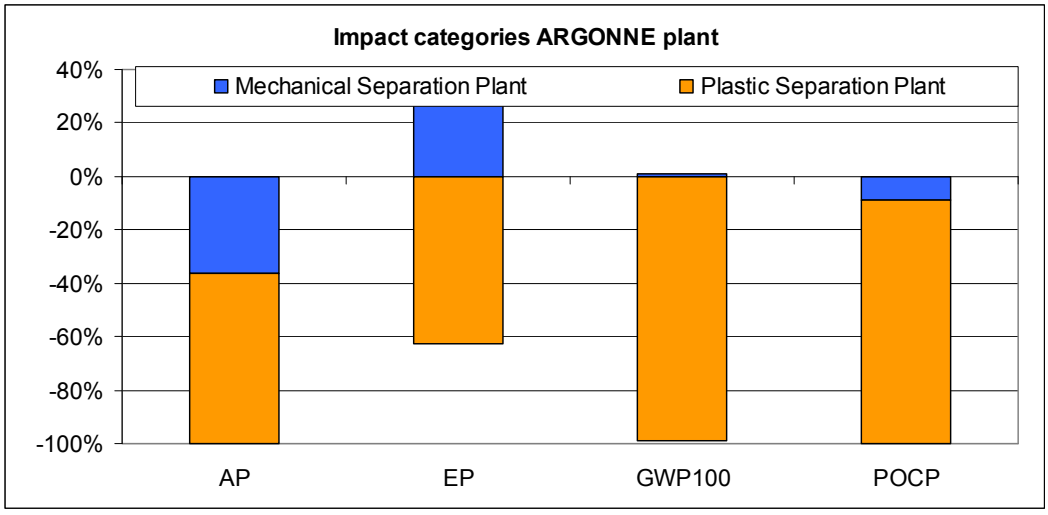

Figure 1. Impact categories of the ANL plant. (AP is acidification potential, EP is eutrophication (depletion of oxygen in water) potential, GWP is global-warning potential and POCP is photochemical ozone creation potential). Y axis indicates increase (+) or decrease (-) in the impact of the different categories.

Table 2. Comparison of the ANL and Salyp processes-Relative Environmental Impact. (A negative value indicates a reduction in the pollution category [an environmental benefit] while a positive value indicates an increase in the pollution category).

	ANL process (mechanical and Froth Flotation)	**Salyp process**
AP [lb SO_2-Equivalent.]	-0.0060	-0.0165
EP [lb Phosphate-Equivalent.]	-0.00011	0.00148
GWP100 [lb CO_2-Equivalent.]	-1.354	0.861
POCP [lb Ethene-Equivalent.]	-0.0026	0.0126

Table 3. Comparison of the ANL Froth Flotation and CWT processes-Relative Environmental Impact. Both processes require mechanical separation of the inorganic fraction. (A negative value indicates a reduction in the pollution category (an environmental benefit) while a positive value indicates an increase in the pollution category).

	ANL process (Froth Flotation*)	**CWT process**
AP [lb SO_2-Equiv.]	-0.01103	-0.00662
EP [lb Phosphate-Equiv.]	-0.00055	-0.00079
GWP100 [lb CO_2-Equiv.]	-4.167	-0.309
POCP [lb Ethene-Equiv.]	-0.0088	-0.0044

*Comparison is done here only with the froth- flotation process because both ANL's froth flotation process and CWT process require mechanical separation of the inorganic materials.

The materials breakdown is summarized in Table 4. By comparison, the materials composition of a production Ford Taurus is summarized in Table 5. Three different recyclability calculations were made (Table 6). The Federal Trade Commission (FTC) recyclability number is the percentage by weight of the material that is currently being recycled, and it includes metals, fluids less fuel, and batteries. The European guidelines include FTC materials plus fuel at 90% of a full tank, plastics that could be recycled, and up to 10% by weight energy recovery.

Table 4. 2004 Toyota Prius materials breakdown.

Materials	Mass (lb)	Percent
Ferrous metals	1713	60.6
Nonferrous metals	507	17.9
Plastics	341	12.1
Elastomers	87	3.1
Inorganic material	77	2.7
Other	62	2.2
Organic materials	42	1.5
Vehicle mass (less fluids)	2829	100.0

Table 5. 2004 Ford Taurus materials breakdown.

Materials	Mass (lb)	Percent
Ferrous metals	2223	70.4
Plastics	340	10.8
Nonferrous metals	312	9.9
Elastomers	152	4.8
Inorganic material	90	2.9
Other	38	1.2
Organic materials	4	0.1
Vehicle mass (less fluids)	3159	100.0

Note that Europe requires 95% recyclability for new vehicles. The feasibility-to-recycle number includes the FTC materials plus plastics that can be recycled. Changes to the current infrastructure would be required to increase recycling beyond the current FTC percentage.

To establish an indication of the impact of lightweight materials on the reference-case recyclability calculations, the 2004 Toyota Prius is compared with a proposed Al-intensive lightweight vehicle and a proposed composite lightweight

vehicle, both of which are also based on the 2004 Prius. The production 2004 Toyota Prius hybrid vehicle body was steel with an Al hood and decklid. The suspension was of steel, except for an Al steering knuckle on the front suspension. This vehicle was used as the base for this study.

Table 6. Reference-case recyclability: 2004 Toyota Prius.

Calculation Method	Recyclability (%)
Federal Trade Commission	80.86
European	97.61
Feasibility of recycling	85.58
Ref. 2000 Ford Taurus	80.50

The Al alternative is for a 2004 Toyota Prius with an Al body and a magnesium (Mg) engine cradle and a rear axle substituted for the production parts. In addition, seat frames, body brackets, and the instrument panel cross-car beam have been changed from steel to Al. As a result, the weight has been reduced by approximately 630 lb or 21%. Because the weight reduction is entirely in the currently- recycled portion of the vehicle, the recyclability is adversely affected and is reduced from 80.86% to 76.10%. No changes were made to the currently non-recycled portion of the vehicle. Al replaced steel at 50% by weight of the original steel.

The composite alternative is for a 2004 Toyota Prius that consists of: 1) a carbon-fiber body with 40% carbon fiber and 60% thermoset polyurethane/urea resin by volume, 49.72% carbon, and 50.28% thermoset polyurethane/urea resin by weight, and 2) a Mg engine cradle and rear axle substituted for the production parts. In addition, seat frames, body brackets, and the instrument-panel cross-car beam have been changed from steel to composite. As a result, the weight has been reduced by approximately 711 lb, or 24%. Because the weight reduction is entirely in the currently-recycled portion of the vehicle, the recyclability is adversely affected and is reduced from 80.86% to 57.20% if none of the composite is recycled or 74% if all of the composite material is recycled. No changes were made to the currently non-recycled portion of the vehicle. The composite material replaced steel at 40 wt% of the original steel.

There are reductions in all three recyclability calculations for lightweighted vehicles, even though the rest of the vehicle is not changed (Table 7). Where the Al and composite material is being recycled, the same amount of material would be disposed of in landfills in each of the three scenarios. The only difference is that the recycled portion of the lightweighted vehicles would be lighter. Although the recyclability would be less, there would be no difference in the amount of material disposed of in landfills, and the lighter vehicles would use less fuel during their life. As can be seen, lightweighting presents challenges in the European market. Note that these calculations do not take into account the downsizing of related components that would accompany any lightweight vehicle, such as powertrains, brakes, and tires. Because the downsized components are high in metallic content, downsizing will further reduce recyclability and make it difficult to meet the European 95% requirement.

In conjunction with this study, additional evaluations are planned by using these data as a starting point for assessing the recyclability of cars of the future. The impact of vehicle lightweighting and material selection on recyclability will be evaluated. In addition, the impact of powertrain changes in future vehicles (including hybrid and fuel-cell alternatives) on recyclability will be determined in comparison to powertrains in current vehicles. An assessment of various alternatives on recycling and the effect on the current recycling infrastructure will be produced. No downsizing of other components was included in this study. Future studies will reflect the downsizing of powertrains, brakes, tires, and other components in recyclability calculations. Items requiring further study resulting from these assessments will support future projects to determine the feasibility of various alternative vehicle configurations and choices of materials.

These results demonstrate the need for technology to recycle new automotive material if recycling mandates are to be met and to ensure that lightweighting materials are not excluded because of the inability to recycle them.

A seminar to address recyclability and recycled content in view of changing automotive materials has been planned.

Table 7. 2004 Toyota Prius recyclability, reference case vs. Al and composite body materials.

Calculation Method	As Produced (%)	Al Body (%)	Composite Body (%)
FTC	80.9	76.1	74.0[a]
European	97.6	96.0	94.5[a]
Recycling feasibility	88.3	85.6	83.9[a]

[a]If the composite material were not recycled, then the numbers would be FTC, 57.2%; European, 78.2%; and feasibility of recycling, 67.1%. Recycling of the composite material would require significant changes in the current recycling infrastructure. In addition, a market for the recycled carbon fibers would need to be developed. Current technology for recycling carbon fibers results in a 20% loss in fiber properties and would limit their reuse to short fiber applications.

Publications

1. *A Life Cycle Look at Making Oil From End-of-Life Vehicles.,* Wheeler, C.S., Simon, N.L., Binder, M., Winslow, G. R., Duranceau, C.M., SAE 2006 World Congress, Detroit, Michigan, 2006. SAE-2006-01-0374.
2. *Modular Life Cycle Model — Basis for Analyzing the Environmental Performance of Different Vehicle End-of-Life Options*, Binder, M.; Simon, N. L.; Duranceau, C. M.; Wheeler, C. S.; Winslow, G. R., Proc. of the 5th International Automobile Recycling Congress, Amsterdam (Mar. 9-11, 2005).
3. Modular Life Cycle Model of Vehicle End-of-Life Phase — Basis for Analysis of Environmental Performance, Wheeler, C. S.; Simon, N. L.; Duranceau, C. M.; Winslow, G. R.; Binder, M., SAE Paper 2005-01-0847.
4. *United States National Life Cycle Inventory Database Project, A Status Report,* Sullivan, J. L.; Wheeler, C. S.; and Simon, N. L., SAE Paper 2005-01-0852.

C. Development of Technology for Removal of PCBs and Other Substances of Concern (SOCs) from Shredder Residue

Principal Investigator: Bassam J. Jody
Argonne National Laboratory (ANL)
9700 S. Cass Ave., Argonne, IL 60439
(630) 252-5279; fax: (630) 252-1342; e-mail: bjody@anl.gov

Field Project Manager: Edward J. Daniels
ANL
9700 S. Cass Ave., Argonne, IL 60439
(630) 252-4206; fax: (630) 252-1342; e-mail: edaniels@anl.gov

Technology Area Development Manager: Joseph A. Carpenter
(202) 586-1022; fax: (202) 586-1600; e-mail: joseph.carpenter@ee.doe.gov

Expert Technical Monitor: Philip S. Sklad
(865) 574-5069; fax: (865) 576-4963; e-mail: skladps@ornl.gov

Participants:
This project is conducted as part of a Cooperative Research and Development Agreement (CRADA) among ANL, the Vehicle Recycling Partnership (VRP) of the United States Council for Automotive Research (USCAR), and the American Chemistry Council-Plastics Division (ACC-PD, formerly the American Plastics Council (APC)).

CRADA Partner Principal Investigators:
Claudia Duranceau, VRP, Ford Motor Co., (313) 390-0504; e-mail: cdurance@ford.com
Nakia Simon, VRP, Chrysler Corp., (248) 576-1869; e-mail: nls8@chrysler.com
Candace Wheeler, VRP, General Motors Corp., (586) 986-1674; e-mail: candace.s.wheeeler@gm.com
James Kolb, American Chemistry Council-Plastics Division, (248) 244-8920; e-mail: james_kolb@americanchemistry.com.
Steve Niemic, The Polyurethane Recycle and Recovery Council (PURCC), (734) 479-4927; email: sfniemiec@wowway.com

---

Contractor: ANL
Contract No.: W-31-109-Eng-38

Objective

- Develop viable strategies and technology for the control and minimization or elimination of polychlorinated biphenyls (PCBs) and other substances of concern (SOCs) from recycled automotive materials.

Approach

- Identify efficient and environmentally-acceptable process solutions for removal of contaminants, including PCBs, from materials recovered from shredder residue.
- Define variances in analytical procedures/test results for PCB analysis.

Accomplishments during this Reporting Period (10/1/06 - 9/30/07)

- Additional bench-scale testing of ANL's two-stage cleaning process has been conducted and has consistently produced plastics from the polypropylene/polyethylene (PP/PE) product with <2 parts per million (ppm) PCBs.

- Tested new methods to clean the plastics and remove the PCBs including:

  -- Conducted preliminary testing of a proprietary process developed by an independent organization

  -- A catalytic process tested at ANL

  -- Cleaning using a bio-degradable solvent

- Developed a design for an apparatus to test ANL's two-stage process at a larger scale (15-25 lb/hr). Quotes for system components have been obtained.

- Hosted and participated in forums and seminars on SOCs including perfluorooctanoic acid (PFOA)/ perfluorooctanesulfonates (PFOS), and brominated fire retardants, emerging lead- and mercury-free technologies.

Prior Accomplishments

Fiscal year (FY) 2006

- ANL developed a two-stage cleaning process which in bench-scale tests has consistently produced plastics from the PP/PE product with <2 ppm PCBs.
- Completed tests in commercial solvent washing equipment using proprietary solvent-based solutions and CO_2
- Cooperated with the Bromine Science and Environmental Forum (BSEF) in preparing the BSEF brochure entitled "Deca-BDE Flame Retardant"

FY 2005

- Completed the study to explain discrepancies in PCBs analytical results
- Initiated testing of commercial solvent washing processes for cleaning plastics
- Conducted a study to understand the interactions between PCBs and plastics
- Identified and initiated testing of alternative methods for PCB removal

FY 2004

- Completed the solvent/detergent screening study for removing PCBs and heavy metals from plastics
- Completed aqueous cleaning tests in commercially-available equipment
- Initiated a study to explain discrepancies in PCBs analytical results

Future Direction

The FY 2008 plan includes:

- Test ANL's two-stage process at a larger scale (15-25 pound test) for the cleaning of the polyolefin concentrate
- Develop a conceptual design and perform cost analysis of the ANL process
- If successful, incorporate the process into the overall process design for recovering materials from shredder residue
- Conduct testing at ECO2 using their proprietary process
- Test a proprietary process developed by an independent organization
- Test vacuum de-volatilization in a screw to remove PCBs

ANL's two-stage process has successfully produced recovered plastics, at least PP/PE materials, with less than 2 ppm PCBs in multiple tests. However, this has been shown only in small-scale experiments. In FY 2008, larger-scale experiments will be conducted to investigate the scalability of the process including required residence time and operating temperatures.

Summary

The objective of this project is to develop techniques and/or technology to identify and/or cost-effectively remove PCBs and other SOCs from recycled automotive materials.

SOCs can impact the recyclability of automotive materials in a number of ways. Certainly, their presence in either recycled materials and/or materials source streams impacts the overall costs of recovering recyclable materials. In some cases, their presence at ppm, such as in the case of PCBs, can prevent the reuse of the recovered materials.

The strategy that is required for control of the SOCs may vary globally. For example, requirements are different in Europe, North America, and Asia for various SOCs. Strategies for controlling SOCs can also depend on the technology used for recycling the automotive material and the materials end use.

The presence of SOCs in vehicles and/or in other durable goods that are presently recycled with end-of-life vehicles (ELVs) is likely to continue to impact the materials recycle stream for the foreseeable future. Consequently, the control of certain SOCs will require technology that will effectively remove the SOCs from recovered materials consistent with current regulatory requirements and consistent with the market requirement for the recovered material.

Other materials that have been in automobiles could also become SOCs in the near future. Examples include some of the brominated biphenyls.

The focus of the work in this project is on the development of technology for the removal of PCBs from potentially recyclable materials recovered from shredder residue. PCBs, at ppm levels, are routinely found in shredder residue. The source of the PCBs is not completely understood, but historically it has been associated with liquid PCB-containing capacitors, ballasts and transformers that inadvertently escape the inspection and control process at the shredders. Unless PCBs are removed from the recovered materials, with the exception of metals, introducing the recovered materials into commerce will not be possible.

Development and Testing of a Two-Stage Process at ANL

The work done so far on washing of polymers recovered from shredder residue suggests that different washing methods and solutions appear to reduce the PCBs concentration down to about 5-10 ppm in a reasonably short time. Further reduction in the concentration of PCBs requires more extensive and prolonged washing in fresh solution. The prolonged washing, particularly in organic solvents, is further complicated by the absorption of the solvent by the plastics which alters the properties and the value of the plastics.

This behavior of PCBs suggests that the PCBs on the plastics are by two different mechanisms. First, some are in the oils and dirt that are on the plastics. Second, some of the PCBs are adsorbed on the plastics and they do not desorb easily during washing. We tested this hypothesis in the lab. We conducted washing tests using several washing solutions and solvents including a non-flammable solvent to wash the plastics under conditions that minimized the absorption of the solvent by the plastics. This reduced the concentrations of PCBs from about 30 ppm to about 5-10 ppm under a range of operating conditions. The washed plastics were then processed in an environment that induces desorption (high temperature and/or reduced pressure). The PCBs concentration was consistently reduced from 5-10 ppm to below 2 ppm. Tests were also conducted where unwashed samples were exposed to the same environment that induces desorption. The PCBs concentration could not be reduced below 2 ppm under the same operating conditions.

A two-stage process, based on this concept, has been developed and tested at the bench scale at ANL It has repeatedly reduced the PCBs concentration in PP/PE samples to less than 2 ppm. For example, at conditions that do not cause the plastics to oxidize, we were able to reduce the PCBs concentration on the recovered polyolefins from about 32 ppm to as low as 0.088 ppm. We developed a preliminary design for an apparatus to test this process at a larger scale (15-25 lb/hr).

Commercially-available equipment that could be adopted with modification to this process has been identified. Quotes for some of the system components have been obtained.

Testing of a New Proprietary Process

An independent organization tested a proprietary process that they developed for cleaning the plastics. Initial tests showed reduction in PCBs on polyolefins from about 22 ppm to 3 ppm. More tests are planned.

We also conducted preliminary tests on a catalytic process to determine if the PCBs can be selectively degraded using ultraviolet (UV) radiation. The initial results were not encouraging. We also conducted tests using a biodegradable solvent. It was successful in reducing the concentration to about 5-10 ppm, but further reduction to below 2 ppm did not appear likely.

The VRP awarded a contract to ECO_2 to conduct tests using their proprietary process.

The criteria for selection of a cleaning method must include: 1) impact of the cleaning process on the properties and marketability of the polymers, 2) nature and cost of disposal of the waste generated by the process, and 3) overall cost of the cleaning process.

Evaluation and Testing of Solvent-Based Washing Systems

Three companies with equipment and/or proprietary washing solvents and solutions that could potentially be used for non-aqueous removal of PCBs from plastics were identified by Troy Polymers, Inc. (TPI):

- Environmental Technology Unlimited (Wilmington, North Carolina);
- Cool Clean Technologies, Inc. (Burnsville, Minnesota); and
- itec Environmental Group, Inc. (Oakdale, California).

Each company was supplied with a sample of plastics with the determined concentration of PCBs of 11 ppm. Samples were washed at the three companies, and the washed samples were evaluated for PCB levels.

Environmental Technology Unlimited performed six treatments of shredder residue plastics, and five out of the six washed samples reduced the PCBs concentration to below 2 ppm. Unfortunately, the company does not have equipment to conduct large-scale testing of the process using plastics. Cool Clean Technologies technology used CO_2 only. The washing failed to remove the PCBs. itec Environmental Group (name changed to ECO_2) reduced PCB levels in the plastics from 11 ppm to 2.8 ppm via solvent washing; no CO_2 treatment, which normally follows the basic process, was used. Further testing was conducted by itec. The plastics were washed using itec's proprietary solvent and then with liquid CO_2. Two samples received by ANL were analyzed and both showed residual PCBs concentration on the order of 5 ppm. Another series of trials was conducted at different process conditions. The residual PCBs were still higher than 2 ppm.

Evaluation and Testing of Commercially-Available, Aqueous-Based Washing Systems

Before testing the solvent-based systems, large-scale cleaning/washing tests were conducted using plastics from shredder residue using aqueous solutions and a surfactant. The objective was to identify the limitations of the various types of existing washing equipment. Testing was done using an ALMCO rotary-drum washer equipped with a dryer and SeKoN centrifuge equipment. The tests were carried out on about 100 lb of plastic chips each. The particles were between 0.2 and 0.5 in. in size. Under a CRADA contract, GraPar Corporation built, for Troy Polymers, Inc. (TPI), and tested a specially designed machine that has a design capacity of about 300 lb/hour of plastics. TPI conducted further testing on this machine in its facilities.

In each of these tests, the washed material was "visually" clean. However, PCBs analyses were highly variable and indicated that, in some cases, the PCBs concentration had increased after washing. As a result, it was determined that the PCBs analysis procedures should be reexamined, as is discussed in the next section.

The results suggest that existing aqueous-based equipment, as is, is not likely to reduce the concentration of PCBs to acceptable levels.

Evaluation of the Variability of PCB Sampling and Analytical Procedures

Experiments were performed to explain the variability in the results, and to develop a consistent procedure for the determination of the concentration of PCBs.

The variability may be due to a number of factors, including sample size, plastics particle size, PCBs extraction procedure, analytical procedures, and/or interference from other compounds. A one-day seminar was held and attended by analytical experts from the United States and overseas to develop recommendations for improved sampling and analysis techniques specific to plastics chips.

To investigate the possible interference of phthalates in the PCBs analysis, a sample of plastics chips derived from shredder residue was thoroughly mixed and then divided into four parts. The first part was analyzed by using gas chromatography and an electron-capture detector (GC-ECD) and by using gas chromatography/mass spectroscopy (GC-MS). The other three parts were spiked with different quantities of phthalates, as shown in Table 1, and the spiked samples were analyzed by using the same two methods. The results show no interference of the phthalates in the PCBs analysis. Interestingly, the GC/MS results were always higher than the GC-ECD results.

Table 1. Effect of phthalates on PCBs analysis.

Weight-Percent of Phthalates added	PCBs Concentration (ppm) by GC/ECD	PCBs Concentration (ppm) by GC/MS
0	4.6+/-0.3	7.9+/-1.0
0.5	4.7+/-0.3	7.4+/-0.2
1.0	5.1+/-0.6	7.0+/-0.4
2.5	4.8+/-0.3	7.4+/-0.3

To investigate the effects of plastics particle size on extraction efficiency of PCBs, a series of laboratory experiments were conducted at TPI on 300-g samples of plastics with two different particle sizes (one made of chips about 0.2 in. in size and the other was granulated to about 0.04 to 0.08 in. in size). Typically in PCBs analyses, extractions are done on a few grams of material, even though the dirt, oil, and the PCBs are not evenly distributed on the shredder residue plastics.

Samples of the plastics before and after washing were analyzed directly by three different laboratories by using standard PCBs analytical procedures. Extracts from nine sonications of 300-g samples were also analyzed for PCBs by three laboratories. The results show that:

1. The results from the three labs are fairly consistent for each set of samples.
2. Direct analysis of the samples from the three labs showed that the concentration of PCBs in the granulated plastics was about 5 ppm and, for the un-granulated, it was 10 ppm. Obviously, the granulated samples have larger surface area per unit mass than the other samples. Therefore, more efficient extraction of PCBs from the plastics would be expected in the case of the granulated chips. Because this was not the case, the results indicate that the particle size does not affect the PCB results. After extraction, the samples all had less than 2 ppm of PCBs, except for one sample that showed 2.8 ppm.
3. Calculation of the concentration of PCBs in the original samples based on the determined PCBs in the hexane extracts (prepared via nine sonications of 300-g samples) showed that the concentrations of PCBs in the granulated samples were comparable with those of the un-granulated samples.
4. These results further indicate that the PCBs are predominantly on the surface and not absorbed in the plastics, otherwise the granulated samples would have shown higher concentrations.

In addition, two of the laboratories identified Aroclor 1242 as the only PCB present, while the third laboratory identified Aroclors 1232 and 1254 as the only two present. TPI also conducted an analysis of various plastics samples by using GC-ECD and GC-MS methods. The results are compared in Table 2. Results from the two methods are in reasonable

agreement, even though the GC-MS method showed higher values.

Evaluation of Soxhlet Method for PCBs Extraction

Successful commercialization of technology for recovering polymers from shredder residue depends on a reliable and inexpensive technique to analyze samples for PCBs in the field. The U.S. EPA and European protocols for PCBs analysis were reviewed and experiments were conducted to understand the requirements for on-site analysis. A Soxhlet-based method appears to be appropriate for testing because of its simplicity and because it is among the methods specified in both the U.S. EPA protocols and in the European protocols (Table 3). Limited experiments to define the operating conditions for the Soxhlet method were conducted. The results are discussed below.

Selection of a Solvent

Two solvents were tested: hexane and toluene. Three 120-g samples were extracted with hexane for 8 hours, and another three 120-g samples were extracted with hexane for 24 hours. Similarly, three 120-g samples were extracted with toluene for 8 hours, and another three 120-g samples were extracted with toluene for 24 hours. All extractions were carried out while maintaining the siphoning time at 8–10-minute intervals. This procedure resulted in 24 samples of extracts and 12 samples of extracted plastics that were analyzed. The results indicated that hexane is a better solvent than toluene.

Table 2. Comparison of PCBs analysis using GC-ECD and GC-MS methods (extraction was carried out using hexane at 2,000 pounds per square inch absolute (PSIA) and 100°C).

Sample Type	PCB Concentration, Using GC-ECD (ppm)	PCB Concentration, Using GC-MS (ppm)
Ungranulated Chips	7.55	9.67
Ungranulated Chips	3.70	5.07
Ungranulated Chips	1.50	3.3
Ungranulated Chips	1.35	2.66
Granulated Chips	7.56	9.37
Granulated Chips	0.93	1.82
Granulated Chips	0.82	2.11
Hexane Solution	9.93	9.50
Hexane Solution	8.3	11.13
Hexane Solution	1.41	1.72
Hexane Solution	0.78	0.92
Hexane Solution	0.53	0.65

Table 3. Protocols for PCBs analysis.

Parameter	European Protocols	U.S. EPA's Protocols	Recommended Protocols
Particle size (mm)	0.5	Not specified	1
Sample size for extraction (g)	3	30	30
Extraction equipment	Soxhlet	Sonication Soxhlet Pressurized fluid	Soxhlet
Extraction time	Not specified	Not specified	>/= 4 h Siphoning cycles at 8–10-min intervals
Solvent	Toluene	Hexane 50/50 Hexane/acetone 50/50 Methylene chloride/acetone	Hexane
Analytical method	MS	GC/ECD MS	MS
Quantification method	6 congeners multiplied by 5	Aroclors	Aroclors

Determination of Extraction Time

Three additional 120-g samples were extracted with hexane for 4 hours each. This procedure resulted in six samples of extracts and three samples of extracted plastics that were analyzed. The results indicate that a Soxhlet extraction time of 4 hours is adequate because it reduced the PCBs concentration in the extracted plastics to below the detectable limits in two of the three samples and reduced it in the third to 1 ppm, even though these samples apparently had more PCBs initially, as evidenced by the higher level of PCBs in the solvent.

Determination of Adequate Sample Size

In addition to the six 120-gram samples extracted for 24 hours discussed above, six additional 60-gram samples and six additional 30-g samples were processed and sampled in the same manner as before (24-hour extraction time and same siphoning intervals) by using hexane. The results indicate that a sample size of 30 g appears to be adequate.

Comparison of the U.S. EPA and the European Quantification Methods

Four of the extracts from the 120-g samples that were extracted with hexane for 24 hours and two of the 120-g samples that were extracted with hexane for 8 hours were also quantified by using the European method. The results were essentially identical within analytical errors (Table 4). These results lead to the following conclusions:

1. A conventional Soxhlet extractor using hexane is effective for PCBs extraction from plastics.
2. A total extraction time of 4 hours with siphoning intervals of 8–10 min is adequate for complete extraction of the PCBs.
3. The EPA and the European quantification methodologies yield close results.

Table 4. Comparison of the U.S. EPA and the European quantification methods.

Extraction Time (h)	PCBs According to the EPA Method (ppm)	PCBs According to the European Method (ppm)
24	10.8	9.8
24	9.8	10.9
24	8.0	10.7
24	11.2	11.5
8	11.7	12.3
8	10.8	10.8

Other Accomplishments

Because of potential concern over other SOCs, the VRP hosted and participated in forums and seminars on several related topics including PFOA/PFOS, brominated fire retardants and emerging lead- and mercury-free technologies.

Publications

1. *Overview of Washing Systems for Commercial Cleaning of Plastics Separated from Automotive Shredder Residue,* Sendijarevic, I.; Sendijarevic, V.; Winslow, G.R.; Duranceau, C.M.; Simon, N.L.; Niemiec, S. F.; and Wheeler, C.S., SAE Paper No. 2005-01-0851.
2. *Screening Study to Evaluate Shredder Residue Materials*, Sendijarevec, V.; Simon, N.; Duranceau, C.; Winslow, G.; Williams, R.; Wheeler, C.; Niemiec, S.; and Schomer, D., SAE Paper No. 2004-01-0468.

D. Compatibilization/Compounding Evaluation of Recovered Polymers

Principal Investigator: Bassam J. Jody
Argonne National Laboratory (ANL)
9700 S. Cass Avenue, Argonne, IL 60439
(630) 252-5279; fax: (630) 252-1342; e-mail: bjody@anl.gov

Field Project Manager: Edward J. Daniels
ANL
9700 S. Cass Avenue, Argonne, IL 60439
(630) 252-4206; fax: (630) 252-1342; e-mail: edaniels@anl.gov

Technology Area Development Manager: Joseph A. Carpenter
(202) 586-1022; fax: (202) 586-1600; e-mail: joseph.carpenter@ee.doe.gov

Expert Technical Monitor: Philip S. Sklad
(865) 574-5069; fax: (865) 576-4963; e-mail: skladps@ornl.gov

Participants:
This project is conducted as part of a Cooperative Research and Development Agreement (CRADA) among ANL, the Vehicle Recycling Partnership (VRP) of the United States Council for Automotive Research (USCAR), and the American Chemistry Council-Plastics Division (ACC-PD, formerly the American Plastics Council (APC)).

CRADA Partner Principal Investigators:
Claudia Duranceau, VRP, Ford Motor Co., (313) 390-0504; e-mail: cdurance@ford.com
Nakia Simon, VRP, Chrysler Corp., (248) 576-1869; e-mail: nls8@chrysler.com
Candace Wheeler, VRP, General Motors Corp., (586) 986-1674; e-mail: candace.s.wheeler@gm.com
James Kolb, American Chemistry Council-Plastics Division, (248) 244-8920; e-mail: james_kolb@americanchemistry.com.

Contractor: ANL
Contract No.: W-31-109-Eng-38

Objectives

- Evaluate the market opportunity for polymers recovered from shredder residue.
- Identify limitations associated with the reuse of the materials as-recovered and determine the need for post-processing technology to upgrade the recovered materials to meet the requirements of the market.

Approach

- Specify standard protocols for material testing, content characterization, and performance properties.
- Determine properties of recovered polymers.
- Conduct blending and pelletizing trials of the recovered polymers.
- Conduct mold trials using recovered polymers.

Accomplishments During This Reporting Period (10/1/06-9/30/07)

- Determined the physical properties of the MBA recovered fractions.

- Provided samples and held discussions with three companies to determine value of recovered polymers as a function of composition of the recovered material.

Prior Accomplishments

Fiscal year (FY) 2006

- Determined the physical properties of the 70% filled acrylonitrile/butadiene/styrene (ABS) fraction.
- Determined the physical properties of two blends of the 70% filled ABS fraction with virgin ABS (10% recovered/90% virgin and 25% recovered/75% virgin).

FY 2005

- Midland Compounding developed a protocol for evaluating the physical properties of recovered plastics.
- Compiled a physical properties database for virgin plastics.
- Determined physical properties of the polyethylene/polypropylene (PP/PE) product recovered from the ANL froth-flotation process and from the PP/PE fraction recovered by the Salyp process.
- Pelletized 1000 pounds of a blend of the ANL-recovered PP/PE product.
- Conducted mold trials of the recovered PP/PE product.

Future Direction

FY 2008 activities will focus on:

- Determine physical properties of upgraded ABS, polystyrene (PS) and polycarbonate(PC)-ABS/PC alloy.
- Pelletize a blend of recovered filled ABS with virgin ABS and compare the properties of the blend with the properties of the virgin material.

Summary

The objectives of this project are (1) to characterize the properties of potentially-recyclable automotive materials and (2) to confirm the technical and economic feasibilities of using those materials in value-added applications.

The project initially focused on establishing the properties of polymeric materials that are recovered as part of the Post-Shred Materials Recovery Technology Development project (see 11.E).

Regardless of the effectiveness of any automotive-materials recovery technology, the materials that will be recovered will be on average 10–15 years old and derived from different sources (automobiles, home appliances and others). In this project, the performance properties of recovered polymers will be compared vis-à-vis new or virgin materials and blends of virgin and recovered materials to establish a database of the properties of recovered automotive polymers. At present, there are few data about the physical properties of polymers recovered from post-consumer durable goods. Absent such data, it is unlikely that sustainable applications for recycled materials will be either identified or developed.

Physical properties testing has been conducted by Midland Compounding, Inc. Midland also conducts composition testing, the results of which are compared with the results of compositional analysis done on recovered materials by ANL.

Blending and pelletizing of the PP/PE recovered from shredder residue by ANL has been tested by Palmer Plastics, Inc. More blending and compounding tests will be done, as required, to achieve the desired performance properties of the recovered materials for target applications. Mold trials using the recovered PP/PE were also done by MGV Enterprises. More molding tests are planned to confirm the technical and economic feasibilities of using recycled polymers in specific applications.

Polymer Physical Properties and Materials Composition Analysis

Typically, 10-lb samples of recovered materials are used to define physical properties and to characterize the composition of the material.

To quantify the physical properties of the recovered material, a sample is extruded on a single-screw extruder, melt-screened through a 40-mesh screen, molded into American Society for Testing and Materials (ASTM) test bars and plaques, and tested. The molded parts and a random selection of regrind chips from each sample are evaluated for material identification by using infrared (IR) spectroscopy.

Common physical properties that are measured for each sample include the following:

- Melt flow rate (MFR),
- Izod impact,
- Flexural modulus,
- Tensile strength at yield,
- Tensile strength at rupture,
- Elongation at rupture,
- Deflection temperature under load (DTUL),
- Gardner impact, and
- Specific gravity (SG).

Physical Properties and Composition of the PP/PE Recovered from Shredder Residue

The physical properties of PP/PE recovered from different shredder residues by ANL and by Salyp were determined for several samples. The results for the ANL materials are given in Table 1. Properties of commercially-available PP and PE virgin (low-density PE (LDPE) and high-density PE (HDPE)) are presented in Table 2 for comparison. The Izod impact of the recovered material is about three times that of the virgin resins, while the tensile strength of the recovered material is lower than the tensile strength of the virgin resins by about 30%. This phenomenon may be attributed, at least in part, to the presence of thermoplastic olefins (TPO) and rubber in the recovered material, which act as impact modifiers. Recovered samples 8, 9, and 10 listed in Table 1 contained about 2% rubber, while samples 1 through 7 contained about 4% rubber.

The results for the more than 20 PP/PE samples recovered by Salyp from different European and U.S. shredder residues are given in Table 3. The properties of the Salyp-recovered PP/PE are equivalent to the properties of the ANL-recovered PP/PE.

Physical Properties and Composition of the Recovered Filled ABS

Filled ABS recovered by the ANL froth-flotation process followed by removal of the rubber by the ANL dry mechanical process contained 70% filled ABS (specific gravity greater than 1.07 and less than 1.1), 1.5% PS, 8% polyphenylene oxide (PPO), 3% rubber, 3% PP, 7% nylon and 7.5% others. The physical properties of this recovered filled ABS were determined. The results are given in Table 4 and are compared with properties of a commercially-available virgin ABS. Table 4 also shows the properties of two blends of the recovered ABS with virgin ABS (25% recovered/75% virgin and 10% recovered/90% virgin). Interestingly, except for elongation-at-rupture and Gardner impact, the properties of the blends were very close to the properties of the virgin material. Operating condition to upgrade the recovered filled ABS to over 90% has been determined. Properties of the upgraded material will also be established.

Physical Properties of the Polymers Recovered by MBA Polymers

During this reporting period the physical properties of the MBA-recovered fractions were determined by MBA Polymers. The results are given in Table 5.

Table 1. Properties of PP/PE recovered by ANL from different shredder residues.

Property	Sample 1	Sample 2	Sample 3	Sample 4	Sample 5	Sample 6	Sample 7	Sample 8	Sample 9	Sample 10	Average
MFR, g/10min, 230°C, 2.16 kg	10.5	14.9	7.7	10.1	11.4	7.2	8.7	7.2	8.7	7.2	9.4
Izod impact, ft-lb/in., 73°F	12.3	10.5	11.9	10.8	9	10.7	13.2	1.7	2.8	3.3	8.6
Flex mod., 1% secant, 1,000 psi	83	73	89	84	82	101	112	126	127	113	99.0
Tensile strength at yield, 1,000 psi	2.6	2.2	2.7	2.6	2.4	2.8	3.1	3.4	3.3	3.1	2.8
Tensile strength at rupture, 1,000 psi	0.8	1.2	2.1	1.9	1.4	2.5	2.0	3.1	3.1	2.9	2.1
Elongation at yield, %	23.0	20.8	21.1	22.8	20. 6	20. 6	17.1	**	**	**	24.3
Elongation at rupture, %	132	78	233	154	82	251	229	12	14	13	119.8
DTUL, °F (at 66 psi)	131	131	134	134	138	147	155	**	171	160	145
Gardner impact, 73°F, in.- lb	104	88	136	96	56	144	184	20	32	40	90.0
SG, g/cc	0.94	0.95	0.94	0.95	0.94	0.93	0.93	0.94	0.94	0.94	0.94

** Not tested

Table 2. Comparison of recovered PP/PE with commercial grades of PP & PE (Boedeker) (http://www.boedeker.com/mtable.htm), unless specified otherwise.

Property	PP Homo-Polymer	PP Co-Polymer	PP Flame Retarded	Standard PP Co-polymer	LDPE	HDPE
MFR, (g/10 min), 230°C	0.5-136*					
Izod impact, ft-lb/in.	1.9	7.5	0.65	0.7	No Break	3
Flex Mod, 1,000 psi	180	160	145	120	200	125
Tensile Strength, 1,000 psi	4.8	4.8	4.3	5.2	2.0	4.6
Elongation, %	12	23	28	600	600	900
DTUL, °F (at 66 psi)	210	173	106	210	110	--
SG, g/cc	0.905	0.897	0.988	0.90	0.92	0.95
Gardner impact, 73°F, in.-lb	0.9-22*					

- Data from http://www.ed-cam.com/materials/propylene_molded.asp. Ranges are for with and without additives.

Table 3. Properties of PP/PE recovered by Salyp from different shredder residues.

Property	**Salyp Data**
MFR, (g/10 min), 230°C	2.3–4.6
Izod impact, (ft-lb/in.) 73°F	4.7–13.3
Flex mod., 1%, secant, 1,000 psi	81.7–116.5
Tensile strength at yield, 1,000 psi	2.4–2.9
Tensile strength at rupture, 1,000 psi	2.2–2.8
Elongation at rupture, %	19–57
DTUL, °F (at 66 psi)	150–169
Gardner impact, 73°F, in.-lb	190–240
SG, g/cc	0.93

Table 4. Properties of recovered filled ABS, virgin ABS and blends of the two materials.

Property	Recovered Filled ABS	Virgin ABS (342 EZ)	90%Virgin/ 10% Recovered	75% Virgin/ 25% Recovered
MFR, g/10min, 230C, 3.8 kg	3.9	6.5	7.6	6.4
Izod Impact, ft.lbs./in., 73F	0.9	3.8	3.0	2.6
Flex Mod, 1% secant, 1,000 psi	324	296	299	302
Tensile strength at yield, psi	4982	5546	5392	5312
Tensile strength at rupture, psi	4956	4459	4544	4930
Elongation at rupture, %	2	56	9	6
DTUL, °F (at 264 psi)	162	165	166	164
Gardner Impact, 73F, in.lbs.	0	>320	32	8
SG, g/cc	1.08	1.05	1.05	1.06

During this reporting period, we also sent samples for evaluation to two plastics recyclers: MRC Polymers, Inc. in Illinois and Enviroplas, Inc. in Indiana. We also held discussions with Standard Plaque, Inc. in Michigan to discuss sample-preparation methodologies for analysis of recovered materials with different levels of impurities.

Polymer Physical Properties Database

A physical properties database has been compiled so that the physical properties of the recovered polymers can be compared with general purpose virgin polymers.

General-purpose physical properties have been compiled for the following plastics:

- ABS,
- Nylon (6 cast, 6/6 extruded, 30% glass filled),
- PPO (unfilled, 30% glass filled),
- PC
- PE, LDPE, HDPE, ultra-high-molecular-weight [UHMW] PE,
- PP,
- PS (general-purpose, high-impact), and
- Polyvinyl chloride (PVC).

The VRP had previously compiled physical properties data on selected polymers that were

recovered during the U.S. field trials. These materials were recovered by disassembly. The data from these polymers are included in the database so that the physical properties of materials recovered by disassembly can be compared with those of materials that are recovered from post-shred operations, Table 6 ("USCAR U.S. Field Trial for Automotive Polymers Recycling," by W.W. Gallmeyer, C.M. Duranceau, R. L. Williams and G.R. Winslow, SAE Paper # 2003-01-0645, 2003). Table 5 gives the properties of PP dismantled from automobiles as part of the USCAR U.S. field trial. The recovered PP was reported to have a specific gravity of 0.915 and it is made of 99.2% PP, 0.4% PE and 0.4% ABS. The differences in the properties of the dismantled PP and the PP/PE recovered from shredder residue are also compared in Table 6.

Table 5. Properties of plastics recovered by MBA.

Sample	ABS	HIPS*	PP filled	PP unfilled
MFR, g/10min, 230C, 3.8 kg	N/A	N/A	N/A	5.5
MFR, g/10min, 200C, 5 kg	N/A	N/A	2.5	N/A
MFR, g/10min, 230C, 2.16 kg	4.6	7.9	N/A	N/A
Izod Impact, ft.lbs./in., 73F	10.3	1.6	1.8	3.4
Flex Mod, 1% secant, 1,000 psi	130	293	315	361
Tensile strength at yield, psi	3029	3779	4319	6291
Tensile strength at rupture, psi	1773	2365	4011	5623
Elongation at rupture, %	50	32	19	6
DTUL, °F (at 264 psi)	N/A	N/A	162	170
DTUL, °F (at 66 psi ,	150	232	N/A	N/A
Gardner Impact, 73F, in.lbs.	216	64	16	16
SG, g/cc	0.94	1.07	1.05	1.06

* HIPS = high-impact polystyrene

Table 6. Properties of PP Dismantled of Cars as Part of the USCAR U.S. Field Trial.

Property	Recovered, Extruded	Recovered Flakes, Sample #1	Average Properties of Recovered PP/PE*
MFR, (g/10 min), 230°C	19.9	17	9.4
Izod impact (ft-lb/in.) 73°F	1.8	1.8	8.6
Flex. Mod., 1%, secant, 1,000 psi	136.9	131.9	99
Tensile Strength at Yield, 1,000 psi	3.130	3.136	2.8
Elongation at Yield, %	19	18	24.3
Tensile Strength at Rupture, 1000 psi	2.388	2.384	2.1
Elongation at Rupture, %	59	60	119.8
DTUL, ^{o}F (at 66 psi)	129.7	136.5	145

* From Table 1

The differences are not significant and do not affect the usefulness of the material. For example, the specific gravity of the material recovered at ANL is about 0.94 compare to 0.915 for the dismantled material. The MFR reflects the largest difference: 17 for one of the two samples of the dismantled flakes versus about 9.4 for the material recovered from shredder residue. The USCAR study also found that the properties of the dismantled PP responded as expected when additives were added to the PP. For example, the Izod impact increased from less than 2 ft-lb/in. to about 11 when 10% of an impact modifier was added, and to about 14 when 20% were added (USCAR U.S. Field Trial for Automotive Polymers Recycling: Interim Findings", by W. W. Orr, SAE Paper # 2000-01-0735, 2000).

Blending and Pelletizing of Recovered PP/PE

250 pounds of PP/PE recovered by ANL were blended with 750 lb of supplemental PP copolymer regrind for 15 minutes. The blended material was then run through an extruder and pelletized. The general appearance of the final pellet was excellent (Figure 1). Properties of the recovered material used in blending and the properties of the regrind and of the resulting pellets are shown in Table 7. Standard pelletizing conditions were used. Barrel heats were set from 365°F at the rear barrel zone and increased progressively to 390°F at the front, with six heat zones in between. Screen-changer and breaker-plate heats were set at 405°F, and die heats were set at 395°F. Melt temperature was recorded as 460°F, and drive-load and screw speed were set at 60% and 67.5% of the maximum values, respectively.

Figure 1. Pelletized PP/PE product recovered from shredder residue.

Material output was recorded as 1,400 lb/h. Extra-fine screen packs were used (20/20/20/60/100/20 mesh screens) to remove impurities because this was the first time this material has been tried.

In addition, while screen changes are typically performed at pressure differences between 500 psi and 1,000 psi, in this test, changes were performed when the pressure exceeded 500 psi to safeguard against puncturing a screen pack and losing material. Because extra-fine screen packs were used in the test, screen changes were required approximately every five minutes. The results indicated that the recovered PP/PE can be blended with other olefinic regrind and pelletized by using standard processes and equipment.

Mold Trials

Three types of auto parts were molded by MGV Enterprises using ANL-recovered PP/PE from shredder residue: knee bolsters, battery trays, and steering column covers (Figure 2). A standard molding machine was used in these trails. No changes to the standard conditions were required to run the recovered material. The limited testing done on the recovered PP/PE fraction shows that quality products, including auto parts, may be produced from the recovered materials. Additives and/or modifiers may be added to meet the specifications of some products.

Recovered Rubber/Plastics Material

A mixed-rubber fraction with about 20% by weight mixed plastics was recovered. A sample of the recovered material was sent for testing by the "TireCycle" process used for recycling rubber. Preliminary tests done on the recovered material indicated that it may be suitable for making construction products, such as roofing shingles. The presence of the plastics in the mixed-rubber material appeared to improve its overall properties, especially its stiffness.

Publications

None.

Table 7. Properties of recovered PP/PE when mixed with regrind.

Property	Argonne, As-Recovered Sample 9 (see Table 1)	Regrind As-Is	Pelletized Blend
MFR (g/10 min), 230°C	8.7	3.1	9.2
Izod impact (ft-lb/in.) 73°F	2.8	13.6	10.4
Flex. mod., 1%, secant, 1,000 psi	127	157	136
Tensile strength at yield, 1,000 psi	3.3	3.7	3.4
Tensile strength at rupture, 1,000 psi	3.1	2.9	2.3
Elongation at rupture, %	14	125	57
DTUL, °F (at 66 psi)	171	197	176
Gardner impact, 73°F, in.-lb	32	>320	132
SG, g/cc	0.94	0.91	0.92

Figure 2. Auto parts molded from PP/PE recovered from shredder residue.

E. Post-Shred Materials-Recovery Technology Development

Principal Investigator: Edward J. Daniels
Argonne National Laboratory (ANL)
9700 S. Cass Ave., Argonne, IL 60439
(630) 252-5279; fax: (630) 252-1342; e-mail: edaniels@anl.gov

Technology Area Development Manager: Joseph A. Carpenter
(202) 586-1022; fax: (202) 586-1600; e-mail: joseph.carpenter@ee.doe.gov

Expert Technical Monitor: Philip S. Sklad
(865) 574-5069; fax: (865) 576-4963; e-mail: skladps@ornl.gov

Participants:
This project is conducted as part of a Cooperative Research and Development Agreement (CRADA) among ANL, the Vehicle Recycling Partnership (VRP) of the United States Council for Automotive Research (USCAR), and the American Chemistry Council-Plastics Division (ACC-PD, formerly the American Plastics Council (APC)).

CRADA Partner Principal Investigators:
Claudia Duranceau, VRP, Ford Motor Co., (313) 390-0504; e-mail: cdurance@ford.com
Nakia Simon, VRP, Chrysler Corp., (248) 576-1869; e-mail: nls8@daimlerchrysler.com
Candace Wheeler, VRP, General Motors Corp., (586) 986-1674; e-mail: candace.s.wheeler@gm.com
James Kolb, American Chemistry Council-Plastics Division, (248) 244-8920; e-mail: james_kolb@americanchemistry.com.

Changing World Technologies (CWT) is cost-sharing on the evaluation of its thermal depolymerization process. The Polyurethanes Recycle and Recovery Council (PURCC) is also participating and cost-sharing on the evaluation of the Troy Polymers, Inc. (TPI), polyurethane glycolysis process.

Contractor: ANL
Contract No.: W-31-109-Eng-38

Objective

- Develop technology for the cost-effective recovery of materials from post-shred residues.

Approach

- Characterize shredder residue (SR) from a number of sources to determine composition variability.
- Conduct bench-scale and large-scale process/technology tests to benchmark technology.
- Build and operate a pilot-plant for the separation of SR to produce recovered materials for market evaluation and to provide "control" samples of materials for testing of alternative technologies, as appropriate.
- Conduct cost and performance analysis of alternative technologies to establish the business case for the technologies and to identify technology gaps.

Accomplishments During this Reporting Period (10/1/06-9/30/07)

- ANL was approached by two shredders who expressed interest in building large-scale plants to validate the results obtained in the ANL pilot-plant. Discussions with the shredders are underway.

- Achievements during this reporting period are given below.

Mechanical Separation of Shredder Residue

- Completed testing of 10,000 pounds of SR out of a 30,000 pound batch from a shredder who is interested in building a plant to validate the ANL technology.
- Completed engineering designs of the basic Mechanical Separation System including equipment specifications, equipment cost, operating requirements, and utility requirements.
- Conducted cost analysis of the process including sensitivity of the cost of producing the polymer concentrate to yield, value of by-products (ferrous, non-ferrous metals) and cost of utilities.
- Completed the recovery of plastics and metals from fines (< 0.25 inch).

Froth-Flotation Separation of the Plastics

- Designed, built and tested a 5,000 lb/hr plastics separation sink/float module.
- Defined process conditions for upgrading the polycarbonate(PC)-acrylonotrile-butadiene-styrene(ABS)/PC alloy concentrate to 90-95%.
- Completed engineering designs of the basic froth-flotation process to include equipment specifications, equipment cost, operating requirements, and utility requirements.
- Proved the technical feasibility of upgrading the filled ABS from 70% to greater than 90% and of the unfilled ABS and polystyrene (PS) from the ABS/PS concentrate, to greater than 90% and 85%, respectively.

CWT's Thermochemical Process for Producing Hydrocarbon Liquids

- Evaluation of the CWT technology was continued. Preparation for the 2,000 lb. test was started.

Emerging Technologies for the Rapid Identification and Sorting of Plastics

- Conducted performance testing and cost analysis of color sorter and near infrared (NIR) systems for plastics, wood and rubber separation.

MBA's Plastics Separation Test

- Tests have been completed and the report was submitted.

Energy Anew Process for Recycling Fines

- Energy Anew completed a study to recover metals and polymers from fines (<7/8 in. in size).

On To Technologies

- The VRP has awarded a contract to OnTo Technology of Bend, Oregon to develop technology to recycle batteries used in hybrid and electric vehicles. Testing has started. Initial results are promising.

Prior Accomplishments

Fiscal Year (FY) 2006

Mechanical Separation of Shredder Residue

- Ran one (1) 10-ton production campaign (fractions supplied to commercial equipment vendors for performance verification).
- Initiated engineering design for full-scale, bulk-separation system.
- Obtained budgetary quotes from vendors for major equipment.
- Confirmed performance of commercial equipment with field trials by vendors/ANL of the as-is SR and of the fractions generated at ANL.
- Conducted preliminary investigation of costs and performance of commercial color sorters, electrostatic separators, and IR sorters for removal of wood and rubber.

- Developed a dry process for separating rubber from plastics.

Froth-Flotation Process for Recovering Plastics

- Ran first campaign of the middling plastics fraction.
- Recovered a 60%-unfilled ABS/PS and a 50%-filled ABS concentrates from the middling plastics.
- Upgraded the filled ABS concentrate from 50% to 70% and defined process conditions to further upgrade this fraction to 90%.
- Defined process conditions for separating and recovering unfilled ABS and PS from the unfilled ABS/PS concentrate, to greater than 90% and 85%, respectively.
- Defined process conditions for recovering an 85% PC-ABS/PC alloy from the middling plastics.

Other Accomplishments

- Completed testing of Troy Polymers' (TPI) process for conversion of urethane foam to polyol initiators. Over 1,200 lb of foam were used and produced over 100 gallons of polyol initiators.
- Conducted pilot-scale testing of CWT process for converting SR to fuels. Pre-processed SR from another shredder was evaluated and shipped to CWT for further testing.
- Completed a large-scale, plastics-separation test at MBA Polymers Inc. using a plastic concentrate produced by Salyp's mechanical-separation system.
- Completed testing of the VW-SiCon plastics-separation process.

FY 2005

Mechanical Separation of SR

- Ran four (4) 15-ton production campaigns and conducted material balance on all runs.
- Modified bulk-separation operation resulting in an increase in polymer yield in concentrate from 40% to over 90%.
- Conducted trials on gravity tables, mineral jigs, and a kinetic density separator in the U.S. and Europe primarily for removal of wood and rubber.

Froth-Flotation Process for Recovering Plastics

- Conducted bench-scale research on settling velocities and density distributions of actual SR polymers including the wood and rubber.
- Ran a production campaign of the base process with polymer concentrate to yield three polymer fractions; the polyolefin fraction: middling plastic fraction, and the heavies plastic fraction.
- Developed a wet process for removal of wood and rubber from the recovered polyolefin fraction.
- Recovered 5,000 pounds of polypropylene(PP)/polyethylene(PE) essentially free of wood and rubber.

Other Accomplishments

- Conducted bench-scale tests and in a five-gallon reactor of TPI's glycolysis process for conversion of urethane foam to polyol initiators.
- Conducted bench and pilot-scale testing of CWT's thermal depolymerization process for converting SR to fuels.
- Developed an Excel-based process cost model that incorporates two primary modules for the recovery of automotive plastics. The first module includes the unit operations required for recovering a plastics concentrate from SR and the second module includes the unit operations required to recover selected plastics from the mixed plastics concentrates.

FY 2004

Mechanical Separation of SR

- Completed construction, shakedown and start-up of the bulk-separation facility.
- Ran six (6) 5-ton trial campaigns.

Froth-Flotation Process for Recovering Plastics

- Completed construction and shakedown of the pilot-plant with electronics plastics.
- Ran a shakedown campaign with SR polymer concentrate.

Other Accomplishments

- Completed large-scale tests of Salyp's "thermoplastics sorting" technology by using residue from two European locations and one U.S. location as feed materials

FY 2003

- Initiated construction of bulk-separation facility.
- Initiated construction of froth-flotation pilot-plant.

Future Direction

The FY 2008 plans are as follows:

Mechanical Separation of SR

- Include recovery of materials from fines in the engineering design.
- Process SR generated by controlled shredding of selected items (autos only).
- Shred automotive nano-composites to determine potential release of nano particles.
- Produce fractions of SR in support of other collaborators.

Froth-Flotation Process for Recovering Plastics

- Produce polymer fractions for property determination and market evaluation.
- Continue development of a predictive simulation model for determining appropriate separation operating and solution conditions that can affect gravity and froth-flotation separation of selected polymer materials for separation and recovery of polymers from a SR concentrate.
- Development of bench-scale experimental design to provide requisite empirical data for the predictive simulation model.
- Conduct process-improvement studies to increase value and reduce cost.

Other Future Plans

- Complete the 2,000-lb sample run. Evaluation of the CWT technology will be completed and recommendations for path forward will be made.
- Develop NIR spectroscopy libraries for SR plastics.
- Evaluate new processes for recycling SR including conversion to fuels and chemicals.
- Determine recycling research needs of new lightweighting materials.
- Identify an industrial partner to demonstrate the ANL technology.
- Continue development of the OnTo technology for battery recycling and Energy Anew fines recycling.

Summary

The objective of this project is to develop technology for the cost-effective recovery of materials from post-shred residues. Research will provide data essential to establishing a business case for sustainable recycling of automotive materials from post-shred residue. Technologies specific to the recovery of materials from post-shred material streams are being evaluated and demonstrated to determine their commercial viability. The performance (e.g., yield, purity, efficiency, and cost) of emerging technologies will be determined to enable the development of an integrated process for recovering materials from shredder residue.

Research has been completed on the Salyp, MBA, Troy Polymers, VW-SiCon and ANL mechanical-

separation processes. Research is ongoing on the ANL froth-flotation, CWT, OnTo, and Energy Anew processes.

Two shredders have expressed interest in building a plant on their sites to validate the results obtained in ANL's pilot-plant. About 5 tons of residue from one of their modern plants was processed to determine if a business case exists.

Characterization of SR

Over 100 tons of SRs from six facilities were processed in ANL's mechanical-separation plant. Table 1 shows the average composition of the different fractions produced. We observed:

- Large variations in fines, metals, rubber and wood, and
- Less variation in the composition of the plastics fraction.

The mass fractions of the polymer concentrate separated from different shredder residues showed little variation, and the weight percent (wt%) of the polymer concentrate recovered from 8 runs totaling 80,000 lbs of shredder residue from a given source conducted over a six-month period was reasonably consistent (41%, 26%, 36%, 39%, 45%, 37%, 43% and 45%,; average 40%). The composition of the different polymer concentrates was also similar, Figure 1.

ANL Pilot-Plant

ANL's pilot-plant consists of a dry mechanical-separation facility and a wet-density/froth-flotation facility. The pilot-plant is used to:

1. Recover materials from shredder residue,
2. Conduct process improvement studies
3. Generate design and scale-up data
4. Produce samples for evaluation,
5. Define the effectiveness of alternative separation technologies and systems, and
6. Serve as a user/demonstration facility.

Mechanical Separation Pilot-Plant

The mechanical-separation facility processes raw SR to yield a polymer concentrate, ferrous and non-ferrous concentrates, a fines fraction and other fractions. The plant achieved over 90% recovery of the thermoplastics targeted for recovery as a polymer concentrate and over 95% recovery of the metals in the SR.

The polymer concentrate included high and varying amounts of wood and rubber. Wood was about 1–4 wt%. In Figure 1, the wood is included in the "non-polymers."

Separation of Wood and Rubber

Trials were conducted on commercially-available air aspirators, air classifiers, gravity tables, and mineral jigs to remove wood and/or rubber from the polymer concentrate. This equipment did not yield satisfactory results. Trials using modified wet-separation approaches removed almost 100% of the wood and over 90% of the rubber with a nominal loss (~ 5%) of the plastics.

A modular dry process for separating rubber from plastics has been tested at rates of up to 200 lb/hr of polymer concentrate. The process is able to separate over 75% of the rubber and produce a rubber fraction containing less than 10% of non-rubber material.

Table 1. Streams produced by mechanical separation of an average shredder residue.

	Shredder Residue	Oversized Heavies	Oversized Foam rich	Fines +	Ferrous Rich	Non-Ferrous Rich	Lights	Polymer Concentrate
Weight (lbs)	40,000	2,148	756	17,640	656	1,468	1,968	10,044
PP	1,075	0	0	0	17	33	129	897
PP (filled)	403	0	0	0	0	0	9	393
ABS	763	0	0	0	5	9	13	737
PE	941	0	0	0	9	18	85	830
HIPS	261	0	0	0	4	8	15	234
Nylon	379	0	0	0	4	9	19	347
PVC	512	0	0	0	0	0	0	511
PPO	139	0	0	0	0	0	4	135
PC-ABS	151	0	0	0	0	0	1	150
PC	212	0	0	0	0	0	12	200
Other Plastics	597	0	0	0	1	0	17	579
Rubber	4,505	20	0	0	6	172	61	4,246
PU	273	3	0	0	1	23	9	237
Wood	239	0	0	0	0	0	0	239
Metals	2,911	1,117	0	0	590	954	0	249
Foam, Fiber and others	21,320	1,008	756	17,640 +	19	241	1,597	59
Moisture	5,320	0	0	0	0	0	0	0
Total	40,000	2,148	756	17,640	656	1,468	1,968	10,044

+ Fines are material smaller than 0.25 inch in size and also contain some polymers and metals. HIPS=high-impact polystyrene, PVC=polyvinyl chloride, PU=polyurethane. See text for other defintions.

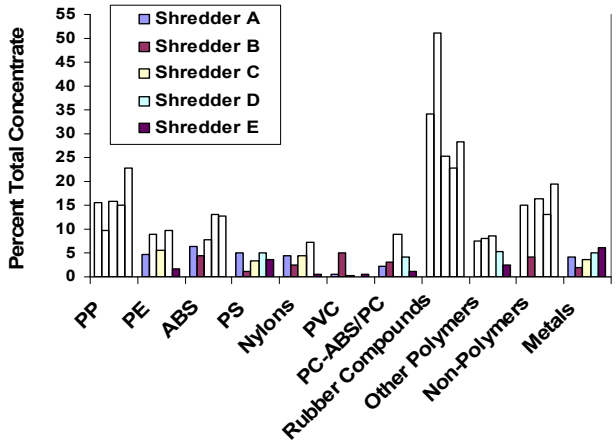

Figure 1. Composition of polymer concentrates from different shredder residues.

Froth-Flotation Pilot Plant

This facility includes six continuous stages for the separation of targeted plastics from the polymer concentrate. A shakedown of the facility was conducted using 4,000 lb of post-consumer electronics and appliance mixed plastics and by using a mixture of colored plastics. These trials confirmed the effectiveness of the basic system.

Over 30,000 lb of polymer concentrate from shredder residue has been processed in this facility. The recovered fractions are described below:

Recovered PP/PE Fraction

More than 5,000 lb of an unfilled PP/PE fraction that is over 95% PP/PE have been consistently

produced. It contains less than 0.2% wood and less than 4% rubber. However, when the material was palletized, most of the rubber in this fraction was compatible with the PP/PE. The recovered PP/PE has properties similar to those of some commercially-available PP materials. The unfilled PP/PE product is about 5%–6% of the starting shredder residue weight. Table 2 summarizes the recoverable plastics from 10,000 pounds of typical shredder residue.

Filled ABS Fraction
ABS that has a specific gravity between 1.07 and 1.1 was isolated by the basic froth-flotation process as an ABS concentrate, Table 2. It contains 50% ABS, 20% rubber, 10% rigid urethane rubber, and 20% of other materials. Removing wood and rubber increased the ABS concentration to 70% and reduced the rubber and urethane to 3% and 2%, respectively. When this material was blended with virgin ABS at 10% and 25% recovered material, the properties of the blends were slightly different from the properties of the virgin ABS. Laboratory tests have established process conditions to increase the ABS concentration to over 90%.

Unfilled ABS and PS
A fraction of ABS, PS and PPO that has a specific gravity between 1.0 and 1.07 (43% ABS, 22% PS, 7% PPO and 28% other materials including rubber and some wood) was produced by the basic process. Lab tests separated this fraction and produced fractions with over 90% ABS and over 85% PS/PPO.

PC-ABS/PC Alloy
Laboratory tests produced a PC-ABS/PC fraction having a combined concentration of over 85%. Work is ongoing to isolate a large sample of ABS/PC-PC fraction for further evaluation.

PVC: Recovery of the above fractions leaves behind a fraction made of high-specific-gravity materials. Rubber constitutes over 50% of the total and metals about 5%. Separating rubber, metals, glass and rocks from this stream leaves a fraction containing over 50% PVC. This fraction is also rich in glass-filled nylons.

Rubber
Recovered-rubber concentrate from the basic process was upgraded by the ANL dry rubber-separation process to over 90% rubber. The other 10% was mostly plastics.
In summary, we have recovered the unfilled polyolefins as a potentially useable product and isolated the filled ABS, unfilled ABS/PS, PC-ABS/PC and PVC into more manageable fractions.

The basic wet process has also produced a styrenics fraction containing over 75% by weight "targeted plastics" primarily ABS, PS, PPO, and filled PP. MBA Polymers established that this fraction can be separated to produce recyclable products. This may be a more cost-effective approach than trying to separate it by froth flotation to produce high-grade ABS and PS.

A 5,000 lb/hr continuous-flotation module has been designed, built and tested. Testing of this module using over 10,000 pounds of various polymer fractions provided necessary information for designing and building a full-scale plant.

Development of a Process Flowsheet

A process conceptual design for a 20 ton/hr mechanical-separation system has been developed. The key steps in the process include: 1) a device to separate large metal chunks and rocks; 2) a screen separator to separate large non-metallic pieces such as fabrics, PU foam and tire rubber pieces; 3) a shredder to size reduce the material; 4) a vibrating screen or a trommel to separate "fines", smaller than ¼ inch; 5) a magnetic separator to recover ferrous metals; 6) an eddy-current separator to recover non-ferrous metals; 7) a granulator to granulate the remaining material; and, 8) an air classifier to remove "lights" from the granulated material. Tests using SR were conducted to evaluate the cost, performance, and maintenance requirements of various equipment that was proposed for the conceptual design.

We also conducted sensitivity of the cost of producing the polymer concentrate to yield per ton of SR, value of the by-products (ferrous, non-ferrous, etc.), cost of utilities, number of operating shifts, cost-of-capital, etc. The production cost can be as low as $0.02 per pound of polymer concentrate recovered for a plant operating three

shifts per day and the polymer concentrate is about 45% of SR, to over $0.075 per pound for a plant operating one shift and the polymer concentrate is only 15% of SR. The value of the recovered metals has a significant impact on the overall cost. The value of the metals will depend on their recoverable concentration in the SR and on the composition of the metal concentrates produced.

Table 2. Composition of an average polymer concentrate and recovered polymer fractions.

	Polymer Concentrate	PP/PE Product	ABS Product	ABS/PC Product	Rubber Product	HIPS/ABS Concentrate	Mixed Plastics	Mixed Stream*
Weight (lbs)	10,044	1,736	141	108	689	856	1,203	5,311
PP	897	827	0	0	0	0	63	7
PP (filled)	393	0	0	0	11	43	194	146
ABS	737	0	105	2	0	365	176	88
PE	830	787	0	0	10	12	21	0
HIPS	234	0	2	0	0	186	25	21
Nylon	347	0	5	0	0	5	42	296
PVC	511	0	0	0	3	0	123	385
PPO	135	0	13	1	0	62	21	37
PC-ABS	150	0	0	6	0	0	0	143
PC	200	0	0	85	1	0	19	94
Other Plastics	579	0	9	2	2	12	8	547
Rubber	4,246	90	2	9	628	104	263	3,149
PU	237	21	4	2	18	0	96	96
Wood	239	0	1	0	17	66	146	8
Metals	249	0	0	0	0	0	0	249
Foam, Fiber and others	59	10	0	0	0	1	5	42
Total	10,044	1,736	141	108	689	856	1,203	5,311

* Rubber and metals are to be recovered from these streams

We conducted performance testing and cost analysis of color sorter and IR sorters. The following systems were tested: 1) Satake (chip monochromatic and IR); 2) Key (chip full-color and laser); 3) MSS (full-color and IR); 4) S+S Separation and Sorting Technology (full-color and IR); 5) NRT (chip full-spectrum and IR – See 11.F); and 6) PROTEC (chip full-spectrum). Based on the results of these tests, the ANL wet separation for wood and rubber removal is the most economical for separating the wood and the rubber from the plastics. The primary reason is the high loss of the targeted plastics by the optical sorters. Further, at this time, these systems can not produce marketable polymer products from the polymer concentrate.

Recycling of Fines

ANL conducted tests to recover polymers and metals from the <0.25 in. fines. The polymer concentrate recovered from the material in the 2-mm to 6-mm size range was about 50 wt% of the weight of the fines fraction. It contained up to 50% by wt rubber and about 20 wt% plastics. A sample of this concentrate was processed in the wet-separation system to produce a polyolefin concentrate, a styrenics concentrate, a mixed plastic and rubber concentrate, and recover the residual metals as a metal concentrate. Twenty percent of the plastics had specific gravity < 1.

The ferrous material, including iron oxides, in the fines has been reduced significantly compared to years ago. This is due to shredders using more-efficient metal-separation equipment.

Processing of Polymer Concentrate at MBA

Salyp built a mechanical-separation plant that started with ANL's original mechanical-separation system and added an optical sorter and a plastics washing system. Salyp's starting SR contained less rubber and wood than the U.S. residue. MBA processed about 40,000 pounds of polymer concentrate produced by Salyp. Five materials were recovered: 1) Polyolefin "A", 2) Polyolefin "B", 3) filled PP, 4) ABS and 5) HIPS. The total yield of these products was estimated to be 48.5%

of the plastics-rich fraction. This yield is 88% of the amounts of these plastics in the feed material. The products were extruded, molded and tested. The properties were reported to be "encouraging" and it is expected that most of the products could be used in some durable-goods applications.

CWT

CWT processed a mixed SR stream after separating the < 1/16-in. fines (~36% by weight). About 700 lb of the remaining material were processed along with 80 lb of tires and 1,700 lb of used motor oil. The products were hydrocarbon oil (84%), a fuel-gas (10%), and a solid carbon product (6%). Distillation of the oil generated gasoline (12%), diesel (32%), heavy-hydrocarbon oils (15%), and gas (3%).

Polychlorinated biphenyls (PCBs) in the input SR were 21.8 parts per million (ppm); however, in the products, the PCBs were below the detection limits. This indicated that PCBs degrade during the process. No measurable concentrations of heavy metals were found in distillate-cut #3. The char contained significant amounts of several metals. The heavy oil from the dissolver contained about 3,200 ppm of total chlorine, but no chlorine was found in the light distillates; only 14 ppm was found in the heavier distillate and 11 ppm in the distillate bottoms. Bromine was found in the heavy oil from the dissolver (~135 ppm). No bromine was found in the output liquid products. Bromine was found in char (87 ppm).

The tire rubber and the oil samples contained 17,200 ppm and 1,600 ppm of sulfur, respectively. This indicates that sulfur compounds degraded in the process.

A pre-processed organic fraction (about 2,000 pounds) derived from SR has been shipped to CWT for next trials. CWT removed the inorganic fines from this material. The prepared organic fraction will be processed to validate the earlier results.

TPI

Foam from SR was converted by the TPI process to polyol initiators at yields of about 88% and 72%, for clean and dirty foam, respectively. Activated carbons reduced the concentration of PCBs in the products to < 2 ppm. Over 1,200 lb of shredder residue foam have been processed in a 5-gallon reactor, and produced over 100 gal of polyol initiator.

Twenty gallons of the polyol initiator were propoxylated. The recycled polyols were successfully tested for making rigid foams. They required less or no catalysts and had better flame resistance than the foams made with virgin polyols. The results established the technical feasibility of the process. Initial economic analysis of the process indicated that the glycolysis process is potentially economical. TPI is working with PU-foam producers to move the technology forward.

Energy Anew Recycling of Fines

Energy Anew conducted tests on 300-pound samples of fines (smaller than 1 in.). SR was screened using a 7/8-in. screen and the material that passed the screen was processed to yield organic- and inorganic-rich fractions. A combination of hydrocycloning, screening, rising current, wet tabling, magnet, and grinding were utilized to give ferrous and non-ferrous metal, organic, and inorganic/sand fractions. Economic analysis of the process showed that recovery of the metal and sand may be viable. Energy Anew is working to scale-up the process.

The ACC-PD has co-funded a study with Plastics Europe to study the synergies of co-combustion of plastics-rich fuels and biomass. The study will review technologies, co-combustion experience, environmental compatibility and synergies of biomass plastics co-combustion

OnTo Technology

The VRP has awarded a contract to OnTo Technology of Bend, Oregon to research and develop technology to recover materials from batteries used in hybrid and electric vehicles. Preliminary tests were conducted during this reporting period and the results are promising.

Publications

1. *Recovery and Recycling of Polymers from Shredder Residue,* Jody, B. J., Pomykala, J. A. Jr., Spangenberger, J. S. and Daniels,

E. J., The Journal of Solid Waste Technology and Management, Vol. 23, No. 4, Nov 2006, PP 228-236

2. *Technologies for Recycling Shredder Residue,* Jody, B. J. and Daniels, E. J., SAE Paper No. 2007-01-0526, 2007 SAE World Congress, Detroit, Michigan, April, 2007
3. *Mass Balance and Composition Analysis of Shredder Residue,* Pomykala, J. A. Jr., Jody, B. J., Spangenberger, J. S. and Daniels, E. J., SAE Paper No. 2007-01-0527, 2007 SAE World Congress, Detroit, Michigan, April, 2007
4. *Metal Recovery from Shredder Residue Fines,* Allen, T., SAE Paper No. 2007-01-0528, 2007 SAE World Congress, Detroit, Michigan, April, 2007
5. *Thermoplastic Separation and Recovery from Various Mixed Scrap by the ANL Developed Froth Flotation Technology,* Pomykala, J. A. Jr., Jody, B. J. and Daniels, E. J., Proc. Of the 13th Annual Global Plastics Environmental Conference (GPEC), Orlando, Florida, March 6-7, 2007
6. *A mechanical Separation Process to Recover Metals and Polymers from Shredder Residue,* Pomykala, J. A. Jr., Jody, B. J., Daniels, E. J., Yang, J. and Spangenberger, J.S. , TMS 2007 Annual Meeting & Exhibition, Orlando, Florida, Feb 25-Mar 1.
7. *Scale Up Study on Converting and Recycling Shredder Residue Into a Fuel Oil*, Winslow, Gerald R., Appel, Brian S., Adams, Terry N., Simon, Nakia L., Duranceau, Claudia M., Wheeler, Candace S., SAE 2006 World Congress, Detroit, Michigan, 2006. SAE-2006-01-1580.
8. *Scale Up Study on Converting and Recycling Shredder Residue into a Fuel Oil*, Winslow, G. R., Appel, B. S., Adams, T. N., Simon, N. L., Duranceau, C. M., Wheeler, C. S., paper # SAE-2006-01-1580.
9. *Recycling of Polyurethane Foams Recovered From Shredder Residue Via Glycolysis Process Into Polyurethanes*, Sendijarevic, V., Sendijarevic, I., Mayne, K., Winslow, G. R., Duranceau, C. M., Simon, N. L. Wheeler, C. S., paper # SAE-2006-01-1579.
10. *Chemical Recycling of Mixed Polyurethane Foam Recovered from Shredder Residue into Polyurethane Polyols,* Sendijarevic, V., Sendijarevic, I., Winslow, G.R., Duranceau, C.M., Simon, N.I., and Wheeler, C.S., SAE paper # 2005-01-0850.
11. *Recycling Shredder Residue Containing Plastics and Foam Using a Thermal Conversion Process,* Winslow, G.R., Appel, B.S., Adams, T., Simon, N.I., Duranceau, C.M., Wheeler, C.S. and Sendijarevic, V., SAE Paper #2005-01-0848.
12. *Advanced Separation of Plastics from Shredder Residue,* Winslow, G.R., Simon, N. l., Duranceau, C. M., Williams, R., Wheeler, C. S., Fisher, M., Kistenmacher, A., and VanHerpe, I., SAE Paper No. 2004-01-0469.
13. *Recycling Automotive Shredder Residue and Plastics Using the CWT Thermal Process,* Winslow, G.R. and Adams, T., Proc. of the 10th Annual Global Plastics Environmental Conference (GPEC), Detroit, MI, February 18, 2004.
14. *Screening Study to Evaluate Shredder Residue Materials*, Winslow, G.R.; Wheeler, C.S., Williams, R.L., Duranceau, C.M., Simon, N.L. and Schomer, D.R., SAE paper # 2004-01-0468.
15. *Processes for Recycling the Non-Metallic Portion of Obsolete Automobiles*, Jody, B. J., Daniels, E. J., and Pomykala, J. A., Jr., U.S. Environment-2003 On-Line Conference, July 14-25, 2003.
16. *Cost Effective Recovery of Thermoplastics From Mixed Scrap*, Jody, B. J., Pomykala, J. A., Jr. and Daniels, E. J., Materials Technology, Volume 18 Number 1, March 2003, pp 18-24.
17. *Separation and Recovery of Thermoplastics From Mixed-Scrap Plastics*, Pomykala, J. A. Jr., Jody, B. J., Daniels, E. J., and Greminger, J., Proc. of the 9th Annual Global Plastics Environmental Conference (GPEC), Detroit, MI, February 26-27, 2003, pp 7-16.

F. Development of High-Speed Multispectral Imaging for Sorting Automotive Plastics

Principal Investigator: Edward J. Sommer, Jr.
National Recovery Technologies, Inc. (NRT)
566 Mainstream Drive, Nashville, TN 372289
(615) 734-6400; fax: (615) 734-6410; e-mail: ejsommer@nrtsorters.com

Technology Area Development Manager: Joseph A. Carpenter
(202) 586-1022; fax: (202) 586-1600; e-mail: joseph.carpenter@ee.doe.gov

Contractor: National Recovery Technologies, Inc.
Contract No.: DE-FG02-06ER84559, Small Business Innovative Research (SBIR) and Small Business Technology Transfer (STTR) Program

Objective

- Develop technology for the cost-effective sorting of automotive plastics recovered from post-shred residues.

Approach

- Determine types of automobile shredder residue (SR) plastics that potentially can be sorted using the proposed multispectral sensing technology.
- Construct a bench-scale unit comprising rudimentary features of the new technology.
- Conduct bench-scale evaluations to determine technical feasibility for development of the proposed technology.
- In Phase II, develop the new high-peed multispectral sensing technology required to perform commercial-scale sorting of automotive plastics recoverable from SR.
- In Phase II, build and test a prototype sorter incorporating the new multispectral sensing technology for application to sorting of plastics recovered from SR.
- Conduct cost and performance analysis of the new sorting technology to establish technical viability and commercial feasibility for deployment and use of the new sorting technology.

Accomplishments During this Reporting Period (10/1/06-9/30/07)

The Phase I research program performance period was from 06/28/2006 through 03/27/2007 and progress reported herein covers this performance period.

Types of Plastics for Sorting Derived from Automobile SR

- Met with personnel from the Transportation Technology R&D Center at Argonne National Laboratory (ANL), toured the Vehicle Recycling Partnership (VRP) plant, and learned about various plastics derived from automobile shredder residue.
- Received and preliminarily evaluated SR plastics samples from ANL.

Bench-Scale System Demonstration and Feasibility Determination

- Determined preliminary technical requirements for an optical module for integration with a sensing module.
- Determined technical feasibility of developing a primary beam-shaping module which collects, collimates, and condenses broadband radiation for transmission to a sensing module.

- Determined the technical requirements for an analog amplification circuit that converts the detector response into an appropriate voltage signal.
- Designed and constructed a bench-scale unit comprising rudimentary features of the proposed detection system.
- Demonstrated technical feasibility for development of the new sensing technology.

Future Direction

Effort in FY2008 will be performed through a recently-awarded SBIR Phase II project. In summary, the Phase II plan is as follows:

- Develop the new high-speed multispectral sensing technology required to perform commercial scale sorting of automotive plastics recoverable from SR.
- Integrate the new sensing technology with an electronics and computing platform incorporating a real-time operating system interfaced to a precision air-jet ejection array system in order to enable high-speed sorting.
- Develop and incorporate sensing, detection, and sorting algorithms and a run-time, human-to-machine, input/output (I/O) interface for system configuration and control.
- Build and test a prototype sorting system incorporating the new multispectral sensing technology with the operating system platform, software, and sorting hardware for application to sorting of plastics recovered from shredder residue.
- Conduct cost and performance analysis of the new sorting technology to establish technical viability and commercial feasibility for deployment and use of the new sorting technology.

Summary

In the Phase I research, NRT has designed and constructed a bench-scale sensing and detection system capable of simultaneously acquiring detection signals from multiple spatial locations thereby potentially enabling high-volume sorting of automotive plastics derived from SR. As a "proof of technology" prototype, this system has enabled us to explore and evaluate the challenges arising from concurrent acquisitions of signals from multiple sensing sites. Assessment of this prototype leads us to believe that it is possible to construct a low-cost, compact, rugged system for industrial processing of automotive plastics.

The project had the following technical objectives:

1. Determine the technical requirements for an optical module that collects the broadband radiation from a plastic sample and couples this information into an optical signal-transmission system. The module should accommodate a "reasonable" field-of-view and depth-of-focus.

2. Determine the technical requirements for a photonic containment array. This array provides for further optical signal processing and allows concurrent monitoring of various spatial locations.
3. Determine the technical feasibility of developing a beam-shaping module which collects and condenses the broadband radiation transmitted from the containment array and presents it to a detector system.
4. Determine the technical requirements for a detector containment array which will be configured to align with the photonic containment array.
5. Determine the technical requirements for an analog amplification circuit that converts the detector response into an "adequate" voltage signal.
6. Construct a rudimentary prototype for the verification of objectives 1 through 5 and determine overall technical feasibility for development of the proposed high-speed multispectral imaging system.

Brief System Description

The multispectral imaging system can be functionally segmented into five modules. These include a collection module, an optical- signal input module incorporating a photonic

containment array, an optical dispersion module, an output optical-signal module, and electro-optical conversion module.

The collection module collects radiation emanating from an irradiated sample and conditions the radiation for presentation to the optical-signal input module. The input module further conditions the optical signals through noise suppression and beam-shaping photonic containment array for redirection and presentation to an optical dispersion module. In the optical dispersion module, the conditioned and redirected optical signals collected from the irradiated sample are dispersed according to energy level and the dispersed optical signals are directed into an output optical signal module. The output optical signal module conditions the dispersed optical signals and aligns the optical signals for presentation to an electro-optical conversion module incorporating a containment detector array which converts the optical signals into electrical signals for analyses by an associated computing system.

System Evaluation

After assembling the prototype and carefully adjusting all mechanical parameters, a "white" and "black" energy spectrum was obtained. The "white" spectrum is acquired when viewing only our radiation source and provides a "perceived" energy signature for that source after transitioning the imaging system. Likewise, the "black" spectrum is acquired when the radiation source is off and provides a "background" signature. Any subsequent data must be "normalized" by subtracting the "black" spectrum, then dividing by the difference of the "white" and "black" spectrum.

Since the primary goal of the prototype was to validate the procedure of simultaneously acquiring independent data from multiple sources, quantifying the crosstalk between channels is essential to evaluating its performance. In particular, the crosstalk we considered could be categorized as electrical, thermal or optical. Electrical crosstalk between the channels is characterized by a voltage change in one channel as a result of applying a signal to another channel. By visual inspection of the various signals, electrical crosstalk seemed negligible.

Thermal crosstalk between the channels is characterized by a voltage change in one channel as a result of the thermoelectric (TE) cooling in another channel. This interaction was difficult to measure, since there seemed to be some signal variance even within a single detector/cooler pair. Perhaps this "drift" was a result of our TE cooling circuitry. However, when the detectors were embedded in an aluminum heat sink, about a one percent signal distortion due to thermal effects was observed.

Optical crosstalk between the channels is characterized by a voltage change in one channel as a result of an intensity change in another channel. To measure the crosstalk of channel *A* on *B*, the radiation entering channel *A* is "chopped" (i.e., cycled on and off) and the change in *B* indicates the distortion. Surprisingly, even after careful alignment of the various system components, the optical crosstalk seemed to range from ten to twenty percent. It is believed that much of the crosstalk is the result of surface effects and that anti-scattering measures, to be incorporated in Phase II, will significantly reduce this distortion.

The next step in system validation involved acquiring "spectra" of some automotive polymers with the prototype and comparing them to "references". To exercise the system, polystyrene (PS), polycarbonate (PC) and polyvinyl chloride (PVC) were selected for this testing. It should be noted that the data analyzed by the system for these polymer samples were acquired simultaneously.

Many physical characteristics (e.g., surface texture, fillers, color) affect the overall shape of the "spectra"; as a result, the system data and reference signals were not expected to be identical. However, certain signatures specific to the polymers were clearly be identifiable. Using these data, the polymers were readily distinguished from one another.

Conclusions

The Phase I research enabled us to investigate a low-cost, high-speed, and effective alternative to current polymer sorting systems. In particular, the prototype has demonstrated that independent, unique signatures can be simultaneously acquired from multiple spatial locations using a multispectral device thereby establishing technical feasibility for development of an operational, near-commercial-scale prototype system in Phase II for high-volume sorting of automotive plastics recovered from automobile SR.

Research using the Phase I bench-scale prototype unit has also highlighted three areas that require more attention in Phase II before constructing an effective industrial-grade sorting system: 1) acquisition speed, 2) channel crosstalk, and 3) number of channels. The prototype system can only acquire approximately 10^3 samples per second per channel; this rate needs to be increased to around 10^4 in the final system. Crosstalk was seen to be as high as twenty percent; a decrease to less than five percent is desired. Finally, the number of simultaneous channels should be increased to at least eight in order to satisfy desired processing rates.

Publications

Phase I Final Report, *Development of High Speed Multispectral Imaging for Sorting Automotive Plastics,* U.S. Department of Energy SBIR Program, Contract DE-FG02-06ER84559, National Recovery Technologies, Inc., Nashville, TN, March 2007.

G. Microwave Assisted Gasification for Recycling Polymer Matrix Composites

Principal Investigator: Sara L. Rolfe
Eltron Research & Development Inc.
4600 Nautilus Court South, Boulder, CO 80301-3241
(303) 530-0263; fax: (303) 530-0264; e-mail: eltron@eltronresearch.com

Technology Area Development Manager: Joseph A. Carpenter
(202) 586-1022; fax: (202) 586-1600; e-mail: joseph.carpenter@ee.doe.gov

---

Contractor: Eltron Research & Development Inc.
Contract No. DE-FG02-07ER84878 Small Business Innovative Research (SBIR) and Small Business Technology Transfer (STTR) Program

---

Objective

- Develop technology for the cost-effective recovery of high strength, full size fibers from polymer matrix composites (PMC).

Approach

- Gasify polymer compositions using microwave gasification and conventional heating.
- Evaluate gas production, liquid composition, and char percentages.
- Determine microwave susceptibility and dielectric heating characteristics of common fiber and particulate materials.
- Determine composite strength using virgin and recycled reinforcements.
- Evaluate whether microwave assisted gasification of PMCs is more energy efficient and economical than conventional pyrolysis.

Accomplishments during This Reporting Period (6/20/07-2/22/08)

Eltron Research and Development has shown proof-of-concept of microwave assisted gasification of polymer matrix composites during this Phase I project. Achievements during this reporting period are given below.

Dielectric Heating Assessment of Fiber and Particulate Compositions

- Selected fiber and particulate reinforcement compositions for testing.
- Determined optimal microwave conditions for heating each composition.
- Prepared new particulate materials with superior dielectric heating capabilities.
- Assessed heating rate and temperature achieved for each composition.

Microwave Assisted Gasification of Polymer Matrix Composites

- Designed, built and tested a laboratory scale microwave gasification reactor.
- Developed microwave thermocouple system.
- Developed experimental method to screen particulate and fiber loading and composition.
- Completed matrix of experiments which show the effect of particulate loading and composition on gas, liquid, and char formation.

Future Direction

The remaining Phase I effort will include the following:

Compare Microwave Gasification to Conventional Pyrolysis

- Design, build and test a laboratory scale pyrolysis reactor using a conventional furnace.
- Complete experiment which shows the effect of heating type (microwave vs. conventional heating) on gas, liquid, and char formation.

Microwave Assisted Gasification of Polymer Matrix Composites

- Continue experiments which show the effect of reinforcement composition, addition of air flow, microwave output power, and polymer composition on gas, liquid, and char formation.

Strength Testing of Composites with Recycled Reinforcements

- Prepare composite samples with virgin and recycled fibers by resin transfer molding.
- Characterize tensile properties according to ASTM D 638-01 for Tensile Properties of Plastics.
- Characterize interlaminar shear strength according to ASTM D2344 for short beam shear testing of high-modulus composite materials.

Feasibility Study Quality Economics for Comparison of Technologies

- Compare the economics of microwave gasification of polymer matrix composites to conventional pyrolysis.

Anticipated Phase II Objectives

- Design, build and test small pilot-scale microwave assisted gasification reactor for scale-up tests to more closely mimic a commercial system.
- Develop methods to microwave gasify composite samples and reclaim fibers from existing commercial products.
- Ascertain the effect of polymer composition, mixed polymer samples, and metal or ceramic content on gas product generation and fiber strength.
- Continue to increase the compositional stability and catalytic activity of particulate reinforcements with dielectric heating capability.
- Determine the feasibility of microwave assisted gasification for other automotive feedstocks such as tires, natural-fiber/polymer composites, and neat polymers.
- Develop a marketing and business plan for commercialization of the technology including feasibility study quality economics for comparison of technologies.

Summary

The objective of this project is to develop a Microwave Assisted Gasification (MAG) process for converting polymer matrix composites (PMC) such as fiber reinforced plastics (FRP) to viable value added products without reducing the size, strength or stiffness of the reinforcement fibers. This will include the development of new fiber or particulate reinforcement compositions that act as internal dielectric heaters when exposed to microwaves.

In this project, the MAG process will efficiently convert the organic matrix of PMCs to usable chemicals or fuels without the degradation in strength or size of the inorganic reinforcement, allowing it to be directly recycled into new composite structures. The microwaves will increase the efficiency and reaction rate of the gasification of the polymer matrix by enhancing the catalytic activity. Fiber or particulate reinforcements will be selected for microwave susceptibility to dielectric heating, so that when exposed to microwaves, the reinforcements will heat the plastic matrix from the inside.

Economically, the MAG process has many benefits to offer versus conventional pyrolysis or mechanical separation methods. Energy costs for microwave heating are comparable to conventional heating methods, but for the proposed MAG process, the costs are offset by quicker, more efficient gasification and savings by eliminating the need for separation, purification, or flotation processes. The MAG process also provides for full-size, high strength and stiffness fiber recycling.

Dielectric Heating Assessment of Fiber and Particulate Compositions

The dielectric heating susceptibility of 27 particulate and fiber compositions were tested at 50% microwave power. As shown in Table 1, six types of compounds were tested. Common particulate additives for polymer matrix composites showed low dielectric heating susceptibility.

Most commercial glass formulations showed low dielectric heating susceptibility. One formulation heated to >50°C, which shows that glass compositions could be optimized for dielectric heating susceptibility.

Metal oxide powders showed varying dielectric heating susceptibility (see Figure 1). The extent of heating depended on metal selection and metal oxidation state. One metal oxide which is a combination of +2 and +3 oxidation states showed a decrease in dielectric heating susceptibility as the M^{+2} oxidized to M^{+3}.

All powders which are well-known dielectric heaters showed heating to >100°C within 5 minutes at 50% microwave power (see Figure 2). These tests illustrated the effect of powder particle size and sample size.

If enough sample was provided, composite reinforcement fibers showed good dielectric heating within 1-2 minutes (see Figure 3).

The best dielectric heaters were proprietary oxygen-storage catalysts (see Figure 4). Most heated to >500°C within 3 minutes at 50% microwave power.

Table 1. Summary of materials tested for dielectric heating.

Type of Particulate or Fiber	Number of Sample Compositions Tested
Commercially available oxides	6
Common particulate reinforcements for composites	2
Well-known dielectric heaters	4
Fibers	3
Proprietary oxygen-storage catalysts	5
Glass compositions	7

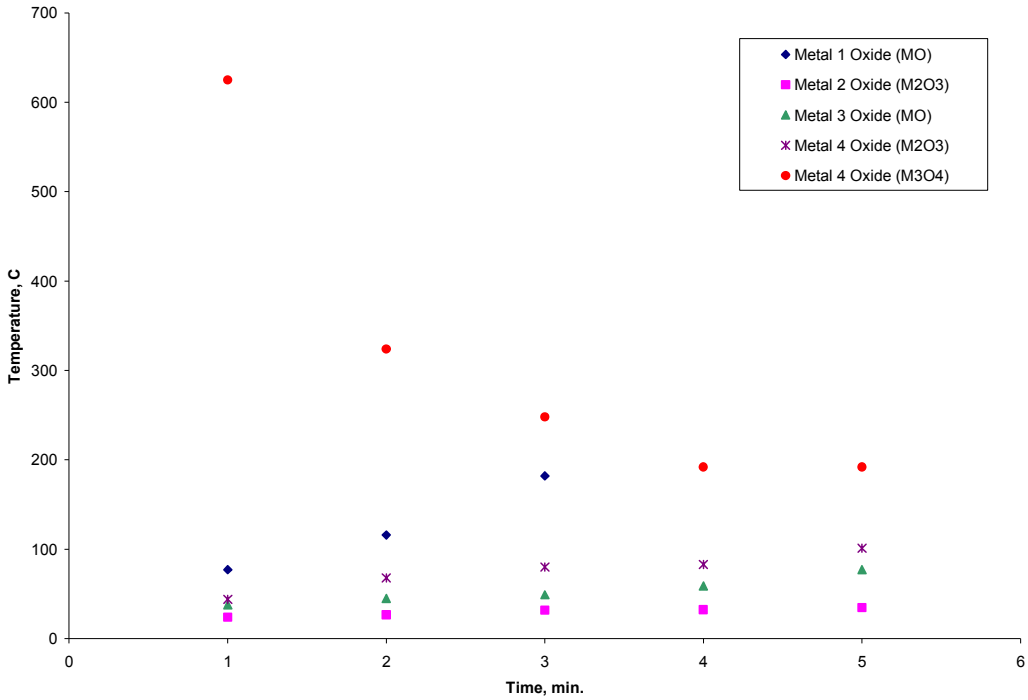

Figure 1. Dielectric heating susceptibility of 5 metal oxide powders.

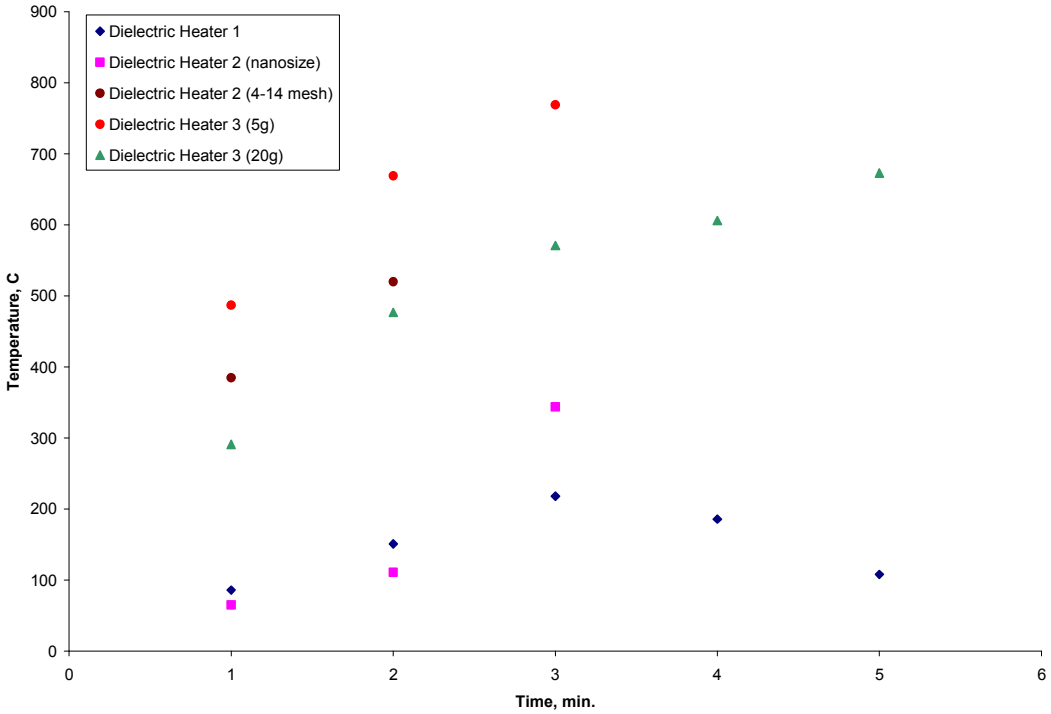

Figure 2. Dielectric heating susceptibility of well-known dielectric heaters.

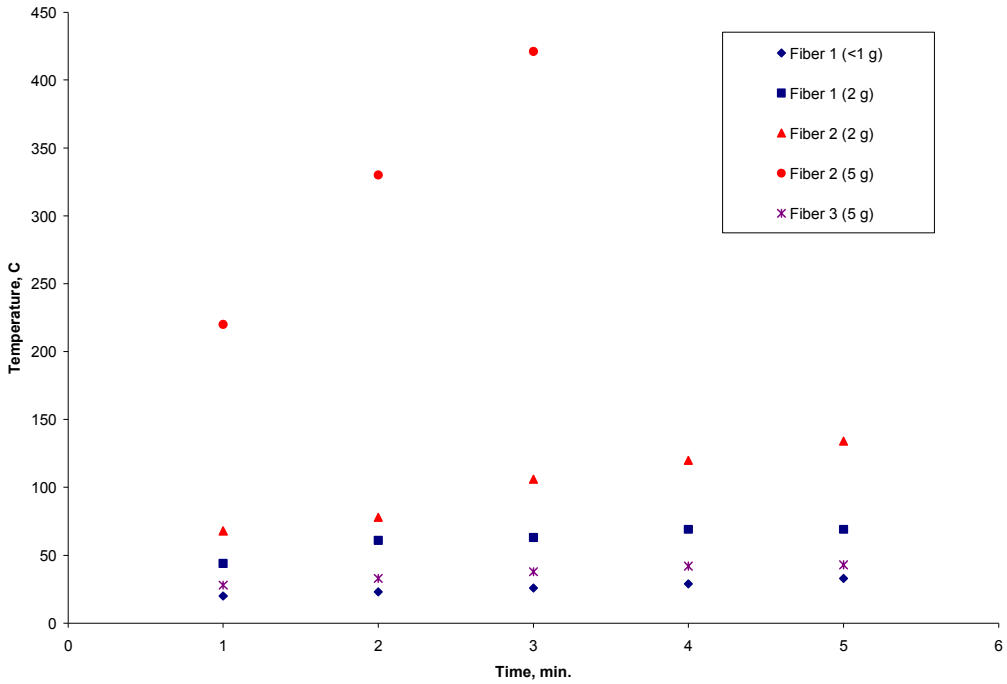

Figure 3. Dielectric heating susceptibility of reinforcement fiber compositions.

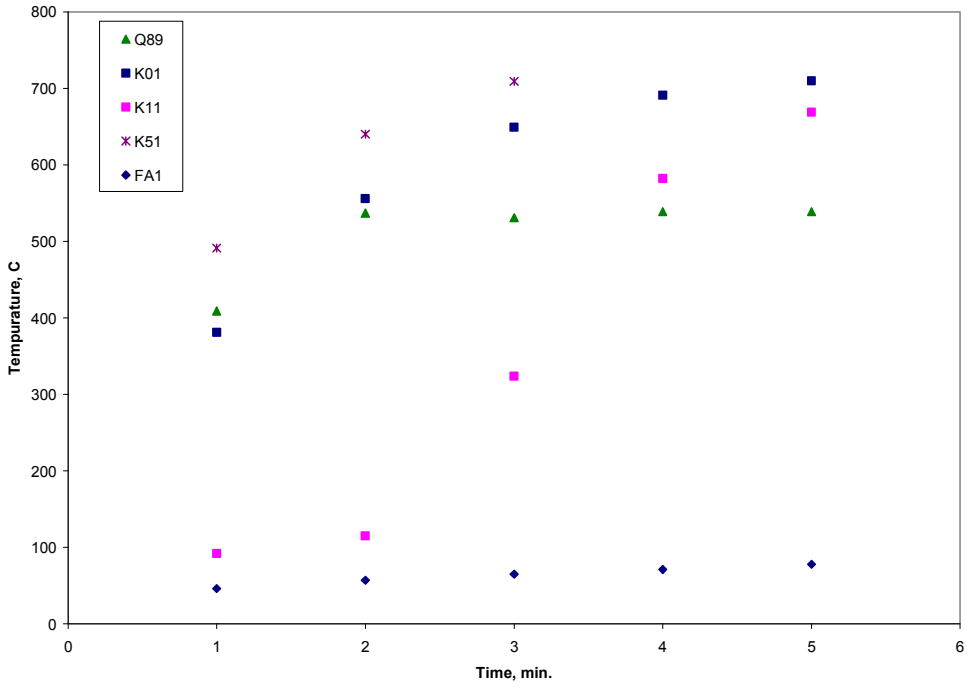

Figure 4. Dielectric heating susceptibility of proprietary oxygen-storage catalysts.

Microwave Assisted Gasification of Polymer Matrix Composites

Many research groups are working on pyrolysis of the organic matrix which is decomposing the polymer in the absence of oxygen. Heating a polymer matrix to 450–500°C can be sufficient to break down many different polymers into a wide range of products including CO, H_2, and hydrocarbons including methane and ethane. However, pyrolysis at 500°C has many waste products that are difficult to separate from the

fibers. Raising the pyrolysis temperature can minimize the creation of byproducts but at higher temperatures, fibers become brittle and lose strength.

Microwave Assisted Gasification can be used to optimize CO and H_2 generation over other gaseous products such as CH_4 or CO_2, increase gaseous versus liquid product generation, and reduce operating temperatures and waste products to generate full-size, high strength fibers with clean surfaces.

At 275–325°C, Microwave Assisted Gasification of epoxy samples showed mostly CH_4 gas generation (see Figure 5). The addition of 1% oxygen-storage catalyst increases the H_2 generation (see Figure 6). Fiber-reinforced composite samples showed the best gas product composition (see Figure 7) and after gasification of the polymer matrix, fibers were undamaged with clean surfaces and no byproducts (see Figure 8).

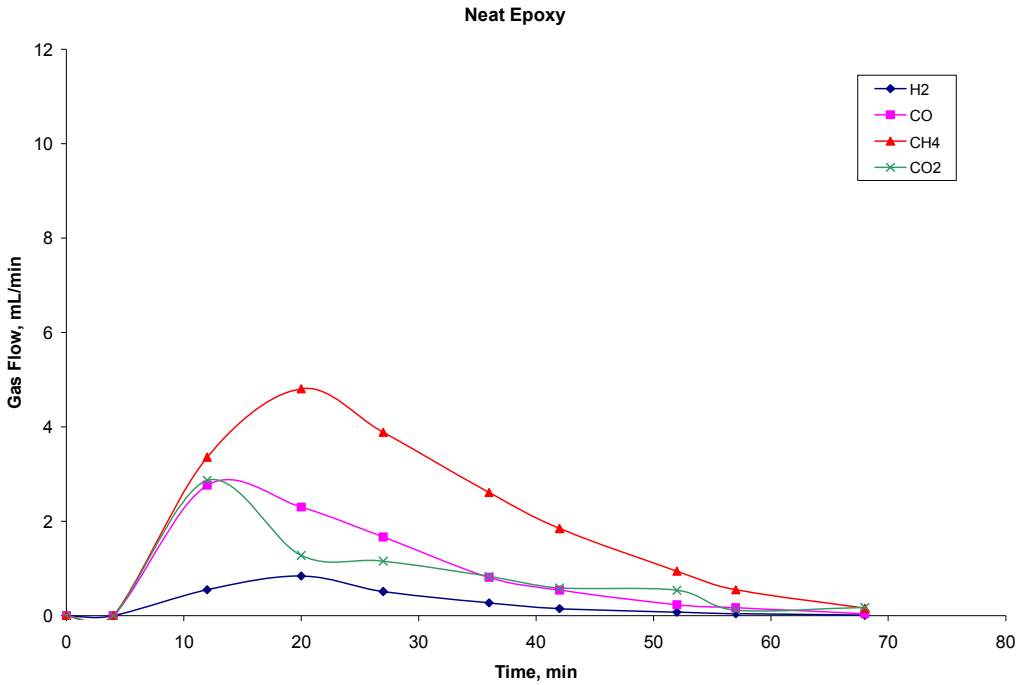

Figure 5. Microwave Assisted Gasification of epoxy sample.

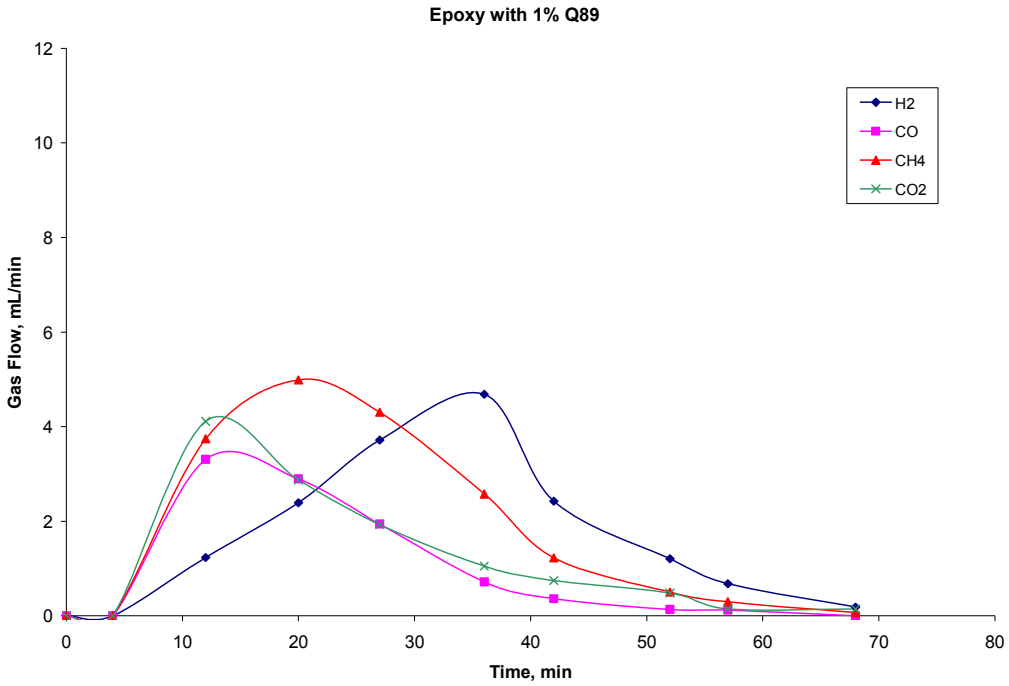

Figure 6. Microwave Assisted Gasification of epoxy sample with 1% Q89 catalyst.

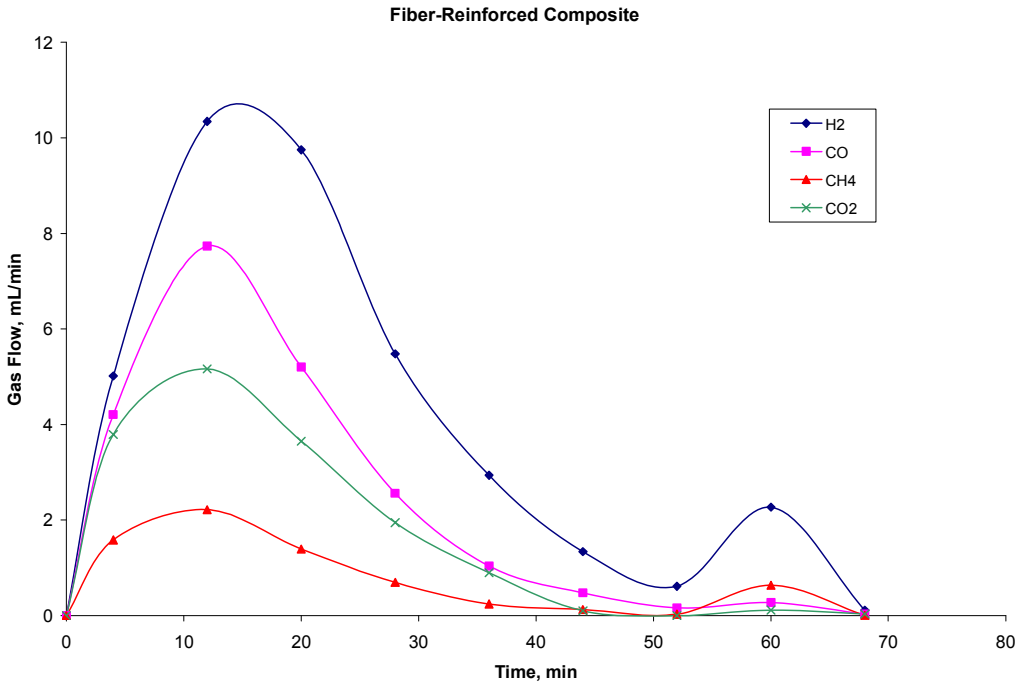

Figure 7. Microwave Assisted Gasification of fiber-reinforced composite sample.

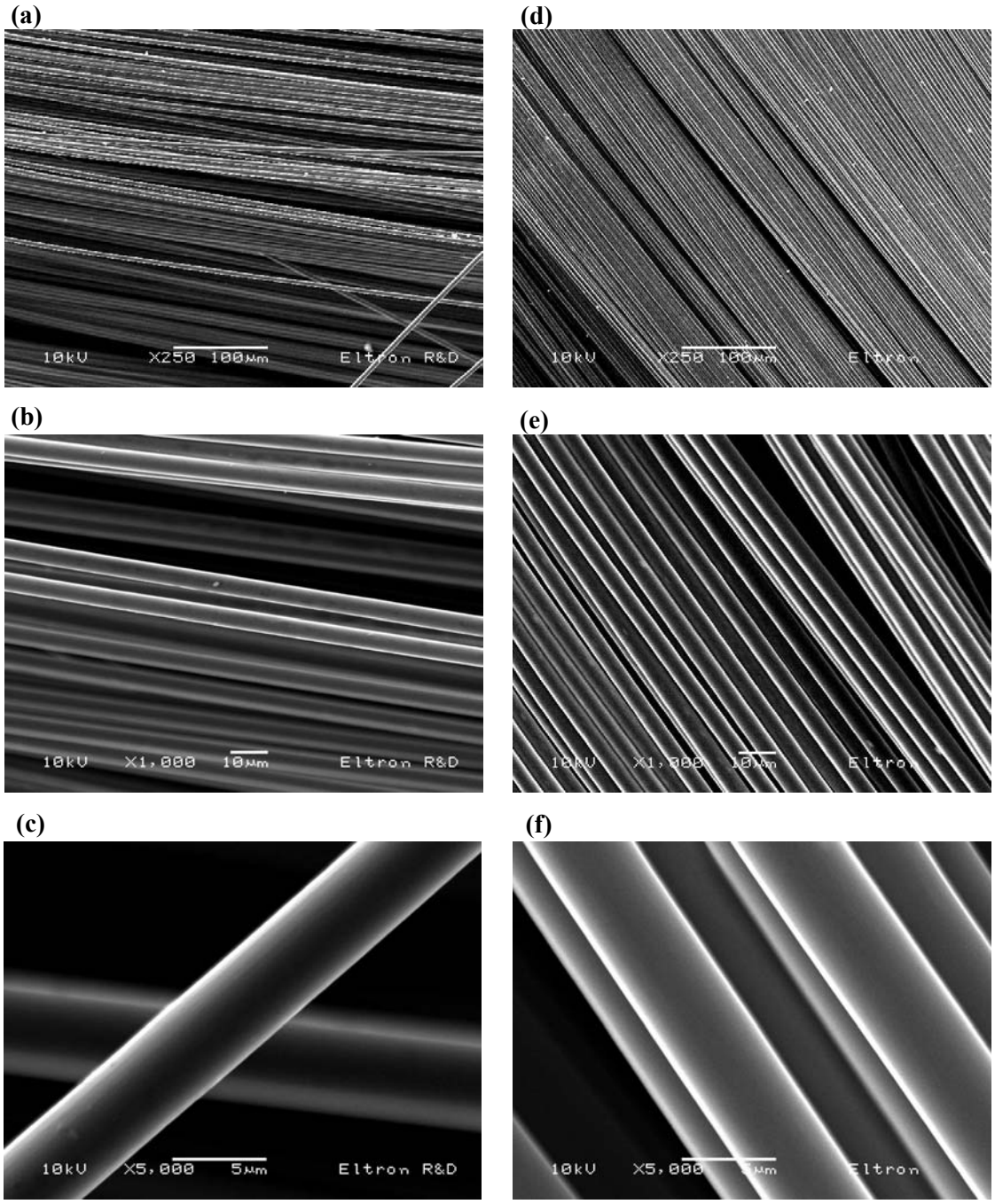

Figure 8. SEM photos of virgin fibers (a, b, c) compared to fibers after Microwave Assisted Gasification of the polymer matrix (d, e, f).

12. MATERIALS CROSS-CUTTING R&D

A. Technical Cost Modeling

Principal Investigator: Sujit Das
National Transportation Research Center (NTRS)
2360 Cherahala Boulevard
Knoxville, TN 37932-6472
(865) 946-1222; fax: (865) 946-1314; e-mail: dass@ornl.gov

Technology Area Development Manager: Joseph A. Carpenter
(202) 586-1022; fax: (202) 586-1600; e-mail: joseph.carpenter@ee.doe.gov

Expert Technical Monitor: Philip S. Sklad
(865) 574-5069; fax: (865) 574-6098; e-mail: skladps@ornl.gov

---

Contractor: Oak Ridge National Laboratory (ORNL)
Contract No.: DE-AC05-00OR22725

Objectives

- Address the economic viability of new and existing lightweight materials technologies.
- Develop technical cost models to estimate the cost of lightweight materials technologies.

Approach

- Address the economic viability of lightweight materials technologies supported by the Lightweighting Materials (LM).
- Use cost modeling to estimate specific technology improvements and major cost drivers that are detrimental to the economic viability of these new technologies.
- Derive cost estimates based on a fair representation of the technical and economic parameters of each process step.
- Provide technical cost models and/or evaluations of the "realism" of cost projections of lightweight materials projects under consideration for LM funding.
- Examine technical cost models of lightweight materials technologies that include (but are not limited to) aluminum (Al) sheet; carbon-fiber precursor and precursor processing methods; fiber-reinforced polymer composites; and methods of producing primary Al, magnesium (Mg), and titanium (Ti) and Mg alloys with adequate high-temperature properties for powertrain applications.

Accomplishments

- An update of primary Mg production-cost estimates for automotive applications was completed. One of the two journal articles submitted based on the last fiscal year (FY) report on the cost-benefit evaluation of the Phase II LM projects funded during the FY 2000-2004 period was accepted for publication in Research Evaluation. Life-cycle inventory data collection for several Mg manufacturing technologies was completed and a paper was published on the preliminary, comparative life-cycle assessment of a lightweight automotive part.

Future Direction

- Complete the life-cycle analysis task for the multinational Mg Front End Research and Development (MFERD) project (see 6.C). A life-cycle assessment of carbon-fiber polymer composites will also be initiated.
- Complete a cost assessment of the proposed LM future vehicle weight reduction goal of 50% by the year 2011, starting with 25 % in 2008.
- Continue individual project-level cost modeling to identify specific technology improvements and major cost drivers that are detrimental to the economic viability of these technologies.

Primary Mg Production Cost Assessment Update

This activity updated earlier, FY 2002 work which focused on primary Mg production cost estimates to provide a sound forecast of the long-term competitiveness of Mg in automotive applications. Competing Mg production technologies are considered in this assessment, with particular emphasis on the long-term viability of the inexpensive supplies using Chinese production technology. Also considered in the comparative production-cost analysis are two yet-to-be-commercialized production processes. Production-cost estimates of competing technologies are disaggregated by major cost categories using the most recent information available from the literature. At first, the recent price trend and the weight-savings potential of competing materials are considered to determine what the primary Mg production costs need to be for Mg to be a viable material/technology option now and in the coming decade. A discussion of the future viability of Mg use in automotive applications based on the potential sources of Mg for the U.S. market, the recent supply trend, production-cost estimates, and potential demand has also been covered in this assessment.

Five primary Mg production processes are considered in this assessment:

- Conventional western electrolytic reduction
- Western Pidgeon (thermal reduction)
- Chinese Pidgeon (thermal reduction)
- Carbothermic, and
- Solid oxygen-ion conducting membrane (SOM) technology developed by Boston University.

The SOM technology, which is still at the laboratory-scale, is electrochemical in nature. A current is passed through a flux containing Mg oxide in a stainless steel crucible, which works as a cathode.

Figure 1 shows an operating cost range of $0.52–$0.87/lb and total production cost range of $0.62–$1.41/lb for the five production processes considered here. Major contributors to cost-effectiveness of the conventional Mg production processes lie in capital and raw material costs for electrolytic and thermal reduction processes, respectively. The lower cost of materials under the electrolytic reduction is due to credits taken for by-products produced. Fluctuations in the market price of raw materials would have greater impact on the total cost of thermal-reduction processes. Numerous processing steps for raw minerals contribute significantly to the higher conventional electrolytic production cost. Because of financial constraints, electrolytic plant expansions are unlikely, although expansion could reduce per-unit overhead costs. Capital costs continue to cause significant financing problems for proposed new electrolytic production capacity in Western economies. The projected Mg cost estimate is consistent with the Mg price projection of $1.27/lb made by North Pacific Alloys for the technical and economic viability of a proposed 150,000 tonnes/year Mg extraction plant from Mg silicates.

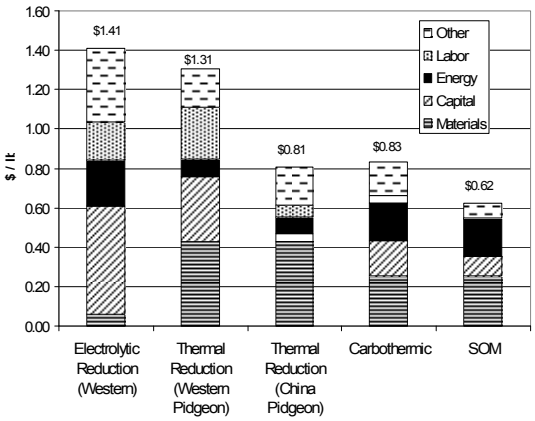

Figure 1. Production cost of major primary Mg production technologies.

The estimated total Chinese Mg production cost is around $0.81/lb—consistent with the Chinese free-market Mg price observed during the past few years. This cost is significantly lower than the estimated Mg production cost of $1.41/lb and $1.31/lb for the Western electrolytic and thermal producers, respectively. China's significantly lower capital and labor costs and its position as the world's biggest producer of ferrosilicon help it to maintain its role as the low-price world Mg supplier. It appears that, in past years, Chinese producers have fully recovered their production costs. With Chinese business becoming increasingly motivated by profits and with Chinese producers having attained significant market share, the Chinese Mg market price has increased and may remain high in the future. In fact, Mg prices in China increased steadily in 2006 after the export rebate on all Mg products was reduced to 5% from 13% at the end of 2005. By the end of the second quarter of 2007, free-market Chinese Mg has increased to $1.18-$1.23/lb range. Energy price increases would affect Chinese Mg production plants less than Western producers that use energy-intensive electrolytic reduction. It is anticipated that any new process could compete with the cheap Chinese Pidgeon process if it could produce Mg with operating costs in the $0.50-$0.75 per pound range.

Two yet-to-be-commercialized Mg production processes could be competitive with the low-cost Chinese Pidgeon production technology. Total estimated Mg production costs for these processes--the carbothermic and SOM processes--are $0.83/lb and $0.50/lb, respectively. The total Mg production cost using the rapid plasma-quench carbothermic process has been reported by Donaldson and Cordes to be $0.72/lb, without consideration of any labor cost associated with production. Both production technologies would have similar raw material costs that would be lower than material costs for the conventional Pidgeon process. As a simpler production technology with lower capital-cost requirements, less processing of the raw material, and lower labor costs, SOM production cost equals about one-third of the conventional electrolytic production cost.

Life-Cycle Analysis of MFERD (See 6.C)

This project is a Canada-China-USA collaborative research and development effort which was kicked-off during the second quarter of FY 2007 as one of the ten enabling technology development tasks to analyze the energy consumption and greenhouse gases effect of Mg production, i.e., CO_2 emissions in primary Mg production (electrolytic process, traditional and improved Pidgeon processes) and SF_6/SO_2 other emissions in Mg casting, wrought-alloy processing as well as recycling. A total life-cycle analysis including vehicle-use and the end-of-life stages will be considered to capture the benefits of light-weighting automobiles such as fuel-economy improvements and associated emission reductions. Environmental performance of the advanced Mg-based front end design of a Cadillac CTS will be compared against the conventional steel-based design. A work plan has been developed jointly in which the US contribution to this task would be in providing: 1) life-cycle inventory data for the baseline conventional steel vehicle; 2) life-cycle inventory data for major Mg part fabrication technologies (e.g., casting, extrusion, and sheet forming, etc.) and for North America electrolytic primary Mg production process; and 3) energy and estimates for the use phase. To date, the preliminary life-cycle analysis framework has been developed using the commercial software SimaPro, and the framework has been populated with some readily-available, public-data databases. In addition, the methodology including data has been developed to estimate energy and emissions at the use life-cycle stage. Preliminary results using the framework have also been presented at an international conference. Life-

cycle inventory data collection for the following Mg production technologies have either been completed or underway from the US side by using a questionnaire developed:

- Chinese Mg-alloy production (AE44, AJ62, AM50, AM60, AZ91)
- Western die casting (AM50, AM60, AZ91)
- Chinese die casting (AE44, AJ62, AM50, AM60, AZ91)
- High-vacuum die casting
- Secondary Mg production
- Conventional sheet forming (AZ31)
- Twin-roll casting
- Extrusion

Conclusions

The potential for Mg use in automotive applications looks promising because the prices of competing lightweight materials are trending upward and the lower-price Chinese Mg remains in good supply and is priced commensurate with its production cost. It is difficult to say how long the strong demand pressure on lightweight materials other than Mg will continue. It is estimated that the Chinese Mg production cost is around $0.80/lb, but higher raw material costs, reduced tax incentives for exports of raw materials, a booming Chinese economy, currency revaluation, and environmental compliance costs may increase the cost of Chinese-produced Mg as seen during 2007. Anticipated inexpensive supplies from the non-Western economies are likely to remove cost from the list of major barriers to wide-range use of Mg in automotive applications. The lack of available financing for the huge capital investment required to expand existing electrolytic plant capacity or add new electrolytic capacity is a barrier to more cost-effective Mg production in the West, even though these higher-capacity plants could offer lower overhead costs. New, cost-effective Mg supply sources appear to be limited, and it is unlikely that some of the yet-to-be-commercialized technologies considered here will come online, although they do hold significant promise to be competitive with the low-cost Chinese Pidgeon process. At the 2006 U.S. price of $1.13/lb, Mg was competitive with Al and galvanized steel sheet for automotive applications. However, since the beginning of 2007, Mg supplies have been tight with major supplies limited to China, Russia, and Israel, resulting in the U.S. western spot price range of $1.64-$1.69/lb – reaching for the first time above the conventional Western Mg production costs of $1.41/lb and $1.31/lb for electrolytic and thermal reduction, respectively. This recent Mg price increase reduces its cost-effectiveness compared to Al and galvanized steel sheet. Currently, anti-dumping duties help Western producers recover their operating costs only. If prices adjust to better reflect full Western production costs as seen during 2007, Mg substitution will become less attractive.

The life-cycle analysis framework, including a majority of the life-cycle inventory data collection for Mg manufacturing technologies, has been completed for the life-cycle analysis of mg front-end research and development. With the availability of Mg front end design, life-cycle analysis will be completed during the coming fiscal year.

Presentations/Publications/Patents

“Preliminary Comparative Life Cycle Assessment of an Automotive Part :Steel, Mg Alloys, Al Alloys, Advanced High Strength Steel**,”** presented at the 3rd International Conference on Light Metals Technology - LMT2007 in Saint-Sauveur, Québec, Canada from September 24-26, 2007.

B. Intermediate-Rate Crush Response of Crash Energy Management Structures

Principal Investigator: J. Michael Starbuck
Oak Ridge National Laboratory (ORNL)
P.O. Box 2009, Oak Ridge, TN 37831-8048
(865) 576-3633; fax: (865)-574-8257; e-mail: starbuckjm@ornl.gov

Project Manager, Composites: C. David Warren
ORNL
P.O. Box 2008, Oak Ridge, TN 37831-6065
(865) 574-9693; fax: (865) 576-4963; e-mail: warrencd@ornl.gov

Technology Area Development Manager: Joseph A. Carpenter
(202) 586-1022; fax: (202) 586-1600; e-mail: joseph.carpenter@ee.doe.gov

Expert Technical Monitor: Philip S. Sklad
(865) 574-5069; fax: (865) 574-6098; e-mail: skladps@ornl.gov

---

Contractor: ORNL
Contract No.: DE-AC05-00OR22725

Objective

- Develop a unique characterization facility for controlled, progressive-crush experiments at intermediate rates of automotive materials (polymer composites, high-strength steels, and aluminum (Al)) and structures.
- Study the deformation and failure mechanisms of automotive materials subjected to crush forces as a function of impact velocity.
- Obtain specific energy absorption (SEA) and strain data and correlate with deformation and failure mechanisms to describe the unknown transitional effects from quasi-static to high loading rates for polymer composites.
- Characterize the strain-rate effects for metallic materials and components.
- Provide access to unique test capabilities to university, industry, and government users for collaborative research.

Approach

- Develop a unique, high-force (500-kN), high-velocity (8-m/s), servo-hydraulic machine to conduct progressive-crush experiments on structural components at intermediate rates.
- Use high-speed imaging to observe and document deformation and damage mechanism during the crush event.
- Conduct strain measurements at discrete locations and explore full-field measurements of strains and curvatures.
- Coordinate polymer composites investigations with the Automotive Composites Consortium (ACC) Energy Management Group (EMWG). (See 8.I).
- Coordinate steel investigations with the Automotive/Steel Partnership (A/SP).

Accomplishments

- Completed preliminary octagonal tube tests in support of the A/SP project. (See 5.G.)
- Completed diagnostic tests on a high-rate (18-meter/second) test machine to better understand inertia effects in the test data.
- Updated the high-rate data-acquisition program to include strain gages and extensometers, and improved interface.
- Completed User Project with Quickstep Technologies.
- Completed User Project with L&L Products.
- Completed User Project with Army Corps of Engineers, Engineering Research and Development Center.
- Completed scoping tests on high-rate tensile coupons for General Motors (GM)/ACC User Project.

Future Direction

- Explore techniques for full-field measurements of strains and curvatures.
- Explore techniques for local strain measurements on the 18-meter/second test machine.
- Complete octagonal tube tests in support of the A/SP project.
- Complete base-metal strain-rate characterization tests.
- Complete User Project with the ACC.
- Complete second User Project with L&L Products.
- Complete second User Project with Army Corps of Engineers

Introduction

Progressive crush is an important mechanism by which the kinetic energy of a traveling automobile is dissipated in a collision to protect the safety of occupants. Unfortunately, the mechanisms governing the progressive-crush response of some emerging automotive materials are not well understood. Additionally, many of these materials are known to exhibit responses that are sensitive to rate of loading.

Understanding the influence of impact velocity on the crush response of materials and structures is critically important for crashworthiness modeling inasmuch as collisions occur at a range of velocities. Additionally, from a structural standpoint, the deformation (or strain) rate is generally not unique from either a spatial or temporal standpoint. Consequently, it is important to quantify the behavior of materials at various strain rates.

Test Machine for Automotive Crashworthiness (TMAC)

Typically, standard test machines are employed for experiments at quasi-static rates, whereas drop towers or impact sleds are the convention for dynamic rates. These two approaches bound a regime within which data, for experiments at constant impact velocity, are not available by conventional experimental practice. This regime is termed herein the intermediate-rate regime and is defined by impact velocities ranging from 1 m/s to 5 m/s. Investigation of rate effects within this regime requires experimental equipment that can supply a large force with constant velocity within these rates.

Using a drop tower or sled at intermediate rates, although technically possible, is problematic due to the prohibitively large mass required to maintain constant velocity during the crush. Consequently, ORNL and the ACC collaborated to define specifications for a unique experimental

apparatus that mitigates the shortcomings of existing equipment. MTS Systems Corporation designed and built the servo-hydraulic test machine, referred to as the TMAC. TMAC is uniquely capable of conducting controlled, progressive-crush tests at constant velocity in the intermediate velocity range (i.e., less than 5 m/s) because of the large energy available at those rates and the sophisticated simulation and control software that permits velocity uniformity to within 10%.

The new experimental facility will be used to understand the crush behavior between the static and dynamic (8-m/s) conditions. The original installation of the TMAC, shown in Figure 1, was at the National Transportation Research Center (NTRC) Knoxville, Tennessee. Since then, TMAC has been relocated to ORNL.

Figure 1. Installation of TMAC in the NTRC composite's lab.

Status

Since the last reporting period, activities have focused on supporting users, developing and promoting user interactions, improving data acquisition, and expanding test capability for higher-rate coupon tests.

Interactions with potential users have taken place with Rutgers, Massachusetts Institute of Technology, SAE High Strain Rate Plastics Consortium, GM, Ford, Imperial College (London, England), Washington University, University of Utah, and L&L Products. Also, discussions continued with the University of South Carolina and Correlated Solutions towards developing a full-field, dynamic-strain measurement using digital image-correlation techniques.

In addition to promoting user programs, continued support was provided to the development of a crashworthiness chapter for the military's composite design guide, CMH-17 (formerly MIL-HDBK-17), and the start of a technical division on the Dynamic Response of Materials within the Society for Experimental Mechanics.

Project Support Activities

Tube tests were completed on TMAC in support of the A/S-P Strain Rate Characterization project (see 5.G). These tubes had an octagonal shape with spot welds down the edges of the tube. Preliminary tests were run to determine the initial folding pattern and appropriate triggering mechanism. These tests were successful and the rest of the tubes needed to complete the test matrix were machined and instrumented. Tests are planned for fiscal year (FY) 2008. In addition to the tube tests, coupon-level strain-rate characterization tests are planned on different high-strength base metals. Dynamic-testing issues associated with these tests are currently being addressed through diagnostic testing.

User Programs

A user project was completed for Quickstep Technologies. Aaron Brighton, Dale Brosius and Ben Ludtka from Quickstep visited ORNL to carry out prismatic-tube crush tests on TMAC. A total of 72 crush tests were run over a range of impact speeds of 0.25, 0.5, 0.75, 1, 2 and 4 m/s. The tubular test specimens were all produced using an Al male mandrel connected to the Quickstep machine. The Quickstep machine utilizes a heat-transfer fluid to provide the required heat to cure the resin system in fiber-

reinforced composites. Two material systems were investigated. The first consisted of a Toray G83C quick-cure resin prepreg with a T700 fiber in a 2x2 twill weave. The G83C resin requires 3 minutes of curing time at temperature with the Quickstep process. The other material system consisted of a St Gobain product called Twintex which is a glass-commingled polypropylene thermoplastic composite. The Twintex is a thermoplastic-matrix material and requires about 30 seconds to cure at temperature. All of the tubes contained four layers of material layered in a "Swiss roll" formation around the mandrel that was then shrink taped. All specimens were machined square at the ends and had a 45-degree chamfer machined in one end. Specimens were approx 240-mm long with a 60-mm inner diameter. Tests were conducted using just the 45-degree chamfer as an initiator and then both the 45-degree chamfer plus a 2.5-mm radius plug as initiator. Testing was 100% successful with no lost specimens, video or data. Figure 2 shows one of the failed specimens being held by one of the Quickstep representatives.

Figure 2. Failed Quickstep tube.

The second user project completed was an exploratory one for L&L Products. L&L products manufactures reinforced, composite/steel box-beam structural components that are integrated into key locations in vehicles to improve vehicle crashworthiness. TMAC can conduct tests at rates higher than normally available from other test methods and can supply the needed structure-performance data necessary for evaluating their product. To help L&L Products define their test plan, 14 exploratory bend-crush tests were conducted to explore the suitability of their custom, three-point bend-test fixture and verify the suitability of the test for collecting the desired high-rate data. Figure 3 shows the test set-up and Figure 4 shows some of the failed specimens. All tests were successful and future testing is scheduled this fall to complete their test matrix consisting of over 100 specimens at various rates up to 8 m/sec. This was the first non-axial crush testing to be preformed on TMAC and was successful in demonstrating its use for studying side impact.

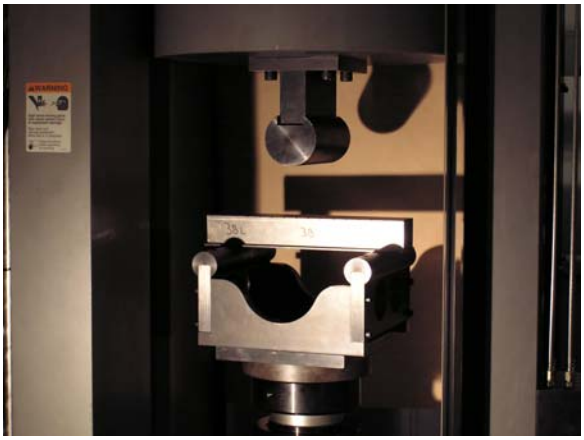

Figure 3. Three-point bend-test set-up on TMAC.

Figure 4. Failed L&L Products specimens.

The third user project completed was for the Army Corps of Engineers, Engineering Research and Development Center. The research objective for this proposal was to investigate the effects of strain-rate and heat-of-deformation and their significance on the energy-absorption process during dynamic progressive-crush deformation. Ductile, metal-alloy structures that rely on controlled, progressive plastic deformation of

material along specific paths or "traveling foldlines" in the geometry can achieve extremely high energy-absorption capability and have significant potential to provide advanced levels of impact and blast-load protection. However, the material response is very complex because, at a particular location in a foldline where most of the energy is absorbed by severe, localized plastic deformation, the material undergoes transient, nonlinear, multiaxial stress/strain history paths in the low-to-high strain-rate range and load magnitudes and energy-absorption capability is influenced by inertia, strain rate, temperature and heat-of-deformation. Currently, there are few data or little understanding of the resulting material response under dynamic, progressive-deformation conditions and both are critical for developing accurate, predictive, computational material models and for obtaining advanced material solutions for protective structures applications.

The experimental approach for the proposed work consisted of performing dynamic axial crush testing on thin-wall, steel box components for a constant geometry (cross-section: 50 mm x 50 mm by 1.40 to 1.65-mm thickness (2 in x 2 in x 0.055-in to 0.065-in thickness) and length of 30.5 cm (12 in)) and four steel materials: A36 structural steel, A513 mechanical steel, 316SS stainless steel and 304SS stainless steel. The tube specimens had groove collapse initiators and were quasi-statically precrushed. For the dynamic tests on TMAC, the tube specimen ends were constrained by end caps. All tests were performed at the constant velocity of 6 meters/second. This was the first user project on TMAC to try incorporating a high-speed infrared camera to capture the heat generated during high-speed deformations in metals. Temperature contours were successfully captured during the test, but calibration of the results needs further investigation.

The GM/ACC user project is to conduct high-rate coupon tests on carbon-fiber braided material. This same material has been used extensively in other ACC projects for tube-crush studies. The data to be generated from these tests are in support of a rate-sensitive material model developed by Stanford University for predicting the crush behavior of carbon-fiber tubes. Preliminary scoping tests were conducted on the high-rate coupon test machine (this equipment is described in the next section). The coupons used for these tests were machined from unidirectional, braided plaques. The test plan consists of 25°, 45°, and 65° off-axis coupons tested at 5 different strain rates (0.01, 0.1, 1.0, 10.0, and 100/second). The preliminary tests were completed to determine load- and strain-measuring requirements and any corresponding data-acquisition modifications. It was determined that updates to the data-acquisition hardware were needed to increase scan rates and that strain gages were the preferred method for measuring strain. The hardware was updated and all specimens were returned to GM to instrument with strain gages. Completion of the test matrix is planned for the first quarter of FY 2008.

High-Rate Coupon Test Machine

To complement the TMAC capability, a high-rate coupon test machine was designed, fabricated by MTS, and installed at ORNL. Where TMAC provides the capability for a large-force (500 kN static), structural-level test, this machine was designed to conduct low-force (40 kN static), coupon-sized tests under primarily tensile loads. A typical size coupon would be a dog-bone strip where the gage section is 15 mm wide with a thickness of 3 mm. This type of test is ideal for generating rate-sensitive stress-strain curves in development of basic material constitutive laws. The machine has a maximum crosshead speed of 18 meters/second with a 400-mm total stroke capacity. The actually working stroke is reduced to 175 mm when installing a slack adapter to allow for the actuator to get up to constant speed before loading the specimen. These specifications were accomplished by a using a 400-gallon/minute (gpm) servo-valve and 50-gallon accumulators (see pictures 5 and 6). Another feature of the test machine is the use of low mass grips designed to reduce ringing in the system thereby minimizing inertial effects in the load signal. The grips were based on a Colorado School of Mines design and are shown in Figure 7.

Figure 5. High-rate (18-meter/second) coupon test machine.

Conclusions

TMAC provides a unique capability to measure the specific energy absorption on crush tubes and other specimen geometries as a function of (constant) impact velocity within a range from quasi-static to 8 meters/second. To complement this capability, another new machine was installed for conducting coupon-level tests up to 18 meters/second.

User interest in this equipment remains very high with follow-on projects and new projects being in the draft stage. TMAC was also instrumental in meeting project objectives for the A/SP. In all of these tests, high-speed video was recorded to document the failure mechanisms using a state-of-the-art, complementary metal-oxide semiconductor (CMOS) camera that was procured for the TMAC installation.

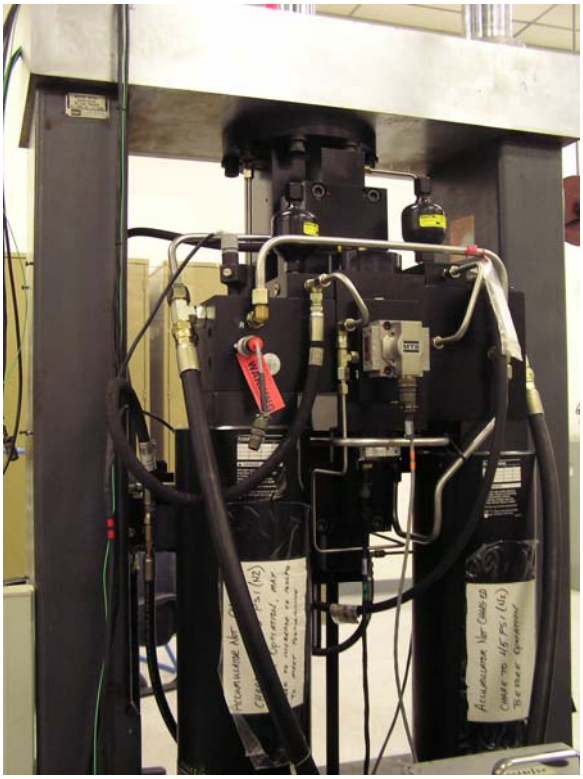

Figure 6. Accumulators and servo-valve for high-rate coupon-test machine.

Figure 7. Low-mass grip used in high-rate coupon test machine.

Presentations/Publications/Patents

None.

C. High-Rate Damage and Fracture, Experimentation, Simulation and Visualization

Philip Gullett: Co-Principal Investigator
Assistant Professor,
Civil and Environmental Engineering
Mississippi State University (MSST)
Walker Bldg., Rm. 235 M
Mississippi State, MS 39762
(662) 325-5486; fax: (662) 325-7189; e-mail: pmgullett@engr.msstate.edu

Mark F. Horstemeyer: Principal Investigator
Center for Advanced Vehicular Systems (CAVS) Chair in Solid Mechanics & Professor, Mechanical Engineering
MSST
206 Carpenter Bldg., PO Box ME
Mississippi State, MS 39762
(662) 325-7308; fax: (662) 325-7223; e-mail: mfhorst@me.msstate.edu

Tomasz Haupt: Co-Principal Investigator
CAVS, MSST
Box 5405, Mississippi State, MS 39762
(662) 325-4524, fax: (662)325-5433, e-mail : haupt@cavs.msstate.edu

David Oglesby: Research Associate II
CAVS, MSST
200 Research Blvd.
Mississippi State, MS 39762
(662) 325-6854; fax: (662) 325-5433; e-mail: doglesby@cavs.msstate.edu

Srdjan Simunovic: Co-*Principal Investigator*
Oak Ridge National Laboratory (ORNL)
1 Bethel Valley Road, Oak Ridge TN 37831-6164
(865) 241-3863, fax: (865) 241-0381; e-mail: simunovics@ornl.gov

J. Michael Starbuck: Co-Principal Investigator
ORNL
P.O. Box 2009, Oak Ridge, TN 37831-8048
(865) 576-3633; fax: (865) 574-8257; e-mail: starbuckjm@ornl.gov

Don Erdman: Co-Principal Investigator
ORNL
P.O. Box 2009, Oak Ridge, TN 37831-8048
(865) 576-4069; fax: (865) 574-0641; e-mail: erdmandl@ornl.gov

Joseph A. Carpenter: Technology Area Development Manager
(202) 586-1022; fax: (202) 586-1600; e-mail: joseph.carpenter@ee.doe.gov

Expert Technical Monitor: Philip S. Sklad
(865) 574-5069; fax: (865) 574-6098; e-mail: skladps@ornl.gov

Contractor: MSST
Contract No.: 4000054701

Objective

- Evaluate the strain rate failure of AZ31 magnesium (Mg) for a various stress states.
- Develop a damage model for stress-state dependence of dynamic damage evolution.
- Evaluate numerical procedures for the modeling of monotonic fracture of Mg.

Approach

- Characterize material behavior using Split Hopkinson Bar experiments in compression, tension and torsion.
- Characterize damage nucleation using molecular dynamics.
- Develop damage-evolution-based fracture.

Accomplishments

- Completed high strain-rate compression, metallurgical evaluation, and torsion testing of Mg AZ31.
- Initiated development of multiscale microstructure-property damage-based fracture simulation.
- Developed procedure for molecular-dynamics simulations of void nucleation at polycrystalline triple junctions.

Future Direction

- High strain-rate torsion and tension of AZ31.
- Implementation of microstructure-property damage-based fracture criteria in fracture-simulation code.
- Evaluate void nucleation, growth, and coalescence at the nano-size scale.

Introduction

This report summarizes the state of the experimental and numerical simulation study of fracture mechanisms in AZ31 Mg. This is a joint effort between ORNL and MSST. The aim is an enhanced, multiscale microstructure-property model that can be implemented into commercial codes and be used in high-fidelity crash simulations for the design and optimization of structural Mg components. The development effort will focus on the AZ31 Mg alloy, and a complementary experimental effort will provide experimental data for other Mg alloys that can be utilized for the development of microstructure-property model parameters.

One of the design aspects integral to the development of highly fuel-efficient vehicles is the reduction of overall vehicle weight. Mg has become a central focus in this effort due to its high strength-to-weight ratio, castability, machinability and damping. On a component basis, Mg can potentially result in 30 to 75% weight savings over conventional iron-, steel-, aluminum- and plastic- based designs (Osborne 2005).

Lightweight automotive designs must meet strength and stiffness performance requirements for normal monotonic and fatigue loading as well as provide acceptable response for abnormal loading conditions that lead to localized failure. Lightweight designs must be optimized with respect to weight and be robust with respect to damage, failure and energy absorption. Thus, the efficient use of Mg or any alloy requires the ability to accurately predict mechanical behavior under service loads as well as damage, failure and energy absorption under extreme loads.

The mechanical performance of structural components under service loads is well understood, as component design is based on well-established principles of linear-elastic solid mechanics. Under safety-critical, extreme-loading conditions such as crash, the mechanical behavior

depends on a complex relationship between component geometry, loading, and material microstructure. In particular, component failure is controlled by microstructural (or smaller-scale) phenomena that vary according to deformation history, temperature, strain rate, and stress state.

The DOE and the United States Council for Automotive Research's (USCAR's) United States Automotive Materials Partnership (USAMP) funded the Structural Cast Magnesium Development (SCMD) project, a broad, multi-faceted effort to address concerns related to the use of structural Mg. One outcome of the SCMD project was the effort lead by Horstemeyer et al. (Horstemeyer, Oglesby et al. 2006) to develop a microstructure-property model that included microstructural details that act as the source of damage progression. Horstemeyer's work included detailed multiscale analysis and model development for several Mg alloys targeted for application in structural automotive components.

This current joint ORNL/MSST effort attempts to build on the experimental and computational work of Horstemeyer et al. (Horstemeyer, Oglesby et al. 2006), by extending the investigation of dynamic failure mechanisms and energy-absorption characteristics of Mg through experiment and simulation, as well as provide experimental data for additional Mg alloys. For this investigation, MSST will (1) experimentally evaluate the dynamic behavior of AZ31 Mg under high strain-rate, monotonic loading in compression, tension and torsion. The experiments will focus on the relationship between high strain-rate damage evolution and stress state, and will utilize Split Hopkinson Bar experiments in compression, tension and torsion. Test-sample evaluation includes interrupted tests as well as metallurgical evaluation.

In addition, MSST will initiate a comparative evaluation of existing numerical techniques for the simulation of component fracture in order to assess relative performance for the prediction of fracture evolution and energy release. Leveraging anticipated FY 2008 funding, ORNL will perform experimental evaluation of additional Mg alloys to provide data by which the damage model from Horstemeyer, Oglesby et al 2006 may be calibrated and assessed.

Experimental Evaluation

Commercial wrought Mg alloy AZ31, Table 1, has gained interest for application in lightweight structural automotive components. Significant attention has been directed toward the composition, processing, and mechanical properties of AZ31 (Styczynski, Hartig et al. 2004; Cao, Qian et al. 2006; Marya, Hector et al. 2006; Yi, Zaefferer et al. 2006; Li, Hsu et al. 2007). This study will be examined for failure processes under quasi-static and high strain-rate loading conditions in compression, tension and torsion.

Table 1. Typical composition (wt.%) of AZ31

Al	2.34 – 2.37
Zn	1.04 – 1.11
Mn	0.12 – 0.14
Si	0.06 – 0.11
Mg	Balance

High strain-rate testing has been initiated on a compressive Split Hopkinson Bar system (Lindholm and Yeakley 1968; Nemat-Nasser 2000). The specimens were disk shaped and were oriented perpendicular to the rolling direction. Specimen surfaces were ungrooved and were lubricated. Figure 1 shows the stress-strain response for strain rates ranging from 1000/s through 3000/s. The data reveal the effect of strain rate on yield stress and hardening properties.

Metallurgical evaluation is currently underway, and will consider changes in microstructural features, as well as failure mechanisms. High strain-rate tension and torsion will commence during the next fiscal year.

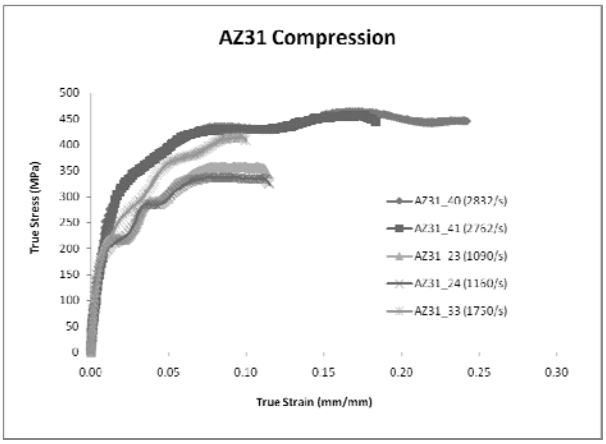

Figure 1. Stress-strain response of AZ31 for various strain rates.

Macroscale Fracture Modeling & Visualization

Ductile fracture initiates from a critical state of void nucleation growth and coalescence. Modeling of localization requires introduction of a length scale to make energy dissipation well defined. The approach taken here utilizes a finite-element framework (Rashid 1997; Rashid 1998) capable of incorporating material-specific, ductile fracture mechanisms into the failure model and that is independent of mesh topology.

Common methods for macroscale crack-growth simulations are reviewed in (Ingraffea 2004). The classical linear-elastic finite-element (Wawrzynek and Ingraffea 1987), enriched finite-element (Belytschko and Black 1999; Moës, Dolbow et al. 1999; Sukumar, Moës et al. 2000) and meshless (Belytschko, Lu et al. 1994; Fleming, Chu et al. 1997) approaches may allow arbitrary crack growth, but are generally limited to empirical representation of the fracture process. The cohesive-zone approaches can include the physically-based failure process models (Varias 1998; Siegmund and Brocks 1999; Pandolfi, Guduru et al. 2000; Zhai, Tomar et al. 2004) of the material-specific failure process, but limits crack growth to element interfaces.

In this work, we utilize the computational framework developed by (Rashid 1997; Rashid 1998). This approach takes the advantages of the approaches listed above: cracks can grow in any direction and physical fracture processes may be incorporated into the model. In this approach, a length scale is introduced in the form of a small "exclusion region" around the crack tip containing an assumed deformation field.
The application of the exclusion-region approach within the context of the finite-element method relies on arbitrary local mesh replacement (ALMR) method. The ALMR method uses two meshes to model a finite-element problem. The first mesh (patch mesh) is used to encompass the crack front and a small area surrounding the crack front. The second mesh is used to represent the entire problem (background mesh). The patch mesh supersedes the background mesh in the finite-element solver, Figure 2. A background element that is partially covered by the patch mesh can be treated utilizing the theory developed in (Rashid 1997; Rashid 1998; Rashid and Gullett 2000; Rashid and Gullett 2002) It should be noted that the exclusion region is a very small area at the center of the patch mesh and not the whole patch mesh.

Crack growth is the result of force balance and does not rely on a user- or discretization-imposed trajectory. This allows prediction of crack trajectory and linking growth to physically-based mechanisms associated with the fracture process in the near-tip region. Thus, the Finite-Element Fracture (FEFRAC) code is capable of predicting crack trajectory.

During the initial stages of this project, we have implemented a visualization technique within the Ensight visualization framework, and have begun development of a multiscale microstructure-property-based fracture criteria.

Nucleation Modeling & Visualization

Previous studies (Gall, Horstemeyer et al. 2000; Horstemeyer, Baskes et al. 2001b) have investigated the connection between the yield strength and the scale size. They observed similarities in deformation kinematics at various length scales despite significant variation of thermodynamic forces (stresses) at these length scales. Nanoscale simulations were shown to give results that agree with the phenomenological attributes of plasticity observed in macroscale experiments.

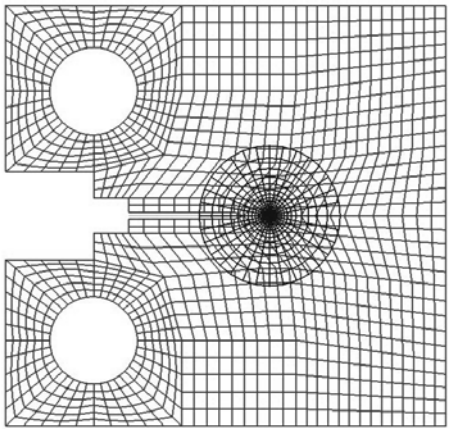

Figure 2. A compact-tension specimen simulated using exclusion-region theory combined with arbitrary local mesh replacement.

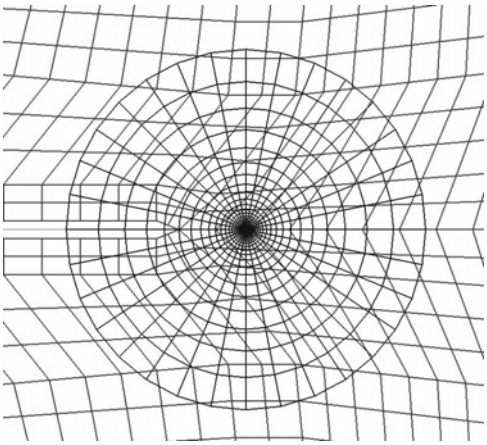

Figure 3. A zoomed-in view of the patch mesh centered at the crack tip.

As an extension of that work, this study utilizes molecular dynamics (MD) to analyze the relationship between dynamic void nucleation and size scale, and examines the applicability of the Horstemeyer-Gokhale continuum void-nucleation model (Horstemeyer and Gokhale 1999) at various nano-size scales.

The onset of damage occurs at the nanoscale by dislocations accumulation in the crystalline lattice. Nanovoids and cracks nucleate in very localized regions near inclusion particles, intermetallics, or at grain-boundary triple junctions. Recent studies (Potirniche, Horstemeyer et al. 2006a; Potirniche, Horstemeyer et al. 2006b) have shown that these voids and cracks grow and coalesce along the main shear bands which experienced intense plastic deformation. Most research efforts have concentrated on dislocation nucleation, e.g., Van Swygenhoven (Van Swygenhoven and Caro 1998; Van Swygenhoven, Spaczer et al. 1999; Van Swygenhoven, Caro et al. 2001), Schiotz (Schiotz, Di Tolla et al. 1998; Schiotz and Jacobsen 2003), Zhu (Zhu, Li et al. 2007), Bringa (Bringa, Caro et al. 2005), and Spearot (Spearot 2005; Spearot, Jacob et al. 2005). Recent efforts to examine high-rate void growth have thus far focused on single- and bi-crystalline systems (Chandler 2007; Chandler, Horstemeyer et al. Accepted; Chandler, Horstemeyer et al. Submitted) which evaluated void growth of nickel.

This work includes a systematic study of void nucleation, growth and coalescence at the nanoscale and microscale levels using modified embedded atom method (MEAM) (Potirniche, Horstemeyer et al. 2006b) based on MD principles. Previous studies (Baskes and Johnson 1994; Horstemeyer, Baskes et al. 2001a) have investigated the connection between the yield strength and the scale size and the kinematics of deformation that seems to be similar at various length scales, even though the thermodynamic forces (stresses) vary at these length scales. Nanoscale simulations were shown to give results that agree with the phenomenological attributes of plasticity observed in macroscale experiments (Horstemeyer 2001).

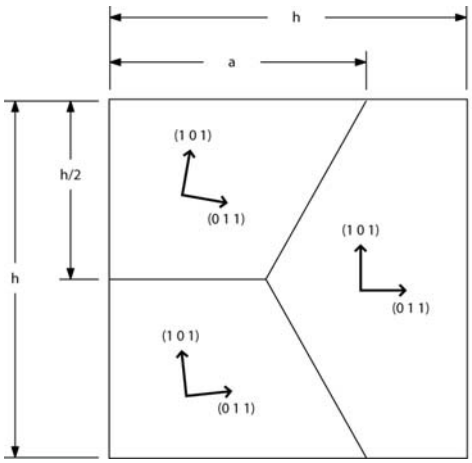

Figure 4. Geometry of polycrystalline specimens with a triple point. The direction vectors indicate the orientation of the crystalline (0 1 1) and (0 1 0) directions.

For this study, we consider computational specimens comprised of single-crystalline, bi-crystalline, and tri-crystalline atomic configurations. For tri-crystalline simulations, the specimen geometry show is shown in Figure 4, which represents lattice orientations with high-angle grain boundaries. Size effects on void growth will be evaluated using specimen sizes shown in Table 2. Atomic interactions will be modeled using the MEAM potential (Baskes 1992). We will consider both uniaxial and biaxial extension.

Table 2. Specimen considered for study of void nucleation at triple junctions.

Number of Atoms			
Simulation	Ni	Al	Mg
Run1	3,544	3,532	2,096
Run2	14,420	14,408	8,252
Run3	57,608	57,596	33,388
Run4	230,424	230,412	133,056
Run5	921,636	921,628	531,882
Run6	3,686,576	3,686,472	2,128,105

Figure 5 shows the initial unstrained configuration with approximately 1 million nickel atoms. The grey scales represent local conformity to the face centered cubic (fcc) structure. Here atoms are grayscaled according to centrosymmetry (Kelchner, Plimpton et al. 1998) which measures local conformity to the fcc structure. Dark grey indicates fcc, while light grey indicates a distortion of the fcc structure.

Preliminary results of biaxial strain simulations are shown in Figure 6 which depicts void nucleation and growth localized at the triple junction, and along grain boundaries.

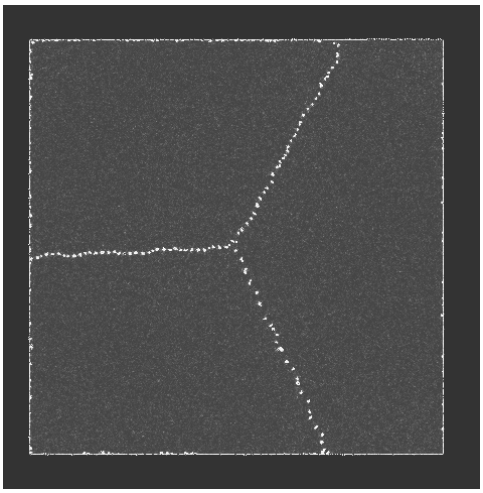

Figure 5. A triple junction with high-angle grain boundaries. Grayscales indicate local fcc structure. Dark grey indicates fcc, light grey indicates a distortion of the fcc structure.

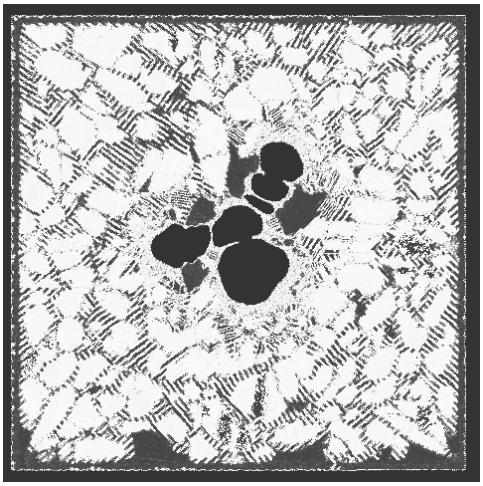

Figure 6. Void nucleation occurs at the triple junction and along grain boundaries when the system is subjected to biaxial loading.

In Figure 7, void volume fraction is plotted against nominal applied strain for five simulation size scales. The plot reveals that size scale has little effect on void growth rates for systems subjected to uniaxial extension loads.

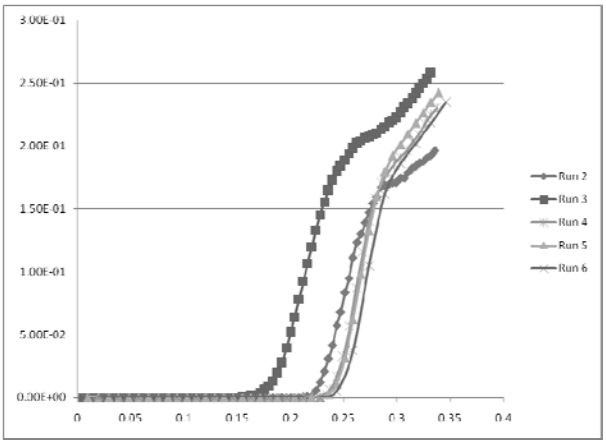

Figure 7. Void growth-rates systems subjected to uniaxial tensile loads reveal relatively minor size scale effects for initial stages of void nucleation and growth.

Conclusions

This is a new program started in the spring of 2007. We have completed compression testing of AZ31 Mg and have begun development of simulation capabilities at the macroscale and the nanoscale in support of development of multiscale modeling techniques for efficient design of lightweight automotive applications. The program is on time and on budget.

Presentations/Publications/Patents

None in FY 2007.

References

1. Baskes, M. I. (1992). "Modified Embedded-Atom Potentials for Cubic Materials and Impurities." Physical Review B-Condensed Matter **46**(5): 2727-2742.
2. Baskes, M. I. and R. A. Johnson (1994). "Modified Embedded-Atom Potentials for Hcp Metals." Modelling and Simulation in Materials Science and Engineering **2**(1): 147-163.
3. Belytschko, T. and T. Black (1999). "Elastic crack growth in finite elements with minimal remeshing." International Journal for Numerical Methods in Engineering **45**(5): 601-620.
4. Belytschko, T., Y. Y. Lu, et al. (1994). "Element-Free Galerkin Methods." International Journal For Numerical Methods in Engineering **37**(2): 229-256.
5. Bringa, E. M., A. Caro, et al. (2005). "Ultrahigh Strength in Nanocrystalline Materials Under Shock Loading." Science **309**(5742): 1838-1841.
6. Cao, P., M. Qian, et al. (2006). "Effect of manganese on grain refinement of Mg-Al based alloys." Scripta Materialia **54**(11): 1853-1858.
7. Chandler, M. Q. (2007). Multiscale Modeling of Hydrogen Enhanced Void Nucleation. Mechanical Engineering. Mississippi State, Mississippi State**:** 157.
8. Chandler, M. Q., M. F. Horstemeyer, et al. (Accepted). "Hydrogen Effects on Nanovoid Nucleation in FCC Single Crystals." Acta Materialia.
9. Chandler, M. Q., M. F. Horstemeyer, et al. (Submitted). "Hydrogen Effects on Nanovoid Nucleation at Nickel Grain Boundaries." Acta Materialia.
10. Fleming, M., Y. A. Chu, et al. (1997). "Enriched element-free GALERKIN METHODS FOR CRACK TIP FIELDS." International Journal for Numerical Methods in Engineering **40**(8): 1483-1504.
11. Gall, K., M. F. Horstemeyer, et al. (2000). "Atomistic simulations on the tensile debonding of an aluminum-silicon interface." Journal of the Mechanics and Physics of Solids **48**(10): 2183-2212.
12. Horstemeyer, M. F. (2001). From atoms to autos: a new design paradigm using microstructure-property modeling. Part 1: Monotonic Loading, Sandia National Labs**:** 260.
13. Horstemeyer, M. F., M. I. Baskes, et al. (2001a). "Computational nanoscale plasticity simulations using embedded atom potentials." Theoretical and Applied Fracture Mechanics **37**(1-3): 49-98.
14. Horstemeyer, M. F., M. I. Baskes, et al. (2001b). "Length scale and time scale effects on the plastic flow of fcc metals." Acta Materialia **49**(20): 4363-4374.
15. Horstemeyer, M. F. and A. M. Gokhale (1999). "A void-crack nucleation model for ductile metals." International Journal of Solids and Structures **36**(33): 5029-5055.
16. Horstemeyer, M. F., D. Oglesby, et al. (2006). From Atoms to Autos: Designing a Mg Alloy Corvette Cradle by Employing Hierarchical

Multiscale Microstructure-Property Models for Monotonic and Cyclic Loads. Mississippi State, Mississippi State University**:** 296.
17. Ingraffea, A. R. (2004). Computational Fracture Mechanics. Encyclopedia of computational mechanics. E. Stein, R. d. Borst and T. J. R. Hughes. Chichester, West Sussex, John Wiley. **2**.
18. Kelchner, C. L., S. J. Plimpton, et al. (1998). "Dislocation nucleation and defect structure during surface indentation." Physical Review B **58**(17): 11085.
19. Li, H., E. Hsu, et al. (2007). "Determination of Active Slip/Twinning Modes in AZ31 Mg Alloy Near Room Temperature." Journal of Materials Engineering and Performance **16**(3): 321-326.
20. Lindholm, U. and L. Yeakley (1968). "High strain-rate testing: Tension and compression." Experimental Mechanics **8**(1): 1-9.
21. Marya, M., L. G. Hector, et al. (2006). "Microstructural effects of AZ31 magnesium alloy on its tensile deformation and failure behaviors." Materials Science and Engineering: A **418**(1-2): 341-356.
22. Moës, N., J. Dolbow, et al. (1999). "A finite element method for crack growth without remeshing." International Journal for Numerical Methods in Engineering **46**(1): 131-150.
23. Nemat-Nasser, S. (2000). Introduction to High Strain Rate Testing. Mechanical Testing and Evaluation Handbook, ASM. **8:** 427-428.
24. Osborne, R. J. (2005). A joint USCAR-USAMP material project with DaimlerChrysler, Ford, General Motors and Industry. Southfield, Detroit.
25. Pandolfi, A., P. R. Guduru, et al. (2000). "Three dimensional cohesive-element analysis and experiments of dynamic fracture in C300 steel." International Journal of Solids and Structures **37**(27): 3733-3760.
26. Potirniche, G. P., M. F. Horstemeyer, et al. (2006a). "Atomistic modelling of fatigue crack growth and dislocation structuring in FCC crystals." Proceedings of the Royal Society, A **462**: 3707-3731.
27. Potirniche, G. P., M. F. Horstemeyer, et al. (2006b). "A molecular dynamics study of void growth and coalescence in single crystal nickel." International Journal of Plasticity **22**: 257-278.
28. Rashid, M. M. (1997). "A new theory for free-surface formation in solid continua." International Journal of Solids and Structures **34**(18): 2303-2320.
29. Rashid, M. M. (1998). "The arbitrary local mesh replacement method: An alternative to remeshing for crack propagation analysis." Computer Methods in Applied Mechanics and Engineering **154**(1): 133-150.
30. Rashid, M. M. and P. M. Gullett (2000). "On a finite element method with variable element topology." Computer Methods in Applied Mechanics and Engineering **190**(11-12): 1509-1527.
31. Rashid, M. M. and P. M. Gullett (2002). Formulation of a Finite Element Method with Arbitrary Element Geometry. Modeling and Simulation-Based Life Cycle Engineering. K. P. Chong and J. E. Harding. London, Spon Press.
32. Schiotz, J., F. D. Di Tolla, et al. (1998). "Softening of nanocrystalline metals at very small grain sizes." Nature **391**(6667): 561-563.
33. Schiotz, J. and K. W. Jacobsen (2003). "A Maximum in the Strength of Nanocrystalline Copper." Science **301**(5638): 1357-1359.
34. Siegmund, T. and W. Brocks (1999). "Prediction of the Work of Separation and Implications to Modeling." International Journal of Fracture **99**(1): 97-116.
35. Spearot, D. (2005). Atomistic Calculations of Nanoscale Interface Behavior in FCC Metals. Mechanical Engineering. Atlanta, Georgia Institute of Technology**:** 276.
36. Spearot, D. E., K. I. Jacob, et al. (2005). "Nucleation of dislocations from [0 0 1] bicrystal interfaces in aluminum." Acta Materialia **53**(13): 3579-3589.
37. Styczynski, A., C. Hartig, et al. (2004). "Cold rolling textures in AZ31 wrought magnesium alloy." Scripta Materialia **50**(7): 943-947.
38. Sukumar, N., N. Moës, et al. (2000). "Extended finite element method for three-dimensional crack modelling." International Journal for Numerical Methods in Engineering **48**(11): 1549-1570.
39. Van Swygenhoven, H. and A. Caro (1998). "Plastic behavior of nanophase metals studied

by molecular dynamics." Physical Review B **58**(17): 11246.
40. Van Swygenhoven, H., A. Caro, et al. (2001). "A molecular dynamics study of polycrystalline fcc metals at the nanoscale: grain boundary structure and its influence on plastic deformation." Materials Science and Engineering A **309-310**: 440-444.
41. Van Swygenhoven, H., M. Spaczer, et al. (1999). "Competing plastic deformation mechanisms in nanophase metals." Physical Review B **60**(1): 22.
42. Varias, A. G. (1998). "Constraint effects during stable transient crack growth." Computational Mechanics **21**(4): 316-329.
43. Wawrzynek, P. A. and A. R. Ingraffea (1987). "Interactive finite element analysis of fracture processes: An integrated approach." Theoretical and Applied Fracture Mechanics **8**(2): 137-150.
44. Yi, S. B., S. Zaefferer, et al. (2006). "Mechanical behaviour and microstructural evolution of magnesium alloy AZ31 in tension at different temperatures." Materials Science and Engineering: A **424**(1-2): 275-281.
45. Zhai, J., V. Tomar, et al. (2004). "Micromechanical simulation of dynamic fracture using the cohesive finite element method." Journal of Engineering Materials and Technology-Transactions of the Asme **126**(2): 179-191.
46. Zhu, T., J. Li, et al. (2007). "From the Cover: Interfacial plasticity governs strain rate sensitivity and ductility in nanostructured metals." PNAS **104**(9): 3031-3036.

D. Multi-Material Vehicle (MMV) Research and Development (R&D) Initiative (MMV 701[i])

Principal Investigator: David A. Wagner, Ph.D.
Ford Research & Advanced Engineering
MD 3137-RIC
2101 Village Road
Dearborn, MI 48121
(313) 845-2547; fax: (313) 337-5581, e-mail: dwagner6@ford.com

Project Technical Coordinator: Manish Mehta, Ph.D.
TRC-National Center for Manufacturing Sciences (NCMS)
3025 Boardwalk
Ann Arbor, MI 48108-3266
(734) 995-4938; fax: (734) 995-1150; e-mail: manishm@ncms.org

Technology Area Development Manager: Joseph A. Carpenter
(202) 586-1022; fax: (202) 586-6109; e-mail: joseph.carpenter@ee.doe.gov

Expert Technical Monitor: Philip S. Sklad
(865) 574-5069; fax: (865) 576-4963; e-mail: skladps@ornl.gov

---

Contractor: U.S. Automotive Materials Partnership (USAMP)[i]
Contract No.: DE-FC05-02OR22910 through the DOE National Energy Technology Laboratory

---

Objective

The MMV R&D Initiative is a new umbrella focal project established in fiscal year (FY) 2007 to connect and relate the USAMP's Auto/Steel Partnership (A/SP), Automotive Composites Consortium (ACC), Automotive Metals Division (AMD) and Non-Destructive Evaluation (NDE) projects together so that they address vehicle issues in addition to materials issues. The project's main near-term objective is to define new opportunities across the various single-area-focused projects that bridge lightweight materials R&D to applications on a donor vehicle and potential future production implementation, addressing integration, joining and assembly, testing and validation, and advanced vehicle design/architectures.

The MMV R&D Initiative deliverables will include:

- Gap/Needs analysis to identify inhibitors to production and manufacturing.
- Attribute performance, mass-reduction and cost implications for multi-material vehicle components, sub-assemblies and systems.
- Vehicle Technical Specifications for donor vehicle for aligning other USAMP projects (crash performance, dynamic stiffness, durability, etc.).
- Computer-aided design (CAD) and computer-aided engineering (CAE) models for the baseline donor vehicle for alignment of other USAMP projects.
- Baseline cost estimates for steel donor vehicle for alignment of other USAMP projects.

Approach

The MMV R&D Initiative will define new opportunities across USAMP that bridge lightweighting materials R&D to applications on a donor vehicle, addressing integration, joining and assembly, testing and validation, and advanced vehicle design/architectures to accommodate alternative energy powertrains. It is anticipated that the MMV will help motivate USAMP's partner organizations (suppliers, academia, and national laboratories) to accelerate research in areas of importance.

- An MMV R&D Steering Committee, consisting of two representatives per original equipment manufacturer (OEM), will be formed to assess the current USAMP project portfolio, identify technology gaps, and to advocate, "bubble-up" and transition new projects in joining, integration and assembly technologies to individual consortia or project teams across USAMP.
- A donor-vehicle platform will form the baseline for affecting the light weighting technology improvements, and will be the focus for the three initial technology "seed" projects addressing major light weighting initiatives: A/SP's Future Generation Passenger Compartment (FGPC; see 5.I), AMD's Magnesium Front End (MFE; see 6.B and 6.C) and the ACC's composite underbody (see 8.A).

Results from demonstration of the three initial seed projects on a large, rear-wheel drive (RWD) passenger vehicle platform will be extrapolated to address light weighting strategies for other vehicle architectures.

Accomplishments

During FY 2007, the MMV project began operations. This year, the accomplishments primarily surround initiating efforts and aligning the three USAMP body subassembly projects.

- Selected a consensus donor-vehicle platform to serve as a benchmark to quantify and compare technology improvements. The selected vehicle is a General Motors (GM) large RWD passenger vehicle.
- A corresponding MMV Technical Specification was collaboratively defined by the MMV team and selected CAE vendor, consisting of required load cases, prioritizations for meeting compliance, and generally tracking the design maturity of MMV modules.
- Initiated a baseline MMV donor-vehicle systems-level manufacturing and assembly cost-modeling project.
- Advocated the technical and business case for new multi-material joining R&D projects by engaging with experts in joining technologies. One new joining R&D concept-feasibility project was selected for sponsorship.

Future Direction

- The MMV R&D initiative will be closely linked in to the emerging needs of the three USAMP MMV "seed" projects, and remain opportunistic in attracting new project ideas from USAMP in multi-material joining technologies.
- A newly-started project to develop a full-vehicle cost model of the MMV baseline-vehicle manufacturing will be tracked closely for comparing with cost performance of lightweight-vehicle body systems resulting from the three MMV "seed" projects.
- Another new project investigating forming metallurgical bonds between steel and cast aluminum as well as between steel and cast magnesium will be initiated.

Introduction

The MMV R&D Initiative is a USAMP umbrella focal project, supporting FreedomCAR goals and timeline, with the primary objective of investigating vehicle weight-reduction opportunities and issues associated with incorporating multiple materials in multiple locations.

The MMV R&D portfolio emphasizes design, joining, corrosion, energy management, manufacturing processes, and other technologies that facilitate mixed-material systems that can support delivery of FreedomCAR goals by 2015.

In its first year since charter in FY 2006, the MMV team was directed by the USAMP to focus on standardization of analytical, design, cost-modeling and benchmarking studies supporting the three 'seed' technology projects. Longer-term focus of MMV R&D will be on integration and joining/assembly technologies as well as new vehicle architectures utilizing lightweight materials and associated processes developed for manufacturing discrete parts and sub-assemblies in high-volume.

Significant accomplishments in program standardization are reported below under each sub-task heading.

Baseline MMV Vehicle

The MMV team identified a common baseline vehicle, the GM unibody (body-frame-integral) RWD vehicle. This provided a single-focus vehicle for each of the following three initial 'seed' projects:

(a) AMD 603 and AMD 604 Magnesium Front End projects.

(b) ACC Composite Underbody.

(c) A/SP Advanced High Strength Steel Future Generation Passenger Compartment.

Figures 1 – 3 illustrate baseline modules being researched within USAMP and being held to engineering-performance targets set by MMV.

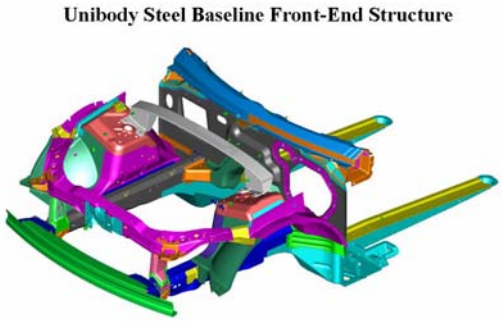

Figure 1. AMD Magnesium Front End project. Steel baseline is shown as the design basis.

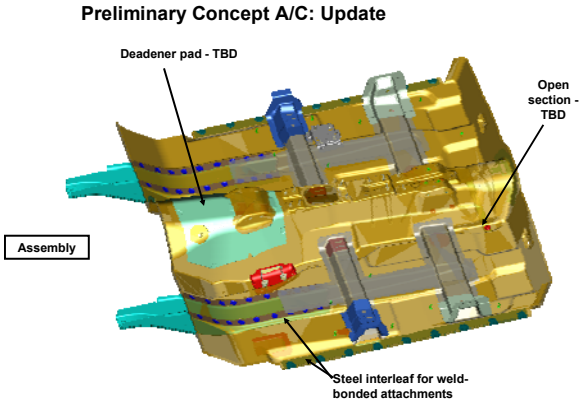

Figure 2. ACC Composite Underbody.

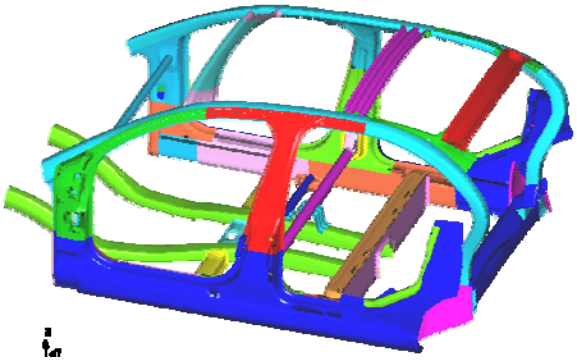

Figure 3. A/SP Advanced High Strength Steel Future Generation Passenger Compartment.

Common MMV Technical Specification

The MMV began FY 2007 by developing a consensus technical specification for comparisons and validation of vehicle performance modeling with respect to the large RWD passenger donor vehicle contributed by GM. The MMV specification was updated by team members to incorporate new Federal Motor Vehicle Safety Standard (FMVSS) requirements, and was then disseminated to all the USAMP consortia over-seeing the three core MMV "seed" projects. The MMV specification is being used to drive design and lightweight materials and manufacturing technology developments across the initial three 'seed' projects that would be compliant to the specification.

Engineering Performance Targets

MMV established the engineering targets and manufacturing goals for each of the three "seed" projects to meet anticipated 2015 functional requirements or match the baseline production-vehicle performance. A tracking mechanism for assessing progress in design maturity towards meeting these targets was also established – a detailed spreadsheet is being maintained by Multimatic (lead design vendor for the ACC underbody project) under contract to the MMV, and involves the regular participation and input of the other two 'seed' project leaders and their respective lead design vendors.

The specific MMV engineering targets relate to:

- Structural Performance (stiffness, dynamic frequencies, mode shapes)
- Manufacturability (cycle time, paint issues, repair procedures in-plant and in-service)
- Safety (front, side, rear, roof, restraints, cargo-retention, bumper requirements)
- Durability and Target Life
- Ride and Handling
- Towing and Trailer

In addition, the three "seed" projects, in proposing new module designs incorporating lightweight materials, must also identify how they could be integrated into a full vehicle-manufacturing scenario capable of producing 100,000 units per year at an affordable cost.

MMV Baseline Cost-Model Development

The MMV Baseline Cost Model development is being led by Camanoe Associates with close oversight and input from the MMV team. Camanoe will estimate the piece costs and assembly costs for the donor vehicle and for each of the subassemblies for the three "seed" projects, the A/SP FGPC, the ACC Composite Underbody and the AMD Magnesium Front End. Having the cost model and estimate as a single project through MMV minimizes the work and costs to each of the three "seed" projects. Also, this effort will provide many inputs for the cost models for each of the three "seed" projects.

The expected results will include cost estimates for the stamped-steel baseline donor-vehicle. Specifically, the cost of each individual part will be estimated based on the material and manufacturing technique, i.e., typical stamping operations. Additionally, the cost of assembly for the full vehicle structure will be estimated based on the donor-vehicle assembly process. Finally, the assembly cost of the three subassemblies matching the three "seed" projects, passenger compartment, underbody and front end, will be estimated.

These estimated costs will be the basis for comparisons with the lightweight investigations in each of the three "seed" projects. By having a consistent baseline estimate, cost opportunities and risks can be identified with respect to the high-volume implementation of the lightweight concepts.

Identification of Critical R&D Gaps

In parallel, the MMV team also began identifying new strategies for promoting mass savings across the USAMP project portfolio which included coordination with the USAMP Materials Technology Team. The MMV team also began resolving design/analytical information discrepancies, as well as assessing critical technology gaps and R&D needs across these three "seed" projects.

The highest priority technology development identified was in multi-material joining technology relevant to the assembly needs of the 'seed' projects. A Joining Technology focus meeting was held with subject matter experts from Edison Welding Institute, Pacific Northwest National Laboratory and the University of Michigan to assess the state-of-the-art and define joining requirements. A future project will address metallurgical joining of cast aluminum to steel and of cast magnesium to steel to address one of the vehicle-integration issues associated with lightweight material introductions.

Conclusion

The USAMP Multi-Materials Vehicle Research and Development Initiative (MMV 701) has been successfully started, with a baseline vehicle

identified, engineering and manufacturing performance targets established, and a consistent source for baseline design, models and engineering performance analysis established.

---

[i] Denotes project 701 of the Multi-Material Vehicle (MMV) Working Group of the United States Automotive Materials Partnership (USAMP), one of the formal consortia of the United States Council for Automotive Research (USCAR, www.uscar.org) set up by Chrysler, Ford and General Motors to conduct joint, pre-competitive research and development.

E. Mission Eggcellence – K-12 Outreach Program

Rosemary Cuicchi
Starkville Junior High School
112 Kirkside Dr
Starkville, MS 39759
(662) 323-6843; email: rcuicchi@gmail.com

Mark F. Horstemeyer
Center for Advanced Vehicular Systems (CAVS) Chair in Solid Mechanics & Professor, Mechanical Engineering
Mississippi State University (MSST)
206 Carpenter Bldg., PO Box ME
Mississippi State, MS 39762
(662) 325-7308; fax: (662) 325-7223; e-mail: mfhorst@me.msstate.edu

Shaik Jeelani: Co-Principal Investigator
Director, Center for Advanced Materials
Vice President, Research and Sponsored Programs
Tuskegee University (TU)
Tuskegee AL 36088
(334) 727-8970; fax: (334) 724-4224; e-mail: jeelanis@tuskegee.edu

Technology Area Development Manager: Joseph A. Carpenter
(202) 586-1022; fax: (202) 586-1600; e-mail: joseph.carpenter@ee.doe.gov

Contract Monitor: Aaron Yocum
(304) 285-4852; fax: (304) 285-4403; e-mail: aaron.yocum@netl.doe.gov

---

Contractor: MSST
Contract No.: 4000054701

Objective

- The Mission Eggcellence Project is designed to develop a commitment from CAVS to the children of the State of Mississippi through curriculum instruction and competitions dealing with the design of a vehicle bumper and/or seatbelt for passenger safety. This instruction and student competitions will create an awareness of the importance of design in safety implications, and of the real-world applications of mathematics, science, and problem-solving skills. Mission Eggcellence will create awareness among the Mississippi school-age population of future job opportunities in the State of Mississippi as well as college majors associated with these jobs.

Approach

- Create a grade-appropriate curriculum with experiments associated with the physics of car crashes for grades K-3 (Objective 1).
- Create a grade-appropriate curriculum with experiments associated with the physics of car crashes for grades 4-6 (Objective 2).
- Develop a Teacher Workshop for grades K-3 teachers for training in use of the grade-appropriate curriculum in the regular classroom. Equipment necessary to conduct the experiments and compete in the competitions is given to each teacher participant (Objective 3).

- Develop a Teacher Workshop for grades 4-6 teachers for training in use of the grade-appropriate curriculum in the regular classroom. Equipment necessary to conduct the experiments and compete in the competitions is given to each teacher participant (Objective 4).
- Design a competition for grades K-3 incorporating bumper design for passenger safety (Objective 5).
- Design a competition for grades K-3 incorporating car design for passenger safety (Objective 6).
- Design a competition for grades 4-6 incorporating bumper design for passenger safety (Objective 7).
- Design a competition for grades 4-6 incorporating car design for passenger safety (Objective 8).
- Create a grade-appropriate curriculum with experiments associated with the physics of car crashes for grades 7-9 (Objective 9).
- Create a grade-appropriate curriculum with experiments associated with the physics of car crashes for grades 10-12 (Objective 10).
- Develop a Teacher Workshop for grades 7-9 teachers for training in use of the grade-appropriate curriculum in the regular classroom. Equipment necessary to conduct the experiments and compete in the competitions is given to each teacher participant (Objective 11).
- Develop a Teacher Workshop for grades 10-12 teachers for training in use of the grade-appropriate curriculum in the regular classroom. Equipment necessary to conduct the experiments and compete in the competitions is given to each teacher participant (Objective 12).
- Design a competition for grades 7-9 incorporating bumper design for passenger safety (Objective 13).
- Design a competition for grades 7-9 incorporating car design for passenger safety (Objective 14).
- Design a competition for grades 10-12 incorporating bumper design for passenger safety (Objective 15).
- Design a competition for grades 10-12 incorporating car design for passenger safety (Objective 16).

Accomplishments

- Completed curriculum for grades K-3 (Objective 1).
- Completed curriculum for grades 4-6 (Objective 2).
- Completed Teacher Workshop for teachers of grades K-3 (Objective 3).
- Completed Teacher Workshop for teachers of grades 4-6 (Objective 4).
- Completed Bumper Design Competition for grades K-3 (Objective 5).
- Completed Car Design Competition for grades K-3 (Objective 6).
- Completed Bumper Design Competition for grades 4-6 (Objective 7).
- Completed Car Design Competition for grades 4-6 (Objective 8).

Work Plan for 2007-08

- Develop curriculum for grades 7-9 (Objective 9).
- Develop curriculum for grades 10-12 (Objective 10).
- Develop Teacher Workshop for teachers of grades 7-9 (Objective 11).
- Develop Teacher Workshop for teachers of grades 10-12 (Objective 12).
- Develop Bumper Design Competition for grades 7-9 (Objective 13).
- Develop Car Design Competition for grades 7-9 (Objective 14).
- Develop Bumper Design Competition for grades 10-12 (Objective 15).
- Develop Car Design Competition for grades 10-12 (Objective 16).

Introduction

The CAVS at MSST is teaming with the local school districts and the Mississippi Children's Museum to develop a sophisticated Science & Technology area in the form of workshops in the museum with teachers to inspire young minds to explore the worlds of math, science, and engineering. We will create powerful, interactive-learning/teaching kits for K-12 students with a program based upon materials design, which will be supported by ASM International (ASM). We already have an ASM-supported program in development entitled ***Mission Eggcellence***. It is worth explaining the Mission Eggcellence notion further as illustrative of our other ideas.

Mission Eggcellence provides students with a hands-on introduction into vehicular crashworthiness through applying basic concepts of physics (students are provided with simple definitions from physics such as mass, velocity, momentum and energy and how they are used during crash), explanations of what actually happens during a crash (using the physics terms and defining what is necessary to enable passengers to survive a crash), and examples of safety devices (explanations and examples of some devices such as bumpers, seatbelts, airbags and safety cages, used in cars and trucks, with simulations to demonstrate how they work). Other explanations provided will include manufacturer goals (creating a vehicle that is lightweight for the lowest price possible, creating a vehicle that demonstrates good fuel efficiency, creating a vehicle that is aesthetically pleasing in appearance) versus consumer goals (a vehicle that is strong enough to protect passengers from impact, a vehicle that is light enough to provide economical fuel consumption, a vehicle that has a pleasing appearance, a vehicle that has a memory of its shape and can be repaired faster, less expensively and easier) and the difficulties involved in balancing these requirements.

Vehicles, materials, eggs, workbooks/worksheets, and instruction will be provided to the students, with which they must design a safety barrier for each team's vehicle that will prevent the egg from breaking upon impact during an impact competition. The vehicles are released upon a ramp, which is elevated to a higher degree of angle, from 15 degrees to 70 degrees, at each step of the impact competition, and the vehicle(s) in which the eggs do not break can win. The winners are determined by the lightweight designs. Competitions are expected to be state-wide. Undergraduates and graduate students will play a large role in communicating the principles and overseeing the activities. They will also be used to help monitor the tournaments and mentor some of the K-12 students.

Each curriculum consists of eight grade-appropriate experiments for the physics concepts of velocity, acceleration, Newton's Third Law, momentum, impulse, elastic and inelastic collisions. These experiments include a bumper design and car design. In the bumper-design competitions for grades K-3 and 4-6, the bumper is tested by rolling a wooden car, with the bumper attached, down a ramp using a raw egg as the passenger. Winner is steepest incline with the egg intact. The tie breaker is lightest mass. In the K-3 and 4-6 car design competitions, a car is designed using Knex pieces from a kit. Winner is steepest incline with egg intact. The tie breaker is lightest mass.

Academic/Research Excellence Basis

An overarching theme of multidisciplinary design integration motivates our research as well as our multilevel educational activities in K-PhD and continuing education. Our educational approach is structured to overcome the knowledge compartmentalization and overspecialization of traditional technical education that stand as barriers to the implementation and dissemination of science-based engineering. Core university collaboration seeks to empower a broad range of students, through a fusion of exciting new science-based tools with design habits of mind, team creativity and effective multidisciplinary communication. Our *Mission Eggcellence* design project work will be enhanced by the emerging technology of a distributed web-based collaborative environment. We have a clear education accountability structure administered by the CAVS Chair Professor, Mark Horstemeyer. In addition, CAVS has a strong extension/ outreach

center in which quick implementation of research is plausible.

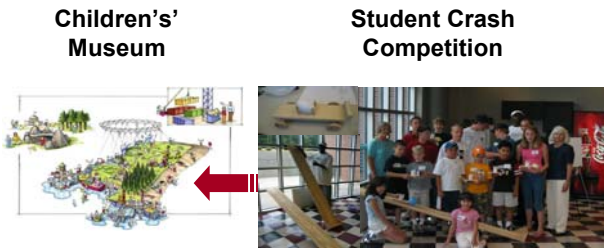

Project Objectives and Expected Outcomes/Impacts

In alignment with the objectives and expected outcomes of this task (which are to empower and inspire all our state's children, regardless of their social, educational or economic background, and to discover their potential through tapping their curiosity and creativity, through hands-on and engaging exhibits and programs), we will create a dynamic and competitive program that will:

- Provide children the opportunity to perform hands-on experiments, to learn the value of mathematics, physics and engineering and how their uses in the experiments correlate with "real world" engineering problems, and to create for themselves the experience of mastering tasks they would normally perceive to be difficult. This will increase their self-esteem, which will be demonstrated by increased performance levels in school.
- Address the needs of Mississippi children, especially in the areas of math, science and engineering.
- Reach children in schools and communities throughout the state through our Outreach Program.
- Complement the mathematics, physics and science programs being taught in school.
- Promote a desire to learn more about the world in which the children live and how it works.

We really need a creative K-PhD program that anticipates the current and future high-tech jobs revolving around the automotive industry in our state. Children need to be excited by math, science, and engineering, and the Mississippi Children's Museum can enkindle that passion. If we can help them develop a passion for learning, they are going to want to understand how things work and how to make things work better. For Mississippi to advance in the science and technology fields, children must become excited about learning, and this is the fundamental mission of a children's museum.

Mission Eggcellence, among other materials-design projects, can provide a science/engineering experience that will inspire children to want to return time and time again; each time that they return, they will learn things about their world that inspires them to want to return and learn more. The imaginative and experimental Mission Eggcellence is relevant to the students' class-work and can be correlated with "real world" safety, reliability, and crashworthiness issues that are faced today within the automotive industries.

Contributions to the Long-Term and Sustainable Engagement of the Team/Unit

MSST is developing an "Automotive Experience" strategic program that includes K-12, undergraduate work, and graduate-level work. A new course and certificate are being developed in real time for this endeavor. For MSST to have an excellent PhD pool, we need to have students aligned in the K-12 pipeline. We are viewing these grant funds as start-up funds only, but the program will continue long into the future.

From the Department of Energy (DOE) - Southern Regional Center for Lightweight Innovative Design (SRCLID) Statement of Program Objectives (SOPO), the transfer of knowledge obtained from leading-edge research to K-12 educational programs is a core requirement. CAVS is required to develop an educational program to integrate lightweighting-design concepts with crashworthiness into student curricula. A K-PhD program will be developed that communicates the important issues of crashworthiness and safety. Crash kits will be developed for appropriate educational levels, and state and regional tournaments will be fostered to further interest in the technology and resultant designs.

Specific subtasks include:

Task 1. Develop crash kits for K-2, 3-6, 7-9, and 10-12.
Task 2. Develop tournaments with crash kits for Mississippi-wide contests.
Task 3. Assist in the development of modules for Mississippi Children's Museum.
Task 4. Assist Choctaw School for Native Americans and the Houston High School Solar Car team in their solar car designs.

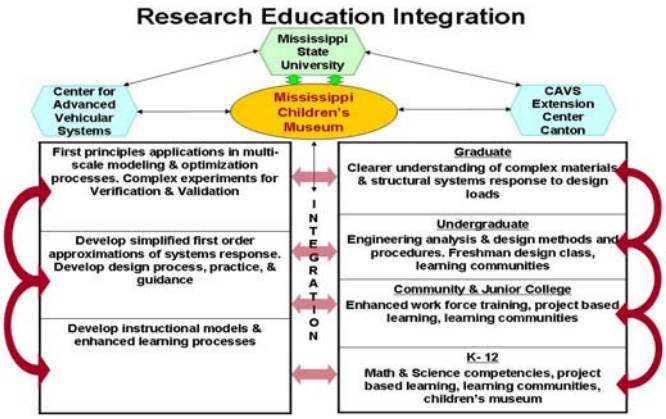

The graphic above represents the integration of education, industry and outreach as they will be applied in technology transfer to the children via the Mississippi Children's Museum.

CAVS will design materials kits and crash kits with their associated documentation (student and instructor) and provide engineering specialists as keynote speakers, trainers, and lecturers. Rosemary Cuicchi (Starkville Jr. High physics instructor and teacher of academically-gifted classes at Armstrong Middle School in Starkville) is involved in developing the program. ASM will also be involved in helping develop the program. Nissan North America (Canton, MS) and Vista Engineering Inc. have both donated in-kind contributions to the SRCLID program with specific interest in the educational development aspects of the program.

The Mississippi Children's Museum administrators and staff will be involved in designing and setting up the exhibits within the museum, as well as establishing agendas for exhibit changes. Dr. Mark Horstemeyer is helping design the regions within the Children's Museum to help explain the math, science, and engineering aspects.

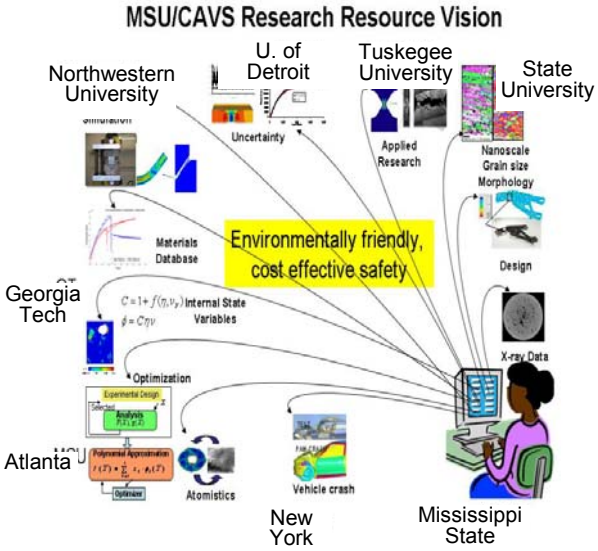

The graphic above represents the CAVS research resource vision through which data, research materials, materials-design methodologies, and basic science aspects will be made available to students through this task, sponsored by DOE and the Mississippi Children's Museum.

Evaluation

The program will be evaluated both internally by MSST staff and externally by partnering organizations, committee members, and visitor surveys. Internal evaluation will take place at monthly meetings where staff members take the opportunity to debrief with the entire group, provide feedback and troubleshoot issues. External evaluations will be completed through a Mississippi Children's Museum Partner Survey. When evaluating the program, staff will review the types of programs/activities offered to ensure that they accurately represent the culture, as well as whether an organization's participation in the program helped to provide access to the Mississippi Children's Museum for members of the community. In addition, staff will track the number of:

- Individuals who participated in the special events, workshops and programming.
- Communities served (Examples are Latino, Native American, African-American, Asian and Caucasian).

- Community-based organizations with which we partner.
- Opportunities created for cross-cultural programming.
- Artists and performers who benefit through participation.
- Number of events we will offer at the museum during the year's Passport programs.
- Number of events/community festivals we will participate in during the next year.

Materials Design Logic Model

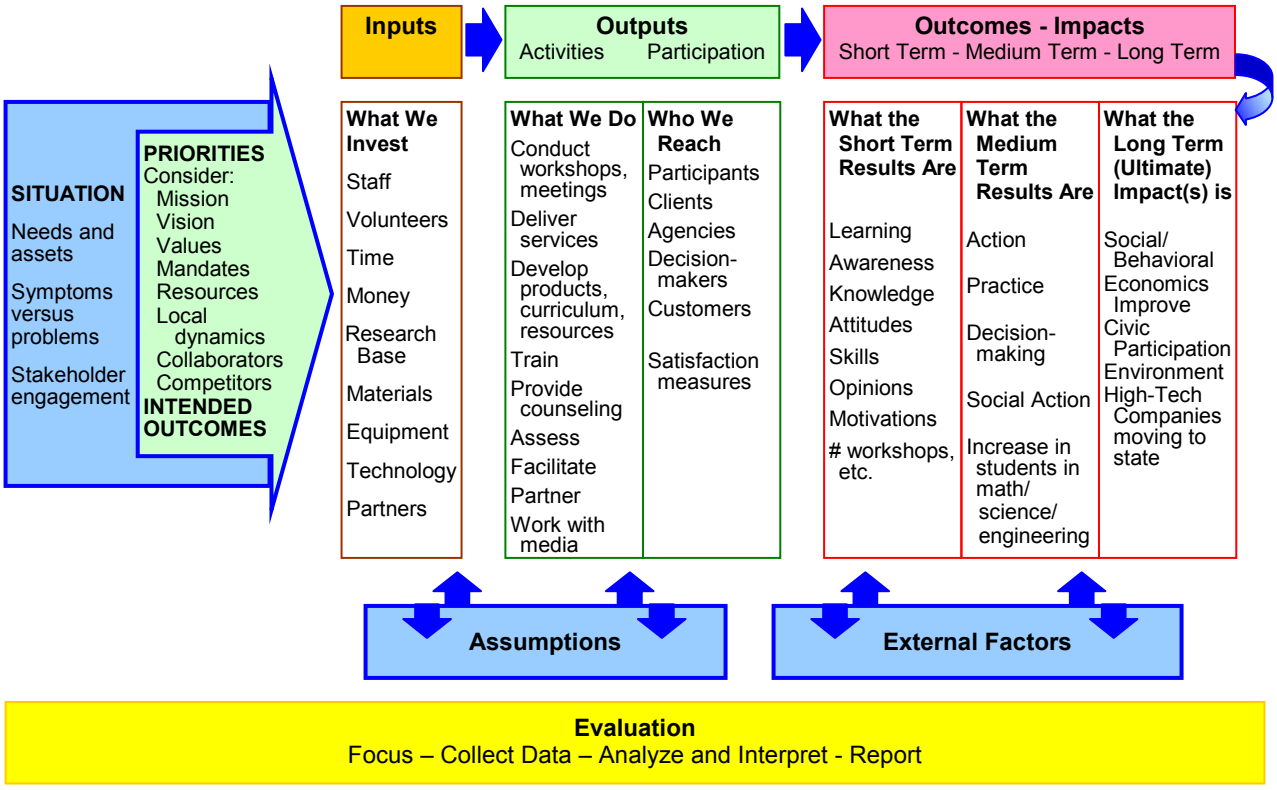

Making a Difference within the Community and the University

University metrics will demonstrate the effectiveness of the program by showing increases in students coming to MSST and other colleges and universities in the fields of math, science and engineering. Within the community, we expect to see a higher rate of students becoming involved in math, science and engineering and, in the long run, expect to see more high-tech companies moving into the state as a result of this program. If we increase the rates of students in math, science and engineering, indicating a more highly educated future work force, the number of incoming high-tech companies will increase.

Interpreting the Accompanying Materials Design Logic Model (see above)

Situation: The situation, as it applies to this project, is that children in Mississippi do not have access to innovative, open-ended, educational hands-on programs in which they can be exposed to viable applications of math, science and engineering. Because the Mississippi public educational system is not considered to be strongly effective in graduating students who are strong in math, science and engineering, few high-tech companies consider Mississippi to be an economically-viable target for relocation or expansion of businesses.

Priorities and Intended Outcomes

The priorities of this project are thoroughly integrated within the mission and vision of CAVS, especially as defined by the DOE-SRCLID Statement of Program Objectives (SOPO). Specifically, the transfer of knowledge obtained from leading-edge research to K-12 educational programs via developing an educational program to integrate lightweighting design concepts with crashworthiness into student curricula will be accomplished by developing crash kits for appropriate educational levels, and by fostering state and regional tournaments to further interest in the technology and resultant designs. The intended outcome will be increased numbers of students at all educational levels who will have a deeper understanding of math, science and engineering and an appreciation of these fields of study in real-world applications.

Inputs: CAVS, MSST, the CAVS Extension (Canton) and the community will integrate into a synergistic teaming effort to provide staff, volunteers, time, money, basic research, materials, equipment, technology and partners to ensure the success of this program.

Outputs – What Will We Do? Personnel from the core facilities mentioned above will conduct workshops and meetings, will deliver services, will develop products, curriculum and provide resources, will provide training, will provide counseling, will assess the program and its effectiveness, will work with the partnering organizations, and will work with media to ensure proper dissemination of information to the public.

Who Will We Reach? We will reach participants (children, parents and teachers), clients, agencies, decision-makers and customers, all of whom should, over time, provide satisfaction feedback.

Outcomes – Impacts – Short Term: We anticipate an increased interest by students in math, science and engineering as demonstrated by improved learning, awareness, knowledge, attitudes, skills, opinions and motivations, as a result of student participation in the workshops, *et cetera*.

Outcomes – Impacts – Medium Term: We anticipate seeing an increase in museum student participation (Actions), an increase in classroom participation (Practice), an increase in understanding and application of lessons-learned by students in their respective schools (decision-making), an increase in awareness of potential impacts upon society of vehicle lightweighting and crashworthiness (social action), and an increase in students interested in math, science and engineering.

Outcomes – Impacts – Long Term: We anticipate students graduating from their respective schools and entering colleges and universities to pursue degrees in math, science and engineering, who will have a stronger working knowledge and understanding of math, science and engineering as they relate to societal/behavioral, economic, civic and environmental impacts, as well as seeing an increase in the number of high-tech companies moving to Mississippi, as a result of having a more-informed and more-highly-educated student labor base from which future employees can be selected.

Evaluation: The effectiveness of this program will be determined by follow-up investigations, over time, to collect data, analyze and interpret the data, and report on the increase in students who enroll in institutions of higher learning in the fields of math, science and engineering.

Conclusions

The Mission Eggcellence Program has been developed for the grades K-3 and 4-6. The Teacher Workshop for these grades was very successful. Eighty percent of the teachers who attended the workshop had students compete in both the bumper-design and car-design competitions. Feedback was excellent. Curriculum and competitions for grades 7-9 and 10-12 are in the developmental process.

Acknowledgement

The authors would like to acknowledge funding from the Center for Advanced Vehicular Systems at Mississippi State University. We also acknowledge valuable curriculum guidance and ramp construction received from Dr. Paul Cuicchi.

We also would like to acknowledge funding and support from CAVS and the Department of Energy.

APPENDIX A: ACRONYMS AND ABBREVIATIONS

^{o}C	degrees centigrade
°F	degrees Fahrenheit
µm	micrometer (micron)
2D	two-dimensional
2DTBC	two-dimensionally triaxially-braided composite
3D	three-dimensional
3DAP	three-dimensional atom probe
3-DEP	Three Dimensional Engineered Preform
A/SP	Auto/Steel Partnership
ABS	acrylonitrile-butadiene-styrene
ACC	Automotive Composites Consortium
ACC-PD	American Chemistry Council, Plastics Division
ACCU	ACC Underbody
AEL	arbitrary Eulerian lagrangian
AFM	atomic-force microscope (microscopy)
AFR	amplified frequency ratio
AFS	American Foundry Society
AHSS	advanced high-strength steel
AISI	American Iron and Steel Institute
AJAX	Asynchronous JavaScript and XML
Al	aluminum
ALMR	arbitrary local mesh replacement
AMD	Automotive Metals Division (of USAMP)
ANL	Argonne National Laboratory
ANOVA	analysis of variance
ANSI	American National Standard Institute
AP	acidification potential
APC	American Plastics Council
API	application program interface
APS	Advanced Photon Source
ARA	Automotive Recycling Association
ARC	(International) Automobile Recycling Congress
ARD	anisotropic rotary diffusion
ARL	Army Research Laboratory
ASTM	American Society for Testing and Materials
ATR-FTIR	attenuated total reflectance Fourier transform infrared (spectroscopy)
AWS	American Welding Society
bcc	body-centered cubic
BCJ	Bammann-Chiesa-Johnson
BDE	brominated diphenyl ethers
BE	blended element
BET	Brunauer-Emmett-Teller
BH	bake hardenable

BIW	body-in-white
BL	black liquor
BLRT	bondline read-through
BOF	body-on-frame
BPEL	Business Process Execution Language
BSEF	Bromine Science and Environmental Forum
CAD	computer-aided design/drafting
CAE	computer-aided engineering
CAFE	corporate average fuel economy
CANMET	The major laboratory of Minerals and Metals Section of Natural Resources Canada
CAVS	Center for Advanced Vehicular Systems
CB	cylinder block
cc	cubic centimeter
CC	continuous-cast(ing)
CCT	continuous cooling transformation
CD	compact disc
CDF	cumulative distribution function
CDC	channel die compression
CF	carbon fiber
CFM	continuous-filament mats
CG	conjugate gradient
CLTE	coefficient of linear thermal expansion
cm	centimeter
CNC	computerized numerical control
CNF	carbon nanofibers
CO_2	carbon dioxide
COE	coefficient of expansion
COM	Conference of Metallurgists
COV	coefficient of variation
CP	commercial purity, complex phase
CPMT	Center for Powder Metallurgy
CPU	central processing unit
CRADA	cooperative research and development agreement
CSM	Composite Spray Molding, Colorado School of Mines
CT	computed tomography, cross-tension
CTE	coefficient of thermal expansion
CVDM	Center for Virtual Design and Manufacturing
CWL	cell-wall loading
CWT	Changing World Technologies
DACE	design and analysis of computer experiments
DAIS	direct-access interface system
DAS	data-acquisition system
DAW	drawn-arc welding
DBMS	Database Management System
DC	direct chill, direct current, die-cast

DFL	dry-film lubricant
DFT	density functional theory
DIC	digital imaging correlation
DLFT	direct long-fiber thermoplastic
DMA	dynamic mechanical analysis, analyzer
DOE	Department of Energy
DoE	design of experiment
DoF	degree(s) of freedom
DP	dual phase
DQ	drawing quality
DQSK	drawing-quality special-killed
DR	dimension reduction
DRIFT®	Direct Reinforced(ment) Fabrication Technology
DS	driver seat
DSC	differential scanning calorimeter, calorimetry
DTA	differential thermal (thermogravimetric) analysis, analyzer
DTUL	deflection temperature under load
E	Young's modulus (of elasticity)
EAM	embedded-atom method
EB	electron beam
EBSD	electron backscatter diffraction
ECD	electron capture detector
EDS	energy dispersive spectra
EDX	energy-dispersive x-ray
EG	electro-galvanized
EGLD	extended generalized lambda distribution
EH&S	environmental, health and safety
EIFS	equivalent initial flaw size
ELV	end-of-life vehicle(s)
EMF	electromagnetic forming
EMT	Eshelby-Mori-Tanaka
EMTA	Eshelby-Mori-Tanaka approach
EP	eutrophication potential
EPA	Environmental Protection Agency
EPFL	Ecole Polytechnic Federal de Lausanne, Swiss Federal Institute of Technology
EPFM	elastic-plastic fracture mechanics
EPR	endpoint reference
ERW	electric resistance welding
ESB	enterprise service bus
EVO	engineering virtual organization
FAME	Flexible Advanced Metamodeling Estimator
fcc	face-centered cubic
FCVT	FreedomCAR Vehicle Technologies
FE	finite element
FEA	finite-element analysis

FEC	front-engine cover
FEFRAC	finite-element fracture
FEG-SEM	field-emission gun scanning electron microscope (microscopy)
FEM	finite-element modeling
FESEM	field-emission scanning electron microscope (microscopy)
FFNN	feed-forward neural network
FFI	full-frontal impact
FGPC	Future Generation Passenger Compartment
FHWA	Federal Highway Administration
FLCA	front-left control arm
FLD	fiber length distribution
FLD	forming-limit diagram
FMEAM	force-matching embedded-atom method
FMVSS	Federal Motor Vehicle Safety Standard
FOD	fiber-orientation distribution
FOTS	first-order Taylor series
FP	Focal Project
FRP	fiber-reinforced plastic
FSP	fiber saturation point
FSW	friction-stir welded, -ing
FSSW	friction-stir spot welding
FTC	Federal Trade Commission
FTIR	Fourier transform infrared
FVF	fiber volume fraction
FWHM	full-width at half maximum
FY	fiscal year
g	gram
GaBi	Ganzheitliche Bilanzerung software
GBD	generalized beta distribution
GC	gas chromatography
GC-ECD	gas chromatography – electron-capture detector
GC-MS	gas chromatograph(y)-mass spectrometer(ry)
GE	General Electric
GGA	generalized gradient approximation
GLD	generalized lambda distribution
GM	General Motors Corporation
GMAS	Group Membership Authorization Service
GMAW	gas metal arc welding
GMSE	generalized mean square error
GND	geometrically necessary dislocation
GP	Guinier-Preston, Gaussian process
GPEC	Global Plastics Environmental Conference
GRAM	grid resource allocation management
gridFTP	grid file transfer protocol
GT4	Global Toolkit 4
GUI	graphical user interface
GWP	global-warning potential

h	hour
H	hydrogen
HAZ	heat-affected zone
HBA	hydroxybenzoic acid
HCF	high-cycle fatigue
hcp	hexagonal close-packed
HDG	heavy duty galvanized, hot-dip galvannealed (galvanized)
HDH	hydride-dehydride
HDPE	high-density polyethylene
HDPE	high-density polyethylene
HEXRD	high-energy x-ray diffraction
HFVFSI	High Fiber Volume Fraction Sequential Inclusion
HI-MAC	high-integrity magnesium automotive castings
HiMECC	Hierarchical, Micro Experimental and Computational Characterization
HIPing	hot isostatic pressing
HIPS	high-impact polystyrene
HMPP	high-modulus polypropylene
HNA	hydroxynaphthoic acid.
HPDC	high-pressure die casting
HPLC	high-performance liquid chromatography
HSB	hot-stamped boron
HSBS	hot-stamped boron steel(s)
HSLA	high-strength low-alloy
HSS	high-strength steel
HTML	High-Temperature Materials Laboratory
HTTP	hypertext transfer protocol
IA	indentation area
IABC	International Automotive Body Congress
IAFR	integrated amplified-frequency ratio
ICME	Integrated Computational Materials Engineering
ICP/MS	induction-coupled plasma/mass spectroscopy
ID	indentation depth, inner diameter
IDDRG	International Deep Drawing Research Group
IF	interstitial-free
IIHS	Insurance Institute for Highway Safety
IISI	International Iron & Steel Institute
IMR	Institute for Metal Research
in.	inch
I/O	input/output
IP	intellectual property
IR	infrared
ISRI	Institute of Scrap Recycling Industries
ISV	internal state variable
IT	information technologies
ITP	International Titanium Powder

J2EE	Java 2 Platform, Enterprise Edition
JBI	Java Business Integration
JCI	Johnson Controls, Inc
JD	Job Descriptor
JMS	Java Message Service, Job Metadata Service, job monitoring service
jpm	jobs per minute
JSDL	Job Submission Description Language
JSS	job status service, Job Submission Service
KBFB	kenaf-bast-fiber bundles
KR	Kriging
Ksi	thousand pounds per square inch
lb	pound
LBNL	Lawrence Berkeley National Laboratory
LC	long crack
LCF	low-cycle fatigue
LDA	local-density approximation
LDH	limited-dome-height
LDPE	low-density polyethylene
LEAP	local-electrode atom probe
LFI	long fiber injection
LFI-PUR	Long Fiber Injection - Polyurethane
LFT	long-fiber thermoplastics
LHS	Latin Hypercube Sampling
LM	lightweighting materials
LRDV	large rear-drive vehicle
LS	lap-shear
LSTC	Livermore Software Technology Corporation
LSEM	large-strain extrusion machining
LTC	large thin casting
LU	laser ultrasonics
LW	laser-welded
LWFS	Lightweight Front Structure
MAG	microwave-assisted gasification
MAP	microwave-assisted plasma
MBC	main bearing cap
MC	moisture content
MC	Monte Carlo
MCS	Monte-Carlo simulations
MD	molecular dynamics
MDS	Multi-scale Design System
MEAM	modified embedded-atom method
MENA	Magnesium Elektron of North America
MFE	Magnesium Front End
MFEDD	Magnesium Front End Design and Development
MFERD	Magnesium Front End Research and Development

MFG	Molded Fiber Glass Companies
MFR	melt flow rate
Mg	magnesium
MHz	mega Hertz
MI	melt index
MIG	metal inert gas
min	minute
M-K	Marciniak-Kuczynski
mm	millimeter
MMI	Michigan Molecular Institute
MMV	Multi-Materials Vehicle
MOE	modulus of elasticity
MOO	multi-objective optimization
MOR	modulus of rupture
MPCC	Magnesium Powertrain Cast Components
MPIF	Metal Powder Industries Federation
MPS	material and process system
MRI	Magnesium Research Institute
MS	mass spectroscopy, characterized length scale of interaction with microstructural Features, martensitic steels, Master of Science
MSC	microstructurally small crack
MSF	multistage fatigue
MSST	Mississippi State University
MS&T	Materials Science and Technology
MTL	Materials Technology Laboratory
MWV	MeadWestvaco
N/D or N.D.	not detected
NA	numerical aperture
NADCA	North American Die Casting Association
NASA	National Aeronautics and Space Administration
NC	numerical control, neighborhood compliance
NCAP	New Car Assessment Program
NCC	National Composite Center
NDE	nondestructive evaluation
NDI	nondestructive inspection
NDT	nondestructive testing
NEXAFS	near-edge x-ray absorption fine structure (spectroscopy)
NFC	natural-fiber composite
NHTSA	National Highway Transportation Safety Administration
NIST	National Institute for Standards and Technology
NIT	nanoindentation test
NIR	near infrared
NOx	nitrogen oxides
NPC	natural-fiber polymer (polyolefin) composite
NTRC	National Transportation Research Center
NUCAPT	Northwestern University Center for Atom Probe Tomography
NVH	noise, vibration and harshness

OD	outside diameter
ODB	oven-dry-base
ODB	oven-dry-basis, Offset Deformable Barrier
OEM	original equipment manufacturer
OFAT	one-factor-at-a-time
OFI	offset frontal impact
OGSA	Open Grid Services Architecture
OGSA-DAI	Open Grid Services Architecture Data Access and Integration
OM	optical microscope/microscopy
ORNL	Oak Ridge National Laboratory
OSU	Ohio State University
P4	Programmable Powdered Preform Process
PA	phased-array, prealloyed
PAH	polycyclic aromatic hydrocarbon
PAN	polyacrylonitrile
PAW	projector augmented wave
PBDEs	polybrominated diphenyl ethers
PBS	portable batch system
PC	polycarbonate
PCBN	polycrystalline cubic boron nitride
PCBs	polychlorinated biphenyls
PDF	probability distribution function
PE	polyethylene
PET	polyethylene terepthalate
PFOA	perfluorooctanoic acid
PFOS	perfluorooctanesulfonates
PIM	powder injection molding, Powder Impression Molding
PM	permanent mold; powder metal, metallurgy
P/M	powder metal, metallurgy
PNGV	Partnership for a New Generation of Vehicles
PNNL	Pacific Northwest National Laboratory
POCP	photochemical ozone creation potential
PP	polypropylene
PP/PE	polypropylene/polyethylene
PPM	parts per million
PPO	polyphenylene oxide
PR	polynomial regression
PS	polystyrene
PSC	Project Steering Committee, physically small crack
psi	pound force per square inch
PSP	processing-structure-property
PTC	Project Technical Committee, project technical coordinator
PTFE	polytetrafluoroethylene
PU	polyurethane
PVC	polyvinyl chloride
QRM	quarterly review meeting

R	stress ratio
R&D	research and development
R&R	repeatability and reproducibility
RaFC	random-fiber composite
RBDO	reliability-based design optimization
RBF	radial basis function
RD	rolling direction
RFQ	request for quote
RH	relative humidity
RMS	root mean square
RMSE	root mean square error
rpm	revolutions/rotations per minute
RS	response surface
RSA	Random Sequential Adsorption
RSC	rear-seal carrier
RSC	reduced strain closure
RSL	RAISE specification language
RSM	response service methodology
RSW	resistance spot weld(ing)
RVE	representative volume element
RWD	rear-wheel drive
SAE	Society of Automotive Engineers
SAML	Security Assertion Markup Language
SBIR	Small Business Innovative Research
Sc	simple cubic
SCC	stress-corrosion cracking
SCMD	Structural Cast Magnesium Development
SD	standard deviation
SDAS	secondary dendrite-arm spacing
SEA	specific energy absorption
Seagull®	a trademark of Herrick Scientific products, Inc.
SEL	solvent extracted lignins
SEM	scanning electron microscope/microscopy
SF_6	sulfur hexafluoride
SG	specific gravity
Sh	rolled sheet per plate
SIR	seat with integrated restraint
SLC	Sub-Liquidus Casting
SLI	starting, lighting, ignition
SMC	sheet molding compound
SO_2	sulfur dioxide
SOA	service-oriented architecture
SOAP	simple object access protocol
SOCs	substances of concern
SOP	structural oil pan, standard operating procedure
SOPO	Statement of Program Objectives
SORPAS	Simulation and Optimization of Resistance, Projection and Spot Welding Processes

SOW	statement of work
SPARC	Strategic Planning and Review Committee
SPBK	support bracket
SPE	Society of Plastics Engineers
SPD	severe plastic deformation
SPR	self-piercing rivet
SQL	structured query language
SRB	Storage Resource Broker
SRCLID	Southern Regional Center for Lightweight Innovative Design
SRIM	structural reaction injection molding
STD	standard seat (without integrated restraint, cf. "SIR" above)
STTR	Small Business Technology Transfer
SUV	sport-utility vehicle
SVDC	Super Vacuum Die Casting
SVR	support vector regression
SWE	Spot Weld Element
SWSG	Structural Weld Sub-Group
T	temperature
TA	transmission area
TAPPI	(previously "the Technical Association of the Pulp and Paper Industry, now just "TAPPI")
TC	transcrystalline region
TD	transverse to rolling direction
TE	thermoelectric
TEM	transmission electron microscope, microscopy
Tg	glass transition temperature
TGA	thermogravimetric analysis, analyzer
ThD	thermal drilling
Ti	titanium
TLCP	thermotropic liquid-crystal polymer
TMAC	Test Machine for Automotive Crashworthiness
TMP	thermo-mechanical pump, processing
TMS	The Minerals, Metals, and Materials Society
TPI	Troy Polymers, Inc.
TPO	thermoplastic olefins
TRC-NCMS	Technologies Research Corporation of the National Center for Manufacturing Sciences
TRIP	transformation-induced plasticity
TRS	transverse rupture strength
TS	tensile strength, thick swelling
TTU	through-transmission ultrasonics
TWB	tailor-welded blank
TWIP	twinning-induced plasticity
TWT	tailor-welded tube
TYE	tensile, yield and elongation

UAB	University of Alabama-Birmingham
UD	unidirectional
UDRDF	uncertainty analysis using dimension reduction and distribution fitting
UDRI	University of Dayton Research Institute
UFG	ultrafine grain
UHMW	ultra-high molecular weight
UHSS	ultra high-strength steel
ULC	ultra-large casting
UMF	uncertainty magnification factor
UPC	uncertainty percentage contribution
UPE	Unsaturated Polyester
URI	uniform resource identifier
URL	uniform resource locator
USAMP	United States Automotive Materials Partnership
USCAR	United States Council for Automotive Research
USPTO	United States Patent Office
UTS	ultimate tensile strength
UT-TT	ultrasonic testing using through-transmission
UV	ultraviolet
UVA	University of Virginia
V&V	verification and validation
VARTM	vacuum-assisted resin-transfer molding
VE	vinylester
VOMS	Virtual Organization Membership Service
VPA	volume per annum
VRP	Vehicle Recycling Partnership
VTP	Vehicle Technologies Program
VW	Volkswagen
WA	water absorption
W/L	ratio of specimen width to length
WPC	woodfiber-reinforced polymer composites
WRC	woodfiber-reinforced composites
WSDL	Web Service Definition/ Description Language
WY	Weyerhaeuser Company
X-EDS	x-ray-electron diffraction spectroscope, spectroscopy, spectrometer
XML	eXtensible Markup Language
XPS	x-ray photoelectron spectrosco(py), (-meter) (-metry)
XRD	x-ray diffraction
XRS	x-ray photoelectron spectroscopy
YAG	yttrium-aluminum-garnet
YE	year-end
YS	yield strength

This document highlights work sponsored by agencies of the U.S. Government. Neither the U.S. Government nor any agency thereof, nor any of their employees, makes any warranty, express or implied, or assumes any legal liability or responsibility for the accuracy, completeness, or usefulness of any information, apparatus, product, or process disclosed, or represents that its use would not infringe privately owned rights. Reference herein to any specific commercial product, process, or service by trade name, trademark, manufacturer, or otherwise does not necessarily constitute or imply its endorsement, recommendation, or favoring by the U.S. Government or any agency thereof. The views and opinions of authors expressed herein do not necessarily state or reflect those of the U.S. Government or any agency thereof.

PRINTED ON
RECYCLED
PAPER

A Strong Energy Portfolio for a Strong America

Energy efficiency and clean, renewable energy will mean a stronger economy, a cleaner environment, and greater energy independence for America. Working with a wide array of state, community, industry, and university partners, the U.S. Department of Energy's Office of Energy Efficiency and Renewable Energy invests in a diverse portfolio of energy technologies.

For more information contact:
EERE Information Center
1-877-EERE-INF (1-877-337-3463)
www.eere.energy.gov